



*Lasers and Electro-Optics Research and Technology Series*

Maxim Thys  
Eugene Desmet  
Editors

# LASER BEAMS

*Theory, Properties and Applications*

NOVA



**LASERS AND ELECTRO-OPTICS RESEARCH AND TECHNOLOGY**

# **LASER BEAMS: THEORY, PROPERTIES AND APPLICATIONS**

No part of this digital document may be reproduced, stored in a retrieval system or transmitted in any form or by any means. The publisher has taken reasonable care in the preparation of this digital document, but makes no expressed or implied warranty of any kind and assumes no responsibility for any errors or omissions. No liability is assumed for incidental or consequential damages in connection with or arising out of information contained herein. This digital document is sold with the clear understanding that the publisher is not engaged in rendering legal, medical or any other professional services.

## **LASERS AND ELECTRO-OPTICS RESEARCH AND TECHNOLOGY**

Additional books in this series can be found on Nova's website under the Series tab.

Additional E-books in this series can be found on Nova's website under the E-books tab.

LASERS AND ELECTRO-OPTICS RESEARCH AND TECHNOLOGY

**LASER BEAMS: THEORY, PROPERTIES  
AND APPLICATIONS**

**MAXIM THYS  
AND  
EUGENE DESMET  
EDITORS**



---

**Nova Science Publishers, Inc.**  
*New York*

Copyright © 2011 by Nova Science Publishers, Inc.

**All rights reserved.** No part of this book may be reproduced, stored in a retrieval system or transmitted in any form or by any means: electronic, electrostatic, magnetic, tape, mechanical photocopying, recording or otherwise without the written permission of the Publisher.

For permission to use material from this book please contact us:

Telephone 631-231-7269; Fax 631-231-8175

Web Site: <http://www.novapublishers.com>

#### **NOTICE TO THE READER**

The Publisher has taken reasonable care in the preparation of this book, but makes no expressed or implied warranty of any kind and assumes no responsibility for any errors or omissions. No liability is assumed for incidental or consequential damages in connection with or arising out of information contained in this book. The Publisher shall not be liable for any special, consequential, or exemplary damages resulting, in whole or in part, from the readers' use of, or reliance upon, this material.

Independent verification should be sought for any data, advice or recommendations contained in this book. In addition, no responsibility is assumed by the publisher for any injury and/or damage to persons or property arising from any methods, products, instructions, ideas or otherwise contained in this publication.

This publication is designed to provide accurate and authoritative information with regard to the subject matter covered herein. It is sold with the clear understanding that the Publisher is not engaged in rendering legal or any other professional services. If legal or any other expert assistance is required, the services of a competent person should be sought. FROM A DECLARATION OF PARTICIPANTS JOINTLY ADOPTED BY A COMMITTEE OF THE AMERICAN BAR ASSOCIATION AND A COMMITTEE OF PUBLISHERS.

Additional color graphics may be available in the e-book version of this book.

#### **LIBRARY OF CONGRESS CATALOGING-IN-PUBLICATION DATA**

Laser beams : theory, properties, and applications / editors, Maxim Thys and Eugene Desmet.

p. cm.

Includes bibliographical references and index.

ISBN 978-1-60876-266-8 (hardcover)

1. Lasers--Industrial applications. 2. Laser beams. I. Thys, Maxim. II. Desmet, Eugene.

TA1675.L335 2009

621.36'6--dc22

2009038668

# CONTENTS

<b>Preface</b>	<b>vii</b>
<b>Chapter 1</b> Computer Modeling of Nanostructuring on Materials with Tightly Focused Energy Deposition <i>D.S. Ivanov, O. Osmani and B. Rethfeld</i>	<b>1</b>
<b>Chapter 2</b> Quantum Kinetics of Multiphoton Processes: Durations of Elementary Processes, Thresholds of Channels Opening and Their Saturations <i>Mark E. Perel'man</i>	<b>95</b>
<b>Chapter 3</b> Two-Dimensional Periodic Nanoscale Patterning of Solid Surfaces by Four-Beam Standing Wave Excimer Laser Lithography <i>Yu. K. Verevkin, E. Ya. Daume, V. N. Petryakov, A. Yu. Klimov, B. S. Gribkov, D. O. Filatov, Yu. Yu. Gushchina, C. Tan, C.S. Peng, M. Pessa, Z. Wang, S. M. Olaizola and S. Tisserand</i>	<b>159</b>
<b>Chapter 4</b> ZnO Nanostructures Deposited by Laser Ablation <i>D. Valerini, A. Cretí, A. P. Caricato, M. Lomascolo, R. Rella and M. Martino</i>	<b>205</b>
<b>Chapter 5</b> Diode Laser Forming of Steel Parts <i>A. Guglielmotti, F. Quadrini, E. A. Squeo and V. Tagliaferri</i>	<b>245</b>
<b>Chapter 6</b> Lasers and Lamps with Excitation by Background-Electron Multiplication Wave <i>A. M. Boichenko</i>	<b>283</b>
<b>Chapter 7</b> Phase Transitions as Possible Sources of High Power Radiation <i>Mark E. Perel'man</i>	<b>313</b>

<b>Chapter 8</b>	Application of Pulsed Laser Deposition for Putting Multi-Layer Coatings on the Inner Surfaces of Hollow Objects <i>Alexandr Alexandrovich Lozovan, Stanislav Vladimirovich Frangulov and Denis Vladimirovich Chulkov</i>	<b>331</b>
<b>Chapter 9</b>	Underground Cavity 3D Detection Using Laser System <i>Liu Xiling, Li Xibing, Anthony Comber and Liu Kewei</i>	<b>351</b>
<b>Chapter 10</b>	Laser Cladding: An Overview <i>L. Santo and J. Paulo Davim</i>	<b>367</b>
<b>Chapter 11</b>	Laser Prototyping of Polymer-Based Nanoplasmonic Components <i>Andrey L. Stepanov, Roman Kiyan, Carsten Reinhardt and Boris N. Chichkov</i>	<b>383</b>
<b>Chapter 12</b>	Structured Beams in Laser Refractography Applications <i>I.L. Raskovskaya, B.S. Rinkevichyus, and A.V. Tolkachev</i>	<b>399</b>
<b>Chapter 13</b>	Optical Breakdown in Gases Induced by High-Power IR CO <sub>2</sub> Laser Pulses <i>J. J. Camacho, L. Diaz, M. Santos, L. J. Juan and J. M. L. Poyato</i>	<b>415</b>
<b>Chapter 14</b>	Machining Steel XC42 by High-Power Continuous CO <sub>2</sub> Laser (Physical Process Description, Energetic and Thermal Modeling) <i>Neila Jebbari, Mohamed Mondher Jebbari, Annie Tarrats-Saugnac and Jean Paul Longuemard</i>	<b>501</b>
<b>Index</b>		<b>517</b>

## PREFACE

This book considers some general laser-induced processes that are involved in laser-matter interactions. A brief review is presented about a very interesting application of laser beams in the fields of materials science: the growth of zinc oxide ( $ZnO$ ) nanostructured films by Pulsed Laser Deposition (PLD). In addition, safe and precise cavity detection, especially of dangerous or inaccessible voids, is essential to safe production in a working mine. The advantages and disadvantages of laser detection systems are analyzed, and a combination of laser scanning techniques and conventional survey methodology is proposed. Other chapters in this book present an overview on laser cladding, a discussion of the applications of structured laser beams in laser refractography technology, a review of some fundamentals of laser-induced breakdown spectroscopy (LIBS) and an analysis of laser forming of steel parts by means of diode lasers.

Chapter 1 - It has been several decades since the first laser was assembled by T. Maiman and his research on generation of coherent radiation by the photoexcited ruby was published in 1960 [1]. Several other works, however, prior to his study were also aimed on creation of Light Amplifier by Stimulated Emission of Radiation (LASER). Thus, one can find the description of laser on ammonia capable of amplifying the microwaves, and therefore called MASER, with induced radiation in works by N.G. Basov and A.M. Prohorov in 1958 [2,3] and in works by C.H. Townes and A.L. Schawlow [4]. And even earlier, the possibility of the existence of induced atomic radiation itself was yet foreseen in 1916 by A. Einstein in his work on the theory of interaction of the electromagnetic radiation with matter [5]. The discovery of laser irradiation in 1960 therefore was a logical conclusion of many years theoretical and experimental research and became one of the most meaningful breakthrough in science and technology in XX century.

Chapter 2 - Kinetics of interaction of powerful light (laser) flux with substance is examined within the frame of microscopic theory of multiphoton processes. It is usually supposed that with growth of radiation intensity its quantum characteristics "become averaged" and consequently their consideration within the scope of quasi-classical theory become allowable and sufficient, that leads to nonlinear theories with corresponding approximations and complications. However, the existence of thresholds of opening of new reaction channels, their saturation and so on requires quantum examination in the scope of linear theory, of quantum electrodynamics, which is less sophisticated in some aspects.

The quantum kinetics of photon flux interaction with substance demands definition of durations of elementary scattering acts and durations of formation of physical states as a

result of such interaction, thus it requires the appeal to quantum electrodynamics and scattering theory. Therefore the general positions of the theory of durations (theory of temporal functions) are briefly considered and the general theory of multiphoton processes on this base is constructed. Then processes of higher harmonics generation and transformations of spectra, multiphoton ionization, multiphoton acceleration of charged particles, pressure of light on absorbing and transparent objects (they are needed for planning of thermonuclear reactions), some features of light reflection are considered. All this visually shows the significance and, simultaneously, the simplicity of used microscopic quantum approach, its perspectives.

The base of offered approach consists in the temporal consideration of interactions and applications of temporal functions, which are rarely yet used. Therefore in the Appendix is shown that these functions allow simple approach and proving of many kinetic relations and characteristics in several branches of physics including general determination of condensed states and some features of phase transitions. This part has, presumably, a methodological character, but opens a new vision or alternative approach to several known kinetics phenomena.

Chapter 3 - The article is devoted to a promising technology for fabrication of two-dimensional nanoperiodic structures on solid surfaces by four-beam standing wave pulsed laser modification. In this method, a large number of spots (up to  $10^7$ ) less than 100 nm in size heated up to several thousand degrees are formed on the modified surface as a result of the interference of the four laser beams incident on the object coherently. Besides a direct laser ablation, various nonlinear mechanisms of surface modification may take place in the standing wave maxima. This way, a nearly perfect two-dimensional pattern can be formed on the modified surface; the pitches of the pattern in both directions can be adjusted easily within the range from a few microns to tens of nanometers by simply varying the beams' incidence angles. This method being developed extensively at present is very promising for application in microelectronics, data storage, integrated optics (including fabrication of the Bragg mirrors, antireflection coating, two-dimensional photonic crystals, etc.) and is considered to be a promising alternative to X-ray lithography in a wide range of applications. The most important advantage of the method is that the nanoperiodic pattern can be formed in a single step (actually, at single laser pulse) by direct laser ablation of the material. However, the method could be applied as well to patterning a resist deposited onto the processed substrate to serve as a lithographic mask. In this article, the authors present some experimental results on patterning various materials, such as metal films on semiconductor and glass substrates, polyimide, and even such a hard material as diamond by direct laser ablation using a XeCl excimer laser. Patterning a resist film, the phase masks on fused silica and the antireflection structures on Si and silica glass have been fabricated. Also, using the effect of stimulation of self-assembling of the semiconductor nanostructures by standing wave laser irradiation discovered by the authors, the authors have fabricated the ordered arrays of nanoislands on the surface of single crystal Si and GaAs and of GaAs/In<sub>x</sub>Ga<sub>1-x</sub>As/GaAs(001) heterostructures with the diameter ranging from 5 to 60 nm.

Chapter 4 - This chapter aims to present a brief review about a very interesting application of laser beams in the field of materials science: the growth of zinc oxide (ZnO) nanostructured films by Pulsed Laser Deposition (PLD), and in particular by means of excimer laser ablation. After an introduction giving an overview on properties and applications of ZnO and its nanostructures and on some growth techniques used to obtain

these materials, this survey will present several results, obtained by different research groups in the world, about nanostructured ZnO grown by excimer laser ablation. Then this study will be focused on the results obtained by the author's research group in this field so far. By properly changing some deposition parameters (substrate temperature, oxygen pressure and ablation laser wavelength) the authors obtained nanostructured films with hexagonal pyramids, columns, hexagonal hierarchical structures and pencils, as well as smooth or rough films. In particular the different ablation laser wavelengths (248 nm of KrF and 193 nm of ArF) are shown to have a deep influence on both morphology and crystal quality of the grown samples. Scanning electron microscopy (SEM), x-ray diffraction (XRD) and photoluminescence (PL) measurements were used to inspect the film properties. Finally, some results about the author's optical gas sensing tests conducted on the grown samples are presented.

Chapter 5 - Laser forming of steel parts by means of diode lasers is discussed from different points of view. The physical mechanisms at the basis of the laser forming processes are depicted, and a description of the state of the art is reported. Many laboratory experiences are presented in the case of diode laser forming of stainless steel sheet metals and tubes. Also slotted tubes were processed to form flares and tongues. Numerical modeling was carried out by means of analytical and finite element models and experimental data were in good agreement with numerical ones. The analytical approach lead to the evaluation of the laser forming efficiency, instead finite element models were used to predict the final shape of the steel parts as a function of the process parameters. In fact, finite element models allow the researchers to thoroughly study the part behavior during forming in the case of sheets, tubes or slotted tubes. In the end, an attempt was made to describe how material analysis helps in the laser forming investigation; residual stresses are mainly discussed as they strongly affect the formed part performances.

Chapter 6 - It was shown earlier that the ionisation propagation in a gas at about the atmospheric pressure may proceed due to the multiplication of the existing electrons with a low background density rather than the transfer of electrons or photons. It is considered the feasibility of using the plasma produced in the afterglow of this background-electron multiplication wave for pumping plasma lasers (in particular, Penning neon laser and  $\text{Xe}_2^*$  excimer lasers) as well as excilamps.

The Penning neon laser was studied in a Ne-H<sub>2</sub> mixture excited by a transverse discharge. Theoretical modeling allowed the conclusion that the laser active medium was excited due to the BEMW passed through the discharge gap. Numerous attempts to pump  $\text{Xe}_2^*$  lasers by a gas discharge instead of a beam have not been successful. Simulations show that it is possible to achieve the laser effect at  $\lambda = 172$  nm as well as to substantially improve the peak specific power of the spontaneous radiation of xenon lamps.

Chapter 7 - Removal of the latent heat at vapor condensation and/or crystallization (with temperature  $T \ll T_c$ ) occurs, as is shown by theoretical calculations and the resulted experimental data, on characteristic frequencies and their higher harmonics'. Intensity of this radiation can be very high and can explain, in particular, the bright flashes at the phenomenon of sonoluminescence. Under the general laws of the quantum theory these processes can be stimulated by resonant frequencies, therefore it is possible to carry out the laser on such "condensation" radiation. Potential capacity and, in principle, simplicity of such devices should attract to them attention of researchers.

Spectral features of atmospheric clouds correspond to characteristic frequencies of water vapor condensation and of CO<sub>2</sub>, CH<sub>4</sub> condensation, etc. Radiative stimulation of their phase transitions can lead to control of atmospheric processes and of heat fluxes from the Earth, to regularization of its thermal regime.

Chapter 8 - Presented here are the analysis results of the ability of Pulsed Laser Deposition methods for putting a multi-layer multi-component coating with single-layer thickness in the nano-scale range as well as micro- and nano-composite coatings on the inner surfaces of hollow objects. Also reviewed are mass-transporting processes, occurring during the application of double-component coatings by Pulsed Laser Deposition methods on the inner surface of long tubes of small diameter (L/d>50 L≈900mm, d≈13mm). With XPS and RBS methods, the structure and composition of double-component multi-layer coatings with single-layer thickness ≈30 nm, obtained on special installation equipped with YAG:Nd+ Laser LTI-207, is investigated. A device to provide target changing during the deposition process without vacuum braking is developed. The authors determined conditions of obtaining multi-layer coatings with single-layer thickness in nano-scale range and methods of preliminary inner surfaces cleaning of said objects by means of hollow cathode glowing discharge with partial plasma filling of cathode cavity. The authors considered different schemes of cleaning inner surfaces of tube-like objects. Possible applications of the presented method for treating of said objects in individual or serial production, instrument decisions providing realization of the presented process and its perspective are discussed.

Chapter 9 - Safe and precise cavity detection, especially of dangerous or inaccessible voids, is essential to safe production in a working mine. Conventional underground cavity detection methods are briefly reviewed and their limitations discussed. Accurate 3D laser measurement systems are introduced. One of these laser systems was used to detect inaccessible underground cavities from the surface through boreholes at Luanchuan molybdenum open pit in China. The results from the scanner demonstrated very well the detailed level of information that can be collected in a cavity using this method, with the cavities' layout under various benches being fully mapped. The processed data can be imported into existing models in SURPAC and CAD and the roof and floor elevations from the model of the cavity was used to output sections which would be required at a later design stage. A minimum number of exploration boreholes can be coordinated based on the scanned data which therefore not only fully details the extent of the cavity, but also saves on the costs of exploration drilling. Finally, the advantages and disadvantages of laser detection systems are analysed, and a combination of laser scanning techniques and conventional survey methodology is proposed to detect these unknown underground cavities.

Chapter 10 - This chapter presents a basic overview on laser cladding. Among laser technologies, laser cladding has received great attention in recent years, mainly due to the reduced costs of laser sources, the increasing potential for material processing, the development of new coating materials, the emergence of rapid prototyping and other manufacturing applications.

In this chapter the process and different systems for laser cladding have been described, some case studies have been discussed, some predictive models have been proposed, and new perspectives have been discussed. Some aspects and advantages of laser cladding process have been highlighted.

Chapter 11 - Growing interest in the field of surface plasmon polaritons comes from a rapid advance of nanostructuring technologies. The application of two-photon polymerization by pulse laser technique for the fabrication of dielectric and metallic SPP-structures, which can be used for localization, guiding, and manipulation of plasmonic waves on a subwavelength scale, are studied. This fast technology is based on nonlinear absorption of near-infrared femtosecond laser pulses. Excitation, propagation, and interaction of SPP waves with nanostructures are controlled and studied by leakage radiation imaging. It is demonstrated that created nanostructures are very efficient for the excitation and focusing of plasmonic waves on the metal film. Examples of passive and active plasmonic components are presented and discussed.

Chapter 12 - In this chapter, the applications of structured laser beams in laser refractography technology are considered. The basic principles of laser refractography, a new method for diagnostics of optically inhomogeneous media and flows are described. This technology is based on the refraction of the structured laser beams in transparent inhomogeneity, digital registration and computer processing of the refraction pattern. The experimental setup allowed quantitative visualization of the transparent media by using 2D- or 3D-refractograms. The 3D-refractograms are used for visualization of the boundary layer near the hot or cold ball in water that are present. The problem of laser sheet (plane structured laser beam) also cylindrical beam propagation in media with radial variation of the temperature and refractive index is solved and the trajectories of geometrical rays are calculated. The comparison of the parameters for experimental and corresponding calculated refractograms allows recognizing the temperature fields in the boundary layer, i.e., gives quantitative information. The method is modified for studying edge effects and micro layers in liquids and gases. Due to nearly inertialess measurements, laser refractography can be used for diagnostics of fast and transient processes.

Chapter 13 - This chapter reviews some fundamentals of laser-induced breakdown spectroscopy (LIBS) and describes some experimental studies developed in the author's laboratory on gases such as nitrogen, oxygen and air. LIBS of these gases at different pressures, in the spectral range ultraviolet-visible-near infrared (UV-Vis-NIR), was excited by using a high-power transverse excitation atmospheric (TEA) CO<sub>2</sub> laser ( $\lambda=9.621$  and  $10.591\text{ }\mu\text{m}$ ;  $\tau\text{FWHM}=64\text{ ns}$ ; and different laser power densities). The spectra of the generated plasmas are dominated by emission of strong atomic, ionic species and molecular bands. Excitation temperatures were estimated by means of atomic and ionic lines. Electron number densities were deduced from the Stark broadening of several ionic lines. The characteristics of the spectral emission intensities from different species have been investigated as functions of the gas pressure and laser irradiance. Optical breakdown threshold intensities in different gases have been measured experimentally. The physical processes leading to laser-induced breakdown of the gases have been analyzed. Plasma characteristics in LIBS of air were examined in detail on the emission lines of N<sup>+</sup>, O<sup>+</sup> and C by means of time-resolved optical-emission spectroscopy (OES) technique. The results show a faster decay of continuum and ionic spectral species than of neutral atomic and molecular ones. The velocity and kinetic energy distributions for different species were obtained from time-of-flight (TOF) OES measurements. Excitation temperature and electron density in the laser-induced plasma were estimated from the analysis of spectral data at various times from the laser pulse incidence. Temporal evolution of electron density has been used for the estimation of the three-body recombination rate constant.

Chapter 14 - Manufacturers who use laser cutting are interested in the optimization of productivity and the subsequent quality of components made by the laser cutting process. Both aspects are governed by the selection of appropriate laser process parameters. These parameters include laser power, assist gas and cutting speed. The last parameter must be able to provide a good quality of machined components. The inert gas is used to minimize the number of laser process parameters. So, only the absorbed energy by steel  $E_a$  contributes in the machining processes.  $E_a$  depends on power laser, interaction time and absorbed coefficient.

Good quality of components made by the laser cutting process is deduced from groove specific characteristic parameters like the width ( $L_s$ ), the groove depth ( $P_r$ ) and the width of the Thermal Affected Zone ( $Z_{TAZ}$ ).

The condition that must be used to write the energy balance is to fix the adequate assumption. The energy balance will give the theoretical values of the characteristic machining parameters and will permit the evaluation of lost energy if the energy quantity able to create the TAZ is calculated from the resolution of the heat propagation equation.

## ***Chapter 1***

# **COMPUTER MODELING OF NANOSTRUCTURING ON MATERIALS WITH TIGHTLY FOCUSED ENERGY DEPOSITION**

***D.S. Ivanov, O. Osmani and B. Rethfeld***

Technical University of Kaiserslautern, Germany.

## **1. INTRODUCTION TO THE THEORY OF NANOSTRUCTURING WITH LASER BEAMS**

### **(a) Laser in Nanostructuring**

It has been several decades since the first laser was assembled by T. Maiman and his research on generation of coherent radiation by the photoexcited ruby was published in 1960 [1]. Several other works, however, prior to his study were also aimed on creation of Light Amplifier by Stimulated Emission of Radiation (LASER). Thus, one can find the description of laser on ammonia capable of amplifying the microwaves, and therefore called MASER, with induced radiation in works by N.G. Basov and A.M. Prohorov in 1958 [2,3] and in works by C.H. Townes and A.L. Schawlow [4]. And even earlier, the possibility of the existence of induced atomic radiation itself was yet foreseen in 1916 by A. Einstein in his work on the theory of interaction of the electromagnetic radiation with matter [5]. The discovery of laser irradiation in 1960 therefore was a logical conclusion of many years theoretical and experimental research and became one of the most meaningful breakthrough in science and technology in XX century.

Since then, the laser technologies have grown to incredible opportunities and applications. Lasers have occupied a significant field in physics and penetrated nearly all scientific areas. Because of their unique properties, laser beams can efficiently serve in medicine as a surgical instrument to perform the tiniest operations [6] and with the same success in industry as a powerful cutter capable of ripping iron sheets of several centimetres thick [7]. Whereas lasers themselves can be effectively used as both diagnostic and research tools their development is still in progress. The requirements to the laser beams as well as the

accuracy in controlling the chosen parameters are varying in a wide range of pulse durations and energies depending on their applications. To nowadays in physics and biophysics the pulse duration has shrunk to attoseconds and energies around 1kJ become possible to be reached in a single pulse. At such high power, of  $10^{12}$  Watt and more, realized upon the absorption of the laser pulse, the matter can undergo a transition to solid dense plasma state that results at least in change of the surface morphology and usually in partial removal of the material (ablation). Especially, the ability of laser beams to serve for a high density energy deposition into a limited area (sub micron scale) and on a very short time scale (less than 10 ps) has been widely exploited in nanostructuring experiments – the process of generation of nanosize features on material surfaces [8].

There is a strong demand for new technologies which can produce 2 and 3-dimensional nanostructures on a wide range of materials [9,10,11,12]. The most common technology of this type is optical lithography. Since the development of this technology, there has been a gradual reduction in the size of the features produced using optical lithographic techniques [13]. This has been achieved mainly by using shorter wavelength of light and it has been predicted that the technology would still be applicable even for feature sizes below 100 nm [14]. The disadvantages are that optical lithography can only be applied to a small range of materials which must have flat surfaces, hence there is a need for the development of new, more broadly applicable nanostructuring technologies based on laser beam technique.

Whereas lasers are well established tools for materials processing. However, the conventional lasers are limited when the highest precision is required due to undesirable effects such as thermal energy dissipation and the formation of heat and shock affected zones. With the introduction of ultrafast lasers (pico-, femto-, and atto-second), it was shown that higher precision features could be produced, thus opening up new applications and possibilities which could not be realized with ordinary laser systems [15,16,17,18].

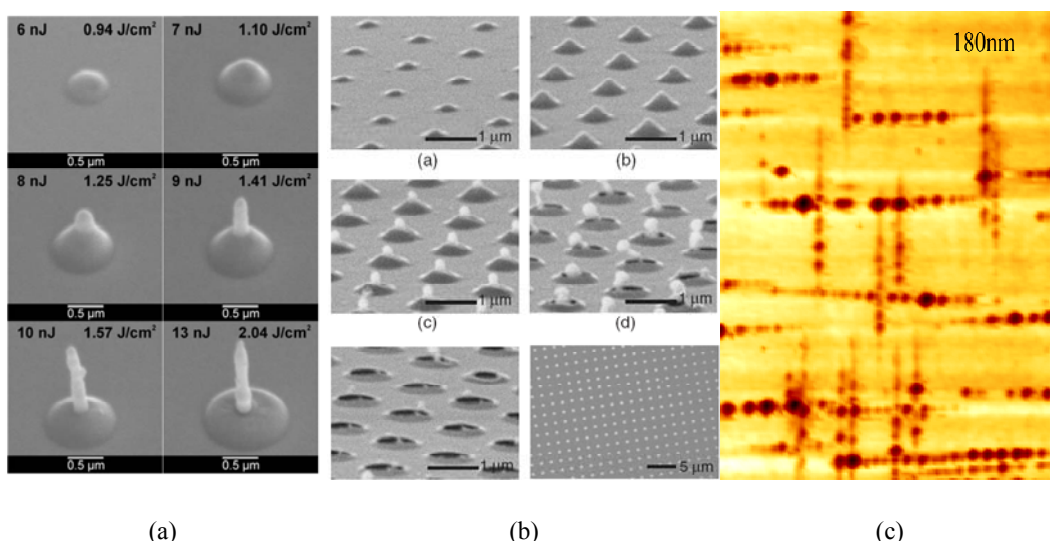


Figure 1. SEM images of an array of micro-shells and nano-jets fabricated in the experiments: (a) by B. Chichkov [9] and (b) by Y. Nakata [11] on thin gold film with femtosecond laser pulses. (c) Formation of nanohillocks on  $\text{SrTiO}_3$  in swift heavy  $\text{Xe}^+$  ions bombardment experiments [19].

Recently, ultrafast laser materials processing has become more attractive due to the rapid development of femtosecond laser systems. At the extreme conditions of matter, however, realized with femtosecond pulsed laser beam focused on a material surface, the physics behind the interaction of laser irradiation with matter is no longer of the classical view as well as the processes of nanostructures formation and the properties of obtained features. In general, high power, short-pulsed, laser-matter interactions are complex, involving mechanical, thermal, and phase perturbations. A number of the non-equilibrium processes induced by a short-pulsed laser beam are impossible to study experimentally and difficult to model at all levels: ab-initio, atomistic, and continuum. In this chapter we address this challenge using new computational techniques that combine advantages of different theoretical approaches. Particularly, we will focus our research on the application of laser beams for the purpose of restructuring materials. We will consider in details which processes are responsible for a change of the surface morphology as result of the laser beam interaction with solid and which physical mechanisms act towards the nanostructuring.

The structure of this chapter can be therefore outlined in the following way. In the beginning we will consider in general laser-induced processes that are involved into laser-matter interaction and thus can be responsible for the change of the surface morphology, Section 1 b) and c). Then, some background on the modelling of laser-matter interaction will be given, including several computational approaches with discussion of their advantages and disadvantages in the scope of description of the nanostructuring processes, Section 2 a)-e). In Section 3 of this chapter, we will present several combined atomistic-continuum theoretical models to study laser-induced changes of the surface morphology. We will demonstrate the applicability of the combined models to study these on different materials as a result of tightly focused energy deposition that can be obtained by any means, either by laser irradiation, Figure 1 a-b), Section 3 b) and c), or by swift heavy ion bombardment of the solid, Figure 1c, Section 3 f). The latter will be considered in a close connection with laser beam nanostructuring experiments since the resulting nanostructures are governed by similar physical mechanisms and can be therefore described within the frames of our combined computational approaches.

## **(b) Processes, Involved into Laser Matter Interaction**

Since it is the electronic system in matter that absorbs the laser pulse energy we shall start our study with a very basic presentation of the electron theory in a solid. In fact, the appropriate description of the dynamics of the excited electronic system occurs to be the most crucial in determining the further evolution of matter upon the laser beam absorption. In this section we describe the process of excitation and relaxation of the conduction band electrons in metals. Later, similar processes in semiconductors and dielectrics will be addressed by analogy in description of nanostructuring of the related materials, Section 3 e) and f).

The classical theory of metallic conductivity was first presented by Drude [20] in 1900. According to his theory, the outer shell electrons (conduction electrons) of atoms that form a metallic solid are able to move freely through the volume of the specimen forming an “electron gas”, governed by Fermi-Dirac statistics. These outer shell electrons are responsible for the conduction of electricity in metals, and are termed “conduction band electrons”, to distinguish from the electrons of the filled shells of the ions, termed “valence

band electrons". The interaction of conduction band electrons with the ion cores of the original atoms is neglected in the free electron approximation, and all calculations are performed under assumption that the conduction electrons are entirely free in space bounded by the surfaces of the specimen. The lattice enters as a periodic background for free moving electrons, responsible therefore for the detailed band structure. There is no direct energy exchange between free conduction band electrons and the atoms constituting the lattice. However, there is an interaction of electrons with quantized modes of vibrations occurring in a lattice that are called phonons [21]. Phonons are wave-like quasiparticles that are governed by Bose-Einstein statistics and their interaction with electrons can be described in terms of the electron-phonon collisions [21]. This interaction becomes especially important in the case of electron-phonon nonequilibrium [22]. Thus, from the point of computational physics we can treat the system of electrons and phonons as two weakly bounded subsystems in the solid.

For long pulse laser irradiation (ns and longer) the excitation rate is comparatively low and both electron-electron and electron-phonon equilibration takes place during the laser pulse. Therefore, both Fermi-Dirac distribution of the electrons and thermal equilibrium between the electrons and the lattice can be safely assumed at any time during and after the laser pulse. For subpicosecond laser pulses, however, one can distinguish three time intervals of material response to a laser irradiation, as schematically shown in Figure 2 [22] where the electron density distribution function is shown at different excitation stages. Immediately upon the laser pulse absorption, there are two processes take place in the electronic system. One process is the ballistic energy transport by highly excited non-equilibrium electrons, and the other one is the establishment of the Fermi-Dirac distribution due to electron-electron collisions (electron thermalization). The characteristic length of the ballistic energy transport can vary for different types of materials. For example it is on the order of 100 nm for noble metals (weak electron-phonon coupling like it is in Au and Cu) and on the order of the optical penetration depth, typically 10-20 nm, for transition metals (strong electron-phonon coupling like it is in Ni and Al). The establishment of the Fermi-Dirac distribution is a general process that occurs by means of collisions of the excited electrons with those around the Fermi level and usually takes few hundred of femtoseconds [23,24,25,26]. The first conditional time interval is over when Fermi-Dirac distribution is established at any depth in the irradiated target and hot electron bath is localized either within the ballistic range or within the optical penetration depth.

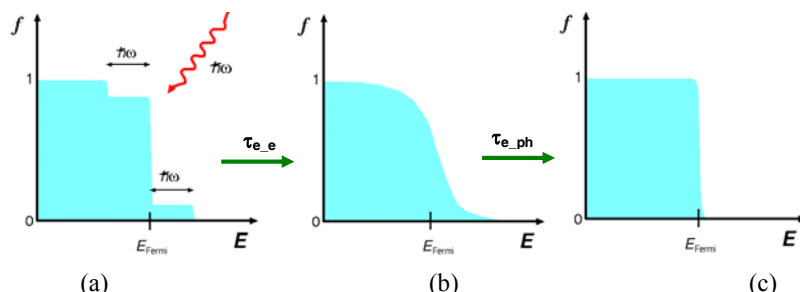


Figure 2. Three stages of the relaxation of optically excited electrons in a metal target irradiated by a femtosecond laser pulse: (a) optical excitation, (b) establishment of the Fermi-Dirac distribution (thermalization process) by means of electron-electron collision process; (c) electron cooling due to the electron heat conduction and the electron-phonon equilibration resulting in lattice heating.

At the same time, the electron-phonon thermalization proceed via electron-phonon collisions but this process takes place on a longer, picosecond time scale which in general depends on the strength of electron-phonon coupling [27,28]. The latter determines the amount of energy transferred between electrons and phonons per unit time per volume, called the electron-phonon coupling parameter, and can vary by more than an order of magnitude for different materials. The second time interval, therefore, is mainly characterized by the difference in temperatures between the hot electrons with the Fermi-Dirac distribution and cold phonons. Due to the large temperature gradient, hot electrons tend to transfer energy deeper into the target by means of the electronic thermal diffusion mechanism. Although at a much slower speed as compared with the ballistic energy transport the electron heat conduction process can nevertheless dissipate a significant amount of energy in a high temperature regime [29,30], when temperature of electrons reaches  $10^4$  K and more. Meanwhile, the electron-phonon equilibration process results in the lattice temperature grow. The diffusion length and the temperature profile of hot electrons before the establishment of the electron-phonon equilibrium is defined therefore by the interplay of the strength of the electron-phonon coupling and the electron heat conduction. Depending on the level of excitation, these two processes have a complex temperature dependence [31,32] and their appropriate theoretical description becomes especially important for the temperature evolution dynamics in the proximity of the material surface [33].

The third time interval can be conventionally defined starting from the time when thermal equilibrium is established between the electrons and phonons. Because of the large difference in heat capacities of electrons and phonons, the rise of lattice temperature is one-two orders of magnitude lower then the electron temperature drop and due to temperature dependence of the electron heat conductiotivity, the established common electron-lattice temperature gradient will result in correspondingly slower heat propagation into the deeper parts of the target.

If a sufficiently high temperature is reached in the solid, it can undergo a phase transition. As energetically favorable, the free surfaces usually serve as nucleation sites for melting with a subsequent propagation of the liquid front into the bulk of the material [34]. Furthermore, homogeneous nucleation of the liquid phase may contribute to the phase transition and regions of liquid phase can appear and grow ahead of the propagating solid/liquid interface [35].

Finally, at even higher excitation, the processes of spallation (chunky material removal) and ablation (gaseous material removal) can take place [36]. In recent study with Molecular Dynamics [37] a close connection between melting, spallation, and ablation processes were considered as a function of fluence. In the case of nanostructuring, however, which is the focus of our work, due to relatively low fluence the contribution of the ablation mechanism will be suppressed whereas the melting process will be dominant. For the same reason of low fluence, the radiation and electron emission losses, usually attributing the ablation mechanisms, will be neglected as comprising less than 0.5% of the laser deposited energy. In the next section, we will consider those processes that we must include into the theoretical description of nanostructuring on materials with tightly focused laser beams.

### (c) Laser-Induced Processes, Contributing to Nanostructuring

The mechanism of nanostructuring in general is a complex interplay of fast concurrent laser-induced processes spawning on a wide time interval, 10 fs – 10 ns, and on a large spatial scale, 10 nm – 10  $\mu\text{m}$ . Since the fluencies used in the nanostructuring processes are rather low, just above the melting threshold [9, 10, 11, 12], the processes of ablation or evaporation will be suppressed. It follows from here that the only possible way of changing the materials surface morphology is the establishment of hydrodynamic motion of the melt or the elasto-plastic deformations of the solid in the proximity of the laser spot. According to [38] upon melting the material's elastic shear modulus vanishes. Therefore, at the moment of phase transformation the crystal structure is lost and material can easily undergo a restructuring and surface modification processes. Upon the phase transition of a particular volume, a part of the solid's thermal energy goes to the latent heat of melting that in turn decreases temperature of the surrounding region. Since the velocity of melting front propagation is a strong function of overheating [39,40], such local temperature decrease along the solid-liquid interface may lead to variation of the velocity of the melting front propagation and development of the melting front instabilities due to thermal energy redistribution across the solid-liquid interface [41]. Such instabilities eventually can lead to the formation of nanofeatures on a material surface that can be studied experimentally [42,43]. The kinetics of liquid phase nucleation and growth, however, as well as the shape of the nuclei are still the subjects of current debates. At high levels of superheating realized in short pulse laser melting, when the size of a critical nucleus becomes comparable to several interatomic distances [44], the applicability of macroscopic kinetic approaches based on classical nucleation theory [45] is questionable and should be verified by a detailed microscopic analysis of the involved processes.

With any laser material processing technology the minimum achievable structure size is determined by the diffraction limit [46] of the optical system and it is generally of the order of the laser wavelength. Apparently, the characteristic length of the established temperature gradient in the solid upon the laser heating will roughly outline the material volume which can potentially undergo to restructuring, if the absorbed fluence was high enough. In this sense, for the purpose of nanostructuring the temperature gradients developed on the nanoscale are of the great preference. This presumes the laser spot size to be at least not greater than temperature gradient range. The focusing of laser beams into the spot of nanosize, however, is not a straightforward task. The diffraction limit defines the lowest possible size,  $x$ , of the laser beam spot focused on a material surface,  $x \geq 1.22\lambda F/D$  [46], where  $F$  is the focal length and  $D$  is the aperture of the optical system. Thus, if working in visible diapason with the wave length  $\lambda = 400 \text{ nm}$  the smallest laser spot that can be obtained in the material surface with a high quality optics of  $F/D = 1.5$  still on the level of 1-3  $\mu\text{m}$  that can barely provide the establishment of temperature gradient on a submicron scale.

In order to overcome the diffraction limit, several advanced techniques were recently introduced into the nanostructuring process. One of the interesting properties of ultrafast laser materials processing is that there is a very well defined melting threshold [9, 11, 22, 47]. This allows for sub-diffraction limited structuring by setting the peak applied laser fluence to be just above the threshold fluence value, like it was accomplished with the use of Gaussian laser pulse tip in the experiments by Chichkov in [9, 10, 60], Figure 1 a). In this case only the central portion of the laser beam can cause any surface modification. In theory, it should be

possible to produce ever-decreasing structure/feature sizes using this technique but in practice a limit exists due to imperfections in the laser beam profile. Alternatively, the interference of four laser beams was used in nanostructuring experiments by Nakata [11, 12], Figure 1 b). Moreover, the recent development of near-field optics [48, 49, 50, 51] broadens the opportunities of tight focusing of the laser energy deposition in nanomodifications of materials.

But probably even more important factor in laser nanostructuring experiments is the time frame within which the laser energy deposition occurs. The effect of laser pulse duration on the character of laser damage (melting, ablation, and spallation) has been considered in several experimental [16, 18, 22, 52, 53] and theoretical [33, 54, 55, 56, 57] works for the last decade. It was justified that ns laser pulses result in a relatively slow heating under electron-phonon equilibrium conditions and eventually in a significant damage of surrounding material due to the excess of thermal energy (melting). This process therefore was attributed to photo-thermal damage and opposed to the photo-mechanical effect where ps or fs laser pulses were used to generate a strong non equilibrium between electrons and phonons. It has been reported that with pico- and femtosecond laser pulses the heating rate can be extremely high, up to  $10^{15}$  K/s, before the systems of electrons and phonons come to the equilibrium. Fast, within tens of ps, heating results in development of significant stresses inside of the material. The relaxation of these laser-induced stresses leads to a local mechanical damage/modification of material with very sharp edges [15, 16, 18, 58]. Apparently, the regime of photo-mechanical influence should be therefore a working mode for the purpose of nanostructuring [9, 10, 11, 12, 16, 18]. From here, the accurate description of laser energy deposition is one of the first and important issues that we must deal with when modeling the material nanostructuring processes.

As highly mobile particles the electrons readily accept the laser energy by means of direct absorption in metals or by additional channels of excitation via one- or multiphoton absorption and impact ionisation in semiconductors and insulators [20, 21]. For short pulses (10 ps and shorter) the resulting temperature difference therefore, developed upon the electron-phonon non equilibrium, can grow as high as two orders of magnitude by the end of the pulse. The further dynamics of the electron and phonon temperatures is defined by energy dissipation via two essential channels: the electron heat conduction and electron-phonon collision mechanisms. Both are strong and complex functions of temperatures [29, 30, 31, 32, 59, 60], and depending on the pulse intensity and duration can significantly alter the resulting lattice temperature profile established by the time of the electron-phonon equilibrium and thus efficiently influence the nanostructuring process [22, 29, 33, 52].

If the excitation of conduction band electrons due to laser irradiation is too strong, the establishment of Fermi distribution can take up to hundreds of femtoseconds [59] and until the electronic system is thermalized, the applicability of Fermi statistics is no longer valid. Additionally, depending on materials the distribution function of free electrons can be influenced by those exited out of valence band (d-band electrons) that enhances nonequilibrium [31, 32]. In order to treat nonthermalized electrons and their interaction with phonons in particular, Boltzmann statistics is proposed, where distribution functions of the systems of electrons and phonons are considered as a function of time [61].

Since the structure size we want to model is on the same scale as the size of the laser spot on the material surface, all these processes: the laser light absorption, the process of thermalization of the electrons, the electron-phonon equilibration, and the electron heat

conduction must be described in 3D space. The relative methods of their description will be considered later in the Section 2 a), d), and e).

When the lattice temperature gradient is established upon the electron-phonon equilibrium, a part of material can undergo to restructuring due to melting or plastic deformations. It was emphasized in Ref. [62] that the essential mechanism of the mechanical damage to the metal film under low-fluence laser irradiation is the relaxation of the stresses, generated with a short laser pulse. The building up of the compressive stresses inside the material in turn is a result of thermal expansion of the lattice in response to laser heating. Such process is a common phenomenon for all classes of the materials: metals, semiconductors, and insulators [63]. If the heating is fast enough, and the thermal expansion of the material is slow, the formation of laser-induced stresses is followed by a propagation of a pressure wave that can cause a mechanical damage of solid or the establishment of a hydrodynamical flow in a melt. In other words, the heating time,  $\tau_h$ , must be shorter than relaxation time (the characteristic time of stress propagation),  $\tau_s$ , that in turn is defined via speed of sound in the solid  $C_s$  and geometrical size of the heated region  $L_c$ ,  $\tau_h < \tau_s = L_c/C_s$ . Such heating is said to be under conditions of stress confinement [64] that triggers the mechanism of relaxation of the laser-induced pressure as a sequence of the compressive/extensive pressure recoils and directly effects the material restructuring.

Finally, the melting and plastic deformations are two separate mechanisms that contribute to the nanostructuring differently and on different spatial scales. If the establishment of a hydrodynamical flow in the molten part of the material is limited to the central part of the formed nanofeature, the most effected by the laser beam [9, 10], the plastic deformation can extend to microns and can form a plateau on which the nanostructure is forming [9, 60]. In nanostructuring experiments, both processes occur under conditions of superheating above the melting point and strong temperature and pressure gradients, and thus proceed at nonequilibrium. The size of liquid nuclear can be as small as several interatomic distances [38, 41, 44] and the melting process itself can be as fast as several hundreds of femtosecond [35]. Therefore, the applicability of Gibbs and classical nucleation theory [45, 65, 66] for description of such melting process is not supported in nanostructuring as well as the elasto-plastic deformations must be described via a realistic stress tensor that includes complex temperature dependences [67]. In the next section, we will present the appropriate physical models that can describe the processes contributing to the nanostructuring. We will outline their advantages and limitation and present the essential impact points on laser-matter interaction obtained with those models.

## 2. MODELING OF MATERIAL PROCESSING WITH A TIGHTLY FOCUSED ENERGY DEPOSITION

### (a) Two-Temperature Model

As discussed in the previous section, upon laser light absorption by the conduction band electrons, the deposited energy quickly, within femtoseconds, is equilibrated among the electrons and, more slowly, is transferred to the atomic vibrations. The latter process is controlled by the strength of the electron-phonon coupling and can take from a fraction of a

picosecond to several tens of picoseconds. Finally, a thermal equilibrium is established between the electrons and phonons, and the heat flow from the surface region into the bulk of the irradiated target can be described as the common thermal diffusion [68]. Based on an energy balance, in 1974, S.I. Anisimov suggested that at the continuum level, the time evolution of the lattice and electron temperatures,  $T_l$  and  $T_e$ , can be described within a so-called Two Temperature model [69,70] (TTM) by two coupled nonlinear differential equations,

$$\begin{cases} C_e(T_e) \frac{\partial T_e}{\partial t} = \nabla [K_e(T_e, T_{ph}) \nabla T_e] - G(T_e, T_{ph})(T_e - T_l) + S(z, t) \\ C_l(T_l) \frac{\partial T_l}{\partial t} = \nabla [K_l(T_l, T_{ph}) \nabla T_l] + G(T_e, T_{ph})(T_e - T_l) \end{cases} \quad (1)$$

where  $C$  and  $K$  are the heat capacities and thermal conductivities of the electrons and lattice as denoted by subscripts  $e$  and  $l$ , and  $G$  is the electron-phonon coupling parameter. The source term  $S(z, t)$  is used to describe the local laser energy deposition per unit area and a unit of time. In the second equation the term responsible for the phonon heat conduction is typically negligible as compared to the electron heat conduction in metals and is often omitted.

The system of differential equations (1) can be solved by a finite difference method and the spatial and time evolution of the electron and lattice temperatures can be obtained. As an illustration of the model predictions in 1D case of heat conduction, the temperature profiles for a 50 nm Ni film irradiated by a 200 fs laser pulse are shown in Figure 3 for the front and rear surfaces of the film. We can see that equilibration between the hot electrons and the lattice takes up to 20 ps for the Ni film, and the heating rate as well as the energy distribution in the film are strongly affected by the equilibration kinetics. A simple description of melting is also included in the model by tracking the fraction of the melted material in any finite difference discretization cell where the equilibrium melting temperature is reached and taking away the latent heat of melting until the complete melting is occurred. The melting process is reflected in regions of the constant-temperature plateau in the lattice temperature profiles. The model predicts that melting of the front surface region starts at 5 ps after the laser pulse and takes 4 ps, whereas melting of the back surface region starts at 8 ps after the laser pulse and takes  $\sim$ 12 ps. As it will be shown in the next section, these predictions on the melting kinetics are very different from the predictions of a more realistic model in which overheating and the effect of pressure on the melting process are included.

Despite its relative simplicity, TTM model can be successfully used in studying the complex mechanism of interplay between channels of the laser-deposited energy dissipation in laser-matter interaction experiments [22]. Particularly, we will demonstrate below that this model predicts the possibility of experimental determination of the strength of the electron-phonon interaction via a direct access to the electron-phonon relaxation time. For this purpose we will consider the interplay between the electron-phonon coupling and the electron heat conduction mechanisms at different conditions, realized during short pulse laser interaction with free standing metal films [33].

Among of four metals chosen to test the process of energy dissipation two of them, Au and Cu, exhibit pure properties of noble type of metals and the rest, Ni and Al, belong to the group of transitional metals. Noble metals have a relatively weak strength of the electron-

phonon coupling, which results in quite high values of the electronic temperatures upon laser light absorption. Transitional metals, on the other hand, exhibit much stronger electron-phonon coupling and much lower electronic temperatures are reached during the laser-matter interaction process.

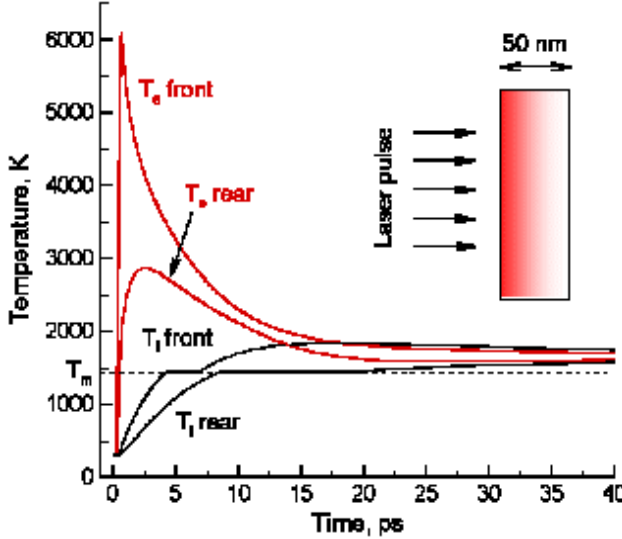


Figure 3. Time dependence of electron and lattice temperatures predicted by TTM for a 50 nm Ni film irradiated with a 200 fs laser pulse at an absorbed fluence of  $43 \text{ mJ/cm}^2$ .

Although, it was discussed that it is the strength of the electron-phonon coupling that plays a determinant role in the character of the laser induced processes [52], its quantitative definition is still a big challenge and only several predictions based on theoretical models were made till nowadays [71,72]. Obviously, that the strength of the electron-phonon coupling is unequivocally related to the electron-phonon relaxation time. The complex and transient character of the electronic and lattice temperature behaviour, however, during the short laser pulses make the experimental determination of this time difficult. Additionally, the fast electron heat conduction mechanism is a strong function of the electronic temperature  $T_e$  and can drastically alter the energy dissipation during the electron-phonon equilibration process. In several theoretical attempts to study the electron heat conduction mechanism [59, 72, 73], it was emphasized that depending on the level of electron excitation (temperature), the conductivity can be approximated either as a constant ( $T_{ph} \sim T_e$ ), or a linear function of  $T_e$  ( $T_{ph} < T_e < T_F$ ), or a function attributed with the electron-electron collision process ( $T_{ph} << T_e < T_F$ ), or a function that behave like plasma conductivity  $\sim T_e^{5/2}$  ( $T_{ph} << T \sim T_F$ ).

In this section the heat conduction mechanism is considered in 1-D here that corresponds to the case of wide laser spot ( $\sim 10 \mu\text{m}$ ) on a metals surface as compare to the laser light absorption depth ( $\sim 10 \text{ nm}$ ). Heat capacities  $C_{ph}$  and  $C_e$  were taken as functions of phonon  $T_{ph}$  and electron  $T_e$  temperatures correspondingly. The dependence of  $C_{ph}$  on  $T_{ph}$  was based on experimental measurements [74]. The dependence of the electron heat capacity  $C_e$  and the strength of the electron-phonon interaction  $G$  on  $T_e$  was accounted for with different theoretical predictions and qualitatively did not affect the results of our calculations: either we used  $G = \text{const}$  [22, 52] and  $C_e = \gamma T_e$  [75] or more complex dependence was considered when

both  $G = f(T_e)$  and  $C_e = f(T_e)$  [31, 32]. The electron heat conductivity  $k_e$  exhibits a strong dependence with temperatures of electrons and phonons and was described with two approximations, depending on the material and, as a result, the temperature of electrons developed upon the absorption of the laser pulse. Namely, if the excitation of electrons leads to the temperature comparable with Fermi temperature  $T_F$ , like it is the case of Au and Cu ( $T_e \sim 10^4$  K), the dependence of  $k_e$  as suggested in [59] is given by Eq. 2:

$$k_e = C \frac{\left(\theta_e^2 + 0.16\right)^{5/4} (\theta_e + 0.44) \theta_e}{\left(\theta_e^2 + 0.092\right)^{1/2} \left(\theta_e^2 + b \theta_{ph}\right)} \quad (2)$$

Where  $\theta_e = T_e/T_F$  and  $\theta_{ph} = T_{ph}/T_F$  and  $C, b$  are material constants, listed in [59,76]. If, however, the excitation is relatively low and the maximum electronic temperature remains negligible as compare to Fermi Temperature  $T_F$ , like it was in the case of Ni and Al ( $T_e \sim 10^3$  K), an ordinary linear dependence of  $k_e$  with electron temperature  $T_e$  can be used [73], Eq.3:

$$k = k_0 \frac{T_e}{T_{ph}} \quad (3)$$

where  $k_0$  is a material constant. The heat conductivities for materials used in the present calculations are shown in Figure 4 a) and b).

In order to exclude any assumption about the melting process, the fluences used in all calculations were chosen to be below the threshold for material modification (melting), and were hold constant for a particular set of calculations where only pulse duration was varying. The source term  $S(z,t)$  for convenience was defined via the absorbed fluence  $F$  that accounts for reflectivity  $R$ :

$$S(z,t) = \sqrt{\frac{\sigma}{\pi}} \frac{F}{L_p} \exp\left(-\sigma \frac{(t-t_0)^2}{t_{pulse}^2}\right) \exp\left(-\frac{z}{L_p}\right) \frac{1}{1 - \exp(-L/L_p)} \quad (4)$$

where  $\sigma = 4Ln2$ ,  $F = F_0(I-R)$  indicates hhe absorbed fluence out of the incident one  $F_0$ , and  $R$  is the reflectivity,  $L_p$  the laser penetration depth,  $L$  is the film thickness,  $t_{pulse}$  is the pulse duration, and  $t_0 = 2.5 t_{pulse}$  is the time of pulse initiation. The first exponent describes Gaussian temporal profile; the second exponent reflects Lambert-Beers law of the laser energy deposition inside a solid; and the last multiplicator accounts for a finite thickness of film, for systems with sizes comparable to the effective energy deposition depth.

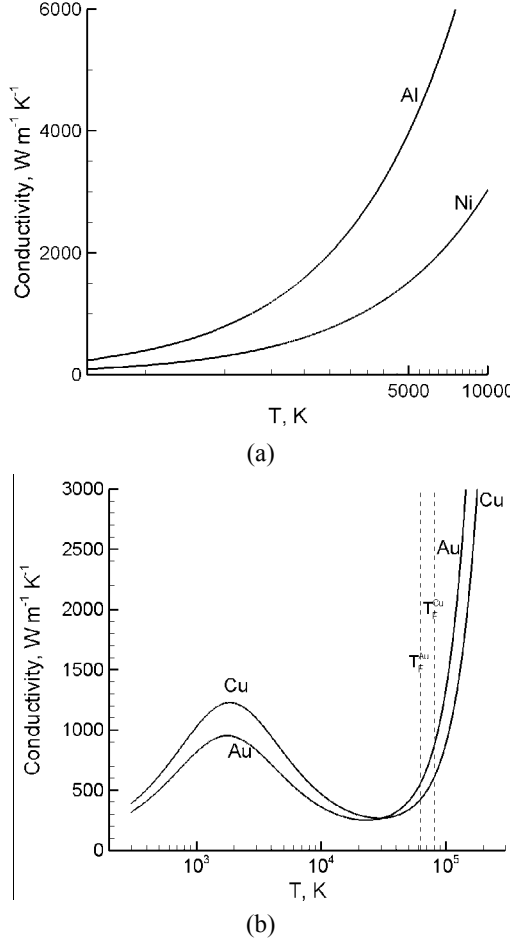


Figure 4. The electron heat conductivities for: a) Ni ( $T_F = 136,000 \text{ K}$ ) and Al ( $T_F = 135,000 \text{ K}$ ); b) Au ( $T_F = 64,000 \text{ K}$ ) and Cu ( $T_F = 81,000 \text{ K}$ ).

Some of the material parameters used in the description of the electron system, Eq. (1) for the case of simple behavior of  $C_e$  and  $G$  with the electron temperature [22, 52]. For Ni,  $C_e = \gamma T_e$  with  $\gamma = 1065 \text{ Jm}^{-3}\text{K}^{-2}$ ,  $K_e = K_0 T_e / T_l$  with  $K_0 = 91 \text{ Wm}^{-1}\text{K}^{-1}$ ,  $G = 3.6 \times 10^{17} \text{ Wm}^{-3}\text{K}^{-1}$ ,  $\lambda_{ball} \sim 0 \text{ nm}$  are used in the simulations; for Au,  $C_e = \gamma T_e$  with  $\gamma = 71 \text{ Jm}^{-3}\text{K}^{-2}$ ,  $G = 2.1 \times 10^{16} \text{ Wm}^{-3}\text{K}^{-1}$ ,  $\lambda_{ball} = 105 \text{ nm}$  are used. In order to describe the dependence of the electron thermal conductivity  $K_e$  on the electron and lattice temperatures in Au we use Eq. (2) with  $C = 353 \text{ Wm}^{-1}\text{K}^{-1}$ ,  $b = 0.16$ , and  $T_F = 64200 \text{ K}$ . The choice of approximations and parameters used for the electron thermal conductivity for Ni and Au was made based on characteristic electron temperatures attainable in calculations at used fluencies. When a more realistic dependence of  $C_e$  and  $G$  with electron temperature had to be considered, we used tabulated data obtained by Z. Lin in his first-principles electronic structure calculations of the electron density of states [31, 32].

The system of TTM equations was solved with the initial and boundary conditions as they are for free standing films. The film thickness  $L$  was chosen so that by the end of modeling the rise of electron temperature on the back surface would not exceed 1% of its initial value. Thus, the calculations were carried out on what is usually understood by thick or bulk metal targets (with  $L$  values 300 nm, 400 nm, 500 nm, and 2000 nm for Ni, Al, Cu, and

Au materials respectively). The time step was chosen based on Neumann stability criterion  $\Delta t \leq 0.5(\Delta X^2)C_e(T_e)/K_e(T_e, T_{ph})$  and ranged in 0.01 - 1 fs.

For each metal we perform a set of calculations at fixed absorbed fluence for a range of pulse durations from 100 fs to 100 ps. Thus, for all of the mentioned materials, there would be pulses much shorter and much longer than the characteristic electron-phonon relaxation times  $\tau_{e-ph}$ . Here we will understand the electron-phonon relaxation time as the time needed for both  $T_e$  and  $T_{ph}$  to equalize (crossover) on the metal surface, see Figure 5b). Being determined in such the way it can be therefore directly detected in experiments when measuring the surface temperature. Thus, we carry out the calculations until the moment when temperatures of electrons and lattice are equal at the surface. The results of simulations of laser pulses interacting with Ni target at the absorbed fluence  $F = 35 \text{ mJ/cm}^2$  are represented in Figure 5a), where the dynamics of transient electron and lattice temperatures on the surface is shown for different pulse durations. The maximum lattice temperature reached at the surface in our simulations as a function of pulse duration can be seen in Figure 5b).

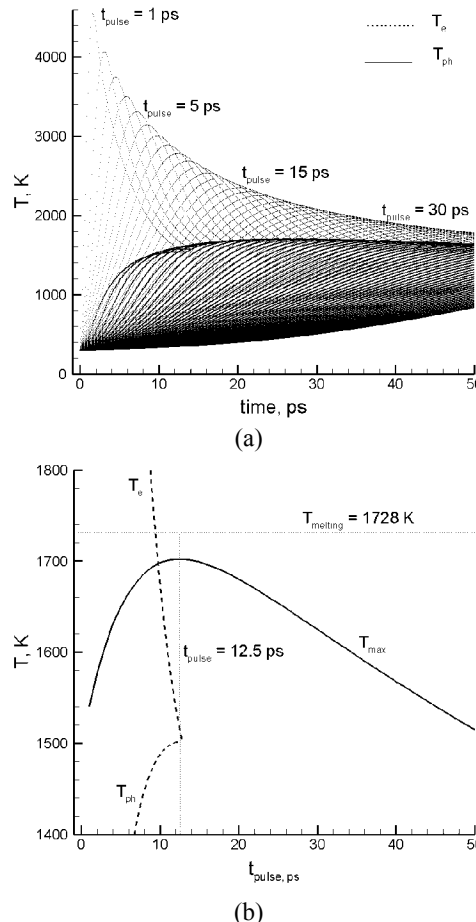


Figure 5. (a) Dynamics of transient electron (dotted) and lattice temperatures (solid) on the surface of Ni for different pulse durations at fixed fluence  $F = 35 \text{ mJ/cm}^2$ . (b) The maximum surface temperature of lattice (solid) of Ni as a function of pulse duration and the electron-phonon temperature dynamics on the surface (dotted) upon instantaneous energy deposition at the same fluence.

The results show that there is a clear peak in the maximum temperature on the target's surface at some pulse duration,  $t_{pulse} = 12.5$  ps, which is very close to electron-phonon relaxation time for Ni material that can be measured from the simulation where the effect of the pulse shape and duration is excluded. For this purpose we distribute the initial electron temperature within the optical absorption depth (13.5 nm for Ni at  $\lambda = 400$  nm) so that the total energy integrated in depth would correspond to the value of the same absorbed fluence and follow the electron-phonon temperature dynamics on the metal surface until equilibration.

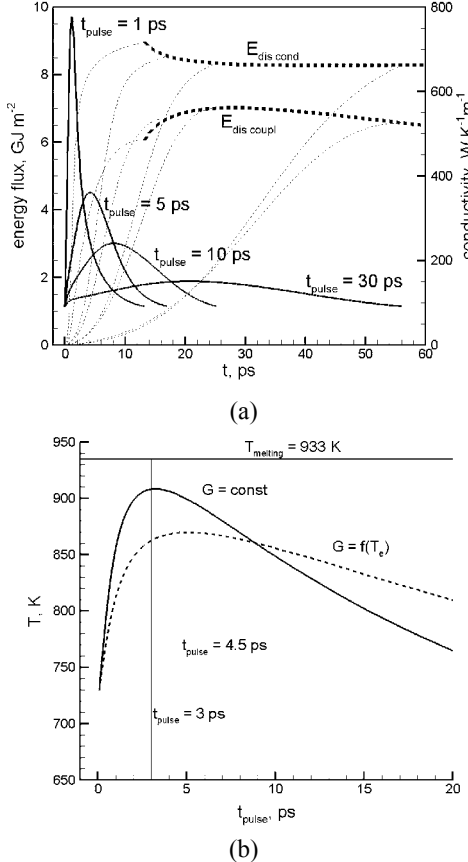


Figure 6. (a) For a set of different pulse durations, the energy dissipated through the electron heat conduction  $E_{dis\ cond}$  (upper dotted line) and through the electron-phonon interaction  $E_{dis\ coupl}$  (lower dotted line). Thin dotted lines connecting them with the zero point indicate their development in the real time from the left to the right for different pulse durations of 1, 5, 10 and 30 ps. For the same value of pulses, the evolution of conductivity function is shown by solid lines. (b) The maximum surface temperature of Al with constant  $G$  (solid) and with  $G = f(T_e)$  (dashed) at the absorbed fluence of 9.5 mJ/cm<sup>2</sup>.

Apparently, the coincidence of the electron-phonon relaxation time with the pulse duration time, at which the maximum lattice temperature on the target's surface is developed, is not accidental. In earlier works by Duff and Zhigilei [77], the fastest cooling rate in laser melting simulations was also observed at the pulse duration on the order of the electron-phonon relaxation time. In order to understand the nature of such coincidence, for different pulse durations, but at the constant fluence, we conduct the calculations while monitoring the

energy fluxes at the surface due to the conduction of hot electrons  $E_{dis\ cond}$  and due to the electron-phonon energy exchange  $E_{dis\ coupl}$ , Figure 6a. The evolutions of these quantities in time are shown by thin dotted lines from the left to the right for different pulse durations corresponding to 1, 5, 10, and 30 ps. For the same pulse durations we also plot the transient values of heat conductivity by the solid lines. As we can see, for pulses shorter than  $\tau_{e-ph}$  defined in Figure 2b, there is a significant part of the energy dissipated from the surface due to high value of the electron heat conductivity (at  $T_e \sim 4,000$  K). Fast energy transfer into the bulk of the material prevents its transfer into the phonon vibrations and the rise of lattice temperature therefore is suppressed. At longer pulses, closer to  $\tau_{e-ph}$ , the energy dissipation from hot electrons to phonons is more pronounced as the electron heat conduction is limited by lower temperature of electrons. In fact, at  $t_{pulse} = \tau_{e-ph}$ , the rate of energy transfer due to electron heat conduction is balanced by the rate of the electron-phonon energy dissipation process. At pulses much longer than  $\tau_{e-ph}$ , however, the electron heat conduction remains roughly on the same level whereas the temperature difference between electrons and phonons developed during the laser pulse is gradually decreasing with the grow of  $t_{pulse}$ , and therefore the energy dissipation from the electrons to the phonons is decreasing as well.

The existence of peak in the maximum temperature reached on the surface can be also observed in similar experiment with Al, another type of material, which exhibit very strong characteristics of transitional metals. Conducting the set of calculations, as we did for Ni, we can plot the temperature of the surface upon the electron-phonon equilibrium for different pulse durations at the absorbed fluence of  $9.5\text{ mJ/cm}^2$ , Figure 6b. Qualitatively, we can find a lot of similarities between Al and Ni, but Al has much shorter pulse duration,  $t_{pulse} = 2.5\text{ ps}$ , at which the peak in lattice temperature was observed. This corresponds to the experimental observation of much faster electron-phonon equilibration in this material [78]. The existence of the maximum still remains if we account for the electronic temperature dependence of the strength of electron-phonon coupling  $G(T_e)$  as it was discussed in [32], Figure 6b, although its position slightly changes to  $t_{pulse} = 4.5\text{ ps}$ . The latter suggests an averaged over time value for the electron-phonon relaxation time,  $\tau_{e-ph}$ , when it is a function of  $T_e$ .

Note, that Figures 5b and 6b were constructed based on monitoring the surface lattice temperature for a range of pulse durations, like it is shown in Figure 5a. From there we can conclude that even though the maximum temperature on the surface is still defined by the pulse duration equal to the electron-phonon relaxation time, the rate of the lattice temperature grow is nevertheless higher for the pulses shorter than  $\tau_{e-ph}$ . This implies that if there is enough space for the temperature gradient development [22, 79, 80], the shorter pulses will induce higher stresses upon the laser heating towards the conditions of inertial stress confinement [64] and after. As it was already mentioned above, physically the condition of inertial stress confinement means that the temperature grow exceeds the rate of thermal expansion of the solid in response to that hearting. The relaxation of overheated solid, apparently, is attributed with a propagation of a strong pressure wave that in turn may cause the mechanical damage. Therefore, the shorter pulse, the stronger laser-induced stresses, and the more photo-mechanical damage is pronounced. The latter complement the condition on inertial stress confinement, when  $\tau_{heating} < L/C_s$  (where  $L$  is geometrical size of the system and  $C_s$  is the speed of sound), given in Ref. [64]. Contrary, the pulses longer than  $\tau_{e-ph}$  result in establishing of temperature gradients on a longer scale and in a longer time. Any damage therefore can be rather addressed with photo-thermal effects, like melting or boiling processes.

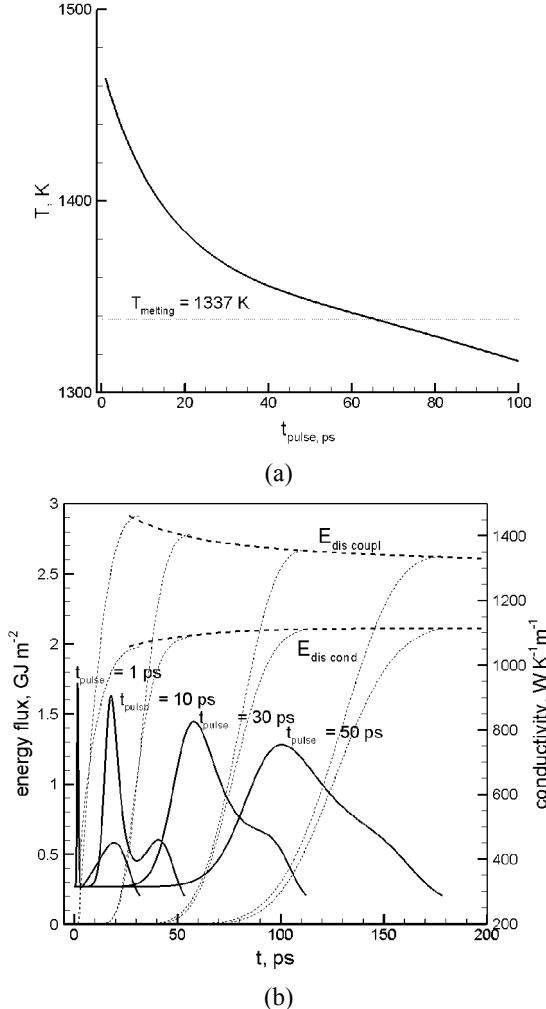


Figure 7. (a) The maximum surface temperature of lattice of Au at  $F = 85 \text{ mJ/cm}^2$  for a range of pulse durations. (b) Similar to Figure 6a, but for pulse durations of 1, 10, 30, and 50 ps.  $E_{dis\ cond}$  is lower dotted line and  $E_{dis\ coupl}$  is upper dotted line.

Now we perform the same type of calculations for noble metals Cu and Au. In Figure 7a we plot the maximum temperature reached at the surface of Au for different pulse durations at constant absorbed fluence of  $85 \text{ mJ/cm}^2$  and constant coupling parameter  $G$ . As we can see, the essential difference with similar calculations on transitional metals Ni and Al, Figure 5b, is that now we do not observe a peak in maximum lattice temperature on the surface when varying the pulse duration. This fact, nevertheless, can be understood with the help of Figure 7b where in real time we plot the energies dissipated from the surface due to the electron heat conduction  $E_{dis\ cond}$  and the electron-phonon interactions  $E_{dis\ coupl}$  along with the value of the electron heat conductivity. As we can see, the dynamics of the electron heat conductivity of Au is very different from that of Ni. Namely, the electron temperatures  $\sim 10,000 \text{ K}$ , realized upon the laser light absorption for pulses on the order of 1 ps, drive the electron heat conductivity into the high temperature regime ( $T_e \sim T_F$ ), resulting in a smaller value of heat conductivity, see Figure 4 b). Thus, the energy dissipation from the surface due to heat

conduction mechanism is suppressed and the heat is confined in the proximity of the surface, resulting in a higher maximum lattice temperature.

This situation drastically changes, however, if we decrease the absorbed fluence down to 1 mJ/cm<sup>2</sup>, pushing the electronic heat conductivity function to the low temperature regime (the electronic temperatures  $T_e$  reaches the value  $\sim 1,000$  K) so that only linear dependence of  $k_e$  with  $T_e$  is realized, Figure 4 b). Now, we can clearly see that there is a peak in the maximum lattice temperature developed on the surface at  $t_{pulse} = 14$  ps, Figure 8 a), that can be related to the electron-phonon relaxation time at this fluence. Qualitatively this behavior can be compared with the presented calculations for transitional metals, also exhibiting the low-temperature behavior of the heat conductivity, as on Figure 4 a). The interplay of the energy dissipation via the electron phonon interaction,  $E_{dis\ coupl}$ , and via electron heat conduction,  $E_{dis\ cond}$ , resulting in a peak behavior of the maximum lattice temperature on the surface for a low fluence regime can be seen in Figure 8 b). Thus, we come to the important conclusion that in the developing of the surface lattice temperature the electron heat conduction mechanism plays as an important role as the process of electron-phonon energy exchange. Similar type of calculations performed for Cu, another metal of noble type, confirmed the dependence of maximum surface temperature with the pulse duration in different fluence regimes. Namely, the absence of maximum surface temperature peak at  $F = 28$  mJ/cm<sup>2</sup> and its presence at  $t_{pulse} = 10$  ps in the low fluence regime  $F = 1$  mJ/cm<sup>2</sup>.

Therefore, there is a fluence regime where we can detect the electron-phonon relaxation time experimentally by means of measuring the lattice temperature reached at the surface for a range of pulse durations at fixed fluence. But even at high excitations the profile of lattice temperature in a wide fluence range can give us important information about  $\tau_{e-ph}$  and its temperature dependence. The necessary picosecond resolution in surface temperature measurements could be achieved in pump probe experiments where optical properties are monitored not only via a signal's amplitude but detecting it's phase as well [81,82]. In these experiments, the abrupt change in fast dynamics of the optical properties would indicate the establishment of equilibrium between the electrons and phonons. Therefore, having the reference points measured at the equilibrium conditions for the same material, the end of fast changing in optical properties could be referred to the value of lattice temperature.

Despite the fact that noble metals exhibit essentially different properties in maximum temperature development when varying the pulse duration, the conclusion drawn concerning the photo-mechanical damage versus photo-thermal one for transition metals still holds valid for noble materials as well. Particularly, if there is enough space for the temperature gradient development upon the laser heating, pulses shorter than  $\tau_{e-ph}$  will induce faster heating and therefore photo-mechanical effects will be more pronounced, whereas pulses longer than  $\tau_{e-ph}$  will result in photo-thermal damage more pronounced. This particular conclusion is very important for the nanostructuring and will be utilized later in this chapter when modeling short pulse laser interaction with thin metal films [62].

While TTM has become a common tool for computational analysis of short pulse laser interaction with metals [22,83,84,85,86,87,88], it is nevertheless based on a number of assumptions and choice of approximations for the temperature dependence of the electron thermal conductivity [59, 73] and coupling parameter [32, 71]. Also, in all calculations we assume that the electron thermalization (establishment of the Fermi-Dirac distribution, Figure 2, takes place instantaneously upon the laser pulse irradiation. This assumption is justified by theoretical calculations presented in [61] were a system of Boltzmann equations was solved

for both electron and phonon gases. It was found that for picosecond and sub-picosecond pulses the difference between the solutions of the Boltzmann equations and TTM calculations can be neglected.

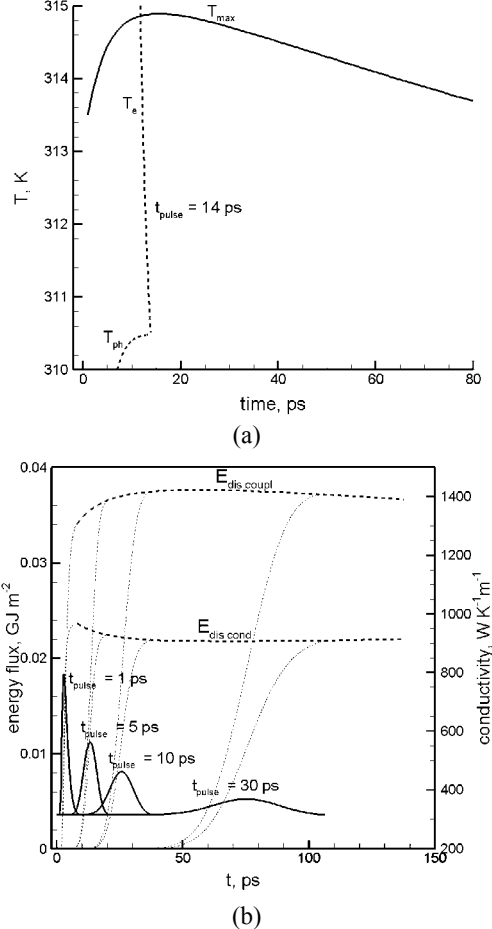


Figure 8. (a) Same as in Figure 5 (b), but at  $F = 1 \text{ mJ/cm}^2$ . The dotted lines are for the electron and lattice temperature dynamics followed by instantaneous energy deposition within the optical penetration depth, including the ballistic energy transfer range. (b) Similar to Figure 6a.

Finally, in addition to the diffusive electron energy transport assumed in TTM, the ballistic motion of the excited electrons can significantly alter the initial energy deposition depth for s/p-band metals [89], where the electron-electron collision rate is relatively small. Before the excited electrons equilibrate due to collisions with other electrons near the Fermi level and form a Fermi-Dirac distribution with a certain electron temperature, they can propagate from the optical absorption depth deeper into the bulk of the irradiated sample with velocities close to the Fermi velocity,  $\sim 10^6 \text{ m/s}$ . This ballistic motion of the excited electrons leads to the fast, within  $\sim 100 \text{ fs}$ , redistribution of the deposited energy within the ballistic range that is defined by the mean free path of the electrons. It has been suggested [22] that the effect of ballistic electrons can be incorporated into TTM by substituting the optical penetration depth  $L_p$  in the source term, Eq. (4), with an effective laser energy deposition

depth defined by both optical absorption and ballistic energy transport,  $L_p + L_b$ , where  $L_b$  is the ballistic range.

As we can see, some of the limitation of TTM model can be overcome by adding “more physics” within the framework provided by TTM. In particular, recent developments include incorporation, through the parameters of TTM, of the description of the surface and grain boundary scattering [90], as well as the energy transfer by ballistic electrons [22, 30, 91], combining TTM with the hot electron blast model [28] and thermoelasticity equations to investigate the conditions for nonthermal damage to thin metal films [83].

Other limitations, on the other hand, are harder to overcome within a continuum model. In particular, the description of phase transformations occurring under highly nonequilibrium conditions induced in the target material by short-pulse laser irradiation is difficult and typically involves several simplifications. Part of the problem is that the physics of ultrafast phase transformations and damage occurring under highly nonequilibrium conditions is not well understood yet and therefore cannot be reliably described by a set of kinetic equations. As already mentioned above, even the basic questions on the kinetics and microscopic mechanisms of melting under conditions of strong overheating continue to remain the subjects of active scientific debates. At the extremely high levels of superheating realized in ultrashort-pulse laser melting, when the melting front propagation approaches speeds on the order of speed of sound and the size of a critical nucleus becomes comparable to several interatomic distances, the applicability of macroscopic kinetic approaches based on classical nucleation theory [35, 45, 92] is rather doubtful. In the next section we describe a computational method that is suitable for description of fast nonequilibrium processes mentioned above.

## (b) Molecular Dynamics Approach

A computational method that is suitable for simulation of fast nonequilibrium processes and therefore can provide insights into the mechanisms of laser-metal interactions at the atomic scale is the Molecular Dynamics (MD) method. In its classical representation, the MD method can be described as the following system of Newton equation of motion:

$$\vec{F}_i = -\nabla U_i(\vec{r}_1, \vec{r}_2, \vec{r}_3, \dots, \vec{r}_N) = m_i \frac{d^2 \vec{r}_i}{dt^2} \quad j = 1, 2, 3, \dots, N \quad (5)$$

where  $m_i$  is the mass of atom  $i$ ,  $U_i$  its total potential energy that can be in general a function of position of the other atoms, and  $F_i$  is the resulting force acting on the atom and  $i$  runs from 1 to  $N$ , the total number of atoms in the system.

The advantage of the MD method is that only details of the interatomic interaction need to be specified, and no assumptions are made about the character of the processes under study. In particular, MD has been demonstrated to be an efficient tool for a microscopic analysis of the melting mechanisms under conditions of overheating in both the bulk of a crystal [99, 100] and in systems with free surfaces [101, 102]. Simulations of boiling, spinodal decomposition and fragmentation of a metastable liquid [103, 104, 105], generation

and propagation of laser-induced pressure waves [106,107], and laser ablation [108, 109, 110] have been also reported.

Therefore, all the thermal and elastic properties of the lattice, such as the lattice heat capacity, elastic moduli, the coefficient of thermal expansion, melting temperature, change of volume, and entropy of melting, as well as the dependence of these characteristics on temperature and pressure are defined by the interatomic interaction, described in most of applications in this chapter by the Embedded Atom Method (EAM) [111, 112] in the form and parameterization of the potential suggested by Johnson [112]. The total energy of the atomic system described via EAM potential can be given as follow:

$$U = \sum_i \Phi_i(\rho_i) + \sum_i \sum_{j \neq i} \varphi_{ij}(\bar{r}_{ij}) \quad \text{and} \quad \rho_i = \sum_{j \neq i} f_i(\bar{r}_{ij}) \quad (6)$$

where  $\Phi_i$  is an embedding functional that approximates the energy required to embed a positively-charged core ion  $i$  into a linear superposition of spherically averaged atomic electron densities given by  $\rho_i$  and  $\varphi_{ij}$  is an ordinary pair potential [113].

One of the most frequently arising questions while dealing with MD is the question about how well the chosen potential describes the material properties. Definitely, one would prefer to have a potential that could accurately reproduce all the properties of the investigated material, but it is difficult to chose an empirical function describing the interatomic interaction so that it would provide a perfect fit to a wide range of properties of the material. Typically, however, the main purpose of an MD simulation is not to describe all the properties of a chosen material as well as it possible, but to reveal some general physical behavior that is not very sensitive to small variations of the parameters of the material system.

In order to perform a quantitative analysis of the simulation results and to relate them to experimental observations, we should start from finding the physical properties of the model material, as predicted by the interatomic potential. As an example of MD application, we reproduce some of the calculations here that help us to analyze the properties of EAM Ni model materials relevant to the melting process, since it is always preceding to a material restructuring.

A series of liquid-crystal coexistence MD simulations has been performed at different pressures to determine the equilibrium melting temperature [114]. In these simulations a system of coexisting liquid and solid phases is allowed to evolve toward the equilibrium state while the energy of the system is conserved. If the temperature of the system is initially above the equilibrium melting temperature, part of the solid phase melts, consuming latent heat of melting and reducing the temperature. If the initial temperature is lower than the equilibrium melting temperature, crystallization of a part of the system leads to the temperature evolution toward the equilibrium melting temperature from below.

Simulation results, shown in Figure 9a, predict a nearly linear dependence of the melting temperature on pressure. This prediction is in a good agreement with calculations based on the Clapeyron equation:

$$\left( \frac{dT}{dP} \right)_m = \frac{\Delta V_m}{\Delta S_m} = \frac{T \Delta V_m}{\Delta H_m} \quad (7)$$

where the volume change and entropy of melting,  $\Delta V_m$  and  $\Delta S_m$ , are determined from the temperature dependences of the volume and internal energy calculated for zero pressure, as shown in Figures 11a and 12a respectively. For example, for the model EAM Ni material, the values of volume change and entropy of melting at zero pressure are found to be  $\Delta V_m = 0.46 \text{ cm}^3/\text{mole}$  and  $\Delta S_m = \Delta H_m/T_m = 10.06 \text{ J/K-mole}$ , comparable to the experimental values for Ni,  $\Delta V_m^{\text{exp}} = 0.32 \text{ cm}^3/\text{mole}$  and  $\Delta S_m^{\text{exp}} = 9.94 \text{ J/K-mole}$  [115]. In simulations we find that both  $\Delta V_m$  and  $\Delta S_m$  are decreasing with increasing pressure, leading to a weak non-monotonous pressure dependence of the slope of the coexistence line with an average value of  $(dT/dP)_m \approx 45 \text{ K/GPa}$ .

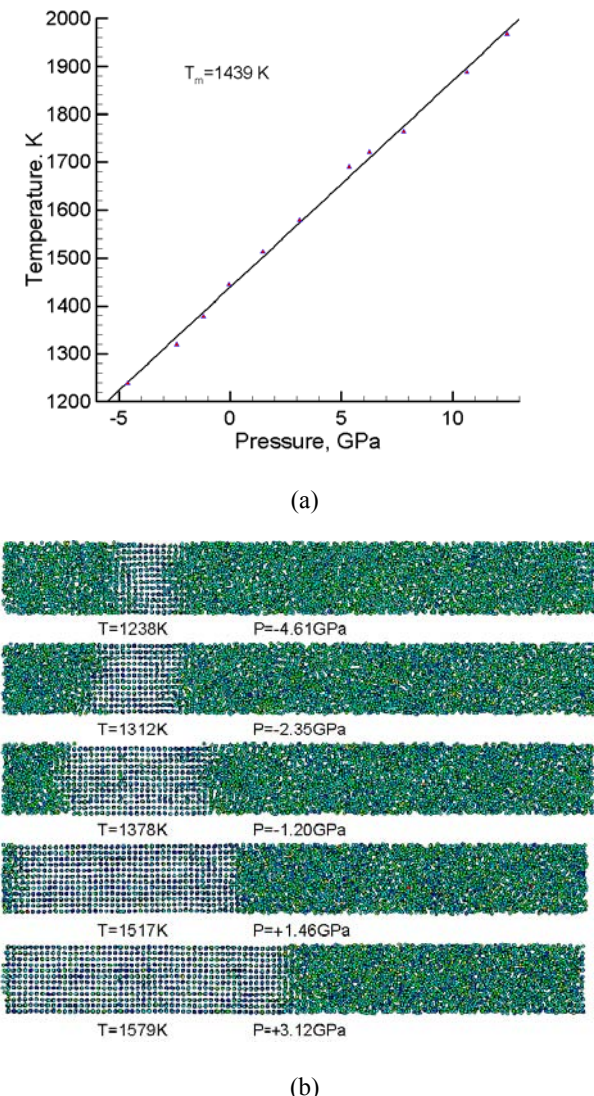


Figure 9. (a) Equilibrium melting temperature of the EAM Ni model material determined in a series of liquid-crystal coexistence simulations. The melting temperature  $T_m = 1439 \text{ K}$  is found at zero pressure. (b) Several snapshots from the liquid-crystal simulations are shown at different pressures.

The dependences of the heat capacity  $C_P$  and the volume coefficient of thermal expansion  $\alpha$  on temperature are calculated for the model materials in a series of constant pressure – constant temperature simulations. The results of these simulations for EAM Ni are shown in Figures 10b and 11b, where the temperature dependences of the volume and internal energy of the system are shown for different pressures. The volume plots, Figure 10, allow us to calculate the volume coefficient of thermal expansion,  $\alpha = (1/V)(dV/dT)_P$  for different temperatures and pressures.

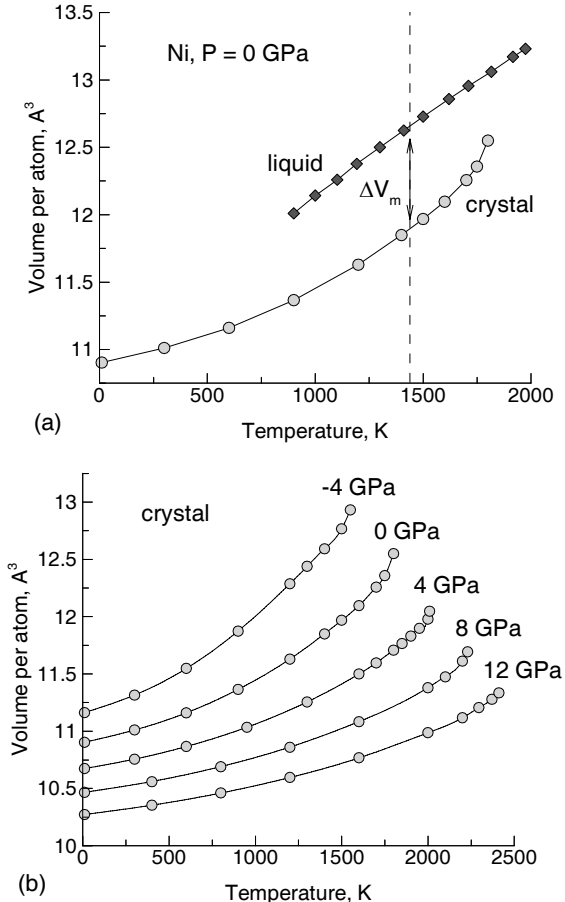


Figure 10. a) The temperature dependence of the volume of the EAM Ni material at zero pressure for both solid and liquid phases. b) Same for several different pressures for the solid phase. The dependences are used to calculate the volume coefficient of thermal expansion at different temperatures and pressures,  $\alpha_v = (1/V)(dV/dT)_P$ , and the volume change of melting,  $\Delta V_m$ , as indicated in a). The vertical dashed line in a) shows the equilibrium melting temperature of the EAM Ni at zero pressure.

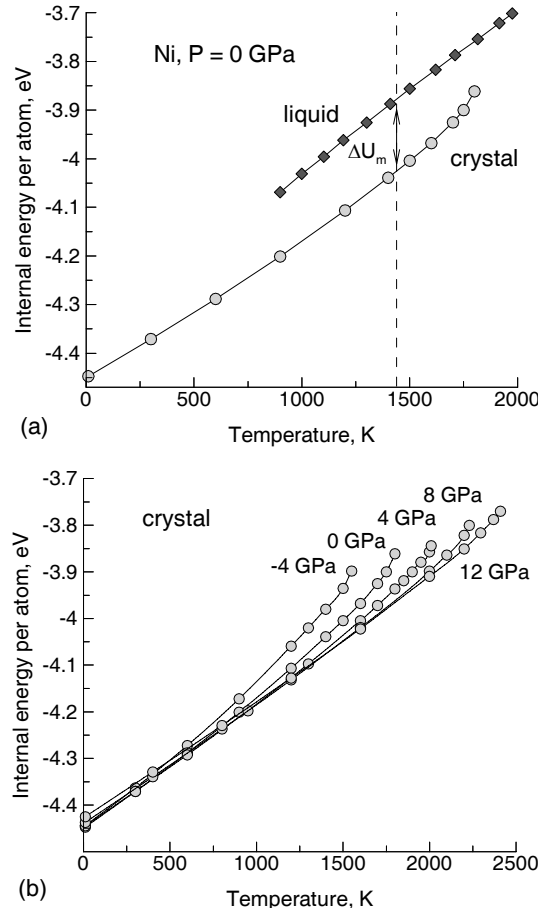


Figure 11. a) The temperature dependence of the internal energy of the EAM Ni material at zero pressure for both solid and liquid phases. b) Same for several different pressures for the solid phase. The dependences are used to calculate the heat capacity at different temperatures and pressures,  $C_p = (dH/dT)_p$ , as well as the latent heat of melting,  $\Delta H_m = \Delta U_m + P\Delta V_m$ , and the entropy change of melting,  $\Delta S_m = \Delta H_m/T_m$ . The vertical dashed line in a) shows the equilibrium melting temperature of the EAM Ni at zero pressure.

The internal energy plots, Figure 11, provide us with the pressure and temperature dependence of the heat capacity,  $C_p = (dH/dT)_p$ . The information on the temperature and pressure dependences of the thermodynamic parameters of the material allows us to perform thermodynamic analysis of processes induced in the surface region of the target by short pulse laser irradiation. In particular, the relaxation of the laser-induced stresses can induce fast adiabatic/isentropic expansion/compression of the material with associated pressure/temperature variations described by the following equation:

$$\left( \frac{\partial T}{\partial P} \right)_s = \frac{VT\alpha_v}{C_p} \quad (8)$$

where  $\alpha_v(T,P)$  is the volume expansion coefficient of the material. The knowledge of  $C_p(T,P)$ ,  $\alpha_v(T,P)$ , and  $V(T,P)$  allows us to integrate this equation and to obtain the temperature-pressure evolution of the system. This analysis is used for interpretation of simulation results on short pulse laser melting considered in Ref. [36, 37, 62, 64, 79, 116, 119] as well as in the next section where simulations of nanostructuring with short laser pulses on metallic surfaces are performed. In Table 1, we combine all the properties that we found from constant temperature – constant pressure and solid-crystal coexistence simulations for EAM Ni and EAM Au materials. As we can see, some of them show a disagreement with their experimental values, but this fact should not disturb the physical picture of melting and nanostructuring processes that we study.

Thus, having now all the properties of the modelled material for a quantitative analysis of the simulation results, we want to demonstrate the applicability of MD method when studying fast nonequilibrium phase transformation processes we perform calculations aimed on isolating two essential mechanism of melting: homogeneous and heterogeneous mechanisms. The objective is to investigate the applicability of the homogeneous nucleation theory [36, 65] for the description of both homogeneous and heterogeneous melting at the strong overheating that can be achieved with short laser pulses. The timescale of the melting process  $t_M$  [36], the density of the liquid phase nuclei and the evolution of the shapes of the liquid regions will be investigated. Microscopic mechanisms of melting will be considered based on the results of several large scale MD simulations performed for EAM Ni material at a high degree of superheating ( $T \approx 1.2T_m$ ).

**Table 1. Some of the material parameters determined for the EAM Ni and Au materials. Values of the equilibrium melting temperature,  $T_m$ , volume change,  $\Delta V_m$ , enthalpy,  $\Delta H_m$ ,**

**and entropy,  $\Delta S_m$ , of melting are given for zero pressure. The dependence of the equilibrium melting temperature on pressure,  $(dT/dP)_m$ , is determined from the liquid-crystal coexistence simulations performed at different pressures and confirmed by the calculations based on the Clapeyron equation,  $(dT/dP)_m = \Delta V_m / \Delta S_m$ . Variations of the coefficient of linear expansion,  $\alpha$ , and heat capacity at zero pressure,  $C_p$ , are given for a temperature range from 293 K to 1000 K for Ni and from 293 K to 950 K for Au.**

**Experimental values are from references [74, 115, 117].**

Properties	$T_m$ , K	$\Delta V_m$ , $\text{cm}^3 \text{ mol}^{-1}$	$\Delta S_m$ , $\text{J K}^{-1} \text{ mol}^{-1}$	$\Delta H_m$ , $\text{kJ mol}^{-1}$
EAM Ni	1439	0.46	10.0	14.47
Experiment Ni	1726	0.452	9.94	17.472
EAM Au	963	0.28	8.69	8.37
Experiment Au	1336	0.55	9.56	12.78

Properties	$(dT/dP)_m$ , $\text{K GPa}^{-1}$	$C_p$ , $\text{J K}^{-1} \text{ mol}^{-1}$	$\alpha$ , $10^6 \text{ K}^{-1}$
EAM Ni	45.73	25.04-36.13	14.4-22.6
Experiment Ni	45.47	25.85-46.50	12.8-17.5
EAM Au	32.19	25.26-32.71	10.3-21.4
Experiment Au	57.53	25.38-31.20	14.2-19.1

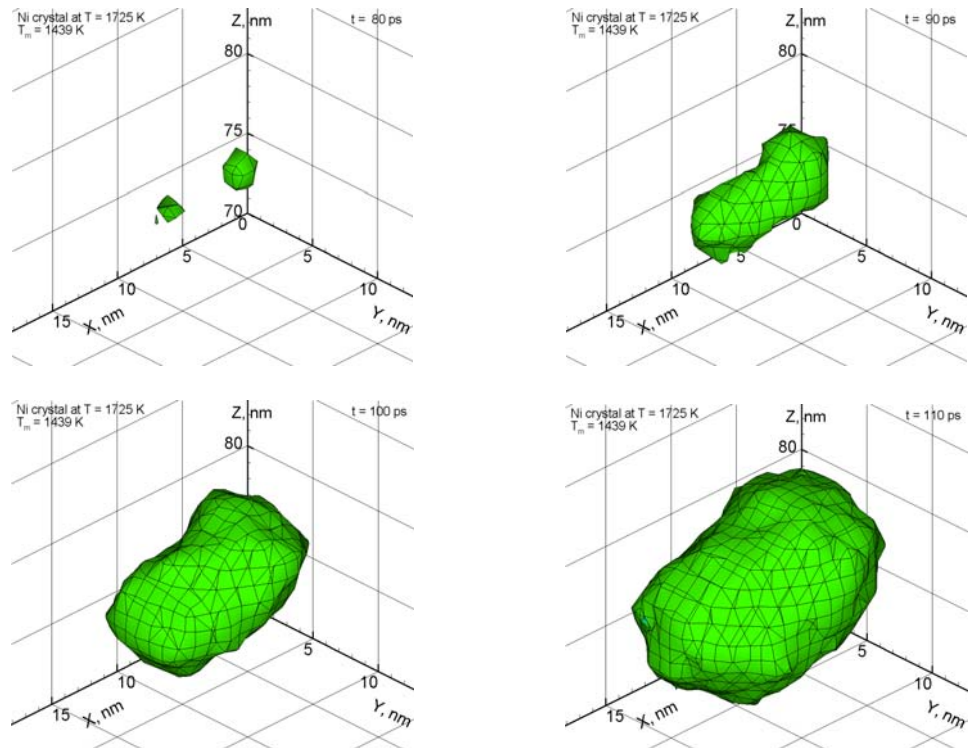


Figure 12. Snapshots taken from a MD simulation of homogeneous nucleation and growth of liquid regions in a Ni crystal at  $T = 1725 \text{ K}$ . The homogeneous nuclei coalesce and develop into a large aspherical volume.

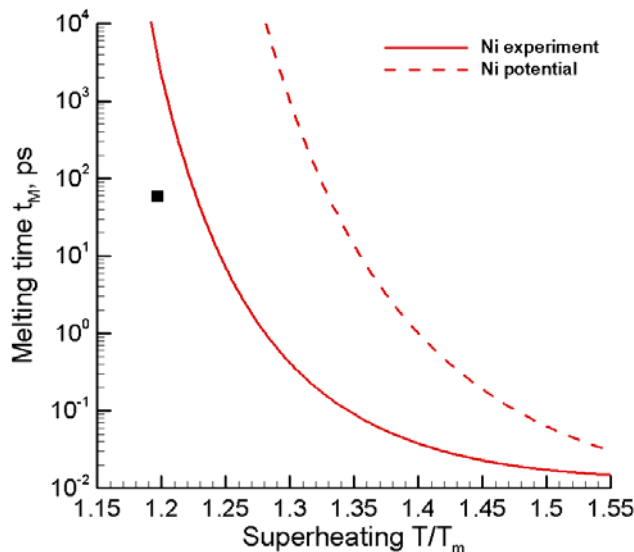


Figure 13. Melting time as a function of overheating  $T/T_m$  as predicted by the homogeneous nucleation theory and calculated as suggested in Ref. [35] for Ni material with experimental parameters (solid line) and parameters given by EAM potential used in this work. The black square point indicates the melting time obtained in MD simulations of homogeneous melting, described here.

Here we present the analysis of homogeneous melting of a Ni crystal with the size of the computational box  $22 \times 22 \times 100$  nm is illustrated in Figure 12. Periodic boundary conditions imposed in all directions, and constant hydrostatic pressure maintained by means of the “Berendsen barostat” algorithm [118]. The sample was slowly heated under constant pressure conditions up to the temperature  $T = 1725$  K, where a spontaneous nucleation of several liquid regions was observed. To analyze the shape of the liquid regions quantitatively the following procedure was developed.

The whole system was first divided into small cells with dimensions of  $0.5 \times 0.5 \times 0.5$  nm. The local order parameter [114] was then averaged for all particles in the cell and the cell is assigned to be a part of a liquid region if the average value of the local order parameter was less than 0.04 (see Appendix at the end of this section) [116]. Connectivity among the cells is then checked and clusters of liquid cells, defined as groups of more than 2 liquid cells connected with each other by sharing a face, are identified. Two clusters identified using the method described above are shown in Figure 12. We can see that two liquid nuclei appear within the volume of the MD computational cell are not spherical as it is assumed in the classical homogeneous nucleation theory [65], but rather coarse and elongated. They grow, coalesce, taking an irregular elongated shape, and fill in the entire volume, thus completing the solid-liquid phase transformation [35].

From two simulations discussed above we can estimate an approximate melting time  $t_M$  of the full volume to be on the order of 50 - 60 ps at an overheating of  $\sim 1.20 T_m$ . In Figure 13, following procedure presented in Ref [35], we replot the data one melting time  $t_M$  as a function of superheating  $T/T_m$  for Ni materials with experimental and EAM parameters including the marked value of the melting time  $t_M$  estimated from the MD simulations. As we can see the melting time by nucleation theory and the one obtained from our MD simulation differ by at least 4 orders of the magnitude. Such a big difference can not be easily attributed to an error in the choice of the material parameters used in Ref. [35] and listed in Table 1. Although not all of the parameters listed in Table 1 can be reliably determined experimentally and the value of melting time  $t_M$  given Ref. [35] is sensitive to the choice of the materials parameters, the difference in 4 orders of magnitude can be hardly eliminated by a simple variation of the parameters within physically reasonable limits. Therefore, the applicability of nucleation theory [35, 65] in description of the homogeneous melting at high degrees of overheating attainable in short laser pulse nanostructuring experiments is questionable.

The heterogeneous melting mechanism, on the other hand, is also difficult to describe at continuum level. The solid-liquid transition may result in a significant ( $\sim 150$  K) local temperature drop since part of the thermal energy goes to the latent heat of melting. It is clear that melting proceeds slower in cooler regions and goes faster in hotter areas. Therefore, while the homogeneous melting front is propagating, due to thermal energy redistribution the instabilities may emerge across the solid-liquid interface. The kinetics of these instabilities may be especially important in the case of strong superheating when heterogeneous melting is about to be supplemented by the homogeneous nucleation of liquid regions ahead of the propagating solid-liquid interface. To elucidate the kinetics of possible instabilities below we perform several large-scale simulations aimed specifically at investigation of the mechanism of heterogeneous melting front propagation [119].

To ensure that periodic boundaries do not affect the kinetics of propagation of the solid-liquid interface and possible appearance of instabilities, we performed simulations for computational cells with three different sizes in the lateral directions:  $14.8 \times 14.8$  nm,  $22 \times 22$

nm, and  $44 \times 44$  nm. Most of the results were obtained on samples containing 3,945,600 atoms and having dimensions of  $22 \times 22 \times 100$  nm. This size of the computational cell was found to give results similar to the ones obtained with larger systems. Simulations were performed for a model EAM Ni material and for a set of different temperatures, 1600 K, 1650 K, 1700 K, 1715 K, and 1725 K.

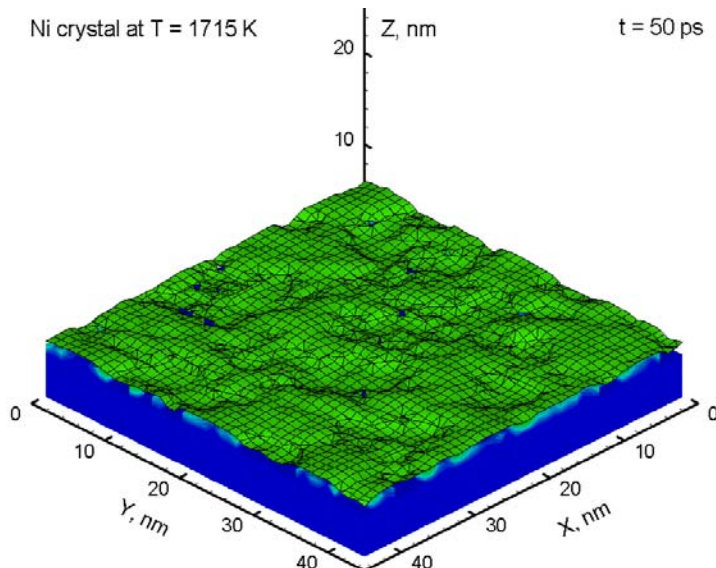


Figure 14. Snapshot of solid-liquid interface taken from a simulation of heterogeneous melting of the sample with size of  $44 \times 44 \times 55$  nm (7 948 800 atoms). The characteristic size of the surface fluctuations is much smaller than the size of the computational box in the lateral directions, in which periodic boundary conditions are imposed.

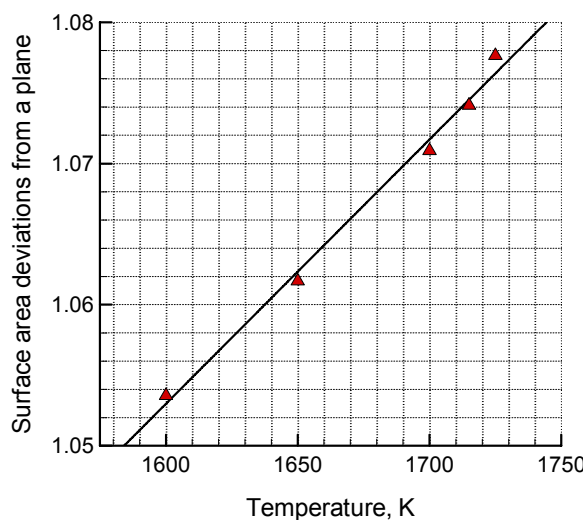


Figure 15. The time averaged deviations of the surface area of the solid-liquid interface from the surface area of a perfect plane shown as a function of temperature. A linear fit is used to extrapolate this dependence down to the equilibrium melting point  $T_m = 1439$  K.

The results of simulations reveal instabilities across the solid-liquid interface that appears as fluctuations of the melting front surface as it can be seen in Figure 14. In this figure we do no show the crystalline part of the system so that the shape of the interface would be clearly visible. In these simulations we assume that a cell is melted if the number of particles that belong to the liquid phase has reached at least half of the total number of particles in this cell. One of the easiest ways to characterize the roughness of the surface is to calculate the deviation of its area from the one of a perfect plane. The calculated quantity,  $A_{s-l\text{ interface}}/A_{\text{plane}}$  is plotted in Figure 15 as a function of temperature.

From data presented in Figure 15 we can deduce that the solid-liquid interface becomes rougher as the melting proceeds more actively, however, we can also see that this dependence is rather weak. Even if we continue to decrease the temperature down to the equilibrium melting point, the linear extrapolation will give us the remaining value of  $\sim 1.025$ . This value is close to 1.032 measured in a large-scale liquid -crystal coexistence simulation ( $T = T_m = 1439$  K,  $P = 0$  GPa) and we consider this value to be inherent solid-liquid interface fluctuations.

A more informative quantitative description of the spatial size of the solid-liquid interface fluctuations during the heterogeneous melting process can be performed with the help of the correlation function  $F(\Delta\vec{r})$ . To calculate the correlation function, we construct the following overlap integral in polar coordinates:

$$F(\Delta\vec{r}) = \frac{1}{\Omega} \int_{\Omega} h(\vec{r})h(\vec{r} + \Delta\vec{r})d\vec{r} \quad (9)$$

where  $h(\vec{r})$  is a position of the solid-liquid interface and  $\Omega$  is the area of the computational box in the lateral directions. By calculating this integral and taking its average over all data points on the surface of the solid-liquid interface we are able to find the correlations, if any, in the spatial distribution of the interface fluctuations. Moreover, since we do not normalize this function to unity, by taking the square root of the main maximum altitude, we thus may estimate the characteristic height of those fluctuations, Figure 16.

For all simulations the correlation function, Figure 16, reveals a similar, very stable behavior that does not deviates significantly even at different temperatures. Averaging the correlation functions over time for each simulation, we may deduce several conclusions. First, the width of the main maximum taken at the half maximum of the correlation function gives us the characteristic radius of the bumps on the solid-liquid interface, the diameter of which we can estimate to be about 3 nm. Second, the characteristic height of the instabilities is merely the square root of the maximum intensity of the correlation function is on the order of 0.2 nm. Third, there is no spatial correlation between the fluctuations. In other words the occurrence of fluctuations across the solid-liquid interface is completely random.

The analysis performed above leads us to the conclusion that instabilities emerging across the solid-liquid interface during a heterogeneous melting process even at a high degree of overheating are still on the order of 0.2 nm in the direction normal to the interface, which is also comparable to the resolution of our method of data analysis (the choice of the size of a cell of the spatial discretization). If there are strong and complex instabilities in the heterogeneous melting front propagation, they must be on the scale much larger than the computational cell used in this work, 44 nm in the lateral directions. Otherwise, the

instabilities we observed in our simulations are on the atomic scale  $\sim 1$  nm. The roughness of the melting front slightly increases with overheating, but this increase is comparable to the inherent solid-liquid interface fluctuations at the equilibrium melting temperature. A more detailed study of the heterogeneous melting process with Molecular Dynamics approach is presented elsewhere [119].

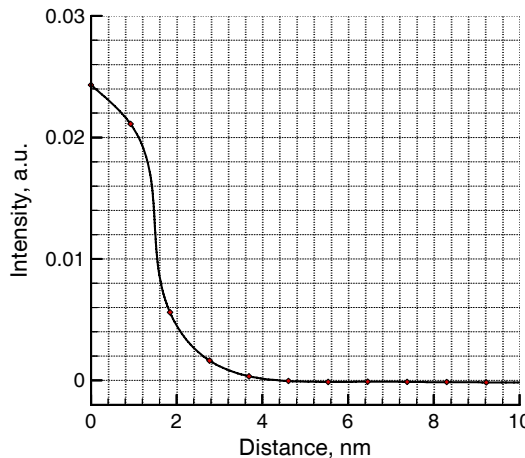


Figure 16. Height-height correlation function averaged over 50 positions of the solid-liquid interface in a simulation of the melting front propagation performed for a Ni sample of  $44 \times 44$  nm dimensions in the lateral directions at a temperature of 1715 K. The function provides information on the characteristic size of the fluctuations, characteristic amplitude of the bumps, and their spatial correlations.

Therefore, as one can see, the accurate and reliable introduction of these tiny details into the nucleation theory at continuum level does not seem to be possible in the set of kinetic equations. This justifies the choice of MD method as a powerful numerical tool in studying non equilibrium phase transformation laser-induced processes that potentially can be involved into the nanostructuring. The classical MD method, however, is not directly applicable for simulation of laser interactions with metals. Since the electronic contribution to the thermal conductivity of a metal is dominant, the conventional MD method, where only the lattice contribution is present, significantly underestimates the total thermal conductivity. This leads to unphysical confinement of the deposited laser energy in the surface region of the irradiated target and does not allow for direct comparison between the calculated and experimental data. Moreover, the laser energy absorption by the conduction band electrons and the transient state of electron-lattice nonequilibrium, briefly discussed above, in Section 2a), cannot be reproduced since the electrons are not explicitly represented in the classical MD model. Additionally, the long range (several microns) elasto-plastic deformation of the solid induced by a short pulse laser nanostructuring processes can not be encompassed by MD calculations because of their high computational cost, but can efficiently contribute to the nanostructuring process [9, 11, 60, 62]. The appropriate method that includes the description of laser-induced nonequilibrium between the electrons and phonons, fast electron heat conduction, and the laser light absorption by conduction band electrons, as it is in TTM model, but on the other hand accounts for long range laser-induced deformations of the solid based on the Macroscopic Continuum Model (MCM) will be presented in the next section.

## APPENDIX: LOCAL ORDER PARAMETER FOR IDENTIFICATION OF SOLID AND LIQUID PHASES

The identification of liquid and crystal regions in the atomic configurations produced in the simulations of ultrafast laser melting is often challenging due to the complex nature of the melting process and the absence of well-defined plane liquid-crystal interfaces (e.g. Figure 17). In this work a distinction between the original fcc structure and the liquid phase is made with the local order parameter defined as [114]:

$$\Psi_i = \left| \frac{1}{6} \frac{1}{Z} \sum_{j=1}^Z \sum_{k=1}^6 \exp(i\vec{q}_k \cdot \vec{r}_{ij}) \right|^2 \quad (59)$$

where the first summation by  $k$  is over a set on six vectors  $\{\vec{q}_k\}$  chosen so that  $\exp(i\vec{q}_k \cdot \vec{r}_{ij}) = 1$  for any vector  $\vec{r}_{ij}$  connecting atom  $i$  with an atom  $j$  in the first or second neighbors shell in a perfect fcc lattice, and the second summation by  $j$  is over all the atoms found within a cutoff distance  $r_{cut}$  chosen so that the first two neighbor shells in a perfect fcc lattice are included. The choice of the six vectors  $\{\vec{q}_k\}$  is not unique, and the following set of vectors was found to provide an optimal sensitivity of the method:

$$\vec{q}_1 = \frac{4\pi}{a_{fcc}} [100] \vec{q}_2 = \frac{4\pi}{a_{fcc}} [010] \vec{q}_3 = \frac{4\pi}{a_{fcc}} [001] \vec{q}_4 = \frac{4\pi}{a_{fcc}} [110] \vec{q}_5 = \frac{4\pi}{a_{fcc}} [011] \vec{q}_6 = \frac{4\pi}{a_{fcc}} [101]$$

where  $a_{fcc}$  is the fcc lattice parameter.

For the method to work in general, three orthogonal vectors are enough. The additional vectors, however, increase the range of basic element  $\{\vec{q}_k\}$  orientation in crystal structure. For example, including vectors looking at the second neighbor shell  $q_4$ ,  $q_5$ , and  $q_6$  into the given set extend the sensitivity of the method against density fluctuations due to shock disturbance [62, 64]. In order words, the resulting value of the local order parameter will be now calculated on the relative orientation of the atomic bonds within the first and second neighbor shells with respect to that of a perfect fcc crystal with orientation [001]. A further increase of the basis range, however, would decrease the method sensitivity with respect to fast homogeneous melting. If this process is attributed with a strong laser-induced pressure relaxation across the system, the nuclei size smaller than diameter of third neighbor shell would be noised out.

Finally, in order to reduce the effect of the thermal atomic vibrations on the result of the structural analysis, the atomic positions used in the calculation of  $\Psi_i$  are averaged over 0.25 ps. Moreover, the local order parameter was by itself averaged over  $Z$  neighbors within first and second neighbor shell, as suggested in [114]:

$$\bar{\Psi}_i = \frac{1}{Z+1} \left( \Psi_i + \sum_{j=1}^Z \Psi_j \right) \quad (60)$$

As shown in Figure 17, the local order parameter defined above provides a quantitative measure of the “degree of crystallinity” of the local atomic configurations that agrees well with a visual analysis. The test atomic configurations were taken from the experiment of 200 fs laser melting of 50 nm free standing Ni film, considered later in this chapter in Section 3 a), Figure 30 and 31. The local order parameter changes from 0.00 to 1.00 with a value of  $\overline{\Psi}_i = 0.04$  chosen in this work to distinguish between the liquid and crystal structures.

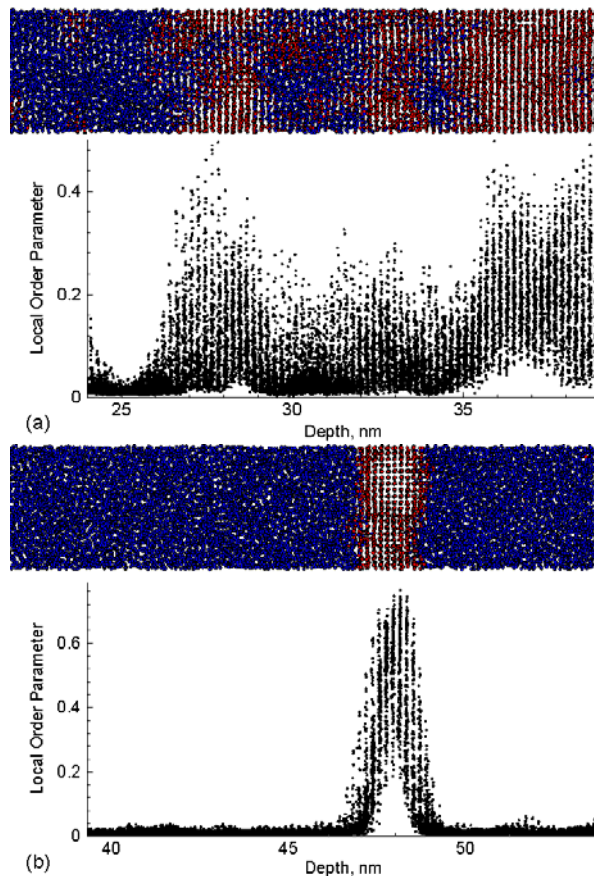


Figure 17. Distribution of the local order parameter for two configurations encountered in the simulations of laser melting in Section 3 a), Figure 31 and 32. Cutoff value of 0.04 is chosen for the local order parameter to distinguish between the crystalline and disordered atomic configurations.

### (c) Continuum Calculations with Microscopic Models

As it was mentioned above, limited by the quality of optical systems, it is difficult to focus a laser beam down to 1 micron in nanostructuring processes. But even a micron-size laser spot would result in the establishment of temperature gradient on the scale of several microns that in turn leads to relaxation of laser-induced stresses even on a bigger scale. The effect of laser-induced pressure waves was considered in Ref. [62, 116] and found to have a

significant influence on the kinetics of short pulse laser melting and therefore, on the nanostructuring process in general. Moreover, the propagation of the laser-induce pressure waves can also influence the resulting nanofeature [9,11,60] on the scale of microns, which is not possible to describe within the scale of Molecular Dynamics method because of its high computational cost.

As a first step, in order to overcome this limitation and to advance the continuum description of the laser-induced pressure waves we introduce the macroscopic-continuum model (MCM) [67, 120] in which the TTM model [70] is incorporated as well. Thus, on one hand, this model accounts for a long range relaxation of the laser-induced stresses, and on the other hand accounts for the electron properties of the solid in description of the heat conduction, electron-phonon nonequilibrium, and the laser-light absorption. In essence, the MCM model is based on three laws of the conservation: the conservation of mass, the conservation of momentum, and the conservation of energy. The governing equations for the MCM model will be as follows [67, 120]:

$$\begin{cases} \frac{d\rho}{dt} + \rho \vec{\nabla} \cdot \vec{v} = 0 \\ \rho \frac{d\vec{v}}{dt} = \vec{\nabla} \times \hat{\Pi} \\ \rho \frac{dw_{ph}}{dt} = \vec{\nabla} \cdot (\hat{\Pi} \times \vec{v}) - \vec{\nabla} \cdot \vec{q}_{ph} + Q_{coupl} \\ \rho \frac{dw_e}{dt} = -\vec{\nabla} \cdot \vec{q}_e + Q_{laser} - Q_{coupl} \\ \frac{d\hat{\Pi}}{dt} = 2\mu_s \left( \hat{E} - \frac{1}{3} \vec{\nabla} \otimes \vec{v} \right) - \frac{J(\hat{T}) - 1}{\tau_r} \hat{T} \end{cases} \quad (10)$$

where  $\rho$  and  $\mathbf{v}$  are the density and velocity,  $w$  and  $\mathbf{q}$  are the specific internal energy and heat flux,  $E$  is the strain rate tensor,  $\mu_s$  is the shear modulus and the subscripts  $ph$  and  $e$  are used for the lattice and electrons respectively. The energy exchange between lattice and electrons due to electron-phonon scattering is described with  $Q_{coupl}$  and the energy absorbed by the conduction band electrons is accounted for in  $Q_{laser}$ . The stress tensor  $\hat{\Pi}$  used in Eq. (10) is a function of lattice temperature  $T_{ph}$  and given by:

$$\hat{\Pi} = -p(\rho, T_{ph}) \hat{I} + \hat{T} \quad (11)$$

where  $p$  is the pressure,  $\hat{I}$  is the unit tensor and  $\hat{T}$  is the deviation part of the stress tensor  $\hat{\Pi}$ , containing the elasto-plastic stresses. The first term in the right part in the last Eq. in (10) describes the production of stresses due to elastic deformation according to Hooke's law. The second term in the right part of this equation describes the fast relaxation of the stresses due to plastic deformation according to von Mises yield condition. The function  $J(\hat{T})$  is defined as:

$$J(\hat{T}) = \begin{cases} 1, & r(\hat{T}) \leq 1 \\ r, & r(\hat{T}) > 1 \end{cases}, \quad r(\hat{T}) = \frac{T_1^2 + T_2^2 + T_3^2}{(2/3)Y^2} \quad (12)$$

where  $T_i$  are the principal components of the tensor  $\hat{T}$  and  $Y$  is the yield stress. Also, for the complete description, Fourier's law, the models of electron energy, and heat conduction, and the equations of state should be added to the system given by Eq. (10). The latter is especially important for an accurate description of the phase transition processes, induced by laser heating.

The solutions of equations (10) are found numerically when the time of stress relaxation to the yield limit tends to zero ( $\tau_r \rightarrow 0$ ). Although this simulation will be performed on the continuum level and thus samples sizes as big as several microns can be used, the calculations implementing the MCM may be as complex as the MD ones. In this approach, however, if a Gaussian pulse is used for the nanostructuring, the central symmetry of the system can be exploited. Therefore, the MCM model can be implemented in 2D in the Hydrodynamic Domain (HD), which significantly reduces the computational cost of the calculations. Therefore, HD calculations will be performed in semiplane schematically shown in Figure 18 on which the description of boundary conditions are indicated as well, similar to [121]. The interaction between the film and the substrate is described with Lennard-Jones potential  $U(r)$  as it was suggested in [17].

In a recent work by Meshcheryakov and Bulgakova [122] the elasto-plastic flow model, similar to the one described above, was applied to describe the nanostructuring mechanism responsible for the formation of nanofeatures in the experiments on Au [9, 11]. The 60 nm gold film was situated on quartz-glass substrate the interaction with which was discarded. The pulse duration of 30 fs was used at the fluencies on the order of  $0.1 \text{ mJ/cm}^2$  in order to simulate the film bending in response to the laser heating. Below, we cite the schematic picture published in [122], Figure 19, in which one can observe the process of formation of a microbump.

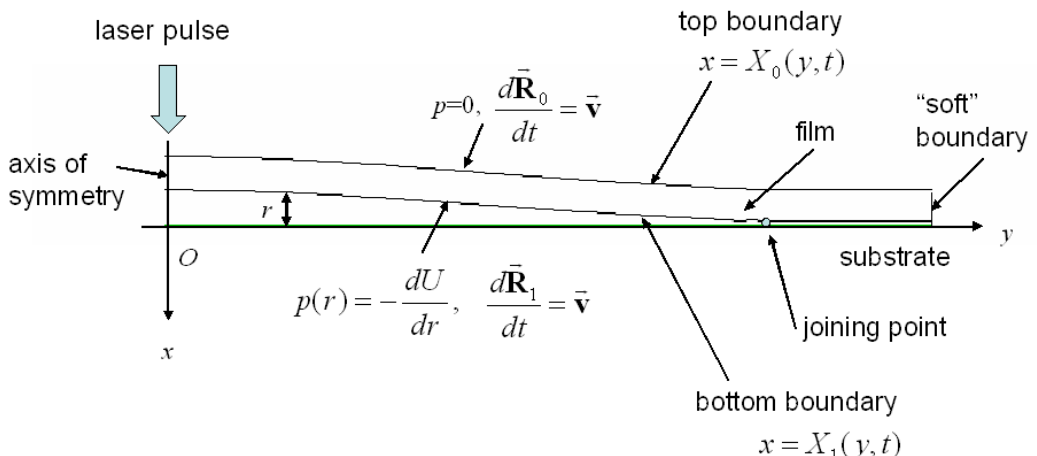


Figure 18. The HD domain in which continuum calculations in 2D will be performed is schematically shown along with the boundary settings according to Ref. [121].

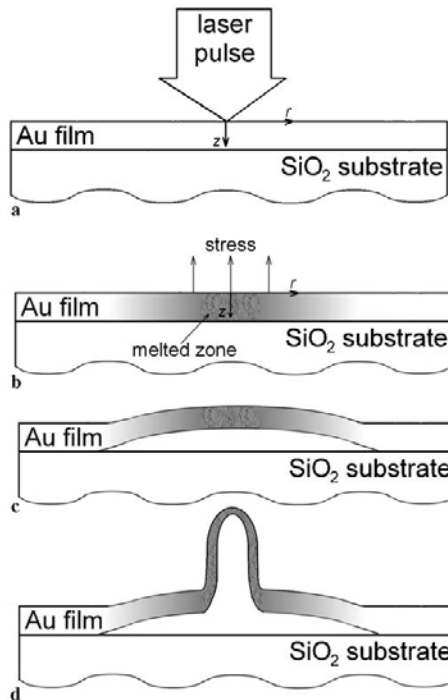


Figure 19. Schematic representation of the nanostructuring process on a thin Au film situated on a quartz-glass substrate published in Ref. [122]. (a) Laser light absorption by conduction band electrons. (b) Bending of the film due to laser heating. (c) Plastic forces seas the motion of solid, but not the molten material in the centre. d) Surface tension forces and cooling mechanisms finalize the formation of jet atop the microbump.

In spite of the obvious advantages of the MCM in computational approach to describe short pulse laser nanostructuring on the scale comparable with the experiment, there are certain difficulties in its successful applications. Calculations based on Macroscopic Continuum Models still require many assumptions to be made. The resulting model can not reliably describe the complex laser-induced nanostructuring processes that involve a series of phase transformation, especially under highly non equilibrium conditions. The description of melting on continuum level is a difficult task since the solid can be overheated far beyond of its equilibrium melting point and the melting mechanism itself can be strongly affected by the relaxation of the laser-induced pressure [62]. Accepting that the model described in [122] is valid for the description of microbumps formation on thin metal films, when metal-silica adhesion energy is negligible, its applicability for the bulk of material, when microshell formation inside of the material must take place, remains questionable. As a result, limited in the description of melting process and working with sub melting temperatures, the continuum model in [122] did not show explicitly the formation of a nanojet feature and the mechanism responsible for the formation of a nanojet is therefore schematically proposed in Figure 19.

A similar problem can be expected when applying the MCM model in description of the nanostructuring process. As it was shown in [36, 37, 116], for pico- and femto- second laser pulses, melting always precedes the spallation of films and bulk metal targets but the description of melting process, occurring under strong degrees of overheating and laser-induced pressure and temperature gradients, is hampered at continuum level.

#### (d) DFT Method for the Energy Deposition Dynamics

As it was mentioned above, the irradiation of solid matter with tightly focused laser beams can result in creation of the structures on nanoscale [9, 10, 11, 12]. The appropriate description of the laser-energy absorption in this case can become crucial for the further description of the system's dynamic. If the use of a laser source in short pulse laser interaction experiments can be reliably described by Eq. 4, Section 2 a), the experiments on nanostructuring with utilization of the near field optics can produce a highly nonequilibrium state of the electronic system when the applicability of the continuum description of the laser source given by Eq. 4 as well as the assumption about instant thermalization of the excited electrons and establishment of the Fermi-Dirac distribution become questionable [42, 48, 49, 50, 51]. For this purpose we suggest to use the Density Functional Theory approach [123] for an accurate description of the energy deposition in to the electronic system. In order to demonstrate the applicability of this method, in this section we present the problem on fast and dense energy deposition into the electronic system with swift heavy ions, probably the most extreme and difficult to describe example of the electronic system excitation.

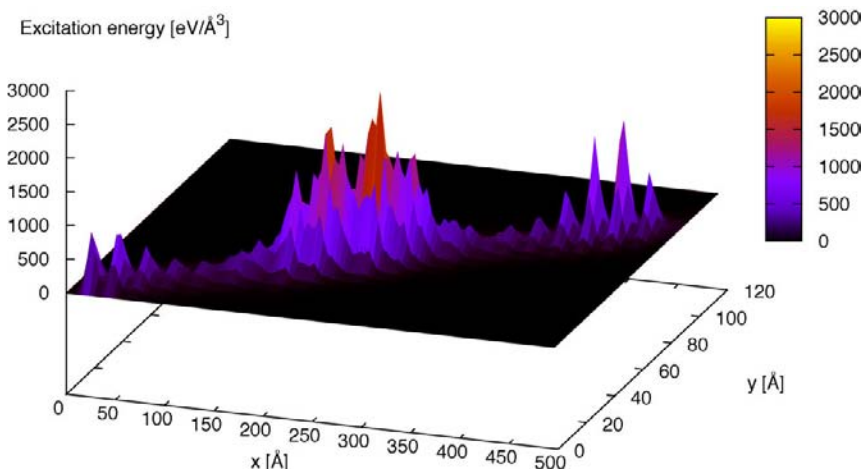


Figure 20. The energy per track length transferred to the electronic system due to the slowing down of the ion. A highly localized character of the energy deposition can be observed [139].

Similarly to the short pulse laser nanostructuring with near field optics, the irradiation of solid with heavy ions of 100 MeV energy is known to create structural modifications ranging from defects and amorphization in the bulk up to the creation of hillocks on the surface[19, 124, 125, 126, 127]. In this energy range, the projectile is slowed down almost exclusively by electronic interactions and the underlying physics of any surface damage/modification, due to intensive electronic excitation, can be therefore described in terms of the generation of a cylindrical zone of electronic excitation along the penetrating ion track. These excitations originate from the transfer of kinetic energy of the projectile to the electronic system of the target which is usually referred to as electronic stopping. The occurrence of surface damage in spite of the fact that this kinetic excitation is limited to a small radial area ( $8\text{--}10\text{ \AA}$ ) around the path of the primary particle indicates that the transport of excitation energy away from the track core must play an essential role in that process.

The standard model for  $\sim 100$  MeV irradiation of a solid surface is the inelastic Thermal Spike Model (TSM) [128, 129]. This model treats the electronic energy loss experienced by the moving projectile as a source of excitation energy of the electronic system assuming an instantaneous thermalization and is used to describe the energy transport heat diffusion in a cylindrical symmetry based on TTM model in Ref. [130, 131, 132]. Although this model has been quite successful in explaining a track radii in various materials created by irradiation perpendicular with respect to the surface [131], such approach requires many approximations as well as the fitting of the strength of the electron-phonon coupling. One of the effects during the high electronic excitation induced by the ion beam is the fact that the energy is deposited on a very small special scale. Therefore by changing the alignment of the incoming ion beam with respect to the target surface results in a drastic change of the energy deposition profile. This has been demonstrated by recent experiments [19, 133, 134] where the irradiation of perovskite crystals ( $\text{ABO}_3$ ) under glancing incidence has been shown to generate chain-like, periodic nanodots at the surface, Figure 1 c) in Section 1 a). In order to understand the nature of such kind of modifications the energy transfer of the ion to the target electrons must be correctly modeled. In particular belowe, we will consider the electronic system excitation in the nanostructuring experiments on  $\text{SrTiO}_3$  surface with swift heavy ions [19].

For ions with a few 100 MeV kinetic energy the stopping occurs via direct inelastic projectile-electron collisions and is often treated in terms of the Lindhard model [135], which gives the electronic stopping cross section as  $S_e = \beta v_p$  with a material parameter  $\beta$  depending on the specific target-projectile combination and  $v_p$  denoting the projectile velocity. For a target containing different elements  $i$  with individual  $\beta^{(i)}$  the effective electronic stopping cross section  $S_{e,\text{eff}}$  must be used. The electronic energy loss per track length,  $dE/dz$  (stopping power), of the projectile along its path through the solid then reads:

$$\left. \frac{dE}{dz} \right|_e = N_e(\vec{r}_p(t)) \beta_{\text{eff}} \left| \dot{\vec{r}}_p(t) \right| \quad (13)$$

where  $N_e(\vec{r}_p(t))$  denotes the electron density of the target at the position of the projectile. From here, it is evident that the electronic density of the target must be known function. Therefore, for its precise calculations DFT calculations were utilized. The electron density  $N_e(\vec{r})$  is calculated for one unit cell of the perovskite using the Abinit package [136] with Perdew-Burke-Ernzerhof (PBE) pseudopotentials from the Fritz-Haber-Institut [137]. Employing a cutoff energy of 2600 eV with a sampling of 512  $k$ -points on a cubic grid, the calculations have been carried out within the Generalized Gradient approximation (GGA) using the PBE functional [138]. The lattice constant of  $\text{SrTiO}_3$  has been determined as 3.905 Å by local energy minimization. The spatial resolution of this electronic density is around 0.1 Å, and was consider therefore to be accurate enought. The calculated density is inserted in Eq.13, which yields the electronic stopping experienced by the moving projectile, and thus the excitation of the electronic system. To calculate the transport of electronic energy away from the track on a large scale (typically track radii are 5 - 20 nm) the output of this DFT calculation is used as a input for a standard 3D TTM model explained in the Section 1 a). The energy transferred to the electrons per unit of track length in nanostructuring experiment on  $\text{SrTiO}_3$  with swift heavy Ions of 100 MeV calculated with the help of DFT method is shown in Figure 20. A very local character of the transferred energy is supporting the use of DFT

method in front of ordinary TSM continuum model for description of the electronic system excitation. More details on this modeling can be found in Ref. [139].

Since the DFT calculations are only performed for the first 10 fs after the excitation, the phononic system remains unchanged and is treated initially at equilibrium at room temperature. The initial electronic temperature for the TTM is taken from the DFT calculations by fitting the electronic excitation energy to local Fermi distributions. This approach, using high resolved DFT electronic density data, provides information regarding the geometric relations of the target material with the incoming ion beam, which are not included in models using a simple homogenous free electron gas. The excitation of the electron system is directly included and can be used for further studies, not only for track radii calculations as it was explained here, but also in any other experiments where highly localized energy deposition must be described, for example in short pulse laser nanostructuring experiment with near field optics [42, 48, 49, 50, 51].

However, it is necessary to remark here that the calculated energy of electronic system by the time of 10 fs is by no means in equilibrium. While a strict DFT calculation of the excited electrons will eventually lead to an equilibrium electron distribution and possibility to use Fermi-Dirac statistics for temperature definition, this kind of calculations take a lot of CPU-time and are still limited to a small spatial area. A more appropriate model based on Boltzmann statistics and aimed on a treatment of the non equilibrated electron systems is presented in the next section.

### (e) Nonequilibrium Electron Dynamics Modelled with Boltzmann Equations

As mentioned in the previous sections, upon strong excitation free electrons in a solid can turn to a highly nonequilibrium state. Applying the two-temperature model, the nonequilibrium between electrons and phonons is accounted for. However, for timescales in the femtosecond regime even the concept of temperature is questionable. Indeed, only a few electrons in the solid will absorb one or several photons. As long as the energy is not redistributed among all free electrons, a Fermi distribution and thus a temperature cannot be determined. This redistribution of energy is caused by electron-electron collisions and called thermalization. Transient changes of distribution functions can be most effectively described in terms of the Boltzmann equation. Several works apply such kinetic approaches to study the effect of a nonequilibrium (i.e. a non-Fermi) distribution in laser-excited solids [24, 26]. In the Boltzmann equation, the changes of distribution function are due to spatial flux on one hand and caused by collisions on the other hand. For the case of ultrafast interaction of laser with metals, mainly three collision processes are relevant. First, is a collision term describing the absorption of a photon by an electron. To fulfill energy and momentum conservation at the same time, a third collision partner is required, given by the lattice. Second, as stated above, collisions in between the free electron gas, i.e. electron-electron collisions play a crucial role to describe the thermalization and thus the transition from the necessity of a kinetic approach to the applicability of the two-temperature model. Third, the energy transfer from the excited electron gas to the lattice, described as electron-phonon collisions starts in the femtosecond regime (the electron-phonon collision time) and has to be accounted for. In the case of kinetic description of laser interaction with semiconductors and/or dielectrics, also the increase of the free electron density by ionization processes as (multi-)photon ionization

across the band gap or electron-electron collision with band transition (impact ionization) have to be included as separate collision terms. For the numerical calculation of the time-dependent Boltzmann equation, spatial transport is neglected. If one assumes also spatial isotropy, the equation depends only on time and energy. The collision term for the electron occupation number  $f$  is composed of collision terms for each considered process. The system of Boltzmann's equation for the calculation of the distribution functions of electron gas and phonon gas reads:

$$\begin{cases} \frac{\partial f(\vec{k})}{\partial t} = \left. \frac{\partial f(\vec{k})}{\partial t} \right|_{el-el} + \left. \frac{\partial f(\vec{k})}{\partial t} \right|_{el-phon} + \left. \frac{\partial f(\vec{k})}{\partial t} \right|_{absorb} \\ \frac{\partial g(\vec{q})}{\partial t} = \left. \frac{\partial g(\vec{q})}{\partial t} \right|_{phon-el} \end{cases} \quad (14)$$

Here,  $f(k)$  and  $g(q)$  are distribution functions of electrons and phonons depending on the modulus of wave vector  $\mathbf{k}$  and  $\mathbf{q}$ , respectively.

The complete Boltzmann collision terms can be found elsewhere [24, 61, 140]. For the electron-electron interaction, the matrix element is given by a screened Coulomb integral. The screening length can be calculated as follows directly from any distribution function [141], thus also as in our case from a strongly nonequilibrium distribution function:

$$k_{sc}^2 = \frac{e^2 m_e}{\pi^2 \hbar^2 \epsilon_0} \int_0^\infty f(\vec{k}) d\vec{k} \quad (15)$$

The electron-phonon interaction can be described by a standard collision term as given by Allen [142]. The matrix element for electron-phonon interaction in metals is given in Ref. [143]. Photon absorption of free electrons requires a third collision partner to provide energy and momentum conservation. To describe photon absorption by free electrons we apply an expression deduced by Epshtain in 1970 [144]. It combines the collision terms for electron-phonon interaction and absorption of laser energy by electrons, resulting in a single electron-phonon-photon collision term, which includes the matrix element of electron-phonon collisions,  $M_{e-ph}(\mathbf{q})$ . The possibility of multiphoton absorption and emission is taken into account, its probability being expressed in Bessel's functions  $J_\ell$ , where subscript indicates  $\ell$  the number of photons absorbed or emitted. The argument of Bessel's function includes the electric field amplitude  $\mathbf{E}_L$  and the frequency  $\omega_L$  of the laser.

$$\begin{aligned} \left. \frac{\partial f(\varepsilon_{\vec{k}})}{\partial t} \right|_{el=phon-phon} &= \frac{2\pi}{\hbar} \sum_{\vec{q}} |M_{e-ph}(\vec{q})|^2 \sum_l J_l^2 \left( \frac{e \vec{E}_L \cdot \vec{q}}{m \omega_L^2} \right) \times \\ &\times \sum_{loss/gain} F \left[ f(\varepsilon_{\vec{k}}), g(\varepsilon_{\vec{q}}), f(\varepsilon_{|\vec{k}+\vec{q}|}) \right] \delta \left( \varepsilon_{|\vec{k}+\vec{q}|} - \varepsilon_{\vec{k}} \pm \varepsilon_{\vec{q}} + l \hbar \omega_L \right) \end{aligned} \quad (16)$$

The functional  $F$  and other details can be found in the article of Epshtain [144]. Note the product  $\mathbf{E}_L \cdot \mathbf{q}$  in the argument of Bessel's function: The electron absorbs energy if the wave

vector  $\mathbf{q}$  of mediating phonon has a component in the direction of electric field  $\mathbf{E}_L$ . Since we do not consider the polarization of the laser at the moment,  $\mathbf{E}_L$  is averaged over all directions. For the case of no irradiation, Eq. (14) turns to a collision term for pure electron–phonon interaction.

In metals, also inverse Bremsstrahlung, where an electron changes its momentum when colliding with an ion core, has to be considered [61]. This absorption can be described by essentially the same collision integral, Eq. 16, where the Matrix element of Coulomb interaction of electron with rigid ion cores is applied. Note, that in our approach collisions of electrons with fixed ions are assumed to change solely the momentum of free electrons. The energy exchange of free electrons and lattice is described through electron-phonon collisions.

Assuming parabolic energy dispersion of electrons and Debye's dispersion relation for phonons, and taking advantage of the assumed isotropy, the dimensions of the collision integrals can be reduced analytically. After that, a numerical treatment of the equation system is possible: Discretizing the energy axes, we transform Eq. 15 into a system of  $\sim 250$  coupled, nonlinear integro-differential equations which we solve with Runge-Kutta integration of fifth order with automatic step-size control [139]. With this procedure, we are able to follow the time evolution of the distribution functions  $f(\varepsilon(\mathbf{k}), t)$  and  $g(\varepsilon(\mathbf{q}), t)$  and observe their changes due to excitation of the electron gas by the laser beam, thermalization of the electron gas by electron-electron collisions and energy exchange between electron gas and phonon gas due to electron-phonon collisions.

The model has successfully been applied for the description of electron dynamics in aluminum, where three free electrons resemble in a good approximation a parabolic dispersion relation. For the calculation of the time evolution of distribution functions in a given metal a few parameters have to be provided. These are the free electron density  $n$ , the wave number at Fermi energy,  $\mathbf{k}_{F,0}$ , the number of free electrons per atom, and Debye's wave number which are taken from standard tables [21, 146]. The effective electron mass and the speed of sound are found from comparison of resulting heat capacities with experimental values. This leads to an effective electron mass of  $m_e = 1.45m_{e,free}$ , as also derived in Ref. [147]. The phonon heat capacity turned out to be best reproduced applying the sound speed of longitudinal phonons. Thus, only parameters describing the unperturbed solid enter the calculation.

To calculate the excitation of the electron gas by laser irradiation we assume a laser pulse of rectangular intensity profile with duration  $\tau_L = 100$  fs and vacuum wavelength  $\lambda = 630$  nm corresponding to a photon energy of  $\hbar\omega_L = 1.97$  eV = 0.245  $\varepsilon_{Fermi}$ . Figure 21 shows the transient behavior of the occupation number of free electrons for an electric laser field of amplitude  $E_L = 1.4 \times 10^8$  V/m, corresponding to an intensity of  $I_L = 7 \times 10^9$  W/cm<sup>2</sup> and an absorbed fluence of  $F_{abs} = 0.7$  mJ/cm<sup>2</sup>. This is a weak intensity far below damage threshold ( $F_{thresh,abs} = 17$  mJ/cm<sup>2</sup>). A function  $\Phi$ , shown in Figure 21, is defined as:

$$\Phi(\varepsilon) = -\ln\left(\frac{1}{f(\varepsilon)} - 1\right) \quad (17)$$

This function increases with increasing  $f$  and is especially suitable to visualize the perturbation of the electron gas: In thermal equilibrium, when electrons obey a Fermi-Dirac-distribution,  $\Phi(\varepsilon)$  equals  $(\varepsilon_{Fermi} - \varepsilon)/(k_B T_e)$ . In this case,  $\Phi(\varepsilon)$  is a linear function with a slope

proportional to the inverse electron temperature  $1/T_e$ . Thus, a deviation of the electron gas from thermal equilibrium is directly reflected in a deviation of  $\Phi(\epsilon)$  from a straight line.

In Figure 21 a) the strong perturbation of the electron distribution immediately after the begin of irradiation can be seen (solid line). In comparison to the straight line representing the Fermi distribution at 300 K, the absorption of photons lead to a step-like distribution function: Electrons below Fermi energy absorb photons, leading to an increase of the occupation number of electrons with energies up to  $\hbar\omega_L$  above Fermi energy. Further absorption of photons by excited electrons lead to an increase of the occupation number for energies up to  $2\hbar\omega_L$  above Fermi energy. The occupation number of electrons below Fermi energy decreases at the same rate, reproducing the Fermi edge in steps of  $\hbar\omega_L$ . A similar step-like electron distribution function for electrons above Fermi energy was found in Ref. [26]. Experimentally the first plateau of excited electrons was observed in gold in Refs. [148, 149], and theoretically reproduced in Ref. [150]. Our log-like plot of the function  $\Phi(\epsilon)$  defined by Eq. 17 has the advantage that not only excited electrons above Fermi energy but also “holes” below Fermi energy can be observed.

Figure 1 b) shows the completion of electron thermalization around the Fermi edge after irradiation. A straight line in  $\Phi(\epsilon)$  and thus a Fermi distribution is established quickly after irradiation ended. Now the effect of electron-phonon interaction is also visible: Cooling of the hot electron gas leads to an increasing modulus of the slope of  $\Phi(\epsilon)$ , corresponding to lower electron temperatures.

The electron cooling, i.e. the energy exchange between electrons and phonons can be studied more in detail as follows: By integrating over the distribution function we find the internal energy of the subsystems at each time step. The energy  $\delta u_{(e,p)}$  is defined as the difference of internal energy  $u_{(e,p)}$  and the internal energy of electrons and phonons, respectively. Thus, for the electrons the internal energy is given as:

$$\delta u_e = u_e - u_e(f_{Fermi,300K}) = \frac{2}{2\pi^2} \int_0^\infty (f(\vec{k}) - f_{Fermi,300K}) \frac{\hbar^2 k^2}{2m_e} k^2 dk \quad (18)$$

The increment of internal energy of phonons,  $\delta u_p$ , is calculated analogously. The sum of both increments of internal energy gives the total absorbed energy,  $\delta u$ . The constancy of  $\delta u$  after irradiation provides a good check of numerical stability.

Figure 22 shows the transient behavior of energy increase for the electron gas, the phonon gas and the total absorbed energy, respectively, for the case of excitation with a laser pulse of 100 fs duration and an intensity of  $I_L = 7*10^9$  W/cm<sup>2</sup>. The absorbed energy  $\delta u$  increases linearly during irradiation with constant intensity. In [151] we studied the absorption characteristics for different intensities. We found linear absorption corresponding to an exponential absorption profile. Also the strength of absorption compares very well with literature.

The energy increase of the electron gas  $\delta u_e$  follows the total absorbed energy, with a slight decrease due to energy transfer to the phonon gas during the pulse. After irradiation, energy transfer from the electron gas to the phonon gas continues until both systems have the same temperature. Because of the large difference in heat capacity, this corresponds to a much lower internal energy of the electron gas than that of the phonon gas. As also shown in Figure 22 the rate of energy transfer from the disturbed electron gas to the phonon gas is

essentially the same as the energy transfer rate from a hot electron gas with Fermi-Dirac distribution of the same initial energy. The absorbed energy of  $\delta u_e$  of the laser excited electron gas corresponds to a Fermi distribution at  $T_e = 3400$  K. We extract an electron-phonon coupling constant  $G$  as used in the TTM model [70] and obtain a value of  $G = 3.1 \times 10^{17}$  J/Ksm<sup>3</sup> for aluminum.

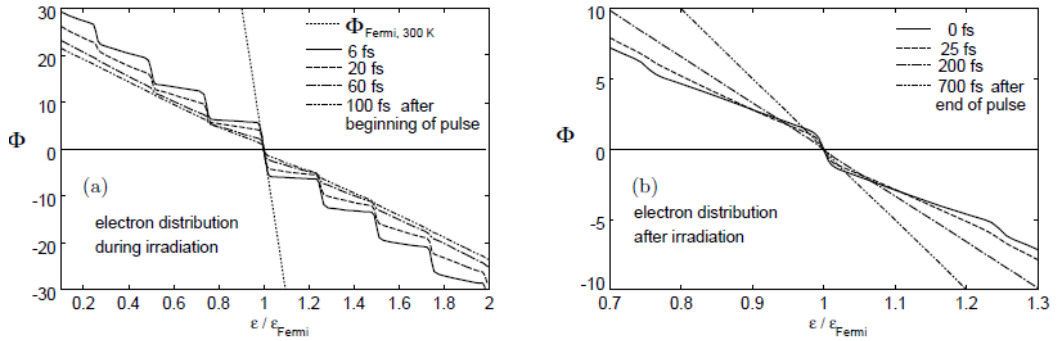


Figure 21. Distribution function of free electrons in aluminum: (a) during and (b) after irradiation. The quantity  $\Phi$ , defined by Eq. 17, is shown as a function of electron energy. A laser pulse with constant intensity of  $I_L = 7 \times 10^9 \text{ W/cm}^2$  of 100 fs duration and a photon energy of  $\hbar\omega_L = 1.97 \text{ eV} = 0.245 \epsilon_{\text{Fermi}}$  was assumed.

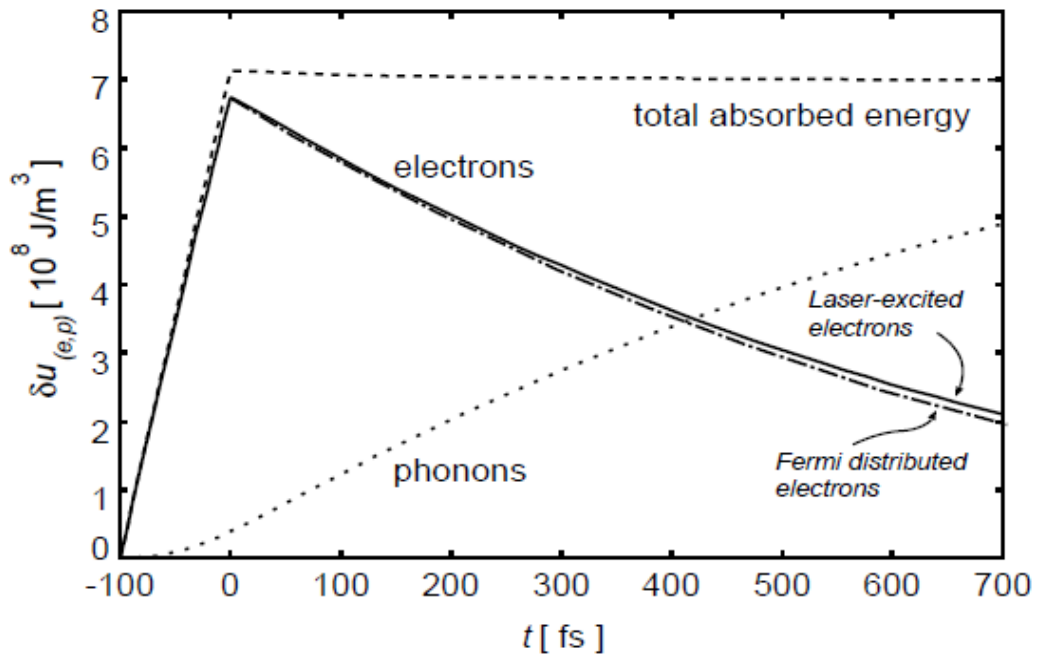


Figure 22. Transient energy increase of electron gas,  $\delta u_e$ , and of phonon gas,  $\delta u_p$ , respectively, and total absorbed energy  $\delta u$ . Additionally the cooling of a Fermi distributed electron gas is shown. The same laser parameters as in Figure 21 were applied.

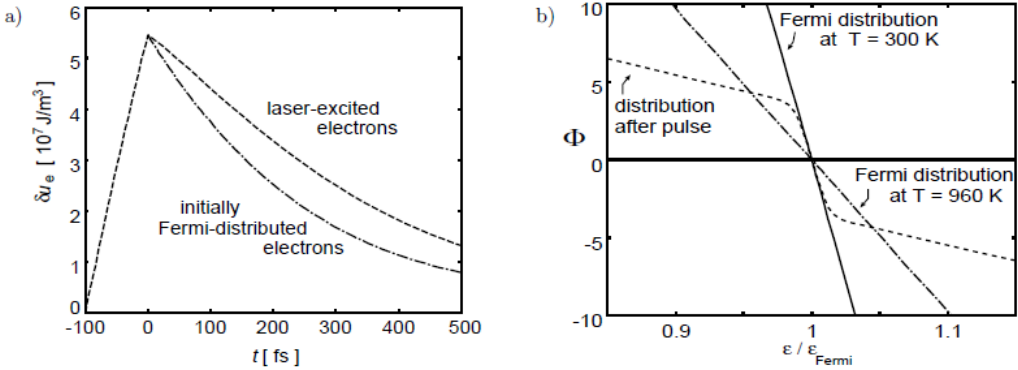


Figure 23. Weak excitations: (a) Transient internal energy of laser-excited electron gas and of the corresponding hot Fermi distributed electron gas. (b) Distribution function of laser-excited electron gas, the corresponding hot Fermi distributed electron gas and Fermi distributed electron gas at room temperature.

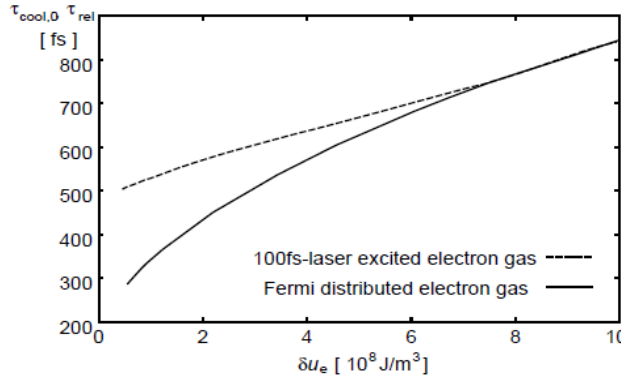


Figure 24. Cooling time of laser-excited electron gas after irradiation of a 100 fs laser pulse with constant intensity (dashed line) and characteristic relaxation time of a Fermi distributed electron gas (solid line) both interacting with a phonon gas at initially 300 K.

For weak excitations, however, we find that the two temperature model does not hold. In Figure 23 we assumed a laser intensity of  $I_L = 5.8 \times 10^8 \text{ W/cm}^2$  leading to an energy increase of  $\delta u_e = 5.5 \times 10^7 \text{ J/m}^3$ , corresponding to a Fermi distribution at  $T_e = 960 \text{ K}$ . Figure 23 a) shows that the initial cooling rate of the laser-heated electron gas is substantially lower than the cooling rate of the corresponding Fermi-distributed electron gas. This is due to the non-equilibrium of the laser-heated electron gas: At  $t = 0$  the electron distribution functions interact with a phonon gas of about 300 K. Thus, at this moment the electron–phonon interaction acts on the electron gas in a way that it tends to establish Fermi distribution with 300 K. To this end, electrons above Fermi energy have to be transferred to states below Fermi energy. However, due to the small phonon energy, the phonons are able to act on the electrons only in a small region around Fermi’s edge. The maximum phonon energy in the case of aluminum is about  $0.08 \epsilon_{\text{Fermi}}$ . Figure 23 b) shows three distribution functions of the electron gas: the laser-excited electron gas at the end of irradiation, the Fermi distributed electron gas of the same energy, and a Fermi distribution of 300 K. As before, the function  $\Phi(\epsilon)$ , defined by Eq. 17, is shown. In the region of one maximum phonon energy ( $0.08 \epsilon_{\text{Fermi}}$ ) around Fermi energy the laser-excited electron gas shows nearly no deviation from the Fermi

distribution at 300 K. Thus, the phonon action on the non-equilibrium electron gas is rather inefficient. In contrast, the corresponding Fermi distribution of a hot electron gas shows a large deviation from the Fermi distribution of 300 K. Therefore here the cooling by the cold lattice is much more efficient. This leads directly to the different cooling rates, i.e. different slopes of energy decay at  $t = 0$  in Figure 23 a). Such delay of energy transfer to the lattice for a laser perturbed electron gas as compared to the TTM model was observed experimentally at low temperatures and for very low intensities [152, 153].

Figure 24 shows the “relaxation time”  $\tau_{rel}$  of the energy between a high-energetic electron gas and the cold lattice. For the laser excited electron gas we prefer the name “initial cooling time”  $\tau_{cool,0}$ , first to pronounce that we refer to the energy decrease directly after the pulse and second, to avoid the impression of a general feature of the heated electron gas. In contrast,  $\tau_{cool,0}$  depends strongly on pulse characteristics. Figure 24 shows the delay of energy transfer between laser excited electron gas and lattice in comparison to the energy transfer between Fermi distributed electron gas and lattice occurs only at weak excitations. For stronger excitations, as also shown in Figure 22, there is no difference between both kinds of excitation and the relaxation time  $\tau_{rel}$  becomes characteristic for the amount of internal energy. It is important to note that all intensities studied here are below melting threshold. Concerning laser induced nanostructuring, we thus conclude, that the energy exchange between electron gas and phonon gas can be described by the well-known TTM model [70].

However, there are several limitations of the applied calculation, leading directly to the future scope of interest in this field. First of all we did not consider spatial behavior. This is a numerically challenging problem, however worth to study since experiments indicate an effect of ballistic motion of hot electrons which are present for non-thermal energy distribution [83]. The comparison of the kinetic approach with the two-temperature model with respect to heat conduction will reveal the influence on nonequilibrium electron distribution on energy dissipation, essential for nanostructuring with ultrashort pulses.

Second, different materials, in particular noble metals with a d-band of electrons in the range of one or two photon energies below Fermi-energy, have to be modelled. Calculations of electron-phonon coupling parameter [31, 32] assuming a Fermi function for the occupation number reveal for high temperatures, that these d-electrons strongly increase the coupling strength. In case of nonequilibrium electron distribution an influence of d-electrons is expected by far lower temperatures, since d-electrons can be excited into free places below Fermi edge, thus increasing the number of free electrons in the conduction band and increasing the energy exchange between electrons and phonons. The modeling of these extensions of the kinetic approach is currently in progress.

### 3. COMBINED MODELS FOR SHORT PULSE LASER NANOSTRUCTURING ON MATERIALS

#### (a) Previously Tested Models and the Strategy of the Models Construction for the Purpose of Nanostructuring

Research efforts towards the development of direct-write laser technologies have yielded a significant progress in fabrication of surface nano- and micro-structures with spatial

resolution exceeding the optical diffraction limit. The spatial resolution achievable in laser surface processing is defined by the ability to concentrate the laser energy deposition in a smallest possible domain. Several approaches have been demonstrated to be instrumental in achieving highly localized laser energy deposition, including the use of tightly focused laser beams with the peak laser fluence close to the threshold for material modification [9, 10, 11, 12, 15] or utilization of the optical near field effects, e.g. a local field enhancement in the vicinity of a probe tip [48, 49, 50, 51] or a deposited nano/micro-particle [148,149] or by means of ion bombardment [19, 124, 125, 126, 127]. While the ability to generate arrays of nanoscale surface features opens up a range of opportunities for practical applications, the processes responsible for the surface nanostructuring are not yet fully understood.

As of the present time, there have been numerous computational methods developed to study laser-induced processes, like laser melting [30, 39, 45, 79, 101, 116, 119], spallation [53, 63, 64, 80], and ablation [28, 35, 37, 54, 56, 57, 59, 116, 156]. None of them, however, meet the challenge of accurately describing a nanojet formation in experiments by Chichkov or Nakata, Figure 1 a) and b), [9, 10, 11, 12, 18, 60], which is the objective of this work. In the work by Meshcheryakov and Bulgakova [122], considered in Section 2 c), the formation of the microbump was ascribed to the development of thermoelastic stresses in the film, resulting in its bending. Although original, the work represents a rather simplified approach to a complex phenomenon. The description of the stress tensor, the central point of the model, was approximated with linear equations and the thermoelasticity itself was only included on the boundaries of the computational domain. Finally, the melting process that was speculatively suggested as a mechanism responsible for the formation of the nanojet in [9, 10, 11, 12], was not explicitly included in the model at all [122].

Another possible explanation of the nanojet grow in experiments was given by the group of Chichkov [9, 10, 18, 60]. The formation of these structures was suggested to be due to the Marangoni effect [157, 158], which is the establishment of a thermocapillary flow, induced by the temperature gradient on the material surface followed by the Gaussian beam intensity profile of the laser beam. The temperature gradient on the surface creates a tension gradient that drives material from the hot centre to the cold periphery or vice versa depending on the material [159]. The formation of the nanojet structures, however, if in the molten phase, must take place on a picosecond time scale in femtosecond laser pulse experiments [35, 160, 161]. Even though observed in nanosecond experiments [162, 163], the establishment of such strong convective flows in the experiments by Chichkov on a nanoscale is considered rather doubtful. The Figure 25, shows the velocity vector filed of the ejected matter at  $t = 50$  ps in nanostructuring simulations, considered later in Section 3 c). The molten part of the material is depicted in particle velocity vectors whereas the atomic configuration of the solid is colored according to the local order parameter, see Appendix in Section 2 b). At this time the hydrodynamic motion of the molten part is established. However we do not observe Marangoni effect in this experiment. This can be seen in Figure 25, where particle velocity vectors are merely directed up, oppositely to the direction of the absorbed laser pulse, and not organizing in anyhow noticeable curls discarding this effect therefore as a possible mechanism of the surface restructuring due to tightly focused short-pulsed laser beams.

Finally, the origin of driving force responsible for the acceleration of molten material followed by the formation of nanofeature in the experiment by Nakata was explained due to pressure of evaporating material between the film and substrate [11, 12]. However, since working with fluencies around threshold for material modification (melting), the evaporation

process is essentially surprised. This is also confirmed in theoretical calculations on short pulse laser melting [37, 116, 119], where no volatile particles are observed even in simulations on spallation of metal targets [36, 64]. Thus, the development of somehow meaningful pressure necessary for material restructuring due to evaporation mechanism in the experiments [11, 12] does not look realistic.

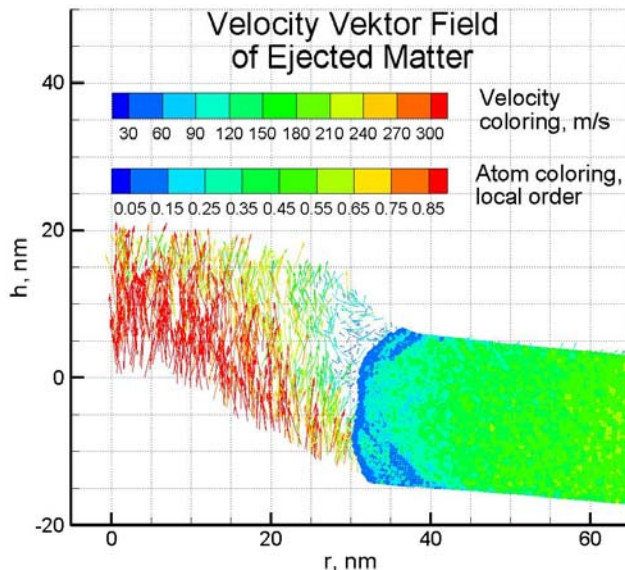


Figure 25. The velocity vector filed of nanostructured sample, showed for a cross section in a randomly chosen radial direction outward the centre. The configuration was taken from the nanostructuring experiment, considered in Section 3 c) at  $t = 50$  ps when the process of ejection matter is completely established.

Therefore, the theoretical models considered above do not account for the essential effects taking place during short pulse laser-metal interactions. As it was considered in Section 1 c), these effects include non equilibrium laser-induced phase transformations, occurring under conditions of strong superheating and fast deformation rates, strong electron-phonon nonequilibrium induced by a short laser pulse, fast electron heat conduction, and the laser energy absorption by the conduction band electrons. To account for these processes in this study, the strategy of computational investigation of the formation of surface nanostructures is outlined below.

Computer modeling of the material response to short pulse laser irradiation indeed has a potential for providing information on the physical processes responsible for the formation of sub-micron frozen surface structures in laser nanotexturing. Depending on the required precision and the available computational power, the same processes in the area of laser-matter interactions can be described on the potentially different levels: from the experimentally visible scale,  $1 - 10^{-6}$  m, with Macroscopic Continuum Models; to atomistic description,  $10^{-6} - 10^{-9}$ , with Molecular Dynamics Method; down to nuclear size,  $10^{-9} - 10^{-15}$  with First Principles, *ab-Initio* calculations [164, 165].

Clearly, computational models based on first principles would provide a precise result on the system's evolution upon the absorption of the laser irradiation. The solution of such system, however, is very costly from the point of computational power. Even the world most

powerful computer at the Lawrence Livermore National Laboratory can reasonable work with a system consisting of only  $\sim 10^3$  atoms since the number of operations grow as fast as  $N^3$  with number of atoms  $N$  and even faster [166].

Calculations based on continuum models, on the other hand, capable of working on experimental scale, requires implementation of many assumptions originating from unclear knowledge of fast nonequilibrium processes involved into short pulse laser nanostructuring experiments. In particular, it is difficult to describe the phase transformations and liquid disruption occurring under conditions of strong superheating and high deformation rates within the conventional hydrodynamic computational models.

Molecular Dynamic (MD) calculations appear to balance the precision of the system analyzed on the atomic level and yet a possibility to compute on a micron scale. One of the advantages of the MD approach is that all the material properties are given *a priori*, via interatomic potential, which in most of the applications presented in this chapter was described via Embedded Atom Method (EAM) with parameterization suggested by Johnson [167]. While being relatively computationally expensive, MD therefore does not require any assumptions to be made about the processes and mechanisms of interest and is well suited for investigation of fast dynamic material response to short pulse laser irradiation.

However, as we could see from Section 2 b), the MD model, when applied alone, do not account for several important processes that can be induced by a short pulse laser interaction with metals and that can play a determinant role in short pulse laser nanostructuring. Particularly, neglecting the free-electron contribution to the transport properties in study by Clancy [168] was reflected in the values of the thermal conductivities of the considered metals being roughly two orders of magnitude lower when compared to their experimental values. The heat conduction due to the free electrons is the main heat transport mechanism in metals and this drawback resulted in the overestimation of the established temperature gradient (sureface heat confinement) during the simulations that in turn certainly affected the melting mechanism in general [168].

To account for the free electron system the Two Temperature Model (TTM) can be applied, see Section 2 a). While the description of free electron system in this model has been successfully applied to investigate the kinetics of the electron and lattice temperature evolution in several theoretical studies and experimental works [29, 83, 84, 85], being realized at continuum level, its application in phase transformation description is hampered. In particular, the physics of ultrafast phase transformations and damage occurring under highly nonequilibrium conditions is not well understood and, therefore, cannot be reliably described by a set of kinetic equations.

In this chapter, therefore, the computational investigation of the formation of the surface nanostructures [9, 10, 11, 12] shall be performed with the hybrid atomistic-continuum models, that possess the advantages of different computational approaches and can act in a wide spawn of time and spatial scales. The strategy of multiscale computational approaches was already successfully tested when studying such complex phenomenon as a crack propagation in crystals [169], plasticity modeling in materials [170], and laser-induced shock waves in a solid [171]. Although requiring a careful implementation and sometimes a complex computational technique, especially at the borders of different numerical schemes, the combined models nevertheless are capable of describing some times nearly incomparable processes. In the next Section 3 a) we present the basic atomistic-continuum method aimed on description of short-pulse laser-metal interaction process. The kinetics of fast non equilibrium

phase transformation processes will be treated at the atomic level with MD, whereas the description of laser light absorption by free carriers, their transport dynamics, and strong laser-induced electron-phonon non equilibrium are accounted for in the continuum part of the model based on TTM approach. The essential laser-induced processes that can potentially act in the nanostructuring mechanism therefore (see Section 1 c) are described within the scale of a single computational approach TTM-MD. This method will become a basic model, which will be then enhanced and modified for the purpose of laser nanostructuring on metals and expanded for further applications to other materials: semiconductors and insulators, see Section 3 e) and f).

## (b) Combined Model for Short Pulse Laser Melting of Metals

Our goal in this section is designing the new computational approach that could overcome the limitations and combine the advantages of traditional TTM and MD methods in description of short pulse laser interaction processes on metals and demonstrating the efficiency of hybrid computational approaches when studying complex and multiscale phenomenon. We developed a computational model (TTM-MD) that combines the classical MD method for simulation of non-equilibrium processes of lattice superheating and fast phase transformations with a continuum description of the laser excitation and subsequent relaxation of the conduction band electrons, based on TTM [116].

In the combined TTM-MD method, schematically illustrated in Figure 26, MD completely substitutes the TTM equation for the lattice temperature, Eq. 1, in the surface region of the irradiated target, where the most active processes are expected to occur. The diffusion equation for the electron temperature  $T_e$  is solved by a finite difference method simultaneously with MD integration of the equations of motion of atoms and the electron temperature enters the coupling term [101], which is responsible for the energy exchange between the electrons and the lattice:

$$\begin{cases} C_e(T_e) \frac{\partial T_e}{\partial t} = \frac{\partial}{\partial z} \left( K_e(T_e) \frac{\partial}{\partial z} \right) - G(T_e - T_l) + S(z, t) \\ m_i \frac{d^2 \vec{r}_i}{dt^2} = \vec{F}_i + \xi m_i \vec{v}_i^T \end{cases} \quad (19)$$

where

$$\xi = \frac{1}{n} \sum_{k=1}^n G V_N (T_e^k - T_l) \Bigg/ \sum_i m_i (\vec{v}_i^T)^2 \quad (20)$$

In Eq. 19,  $m_i$  and  $\vec{r}_i$  are the mass and position of an atom  $i$ , and  $\vec{F}_i$  is the force acting on atom  $i$  due to the interatomic interaction. An additional term, added to the ordinary MD equations of motion, accounts for the electron-phonon coupling. A modified, as compared to

earlier works [101], formulation of the coupling term is used in the model and is described below.

In this section for the beginning we assume the laser spot size, as it is in the typical short-pulsed laser-matter interaction experiment, to be much larger as compared to the depth affected by the laser heating. Thus a one-dimensional version of the diffusion equation for electron temperature, Eq. 1, is used here, in Eq. 19.

In the combined TTM-MD model the cells in the finite difference discretization are related to the corresponding volumes of the MD system and the local lattice temperature is defined from the average kinetic energy of thermal motion of atoms,  $K^T$ :

$$T_1 = \frac{2K^T}{3k} = \sum_i m_i (\bar{v}_i^T)^2 / (3kN^{\text{cell}}) \quad (21)$$

where the summation is performed over all the  $N^{\text{cell}}$  atoms in a given cell. In this definition, it is important to distinguish between the thermal velocities of the atoms,  $\bar{v}_i^T$ , and the velocities of the collective motion of atoms in a cell. For any atom, the thermal velocity is defined as  $\bar{v}_i^T = \mathbf{v}_i - \mathbf{v}_c$ , where  $\mathbf{v}_i$  is the actual velocity of an atom  $i$ , and  $\mathbf{v}_c$  is the velocity of the center of mass of a cell to which atom  $i$  belongs.

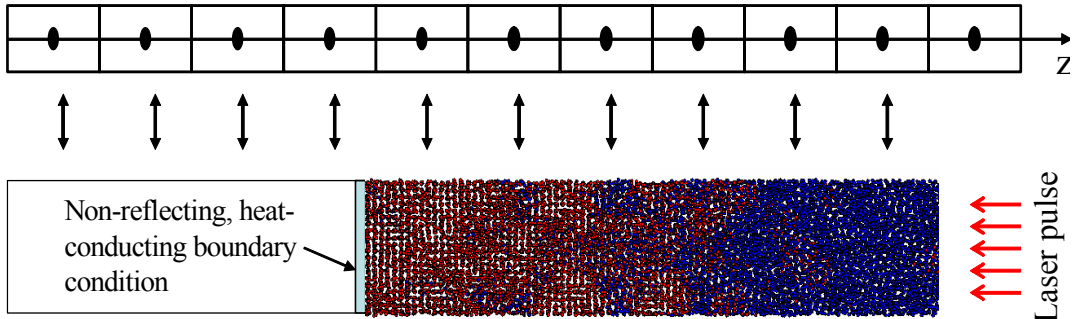


Figure 26. Schematic representation of the combined atomistic-continuum model. The evolution of electron temperature is described by a non-linear differential Eq. 19, whereas the atomic motions are described by the MD method with additional forces that account for the energy exchange due to the electron-phonon coupling. Spatial discretization in the continuum model (typically  $\sim 1$  nm) and size of the atomistic region are not drawn to scale. Non-reflecting boundary conditions are described in Refs. [76, 109].

The energy exchange between the electrons and the lattice is described in the model by two coupling terms,  $-G(T_e - T_l)$  in the diffusion equation for Eq. 19, and  $\xi m_i \bar{v}_i^T$  in the equation of motion of the atoms, Eq. 19. The latter term serves the same purpose as does the coupling term  $G(T_e - T_l)$  in the equation for the lattice temperature in Eq. 1. In order to define the coefficient  $\xi$  in the coupling term given by Eq. 20 for each cell in the MD system, we have to relate the coefficient to the rate of the energy exchange and to make sure that this rate matches the one described by the coupling term  $G(T_e - T_l)$  of the continuum equations. Since the coupling term affects the thermal velocities of the atoms, let us consider the rate of the thermal kinetic energy change in a given cell of the MD system:

$$\frac{d}{dt} K^T = \frac{d}{dt} \sum_i \frac{m_i (\vec{v}_i^T)^2}{2} = \sum_i m_i \vec{v}_i^T \frac{d\vec{v}_i^T}{dt} = \sum_i m_i \vec{v}_i^T \frac{d\vec{v}_i}{dt} - \sum_i m_i \vec{v}_i^T \frac{d\vec{v}^c}{dt} \quad (22)$$

Since the thermal velocities of atoms in a cell have random directions, the second term in the above equation can be neglected for sufficiently large cells. Therefore, using the equation of motion Eq.19 and defining the rate of the energy deposition/extraction in a cell of a volume  $V_N$  according to the electron-phonon coupling term, we have:

$$\frac{d}{dt} K^T = \sum_i m_i \vec{v}_i^T \frac{d\vec{v}_i}{dt} = \sum_i \vec{v}_i^T (\vec{F}_i + \xi m_i \vec{v}_i^T) = \sum_i \vec{v}_i^T \vec{F}_i + \xi \sum_i m_i (\vec{v}_i^T)^2 = G V_N (T_e - T_l) \quad (23)$$

expressing the coefficient  $\xi$  from this equation we have

$$\xi = \frac{G V_N (T_e - T_l)}{\sum_i m_i (\vec{v}_i^T)^2} - \frac{\sum_i \vec{v}_i^T \vec{F}_i}{\sum_i m_i (\vec{v}_i^T)^2} \quad (24)$$

The second term in this equation is not related to the energy exchange with the electron sub-system of the model and is the result of the constraint on the thermal kinetic energy introduced by Eq. 23. This constraint prevents any temperature fluctuations and limits the thermal kinetic energy variations to the controlled energy deposition due to the electron-phonon coupling. Actually, the second term in Eq. 24 corresponds to a well-known Gaussian thermostat method for constant temperature simulations [172]. In our model we do not want to prevent the natural temperature fluctuations in the system as well as temperature changes due to the phase transformations (e.g. melting leads to the transfer of a part of the kinetic energy to the latent heat of melting). Therefore we omit the second term in Eq. 24 and leave only the term that is responsible for the controlled energy deposition due to the electron-phonon coupling:

$$\xi = \frac{G V_N (T_e - T_l)}{\sum_i m_i (\vec{v}_i^T)^2} = \frac{G V_N (T_e - T_l)}{2 K^T} \quad (25)$$

where the lattice temperature is defined by Eq. 21 and the coupling coefficient  $\xi$  is recalculated at each MD integration time-step for each cell defined by the finite difference discretization.

The time-step of the finite difference integration of Eq. 19 is typically  $n$  times (1 - 100) smaller than the one used in the MD part of the model,  $\Delta t_{MD} = n \times \Delta t_{FD}$ , and the electron temperature can change during one MD time-step. Therefore, the actual implementation of the algorithm involves averaging over a number of finite difference integration time-steps that fits to one MD time-step. The coefficient  $\xi$  is chosen so that the energy added to (or removed from) each cell of the MD system at each integration step,  $\Delta t_{MD}$ , would match the energy transferred between the electrons and the lattice during  $n$  steps of the finite difference integration:

$$\Delta E^{e-ph} = \sum_{k=1}^n \Delta t_{FD} G V_N (T_e^k - T_l) \quad (26)$$

which leads to the following final expression for  $\xi$  used in this work,

$$\xi = \frac{\frac{1}{\Delta t_{MD}} \sum_{k=1}^n \Delta t_{FD} G V_N (T_e^k - T_l)}{2 K^T} = \frac{\frac{1}{n} \sum_{k=1}^n G V_N (T_e^k - T_l)}{2 K^T} \quad (27)$$

Finally, we would like to emphasize the importance of making the distinction between the thermal and collective motion of atoms that has not been taken into account in earlier works [76, 101]. Scaling the total velocities of atoms can introduce significant artifacts into the simulation results and cause unphysical overheating [173] of fast moving material parts and clusters followed by ablation or spallation phenomenon. As shown below, the relaxation of the laser-induced pressure in the irradiated films leads to large acoustic vibrations and, at high fluences, disintegration of the films. The energy of the collective motion of atoms associated with these processes can be comparable to the energy of the thermal motion of atoms, as it will be seen later in Figure 28. Therefore, scaling the total velocities would artificially pump the energy into the energy of the acoustic vibrations, facilitate disintegration of the films, and accelerate any cluster that would form before the equilibrium between the local electron and lattice temperatures is reached. It is also essential to make the distinction between the thermal velocities and the velocities of collective motion of atoms in the definition of temperature, Eq. 21, and pressure, defined in MD simulations through the virial equation.

Now, after the coupling term has been defined, we will further discuss the TTM-MD algorithm illustrated in Figure 26. In the combined model, the cells in the finite difference discretization are related to the corresponding volumes in the MD system. The lattice temperature and coefficient  $\xi$  are defined for each cell of a volume  $V_N$ , and the summation  $\sum_i$  in the Eq. 19 is performed over all the atoms in a given cell. The expansion, density variations along the  $z$  axes, and, at higher fluences, disintegration of the irradiated target predicted in the MD part of the model are accounted for in the continuum part of the model. New cells are activated when the number of atoms in the corresponding MD regions exceeds a certain critical number, taken in this work to be 10% of the average number of atoms in a cell in the initial system. Cells are deactivated when the number of atoms in the corresponding MD region falls below the critical number. The atoms in the deactivated cells are included in the nearest active cell if they are located within a distance equal to half the size of a cell from the active cell.

The step of the spatial discretization in the finite difference integration of Eq. 19 can be estimated based on the von Neumann stability criterion,  $\Delta t_{FD} \leq 0.5 (\Delta x_{FD})^2 C_e(T_e) / K_e(T_e, T_l)$  for the values of the heat capacity and thermal conductivity giving the smallest time-step. The maximum time-step that can be used in the finite difference integration is typically smaller than the values of the time-step used in the integration of the MD equations of motion, Eq. 19. Therefore, the time-steps in the two parts of the combined model are chosen so that one MD time-step would correspond to an integer number of finite difference time-steps,  $\Delta t_{MD} = n \times \Delta t_{FD}$ . In each finite difference discretization cell, the energy transferred between the

electrons and the lattice due to the electron-phonon coupling is accumulated for  $n$  steps of integration,  $\Delta E^{e-ph} = \sum_{k=1}^n \Delta t_{FD} G V_N (T_e^k - T_l)$ . The accumulated energy is then transferred to (or extracted from) the energy of the atomic motion in the corresponding part of the MD system by means of the coupling term added to the MD equations of motion, Eq. 19, as it was explained before. Note that although a smaller time-step is used in the finite difference integration, the computational efficiency of the combined TTM-MD model is defined almost entirely by the MD part. A Gaussian temporal profile is used in the simulations to describe the laser energy deposition, as it was described in the Section 2 a).

In the case of a bulk sample irradiated by a laser pulse, the MD method is used only in the very surface region of the target, where active processes of laser melting and ablation are taking place, whereas the diffusion equation for electron temperature is solved in a much wider region affected by the thermal conduction from the absorbing surface layer, Figure 26. In order to avoid reflection of the pressure waves propagating from the irradiated surface, dynamic boundary conditions that mimic the interaction of the atoms in the boundary region with the outer “infinite elastic medium” [116] are applied at the bottom of the MD region. The energy carried away by the wave is monitored, allowing for control over the energy conservation in the combined model. Free boundary conditions are used at the surface exposed to laser irradiation. In the simulations performed for free-standing thin metal films free boundary conditions are applied at both surfaces of the film. Periodic boundary conditions are imposed in the directions parallel to the free surface(s). These conditions simulate the situation in which the laser spot diameter is much larger as compared to the depth of the laser energy deposition so that the effects of the edges of the laser beam can be neglected.

The hybrid approach, briefly described above, combines the advantages of the two-temperature model and the MD method. The two-temperature model provides an adequate description of the laser energy absorption by the conduction band electrons, energy exchange between the electrons and phonons, and fast electron heat conduction in metals, whereas the MD method is appropriate for simulation of non-equilibrium processes of lattice superheating and melting.

Before proceeding to the simulations of short-pulsed laser nanostructuring on metals we want to justify its applicability in experiments on laser melting of Ni and Au films and bulk targets, discussed below. But first, we briefly discuss a simulation that can serve as a test of the model that we developed, and which was already considered at continuum level in Section 2 a), Figure 3. In this discussion we will focus on the energy conservation in the joint electron-lattice system. The total energy conservation can be used as a main test of the correct implementation of the algorithm discussed in this section.

The initial MD system used in the simulation discussed here is an FCC crystal composed of 56800 atoms with dimensions  $3.53 \times 3.53 \times 50.14$  nm and periodic boundary conditions imposed in the directions parallel to two (100) free surfaces. Before applying laser irradiation, the system is equilibrated at 300 K. The evolution of the electron and lattice temperatures is shown in Figure 27. While the temperature profiles are similar to that in Figure 3, where the results of a TTM simulation are shown for the same irradiation conditions, the MD description gives a much more realistic representation of the lattice response to the laser heating, including thermal expansion, overheating, melting, and disintegration, as discussed

in the following sections. The size of the relative temperature fluctuations in Figure 27 is determined by the number of atoms in cells within the MD system, for which temperature is calculated,  $\sqrt{\langle (\Delta T)^2 \rangle} / \langle T \rangle \sim 1 / \sqrt{N_{\text{cell}}}$  [168]. The size of the fluctuations can be reduced by increasing the lateral size of the MD system or the step of spatial discretization used in the finite difference integration of Eq. 19, Figure 26. The step of spatial discretization used in this work is  $\Delta X_{FD} = 1$  nm, and the average number of atoms in a cell is 1159 in the initial equilibrated system, before laser irradiation.

The time-step in the finite difference integration of Eq. 19,  $\Delta t_{FD} = 1.25$  fs for Ni and  $\Delta t_{FD} = 0.025$  fs for Au, and the time-step in the integration of the MD equations of motion, Eq. 19,  $\Delta t_{MD} = 2.5$  fs, are chosen so that the von Neumann stability criterion and the synchronization requirement  $\Delta t_{MD} = n \times \Delta t_{FD}$  are satisfied, and the total energy in the combined model is conserved with the maximum energy drift of less than 0.3% during any of the simulations discussed in this section.

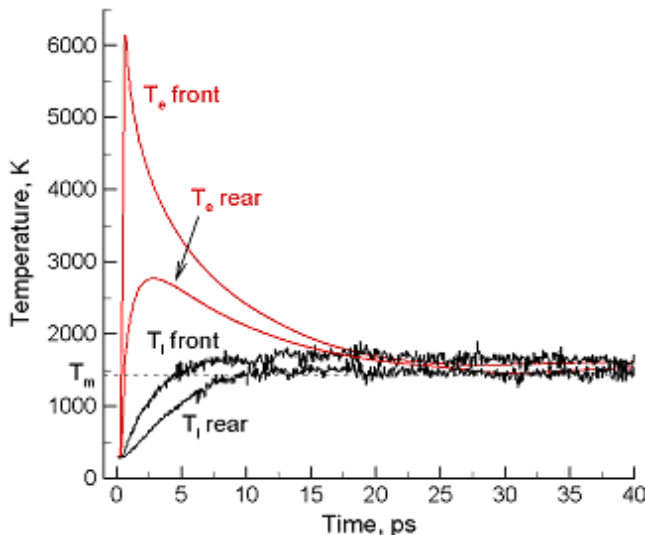


Figure 27. Time dependence of electron and lattice temperatures predicted by the combined TTM-MD method for a 50 nm Ni film irradiated with a 200 fs, laser pulse at an absorbed fluence of 43 mJ/cm<sup>2</sup>. Dashed lines show the melting temperature by EAM Ni.

The energy balance in a combined TTM-MD simulation is illustrated in Figure 28 for the simulation, for which the surface temperatures are shown in Figure 27 [175]. The total energy of the entire system is shown along with contributions from the thermal energy of the electrons,  $E_e$ , the energy (kinetic and potential) associated with the thermal motion of the atoms,  $E^h_a$ , the energy (kinetic and potential) of the collective atomic motion due to the elastic vibrations of the film induced by the fast laser energy deposition,  $E^c_a$ , and the energy that goes to the latent heat of melting,  $E_m$ . Both  $E^h_a$  and  $E^c_a$  include contributions from the kinetic and potential energies of the MD system and the approximate separation of the MD energy into the energies of the thermal and collective motion is based on the virial theorem [176]. The energy spent on melting is determined by multiplying the fraction of the liquid phase in the system at any given time by the latent heat of melting of the model material.

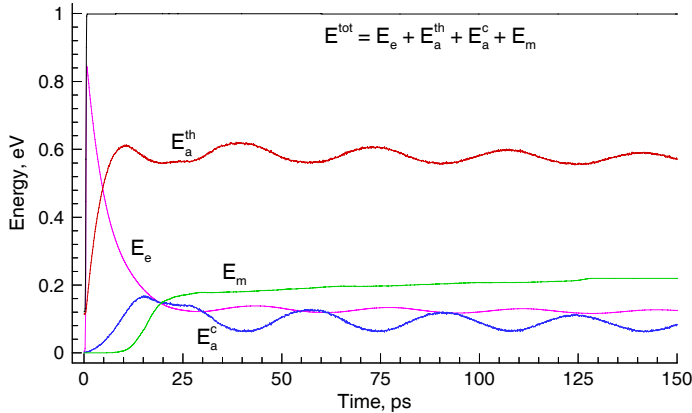


Figure 28. Energy redistribution in a 50 nm Ni film irradiated with a 200 fs, laser pulse at an absorbed fluence of  $43 \text{ mJ/cm}^2$ . The thermal energies of the electrons,  $E_e$ , and the atoms,  $E_a^{\text{th}}$ , the energy of the collective atomic motion due to the elastic vibrations of the film,  $E_a^c$ , the energy that went to the latent heat of melting,  $E_m$ , and the total energy of the system,  $E^{\text{tot}} = E_e + E_a^{\text{th}} + E_a^c + E_m$  are shown. Energies are normalized to the total energy absorbed by the film,  $E^{\text{tot}} = F_{\text{abs}} \times S$ , where  $S$  is the surface area of the MD system and  $F_{\text{abs}}$  is the absorbed laser fluence.

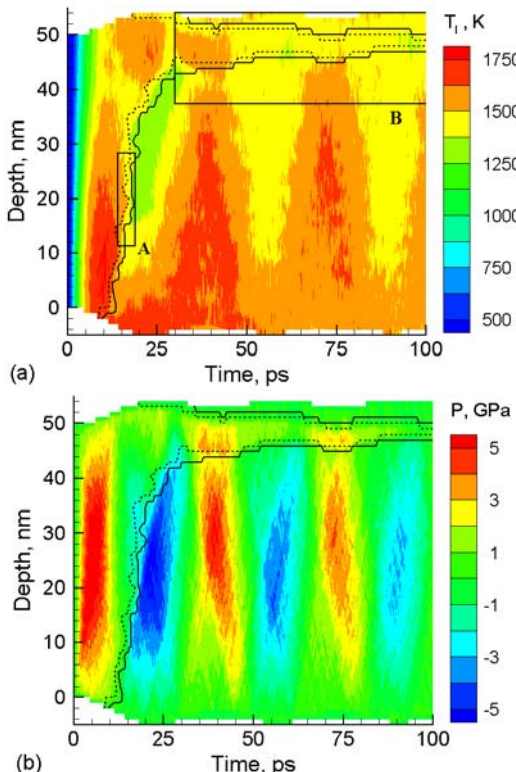


Figure 29. Contour plots of (a) lattice temperature and (b) pressure for simulation of laser melting of a 50 nm Ni film irradiated with a 200 fs laser pulse at an absorbed fluence of  $43 \text{ mJ/cm}^2$ . Solid and dashed lines show the beginning and the end of the melting process. Rectangles A and B in (a) show the areas of the film and times for which snapshots are shown in Figures 31 and 32 respectively. The laser pulse is directed along the Y axes, from the bottom of the contour plots.

The fraction of the liquid phase is determined based on the local order parameter, defined in Appendix of Section 2, whereas the latent heat of melting is calculated from the internal energy plots, Figure 11, as discussed in Section 2 b). Figure 28 shows that the total energy is conserved following the laser energy deposition occurring during the first ps. Initially all the laser energy is deposited into the energy of electrons and then, within  $\sim 20$  ps, is transferred to the thermal energy of the atomic motion. The fast temperature increase leads to the buildup of the compressive pressure in the middle of the irradiated film (see below in this section) and induces acoustic vibrations of the film. The vibrations are gradually dissipating into heat, which is reflected in a gradual transfer of energy from  $E_a^c$  to  $E_a^h$ . This energy transfer does not lead to the increase of the thermal energy,  $E_a^h$ , since it is offset by the transfer of energy from  $E_a^h$  to  $E_m$ . The time dependence of the energy of melting,  $E_m$ , reflects the two-step character of the melting process. A fast melting of  $\sim 80\%$  of the film that takes place from  $\sim 10$  ps to  $\sim 25$  ps, and is followed by a much slower melting of the remaining part of the film. A detailed analysis of the melting mechanisms is flowed up.

We will now apply TTM-MD model to describe short-pulses laser melting of metal targets, the central point of the mechanism of nanostructuring with laser beams. The following simulations in this section are performed for 50 nm Ni free-standing films irradiated with laser pulses of 200 fs. The effect of ballistic energy transport is negligible in Ni and the source term, Eq. 4, with the optical penetration depth of 13.5 nm is used in the simulations of laser irradiation of Ni films. The range of laser fluences used in the simulations is chosen so that the lowest fluence would be close to the threshold for the surface melting of the irradiated film, whereas the highest fluence would be close to threshold of the film spallation/disintegration. Thus, the range of absorbed fluences,  $F_{abs} = (I - R_{ref})F$ , used in this work, is for Ni from  $18.1 \text{ mJ/cm}^2$  (surface melting on a 30 nm film) to  $193.5 \text{ mJ/cm}^2$  (the onset of spallation on a bulk target). The initial MD system used in the simulations of laser irradiation of Ni films is an FCC crystal composed of 56800 atoms with dimensions  $3.53 \times 3.53 \times 50.14 \text{ nm}$  and periodic boundary conditions imposed in the directions parallel to two (100) free surfaces. Before applying laser irradiation, all systems are equilibrated at 300 K.

The following discussion of the redistribution of the absorbed laser energy and the mechanism of laser melting is given below for a simulation performed for a 50 nm free-standing Ni film irradiated with a 200 fs laser pulse at an absorbed fluence of  $43 \text{ mJ/cm}^2$ . This fluence is chosen so that we have a complete melting of the film by the end of the simulation. The laser energy absorption by the conduction band electrons, fast electron heat conduction and gradual energy transfer to the lattice vibrations due to the electron-phonon coupling are reflected in Figure 27, where the evolution of the electronic and lattice temperatures at the front and rear surfaces of the film is shown. The laser energy absorption results in a sharp increase in the electronic temperature near the irradiated front surface. The fast temperature-dependent electron heat conduction leads to the redistribution of the deposited energy within the film as reflected by the rise of the electronic temperature near the rear surface of the film. The process of the energy redistribution within the electronic system is occurring simultaneously with a more gradual energy transfer to the lattice vibrations due to the electron-phonon coupling. As can be seen from Figure 27 and Figure 28, most of the energy is transferred to the lattice within  $\sim 5$  ps, whereas complete equilibration between the hot electrons and the lattice takes up to 20 ps. As briefly discussed above, the energy transferred to the lattice splits into three parts in Figures 28; the energy of the thermal motion of the atoms, the energy of melting, and the energy of the collective atomic motion associated with

elastic vibrations of the film. The latter part is associated with the relaxation of the laser-induced pressure and is decreasing with increasing laser pulse duration [116] or decreasing strength of the electron-phonon coupling [116].

The temporal and spatial evolution of the lattice temperature and pressure in the irradiated film is shown in the form of contour plots in Figure 29. The complexity of the temperature plot, Figure 29a, reflects the interplay of several processes that are responsible for the lattice temperature evolution.

First, the energy transfer from hot electrons to the lattice leads to the initial temperature increase. A relatively small thermal diffusivity and strong electron-phonon coupling in Ni (as compared to other metals) leads to a rapid transfer of the absorbed energy to the lattice and the development of a temperature gradient within the 50 nm film during the first 10 ps of the simulation, Figure 29a.

Second, the onset of melting leads to a local decrease of the lattice temperature due to the transfer of a part of the thermal energy to the latent heat of melting, Figure 28. A transient decrease of temperature due to the melting can be seen in Figure 29a, where the beginning and the end of the melting process are shown by the dashed and solid lines respectively. The dashed line goes through the regions in the film where 10% of atoms have a “liquid-like” environment (as defined by the local order parameter, described in Appendix of Section 2 b), whereas the solid line connects the regions where 90% of atoms belong to the liquid phase.

Third, the elastic vibrations of the irradiated film caused by the relaxation of the laser-induced pressure have a significant effect on the temperature evolution in the film. Strong electron-phonon coupling in nickel leads to the steep rise of the lattice temperature during the first ~5 ps after the laser pulse, Figure 27, Figure 28 and Figure 29a. The time of the lattice heating is shorter than the time needed for the film to expand in response to the corresponding thermoelastic stresses and, in the central part of the film, the heating takes place under conditions of the inertial stress confinement [109, 177]. The heating under the condition of inertial stress confinement results in the buildup of high, up to 6 GPa, compressive pressure, Figure 29b. Relaxation of the compressive pressure leads to the expansion of the free-standing film with tensile stresses concentrating in the central part of the film. The following gradually dissipating oscillations of the film can be described as propagation of two unloading pressure waves trapped within the film and changing their signs from compressive to tensile and vice versa at each reflection at the free surfaces. The dissipation of the oscillations is reflected in the gradual energy transfer from the energy of the collective atomic motion,  $E^c_a$ , to the energy of the thermal motion of the atoms,  $E^{th}_a$ , as can be seen from Figure 28. The energy of the film oscillations decreases from ~15% of the total energy deposited by the laser pulse at 15 ps down to less than 10% by the time of 150 ps. A direct correlation between the pressure and temperature variations in the film is apparent from comparison of Figures 29a and 29b. Compression leads to the temperature increase whereas expansion corresponds to cooling. Neglecting viscosity and dissipation of the energy of the elastic waves and considering the compression and expansion of the solid and liquid parts of the film as isentropic processes, the temperature variation with pressure can be estimated from classical thermodynamics, Eq. 8.

The knowledge of  $C_p(T,P)$ ,  $\alpha(T,P)$ , and  $V(T,P)$  allows us to integrate the equation for isentropic expansion and the results of the integration are shown in Figure 30, where the isentropes are shown for the crystal phase by dashed lines for several initial values of entropy. For a pressure variation from -5 to 5 GPa, observed in Figure 29b, the range of the

temperature variation of  $\sim 200$  K is predicted for the isentropic process of expansion/compression for both crystal, Figure 30, and liquid (not shown) phases, in agreement with the temperature variation observed in Figure 29a.

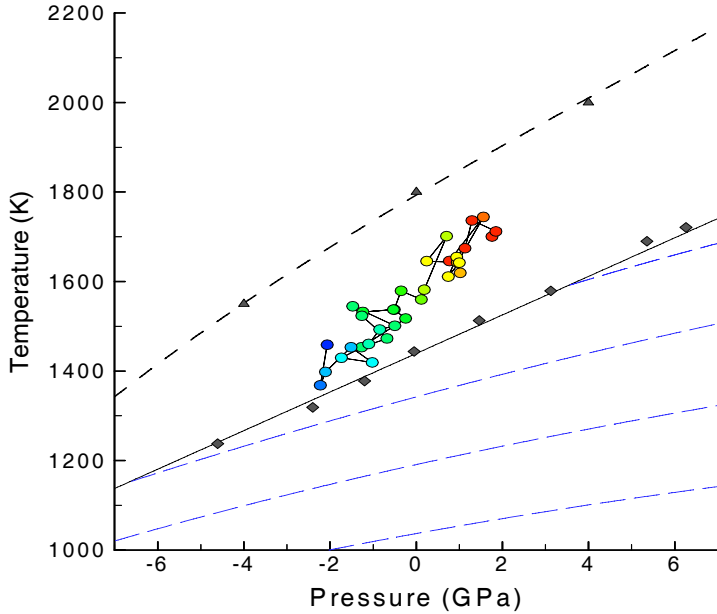


Figure 30. Conditions of equilibrium and nonequilibrium melting observed in simulations performed for the EAM Ni material. Black diamonds correspond to the conditions obtained in liquid – crystal coexistence simulations, Figure 9. Solid line shows the melting curve calculated from the Clapeyron equation. Blue dashed lines are isentropes plotted for the crystal phase for four different values of entropy. Black triangles connected by the black dashed line correspond to the maximum overheating of crystal observed in simulations performed with 3D periodic boundary conditions, Figure 9. Color circles correspond to the conditions leading to the onset of homogeneous melting in the simulation of laser irradiation of a 50 nm Ni film at the absorbed fluence of  $43 \text{ mJ/cm}^2$ . The conditions for the onset of homogeneous melting are realized along the dashed lines in Figure 29 up to the depth of 35 nm. The circles are connected by lines and colored from red to blue in the order of the increasing depth under the surface.

The analysis performed above indicates that the complex temperature evolution in the irradiated film is defined by the interplay of the fast energy transfer from the excited electrons to the lattice vibrations, transfer of a part of the lattice thermal energy to the latent heat of melting, and the temperature variations related to the relaxation of the laser-induced pressure. The temperature and pressure evolution, in turn, define the kinetics and the mechanisms of laser melting, as discussed below.

Turning to the analysis of the mechanisms of laser melting, we can see from the dashed and solid lines separating the liquid and solid-state regions in the contour plots shown in Figure 29 that the melting process occurs in two steps. An ultrafast melting of  $\sim 80\%$  of the film occurring within  $\sim 15$  ps is followed by a much slower melting of the remaining crystalline region near the back surface of the film that takes more than 100 ps.

The irradiated side of the film starts to melt  $\sim 10$  ps after the laser pulse, when the temperature reaches  $\sim 1650$  K, significantly above the equilibrium melting temperature of 1439 K, determined for the EAM Ni from a liquid-crystal coexistence simulation at zero

pressure. During the following 15 ps a big part of the film melts and only a small layer near the back surface remains in a crystalline form. Although, at first sight, the melting seems to proceed by propagation of the melting front from the irradiated surface, a closer look at a series of snapshots of the atomic-level structure of the region undergoing ultrafast melting, Figure 31, reveals a more complex characteristic picture of homogeneous melting. Small liquid regions appear and grow ahead of the “melting front” leading to a very high apparent “melting front” propagation velocity of ~4000 m/s.

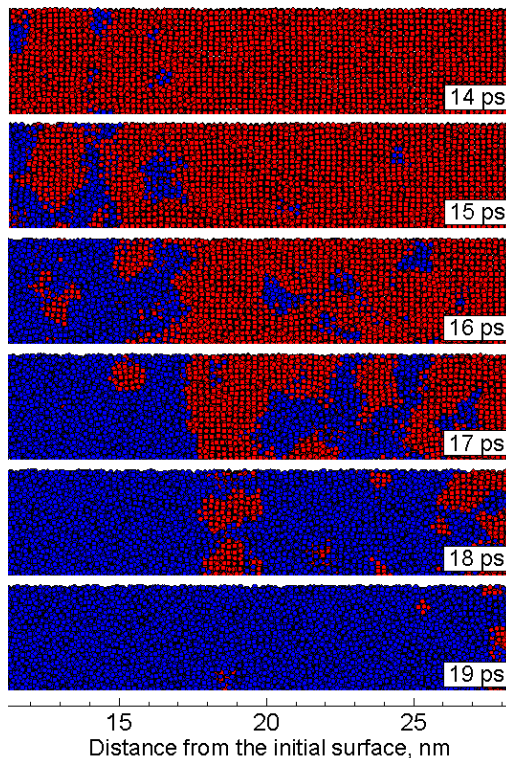


Figure 31. Snapshots from simulation of a 50 nm Ni film irradiated with a 200 fs laser pulse at an absorbed fluence of  $43 \text{ mJ/cm}^2$ . Snapshots are taken at times and locations marked by rectangle A in Figure 29a. Atoms are colored according to the local order parameter - red atoms have local crystalline surroundings, blue atoms belong to the liquid phase. In these and other snapshots the atomic positions are averaged over 100 MD integration timesteps (0.25 ps) in order to reduce the effect of thermal oscillations of atoms.

From the temperature contour plot, Figure 29a, we see that although the homogeneous melting starts near the irradiated surface at a temperature of ~1650 K, it proceeds at significantly lower temperatures that, in the central part of the film, become as low as ~1300 K. This observation can be explained based on the pressure dependence of the equilibrium melting temperature. Simulation results, shown by diamonds in Figure 30, predict a nearly linear dependence of the melting temperature on pressure. This prediction is in a good agreement with calculations based on Clapeyron equation,  $(dT/dP)_m = \Delta V_m / \Delta S_m$ , where the volume change and entropy of melting,  $\Delta V_m$  and  $\Delta S_m$ , are determined from the temperature dependences of the volume and the internal energy calculated for zero pressure, as shown in Figure 10a and Figure 11a respectively.

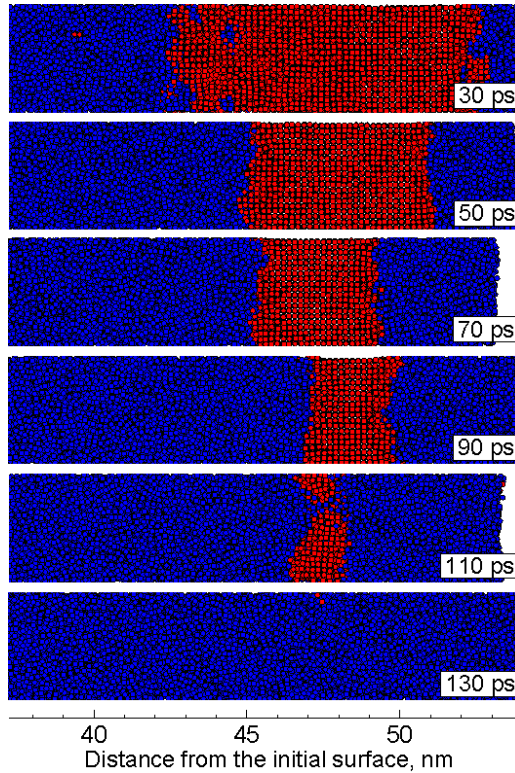


Figure 32. Snapshots from simulation of a 50 nm Ni film irradiated with a 200 fs laser pulse at an absorbed fluence of  $43 \text{ mJ/cm}^2$ . Snapshots are taken at times and locations marked by rectangle B in Figure 29a. Atoms are colored according to the local order parameter - red atoms have local crystalline surroundings, blue atoms belong to the liquid phase.

A region near the back surface of the irradiated film is not affected by the ultrafast homogeneous melting discussed above, and a much slower conventional heterogeneous melting takes place. A thin crystalline layer with two well-defined crystal-liquid interfaces is observed in a snapshot taken at 30 ps after the laser pulse in Figure 32. The subsequent snapshots show that two melting fronts are propagating from the back surface of the film and from the homogeneously melted part of the film, leading to a gradual decrease of the size of the crystalline region and complete vanishing of the crystalline layer by the time of  $\sim 115$  ps after the laser pulse. The heterogeneous melting is also affected by the pressure variations. The decrease in the thickness of the crystalline region typically coincides with the expansion of the region. This is related to the steeper slope of the coexistence line as compared to isentropes,  $(dT/dP)_m > (dT/dP)_s$ , Figure 30. Therefore, an adiabatic expansion of a region of the liquid-crystal coexistence facilitates melting and induces the advancement of the melting front.

From the analysis preformed in this subsection we can conclude that the interplay of homogeneous and heterogeneous melting mechanisms is responsible for the laser melting of thin metal films. Ultrafast homogeneous melting takes place almost simultaneously in a wide area of the overheated crystal and proceeds by nucleation and growth of liquid regions inside the crystal. It is followed by a slower heterogeneous melting that proceeds by the propagation

of the liquid-crystal interfaces (melting fronts) from the back surface of the film and from the homogeneously melted part of the film.

We shall now discuss the effect of laser-induced stresses relaxation on the melting process using the simulation performed for a 50 nm Ni film and discussed in the previous section as an example. The temperature and pressure conditions leading to the onset of the ultrafast homogeneous laser melting are shown in Figure 33 by colored circles. This figure is analogous to Figure 30, with some additional information related to the effect of laser-induced stresses on the melting process shown. The conditions for the onset of homogeneous melting are calculated along the dashed line in Figure 29 a) for the depth under the irradiated surface up to 35 nm. At all pressures, the homogeneous melting starts under conditions of overheating above the liquid-crystal coexistence line. The circles are connected in the order increasing depth. The overheating required for the initiation of the homogeneous melting in this simulation is found to range from  $1.05 T_m$  to  $1.18 T_m$ . These values of overheating are significantly lower than the highest temperature at which no homogeneous melting is observed in constant-pressure simulations performed with three-dimensional periodic boundary conditions. A series of such simulations has been performed for different values of hydrostatic pressure and the observed temperatures required to melt the system,  $1.21 - 1.25 T_m$ , are shown by red squares connected by the black dashed line in Figure 33. The temperatures at which melting takes place in a system with no external boundaries and internal defects correspond to the limit of thermal stability of the crystal lattice [66], and can be considered as the maximum possible overheating achievable in a system. The maximum overheating of  $\sim 1.25 T_m$  is observed at pressures from 0 to 10 GPa, whereas a gradual decrease of the overheating down to 1.21 GPa at -5 GPa is observed for negative pressures. The reasons for the discrepancy between the maximum overheating and the one required for the initiation of homogeneous melting under laser irradiation conditions can be explained by the dynamics of the relaxation of the laser-induced pressure, as shown below.

The strong pressure gradients transiently realized in the irradiated films, Figure 29 b), and associated complex stress conditions can destabilize the lattice and promote melting at lower overheatings. Moreover, for a typical laser spot diameter of  $10 - 100 \mu\text{m}$  the fast relaxation of the laser-induced pressure can only proceed in the direction normal to the surface. This uniaxial expansion and associated anisotropic lattice distortions can additionally reduce the lattice stability against the initiation of melting. Indeed, the melting process in the simulation proceeds simultaneously with the uniaxial expansion of the film, Figure 29b, leading to the decrease of the overheating needed for the initiation of the homogeneous melting. This scenario is supported by the data shown in Figure 30 and Figure 33, where the points corresponding to the onset of the homogeneous melting are approaching the coexistence line as depth (and time) increases.

In order to test this hypothesis, we performed a series of constant-pressure simulations under conditions of uniaxial expansion, when the sizes of the computational cell in the lateral directions were fixed at values that correspond to zero pressure at a temperature of 300 K and relaxation is only allowed in one direction. These simulations predict the conditions for the onset of homogeneous melting (green diamonds in Figure 33) that fit well with the conditions realized in the simulation (color circles in Figure 33). Note, that under conditions of uniaxial expansion the value of pressure, defined as negative one third of the first invariant of the stress tensor,  $P = -(\sigma_{xx} + \sigma_{yy} + \sigma_{zz})/3$ , contains different contributions from different diagonal components of the stress tensor. For example, for melting conditions at zero pressure the

lattice parameter in lateral ( $X$  and  $Y$ ) directions is fixed at  $a_0 = 0.353$  nm, lattice parameter in  $z$  direction is  $a_1 = 0.394$  nm, and stresses are  $\sigma_{xx} = \sigma_{yy} = -0.66$  GPa, and  $\sigma_{zz} = 1.32$  GPa.

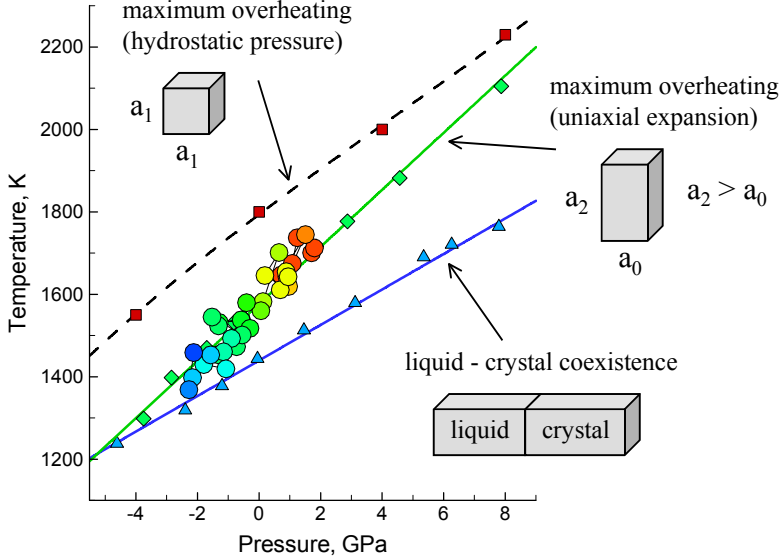


Figure 33. Pressure/temperature conditions for equilibrium and nonequilibrium melting observed in simulations performed for EAM Ni material. Blue triangles correspond to the conditions of equilibrium melting obtained in liquid-crystal coexistence simulations. Red squares connected by the black dashed line correspond to the maximum overheating of a crystal observed in simulations performed with 3D periodic boundary conditions and constant hydrostatic pressure. Green diamonds show the conditions for homogeneous melting in simulations of uniaxial expansion. Colored circles show the conditions leading to the onset of homogeneous melting in the simulation of laser melting illustrated in Figures 29 a) and b). The circles are connected by lines and colored from red to blue in the order of increasing depth under the surface.

Therefore, we can conclude that the dynamics of the relaxation of the laser-induced pressure has a profound effect on the melting processes. The homogeneous nucleation of liquid regions inside the crystalline material is assisted by anisotropic lattice distortions induced by the short pulse laser irradiation. The anisotropic uniaxial expansion reduces the overheating required for the onset of homogeneous melting down to less than  $1.05 T_m$ . Thus, our simulations suggest that homogeneous melting can be induced at significantly lower values of overheating and larger range of irradiation parameters as compared to the predictions based on the classical nucleation theory [35]. The reduced lattice stability under conditions of short pulse laser irradiation has important implications for the interpretation of experimental data on the kinetics of laser melting.

The complete study of short-pulsed laser melting, including the simulations presented in this section can be found in Refs. [62, 116], where the effect of pulse duration and the strength of the electron-phonon coupling were also considered. The TTM-MD was successfully utilized when finding the threshold for the surface modification of metal films of different thickness [79]. The onset of the interfacial stress confinement in short pulse laser melting, spallation, and disintegration of metal films was largely investigated in Refs [36, 37, 63, 64] with TTM-MD and the results are vastly applicable in surface nanostructuring experiments with laser beams. Finally, the model was found to be applicable in investigation

of shock melting of grain boundaries in metal targets [178, 179]. In fact, the applicability of the combined atomistic-continuum model can be justified in any experiments where the interplay of transient electron-phonon dynamics is perturbed with nonequilibrium phase transformation processes. The existence of Fermi Distribution in the electronic system, however, is assumed for TTM-MD during whole simulation process. In the next section we will present the atomistic-continuum model suitable to study nanostructuring processes generated in the experiments by Chichkov and Nakata [9, 10, 11, 12].

### (c) Combined Model for Nanostructuring on Metals

Although MD calculations are a way ahead of *ab-initio* ones from the point of view of the sample size that can be modeled, even the largest MD job performed on Los Alamos National Laboratory Super Facility [180] in fact is only on the micron scale, which is on the verge of the experimental measurements. As we can see, for their close comparison, it is an extremely difficult task to perform MD calculations on the scale attainable by an experiment. In our case, in order to observe the formation of surface nanostructures, the sample has to be big enough to accommodate the concurrent laser-induced processes like homogeneous melting, propagation of the solid-liquid interface, relaxation of the laser-induced pressure, and other possible processes resulting in a hydrodynamic motion of matter and leading to the formation of nanostructures. It can be estimated that if we want to fit the experimental scale of the microbumps/nanojets on Au [9, 10, 11, 12] into MD calculations, it would require an enormous number of atoms in the computational cell. For example, a circular slab of gold film with thickness of 50 nm and diameter of 1  $\mu\text{m}$  consists of approximately  $2.3 \times 10^9$  atoms, which is of immense computational cost to process with MD in a reasonable time. However, if we chose Ni to suit our challenges, we can study the process of surface laser nanotexturing in general, but on a smaller scale that fits the MD approach. Strong electron-phonon coupling of Ni (one order of magnitude stronger than that of Au) and negligible contribution of the ballistic energy transport (the range of ballistic electrons in Au is  $\sim 100$  nm [22]) result in a fast lattice heating and a high degree of laser energy localization near the laser spot. To quantitatively characterize the extent of spatial energy redistribution during the time of the electron-phonon equilibration, one can consider the effective penetration depth of hot electrons,  $L_c$ , introduced in Ref. [181]. This quantity is a material property and was shown to be the key parameter defining the surface melting thresholds for films of different thickness and for the melting/recrystallization mechanism observed in a bulk of material. Although derived in 1D, both the physical meaning and quantitative value of the quantity  $L_c$  holds for a multidimensional diffusion process as well and can be used to justify the choice of Ni as an investigated material in the problem of microbumps/nanojets formation. Indeed, following the procedure described in [22, 79, 181], the values of  $L_c$  can be estimated to be  $\sim 50$  nm for Ni and  $\sim 700$  nm for Au. Therefore, in contrast with a recent continuum-level study presented in [122] where a sample of Au of  $\sim 1\mu\text{m}$  in diameter was used, to observe nanotexturing processes similar to [9, 10, 11, 12] but on Ni surface, a sample of  $\sim 250$  nm in diameter is enough. A 20 nm thick circular slab of EAM Ni material, 250 nm in diameter provides an adequate description of the laser-induced phase transformations and plastic deformation

following a localized laser energy deposition and still contains 85,158,528 atoms, a number that can be treated in a large-scale parallel MD simulation [182].

Since the sample size is reduced by one order of magnitude, to observe the nanostructuring process similar to [9, 10, 11, 12], the diameter of the laser beam in the MD simulation is also reduced by the same order. The simulation is performed with 200 fs laser pulse having Gaussian spatial and temporal profiles and a laser beam diameter  $b$  (full width at half maximum) equal to 10 nm. Thus, the source term in the continuum part of MD-TTM model can be written in cylindrical coordinates,  $\vec{x} = (r, z)$ , as the following:

$$I(\vec{x}, t) = I_0(r, t) \frac{1}{\alpha} \exp(-\alpha z) \text{ and} \quad (28)$$

$$I_0(r, t) = \sqrt{\frac{\omega}{\pi}} \frac{(1-R)F}{\pi b^2 t_{pulse}} \exp\left(-\frac{r^2}{b^2}\right) \exp\left(-\omega \frac{(t-t_0)^2}{t_{pulse}^2}\right) \quad (29)$$

where  $R$  is reflectivity that was not considered in this modeling. Instead we worked with the absorbed fluence that was taken to be 3.1 J/cm<sup>2</sup> and that can be easily transferred to the incident one with known function of reflectivity, and  $\omega = 4Ln2$ .

Thus, the computational model can be considered to be a scaled down version of the experimental setup used in nanostructuring of Au films. While the difference in the length-scale and material properties of EAM Ni does not allow us to establish direct quantitative connections between the computational results and experimental data, the scaled down model can be expected to capture the basic mechanisms responsible for formation of the surface nanostructures. Although the immediate goal of this work is to provide insights into the mechanisms responsible for nanobump formation in experiments reported in Refs. [9, 10, 11, 12], the results of the simulation may also have implications for other laser processing techniques, particularly for surface nanostructuring based on optical near-field effects [15, 18, 50, 51].

Despite the fact that the atomistic-continuum model TTM-MD developed in the previous Section 3 a) [116] was successfully applied to study various ultrafast nonequilibrium phenomena induced during laser-matter interaction, including laser-induced melting [79, 116, 119], spallation [63, 64], and even ablation of metal targets [36, 37, 64], it is in need of further development to study the nanojets formation mechanism. Namely, in the case of short pulse laser nanostructuring the size of laser spot becomes comparable with the characteristic size of the studied features. The solution of the diffusion equation for the electrons, therefore, is no longer valid in 1-D and, since there will be a significant temperature gradient established in the vicinity of the modeled structures, the description of the electron heat conduction process in 3D is required.

Furthermore, it is important to exclude the artificial effect of multiple reflections of the laser-induced pressure recoil from the system's boundaries that can certainly affect the formation of the nanostructures. In [109, 116], where as a result of the laser heating the establishment of temperature gradient took place in 1D, the propagation of a plane wave through the dynamic boundary was successfully applied. When studying the nanojets, however, the conduction due to hot electrons in 3-D results in the establishment of a

temperature gradient in 2D for thin and in 3D for thick films. The terms “thin” and “thick” are applicable when comparing film thickness,  $d$ , with the distance  $L_c$ , the effective penetration depth of hot electrons by the time of electron-phonon equilibrium [22, 79, 181]. In thin films ( $d < L_c$ ), the laser-induced pressure recoil is expected to take place in radial directions, and the nonreflective boundary, therefore, can be represented in the form of a ring. Alternatively, in the case of thick films ( $d > L_c$ ), the dynamical boundary must take a spherical shape. Such boundary conditions require thorough development and is considered for development in the MD-TTM application for the surface laser nanostructuring for the first time. Therefore, with all the modifications described above, the preliminary atomistic-continuum MD-TTM model has been used for the case of thin film ( $d < L_c$ ) to study the formation of the nanojets structures in the experiments [9, 10, 11, 12].

A schematic representation of the computational cell used in the simulation is shown in Figure 34 [182]. The simulations are performed for a 20 nm Ni film deposited on a transparent substrate. The initial MD part of the model is a circular slab of 250 nm in diameter, where atoms are arranged in the FCC crystal structure with (001) surface oriented parallel to the substrate. The thermal and elastic properties of the Ni film are defined by the interatomic interaction potential, described in this work by the embedded-atom method (EAM) [112]. Some of the parameters of the model EAM Ni material are reported in [64, 116] and also above in the Section 2 b). The parameters used in the TTM equation for the electron temperature are given in [116] and in the Section 2 a). The top surface of the film, exposed to the laser irradiation, is free to move, whereas the interaction of the bottom side of the film with the substrate is described by Lennard-Jones potential. The parameters of the Lennard-Jones potential are chosen to represent an adhesion of a Ni film to the substrate and set to be 10 times weaker than the effective strength of Ni-Ni interaction that roughly corresponds to the estimations from experimental results on adhesia. The substrate is kept rigid during the simulation and the energy exchange between the metal film and the substrate is not allowed. This assumption of the model is justified by the short characteristic time of the processes responsible for the nanobump formation and relatively slow heat exchange between a metal film and a glass substrate.

While the size of the MD part of the combined model is limited to 250 nm in diameter, the TTM equations for the electron and lattice temperatures are solved in a much wider region affected by the thermal conduction, up to more than 300 nm from the center in the radial direction, Figure 34. A special non-reflective boundary (NRB) condition is applied circumferentially around the MD computational cell. This boundaries imitates the propagation of the laser-induced radial/circular pressure wave from the MD region to the continuum part of the model and eliminates the artificial effect of the multiple reflections of the waves.

Note that the TTM-MD simulation involving 85,158,528 atoms interacting by a realistic many-body EAM potential presents a significant computational challenge that can only be addressed with access to advanced computational facilities. The simulation reported in this work is performed with an MPI parallel TTM-MD code optimized for the IBM eServer cluster 1350 recently build at the National Facility at Irish Centre for High End Computing. Using an optimized linked list neighbor search and improved memory consumption, the code has reached a competitive time of  $\sim 8 \mu\text{s}$  spent by a single processor per atom per time step. The simulation was run across 128 processors and required  $\sim 1,000$  hours of calculations [182].

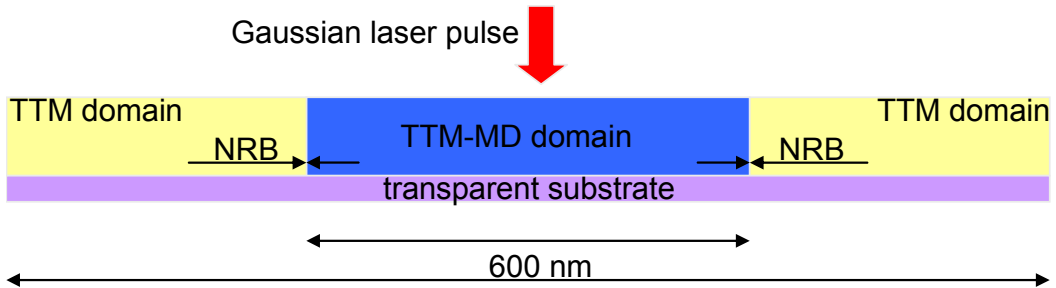


Figure 34. Schematic representation of the computational setup used in MD-TTM [182].

The visual picture of the laser-induced processes is shown in Figure 35. In order to provide a clear view of the film separation from the substrate and nanobump formation, only a thin 5 nm slice cut through the center of the MD part of the model is shown in the snapshots taken from the simulation. The atoms in the snapshots are colored according to the local order parameter (see appendix in Section 2 b) [114], with blue color indicating the destruction of the original FCC crystalline order due to the fast melting. The melting starts within 2-3 ps after the laser pulse and the radius of the melted region reaches its maximum size of ~32 nm by the time of ~20 ps. The melting process proceeds simultaneously with the separation of the central part of the film from the substrate and generation of a pronounced hollow nanobump due to the rapid bloating of the melted region away from the substrate. Some limited plastic deformation, proceeding mainly by emission of dislocation from the melting front, is observed in a relatively narrow layer adjacent to the melted region.

The insights into the physical mechanisms responsible for the nanobump formation can be obtained by considering the evolution of the electron and lattice temperatures, pressure, and velocity in the direction normal to the substrate. The values of the parameters plotted in Figure 36 are averaged over a central part of the film with a radius of 2 nm. Due to the small heat capacity of the electrons, the laser excitation results in a large spike of the electron temperature that reaches ~16,000 K by the end of the pulse. The sharp drop of the electron temperature during the first 10 ps of the simulation, Figure 36 a), is mainly due the fast energy transfer from hot electrons to the lattice. By the time of 12 ps, the electron temperature in the central part of the system drops below the lattice temperature and further decrease of the electron temperature is defined by the two-dimensional electron heat conduction in the radial direction. The fast energy transfer from the electrons to the lattice is also reflected in the initial increase of the lattice temperature, that exceeds the melting temperature of the EAM Ni material,  $T_m = 1439$  K [116], at 1 ps after the beginning of the laser pulse and reaches the maximum level of  $2.26T_m$  by the time of 15 ps. At later times the heating turns into cooling, with the electron heat conduction and energy transfer from the lattice to the electrons being the dominant cooling mechanisms.

The fast localized heating of the film takes place under conditions of the partial inertial stress confinement [62, 63, 64, 109], when the heating time is shorter than the time needed for the film to expand in response to the thermoelastic stresses. The confinement of the thermoelastic stresses, combined with an additional pressure coming from the suppressed volume expansion associated with the melting process [116], results in the buildup of high, up to 8 GPa, compressive stresses during the first several picoseconds of the simulation, Figure 36 b) and d). The relaxation of the compressive stresses proceeds by expansion in both radial

direction and normal to the substrate. In the presence of the rigid substrate, the normal expansion of the film results in the upward acceleration of the film up to a velocity exceeding 300 m/s, Figure 36 c). The expansion of the film may be described in terms of an unloading wave propagating from the free surface toward the substrate. The reflection of the unloading (tensile) wave from the rigid substrate results in the concentration of the tensile stresses at the film-substrate interface and leads to the separation of the film from the substrate.

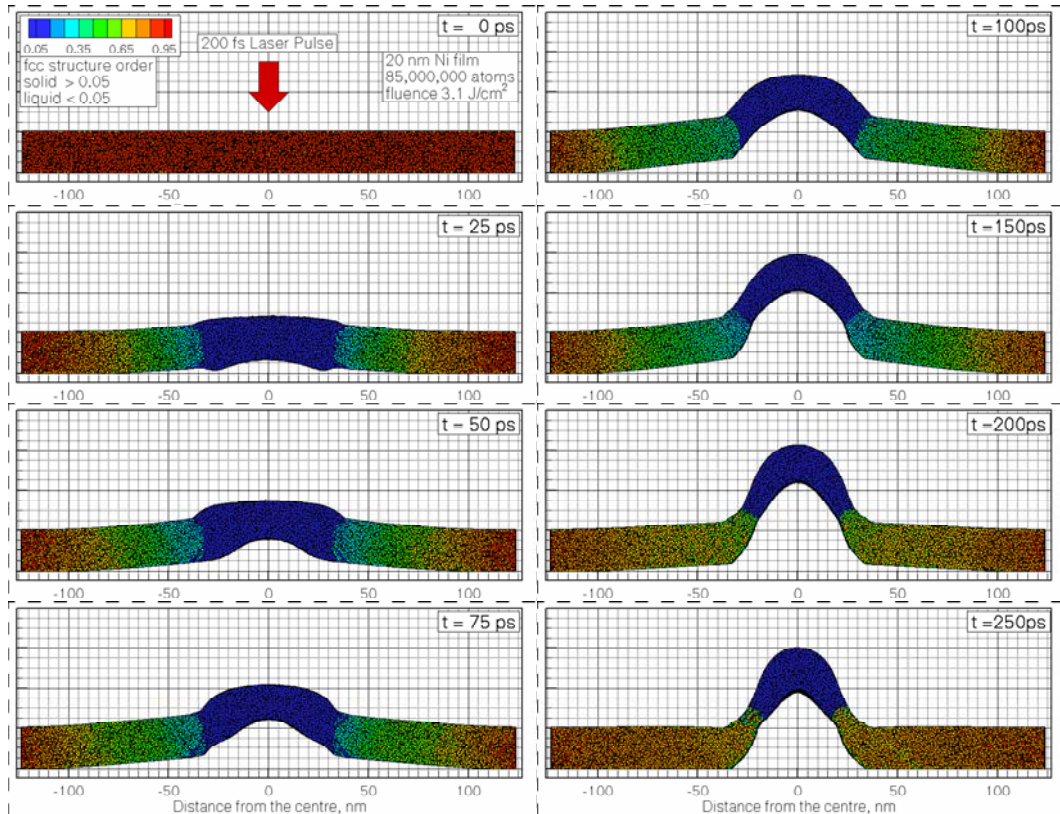


Figure 35. Snapshots from a TTM-MD simulation of a 20 nm Ni film on a transparent substrate irradiated with a 200 fs laser focused on a 10 nm spot in the middle of the computational cell. The average fluence absorbed within the beam diameter is  $3.1 \text{ J/cm}^2$ . Atoms are colored according to the local order parameter [114] - red atoms have local crystalline surroundings, blue atoms belong to the liquid and, in the last snapshot, to small crystallites disoriented with respect to the original crystalline structure of the film [183].

An apparent correlation between the time of the film acceleration and the first peak of the compressive pressure, Figure 36 d), provides clear evidence that the relaxation of the laser-induced compressive stresses generated under conditions of the inertial stress confinement is responsible for the initial acceleration of the central part of the film. Following the initial acceleration, the vertical velocity slowly decreases during the remaining part of the simulation, Figure 36 c). The decrease of the velocity is related to the resistance of the colder parts of the film to the separation from the substrate. The upward displacement of the central part of the film leads to the elastic deformation of the surrounding areas which relaxes by pooling the film back toward the substrate, Figure 35. In the melted part of the film, however,

the initial momentum induces a hydrodynamic flow of the molten material leading to the formation of a distinct nanobump.

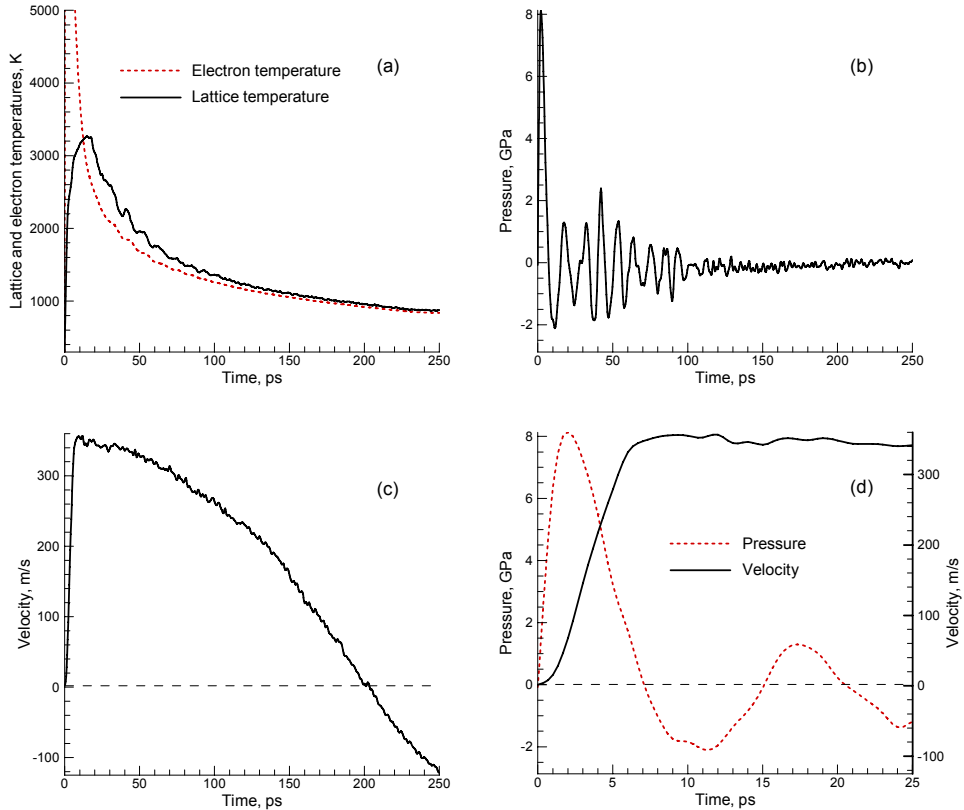


Figure 36. (a) The time dependences of the electron and lattice temperatures, (b) pressure, and (c) velocity in the direction normal to the substrate, averaged over a part of the film within 2 nm from the center of the laser spot. (d) The initial changes of pressure and velocity during the first 25 ps of the simulation are shown with higher resolution.

Strong electron temperature gradients established in the radial direction following the initial localized laser energy deposition result in a fast cooling of the electrons and the lattice at later times. At  $\sim 50$  ps the lattice temperature at the periphery of the melted region drops below the equilibrium melting temperature, starting a slow process of epitaxial crystallization. At the same time, the fast two-dimensional electron heat conduction continues to cool the melted region, with the lattice temperature in the center of the laser spot dropping down to  $T_m$  by 90 ps and down to  $0.6T_m$  by the end of the simulation at 250 ps. At such strong undercooling, the slow epitaxial recrystallization gives way to a massive homogeneous nucleation of multiple crystallites within the undercooled liquid region, resulting in a rapid solidification of the nanobump. A detailed description of the presented model and the nanostructuring mechanism can be found in Ref. [182] whereas the analysis of the solidification process producing a nanocrystalline nanobump is presented elsewhere [183].

In this large-scale parallel molecular dynamics simulation of the nanobump formation with a short-pulsed laser beam we can now surely relate the results of the simulation to the alternative mechanisms of nanobump formation proposed in literature. We note that, contrary

to the suggestions on the dominant contribution from the pressure of evaporating material [11, 12] or plastic deformation [122], we observed neither of them in the presented TTM-MD simulation. The area of the nanobump undergoes a transient melting, and the hydrodynamic motion of the melted part of the film prior to the resolidification, rather than plastic deformation, is defining the shape of the nanobump. The upward acceleration of the melted film is provided by the relaxation of the initial compressive stresses generated by the fast laser heating, with Marangoni effect not involved into the process of restructuring [9, 10]. The results of the simulation do not exclude, however, the possibility that under different irradiation conditions or for different material system the above mentioned effects may contribute to the generation of surface structures in short pulse laser nanostructuring.

Finally, the results of a large scale TTM-MD simulation performed for a thin metal film irradiated by a tightly focused femtosecond laser pulse reveal the physical processes involved in the formation of a nanobump with dimensions comparable to the laser spot. The relaxation of the compressive stresses generated under conditions of the inertial stress confinement is identified as the main driving force responsible for the acceleration of a transiently melted region of the film which results in the bloating of a hollow nanostructure. Two-dimensional electron heat conduction provides the conditions for the fast cooling of the melted region and rapid solidification of a surface feature generated in the process of hydrodynamic motion of the liquid metal. While in the simulation discussed in this work the growth of the nanobump stops at  $\sim 200$  ps, one can expect that, at higher excitation levels, the hydrodynamic motion induced by the relaxation of the laser-induced compressive stresses may result in a stronger acceleration and a more active hydrodynamic flow leading to the emergence of jet-like structures that have been observed on top of hollow microbumps in experiments performed at sufficiently high laser fluencies.

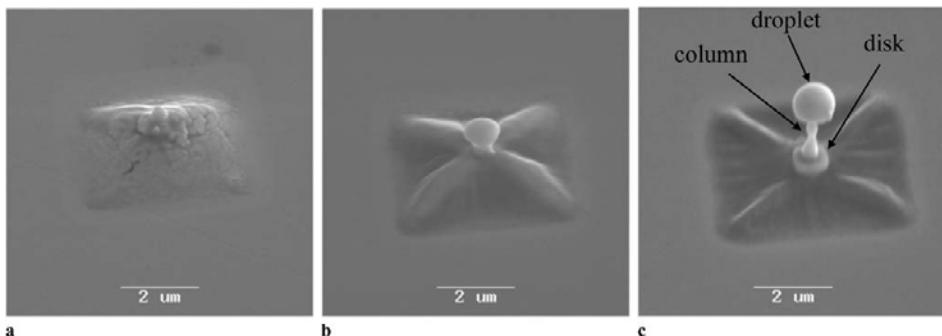


Figure 37. Structures obtained by irradiation of a 60 nm gold film with single femtosecond laser pulses having square-shaped intensity distribution. The laser fluencies on the sample surface are (a) 0.19 J/cm<sup>2</sup>, (b) 0.195 J/cm<sup>2</sup>, and (c) 0.2 J/cm<sup>2</sup> [60].

The results of the simulation performed above, nevertheless, still do not allow for a direct theory-experiment comparison. The necessity of switching material from Au as it is in the experiments [9, 10, 11, 12] to EAM Ni, the structuring of which was retarded in the experiments by Koch [9, 10], was justified from the point of computational power accessible for the moment of study. The further experiments of Kuznecov [60], however, reveal a complicated dependence of the formed nanojet aspect-ratio as a function of fluence, Figure 37, that again bring the question on the mechanism of nanostructuring on thin Au film on the

experimental scale back to the agenda of our current theoretical research. In particular, the necessity of working with Au material, as it is in the experiment by Koch and Kuznecov, and on the same scale, therefore completely reproducing the experimental conditions, now looks obvious for a deeper understanding of the processes underlying the nanostructuring of gold films [9, 10, 16, 18, 60]. In the next section we will present two computational approaches of the extension of the combined atomistic-continuum model to the possibility of modeling on the experimental scale (microns) for a direct theory-experiment comparison.

#### **(d) Extension of the Combined Atomistic-continuum Model for Nanostructuring on Metals to the Experimental Scale**

The complexity of the nonreflective boundaries with circumferential or spherical shape, described in the previous section, limits their application and still implies some assumptions concerning the symmetries of the laser-induced pressure recoil. A more advanced model, therefore, capable of including the processes related to free electrons, nonequilibrium phase transformations, and long range laser-induced elasto-plastic deformations within the frames of one computational approach, is needed. In order to overcome this limitation and to advance the continuum description of the laser-induced pressure waves, it is possible to merge the atomistic-continuum TTM-MD [116] model with the hybrid macroscopic-continuum model (MCM) [67, 120] in which the TTM model [70] and elasto-plastic flow model [122] are incorporated as well. Similar to TTM-MD, at the atomic level at the very central part of the computational cell this model accounts for the kinetics of fast laser-induced nonequilibrium processes such as phase transformation, spallation, and ablation with Molecular Dynamics by means of TTM-MD model along with the effects related to the free electrons. However, in addition to the TTM-MD model, in which no plasticity effects can be considered beyond MD boundary, by adding the description of elasticity within the frames of MCM model, where no phase transformations shall take place, the long range elasto-plastic deformations will be treated with continuum hydrodynamic approach. With the combined atomistic-continuum TTM-MD and macroscopic-continuum model MCM model therefore, we can align our calculations to what is experimentally accessible, and compare our results directly with the experiments [9, 10, 11, 12, 16, 18, 60]. The computational set up for the combined TTM-MD-MCM model is schematically shown in Figure 38.

The basic theses and governing equations of MCM model were described in Section 2 c). In order to combine the atomistic-continuum TTM-MD and macroscopic-continuum MCM implementing the elasto-plastic flow model, we set a common area for MD and HD domain. Hence, these two domains overlap for the purpose of exchange with the input/output information, organizing therefore a feed back to ensure the accuracy of the calculations. In the coupled TTM-MD and MCM models the time step will be synchronized for the HD and MD calculations. Each step, MD will average necessary data over all angles (due to the central symmetry) within the common MD/HD area and pass this information to the HD domain as in input, where it is treated in 2D. After the HD step, the related output data will be interpolated for the all atoms in the MD/HD area and passed to the MD domain for processing on the next time step. Due to this synchronization we have a permanent connection between HD and MD domains within the boundaries separating the atomistic and continuum

description of the same analyzed system. The complete description of the TTM-MD-MCM model will be given elsewhere [184].

In spite of the obvious advantages of such the combined computational approach to describe short pulse laser nanostructuring on the scale comparable with the experiment [9, 10, 11, 12, 16, 18, 60], there is a certain difficulties in its successful applications. The originality of the essential problem arises from the nature of discrete and continuum approaches themselves. Namely, it was indicated in [116] that the limited number of atoms (50-100) in a unit cell of TTM-TTM model results in fluctuations of such macroscopic parameters as temperature, pressure, and density. Those fluctuations do not affect the continuum part of the MD-TTM model since they get averaged in time during the MD integration. However, the jumps in definition of temperature, pressure, and especially density are very harmful for MCM part implementing the elasto-plastic flow model. Particularly, McCormack scheme used for the integration of the system, given by Eg. 10 in Section 2 c), becomes unstable. In order to get a higher stability and keep the processing safe we propose to interpolate the macroscopic parameters determined along the MD/HD zone by means of the least squares method. Thus, yet before we pass them from MD to HD domain, we smoothen the fluctuations of the temperature, pressure, and density after their averaging over all angles. Furthermore, we can get an even higher stability, if averaging those parameters over time as well. We may record the change of macroscopic variable within the MD/HD zone for the last several steps and get their weighted average every MD step. Therefore, we believe that the problems on the connection of MD and HD domains can be eventually overcome and the description of laser-induced pressure relaxation can be extended, as compare to the MD-TTM model, over the experimental scale. In the same time, since MD calculations proceed only in the central part of the system and HD calculations take place 2D, the computational cost of such processing remains very reasonable at significantly fewer number of atoms as compared to TTM-MD model describing the nanostructuring on metals, Section 3 a). The latter gives us broad opportunities to vary the laser input parameters and playing with different initial conditions have our calculations compared directly with the experimental data [9, 10, 11, 12, 16, 18, 60].

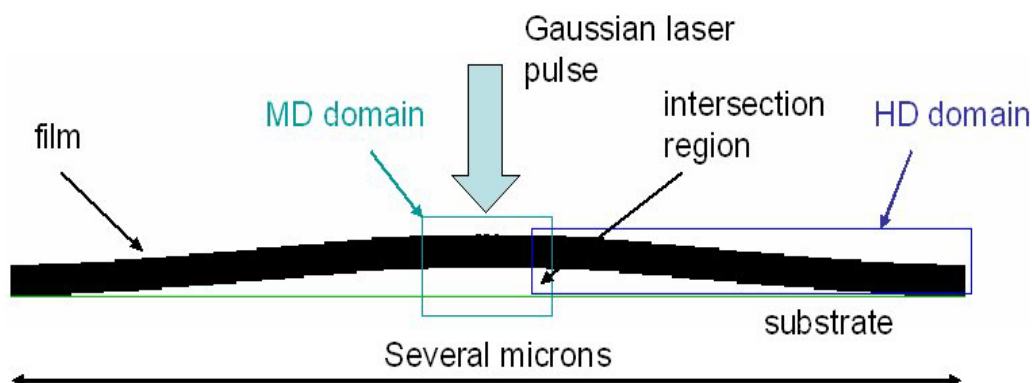


Figure 38. Comparative position of the areas of the computational cell treated with MD and HD approaches.

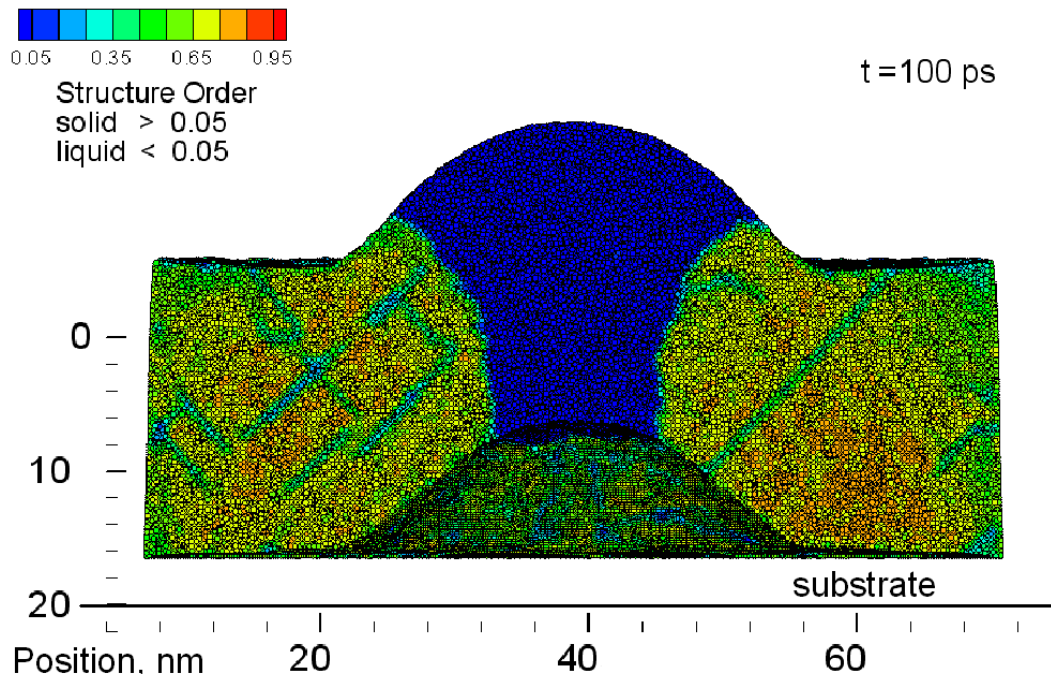


Figure 39. Position of the MD domain in the frames of TTM-MD-MCM model at the final time  $t = 100$  ps. The nanobump is formed and the solidification process is nearly finished. The atoms are colored according to their local order parameter, Section 2 b), [114] that shows atoms with disordered ambient in blue color. Coloring other than that indicates the solid with the initial [001] crystal orientation. The HD domain is not shown.

In order to validate the applicability of TTM-MD-MCM model to study the processes of nanostructuring on the example of nanojets, we perform a trial modeling of 20 nm Ni film situated on a silica substrate irradiated with 200 fs laser pulse at the absorbed fluence  $2.5 \text{ J/cm}^2$ . With this fluence, assuming a realistic metal-silica adhesion, we allow for a complete separation of the MD domain off the substrate. This separation, if happens in the case of TTM-MD model, Section 3 a), makes our further calculations no longer valid. In TTM-MD-MCM model however, the metal-substrate interaction of MD domain would still have the place via HD domain and the formation of a microbump and a nanojet can be therefore described, Figure 39. The diameters of MD domain and the laser spot was taken to be 75 nm and 10 nm respectively. The former results in the number of atoms in MD part to be just 5,997,600 that significantly simplifies calculations of MD part and the model in overall as compare to TTM-MD approach described in the previose section..

In this modeling, the separation of central part of the film, describe within MD domain, took place at 8 ps as a crack. Further monitoring of the MD domain revealed a gradual increase of this crack until it reached its maximum diameter of 110nm by the time  $t = 15$  ps, Figure 40. The initial position of the MD domain is indicated by the black solid line at the level of -20 nm. The final lattice temperature distribution is shown by color and validates an accurate connection of TTM-MD and MCM models. In spite of the mosaic-like field of temperature in MD domain [116], it can be seen that in average the lattice temperature is a continuous function at the MD/HD border.

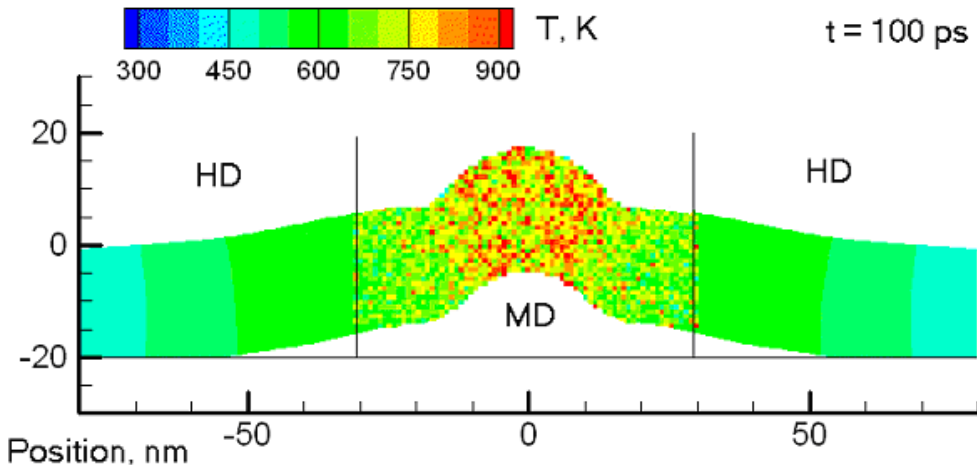


Figure 40. The overall view on the MD and HD domains at the final time  $t = 100$  ps. The color represents the lattice temperature. Two vertical solid lines indicate the borders where HD and MD domains are connected. The solid horizontal line represents the surface of substrate where the film was initially situated.

Similar, to the case with TTM-MD, in this run the electronic temperature eventually goes significantly below the lattice one, Section 3 a), and acts as an extensive cooler for the molten material in the area of nanojet formation. The difference between electron and lattice temperatures,  $\Delta T = 350$  K, was reached by  $t = 50$  ps. Therefore, in this run we reproduced the effects we have already seen with TTM-MD model, but in same time, the employed model is able to work with higher fluencies due to correct description of both the plastic deformation and the electron heat conduction in HD domain on the scale archivable in the experiments.

The problem of connecting the MD and HD domains due to nature of atomic-continuous connection, limits the absorbed fluencies at the moment to the values not exceeding  $3,1 \text{ J/cm}^2$ . A higher excitation results in strong fluctuations in definition of macroscopic parameters at the border of MD part and as a result unstable solution in HD domain. Moreover, higher fluencies would require a bigger MD domain for a possible wider propagation of the melting front. The problem of unstable numerical solution in the connecting area of TTM-MD-MCM is in the process of elaboration now, and application of a more advanced and stable algorithms against of strong fluctuations, like TVD and Godunov-based methods, can probably increase the efficiency of TTM-MD-MCM method.

Nevertheless, the possibility of a direct comparison between the experimental data on nanostructuring process [9, 10, 11, 12, 16, 18, 60] and the theoretical models implementing the atomistic-continuum numerical approach still remains within the frames of TTM-MD approach only. Particularly, in the experiment by Kuznecov [60], a nanobarrier structures on 60 nm Au film were obtained with a single femtosecond laser pulse with an intensity distribution strongly elongated perpendicular to the beam axes. The application of symmetrical boundaries (mirror type) along the obtained structure and periodic boundaries in one of the lateral direction makes the modeling on the experimental scale possible with MD-TTM approach, Figure 41.

In order to model a segment of  $60 \times 2500 \times 60$  nm, shown in Figure 41 a), the computational cell must have dimensions of  $147 \times 6125 \times 147$  lattice parameters ( $4.05 \text{ \AA}$ ) in X, Y, and Z direction respectively, accounting for about 530,000,000 atoms totally, Figure 41

b). The Au sample will have polycrystalline structure [185], for a realistic simulation of short pulse laser nanostructuring of thin Au film [60]. The film is situated on a silica substrate with which the atoms are interacting via Leonard-Johns potential, as it was done in [182]. The nonreflective (NRB) boundaries [109, 110] are applied on the right side of the model to ensure for absorption of the laser-induced pressure wave as it was done in simulation of bulk in Ref. [36, 37, 63, 64]. Since the parameter  $L_c$  [22, 79, 181] for Au material is on the order of 700 nm, the electron heat conduction therefore, must be described in continuum on a much grater scale, up to 15 microns. A special new type of mirror boundaries is necessary for simulating the presence of the material on the left at the atomic scale. To our best knowledge such type of the boundaries has not been yet implemented in Molecular Dynamics and will be elaborated and introduced in this model for the first time. Since, in the experiment, the laser pulse has intensity distribution strongly elongated perpendicular to the beam axes, the application of periodic type of boundaries in the same direction looks natural. In order to observe the formation of liquid nuclei without any possible effect form the limited size of the periodic boundaries, however, we must set their length at least equal to the film thickness [119].

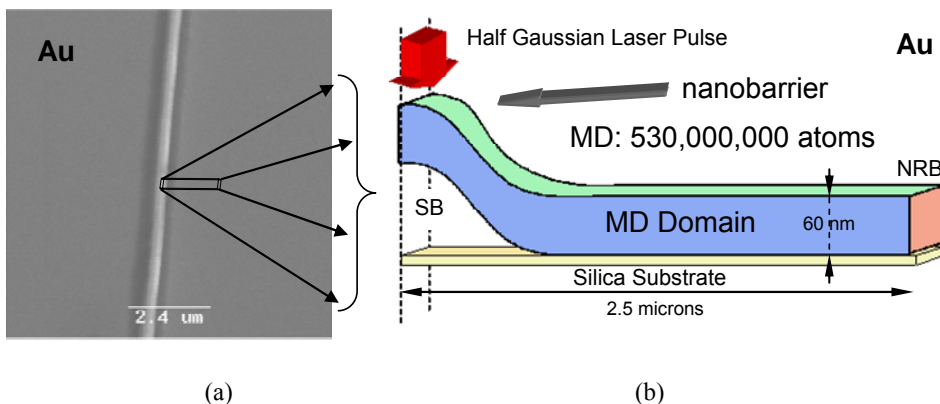


Figure 41. (a) Nanobarrier obtained at Laser Zentrum Hanover in experiments, (b) schematic representation of the model allowed for a direct comparison the results.

Finally, in order to get a possibility for a direct simulation-experiment comparison, we need to have the experimental properties of the material reproduced via EAM potential as close as it possible. Although the EAM potential for Ni and Au, developed by Johnson and utilized in [116] described some of the material thermodynamics properties close to their experimental values, it also showed a quite discrepancy for the melting temperature and the enthalpy of melting, which can be harmful in the task we pursue in our modeling on a direct simulation-experiment comparison. Recently, however, a new EAM potential by Zhakhovskii [186] was developed and discovered a good fit for several materials like Ni, Al, Au, and Pt to their experimental properties and will be therefore employed in our simulation.

Thus, in this computational approach, the complete process of femtosecond laser nanostructuring of Au film on a substrate can be modeled on the experimental scale in a super-large scale simulation based on Molecular Dynamics. The code implementing the atomistic-continuum model for nanostructuring [182] is adapted for multiprocessing and is planned for submission at Juelich Supercomputing Centre (Germany) across 4,000 processors

and more in order to process the system of  $0.5 \times 10^9$  Au atoms [187] for at least 1 ns for observation of the complete process of resolidification of the nanojet, as it is in the experiments [60]. Thus, this modeling become one of the biggest MD-based modeling up to now. It is important to notice here, that models presented above in these sections are yet in the process of elaboration and applications. Some of the details therefore may slightly change in their final versions. Especially it concerns the application of mirror type of the boundaries in modeling on direct simulation-experiment comparison of the obtained nanostructures, since a straightforward imaging of the atoms in the set plane mirror may introduce unphysical phenomenon resulted form correlated atomic motion. This can be avoided by setting the image particle velocities at the mirror type of boundaries randomly oriented, thus forcing them for uncorrelated motion, however at the same kinetic energy as thire real hosts. In the next section, we will introduce you the method of extension of the atomistic-continuum type of models for a simulation of nanostructuring processes on semiconductors and insulators.

### (e) Extension of the Combined Atomistic-Continuum Model for Nanostructuring on Semiconductors

This section we begin with the extension of the atomistic-continuum model [116] for simulation of nanostructuring processes on semiconductors [188]. Similarly to that with metals, the essential idea of the atomistic-continuum model application for other materials holds the same. Namely, within the frames of a single computational approach we describe the processes of different special scales and time intervals.

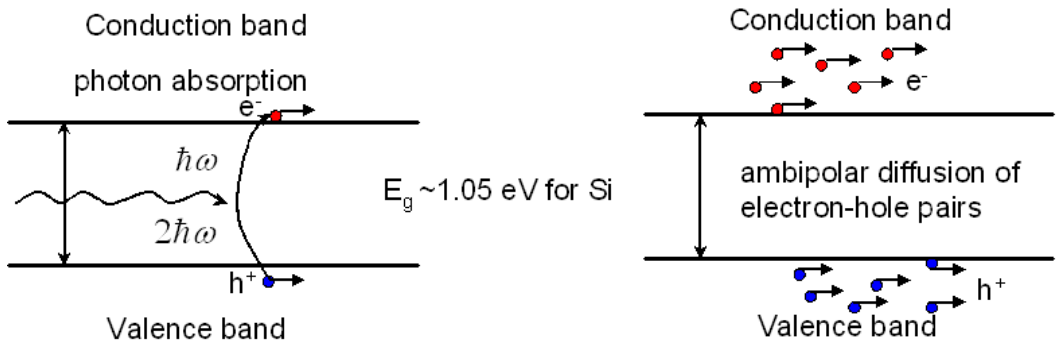


Figure 42. Schematic illustration of the electron-hole carrier excitation due 1 or 2 photon absorption in Si with a laser pulse of a sufficient energy. The further dynamics of the electron-hole condensate can be described as the ambipolar diffusion process.

For simulation of short pulse laser interaction with semiconductors, therefore, we must account for nonequilibrium phase transformation, generated with a short laser pulse, and the process of energy dissipation by free-carrier transport, similarly to that in metals on the other hand. As it was developed in [69, 70], the free carriers (electrons), when thermalized upon laser energy absorption, form a distribution governed by Fermi-Dirac statistics. Thus we could prescribe a temperature definition according to the possessed energy, and based on the energy balance the TTM model was proposed [189, 190, 191] for description of a temperature dynamics of the electrons and the phonons in metals. In essence, the TTM model states that

the local energy change in the electronic subsystem is due to three essential processes: the energy transport by electron heat conduction, the energy exchange with the phononic subsystem, and the energy gained due to the laser light absorption.

In the experiment with Si, on the other hand, one has to consider the energy gap  $E_g = 1.05$  eV. But under laser irradiation of sufficiently high energy one can promote quite a few electrons into the conduction band by means of 1 or 2 photon absorption, Figure 42. The latter results in the establishment of electron-hole condensate that is governed by Fermi-Dirac statistics. Thus, the dynamics of the electron-hole carrier transport can be described as an ambipolar diffusion process [190] and a model, similar to TTM, based on the energy balance can be proposed. Similarly, to TTM [70], the change of total energy of the electron-hole condensate will be accounting from: 1) the energy gained from the laser irradiation due to one or multiphoton absorption processes and direct laser light abortion by free carriers, 2) equilibration of free carrier's density and temperature gradient, and 3) the energy exchange between electron-hole carriers and phonons. The processes of impact ionization and Auger recombination processes must be added to the calculation of electron-hole carrier density. The complete Self Consistent Model (SCM) model can be found in Ref. [190, 191] and it has the following governing system of equations in 1D:

$$\left\{ \begin{array}{l} \frac{\partial n}{\partial t} = \frac{\alpha I(z, t)}{h\nu} + \frac{\beta I^2(z, t)}{2h\nu} - \gamma n^3 + \theta n - \nabla \cdot \bar{J}(n, T_e, E_g) \\ \frac{\partial U_e(n, T_e, E_g)}{\partial t} = (\alpha + \Theta n)I(z, t) + \beta I^2(z, t) \\ - \nabla \cdot \vec{W}(n, T_e, E_g) - \frac{C_{e-ph}(n, T_e, E_g)}{\tau_{e-ph}}(T_e - T_l) \\ C_l \frac{\partial T_l}{\partial t} = \nabla \cdot (k \bar{\nabla} T_l) + \frac{C_{e-ph}(n, T_e, E_g)}{\tau_{e-ph}}(T_e - T_l) \end{array} \right. \quad (30)$$

where subscripts  $\underline{e}$  and  $\underline{l}$  stay for the electron-hole and phonon systems respectively.  $n$  is the free carrier (electron-hole pairs) density,  $U_e$  the total free carrier energy density,  $T$  is temperature, and  $E_g$  is the energy gap. The ratio of the electron-hole heat capacity  $C_{e-ph}$  and electron-hole relaxation time  $\tau_{e-ph}$  defines the rate of energy transfer form hot electron-hole carriers to the energy of phonon vibrations, or in other words lattice temperature, and  $I(\mathbf{r}, t)$  is the laser intensity.

The first equation describes density of the electron-hole carriers via one or two photon absorption given by first and second terms respectively with material parameters  $\alpha$  and  $\beta$ . The third term describes the Auger recombination with parameter  $\gamma$ , forth term gives the impact ionization with parameter  $\theta$ , and finally the last term described the loss mechanism due to carrier current. Note, that applicability of the term describing impact ionization need to be confirmed depending on intensity and pulsed duration [186]. The second equation stays for the balance of total energy of the electron-hole pairs. Similarly to the first equation, it accounts for the processes of one and two photon absorption, the energy flux  $W$  and the energy exchange with lattice. Third equation describes the energy balance of lattice in the same form as it is in TTM [70], Eq. 1, Section 2 a). Follow the formulation of ultrafast transport dynamics presented in [188, 189], the carriers current is given by:

$$\vec{J} = -D \left\{ \begin{array}{l} \bar{\nabla} n + \frac{n}{k_b T_e} [H_{-1/2}^{1/2}(\eta_e) + H_{-1/2}^{1/2}(\eta_h)]^{-1} \bar{\nabla} E_g \\ + \frac{n}{T_e} \left\{ 2 [H_0^1(\eta_e) + H_0^1(\eta_h)] / [H_{-1/2}^{1/2}(\eta_e) + H_{-1/2}^{1/2}(\eta_h)] - \frac{3}{2} \right\} \bar{\nabla} T_e \end{array} \right\} \quad (31)$$

where the ambipolar diffusion coefficient D is given by:

$$D = \frac{k_b T_e}{q} \frac{\mu_e^0 \mu_h^0 H_{1/2}^0(\eta_e) H_{1/2}^0(\eta_h)}{\mu_e^0 H_{1/2}^0(\eta_e) + \mu_h^0 H_{1/2}^0(\eta_h)} [H_{-1/2}^{1/2}(\eta_e) + H_{-1/2}^{1/2}(\eta_h)] \quad (32)$$

the reduced Fermi Levels  $\mu_c$  can be found from the local carrier density, obtained by integrating over the microscopic quasi-equilibrium distribution functions [192]

:

$$n_c = 2 \left[ \frac{m_c^* k_b T_c}{2\pi\hbar^2} \right]^{3/2} F_{1/2}(\eta_c) \quad (33)$$

where

$$F_\xi(\eta_c) = \frac{1}{\Gamma(\xi+1)} \int_0^\infty \frac{x^\xi}{1 + \exp(x - \eta_c)} dx \quad \text{and} \quad F_\xi(\eta_c)/F_\zeta(\eta_c) = H_\zeta^\xi(\eta_c) \quad (34)$$

The energy current is defined by carrier's density gradient leading to the ambipolar diffusion and temperature gradient causing the heat transport. Given by the sum of the carrier energy current in electrons and holes it is resulting therefore in:

$$\bar{W} = \{E_g + 2k_b T_e [H_0^1(\eta_e) + H_0^1(\eta_h)]\} \bar{J} - (k_e + k_h) \bar{\nabla} T_e \quad (35)$$

where  $k_e$  and  $k_h$  are the conductivities of the electrons and holes respectively.

Since the total energy density  $U_e$  in the electron-hole pairs is the product of the carrier number density number  $n$  and the sum of the band gap  $E_g$  energy per unit volume and the kinetic energy is given by:

$$U_e = n \left\{ E_g + \frac{3}{2} k_b T_e [H_{1/2}^{3/2}(\eta_e) + H_{1/2}^{3/2}(\eta_h)] \right\} \quad (36)$$

Substituting Eq. 36 into the second equation of Eq. 30 and bearing in mind that the heat capacity of the electron-hole pairs  $C_{e-h} = \partial U_e / \partial T_e|_{n=const}$  we can write an explicit energy balance equation with respect to temperature of the electron-hole free carriers,  $T_e$ :

$$\begin{aligned}
C_{e-h}(n, T_e, E_g) \frac{\partial T_e}{\partial t} = & (\alpha + \Theta n) I(z, t) + \beta I^2(z, t) - \nabla \cdot \vec{W}(n, T_e, E_g) \\
& - \frac{C_{e-h}(n, T_e, E_g)}{\tau_e} (T_e - T_l) - n \left( \frac{\partial E_g}{\partial n} \frac{\partial n}{\partial t} + \frac{\partial E_g}{\partial T_l} \frac{\partial T_l}{\partial t} \right) \\
& - \frac{\partial n}{\partial t} \left\{ E_g + \frac{3}{2} k_b T_e [H_{1/2}^{3/2}(\eta_e) + H_{1/2}^{3/2}(\eta_h)] \right\}
\end{aligned} \tag{37}$$

with

$$\begin{aligned}
C_{e-h}(n, T_e, E_g) = & n \frac{\partial E_g}{\partial T_e} + \frac{3}{2} n k_b \{ H_{1/2}^{3/2}(\eta_e) + H_{1/2}^{3/2}(\eta_h) \} \\
& - \frac{3}{2} n k_b \{ \eta_e [1 - H_{1/2}^{3/2}(\eta_e) H_{1/2}^{-1/2}(\eta_e)] + \eta_h [1 - H_{1/2}^{3/2}(\eta_h) H_{1/2}^{-1/2}(\eta_h)] \}
\end{aligned} \tag{38}$$

Although the Eq. 37 gives an explicit relation with respect to  $T_e$ , the energy density balance via formulation 37 is a nonconservative scheme, so that the control of the numerical scheme through the conservation of energy is not possible. In this sense, the energy density balance given by second equation in Eq. 30 is of a better preference.

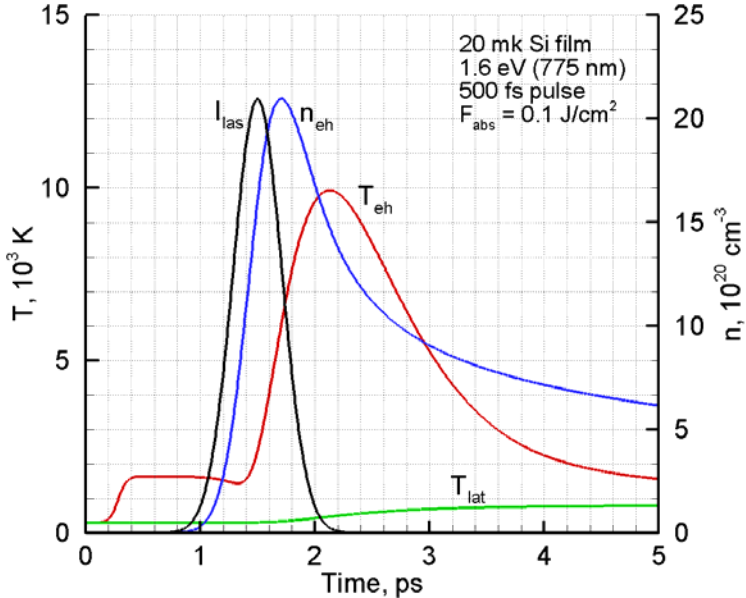


Figure 43. Electron-hole (red) and lattice (green) temperature along with density of free carriers (blue) dynamics is presented according to Self Consistent Model in [191]. The calculations are performed for 20  $\mu\text{m}$  free standing Si film at 500 fs 775 nm laser pulse at the absorbed fluence of  $0.1 \text{ J/cm}^2$ . The laser intensity is shown in black and not in scale.

Finally, for a volume-absorbing material, the laser attenuation in the direction of propagation  $z$  can be obtained by solving the following differential equation that describes losses due one- or two-photon absorption and free carrier absorption [191]:

$$\frac{\partial I(z,t)}{\partial z} = -(\alpha + \Theta n)I(z,t) - \beta I^2(z,t) \quad (39)$$

For the constant values of  $\alpha$ ,  $\beta$ , and  $\Theta$  a closed-form solution of the Eq. 39 can be derived [191]:

$$I(z,t) = -\frac{(\alpha + \Theta n)I_0(r,t)\exp(-(\alpha + \Theta n)z)}{(\alpha + \Theta n) + \beta[1 - \exp(1 - ((\alpha + \Theta n)z))]} \quad (40)$$

where  $I_0(r,t)$  is the incident intensity of the laser beam at the material surface,  $z = 0$ , given by Eq. 29 in Section 3 b).

Following the numerical procedure described in Ref. [191], one can obtain the solution of Eq. 30 for a 500 fs 775nm laser pulse interacting with a 20mk free standing Si film. The expensive calculations of reduced chemical potential  $\eta_c$  in SCM model from transcendental Eq. 33 can be tabulated in order to increase the efficiency of the numerical scheme, which was realized in finite differences method here. Together with the electron-hole temperature dynamics at the surface, Figure 39 shows the lattice temperature dynamics and the transient carrier density of laser-generated free carriers. The laser intensity reflecting Gaussian temporal profile is not in the scale, but rather an eye guide. The material parameters for in present SCM calculations are taken from Ref. [190, 191].

The unusual double peak behavior in the electron-hole temperature dynamics, as it can be seen from Figure 43, clearly correlate with the laser pulse shape. When number of free carriers  $n$  is negligible, their heat capacity  $C_{e-h}$  is low and the temperature of the electron-hole pairs easily goes up. When the number of free carriers become sufficiently high, their temperature growth cease for a moment and energy dissipation via heat conductivity mechanism comes to place, that is reflected in a transient temperature decrease. The further increase in the number of free carriers in the conduction band, however, results in a direct laser light absorption as a dominant absorption mechanism and the temperature of electron-hole pairs is rising again following the laser pulse, similarly to the electron temperature dynamics in TTM model for metals, Section 2 a). The lattice temperature is gradually increasing until it equilibrates with temperature of free carriers roughly by the time of 20 ps, that is associated with free carriers phonon equilibration time,  $\tau_e$ .

The interesting behavior of the electron-hole temperature dynamics during short pulse laser interaction with Si opens up a wide range for research opportunities from the point of view of both the fundamental physics and the practical application for the purpose of nanostructuring. In order to have this model applicable in nanostructuring experiment however, we must deal with basically same essential physical mechanisms that were found to be responsible for the structuring on metals. They are transient laser-induced nonequilibrium phase transformation under condition of strong superheating and fast deformation rates on one hand, and fast electron-hole heat conduction, laser light absorption, and laser-induced nonequilibrium between electron-holes and phonons. On the other hand, all these processes can be, similarly to TTM-MD, described within the scale of a single computational approach, where phase transformations are taken care of at the atomic level with MD approach, and processes due to free carriers are treated in continuum with SCM model. The atomistic-continuum model for semiconductors therefore, by analogy with TTM-MD, can be composed by substituting the last equation for lattice in Eq. 30 by MD integration in which the energy

exchange between the electron-hole free carriers and phonons vibrations is accounted for by adding an additional friction term expressed via thermal velocities, as it was described in Section 3 b):

$$\left\{ \begin{array}{l} \frac{\partial n}{\partial t} = \frac{\alpha I(z,t)}{h\nu} + \frac{\beta I^2(z,t)}{2h\nu} - \gamma n^3 + \Theta n - \nabla \cdot \vec{J}(n, T_e, E_g) \\ \frac{\partial U_e(n, T_e, E_g)}{\partial t} = (\alpha + \Theta n)I(z,t) + \beta I^2(z,t) \\ - \nabla \cdot \vec{W}(n, T_e, E_g) - \frac{C_{e-h}(n, T_e, E_g)}{\tau_e} (T_e - T_l) \\ m_i \frac{d^2 \vec{r}}{dt^2} = \vec{F}_i + \xi m_i \vec{v}_i^T \end{array} \right. \quad (41)$$

where

$$\xi = \frac{\frac{1}{n} \sum_{k=1}^n V_N \frac{C_{e-h}}{\tau_e} (T_e^k - T_l)}{\sum_i m_i (\vec{v}_i^T)^2} \quad (42)$$

When merging these two models MD and SCM, however, one must carefully consider the effect the excited free carriers on the weakening of the atomic bonding, that for the case of silicon will be described by Stillinger-Webber potential [193]. In the work by Loras [194], the attractive part of the Stillinger-Webber potential was simply discarded upon the electron-hole pair excitation. Such a rude approximation was not supported in *ab-initio* calculations by Louie [195] where role of the electorn-hole interaction was investigated followed by optical excitation. In the atomistic-continuum model for the nanostructuring on Si therefore, one must fit the Stillinger-Webber potential in MD calculations for Si in accordance with *ab-initio* calculations in which the effect of photoexcited electron-hole pairs is thoroughly considered. In the next section, we describe how to extent the applicability of the combined atomistic-continuum computational technique to study the nanostructuring processes on insulators.

## (f) Extension of the Combined Atomistic-Continuum Model for Nanostructuring of Insulators

The strategy of the hybrid atomistic-continuum modeling of the complex laser-induced transient processes resulted in extention of the applicability of the TTM-MD model to the nanostructuring on metals on the experimental scale and on semiconductors, Section 3 b)-e). Moreover, recent experiment with near-field optics involved into nanostructuring process [48, 49, 50, 51 ] allows us for a direct comparison of the calculation with the experimental data already with models described in Section 3 c) and d), that reinforce the position of the atomistic-continuum modeling as an advanced computational tool in investigation of short pulse laser materials interactions for the pulpous of studying the ultrafast phenomenon in

nanostructuring experiments [9, 10, 11, 12, 16, 18, 60]. But even beyond the laser applications, the TTM-MD-based model can be applicable to a broader range of phenomena. In fact, this model will be applicable everywhere where fast and localized energy deposition occurs, from ion beam surface nanomodifications and cluster deposition to the analysis of damage to a spacecraft shielding material from hypervelocity impacts by energetic particles.

In Section 2 e) we considered DFT method in description of fast and localized energy deposition with swift heavy ions in nanostructuring experiments on the surface of SrTiO<sub>3</sub> material [19,]. In his model, however, Osmani used the TTM model for the description of fast electron heat conduction and electron-phonon nonequilibrium. While accepting such the model as a first approximation of quite complex phenomena, the applicability of the TTM model is limited here by the absence of local thermal equilibrium everywhere in the proximity of restructured surface within any volume comprising 50-100 atoms for a meaningful determination of lattice temperature. The same problem is related to the electronic system as well. Strong excitation with heavy swift ions can promote the electrons into the conduction band, where yet before the establishment of Fermi-Dirac distribution, a significant energy transport due to heat conduction or ballistic energy transport can occur [22, 59]. Apparently, within the scope of our review, the description of nonthermalized electrons should be given with Boltzmann system, Section 2 d). Finally, for a reliable treatment of fast transient processes of melting and formation of the nanohillocks, the Boltzmann approach for nonthermalized electrons must be utilized in a coupling with atomic description based on MD approach, similarly to that was done when linking TTM and MD models in nanostructuring on metals and semiconductors. The problem of Boltzmann system numerical applicability, however, is that it is written in *K* space, Eq. 14, whereas both DFT and MD methods are working in real space. Therefore, in order to bring all these three methods in one computational approach, we suggest solving the Boltzmann system in each numerical cell where treatment of the nonequilibrium electronic system is considered to be necessary, obtaining therefore the local solution of Boltzmann system for the real space.

The MD computational approach, on the other hand, can be used for description of fast nonequilibrium processes of phase transformation at the atomic level. The crystal structure of SrTiO<sub>3</sub> is related to the group of Perovskite type, which is fcc with Sr in corners and Ti in the center of the cubic cell, Figure 44.

The simulation of this crystal structure with molecular dynamic approach was described in Ref. [196], where ionic crystal model was proposed for the treatment of interatomic interaction:

$$U_{ij} = \frac{1}{4\pi\epsilon} \frac{Z_i Z_j e^2}{r_{ij}} + f_0(b_i + b_j) \exp\left(\frac{a_i + a_j - r_{ij}}{b_i + b_j}\right) - \frac{c_i c_j}{r_{ij}^6} + D_{ij} \left\{ \exp[-2\beta_{ij}(r_{ij} - r_{ij}^*)] - 2 \exp[-\beta_{ij}(r_{ij} - r_{ij}^*)] \right\} \quad (43)$$

The first term represents the Coulomb interaction, where  $Z_i$  and  $Z_j$  are the effective charges of ions I and j, respectively and  $r_{ij}$  is the interatomic distance between the ions. The second term represents the short range repulsion potential. The parameters  $a_i$  and  $a_j$  reflect the radii and  $b_i$  and  $b_j$  reflect the hardness of the ions i and j and  $f_0 = 0.043364$  eV\*A. Their term represents the dipole induced dispersion potential based on the van der Waals interaction. The

last term is the Morse potential for description of covalent bonding for Ti-O bonds only, where  $D_{ij}$ ,  $b_{ij}$ , and  $r_{ij}^*$  are the specific parameters for the Ti-O bond. The parameters of the interatomic potential given by Eq. 43 are listed in the Table 2 for SrTiO<sub>3</sub> material.

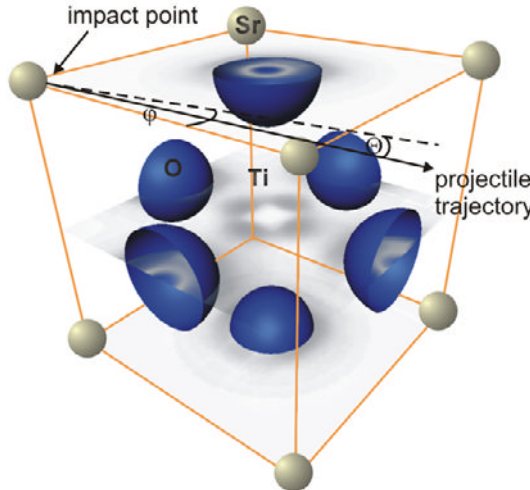


Figure 44. Schematic representation of the Ionic Crystal cell [139]. The direction of projectile is indicated by an arrow.

**Table 2. Parameters for SrTiO<sub>3</sub> material described via Ionic Crystal Model, Eq. X23.**  
For Ti-O bonds, the parameters are:  $D_{ij} = 1.1193 \text{ eV}/\text{at}$ ;  $\beta_{ij} = 2.0 \text{ \AA}^{-1}$ ;  $r^* = 1.6 \text{ \AA}$ .

Parameter	Z	a, Å	b, Å	C, eV <sup>1/2</sup> Å <sup>3</sup> at <sup>-1/2</sup>
O	-1.4	1.850	0.18	8.5569
Ti	2.2	1.385	0.10	0.0
Sr	2.0	1.846	0.13	5.9083

Similarly to that in Section 3 b) when constructing the atomistic-continuum TTM-MD model, the energy conservation law is utilized for controlling the accuracy of the calculations that is specifically important for ionic crystal type of potentials since it involves the summation of long range interactions  $\sim 1/r$ , originating from Coulomb interaction, given by first term of Eq. 43. An advanced Ewald summation method is suggested in Ref. [197] to take care of long range electrostatic forces. Although, the classical Ewald method results in a poor scaling with number of particles  $N$  in the system, leading to number of calculation  $\sim N^2$ , there are schemes that allow for speeding up the Ewald Summation with Fast Fourier Transformation and increasing the efficiency of the calculations up to  $\sim NLog(N)$  and even better [192,193,194,195]. Several theoretical groups, however, consider a straight forward Ewald method summation as is inefficient when crystal structure is vanishes due to melting process. Thus, a more advanced and computationally favorable method Particle-Particle-Particle-Mesh (P<sub>3</sub>M) [198, 199, 200, 201] method looks reasonable for studing nanostructuring processes on insulators.

Thus, by merging all three model in a single computational approach, we are able to simulate fast and localized ion energy deposition in the electronic system of SrTiO<sub>3</sub> with DFT method, fast ballistic transport with nonthermalized electrons under conditions of the

electron-phonon nonequilibrium with the system of Boltzmann equations in a real space, and transient nonequilibrium induced phase transformation processes at the atomic level with Molecular Dynamics. We believe that this atomistic-continuum computational model will allow for a simulation of the nanostructuring processes induced by not only in ion bombardment experiments [19], but also in atto- and femto-second pulse laser experiments, in essence as soon as fast and localized energy deposition take place.

## CONCLUSION

In conclusion we want to indicate that the presented strategy of combination of the potentially different models for description of fast surfaces nanostructuring processes different in respect to temporal and special scale has found a significant support of its applicability. The combined atomistic-continuum models allowed for simultaneous description of the laser light absorption, laser-induced electron-phonon nonequilibrium, and fast free carrier heat conduction processes in continuum on one hand with the Two Temperature Model, and transient nonequilibrium phase transformations at the atomic scale with Molecular Dynamic approach on the other hand. Moreover, nonequilibrium processes induced by very intensive and localized energy deposition on the scale of angstroms can be accounted for by means of adding Density Functional Theory description or Boltzmann kinetic approach and long range laser induced elasto-plastic deformations occurring in micron spawn can be described by Macroscopic Continuum Models. With the multiscale methodic outlined in this chapter therefore, we have a very powerful computational tool for studying nanostructuring processes on material surfaces induced with a short pulse laser beams or other means of fast and dense energy deposition.

The results of TTM-MD model application for investigation of short pulse laser nanostructuring processes on metals suggest that the essential mechanism of the nanojet and nanobump formation is the interplay of two laser-induced processes. Fast energy deposition followed by the recoil of compressive/tensile pressure waves in both radial and vertical directions results in the establishment of the hydrodynamic motion of the molten material that is an essential driving force responsible for the acceleration of the melt and formation of the nanojet. The nanojet solidification, on the other hand, is essentially due to fast electron heat conduction in multidimensional space. The electron temperature goes significantly below (up to  $\sim 500$  K) the temperature of melted lattice in the vicinity of the forming nanofeature, which results in a very strong cooling of the melt and very fast (within tens of picoseconds) solidification of the nanojet due to homogeneous phase nucleation mechanism. The resulting nanostructure therefore exhibit a nanocrystalline character. Finally, the establishment of a strong temperature gradient in the vicinity of the laser spot lead to the long range elasto-plastic deformation of the film on the micron scale and formation of a microbump on which the nanostructures appear.

The effect of electron heat conduction on the nanojet solidification process can be significantly increased if developed in 3D. In the modeling presented in Section 3 c), the film thickness of 20 nm is rather small comparatively with the distance  $L_c$ , which is 50 nm for Ni. Therefore, no temperature gradient is developed in the vertical, Z, direction upon the electron-phonon equilibration and heat conduction proceeds in radial, 2D, direction only. If we take a

thicker film, however, 50 nm and more, the electron heat conduction will proceed in both radial and vertical direction resulting in much stronger, 3D, cooling of the electrons. In this case, the temperature difference reached between the electrons and lattice can be much greater and extremely fast cooling and resolidification can potentially induce the appearance of metastable structures.

Note, that although the presented results on nanostructuring experiments on metals in Section 3 were yet limited in size by computational power, recent development of subwavelength structuring and nearfield optics allow for a direct simulation-experiment comparison already at this stage. The inclusion of the Macroscopic Continuum Model into consideration will significantly increase the scale of the model applicability up to microns with decrees of the computational cost at the same time. Nevertheless, the computational cell set-up presented in the Section 3 d) will allow for a direct simulation-experiment comparison of the modeled features in a super large scale modeling on advanced computational facilities (Juelich Supercomputer Centre, Aachen, Germany) already at this stage within the frames of the atomistic-continuum TTM-MD model.

Moreover, beyond the laser applications on metals, the TTM-MD-based models can be applicable to a broad range of phenomena and materials. The discussions on the atomistic-continuum computational approach when modeling nanostructures on metals by analogies where carried out in the application on semiconductors, that additionally reinforces the position of the atomistic-continuum modeling strategy. In fact, this model will be applicable everywhere where fast energy deposition takes place, from ion beam surface nanomodifications and cluster deposition to the analysis of damage to a spacecraft shielding material from hypervelocity impacts by energetic particles, that was considered on the example of the TTM-MD-based model application to study nanostructuring processes on the surface of  $TiSrO_3$  with swift heavy ions.

## REFERENCES

- [1] Maiman, T. H. (1960) "Stimulated Optical Radiation in Ruby", *Nature*, 187, 493.
- [2] Basov, N. G. & Prohorov, A. M. (1955) "Possible Methods of Obtaining Active Molecule doe a Molecular Oscillator", *Sov. Phys. JETP*, 1, 184.
- [3] Basov, N. G. & Prohorov, A. M. (1955) Theory of the Molecular Generator and the Molecular Power Amplifier", *Sov. Phys. JETP*, 3, 426.
- [4] Townes, C. H. & Schawlow, A. L. (1958) "Infrared and Optical Masers" *Phys. Rev.*, 112, 1940.
- [5] Einstein, A. (1917). "Zur Quantentheorie der Strahlung", *Physika Zeitschrift*, 18, 121.
- [6] Berlien, H. P. & Mueller, G. J. (2003) *Applied Laser Medicine*, Springer-Verlag, Berlin, Heidelberg, New York.
- [7] Powel, J. (1998) "CO<sub>2</sub> Laser Cutting", Springer London Ltd, 2nd Revised edition.
- [8] Wolf, E. L. (2006) *Nanophysics and Nanotechnology: Introduction to Modern Concepts in Nanoscience*, Weinheim : Wiley-VCH , 2nd updated and enl. Ed.
- [9] Korte, F., Koch, J. & Chichkov, B. N. (2004) "Formation of Microbumps and Nanojets on Gold Targets by Femtoseccond Laser Pulse", *Appl. Phys. A*, 79, 879.

- [10] Koch, J., Korte, F., Bauer, T., Fallnich, C., Ostendorf, A. & Chichkov, B. N. (2005) "Nanotexturing of Gold Films by Femtosecond Laser-Induced Melt Dynamics", *Appl. Phys. A*, **81**, 325.
- [11] Nakata, Y., Okada, T. & Maeda, M. (2002) "Fabrication of Dot Matrix, Comb, and Nanowire Structures Using Laser Ablation by Interfered Femtosecond Laser Beams," *Appl. Phys. Lett.*, **81**, 4239.
- [12] Nakata, Y., Miyanaga, N. & Okada, T. (2007) "Nano-Structured Surfaces on Ni-Ti Generated by Multiple Shots of Interfering Femtosecond Laser", *Appl. Surf. Sci.*, **253**, 6555.
- [13] Björk, G., Sánchez-Soto, L. L. & Söderholm, J. (2001) "Entangled-State Lithography: Tailoring Any Pattern with a Single State", *Phys. Rev. Lett.*, **86**, 4516.
- [14] Björk, G., Sánchez-Soto, L. L. & Söderholm, J. (2001) "Subwavelength Lithography Over Extended Areas", *Phys. Rev. A*, **64**, 013811.
- [15] Pronko, P. P., Dutta, S. K., Squier, J., Rudd, J. V., Du, D. & Mourou, G. (1995) "Machining of Sub-Micron Holes Using a Femtosecond Laser at 800 nm", *Optics Comm.*, **114**, 106.
- [16] Nolte, S., Momma, C., Jacobs, H., Tünnermann, A., Chichkov, B. N., Wellegehausen, B. & Welling, H. (1997) "Ablation of Metals by Ultrashort Laser Pulses", *J. Opt. Soc. Am. B*, **14**, 2716.
- [17] Stuart, B. C., Feit, M. D., Herman, S., Rubenchik, A. M., Shore, B. W. & Perry, M. D. (1996) "Optical Ablation by High-Power Short-Pulse Lasers", *J. Opt. Soc. Am. B*, **13**, 459.
- [18] Korte, F., Serbin, J., Koch, J., Egbert, A., Fallnich, C., Ostendorf, A. & Chichkov, B. N. (2003) "Towards Nanostructuring with Femtosecond Laser Pulses", *Appl. Phys. A*, **77**, 229.
- [19] Akcöltekin, E., Akcöltekin, S., Osmani, O., Duvenbeck, A., Lebius, H. & Schleberger, M. (2008) "Swift Heavy Ion Irradiation of SrTiO<sub>3</sub> Under Grazing Incidence", *New J. Phys.*, **10**, 053007.
- [20] Drude, P. (1900) "Electron Theory of Metals", *Ann. Physik.*, **1**, 566.
- [21] Kittel, C. (1996) "Introduction to Solid State Physics", 7th ed., John Wiley and Sons, New York.
- [22] Hohlfeld, J., Wellershoff, S. S., Gudde, J., Conrad, U., Jahnke, V. & Matthias, E. (2000) "Electron and Lattice Dynamics Following Optical Excitation of Metals", *Chem. Phys.*, **251**, 237.
- [23] Fann, W. S., Storz, R., Tom, H. W. K. & Bokor, J. (1992) "Electron Thermalization in Gold", *Phys. Rev. B*, **46**, 13592.
- [24] Sun, C. K., Valle'e, F., Acioli, L. H., Ippen, E. P. & Fujimoto, J. G. (1994) "Femtosecond-Tunable Measurement of Electron Thermalization in Gold", *Phys. Rev. B*, **50**, 15337.
- [25] Bejan, D. & Raseev, G. (1997) "Nonequilibrium Electron Distribution in Metals", *Phys. Rev. B*, **55**, 4250.
- [26] Lugovskoy, A. V. & Bray, I. (1999) "Ultrafast Electron Dynamics in Metals Under Laser Irradiation", *Phys. Rev. B*, **60**, 3279.
- [27] Bonn, M., Denzler, D. N., Funk, S., Wolf, M., Wellershoff, S. S. & Hohlfeld, J. (2000) "Ultrafast Electron Dynamics at Metal Surfaces: Competition Between Electron-Phonon Coupling and Hot-Electron Transport", *Phys. Rev. B*, **61**, 1101.

- [28] Falkovsky, L. A. & Mishchenko, E. G. (1999) "Electron-Lattice Kinetics of Metals Heated by Ultrashort Pulses", *Zh. Eksp. Teor. Fiz.*, **115**, 149.
- [29] Schmidt, V., Husinsky, W. & Betz, G. (2002) "Ultra Short Laser Ablation of Metals: Pump-Probe Experiments, the Role of Ballistic Electrons and the Two Temperature Model", *App. Surf. Sci.*, **145**, 197-198.
- [30] Chen, J. K. & Beraun, J. E. (2001) "Numerical Study of Ultrashort Laser Pulse Interactions with Metal Films", *Numerical Heat Transfer, Part A*, **40**, 1.
- [31] Lin, Z. & Zhigilei, L. V. (2007) "Temperature Dependences of the Electron-Phonon Coupling, Electron Heat Capacity and Thermal Conductivity in Ni under Femtosecond Laser Irradiation", *Appl. Surf. Sci.*, **253**, 6295.
- [32] Lin, Z., Zhigilei, L. V. & Celli, V. (2008) "Electron-Phonon Coupling and Electron Heat Capacity of Metals under Conditions of Strong Electron-Phonon Nonequilibrium", *Phys. Rev. B*, **77**, 075133.
- [33] Ivanov, D. S. & Rethfeld, B. C. (2008) "The Effect of Pulse Duration on the Character of Laser Heating: Photo-Mechanical vs. Photo-Thermal Damage of Metal Targets", online *Appl. Surf. Sci.*, **255**, 9724.
- [34] Ma, D. & Li, Y. (2000) "Heterogeneous Nucleation Catastrophe on Dislocations in Superheated Crystal", *J. Phys.: Condens. Matter*, **12**, 9123.
- [35] Rethfeld, B., Sokolowski-Tinten, K., von der Linde, D. & Anisimov, S. I. (2002) "Ultrafast Thermal Melting of Laser-Excited Solids by Homogeneous Nucleation", *Phys. Rev. B*, **65**, 092103.
- [36] Zhigilei, L. V., Lin, Z. & Ivanov, D. S. (2006) "Molecular Dynamics Study of Short Pulse Laser Melting, Recrystallization, Spallation, and Ablation of Metal Targets", *Proceedings of the 2006 ASME International Mechanical Engineering Congress and Exposition (IMECE2006)*, ASME paper IMECE16305.
- [37] Zhigilei, L. V., Lin, Z. & Ivanov, D. S. (2009) "Atomistic Modeling of Short Pulse Laser Ablation of Metals: Connections Between Melting, Spallation, and Phase Explosion", *J. Chem. Phys. C*, **113**, 11892.
- [38] Born, M. (1939) "Thermodynamics of Crystals and Melting", *J. Chem. Phys.*, **7**, 591.
- [39] Bucksbaum, P. H. & Bokor, J. (1984) "Rapid Melting and Regrowth Velocities in Silicon Heated by Ultraviolet Picosecond Laser Pulses", *Phys. Rev. Lett.*, **53**, 182.
- [40] Kapat, J. S., Wei, Z. & Kumar, A. (1998) "Role of Kinetics in Laser Processing", *Appl. Surf. Sci.*, **212**, 127-129.
- [41] Lin, Z. & Zhigilei, L. V. (2006) "Time-Resolved Diffraction Profiles and Atomic Dynamics in Short Pulse Laser Induced Structural Transformations: Molecular Dynamics Study", *Phys. Rev. B*, **73**, 184113.
- [42] Bennett, T. D., Grigoropoulos, C. P. & Krajnovich, D. J. (1995) "Near-Threshold Laser Sputtering of Gold", *J. Appl. Phys.*, **77**, 849.
- [43] Vorobyev, A. Y. & Guo, C. (2007) "Femtosecond Laser Structuring of Titanium Implants", *Appl. Surf. Sci.*, **253**, 7272.
- [44] Lindemann, F. A. (1910) "The Calculation of Molecular Vibration Frequencies", *Z. Phys.*, **11**, 609.
- [45] Lu, K. & Li, Y. (1998) "Homogeneous Nucleation Catastrophe as a Kinetic Stability Limit for Superheated Crystal", *Phys. Rev. Lett.*, **80**, 4474.
- [46] Born, M. & Wolf, E. (1965) "Principles of Optics", Pergamon Press, New York.

- [47] Mannion, P., Magee, J., Coyne, E., O'Connor, G. & Glynn, T. J. (2004) "The Effect of Damage Accumulation Behavior on Ablation Thresholds and Damage Morphology in Ultrafast Laser Micro-Machining of Common Metals in Air", *Appl. Surf. Sci.*, 233, 275.
- [48] Yin, X., Fang, N., Zhang, X., Martini, I. B. & Schwartz, B. J. (2002) "Near-Field Two-Photon Nanolithography Using an Apertureless Optical Probe", *Appl. Phys. Lett.*, 81, 3663.
- [49] Jersch, J., Demming, F., Hildenbrand, J. & Dickmann, K. (1997) "Nano-Material Processing with Laser Radiation in the Near Field of a Scanning Probe Tip", *Opt. Laser Technol.*, 29, 433.
- [50] Chimalgi, A., Choi, T. Y., Grigoropoulos, C. P. & Komvopoulos, K. (2003) "Femtosecond Laser Apertureless Near-Field Nanomachining of Metals Assisted by Scanning Probe Microscopy", *Appl. Phys. Lett.*, 82, 1146.
- [51] Huang, S. M., Hong, M. H., Lu, Y. F., Lukyanchuk, B. S., Song, W. D. & Chong, T. C. (2002) "Pulsed-Laser Assisted Nanopatterning of Metallic Layers Combined with Atomic Force Microscopy", *J. Appl. Phys.*, 91, 3268.
- [52] Wellershoff, S. S., Hohlfeld, J., Gudde, J. & Matthias, E. (1999) "The Role of Electron-Phonon Coupling in Femtosecond Laser Damage of Metals", *Appl. Phys. A*, 69, S99.
- [53] Yingling, Y. G., Conforti, P. F. & Garrison, B. J. (2004) "Theoretical Investigation of Laser Pulse Width Dependence in a Thermal Confinement Regime", *Appl. Phys. A*, 79, 757.
- [54] Gamaly, E. G., Rode, A. V., Tikhonchuk, V. T. & Luther-Davies, B. (2002) "Electrostatic Mechanism of Ablation by Femtosecond Lasers", *Appl. Surf. Sci.*, 699, 197-198.
- [55] Bulgakova, N. M., Stoian, R., Rosenfeld, A., Campbell, E. E. B. & Hertel, I. V. (2004) "Model Description of Surface Charging during Ultra-Fast Pulsed Laser Ablation of Materials", *Appl. Phys. A*, 79, 1153.
- [56] Lukyanchuk, B. S., Anisimov, S. I. & Lu, Y. F. (2001) "Dynamics of Subpicosecond Laser Ablation, Examined by Moments Technique", *Proc. SPIE*, 4423, 141.
- [57] Nedjakov, N. N., Imamova, S. E., Atanasov, P. A., Heusel, G., Breitling, D., Rut, A., Hugel, H., Dausinger, F. & Bereger, P. (2004) "Laser Ablation of Iron by Ultrashort Laser Pulses", *Thin Sol Films*, 496, 453-454.
- [58] Hirayama, Y. & Obara, M. (2005) "Heat-Affected Zone and Ablation Rate of Copper Ablated with Femtosecond Laser" *J. Appl. Phys.*, 97, 064903.
- [59] Anisimov, S. I. & Rethfeld, B. (1997) "On the Theory of Ultrashort Laser Pulse Interaction with a Metal", *Proc. SPIE*, 3093, 192.
- [60] Kuznetsov, A. I., Koch, J. & Chichkov, B. N. (2009) "Nanostructuring of Thin Gold Films by Femtosecond Lasers", *Appl. Phys. A*, 94, 221.
- [61] Rethfeld, B., Kaiser, A., Vicenek, M. & Simon, G. (2002) "Ultrafast Dynamics of Nonequilibrium Electrons in Metals Under Femtosecond Laser Irradiation", *Phys. Rev. B*, 65, 214303.
- [62] Ivanov, D. S. & Zhigilei, L. V. (2003) "Effect of Pressure Relaxation on the Mechanisms of Short-Pulse Laser Melting", *Phys. Rev. Lett.*, 91, 105701.
- [63] Leveugle, E., Ivanov, D. S. & Zhigilei, L. V. (2004) "Photochemical Spallation of Molecular and Metal Targets: Molecular Dynamic Study", *Appl. Phys. A*, 79, 1643.

- [64] Zhigilei, L. V., Ivanov, D. S., Leveugle, E., Sadigh, B. & Bringa, E. M. (2004) “Computer Modeling of Laser Melting and Spallation of Metal Targets”, *High Power Laser Ablation V, Proc. SPIE*, 5448, 505.
- [65] Gibbs, J. W. (1931) “Collected Works”, Vol. 1, 55-372, Longmans, New York.
- [66] Jin, Z. H., Gumbsch, P., Lu, K. & Ma, E. (2001) “Melting Mechanism at the Limit of Superheating”, *Phys. Rev. Lett.*, 87, 055703-1.
- [67] Wilkins, M. L. (1964) “*Methods in Computational Physics*”, vol. 3, Academic press, New York, 211-261.
- [68] Pilipovich, V. A., Malevich, V. L., Ivlev, G. D. & Zhidkov, V. V. (1985) “Dynamics of Nanosecond Laser Annealing of Silicon”, *J. Eng. Phys. Thermophys.*, 48, 228.
- [69] Kaganov, M. I., Lifshitz, I. M. & Taranov, L. V. (1956) “Relaxation Between Electrons and the Crystalline Lattice”, *Zh. Eksp. Teor. Fiz.*, 31, 232 [*Sov. Phys. JETP*, 4, 173 (1957)].
- [70] Anisimov, S. I., Kapeliovich, B. L. & Perel'man, T. L. (1974) “Electron Emission from Metal Surfaces Exposed to Ultrashort Laser Pulses”, *Zh. Eksp. Teor. Fiz.*, 66, 776 [*Sov. Phys. JETP*, 39, 375 (1974)].
- [71] Allen, P. B. (1987) “Theory of Thermal Relaxation of Electrons in Metals”, *Phys. Rev. Lett.*, 59, 1460.
- [72] Wang, X. Y., Riffe, D. M., Lee, Y. S. & Downer, M. C. (1994) “Time-Resolved Electron-Temperature Measurement in a Highly Excited Gold Target Using Femtosecond Thermionic Emission” *Phys. Rev. B*, 50, 8016.
- [73] Groeneveld, R. H. M., Sprik, R. & Lagendijk, A. (1995) “Femtosecond Spectroscopy of Electron-Electron and Electron-Phonon Energy Relaxation in Ag and Au”, *Phys. Rev. B*, 51, 11433.
- [74] Touloukian, Y. S. (1970) Thermophysical Properties of Matter 4: Specific heat: metallic elements and alloys (New York: IFI/Plenum).
- [75] Gray, D. E. (Ed.). *American Institute of Physics Handbook*, 3rd ed. (McGraw-Hill, New-York 1972).
- [76] Schäfer, C., Urbassek, H. M. & Zhigilei, L. V. (2002) “Metal Ablation by Picosecond Laser Pulses: A Hybrid Simulation”, *Phys. Rev. B*, 66, 115404.
- [77] Duff, W. H. & Zhigilei, L. V. (2007) “Computational Study of Cooling Rates and Recrystallization Kinetics in Short Pulse Laser Quenching of Metal Targets”, *J. of Phys. : Conference Series*, 59, 413.
- [78] Girardeau-Montaut, J. P., Afif, M., Girardeau-Montaut, C., Moustazis, S. D. & Papadogiannis, N. (1996) “Aluminium Electron-Phonon Relaxation-Time Measurement from Subpicosecond Nonlinear Single-Photon Photoelectric Emission at 248 nm”, *Appl. Phys. A*, 62, 3.
- [79] Ivanov, D. S. & Zhigilei, L. V. (2004) “Combined Atomistic-Continuum Model for Simulation of Laser Interaction with Metals: Application to Calculation of Melting Thresholds in Ni Targets of Varying Thickness”, *Appl. Phys. A*, 79, 977.
- [80] Corkum, P. B., Brunel, F., Sherman, N. K. & Srinivasan-Rao, T. (1988) “Thermal Response of Metals to Ultrashort Laser Excitation”, *Phys. Rev. Lett.*, 61, 2886.
- [81] Agranat, M. B., Anisimov, S. I., Ashitkova, S. I., Zhakhovskii, V. V., Inogamov, N. A., Nishihara, K., Petrov, Yu. V., Fortov, V. E. & Khokhlov, V. A. (2007) “Dynamics of Plume and Crater Formation After Action of Femtosecond Laser Pulse”, *Appl. Surf. Sci.*, 253, 6276.

- [82] Horn, A., Mingareev, I., Gottmann, J., Werth, A. & Brenk, U. (2008) "Dynamical Detection of Optical Phase Changes During Micro-Welding of Glass with Ultra-Short Laser Radiation", *Meas. Sci. Technol.*, 19, 015302.
- [83] Hohlfeld, J., Müller, J. G., Wellershoff, S. S. & Matthias, E. (1997) "Time-Resolved Thermoreflectivity of Thin Gold Films and its Dependence on Film Thickness", *Appl. Phys. A*, 64, 387.
- [84] Hostetler, J. L., Smith, A. N. & Norris, P. M. (1998) "Simultaneous Measurement of Thermophysical and Mechanical Properties of Thin Films", *Int. J. Thermophys.*, 19, 569.
- [85] Eesley, G. L. (1986) "Generation of Nonequilibrium Electron and Lattice Temperatures in Copper by Picosecond Laser Pulses", *Phys. Rev. B*, 33, 2144.
- [86] Hostetler, J. L., Smith, A. N., Czajikowsky, D. M. & Norris, P. M. (1999) "Measurements of the Electron-Photon Coupling Factor Dependence on Film Thickness and Grain Size in Au, Cr, and Al.", *Applied Optics*, 38, 3614.
- [87] Hodak, J. H., Henglein, A. & Hartland, G. V. (2000) "Electron-Phonon Coupling Dynamics in Very Small (between 2 and 8 nm diameter) Au Nanoparticles", *J. Chem. Phys.*, 112, 5942.
- [88] Antaki, P. J. (2002) "Importance of Nonequilibrium Thermal Conductivity During Short-Pulse Laser-Induced Desorption From Metals", *Int. J. Heat Mass Transfer*, 45, 4063.
- [89] Thomas, D. A., Lin, Z., Zhigilei, L. V., Gurevich, E. L., Kittel, S. & Hergenröder, R. (2009) "Atomistic Modeling of Femtosecond Laser-Induced Melting and Atomic Mixing in Au Film - Cu Substrate System", *Appl. Surf. Sci.* in press.
- [90] Qiu, T. Q. & Tien, C. L. (1993) "Size Effects on Nonequilibrium Laser Heating of Metal Films", *J. Heat Transfer*, 115, 842.
- [91] Chen, J. K., Beraun, J. E., Grimes, L. E. & Tzou, D. Y. (2002) "Modeling of Femtosecond Laser-Induced Nonequilibrium Deformation in Metal Films", *Int. J. Solids Struct.*, 39, 3199.
- [92] Turnbull, D. (1956) "Phase Changes", *Solid State Phys.*, 3, 225.
- [93] Kudryashov, S. I., and Emel'yanov, V. I. "Electron Gas Compression and Coulomb Explosion in the Surface Layer of a Conductor Heated by Femtosecond Laser Pulse", *JETP Lett.* 73, 666 (2001).
- [94] Miotello, A. and Kelly, R. "Limit of Overheating and the Threshold Behavior in Laser Ablation", *Appl. Phys. A: Mater. Sci. Process.* 69, S67 (1999).
- [95] Kelly, R. and Miotello, A. "Does Normal Boiling Exist Due to Laser-Pulse or Ion Bombardment?", *J. Appl. Phys.* 87, 3177 (2000).
- [96] Bulgakova, N. M. and Bulgakov, A. V. "Pulsed Laser Ablation of Solids: Transition From Normal Vaporization to Phase Explosion", *Appl. Phys. A: Mater. Sci. Process.* 73, 199 (2001).
- [97] Vidal, F., Johnston, T.W., Laville, S., Barthe'lemy, O., Chaker, M., Le Drogoff, B., Margot, J., and Sabsabi, M. "Critical-Point Phase Separation in Laser Ablation of Conductors", *Phys. Rev. Lett.* 86, 2573 (2001).
- [98] Sokolowski-Tinten, K., Bialkowski, J., Cavalleri, A., von der Linde, D., Oparin, A., Meyer-ter-Vehn, J., and Anisimov, S.I. "Transient States of Matter during Short Pulse Laser Ablation", *Phys. Rev. Lett.* 81, 224 (1998).

- [99] Kluge, M. D., Ray, J. R. & Rahman, A. (1987) "Pulsed Laser Melting of Silicon: A Molecular Dynamics Study", *J. Chem. Phys.*, **87**, 2336.
- [100] Jin, Z. H. & Lu, K. (1998) "Melting of Surface-Free Bulk Single Crystals", *Philos. Mag. Lett.*, **78**, 29.
- [101] Häkkinen, H. & Landman, U. (1993) "Superheating, Melting, and Annealing of Copper Surfaces", *Phys. Rev. Lett.*, **71**, 1023.
- [102] Abraham, F. F. & Broughton, J. Q. (1986) "Pulsed Melting of Silicon (111) and (100) Surfaces Simulated by Molecular Dynamics", *Phys. Rev. Lett.*, **56**, 734.
- [103] Abraham, F. F., Schreiber, D. E., Mruzik, M. R. & Pound, G. M. (1976) "Phase Separation in Fluid Systems by Spinodal Decomposition: A Molecular-Dynamics Simulation", *Phys. Rev. Lett.*, **36**, 261.
- [104] Blink, J. A. & Hoover, W. G. (1985) "Fragmentation of Suddenly Heated Liquids", *Phys. Rev. A*, **32**, 1027.
- [105] Ashurst, Wm. T. & Holian, B. L. (1999) "Droplet Formation by Rapid Expansion of a Liquid", *Phys. Rev. E*, **59**, 6742.
- [106] Zhigilei, L. V. & Garrison, B. J. (1999) "Pressure Waves in Microscopic Simulations of Laser Ablation", *Mater. Res. Soc. Symp. Proc.*, **538**, 491.
- [107] Etcheverry, J. I. & Mesaros, M. (1999) "Molecular Dynamics Simulation of the Production of Acoustic Waves by Pulsed Laser Irradiation", *Phys. Rev. B*, **60**, 9430.
- [108] Herrmann, R. F. W., Gerlach, J. & Campbell, E. E. B. (1998) "Ultrashort Pulse Laser Ablation of Silicon: an MD Simulation Study", *Appl. Phys. A: Mater. Sci. Process*, **66**, 35.
- [109] Zhigilei, L. V. & Garrison, B. J. (2000) "Microscopic Mechanisms of Laser Ablation of Organic Solids in the Thermal and Stress Confinement Irradiation Regimes", *J. Appl. Phys.*, **88**, 1281.
- [110] Zhigilei, L. V. (2003) "Dynamics of the Plume Formation and Parameters of the Ejected Clusters in Short-Pulse Laser Ablation", *Appl. Phys. A: Mater. Sci. Process*, **76**, 339.
- [111] Foiles, S. M., Baskes, M. I. & Daw, M. S. (1986) "Embedded -Atom-Method Functions for fcc Metals Cu, Ag, Au, Ni, Pd, Pt, and Their Alloys", *Phys. Rev. B*, **33**, 7983.
- [112] Zhou, X. W., Wadley, H. N. G., Johnson, R. A., Larson, D. J., Tabat, N., Cerezo, A., Petford-Long, A. K., Smith, G. D. W., Clifton, P. H., Martens, R. L. & Kelly, T. F. (2001) "Atomic Scale Structure of Sputtered Metal Multilayers", *Acta Mater.*, **49**, 4005.
- [113] Lennard-Jones, J. E. & Devonshire, A. F. (1924) "On the Determination of Molecular Fields. II. From the Equation of State of a Gas", *Proc. Roy. Soc. A*, **106**, 463.
- [114] Morris, J. R. & Song, X. (2002) "The Melting Lines of Model Systems Calculated from Coexistence Simulations", *J. Chem. Phys.*, **116**, 9352.
- [115] Smithell's Metal Reference Book, 6th edition, E. A. Brandes, ed. London: Butterwoths, 1983.
- [116] Ivanov, D. S. & Zhigilei, L. V. (2003) "Combined Atomistic-Continuum Modeling of Short-Pulse Laser Melting and Disintegration of Metal Films", *Phys. Rev. B*, **68**, 064114.
- [117] Touloukian, Y. S. (1975) Thermophysical Properties of Matter 12: Thermal expansion: metallic elements and alloys (New York: IFI/Plenum).

- [118] Berendsen, H. J. C., Postma, J. P. M., van Gunsteren, W. F., DiNola, A. & Haak, J. R. (1984) "Molecular Dynamics with Coupling to an External Bath", *J. Chem. Phys.*, **81**, 3684.
- [119] Ivanov, D. S. & Zhigilei, L. V. (2007) "Kinetic Limit of Heterogeneous Melting in Metals", *Phys. Rev. Lett.*, **98**, 195701.
- [120] Wang, X. & Xu, X. (2001) "Thermoelastic Waves Induced by Pulsed Laser Heating", *Appl. Phys. A*, **73**, 107.
- [121] Preuss, S., Demchuk, A. & Stuke, M. (1995) "Sub-Picosecond Laser Ablation of Metals", *Appl. Phys. A*, **61**, 33.
- [122] Meshcheryakov, Y. P. & Bulgakova, N. M. (2005) "Thermoelastic Modeling of Microbump and Nanojet Formation on Nanosize Gold Films under Femtosecond Laser Irradiation", *Appl. Phys. A*, **82**, 363.
- [123] Burke, K., Werschnik, J. & Gross, E. K. U. (2005) "Time-Dependent Density Functional Theory: Past, Present, and Future", *J. Chem. Phys.*, **123**, 062206.
- [124] Awazu, K., Wang, X., Fujimaki, M., Komatsubara, T., Ikeda, T. & Ohki, Y. (2006) "Structure of Latent Tracks in Rutile Single Crystal of Titanium Dioxide Induced by Swift Heavy Ions", *J. Appl. Phys.*, **100**, 044308.
- [125] Khalfaoui, N., Goerlich, M., Mueller, C., Schleberger, M. & Lebius, H. (2006) "Latent Tracks in CaF<sub>2</sub> Studied with Atomic Force Microscopy in Air and in Vacuum", *Nucl. Instrum. Methods B*, **245**, 2469.
- [126] El-Said, A. S., Cranney, M., Ishikawa, N., Iwase, A., Neumann, R., Schwartz, K., Toulemonde, M. & Trautmann, C. (2004) "Study of Heavy-Ion Induced Modifications in BaF<sub>2</sub> and LaF<sub>3</sub> Single Crystals", *Nucl. Instrum. Methods B*, **218**, 4927.
- [127] Mueller, A., Neumann, R., Schwartz, K. & Trautmann, C. (1998) "Scanning Force Microscopy of Heavy-Ion Tracks in Lithium Uoride", *Nucl. Instrum. Methods B*, **146**, 3938.
- [128] Lucchese, R. R. (1987) "Thermal spike model for heavy ion induced desorption from surfaces", *J. Chem. Phys.*, **86**, 443.
- [129] Tucker, O. J., Ivanov, D. S., Johnson, R. E., Zhigilei, L. V. & Bringa, E. M. (2005) "Molecular Dynamics Simulation of Sputtering from a Cylindrical Track: EAM vs. Pair Potentials", *Nucl. Instr. Meth. B*, **228**, 163-169.
- [130] Seitz, F. & Koehler, J. (1956) "Displacement of Atoms During Irradiation Solid", *State Phys.*, **2**, 305.
- [131] Toulemonde, M., Dufour, C. & Paumier, E. (1992) "Transient Thermal Process After a High-Energy Heavy-Ion Irradiation of Amorphous Metals and Semiconductors", *Phys. Rev. B*, **46**, 14362.
- [132] Meftah, A., Constantini, J. M., Khalfaoui, N., Boudjadar, S., Stoqert, J. P., Studer, F. & Toulemonde, M. (2005) "Experimental Determination of Track Cross-Section in Gd<sub>3</sub>Ga<sub>5</sub>O<sub>12</sub> and Comparison to the Inelastic Thermal-Spike Model Applied to Several Materials", *Nucl. Instrum. Methods B*, **237**, 563.
- [133] Akcilekin, E., Peters, Th., Meyer, R., Duvenbeck, A., Klusmann, M., Monnet, I., Lebius, H. & Schleberger, M. (2007) "Creation of Multiple Nanodots by Single Ions", *Nat. Nanotechnol.*, **2**, 2904.
- [134] Carvalho, A. M. J. F., Marinoni, M., Touboul, A. D., Guasch, C., Lebius, H., Ramonda, M., Bonnet, J. & Saign, F. (2007) "Discontinuous Ion Tracks on Silicon Oxide on

- Silicon Surfaces After Grazing Angle Heavy Ion Irradiation”, *Appl. Phys. Lett.*, **90**, 073116.
- [135] Lindhard, J. & Schar, M. (1961) “Energy Dissipation by Ions in the keV Region”, *Phys. Rev.*, **124**, 128.
- [136] Gonze, X., Beuken, J. M., Caracas, R., Detraux, F., Fuchs, M., Rignanese, G. M., Sindic, L., Verstraete, M., Zerah, G., Jollet, F., Torrent, M., Roy, A., Mikami, M., Ghosez, Ph., Raty, J. Y. & Allan, D. C. (2002) “First-Principles Computation of Material Properties: the ABINIT Software Project”, *Comput. Mater. Sci.*, **25**, 47892.
- [137] Fuchs, M. & Schefer, M. (1999) *Comput. Phys. Commun.*, **119**, 6798.
- [138] Perdew, J. P., Burke, K. & Ernzerhof, M. (1996) “Generalized Gradient Approximation Made Simple”, *Phys. Rev. Lett.*, **77**, 3865.
- [139] Osmani, O., Duvenbeck, A., Akcoeltekin, E., Meyer, R., Lebius, H. & Schleberger, M. (2008) “Calculation of Electronic Stopping Power Along Glancing Swift Heavy Ion Tracks in Perovskites Using *Ab-Initio* Electron Density Data”, *J. Phys.: Condens. Matter*, **20**, 315001.
- [140] Snone, D. W., Ruehle, W. W., Lu, Y. C. & Bauser, E. (1992) “Evolution of a Nonthermal Electron energy Distribution in GaAs,” *Phys. Rev. B*, **45**, 10979.
- [141] Binder, R., Koehler, H. S., Bonitz, M. & Kwong, N. (1997) “Green’s Function Description of Momentum-Orientation Relaxation of Photoexcited Electron Plasmas in Semiconductors,” *Phys. Rev. B*, **55**, 5110.
- [142] Allen, P. B. (1987) “Theory of Thermal Relaxation of Electrons in Metals,” *Phys. Rev. Lett.*, **59**, 1460.
- [143] Ashcroft, N. & Mermin, N. (1976) *Solid State Physics*, Saunders College Publishing.
- [144] Epshteyn, E. M. (1970) “Scattering of Electrons by Phonons in a Strong Radiation Field”, *Sov. Phys. Solid State*, **11**, 2213.
- [145] Press, W. H. & Teukolsky, S. A. (1992) *Numerical Recipes in C*, Cambridge University Press, New York.
- [146] Grigorev, I. S. & Mejlikhov, E. Z. (1991) “*Fizicheskie Velichini.*” Moskau Energoatomizdat.
- [147] Ashcroft, N. W. & Wilkins, J. W. (1965) “Low Temperature Electronic Specific Heat of Simple Metals,” *Physics Letters*, **14**, 285.
- [148] Fann, W. S., Storz, R., Tom, H. W. K. & Bokor, J. (1992) “Electron Thermalization in Gold,” *Phys. Rev. B*, **46**, 13592.
- [149] Fann, W. S., Storz, R., Tom, H. W. K. & Bokor, J. (1992) “Direct Measurement of Nonequilibrium Electron-Energy Distribution in Subpicosecond Laser-Heated Gold Films,” *Phys. Rev. Lett.*, **68**, 2834.
- [150] Bejan, D. & Raseev, G. (1997) “Nonequilibrium Electron Distribution in Metals”, *Phys. Rev. B*, **55**, 4250.
- [151] Rethfeld, B., Kaiser, A., Vicanek, M. & Simon, G. (1999) “Femtosecond Laser-Induced Heating of Electron Gas in Aluminium”, *Appl. Phys. A*, **69 [Suppl.]**, S109.
- [152] Groeneveld, R. H. M., Sprik, R. & Lagendijk, A. (1992) “Effect of a Nonthermal Electron Distribution on the Electron-Phonon Energy Relaxation Process in Noble Metals”, *Phys. Rev. B*, **45**, 5079.
- [153] Groeneveld, R. H. M., Sprik, R. & Lagendijk, A. (1995) “Femtosecond Spectroscopy of Electron-Electron and Electron-Phonon Energy Relaxation in Ag and Au”, *Phys. Rev. B*, **51**, 11433.

- [154] Huang, S. M., Hong, M. H., Lukiyanchuk, B. & Chong, T. C. (2003) "Nanostructures Fabricated on Metal Surfaces Assisted by Laser with Optical Near-Field Effects", *Appl. Phys. A*, 77, 293.
- [155] Lu, Y. & Chen, S. C. (2003) "Nanopatterning of a Silicon Surface by Near-Field Enhanced Laser Irradiation", *Nanotechnology*, 14, 505.
- [156] Povarnitsyn, M. E., Itina, T. E., Khishchenko, K. V. & Levashov, P. R. (2007) "Multi-Material Two-Temperature Model for Simulation of Ultra-Short Laser Ablation", *Appl. Sur. Sci.*, 253, 6343.
- [157] Bennett, T. D., Krajnovich, D. J. & Grigoropoulos, C. P. (1997) "Marangoni Mechanism in Pulsed Laser Texturing of Magnetic Disk Substrates", *J Heat Transfer*, 119, 589.
- [158] Lu, Y., Theppakuttai, S. & Chen, S. C. (2003) "Marangoni Effect in Nanosphere-Enhanced Laser Nanopatterning of Silicon", *Appl. Phys. Lett.*, 82, 4143.
- [159] Kingery, W. D. (1959) "Surface Tension of Some Liquid Oxides and Their Temperature Coefficients", *J. Am. Ceram. Soc.*, 42, 6.
- [160] Sokolowski-Tinten, K., Blome, C., Blums, J., Cavalleri, A., Dietrich, C., Tarasevich, A., Uschmann, I., Förster, E., Kammler, M., Horn-von-Hoegen, M. & von der Linde, D. (2003) "Femtosecond X-ray Measurement of Coherent Lattice Vibrations near the Lindemann Stability Limit", *Nature*, 422, 287.
- [161] Siwick, B. J., Dwyer, J. R., Jordan, R. E. & Miller, R. J. D. (2003) "An Atomic-Level View of Melting Using Femtosecond Electron Diffraction", *Science*, 302, 1382.
- [162] Schwarz-Selinger, T., Cahill, D. G., Chen, S. C., Moon, S. J. & Grigoropoulos, C. P. (1999) "Micron-Scale Modifications of Si Surface Morphology by Pulsed-Laser Texturing", *Phys. Rev. B*, 64, 155323.
- [163] Willis, D. A. & Xu, X. (2000) "Transport Phenomena and Droplet Formation During Pulsed Laser Interaction With thin Films", *J. Heat Transfer*, 122, 763.
- [164] Valavalas, P. K. & Odegard, G. M. (2005) "Modeling Techniques for Determination of Mechanical Properties of Polymers Nanocomposites", *Rev. Adv. Mater. Sci.*, 9, 34.
- [165] Xu, X. & Liao, K. (2004) "Molecular and Continuum Mechanics Modeling of Graphene Deformation", *Mater. Phys. Mech.*, 4, 148.
- [166] Bohm, E., Bhatele, A., Kalé, L. V., Tuckerman, M. E., Kumar, S., Gunnels, J. A. & Martyna, G. J. (2008) "Fine-Grained Parallelization of the Car-Parrinello Ab Initio Molecular Dynamics Method on the IBM Blue Gene/L Supercomputer", *IBM J. Res. and Dev.*, 52, 159.
- [167] Zhou, X. W., Wadley, H. N. G., Johnson, R. A., Larson, D. J., Tabat, N., Cerezo, A., Petford-Long, A. K., Smith, G. D. W., Clifton, P. H., Martens, R. L. & Kelly, T. F. (2001) Atomic scale structure of sputtered metal multilayers, *Acta Mater.*, 49, 4005.
- [168] Richardson, C. F. & Clancy, P. (1992) "Contribution of Thermal Conductivity to the Crystal-Regrowth Velocity of Embedded-Atom-Method-Modeled Metals and Metal Alloys", *Phys. Rev. B*, 45, 12260.
- [169] Rafii-Tabar, H., Hua, L. & Cross, M. (1998) "A multi-scale numerical modelling of crack propagation in a 2D metallic plate", *J. of Comp.-Aided Mat. Design*, 4, 165.
- [170] Kuchnickia, S. N., Radovitzky, R. A. & Cuitiño, A. M. (2008) "An Explicit Formulation for Multiscale Modeling of bcc Metals", *Int. J. Plasticity*, 24, 2173.
- [171] Tang, Z. & Xu, J. (2006) "A Combined DEM/FEM Multiscale Method and Structure Failure Simulation under Laser Irradiation", *AIP Conf. Proc.*, 845, 363.

- [172] Evans, D. J. (1983) "Nonequilibrium Molecular Dynamics via Gauss's Principle of Least Constraint", *Phys. Rev. A*, 28, 1016.
- [173] Amorusso, S., Buzzese, R., Wang, X., Nediakov, N. N. & Atanasov, P. A. (2007) "Femtosecond Laser Ablation of nickel in Vacuum", *J. Phys. D: Appl. Phys.*, 40, 331.
- [174] Landau, L. D. & Lifshitz, E. M. (1999) "Statistical Physics: Part I", 3d ed., Oxford: Butterworth-Heinemann.
- [175] Zhigilei, L. V. & Ivanov, D. S. (2005) "Channels of Energy Redistribution in Short-Pulse Laser Interactions with Metal Targets", *Appl. Surf. Sci.*, 248, 433-439.
- [176] Landau, L. D. & Lifshitz, E. M. (1976) "Mechanics", 3d ed., Oxford; New York: Pergamon Press.
- [177] Paltauf, G. & Dyer, P. E. (2003) "Photomechanical Processes and Effects in Ablation", *Chem. Rev.*, 103, 487.
- [178] Ivanov, D. S., Zhigilei, L. V., Bringa, E. M., De Koning, M., Remington, B. A., Caturla, M. J. & Pollaine, S. M. (2004) "Molecular Dynamic Simulations of Shocks Including Electronic Heat Conduction and Electron-Phonon Coupling", *Shock Compression of Condensed Matter 2003, AIP Conf. Proc.*, 706, 225.
- [179] Remington, B. A., Bazan, G., Belak, J., Bringa, E., Caturla, M., Colvin, J. D., Edwards, M. J., Glendinning, S. G., Ivanov, D. S., Kad, B., Kalantar, D. H., Kumar, M., Lasinski, B. F., Lorenz, K. T., McNaney, J. M., Meyerhofer, D. D., Meyers, M. A., Pollane, S. M., Rowley, D., Schneider, M., Stolken, J. S., Wark, J. S., Weber, S. V., Wolfer, W. G., Yaakobi, B. & Zhigilei, L. V. (2004) "Materials Science Under Extreme Conditions of Pressure and Strain Rate", *Metall. Mater. Trans. A*, 35, 2587.
- [180] Kadau, K., Germann, T. C. & Lomdahl, P. S. (2004) "Large-Scale Molecular-Dynamics simulation of 19 Billion Particles", *Int. J. Mod. Phys. C*, 15, 193.
- [181] Corkum, P. B., Brunel, F., Sherman, N. K. & Srinivasan-Rao, T. (1988) "Thermal Response of Metals to Ultrashort-Pulse Laser Excitation", *Phys. Rev. Lett.*, 61, 2886.
- [182] Ivanov, D. S., Rethfeld, B. C., O'Connor, G. M., Glynn, T. J., Volkov, A. N. & Zhigilei, L. V. (2008) "The Mechanism of Nanobump Formation in Femtosecond Pulse Laser Nanostructuring of Thin Metal Films", *Appl. Phys. A*, 92, 791.
- [183] Ivanov, D. S., Rethfeld, B., O'Connor, G. M., Glynn, T. J., Lin, Z. & Zhigilei, L. V. (2009) "Microstructure of a Nanobump Generated by Focused Laser Irradiation of a Metal Film", in print *J. Appl. Phys.*
- [184] Ivanov, D. S., Rethfeld, B., Volkov, A. & Zhigilei, L. V. (2010) "The Mechanism of Microbump/Nanojet Formation due to Short Pulse Laser Surface Nanostructuring", in preparation for *Phys. Rev. B*.
- [185] Lin, Z., Bringa, E. M., Leveugle, E. & Zhigilei, L. V. (2009) "Molecular Dynamics Simulation of Laser Melting of Nanocrystalline Au", in preparation.
- [186] Zhakhovskii, V. V., Inogamov, N. A., Petrov, Yu. V., Ashitkov, S. I. & Nishihara, K. (2009) "Molecular Dynamics Simulation of Femtosecond Ablation and Spallation with Different Interatomic Potentials", in print *Appl. Surf. Sci.*
- [187] Ivanov, D. S., Rethfeld, B. C. & Kuznecov, A. (2009) "Direct Comparison of a Super Large Scale Modeling of Nanostructuring on Au Films with the Experiment", in preparation.
- [188] Gottmann, J. & Wagner, R. (2006) "Sub-Wavelength Ripple Formation on Dielectric and Metallic Materials Induced by Tightly Focused Femto-Second Laser Radiation", *Proc. of SPIE*, 6106, 61061R .

- 
- [189] Drabble, J. R. & Goldsmid, H. J. (1961) "Thermal Conduction in Semiconductors", Pergamon Press, Oxford.
  - [190] Young, J. F. & Driel, H. M. (1982) "Ambipolar Diffusion of High-Density electrons and holes in Ge, Si, and GaAs: Many-body Effect", *Phys. Rev. B*, **26**, 2147.
  - [191] Chen, J. K., Tzou, D. Y. & Beraun, J. E. (2005) "Numerical Investigation of Ultrashort Laser Damage in Semiconductors", *Int. J. of Heat and Mass Transfer*, **48**, 501.
  - [192] Rethfeld, B. (2006) "Free-Electron Generation in Laser-Irradiated Dielectrics", *Phys. Rev. B*, **73**, 035101.
  - [193] Stillinger, F. & Weber, T. A. (1985) "Computer Simulation of Local Order in Condensed Phases of Silicon", *Phys. Rev. B*, **31**, 5262.
  - [194] Lorazo, P., Lewis, L. J. & Meunier, M. (2006) "Thermodynamic Pathways to Melting, Ablation, and Solidification in Absorbing Solids under Pulsed Laser Irradiation", *Phys. Rev. B*, **73**, 134108.
  - [195] Louie, S.G. (2001) "Ab Initio Study of Optical Excitations: Role of Electron-hole Interaction", in Conference Proceedings (no. 577), Density Functional Theory and Its Appl. to Materials, eds. V.E. Van Doren, K. Van Alsenoy, and P. Geerlings (American Institute of Physics, Melville, N.Y., 151.
  - [196] Kawamura, K. (1990) *Proc. of the 13th Taniguchi Symp. Kashikojima*, Japan 6-9, 88.
  - [197] Katsumata, T., Inaguma, Y., Itoh, M. & Kawamura, K. (1998) "Molecular Dynamic Simulation in SrTiO<sub>3</sub>", *Sol. State Ionics*, **108**, 175.
  - [198] Toukmaji, A. Y. & Poard, J. A. Jr. (1996) "Ewald Summation Techniques in Perspective: a Survey", *Comp. Phys. Comm.*, **95**, 73.
  - [199] Duan, Z. H. & Krasny, R. (2003) "A Treecode Algorithm for Computing Ewald Summation of Dipolar Systems", Proceedings of the *2003 ACM Symposium on Applied Computing*, 172.
  - [200] Deserno, M. & Holm, C. (1998) "How to Mesh Up Ewald Sums (I): A Theoretical and Numerical Comparisons of Various Particle Mesh routines", *J. Chem. Phys.*, **109**, 7678.
  - [201] Deserno, M. & Holm, C. (1998) "How to Mesh Up Ewald Sums (II): An Accurate Error Estimate for the P3M Algorithm", *J. Chem. Phys.*, **109**, 7694.



## ***Chapter 2***

# **QUANTUM KINETICS OF MULTIPHOTON PROCESSES: DURATIONS OF ELEMENTARY PROCESSES, THRESHOLDS OF CHANNELS OPENING AND THEIR SATURATIONS**

***Mark E. Perel'man\****

Racah Institute of Physics, Hebrew University, Givat Ram, Jerusalem, Israel.

## **ABSTRACT**

Kinetics of interaction of powerful light (laser) flux with substance is examined within the frame of microscopic theory of multiphoton processes. It is usually supposed that with growth of radiation intensity its quantum characteristics "become averaged" and consequently their consideration within the scope of quasi-classical theory become allowable and sufficient, that leads to nonlinear theories with corresponding approximations and complications. However, the existence of thresholds of opening of new reaction channels, their saturation and so on requires quantum examination in the scope of linear theory, of quantum electrodynamics, which is less sophisticated in some aspects.

The quantum kinetics of photon flux interaction with substance demands definition of durations of elementary scattering acts and durations of formation of physical states as a result of such interaction, thus it requires the appeal to quantum electrodynamics and scattering theory. Therefore the general positions of the theory of durations (theory of temporal functions) are briefly considered and the general theory of multiphoton processes on this base is constructed. Then processes of higher harmonics generation and transformations of spectra, multiphoton ionization, multiphoton acceleration of charged particles, pressure of light on absorbing and transparent objects (they are needed for planning of thermonuclear reactions), some features of light reflection are considered. All this visually shows the significance and, simultaneously, the simplicity of used microscopic quantum approach, its perspectives.

The base of offered approach consists in the temporal consideration of interactions and applications of temporal functions, which are rarely yet used. Therefore in the

---

\* Corresponding author. E-mails: m.e.perelman@gmail.com; mark\_perelman@mail.ru.

Appendix is shown that these functions allow simple approach and proving of many kinetic relations and characteristics in several branches of physics including general determination of condensed states and some features of phase transitions. This part has, presumably, a methodological character, but opens a new vision or alternative approach to several known kinetics phenomena.

## 1. INTRODUCTION

Basic calculations in the laser theory and, more generally, in quantum optics and in the theory of multiphoton processes are usually executed in the quasiclassical frames. Such approaches are very effective, but in this course can be missed valuable details (let's remember the famous maxim of Albert Einstein: "Things should be as simple as possible, but not simpler"). The used assumptions of sufficiency of quasiclassical description can represent an excessive simplification, and therefore a support of many positions or even the reconsideration of them by methods of quantum electrodynamics is very desirable or even necessary.

Quantum electrodynamics (QED) examines, as a rule, processes with two particles in an initial state. From here, apparently, had been appeared a conviction that processes with big numbers of initial particles are the following terms of a general decomposition of S-matrix over parameter of interaction  $\alpha = 1/137$ . Therewith, a direct calculation, for example, of the higher harmonics generation with matrix element containing  $\alpha^N, N \gg 1$ , is seemed senseless. Probably therefore multiphoton processes (MPPs) are examined as the extremely nonlinear effects that are demanding the description by averaged functions such as nonlinear susceptibilities (e.g., the general reviews with the detailed bibliography [1,2]).

So for the description, for example, of process  $N\gamma(\omega) + e \rightarrow e + \gamma(N\omega)$  the matrix element of  $(N + 1)$ -order is the basic one; but it is not the  $N$ -term of  $S$ -matrix perturbative decomposition (perturbative decompositions lead to appearance of additional internal lines in the Feynman graphs only). With taking into account the fluxes density of incident particles, i.e. at the correct transition to limits of the quantization volumes, the smallness of constants of interaction will be compensable by other factors [3]. Among these factors the most physically interesting was the automatic appearance of the delays time of scattering process at summation of an infinite  $S$ -matrix series that determine the radius of convergence and therefore the thresholds of new channels of MPPs reactions.

All this shows an opportunity of the consideration of MPPs in the frameworks of QED with the strict observance of all its instructions. The analysis of received results can be carried out most simply and physically evidently, in our opinion, with taking into account the conception of duration of interaction, which should be included into general field theory.

Temporal characteristics of process of scattering should contain, as minimum in principle, two types of magnitudes: duration of a delay of colliding particles during their interaction (their temporal virtual joining) and duration of formation (dressing) of products of reaction. Formation of dressed (physical) state can require also an account of durations of establishment of other parameters: the momentum at ionization, etc. Their research has an uneasy history: in the beginning of development of quantum theory McColl had shown that the calculation of duration of tunnel transition leads to negative values [4]. Therefore during long time was factually postulated that any estimations of temporal characteristics, besides

the uncertainty principles, are practically not necessary or even impossible. Moreover, in the MPPs theory is usually implied that all  $N$  photons at process of higher harmonics generation are absorbed within one-stage interaction, instantaneously, that completely contradicts the paradigm of QED.

This problem must be investigated on the base of field theory. And the offered approach must be reinforced via revealing of real presence of temporal parameters in others, even common theories (these problems are considered in the Appendix).

The first appearing of this problem must be connected with the famous article of Frank [5], where in the theory of Čerenkov radiation is introduced the notion of path length (or duration), necessary for a gradual formation of real photon by "a superluminal in media" electron. Without such concept the discrete character of this emission was incomprehensible, and Frank had been forced to estimate the interference picture of continuously emitted (virtual) waves that can lead to the real emission of single photons in resonance conditions.

However this theory had been remaining without further researches and developments onto many years. The first, as far as I know, quantum investigation in this direction has been executed and published by Moshinsky [6]. He had calculated, through the non-stationary Schrödinger equation, the time duration needed for establishment of the definite state of electron after its transition onto upper level with some damped oscillations ("temporary diffraction"), i.e. the duration of resulted state formation.

The first (semi-qualitative) consideration of time delay in processes of tunneling had been performed, as far as I know, by Bohm [7]. Then Ter-Mikaelyan and Landau and Pomeranchuk [8] had considered the duration of photon formation in the theory of bremsstrahlung: it is the time duration needed for formation of virtual coat around particle, its dressing.

The more constructive and physically more transparent approach to magnitude of time delay under an elastic scattering was introduced by Wigner [9] through the partial phase shifts,  $\tau_l(\omega) = d\delta_l/d\omega$  and generalized by Smith [10] via  $S$ -matrix as

$$\tau^1(\omega) = \text{Re} \left( \frac{\partial}{i\partial\omega} \right) \ln S. \quad (1.1)$$

Next Goldberger and Watson had deduced on the base of (1.1) a "coarse-grain" Schrödinger equation which shown the generality of this definition [11]. But at their approach the magnitude (1.1) had been however introduced artificially, by the serial decomposition of Fourier transformed response function  $S(t)$  of linear relation,

$$O(t) = S(t) \otimes I(t) = \int dt' S(t' - t) I(t'), \quad (1.2)$$

or its logarithm near the selected frequency without discussion of its imaginary part, higher terms and dependence on spatial variables.

Another approach, which seems at first glance to be distinguished from the Wigner-Smith one, was suggested by Baz' [12] for consideration of nonrelativistic tunneling processes: to a scattering particle is attributed magnetic moment and its rotation within the scattering process is analyzed (the method of "Larmor clocks").

Another problem is connected with the definite duration of state formation ("dressing") expressed as

$$\tau_2 = \text{Im}(\partial \ln S / i\partial\omega). \quad (1.3)$$

As far as I know, the similar expression for  $\tau_2$  was introduced, for the first time, by Pollak and Miller [13] and was interpreted as the duration of tunneling process. (Note that the duration of particle formatting can be calculated by dynamical considerations, it presents the special direction in the high energy physics, cf. the review [14].)

After these initial investigations a number of various definitions of duration of scattering processes and interaction were offered, different determinations of duration of interactions are introduced, e.g. the reviews collected in [15].

Our purpose in the series of papers, generally reviewed in [16], was to reveal that functions describing duration of scattering processes and formation of new states are present in already existing theories: if these concepts reflect essential features of a reality they should be found in the theories, which adequately describe several experiments. (Just with this aim the simplest well-known expressions are considered in the Appendix.)

On the other hand, however, it is necessary to show that the direct use of temporal functions at analyses, at least, of some processes has practical and not only a gnostic sense. On their basis the theory of optical dispersion had been established [17], the features of frustrated total internal reflections [18] and singularities of so named left-handed materials [19] are explained. The notion of temporal functions allows consideration of phase transitions by analogy with radiative quantum transition, including MPPs, and their thresholds; it leads to the theory of critical indices [20] and predicts characteristic radiation of latent energy, existence of which is experimentally proven ([21] and references therein).

Among other possibilities the opportunity of the "nonlocality in the small", i.e. instantaneous tunneling jumps of excitations within the scope of near field, has been shown [22]. As it is proven, the superluminal transfer of excitations (jumps) through a linear passive substance can be affected by nothing but by the instantaneous tunneling of virtual particles. The tunneling distance  $c|\tau_2|$  is expressed via the deficiency in the energy relative to the nearest stable (resonance) state  $\Delta(\hbar\omega)$  as the relation of uncertainty type:  $\tau_2\Delta\omega = \pi$ , the nonlocality of the electromagnetic field must be described by the 4-potential  $A_\mu$ , whereas the fields **E** and **B** remain unconnected to the near field.

Nevertheless the existence of two independent expressions (1.1) and (1.3) even logically seems unsatisfactory: delay at scattering and duration of formation should be in some way or other interrelating. Formally they can be combined as  $\tau_1(\omega, \mathbf{r}) + i\tau_2(\omega, \mathbf{r}) = (\partial / i\partial\omega)\ln S(\omega, \mathbf{r})$ , which appears as an equivalent of the equation

$$\partial S(\omega, \mathbf{r}) / i\partial\omega = \hat{\tau}(\omega, \mathbf{r})S(\omega, \mathbf{r}), \quad (1.4)$$

as though it is the analog or reciprocal form of the Schrödinger equation for S-matrix, rewritten via the Legendre transformation of  $t \leftrightarrow \omega$  type and with a "temporal" operator

$\hat{\tau}(\omega, \mathbf{r})$  instead the Hamiltonia [18]. Just this equation is the basic one in the microscopic theory of MPPs.

The general overview of the theory of temporal functions is given in the Section 2. These general expressions will be needed at the QED approach to the general theory of MPPs in the Section 3.

The Section 4 is devoted to the detailed calculations of stimulated radiation in two-level systems [3]. These calculations allow to revealing the most general sense of MPP in the scope of QED, including an appearance of singularities of reaction rates and thresholds of new processes as functions of flux power. In the Sections 5 and 6 the main MPPs on single atoms and free electrons, the higher harmonics generation (HHG) and multiphoton ionization (MPI), are considered. In the Section 7 are briefly considered possibilities of laser acceleration of single charged particles, but since such phenomena are really realizable in plasma, here are described elementary acts only. The Section 8 is devoted to problems of radiation pressure at absorption and on transparent surfaces; this last problem has a long and casuistic history and now is more demanded in connection with perspectives of laser inducing compression for realization of thermonuclear reactions. In the Section 9 some problems connected with light reflection are described.

As our approach is based on the temporal notions and they are not yet common known and/or are rarely used, in the Appendix is shown that several different physical laws and expressions can be considered and simply prove with the use of temporal notions. It can give new possibilities of their interpretations and understanding.

It must be noted that the basic content of Sections 4 - 6 corresponds to [17] with some corrections and additions. The results and some perspectives are summed in the Conclusions.

## 2. PHOTON GREEN FUNCTIONS AND DURATIONS

Temporal functions are introducing in general form via the response functions or matrix elements of scattering processes as transfer functions in the frequency's representation,  $S(\omega) = |S(\omega)|\exp(i\Phi(\omega))$ , other variables are omitted:

$$\tau(\omega) \equiv \tau_1 + i\tau_2 = (d/d\omega) \ln S(\omega). \quad (2.1)$$

In this expression

$$\tau_1 = \operatorname{Re} \tau(\omega) = d\Phi/d\omega \text{ and } \tau_2(\omega) \equiv \operatorname{Im} \tau(\omega) = (d/d\omega) \ln |S(\omega)| \quad (2.2)$$

that describe, correspondingly, the delay duration at the scattering process via the variation of response phase and the duration of outgoing particle formation (its "dressing" or "redress") via the amplitude alteration.

As the simplest illustrative examples of temporal functions, the propagators in the nearest order in the  $(\omega, \mathbf{k})$  representation could be considered. So the causal photon's propagator of the lowest order in the Feynman gauge,  $D_c(\omega, \mathbf{k}) = 4\pi/(\omega^2 - c^2\mathbf{k}^2 - i0)$ , leads to the temporal functions:

$$\begin{aligned}\tau_1 &= 2\pi\omega\delta(\omega^2 - c^2\mathbf{k}^2) = \pi(\delta(\omega - c|\mathbf{k}|) + \delta(\omega + c|\mathbf{k}|)); \\ \tau_2 &= 2\omega/(\omega^2 - c^2\mathbf{k}^2) = 1/(\omega - c|\mathbf{k}|) + 1/(\omega + c|\mathbf{k}|).\end{aligned}\quad (2.3)$$

The time delay  $\tau_1$  is non-zero for real photons only ( $\omega^2 = c^2\mathbf{k}^2$ ) and for the static Coulomb field ( $\omega = \mathbf{k} = 0$ ). The duration of dressing  $\tau_2$  is finite for virtual photons with  $\omega^2 \neq c^2\mathbf{k}^2$ , it's negative sign at  $\omega < c|\mathbf{k}|$  corresponds to tunneling processes (the case of anomalous dispersion as example).

The interpretation of temporal functions can be achieved also by the presentation of temporal functions (2.3) in  $x$ -space via the Green functions of Klein-Gordon equation:

$$\tau_1(x) = i\partial_i(D_{ret}(x) + D_{adv}(x)); \quad \tau_2(x) = i\partial_i(D^{(+)}(x) - D^{(-)}(x)) \quad (2.4)$$

These relations present the delay duration at scattering process as the jointed decay of retarded and generation of advanced waves or vice versa in the light cone limits. But the duration of formation (dressing) shows that the physical particle formation requires waves with different signs of energy, i.e. vacuum fluctuations including out-of-cone ones are take part in them, therefore superluminal effects in these processes cannot be excluded. (These examinations are shown, in particular, that superluminal phenomena should be present and, in principle, may be observed at all scattering processes, not only in the QED.)

Temporal functions allow certain specification of properties of the basic singular functions of field theory. Let us determine their corresponding temporal functions in the  $(\omega, \mathbf{r})$  representation ( $\hbar = c = 1$  below):

$$\tau(D_{R,A}|\omega, \mathbf{r}) = \pm r; \quad \tau(D_c|\omega, \mathbf{r}) = \pm r \cdot \text{sgn}\omega; \quad (2.5)$$

$$\tau(D, D_1, D^{(\pm)}|\omega, \mathbf{r}) = -ir \cdot \cot(\omega r); \quad (2.6)$$

$$\tau(\bar{D}|\omega, \mathbf{r}) = ir \cdot \tan(\omega r). \quad (2.7)$$

The representations (2.5) demonstrate that propagators of “dressed” photons can be considered classically: they describe passage of photons without any reformations.

The representations (2.6) show that commutations of field intensities described by the Pauli-Jordan function are connected with their formation or reformations without delay. The Coulomb field is infinitely in the undressed state and therefore the term  $1/\omega$  leading to the Coulomb pole in (2.6) must be subtracted. The subtraction can be performed with the decomposition of cotangent:  $\cot(x) = 1/x + 2x \sum_1^\infty 1/(x^2 - \pi^2 n^2)$ . It leads to the renormalized expression for (2.6):

$$\tau_2^{(renorm)}(\omega, \bar{r}) = -2\omega \sum_1^\infty 1/(\omega^2 r^2 - \pi^2 n^2), \quad (2.8)$$

which shows that the first pole of (2.6) is at the point  $\omega r = \pi$ . Therefore it can be taken that the formation path for photon is of the order

$$\Delta l \sim \pi/\omega = \lambda/2. \quad (2.9)$$

As this process is instantaneous, it corresponds to the jump of photon at the act of formation on the distance  $\lambda/2$  (cf. [23], where this estimation is proven by the covariant dispersion relations). Really it means impossibility of gradual photons formation that completely corresponds to quantum paradigm.

As must be underlined, (2.9) and (2.3) strictly correspond to duration of Čerenkov photon formation that justifies results of classical approach to this phenomenon.

For analysis of near field the usual decomposition can be written out (e.g. [23], compare [24,25], certain problems of near field are considered in [26]):

$$D_{ij}(\omega, \bar{r}) = \left\{ (\delta_{ij} + e_i e_j) - \frac{i}{\omega r} P_{ij} \cot(\omega r) + \frac{1}{(\omega r)^2} P_{ij} \right\} D(\omega, \bar{r}) \quad (2.10)$$

with directing  $e = x_i/r$  and the tensor  $P_{ij} = \delta_{ij} - 3e_i e_j$ . Three terms of (2.10) are related, correspondingly, to far, intermediate and near fields. The Sommerfeld condition of radiation,

$$(\mathbf{r} \cdot i\nabla_{\mathbf{r}})U(\mathbf{r}) = |\mathbf{k}| |\mathbf{r}| U(\mathbf{r})$$

at  $r \rightarrow \infty$ , selects within these terms the far field only.

Near field part corresponds to the function entered by Schwinger in [27]:

$$D_N(\omega, \bar{r}) = -(1/2\pi\omega^2 r^3) \sin(\omega r). \quad (2.11)$$

Corresponding duration,

$$\tau(D_N | \omega, \bar{r}) = i \left( \frac{2}{\omega} - r \cot(\omega r) \right), \quad (2.12)$$

shows that formation of near field requires duration 4-times bigger the uncertainty value in addition to (2.12). Therefore this value can be measurable.

Note that intermediate and near fields have space-like parts, corresponding instantaneous jumps (2.9), the singular function (2.11) describes connection of atoms in near field and transferring of excitations that can be instantaneous [23].

It can be noted that the spontaneous breaking of symmetry that leads to phase transitions of the first kind into more ordered states, at least, is executed by emission of photons [21], i.e. it corresponds to the Higgs mode.

Electromagnetic interactions in media can be examined via the dielectric susceptibility:

$$\epsilon(\omega; \bar{r}_1, \bar{r}_2) = f(\bar{r}_1, \bar{r}_2) / i[(\omega_0 + i\Gamma/2)^2 - \omega^2] \quad (2.13)$$

(we consider for brevity the two-level system only), which can be considered as the response function and for which temporal functions can be expressed just as above, but in the  $(\omega, \mathbf{r})$  representation. Thus the logarithmic derivative of (2.13) leads to

$$\tau_1(\omega) = \frac{\Gamma/2}{(\omega - \omega_0)^2 + \Gamma^2/4}; \quad \tau_2(\omega) = \frac{\omega - \omega_0}{(\omega - \omega_0)^2 + \Gamma^2/4}. \quad (2.14)$$

These forms will be used below.

Although several different possibilities for establishment of temporal functions had been considered in [18], it seems that the most short and the closest one to canonical theory follow the Ward identity.

Let's consider the simplest Ward-Takahashi identity:

$$k_\mu \Gamma_\mu(p, q, k) = G^{-1}(p) - G^{-1}(q), \quad (2.15)$$

where  $\Gamma_\mu$  is the vertex part and  $G(p)$  is the causal propagator. At  $q \rightarrow p$  its right part can be transformed as

$$k_\mu \frac{\partial}{\partial k_\mu} G^{-1} = -iG^{-1} k_\mu \frac{\partial}{i\partial k_\mu} \ln G = -iG^{-1} k_\mu \xi_\mu, \quad (2.16)$$

i.e. can be rewritten via the covariant temporal function, corresponding to 4D generalization of (2.1) and (1.4) as

$$\xi_\mu = (\partial / i\partial_\mu) \ln S \quad \text{and} \quad \partial S / i\partial k_\mu = \hat{\xi}_\mu S, \quad (2.17)$$

where  $\xi_\mu = (\tau, \vec{\xi})$  is the 4D temporal-spatial function.

The corresponding operator  $\hat{\xi}_\mu$  is canonically conjugated with the operator of energy-momentum. So, evidently,

$$i[\hat{\tau}, \hat{H}] = 1 \quad (2.18)$$

and the executing of this obligatory condition underlines the uniqueness of considered operator: it has no place with another artificially introduced duration operators [16]. Note that both operators in (2.18) describe interactions with another objects and with vacuum fluctuations, hence they must act onto S-matrix.

Thus, with these substitutions the Ward-Takahashi identity can be rewritten as

$$k_\mu \xi_\mu(p) = iG(p) k_\mu \Gamma_\mu(p, p', k) \quad (2.19)$$

that at  $k_\mu \rightarrow 0$  leads to the main definition:

$$\xi_\mu(p) = iG(p) \Gamma_\mu(p, q \rightarrow p) \quad (2.20)$$

(it can be deduced directly from the Ward identity, but the used way visually shows that the strong equality  $k = 0$  is not necessary).

Physical sense of duration operator can be précised by the QED representation  $\Gamma_\mu(p, q) = \gamma_\mu + \Lambda_\mu(p, q)$  with the Ward identity  $\Lambda_\mu(p, p) = -\partial\Sigma(p)/\partial p_\mu$ , where  $\Sigma(p)$  is the mass operator:

$$\xi_\mu = iG(p)\left(\gamma_\mu - \partial\Sigma(p)/\partial p_\mu\right). \quad (2.20')$$

Thus, the durations of scattering process are connected with reorganization of scatterer and with formation of emitted particle. On the other hand (2.20) is close to the expression of current  $j_\mu \sim \text{Tr}(\Gamma_\mu(x)G(x))$ , i.e. each measurement corresponds to the addition of zero energy vertex to corresponding line of the Feynman graph, that justifies the “Larmor clocks” method [13].

The structure of (2.20) shows possibilities of its generalization by the standard substitutions  $p \rightarrow p - ieA$  with further decomposition over degrees of charge, etc.

Let us consider the principal significance of locality features corresponding to (2.20). The component  $\xi_0 \equiv \tau$  describes temporal properties of interaction, other components are related with its spatial lengths, but they can be expressed via the temporal functions and group velocity:

$$\bar{\xi} = i \frac{\partial}{\partial \vec{p}} \ln G(p) = i \frac{\partial}{\partial E} \ln G(p) \frac{\partial E}{\partial \vec{p}} \rightarrow -\tau(E) \vec{v}. \quad (2.21)$$

Analogically, for particle of spin  $1/2$  from (2.20) follows:

$$\bar{\xi} = iG(p)\bar{\Gamma}(p, q \rightarrow p) \rightarrow -\tau(E)\bar{\alpha}. \quad (2.22)$$

These expressions allow to writing the covariant representation:

$$\xi_\mu^2 = \tau^2(E)\left(1 - v^2/c^2\right), \quad (2.23)$$

i.e.  $\xi_\mu$  is the 4-vector of proper duration (cf. [28]).

### 3. OVERVIEW OF GENERAL THEORY

Let's consider interaction of  $n$  photons with electron, free or bound:

$$\gamma(\omega_1, \mathbf{k}_1) + \dots + \gamma(\omega_n, \mathbf{k}_n) + e(E, \mathbf{p}) \rightarrow e(E', \mathbf{p}') + \gamma(\omega_1', \mathbf{k}_1') + \dots + \gamma(\omega_m', \mathbf{k}_m'). \quad (3.1)$$

In the lowest order this process is described by the standard matrix element:

$$S_{n+m} = \frac{(-e)^{n+m}}{(n+m)!} \int dx_1 \dots dx_{n+m} T\{N(\bar{\Psi} A \Psi)_1 \dots N(\bar{\Psi} A \Psi)_{n+m}\}. \quad (3.2)$$

For processes on a bound (atomic) electron its propagator in the Furry representation can be taken in the Low form [29] as

$$G(x_1, x_2) \approx \frac{1}{2\pi i} \sum_n \psi_n(\mathbf{r}_1) \bar{\psi}_n(\mathbf{r}_2) \int_{-\infty}^{\infty} d\omega \frac{\exp[i\omega(t_1 - t_2)]}{E_n + \omega - i\Gamma_n/2}, \quad (3.3)$$

external electromagnetic field can be quantized in the volume  $V$  in the plane wave representation:

$$\mathbf{A}_{i,f} = \sum_{\mathbf{k}} \frac{e a^{(\pm)}}{\sqrt{2\omega_{i,f} V}} \exp\{\pm i(\mathbf{k}_{i,f} \mathbf{R} - \omega_{i,f} t)\}, \quad (3.4)$$

where  $\mathbf{R}$  is the radius-vector of the center of atom.

After integration over all time variables

$$S_{n+m} = 2\pi Q_{n+m} V^{-\frac{n+m}{2}} \delta(\sum \omega_n + E_0 - \sum \omega_m - E_f), \quad (3.5)$$

where

$$Q_{n+m} = i(ie)^{n+m} \frac{C_{n,m}}{(n+m)} \frac{\langle f | e \exp(i\mathbf{k}_m \mathbf{R}) | n+m-1 \rangle}{\sqrt{2\omega_{n+m}}} \prod_{q=1}^{n+m-1} \sum_{l \neq q} \frac{\langle l | e \exp(i\mathbf{k}'_m \mathbf{R}) | \lambda \rangle}{\sqrt{2\omega_q} (E_l - E_0 - \sum_i^q \omega_k - i\Gamma_q/2)}, \quad (3.6)$$

at photons absorption and emission  $\omega_q \geq 0$ , the standard designations of partial matrix elements are used, the factorials corresponding to permutations of identical particles are grouped in the  $C_{n,m}$ .

The reaction rate is determined as

$$dR_{n+m} = \lim 2\pi |Q_{n+m}|^2 \frac{dN_1}{V} \cdots \frac{dN_n}{V}, \quad (3.7)$$

$dN_i$  is the number of incident photons of type  $i$  in the energy interval  $(\omega_i, d\omega_i)$ , the matrix element is averaged over polarization of initial photons and summed over polarizations of outlet photons interacting with single electron:

$$|Q_{n+m}|^2 = \frac{2j_f+1}{2^{n+m}(2j_i+1)} |Q_{n+m}(e \rightarrow \gamma_v)|^2. \quad (3.8)$$

At calculation of processes with two-particle initial states, it is possible to omit  $V$  in (3.7) by the known procedures, however in general case the situation is more complicated. The transition  $V \rightarrow \infty$  is performed for outlet and incident photons, respectively, as

$$\frac{1}{V} \rightarrow \frac{d\mathbf{k}_f}{(2\pi)^3}, \quad \frac{dN_i}{V} \rightarrow f(t, \mathbf{r}|\omega, \mathbf{k}) d\mathbf{k}_i. \quad (3.9)$$

For unidirectional monochromatic laser flux of photons density  $\rho$  the last distribution is simplified,

$$f(t, \mathbf{r}|\omega, \mathbf{k}) \rightarrow \rho \delta(\mathbf{k} - \mathbf{k}_0), \quad (3.10)$$

but can be generalized for the case of some fluxes with different frequencies and directions, in thermal field it would be expressed via the Planck distribution and so on.

If the interference between levels in (3.6) can be neglected, all integrations over angles in (3.8), except transitions into the continuous spectrum, can be executed:

$$\int d\Omega | < l | \gamma_\mu e^{ikR} | \lambda > |^2 \rightarrow 8\pi^2 \Gamma_l / e^2 \omega_{l\lambda}. \quad (3.11)$$

The integration over frequencies can be executed by (3.10) and/or by the Lorentz profiles in the square of expression (3.6).

For the reactions in the continuous flux, where number of interacting photons is not fixed, the complete reaction rate can be determined, after all integrations, as

$$R(j) = \sum_{n,m=0}^{\infty} R_{n,m} \rightarrow \sum_0^{\infty} a_n \rho^n, \quad (3.12)$$

i.e. as the virial decomposition over the photons density  $\rho = j/c$  in vacuum.

At calculation of (3.12) the question of convergence of these series appears. The radius of convergence determines saturation of corresponding process and an opportunity of opening of new channels of reactions. Notice that the presence of thresholds on number of particles is the feature of the MPPs theory; in nuclear physics, for example, thresholds are determined by the energy of single incident particle.

Some basic features of MPPs can be revealed at consideration of such example.

Let's consider the most usual MPP of type

$$\gamma(\omega_1) + \dots + \gamma(\omega_n) + A \rightarrow B + C. \quad (3.13)$$

As the main graph of the process is one-connected, its matrix element

$$S_{fi}^{(n)} = M \prod_{q=1}^n \{ G(p_q) \Gamma_\mu(p_q, p_q + k) A_\mu(k) \} \Phi_{in}(p_0), \quad (3.14)$$

where  $\Phi_{in}(p_0)$  is the wave function of initial state of scatterer, bound or free,  $M$  is the matrix element of decay of excited intermediate state into the final state:  $A^* \rightarrow B + C$ .

In the low frequencies limit ( $\hbar\omega/mc^2 \ll 1$ ,  $\lambda/r_0 \gg 1$ ) it can be taken in the accordance with (1.4) that

$$\Gamma_\mu(p, p + k) G(p) \Gamma_\mu(p, p) G(p) = i G^{-1}(p) \xi_\mu(p), \quad (3.15)$$

i.e. the temporal function can be naturally introduced. In our limit  $\xi_\mu(p) \rightarrow \tau(\omega)$ . Hence each absorbed photon introduces into reaction rate the factor:

$$\frac{4\pi e^2}{2\omega V} e_\mu \Gamma_\mu(p, p + k) G(p) e_v \xi_v(q\omega) \approx \frac{4\pi}{2\omega V} M' \tau, \quad (3.16)$$

where  $M'$  corresponds to the matrix element of elastic  $e\gamma$  scattering and in the considered limit for it the classical Thompson amplitude  $r_0 = e^2/mc^2$  can be taken. For nonpolarized photons, in accordance with the optical theorem of QED,  $4\pi r_0/2\omega = c\sigma_{\text{tot}}$ .

It shows that the reaction rate represents the series over

$$j/j_0(\omega) \equiv j\sigma_{\text{tot}}\tau_2(\omega), \quad (3.17)$$

and therefore clears up the physical sense of (3.12): the magnitude of  $j_0 = 1/\sigma_{\text{tot}}\tau_2$  represents the saturation value of photon flux.

Thus suggested theory can be characterized as the  $S$ -matrix decomposition over the parameter  $(j/j_0)$  and can be comparing with other ones.

In the early period of MPPs investigations the processes of MPI were modeled in the quasiclassic theory by consideration of electron liberation from the potential well of depth  $I$  in the field  $E = E_0 \cos \omega t$ . These calculations are leading to the famous Keldysh adiabatic parameter [30]:

$$\xi_0^2 = 2m\omega^2|I|/e^2E_0^2. \quad (3.18)$$

In the scope of QED this parameter can be rewritten as

$$\xi^2 = j_0^{(N)} / j \equiv 1 / j \sigma_{\text{tot}} \tau_0(N),$$

where  $\tau_0(N) = 1/2N\omega$  corresponds to the uncertainty principle. Such representation shows that these theories propose the simultaneous absorption of  $N$  photons, without any spans between elementary acts. Such conjecture can be justified in the definite cases, but can not be the universal one.

At the further investigations (e.g. [31], and references therein) this parameter was slightly generalized by including the complete absorbed energy  $\Sigma = N\hbar\omega$ :

$$\xi_0^2 = 2m\omega\Sigma/e^2E^2 \rightarrow J/U_p, \quad (3.19)$$

where  $U_p$  is the ponderomotive potential.

The introduction of a free electron's intensity parameter [32] as

$$Z = 2U_p/mc^2 \rightarrow (1/2mc^2)\sigma j \quad (3.20)$$

supposes that the duration of process is determined by the Compton time  $\tau_C = \hbar/mc^2$ . This conjecture seems very artificial one and must be proven for concrete processes.

It must be concluded that none of these parameters take into account the momentum acquisition at MPI. Therefore, they can be suitable, in principle, for the HHG examination, but not to distinguishing between HHG and MPI at all. These parameters, as may be added, do not contain the characteristics of scatterers and it complicates the consideration of such phenomenon as atomic stabilization. (Some other parameters are considered in [33].)

The non obvious proposition of simultaneousness permits to use the usual one-time Schrödinger equation with the Hamiltonian of interaction  $H'' \sim \mathbf{dE}$  instead of  $H' \sim \mathbf{pA}$ . The transition from one form to another can be carried by the unitary transformation

$$\Psi_1(t, r) \approx \exp [-(i/c) \mathbf{A}(t) \mathbf{r}] \Psi_2(t, r),$$

if  $\mathbf{A}$  does not depend on the spatial variables, but it is known that these forms are not equivalent, for example, in the calculations of photonuclear reactions [34], which are formally similar to MPPs, and it can be connected just with duration of these reactions: as this transformation is non local, it can not be so produced for time and spatial extended process. Hence if MPPs are determined by the sequential photons absorption, they must be calculated via  $H'$ .

Let's define for further examinations the conditions at which the atom can be considered as an isolated object relative to MPP. The volume, in which occurs single non-resonant e- $\gamma$  interaction, can be determined as

$$V_{\text{int}} = \sigma_T c \tau_2 \rightarrow (4\pi c^2 / \omega^2) r_0. \quad (3.21)$$

Process can be examined as happening on the isolated atom, if the density  $\rho_a$  [atoms/cm<sup>3</sup>] of considered substance (or, more precisely, the density of upper electrons) is those, that

$$\rho_a V_{\text{int}} \leq 1. \quad (3.22)$$

This condition can be rewritten in a more simply and physically evident form through the plasma frequency as

$$\omega \geq \omega_p. \quad (3.23)$$

Thus, the execution of MPPs should go faster than excitation of plasma waves and transferring of energy into collective oscillations.

#### 4. STIMULATED RADIATION

The notion of stimulated (induced) radiation appears at consideration of resonant processes:

$$\gamma(\omega_0) + e_B^*(E_1) \rightarrow e_B(E_0) + 2\gamma(\omega_0) \quad (4.1)$$

at  $\omega_0 = E_1 - E_0$ .

Its probability is defined in the resonance field of intensity  $J = \hbar \omega j(\omega)$  by the Einstein coefficients [35] as

$$W = A + Bj(\omega_0). \quad (4.2)$$

The linear dependence on photons intensity can be generalized onto more complicated processes (cf. [36]). So, the consideration of processes in an intensive monochromatic field requires an account of possibilities of additional absorption-reemission of photons:

$$N\gamma(\omega_0) + e_B^* \rightarrow e_B + (N+1)\gamma(\omega_0). \quad (4.3)$$

Its probability must be examined in a more general form comparable with (2.13):

$$W = A + \sum_n B_n(\omega, \omega_0, \Gamma) j^n(\omega), \quad (4.4)$$

i.e. in the form of "virial" series with  $B_n$  as functions of parameters of scatterers considered for simplicity as two-level systems.

Such representation, if it would be summed, can lead to the radius of convergence for processes of stimulated radiation, to their saturation and to thresholds of another processes. Let's consider its deduction in some details.

The amplitude of transition (4.3) can be written in the form of clusters decomposition as

$$\langle (N+1)\gamma, e | S | N\gamma, e^* \rangle = 2\pi i \sum_1^N \frac{n!(n+1)!}{(2n+1)!} \langle (n+1)\gamma, e | T | n\gamma, e^* \rangle Q_n \delta(\sum E_f - \sum E_i), \quad (4.5)$$

where  $Q_n$  corresponds to the density of states, initial and final, i.e. is determined via densities of incident photons. By taken into account its further squaring

$$Q_n^2 = \prod_1^n \frac{\rho_i(k) dk_i}{2\omega_i} \prod_1^{n+1} \frac{dk_f}{2\omega_f (2\pi)^3}, \quad (4.6)$$

where  $\rho_i(k)$  is the density of photons of type  $i$ , in the monochromatic coherent flux  $\rho_i(k) = \rho \delta(k - k_0)$ .

At  $|\omega - \omega_0| < \Gamma/2$  all diagrams of (4.5) with nonresonant factors instead of resonant ones and all S-matrix terms with  $A_\mu^2$  in the Hamiltonian can be omitted. With these approximations the reaction rate with  $N = 1$  gives

$$R_{2,1} = \frac{64\pi}{9\omega^2} j \Gamma \frac{\Gamma}{(\omega - \omega_0)^2 + \Gamma^2/4}. \quad (4.7)$$

For  $n \gg 1$  with only resonant terms taken into account the partial reaction rate

$$R_{n+1,n} \approx \pi \Gamma n (j/j_0)^n \quad (4.7')$$

and the complete reaction rate is summed at  $j < j_0$  via the higher hypergeometric function:

$$R = \sum_0^\infty R_{n+1,n} = {}_3F_2(2,2,1; 3/2, 3/2; j/j_0) \approx \pi \Gamma \frac{j/j_0}{(1 - j/j_0)^2}, \quad (4.8)$$

here the designation

$$j_0 = \frac{\omega^2}{\pi c^2((\omega - \omega_0)^2 + \Gamma^2/4)/\Gamma} \rightarrow \frac{1}{\sigma_{el}\tau_1} \quad (4.9)$$

is introduced. (To simplify the writing, here and below we omit factors arising from averaging over the initial polarizations and summing over the final polarizations.)

The expression of  $j_0$  via the cross-section of elastic scattering  $\sigma_{el}$  and the duration of time delay at this process  $\tau_1$  (cf. (1.2)) evidently visualizes the physical sense of the non-removable pole of reaction rate: this flux density corresponds to the saturation of induced radiation and, as can be demonstrated, the possibility of opening of new channel, the higher harmonics generation.

The most interesting physical result consists here in the natural appearance of temporal characteristic of scattering process, which is usually introduced in the theory ad hoc, by hands only.

Thus the parameter of multiphoton reaction rates decomposition must be of the order  $(j/j_0)$ , i.e. must contain temporal characteristics of interactions (further decomposition of each partial matrix element goes, naturally, over degrees of  $e^2/\hbar c$ ). These results are deduced in [3, 37] by another method also, there is considered also stimulated radiation at irradiation in restricted time and so on.

Threshold of the beginning of induced radiation at the strictly resonant irradiation of excited gas is enough low. So, at  $\omega_0 = 10^{15}$  and  $\Gamma = 10^8$  it is received that

$$I_{min} = \hbar\omega_0 j(\omega_0) = \frac{\hbar\omega_0\Gamma}{4\pi c^2} \sim 10^{-3} \text{ [W/cm}^2\text{].}$$

Therefore these phenomena could be in part investigated up to the invention of lasers.

Our consideration, certainly, is much idealized: it is assumed that values of  $j$  are independent of time, i.e. their fluctuations are small on time intervals  $\tau_2 \sim 1/\omega_0$ , when the electron can be considered as virtual. If the distance between inlet photons is more  $c\tau_2$ , the matrix element is splitted onto product of independent multipliers.

The formal requirement to uniformity and intensity of radiation flux can be expressed as the condition:

$$\int_0^{\tau_2} j(t, \omega) dt \geq 1/\sigma(\omega) \quad (4.10)$$

Now we shall consider the parameters of levels, their widths and shifts in the field. In the asymptotically weak field these magnitudes are described, in accordance with Low, as

$$\delta\omega_n - (i/2)\Gamma_n = \frac{e^2}{16\pi^2} \int \frac{dk}{k} \sum_m \frac{|\langle n | \gamma_\mu e^{ikR} | m \rangle|}{\omega_n^0 - \omega_m^0(1 - i0) - k \operatorname{sgn} \omega_m^0}. \quad (4.11)$$

External field can be taken into account by the substitution:  $k_\mu \rightarrow k_\mu - ieA_\mu$ , at which the nominator of (4.11) receives additive terms that in the dipole approximation are of the type of  $\Omega_{n,m} = \langle n|\mathbf{dE}|m \rangle$  and its square. Therefore the widths of levels and their shifts become to

$$\begin{aligned}\Gamma_n &= \Gamma_n^0 + 2 \sum_m \Omega_{n,m} + \frac{a \sum_m \Omega_{n,m}^2}{\omega} + \dots, \\ \delta\omega_n &= \delta\omega_n^{(0)} + \alpha j^{1/2} + \beta j + \dots\end{aligned}\quad (4.12)$$

Note that in the high frequencies field (4.12) correspond to so-called theorem of squares:

$$\Gamma t \rightarrow 2 \int_0^t (\mathbf{dE})_{21} dt \quad (4.13)$$

that naturally leads to  $\Delta\Gamma \sim j^{1/2}$ .

In the two-level system  $\Gamma^{(0)} \ll \Omega \ll \omega$  in an intensive field usually, and therefore the half-width of level can be replaced by the Raby frequency  $\Omega = (\mathbf{dE})_{21}$ . In a more general case it can be taken that  $\Gamma \rightarrow 2\langle n|\mathbf{dE}|m \rangle$  and near to the resonance ( $\Gamma > |\Delta\omega|$ ) such substitution is possible:

$$\tau_1 = \frac{\Gamma/2}{\Delta\omega^2 + \Gamma^2/4} \rightarrow \frac{1}{\sqrt{\Delta\omega^2 + \Omega_{nm}^2}}. \quad (4.14)$$

It shows that atomic electrons in the intensive field must be in continuous beatings with frequency  $1/\tau_1$  between levels, i.e. in the sequential absorption-reemission processes. This result completely coincides with the quantum mechanical calculation [38]. But our consideration shows that such beatings take place at  $j \leq j_0$  only, higher fields must be examined additionally.

Let us consider now the dependence of level parameters on flux intensity via the substitution of (4.9) into (4.8) that can be rewritten at  $j < j_0$  in the Lorentz form:

$$R \approx Aj/[(\Delta\omega - \delta\omega(j))^2 + \gamma^2(j)/4] \quad (4.15)$$

with nonresonant factor  $A = \pi\sigma_{\text{res}}\Gamma^2(\Delta\omega^2 + \Gamma^2/4)/(\Delta\omega + \delta\omega)^2$  and with shifts of effective levels and width:

$$\begin{aligned}\delta\omega &= \sqrt{j\sigma_{\text{res}}\Gamma}; \\ \gamma^2(j)/4 &= \frac{\Delta\omega - \delta\omega}{\Delta\omega + \delta\omega} \cdot \frac{\Gamma^2}{2} + \frac{\Gamma^4}{16(\Delta\omega + \delta\omega)^2}.\end{aligned}\quad (4.16)$$

These expressions demonstrate that reemission processes lead to the renormalization of parameters of electron levels. At the strict resonance  $\Delta\omega = \delta\omega$ ,  $\gamma_{\text{res}} = \Gamma^2/4\delta\omega$

and  $\delta\omega_{\text{res}} = (j\sigma_{\text{res}}\Gamma^2)^{1/3}$ , which show, in comparison with (4.12), that the functional forms are changing directly at the resonance.

Now we will consider processes of higher field intensity, at  $j > j_0$ .

As it can be showing, each (nonresonant) act of absorption-reemission adds to (4.8) the multiplier

$$\frac{j}{j^{(1)}} = \frac{\pi c^2 j}{\omega^2} \frac{\Gamma}{(\omega + \omega_0)^2 + \Gamma^2/4} \approx \frac{j}{j_0} \frac{\Gamma^2}{16\omega_0^2}. \quad / \quad (4.17)$$

So, if between two resonant transitions appears  $q$  nonresonant transitions of the same frequency, the radius of convergence will be increased on the factor of (4.17) in the degree  $q$ . Therefore it seems that the convergence of this new reaction rate is possible if the expression (4.17) is not bigger than one, i.e. the radius of convergence with taken into account nonresonant scatterings would be

$$j_1 = j_0(4\omega_0/\Gamma)^2. \quad (4.18)$$

This magnitude is so big (in the optical range  $j_1 \sim 10^{15}j_0$ ) that if only these processes played a role, stimulated radiation would be possible at all practically achievable intensities.

But on the other hand an intensity of irradiation should be lower than the threshold of harmonics generation. At the absence of any additional levels of system, harmonics can arise in the non-resonant way if the distance between consistently suitable quanta is lesser  $c\tau_1$ , i.e. if

$$j \geq j_{\text{harm}} = 1/\tau_1\sigma_{\text{tot}}, \quad (4.19)$$

where  $\sigma_{\text{tot}} = 4\pi cr_0/\omega_0$ . As the magnitude of (4.19) is usually much lesser (4.18), it represent natural upper threshold of stimulated radiation connected with opening of a new channel, of HHG.

Notice, that the analogical calculation of stimulated absorption, i.e. of (4.3) with  $N \leftrightarrow N + 1$ , shows that corresponding partial rates

$$\frac{R(n \rightarrow n+1)}{R(n+1 \rightarrow n)} = \frac{n+1}{n}, \quad (4.20)$$

i.e. it confirms the validity of the Einstein solution (4.2) of thermodynamic Diophantine equation.

## 5. PROCESSES OF HIGHER HARMONICS GENERATION

Generation of higher harmonics, especially at single electrons, can be considered by an analogy with a multiphoton Compton scattering and therefore some problems of its

kinematics can be directly transferring from the one-photon processes description. But the dependence on densities of photon fluxes represents some new problems.

Consideration of HHG processes is usually carried out variously for different energies. For harmonics with energy smaller the ionization threshold is usually suggested that the electron, which has virtually absorbed some photons, is transferring downwards in the same atom with emission of the total saved up energy as one photon. However the HHG of significant big energies is usually considered through three steps: (1) tunnel or barrier-suppression ionization, (2) acceleration by the laser field and return to the ion, and (3) recombination with the ion. The excess energy of the recombination process is emitted as short wavelength radiation (e.g. [39,40]). The HHGs at the accelerator energy had been also investigated [41].

As we shall show, such complications are not necessary: HHG at all energies can be considered as a process when virtually excited electron does not leave the atom, and simply, as well as in the case of weak excitation, comes back onto the place. The developed approach does not conduct to spectral expansion of the higher harmonics, inevitable at three-stage processes.

However for harmonics of very high numbers and for an explanation of so-called plateau in the harmonics spectrum it is more convenient to use the statistical approach in the frame of QED. Therewith, it appears that there is original rather short-term effect of an equipartition of energy on "degrees of freedom" of electronic gas, which are represented as the number of virtually seized photons.

For comparatively low intensity of laser flux ( $J \ll 10^{13} \text{ W/cm}^2$ ), at which atomic levels have significant role, the calculations can be proceeding in accordance to general rules described above. So for the elementary act of frequency doubling (really such process is possible under special conditions in media only):

$$2\gamma(\omega) + e_B \rightarrow \gamma(2\omega) + e_B \quad (5.1)$$

we can formally write:

$$R_{1,2} \simeq \frac{2j_f+1}{4(2j_i+1)^2} \frac{\pi^2 j_i^2}{9\omega^4} \frac{\Gamma^2}{(\omega - \omega_0)^2 + \Gamma^2/4} \frac{\Gamma}{(\omega - 2\omega_0)^2 + \Gamma^2/4} \sim Q\Gamma(j/j_0^{(2 \rightarrow 1)})^2, \quad (5.2)$$

where  $Q$  include all multipole factors and the critical flux density

$$j_0^{(2 \rightarrow 1)} = 1/\sqrt{\sigma(\omega)\tau(\omega) \cdot \sigma(\omega)\tau(2\omega)} \quad (5.3)$$

is the geometrical average over one-photon densities.

Reaction rates for generation of higher harmonics on isolated scatterer can be written analogously:

$$R_{1,n} \sim Q\Gamma j^n / j_0^{(n \rightarrow 1)} \simeq Q\Gamma j^n \sigma^n(\omega) \prod \tau(\omega + k\omega_0). \quad (5.4)$$

This approach can be essentially simplified. As a matter of fact from QED is required only the concept of time of delay and the formations of final states applied to statistical consideration of processes. Simultaneously such consideration reveals some features of MPPs.

Let's consider a set of free electrons irradiated by a monochromatic photon flux  $J = \hbar\omega$  of high intensity. Process of elastic scattering occurs as absorption of a photon and its emission through time of delay  $\tau_1$ . But if the density of photons flux is such that during this time the scattering of second photon on the same electron takes place, this electron will retain onto a time duration  $\tau/2$  double energy, which will be let out, with greater probability, as one photon of the double frequency. Thus, the electron can retain energy  $E_K = K\hbar\omega$ ,  $K = 1, 3, 5, \dots$ , sufficient for HHG, and corresponding momentum, the oddness of  $K$  guarantees the parity conservation. This process goes by one stage, can be described by the single Feynman graph and there is not necessity for splitting it onto subprocesses of various nature.

According to the uncertainty principle if the electron absorbs  $K$  photons of energy  $\hbar\omega$ , it can keep their energy during the time  $T'_K = 1/2K\omega$ . The theory of temporal functions overviewed in the Section 2 gives twice bigger value till the end of particle formation (its "dressing"):  $T''_K = 1/K\omega$ . Hence we can estimate the duration of holding time for accumulated energy as

$$T_K = 1/\eta K\omega \quad (1 \leq \eta \leq 2). \quad (5.5)$$

Over this time  $N_K$  photons are transferring through the maximally possible cross-section  $S_0 = \alpha\pi\lambda^2$  of e- $\gamma$  interaction ( $\alpha$  is the fine structure constant):

$$N_K = j\xi S_0 T_K, \quad (5.6)$$

where  $\xi$  characterizes a competition in photons capture with other sufficiently closely located scatterers (it will be considered below and can be omitted at consideration of rarefied gas).

The probability of each virtual absorption (capture) is proportional at considered frequencies and at absence of resonances to the total cross-section of the single photon scattering  $\sigma_{\text{tot}} = 4\pi c r_0 / \omega$  and can be represented as

$$p \simeq \sigma_{\text{tot}} / S_0 = (2/\pi)\lambda_C / \lambda, \quad (5.7)$$

$\lambda_C$  is the Compton wave length, in considered processes  $\lambda \gg \lambda_C$ .

The probability of virtual absorption of  $K$  photons, from among  $N_K$  quanta passing through the maximal possible interaction cross-section, is expressed by the binomial distribution (e.g. [42]; for its approximations we use, actually, the conservation laws only):

$$B_K(N_K) = (N_K/K)p^K(1-p)^{N_K}. \quad (5.8)$$

This distribution corresponds to a fast decreasing of intensity of lower frequencies harmonics, but for big  $N_K \gg 1$  and with  $pN_K \ll 1$  this decreasing is sharply slowing down. So

the distribution (5.8) can be approximated at these conditions by the Poisson distribution with the mean value of virtually absorbed photons forming the K harmonic:

$$n_K = pN_K = j\sigma_{tot}T_K = (J/\hbar\omega) \frac{4\pi c r_0}{\eta K\omega^2}. \quad (5.9)$$

It means that the mean energy of this harmonic

$$E_K = K\hbar\omega n_K = J \frac{4\pi c r_0}{\eta\omega^2} = J \frac{\sigma_{tot}}{\eta\omega}, \quad (5.10)$$

i.e. this mean that the energy does not depend on the harmonics number in the considered part of the HHG spectrum and forms the observed plateau. (To this value can be added, of course,  $I/\hbar\omega$ , where  $I$  is the ionization potential.)

Hence each harmonic in this region of spectrum can be considered as the "degree of freedom" of photonic gas with the equipartition law of their description when the interaction between scatterers is negligible. Moreover (5.10) does not contain  $\hbar$  and therefore appears as the classical magnitude in the concordance with the classical, generally speaking, notion of degrees of freedom.

This expression can be rewritten as  $E_K = (4/\eta)U$ , where  $U$  is the ponderomotive potential. Note, that in so called "simple man's theory" [43] this energy is introduced for description of the experimental data as  $3.17U$ . It means that the coefficient  $\eta$  is precisely in the limits of (5.5),  $\eta \in [1, 2]$ , and that, consequently, our result qualitatively, at the least, conforms to the experimental data and therefore further numerical comparisons are not required.

The higher frequencies tail of (5.8) at big  $K$  and  $n_K$ , but with  $K/n_K \rightarrow 1$ , can be approximated by the Gaussian:

$$B_K(N_K) \rightarrow (2\pi n_K)^{-1/2} \exp(-(K - n_K)^2/2n_K). \quad (5.11)$$

It evidently corresponds to the observed decreases of energy of harmonics with the rising of  $K \rightarrow N_K$  after the plateau.

Let's consider now the low-frequencies tail of harmonics spectra. With the lowering of kept energy the duration of their keeping will increase, and therefore possibilities of their partial transferring to another scatterers will also increase; it will lead to a distortion of the harmonics' profile, to formation of quasi-continuous spectrum.

This transferring is effective for such accumulated energy only, for which  $cT_K$  is bigger  $\rho_e^{-1/3}$ , the mean distance between scatterers. Therefore we can expect that the clear harmonics comb begin only with  $K$  bigger

$$K_{min} \sim (c/\eta\omega)\rho_e^{1/3}. \quad (5.12)$$

Hence we had finished, in principle, the description of the main parts of HHG spectra for rarified scatterers set. For consideration of HHG processes in more dense media a coefficient  $\xi$  in (5.6) must be estimated.

The simplest case is a rarified medium of the scatterers' density  $\rho_e$ , when the free path length of photon  $\ell=1/\rho_e\sigma_{\text{tot}}$  is bigger the target depth  $L$ , then the coefficient  $\xi=L/\ell$ .

For more dense targets, but with  $L \leq \ell$  and when the photon wavelength  $\lambda \gg \rho_e^{-1/3}$ , the sufficiently thin target gas layer can be subdivided onto "interaction pipes" of cross sections  $S_1 = \pi\rho_e^{-2/3}$ , so it can be assumed that each photon can interact in an each "pipe" with a single scatterer only. If we shall accept, for simplicity, that  $\rho_e = Z\rho$ ,  $\rho$  is the atomic density,  $Z$  is a number of electrons taking part in the process (note that at sufficient energies all atomic electrons, not only valent ones, can be involved in the reaction), then into the expression (5.6) would be inserted

$$\xi = (Z\rho)^{-2/3}/\alpha\lambda^2, \quad (5.13)$$

and the probability of single photon virtual capture will be now, instead of (5.7), determined as  $p_1=\sigma_{\text{tot}}/S_1$ .

According to (5.6) the maximal photons quantity, that are passing through the "interaction pipe" and can be virtually captured by the scatterer, will be equal to

$$N_{\max} = jS_1 T_{\min} \simeq jS_1 / \eta\omega N_{\max}, \quad (5.14)$$

i.e. the highest harmonic of plateau in the HHG process will be of the order

$$N_{\max} \simeq (\pi/\eta)^{1/2} (J/\hbar\omega^2)^{1/2} (Z\rho)^{-1/3}. \quad (5.15)$$

Hence the numbers of higher harmonics are proportional to the strength of laser field, instead of its power. Such dependence seems physically natural for the common classical representations that the energy of electron is determined by its acceleration in the laser field.

The dependence  $Z^{-1/3}$  for the highest achievable harmonic (5.15) can be comparable with some experimental data. In the article [44] the highest numbers of harmonics formed by the various gas targets are concerned as Ar : Kr : Xe = 1 : 0.85 : 0.71, the expression (5.15) results in ratio 1 : 0.79 : 0.69. In the article [45] the ratio of the highest harmonics numbers on targets He : Ne = 0.58, our formula gives for them 0.52. According to [46] such relation was measured for gases Ne : Ar  $\geq 0.75$  (uncertainty is connected to alterations of gas density in this research), the relation (5.15) gives 0.75.

With dependence on frequency the situation is more complicated: the estimation (5.15) results in dependence  $1/\omega$ , but for the highest harmonics and in sufficiently dense medium only. The similar estimation for rarefied gases (5.9) leads to  $1/\omega^2$ , which is closer to the "simple man's theory", where  $N_{\max} \sim I/\hbar\omega + a\sigma J/4\hbar\omega^2$ , with  $a \sim 2 \div 3$ . The dependence of  $N_{\max}$  on wavelength with equal other conditions was measured in [47] at  $J = 4 \cdot 10^{14} \text{ W/cm}^2$  for wavelengths 0.8 and 1.51 nm: the cutoff of harmonics set occurs, correspondingly, on energies of 64 eV and close to 160 eV that corresponds to  $\lambda^{1.8}$  and is close enough to square-law dependence in (5.10), but not to (5.15). This observation can be interpreted as the obvious minimization of the role of interaction with neighbor scatterers at higher frequencies with their shorter durations for such interactions, but evidently requires further investigation.

For numerical estimations, however, the more precise dynamical models are needed. Nevertheless, for a characteristic set of used parameters:  $J = 10^{14} \text{ W/cm}^2$ ,  $\hbar\omega = 1 \text{ eV}$ ,  $Z = 18$ ,  $\rho = 10^{18} \text{ cm}^{-3}$ , and at assumption that all processes are channeled only in the HHG we receive that  $N_{\max} \geq 200$ . This estimation does not seriously contradict observed values, especially since even the account of polarization of a laser beam and its angular divergence can reduce this value. (Notice that for the mean number of accumulated photons the expression (5.9) gives more adequate answers.)

It must be underlined that all above is conditioned by a shortness of laser pulse. If its duration would be longer, it can stimulate the partial exchange of surplus energy between electrons and accelerate the leveling of harmonics comb. It is not excluded that just such reasons can explain the phenomena, observed in some experiments [1], when the intensity of harmonics at the light impulse in 7 fs is approximately on the 0.5 orders above than at the impulse in 30 fs. Note that inasmuch as at the initial stage of dissipation its speed corresponds to the plasma frequency of electronic components  $v_p = (e^2 \rho / \pi m)^{1/2}$ , the condition of smallness of thermalization can be estimated through smallness of laser pulse duration in comparison with  $1/v_p$ .

The described picture can be evidently generalized on the case of two or more laser beams of different frequencies: the spectrum of harmonics will be more complex, inasmuch as, in the accordance with the composition law of binomial distributions, the new and more complicate set of "the degrees of freedom" can appear, but it does not change the general approach and observed picture.

The processes of summation of high harmonics quanta (including quanta of different frequencies) with each other are also possible. Probably, the mechanism of some harmonics amplification in the research [48], where the HHG was spent out in the long capillary with gas, is just those that increased the probability of virtual absorption and subsequent addition of previously formed quanta of higher frequencies.

At processes of HHG in the unidirectional flux all consideration is facilitated by the concordance of energy and momenta of harmonics quanta. In other cases, at the ATI and even in the crossed laser beams, the accumulation of additional momentum via interaction with parent ions or with neighbors is needed; it can accelerate the thermalization effects and widening of single harmonics (the extreme case of crossed light beams are processes in the opposite directed laser beams, [49]). The kinematics of such processes is evident and can be omitted.

We did not consider above the dependence of sequential photons capture on their polarization. As the virtual absorption of the first photon polarizes electron, it becomes necessary to take into account that the probability of following photon absorption would be proportional to probabilities of polarized photons scattering on polarized electrons. This circumstance, it is possible to think, changes the intensity of HHG at division of focuses of laser fluxes with different linear polarizations and at circular polarization in comparison with linear. But it also does not alter basically the described picture.

The revealed features can be considered as the extending of the Rayleigh-Jeans theory of the equilibrium low-frequency thermal radiation to the rapid energies reallocation at power laser flux interaction with electrons set. At the considered phenomenon the role of black body

fulfill scatterers with opportunities of only discrete and equidistant, on the frequencies  $K\omega$ , virtual energy accumulations. Note that the rescattering phenomena as the cause of plateau formation (e.g. [50] and references therein) and our approach lead to different temporal dependences, but we did not see yet sufficient experimental data for the choice between them.

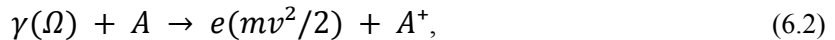
It can be interesting to note that in the articles of Jeans [51], where for the first time the fluctuations of "ether" in the resonator and their harmonics had been considered, only the equality of possible energies, without their equating to  $\kappa T/2$ , was accepted.

Some other peculiarities of the MPPs consist in the dependence of maximal number of these virtual degrees of freedom on the density of photon gas, on the target parameters and on the specific short-term condition of "thermodynamic balance". It is remarkable that in an accord with the classical definition of degrees of freedom their energies are classical magnitudes.

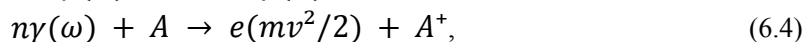
## 6. MULTIPHOTON IONIZATION: PROBLEM OF MOMENTUM

Consideration of processes of multiphoton ionization (MPIs) can be beginning with comparisons of reaction rates of one-photon processes and HHG on single scatterers with equal final energies and the same energy of an intermediate state:

- 1) one-photon processes with rates  $R_{el} = j\sigma_{el}$  and  $R_{ion} = j\sigma_{ion}$ ,



- 2) multiphoton processes with rates  $R_{HHG}$  and  $R_{MPI}$ ,



where  $n\hbar\omega = \hbar\Omega = I_0 + mv^2/2$ ,  $I_0$  is the potential of ionization.

Their rates must be connected by the ratio:

$$R_{el}/R_{ion} \simeq R_{HHG}/R_{MPI}, \quad (6.5)$$

it follows unitarity of  $S$ -matrix since all four processes have almost identical (last for (6.3-4) graphs) intermediate states of an electron virtually absorbing energy  $\hbar\Omega$  with duration of this stage  $1/2\hbar\Omega$ . The ratio can be comparable with the Fermi-Watson theorem for  $\pi$ -mesons photoproduction [52].

In the spite of our general approach we shall begin with the most power processes and then will turn to lower intensities, for which calculations and comparison with experimental data are simpler.

The rates of one-photon processes are well known and if the HHG process also would be well examined, the rate of MPI could be described via them. If this ratio is not executed, it would mean that MPI goes, completely or in part, as a multi-stage process, i.e. via the initial formation of sufficient high harmonics and subsequent ionization by one or even some different photons of high harmonics.

For the MPP with such (last) intermediate state as the combination of (6.3) and (6.2), the reaction rate can be estimated:

$$R_{\text{MPI}}^{(1)} \sim R_{\text{HHG}} T_{\text{HHG}} R_{\text{ion}}, \quad (6.5')$$

where  $T_{\text{HHG}}$  is the duration of (6.3) that via the uncertainty principle can be approximated as  $1/2\Omega$ . Hence, with taking into account (6.5) and  $R_{el} = j\sigma_{el}$ , where  $\sigma_{el} \approx \sigma_T$ , the classical Thomson cross-section,

$$R_{\text{MPI}}^{(1)} \sim \frac{1}{2\Omega} R_{\text{HHG}} R_{\text{ion}} = (j\sigma_T / 2N\omega) R_{\text{HHG}} \quad (6.5'')$$

and it can be generalized on more number of intermediate states.

Let's consider now the direct calculation of  $R_{\text{MPI}}$ . It can be approximately represented as

$$R_{\text{MPI}} \rightarrow R_{\text{HHG}}(E) D(E, \mathbf{p}), \quad (6.6)$$

where  $E = \hbar\Omega - I$  is the kinetic energy of photoelectron,  $p = \sqrt{2mE}$  is its momentum,  $D(E, \mathbf{p})$  is the probability of momentum accumulation via interaction with atomic reminder and so on.

The problem of momentum accumulation by freed electron had been the item of discussing from the very beginning of quantum electrodynamics ([53]), and even earlier, in the theory of one-photon photoeffect (e.g., [54], the modern statement [55]) and in the theory of molecules photo-dissociation. As can be represented, the most direct decision of this problem can be achieved by the Landau method advanced in the theory of predissociation [37]; therefore the state of an electron that receives enough energy, but the corresponding momentum has not accumulated up yet, can be named the pre-ionization state.

Let's try to estimate  $D(E, \mathbf{p})$  in (6.6) by the Landau method.

Let  $\psi_b$  and  $\psi_f$  describe states of an electron in discrete and continuous spectra,

$$(H_0 + V)\psi_{b,f} = U_{b,f}\psi_{b,f}. \quad (6.7)$$

If  $\psi_{0,b}$  and  $\psi_{0,f}$  are self-functions, and  $U_{0b}$  and  $U_{0f}$  are self-values of the Hamiltonian  $H_0$ , it is possible to search for wave function as the superposition  $\psi = c_b\psi_{0,b} + c_f\psi_{0,f}$ . Multiplying the equation (6.7) at the left serially on the functions

conjugated to  $\psi_{0,b}$  and  $\psi_{0,f}$ , we receive system of two homogeneous equations and the condition of their compatibility results in the expression:

$$U_{b,f}(\mathbf{r}) \equiv U \pm \Delta U = (U_{0b} + U_{0f})/2 \pm [(U_{0b} - U_{0f})^2 + 4U^2]^{1/2}, \quad (6.8)$$

where  $U(\mathbf{r})$  is the matrix element of interaction operator  $V$ , and all magnitudes are functions of  $\mathbf{r}$ .

The start of photoelectron is possible from the point, in which  $\Delta U = 0$ . Near to this point the difference  $(U_{0b} - U_{0f})$  as function of  $\xi = |\mathbf{r} - \mathbf{r}_0|$  can be approximated as

$$U_{0b} - U_{0f} \approx (\mathfrak{J}_f - \mathfrak{J}_b)\xi,$$

where  $\mathfrak{J} = -(dU/d\mathbf{r})$  is the force of interaction between an electron and atomic reminder. As this process can be considered as nonrelativistic, it becomes possible to accept  $\xi = vt$ . Then the equality  $\Delta U = 0$  shows that the transition occurs during (pure imaginary) moment of time

$$t_0^{(\pm)} = \pm 2i|U|/v |\mathfrak{J}_f - \mathfrak{J}_b| \equiv \pm i\tau(\mathbf{p}), \quad (6.9)$$

its completely imaginary form corresponds to the duration of final state formation  $\tau_2$  described in the Section 2 [18].

If  $\mathfrak{J}_f \ll \mathfrak{J}_b$  in (6.9) also, it is possible to assume that  $2|U|/v$  is about the momentum, which has been accumulated up by an electron at a starting from atom; then  $\tau(\mathbf{p})$ , in the full conformity with the Second law of dynamics, shows the duration of time necessary for accumulation of the momentum corresponding to the kinetic energy of electron:

$$\tau_n(\mathbf{p}) = \Delta p_n / \mathfrak{J}_b, \quad (6.10)$$

where  $\Delta p_n \approx \sqrt{2m(\hbar\Omega - E_n)}$  at ionization within the state with the main quantum number  $n$ . Thus it can be assumed that  $\mathfrak{J}_b \sim E_n/a_n = \frac{1}{2}(Z\alpha)^2 \cdot Ze^2/(n^2\lambda_C)^2$ , i.e. the duration of time, necessary for momentum accumulation, sharply increases with transition to highest levels that result in a relative stabilization of the Rydberg levels concerning opportunity of MPI.

Accepting to  $\Delta p_n \sim \sqrt{2m\hbar\Omega}$  it is received that

$$\tau_n(\mathbf{p}) \approx 1.3 \cdot 10^{-17} n^4 Z^{-3} \sqrt{\hbar\Omega}, \quad (6.10')$$

where  $\hbar\Omega$  is expressed in the eV's.

This magnitude is the major parameter since it is obvious that for realization of considered reaction the durations of momentum and energy accumulations should be coordinated.

Now it is possible to search for the solution of the Schrödinger temporal equation, needed for their coordination:

$$i\hbar \frac{\partial \Psi}{\partial t} = [H_0(t) + V(t)]\Psi, \quad (6.11)$$

in the form

$$\Psi = b(t)\psi_b + f(t)\psi_f \quad (6.11')$$

with the initial conditions  $b(-\infty) = 1, f(-\infty) = 0$ , such that  $|f(\infty)|^2$  is the probability of electronic transition in a point  $\mathbf{r} = \mathbf{r}_0$  into the state  $\psi_f$ , and  $|b(\infty)|^2 = 1 - |f(\infty)|^2$  is the probability of electron that further stays in the atom.

According to the quasiclassical Landau method for the solution of such equations, it is necessary to proceed in the factor

$$b(t) = \exp\left\{-\left(\frac{i}{\hbar}\right) \int_{-\infty}^t U(t)dt\right\} \quad (6.12)$$

at big  $t < 0$  into the complex plane with detour the point  $t_0^{(+)}$  from above. Thus  $b(t)$  passes in  $f(t)$  that conducts to the expression:

$$|f(\infty)|^2 = \exp\left\{-\left(i/\hbar\right) \int_{-\infty}^{i\tau(p)} \Delta U(t)dt\right\} \rightarrow \exp\{-\pi\Omega\tau(\mathbf{p})\}, \quad (6.13)$$

where  $t' = 0$  is accepted.

It is natural to assume, in accordance to the uncertainty principle, that duration of holding of virtually absorbed energy of N photons by an electron, i.e. duration of formation of a free electron state with kinetic energy  $\hbar\Omega \simeq p^2/2m$ , is about  $\tau_2 = 1/2\Omega$ . Hence, the parameter exhibitors in the expression (6.13) are determined by the ratio of durations necessary for accumulation of mutually corresponding momentum and energy of the taking off electron. According to (6.10') this key parameter of the theory can be appreciated as

$$\zeta \equiv \tau_n(\mathbf{p})/\tau_2 \approx 0.04n^4Z^{-3}(\hbar\Omega)^{3/2}. \quad (6.14)$$

The full probability of pre-ionization can be determined according to the Landau-Zener definition of probability of predissociation as

$$P_{LZ} = 2|f(\infty)|^2(1 - |f(\infty)|^2) \equiv 2\exp(-\pi\zeta/2)[1 - \exp(-\pi\zeta/2)]. \quad (6.15)$$

The expression (6.15) has the flat maximum equals  $\frac{1}{2}$  at

$$\zeta = (2/\pi)\ln 2 \approx 0.44, \quad / \quad (6.16)$$

weakly varies at  $\tau(\mathbf{p})/\tau_2 \sim 0.2 \div 0.8$  in an interval about  $\zeta = 0.4 \div 0.44$  and decreases on the order at  $\zeta < 0.1$  and  $\zeta > 3$ . From last condition it follows that the efficiency of the direct MPI should fall down essentially at

$$\hbar\Omega_{\max} \geq 75n^{-4}Z^3 \text{ [eV].} \quad (6.17)$$

Thus, MPIs at big energies should, basically, pass through stages of accumulation of energy, virtually corresponding to HHGs, and the subsequent one-quantum photoeffect. Therefore the spectra of MPIs have the plateau analogically to HHGs processes. Notice that the stabilization of the Rydberg levels at MPI and necessity of transition to heavier atoms for increasing the output of photoelectrons also follows (6.17).

Thus, this factor shows definite reduction of probability of ionization with growth of energy in comparison with probability of HHG. However, speed of this falling off is proportional  $N^{-1}$ , i.e. obviously is slower than at three stages MPI processes: so it can be concluded that the basic role in MP I in the field of low frequencies executes direct liberation of electron that accumulated energy of absorbed photons in atom.

Let's turn to direct calculations of MPPs rates at comparatively lower power. In accordance with (6.6)

$$\sigma_{\text{ion}}/\sigma_{\text{elast}} \approx (2^4/\pi n^3 \alpha^2) (Ry/N\hbar\omega)^{7/2}, \quad (6.18)$$

And therefore the rate of MPP ionization can be written as

$$R_N \equiv \sigma_N j^N \approx \frac{2^5 N \omega}{5\pi n^3 \alpha^2} \left( \frac{Ry}{N\hbar\omega} \right)^{7/2} \frac{1}{N!} \left( \frac{\lambda^2 r_0}{2\pi c} j \right)^N, \quad (6.19)$$

in which under  $N\hbar\omega$  near to the ionization potential  $I$  must be included the Wigner threshold factor  $\sqrt{1 - I/N\hbar\omega}$ .

**Table 1. Logarithm of the generalized cross-sections (6.19) in comparison with the experimental data from [56], pp 101, 109, 110; ( $K = [I/\hbar\omega + 1]$ ,  $I$  is the energy of ionization,  $\hbar\omega$  is the energy of the laser quanta, both in eV's.)**

Atom	I	$\hbar\omega$	K	$-\lg \sigma_{\text{calc}}$	$-\lg \sigma_{\text{experim}}$
Na	5.14	2.34	3	81.1	$80.4 \pm 0.1$
		1.17	5	143.7	$140.1 \pm 1.7;$
K	4.43	2.34	2	48.9	$47.5 \pm 0.8; 49.1 \pm 0.8$
		1.17	4	111.7	$105.6 \pm 1.2; 109.2 \pm 0.8$

Cs	3.89	1.17	4	111.6	108.4±0.2; 109.5±0.2
Ca	6.113	2.34	3	81.2	78.4±0.5
		1.17	6	175.9	172.3±1.5
Ba	5.21	2.34	3	76.7	78.6±0.4
		1.17	5	143.7	140.0±1.0
Sr	5.69	1.17	5	144.0	142.7±1.5
Kr	14.0	4.2	4	115.5	115.1±0.6
Xe	12.13	6.37	2	50.3	49.4; 52.0
		4.2	3	82.7	82.7±0.1
		2.11	6	178.3	170.2±0.6; 169
		1.17	11		336±2.0
		0.62	19	589.5	585

For the direct comparison of (6.19) with the experimental data the averaging of reaction rate is needed: 1) over numbers ( $N - K$ ), since if in the experiment are fixed the numbers of ions, the numbers of photons absorbed above  $K$  is unknown; 2) over principal quantum numbers, since all atomic electrons are virtually free for a short time interval and inner electrons easier grow needed momentum for liberation; 3) over spatial and time distribution of photon flux density, etc.

As the main critical is the dependence on number of absorbed photons  $N$ , the experimental verification of the relation seems interesting:

$$\frac{R_{N+1}}{R_N} = \sqrt{\frac{1 - I/(N+1)\hbar\omega}{1 - I/N\hbar\omega}} N^{5/2} (N + 1)^{-7/2} \quad (6.20)$$

This relation was measured near the threshold at the atoms of Cs ( $N = K = 4$ ) under  $J = 5 \cdot 10^{14}$  W/cm<sup>2</sup> and was founded to be 0.03 [57], which is close to an estimation of (6.20) of order 0.025.

For the direct comparison of (6.19) with the experimental data the averaging of reaction rate is needed: 1) over numbers ( $N - K$ ), since if in the experiment are fixed the numbers of ions, the numbers of photons absorbed above  $K$  is unknown; 2) over principal quantum numbers, since all atomic electrons are virtually free for a short time interval and inner electrons easier grow needed momentum for liberation; 3) over spatial and time distribution of photon flux density, etc.

But if, without all these procedures, it will be proposed for the rough comparison that the subprocess of many photons absorption is the most characteristic one, then we would compare the expression (6.19), in fact the Poisson distribution, with the experimental data of MPP ionization. And this comparison (the Table 1) gives surprising fine results for such approximated estimations, which corroborate our approach and, in particular, the QED spirit for choice of elementary acts parameters: the total cross-section and the time of formation.

The choice of the formation duration can be supported by the analysis of above threshold ionization in a two-color laser field, where usually  $\mathbf{E}(t) = \mathbf{E}_1(\omega) \cos \omega t + \mathbf{E}_2(n\omega) \cos(n\omega t + \phi)$ . Since under N-photon processes the duration time is of order  $\tau_2 \sim 1/N\omega$ , it is evident that photons from both fluxes will be absorbed independently and just such picture is observed in the experiments [58,59] at  $\phi = \pm \pi/2$ , when the electrons can absorb photons from one flux only. Such picture is evidently seen on the Figures of [56] (in these experiments  $J_1 \approx J_2$  and  $n = 2$ ): the peaks  $R_{13}(\omega) \approx R_7(2\omega)$  under such phase difference and it leads to  $J/J_0(\omega) = 1.14$ , which is of the order of used values. At  $\phi = \pi$   $R_7(2\omega) > R_{13}(\omega)$  and at  $\phi = 2\pi$ , inversely,  $R_7(2\omega) < R_{13}(\omega)$ . It can be interpreted by the parity requirements. The absolute rates of such processes can be calculated with account of product  $w_{N'}(\omega) w_{N''}(2\omega)$ , where  $N'$  and  $N''$  are functions of  $t$  and  $\phi$ .

It must be noticed that although from the classical point of view the interference between these two fields leads to frequencies  $\omega/2$ , such peaks were not fixed. More once it says that classical approach to MPPs is impossible.

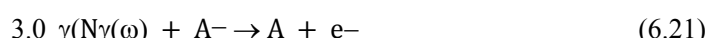
All these results are related to high intensity fields. In weaker fields such interesting events was registered. So, in the early experiments were usually defined so named index of multiphotonics  $K = \delta \ln R_N / \delta \ln J$ , which at first sight can not be bigger than  $N$ . But there were fixed bigger values (e.g. [60]). And really as can be shown at  $j < j_1$   $K = N + J/J_1(1 - J/J_1)$  and shows the possibilities of additional photons reemissions. On the other side, if there is a level, which can be in resonance with some number of absorbed photons, then in the relative weak field  $K$  can be less than  $N$ , since the process of ionization will go from the excited state of atom with lesser ionization potential.

**TABLE 2. Logarithm of the generalized cross-sections of multiphoton detachment from negative ions of halogens and limits of experimental data from [55], p. 61.**

Ion	I	$\hbar\omega$	K	$\lg \sigma_{(\text{theor})}$	$\lg \sigma_{(\text{exp})}$
$F^-$	3,45	2,44	2	- 48,3	- 49,7
		1,22	3	- 80,1	- (81,6 - 82,4),
$Cl^-$	3,61	2,44	2	- 48,1	- (49,7 - 50),
		1,22	4	- 112,1	- (112,1 - 112,5),
$I^-$	3,08	2,44	2	- 48,4	- (48,4 - 48,7),
		1,22	3	- 79,8	- (81,3 - 81,7),
$Br^-$	3,37	1,22	3	- 79,3	- (81,6 - 82),

1.0 MPPs photo detachment of electron from the negative ion

2.0



4.0

5.0 is distinguished from considered above by the interaction in final state. Therefore it can be estimated on the same base: the comparison of calculated and experimental data is given in the Table 2.

Let us consider in some details the unique investigation of (6.21) on the negative ion  $H^-$ , carried on the ion accelerator under continuous shifted photons energy from 0.043 eV till 0.39 eV, e.g. for  $K = 2 \div 5$  under the affinity energy  $E_0 = 0.75$  eV [61].

For the peculiarities of kinematics the probability of photodetachment is equal to zero at the threshold, come up to a slope maximum at  $N_s = \beta K$ ,  $\beta \geq 2$ . Hence the saturation of process arrives at  $j = 1/\sigma_{\text{tot}}(\omega) \tau(N_s \omega)$  and it leads to the expression

$$N = 4\pi c r_0 J / \hbar \omega^3 = 8\pi \bar{W} / \hbar \omega \quad (6.22)$$

where  $\bar{W} = c r_0 J / 2\omega$  is the relativistic invariant photon energy.

In the experiment [59]  $\bar{W} = 0.105$  eV and therefore  $\beta = 3.5$ . The relative peaks probability can be estimated as

$$p_N(N_s) = R_N / \sum R_N \approx (1/N!) N_s^N \exp(-N_s). \quad (6.23)$$

Hence the relative probability  $p_N/p_{N+1} \sim 0.11$ , which does not contradict to the experiment.

## 7. ACCELERATION OF FREE ELECTRONS

Real processes of electrons acceleration can take place within plasma targets and include many different subprocesses (e.g. [62,63]). Their consideration leaves far beyond our tasks, therefore we shall be limited to the elementary cases that demonstrate some features of multiphotonics (cf. [64]).

If on a free electron will fly photons flux  $J_0 = \hbar \omega j_0$ , the electron can keep virtually absorbed single photon during the time  $\tau_1 = 1/\omega$ . After this time the Compton scattering is executed with division of energy and momentum between electron and secondary photon (e.g. [65]).

With rising of the flux intensity some additional photons can be virtually absorbed till executing of the process: it is the multiphoton Compton scattering,

$$n\gamma(\omega) + e_F \rightarrow e_F(mv^2/2) + \gamma(n\omega - mv^2/2), \quad (7.1)$$

with corresponding distribution of final momenta. Thresholds of (7.1) are identical with considered above.

For increase in energy of electrons it is necessary to find a way of transfer the momentum to it. It can be the static Coulomb field  $\mathbf{E}$  in a direction of electrons movement. In such field electron receives momentum  $\Delta p = e\mathbf{E}\Delta t$  and energy  $\Delta E = e\mathbf{E}\Delta s \approx e\mathbf{E}(\Delta p/2m)\Delta t$ . Hence the duration of photons energy accumulation decreases:

$$\tau_n^{(field)} \sim \hbar / (n\hbar\omega + \Delta E) \quad (7.2)$$

and with substitution  $\Delta t \rightarrow \tau_n^{(field)}$  it represents the possibilities for estimation of parameters of acceleration process in a very idealized case of separated free electrons in the Coulomb field.

At higher intensities the relativistic Doppler shift of frequencies of inletting photons must be taken into account, therefore the electron, that holding  $n$  photons, perceives the frequency of subsequent  $(n + 1)$ 's photon as

$$\omega_{n+1} = \omega_0 \sqrt{(1 - \beta_n)/(1 + \beta_n)}, \quad (7.3)$$

where  $\beta_n = vn/c \approx n\hbar k/mc \equiv na$  and  $a = \hbar\omega_0/mc^2$ ; the density of photons flux in the electron self frame is shifted as

$$j_n = j_0 [(1 - \beta_n)^2/(1 + \beta_n^2)]. \quad (7.4)$$

For  $\lambda = 800$  nm and  $\hbar\omega_0 = 1.55$  eV the main parameter  $a = 3 \cdot 10^{-6}$  and consequently for  $\beta \equiv Na \ll 1$  relativistic corrections can be omitted.

The complete energy holding by electron after virtual absorption of  $N$  photons in its own frame is equal to

$$\hbar\Omega_N = \sum_1^N \hbar\omega_n = \hbar\omega_0 \sum_1^N \sqrt{(1 - na)/(1 + na)}. \quad (7.5)$$

With replacement of summation by integration for  $N \gg 1$  and with  $\beta = Na < 1$  we come to the expression:

$$\begin{aligned} \hbar\Omega \rightarrow \hbar\omega_0 \int_1^N \frac{dx}{a} \cdot \sqrt{\frac{1 - xa}{1 + xa}} &= \frac{\hbar\omega_0}{a^2} \Phi(N, a); \\ \Phi(N, a) &= \left[ \sqrt{1 - N^2 a^2} - \sqrt{1 - a^2} + 2 \sin^{-1} \left( (\sqrt{1 + \beta} - \sqrt{1 + a}) / \sqrt{2} \right) \right]. \end{aligned} \quad (7.6)$$

The virtual holding of this energy requires such density of photons flux:

$$j_N \approx 1/\sigma_{tot} N \tau \rightarrow \Omega / \sigma_{tot}, \quad (7.7)$$

where  $\sigma_{tot}$  is the total cross-section (the mass of electron is invariant in its own frame).

The suspension of virtual photons energy accumulation onto single electron becomes possible when the flux density will be less or of the order of (7.7), its possibility of energy keeping. The equaling of these expressions allows an estimation of limiting density of photon flux  $j_0$  in the L-system. Thus the power needed for  $N$  photons accumulation

$$J_0^{(N)} = \hbar\omega_0 j_N = \frac{\hbar\omega_0^3}{4\pi c r_0} f^{(N)}(\beta) \quad (7.8)$$

with

$$f^{(N)}(\beta) = \frac{1+\beta^2}{a^2(1-\beta)^2} \Phi^2(\beta, a). \quad (7.9)$$

At  $\beta \ll 1$

$$f^{(N)}(\beta) \approx \beta^2 / 2a^2 = N^2 / 2$$

and with  $\hbar\omega_0 = 1.55$  eV the needed power can be estimated for the N-photon processes on a free electron as

$$J_0^{(N)} \sim 1.3 \cdot 10^{13} N^2 \text{ [W/cm}^2\text{].} \quad (7.10)$$

It must be underlined that for multiphoton processes on bound electrons the numerical factor in (7.10) can be essentially less, since the duration of virtual energy holding  $\tau_N$  can be sufficiently bigger.

At the taking into account the Doppler shift it should be concluded that the maximal acceleration might be achieved if the laser flux will be directed *oppositely* to the electrical field and electrons flux ( $a \rightarrow -a$  above). It appears as paradox at the first glance, but should be remembered that the electron receives its momentum from the field and only its energy from the laser flux, which therefore does not determine the moving direction of electron. Thus the considered case can be considered as the rising of electron energy during its acceleration in a linear accelerator, etc.

## 8. LIGHT PRESSURE ON MEDIA CONDITIONED BY FEATURES OF PHOTONS KINETICS

One of the perspective applications of high power lasers consists in targets compression for initiation of thermonuclear reactions. Therefore problems of light pressure must be considered more scrupulously.

Examinations of light pressure on transparent media have a centenary history, basically as discussions of so called Abraham-Minkowski controversy (e.g. [66]). Two different determinations of classical energy-momentum tensor of electromagnetic field, by Minkowski and by Abraham, lead to different linear momenta of photons in isotropic transparent media:  $p_M = n\hbar k/n_g$  and  $p_A = \hbar k/n n_g$ , where  $n = c/u$  and  $n_g = c/v$  are the phase and group indices of refraction,  $u = \omega/k$  and  $v = d\omega/dk$  are the phase and group velocities. In accordance with the approach of Minkowski the full momentum is connected to the "photon in medium"; but at the Abraham picture the definite part of this momentum during time of passage is related to the medium. This difference leads to the opposite directions of movement of transparent body at the time of pulse propagation.

This controversy can be presented in the evidently paradoxical form. Let's consider the passage of light flux through a transparent medium with the phase velocity  $u \leq c$ : in accordance with the Maxwell equations, the light momentum in a medium can be bigger than in vacuum and in accordance with the momenta conservation this body should move against a direction of light (Minkowski). But on the other hand such presentation also seems correct: if light is passing through the medium for greater time than in vacuum, the conservation of movement of the center of masses or inertia requires that the body should move in a direction of light flux (Abraham).

Hence this paradox means the necessity of some correction or even a re-examination of light propagation theory.

The experimental data are so inconsistent that the general comparison with them is impossible. So, in the recent experiments of Ketterle group [67] was shown that at reflection by a mirror and at absorption by an atom, a photon in a dispersive medium behaves as though had a momentum of  $n\hbar k$  according to Minkowski. But in the subsequent experiment [68] photons that go out from waveguides lead to the recoil in accordance with the Abraham proposition. These inconsistencies together with discrepancy of former experiments, cited in [67, 68] show that the direct experimental verification of situation is very complicated and intricate; therefore the proper theoretical analysis, with possible revision of established notions and/or outside the scope of macroscopic electrodynamics, seems desirable or even necessary.

It can be suggested that, possibly, the initial implicit representation of transparent media as the un-structured substance, the classical “black box”, is inadequate, i.e. by another words, the description of process via the mean velocities corresponding to the classical Maxwell equations is non-sufficient: the kinetics of light passage through medium must be considered in more details. Really, a photon in media may be a part of time, at least, in virtual state, to which classical description is not applicable; hence quantum peculiarities of light interaction with constituents of medium must be taken into account.

From the microscopic point of view [17] single photon is flying from one scatterer to another with the speed  $c$  on distances of the free path  $\ell = 1/\rho\sigma$  ( $\rho$  is the density of scatterers, free and valent electrons,  $\sigma$  is the cross-section of elastic unbiased scattering). After that it will be detaining on scatterer on the delay time  $\tau_1$ , determined by (2.7) or by a similar expression for more realistic model. If  $\tau_2 > 0$ , to the free path length must be added the distance  $c\tau_2$ , after passing of which photon becomes real, at  $\tau_2 < 0$  it instantaneously jumps over the distance  $c|\tau_2|$ . Thus this photon undergoes  $N = L/(\ell + c|\tau_2|)$  acts of elastic unbiased scattering with delays  $\tau_1$  by each of them, and therefore the complete duration of its transmission at  $\tau_2 > 0$  on the distance  $L \gg \ell$  becomes

$$T = L/c + N\tau_1 \quad (8.1)$$

(for the case of  $\tau_2 < 0$  the substitution  $L \rightarrow L - Nc|\tau_2|$  is needed, but we do not consider this case further).

Such representation leads to the group refraction index for the region of normal dispersion:

$$n_g = cT/L = 1 + c\tau_1/(\ell + c\tau_2). \quad . \quad (8.2)$$

If  $\ell \gg c\tau_2$  this expression can be approximately rewritten, sufficiently far from resonances, as

$$n_g \cong 1 + c\rho\tau_1(\omega)\sigma(\omega). \quad (8.2')$$

These magnitudes allow the estimation of group velocities of photons in transparent media and of corresponding indices of refraction. (Note that, as it was experimentally shown, photon really passes in media with the group velocity [69].)

The phase index of refraction can be determined through the group index as

$$n(\omega) - n_g(0) = \frac{1}{\omega} \int_0^\omega n_g(\omega)d\omega, \quad (8.3)$$

i.e. by its averaging over the frequencies interval  $(0, \omega)$  at assumption  $n_g(0) = 0$  or with a subsequent subtraction.

At the periods of time  $N\tau_1$ , when the photon is virtually captured, its momentum is transmitted into the medium. But if from the Abraham point of view the part of momentum is transmitted into media onto full duration of photon passage, in the offered approach it takes place at saltatory virtual regime. If only these times are taken into account, then such part of linear momentum of photon will be related to body:

$$N\tau_1/T = (n_g - 1)/n_g = 1 - 1/n_g. \quad (8.4)$$

Hence during the time of photon's pass inside the body, it will possess the momentum

$$p = (1 - 1/n_g)\hbar k \cong \hbar k - \Delta(\hbar k) \quad (8.5)$$

directed to the flux under  $n_g > 1$  and oppositely under  $n_g < 1$ . It will lead to the displacement of body onto the distance

$$\delta S = pT/M = \pm N\tau_1 \hbar k / M, \quad (8.6)$$

where  $M$  is the mass of displaced body, and as  $N \sim L(n_g - 1)/c\tau_1$ , the relative displacement of this body at the single photon passage can be expressed as

$$\delta S/L \sim (n_g - 1) \cdot \hbar\omega/Mc^2. \quad (8.7)$$

Into this expression must be included, generally speaking, displacements caused by the surface effects considered below.

This picture, as must be underlined, simultaneously corresponds to both laws of conservations, the linear momenta and the uniform motion of center of inertia. At the same time it allows the consistent determination of indices of refraction describing the average duration of radiation passage through media.

Notice that the additional momentum in (8.5) is curiously connected with the Abraham and Minkowski momenta:

$$\Delta(\hbar k) = \hbar k / n_g = |p_M \cdot p_A|^{1/2}. \quad (8.8)$$

At the real absorption by an isolated scatterer (the Bose condensate in [67] must be considered as a single scatterer) the photons' virtual coat, the evanescent waves (see below), must be absorbed together with the energy-momentum (8.5). Therefore at this act, in accordance with conservation laws,  $\omega^2 = c^2 k^2$ , hence formally  $n_g = 1/n$  and therefore

$$\Delta(\hbar k)^{abs} = n \hbar k, \quad (8.9)$$

i.e. the momentum of body, in accordance with (8.5), will be equal to  $p = (1 - n) \hbar k$ , just as it is describable by the conception of "photons in medium". So the complete momentum of system after absorption is equal to  $\hbar k$ , just as it is needed. Notice that such division corresponds to the Minkowski picture, but just as the Abraham picture described above, it is not universally true: both pictures are correct along the definite and different moments and for parts of the total path of photon.

Thus, at the real absorption of single photon by an isolated scatterer of mass M

$$\hbar\omega = (n \hbar k)^2 / 2M + \Delta U, \quad (8.10)$$

where  $\Delta U$  is the energy of inner reconfiguration of scatterer. The term of absorbed kinetic energy can be expressed via the energy of recoil  $\hbar\Omega$  and with the explicit accentuation of refraction index factor  $\Omega = n^2\Omega'$  it leads to the representation:

$$\hbar\omega = n^2 \hbar\Omega' + \Delta U, \quad (8.10')$$

that conforms to the results of the experiments [67]. Nevertheless, contrary to the conclusions of this article, it does not mean yet that the photon's self-momentum in media is constantly equal to  $n \hbar k$ : such significance appears at the absorption only, by an integration of parameters of photon self-momentum and of corresponded evanescent waves.

The appearance of evanescent waves propagating mutually with a bare photon can be demonstrated in the frame of QED. The concept of "photons in medium" requires the replacement of the momentum on the pseudo-momentum:  $k \rightarrow n(\omega)k$ . This replacement corresponds to the transformation of causal propagator:

$$D_c(\omega, \vec{k}) \sim \delta_+(\omega^2 - c^2 k^2) \longrightarrow D_c(\omega, n(\omega)\vec{k}) \sim \delta_+(\omega^2 - c^2 n^2 k^2). \quad (8.11)$$

Inside the medium, far from borders, it is possible to accept  $n = ck/\omega$ . Then by use the properties of  $\delta$ -function at  $\omega \neq 0$  the propagator in transparent isotropic media can be decomposed as

$$D_c(\omega, n\vec{k}) = \frac{1}{2} \left\{ D_c(\omega, \vec{k}) + D_c(\omega, i\vec{k}) \right\}. \quad (8.12)$$

The first term corresponds to the photon's free flight between scatterers with the vacuum speed  $c$ . The second term of (8.12) describes, accordingly, the field of evanescent waves, caused by photons flight through media; these waves can be attributed to the near field photon's dressing in media:

$$D_c(\omega, i\mathbf{k}) \rightarrow D^{(near)}(\omega, \mathbf{k}).$$

Notice that this term describes the Coulomb field also, in as much as  $\delta(\omega^2 - c^2 k^2) \sim \delta(\omega) \delta(c|k|)$  at  $\omega \rightarrow 0$ .

Evanescence waves are characterized by imaginary momenta. As a contrast to the evanescent waves at the FTIR [19] here all components are imaginary. From the formal point of view the Green function  $D^{(near)}(\omega, \mathbf{k})$  corresponds to the 4-D Laplace equation for space instantons of zero mass (cf. [70]), it demonstrates that corresponding excitations are transmitting instantaneously.

The difference between two terms of (8.12) is more visual in the mixed  $(\omega, \mathbf{r})$  representation:

$$D_c(\omega, \vec{r}) = (1/4\pi r) \exp(i|\omega|r/c); \quad D^{(near)}(\omega, \vec{r}) = (1/4\pi ir) \exp(-|\omega|r/c) \quad (8.13)$$

that obviously shows the space-like character of near field and its fast attenuation, on account of which near field does not contribute in the far field of sources [71]. Notice that these phenomena on such distances do not overflow the uncertainties limits; therefore the observance of conservation laws is not here required.

\* \* \*

Let's turn now to consideration of reflection and refraction and begin with the Fresnel formulae, for the clearness and better comprehension of physical content we do not go

beyond the normal incident onto flat surface (conditions of their applicability are discussed, for example, in [72]).

The transient functions of refraction and reflection processes depend on the phase index of refraction only. Therefore the duration of transmitted or refracted waves' formation can be expressed in the form:

$$\tau^{(o)} = \frac{\partial}{\partial\omega} \ln |S^{(o)}(\omega)| = \frac{\partial}{\partial n} \ln |S^{(o)}(n)| \cdot \frac{dn}{d\omega}, \quad (8.14)$$

where by definition inside isotropic media

$$\frac{dn}{d\omega} = \frac{c}{\omega} \left( \frac{1}{v} - \frac{1}{u} \right) = \frac{n_g - n}{\omega}, \quad (8.15)$$

$v$  and  $u$  are the group and phase velocities correspondingly. Hence the sign and the value of  $\tau^{(o)}$  depend on discrepancy between them, (8.15) is positive for regions of normal dispersion.

At crossing of boundary between media this function can be formally represented as

$$\frac{dn}{d\omega} = \lim_{\delta \rightarrow 0} \frac{d}{d\omega} (n_1(\omega, x + \delta) - n_2(\omega, x - \delta)) \xrightarrow{\sim} \frac{1}{\omega} ((n_{g1} - n_{g2}) - (n_1 - n_2)), \quad (8.16)$$

really, of course, this transition must be more smoothing (e.g [20]). If the medium is bordered with vacuum, one of  $n$ 's is equal to 1 and we come back to (8.15), sign of which depends on direction of ray.

Let's begin with the consideration of reflection. The relative amplitude of reflection  $|S^{(R)}| = |(n - 1)/(n + 1)|$  leads to the duration of reflecting wave formation:

$$\tau_2^{(R)} = -2(n^2 - 1)^{-1} (dn/d\omega)^{(R)}. \quad (8.16')$$

As photons are twice transmitted through the transient zone,  $(dn/d\omega)^{(R)} = 2dn_1/d\omega$  and is positive. The negativity of (8.16') means that the emission of reflected photons is instantaneous and just therefore they remain coherent with the initial flux (phase is changed on  $\pi$  and so on).

The force acting on reflecting medium,

$$F^{(R)} = \frac{2\hbar\omega}{\tau_2^{(R)}} = \frac{\hbar\omega^2}{2c} \cdot \frac{n^2 - 1}{n - n_g}, \quad (8.17)$$

leads to appearance of perturbation or recoil wave directing into the medium and inducing its temporary polarization. Such processes would induce the cooling of transient layer (the

possibility of cooling by wave reflection, as far as I know, never was observed, its searching could be used for direct measuring of duration of formation).

Notice that in the addition to this recoil photon, an acoustic wave into a medium can appear (a polarization wave, cf. [73]), the direct usage of energy-time uncertainty relation and conservation laws can present difficulties and therefore at an initial analysis may be avoided. However, elastic reflection leads to appearing of momentum of reflecting media, i.e. to appearing of its kinetic energy, therefore the source of this energy must be examined.

Let's proceed to the phenomena on refraction surfaces.

For wave incoming from vacuum  $|S^{(T,in)}| = 2/(n+1)$ , hence

$$\tau^{(T,in)} = -(n+1)^{-1} (dn/d\omega)^{(T,in)}, \quad (8.18)$$

which is negative for the case of normal dispersion. For out-going wave  $|S^{(T,out)}| = 2n/(n+1)$  the duration of disguising of photons that exiting medium becomes

$$\tau^{(T,out)} = n^{-1}(n+1)^{-1} (dn/d\omega)^{(T,out)}, \quad (8.19)$$

but as  $dn/d\omega$  changes sign at transition from (8.18) to (8.19), the signs of durations coincide.

The nonzero duration of wave formations must lead to appearance of inversely oriented optical transient zones on both surfaces of body (cf. [19]):

$$\Delta x^{(in,out)} = c\tau^{(T,in,out)}. \quad (8.20)$$

Another connected phenomenon is the occurrence of forces of light pressure on surfaces, differing for in- and out-surfaces with taking into account the altering of momenta:

$$F^{(in)} = (1-n)\hbar\omega/c\tau^{(in)}, \quad F^{(out)} = -F^{(in)}. \quad (8.21)$$

Thus in both cases the pressure is directed into the media, squeezing it. It just corresponds to results of the experiment [68].

\* \* \*

Thus the researches of dispersion phenomena necessitate more profound consideration of light interaction with substance even the transparent one: they show inapplicability of concepts of macroscopic electrodynamics to theory of dispersion [17]. The appeal to more deep concepts of quantum electrodynamics with usages of temporal functions allows the description of kinetics of photons propagation and determination of light pressure with simultaneous feasibility of all conservation laws.

The continue discussions of Abraham-Minkowski controversy on the base of classical energy-momenta tensors have not direct physical sense: neither the Abraham momentum nor the Minkowski momentum is conservable. Both expressions are wrongful as general ones and

new researches must be basing on microscopic considerations or correspond to them (the problem of correct form of macroscopic energy-momenta tensor remains open).

The most interesting and new in these considerations seems such result: processes of photons dressing or their redress on borders of media lead to formation of oppositely oriented effective transient zones on boundaries. They represent double electric layers, dipoles or other moments of which absorb falling waves and emit new ones, reflected or refracted. Some other processes of reflection can be considered on an analogical base. So, it can be noted that the mirror reflection by metal surfaces requires a more scrupulous consideration of photon interaction with the group of scatterers: this process takes place in the depth of skin-layer  $\delta \approx \sqrt{2c^2/\omega_2^2}$  and  $\text{Re } \delta = \text{Im } \delta$  [74]. The time delays at scattering and the duration of outlet photon formation are equal; therefore such process does not destroy the coherence of reflected light flux.

The inside directed surface pressure by the incident light may be useful for precise designing of the laser-induced inertial-confined fusion. It must be taken into account at consideration of certain astrophysical problems also.

It must be underlined that the used approach is of probabilistic type and more scrupulously it would be described as the Poisson process. Therefore the outgoing pulse must be represented as the Poisson comb, i.e. by its envelope with some inevitable smearing of initial pulse. The probability of  $N$  scattering acts on the distance  $L$ , if  $N$  is sufficiently big, are describable, in general, by the Gauss distribution of magnitude  $N\ell/L$ . Hence there is a finite probability of appearance of "precursors", i.e. photon passing through media without scattering, with only one scattering and so on. It can lead to observation of signal passing with the vacuum speed  $c$  through sufficiently thin medium. Probably, just such observation is described in [75], at which one bit of information was transferred with the speed  $c \gg v$  through the thin layer of resonant slow-light medium. However, it does not mean the possibility of introduction of the signal or information velocity  $v_i \sim c$ : the conditions of this experiment, the low optical thickness of intermediate layer, is too restricted for such wide generalization; the increasing of this thickness inevitably would lead to such attenuation of signal that will do it non-measurable. Such description of precursors seems more adequate in quantum theory than the classical ones, which present the existence of precursors via unavoidable presence of high frequencies in the abrupt front of pulses [76] (last experiments [77]).

All above was considered at the condition of comparatively big free path length,  $\ell \gg c|\tau_2|$ . What can be expected at sizeable decreasing of  $\ell$ ? In the Anderson theory of localization [78] a possibility of such interference and self-interference picture was predicted, when photons will be, at least, delaying in substance. For the effect of localization is known the empirical Joffe - Regel criterion:  $\ell k \sim 1$ . Just this phenomenon was observed in [79] (therein are given references on preceding investigations). In the scope of offered approach the phenomenon of Anderson's localization can be considered on a slightly another base. So, if  $\ell \ll c|\tau_2|$  the photon will undergo repeating interaction acts without completion of its physical formation between them that must delay its exit out of medium. The criterion of delay is determined [23] as  $\Delta\omega\tau_2 = \pi$ , which can be rewritten with  $\Delta\omega \rightarrow ck$  and

$c|\tau_2| \rightarrow \ell k \sim \pi$ . Notice that this condition is nearer to the experimental results [19] than the Joffe - Regel criterion.

## 9. THRESHOLDS OF LIGHT REFLECTION

Let's consider some features of occurrence of specular reflection at metal surface. We assume that each act of reflection is the collective effect of the group of M scatterers. The depth of skin-layer in substance with dielectric susceptibility  $\varepsilon(\omega) = \varepsilon_1 + i\varepsilon_2$  is equal  $\delta = \sqrt{2c^2/\omega^2\varepsilon_2(\omega)}$  by the definition, at complex description  $\text{Re}\delta = \text{Im}\delta$  and therefore the delay at scattering coincides with the duration of formation of reflected signal. The duration of reflection process (absorption of ingoing photon and formation of outgoing) can be determined as

$$\tau_{refl} = \frac{2\delta}{v} = \sqrt{2^3\varepsilon_1(\omega)/\omega^2\varepsilon_2(\omega)}, \quad (9.1)$$

where  $v = c/\sqrt{\varepsilon_1}$  is the light velocity in reflecting layer of metal. Here must be underlined that in (9.1) contains the relation  $(\varepsilon_1/\varepsilon_2)$ , i.e. resonance denominators are cancelled and  $\tau_{refl}$  is sufficiently flat function (absence of sharp maxis of reflection is natural for metals).

The size of scatterers group M can be determined via comparison of thresholds of MPP at reflection estimated by different methods.

Let's consider an area  $S$  of skin-layer of depth  $\delta$ , on which the flux  $j$  falls. As the duration of interaction of each photon is equal  $\tau_{refl}$ , in this volume simultaneously can be  $m = jS\tau$  quanta and  $m_{max} = j_0S\tau$ . On the other hand maximal number of independently reflected photons must be equal to number of reflecting groups in the volume  $S\delta$ ; i.e.  $m_{max} = NS\delta/M$ . The equating of both relations leads to an estimation:

$$j_0 \approx N\delta/M\tau. \quad (9.2)$$

In the Drude model all outer electrons in metal can be considered as free ones. Therefore the amplitude of scattering on the group close to saturation is M-fold bigger than the amplitude of scattering on single electron  $r_0$ , i.e. the cross-section on such group  $\sigma_M = M^2\sigma_T$ . Thus the threshold density of reflecting photon flux

$$j_0 \approx c/\sigma_M v\tau. \quad (9.3)$$

Equating of these expressions leads to an estimation:

$$M = \frac{c}{N\delta\sigma_T v} \approx \frac{3\lambda}{4r_0} \cdot \frac{\varepsilon_1(\omega)}{\varepsilon_2(\omega)}, \quad (9.4)$$

where  $N$  is the number of dispersive electrons and approximately

$$N = \int_0^\infty f(\omega) d\omega = \int \frac{f(\omega)}{\tau} \tau d\omega \approx \frac{f(\omega)}{\tau}$$

as for coherent interactions  $\tau d\omega \sim 1$  in analogy with  $\Delta\omega \cdot \Delta t \sim 1$ .

Let's consider the flux  $j$ , part of which is entering into rays tube, i.e. into the cylinder of diameter  $\lambda$ . If on this area is a heterogeneity, the silver grain, for example, with  $M$  dispersive electrons, it quasi-resonantly interacts with this part of flux and the threshold of nonlinear processes goes down:

$$j_0^{(eff)} = \frac{\sigma_M}{\pi\lambda^2/4} j_0 = 6 \left( \frac{\varepsilon_1(\omega)}{\varepsilon_2(\omega)} \right)^2 j_0. \quad (9.5)$$

Hence the presence of grains of definite sizes on reflecting surface can lower threshold of nonlinear processes in  $(\varepsilon_1/\varepsilon_2)^2$ -fold. It is the gigantic effect of harmonics generation (e.g. [80]).

Considered mechanism can explain also the known Wood effect: transition from diffuse reflection to mirror one with growing of density of mercury gas [81] (further investigations are reviewed e.g. in [82]).

For this purpose the density of atoms-scatterers  $N_1$  with  $\lambda^3 = M$  needed for beginning of mirror reflectance must be estimated. As mercury in considered case can be represented as an ideal gas, this density is determined via pressure as  $N_1 = p/\kappa T$  and therefore

$$p_{crit} = \frac{3}{4} \cdot \frac{\kappa T}{\lambda^2 r_0} \cdot \frac{\varepsilon_1(\omega)}{\varepsilon_2(\omega)}, \quad / \quad (9.6)$$

This expression is in a qualitative conformity with the Fermi calculations [83].

It can be noted that the generation of higher harmonics must be sharply increased at approach to thresholds of selective reflection. As far as I know, such effect was not experimentally examined.

## CONCLUSIONS

Let us enumerate examined problems and the main results.

1. Microscopic consideration of lasers and, more generally, of interactions of intensive radiation flux with matter requires the examination of QED processes with  $N$  incident photons ( $N \geq 2$ ) in the initial state. With this aim the clarification of transition to the infinite volume of field quantization is executed. The refined procedure leads to appearance of dependence of reaction rate on densities of photons fluxes  $j(\omega)$  [quant/cm<sup>2</sup>s].

2. Calculations of MPPs naturally lead to appearing of the time durations of elementary processes which, as all primary physical magnitudes, must be initially contained in the QED and their ad hoc introduction is not needed.
3. Calculation of MPP rates in laser fields leads to the "virial" series over  $(j/j_0)$ . Characteristic photon flux density is presented as  $j_0 = 1/\sigma(\omega)\tau(\omega)$ , where  $\sigma(\omega)$  and  $\tau(\omega)$  are the cross-section and time duration of elementary act of elastic e- $\gamma$  scattering.
4. Reaction rates are characterized by the irremovable pole at  $j = j_0$ . This pole corresponds to saturating of considered process and/or to opening of new channel of interactions and can be naturally interpreted via magnitudes of durations and cross-sections of scattering.
5. The HHGs can be interpreted via virtual absorption of many quanta during the time of keeping of their total energy by bound or free electron in accordance with the uncertainty principles. The emission of all this energy by one photon is the most probable. The HHG on bound electron can completely be executed in the scope of the same atom.
6. The reaction rates of HHGs are expressed via the binomial distribution that leads under big  $N$  to the plateau in HHG spectra far from both their tails.
7. The MPI process is complicated by the accumulation of momentum of liberated electron corresponding to energy of virtually absorbed quanta. The computation of this process is executed by the Landau theory of predissociation that leads to revealing of time duration of momentum accumulation. The reaction rate depends on conformity of both durations.
8. Acceleration of charged particles by laser field is also describable by two mutual subprocesses: the accumulation of energy by virtual absorption of photons of laser flux and an acquisition of corresponding momentum via interaction with ions of plasma and/or by external electric field. Last case is considered in some details.
9. The QED consideration of radiation pressure on transparent objects can resolve the very old Abraham-Minkowsky paradox and gives correct expressions for several cases. This problem can be valuable at consideration of laser induced thermonuclear reactions.
10. As the offered approach is based onto the theory of temporal functions, the demonstration of their significance seems desirable. With these aims in the Appendix their application to general structure of condensed states and to several kinetic processes, mostly well known, are examined. This consideration demonstrates the possibilities that can lead to new understanding of some old problems.

## ACKNOWLEDGMENTS

Problems considered in this article had been studied during long times and had been discussed, at different directions, with many colleagues. The most valuable comments were expressed by N. B. Delone, G. Mainfray, V. A. Kovarsky, S. G. Matinyan, E. Pollak, I. Royzen, M. Ya. Amusia and, constantly, by G. M. Rubinstein. I am deeply indebted to them.

## APPENDIX: QUANTUM KINETICS OF CONDENSED STATES: ROLE OF DURATIONS OF ELEMENTARY PROCESSES

### A-1. Overview

The most interactions between atoms/molecules in condensed substances can be considered as exchanging of virtual photons within the near field of constituents charges. Therefore durations of interaction and "dressing" of particles, considered above, are the main determinative that lead to definition of effective volume of such interaction  $V$  expressed through the total cross-section of (low frequencies) scattering  $\sigma_{tot} \sim 1/\omega$  of virtual photons and duration of this interaction  $\tau_2 \sim 1/\omega$ , i.e.  $V_\gamma \approx c\tau\sigma_{tot} \sim 1/\omega^2$ . Hence radii of electronic correlations  $R_\gamma \sim \omega^{-2/3}$ ; they determine a set of critical indices under phase transitions, lead to somewhat précised form of the Landau-Ginzburg theory of phase transitions and so on.

Offered approach, just as in the case of multiphoton processes, allows estimation of saturations of interactions and determining thresholds of new channels opening for certain processes. Therefore several expressions can be deduced for transition points of dielectric and magnetic susceptibilities of different media, electrical conductivity including superconductivity and Anderson transitions, heat conductivity, certain limit significances of physical parameters and so on. The offered theory allows also the consideration of Bose-Einstein condensate of rarified gases via virtual photons exchange between atoms.

It should be noted that although all interactions between components of such states are electromagnetic ones, however the direct use of QED concepts, just as for the theory of MPPs, is usually presented a priori impossible or inconvenient and with excessive complication. Here we try to demonstrate possibilities and perspectives of the QED approach to certain more or less known problems. The general aim of QED should consist in describing of all phenomena, except nuclear and gravitational ones, by the photons exchange and influence of static fields. At application to definition of condensed states this program can be expressed in such form:

*The stationary state can be called the condensed formation, if each part of an unrestricted, in principle, isotropic set of its constituents has lesser mass than in free or isolated states, i.e. at sufficiently far distance between them.*

Such definition means the consideration of mass defect as the negative binding energy. The lesser value of mass can be interpreted, on the quantum language, dynamically: these particles are in the processes of "development" into separate physical particles, are at the formation status. Therefore they are inter-connected by virtual field quanta of near field that are also in the status of formation. Differently, the virtual "coat" of individual particles is not completed or such "dressing" is integrated for a set of constituents and therefore the virtual dressing of each particle is not required, as though particles lost self-individuality or identification.

For demonstration of the offered program we shall use basic determinations and features of near field and temporal functions describing processes of formation (dressing) of particles and states given in the Section 2. The most needed for us is the simplest case of two-level systems:

$$\tau(\omega) = 1/(i(\omega - \omega_0) + \Gamma/2), \quad (\text{A.1.1})$$

After averaging over the Boltzmann distribution it leads to the usable expression:

$$\bar{\tau}_2(\omega) = \frac{\omega_0}{(\omega - \omega_0)^2 + \Gamma^2/4}, \quad (\text{A.1.2})$$

with  $\bar{\tau}_2(\omega) \gg \bar{\tau}_1(\omega)$ .

In a majority of cases below will be enough the simplest forms:

$$\bar{\tau}_2(\omega) \sim 1/\omega_0, \quad (\text{A.1.3})$$

the magnitude (A.1.3) will be only used for examination of problems of dressing, index and average sign will be omitted.

The general consideration of these notions is given in the Subsection A.2 [16]. In the Subsection A.3 they are expressed in more precise forms for different types of interactions, [20], which allow determination of radii of correlations for these interaction types at comparing of their relative values.

In the Subsections A.4 and A.5 certain well known expressions of different branches of solid state physics (cf. [84]) are expressed via temporal functions and corresponding radii of correlations and thresholds. Such way of their derivation demonstrates possibilities of method and can lead to some new interpretations of known phenomena.

The phenomenon of Bose-Einstein condensation (BEC) in rarefied atomic gases [85] is separately examined in the Section 6. The QED approach to this phenomenon can be connected to our general assumption of impossibility of existence of links without an exchange of excitations, of virtual photons [18].

All these results and certain further perspectives are summed in the concluding section of the Appendix.

## A-2. General consideration

Let us examine the peculiarity of (virtual) photons exchange (we follow [20]). The mean free flight path of photons is determined by the total cross-section of e- $\gamma$  interactions and the density of scatterers (outer electrons) as  $\ell = 1/\sigma_{tot}N$ . The total cross-section is determined by the optical theorem of scattering theory as

$$\sigma_{tot}(\omega) = (4\pi c/\omega) \cdot \text{Im}A(0), \quad (\text{A.2.1})$$

$A(0)$  is the amplitude of elastic scattering on the zero angle. For low frequencies, interesting for our consideration in the most cases, can be taken that  $\text{Im}A(0) = r_0$  with  $r_0 = e^2/mc^2$ , the classical radius of electron.

Interchanging photons will be in a formation stage if

$$\tau_2 \geq \ell/c. \quad (\text{A.2.2})$$

and this condition is the basic one for the offered theory, exactly corresponds (2.14), etc. (Some other deductions of this main physical notion will be given below.)

The definition (A.2.2) leads to the basic inequality corresponding to the proposed definition of condensed state:

$$c\tau\sigma_{\text{tot}}N \equiv V \cdot N \geq 1, \quad (\text{A.2.3})$$

where  $V(\omega)$  may be named "the effective volume of electromagnetic (EM) interactions on the frequency  $\omega$ " or, more shortly, "the volume of interaction".

From the definition (A.2.3) the effective radius of EM correlations (the length of EM interactions) on frequency  $\omega$  follows:

$$R(\omega) = (3c\tau\sigma_{\text{tot}}/4\pi)^{1/3}, \quad (\text{A.2.4})$$

and conditions for saturation of interactions on this frequency as

$$V(\omega) \cdot N = 1 \quad \text{or} \quad \sum_k V_k(\omega) \cdot N_k = 1 \quad (\text{A.2.5})$$

as several types of interactions are possible. (We do not take here into account the space-time dependencies and anisotropy of states, polarization effects, etc.)

The induction of external influence in medium can be defined as

$$F = \sum_1^\infty (VN)^n I = \frac{VN}{1 - VN} I \equiv \chi I, \quad (\text{A.2.6})$$

$\chi(\omega)$  is the generalized susceptibility of medium. Therefore the conditions of phase transitions can be determined as singularities of  $\chi(\omega)$  and/or as situations when  $R(\omega) \rightarrow \infty$  at definite frequency.

As  $\tau, \sigma$  and, more generally,  $N$  are functions of the frequency  $\omega$ , the natural question arises: which frequency must be inserted into (A.2.1)? It can not be, of course, frequencies, connected with the heat radiation that corresponds to kinetic energy of particles. As this frequency is the representative of the (negative) potential energy, it must be connected with latent heat, energy of atomization and so on.

By a very surprising manner the volume of interaction for single electron  $V_e$  can be defined as the volume within which the mass of electron (the complete mass of free physical particle) is assembled in the averaged result of pure Coulomb interaction:

$$mc^2 = \frac{1}{V_e} \int d\mathbf{r} \frac{e^2}{r} e^{-k^2 r^2/2} = 4\pi \frac{e^2}{k^2 V_e} \equiv \phi(k)/V_e, \quad (\text{A.2.7})$$

where  $\phi(k) = 4\pi/k^2$  is the Coulomb potential (choice of the averaging procedure is not very critical, the density of averaging  $f(\mathbf{k}, \mathbf{r})$  must be chosen so that  $\int d\mathbf{r} \cdot r^{-1} f(\mathbf{k}, \mathbf{r}) \sim k^{-2}$  only). This relation undoubtedly shows that the volume included in it corresponds to such physical interpretation:

$$V_e = 4\pi e^2 / k^2 mc^2 \equiv \sigma_{\text{tot}} c \tau, \quad (\text{A.2.8})$$

+

where  $\text{Im } A(0) = r_0 = e^2/mc^2$  is substituted and  $\tau = 1/\omega$  is the duration of physical particle formation at this frequencies range (A.1.3) (the uncertainty principles interpretation of this factor is not excluded).

The expression (A.2.8) can be also calculated for electrons in EM fields via the factor expressing the absorbed energy  $W$  of density of electromagnetic flux  $J(\omega) = (c/4\pi)|\mathbf{E}|^2$  penetrating into the volume:

$$W = (J/c)V_e. \quad (\text{A.2.9})$$

Let's assume that the electron is absorbing this energy as one quantum:  $W = \hbar\omega$ . For its keeping an accumulation of momentum  $\Delta p = \sqrt{2mW}$  from surrounding particles or fields at the course of the time duration  $\Delta t \leq 1/2\omega$  is needed. Substitution of these magnitudes in (A.2.9) with taking into account the Second Law,  $\Delta\mathbf{p}/\Delta t \rightarrow e\mathbf{E}$ , leads just to the expression (A.2.8). (It must be emphasized that  $W \sim J/\omega^2$  is the relativistic invariant.)

The expression (A.2.8) leads to the radius of bonds (or correlations) as

$$R = (3V_e/4\pi)^{1/3} = (3c^2 r_0)^{1/3} \omega^{-2/3} = 0.28 \cdot 10^{-4} \lambda^{2/3} [\text{cm}]. \quad (\text{A.2.10})$$

For usual distances  $R \sim 10^{-7}$  cm between atoms/molecules in condensed state the relation (A.2.10) leads to  $\lambda \sim 2$  mcm, of a right order of magnitude for interatomic bonds.

In processes of photons exchanging between particles with magnetic moment  $\mu$  and under exchanging between spherical rotators with dipole moment  $\mathbf{d}$  and moment of inertia  $I$  the corresponding amplitudes are:

$$A_m = \frac{4\mu^2 \omega}{\hbar c^2}; \quad A_d = \frac{4\omega^2 d^2}{c^2} \frac{I}{|\hbar^2 - \omega^2 I^2|}. \quad (\text{A.2.11})$$

For the first estimations can be taken that  $|\mu| \sim e\hbar/2mc$ ,  $I \sim \hbar^2/mc^2$  and  $\omega d \sim ev$ , then

$$A_m \sim A_d \sim r_0(v/c)^2 \quad (\text{A.2.11}')$$

and therefore the effective volume for these interactions remains equal to (A.2.8). It can be even assumed that these more weak interactions would lead to phase transitions of the second kind, etc.

A slightly another interpretation of the interaction volume can be represented via the energy of black body radiation  $P(\omega, T)$  filling up the volume of interaction:

$$E_T = \int_0^\infty d\omega V_e(\omega) P(\omega, T) = \frac{2\pi}{3} r_0 \frac{\hbar}{c} \left( \frac{\hbar}{kT} \right)^2. \quad (\text{A.2.12})$$

The expression (A.2.12) can be rewritten via the ratio of durations:

$$E_T/kT = \left( \frac{2\pi}{3} \right) \tau_{\text{class}}/\tau_T, \quad (\text{A.2.13})$$

where  $\tau_{\text{class}} = r_0/c$  and  $\tau_T = \hbar/kT$ . It can be considered, in particular, as proportionality of the magnitudes of action:  $E_T \cdot \tau_T \sim kT \cdot \tau_{\text{class}}$ .

Note that the order and the sense of  $V$  can be noted also by such simple estimation. For hydrogen and hydrogen-like atoms the binding energy  $E = e^2/a_B$ , where  $a_B = \hbar^2/me^2$  is the Bohr radius, and the transition frequency  $\omega_B = E/\hbar$ . These values lead to a limiting estimation:  $V_e \simeq 4\pi a_B^3$ , i.e. the mean interaction volume is of the order of the Bohr volume.

It may be noticed that the strange, at first glance, dependence:  $V_e \sim k^{-2}$  and therefore the proportionality  $V_e \sim R^2$  could be foreseen by the well-known dependence of the Fermi energy:  $E_F \sim (N/V)^{2/3} \sim R^{-2}$ .

### A-3. Radii of thermal and field correlations

The mole latent energy of phase transitions is determined as  $\Delta = T(S_2 - S_1)$ , where  $S_k$  is the entropy of  $k$  phase. If at approach to the critical temperature  $T_c$  this difference smoothly aspires to zero, the latent energy per atom/molecule can be presented as

$$W = T\Delta S/N_A = T(\partial S/\partial T)(T_c - T) \rightarrow T_c^2(\partial S/\partial T)_{T=T_c} \cdot \Delta, \quad (\text{A.3.1})$$

where  $\Delta = (T_c - T)/T_c \geq 0$ .

Let's suppose that this energy plays the role of  $n$  quanta (of equal frequencies, for simplicity) that execute connections in (A.2.8) as  $\hbar\omega \rightarrow W/n$ . This assumption leads to such expression of the volume of interaction:

$$V(W/n) = V'\Delta^{-2}, \quad (\text{A.3.2})$$

$V' \approx \text{const}$ , and to the radius of virtual photon's correlations:

$$R_c(T) = (3V/4\pi)^{1/3} = R_0\Delta^{-2/3}. \quad (\text{A.3.3})$$

. For the phase transitions of second kinds the thermal energy of a single atom may be determined close to the critical temperature as

$$W = \frac{1}{N_A} \int_T^{T_c} C dT \approx (CT_c/N_A)\Delta,$$

i.e. it leads to the similar form of expressions for the radius of correlations.

Similar quantities may be determined for some other types of interactions. So for the electrical and magnetic dipole interactions, correspondingly,  $\hbar\omega \rightarrow \mathbf{dE}$  and  $\hbar\omega \rightarrow \mu\mathbf{H}$ . It naturally leads to the radii of correlations:

$$R_{c,d} = R_{0,d}(\mathbf{dE})^{-2/3}; \quad R_{c,m} = R_{0,m}(\mu\mathbf{H})^{-2/3}. \quad (\text{A.3.4})$$

If there is such medium, where the main role plays the exchange of electrons (polymer molecules?), the corresponding matrix element and correlation radius will be of the form:

$$A_{ee} = e^2/mv^2 \rightarrow e^2/3kT; \quad R_{c,T} = R_{0,T}T^{-2/3}. \quad (\text{A.3.5})$$

Thus, in all these cases the critical index of correlations is of the universal type:

$$R \sim \Delta^{-v}, \quad v = 2/3 \quad (\text{A.3.6})$$

- the conclusion, which supports, in the scope of offered theory, the known hypothesis of transitions similarity. This result predetermines the estimations of other critical indices [20].

The definition of volume of interaction allows estimating of some other physical quantities. So, for example, the maximal temperature, when the existence of chemical bonds is still possible, can be estimated.

Let's define for this aim the e-e interaction volume averaged over the Maxwell distribution that implies the substitution  $\hbar/p \rightarrow \hbar/\sqrt{2\pi m k T}$  and therefore the volume of interaction, written with taking into account (A.3.5), can be expressed as

$$V = 4\pi(\hbar/p)^2 A_{ee} \rightarrow \langle V \rangle_T = (2/3)r_0(c\tau_T)^2. \quad (\text{A.3.7})$$

It shows that the electron exchange interactions at distances  $R > 10^{-8}$  cm are possible when  $T_{max} < 10^4$  K only. (Note that on this base can be determined the maximal temperature for  $\mu$ -mesoatoms interactions also, etc.) Such estimations should be more probable than the usual ones of type  $\kappa T_m \sim \Lambda/N_A$ , where  $\Lambda$  is the mole energy of atomization.

The condition  $\ell \leq R_c$ , natural for the offered approach, can be rewritten as

$$\hbar\omega_{max} \leq \hbar c [3(4\pi)^3 N^3 r_0^4]^{1/5}, \quad (\text{A.3.8})$$

which for medium density  $N=10^{21}\div 10^{24}$  particles/cm<sup>3</sup> leads to the bond energy of order 0.04÷2.6 eV or to the maximal latent heat  $\Lambda = N_A \hbar\omega_{max} \sim 3.7 \div 230$  kJ/mole.

These estimations seem rough ones, but not contradictory.

The limit case of narrow cooperation should be noted when  $V_\gamma \rightarrow \infty$ , but  $N/V_\gamma$  remains non-zero. In such case  $r_0 \rightarrow r_0(N/V_\gamma)$  and therefore

$$R_0^{\text{narrow}} = (2\pi r_0 N)^{1/6} (c/\omega)^{1/3}, \quad (\text{A.3.9})$$

i.e. the index is twice lesser than nearby of usual critical points. It means that the corresponding index can vary, in general, between 2/3 and 1/3.

It is necessary to underline that determination of the radius of correlations allows the expanding of density of thermodynamic potentials over the order parameter as

$$\Omega = \Omega_0 + (\alpha/R_0^2)\varphi^2 + b\varphi^4 + g(\partial\varphi/\partial r)^2 - 2\varphi h, \quad (\text{A.3.10})$$

where as distinguished from the famous Landau theory the expansion goes not over the artificial parameter  $\Delta = (T_c - T)/T_c$ , but over physically founded magnitude  $R_0^{-1} \sim \Delta^{2/3}$ .

From the definition (A.2.9) follows that  $(\Omega - \Omega_0) \sim V_0 \sim \Delta^2$  and therefore

$$\varphi \sim \varphi_0 \Delta^\beta, \quad \beta = 1/3. \quad (\text{A.3.11})$$

This approach leads to certain refinements of the Ginsburg-Landau theory; they are in more details described in our article [20] and therefore are here omitted.

#### A-4. Some applications: electromagnetic properties

In the accordance with (A.2.11), (A.2.8), (A.2.12) and (A.3.5) such expressions for volumes of different interaction types can be represented:

$$\begin{aligned}
 V_\gamma &= 4\pi e^2/m\omega^2; \\
 V_m &= 16\pi\mu/\hbar\omega; \\
 V_d &= 16\pi d^2 I/3|\hbar^2 - \omega^2 I^2|; \\
 V_e &= 4\pi c^2 e^2/mv^2\omega^2 \rightarrow 4\pi c^2 e^2/3\omega^2\kappa T.
 \end{aligned} \tag{A.4.1}$$

These magnitudes lead to the dimension-less parameters

$$X_k = V_k N_k \quad (k = \gamma, m, d, e), \tag{A.4.2}$$

where  $N_k$  is the density of corresponding particles or complexes. It means that such quantities as susceptibilities and some other characteristics of media must be expressed via (A.4.2), and the equality  $X_k = 1$  should signify the singularity of considered quantity.

We shall illustrate these propositions by some more or less evident examples.

### A-4-1. Dielectric susceptibility

Dielectric susceptibility of rarefied plasma on high frequencies can be represented as

$$\epsilon(\omega) = 1 - 4\pi e^2 N_e / m\omega^2 \equiv 1 - \omega_p^2 / \omega^2 \rightarrow 1 - V_\gamma N_e. \tag{A.4.3}$$

This conformance leads to a macroscopic definition of the volume of interaction:

$$V_\gamma = -\partial\epsilon / \partial N_e. \tag{A.4.4}$$

In the more general case, when the multiple interaction acts are possible, the induction (in isotropic linear media) must be written as

$$D = \sum_0^\infty (V_\gamma N_e)^n \equiv \epsilon E; \quad \epsilon(\omega) = 1 + \omega_p^2 / (\omega_p^2 - \omega^2). \tag{A.4.3'}$$

These expressions can be easily generalized on more complex cases. So, for crystals in the Drude - Kronig theory of free charge carriers the effective electron mass  $m^*$  and the damping caused by frequent electron-lattice collisions  $\varpi$  must be taken into account. Therefore

$$\tau = \frac{\omega}{\omega^2 + \varpi^2}; \quad V_\gamma = c\sigma\tau = \frac{4\pi e^2}{m^*} \cdot \frac{1}{\omega^2 + \varpi^2},$$

from which the known expression for  $\epsilon(\omega)$  follows, where the density of oscillators  $N$  can be taken into account.

Molecule with the constant dipole moment  $d$  can be considered as the spherical rotator. If its moment of inertia is  $I$ , the amplitude of forward scattering  $A_d \sim d^2/Ic^2$ . In the static case  $I\omega^2 \rightarrow 3\kappa T$  and therefore

$$\varepsilon_{st} - \varepsilon_\infty = 4\pi d^2 / 3\kappa T \quad (\text{A.4.5})$$

For the dielectric analysis can be used the following form of partial contribution of molecules of either type into the dielectric susceptibility:

$$\Delta\varepsilon_q = \sum_1^\infty X_q^n = 4\pi d^2 I / (I\omega^2 - 4\pi d^2 N). \quad (\text{A.4.6})$$

Addition of  $n$  links leads to change of the moment of inertia  $I \rightarrow nI$  and to the variation of resonance frequency  $\omega \rightarrow \omega/\sqrt{n}$ , which allows an estimation of the degree of polymerization.

The formulae (A.4.3) - (A.4.6) are related to sufficiently rarefacted media, to systems of non-interacted dipoles. The account of their interactions leads to the usual Lorentz factor.

#### A-4-2. Debye radius of screening

Debye's radius of screening determines the space distance of saturation of e-e interaction (A.2.3) that leads to the expressions for cases of one type and for mixture of scatterers, respectively:

$$R_{D,n}^{-2} \equiv k^2 = 4\pi e^2 N_e / \kappa T; \quad R_D^{-2} = \sum_n R_{D,n}^{-2}. \quad (\text{A.4.7})$$

Notice that this condition determines the skin-layers depth in metals. At the absence of external fields this equality permits longitudinal waves propagation, i.e. the presence of near field.

For a quantitative comparison with the usual theory is needed to take into account that the path length in molecular dynamics is determined as

$$\ell = \frac{1}{4} \cdot \sqrt{2} \sigma N \rightarrow 3\kappa T / 4 \cdot \sqrt{2} \cdot 4\pi e^2 k N.$$

This expression leads to the Debye radius, differs on the factor of order  $\sqrt[4]{8/9}$  from the usual one.

#### A-4-3. Magnetic susceptibility

If atoms of medium do not have magnetic moments,  $\mu = 0$ , photons scattering induces electric dipole moments  $d$  and features of medium are determining via  $V_d$ . If  $\omega I \ll \hbar$  the volume of interaction and consequently magnetic susceptibility  $\chi$  do not depend on frequency, it is so named Van Vleck's paramagnetism.

Under rising of  $\omega$  (or temperature) or under excitation of higher levels with rising of  $I$  the enhancement of  $\chi(\omega)$  should be observed:

$$\chi \sim (d/\hbar)^2 I / [1 - (\omega I/\hbar)^2]. \quad (\text{A.4.8})$$

If  $\mu \neq 0$  and  $V_m > V_d$ , it can be concluded that

$$\chi_{\text{para}} = (\mu^2/\omega)N \rightarrow (\mu^2/\kappa T)N_{\text{eff}}, \quad N_{\text{eff}} = (3/2)N\kappa T/E_{\text{max}}. \quad (\text{A.4.9})$$

This expression can be generalized as

$$\chi_{\text{para}} = \frac{1}{4\pi} \sum_1^\infty (V_m N_m)^n = \frac{\mu^2 N}{\hbar\omega - 4\pi\mu^2 N}, \quad (\text{A.4.9}')$$

which shows the possibility of saturation and at  $\hbar\omega \rightarrow \kappa T$  leads to the Curie-Weiss law:

$$\chi \sim 1/(T - \Theta), \quad \Theta = 4\pi\mu^2 N/\kappa. \quad (\text{A.4.10})$$

For diamagnetics, correspondingly, can be concluded that

$$\chi_d = V_d N = -d^2 I N / \hbar^2 \simeq -d^2 N / mc^2 \rightarrow -(e^2 / 6mc^2) \sum \langle r_n^2 \rangle. \quad (\text{A.4.8}'')$$

#### A-4-4. Polaron

The function  $V_d$  and the corresponding radius of correlation arrive at maximum on the frequency  $\omega_0 = I/\hbar$ , i.e. at the "particle" radius

$$r^* \sim \sqrt{\hbar/m^*\omega}. \quad (\text{A.4.11})$$

Just such excitation is named polaron.

The value of  $\omega_0$  corresponds to the characteristic temperature of rotation  $\kappa\theta_{\text{rot}} = \hbar^2/2I$  and to the self energy of rigid rotator  $E_{\text{rot}} = (\hbar^2/2I)j(j+1)$ ,  $j = 0, 1, 2, \dots$

#### A-4-5. Electrical conductivity and Anderson transitions

Electro-conductivity can be determined via the dielectric susceptibility as

$$\sigma(\omega) = \frac{\omega}{4\pi} [\varepsilon(\omega) - 1] = \frac{\omega}{4\pi} V_\gamma N_e. \quad (\text{A.4.12})$$

For the direct current it leads at  $\omega \rightarrow \kappa T/\hbar$  to the known relation:

$$\sigma(0) = (\kappa T / 4\pi\hbar) V_\gamma N_e = e^2 N \tau_T / m^*. \quad (\text{A.4.13})$$

where  $\tau_T = \hbar/\kappa T$  is of the order of time of the electron free path  $\ell/c$  at the Fermi energy. (Notice that the account of e-e scattering leads to the substitution  $A_e = 3e^2/\kappa T$  instead of  $A_\gamma$  and to dependence of the corresponding part of conductivity on temperature as  $\sigma_1 \sim T^{-2}$ .)

For adjusting (A.4.13) to the elementary theory of conductivity the substitution  $\tau_T \rightarrow \ell/v$  can be taken, where  $\ell$  is the free path length and  $v$  is the velocity on Fermi surface. Under a more successive consideration the quantity  $N$  or  $N/\omega$  must be replaced by corresponding distributions, by the integrals of overlapping and so on.

It is physically evident that for metallic conductivity the overlap of particles electromagnetic volumes is needed:  $VN \geq 1$ . And really for metals  $\sigma(0) \sim 10^{-6} \div 10^{-7} \text{ sec}^{-1}$  at the room temperature, which correspond to (A.4.13) at  $VN \sim 1$ .

Since  $V$  and  $N$  depend on thermodynamic parameters, external fields and chemical composition, it leads to possibilities for control of processes of electrons delocalization, i.e. the processes of dielectric-metal transitions:  $(V_\gamma N_e < 1) \rightleftarrows (V_\gamma N_e \geq 1)$ .

The most known of them are transitions of enough quantity of electrons into the conduction band (photoconduction, thermal and electrical breakdown, etc.).

As  $V$  and  $N$  are functions of frequency, it is possible that the condition  $VN > 1$  will be executed in the definite frequencies interval only. So, if in the expression for  $V_\gamma$  would be taken into account that the energy of electrons is constrained by the edge of mobility  $E_g$ , the replacement  $\hbar\omega \rightarrow E_g - E$  leads to the radius of correlations:

$$R_{c,g} = (3V_\gamma(E)/4\pi)^{1/3} \sim |E_g - E|^{-2/3}. \quad (\text{A.4.14})$$

Such dependence is revealed in the known theory of Freed [86]. The coincidence of the degree in (A.4.14) with the critical index  $\beta$  allows to naming the process of energy transition over  $E_g$  as the Anderson phase transition.

The control of conductivity is evidently possible by modification of relative contents of components of medium, when, for example,  $N = xN_1 + (1-x)N_2$ , where  $N_1$  and  $N_2$  are density of metal and dielectric atoms correspondingly. At such cases  $\sigma = \sigma(x)$  and the control of conductivity is feasible via the variation of medium composition.

## A-4-7. Superconductivity

The conditions for superconductivity existence (at  $T = 0$ ) must be written as (A.2.3):

$$V_s N_s = 1, \quad (\text{A.4.15})$$

where  $V_s = (4\pi/k)r_0^*c\tau$ , and for the Cooper pairs  $r_0^* = (e^*)^2/m^*c^2$ , (here  $e^* = 2e$ ,  $m^* = 2m$ ,  $N_s = N/2$ ).

For ions of mass  $M_i$  this volume is equal to

$$V' = 4\pi e^2/\omega^2 M_i = 4\pi e^2 \hbar^2 N_A / C^2 (T_c - T) M_i$$

and therefore at  $T \rightarrow 0$  from the condition  $V'_s N_s = 1$  follows

$$T_c^2 M_i = \text{const}, \quad (\text{A.4.16})$$

which corresponds to the known Fröhlich isotopic effect.

Magnetic field in the domain (A.4.15) can be represented as

$$\mathbf{H} = \int d\mathbf{k} \mathbf{H}_0 \delta(k^2 - 4\pi N r_0) \exp(i\mathbf{k}\mathbf{r}),$$

which satisfies the well-known London's equation:

$$\nabla^2 \mathbf{H} = \Lambda^{-2} \mathbf{H}; \quad \Lambda(0) = k_s^{-1} (4\pi N r_0)^{-1/2}, \quad (\text{A.4.17})$$

$\Lambda(T)$  is the field penetration depth.

In the Ginzburg-Landau theory the equation for macroscopic  $\Psi$ -function is of the form:

$$-(\hbar/2m^*)(d/dz)^2\Psi + B_2(T)\Psi + B_4|\Psi|^2\Psi = 0, \quad (\text{A.4.18})$$

and in accordance with (A.3.10) can be taken that

$$1/B_2(T) = (2m^*/\hbar^2)R_c^2(T) = (T_c^4 C^4 \hbar / 2^8 3^2 m e^4) \Delta^{-2/3}. \quad (\text{A.4.19})$$

From (A.4.18) follows that  $N_s^* = |\Psi_{-\{\infty\}}| = -B_2(T)/B_4$ . Therefore the penetration depth

$$\Lambda(T) = (8\pi N_s^* r_0)^{-1/2} \approx (B_4 / 8\pi r_0 B_2(0))^{1/2} \Delta^{-1/2},$$

which is noticeably different from the usual expression, but the Ginzburg-Landau parameter  $\xi = \Lambda(T)/R_c(T)$  does not depend on  $\Delta(T)$  and the corresponding quantities are not modified.

As in the BCS theory the energy gap at  $T = 0$  is equal to  $2\Delta = 3.5\kappa T_c$ , it becomes possible to determine the numerical value of the radius of correlation as

$$R_c(\hbar\omega = 2\Delta) = \left[ \frac{6e^2\hbar^2}{m(3.5k)^2} \right]^{1/3} (T_c - T)^{-2/3} \approx 2 \cdot 10^{-5} (T_c - T)^{-2/3} \text{ cm.}$$

(A.4.20)

It leads to  $R_c$  that can be bigger the distance between atoms even till the room temperatures! But we can not claim that it should lead to an explanation of the high temperature superconductivity.

## A-5. Some applications: thermodynamic properties

### A-5-1. Fermi sphere

Under  $T = 0$  the concentration of electrons is determined as  $N_F = 2(4\pi/3)[k_F/2\pi]^3$  and from the condition of saturation,  $V_\gamma(k_F)N_F = 1$ , follows

$$k_F = 3\pi/4r_0. \quad (\text{A.5.1})$$

The condition of saturation  $V_e(k_F)N_F = 1$  for e-e interactions leads to the length

$$L_F = 2\pi/k_F = (3\pi^2/2)a_B, \quad (\text{A.5.2})$$

from which follows the maximal energy  $E_F = \hbar^2 k_F^2 / 2m \approx 10 \text{ eV}$ .

Note that (A.5.2) defines the limit distance, at which electrons are connected by the Pauli principle. It means that in any media atoms cannot be compressed on distances lesser than (A.5.2), i.e. it determines the maximal density of atomic media.

### A-5-2. Sound velocity and Debye temperature

Let's consider such situation when, at very low temperatures, ions/atoms of medium obtain energy via collisions with electrons only. If an electron transfers at collision the energy  $E = \hbar^2 k^2 / 2m$  to ion, the momentum of ion, with  $E = \hbar^2 q^2 / 2M$ , will be equal to

$$\hbar q = \hbar k \sqrt{M/m} \approx \hbar k \sqrt{2 \cdot 10^3 \mu}, \quad (\text{A.5.3})$$

$\mu$  is the molecular mass.

Since  $k$  can be determined by the condition  $V_\gamma n \approx 1$ , where  $n = N_A \rho / \mu$  is the number of ions/atoms in the volume  $V_\gamma$ ,

$$q = \sqrt{8 \cdot 10^3 \pi r_0 N_A \rho}. \quad (\text{A.5.4})$$

Therefore the analog of the Debye temperature can be defined as

$$\kappa\Theta_D' = s\hbar q, \quad (\text{A.5.5})$$

where  $s$  is the mean sound velocity. The last two relations lead to the definition:

$$\kappa\Theta_D' = 4.7 \cdot 10^{-4} s \rho^{1/2}, \quad (\text{A.5.6})$$

i.e. to a qualitative conformity with the Debye temperature for simple media.

### A-5-3. Heat conductivity

Let's attempt to consider the quantities  $V$  and  $N$  for phonons flux. The dispersion law for phonons can be written as  $\omega = sk$ . Since it can be taken that  $ms^2 = akT$ , where  $a \sim 1$ , we have that

$$X_s = (4\pi/k^2)AN_s = (4\pi a k T / m \omega^2)AN_s. \quad (\text{A.5.7})$$

As in the case of electrical conductivity, the coefficient of thermal conductivity can be determined from the relation for thermal flux:

$$\mathbf{q} = \xi \nabla T; \quad \xi = (\omega/4\pi)X_s L, \quad (\text{A.5.8})$$

where  $L$  is of interatomic order.

It seems, that the classic Wiedemann-Franz relation

$$\xi/\sigma = (\pi^2/3)(\kappa^2 T/e^2)$$

is fulfilled for obtained estimations. In every case they allow to estimate amplitude of phonons scattering on distinguished scatterers.

### A-5-4. Energy and heat capacity of electron gas

Let's designate

$$V_\gamma = V_0 mc^2/E, \quad V_0 = 2\pi r_0 \lambda_c^2; \quad E = \hbar^2 k^2 / 2m. \quad (\text{A.5.10})$$

Electron states number  $n(E)$  in the volume  $V$  and their density  $N(E)$  on the energy interval are naturally written as

$$n(T) = V/V_\gamma(E) = (V/V_0)E/mc^2 = EN. \quad (\text{A.5.11})$$

Complete energy of electron gas in the volume  $V$  under  $\mu/\kappa T \gg 1$  is equal to

$$E = N \int_0^{\infty} dE \frac{E}{\exp\{(E - \mu)/kT\} + 1} \approx N[\mu^2/2 + (\pi kT)^2/6], \quad (A.5.12)$$

and hence immediately follows heat capacity of degenerate electron gas:

$$C = T(\partial/\partial T)^2 E = (\pi^2/3)Nk^2 T. \quad (A.5.13)$$

Let us calculate now the internal energy of electron gas and compare it with the energy of heat radiation. If it will be assumed that the electrons kinetic energy is completely caused by photons of the internal field, the complete energy of this field must be calculated as the analogue with (A.5.12), with substitution  $E \rightarrow \hbar^2 k^2 / 2m$  and the averaging over the Bose-Einstein distribution:

$$E_{\gamma e} = \frac{Nh^2}{2m^2} \int_0^{\infty} dk \frac{k^3}{\exp(\hbar ck/kT) - 1} = \sigma_{SB}(\hbar c/e^2) \pi T^4 V/c. \quad (A.5.14)$$

Thus, this energy surpasses the Planck radiation energy at, approximately, 137-fold:

$$E_R = (e^2/\hbar c)(4/\pi)E_{\gamma e}. \quad (A.5.15)$$

This relation, with precision till  $(4/\pi)$ , is natural from the QED point of view: irradiation leads to the additional vertex at any Feynman graph.

#### A-4-5. Fermi gas

Under  $T = 0$  the density of Fermi gas is determined via the top momentum as  $n_F = p_F^3 / 3\pi^2 \hbar^3$ . If it would be taken that the main frequency, which determines the volume  $V_\gamma$ , depends on the limit energy of Fermi gas  $E_F = p_F^2 / 2m^*$ , then the saturation condition  $n_F V_\gamma = 1$  with  $\omega \rightarrow E_F / \hbar$  leads to the expression ( $\alpha = e^2 / \hbar c$ ):

$$p_F = \frac{16}{3\pi} \alpha \left( \frac{m^*}{m} \right)^2 mc. \quad (A.5.16)$$

It leads to such EM volume of one fermion:

$$V_\gamma = 4\pi e^2 \hbar^2 / m E_F^2 = (4\pi/3) a_B^3 C_1, \quad (A.5.17)$$

where  $C_1 = 12(3\pi/16)^4 (m^*/m)^3$  and at  $C_1 \rightarrow 1$  the mass renormalization in such system is turn out:

$$m^* = 1.042 m. \quad (A.5.18)$$

It must be noticed that the analogical form of  $V_\gamma$  with slightly different coefficient  $C_1$  can be formed by inclusion in  $V_\gamma$  the Coulomb energy  $\hbar\omega = e^2/r_C$  with  $r_C = (3/4\pi)n^{-1/3}$  instead of irradiation energy.

#### **A-5-6. Maximal binding energy and maximal self-frequency**

The mole energy of atomization  $\Lambda$  may correspond to such EM volume, for which the correlation radius is of the order of the Bohr radius:  $V = (4\pi/3)a_B^3$  and  $\hbar\omega = \Lambda/N_A$ . It leads to such estimations:

$$\Lambda \approx 426 \text{ kJ/mole}, \quad \hbar\omega_{\max} \approx 4.4 \text{ eV}. \quad (\text{A.5.19})$$

It can be reminded that under the normal conditions (absence of external pressure) the maximal atomization energy has Wolfram  $W$ , it is of the order 857 kJ/mole. The duplicating of  $\Lambda$  can be achieved by more scrupulous consideration of interatomic distances. With taking into account this possibility it can be stated that the maximal self-frequency in condensed media must correspond to photons energy of order of 8÷9 eV.

#### **A-5-7. Green functions and quasiparticles**

The dispersion law for quasiparticles is usually determined via poles of thermodynamic Green functions in momentum space, i.e. by the equation

$$G^{-1}(\varepsilon, \mu, p) = 0. \quad (\text{A.5.20})$$

More visual will be such proposition: the elementary excitation can be freely transferring via media if its (macroscopic) delay time is equal to zero:

$$\tau_1 = \operatorname{Re} \left( \frac{\partial}{i\partial\omega} \right) \ln G(\varepsilon, \mu, p) \equiv [G_1 G_2' - G_1' G_2] / |G|^2, \quad (\text{A.5.21})$$

where  $G_1$  and  $G_2$  are the real and imaginary parts of  $G$  and  $G_n'$  are corresponding derivatives.

The equality (A.5.22) leads to three possibilities of quasiparticles formation:

$$1/G_1 \rightarrow 0; \quad 1/G_2 \rightarrow 0; \quad G_1 = \text{const} \cdot G_2, \quad (\text{A.5.22})$$

and the third possibility, as far as I know, was not considered yet. It seems that this condition can be connected with peculiarities of skin layers, etc.

### **A-6. Bose-Einstein Condensation of Gases: Interconnection of Constituents**

Let's consider the BEC formation as the process of virtual photons exchange that links spacially distributed systems of oscillators [87]. The conditions of virtuality leads to the main restriction on density of identical particles in considered medium  $n \sim \lambda^{-3}$ , which should be close to the condition of Bose condensate formation defined by Einstein [88] as

$$n\lambda^3 = 2.615, \quad (\text{A.6.1})$$

where  $\lambda = \hbar (2\pi/mkT)^{1/2}$  is the length of de Broglie thermal wave.

The combination of these conditions leads to our main condition: BEC of rarified atomic gases can be formed by coordination of thermal excitation (thermal wave length) and the energy of the lowest, but sufficiently effective level of atom (the  $ns \leftrightarrow np$  transitions).

Let's consider this assumption in more detail. Each atom has, on the average, the kinetic energy  $E_1 = p_1^2/2m = \xi kT$ , where  $\xi$  is the coefficient of proportionality; probably, in view of condensation,  $\xi = 1.348/2.615 \approx 1/2$ , its magnitude introduces certain uncertainty not very important for further examination. Therefore at entering into the condensate each atom must get rid of corresponding momentum,

$$p_1 = \sqrt{2mE_1} \rightarrow \sqrt{2\xi mkT}, \quad (\text{A.6.2})$$

by atomic collisions that are very rare at the considered situation, or by a transfer of this momentum via a virtual photon emission to any other constituent.

The energy of photon with momentum (A.6.2) may correspond therefore to the wavelength of the strongest level of recipient atom  $\lambda_0$ :

$$\lambda_0 = 2\pi\hbar/p_1 = 2\pi\hbar/\sqrt{2\xi mkT}. \quad (\text{A.6.3})$$

Additionally we must suggest that the transfer of this excitation will be the most effective on a distance of photon wavelength, i.e. if all interacting atoms of BEC are in the near field of exchanging photons:

$$\lambda_0 \sim n^{-1/3}. \quad (\text{A.6.4})$$

The comparison of the estimations (A.6.3) and (A.6.4) for the most suitable, as seems, lines with experimental data [84] shows a qualitative accordance of the data for Na, Cr and Rb or, more carefully, an absence of essential contradictions.

\* \* \*

The considerations described in the Appendix lead to such conclusions.

All dynamical interactions between atoms/molecules in condensed substances can be considered as the exchanging by virtual photons in the frame of QED. Such approach allows the determining of effective radii of correlations for different types of interaction and effective volumes of such interactions. These magnitudes are directly determined via durations of interaction: the duration of delay at elastic scattering and the duration of final state formation. It evidently demonstrates the significance of temporal conceptions for fundamental science.

The derived radii of correlations determine critical indices of phase transitions. It univocally demonstrates their physical sense and proves the offered conception. The deduced

radii of interactions correspond to volumes of interactions and allow a specification of thresholds of different processes. The offered approach leads, in particular, to certain specification of the Ginzburg-Landau theory of phase transitions.

For obvious demonstration of possibilities of this conception, the simplified deduction of some known results in different branches of physics is represented. These results represent also certain new possibilities of phenomena interpretations. The most obvious example of the offered approach represents the Bose-Einstein condensation of gases; therefore it is described in the special Section.

It can be noted that constituents dressing can be considered as a direction to their decoherence. Therefore the theories of decoherence (e.g. [89]) can be formally close to the offered approach.

The negative values of durations are not considered here. They correspond to processes of tunneling, are partly examined in [18] and require special consideration. Note, that the offered scheme can be evidently generalized on non-electromagnetic interactions also.

## REFERENCES

- [1] Brabec, T. & Krauz, F. (2000). Rev. Mod. Phys., 72, 545.
- [2] Dell'Anno, F., De Siena, S. & Illuminati, F. (2007). arXiv: quant-ph/0701050v1.
- [3] Perel'man, M. E. (1970). Sov. Phys. JETP, 31, 1155.
- [4] McColl, L. A. (1932). Phys. Rev., 40, 261. A more recent calculations, for example: E. O. Kane in "*Tunneling phenomena in solids*" (E. Burstein, S. Lundqvist, Ed's). Plenum Press, NY, 1969.
- [5] Frank, I. M. (1942). Izvestia Akademii Nauk SSSR, ser. fizich., 6, 10.
- [6] Moshinsky, M. (1951). Phys. Rev., 81, 347, 84, 525 (1951). See, also, a recent interpretation of this phenomenon: V. Man'ko, M. Moshinsky & A. Sharma. *Phys. Rev.*, A 59, 1809 (1999)
- [7] Bohm D. *Quantum theory*. Prentice-Hall, NY: 1952, Ch.11.
- [8] Ter-Mikaelyan M. L. Zh. Eksp. Teor. Fiz., 25, 289 (1953). Landau L. D. & Pomeranchuk I. Ya. DAN SSSR, 92, 535, 735 (1953)
- [9] Wigner E. P. Phys.Rev., 98, 145 (1955), Wigner cited in this connection the unpublished theses of L.Eisenbud.
- [10] Smith F. T. Phys. Rev., 118, 349; 119, 2098 (1960).
- [11] M. L. Goldberger & K. M. Watson. *Collision Theory*. Wiley, NY, 1964.
- [12] A. I. Baz'. Sov.J.Nucl.Phys., 4, 229 (1967)
- [13] E. Pollak, W. H. Miller. Phys. Rev. Lett., 53, 115 (1984); E. Pollak. J. Chem. Phys. 83, 1111 (1986).
- [14] V. N. Baier, V. M. Katkov. Phys. Rep., 409, 261 (2005).
- [15] J. G. Muga et al., Ed's, 2002. Time in Quantum Mechanics. NY: Springer.
- [16] M. E. Perel'man. Int J Theor Phys 47, 468 (2008).
- [17] M.E. Perel'man, G.M. Rubinstein, Sov. Phys. Dokl. 203 798 (1972); M.E. Perel'man, G.M. Rubinstein, in: W.T. Arkin (Ed.), *New Research on Lasers and Electro Optics*, Nova Science, New York, 2006, pp. 229–267.
- [18] M. E. Perel'man. Phys. Lett. A 373, 648 (2009)

- [19] M. E. Perel'man. Phys. Lett. A 370, 528 (2007)
- [20] M. E. Perel'man. Phil. Mag., 87, 3129 (2007).
- [21] M. E. Perel'man, V.A. Tatartchenko. Phys. Lett. A 372, 2480 (2008); M. E. Perel'man, V.A. Tatartchenko. arXiv: 0711.3570. M. E. Perel'man, G. M. Rubinstein, V.A. Tatartchenko. Phys. Lett. A 372, 4100 (2008)
- [22] M. E. Perel'man. Ann. Phys. (Leipzig), 14, 733 (2005); quant-ph/0510123.
- [23] L. D. Landau , E. M. Lifshitz. *The Classical Theory of Fields*. 4 Ed. Pergamon, Oxford, 1975
- [24] O. Keller. J. Opt. Soc. Am. B, 16, 835 (1999)
- [25] H. E. Arnoldus. J. Opt. Soc. Am. B, 18, 547 (2001)
- [26] M. E. Perel'man. Ann. Phys. (Leipzig) 16, 350 (2007); quant-ph/0611098
- [27] J. Schwinger. Phys. Rev., 74, 1439 (1948)
- [28] J. Schwinger. Phys. Rev., 82, 664 (1951)
- [29] F. Low. Phys. Rev., 88, 28 (1952).
- [30] L. V. Keldysh. Sov.Phys.JETP, 20, 1307 (1965).
- [31] P. Salieres, et al. Adv. Atomic, Mol. Opt. Phys., 41, 89 (1999).
- [32] H. R. Reiss. Prog. Quant. Electr., 18, 17 (1992).
- [33] M.E. Perel'man, V. G. Arutyunian. Sov. Phys. JETP, 35, 260 (1972).
- [34] J. Levinger. Photonuclear reactions, 1960; I.Schicher. In: *Quantum Electrodynamics and Quantum Optics*. NY, Boulder, 1984, p.405. Comp.: W.R.Lamb, R.R.Schlischer, M.O.Scully. Phys.Rev.A, 36, 2763 (1987).
- [35] A. Einstein. Phys. Zs., 18, 121 (1917).
- [36] A. Einstein, P. Ehrenfest. Zs. Phys., 19, 301 (1923).
- [37] M. E. Perel'man. arXiv: quant-ph/0903.1823.
- [38] L. D. Landau, E.M.Lifshitz. Quantum Mechanics (Non-Relativistic Theory). 3rd ed. Pergamon Press. Oxford, 1991.
- [39] P. Agostini, L. F DiMauro. Rep. Prog. Phys., 67, 813 (2004).
- [40] A. Scrinzi, et al. J. Phys. B: At. Mol. Opt. Phys. 39, R1 (2006).
- [41] Ch. Bula. E144 Collaboration. SLAC-PUB-7219, Jul 1995. 23pp.
- [42] W. Feller. An Introduction to Probability Theory and its Applications. NY: Chapman, 1961.
- [43] K. C. Kulander, K. J. Schafer, J. L. Krause. In: Super-intense Laser-Atom Physics. NATO ASI Series B, 316, 95 (1993).
- [44] J. Peatross, D. D. Meyerhofer. Phys. Rev. A, 51, R-906 (1995).
- [45] Z. Chang et al. Phys. Rev. Lett., 79, 2967 (1997).
- [46] P. B. Corcum. Phys. Rev. Lett, 71, 1994 (1993).
- [47] B. Shan, Z. Chang. Phys. Rev. A, 65, R-011804 (2002).
- [48] R. Bartels et al. Nature, 406, 164 (2000).
- [49] S. L. Voronov et al. Phys. Rev. Lett., 87, 133902 (2001).
- [50] A. Gazibegović-Busuladžić, D. B. Milošević, W. Becker. Phys. Rev. A, 70, 053403 (2004).
- [51] J. H. Jeans. Phil. Mag., 10, 91 (1905); 17, 229 (1909).
- [52] E. Fermi. Suppl. N. Cimento, 2, 17 (1955).
- [53] N. Bohr, L. Rosenfeld. Kgl. Danske Videnk. Selskab., Math.-Fys. Medd., 12, No 8 (1933).
- [54] A. Sommerfeld. *Atombau und Spektrallinien*. B.2. Braunschweig, 1960.

- [55] M. Ya. Amusia. *Atomic Photoeffect*. Plenum, NY. 1990.
- [56] Delone, N. B. & Krainov, V. P. (1993). *Multiphoton processes in atoms*, Berlin: Springer.
- [57] G.Petite et al. Phys.Rev.A, 29, 2677 (1984).
- [58] H.G.Muller, P.H.Bucksbaum, D.W.Schumacher, A.Zavriyev. J.Phys.B, 23, 2761 (1990).
- [59] Watanabe et al. Phys.Rev.Lett. 73, 2692 (1994).
- [60] G.Mainfray. J.Phys.(France) 43, S.2-367 (1982).
- [61] C.Y.Tang et al. In: *Multiphoton processes* (G.Mainfray, P.Agostini, Eds.) Paris: CEA, 1991, p.69.
- [62] D. Umstadter. Phys. Plasm., 8, 1774 (2001); J. Phys. D: 36 , R151 (2003),
- [63] S. V. Bulanov, T. Zh. Esirkepov et al. arXiv: 0812.14.21v.3
- [64] M. Pardy. hep-ph/0207274
- [65] T. Plettner et al. Phys. Rev. Lett. 95, 134801 (2005)
- [66] S. R. de Groot, L. G. Suttorp. *Foundations of Electrodynamics* (North-Holland, Amsterdam, 1972), Ch. V.7; I. Brevik. Phys. Rep., 52, 133 (1979); V. L. Ginzburg. Applications of Electrodynamics in Theoretical Physics and Astrophysics (Gordon & Breach, NY, 1989)
- [67] G. K. Campbell, A. E. Leanhardt, J. Mun, M. Boyd, E. W. Streed, W. Ketterle, D. E. Pritchard. Phys. Rev. Lett., 94, 170403 (2005).
- [68] Weilong She, Jianhui Yu, Raohui Feng. Phys. Rev. Lett. 101, 243601 (2008).
- [69] A. M. Steinberg, P. G. Kwiat, R. Y. Chiao. Phys. Rev. Lett. 68, 2421 (1992).
- [70] R. Rajaraman. *Solitons and Instantons* (North-Holland, Amsterdam, 1982).
- [71] M. E. Perel'man. Ann. Phys. (Leipzig) 16, 350 (2007).
- [72] A. Zangwill. *Physics at Surfaces*. Cambridge Univ. Press, NY, 1988..
- [73] V. V. Zheleznyakov et al. Sov. Phys. Usp. 32, 835 (1989) (UFN, 159, 194 (1989)).
- [74] L. D. Landau, E.M. Lifshitz. *Electrodynamics of continuous media* (Pergamon, London, 1984).
- [75] M. D. Stenner, D. J. Gauthier, M. A. Neifeld. Phys.Rev.Lett., 94, 053902 (2005).
- [76] L. Brillouin. *Wave Propagation and Group Velocity*. Academic Press, NY, 1960.
- [77] S. -H. Choi, U. Österberg. Phys.Rev.Lett., 92, 193903 (2004).
- [78] P. W. Anderson. Phys. Rev., 109, 1492 (1958).
- [79] M. Störzer et al. Phys. Rev Lett., 96, 063904 (2006); cond-mat/0511284.
- [80] C. K. Chen et al. Phys. Rev. Lett., 46, 145 (1981)
- [81] R. W. Wood. Phil. Mag., 23, 689 (1912); *Physical Optics* (Macmillan, NY, 1934).
- [82] V. A. Kizel'. *Otrazhenie sveta (Light Reflection)*. Moscow, 1973 and references therein.
- [83] E. Fermi. Rend. Lincei, 33, 90 (1924).
- [84] L. D. Landau, E. M. Lifshitz. *Statistical Physics. 1.* L. Pergamon, 1980; Electrodynamics.of Continious Media. L.: Pergamon, 1981.
- [85] E. A. Cornell, C. E. Wieman. Rev. Mod. Phys. 74, 875 (2002); E. A. Cornell, J. R. Ensher, C. E. Wieman. Proc. Intern. School of Physics "Enrico Fermi ", Course CXL (Eds M. Inguscio, S. Stringari, C. E. Wieman) (Italian Phys. Soc., 1999) pp.15 -- 66; In: arXiv/9903109.
- [86] K. F. Freed. Phys. Rev., 135, 4802 (1972).
- [87] M. E. Perel'man. In: arXiv/ 0804.1908 (2008).

- [88] A. Einstein. Sitzungsber. K. Preuss. Akad. Wiss. Phys. Math. Kl., 1924, 261; 1925, .
- [89] Ph. Blanchard, et al. (Eds.). *Decoherence: theoretical, experimental, and conceptual problems* (Lecture notes in physics; 538). Berlin et al.: Springer, 2000.



## ***Chapter 3***

# **TWO-DIMENSIONAL PERIODIC NANOSCALE PATTERNING OF SOLID SURFACES BY FOUR-BEAM STANDING WAVE EXCIMER LASER LITHOGRAPHY**

**<sup>1</sup>Yu. K. Verevkin, <sup>1</sup>E. Ya. Daume, <sup>1</sup>V. N. Petryakov, <sup>2</sup>A. Yu. Klimov,  
<sup>2</sup>B. S. Gribkov, <sup>3</sup>D. O. Filatov, <sup>3</sup>Yu. Yu. Gushchina, <sup>4</sup>C. Tan,  
<sup>4</sup>C.S. Peng, <sup>4</sup>M. Pessa, <sup>5</sup>Z. Wang, <sup>6</sup>S. M. Olaizola and <sup>7</sup>S. Tisserand**

<sup>1</sup>Institute for Applied Physics, Russian Academy of Science, Nizhny Novgorod, Russia

<sup>2</sup>Institute for Physics of Microstructures, Russian Academy of Science,  
Nizhny Novgorod, Russia

<sup>3</sup>Research and Educational Center for Physics of Solid State Nanostructures,  
N. I. Lobachevskii University of Nizhny Novgorod, Nizhny Novgorod, Russia

<sup>4</sup>Optoelectronics Research Centre, Tampere University of Technology, Tampere, Finland

<sup>5</sup>Manufacturing Engineering Centre, Cardiff University, Cardiff, UK

<sup>6</sup>CEIT and Tecnun, University of Navarra, San Sebastian, Spain

<sup>7</sup>SILIOS Technologies, Peynier, France

## **ABSTRACT**

The article is devoted to a promising technology for fabrication of two-dimensional nanoperiodic structures on solid surfaces by four-beam standing wave pulsed laser modification. In this method, a large number of spots (up to  $10^7$ ) less than 100 nm in size heated up to several thousand degrees are formed on the modified surface as a result of the interference of the four laser beams incident on the object coherently. Besides a direct laser ablation, various nonlinear mechanisms of surface modification may take place in the standing wave maxima. This way, a nearly perfect two-dimensional pattern can be formed on the modified surface; the pitches of the pattern in both directions can be adjusted easily within the range from a few microns to tens of nanometers by simply varying the beams' incidence angles. This method being developed extensively at present is very promising for application in microelectronics, data storage, integrated optics (including fabrication of the Bragg mirrors, antireflection coating, two-dimensional photonic crystals, etc.) and is considered to be a promising alternative to X-ray

lithography in a wide range of applications. The most important advantage of the method is that the nanoperiodic pattern can be formed in a single step (actually, at single laser pulse) by direct laser ablation of the material. However, the method could be applied as well to patterning a resist deposited onto the processed substrate to serve as a lithographic mask. In this article, we present some experimental results on patterning various materials, such as metal films on semiconductor and glass substrates, polyimide, and even such a hard material as diamond by direct laser ablation using a XeCl excimer laser. Patterning a resist film, the phase masks on fused silica and the antireflection structures on Si and silica glass have been fabricated. Also, using the effect of stimulation of self-assembling of the semiconductor nanostructures by standing wave laser irradiation discovered by the authors, we have fabricated the ordered arrays of nanoislands on the surface of single crystal Si and GaAs and of GaAs/In<sub>x</sub>Ga<sub>1-x</sub>As/GaAs(001) heterostructures with the diameter ranging from 5 to 60 nm.

PACS: 42.55.Gp, 42.62.-b, 42.79.Dj, 68.65.Hb, 81.16.Nd, 81.16.Dn, 85.40.Hp

## 1. INTRODUCTION

The periodic submicron structures have found a wide range of applications in science and technology [1]. Among the applications of these arrays, one could mention Bragg mirrors, photonic crystals, data storage, etc. For formation of the periodic arrays of the nanometer-sized elements, E-Beam lithography and X-Ray Lithography are used the most often. One of the promising methods for forming the submicron periodic arrays on the solid surfaces is Standing Wave or Interference Lithography [2]. In this method, the periodic pattern on the surface to be processed is provided by the interference of two (or more) coherent laser beams. In the case of two beams, the interference pattern is suitable for forming various gratings, first of all, for the integrated and fiber optics [3,4], including the Bragg mirrors, beam couplers, etc. As follows from a simple geometrical consideration (Fig. 1), the period of the standing wave in the symmetric scheme  $d = \lambda/[2\sin(i)]$  where  $\lambda$  is the wavelength of the radiation used and  $i$  is the angle of incidence. So far, one can vary the period of the grating formed within a rather wide range simply adjusting  $i$ . The minimum  $d_{min} = \lambda/2$  is reached at  $i \rightarrow \pi/2$ . Using an immersion medium reduces  $d_{min}$   $n$  times where  $n$  is the refractive index of the immersion medium.

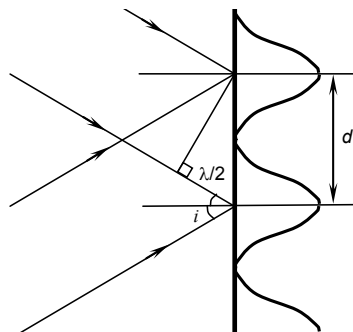


Figure 1. Schematic representation of two-beam interference in the symmetric scheme.

In the four-beam Standing Wave Lithography, the material to be patterned is subjected to the two pairs coherent laser beams incident on the surface under relatively large angles. So

far, the energy of the laser beams is localized in a huge number of spots of  $\sim \lambda/4$  in size. When the excimer ultraviolet (UV) lasers are used, the light can be localized in the spots of less than 40 nm in size. Using the 4<sup>th</sup> (or even the 5<sup>th</sup>) harmonic of a solid state laser radiation represents an alternative approach.

It should be noted that E-Beam Lithography and X-Ray Lithography exceed the standing wave lithography in the spatial resolution. The forthcoming generation of the semiconductor devices will be based on sub-50-nm critical dimensions [5]. These critical dimensions are planned to be achieved using nonlinear effects in Extreme UV lithography. The above listed techniques have higher spatial resolution limit than UV Standing Wave Lithography. On the other hand, the main advantage of the last method compared to E-Beam Lithography is higher productivity because the latter is based on the scanning principle.

In this article we present some experimental results on patterning various materials, by Four Beam Standing Wave Lithography using a powerful UV XeCl excimer pulsed laser with the emission wavelength  $\lambda = 308$  nm. The apparatus used in these experiments is described in Sec. II. Also, some features of the interference of four laser beams and the mechanisms of the surface modification under pulsed interfering UV excimer laser radiation are discussed briefly. Finally, in Sec. II the heat dissipation in a thin film on a heat conducting substrate subjected to a spatially periodic standing wave of pulsed laser radiation [6] is considered in detail. It was shown that this process governs all the processes of the film modification (first of all, direct ablation of the film material) and is important for interpreting the experimental results presented below.

There are two main techniques of Standing Wave Laser Lithography. In the first technique, the surface to be patterned is covered by a photoresist and exposed to the interfering laser radiation. Then the exposed resist undergoes development followed by further processing as in routine UV lithography [7,8,9]. The possibility of easy incorporation into a standard UV photolithographic process is a considerable advantage of Standing Wave Lithography. An alternative technique is direct (single pulse) modification of the patterned surface by laser irradiation [10,11,12,13]. In the studies presented in this article, both techniques have been applied. The first technique employs CW and pulsed lasers, whereas the second one needs high-power pulsed lasers. The high sensitivity of the photoresists makes it possible to use relatively low pulse energy densities and therefore to spread the processed area up to more than 10 cm in diameter [2, 9, 12]. This approach is promising for forming the large area regular arrays of the nanostructures (e.g., for flat panel displays [14]). However, this multistage process is rather complicated and expensive.

In the present article, we applied this technique to pattern the surface of fused silica [15]. Also, we used two-beam Standing Wave Laser Lithography to form the one-dimensional phase masks on fused silica and on Si and the antireflection gratings on Si [16]. These objects are promising for applications in planar integrated optics [17,18]. The reason for using the photoresist is that the above applications require high enough aspect ratio of the surface relief that could hardly be obtained by direct ablation. The results of these studies are presented in Sec. III.

The second approach enables one to form sub-100-nm periodic arrays of the surface nanostructures in a single step (actually, at a single pulse) in a variety of environments, including vacuum and ambient air. In Sec. IV we present the results of direct four-wave pulsed laser modification of the Fe—C films on Si substrates [6], of the polyimide films on

the fused silica substrates, and of even such a hard material as diamond [15]. The submicron periodic regular arrays of the nanodimensional features of the surface morphology were obtained. Such structures are interesting in both fundamental and applied aspects. Fe—C films are promising for magnetic data storage applications. Also, investigation of the effect of the pulse energy density and duration on the resulting film morphology turned to be useful to verify the theory of heat dissipation in the thin films on various substrates presented in Sec. II. The polyimide films are promising as the high-contrast photoresists useful for application in various purposes. It was demonstrated that the mechanisms of the effect of the standing wave laser radiation on the polyimide film surface are different for various beam energy densities. Diamond has been considered to be a promising wide-gap semiconductor material for several decades. One of its features is extreme radiation hardness that makes it especially promising for application in nuclear engineering, in high energy physics, in the space applications, etc. At present the epitaxial films of the artificially synthesized diamond of nanometer scale thickness are considered to be a promising material for future nanoelectronics, first of all, due to high thermal conductivity of diamond. On the other hand, hardness of diamond caused considerable problems in processing these films. The results presented in this article demonstrate the possibility of direct patterning of diamond by Standing Wave Laser Ablation. Besides, this technique can be applied to secret marking of the diamonds used in jewelry.

Investigations and applications of the self-assembling of nanostructures is now one of the dominant trends in the development of nanotechnology [19]. Starting from self-assembling of InAs/GaAs(001) quantum dots (QDs) [20] and GeSi/Si(001) nanoislands [21] driven by the elastic strain in the process of the heteroepitaxy of the highly mismatched materials [22] in the early 1990s, to date it has grown into a broad field of science and technology promising a wide range of applications in nanoelectronics [23], nanophotonics [24], etc. In recent years, extensive investigations have been devoted to finding the conditions for self-assembling of the spatially-ordered arrays of the self-assembled nanoislands in various material systems [25,26,27]. As a result of these studies, some self-assembling mechanism stimulating improvement of the size uniformity of the islands and their arrangement in regular arrays on the growth surface have been discovered [28,29]. Nevertheless, the problem of forming the uniform regular arrays of self-assembled semiconductor nanoisland still remains a vital one. Among various approaches to the solution of this problem, one could mention substrate prepatternning [30] using lithography [31,32], masking [33], growth on the vicinal surfaces [34], using the artificial substrates such as  $\text{Ge}_x\text{Si}_{1-x}/\text{Si}(001)$  buffers for growing spatially ordered GeSi nanoislands [35], etc. Pedraza et al. have studied the self-assembling of the nanoislands on Si under high-power UV pulsed laser radiation in the regime of surface wave excitation [36]. The self assembling effect was observed after  $> 200$  laser pulses with the pulse energy density  $\sim 1 \text{ J}\cdot\text{cm}^{-2}$ .

Recently a novel approach to forming near perfectly ordered periodic arrays of self-assembled semiconductor nanoislands has been proposed by the authors of the present article [37]. This is the self assembling of the semiconductor nanoislands under four-beam standing wave pulsed laser radiation. In Sec. V the experimental results on the formation of the two-dimensional regular periodic arrays of the semiconductor nanoislands on the single crystal Si(001) and GaAs(001) through self-assembling stimulated by the standing wave pulsed XeCl excimer laser radiation are presented. The surface stresses due to the local thermal expansion of the single crystal surface in the standing wave maxima were considered to be the driving force for ordered nanoisland array formation. Also the results of the four beam standing wave

pulsed laser modification of a GaAs/InGaAs/GaAs(001) strained heterostructure grown by Molecular Beam Epitaxy (MBE) are presented in Sec. V. The complex two-dimensional periodic nanoscale patterns were formed. Within each cell of the standing wave induces pattern, a number of self-assembled nanoislands having a bimodal size distribution were observed. The islands of smaller size ( $\approx 5$  nm in diameter) were concentrated in the center of each cell whereas the larger islands ( $\approx 15$  nm in diameter) were located at the boundaries of the cells. The results were explained by the interaction of the intrinsic elastic strain in the CaAs/InGaAs/GaAs heterostructure with the standing wave induced thermal field.

## II. STANDING WAVE PULSED LASER MODIFICATION OF THE SOLID SURFACES: APPARATUS AND BASICS

### A. Apparatus

The techniques for laser modification of the solid surfaces can be classified according to the number of the laser beams employed. The methods using a single focused laser beam are the most developed ones [38]. The nonlinear mechanisms of modification of the solids under the focused laser beams provide the possibility to reduce the modified area down to the sizes comparable to the wavelength of the laser radiation used [39]. Using laser beam scanning and/or the motorized stages one can produce any complex structure including the Bragg mirrors for the infrared (IR) and visible wavelength bands. The main drawback of this approach is poor productivity that is an attribute of all technologies based on the scanning principle.

Another approach to forming the one-dimensional Bragg mirrors, gratings, etc. is using the interference of two coherent laser beams [40,41,42]. This way, a perfectly periodic pattern over the area of several centimeters in diameter can be formed. Also, the Bragg mirrors with the spatially modulated period can be formed using the interference of the two laser beams with the different non-planar wave fronts [43]. The optical filters with complex transmission spectra can be created using the interference of two beams having several narrow lines in their emission spectra [44]. The same results can be obtained using the interference of three (or more) coherent monochromatic laser beams aligned in a single plane of incidence.

The interference of three and more coherent laser beams incident onto the surface to be modified in difference planes opens a way to create large two dimensional arrays of the submicron elements [45,46,47]. Also, the interference of the surface electromagnetic waves can be used in these purposes [48,49]. The latter mechanism can be used to create novel measuring and imaging systems on the basis of the method of the aperture synthesis. For instance, using many-beam interference one can create the holographic beam splitters for the master oscillators in the complex powerful laser systems.

In the experiments described in the present article a three-cascade UV XeCl pulsed excimer laser designed and built at the Institute of Applied Physics, Russian Academy of Sciences (Nizhny Novgorod, Russia) have been employed. The laser parameters were the following: the emission wavelength  $\lambda \approx 308$  nm, the coherence length  $> 30$  cm, the laser radiation bandwidth  $\approx 0.02$  cm $^{-1}$ , the pulse duration ranging from 2 to 45 ns, the pulse energy

up to 100 mJ, the beam divergence was close to the diffraction limit. The schematic drawing of the experimental setup is presented in Fig. 2.

The laser system consisted of a master oscillator, of two cascades of the optical amplifiers, and of the optical elements for forming the laser beam(s) geometry and properties for matching between the amplification cascades. The master oscillator (MO) (1) consists of an amplifying module (2) with pumping by a transverse charge and automatic ionization of the active volume ( $33 \times 2.8 \times 0.7 \text{ cm}^3$ ). The cavity consisted of two planar mirrors with the reflection coefficients of 98% (3) and 50% (4). The cavity was formed by two planar mirrors with reflection coefficients of 98% (3) and 50% (4).

In contrast to the conventional design, which utilizes the diffraction gratings in the master oscillator as the spectrum purifiers [50,51] two Fabry — Perot interferometers (FPs) (5, 6) with the sharpness  $\approx 10$  were employed were used for the laser spectrum rectification. This approach allowed improving the stability of the output radiation mode structure considerably. The FPs were placed inside the thermostats with the temperature stability  $\approx 0.1 \text{ }^\circ\text{C}$  at the ambient temperature variations of  $\approx 3 \text{ }^\circ\text{C}$ . The design of two FPs and thermostats implemented in the laser setup ensures the stability of the spectral characteristics of the laser radiation for about one week. After this time, the FPs required readjustment. A diaphragm of 1.5 mm in diameter (7) was used to select a single transverse mode in the cavity. An optical dielectric polarizer (8) was installed inside the cavity to select the radiation polarization. The total cavity length was  $\approx 1.5 \text{ m}$ .

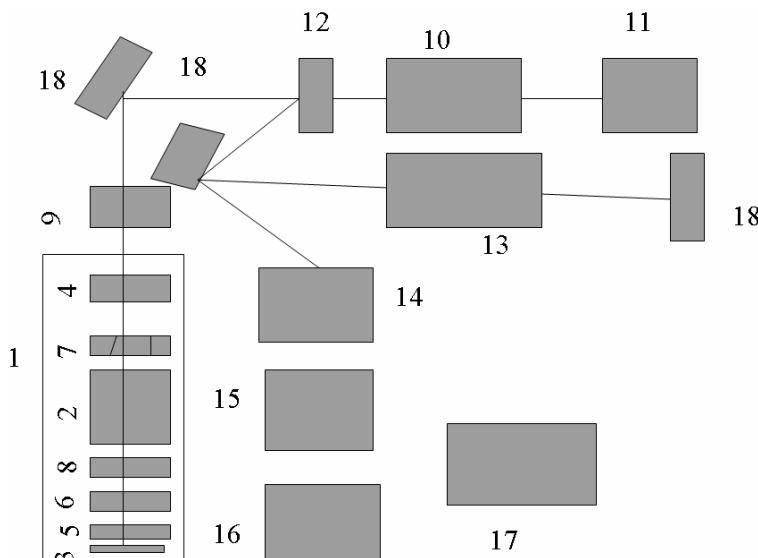


Figure 2. The schematic diagram of the laser system for four-beam standing wave XeCl pulsed excimer laser modification of the solid surfaces. 1 — the master oscillator (MO); 2 — the amplifying module; 3 and 4 — the back and the front mirrors of the cavity, respectively; 5, 6 — the Fabry-Perot etalons (FPs); 7 — the mode selection diaphragm; 8 — the polarizer; 9 — the beam expander; 10 — the first stage optical amplifier; 11 — the phase conjugation (PC) scheme; 12 — the beam decoupler; 13 — the second stage optical amplifier; 14 — the modified object; 15 — synchronization; 16 — the vacuum system; 17 — the scheme for measuring the spatial distribution of the laser radiation; and 18 — the mirrors.

A beam expander (a co-focal telescope, 9) with the spatial filter for increasing the beam diameter and decreasing the level of amplified spontaneous radiation appeared in the MO was placed between the MO and the mirror (18).

The first stage amplifier (10) had the active volume of  $33 \times 2.8 \times 1.4 \text{ cm}^3$ . The radiation passed around the amplifier twice. The second pass was provided by a phase-conjugation (PC) scheme (11) where the radiation was extracted due to rotation of the beam polarization plane by  $90^\circ$  (12). Compressed SF<sub>6</sub> under the pressure of  $\approx 175$  psi had been employed for PC.

The four-way second stage optical amplifier (13) had an active volume of  $65 \times 3.5 \times 1.6 \text{ cm}^3$ . The radiation was extracted by a stimulated Brillouin scattering (SBS) mirror. After the second stage amplifier, the radiation was directed into the optical scheme and split into the required number of beams. The beams were then joined together onto the surface to be modified (positioned vertically, 14). The optical scheme consisted of four dielectric mirrors in the case of the two beam interference and of 11 mirrors in the case of the four beam one. The dielectric mirrors with the reflectivity  $R \approx 0.5$  were employed as the beam splitters and in order to direct the two resulting coherent beams onto the surface to be patterned the high reflectivity ( $R \approx 0.99$ ) dielectric mirrors were used.

A high-voltage switch with a set of the cable delay lines (15) was used to synchronize the MO and the amplifiers. A vacuum system with one vacuum pump (16) was used to manufacturing and circulating the working-gas mixtures in the amplifiers.

The setup included also a high-resolution grating spectrograph, a calorimeter for measuring the pulse energy, several multi-channel oscilloscopes with the high-speed photodetectors for recording the radiation kinetics, and a scheme for measuring the spatial distribution of the laser radiation (17). Also the setup included a number of the dielectric mirrors (18).

The laser was initiated by feeding a high-voltage start-up pulse to the active-volume discharger of the master oscillator. The delay of the start-up of the first and the second stage amplifiers with respect to the MO depended on the rise time of the radiation in the MO and on the light propagation time from the MO to the corresponding amplifier. Usually, this delay was several tens of nanoseconds. The stability of the delay of the control pulses was  $\approx 2$  ns. The application of the thermally stabilized optics, of the spectral and spatial filtering, and of the SBS mirror made it possible to maintain a high quality of the laser beams during amplification. The SBS mirror was also used to shorten the laser pulses and to filter out the amplified spontaneous radiation. In most experiments the pulse duration was  $\approx 7$  ns unless other values were specified. All the experiments described below were performed in the ambient air at room temperature. Typically, the modified area on the sample surface was of several square millimeters.

Generally, the interference of four beams is described by more than 20 parameters [2]. When one creates a nonmodulated uniform periodic two-dimensional structures, it is sufficient to consider three simplified interference schemes characterized by a much smaller number of parameters:

- (i) In the first scheme, two pairs of the beams lie in two different planes of incidence. These planes are perpendicular to each other, and the bisectors of the angles between the beams in each of the incidence planes are perpendicular to the sample surface.

- (ii) The second scheme differs from the first one in that the bisector between the beams in one of the pairs is not perpendicular to the sample.
- (iii) In the third scheme, the planes of incidence are not perpendicular to each other.

The mathematical procedure in describing the interference patterns in these cases is obvious and can be found, for instance, in [2]. Without going into the details of trigonometric calculations here, we shall mention several specific features of the interference of the four laser beams in the cases listed above. In the first scheme of interference, all the maxima have equal amplitudes and are separated by equal intervals. In the second and the third schemes, the amplitudes of intensity maxima in the plane of the sample and the separations between these maxima vary periodically.

In all the above schemes, the interference pattern is highly sensitive to the polarizations of the interfering beams. Let us consider the following two cases: [46] i) the polarization planes of both pairs of the beams are perpendicular to the respective incidence planes (below referred to as TE—TE interference); and ii) the direction of polarization in one pair of beams is perpendicular to the plane of incidence of these beams, while in the other pair of the beams it is parallel to the plane of incidence of these beams (TE—TM interference).

In [19] the pulsed laser modification of the surface of a Fe—C film with a thickness of several tens of nanometers deposited onto Si substrate in the TE—TM four-beam interference polarization scheme was studied experimentally. Fig. 3 shows the profiles of the modified Fe—C film surface measured by Maxim GP 200 profilometer with  $\approx 0.5 \mu\text{m}$  in-plane resolution and  $\approx 0.2 \text{ nm}$  vertical one. Fig. 3 (a) and (b) correspond to the case when the bisector of one of the beam pairs is not perpendicular to the sample surface. In this case, the depth of surface modification varies across the sample. These variations became less expressed with decreasing angle between the bisector and the normal to the sample surface [Fig. 3 (c)]. From these experiments, one can conclude than in order to achieve the acceptable scatter of the intensity in the interference pattern maxima within 10%, the deviation of the angular beam alignment should be less than  $1^\circ$ .

Most papers cited above were devoted to Standing Wave Laser Lithography where the interfering laser radiation was used to pattern a photoresist followed by development and further processing as in standard UV lithography. In this article we present mostly the results of forming the submicron periodic structures (including almost perfectly arranged periodic arrays of the holes in the metal films and of the semiconductor nanoislands) by direct Standing Wave Laser Modification using a powerful pulsed UV laser. Let us consider briefly the mechanisms of the solid surface modification in this process.

The interest to the effect of the laser radiation on the surface of various materials originates from the development of the laser technologies in the 1960-s. Many fundamental and applied problems have been considered since that time [39, 52].

A powerful standing wave laser pulse results, first of all, in rapid (up to  $10^{11} \text{ }^{\circ}\text{C}\cdot\text{s}^{-1}$ ) heating up of the patterned surface in the local nanometer sized areas. This heating may result in the material evaporation [53], in the recrystallization of the films of various chemical composition [54,55,56], in the acceleration of the chemical reactions (in particular, in the laser-induced oxidation), in enhancement of the surface diffusion, etc. For example, this method was applied to the local nanodimensional modification of paramagnetic films with their conversion into the ferromagnetic state that is promising for magnetic data storage [57].

However, the effect of the laser radiation on a solid surface may not be limited to a pure thermal heating only. As well, it may result in a photochemical effect.

In order to understand these processes, it is important to know the temperature distribution in the structures subjected to the standing wave pulsed laser radiation. Knowing this distribution is also useful in studying the thresholds for the laser destruction of the metal coatings [58] and for excitation of the surface waves.

In the next subsection a detailed two-dimensional calculations of the heat release in a metal film on a heat-conducting substrate [59] are presented. Then this theory will be applied to analysis of the experimental results presented in the following sections. It will be demonstrated that thermal physical properties both of the film and of the substrate play an important role when a standing wave laser radiation is employed to produce a submicron structures on the surface.

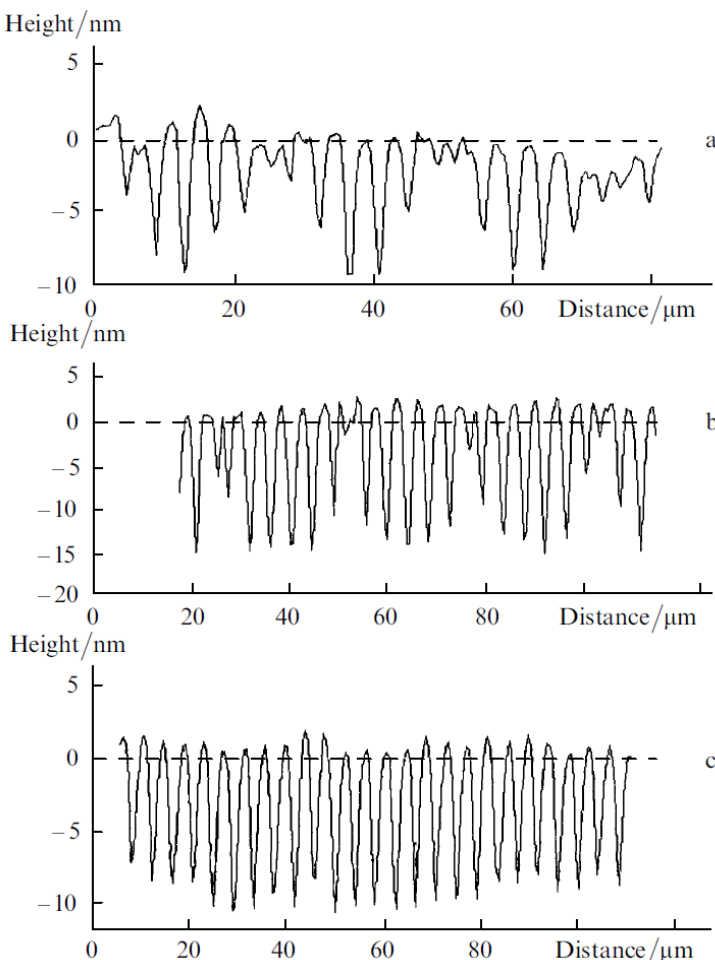


Figure 3. The effect of the deviation of the bisector of the angle between the two laser beams lying in the same plane of incidence from the normal to the sample surface on the relief of a Fe—C film patterned by direct single-pulse two-beam laser ablation: the bisector was not perpendicular to the sample surface (the deviation  $\approx 2^\circ$ ) (a, b) and the bisector was almost perpendicular to the sample surface (the deviation  $\approx 30^\circ$ ) (c).

## B. The Spatial Distribution of the Temperature in a Film on a Substrate Heated by a Surface Standing Wave of Laser Radiation

This subsection is devoted to an analysis of the heat transfer in a film of finite thickness on a semi-infinite substrate. Here we assume that the film surface is heated from the surface by a spatially periodic (in the film surface plane) heat source (namely, the standing wave of the laser radiation). This approximation is valid when the absorption length of the laser radiation employed  $\beta(\lambda)^{-1} \ll L$  where  $\beta$  is the optical absorption coefficient of the modified material at the wavelength of  $\lambda$  and  $L$  is the film thickness. For  $\lambda = 308$  nm this conditions is satisfied well for most metals (at reasonable  $L$ ) and semiconductors. Here we limited our analysis to considering the thermal effects only neglecting other effects of laser radiation on the film material listed in the previous subsection.

The schematic drawing of the configuration of the film on the substrate is shown in Fig. 4. The film has its boundaries at  $x = 0$  and at  $x = L$ , and the substrate is located in the region  $x < 0$ . The thermal parameters of the film and of the substrate are indicated by the subscripts "1" and "2", respectively. Let us assume that the thermal flux  $q_{in}$  incident onto the film surface at  $x = L$  is spatially modulated along the  $y$  axis as

$$\begin{cases} q_{in}(y) = A + B \cos\left(\frac{2\pi y}{d}\right) \\ A \geq B \geq 0 \end{cases} \quad (1)$$

where  $d$  is the period of the standing wave.

A two-dimensional heat conduction equation describing the spatial distribution of the temperature as a function of the time  $t$   $T(x, y, t)$  can be written as

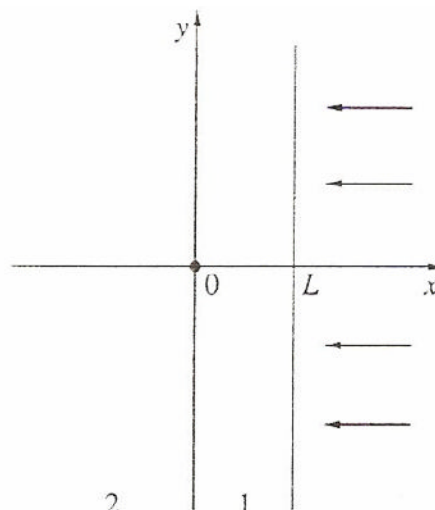


Figure 4. A schematic drawing of a film of the thickness  $L$  on a semi-infinite substrate. Region (1) is the film and region (2) is the substrate. The direction of the heat flux incident onto the film surface at  $x = L$  is indicated by the arrows.

$$\frac{\partial T_{1,2}}{\partial t} = \alpha_{1,2} \left( \frac{\partial^2 T_{1,2}}{\partial x^2} + \frac{\partial^2 T_{1,2}}{\partial y^2} \right), \quad (2)$$

where  $\alpha_{1,2} = k_{1,2} [\rho_{1,2} c_{1,2}]^{-1}$  are the temperature conductivities,  $k_{1,2}$  are the heat conductivities,  $\rho_{1,2}$  are the densities, and  $c_{1,2}$  are the specific heat capacities for the film material and for the substrate one, respectively.

The initial condition for the problem considered is that the temperature in both the film and the substrate are constant at  $t = 0$ :

$$T_{1,2}(x, y, 0) = T_0. \quad (3)$$

The boundary conditions are written as follows. For  $x = L$ , the heat flux entering the film is

$$k_1 \frac{\partial T_1}{\partial x} = q_{in}. \quad (4)$$

For  $x = 0$ , the continuity condition for the heat flux

$$k_1 \frac{\partial T_1}{\partial x} = k_2 \frac{\partial T_2}{\partial x} \quad (5)$$

and the condition of equal temperatures

$$T_1(0, y, t) = T_2(0, y, t) \quad (6)$$

should be satisfied. For  $x \rightarrow -\infty$ , the temperature of the substrate should tend to  $T_0$ :

$$T_2(x, y, t)_{x \rightarrow -\infty} \rightarrow T_0. \quad (7)$$

Under these conditions, the solution of Eq. (2) is

$$T_{1,2}(x, y, t) = T_{1,2}^c(x, t) + T_{1,2}^a(x, t) \cos\left(\frac{2\pi y}{d}\right) \quad (8)$$

Applying the Laplace transformation with respect to the time  $t$  to Eq. (2) and to the boundary conditions (4) — (7), one can obtain the equations for the images  $T_{1,2}^c(x, p)$  and  $T_{1,2}^a(x, p)$ .

The solutions of Eq. (2) have different forms in the regions 1 and 2. Here we consider the solution for the temperature distribution in the film ( $0 < x < L$ ) only:

$$T_1(x, y, t) = T_1^c(x, t) + T_1^a(x, t) \cos\left(\frac{2\pi y}{d}\right). \quad (9)$$

The constant component  $T_1^c$  is given by the following expression:

$$T_1^c(x, t) = T_0 + \frac{A}{k_1} \sum_{n=0}^{\infty} \gamma^n \left\{ 2\sqrt{\frac{\alpha_1 t}{\pi}} \left[ \exp \left\{ \frac{[(2n+1)L-x]^2}{4\alpha_1 t} \right\} + \gamma \exp \left\{ \frac{[(2n-1)L+x]^2}{4\alpha_1 t} \right\} \right] - \right. \\ \left. - [(2n+1)L-x] \operatorname{erfc} \left[ \frac{(2n+1)L-x}{2\sqrt{\alpha_1 t}} \right] - \gamma [(2n+1)L+x] \operatorname{erfc} \left[ \frac{(2n+1)L+x}{2\sqrt{\alpha_1 t}} \right] \right\} \quad (10)$$

where

$$\gamma = \frac{1-\sigma}{1+\sigma}, \quad (11)$$

and

$$\sigma = \sqrt{\frac{k_2 \rho_2 c_2}{k_1 \rho_1 c_1}}. \quad (12)$$

The amplitude of the oscillating component of the temperature distribution along the  $y$  axis  $T_1^a$  is given by

$$T_1^a(x, t) = \frac{B}{k_1} (D - I - Q) \quad (13)$$

where

$$D = \frac{d}{2\pi} \cdot \frac{\cosh \left( \frac{2\pi x}{d} \right) + \delta \sinh \left( \frac{2\pi x}{d} \right)}{\sinh \left( \frac{2\pi L}{d} \right) + \delta \cosh \left( \frac{2\pi L}{d} \right)} \quad (14)$$

and  $\delta = k_2/k_1$ . The form of the functions  $I$  and  $Q$  depends on the relationship between the thermal conductivities  $\alpha_1$  and  $\alpha_2$ . This effect is related to the fact that the number of poles and branching points of the function  $T_1^a(x, p)$  depends on the above relationship. When  $\alpha_1 > \alpha_2$

$$I = \frac{2\delta L}{\pi} \int_0^\infty \exp \left\{ -\frac{\alpha_1 t}{L^2} \left[ \left( \frac{2\pi L}{d} \right)^2 + u^2 \right] \right\} \beta(u) \cos \left[ u \left( 1 - \frac{x}{L} \right) \right] \times \\ \times \overline{\left[ \left( \frac{2\pi L}{d} \right)^2 + u^2 \right] (u^2 \sin^2 u + \delta^2 \beta^2(u) \cos^2 u)} \quad (15)$$

$$Q = \frac{2\delta L}{\pi} \int_0^\varepsilon \exp \left\{ -\frac{\alpha_1 t}{L^2} \left[ \left( \frac{2\pi L}{d} \right)^2 - u^2 \right] \right\} \tilde{\beta}(u) \cosh \left[ u \left( 1 - \frac{x}{L} \right) \right] \times \frac{u \partial u}{\left[ \left( \frac{2\pi L}{d} \right)^2 - u^2 \right] \left( u^2 \sinh^2 u + \delta^2 \tilde{\beta}^2(u) \cosh^2 u \right)} \quad (16)$$

where

$$\varepsilon = \frac{2\pi L}{d} \sqrt{1 - \frac{\alpha_2}{\alpha_1}}, \quad (17)$$

$$\beta(u) = \sqrt{\left( \frac{\alpha_1}{\alpha_2} - 1 \right) \left( \frac{2\pi L}{d} \right)^2 + \frac{\alpha_1}{\alpha_2} u^2}, \quad (18)$$

and

$$\tilde{\beta}(u) = \sqrt{\left( \frac{\alpha_1}{\alpha_2} - 1 \right) \left( \frac{2\pi L}{d} \right)^2 - \frac{\alpha_1}{\alpha_2} u^2}. \quad (19)$$

When  $\alpha_1 < \alpha_2$ , the following expressions can be obtained:

$$I = \frac{2\delta L}{\pi} \int_\omega^\infty \exp \left\{ -\frac{\alpha_1 t}{L^2} \left[ \left( \frac{2\pi L}{d} \right)^2 + u^2 \right] \right\} \beta(u) \cos \left[ u \left( 1 - \frac{x}{L} \right) \right] \times \frac{u \partial u}{\left[ \left( \frac{2\pi L}{d} \right)^2 + u^2 \right] \left( u^2 \sin^2 u + \delta^2 \beta^2(u) \cos^2 u \right)} \quad (20)$$

where

$$\omega = \frac{2\pi L}{d} \sqrt{\frac{\alpha_1}{\alpha_2} - 1}, \quad (21)$$

and

$$Q = \sum_i \frac{\exp(-\rho_i t)}{C_i} [r_i \cos(r_i x) + \delta l_i \sin(r_i x)], \quad (22)$$

$$r_i = \sqrt{\frac{\rho_i}{\alpha_1} - \left(\frac{2\pi}{d}\right)^2}, \quad (23)$$

$$l_i = \sqrt{\left(\frac{2\pi}{d}\right)^2 - \frac{\rho_i}{\alpha_2}}, \quad (24)$$

and  $\rho_i$  are the roots of the equation

$$\sqrt{\frac{\rho}{\alpha_1} - \left(\frac{2\pi}{d}\right)^2} \operatorname{tg} \left[ L \sqrt{\frac{\rho}{\alpha_1} - \left(\frac{2\pi}{d}\right)^2} \right] = \delta \sqrt{\left(\frac{2\pi}{d}\right)^2 - \frac{\rho}{\alpha_2}}. \quad (25)$$

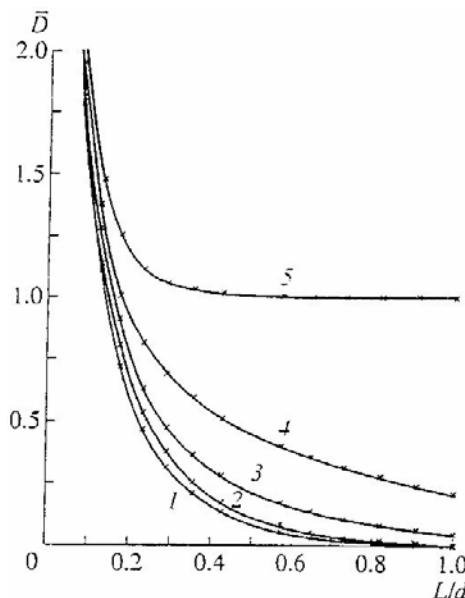
All roots  $\rho_i$  of Eq. (25) should be determined, and the summation in Eq. (22) should be performed over the whole range of  $i$ . The roots  $\rho_i$  fall into the range from  $\rho = \alpha_1(2\pi/d)^2$  to  $\rho = \alpha_2(2\pi/d)^2$ . The total number of roots of Eq. (25) is  $[z] + 1$ , where  $[z]$  is the integer part of  $2L/d(\alpha_2/\alpha_1 - 1)^{0.5}$ .

The solution  $T_2(x, y, t)$  for the substrate that is not written here also satisfies Eq. (2). The boundary conditions (3) — (7) are also satisfied by the solutions found. We failed to verify the fulfillment of the initial condition  $T_{1,2}(x, y, 0) = T_0$  analytically, but the computer calculation demonstrated that this condition was satisfied as well. If one considers the condition (3) to be satisfied, the improper integrals in (15) and (17) for  $t = 0$  can be expressed in terms of function (14) and, correspondingly, in terms of (16) and (18).

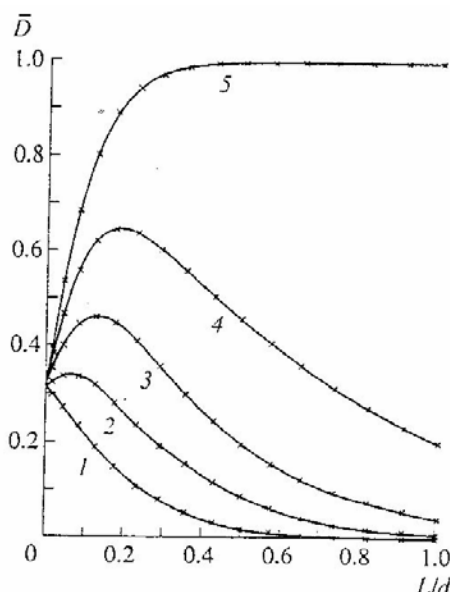
It should be noted that the integrals  $I$  and  $Q$  entering expression (13) for the amplitudes  $T_1^a(x, t)$  tend to zero at  $t \rightarrow \infty$ . This means that  $T_1^a(x, \infty) = BD/k_1$  is a steady-state value of the amplitude of the temperature distribution component oscillating with varying  $y$ .

Fig. 5(a) and (b) show  $\bar{D} = 2\pi D/d$  as a function of  $L/d$  for various values of depths  $x$  normalized to the film thickness  $L$  for a metal film on the silica glass substrate and on the Si one, respectively. These ones represent the behavior of the steady-state value of the temperature distribution component varying along  $y$  direction for the metal films on various substrates. A dramatic effect of thermal properties of the substrate on the spatial distribution of the film temperature is seen clearly. In the case of the silicon substrate  $k_1 < k_2$  and  $D$  decreases with decreasing  $L/d$  starting with a certain value of  $L/d$ . In this case,  $\bar{D} \rightarrow k_1 k_2$ . For the silica glass substrate,  $k_1 > k_2$  and  $D$  increases with decreasing  $L/d$ .

One can see from Eqs. (15) — (20) that the settling time for the steady-state value of  $T_1^a(x, t)$  is determined by the two parameters: by  $t_L = L^2/\alpha_1$  and by  $t_d = d^2/(2\pi)^2 \alpha_1$ . The effect of the latter parameter  $t_d$  is related to the presence of an exponential factor that does not enter the integrand. The effect of  $t_L$  entering the integrand, which is a function of four thermal physical parameters and of the quantity  $2\pi L/d$ , is more complicated. As follows from computer simulation, the settling time for the steady-state value of  $T_1^a(x, t)(t_{st})$  for the metal film on the silica glass substrate decreased from  $5t_d$  down to  $2t_d$  as  $L/d$  increased from 0.025 to 0.25. For the silicon substrate, a different behavior of  $t_{st}$  was obtained. Namely,  $t_{st}$  increased from  $0.3t_d$  up to  $\approx t_d$  as  $L/d$  increased within the limits indicated above.



(a)



(b)

Figure 5. The effect of the metal film thickness  $L$  and of the period of the spatial modulation of the heat flux  $d$  on the steady-state amplitude of the temperature distribution in the  $y$  direction for various depths  $x$ . Substrate material: (a) — silica glass; (b) — silicon.  $x/L$ : 1 — 0, 2 — 1/4, 3 — 1/2, 4 — 3/4, and 5 — 1.

For certain applications, the parameter  $M = T_1^a(x, t)/[T_1^c(x, t) - T_0]$  characterizing the depth of spatial modulation of the temperature is important. For the boundary conditions (3) — (7),  $T_1^c(x, t) \rightarrow \infty$  for  $t \rightarrow \infty$ , and, consequently,  $M \rightarrow 0$  for  $t \rightarrow \infty$ . This means that in order to

obtainin a desired value of  $M$  the duration of heating should be limited. The effect of the substrate parameters on  $M(L, t)$  for various values of  $L$  and  $d$  is shown in Fig. 6 and Fig. 7. Note that the relative effect of the substrate is more pronounced as  $d$  decreases (Fig. 6).

For  $d = 200$ , 400, and 800 nm the parameter  $t_d$  is 0.085, 0.34, and 1.35 ns, respectively. As follows from Fig. 4 and Fig. 5, the modulation depth is 15-20% for the heating time  $t < 10t_d$ .

The main conclusions from the analysis and computer simulation presented in this subsection are as follows:

- (i) The parameter  $L/d$  should be smaller than 0.1 for heating to be sufficiently uniform over the film thickness.
- (ii) The heating time  $t$  should be less than  $10t_d$  in order to provide the modulation depth of the film temperature (in the  $y$  direction) greater than 15%.
- (iii) When the structures with the period  $d < 500$  nm are produced, the modulation depth  $M$  for the silicon substrates is 2 to 4 times greater than for the silica glass ones. The effect is attributed to higher heat conductivity of silicon than the one of silica glass.

Finally, it should be noted that the problem considered here can be extended to the case when the input flux  $q_{in}$  is an arbitrary function of  $y$ . This can be done by representing it in terms of a Fourier integral and carrying out inverse transformation of Fourier images obtained from the solutions of the heat conduction equations (13) — (25). The time dependence of the input heat flux  $q_{in}$  can also be included with the use of Duhamel's integral.

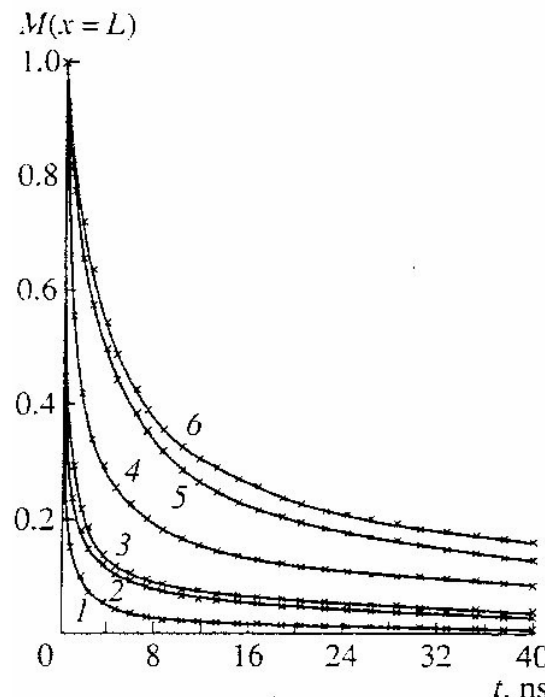


Figure 6. The depth of spatial modulation of the temperature  $M$  with the period  $d$  for an iron film of thickness  $L = 20$  nm on silica glass (1 and 5), iron (2 and 6), and silicon (3 and 4) substrates as a function of the heating time  $t$ . The modulation period  $d = 200$  nm (1, 2, and 3) and  $d = 800$  nm (4, 5, and 6).

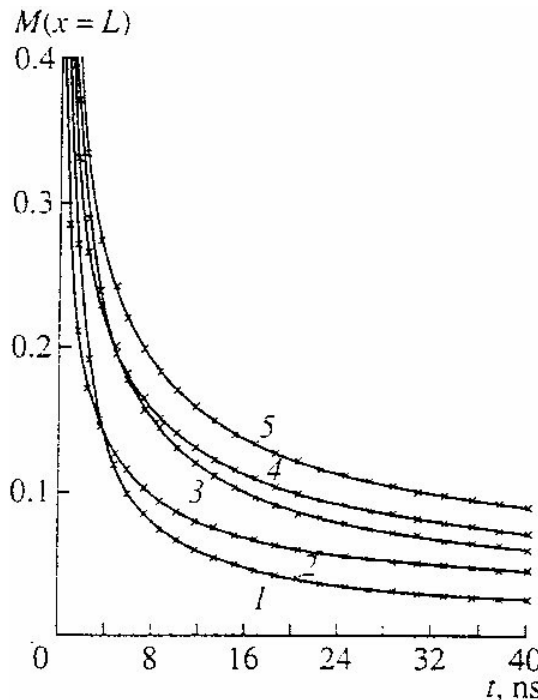


Figure 7. The depth of spatial modulation of the temperature  $M$  with the period  $d = 400$  nm for an iron film of thickness  $L$  on a glass substrate with  $L = 40$  nm (1) and  $10$  nm (2) and a silicon substrate with  $L = 10$  nm (3),  $40$  nm (4), and  $200$  nm (5) as a function of the heating time  $t$ .

### III. FORMING THE ONE- AND TWO-DIMENSIONAL PERIODIC RELIEF ON THE FUSED SILICA AND Si SURFACES BY STANDING WAVE PULSED LASER LITHOGRAPHY

#### A. One-dimensional Periodic Nanorelief on the Fused Silica and Si: the Phase Masks and the Antireflection Coatings

In this subsection the results on forming of the phase masks on the fused silica and of the antireflection coatings on fused silica and on Si using the two-beam standing wave UV pulsed laser radiation to expose the photoresist on the fused silica and Si substrates followed by a standard lithographic process including the development of the exposed resist and by dry etching. One of the most promising applications of this technology is fiber and integrated optics, namely forming the phase masks and Bragg mirrors with controlled reflection/transmission spectra. Such gratings made from Si are promising for various applications in the IR wavelength band, for instance, in the solar cells as the antireflection coatings [60] and in the integrated optics, especially, in Si based photonics, which is a new field of science and technology developed rapidly in recent years [61]. There the regular surface relief can be applied as the Bragg mirrors in the Si based planar and ridge waveguides (in the photodetectors, multiplexors, etc.), in distributed feedback (DFB) for the Si-based lasers, in the one-dimensional photonic crystals, etc.

For forming the phase masks E-Beam Lithography is used the most widely. The studies presented in this subsection were devoted to development of simple and cost-effective method of Standing Wave Lithography using a powerful XeCl excimer pulsed laser for forming the one-dimension gratings. One of the advantages of the Standing Wave Pulsed Laser Lithography is much less effect of the vibration environment on the nanoscale pattern quality. Besides, using a powerful lasers allows increasing the pulse energy up to several tens of joules that in turn would allow exposing relatively large areas (up to  $1000 \text{ cm}^2$ ) at a single pulse. On the other hand, the breakdown threshold for fused silica exposed to the UV standing wave laser radiation with  $\lambda = 308 \text{ nm}$  is  $\approx 15 \text{ J}\cdot\text{cm}^{-2}$ . Such a high value does not allow the formation of a regular periodic relief over an area greater than  $\sim 1 \text{ cm}^2$  by direct Standing Wave Laser Ablation.

Let us first estimate the parameters of the surface nanorelief required for the efficient phase masks and antireflection coatings. For the phase masks, the condition of minimum transmission in the zero order of diffraction (MTZOD) is an obligatory one. The quality of the phase mask can be considered to be satisfactory when MTZOD is less than 10%. From the elementary physics considerations, MTZOD is obtained when the corrugation depth  $h \approx \lambda / 2(n - 1)$  where  $\lambda$  is the wavelength of the incident light used for the pattern transfer and  $n$  is the refractive index of the phase mask material. This condition provides MTZOD at normal incidence of the light onto a phase mask with a rectangular relief. However, this estimate is rather rough; and modern technological developments require more accurate theory as well as the experimental verification of the latter.

For the antireflection coatings the following two conditions are to be satisfied. First, the period of the surface relief  $d$  should be less than  $\lambda_a/n$  where  $\lambda_a$  is the wavelength of the light, which the antireflection coating is designed for. Second, the corrugation height  $h$  should equal approximately to  $\lambda_a/4$ . The first condition is required in order to suppress the diffraction of the higher orders inside the coated material while the second one provides the MTZOD at the normal incidence.

The forming of the relief on the surfaces of the silica glass substrates was performed using a double layered resist mask consisting of a Cu film of  $\approx 50 \text{ nm}$  in thickness deposited onto a photo resist film  $\approx 400 \text{ nm}$  thick. We have used the two-beam XeCl laser interference scheme with the energy densities  $\approx 30 \text{ mJ/cm}^2$ . The exposed resist was developed in an alkaline water solution and Cu film was etched using  $\text{Ar}^+$  ion beam. The silica glass was etched using Reactive Ion Beam Etching in a flux of  $\text{CF}_4 - \text{O}_2$  gas mixture. The etching rates were  $\approx 30 \text{ nm/min}$  for fused silica and for the photo resist and  $\approx 3 \text{ nm/min}$  for Cu. This way, the relief on the surface of the fused silica substrate up to  $\approx 500 \text{ nm}$  in depth was formed.

In Fig. 8 (a) and (b) AFM image and line profile, respectively of a phase mask formed on a fused silica substrate by the process described above are presented. The period of the grating  $d$  was  $\approx 460 \text{ nm}$  and the averaged grove depth  $h$  was  $\approx 280 \text{ nm}$ . It should be noted that the width of the grooves and the one of the ridges are not equal to each other. These parameters depend on the conditions during developing of the photoresist and etching of the metal mask and of silica glass. In order to optimize the phase mask relief further experiments are necessary.

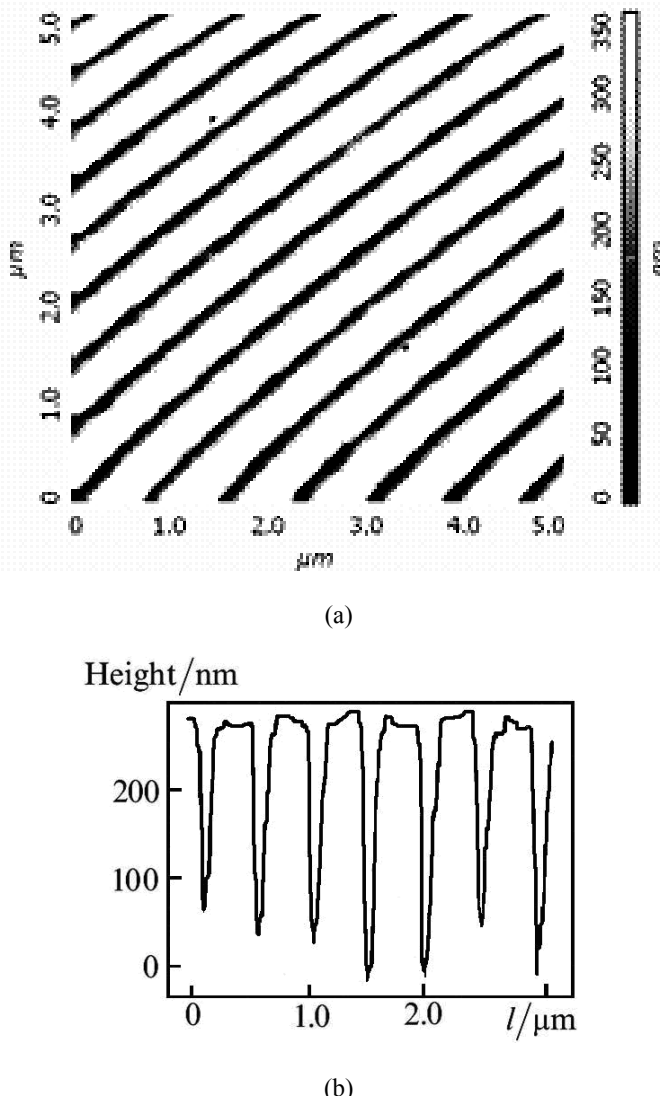


Figure 8. An AFM image (a) and a line profile (b) of a phase mask on the surface of a silica glass substrate formed by Standing Wave Excimer XeCl Pulsed Laser Lithography with reactive ion etching.

The optical transmission measurements in the zero order of diffraction have been carried out using Specord M40 Carl Zeiss Jena spectrophotometer. Also, a special measurement has been carried out using XeCl laser as a probing light source. In the latter case, the beam diameter was expanded to  $\approx 5$  mm. In order to increase the measurement accuracy, a double beam technique with a reference beam was applied. The results of the optical transmission measurements are presented in Fig. 9. Curve 1 represents the optical transmission spectrum of a flat fused silica substrate served as a reference sample. Curve 2 represents the transmission spectrum of the sample shown in Fig. 8. The minimum TCZOD took place at  $\lambda \approx 250$  nm and the antireflection properties were observed at  $\lambda_a > 630$  nm. So far, the structure obtained can serve both as a phase mask at  $\lambda \approx 250$  nm and as an antireflection coating at  $\lambda > 630$  nm at the same time.

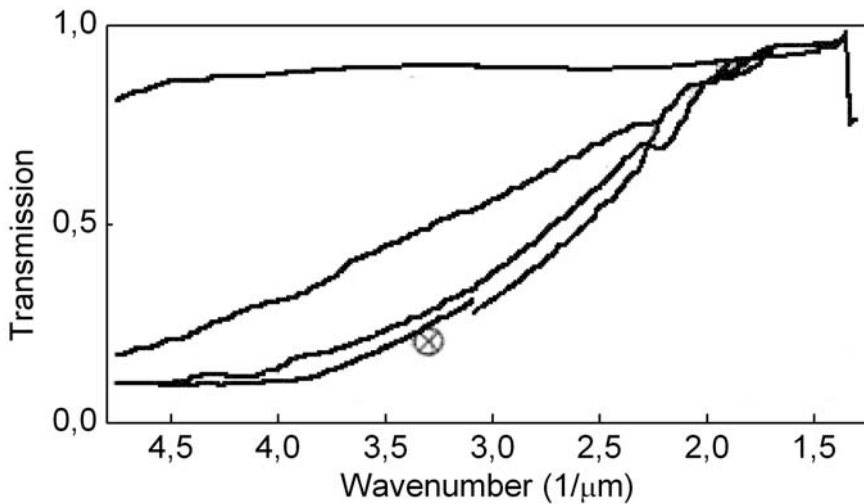


Figure 9. The optical transmission spectra of the reference sample (the initial fused silica substrate) (1) and of the phase mask formed by Standing Wave Excimer XeCl Pulsed Laser Lithography with reactive ion etching, the morphology of which is presented in Fig. 13 (2).  $\otimes$  — the result of the measurement with XeCl laser as a probing light source.

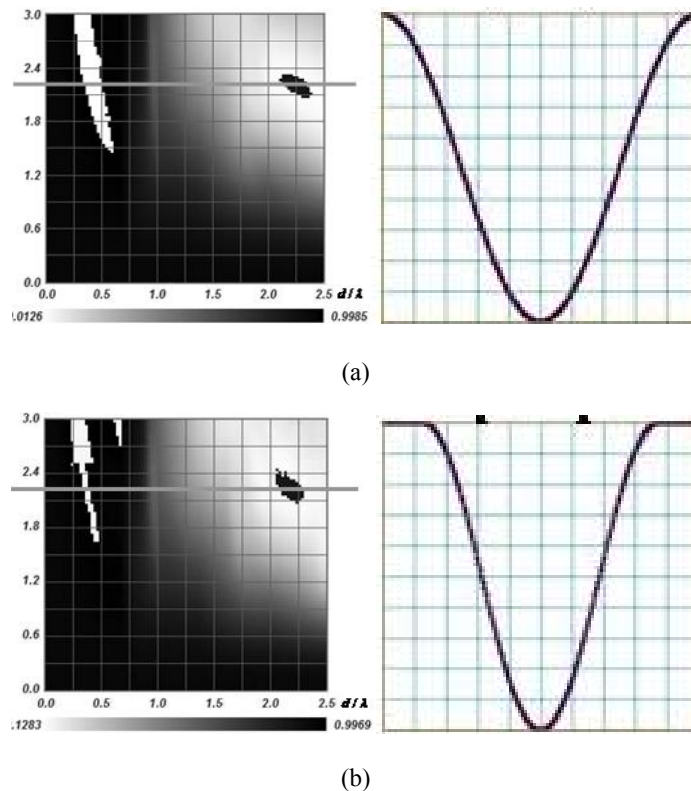


Figure 10. The calculated grayscale diagrams of the optical transmission of the goffered fused silica substrate for the sinusoidal model surface profile (a) and for the truncated sinusoidal one (b). The fields close to the maximum and the minimum transmissions are highlighted by the inverted colors.

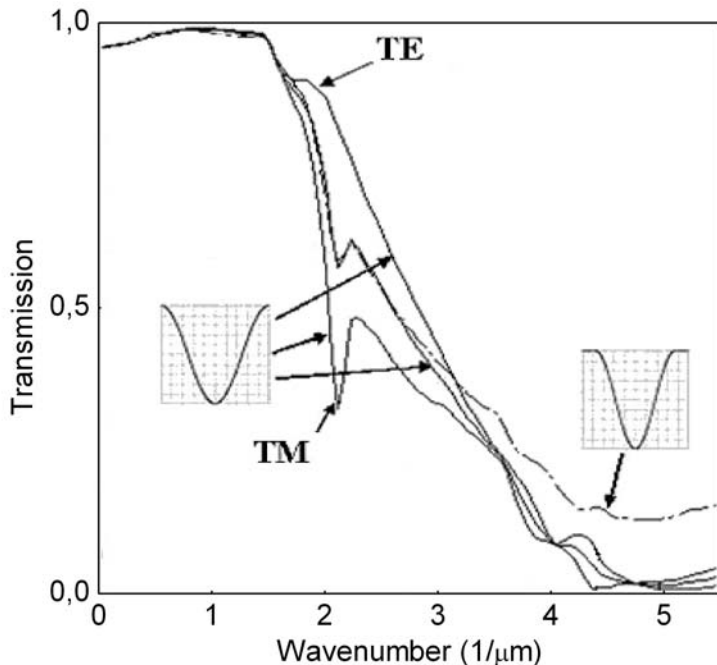


Figure 11. The calculated optical transmission of a goffered fused silica surface versus  $d/\lambda$  ratio for the relief heights providing the minimum transmission (corresponding to the gray lines in Figure 11).

The transmittance of a goffered fused silica surface has been calculated by the numerical solving of the integral equation for diffraction of a plane wave on a goffered surface [62]. The calculations were carried out for the two corrugation profiles: i) for the sinusoidal one [Fig. 10 (a)] and ii) for a truncated sinusoid [Fig. 10 (b)]. The latter was selected as a model profile to approximate the measured one presented in Fig. 8 (b). The refractive index of fused silica  $n$  was assumed to be 1.46 over the whole wavelength band which the calculations were carried out for. The optical absorption in fused silica was neglected. The refractive index of the ambient medium was assumed to be equal to unity.

The calculated dependencies of the power transmittances  $T$  (averaged over the TE and TM polarization modes of the incident light) on the dimensionless parameters of the phase mask  $h/d$  and  $d/\lambda$  are presented in Fig. 10 as the grayscale maps for the respective corrugation profiles presented nearby. The fields of the near-maximum transmittance and of the near-minimum one are denoted by the inverted grayscale palette tones for clarity. In both cases of the sinusoidal surface profile and of the profile close to the one obtained in the experiment the calculated  $T$  is close to unity within a rather wide range of the model parameters  $\lambda > d$ ,  $h > \lambda$ , and  $h > d/2$ . The general pattern of the  $T(h/d, d/\lambda)$  chart depends on the exact shape of the surface profile weakly. For the ideal sinusoidal profile  $T$  reaches its minimum ( $T \rightarrow 0$ ) when  $d/\lambda \approx 2.25$  and  $\pi h/d \approx 2.21$ . For the actual corrugation profile minimum  $T$  is greater than 0,13 and its position in the  $h/d$  —  $d/\lambda$  axes is shifted to lower  $d/\lambda$  as compared to the case of the ideal sinusoidal profile.

In Fig. 11 the calculated profiles of  $T(d/\lambda)$  along the lines shown in Fig. 10 (for the values of  $h$  providing the minimum transmission) are presented. For the structure studied in

the experiment  $d \approx 460$  nm and  $h \approx 320$  nm (i. e.  $\pi h/d \approx 2.21$ ). Curve 1 (the bold line) presents T vs  $d/\lambda$  for the sinusoidal profile and curve 2 (the dashed bold line) — for the truncated sinusoidal one. These two curves represent the optical transmission spectra averaged over the TE and the TM modes to simulate the non-polarized natural light transmission. The respective solid curves represent the results of calculations for the TE and the TM modes, respectively calculated for the sinusoidal profile. The difference between these two curves is the most pronounced near  $\lambda_1 \approx d$ , which is the cut-off wavelength for the first diffraction maximum in vacuum. There is a narrow dip in the  $T(d/\lambda)$  curve at  $\lambda_1$  for the TE mode while a smoothed step takes place for the TM one. It should be noted that the dip is seen in the averaged  $T(d/\lambda)$  curve at  $\lambda_1$  as well although the dip is less pronounced.

A rapid decreasing of T with decreasing  $\lambda$  takes place at transition from the longer wavelengths where  $T \rightarrow 1$  to the shorter ones. Another critical point important for the experimental data analysis is  $\lambda_2 = nd$ , which corresponds to the cut-off for the first harmonic in the substrate material. The calculations predict a step or even a peak in the  $T(d/\lambda)$  curves near  $\lambda_2$  for both surface profile shapes considered above and for both incident lightwave polarizations.

Having measured  $\lambda_2$ , one can determine  $n$  if the period of the grating is known. For the sample studied in the present work,  $\lambda^* = dn \approx 650$  nm,  $d \approx 460$  nm, and  $n \approx 1.46$ . This value was used in the calculations.

In Fig. 9 besides the measured optical transmission spectra of the goffered fused silica substrate the calculated ones are presented (curves 3 and 4). The latter were calculated by numerical solving of the integral equation for diffraction of light on a fused silica plate of finite thickness with a goffered front side taking into account the parasitic reflection of the transmitted light from the flat back side. The model optical transmission spectra were calculated for the truncated sinusoidal surface profile approximating the one of the experimental sample. The behavior of the measured curve indicates the domination of the TM-polarized radiation in the probing light since the dip near  $\lambda = d$  featuring the TE-polarized light is not expressed. Fitting of the measured transmission spectrum by the calculated one revealed the TE/TM ratio in the probing light to be  $\approx 1 : 4$ .

Curve 3 was calculated for  $h = 280$  nm and curve 4 — for  $h = 390$  nm. Curve 3 is consistent with the experimental transmission spectrum (curve 2) within the longer wavelength band however at shorter wavelengths the calculated transmission was greater than the measured one. On the contrary, curve 4 concedes with the measured curve 2 better as shorter wavelengths and worse at longer ones. This disagreement could be attributed to not accurate enough approximation of the actual surface profile by the model one (the truncated sinusoid). Also, the scatter of the groove depth and width was not taken into account in the calculations.

In Fig. 12 (a) and (b) an AFM image and a surface profile of a grating formed on the surface of a single crystal Si wafer are presented. The patterned area was  $\approx 6$  mm in diameter. The period of the grating  $d$  was  $\approx 460$  nm and the groove depth  $h$  was  $350 - 370$  nm. Using the formulae given above, one can estimate the cut-off wavelength for the antireflection band to be  $\lambda_1 \approx 1.5$   $\mu\text{m}$ .

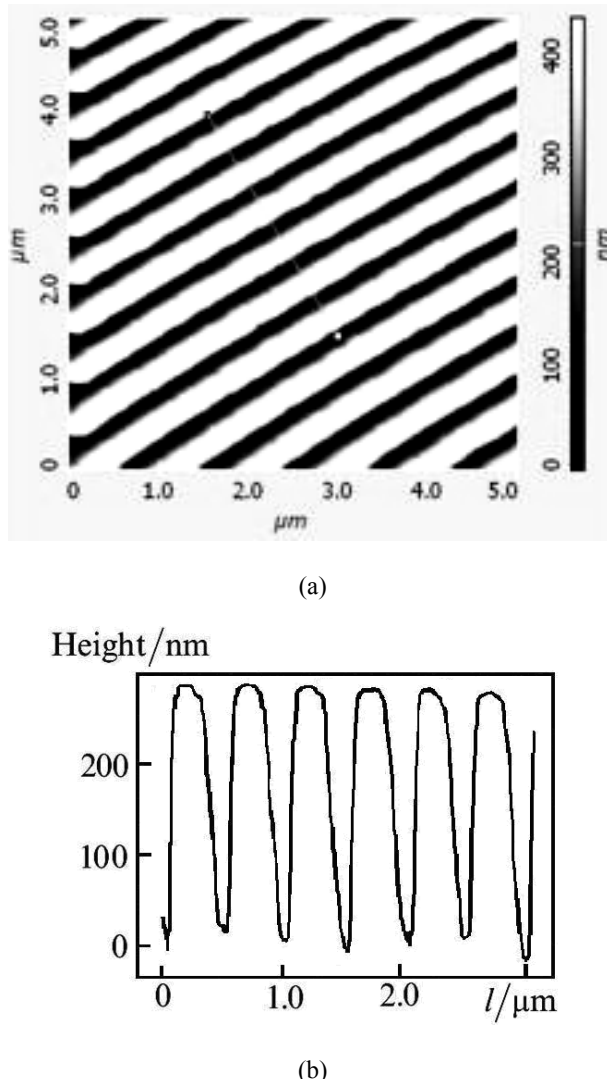


Figure 12. An AFM image (a) and a surface profile (b) of a one-dimensional grating on a Si single crystal substrate formed by Two-Beam Standing Wave Pulsed Laser Lithography using XeCl excimer laser to pattern the photoresist film on Si and subsequent  $\text{Ar}^+$  ion etching.

In Fig. 13 the IR transmission spectra of the Si wafers measured using LOMO SP-20 spectrophotometer and the calculated ones are presented. Curve 1 presents the measured transmission spectrum of a flat Si wafer. Curves 2 and 3 are the measured transmission spectra of the patterned Si wafers with  $h \approx 350$  nm and  $h \approx 400$  nm, respectively. A significant increase in the light transmission at  $\lambda > 1.5 \mu\text{m}$  has been observed in curves 2 and 3 that is in a good agreement with the rough estimate given above. More detailed analysis of the measured transmission spectra revealed the cut-off wavelength of the first harmonic in the substrate  $\lambda_2 = nd \approx 1.53 \mu\text{m}$ . From  $d \approx 466 \text{ nm}$  [see Fig. 12 (b)] one can estimate  $n \approx 3.28$ . The model transmission spectra (curves 4 and 5 in Fig. 13) were calculated just for this particular value of  $n$  and for the relief profile close to the one presented in Fig. 12 (b). The latter was approximated by a truncated sinusoid with the length of the plateaus on the tops

equal to  $d/5$  (as shown in the inset in Fig. 14) for the two values of  $h = 350$  and  $h = 400$  nm. The calculated IR transmission spectra were weighted averaged of the ones for the TE and the TM modes (5 TE : 1 TM) as in the probing light used in the IR transmission measurements. In Fig. 14 the model IR transmission spectra for the TE and the TM modes calculated for the two values of  $h = 350$  nm and  $h = 400$  nm are presented. The calculations were performed for  $\lambda > 1.15 \mu\text{m}$  where the measured transmission spectrum of the flat Si wafer was almost constant (see Fig. 13, curve 1). The optical absorption in Si was not taken into account since Si is almost transparent in the wavelength band of interest. The calculations demonstrated the IR transmission spectra to be different for the TM and TE modes essentially. On the other hand, a little difference was found between the transmission spectra calculated for  $h = 350$  nm and for  $h = 400$  nm.

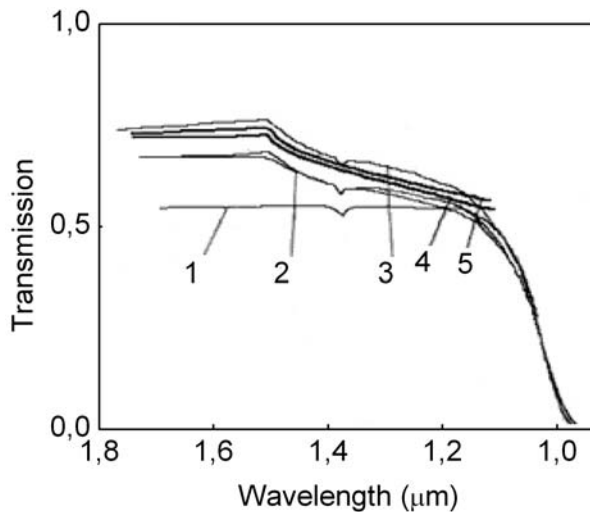


Figure 13. The measured optical transmission spectra of the flat Si wafer (1) and the ones for the goffered Si wafers (2 — 4); the calculated optical transmission spectra for the sinusoidal model surface profiles with  $h = 350$  nm (5) and with  $h = 400$  nm (6).

Concluding, a promising technology for forming the one-dimensional submicron periodic relief on fused silica substrates and on the Si ones using Standing Wave Pulsed Laser Lithography have been developed. Comparing the experimental results on the optical properties of the test samples with the results of computer simulations demonstrates applicability of the structures made by the above technology as the phase masks for the fiber and integrated optics and as the antireflection coatings.

## B. Formation of the Two-dimensional Periodic Arrays of the Nanometer Sized Pits with High Aspect Ratio in Fused Silica

In this subsection, we present the experimental results of forming the two-dimensional submicron periodic relief on the fused silica substrates by Four-Beam Standing Wave Pulsed Laser Lithography using the four beam standing wave XeCl laser radiation to expose an UV

photoresist film on the fused silica surface followed by development and wet or Ar<sup>+</sup> ion etching. The periodic arrays of the nanometer sized pits in the fused silica surface were obtained.

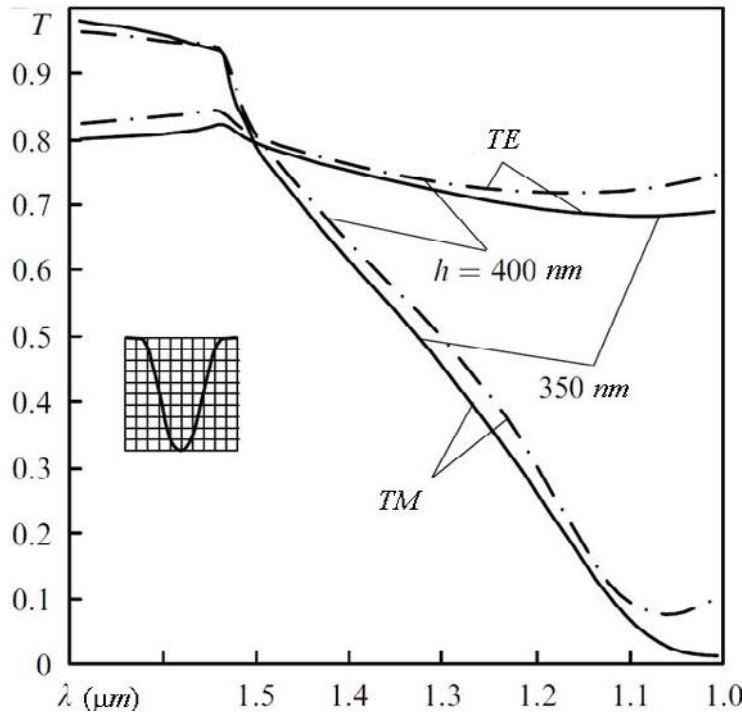


Figure 14. The calculated optical transmission spectra of a goffered Si surface for the model surface profile shown in the inset for different polarization modes.  $h$ , nm: 1 — 350; 2 — 400.

The nanometer scale periodic patterning of the fused silica surface is an important applied problem. The relevant technology could be applied to formation of various integrated optical and electronic devices. Its potential applications include, first of all, the phase masks for forming the Bragg mirrors for the planar optical waveguides [63,64,65], the planar photonic crystals, the punches for the nanoimprint technology [66,67,68] the broadband antireflection coatings [69,70] etc. [71,72]. From the technological viewpoint, the direct patterning of fused silica surface by Four Beam Standing Wave Laser Ablation would be extremely promising. However, the relatively large value of the breakdown threshold for fused silica at  $\lambda \approx 308$  nm ( $\approx 15$  J·cm<sup>-2</sup>, as had already been mentioned above) would make us to reduce the patterned area down to  $\sim 1$  mm<sup>2</sup> (at the maximum pulse energy of the laser available  $\approx 300$  mJ) and therefore to lose in the main advantage of the direct modification namely, in the productivity. So far, in order to make a periodic pattern on the fused silica surface of a considerable area ( $\sim 1$  cm<sup>2</sup>), we selected using a photoresist. We used FP-4-04-V positive UV photoresist spread over the fused silica substrates by spinning. The photoresist film thickness was 800 – 1000 nm.

After the standing wave laser irradiation with the pulse energy density of  $\approx 20$  mJ·cm<sup>-2</sup> the swellings on the photoresist surface of  $\approx 50$  nm in height have been observed by AFM [Fig. 15 (a)]. The wet development in the KOH solution resulted in appearance of the holes in

the photoresist [Fig. 12 (b)]  $\approx 1000$  nm in depth. In addition, some number of shallow pits attributed to the action of the laser beams reflected from the back surface of the substrate and interfering with the incident ones has been observed.

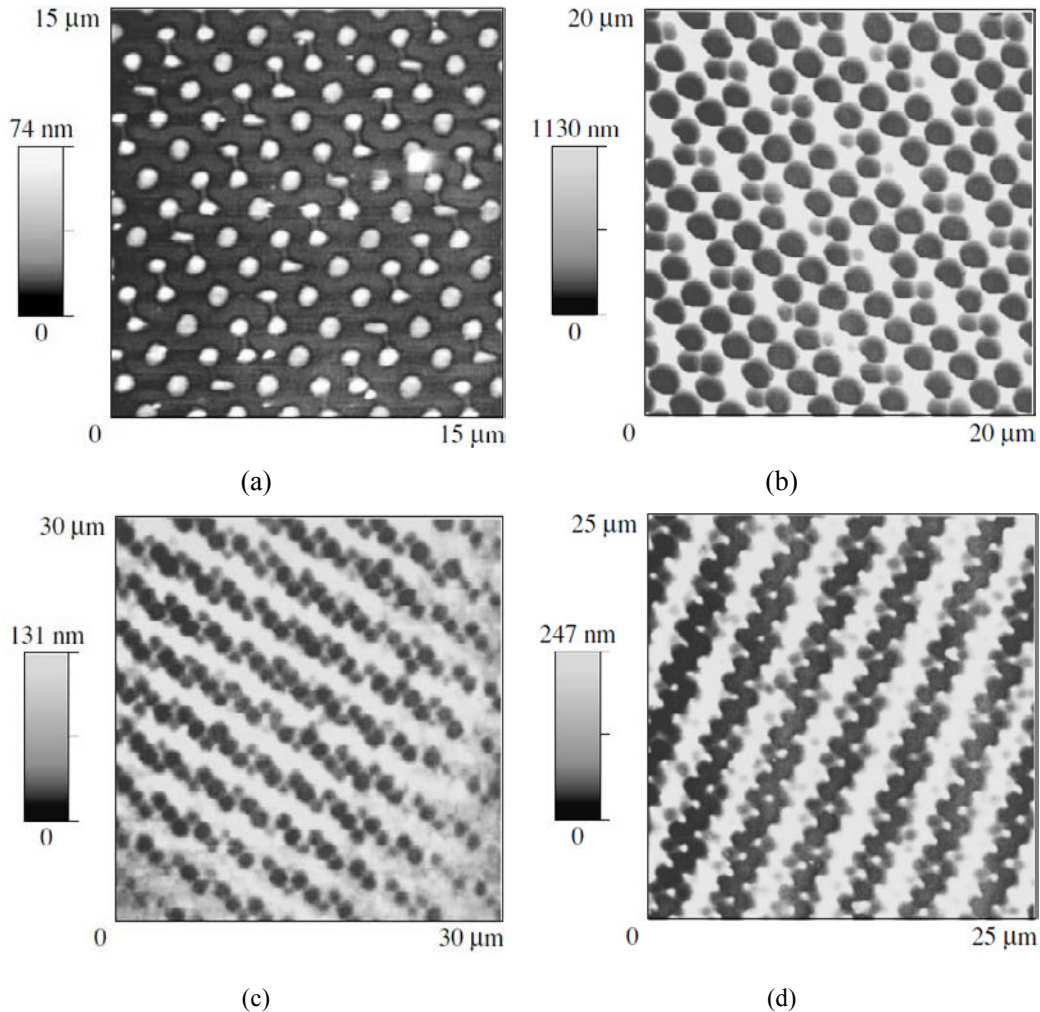


Figure 15. The AFM images of a UV photoresist film on a fused silica substrate exposed to a standing wave pulsed XeCl laser radiation with the energy density  $\approx 20 \text{ mJ}\cdot\text{cm}^{-2}$  (a) and after the development (b); the fused silica substrate after etching in hydrofluoric acid (c) and after Ar<sup>+</sup> ion etching (d).

After the wet development, the forming of the relief in the fused silica was performed by the following two methods: i) by wet etching in the hydrofluoric acid (HF) and ii) by Ar<sup>+</sup> ion etching at the dose of  $(4.4\text{--}5.0) \times 10^4 \text{ cm}^{-2}$  and the ion energy of 2.5 – 3.0 keV for 12 hours in URM 3.279.029 ion milling machine. Fig. 15 (c) presents an AFM image of the fused silica substrate surface etched through the holes in the developed photoresist film in HF. In this case, the maximum depth of the etched pits was  $\approx 100$  nm. In Fig. 12 (d) the surface of the fused silica substrate after Ar<sup>+</sup> ion etching is presented. Unlike etching in HF, in the case of ion etching the pit depth is greater than 200 nm. It was found that when radiation with the wavelength  $\lambda = 308$  nm was diffracted by the ion-etched relief,  $\approx 50\%$  of the incident light

energy was concentrated in the zero order of diffraction. Along with the estimates given in the previous subsection, these results indicate that Four Beam Standing Wave Pulsed Laser Lithography is a promising technology for production of the efficient two-dimensional phase masks on the fused silica substrate.

Concluding, a periodic relief on the fused silica surface was obtained with an UV photoresist exposed to four beam standing wave XeCl pulsed laser radiation and wet and Ar<sup>+</sup> ion etching. It should be noted that this technology could be applied not only to formation of the periodic gratings for integrated optics applications, but also to formation of the regular arrays of various semiconductors nanostructures, including the QDs [73,74]. For example, the regular arrays of the GeSi nanoislands on the Si substrates were formed from an epitaxial Si/GeSi/Si(001) quantum well (QW) heterostructure by Standing Wave Laser Lithography and dry etching [75].

#### **IV. THE TWO-DIMENSIONAL PERIODIC PATTERNING OF THE SOLID SURFACES BY DIRECT FOUR-BEAM STANDING WAVE EXCIMER LASER MODIFICATION**

In this section, the results of the investigations of direct four-beam standing wave pulsed excimer laser patterning of the metal films on Si substrates, of the synthetic polycrystalline diamond films on the single crystal diamond substrates, and of the polyimide films on the fused silica substrates are presented.

##### **A. The Fe—C Films on Si Substrates**

In this subsection, we present the results of the periodic patterning of the Fe—C films with the thickness of several tens of nanometers on the Si substrates by direct Four-Beam Standing Wave Pulsed Laser Ablation. These studies continue the series of investigations devoted to the development of the technology for the fabrication of the regular arrays of the ferromagnetic nanoparticles with the submicron period by modifications of the thin metal films by direct four beam standing wave XeCl excimer pulsed laser modification [76,77]. In this subsection, forming of the two-dimensional periodic arrays of the holes in the Fe—C films with different shape and periods in different directions are reported. The effect of the geometry of the optical scheme of the laser setup on the nanostructure morphology has been studied. It was demonstrated that the two-dimensional periodic arrays with the variable geometrical parameters of the elements can be formed by varying the orientation of the bissector of the angle between the laser beams with respect to the modified sample surface. The possibility of varying the incident angles and, so far, the period(s) of the arrays and/or the aspect ratio of the formed nanoparticles is an important advantage of the four-beam technique useful for some applications. An example of such applications is the periodic arrays of elongated ferromagnetic nanoparticles for dense magnetic data storage elements [6]. The features of the nanostructure morphology were shown to be highly sensitive to the duration and energy of the laser pulses. The conditions for the forming of near perfectly periodic two-dimensional arrays of the submicron structures in the thin Fe—C films are determined.

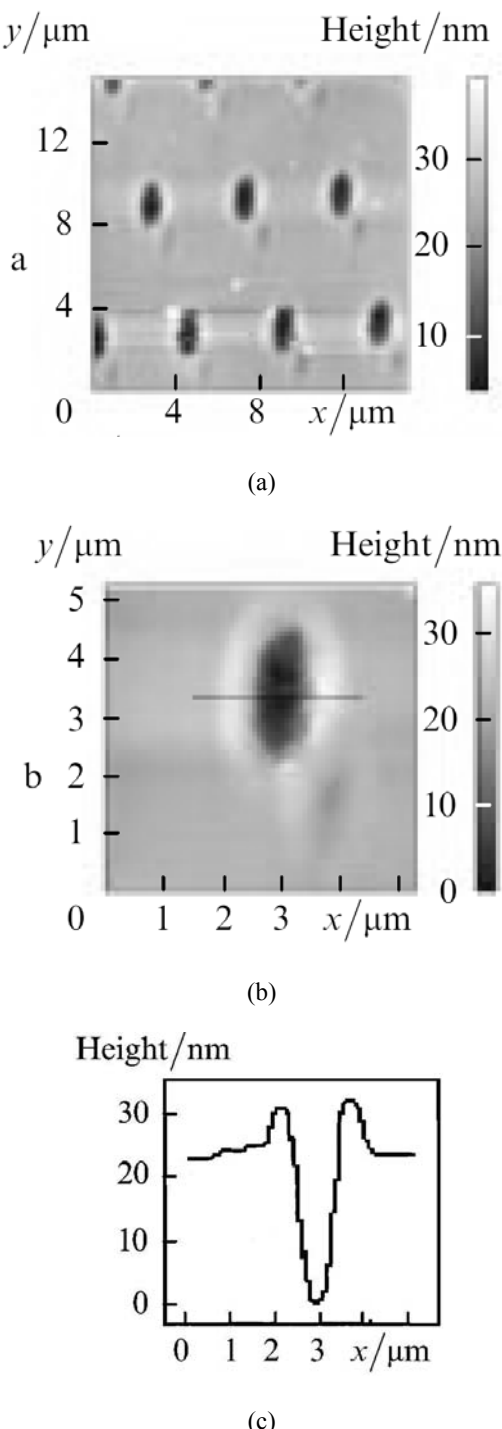


Figure 16. The AFM images (a, b) and the surface profile (c) of a Fe—C film on a Si substrate patterned by Standing Wave Pulsed Laser Ablation.

The main processes responsible for the modification of the metal film surface are usually determined by the heat release process. As it was demonstrated in Sec II, the submicron

spatial modulation of the temperature with a considerable modulation depth can be achieved when the duration of the heating pulses does not exceed several nanoseconds. This requirement dictates the choice of the operation mode of the excimer laser used for the metal film patterning.

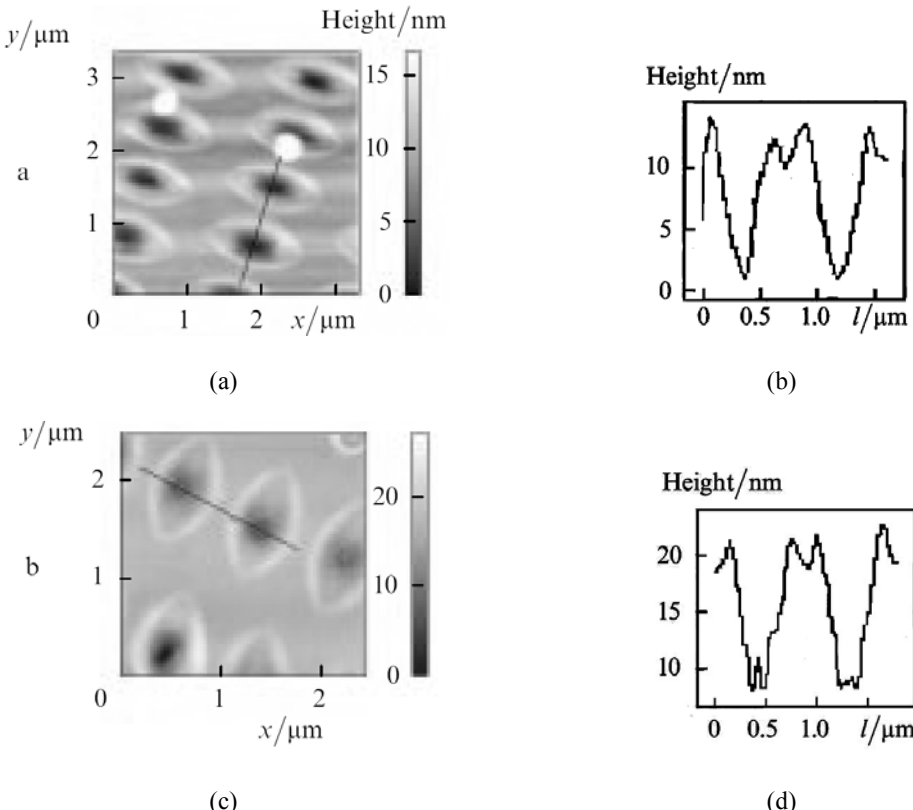


Figure 17. The effect of the laser pulse energy density on the morphology of the pits in the Fe—C film on the Si substrate patterned by Standing Wave Pulsed Laser Ablation. The laser pulse energy density,  $\text{J cm}^{-2}$ : (a, b) — 0.3; (c, d) — 0.5.

In Fig. 16 an AFM image of the surface of a Fe—C film on a Si substrate modified by a single laser pulse is presentd. Fig. 16 (c) presents a surface profile across a pit along the line shown in Fig. 16 (b). The width and the depth of the pits were  $\approx 0.8 \mu\text{m}$  and  $\approx 25 \text{ nm}$ , respectively. The ellipticity of the pits was  $\approx 0.3$  that is close to the ratio of the interference pattern periods in the respective directions. The ratio of the size of the modified area to the period of the array for typical experimental conditions was  $\approx 0.25$ .

An important feature of the pit morphology is a swell around each pit. The AFM measurements revealed that approximately  $\frac{1}{4}$  of the material removed in the process of the pits' formation was transferred to the swells. The rest material was ablated.

The morphology of the swells has been found to depend on the laser beam parameters strongly. In Fig. 17 the AFM images and the surface profiles of the pits formed at different laser pulse energy densities are presented. The samples shown in Fig. 17 (a) and (c) were formed at the laser pulse energy densities in the maxima of the interference pattern of  $\approx 0.3$

$\text{J}\cdot\text{cm}^{-2}$  and  $\approx 0.5 \text{ J}\cdot\text{cm}^{-2}$ , respectively. Both the depth and the width of the pits increased with increasing pulse energy density. In the samples shown in Fig. 17 about 20% of the material removed from the film was transferred into the swells around the pits.

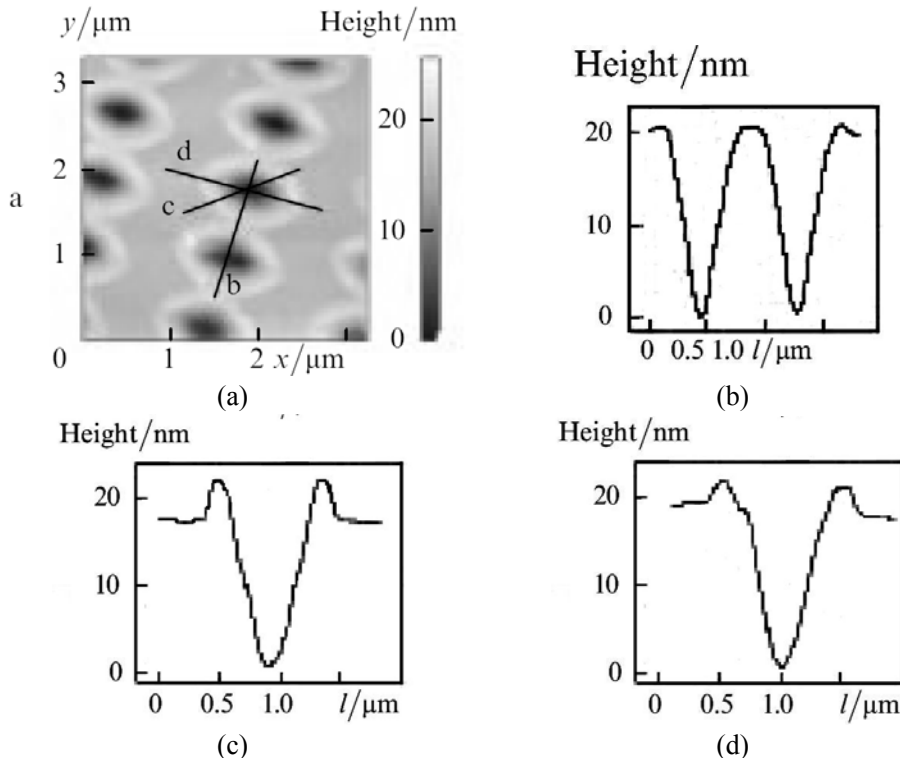


Figure 18. An AFM image (a) and the surface profiles (b — d) along the lines labeled with the respective letters in the AFM image (a) of a Fe—C film on Si substrate patterned by Standing Wave Pulsed Laser Ablation under conditions of sufficient heat dissipation during the laser pulse.

The laser pulse duration in the experiments on the modification of the samples shown in Fig. 17 was selected to be short enough ( $\approx 3 \text{ ns}$ ) to ensure a weak heat dissipation during the laser pulse. In Fig. 18 an AFM image and the surface profiles of a Fe—C film modified at the laser pulse duration of  $\approx 7 \text{ ns}$  and the pulse energy density of  $\approx 0.44 \text{ J}\cdot\text{cm}^{-2}$  are presented. Comparing the image in Fig. 18 to the ones presented in Fig. 17 one can see that the width and the height of the swells around the pits are much greater in the former case so that the swells around any two adjacent pits even tend to overlap [see Fig. 18 (b)]. The ellipticity of the pits in Fig. 18 was  $\approx 0.5$  although the ratio of the periods in the interference pattern of the laser radiation was  $\approx 0.25$ .

The results presented in Fig. 17 and Fig. 18 allowed us to estimate the heat diffusion length to be  $\approx 0.25 \mu\text{m}$  that is consistent with the results of the calculations presented in Sec. II. The maximum temperature of the film in the interference maxima can be estimated to be close to the boiling point of iron. The parameter of the two-phase destruction [52]  $\chi = (h/D)(v_l/v_v) < 0.7$  where  $h$  is the film thickness,  $D$  is the diameter of the heated area,  $v_l$  is the velocity of melt flowing out of the irradiated area, and  $v_v$  is the evaporation rate. The calculated ratio of the mass of the removed liquid metal to the mass of the removed vapor is

less than 0.3. The latter estimate agrees well with the measured ratio of the volume of the swells around the pits to the volume of the entire pit [Fig. 16 (c)]. Knowing the mean velocity of the melt rolling [52] ( $v_l \approx 250 \text{ m s}^{-1}$ ) and the pit radius ( $r \approx 0.5 \mu\text{m}$ ) one can estimate the time of rolling of the liquid metal to be  $\approx 2 \text{ ns}$  that is close to the duration of the laser pulse. Note that the role of the heat diffusion under the conditions of the experiments described here becomes much less important when both periods of the interference pattern exceed  $\approx 2 \mu\text{m}$  (see Fig. 16).

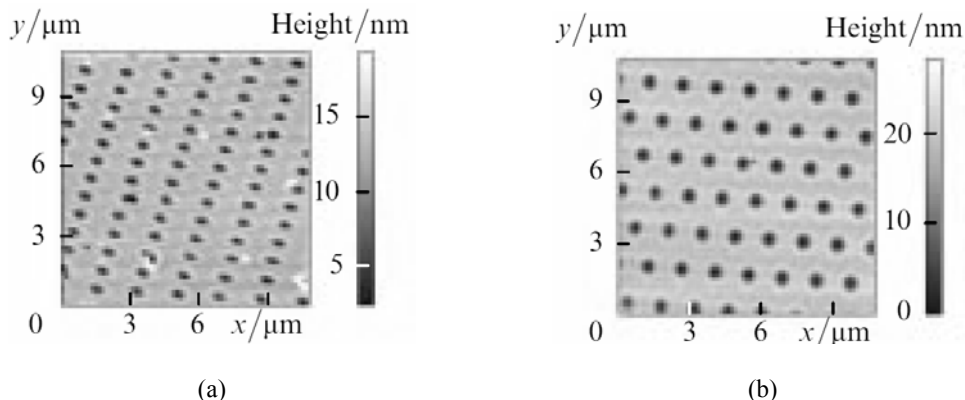


Figure 19. The AFM images of the Fe—C films on Si patterned by Standing Wave Pulsed Laser Ablation. The ratio of the periods of the interference pattern in different directions  $Q_i$ : *a* — 0.25; *b* — 0.5.

Thus, based on the study reported, we have determined the conditions necessary for the formation of the nearly perfect two-dimensional periodic submicron arrays of the pits in the Fe—C films on the Si substrates by Four Beam Standing Wave Pulsed Laser Ablation. The primary mechanism of the pits' formation was associated with the two-phase destruction of the metal film material. In Fig. 19 the AFM images of the Fe—C films on the Si substrates patterned by Standing Wave Pulsed Laser Ablation with different values of the ratio of the periods of the interference pattern in different directions  $Q_i$  are presented. It is worth to note a remarkable uniformity of the patterned film surface over the whole AFM images.

## B. The Polyimide Films on the Fused Silica Substrates

The objects to be modified were 1-μm-thick polyimide films deposited onto the fused silica substrates. The experiments on the standing wave pulsed laser modification of the polyimide films have shown that there exist two different modes of the modification subject to the pulse energy density. At the pulse energy densities less than  $100 \text{ mJ cm}^{-2}$ , the swelling of the film surface has been observed, the most probably originating from the destruction of polyimide. In Fig. 20 (a) an AFM image of the polyimide film on the fused silica substrate modified at the pulse energy density of  $\approx 100 \text{ mJ cm}^{-2}$  is presented. The height of the swellings depended on the pulse energy density and ranged from 300 to 1000 nm. At the energy densities greater than  $100 \text{ mJ cm}^{-2}$ , the regular arrays of the holes in the polyimide film have been observed. In Fig. 20 (b) an AFM image of the polyimide film modified in the

the regime specified above is presented. Such objects can be used as the resist masks in the submicron lithography. Unlike the conventional Standing Wave Lithography where such masks are formed in the two-step process (the first step is the exposing of the resist and the second one is the development), direct Standing Wave Pulsed Laser Ablation allows a single-step mask formation that is highly appreciable from the viewpoint of the cost reduction.

### C. Polycrystalline Diamond

Diamond has been being considered to be a promising wide-gap semiconductor material for decades. In particular, the ultrathin epitaxial films of the synthetic diamond are considered now to be a promising material for some advanced microelectronic applications. Diamond is featured by outstanding thermal and radiation hardness as well as by high thermal conductivity. The latter property is extremely valuable for the very large scale integrated circuits (VLSICs) where the problem of the heat sink is now a critical one.

Here it was demonstrated that a regular periodic relief can be formed on the surface of the synthetic diamonds by direct Standing Wave Pulsed Laser Ablation. The importance of this result follows from the fact that radiation and chemical hardness of diamond causes considerable problems in its processing by the standard microelectronic techniques (such as dry etching, etc.).

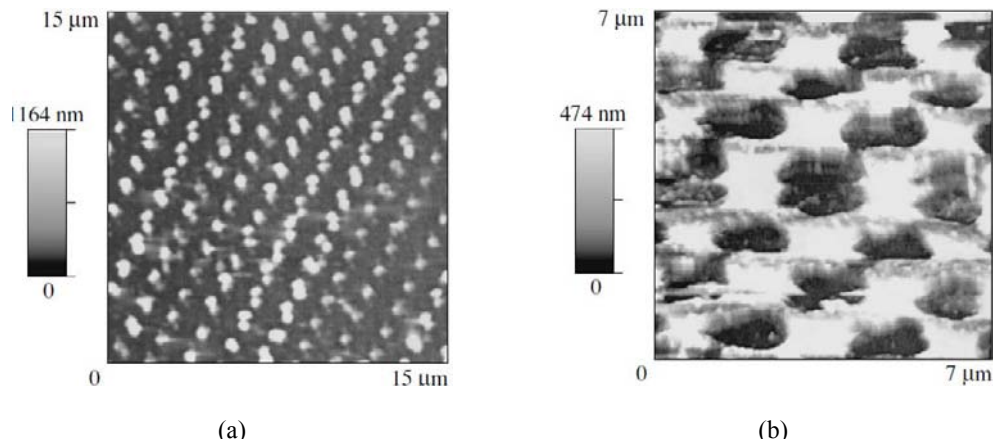


Figure 20. The AFM images of the polyimide films on the fused silica substrates modified by the four beam standing wave pulsed laser radiation at the pulse energy density of (a)  $60 \text{ mJ cm}^{-2}$  and (b)  $120 \text{ mJ cm}^{-2}$ .

In Fig. 20 the AFM images of the surface of the synthetic polycrystalline diamond exposed to the standing wave pulsed laser radiation with the energy density of  $\sim 10 \text{ J cm}^{-2}$ , which corresponds to the radiation induced damage threshold for the single crystal diamond are presented. At such an energy density, different places of the polycrystalline diamond surface exhibited different types of damage. There were the areas where the damage pattern correlated with the standing wave one well [Fig. 21 (a)]. These were the surfaces of single crystal grains in the polycrystalline diamond film. In some places, a severe damage independent on the incident radiation spatial structure has been observed [Fig. 21 (b)]. These

places were associated with the inclusions of graphite between the diamond grains highly absorbing the laser radiation while the single crystal diamond is transparent to the 308-nm radiation.

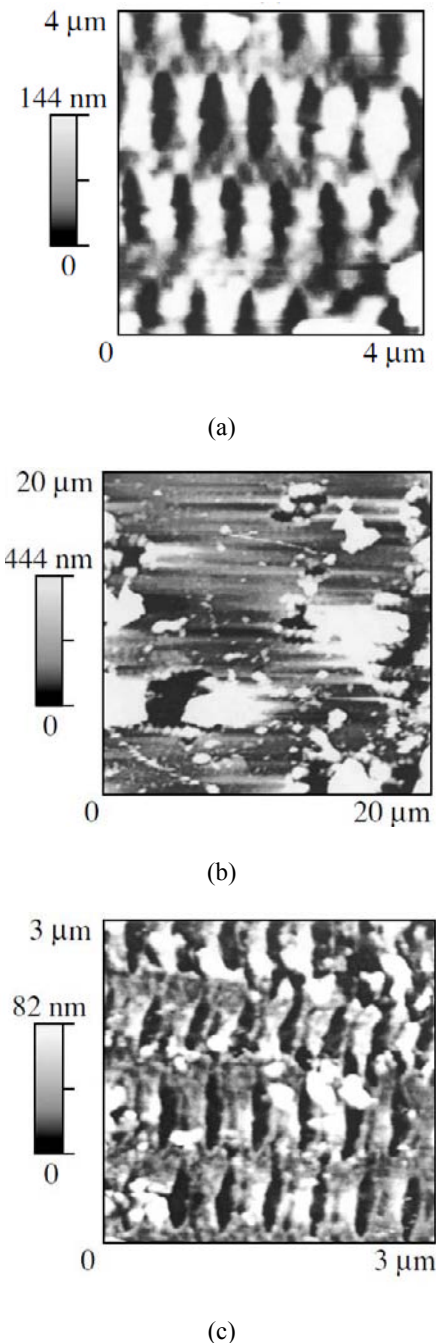


Figure 21. The AFM images of the modified surface of synthetic polycrystalline diamond: (a) the modified surface of a single crystalline grain; (b) severe damaged surface of a graphite inclusion between the crystalline grains, and (c) at the boundary between two adjacent single crystal grains. The pulse energy density was  $\approx 10 \text{ mJ/cm}^2$ .

In Fig. 21 (c) a fragment of the modified polycrystalline diamond surface between the single crystal grains where the absorbing graphite layer and, so far, the severe damage were absent is presented.

In conclusion, it was demonstrated that using the direct Four Beam Standing Wave Pulsed UV Laser Ablation, one can form a two-dimensional periodic relief with a submicron period on the diamond surface. In particular, this technology could be applied for secret marking of the diamonds used in jewelry.

## V. SELF ASSEMBLING OF THE PERIODIC ARRAYS OF THE NANOMETER SIZED SEMICONDUCTOR ISLANDS STIMULATED BY STANDING WAVE UV LASER RADIATION

In this section, we present the results on the formation of the two-dimensional regular periodic arrays of the semiconductor surface nanoislands formed by self-assembling stimulated by four coherent interfering pulsed laser beams incident onto the silicon and gallium arsenide single crystal wafers. The lateral size of the islands ranged from 60 to 100 nm and the height from 6 to 12 nm that was 5 – 10 times smaller than the period(s) of the standing wave. The island formation was attributed to the effect of the elastic strain at the crystal surface induced by the non-uniform heating of the substrate by the standing wave laser radiation. The effect of the laser beam parameters including the polarization of the interfering laser beams on the resulting nanoisland array morphology has been investigated. It has been already mentioned above (see Sec. II) that the distribution of radiation in the standing wave field depends on the polarization of interfering laser beams significantly. The analytical expressions and the computer calculations of the spatial distribution of the standing wave intensities for various polarization configurations can be found in [45]. In our experiments, both the TE—TE configuration and the TE—TM one had been explored. The conditions for obtaining the uniform nearly perfectly periodic arrays of Si and GaAs nanoislands on the Si(001) and GaAs(001) substrates, respectively, had been determined.

### A. Silicon

The results presented in this subsection were obtained using single laser pulses with the duration of 10 ns and the energy density of  $(1.0 - 1.5) \text{ J} \cdot \text{cm}^{-2}$ . In Fig. 22 a typical AFM image of Si(001) surface patterned by four-beam standing wave UV pulsed laser radiation in the TE—TE polarization configuration is presented. The standing wave pattern in this case corresponds to the two series of stripes perpendicular to each other. The AFM image in Fig. 22 (a) as well as the two surface profiles along the lines 1 and 2 in the main image [Fig. 22 (b) and (c), respectively] demonstrate the nanoislands with the diameter of 40 – 60 nm to form in the maxima of the standing wave intensity. The islands were separated by the almost flat regions of the substrate with the dimensions of  $\approx 30 \times 150 \text{ nm}^2$ . An essential feature of the self-assembling in this particular regime is the appearance of the pits of various shapes and dimensions near the islands. The pits have lateral dimensions more than 30 nm and the depth

of 4–6 nm. As can be seen in Fig. 22, the pits are located at different sides of the neighboring islands.

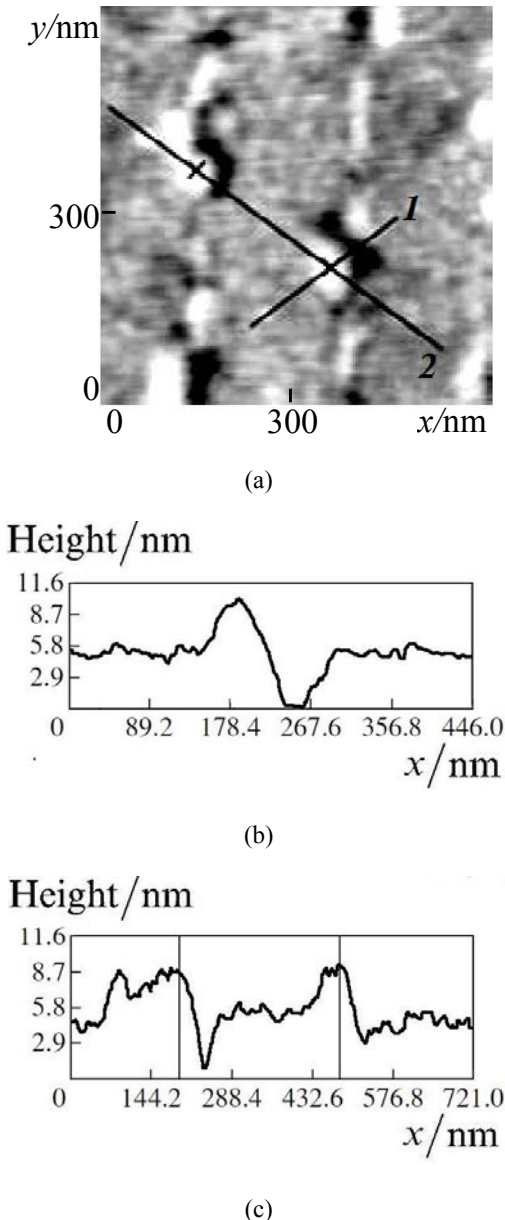


Figure 22. An AFM image (a) and the surface profiles (b, c) of Si(001) surface patterned by the four-beam standing wave UV pulsed laser radiation in the TE–TE polarization configuration.

This pattern of modification of the crystal surface differs significantly from the results of the standing wave laser modification of the amorphous materials (see Sec. IV.A) where the symmetric swells were formed around the pits [6]. A substantially different character of self-assembling was observed in the case of using the beams with the TE–TM polarization configuration. In this case, the sites of maximum intensity are well localized and surrounded

by the lines of zero intensity. As a result of such an intensity distribution, the self assembled Si nanoislands are better defined in this case.

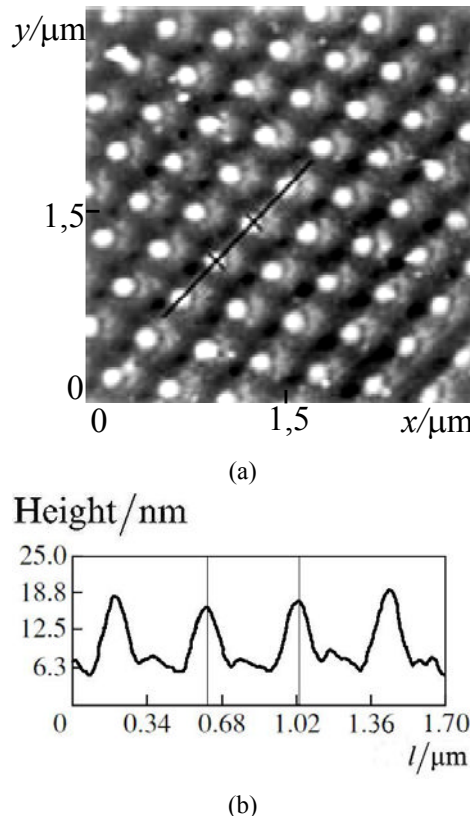


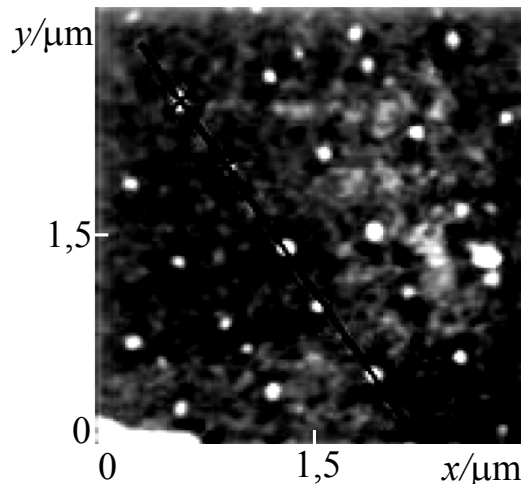
Figure 23. An AFM image (a) and a surface profile (b) of Si(001) surface patterned by the four-beam standing wave UV pulsed laser radiation in the TE—TM polarization configuration.

In Fig. 23 a typical AFM image and a surface profile of Si(001) surface patterned in the TE—TM polarization configuration is presented. The AFM image revealed a nearly perfect two-dimensional periodic array of islands with the diameter below 100 nm and the height of  $\approx 12$  nm. It should be noted that all islands in the array are located at the same side of the adjacent pits that indicates that the conditions of diffusion for silicon atoms were the same over the whole AFM image.

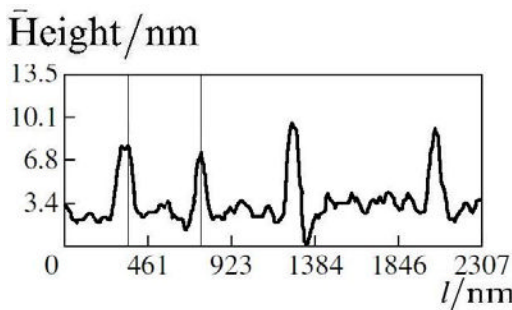
## B. Gallium Arsenide

In Fig. 24 an AFM image of GaAs(001) single crystal surface patterned by four-beam standing wave UV pulsed laser radiation in the TE—TM polarization configuration is presented. The islands observed on the GaAs surface had the lateral dimensions of  $\approx 60$  nm and the height of  $\approx 7$  nm. The surface profile showed that the positions of the islands with respect to the interference pattern knots scattered within  $\approx 30$  nm.

The results presented above demonstrate that the minimum lateral size of the islands is 5 – 10 times smaller than the period of the standing wave of the laser radiation. In the case of laser modification of the amorphous or polycrystalline films [15, 78], the typical size of the region of modification usually amounts to 50% of the standing wave period. This significant difference between the results of the laser modification of the single crystal and of the amorphous surfaces leads to a conclusion that the resulting surface morphology in the laser modification of single crystals is affected by the inhomogeneous laser-induced strain field arising from the local heating of the crystal surface by the standing wave radiation. This heating results, first, in the thermal expansion of the near-surface layers inducing the elastic stress, and second, in the stimulation of the diffusion of the atoms of the modified material in the elastic strain field developed in the surface layer of the crystalline substrate. The simultaneous action of the two factors listed above makes possible the formation of the nanoislands with the sizes significantly smaller than the standing wave period. Note that the island formation can not be explained by the effect of the thermal threshold for the laser modification only since the nanoisland size remained almost the same when the energy density of the laser radiation increased two times. So far, such a modification is possible in the presence of the surface stress only.



(a)



(b)

Figure 24. An AFM image (a) and a surface profile (b) of GaAs(001) surface patterned by four-beam standing wave UV pulsed laser radiation in the TE—TM polarization configuration.

### C. InGaAs/GaAs Epitaxial Heterostructures

In this subsection, the results of the four beam standing wave pulsed laser modification of the strained GaAs/InGaAs/GaAs quantum well (QW) heterostructures are presented. These studies were the further development of the ones described in the previous subsections and were aimed at confirming the suggestion of the laser-induced local thermal expansion of the surface as the key driving force for the nanoisland formation. In these purposes, the GaAs/InGaAs/ GaAs heterostructures where the elastic stress was present *ab initio* were grown on GaAs(001) substrates by Molecular Beam Epitaxy (MBE).

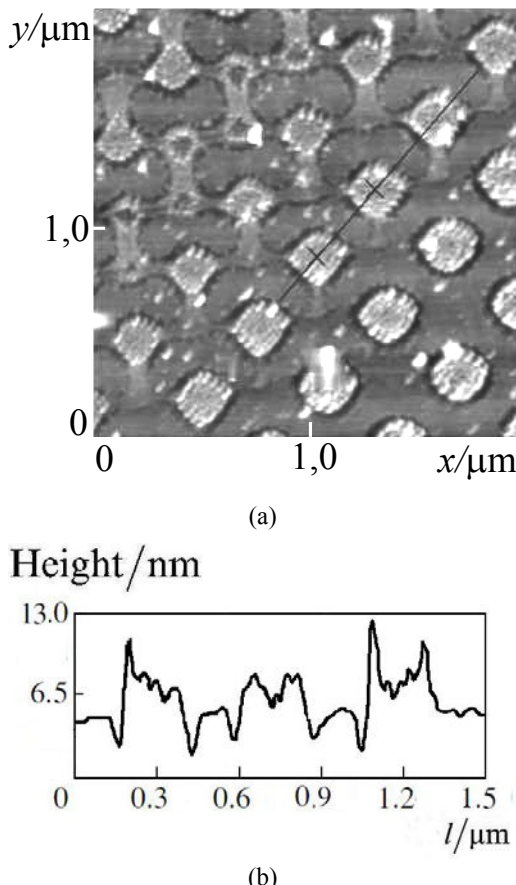


Figure 25. An AFM image (a) and a surface profile (b) of the GaAs/InGaAs/GaAs heterostructure surface modified by four beam standing wave XeCl pulsed laser radiation.

The experiments on modification of the GaAs/InGaAs/GaAs(001) epitaxial heterostructures were carried out on the four samples. The  $n$ -GaAs(001) epi-ready substrates were used for the epitaxial growth by all-solid-source MBE. After the thermal removing of the native oxide from the GaAs substrate surface in the As flow, the 100 nm GaAs buffer layers were grown at 580°C followed by deposition of the 3 nm thick  $\text{In}_{0.35}\text{Ga}_{0.65}\text{As}$  QWs at 520°C. Finally, the GaAs cap layers of 5, 10, 20, and 40 nm in thickness were grown at the same temperature as the  $\text{In}_{0.35}\text{Ga}_{0.65}\text{As}$  layer. The conditions of the four beam laser

modification were the same as in the experiments on modification of the single crystal Si and GaAs wafers (see Sec. V A and B for details) but the laser pulse duration was varied within the range from 10 to 15 ns.

Within the accuracy of the AFM measurements, the general pattern of the modified surface morphology did not depend on the GaAs cap layer thickness. Below the results of the laser modification of the heterostructure with the 20 nm thick cap are presented.

When the TE—TM polarization configuration was selected, the intensity distribution in the plane of the sample surface can be treated in the first-order approximation as the sinusoidal one along both directions [45]. In Fig. 25 (a) and (b) an AFM image and a surface profile of the GaAs/InGaAs/GaAs heterostructure surface modified by four beam standing wave pulsed laser radiation with the pulse energy density of  $\approx 1.5 \text{ J}\cdot\text{cm}^{-2}$  are presented. Note that in this experiment the bissector between the incidence angles of one pair of the beams was tuned off the normal to the sample surface. This resulted in the modulation of the intensity in the standing wave pattern maxima in the diagonal direction from the upper left corner of the AFM image to the lower right one; the modulation period was doubled relative to the basic period of the standing wave pattern. That is why the corresponding modulation of the surface modification pattern can be observed in the AFM image in Fig. 25 (a).

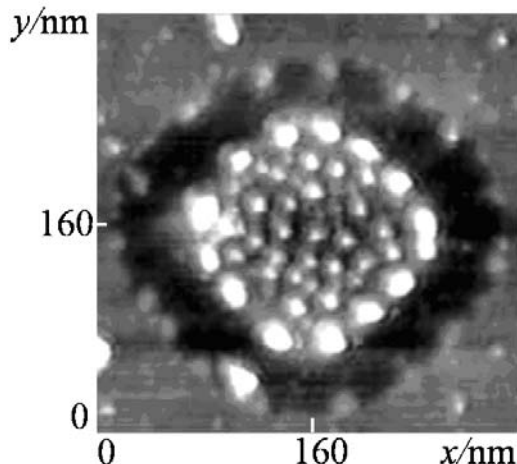


Figure 26. A typical AFM images of a modified area on the surface of GaAs/InGaAs/GaAs heterostructure.

In Fig. 26 a typical AFM image of a modified area on the GaAs/InGaAs/GaAs heterostructure surface is presented. Let us consider the following two features of the morphology of the modified heterostructure surface. First, the outer boundary of the modified areas (corresponding to the interference maxima) had a nearly rectangular shape, while the calculated intensity distribution near the standing wave maxima had a circular symmetry. The second important feature is that a considerable number of islands appeared inside the modified areas, whereas no islands had been observed between these ones. It should be mentioned here that the general pattern of the modification on the surface of the strained heterostructure differs drastically from the one of the single crystal GaAs and Si as well as from the one of the amorphous films. In the case of the crystalline semiconductors, the single islands appeared near each interference maximum and a pit in the substrate was formed

straight in the maxima (see Sec. V A and B). This was considered as the evidence of the crystalline material transfer. In the case of the amorphous metal films, the pits on the film surface surrounded by the swells (like in the case of an explosion) were formed (see Sec. IV A).

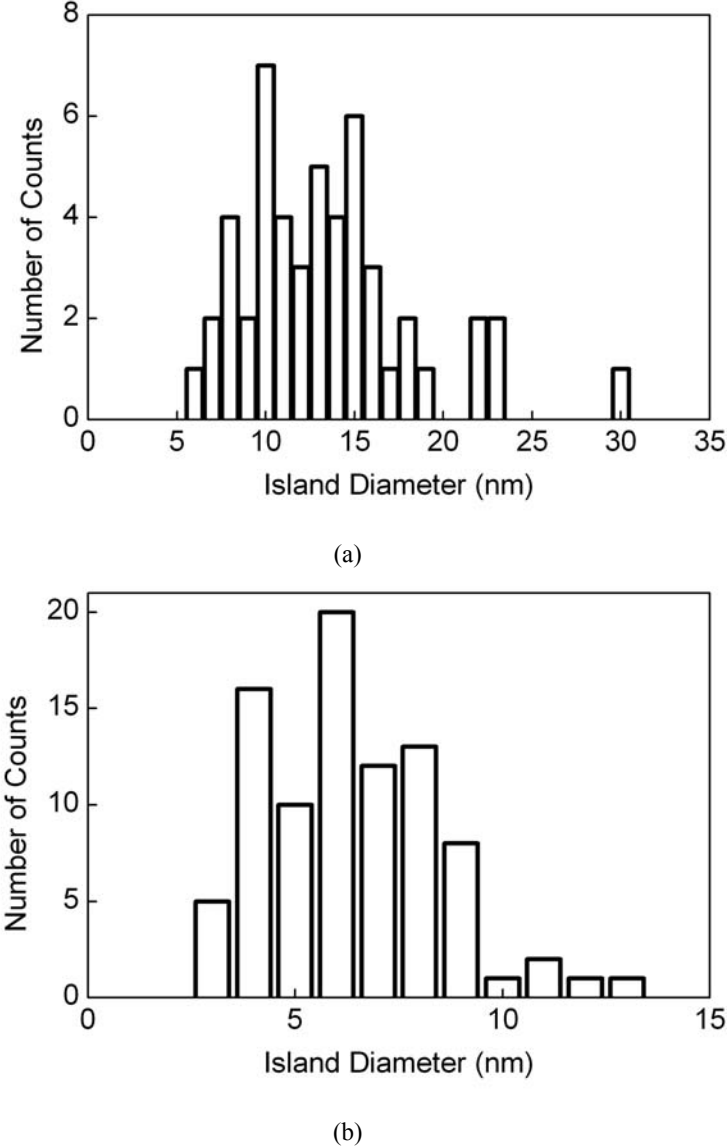


Figure 27. The histogram of the lateral size distribution for the peripheral (large) islands (a) and of the internal (small) ones (b) on the surface of GaAs/InGaAs/GaAs QW heterostructure modified by four-beam standing wave pulsed XeCl laser radiation in the TE—TM polarization configuration.

The statistical analysis of the island sizes in the AFM images shown in Fig. 26 revealed a bimodal island size distribution. The sizes of the islands located in the periphery of the modified area (7 to 20 nm in diameter) differed significantly from the sizes of the islands located inside this area (3 to 8 nm, respectively). The size distributions of the peripheral

(large) islands and of the internal (small) ones are presented in Fig. 27 (a) and (b), respectively. The surface densities of the peripheral islands and of the internal ones are close to  $1 \times 10^{10} \text{ cm}^{-2}$  and to  $5 \times 10^{10} \text{ cm}^{-2}$ , respectively.

From the experimental data presented here, one can make the following conclusions regarding the island formation process. First of all, under the conditions of these experiments, the ablation (i.e., removing the material from the processed surface) was absent. So far, the resulting surface morphology could be attributed to the material transfer on the surface only. The lateral sizes of the islands were 20 to 60 times smaller than the standing wave period(s). These sizes of the islands cannot be determined by a pure thermal effect since similar islands were obtained when the laser pulse energy density was increased two times.

As in the case of the laser modification of the single crystal GaAs and Si, understanding the modification process of the strained heterostructures requires consideration of the surface stresses as the driving forces of the nanoislands' self assembling. The process of island formation during the four-beam standing wave laser modification can be understood in terms of the Stranski-Krastanow growth. It is well known that the surface of a single crystal is in a stressed state. These surface stresses are related to the difference in the coordination of the atoms located in the bulk and on the surface of the crystal. The higher the quality of the single crystal surface, the greater the magnitude of surface stresses. Actually, the stresses relax at the defects of the single crystal surface that arise during growth and processing of a single crystal substrate. Any defects of any type known in crystallography can act as the stress relaxation centers. In this case, the spatial scale of the stress variations across the single crystal substrate surface depends on the quality of the substrarte. In the case of the substrate of high enough quality, the stress relaxation scale can be commensurable with the substrate dimensions. This is exactly what has been observed for the Si and GaAs single crystal substrates.

Unlike the homogeneous single crystals, the primary origin of the surface stresses in the heteroepitaxial films is the lattice mismatch between the film and the substrate. For InAs, the lattice constant  $a_1 \approx 0.60584 \text{ nm}$  and for GaAs  $a_2 \approx 0.56534$  (at 293K). The spatial scale of the stress variations is determined by the beats between the two lattice constants  $a_1$  and  $a_2$ . In this approximation, one can easily obtain an expression for the minimum period of the spatial strain fluctuations to be  $2a_1a_2/(a_1 - a_2)$ . This estimate yields a value of  $\approx 17 \text{ nm}$ . In the samples used in the experiments described here, the averaged lattice constant of the  $\text{In}_{0.35}\text{Ga}_{0.65}\text{As}$  alloy was  $\approx 0.57952 \text{ nm}$  (at 293K) that yields the period of the spatial variation of the elastic strain to be  $\approx 51 \text{ nm}$ . This value agrees fairly well with the averaged distance between the islands (presented in Fig. 26) measured experimentally by AFM. Such a coincidence can be treated as an additional argument that surface stresses play a key role in the standing wave laser assisted self assembling observed in the experiments described here. In this scope, the scatter in the distances between the adjacent islands can be attributed to the local variations in the InGaAs alloy composition.

## CONCLUSION

The results of the studies presented in this article demonstrate the capabilities and versatility of Four Beam Standing Wave XeCl Pulsed Excimer Laser Lithography in the periodic patterning of various materials. These results supported by the theoretical

calculations have demonstrated that using the four-beam interference of the high-power coherent pulsed UV laser radiation one can form the nearly perfect periodic arrays of the nearly identical surface nanoobjects in an extremely wide range of the material systems. The lateral dimensions of these nanoobjects as well as the array periods in both directions can be controlled precisely by adjustment of the optical scheme of the interference (namely, of the angles of incidence of the laser beams onto the illuminated area) and of the beam parameters (such as the beam polarizations, the pulse energy, and the pulse duration). For the XeCl laser with the emission wavelength  $\lambda = 308$  nm the minimum array period is  $\approx 150$  nm and as low relative uncertainty in the array period as  $\sim 10^{-4}$  is achievable.

Although E-beam Lithography, X-Ray Lithography, and even Extreme UV Optical Lithography (again, the two latter techniques use the photomasks recorded by E-Beam Lithography) provide potentially much lower limits of the critical dimensions, the typical element size range of the UV Standing Wave Laser Lithography of 100 to 1000 nm covers a wide range of applications, first of all, in the integrated optics of the visible and of the near IR wavelength bands. Next, E-Beam Lithography is featured by infinite flexibility (i.e., any desired picture can be drawn by the electron beam scanning). This feature is inherited by X-Ray and UV Lithographies along with the photomasks. In this scope, the capabilities of the Standing Wave Lithography are limited to the rather simple periodic patterns. However, in this particular case, Standing Wave Lithography takes an important advantage of the array period reproducibility. The last (but not least) Standing Wave lithography is much more cost effective compared to the other techniques listed above, especially when the direct surface modification is feasible. The studies presented in this article demonstrate that even such hard material as diamond can be patterned using direct Standing Wave Pulsed Laser Ablation. This method can be applied not only in the semiconductor diamond technology but also for secret marking of the diamonds used in jewelry for security and customs purposes, etc.

The process of modification of the solid surfaces in the direct Standing Wave Pulsed Laser Modification is governed by the thermal processes near the surface. The theoretical investigations of the heat transfer in the thin films on the heat conducting substrates heated by a spatially periodic pulsed heat source helped us to find the conditions for the forming of the arrays of the surface nanostructures with necessary morphological parameters in various film and substrate material systems.

Application of the four-beam standing wave laser radiation to stimulate the self assembling of the semiconductor nanoislands opens new prospects in control of the self-assembling process and therefore in increasing the size uniformity of the nanoislands and the degree of their ordering in the substrate plane. The results of our experiments demonstrated the possibility of controlled self-assembling of the two-dimensional arrays of the nanoislands on the surface of single crystal Si(001) and GaAs(001) stimulated by pulsed standing wave UV laser radiation. Self assembling mechanism of the nanoisland formation provides the small nanoisland sizes down to  $\approx 40$  nm that is  $\sim 10$  times smaller than the standing wave period while the typical size of the nano relief features produced by direct Standing Wave Laser Ablation is  $\approx 1/4$  of the array period. So far, utilization of self-assembling reduces the lower limit for the size of the nanoislands formed by Standing Wave Laser Modification drastically. On the other hand, the standing wave pattern dictates the spatial arrangement of the nanoislands on the substrate and provides the uniform islands to arrange in nearly perfect two-dimensional superlattice. One can control both periods of this superlattice by adjusting

the angles of incidence of the laser beams onto the patterned substrate. Also, the resulting nanoisland array morphology has been demonstrated to depend on the polarization of the interfering laser beams that opens additional opportunities for controlling the self-assembling process. The experiments on the four-beam standing wave pulsed laser stimulation of the self-assembling on the surface of GaAs/InGaAs/GaAs(001) strained quantum well heterostructures demonstrated that the interaction of the intrinsic strain field with the standing wave induced thermal one results in a rather complex pattern of the surface nanostructures.

It should be stressed here that the four-beam laser setup could be combined quite easily with any growth chamber for MBE as well as for Vapor Phase Epitaxy just passing the laser beams through the appropriate viewports. Thus, standing wave assisted self assembling can be performed *in situ*, and the resulting nanoisland arrays could be built in any multilayered structure including the device ones. Taking into account all the above, we can conclude that the four beam standing wave laser assisted self-assembling is a very promising technique for various applications in nanotechnology.

## ACKNOWLEDGMENTS

The studies presented in this article have been supported in part by European Community FP-6 IST-4 No.027976 “Development of Lithography Technology for Nanoscale Structuring of Materials Using Laser Beam Interference (DELILA)”, by Russian Academy of Science (Division of Physics Sciences) under Nonlinear Optics of Unique Laser Systems Program, by Russian Foundation for Basic Research (L-EN 96-15-96594, 98-02-16306, and 02-02-17139), and by Joint Russian – American Program “Basic Research and Higher Education”(BRHE) funded in parity by US Civilian Research and Development Foundation (CRDF) and by Ministry of Education, Russian Federation (REC-NN-001).

## REFERENCES

- [1] Zaidi, S. H., Brueck, S. R. J., Hill, T. & Shagam, R. N. (1998). *Proc. SPIE*, 3331, 371-382.
- [2] Brueck, S. R. (2005). *J. Proc. IEEE*, 93, 1704-1721.
- [3] Zhang, L., Sugden, K., Williams, J. A. R., Bennion, I., Reid, D. C. J. & Ragdale, C. M. (1995). *Opt. Lett. A*, 20, 1927-1929.
- [4] Askins, C. C., Tsai, T. E., Williams, G. M., Putnam, M. A., Bashkansky, M. & Friebel, E. (1992). *J. Opt. Lett.*, 17, 833-835.
- [5] Luryi, S., Xu, J. & Zaslavsky, A. (2007). *Future Trends in Microelectronics: Up the Nano Creek*. Wiley-IEEE Press: Hoboken, NJ, 14.
- [6] Bredikhin, V. I., Verevkin, Yu. K., Daume, E. Ya., Kuznetsov, S. P., Mal'shakova, O. A., Petryakov, V. N., Vostokov, N. V. & Polushkin, N. I. (2000). *Quantum Electron.*, 30, 333-339.
- [7] Savas, T. A., Farhoud, M., Smith, H. I. & Ross, C. A. (1999). *J. Appl. Phys.*, 85, 6160-6165.

- [8] Fernandez, A., Bedrossian, P. J., Baker, S. L., Vernon, S. P. & Kania, D. R. (1996). *IEEE Trans. Magn.*, **32**, 4472-4475.
- [9] Smith, H. I. (2001). *Phys. E*, **11**, 104-109.
- [10] Zheng, M., Yu, M., Liu, Y., Liou, S. H., Sellmyer, D. J., Petryakov, V. N., Verevkin, Yu. K., Polushkin, N. I. & Salashchenko, N. N. (2001). *Appl. Phys. Lett.*, **79**, 2606-2608.
- [11] Phillips, H. M., Callaham, D. L. & Sauerbrey, R. (1992). *Appl. Phys. A*, **54**, 158-163.
- [12] Ezaki, M., Kumagai, H. & Toyoda, K. (1993). *Jpn. J. Appl. Phys.*, **32**, 1308-1315.
- [13] Pelissier, S., Biauc, D., Andrews, M. P., Najafi, S. I., Tishchenko, A. V. & Parriaux, O. (1999). *Appl. Opt.*, **38**, 6744-6746.
- [14] Fernandez, A., Nguyen, H. T., Britten, J. A., Boyd, R. D., Perry, M. D., Kania, D. R. & Hawryluk, A. M. (1997). *J. Vac. Sci. Technol. B*, **15**, 729-734.
- [15] Verevkin, Yu. K., Bronnikova, N. G., Korolikhin, V. V., Gushchina, Yu. Yu., Petryakov, V. N., Filatov, D. O., Bityurin, N. M., Kruglov, A. V. & Levichev, V. V. (2003). *Tech. Phys.*, **48**, 757-761.
- [16] Verevkin, Yu. K., Klimov, A. Yu., Gribkov, B. A., Petryakov, V. N., Koposova, E. V. & Olaizola, S. M. (2008). *Quantum Electron.*, **38** (*in press*).
- [17] Brundrett, D. L., Gaylord, T. K. & Glytsis, E. N. (1998). *Appl. Opt.*, **37**, 2534-2538.
- [18] Xu, Y., Sun, H., Ye, J., Matssuo, S. & Misawa, H. (2001). *J. Opt. Soc. Am. B*, **18**, 1084-1090.
- [19] *Nano-optoelectronics: Concepts, Physics, and Devices*. Grundmann, M., Ed., Springer: Berlin - Heidelberg, 2004.
- [20] Ledentsov, N. N., Ustinov, V. M., Shchukin, V. A., Kop'ev, P. S., Alferov, Zh. I. & Bimberg, D. (1998). *Semicond.*, **32**, 343-361.
- [21] Pchelyakov, O. P., Bolkhovityanov, Yu. B., Dvurechenskii, A. V., Sokolov, L. V., Nikiforov, A. I., Yakimov, A. I. & Voigtländer, B. (2000). *Semicond.*, **34**, 1229-1247.
- [22] Teichert, C. (2002). *Phys. Rep.*, **365**, 335-369.
- [23] Cerofolini, G. F., Arena, G., Camalleri, M., Galati, C., Reina, S., Renna, L., Mascolo, D. & Nosik, V. (2002). *Microel. Eng.*, **81**, 405-429.
- [24] *Semiconductor Nanostructures for Optoelectronic Applications*. Steiner, T. D., Ed., Artech House Semiconductor Materials and Devices Library, Artech House: Norwood, MA, 2004.
- [25] Ustinov, V. M. (2004). *Semicond.*, **38**, 923-927.
- [26] Kryzhanovskaya, N. V., Gladyshev, A. G., Blokhin, S. A., Musikhin, Yu. G., Zhukov, A. E., Maksimov, M. V., Zakharov, N. D., Tsatsul'nikov, A. F., Ledentsov, N. N., Werner, P., Guffart, F. & Bimberg, D. (2004). *Semicond.*, **38**, 833-835.
- [27] Sgartato, A., Szkutnik, P. D., Balzarotti, A.; Motta, N. & Rosei, F. (2004). *Appl. Phys. Lett.*, **83**, 4002-4004.
- [28] Shchukin, V. A., Borovkov, A. I., Ledentsov, N. N. & Kop'ev, P. S. (1995). *Phys. Rev. B*, **51**, 17767-17770.
- [29] Capellini, G., De Seta, M., Spinella, C. & Evangelisti, F. (2003). *Appl. Phys. Lett.*, **82**, 1772-1774.
- [30] Patella, F., Szkutnik, A. & Sgarlata, E. (2004). *J. Phys. Condens. Matter*, **16**, S1503-1505.
- [31] Kitajima, T., Lu, B. & Leone, S. R. (2002). *Appl. Phys. Lett.*, **80**, 497-499.

- [32] Zhoug, Z., Halilovic, A., Fromherz, T., Schäffler, F. & Bauer, G. (2003). *Appl. Phys. Lett.*, *82*, 4779-4781.
- [33] Li, Q., Han, S. M., Bruek, S. R. J., Hersee, S., Jiang, Y. B. & Xu, H. (2003). *Appl. Phys. Lett.*, *83*, 5032-5034.
- [34] Liu, F. & Lagally, M. G. (1997). *Surf. Sci.*, *386*, 169-175.
- [35] Drozdov, Yu. N., Krassil'nik, Z. F., Lobanov, D. N., Novikov, A. V., Shaleev, M. V. & Yablonskiĭ, A. N. (2006). *Semicomd.*, *40*, 338-342.
- [36] Pedraza, A. J., Fowlkes, J. D. & Guan, Y. E. (2003). *Appl. Phys. A*, *77*, 277-279.
- [37] Verevkin, Yu. K., Daume, E. Ya., Petryakov, V. N., Gushchina, Yu. Yu. & Tikhov, S. V. (2005). *Tech. Phys. Lett.*, *31*, 759-762.
- [38] Bauerle, D. (1996). *Laser Processing and Chemistry*. Springer: Berlin - Heidelberg.
- [39] Mullendorn, M., Birkelund, K., Grey, F. & Madsen, S. (1996). *Appl. Phys. Lett.*, *69*, 3013-3015.
- [40] Meltz, G., Morey, W. W. & Glenn, W. H. (1989). *Opt. Lett.*, *14*, 823-825.
- [41] Askins, G. G., Tsai, T.-E., Williams, G. M., Putnam, M. A., Bashkausky, M. & Friebel, E. Y. (1992). *Opt. Lett.*, *17*, 833-835.
- [42] Dong, L., Archambault, Y. L., Reekie, L., Russell, P. S. Y. & Payne, D. N. (1993). *Electron. Lett.*, *29*, 1577-1579.
- [43] Zhang, L. S., Williams, Y. A. R., Denion, Y., Reid, D. C. Y. & Ragdale, C. M. (1995). *Opt. Lett.*, *20*, 1927-1929.
- [44] Othonos, A. & Lee, X. (1995). *Rev. Sci. Instr.*, *66*, 3112-3116.
- [45] Fernandez, A. & Phillion, D. W. (1998). *Appl. Opt.*, *37*, 473-478.
- [46] Baker, K. M. (1999). *Appl. Opt.*, *38*, 352-355.
- [47] Meier, M., Mekis, A., Dodabalapur, A., Timko, A., Slusher, R. E., Yoannopoulos, Y. D. & Nalamasu, O. (1999). *Appl. Phys. Lett.*, *74*, 7-9.
- [48] Ezaki, M., Kumagai, H., Toyoda, K. & Obara, M. (1993). *Jpn. J. Appl. Phys.*, *32*, 1308-1312.
- [49] Seminogov, V. N., Panchenko, V. Ya. & Khudobenko, A. N. (1997). *JETP*, *111*, 174-181.
- [50] Bychkov, Yu. I., Losev, V. F. & Panchenko, Yu. N. (1992). *Sov. J. Quantum Electron.*, *22*, 638-642.
- [51] Perrone, M. R. & Yao, Y. B. (1994). *IEEE J. Quantum Electron.*, *30*, 1327-1330.
- [52] Veiko, S. M. & Metev, S. M. (1991). *Laser Technologies in Microelectronics*. Sofia: Bulgarian Academy of Science Publishing.
- [53] Phillips, H. M., Callahan, D. L., Sauerbrey, R., Szabo, G. & Bor, Z. (1992). *Appl. Phys. A*, *54*, 158-161.
- [54] Chung, Y. & Shi-Woo, R. (2001). *J. Mater. Sci. Mater. Electron.*, *12*, 697-700.
- [55] Lee, M., Moou, S., Haatana, M. & Grigoropoulos, C. P. (2001). *Appl. Phys. A*, *73*, 317-321.
- [56] Efremov, M. D., Bolotov, V. V., Volodin, V. A., Kochubei, S. A. & Kretinin, A. V. (2002). *Semicond.*, *36*, 102-106.
- [57] Alekseev, A. M., Verevkin, Yu. K., Vostokov, N. V., Petryakov, V. N., Polushkin, N. I., Popkov, A. F. & Salashchenko, N. N. (2001). *JETP Lett.*, *73*, 192-195.
- [58] Boyd, R. D., Britten, Y. A., Decker, D. E., Shore, B. W., Stuart, B. C., Perry, M. D. & Li, L. (1995). *Appl. Opt.*, *34*, 1697-1700.
- [59] Verevkin, Yu. K. & Daume, E. Ya. (1998). *Opt. Spectrosc.*, *85*, 239-244.

- 
- [60] Wang, S., Zhou, C., Zhang, Y. & Ru, H. (2006). *Appl. Opt.*, **45**, 2567-2569.
  - [61] Silicon Photonics. L. Pavesi, & D. J. Lockwood, (Eds.), Springer: Berlin - Heidelberg, 2004.
  - [62] Vlasov, S. N. & Koposova, E. V. (2003). *Radio Phys. Quantum Electron.*, **46**, 5-14.
  - [63] Dragomir, N. M., Rollinson, C. & Wade, S. A. (2003). *Opt. Lett.*, **28**, 789-791.
  - [64] Park, D. & Kim, M. (2004). *Opt. Lett.*, **29**, 1849-1851.
  - [65] Haro-Poniatowski, E., Fort, E., Lacharme, J. P. & Ricolleau, C. (2005). *Appl. Phys. Lett.*, **87**, 3103-3105.
  - [66] Guo, L. J. (2004). *J. Phys. D Appl. Phys.*, **37**, R123-159.
  - [67] Pisignano, D., Maruccio, G. & Mele, E. (2005). *Appl. Phys. Lett.*, **87**, 3109-3111.
  - [68] Heon, L., Hong, S. & Yang, K. (2006). *Appl. Phys. Lett.*, **88**, 3112-3114.
  - [69] Kanamori, Y., Sasaki, M. & Hane, K. (1999). *Opt. Lett.*, **24**, 1422-1424.
  - [70] Kintaka, K., Nishii, J., Mazutani, A., Kikuta, H. & Nakano, H. (2001). *Opt. Lett.*, **26**, 1642-1644.
  - [71] Rastei, M. V., Meckenstock, R., Bucher, J. P., Devaux, E. & Ebbesen, T. (2004). *Appl. Phys. Lett.*, **85**, 2050-2052.
  - [72] Kim, D. (2005). *Appl. Opt.*, **44**, 3213-3217.
  - [73] Zeng, L., Hong, Y., Liu, J., Feng, N., Duan, X., Kimerling, L. & Alamariu, B. (2006). *Appl. Phys. Lett.*, **89**, 1111-1113.
  - [74] Guise, P., Yates, J., Levy, J., Ahner, J., Vaithynathan, V. & Schlom, D. (2005). *Appl. Phys. Lett.*, **87**, 1902-1904.
  - [75] Zhong, Z., Katsaros, G., Stoffel, M., Costantini, G., Kern, K., Schidt, G., Jin-Phillipp, N. & Bauer, G. (2005). *Appl. Phys. Lett.*, **87**, 3102-3104.
  - [76] Polushkin, N. I., Gusev, S. A., Drozdov, S. A., Verevkin, Yu. K. & Petryakov, V. N. (1997). *J. Appl. Phys.*, **81**, 1-3.
  - [77] Verevkin, Yu. K., Petryakov, V. N. & Polushkin, N. I. (1998). *Tech. Phys. Lett.*, **24**, 460-463.
  - [78] Bredikhin, V. I., Burenina, V. N., Verevkin, Yu. K., Kirsanov, A. V., Petryakov, V. N., Vostokov, N. V., Dryakhlin, V. F. & Klimov, A. Yu. (2004). *Tech. Phys.*, **49**, 1191-1197.

## **Chapter 4**

# **ZNO NANOSTRUCTURES DEPOSITED BY LASER ABLATION**

**D. Valerini<sup>1\*</sup>, A. Creti<sup>2</sup>, A. P. Caricato<sup>1</sup>, M. Lomascolo<sup>2</sup>, R. Rella<sup>2</sup>,  
and M. Martino<sup>1</sup>**

<sup>1</sup>Department of Physics, L3 group, University of Salento,  
Via Arnesano, 73100 Lecce, Italy.

<sup>2</sup>IMM-CNR, Institute for Microelectronics and Microsystems,  
Department of Lecce, Via Arnesano, 73100 Lecce, Italy.

## **ABSTRACT**

This chapter aims to present a brief review about a very interesting application of laser beams in the field of materials science: the growth of zinc oxide (ZnO) nanostructured films by Pulsed Laser Deposition (PLD), and in particular by means of excimer laser ablation. After an introduction giving an overview on properties and applications of ZnO and its nanostructures and on some growth techniques used to obtain these materials, this survey will present several results, obtained by different research groups in the world, about nanostructured ZnO grown by excimer laser ablation. Then this study will be focused on the results obtained by our research group in this field so far. By properly changing some deposition parameters (substrate temperature, oxygen pressure and ablation laser wavelength) we obtained nanostructured films with hexagonal pyramids, columns, hexagonal hierarchical structures and pencils, as well as smooth or rough films. In particular the different ablation laser wavelengths (248 nm of KrF and 193 nm of ArF) are shown to have a deep influence on both morphology and crystal quality of the grown samples. Scanning electron microscopy (SEM), x-ray diffraction (XRD) and photoluminescence (PL) measurements were used to inspect the film properties. Finally, some results about our optical gas sensing tests conducted on the grown samples are presented.

---

\* Corresponding author : currently at Italian National Agency for New Technologies, Energy and Sustainable Economic Development (ENEA), Research Centre of Brindisi, S.S. 7 Appia - km 706, 72100 Brindisi, Italy.

## INTRODUCTION

A very interesting application of laser beams can be found in the field of materials science, where they can be valuably used as means to grow a wide range of materials with controllable physical properties, which can be consequently used for a huge number of technological applications. This chapter deals with the use of a laser-based growth technique (the Pulsed Laser Deposition technique) for the realization of nanostructured zinc oxide. In order to introduce the matter examined in this chapter, we first present a general overview about properties and applications of ZnO and its nanostructures and about some growth techniques used to obtain these materials.

### 1.a. Properties and Applications of Zinc Oxide and Its Nanostructures

Nanostructured zinc oxide (ZnO) has attracted great attention over the recent years because of its interesting properties making this kind of material particularly appealing for a wide range of applications in several technological fields, like e.g. optoelectronics and biochemical sensing. This is also evidenced by the huge number of scientific publications about this matter [1].

ZnO, even in its non-nanostructured form, is a very attractive material thanks to its features, like wide band gap, large exciton binding energy, chemical stability, biocompatibility, piezoelectricity, nonlinear optical effects, radiation hardness. Moreover, when passing from bulk material to nanostructures, the interest becomes strongly enhanced, since the properties deriving from the reduced dimensionality of nanostructures add to the intrinsic ZnO properties. Furthermore, the intense studies in this research field are promoted by the possibility to realize a very broad variety of ZnO nanostructures, such as dots, wires, rods, tetrapods, belts, combs, tubes, needles, hierarchical structures and so on. Some examples of ZnO nanostructures are displayed in Figure 1.

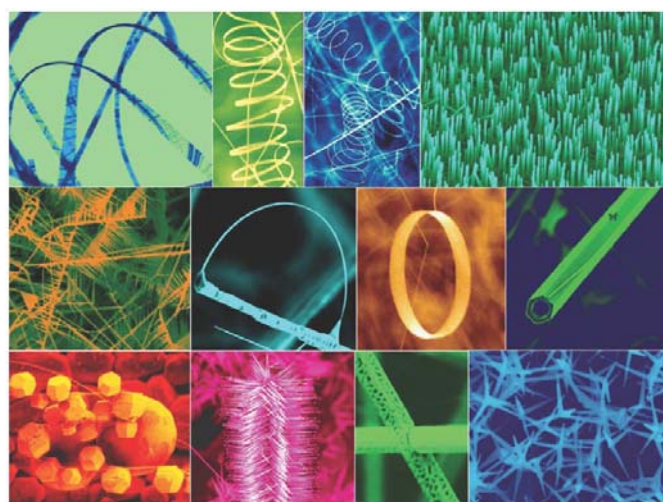


Figure 1. Some examples of ZnO nanostructures. (Reprinted with permission from [58], copyright 2004, Elsevier).

ZnO, as bulk material or film, is very appealing for electronic and opto-electronic devices, such as Ohmic contacts [2], Schottky contacts [3], LEDs [4], LASERs [5], transparent FETs [6], photodetectors [7] and solar cells [8]. Dealing with ZnO nanostructures, a lot of different possible electronic and opto-electronic applications have been explored. The possibility to realize Ohmic or Schottky metal nano-contacts onto ZnO nanostructures has been reported [9]. Electroluminescence for LED applications has been extensively studied with devices based both on ZnO nanorod arrays [10] and on single ZnO nanorod [11]. Thanks to the ZnO high refractive index ( $\sim 2.0$ ) and to the well-faceted ends of the nanowires acting as reflecting mirrors, ZnO nanowires can work as ideal optical resonance cavities; indeed lasing action at room temperature has been demonstrated on ZnO aligned nanorod arrays [12] and single nanorods [13], but also in random oriented nanorod arrays [14] and other nanostructures [15,16]. Even random lasing in ZnO nanoparticle films has been studied [17]. Field effect transistors (FETs) based on single ZnO nanorods [18], nanobelts [19], and hybrid ZnO tetrapods/polymer blends [20] have been realized. ZnO nanorods/nanowires have been studied for applications as ultraviolet photodetectors and optical switches [21,22]. UV photodiodes based on ZnO nanotetrapods with Schottky contacts have been reported [23]. For applications of ZnO nanostructures to solar cells, it is believed that aligned nanorods can highly improve the solar energy conversion efficiency through a faster electron transport than conventional solar cells; for this reason many studies are conducted towards this application [24,25]. By combinations of metal-semiconductor Schottky diodes or FETs, ZnO nanorods have been also used to realize logic circuits [26].

Due to its high refractive index ZnO is also useful for optical waveguides. Thus, for example, light can be guided inside a nanowire, acting like an optical nano-fiber. Even light coupling between nanostructures of different materials (like ZnO and SnO<sub>2</sub>) has been reported [27]. This is particular appealing for nanoscale photonics integration [27].

Since zinc oxide presents strong piezoelectric properties [28] it can be suitable for electro-mechanical transducers, sensors and actuators [29] and for surface acoustic wave (SAW) devices [30]. The piezoelectric properties of ZnO nanostructures have been widely explored [31]. A method to convert mechanical energy into electrical energy through piezoelectricity of ZnO nanowires has been showed [32], suggesting the possibility to convert biological mechanical energy, acoustic vibration energy, and bio-fluid hydraulic energy into electricity at nanoscale levels. Piezoelectricity can be also used for pressure or force sensors [33]. ZnO nanostructures are also interesting for use as nano-cantilevers [34], for example for atomic force microscopy (AFM), thanks to their piezoelectric properties and smaller dimensions than conventional cantilevers (e.g. made of Si<sub>3</sub>N<sub>4</sub> or SiC).

Bulk zinc oxide and films present large nonlinear optical coefficients, suggesting their potential application in quantum electronics and integrated optical devices. Second harmonic generation (SHG) in bulk ZnO [35] and films [36] and third harmonic generation (THG) [37] have been reported, hence showing the possibility to use this material, which is cheaper and easier to be integrated than other nonlinear optical single crystals like LiNbO<sub>3</sub> and LiTaO<sub>3</sub>, in this technological field. Optical nonlinearity has been studied in ZnO nanostructures as well; for example SHG and THG have been reported for ZnO nanowires [38].

Ferromagnetism in doped ZnO has been theoretically studied [39] and experimentally evidenced at room temperature in doped ZnO films [40] as well as nanostructures [41], thus showing possible appliance in spintronics.

Another useful ZnO property is its radiation hardness [42,43], making it interesting for devices to be used in space applications.

Zinc oxide is also reported to be a biosafe and biocompatible material [44], hence supporting the possible use of ZnO for biomedical applications [45,46]. However further studies are still required in this direction, since possible damages of ZnO nanoparticles on human cells have been observed [47].

The possibility to realize very ordered arrays of ZnO nanostructures is particularly useful for realization of photonic crystals. Theoretical and experimental results have shown the possibility to obtain photonic structures by means of ZnO inverted opals [48] and ZnO nanopillar arrays [49].

Another very interesting possible application of ZnO nanostructures is as field emitters to be used, for example, for flat panel displays, cold cathodes and other photoelectric devices. Oxide nanostructures may have high efficiency, reduction of cost and device sizes in comparison with conventional thermo-ionic emitters, and they are more stable in harsh environment and controllable in electrical properties compared, for example, to carbon nanotubes [50]. The great interest derives also from the fact that many nanostructures have a needle-like tip, so that the electron field emission is highly enhanced due to the local field enhancement on their tips. Several reports exist about field emission from different ZnO nanostructure arrays, such as nanowires [50], nanopencils [51], nanoneedles [52] and other nanostructures [53,54,55].

Other possible applications of ZnO nanostructures are related to their wettability properties, since hydrophilic or hydrophobic materials are interesting for microfluid devices, chemical sensors or biosensors and for industrial uses like cleaning, drying etc. Conversion from hydrophobic to hydrophilic surface of ZnO nanorod arrays by UV illumination [56] or by oxygen plasma treatment or annealing [57] have been reported.

Certainly one of the most attractive applications of zinc oxide is for chemical or biological sensors. More details about this aspect will be given in par. 3.d.

## 1.b. Growth Techniques for Zinc Oxide Nanostructures

Several growth techniques have been reported in literature for the growth of ZnO nanostructures. Here we list some examples.

A technique extensively used for the growth of ZnO nanostructures is *thermal evaporation*. In this vapor-phase method the species evaporated from the source material, e.g. zinc or zinc oxide, in a furnace are transported onto the substrate, maintained at the chosen temperature, through a flux of an inert gas or of a mixture containing a gas which must interact with the evaporated species (for example oxygen if only zinc is evaporated). By properly tuning the growth parameters, the condensation of the gaseous species on the substrate leads to the growth of different nanostructures [58]. Often, in order to get nanostructures, the growth must be aided by a catalyst. For example sometimes the catalyst is dispersed together with ZnO in the source material (e.g. graphite mixed with ZnO powder [59] and, during the condensation process, it catalyzes the nanostructure growth. In other cases a thin layer of a catalyst (e.g. Au, Cu, Ni, Sn, Pt, etc.) is previously deposited on the substrate. Typically the growth process in this technique is reported to be related to a vapor-liquid-solid (VLS) mechanism [59], that is: on the substrate the catalyst forms liquid droplets

which promote the adsorption of the gaseous molecules; when supersaturation is reached, the nucleation and subsequent growth of nanometric structures start. Usually, when no catalyst is used during the growth, a vapor-solid (VS) sublimation mechanism is proposed [58]. In order to aid the nanostructure formation or to modify their properties (like density on the substrate, dimensions, etc.), sometimes a ZnO film (buffer layer) is deposited on the substrate before the nanostructure deposition [60]. Thermal evaporation is a very simple technique, but it usually requires high temperatures (even  $\sim 900^{\circ}\text{C}$  or more) in order to evaporate the source material or to form the liquid catalyst droplets on the substrate. The nanostructures shown in Figure 1 were obtained by this growth technique.

*Chemical Vapor Deposition (CVD)* [61] and *Metalorganic CVD (MOCVD)* [62,63] are also widely used for the growth of ZnO nanostructures. In these techniques the volatile precursors containing the elements of the material to be deposited are transported onto the heated substrate where they react allowing the growth of the material. As for thermal evaporation, even in this case catalysts are sometimes used, and VLS or VS (for catalyst-free CVD) mechanisms are proposed as possible growth processes. Also *plasma-enhanced CVD (PECVD)*, in which a plasma is used in order to enhance the chemical reaction rates of the precursors, has been employed to obtain ZnO nanostructures [64]. Figure 2 shows some ZnO nanostructures grown by these techniques.

*Molecular Beam Epitaxy (MBE)* has been used to realize ZnO nanostructures. Even in the MBE growth a catalyst can be used to aid the nanostructure formation. For example the cation flux coming from a zinc source is oxidized in a plasma of ozone/oxygen mixture and the material deposits on a catalyst-coated (e.g. Ag) heated substrate [65].

ZnO micro/nanostructure deposition can be obtained by *sputtering* of a ZnO target. As examples, RF magnetron sputtering has been used to grow ZnO nanorods on Cu-coated silicon substrates [66] or hexagonal micropyramids on alumina substrates [67].

*Pulsed Laser Deposition (PLD)*, in which a high-power pulsed laser beam is focused onto a target material (for example metallic zinc or sintered/ceramic zinc oxide) placed in a vacuum chamber, causing the ablation (ejection) of the material which interacts with the background atmosphere (for example oxygen) and deposits on a substrate, is a very powerful technique for the growth of ZnO nanostructures. Nanostructured ZnO has been obtained by PLD by using different lasers (excimer, Nd:YAG and femtosecond lasers) in conventional or unconventional systems, with or without the use of catalysts, in different background atmospheres, etc. The growth of ZnO nanostructures by this technique will be discussed in more details in the next paragraphs.

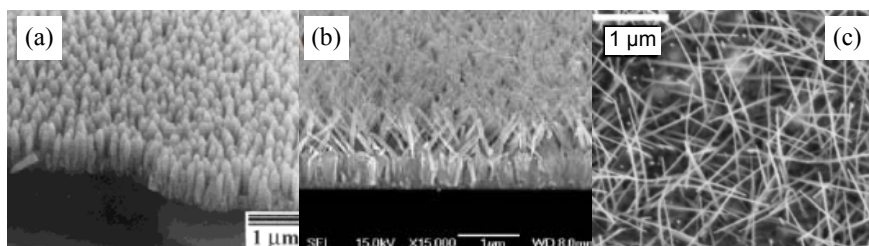


Figure 2. SEM images of some ZnO nanostructures grown by (a) CVD, (b) MOCVD, (c) PECVD. (Reprinted with permission from: (a) [61], copyright 2002, Wiley-VCH Verlag GmbH & Co. KGaA.; (b) [62], copyright 2007, Institute Of Physics (IOP); (c) [64], copyright 2004, American Institute of Physics (AIP)).

Also direct *oxidation* of zinc powders has been showed to allow the realization of ZnO nanostructures. For example ZnO tetrapods have been obtained by heating zinc powders in a furnace at 850–900°C in oxygen atmosphere [68].

ZnO nanostructures have been synthesized by *hydrothermal methods* [69], which consist in the growth from hot (~90°–300°C) aqueous solutions at high vapor pressures (~1 atm or more). The aqueous solution contains the precursors for the growth of the material of interest, which dissolve in the high-temperature solution and condense in the cooler part of the chamber.

Apart from hydrothermal synthesis, other *solution-based methods* have been used to synthesize ZnO nanostructures, like *electrochemical methods* (or *electrodeposition*) [70], *sol-gel methods* [71,72], *sonochemical synthesis* and *microwave-assisted synthesis* [73], and other solution-based chemical routes [74].

Zinc oxide nanostructures have been also realized by using *template-directed methods*, in which a periodic structured template (for example an anodic alumina membrane or a polymeric membrane) is exploited to lead the growth of the material. The pores of the template can be filled by using other techniques. For example nanodots have deposited by PLD using an anodic alumina membrane [75] and nanorods have been obtained by evaporation on a gold membrane [76].

Finally, it must be added that different methods, other than the previous ones, have also been used to deposit ZnO nanostructures and that techniques made by combinations of different methods can be used. For example ZnO nanorods have been grown by chemical vapor deposition combined with pulsed laser deposition [77]. Another example of a mixed technique is a combination between laser ablation and chemical synthesis (see par. 2.b).

Some examples of ZnO nanostructures grown by different techniques are displayed in Figure 3.

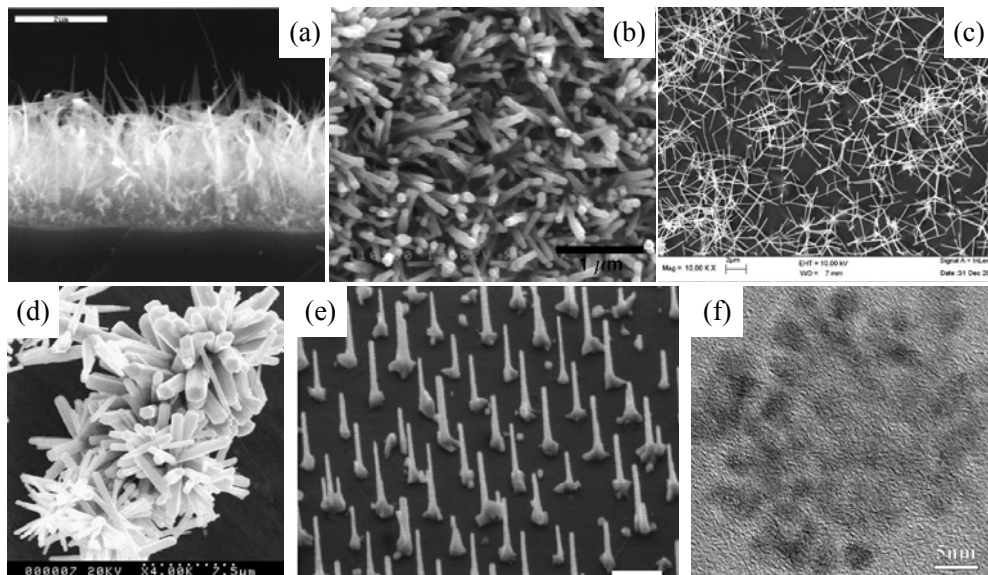


Figure 3. (a)-(e) SEM and (f) TEM images of ZnO nanostructures grown by (a) MBE, (b) sputtering, (c) oxidation of Zn powders, (d) hydrothermal method, (e) template-directed thermal evaporation, (f) sol-gel method. (Reprinted with permission from: (a) [65], copyright 2002, American Institute of Physics (AIP); (b) [66], copyright 2006, Elsevier; (c) [68], copyright 2002, Elsevier; (d) [69], copyright 2006, Elsevier; (e) [76], copyright 2005, Institute Of Physics (IOP); (f) [71], copyright 2005, Elsevier).

## ZINC OXIDE NANOSTRUCTURES BY LASER ABLATION

As already mentioned in the previous paragraph, the PLD technique represents a very functional method to grow ZnO nanostructures. Here we provide a brief general description of the PLD technique and then we present some results, obtained by different research groups in the world, about nanostructured ZnO grown by PLD (in particular by excimer laser ablation).

### 2.a. The Pulsed Laser Deposition Technique

The Pulsed Laser Deposition (PLD) technique is a very versatile technique for the deposition of thin films and it was applied to a wide range of materials and applications [78,79]. Some of the historical applications of the PLD technique are, just as examples, in the fields of superconductivity [80], diamond-like coatings [81], nitride thin films [82], and so on.

In a standard pulsed laser deposition set-up (Figure 4) a high-power laser beam, for example an UV laser with nanosecond pulse duration like KrF or ArF excimer lasers, is directed onto a target placed inside a vacuum chamber.

The main components of a standard PLD setup are:

- an ablation laser;
- a lens focusing the laser beam onto the target surface;
- a variable attenuator, varying the laser energy on the target and thus controlling the laser fluence;
- a stainless steel high vacuum chamber ( $\sim 10^{-5} \div 10^{-4}$  Pa);
- reaction gases inlets;
- a rotating target holder;
- a substrate holder, possibly equipped with a heater and a motion system.

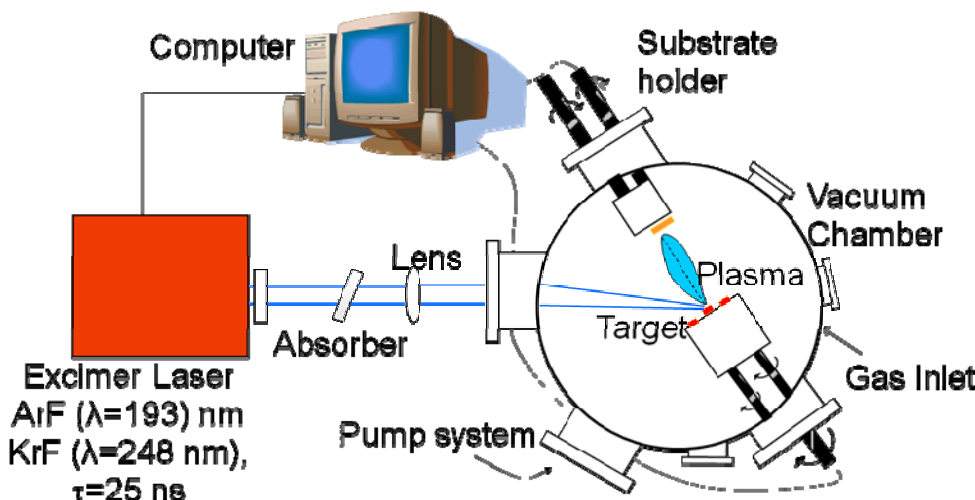


Figure 4. Schematization of a typical PLD experimental apparatus.

UV light is strongly absorbed by many metals and other materials in contrast to IR light [79], for this reason the UV lasers are very attractive for materials processing, and the film production by PLD is widely based on the use of ns laser pulses in the UV range. Typical wavelengths for laser ablation are obtained from excimer lasers at 248 nm (KrF) and 193 nm (ArF), or also by Nd:YAG lasers (e.g. tripled Nd:YAG at 355 nm) or femtosecond lasers.

A comprehensive review on the fundamental aspects of laser-solid interaction is given in [83]. The laser-target interaction causes the ejection of material from the target. The material ejected from the target due to this “explosive removal” (ablation) expands perpendicularly to the target surface, creating a plasma plume, and it is collected onto a substrate placed in front of the target. The deposition of this ablated material on the substrate from a large number of laser pulses leads to the gradual formation of the film.

Several parameters play a key role on the quality of pulsed laser deposited thin films, namely the laser fluence, the background gas and the substrate temperature. The presence of a gas, for example an inert gas as argon, during laser ablation changes the dynamic expansion of the plume as a consequence of the collisions between plume particles and background gas molecules. In this case the gas acts as a moderator reducing the high impact energy of the ablated species [84,85]. Moreover a suitable gas can be inserted in the process chamber in order to also induce chemical reactions between the plume species and the gas molecules during the transfer of the target material to the substrate. In the case of oxide materials, a background O<sub>2</sub> pressure of few Pa is generally used during the deposition in order to maintain the oxygen content in the growing film.

A unique feature of the PLD technique is the high kinetic energy of the ablated particles, which strongly depends of the laser fluence. Time-of-flight analyses evidenced kinetic energies of the ablated species exceeding 100 eV even at relatively low fluences ( $\sim 2 \text{ J/cm}^2$ ) [86]. The collisions within the plasma and with the background gas reduce the energy of the ablated species, therefore the substrate surface can be heated in order to increase the surface mobility of the adatoms.

The PLD technique presents several advantages with respect to other thin film deposition methods:

- The ablated species (ions and atoms in the plume) have very higher kinetic energy and internal excitation energy with respect to other techniques, like sputtering, consequently thin films with a good adhesion on the substrate and good crystalline quality can be deposited also at relatively low temperature.
- Materials with complex stoichiometry can be deposited in a single step, since the laser-target interaction causes the simultaneous evaporation of all the target constituents (congruent ablation). However deficiency of the lighter and most volatile elements (like oxygen) in the plume can occur in the final film composition, so the use of a suitable background gas can overcome these deficiency.

- Reactive PLD is possible using suitable background gases (e.g. nitride compounds in N<sub>2</sub> or NH<sub>3</sub> atmosphere), moreover since PLD is a non-equilibrium process, the formation of new compounds and metastable phases is possible [87].
- Multilayer thin films can be easily deposited by means of multi-target systems.

Two major drawbacks are related to the PLD process and should be considered.

Droplets and particulate can be deposited along with the film. However a careful choice of the deposition parameters (laser wavelength and fluence, repetition rate, background pressure) can reduce or eliminate this problem.

The thickness profile of the deposited films on large areas is inhomogeneous. In fact the angular distribution of the ablated material has a strong peak in the forward direction, with an angular dependence  $\sim \cos^n(\theta)$ , where  $\theta$  is the angle respect to the target surface normal, and n ranges from 2 to 20 (in vacuum) even if higher values have been also reported [88]. It is possible to improve the film thickness uniformity by changing the relative position between target and substrate (e.g. by a suitable motion of the substrate), so that it is possible to achieve uniform thin films on a large deposited areas too.

## 2.b. Nanostructured Zinc Oxide by PLD in the World

The previous paragraph presented a description of the “classical” PLD technique. However, due to the versatility of this growth method, also some variants have been reported to deposit ZnO nanostructures. For example, the laser ablation of the target can be conducted in a liquid medium instead of a gaseous environment. ZnO nanoparticles have been obtained by laser ablation of a zinc oxide target in pure liquids, like deionized water or ethanol [89]. Also laser ablation of metallic zinc in aqueous solutions containing other surfactants has been reported for the growth of ZnO nanostructures, such as nanoparticles [90], nanoleaves [91], nanorods and other nanostructures [92]. This technique, in which the ablated species interact with the surfactants, for example preventing further growth of the ablated species thus allowing the formation of nanometric clusters, can be considered as a mixed method between laser ablation and chemical routes. Further variants have been reported in literature, like e.g. RF plasma assisted PLD [93], bias voltage assisted PLD [94], and others [95].

Dealing with the classical PLD technique, ZnO nanostructures have been deposited by using different lasers as ablation sources, such as KrF or ArF excimer lasers (see below for details), Nd:YAG [96,97] and femtosecond lasers [98,99].

Some examples of ZnO nanostructures obtained by laser ablation in liquid or by ablation with Nd:YAG or femtosecond lasers are reported in Figure 5.

Focusing the attention on PLD with excimer lasers as ablation sources, different research groups in the world have reported the growth of ZnO nanostructures, in particular nanorods or nanowires, by the use of different process parameters (laser wavelength and fluence, kind of target and substrate, background atmosphere, substrate temperature, etc.), without or with the use of a catalyst for the nanostructure growth,

and performing the depositions in conventional or unconventional PLD set-ups. Here we intend a “conventional” apparatus as a PLD system like that one described in par. 2.a, while an “unconventional” apparatus is intended as a modified PLD set-up, like for example systems with a hot-walled vacuum chamber similar to a furnace (instead of a direct heating of the substrate) or systems with particular shapes or geometries (see later for more details).

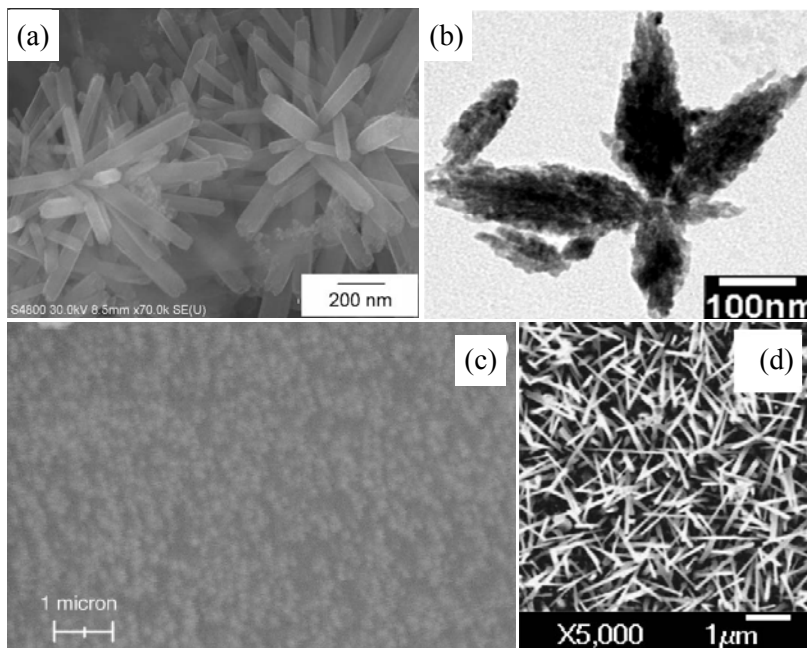


Figure 5. (a) SEM and (b) TEM images of different nanostructures grown by laser ablation in liquid media. (c) and (d): SEM images of nanostructures deposited by Nd:YAG and femtosecond laser ablation respectively. (Reprinted with permission from: (a) [92], copyright 2006, Elsevier; (b) [91], copyright 2007, Institute Of Physics (IOP); (c) [96], copyright 2006, Elsevier; (d) [98], copyright 2005, American Institute of Physics (AIP)).

Table 1 summarizes the deposition parameters used by some research groups to grow ZnO nanorods/nanowires. The different groups are labeled with capital letters from *A* to *M*, and the subscripts indicate different references related to the same group. In the column named “Laser parameters”, the excimer laser wavelength (248 nm for KrF, 193 nm for ArF), the laser fluence (energy per unit area) on the target and the repetition rate of the laser pulses are reported.  $D_{T-S}$  is the target-to-substrate distance. In the last column the proposed growth mechanism is also summarized, whether reported in the corresponding papers. The values reported in square brackets in the columns “ $T_{\text{substrate}}$ ” and “Background atmosphere” represent the optimal values found in the corresponding reference for the nanorod growth. The gray-shaded rows indicate references where unconventional PLD systems have been used.

Some comments about the results obtained by the different groups and about the different proposed growth mechanisms are reported below.

**Table 1. Deposition parameters used by different research groups (labeled with letters from *A* to *M*) for the growth of ZnO nanostructures by excimer PLD. See text for details.**

Refs.	Laser parameters		Target	Substrate	Catalyst	T <sub>substrate</sub>	D <sub>F-S</sub> (mm)	Background atmosphere	Proposed growth mechanism
A	1	KrF, 20 Hz, 3 J/cm <sup>2</sup>	sintered ZnO or metallic Zn	sapphire (0001) or (11 $\bar{2}$ 0), or silica	/	400-800°C [600-700°C]	20-70	O <sub>2</sub> or He 13.3-2700 Pa [100-1300 Pa]	Nanoparticle-assisted
	2	KrF, 20 Hz, 3-4 J/cm <sup>2</sup>	sintered ZnO	sapphire (0001) or (11 $\bar{2}$ 0), silica, silicon	Au particles on silicon	T <sub>furnace</sub> =600-1200°C	10-30	Ar 30000-67000 Pa or N <sub>2</sub>	Nanoparticle-assisted
	3	KrF, 20 Hz, 3 J/cm <sup>2</sup>	sintered ZnO	sapphire	/	T <sub>substrate</sub> =700°C	20	O <sub>2</sub> 130-1300 Pa	Nanoparticle-assisted
		KrF, 20 Hz, 4 J/cm <sup>2</sup>	sintered ZnO	sapphire	/	T <sub>furnace</sub> =800°C	/	Ar 20000-47000 Pa	
B	ArF, 10 Hz, 1-20 J/cm <sup>2</sup>		ceramic ZnO	silicon (100) with or without a ZnO buffer layer, or (0001) sapphire	/	300-750°C [600°C]	20-60	O <sub>2</sub> 1.33 Pa	VLS catalyzed by Zn droplets on bare Si. VS on ZnO-coated Si.
C	1	KrF	ZnO	silicon	/	150-800°C [500°C]	25	O <sub>2</sub> 133-933 Pa	Nanoparticle-assisted
	2	ArF, 10 Hz, ~2-3 J/cm <sup>2</sup>	ZnO	silicon (100), copper, or tungsten	/	600°C	40	2.7×10 <sup>-3</sup> Pa	Volmer-Weber on Si. Stranski-Krastanov on Cu and W. (VS)

**Table 1. (Continued)**

D	ArF, 10 Hz	ZnO	sapphire (0001)	/	500°C	/	Ar 10 Pa	Nanoparticle-assisted (VS) Stranski-Krastanov
E	KrF, 1-5 J/cm <sup>2</sup>	sintered ZnO	silicon	without or with Au (5-30 Å)	500-900°C [800-900°C without Au] [700-900°C with Au]	/	O <sub>2</sub> 26.6-1300 Pa	VLS (atypical)
F	KrF, 3-10 Hz, 2 J/cm <sup>2</sup>	sintered ZnO	sapphire (0001), (11 2 0) or (11 1 0) (off-axis)	Au film (10 Å), or Au seed particles	690-950°C	5-35	Ar or O <sub>2</sub> /Ar 2500-50000 Pa	Importance of Au only in the nucleation steps when using an Au film. VLS when using Au particles.
G	KrF	sintered ZnO	sapphire (0001) or silicon (001)	/	400-780°C [600-700°C]	20-42	O <sub>2</sub> 33-2700 Pa [667-1330 Pa]	Growth related to supersaturation
H	KrF, 5 Hz, 1-3 J/cm <sup>2</sup>	sintered ZnO	sapphire (0001) with a ZnO layer	/	500-800°C	20-50	O <sub>2</sub> , Ar, or O <sub>2</sub> /Ar 20-67 Pa [67 Pa]	Not VLS
I	KrF, 3 J/cm <sup>2</sup>	sintered ZnO	silicon (100) with annealed ZnO powder (off-axis)	/	650°C	40	Ar 1.33 Pa	VS on the seed particles
J	KrF, 10 Hz	sintered ZnO	silicon (100) (off-axis)	Au (300 Å)	600-800°C	50	O <sub>2</sub> 20 Pa	/

**Table 1. (Continued)**

K	KrF, 10 Hz, 4 J/cm <sup>2</sup>	metallic Zn	sapphire (0001)	/	600°C	50	O <sub>2</sub> 13-27 Pa	VLS catalyzed by Zn droplets
L	KrF, 5 Hz, 2.5 J/cm <sup>2</sup>	ceramic ZnO	InP (001) with a ZnO seed layer	/	400°C	50	O <sub>2</sub> 30 Pa	The droplets of the seed layer act as self-catalyst
M	KrF, 10 Hz, 4.3 J/cm <sup>2</sup> or ArF, 10 Hz, 1.6 J/cm <sup>2</sup>	sintered ZnO	silicon (100)	/	500-700°C	45	O <sub>2</sub> 1-100 Pa	Growth started from Zn or zinc suboxide droplets at low pressure.  Nanoparticle-assisted at high pressure.  (see text for details)

---

**A) Kyushu University (Fukuoka, Japan), Fudan University (Shanghai, China), University of Miyazaki (Miyazaki, Japan)**

**A1) Refs. [100,101,102,103]**

Ablating a ZnO target, on sapphire substrate the authors observed the growth of c-axis oriented hexagonal rods with mean diameter of  $\sim 300$  nm and lengths of  $\sim 6$   $\mu\text{m}$  on a thin ZnO layer at an oxygen background pressure of 665 Pa and substrate temperature of 700°C. At lower temperatures only ball-like structures, hexagonal structures or particles were obtained. Rayleigh scattering measurements showed that, at high background pressure, nanoparticles were formed in the gas-phase and transported onto the substrate. On the base of this observation it was assumed that these nanoparticles stacked on the substrate and, since their melting temperature is far lower than the bulk ZnO melting temperature, they fused forming the nanorods. As a consequence, the formation of nanorods was possible only at background pressures high enough (from  $\sim 100$  Pa) to allow the formation of the nanoparticles in the gas-phase. At lower pressure ( $\sim 13.3$  Pa) micro-crystals on a smooth film were grown while at too high pressure ( $> 1300$  Pa) the rods fused together and the surface became flattened. By using helium as background gas instead of oxygen, no rods were observed, while only smooth films, hexagonal micro-crystals or meshlike structures were obtained. When a metallic zinc target was ablated, the rods on sapphire were similar to those grown from a ZnO target, while on silica substrate the rods were bigger (diameter  $\sim 1$   $\mu\text{m}$ ) and somewhat tilted from the substrate normal.

**A2) Refs. [104,105,106,107,108,109]**

Here the authors used a modified PLD system, consisting of a quartz furnace where a ZnO target was ablated. In this way the laser ablation occurred in a high-temperature gas background. Moreover the depositions were performed at very high background pressures and with different substrate positions. In argon atmosphere of 36000 Pa and at a furnace temperature of 1000°C, on sapphire (0001) substrate a web-like structure of nanowires with diameters of  $\sim 50$  nm together with some large crystals ( $\sim 200$  nm), or bigger wires ( $\sim 500$  nm) with smaller wires ( $< 100$  nm) on their top were deposited for different substrate positions. On sapphire (11 $\bar{2}$ 0) substrate, cone-shaped crystals perpendicular to the substrate surface were obtained. On silicon substrate, nanowires grew only in the regions covered by Au nanoparticles acting as catalyst. On sapphire substrate annealed at 1000°C for 1 h, nanonails with root diameter of  $\sim 500$  nm and stem diameter of  $\sim 150$  nm were grown. On silica substrate annealed at 1000°C for 1 h, nanowires lying on the substrate were observed. The density of vertically aligned nanowires was found to increase with the increasing laser energy, and vertically aligned nanowires were grown in N<sub>2</sub> atmosphere too. Also horizontally aligned nanowires, with lengths up to more than 8  $\mu\text{m}$ , were obtained on annealed sapphire substrates, while on not-annealed sapphire substrates only nanodots appeared.

**A3) Ref. [110]**

In a conventional PLD apparatus, rods (with diameters of  $\sim 300$ -500 nm at oxygen pressure of 133 Pa,  $\sim 500$ -1000 nm at 667 Pa, and length of several  $\mu\text{m}$ ) were grown on sapphire, while at higher pressure (1330 Pa) the rods fused together. In an unconventional apparatus, that is laser ablation in a quartz furnace, a web of nanowires with diameters of  $\sim$

50-100 nm and several  $\mu\text{m}$  long were obtained in an Ar pressure range of 20000-47000 Pa, together with some large crystallites of  $\sim 500$  nm.

**B) University of Bristol (Bristol, UK), refs. [111,112,113,114,115]**

At silicon substrate temperature of 600°C, the authors observed the growth of rods (base diameter  $\sim 60$  nm, length  $\sim 200$ -800 nm) after a thin ZnO layer. At lower temperatures polycrystalline films or with a network-like morphology were grown, and at higher temperatures irregularly shaped larger particles were observed. On the tip of the rods, ZnO capping particles were present: on the base of this observation the growth was attributed to a VLS mechanism, catalyzed by Zn liquid droplets where adsorption of oxygen took place. On silicon substrate intentionally pre-coated with a thin ZnO film (deposited at 300°C for 1 minute), the grown nanorods were denser, thinner (base diameter of  $\sim 20$  nm) and longer ( $\sim 1$ -1.2  $\mu\text{m}$ ) than those obtained on uncoated silicon. Moreover in this case no capping particles were observed, thus suggesting that the growth occurred by a VS mechanism, with rods starting to grow from nanosized crystallites, acting as nucleation sites, on the ZnO layer. The nanorod diameters were found to increase from  $\sim 10$  nm to  $\sim 50$  nm with increasing the laser fluence from  $\sim 4 \text{ J/cm}^2$  to  $\sim 11 \text{ J/cm}^2$ , whereas at further higher fluence ( $\sim 20 \text{ J/cm}^2$ ) large hexagonal nanostructures ( $\sim 100$  nm) were observed. At the same time, the density of nanorods and nanostructures decreased with increasing the fluence. These trends with laser fluence were ascribed to a higher bombardment effect of high energy species in the plume at higher fluences, thus allowing only the bigger rods to survive. On sapphire substrate, with a laser fluence of  $\sim 2.5 \text{ J/cm}^2$  nanorods (diameter  $\sim 20$  nm, length  $\sim 100$ -200 nm) grew after an ablation of 10 minutes, while for longer ablation times a porous ZnO network or a smooth film were grown. Some images are reported in Figure 6.

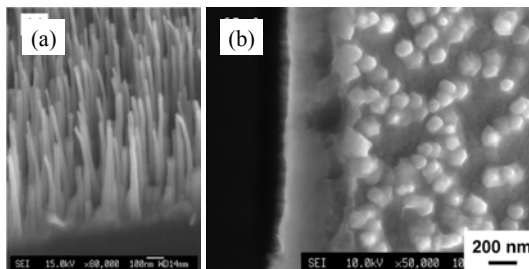


Figure 6. SEM images of nanostructures grown by the group labeled with *B*. (Reprinted with permission from: (a) [111], copyright 2004, Elsevier; (b) [113], copyright 2007, Elsevier).

**C) University of Delhi (Delhi, India), University of Puerto Rico (San Juan, Puerto Rico), Harbin Institute of Technology (Harbin, China)**

**C1) Refs. [116,117]**

In oxygen atmosphere of 665 Pa, rough and porous polycrystalline films were obtained at low substrate temperature ( $< 450^\circ\text{C}$ ), rods with a low size dispersion ( $\sim 120$ -200 nm) at  $\sim 500^\circ\text{C}$ , rods with high size dispersion ( $\sim 70$ -350 nm) at  $\sim 600^\circ\text{C}$ , and a film having densely packed large size grains at  $\sim 800^\circ\text{C}$ . As in references of group *A*, the growth mechanism was

ascribed to the nucleation of the nanoparticles formed during the scattering events in the high background pressure.

### C2) Refs. [118]

Different nanostructures were grown on the different substrates. On Si (100), needle-like nanostructures with lengths of  $\sim$  1-5  $\mu\text{m}$  were arranged in flower-like structures with a diameter of  $\sim$  4-8  $\mu\text{m}$ . The single needle presented a root and a tip of  $\sim$  50-100 nm and 20-50 nm respectively. Nanowires with diameter of  $\sim$  50-70 nm and length of  $\sim$  5-10  $\mu\text{m}$  were grown on W substrates. Micro-flowers of  $\sim$  1-3  $\mu\text{m}$  with leaves with a base of  $\sim$  150-200 nm were obtained on rough Cu substrates, while particles of  $\sim$  300-500 nm were observed on smooth Cu substrates. The growth was supposed to be governed by a Volmer-Weber mechanism on Si, and by a Stranski-Krastanov mechanism on W and Cu due to their enhanced free surface energy in comparison to Si. The different morphologies observed on W and Cu were ascribed to the different thermal expansion coefficients of the two substrates, thus differently affecting the cracking of the initial layer from which the nanostructure growth took place.

Some images are reported in Figure 7.

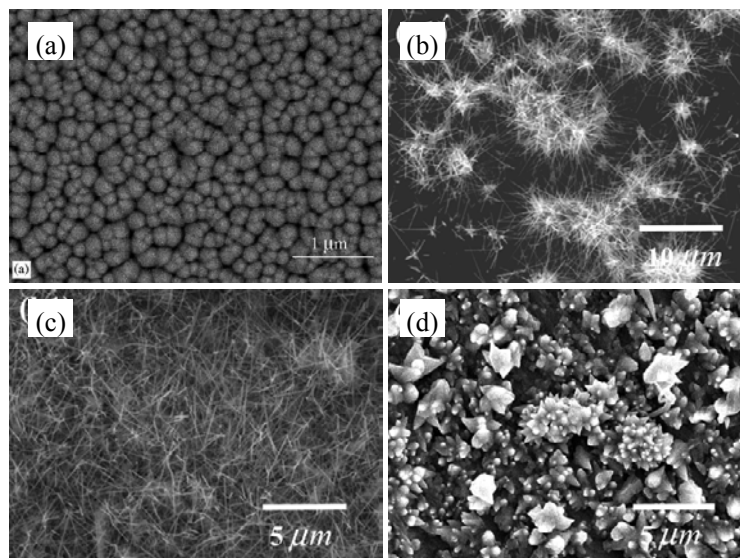


Figure 7. SEM images of nanostructures grown by the group labeled with C. (Reprinted with permission from: (a) [117], copyright 2005, Elsevier; (b), (c) and (d) [118], copyright 2009, Institute Of Physics (IOP)).

### D) Osaka University (Osaka, Japan), Chiang Mai University (Muang Chiang Mai, Thailand), ref. [119]

In argon atmosphere the authors obtained rods with diameter  $\sim$  500-700 nm at high fluences and  $\sim$  40-100 nm at low fluences, while only 3D hexagonal islands where observed in oxygen atmosphere. They explained this behavior observing that the mean free path of the particles in the plume was shorter in argon atmosphere than in oxygen, thus allowing more scattering events and the consequent formation of nanoparticles and zinc sub-oxide species in

the gas phase; these nanoparticles started the growth on the substrate and then acted as nucleation sites for the growth of the rods. Therefore the authors attributed the growth to a Stranski-Krastanov mechanism allowed by the formation of nanoparticles in argon atmosphere. Figure 8 displays the ZnO sample grown in Ar atmosphere.

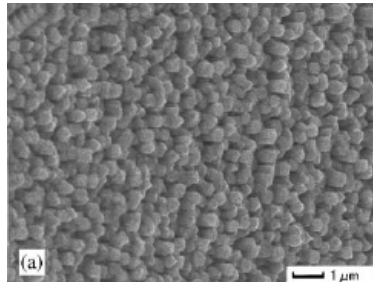


Figure 8. SEM image of a nanostructured ZnO sample reported by group labeled with D. (Reprinted with permission from [119], copyright 2005, Elsevier).

#### E) Korea Institute of Science and Technology (Seoul, Republic of Korea), ref. [120]

As in references labeled with  $A_2$ , the unconventional PLD system here used was a furnace where the ablation of the target was performed. Here ZnO rods were deposited either without or with a 5-30 Å layer of Au catalyst. Without the catalyst, rods with diameters of  $\sim$  200-600 nm were deposited in the temperature range of 800-900°C with a fluence of  $\sim$  3-5 J/cm<sup>2</sup>, while at lower temperatures a wrinkled patterns (600-800°C) or rough or grain-shaped films (500-600°C) were observed. With the catalyst, thinner nanorods ( $\sim$  30-100 nm) were grown with a fluence of  $\sim$  2-5 J/cm<sup>2</sup> in the temperature range of 700-900°C, and again wrinkled patterns or rough films were obtained at lower temperatures. When the Au catalyst was used the authors supposed a VLS growth mechanism but, since no Au presence was revealed on the rod tips, they retained that the catalyst had an important role only during the initial growth of the rods, thus remaining at their bottom.

#### F) Universität Leipzig (Leipzig, Germany), Martin-Luther-Universität (Halle (Saale), Germany), refs. [121,122,123]

The unconventional PLD system here used was a T-shaped quartz furnace in which the laser ablation was performed. The authors obtained the growth of rods or needles only in the regions of the substrate covered by a sputtered Au film acting as catalyst, while only a wetting layer was observed on the uncoated regions. No Au particles were detected on the top of the rods, while gold nanodrops were identified near the ZnO wetting layer, so the authors supposed that gold had an important role only in the nucleation steps of the rods. The Au catalyst was also pre-arranged in an ordered array of seeds by means of polystyrene nanosphere lithography. By using this catalyst, ZnO nanorods with diameters of  $\sim$  60-150 nm and lengths of  $\sim$  1 μm grew perpendicularly aligned to the substrate through a VLS mechanism. By depositing on sapphire (10̄10) substrates, the authors found that the grown rods were 30°-inclined to the right or to the left with respect to the substrate normal. By increasing the furnace temperature, the mean rod dimensions (both diameter and length) increased. By decreasing the total pressure in the tube below 10000 Pa, the rods began to

coalesce, while, fixing the total pressure at 10000 Pa, an increase of the lateral rod dimensions was observed with increasing the oxygen partial pressure. Two samples are shown in Figure 9.

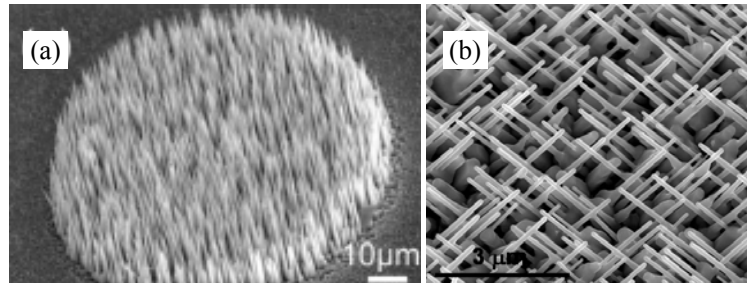


Figure 9. SEM images of two samples deposited by group labeled with *F*. (Reprinted with permission from: (a) [121], copyright 2005, American Institute of Physics (AIP); (b) [123], copyright 2007, Institute Of Physics (IOP))

#### **G) National University of Singapore (Singapore), Nanyang Technological University (Singapore), refs. [124,125]**

On sapphire substrate at 700°C, rods with a mean diameter of ~ 400 nm were obtained at oxygen background atmosphere of 1330 Pa, while increasing the oxygen pressure the rods started to contact each other forming a continuous film. Also at pressure lower than 667 Pa a continuous film was deposited. In the pressure range ~ 667-2700 Pa the rod diameter increases from ~ 300 nm to ~ 1000 nm. At oxygen pressure of 1330 Pa the authors observed the growth of rods at sapphire temperature of 600-700°C, hexagonal crystals at 550°C and continuous films at temperatures lower than 500°C or higher than 750°C. In the temperature range ~ 550-700°C the rod diameter increased almost linearly from ~ 100 nm to ~ 500 nm with the increasing temperature. On silicon substrate at 600°C in 1330 Pa of oxygen, rods with a mean diameter of ~ 400 nm were observed. Increasing the laser energy, the pulse repetition rate or the target-to-substrate distance, the rod dimensions increased. The growth mechanism, and thus the film morphology, was assumed to be strongly dependent on the supersaturation conditions, which strongly influences the coalescence processes of the nucleation sites. The ZnO grains were found to be separated in the early stages of the growth, then the rods with favorable orientation grew faster, dominating the growth process. The radial growth of these rods suppressed the growth of the others, and a compact nanorod array was finally formed. Two examples of rod arrays are shown in Figure 10.

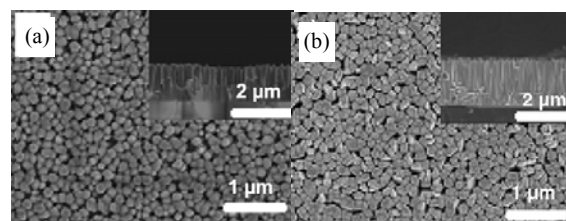


Figure 10. SEM images of two samples deposited by group labeled with *G*. (Reprinted with permission from [125], copyright 2007, Elsevier).

**H) National Dong Hwa University (Shoufeng, Taiwan), University of Florida (Gainesville, Florida, USA), ref. [126]**

A ZnO layer (75-200 nm) was deposited on the substrate at 450°C in 4 Pa of oxygen before the rod growth. C-axis oriented nanowires, perpendicularly aligned to the substrate, were grown at 800°C in 67 Pa of oxygen, argon, or O<sub>2</sub>/Ar mixture. The nanorods had diameters in the range 50-90 nm and length of some μm. Fixing the substrate temperature at 800°C, a smooth film was obtained at an oxygen pressure of 20 Pa, hexagonal microcrystals were observed at 40Pa, nanowires grew at 67 Pa, while only few nanowires were observed at 133 Pa. Fixing the oxygen pressure at 67 Pa, the rods diameter was found to decrease from ~ 500 nm at substrate temperature of 550°C, to ~ 150 nm at 750°C, to less than 100 nm at 800°C. Since no particles were observed on the tips of the nanowires, the VLS mechanism was excluded.

**I) Keio University (Yokohama, Japan), ref. [127]**

The silicon substrate was firstly coated with ZnO powder and annealed at 1150°C for one hour, then the deposition was performed at 650°C. Without the annealing process, nanorod arrays were not grown, and only a ZnO thin film or particles were obtained. Also, no nanorods grew on the uncoated regions of the substrate. The rod diameters and lengths were found respectively to decrease from ~ 700 nm to ~ 50 nm and to increase from ~ 2 μm to ~ 10 μm with increasing the distance of the substrate from the central position. The growth was ascribed to a VS mechanism in which, in the initial stages, the plume particles condensed on the seeds present on the coating layer, then the rods continued the growth along the c-axis. Some samples are shown in Figure 11.

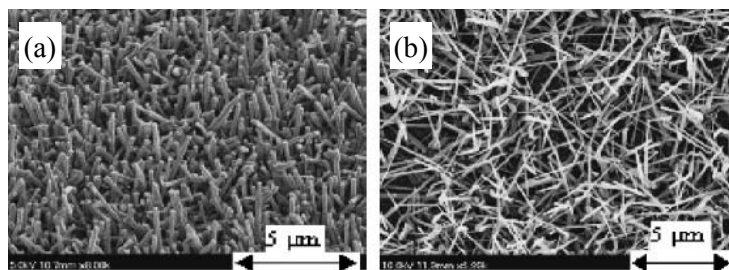


Figure 11. SEM images of two samples grown by group labeled with I. (Reprinted with permission from [127], copyright 2008, Japan Society of Applied Physics).

**J) Jawaharlal Nehru Centre for Advanced Scientific Research (Bangalore, India), ref. [128]**

A 30 nm Au catalyst layer was sputtered on the silicon substrate. C-axis oriented nanorods with diameters of ~ 30-50 nm and lengths of ~ 100-300 nm were grown at substrate temperature of 600°C, diameters of ~ 40-60 nm and lengths of ~ 200-400 nm at 700°C, and diameters of ~ 30-70 nm and lengths of ~ 200-400 nm at 800°C. Figure 12 shows some samples.

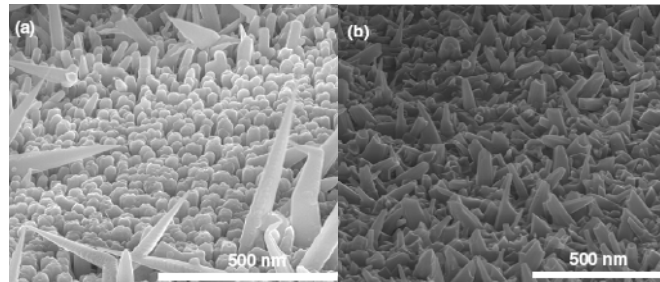


Figure 12. SEM images of ZnO nanorod samples grown by group labeled with J. (Reprinted with permission from [128], copyright 2008, Institute Of Physics (IOP)).

**K) University of Canterbury (Christchurch, New Zealand), The MacDiarmid Institute of Advanced Materials and Nanotechnology (New Zealand), ref. [129]**

Here nanostructured ZnO films were grown either by the standard PLD technique or by the eclipse PLD technique (EPLD), in which a shadow mask is placed between the target and the substrate to block the large particulate produced during the target ablation. By PLD, rods with a base of  $\sim 200$  nm, a tip of  $\sim 50$  nm and a length of  $\sim 900$  nm grew with a good perpendicular alignment, but many particulates were observed in the sample. The film grown by EPLD was particulate-free and constituted by rods, with diameter of  $\sim 80\text{-}90$  nm, which clumped up in micron-sized circular zones. Among the microclumps, hexagonal pyramids with a base diameter of  $\sim 150\text{-}200$  nm, height of  $\sim 100\text{-}200$  nm and tip of  $\sim 60\text{-}70$  nm were observed. These tips were considered as capping particles due to a VLS mechanism starting from Zn droplets. Two samples are reported in Figure 13.

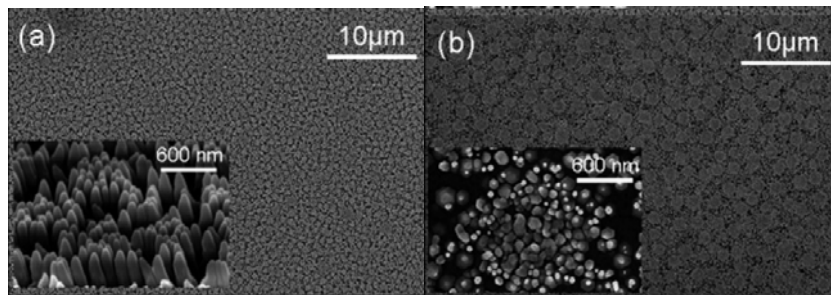


Figure 13. SEM images of two films grown by group labeled with K. (Reprinted with permission from [129], copyright 2008, Elsevier).

**L) University of Technology (Dalian, China), ref. [130]**

A ZnO buffer layer was grown on an InP substrate at  $300^{\circ}\text{C}$ , then the substrate temperature was increased to  $400^{\circ}\text{C}$  for the nanorod growth. The buffer layer was constituted of ZnO droplets, acting as self-catalysts and thus as seed-crystals for the growth of the nanorods, having a diameter of  $\sim 400$  nm. A SEM image is shown in Figure 14.

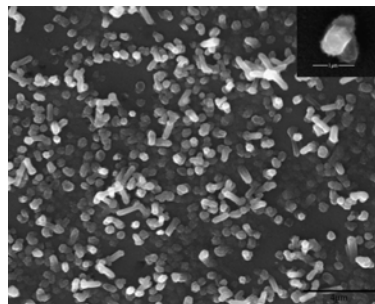


Figure 14. SEM image of ZnO nanorods grown by group labeled with L. (Reprinted with permission from [130], copyright 2008, Elsevier).

#### **M) University of Salento (Lecce, Italy), refs. [131,132]**

Different kinds of nanostructures were obtained by our research group by changing the deposition parameters. The details of our results are reported in the next paragraphs.

As seen in the discussion above, different mechanisms have been proposed to explain the growth of ZnO nanorods: formation of nanoparticles in the plume which form nucleation sites on the substrate for the nanorod growth (for example in a Stranski-Krastanov mode), other VS mechanisms (for example in a Volmer-Weber mode), VLS mechanism catalyzed by zinc droplets, or atypical VLS with the Au catalyst on the bottom of the rods instead of the top as in classical VLS. It should be noticed that formation of nanoclusters in the gas phase during ablation of a ZnO target has been also demonstrated by photoluminescence measurements [133].

Moreover, it is evident that several different sets of deposition parameters have been used to successfully grow ZnO nanostructures. This implies that, obviously, it is not possible to choose a unique set of parameters to get the PLD-growth of ZnO nanostructures and that the suitable set of deposition parameters must be found and optimized on one's own experimental system. Anyway, by a comparison of the parameters used by the different research groups, it is possible to draw some observations:

fluences from  $\sim 1$  to  $5 \text{ J/cm}^2$  were used for KrF ( $\lambda = 248 \text{ nm}$ ) laser ablation, and from  $\sim 1$  to  $20 \text{ J/cm}^2$  for ArF ( $\lambda = 193 \text{ nm}$ ) laser ablation;

usually a zinc oxide target was ablated for the depositions, although reports with the use of a metallic zinc target are present;

the possibility to deposit ZnO nanostructures on different substrates (silicon, sapphire, silica, etc.) was showed;

the optimal substrate temperature was around  $600^\circ\text{C}$ , and nanorod/nanowire growth was not observed for substrate temperatures lower than  $500^\circ\text{C}$ ;

the help of a pre-deposited catalyst on the substrate was not essential to allow the growth of nanostructures;

nanorod growth was obtained in both low ( $\sim 1 \text{ Pa}$ ) or high ( $\sim 100 \text{ Pa}$  or more) oxygen background pressure; also some reports with the use of Ar or  $\text{N}_2$  background atmosphere are present;

the target-to-substrate distance was usually in the range  $\sim 20$ - $60 \text{ mm}$ , although also shorter or longer distances were reported.

## OUR RESULTS

The last row in Table 1 summarized the deposition parameters and the proposed growth mechanism in our research activity. More details on our results and discussion are reported here.

### **3.a. Experimental PLD Set-Up and Deposition Parameters**

The experimental set-up here used for the growth of nanostructured ZnO films was a conventional PLD system, similar to that one described in par. 2.a and schematized in Figure 4.

The excimer laser used for the target ablation was a Lambda-Physik LPX 305 I, with the possibility to change the working gas mixture (KrF or ArF) and thus the corresponding output wavelength: 248 nm ( $\sim 5$  eV) for KrF, 193 nm ( $\sim 6.4$  eV) for ArF. The laser pulse duration was  $\sim 25$  ns. The laser beam was shaped through a mask with a  $1\text{cm} \times 1\text{cm}$  aperture in order to select the most uniform region of the beam, which was focused onto the target by a  $f = 30$  cm lens. The target was placed inside a stainless steel vacuum chamber and put on a target-holder rotated and translated to avoid continuous ablation on the same point. The chamber was evacuated by a pumping system, constituted of a scroll pump and a turbomolecular pump, and filled with oxygen gas with 99.999% purity to obtain the desired background atmosphere. The substrate was placed on a substrate holder/heater allowing to set the substrate temperature up to  $\sim 700^\circ\text{C}$ . A K-type thermocouple was fixed on the front face of the substrate holder, nearly in direct contact with the substrate (distance  $\sim 1$  mm) in order to measure the actual substrate temperature, and protected against the incoming ablated material. The thermalization of the heater surface and substrate was assured awaiting one hour after the desired temperature was reached, before starting the target ablation. The value of the laser fluence on the target was estimated by measuring, before evacuating the vacuum chamber, the laser energy arriving onto the target by a joulemeter and the area of the laser spot directly on the target surface by a caliper.

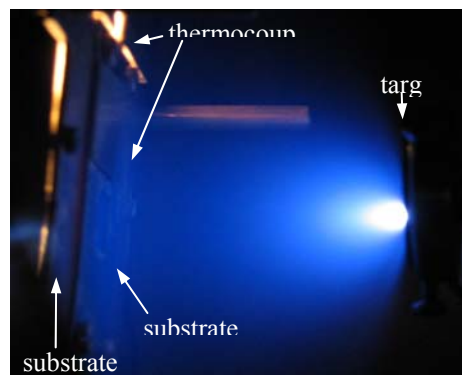


Figure 15. A detail of the experimental set-up inside the vacuum chamber and of the ZnO plume during a PLD process. Some elements of the set-up are indicated in the picture.

The photo in Figure 15 displays a detail of the experimental set-up, showing the target and the substrate on the heater during a ZnO deposition. The plasma plume in the photo was produced by the ablation of the ZnO target by the KrF excimer laser beam in an oxygen background pressure of 1 Pa.

In our study, ZnO nanostructured films were grown without the aid of any catalyst, by using two different excimer laser wavelengths (KrF mixture or ArF mixture) for the target ablation, by varying the substrate temperature and by performing the depositions at low and relatively high oxygen background pressure, while all the other deposition parameters were kept constant. In particular, the used deposition parameters are listed below.

Fixed parameters:

- Target = sintered ZnO (99.999% purity, bought from M.C.S.E.)
- Repetition rate of laser pulses = 10 Hz
- Laser spot dimensions on the target:  $\sim 4.2 \text{ mm}^2$  with KrF,  $\sim 4.5 \text{ mm}^2$  with ArF
- Laser fluence on the target:  $\sim 4.3 \text{ J/cm}^2$  with KrF,  $\sim 1.6 \text{ J/cm}^2$  with ArF
- Substrate = Si (100), area  $1\text{cm}\times 1\text{cm}$
- Target-to-substrate distance = 45 mm
- Number of pulses for each deposition = 25000
- No catalyst used

Varied parameters:

- Laser wavelength = 248 nm (KrF) or 193 nm (ArF)
- Substrate temperature = 500-700°C
- Oxygen background pressure = 1, 5, 50, 100 Pa

The low fluence value used for the ArF depositions was due to limitations in the experimental set-up: indeed the laser output energy obtained with the ArF mixture was lower than that one obtained with KrF, and the spot was chosen in order to get the minimum spot dimensions obtainable having a regular (rectangular) shape and without evident non-homogeneous zones in the ablated region. In these conditions the minimum spot dimension was around  $4.5 \text{ mm}^2$ , resulting in a fluence of about  $1.6 \text{ J/cm}^2$ .

Before the depositions, the silicon substrates were cleaned by ultrasonic baths for 10 minutes in acetone and 10 minutes in isopropyl alcohol.

The vacuum chamber was evacuated to a base pressure of  $\sim 4\times 10^{-5} \text{ Pa}$ , which rose up to  $\sim 4\times 10^{-4} \text{ Pa}$  when the substrate was heated, due to desorption inside the vacuum chamber.

Before starting each deposition, the substrate was shut by a steel mask and a preliminary ablation was performed spanning the target surface for two cycles. This preliminary ablation had two purposes. First, the target surface was cleaned of possible environmental contaminants. Second, since it has been reported [134] that the ZnO target surface becomes Zn-enriched after just a few laser shots due to backscattered zinc from the plume onto the target surface, a preliminary target ablation ensured that the composition of the ablated species and the deposition rate were almost constant throughout the deposition [135].

After the film deposition, the substrate cooled down to room temperature with a rate of about  $14^\circ\text{C}/\text{min}$  at the same oxygen pressure used during the deposition.

The following notation will be used hereafter to label the deposited samples: the first letter refers to the laser wavelength used for the target ablation (K for KrF, A for ArF), then the substrate temperature and the background oxygen pressure are reported in the label. For example, the sample labeled as “K600\_1” indicates the sample grown by KrF laser ablation at substrate temperature of 600°C and oxygen pressure of 1 Pa.

### 3.b. Morphology

The morphology of the deposited samples was investigated by Scanning Electron Microscopy, by a JEM JEOL 6500F instrument equipped with a Schottky Field Emission Gun (SEM-FEG), used in the secondary electron detection mode and with an accelerating voltage of 5 kV.

#### 3.b.1. KrF-deposited samples ( $\lambda = 248 \text{ nm}$ , $E = 5 \text{ eV}$ )

Figure 16 reports the SEM images of three samples deposited at substrate temperatures of 500°C, 600°C and 700°C in 1 Pa of oxygen background atmosphere.

The sample deposited at 500°C (K500\_1) appears as a smooth film with a “jigsaw”-like morphology. This morphology is similar to that one reported for metal films grown by physical vapor deposition techniques in a growth regime of transition from islands to percolation [136]. It has been reported that metal films deposited by this kind of techniques on substrates such as silicon, glass or graphite, in certain ranges of temperature have an initial growth consisting in droplets forming small islands which touch and coalesce to create larger islands. When the growth proceeds these islands can further coalesce forming elongated structures with gaps between the different structures (this process is called percolation). The coalescence stops when the islands reach a certain critical size, and the resulting film morphology depends on the competition between island coalescence due to surface diffusion and island growth due to deposition. This observation suggests that, in our case, zinc and zinc sub-oxide ( $\text{Zn}_x\text{O}_y$  with  $y < x$ ) species, created in high amount in the plasma plume [137], form small droplets on the substrate since their melting temperature is very low (about 419°C [138] like the zinc melting point, or slightly higher for bigger and more stoichiometric clusters); these droplets coalesce in the very early stages of the growth and form the islands acting as nucleation sites for the subsequent ZnO film growth. As a consequence the final morphology resembles these islands formed in the early stage of the growth. Of course some differences can be observed in sample K500\_1 with respect to the metal films mentioned above: the “pieces” forming the jigsaw morphology are smaller (sizes of the order of ~ 10-100 nm) than those observed in metal films (more than 1 μm) and no gaps among them are observed. These differences can be explained observing that, in our case, the adatoms depositing on the substrate are mainly constituted by oxide (or sub-oxide) species and not only by pure metal species; therefore the tendency to coalesce is slower than for pure metals and thus smaller and closer islands are formed.

At substrate temperature of 600°C (sample K600\_1) the same jigsaw morphology is still present (see inset of Figure 16(b)) but some structures, with dimensions ranging from few tens of nm to ~ 100 nm, emerge from the surface. The appearance of these nanometric structures is in accordance with a known behavior: the depositing species need higher

energies to allow the growth of nanostructured samples. In this case, this energy is provided to the adatoms by two ways. The first one is, of course, the higher temperature of the substrate itself, thus supplying more energy to the species arrived on the substrate. A second mechanism can be related to the observation that, for ablation of oxide materials in oxygen background atmosphere, the substrate heating also influences the plume propagation, as reported in ref. [139]: at higher temperatures the background gas resistance to plume propagation is reduced, leading to an increased velocity, and hence kinetic energy, of the species reaching the substrate during the film growth.

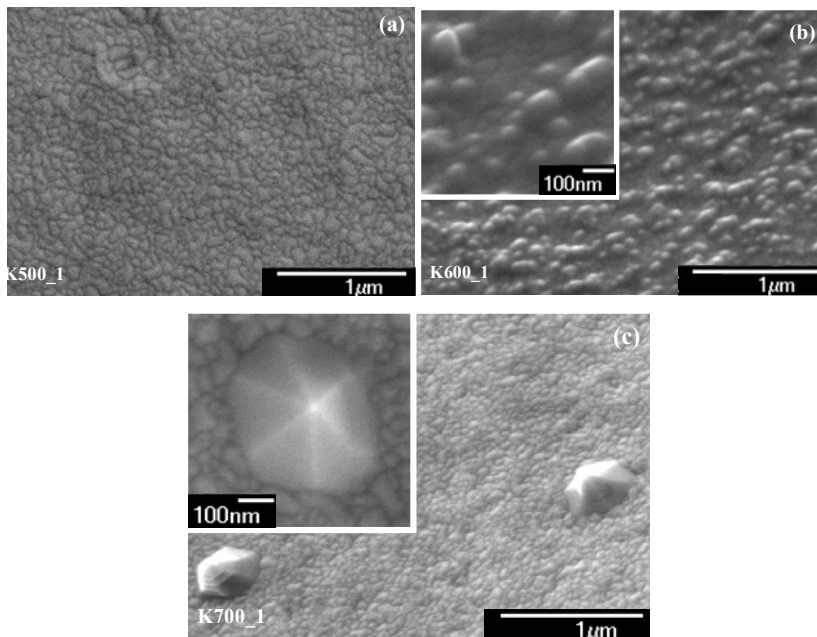


Figure 16. SEM images of KrF-deposited ZnO films in 1 Pa of oxygen at substrate temperature of (a) 500°C, (b) 600°C and (c) 700°C. Image (b) and main panel of (c) are 45°-tilted views. Insets of (b) and (c) are at higher magnifications with respect to the corresponding main panels.

When the substrate temperature is further increased to 700°C (sample K700\_1), the same jigsaw morphology is still observed, but sparse pyramids with a nearly perfect hexagonal base of  $\sim 400$  nm are present. By carefully observing these structures, it seems they are not grown on the sample surface, while they seem to emerge from the bottom of the sample. It is reasonable that hexagonal columns starts directly from the substrate surface or just after some few layers of material, and that the observed hexagonal pyramids are their tops, like a sort of pencils with a diameter of  $\sim 400$  nm. These structures can be thought as deriving from the formation of bigger clusters, due to coalescence of the depositing species in the early stage of the growth, and, because of the high substrate temperature, these bigger clusters receive enough energy to be arranged in nearly perfect hexagonal crystals as the ZnO wurtzite structure. Due to their hexagonal base, it can be deduced that the observed structures are grown along the ZnO wurtzite c-axis, perpendicular to the substrate surface.

The SEM images of ZnO samples deposited at fixed substrate temperature of 600°C and at oxygen pressures of 5, 50 and 100 Pa are shown in Figure 17.

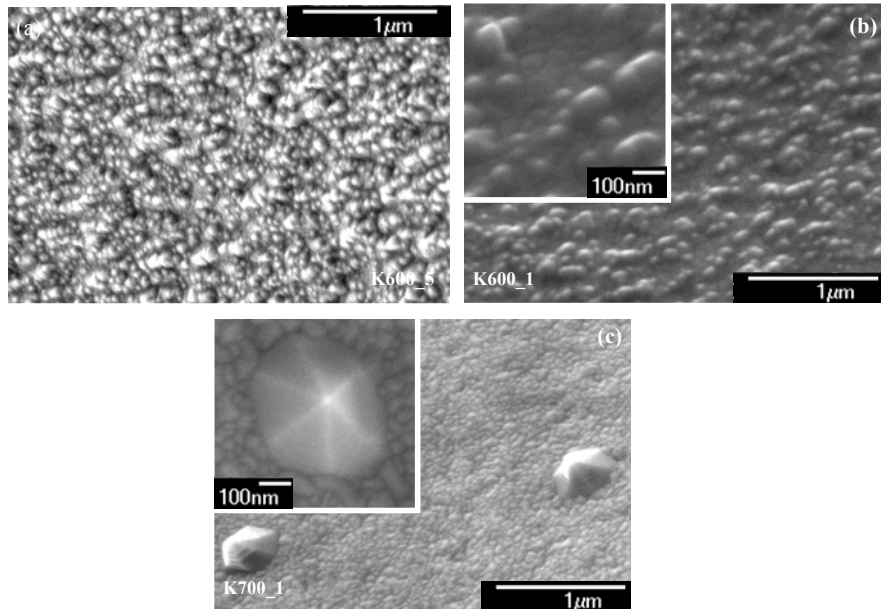


Figure 17. SEM images of KrF-deposited ZnO films at substrate temperature of 600°C and oxygen background pressure of (a) 5 Pa, (b) 50 Pa and (c) 100 Pa. Image (a) is a 45°-tilted view. Insets of (b) and (c) are 40°-tilted view in proximity of intentionally-made scratches on the sample surface.

The surface of the sample deposited at 5 Pa (K600\_5, Figure 17(a)) is rougher than that one deposited at 1 Pa at the same substrate temperature (K600\_1, Figure 16(b)), as expected due to the higher presence of particulates in a higher oxygen pressure. At further higher oxygen pressures (samples K600\_50 and K600\_100) the films show a columnar structure, evident in the insets of Figures 17 (b) and (c), and at 100 Pa the film is made by a rod array directly starting from the substrate surface. The rods of sample K600\_100 have diameters in the range  $\sim$  100-400 nm and their tops have a nearly hexagonal shape, suggesting that the columns are grown in the wurtzite structure with the c-axis perpendicular to the substrate surface. The morphology of sample K600\_100 is very similar to that one reported in the literature for nanostructured ZnO films grown by PLD in high oxygen pressure ( $\sim$  100-700 Pa) (see e.g. groups labeled with *A1* and *C1* in par. 2.b). This kind of growth was attributed to the high number of collisions of the ablated species in the high background pressure causing the formation, in the gas phase, of nanoparticles that stack on the substrate and fuse to form the rods. The height of the rods of sample K600\_100 is about 3.5  $\mu$ m near the center of the sample, while it decreases to about 2.7  $\mu$ m in the border proximity. Moreover, at the center of the sample the columns are well oriented perpendicularly to the substrate surface, whereas, very close to the sample borders, they tend to slightly tilt toward the center. Further details and discussion about these features can be found in ref. [132].

### 3.b.2. ArF-deposited samples ( $\lambda = 193$ nm, $E = 6.42$ eV)

Figure 18 shows the SEM images of three samples deposited by ablating the target with the ArF laser beam at substrate temperatures of 500°C, 550°C and 600°C in 1 Pa of oxygen background atmosphere. For all the three samples, nanostructures constituted by hexagonal

terraces (“hexagonal hierarchical nanostructures”) are visible. These structures are particularly evident in the insets of Figs. 18 (b) and (c).

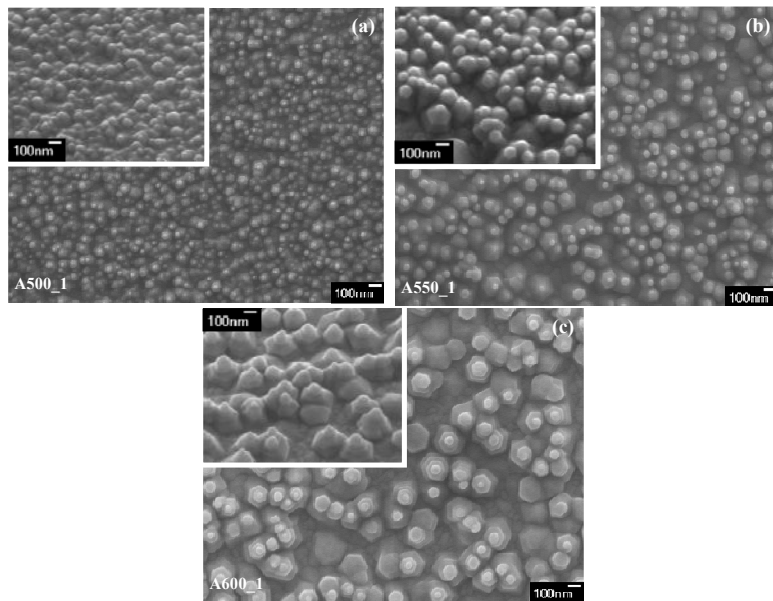


Figure 18. SEM images of ArF-deposited ZnO films in 1 Pa of oxygen at substrate temperature of (a) 500°C, (b) 550°C and (c) 600°C. Insets of (a), (b) and (c) are 40°, 30° and 45° -tilted views, respectively.

It can be noticed that the nanostructure diameter increases with increasing the growth temperature. In sample A600\_1 these structures have a base diameter of ~ 200 nm and a tip of ~ 30-40 nm. The perfect hexagonal shape of the terraces indicates that, like in other samples shown above, the structures grew in the wurtzite structure with the c-axis perpendicular to the substrate. Moreover it can be seen that these hierarchical structures sprout from a jigsaw-like film, similar to that one observed for the KrF-deposited samples, thus suggesting a similar growth mechanism for both the ablating wavelengths. Again it can be assumed that the species arriving onto the substrate coalesce forming the islands acting as nucleation sites for the subsequent film growth. However samples grown by the ArF ablating beam clearly exhibit a higher degree of nanostructuration, also at lower substrate temperatures, in comparison with the KrF-deposited ones, thus denoting a better tendency towards the growth of nanostructures when the 193 nm wavelength is used in comparison to the 248 nm wavelength. This occurrence can be ascribed to several reasons. Firstly, since the ArF photon energy is higher than the KrF one (6.42 eV versus 5 eV), during the depositions with ArF the target material is ablated by higher-energy photons and, in addition, the ablated species absorb higher-energy photons from the subsequent laser pulses. Secondly, the lower ArF laser fluence can be partially balanced by a higher absorption of the ArF laser beam per unit volume of the ZnO target, with respect to KrF. In a further addition, the higher energy of the ArF photons can also cause the production of more ionized species and more electronically excited species (Rydberg atoms or ions) in the plasma plume; this feature can lead to a higher Coulombic repulsion and thus probably to higher plume velocities (at least for the charged

components). As a consequence of all these factors, it may be supposed that during the depositions with the ArF laser beam, despite the lower fluence and the lower substrate temperature, the species depositing onto the substrate have a higher kinetic energy with respect to KrF. Therefore, the formation of nanostructures and the possibility to get clusters having enough energy to arrange in hexagonal wurtzite crystals are favored when using the ArF ablating beam. Besides, it can be also underlined that the higher degree of plume ionization and a better dissociation of the oxygen molecules (as better explained in par. 3.c) lead to a greater reactivity between the ablated species and the background atmosphere, hence the depositing species can be also different when the ArF or KrF lasers are used to ablate the target.

About the terrace growth observed for the hierarchical structures, a possible explanation can be found in the competition between two processes, suggested to explain the growth of hierarchical structures by vapor phase technique: *ledge-flow mode* and *nucleation on the terrace* [140]. When a terrace is formed, the other incoming species can diffuse from the terrace to its edge (ledge-flow mode) or can coalesce starting to form a new terrace (nucleation on the terrace). The competition between these two processes depends on the ratio of the diffusion time of an adatom from the terrace to the edge and the interval time between adatoms arriving at the terrace, thus determining the morphology of the film. This mechanism can also explain the increasing nanostructure size with the substrate temperature observed in Figure 18: indeed, increasing the substrate temperature the surface mobility of the depositing species increases, thus increasing the rate of the diffusion process of adatoms to the edge of the ledge and consequently increasing the nanostructure diameter.

Another interesting feature is the slight inclination of the nanostructures near the sample border towards the center, similarly to what observed for sample K600\_100. This tilt from the substrate normal is shown in Figure 19, whose inset also evidences how the structures partially lose the well-defined hierarchical structure observed at the center of the sample.

When the substrate temperature is further increased to 650°C (sample A650\_1), the nanostructure formation is inhibited and the film-like growth becomes more favorable, thus resulting in a smooth film with only few sparse pyramidal nanostructures coming out, as observable in Figure 20. The inset evidences that the residual structures still preserve a hierarchical construction, although less sharp and less well-defined than in the previous samples.

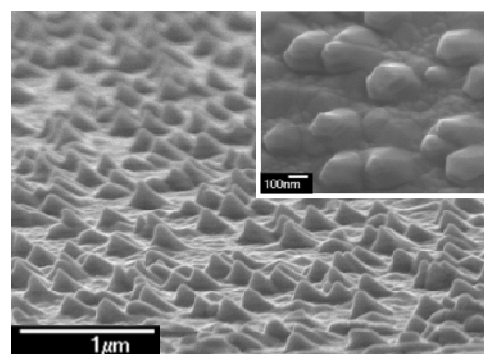


Figure 19. SEM image of sample A600\_1 near the sample border. Inset: higher magnification very near to the sample border.

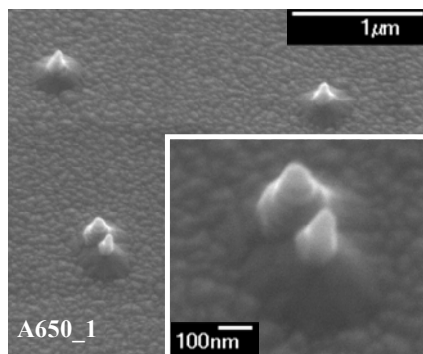


Figure 20. 45°-tilted view SEM image of ArF-deposited sample at substrate temperature of 650°C and 1Pa of oxygen background pressure. Inset: higher magnification.

Figure 21 shows the SEM images of samples deposited at substrate temperature of 600°C at increased oxygen pressure of 50 and 100 Pa.

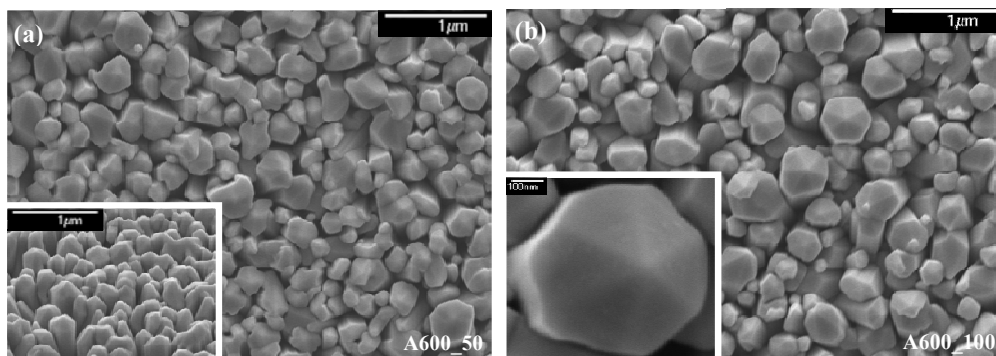


Figure 21. SEM images of ArF-deposited samples at substrate temperature of 600°C and oxygen background pressure of (a) 50 Pa and (b) 100 Pa. Inset of (a) is a 45°-tilted view, inset of (b) is a higher magnification on the top of a pencil.

Similarly to the KrF-deposited samples at the same temperature and pressures, these samples show the same tendency to grow forming a pencil-array. The columns are somewhat non-uniform in shape and size, with column diameters in the range from ~ 80 to ~ 500 nm, and rather randomly tilted from the substrate normal. Clear evidence of a hexagonal shape can be observed from the images, thus indicating that the pencil axis is the c-axis of the wurtzite structure. Comparing the samples grown in 50 and 100 Pa, it can be noticed that sample A600\_100 has a better uniformity in shape and size and a more evident tendency to grow in a nearly perfect hexagonal structure (see also inset in Figure 21(b)). This behavior is similar to what observed also in samples K600\_50 and K600\_100, and it is consistent with the growth mechanism assuming, at higher background pressures, the formation of a larger amount of nanoparticles in the gas-phase forming the nucleation sites for the growth of the columns.

Even if the samples deposited at a substrate temperature of 600°C in 100 Pa of oxygen by the KrF and ArF wavelength show the same trend to grow in a pencil-like way, the

differences between samples K600\_100 and A600\_100 are evident: in the former, the columns are almost perfectly aligned, oriented perpendicularly to the substrate surface and very close-packed, while in the latter the columns are misaligned, not perpendicular to substrate surface and more separated one each other. Moreover the hexagonal shape is much more evident in the ArF-deposited sample. All these differences are compatible with the suggestion made above, supposing more energetic depositing species when the 193 nm laser beam is used instead of the 248 nm for the target ablation. Indeed it can be assumed that, due to the higher energy of the species depositing on the substrate, there is a more favorable tendency to arrange in hexagonal wurtzite big crystals but, at the same time, there is also a higher tendency to grow with less ordered alignment and orientation during the ablation by the ArF laser beam with respect to the KrF one.

By cross-sectional SEM inspections it is observed that, unlike the array of sample K600\_100, in proximity of the border of sample A600\_100 the rods do not show any tendency to grow inclined toward the center of the sample, while they are still somewhat randomly oriented as in the center of the sample. In addition, the difference in thickness is almost imperceptible in this case: a thickness of  $\sim 1.2\text{-}1.3 \mu\text{m}$  and  $\sim 1.15 \mu\text{m}$  is measured near the center and near the border respectively, corresponding to a difference of about 4-11% from the thickness measured at the center, while it was around 23% in sample K600\_100. Again, this observation can be attributed to the possible higher energy of the ablated material, thus allowing that a higher amount of material can reach the more distant regions of the substrate. Anyway it must be taken into account that sample K600\_100 is thicker than A600\_100 ( $\sim 3.5 \mu\text{m}$  versus  $\sim 1.25 \mu\text{m}$ , measured at the center of the two samples) so it cannot be excluded that the per-cent difference in thickness between the center and the border should become higher for a thicker ArF-deposited sample.

### **3.b.3. Comparison between KrF and ArF -deposited samples**

Some comparisons about the samples deposited by KrF and ArF laser ablation were already made in the previous paragraph. The important observations are re-summarized here.

By KrF laser ablation a weak sample nanostructuration was observed at low oxygen background pressure (1-5 Pa), while at high pressure (50-100 Pa) the samples grew in columnar structures and a rod array was obtained at 100 Pa. On the contrary, by ArF laser ablation the tendency toward the growth of nanostructures is stronger, also at low oxygen pressure and low substrate temperature. A possible explanation for this behavior was discussed in the previous paragraph and attributed to the ArF higher photon energy.

At the same time, some common features were observed in samples deposited by the two ablating laser beams. For depositions at low oxygen pressure, a similar jigsaw-like film has been observed as background in samples grown by both laser wavelengths, suggesting a similar growth mechanism, but leading anyway to very different final morphologies. In the same way, at high oxygen pressure, for both laser wavelengths the films showed the formation of rod-arrays but, while with KrF the columns were well oriented perpendicularly to the substrate surface, with ArF the structures were tilted in a more disordered way. Moreover the hexagonal shape was more evident in the ArF-deposited films. As discussed in the previous paragraph, also for these behaviors a possible explanation was suggested in the higher photon energy of the ArF laser beam.

### 3.c. Summary of Other Characterizations

X-ray diffraction measurements (XRD) were performed to give information about the sample crystal quality and orientation. A Rigaku diffractometer with  $\text{CuK}\alpha_1$  radiation ( $\lambda = 1.5405 \text{ \AA}$ ) was used over a  $2\theta$  range from  $30^\circ$  to  $80^\circ$ . Figure 22 shows the XRD spectra of samples K600\_100 and A600\_1.

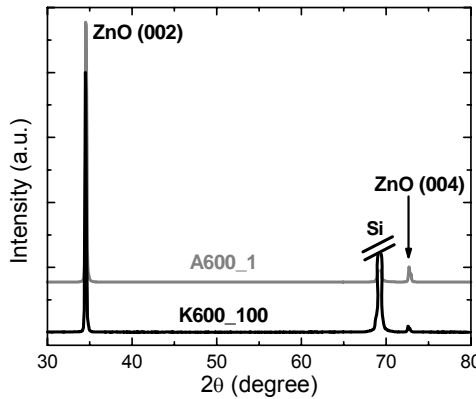


Figure 22. XRD spectra of samples K600\_100 and A600\_1. The spectra are normalized on the first peak and vertically translated for clarity.

Apart from the peak at  $\sim 69.1^\circ$  coming from the silicon substrate, only the (002) and (004) diffraction peaks of the zinc oxide wurtzite crystal structure are visible, indicating the good film crystal quality and that the samples are grown along the wurtzite c-axis perpendicular to the substrate surface, as also previously suggested by SEM inspections. About sample A600\_1, since it is expected that the jigsaw-like film under the hexagonal structures (see Figure 18(c)) provides a significant contribution to the XRD spectrum, the absence of any other peak besides the (002) and (004) ones suggests that this underlying film is c-axis oriented as well.

Photoluminescence (PL) measurements were conducted at room temperature (RT) and 7 K by exciting the samples with the 325 nm line delivered by a continuous wave He-Cd laser (Kimmon IK Series). The laser beam was focused onto the sample resulting in a spot dimension of  $\sim 130 \mu\text{m}$  and a power of  $\sim 6 \text{ mW}$ . The PL was collected by a Jobin Yvon SPEX TRIAX320 monochromator, with a 1200 lines/mm grating and  $100 \mu\text{m}$  slits. The nominal resolution of the instrument was 0.6 nm at 500 nm. All the recorded PL spectra were corrected with the spectral efficiency curve of the grating inside the monochromator.

Figure 23 shows the low temperature (7 K) PL spectra of some samples deposited by KrF laser ablation. In order to make a comparison of the spectra, the intensities were normalized on the peak positioned at  $\sim 3.37 \text{ eV}$ .

The spectra evidence the donor-bound exciton emission at  $\sim 3.37 \text{ eV}$  and two defect bands: a wide band centered at  $\sim 2.3\text{-}2.4 \text{ eV}$  (usually called “green band”) and a violet-blue band centered at  $\sim 3.1 \text{ eV}$ . For sample K500\_1, both defect bands are very intense, thus pointing out the low quality of this sample. For samples deposited at higher temperatures, the relative intensity of the violet-blue band with respect to the excitonic peak decreases with increasing the substrate temperature, while, apart for sample K500\_1, the green band remains

almost unaffected by the deposition temperature (see also [132]). On the contrary, the intensities of both bands decrease with increasing the oxygen pressure. The green band can be attributed to emission related to oxygen vacancies, while the violet-blue band can be ascribed to emission from zinc-related defects like zinc interstitials or vacancies [132].

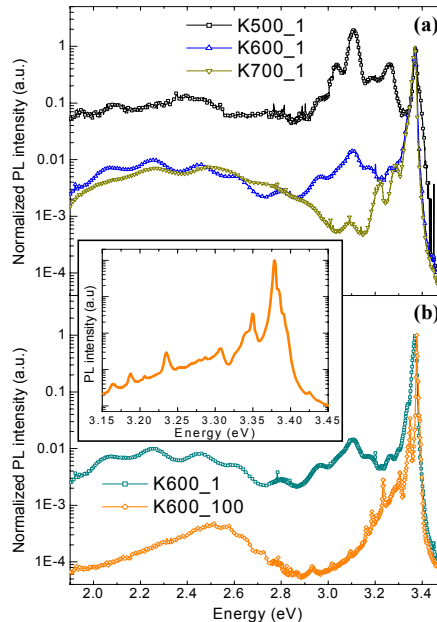


Figure 23. PL spectra at sample temperature of 7 K of KrF-deposited films, (a) at fixed oxygen pressure of 1 Pa and substrate temperature of 500°C (black spectrum), 600°C (blue) and 700°C (green), and (b) at fixed substrate temperature of 600°C and oxygen pressure of 1 Pa (cyan) and 100 Pa (orange). Inset: magnification of the PL spectrum of sample K600\_100 in the range 3.15–3.45 eV.

The PL spectrum of the rod-array grown at 100 Pa (sample K600\_100) is typical of high quality ZnO films [141]: narrow full width at half maximum (FWHM), low defect emission, and several transitions clearly detectable in the excitonic region as evident in the inset of Figure 23.

Similar trends are also observed for the ArF-deposited samples. However, in this case, even the samples deposited at low substrate temperatures and low oxygen pressures show PL spectra with typical features of high-quality ZnO films (see e.g. the PL spectrum of sample A600\_1 at 7 K reported in Figure 24). Several transitions are clearly detectable in the excitonic region (as observed for sample K600\_100 too), and narrower excitonic peaks and lower defect emission are observed in comparison with the PL spectra of samples deposited by KrF laser ablation at the same substrate temperatures and oxygen pressures, thus indicating an improved crystal quality for the ArF-deposited samples [131]. This can be ascribed to the higher energy of the depositing species during the ArF laser ablation as suggested above, and to the fact that the higher ArF photon energy (6.1 eV) can promote (i) a higher production of ionized and electronically excited species and (ii) a better dissociation of the O<sub>2</sub> molecules, having a dissociation energy of 5.1 eV, with respect to KrF photons (energy of 5 eV). These two effects lead to a better reactivity between the ablated species and the background oxygen molecules, thus allowing for the growth of higher quality films.

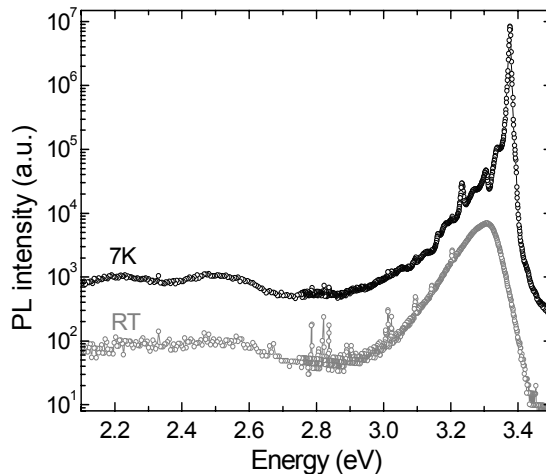


Figure 24. PL spectra at 7 K (black circles) and at room temperature (gray circles) of sample A600\_1.

The room temperature PL spectra (see e.g. the RT spectrum of sample A600\_1 in Figure 24 and the spectra in ref. [131]) show lower emission intensities with respect to the low-temperature spectra due to the increasing effect of non-radiative relaxations, the excitonic emission is shifted to lower energy as expected due to band-gap shrinkage and it appears as a broader and unstructured band due to the broadening of the different peaks in this spectral region.

### 3.d. Gas Sensing Tests

As stated in the first paragraph of this chapter, one of the most appealing applications of ZnO nanostructures is related to gas and biological sensing. In general, semiconductor nanostructures, and particularly metal oxide semiconductors, are very interesting materials for chemical and biological gas sensing applications [44, 142]. In particular, zinc oxide and its nanostructures are extensively investigated as active material for gas sensors, as demonstrated by the great number of tested gases and vapors, like hydrogen, ammonia, carbon monoxide, ethanol, methanol, acetone, butane etc. (see e.g. [143,144,145,146]). Dealing with biological sensing, ZnO has been employed for species like e.g. glucose, cholesterol etc. [147,148].

When gas molecules or biological species interact with the surface of the active material of the sensor, they can induce a change in several physical properties of the material, such as the charge-carrier density, inducing variations in the electrical conductance and/or optical emission. As a consequence, different transduction mechanisms can be exploited in order to reveal the presence of the analyte in the environment. By using ZnO as active material, different transduction mechanisms have been studied, such as the measurements of the variations of the electrical resistance, the Surface Plasmon Resonance (SPR) technique, or the measurements of the variations in the photoluminescence (PL) emission [143-146]. In particular, when molecules of an oxidizing gas, like nitrogen dioxide ( $\text{NO}_2$ ), bind to the ZnO surface, which is an intrinsic n-type material due to native lattice defects like oxygen vacancies and zinc interstitials, they act as electron trappers, thus decreasing the number of

charge-carriers which can radiatively recombine. As a consequence the NO<sub>2</sub> adsorption process on the ZnO surface induces a quenching of the PL intensity. By a real-time monitoring of the integrated PL intensity in a fixed emission wavelength range, it is then possible to reveal the presence/absence of the gas through the decrease/increase of the PL signal.

We tested the room temperature NO<sub>2</sub> sensing properties, at concentrations as low as 3 ppm, of some samples shown in the previous paragraphs by means of PL measurements. The tested sample was placed inside an aluminum sealed chamber where it was exposed to dry air or to a proper mixture of NO<sub>2</sub> and dry air, and excited by the same He-Cd laser (325 nm) used for the PL measurements reported above. The laser beam was split in two paths: a part was sent to excite the sample with a focus spot of about 3 mm<sup>2</sup>, the second beam was sent to a silicon photodiode in order to take into account the fluctuations of the laser power during the sensing measurements. The PL emission was measured by a spectrometer (Avantes MC2000) with a 75 mm focal length, a 600 lines/mm grating, 200 μm slit, a 2048 pixels CCD linear array detector, and a spectral resolution of 4 nm. The integral under the PL spectrum in a fixed wavelength range was periodically acquired at fixed time intervals of 3 seconds. The desired gas concentration in the chamber was obtained by mixing different flows of dry air and NO<sub>2</sub> through a bank of three mass flow controllers (Brooks Instrument 5850S). Each controller could operate in the flow range ~ 2.5-50 ml/min with an accuracy of ±0.2%. Two different total flows (50 ml/min and 100 ml/min) were used. The maximum used NO<sub>2</sub> concentration in dry air was 114 ppm, while the minimum obtainable concentration was about 5 ppm with a total flow of 50 ml/min and 3 ppm with 100 ml/min. Before each measurement, the tested samples were exposed for 15 minutes in dry air flux in order to get sample stabilization. Then, for each selected NO<sub>2</sub> concentration, an exposure of 5 minutes to the gas flux was followed by a recovery of 5 minutes in dry air flux. These periods were long enough to get detectable sensor response and recovery for the probed samples. Due to the high crystal quality of the films considered in this study, the PL signal in the ultraviolet range, resulting from band-edge emission, was very intense while the defect-related green band was very low, as observed in the previous paragraph. As a consequence, in our sensing measurements, the integrated area in the excitonic range, i.e. 360-420 nm was monitored. During the sample exposure to the NO<sub>2</sub> gas, the only significant effect observed in the emission spectrum was a reduction of the PL intensity, while no shift of the emission peak or change in its lineshape were observed.

Figure 25 shows the integral of the PL emission vs. time during the sensing measurements for five selected samples, whose SEM images are recalled beside the corresponding spectra. Six different NO<sub>2</sub> concentrations, from 11 ppm to 114 ppm, were tested with a total flow of 50 ml/min. The spectra were normalized assuming a value of 1 for the integrated area at the beginning of the measure. All the graphs are reported with the same scale on the Y-axes in order to make a comparison of the different signals. As observable in the figure, when NO<sub>2</sub> was introduced into the chamber, the PL integral sharply decreased and, after about 2 minutes, it reached a rather stable value. When dry air was flowed again, the integral partially recovered its initial value. The sensor response  $S_C$  at a fixed gas concentration  $C$  can be defined as the percentage variation of the PL integrated area during the gas exposure with respect to the initial value in air. The values of  $S_{II}$ , that is the sensor response at NO<sub>2</sub> concentration of 11 ppm, are reported inside each graph.

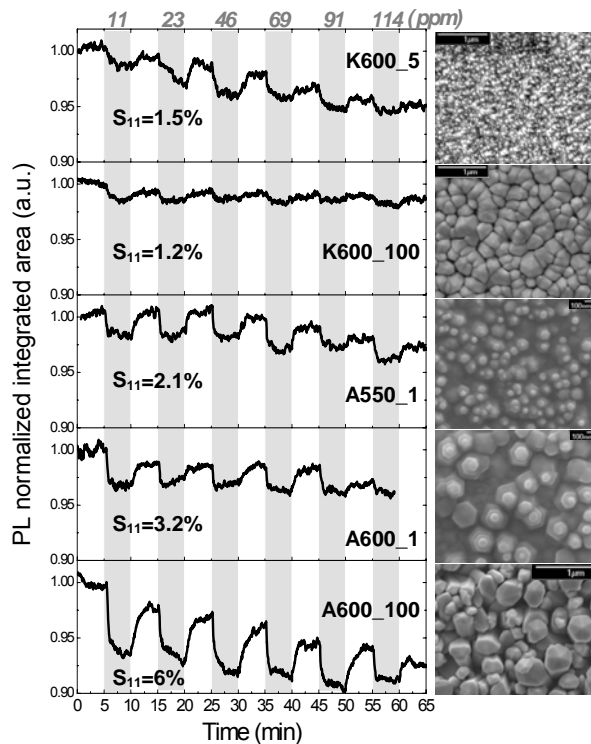


Figure 25. Room temperature NO<sub>2</sub> PL sensing measurements for some deposited samples at gas concentrations from 11 to 114 ppm, with a gas flow of 50 ml/min. The time intervals of NO<sub>2</sub> exposure are gray-shaded and the corresponding gas concentrations are reported on the top of the graph, while the white regions indicate the recovery in dry air. The values  $S_{11}$  of the response measured at the lowest NO<sub>2</sub> concentration (11 ppm) are reported inside each graph. An excerpt of the SEM image of each sample is reported beside the corresponding graph.

The best responses are measured for samples A550\_1, A600\_1 and A600\_100, which, thanks to their highly nanostructured morphology, have a higher total exposed surface than samples K600\_5 and K600\_100. Although sample K600\_100 is constituted by a rod array, thus having a high surface-to-volume ratio and a high total surface, it presents the worse response to the gas, probably because the rods are tightly close one each other, thus allowing only a small fraction of the incoming molecules to bind to their surface. A low sensitivity is also revealed for sample K600\_5, having a non-nanostructured surface although quite rough. On the contrary, the sensitivity increases in the last three samples shown in Figure 25, and the highest response (about 6% at 11 ppm) is obtained for the pencil-array (sample A600\_100). This behavior can be ascribed to the well separated pencils which constitute the sample surface, resulting in a very high surface-to-volume ratio and a very wide total surface available for gas molecule adsorption.

Two other important features can be observed in Figure 25: in all the signals, the quenching of the PL integrated area, or in other words the response, decreases as the gas concentration increases in the range 11-114 ppm; in addition, beside the sharp variations of the PL integrated area, the sample radiative emission continuously decreases during the experimental run-time (with a final reduction of about 3-7 %). These observations suggest that the process of NO<sub>2</sub> adsorption is not fully reversed during the sample recovery in dry air.

In other words probably not all the adsorbed molecules are released during the recoveries in dry air and consequently a complete retrieval of the initial PL integral was not allowed, thus causing a worsening of the sensor response. More details will be reported elsewhere [149].

Sample A600\_100, which showed the highest sensor responses, was tested at lower gas concentrations (from 3 to 20 ppm) and with a higher gas flux (100 ml/min). Figure 26 shows the sensing measurements at NO<sub>2</sub> concentrations in the range 5-20 ppm with a total flow of 50 ml/min, and in the range 3-20 ppm with a total flow of 100 ml/min.

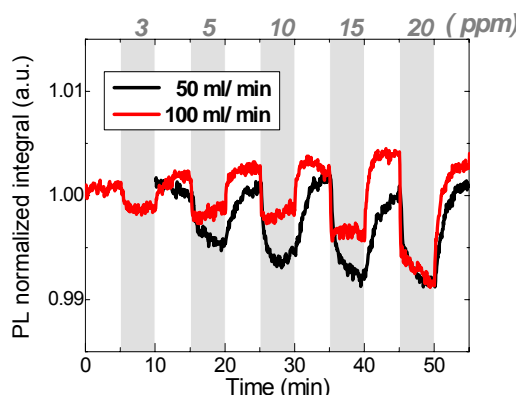


Figure 26. Room temperature NO<sub>2</sub> PL sensing measurements for sample A600\_100 at gas concentrations from 3 to 20 ppm, with gas flows of 50 ml/min (black line) and 100 ml/min (red line).

From these measurements, a low sensor response is obtained in comparison to that one obtained from the last spectrum of Figure 25: at 50 ml/min the response value is about 0.7% and 0.9% at 10 and 15 ppm NO<sub>2</sub> concentrations respectively, far lower than the 6% value observed in the previous measurement at 11 ppm. This decrease is supposed to derive from the incomplete release of NO<sub>2</sub> molecules adsorbed in the previous measurements. Anyway, in spite of these low responses, the variations of the PL integrated area when switching between NO<sub>2</sub> and dry air result to be still sharp, thus allowing to clearly detect the NO<sub>2</sub> presence also at the lowest tested concentration (3 ppm).

Further inspections show that, as expected, the effects of the incomplete reversibility of NO<sub>2</sub> adsorption are reduced at lower tested NO<sub>2</sub> concentrations and higher gas flux [149].

## CONCLUSION

A brief review has been presented about properties, applications and growth methods of nanostructured ZnO. The attention has been then focused on the growth of this material by the Pulsed Lased Deposition technique, and results obtained by different research groups have been reported. The results obtained by our research group have been described in a deeper extent. Smooth or rough films, as well as nanostructured films with hexagonal pyramids, columns, hexagonal hierarchical structures and pencils have been obtained by changing the ablation laser wavelength, the substrate temperature and the oxygen pressure. The morphology of the deposited samples has been investigated to get information about the

growth mechanisms, and some characterization analyses have been reported in summary to obtain information about the sample quality. Films deposited by ablation with the ArF laser beam showed a better tendency to grow in nanostructured forms and a higher quality than those grown by using the KrF laser beam. The differences observed between samples deposited by the two ablating wavelengths have been discussed and related to the ArF higher photon energy. Finally, some NO<sub>2</sub> gas sensing tests exploiting the variations in the PL emission of the deposited samples have been reported, showing better responses for nanostructured samples with high surface-to-volume ratio and wide total surface available for gas molecule adsorption.

## ACKNOWLEDGMENTS

Many thanks are due to Prof. A. Luches, Dr. A. Taurino, Dr. F. Romano, Dr. T. Tunno, M. Corrado and F. Casino for helpful discussions and assistance.

## REFERENCES

- [1] On June 3 2009, about 8700 results were found when searching for “ZnO AND nano\*” in the field ‘Article Title, Abstract, Keywords’ on Scopus ([www.scopus.com](http://www.scopus.com)) or in the field ‘Topic’ on ISI Web of Knowledge (<http://www.isiknowledge.com>)
- [2] Akane, T; et al., *J. Vac. Sci. Technol. B*, 18, 1406 (2000).
- [3] Sheng, H; et al., *Appl. Phys. Lett.*, 80, 2132 (2002).
- [4] Xu, WZ; et al., *Appl. Phys. Lett.*, 88, 173506 (2006).
- [5] Bagnall, DM; et al., *Appl. Phys. Lett.*, 70, 2230 (1997).
- [6] Hoffman, RL; et al., *Appl. Phys. Lett.*, 82, 733 (2003).
- [7] Zheng, XG; et al., *Appl. Surf. Sci.*, 253, 2264 (2006).
- [8] Minami, T; et al., *Thin Solid Films*, 494, 47 (2006).
- [9] Park, WI; et al., *Appl. Phys. Lett.*, 82, 4358 (2003).
- [10] Park, SH, *Nanotechnology* 18, 55608 (2007).
- [11] Bao, J; et al., *Nano Lett.*, 6, 1719 (2006).
- [12] Huang, MH; et al., *Science* 292, 1897 (2001).
- [13] Johnson, JC; et al., *J. Phys. Chem., B* 105, 11387 (2001).
- [14] Hsu, HC; et al., *J. Appl. Phys.* 97, 64315 (2005).
- [15] Yan, H; et al., *Adv. Mater.*, 15, 1907 (2003).
- [16] Yu, D; et al., *Appl. Phys. Lett.* 91, 91116 (2007).
- [17] Chelnokov, EV; et al., *Appl. Phys. Lett.*, 89, 171119 (2006).
- [18] Cha, SN; et al., *Appl. Phys. Lett.*, 89, 263102 (2006).
- [19] Arnold, MS; et al., *J. Phys. Chem. B*, 107, 659 (2003).
- [20] Xu, ZX; et al., *Appl. Phys. Lett.* 90, 223509 (2007).
- [21] Hsu, CL; et al., *Chem. Phys. Lett.* 416, 75 (2005).
- [22] Kind, H; et al., *Adv. Mater.*, 14, 158 (2002).
- [23] Newton, MC; et al., *Appl. Phys. Lett.*, 89, 72104 (2006).
- [24] Law, M; et al., *Nat. Mater.*, 4, 455 (2005).

- [25] Baxter, JB; et al., *Nanotechnology*, 17, S304 (2006).
- [26] Park, WI; et al., *Adv. Mater.*, 17, 1393 (2005).
- [27] Law, M; et al., *Science*, 305, 1269 (2004).
- [28] Dal Corso, A; et al., *Phys. Rev. B*, 50, 10715 (1994).
- [29] Minne, SC; et al., *Appl. Phys. Lett.*, 67, 3918 (1995).
- [30] Krishnamoorthy, S; Iliadis, AA. *Solid-State Electron.*, 50, 1113 (2006).
- [31] Wang, ZL; et al., *Materialstoday*, 10, 20 (2007).
- [32] Wang, ZL; Song, J. *Science*, 312, 242 (2006).
- [33] Wang, X; et al., *Nano Lett.*, 6, 2768 (2006).
- [34] Hughes, WL; Wang, ZL. *Appl. Phys. Lett.*, 82, 2886 (2003).
- [35] Wang, G; et al., *Appl. Opt.*, 40, 5436 (2001).
- [36] Cao, H; et al., *Appl. Phys. Lett.*, 73, 572 (1998).
- [37] Larciprete, MC; et al., *Appl. Phys. B*, 82, 431 (2006).
- [38] Johnson, JC; et al., *Nano Lett.*, 2, 279 (2002).
- [39] Dietl, T. *Semicond. Sci. Technol.*, 17, 377 (2002).
- [40] Ueda, K. et al., *Appl. Phys. Lett.*, 79, 988 (2001).
- [41] Chawla, S; et al., *Phys. Rev. B* 79, 125204 (2009).
- [42] Look, DC; et al., *Appl. Phys. Lett.*, 75 (1999).
- [43] Tuomisto, F; et al., *Physica B*, 401, 604 (2007).
- [44] Wang, ZL. *Appl. Phys. A*, 88, 7 (2007).
- [45] Hanley, C; et al., *Nanotechnology*, 19, 295103 (2008).
- [46] Wu, YL; et al., *Nanotechnology*, 19, 345605 (2008).
- [47] Sharma, V; et al., *Toxicol. Lett.*, 185, 211 (2009).
- [48] García, PD; López, C. *J. App. Phys.*, 99, 046103 (2006).
- [49] Cui, J; Gibson, U. *Nanotechnology*, 18, 155302 (2007).
- [50] Ham, H; et al., *Chem. Phys. Lett.*, 404, 69 (2005).
- [51] Wang, RC; et al., *Appl. Phys. Lett.*, 87, 013110 (2005).
- [52] Zhu, YW; et al., *Appl. Phys. Lett.*, 83, 144 (2003).
- [53] Wei, A; et al., *Appl. Phys. Lett.*, 88, 213102 (2006).
- [54] Hou, K; et al., *Nanotechnology*, 18, 335204 (2007).
- [55] Xu, F; et al., *Nanotechnology*, 17, 2855 (2006).
- [56] Feng, X; et al., *J. Am. Chem. Soc.*, 126, 62 (2004).
- [57] Meng, XQ; et al., *Chem. Phys. Lett.*, 413, 450 (2005).
- [58] Wang, ZL; et al., *Materialstoday*, 7, 26 (2004).
- [59] Huang, MH; et al., *Adv. Mater.*, 13, 113 (2001).
- [60] Cheng, HM; et al., *Nanotechnology*, 16, 2882 (2005).
- [61] Wu, JJ; Liu, SC. *Adv. Mater.*, 14, 215 (2002).
- [62] Kim, DC; et al., *Nanotechnology*, 18, 015603 (2007).
- [63] Park, WI; et al., *Adv. Mater.*, 14, 1841 (2002).
- [64] Liu, X; et al., *J. Appl. Phys.*, 95, 3141 (2004).
- [65] Heo, YW; et al., *Appl. Phys. Lett.*, 81, 3046 (2002).
- [66] Chen MT; Ting, JM. *Thin Solid Films*, 494, 250 (2006).
- [67] Kim, D; et al., *Appl. Phys. Lett.*, 90, 101918 (2007).
- [68] Dai, Y; et al., *Chem. Phys. Lett.*, 358, 83 (2002).
- [69] Liu, C; et al., *Mater. Lett.*, 60, 1394 (2006).
- [70] Wong, MH; et al., *Nanotechnology*, 14, 968 (2003).

- [71] Lin, KF; et al., *Chem. Phys. Lett.*, 409, 208 (2005).
- [72] Bae, CH; et al., *Appl. Surf. Sci.*, 253, 1758 (2006).
- [73] Hu, XL; et al., *Mater. Chem. Phys.*, 88, 421 (2004).
- [74] Green, LE; et al., *Inorg. Chem.*, 45, 7535 (2006).
- [75] Bae, CH; et al., *Nanotechnology*, 17, 381 (2006).
- [76] Fan, HJ; et al., *Nanotechnology*, 16, 913 (2005).
- [77] Hirate T; et al., *Superlattices Microstruct.*, 42, 409 (2007).
- [78] Chrisey, DB; Hubler, GK. *Pulsed Laser Deposition of Thin Films*; Wiley, New York (1994).
- [79] Bäuerle, D. *Laser Processing and Chemistry*; 3<sup>rd</sup> edition, Springer, Berlin (2000).
- [80] Hor, PH; et al., *Phys. Rev. Lett.*, 58, 911 (1987).
- [81] Voevodin AA; Donley, MS. *Surf. Coat. Tech.*, 82, 199 (1996).
- [82] Perrone, A. *Jpn. J. Appl. Phys.*, 41, 2163 (2002).
- [83] Schou, J. *Laser Beam-Solid Interactions: Fundamental Aspects in Materials Surface Processing by Directed Energy Techniques*; edited by Y. Pauleau; Elsevier (2005).
- [84] Kools, JCS. *J. Appl. Phys.*, 74, 6401 (1993).
- [85] Gonzalo, J; et al., *J. Appl. Phys.*, 81, 951 (1997).
- [86] Hansen, TN; et al., *Appl.Phys. Lett.*, 72, 1829 (1998).
- [87] Gonzalo J; et al., *Appl. Phys. A*, 76, 943 (2003).
- [88] K.L. Saenger in *Pulsed Laser Deposition of Thin Films*; Editors D.B. Chrisey and G.K. Hubler; Wiley, New York (1994).
- [89] Said, A; et al., *J. Phys: Conf. Ser.*, 59, 259 (2007).
- [90] He, C; et al., *Appl. Surf. Sci.*, 254, 2196 (2008).
- [91] Yang, L; et al., *Nanotechnology* 18, 215602 (2007).
- [92] Ishikawa, Y; et al., *J. Colloid. Interf. Sci.*, 300, 612 (2006).
- [93] Epurescu, G; et al., *Superlattices Microstruct.*, 42, 79 (2007).
- [94] Yamaguchi, H; et al., *Physica B*, 401-2, 391 (2007).
- [95] Suzuki, K ; et al., *J. Nanopart. Res.*, 11, 1349 (2009).
- [96] O'Haire, R; et al., *Superlattices Microstruct.* 39, 153 (2006).
- [97] Premkumar, T; et al., *Appl. Surf. Sci.*, 255, 6819 (2009).
- [98] Zhang, Y; et al., *Appl. Phys. Lett.*, 87, 133115 (2005).
- [99] Liu, B; et al., *Appl. Phys. A*, 93, 813 (2008).
- [100] Kawakami, M; et al., *Jpn. J. Appl. Phys.*, 42, L33 (2003).
- [101] Hartanto, AB; et al., *Appl.Phys. A*, 78, 299 (2004).
- [102] Okada, T; et al., *Appl. Phys. A*, 81, 907 (2005).
- [103] Okada, T ; et al., *Jpn. J. Appl. Phys.*, 44, 688 (2005).
- [104] Okada, T; et al., *Thin Solid Films*, 506-507, 274 (2005).
- [105] Okada, T; Suehiro, J. *Appl. Surf. Sci.*, 253, 7840 (2007).
- [106] Guo, RQ ; et al., *Appl. Phys. A* 89, 141 (2007).
- [107] Guo, RQ; et al., *Appl. Surf. Sci.*, 254, 3100 (2008).
- [108] Guo, RQ; et al., *Appl. Phys. A*, 93, 843 (2008).
- [109] Guo, RQ ; et al., *Appl. Surf. Sci.*, 255, 9671 (2009).
- [110] Sakai, K; et al., *Physica E*, 40, 2489 (2008).
- [111] Sun, Y; et al., *Chem. Phys. Lett.* 396, 21 (2004).
- [112] Sun, Y; et al., *Superlattices Microstruct.*, 39, 33 (2006).
- [113] Sun, Y; et al., *Chem. Phys. Lett.*, 447, 257 (2007).

- [114] Sun, Y; Ashfold, MNR. *Nanotechnology*, 18, 245701 (2007).
- [115] Doherty, RP; et al., *Appl. Phys., A* 89, 49 (2007).
- [116] Gupta, V; et al., *Mat. Res. Soc. Symp. Proc.*, 818, M8.26.1 (2004).
- [117] Gupta, V; et al., *J.Cryst.Growth*, 287, 39 (2005).
- [118] Yang, B; et al., *J. Phys. D: Appl. Phys.*, 42, 045415 (2009).
- [119] Choopun, S; et al., *J. Cryst. Growth*, 274, 167 (2005).
- [120] Park, JH; et al., *J. Cryst. Growth*, 276, 171 (2005).
- [121] Lorenz, M; et al., *Appl. Phys. Lett.*, 86, 143113 (2005).
- [122] Rahm, A; et al., *Appl. Phys. A*, 88, 31 (2007).
- [123] Zúñiga-Pérez, J ; et al., *Nanotechnology*, 18, 195303 (2007).
- [124] Liu, ZW; et al., *Appl. Phys. Lett.*, 88, 53110 (2006).
- [125] Liu, ZW; Ong, CK. *Mater. Lett.*, 61, 3329 (2007).
- [126] Tien, LC; et al., *J. Mater. Sci.*, 43, 6925 (2008).
- [127] Nishimura, R; et al., *Jpn. J. Appl. Phys.*, 47, 4799 (2008).
- [128] Rout, CS; Rao, CNR. *Nanotechnology*, 19, 285203 (2008).
- [129] Mendelsberg, RJ; et al., *Superlattices Microstruct.*, 43, 594 (2008).
- [130] Yu, D; et al., *Mater. Lett.*, 62, 4063 (2008).
- [131] Valerini, D; et al., *Appl. Phys. A*, 93, 729 (2008).
- [132] Valerini, D; et al., *Appl. Surf. Sci.*, 255, 9680 (2009).
- [133] Ozerov, I; et al., *Appl. Surf. Sci.*, 247, 1 (2005).
- [134] Claeysens, F; et al., *J. Appl. Phys.*, 92, 6886 (2002).
- [135] Ohtomo, A; Tsukazaki, A. *Semicond. Sci. Technol.*, 20, S1 (2005).
- [136] Jeffers, G; et al., *J. Appl. Phys.*, 75, 5016 (1994).
- [137] Aubriet, F ; et al., *Appl. Surf. Sci.*, 186, 282 (2002).
- [138] Yao, BD; et al., *Appl. Phys. Lett.*, 81, 757 (2002).
- [139] Sambri, A; et al., *Appl. Phys. Lett.*, 91, 151501 (2007).
- [140] Yang, YH; et al., *Nanotechnology*, 17, 5556 (2006).
- [141] Özgür, Ü; et al., *J. Appl. Phys.*, 98, 041301 (2005).
- [142] Patolsky, F; Lieber, CM. *Materialstoday*, 8, 20 (2005).
- [143] Wang, JX; et al., *Nanotechnology*, 17, 4995 (2006).
- [144] Li, CC; et al., *Appl. Phys. Lett.*, 91, 32101 (2007).
- [145] Sberveglieri, G ; et al., *Sens. Actuators B*, 121, 208 (2007).
- [146] de Julián Fernández, C. et al., *Sens. Actuators B*, 130, 531 (2008).
- [147] Wang, JX; et al., *Appl. Phys. Lett.* 88, 233106 (2006).
- [148] Singh, SP; et al., *Appl. Phys. Lett.* 91, 63901 (2007).
- [149] Valerini, D; et al., accepted for publication on *Sens. Actuators, B*.

## ***Chapter 5***

# **DIODE LASER FORMING OF STEEL PARTS**

***A. Guglielmotti, F. Quadrini, E. A. Squeo and V. Tagliaferri***

Department of Mechanical Engineering, University of Rome Tor Vergata, Via del Politecnico 1, 00133 Rome, Italy.

## **ABSTRACT**

Laser forming of steel parts by means of diode lasers is discussed from different points of view. The physical mechanisms at the basis of the laser forming processes are depicted, and a description of the state of the art is reported. Many laboratory experiences are presented in the case of diode laser forming of stainless steel sheet metals and tubes. Also slotted tubes were processed to form flares and tongues. Numerical modeling was carried out by means of analytical and finite element models and experimental data were in good agreement with numerical ones. The analytical approach lead to the evaluation of the laser forming efficiency, instead finite element models were used to predict the final shape of the steel parts as a function of the process parameters. In fact, finite element models allow the researchers to thoroughly study the part behavior during forming in the case of sheets, tubes or slotted tubes. In the end, an attempt was made to describe how material analysis helps in the laser forming investigation; residual stresses are mainly discussed as they strongly affect the formed part performances.

## **INTRODUCTION**

Laser forming is a no-contact technique for sheet metal and tube forming: the bending is obtained because of the difference between the very fast heating rate (during laser exposure) and the subsequent slow cooling rate after the laser removal. It gives the possibility to implement highly automated manufacturing processes and to reduce tooling costs for rapid prototyping and small-batch production. Thanks to the laser system flexibility, a lot of applications (such as soldering, brazing and hardening) can be performed by means of the same apparatus. In the last 15 years, laser forming has been investigated more and more; the interest of manufacturing industries in laser forming applications has increased thanks to the high degree of control over the energy transfer, the high accuracy and reliability, and the very

high flexibility. Moreover, the no-contact nature of the process makes hard tooling not necessary and small batch production runs and rapid prototyping are very effective applications.

## THE LASER FORMING PROCESS

The mechanism of laser forming is based on laser-induced thermal stresses; in particular, as Shi et al. reported [1], there are three main laser forming mechanisms associated with metal plates: temperature gradient mechanism (TGM), buckling mechanism (BM) and upsetting mechanism (UM).

The TGM is present if the laser beam diameter is in the order of the sheet metal thickness. In the TGM, a fast scan of a plate on a line by the laser beam forms a steep thermal gradient across the thickness thus producing differential thermal expansion, which in turn generates a gradient of compressive stresses on the laser-processed area, along the thickness. These compressive stresses are caused by the restriction of the surrounding material which prevents the thermal expansion of the laser exposed material. When these stresses reach the temperature-dependent flow-stress, a gradient of plastic compressive deformation along the thickness occurs, which is greater on the top surface. After laser passing, the material starts to cool and contracts, but the plastic deformation cannot recover, therefore the plate bends around the laser scanned line towards the laser beam.

In the BM, the spot diameter is greater than the plate thickness and the heated zone takes up the entire thickness because of a slow scanning speed. The heated area expands, up to the limit allowed by the surrounding material. The plastic deformation is maximum at the top surface and, during cooling, the plate starts to bend either away from or towards to the laser beam.

The UM uses process parameters similar to BM, but the heated area is much smaller than the plate thickness; the geometry of the plate would prevent buckling due to the increased moment of inertia. Also in this case, the material in the non-processed zone restricts the thermal expansion of the heated area, which exhibits a nearly constant strain along the thickness. The material of heated area shortens and increases its thickness during cooling; moreover, the material on top zone starts to contract earlier than the bottom one and the plate starts to bend toward the laser beam. A combination of TGM and UM was also proposed by Shi et al. as the coupling mechanism (CM) [1].

In the last years, the scientific interest on the laser forming process is enormously increased but a full industrial application is still far to come. This limitation is probably due to the complexity of process design and to the equipment cost.

In 2000, Magee et al. already proposed a prototype laser forming system to demonstrate the process feasibility on large primitive shape [2]. Laeng et al., in their review, concluded that the laser-based metal forming process is a technique that has the potential to produce fully functional models directly from a CAD system and eliminate the need for an intermediate step [3].

In 2001, Lawrence et al. discussed the bending of mild steel sheets by using a high power diode laser [4]. They only evaluated the effect of the process parameters on the bending angle, but it was evident that diode lasers gave high process efficiency. Even if this kind of

laser source has also other advantages, it is rarely mentioned in scientific papers. In the same year, Li and Yao deepened the laser forming of AISI 1010 steel sheets with constant line energy by using a CO<sub>2</sub> laser [5]. They observed that under the condition of constant line energy, the bending angle increases with scanning velocity, but the degree of increase reduces with velocity increase.

In 2002, Lee and Lin simulated the transient deformation of thin AISI 304 stainless steel sheet metals by a single pulse of a CO<sub>2</sub> laser forming [6]; however the application of a single pulse simplifies the thermo-mechanical simulation. In the following year, 2003, Dearden and Edwardson, in their review on laser forming, described a number of new developments for both macro- and micro-scale applications [7].

In 2004, Geiger et al. discussed some developments in the laser forming of aluminum alloys [8]. Zhang and Michaleris proposed 3D Eulerian and Lagrangian finite element models to simulate the forming process [9]. Both models took into account only the transient thermal and the elasto-plastic analysis, whereas the effect of the laser heating on the material annealing was not considered. This is a general assumption of all the thermo-mechanical numerical models, in the previous and following studies as well. In the same year, Hsieh and Lin investigated experimentally and numerically the vibration phenomenon during pulsed laser forming of thin metal plates [10]; the metal plates were made of AISI 304 stainless steel and were heated by a CO<sub>2</sub> laser.

In 2005, McBride et al. introduced a simplified analytical model to characterize bending by the thermal gradient mechanism [11]. Experimental tests were performed on mild steel coupons by means of a CO<sub>2</sub> laser. Moreover, Yanjin et al. deepened the influence of material properties on the laser forming process by means of numerical simulations [12]. Zhang et al. proposed a model to predict the fatigue behavior of sheet metals after laser forming [13]. In fact, microstructure as well as the distribution of residual stresses changes during the process; they incorporated some results from microstructure integrated finite element modeling in the fatigue life model. Tests on low carbon steel were used to validate the model.

A lot of numerical studies were carried out on laser forming in 2006. Edwardson et al. deepened the problem of the variation of the bending angle per pass during multiple passes along a single irradiation track [14]. Costa Santos et al. proposed a review on rapid manufacturing by laser forming [15]. A research on the related mechanisms was proposed by Shi et al. by means of a numerical and theoretical approach [1]. A numerical model was also proposed by Shi et al. who studied the straight-line laser forming under the TGM [16], and applied the similarity theory in the forming process [17]; by Shen et al. who introduced an analytical approach for estimating the deformation [18], a finite-element model for two-scan laser forming with different intervals along the same path [19], and a fuzzy logic model to predict the bending angle [20]. Another finite element model was also proposed by Liu et al. to simulate the laser forming of aluminum matrix composites [21]. A last mention has to be made of the study by Cheng et al. who discussed experimentally and numerically the laser forming of varying thickness plates [22], and proposed a strain-based strategy for process design [23].

Also the last contributions are mainly numerical. In 2007, Shen et al. proposed a 3D non-linear, indirectly coupled thermal model to investigate the edge effects of the laser bending [24], and the overlapping of two sequential scans [25]. More recently, Korsunsky et al. have proposed a beam-bending eigenstrain analysis of residual elastic strains in multi-scan laser-formed steel samples [26]. The authors observed that a key challenge in the development of

laser forming is the characterization of the relationship between process parameters and the resulting state of the material. In conclusion, Labeas has developed a 3D numerical model for the laser forming of aluminum components [27].

Not only laser forming of sheets is studied, several scientific studies deal with laser bending of tubes and the related physical mechanisms. In 2001, Li and Yao discussed in detail the mechanism at the basis of laser tube bending by stress analysis [28]. They studied the laser bending of low carbon steel tubes by a CO<sub>2</sub> laser with a power of 1.5 kW, and discussed the dependence of the bending angle on scanning speed and laser power. Particularly they investigated the tube ovalization, and concluded that wall thickness reduction seems to be avoided and lesser ovalization results in comparison with mechanical bending. A thermo-mechanical finite element simulation to correlate stress arising in the tube and thermal gradients was performed in 2003 by Hao and Li [29], who also developed an analytical model for laser tube bending by a 400 W Nd-YAG laser source [30]. In 2005, Hsieh and Lin studied BM in laser tube forming, which occurs in the case of thin tubes [31]; experimental tests were carried out on stainless steel tubes by means of a CW CO<sub>2</sub>.

Laser bending of tubes is normally achieved through the UM. In the most common laser scanning scheme, the tube rotates 180 degrees when its outer circumference is heated by a laser beam with a spot size greater than the tube thickness. The scanned region is heated homogeneously in the thickness direction, plastic compressive deformation arises and the wall thickens because the surrounding material prevents the thermal expansion. The consequent shortening of the scanned region in the axial direction of the tube during cooling causes the tube to bend towards the laser beam. Other scanning schemes (such as the axial scanning scheme) were evaluated by Zhang et al. in 2006 [32] and by Safdar et al. in 2007 [33]. In the former case, a CO<sub>2</sub> laser was used to bend low carbon steel tubes, and the effect of the scanning scheme on the ovalization was experimentally measured (in all cases lower than 1%). In the latter study, a fiber optic coupled high power diode laser was used to bend stainless steel tubes. The latter also discussed the main parameters to control the bending process and the correlation between thermal stresses, laser beam geometry and scanning direction.

## APPLICATION OF HIGH POWER DIODE LASERS (HPDLS)

In 2000, Li discussed the application of HPDLs in material processing such as soldering, surface treatment, welding, marking, sheet metal bending [34]. As Bachman observed in 2003, HPDLs have entered the industrial manufacturing area [35]. Because of their unique features (small size and low weight), high efficiency and reliability, diode lasers gained high interests as new sources for material processing. The investment costs of HPDL systems are not very lower than those of CO<sub>2</sub> lasers but considerably less than Nd-YAG lasers. Running costs are much less than those of conventional lasers, because of their high efficiency (above 30%). Many industrial applications are possible, from brazing to cladding and hardening. As a consequence of the rather poor beam quality, applications as cutting and high speed deep penetration welding are not yet available as a market for HPDL. Instead, hardening is a typical application, as reported by Pashby et al. who studied surface hardening of steel using a 1.2 kW diode laser [36]. Recently Zhu et al. have suggested an interesting comparison

between CO<sub>2</sub> and diode laser welding of AZ31 magnesium alloy [37]. Keyhole welding can be obtained using the CO<sub>2</sub> laser, whereas only conduction welding is possible with the diode laser. Conduction mechanism is a limit for cutting and welding, but it is an advantage for other diode laser applications, such as forming. In particular, as suggested by Zhang et al. [32], diode lasers are suitable for tube bending due to the rectangular laser beam shape. In the study of Zhang et al., the case of low carbon steel tube forming is discussed.

## EXPERIMENTAL

In the following, many experimental and numerical results related to the case of diode laser forming of sheet metals and tubes made of steel are discussed. The effect of the main process variables was evaluated and the related forming mechanisms were investigated [38-43].

Laser forming tests were all carried out on AISI 304 stainless steel sheet metals and tubes. The laser system used was a 1.5 kW diode laser source (Rofin-Sinar, DL 015) with 940 nm wavelength. The laser source had an almost rectangular spot due to the superposition of two different rays, each one coming from a 750 W emitter diode. A 63 mm long focus lens was used to maximize the depth of field. Nominally, in the focalization condition, the spot maximum axis was 3.8 mm in length and the minimum axis was 1.2 mm.

Dealing with line bending (i.e. bending a sheet metal around a line), tests were performed by focusing the diode laser on AISI 304 stainless steel sheets with different area (100x35 mm<sup>2</sup> and 100x80 mm<sup>2</sup>) and thickness (1.20 mm and 1.50 mm, respectively). Before testing, samples were cleaned by means of acetone to remove any grease stain. No coating was applied on the sheets. Sheet metals were fixed on a CNC motion table along the smaller edge as reported in Figure 1. The samples were then laser scanned in the middle, backward and forward by moving them under the motionless laser source. Each scan was longer than the sample length: in this way the motion inversion occurred externally to the sample, avoiding over-heating on the edges. During the experimentation, several process parameters were changed, such as the scanning rate, the laser power and the spot orientation, which is expressed as the angle between the spot maximum axis and the laser path direction. The images of the bent samples, after each series of laser passes, were captured and the resulting bending angles were measured using an image processing software. During image acquisition the samples were left cooling in air, to avoid excessive pre-heating in successive scans.

Considering the spot area and the small sample thickness, the TGM can be considered as the forming mechanism for the laser induced bending. In fact the TGM is present when the spot diameter is in the order of the sheet metal thickness. A steep temperature gradient occurs in the laser exposed area producing a non-uniform thermal expansion through the thickness. In this phase the sheet exhibits a counter bending. The constraining effect of the non heated surrounding material determines the presence of an elastic stress. At high temperatures the material yield stress decreases and therefore the pure elastic strains are converted into plastic ones. When the laser spot proceeds along its path and the initial irradiated portion of the sheet cools, the elastic strains are recovered but not the plastic ones. During cooling, the difference in thermal contraction between the upper and lower sheet layers, generates a bending angle towards the laser beam source.

In Figure 2 the total bending angle for 1.5 mm thick stainless steel sheets is reported as a function of pass number in four different conditions.

The bending angle increases with the number of scanning passes and the increase in laser power, whereas it decreases as the scanning rate increases. By increasing the pass number and laser power and decreasing the laser scanning rate, the energy amount provided to the sample increases, as well as the total bending angle. If two samples are bent in different conditions but with the same energy amount per unit length, similar bending curves could be obtained. For a given spot orientation, energy amount per unit length (i.e. the laser fluence) can be evaluated by means of the ratio  $P/v$ . In Figure 3 two bending curves, obtained at different powers and scanning rates but the same  $P/v$  value, seem to be superimposed. However this experimental evidence cannot be considered a general conclusion. In fact it was shown, experimentally and numerically, that under the condition of constant line energy, the bent angle increases with scanning velocity. Moreover the degree of increase reduces with velocity increase [5]. Evidently the investigated power and scan rate ranges are too small for the evaluation of the scan rate in condition of constant line energy.

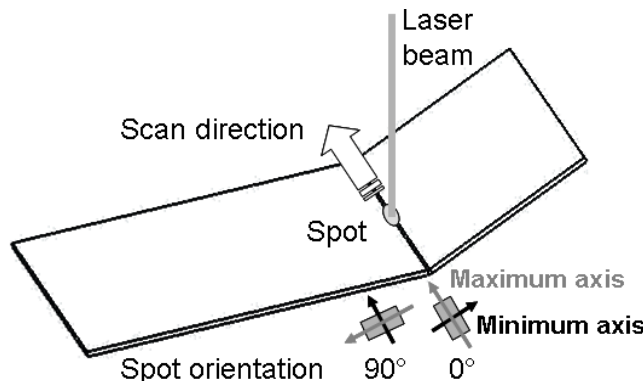


Figure 1. Experimental configuration for diode laser forming of stainless steel sheet metals.

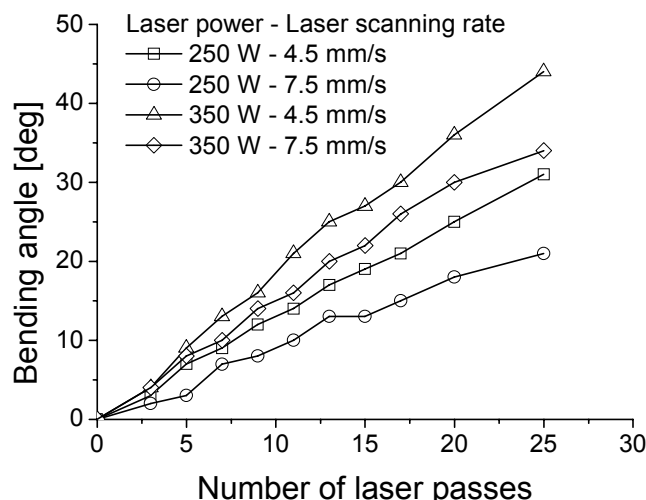


Figure 2. Total bending angle as a function of pass number for 1.5 mm thick stainless steel sheets at different laser powers and scanning rates (90° spot orientation).

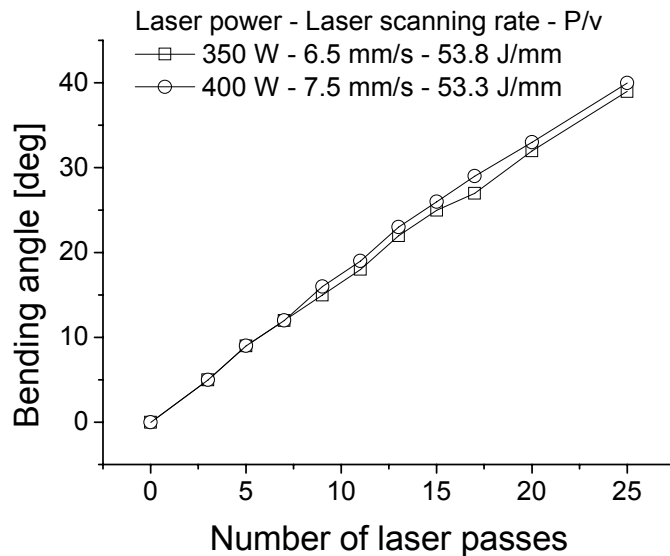


Figure 3. Total bending angle as a function of pass number for 1.5 mm thick stainless steel sheets at equal fluence (90° spot orientation).

A significant loss in bending efficiency is visible when melting appears on the laser exposed surface. Figure 4 shows the comparison between two different experimental curves, the first curve obtained at higher power and lower scanning rate than the second curve. Even if, in the first case, a greater energy amount per time unit is provided to the sample, the corresponding bending curve lies in the lower part of the graph. Surface melting partially nullifies thermal gradient effect because melting relaxes thermal stresses.

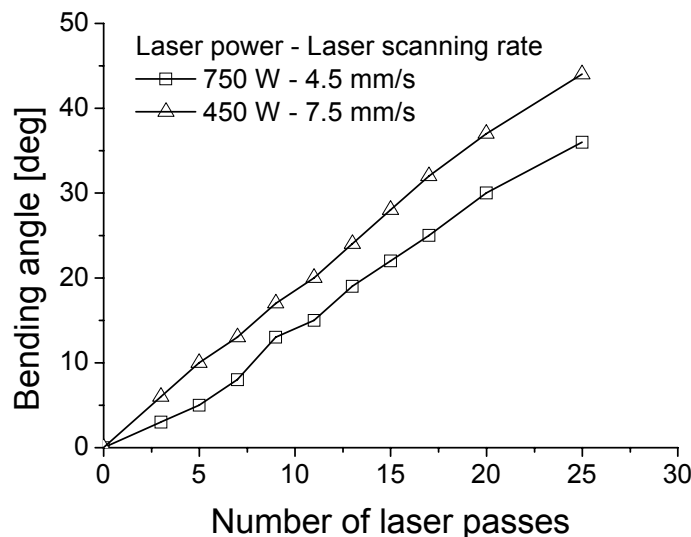


Figure 4. Total bending angle as a function of pass number for 1.5 mm thick stainless steel sheets, with (upper curve) and without (lower curve) surface melting (90° spot orientation).

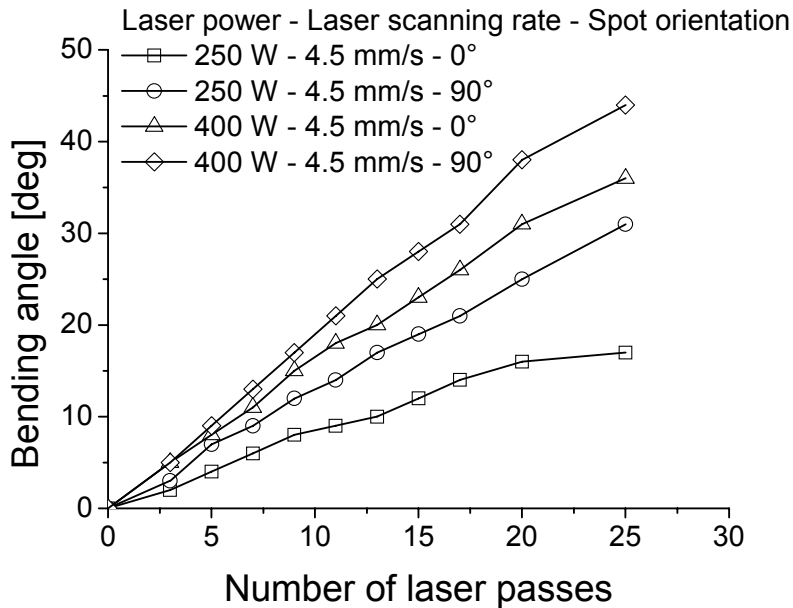


Figure 5. Total bending angle as a function of pass number for 1.5 mm thick stainless steel sheets at different laser powers and spot orientations.

Also spot orientation is an important parameter for an efficient bending process. In fact 90° spot orientation allows a greater material area to be treated, reducing surface melting occurrence. Figure 5 shows that at a fixed laser power and scanning rate for stainless steel samples, 90° spot orientation gives higher bending angles than 0° spot orientation. When surface melting is generated, a similar bending curve is obtained in both cases (0° and 90° spot orientation), as Figure 6 shows.

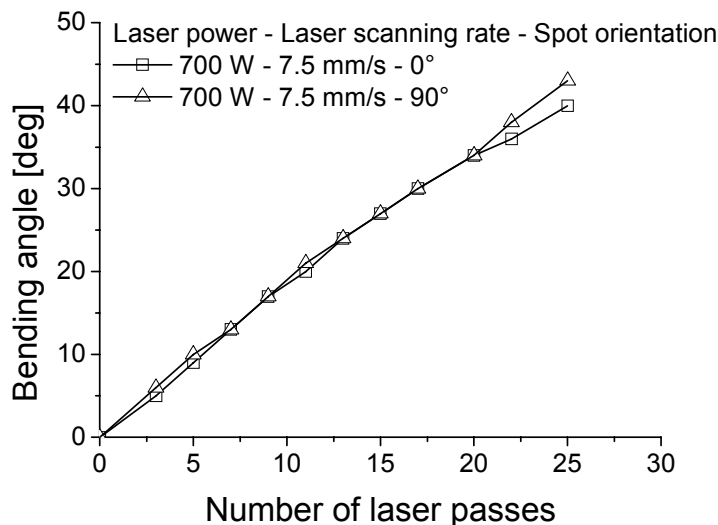


Figure 6. Total bending angle as a function of pass number for 1.5 mm thick stainless steel sheets at different spot orientations in presence of surface melting.

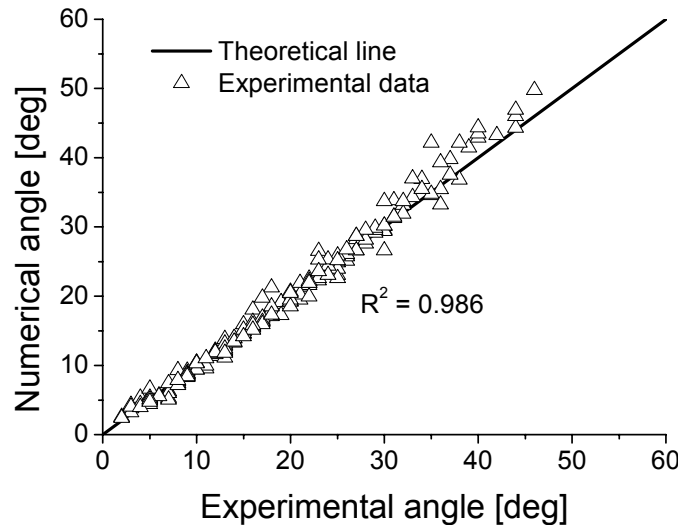


Figure 7. Comparison between experimental data and numerical data extracted from the average single pass (1.5 mm thick stainless steel sheets).

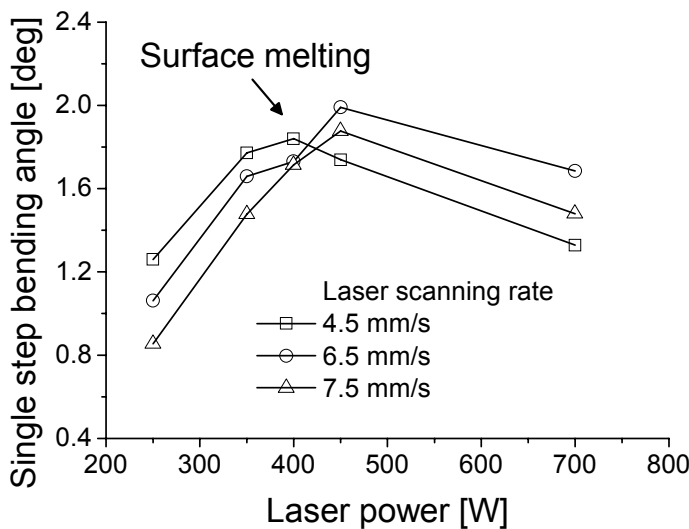


Figure 8. Bending angle after a single laser pass as a function of laser power for 1.5 mm thick stainless steel sheets at different laser scanning rates (90° spot orientation).

For all the experimental curves, with and without surface melting occurrence, a uniform increase in bending angle was observed, increasing the laser passes. After the first passes, the same increase in bending angle is obtained for all the subsequent single passes. This fact is shown in Figure 7 where the experimental angle is reported together with the numerical one. The numerical angle is simply the product between the number of laser passes  $n$ , and the average of the single pass bending angle increase  $\gamma_s$ . The experimental angle is almost equal to the numerical one for all the experimental points of the bending curves, as Figure 7 shows. This fact suggests to use the bending angle increase, after a single laser pass, as a significant experimental parameter for bending condition comparison. Figure 8 shows the single step

bending increase as a function of laser power and scanning rate. In this case, surface melting occurrence is clearly visible by the curve trends. At a given scanning rate, a maximum is present for the optimal bending power. After the maximum, the curve drop is the highest at the lowest scanning rate.

As Figure 9 shows, by reducing the sheet thickness, high bending angles may be obtained at lower laser powers after few scans. However, in this case, surface melting more easily occurs, limiting the process window.

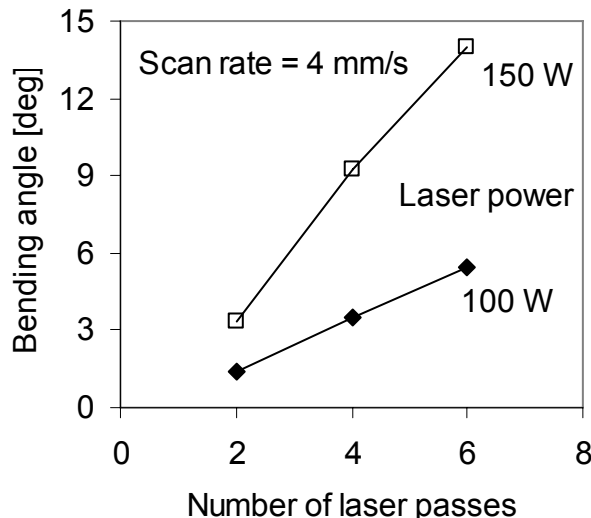


Figure 9. Bending angle as a function of laser passes for 1.2 mm thick stainless steel sheets (90° spot orientation).

Laser forming of tubes was performed by putting into rotation steel tubes made of AISI 304, under the focused HPDL beam. The tubes were 20 mm in outer diameter, 60 mm in length and 1 mm in thickness. The experimental apparatus for laser forming is shown in Figure 10a together with the configuration for the tube temperature measurement under laser exposure (Figure 10b). The tubes were clamped to a stepper motor that provided the rotational speed, which ranged from 9 to 60 deg/s in 5 steps. A comparator was used to measure the vertical displacement of the free tube end so as to extract the bending angle.

The maximum axis of the spot was aligned to the tube axis (i.e. the spot orientation was fixed to 90°). The tube clamping length was about 15 mm. Fifty consecutive scans were performed for each combination of laser power and tube rotational speed, whereas the angular displacement under heating was fixed to 180 deg. Every 2 scans the measure of the tube end displacement was acquired, and the tube was left to cool in air before further scans. Laser bending tests were also carried out by moving the laser source along the tube axis after 20 consecutive circumferential scans. In this case the laser power was fixed to 150 W, the rotational speed to 36 deg/s, and 20 series of 20 laser scans were performed at a distance of 2 and 3 mm one from the other. A sum of 400 scans were performed for each test, the tube was left to cool for 5 min between two consecutive series.

Figure 11 shows the experimental results in terms of tube bending angle in dependence of the number of scans at different values of rotational speed and laser power. In this case a

single circumferential band was laser treated and no longitudinal motion was applied to the tube. The bending angle increases with decreasing the rotational speed and increasing of the laser power; however, too high powers or too low rotational speeds lead to the tube surface melting in the first scans. This occurrence limits the maximum value of the power to 175 W and the minimum value of the rotational speed to 9 deg/s, but also in this condition only few scans were performed at 18 deg/s and 175 W and no one at 9 deg/s and 175 W. At high laser powers and low rotational speeds, if the surface melting is avoided, high laser bending efficiencies are obtained, but high cycle times are necessary to cool the tube between successive scans or series of scans. The effect of multiple scans on the laser forming efficiency was also discussed by Edwardson et al. (2006) who observed the decrease in bending angle per pass after many irradiations for a given set of process parameters [14]. For this reason, large tube deformations were achieved at medium values of laser power (150 W) and rotational speeds (36 deg/s). It is clearly observable when surface melting occurs during laser forming, but this phenomenon is not the only one affecting the material integrity. Surely melting leads to catastrophic effects; nevertheless at lower temperatures phase transformations may occur, and the final material properties may be negatively influenced.

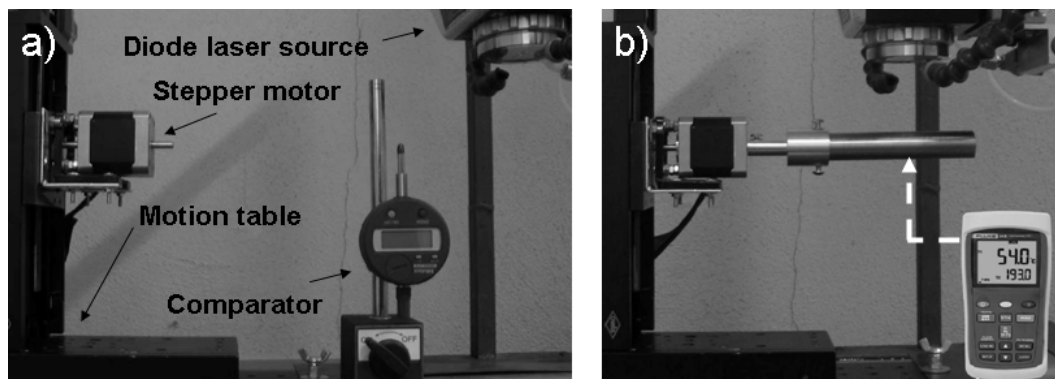


Figure 10. Experimental set-up for tube laser bending (a) and temperature acquisition (b).

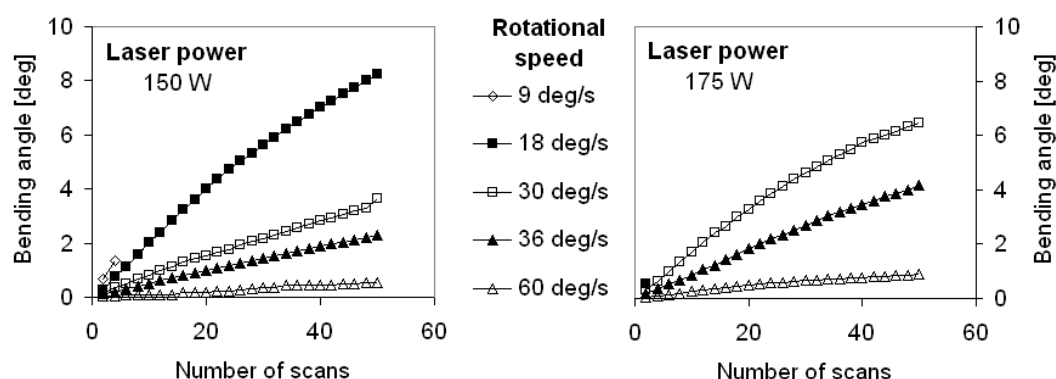


Figure 11. Tube bending angle as a function of the number of scans at different values of rotational speed and laser power in the case of a single treated band.

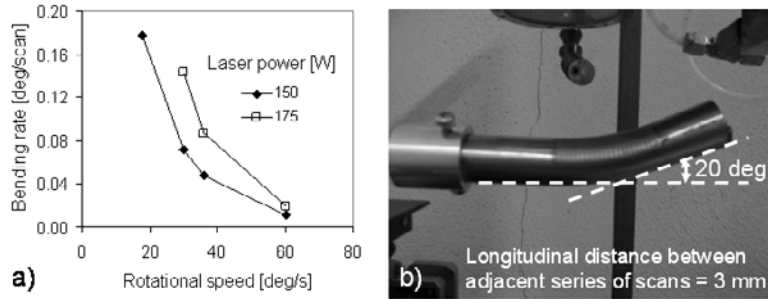


Figure 12. Bending rate as a function of the rotational speed (a), and bent tube after 300 scans (b).

At a fixed value of rotational speed and laser power, the bending angle is linearly dependent on the number of scans as discussed in [28]. Fig.12a shows the slope of the curves of Fig.11 as a function of the rotational speed for both laser powers. The linear fitting was performed by considering the intersection at the origin, and correlation factor of the linear fitting were always higher than 0.93 (up to 0.997). The lowest values were found for those curves of Fig.11 which start to decrease their slope at high number of scans due to the sudden increase of the tube average temperature. However this effect was sufficiently limited during the experimentation.

Even if the bending angle is linearly dependent on the number of scans (Figure 11), it is not possible to normalize the bending rate by means of the input energy (which is related to the ratio between laser power and rotational speed). The contribution of these two process variables is always well distinct. Data of Figure 12a may be used to calculate the final bending angle for the different process conditions. In the case of 150 W, 36 deg/s and 400 scans, a value of 19 deg is extracted. Experimental tests provided a value about 20 deg independently from the longitudinal distance that was applied between two successive series of scans. In Figure 12b, the case of the 3 mm distance is shown with the tube at the end of the laser processing. Therefore, a good agreement is present between the interpolated datum from Figure 12a and the experimental evidence of Figure 12b. This occurrence suggests that a numerical model can simulate the behavior of the tube under complex processing conditions if it is correctly calibrated by using laser tests on a single band. Up to 400 scans were performed on the steel tube of Figure 12b at 150 W of laser power and 36 deg/s of rotational speed, whereas 70 s of cooling were applied between two consecutive scans. Therefore, about 10 hr were necessary to bend a steel tube (20 mm in outer diameter, 1 mm in thickness) up to 20 deg without surface melting. Evidently, for an industrial application, this time has to be reduced and the tube has to be cooled by water and not left to cool in air.

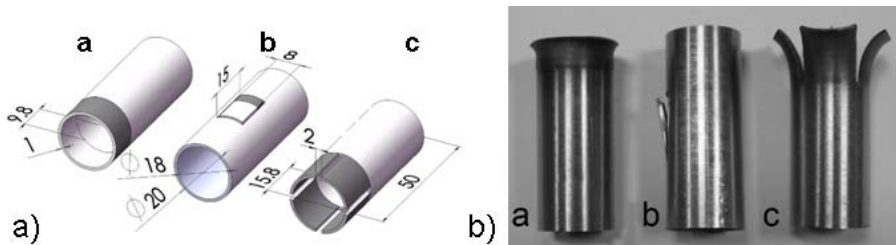


Figure 13. Slotted tubes (a) and aspect of the tubes after laser processing (b).

In a further development of laser forming, it is possible to combine line bending and tube bending to perform a slotted tube bending. In fact, if a U-shaped slot is cut in a tube, a tongue is obtained. The side of the tongue continuous with the tube can be laser processed by means of a HDPL, to carry out the tongue bending. The laser bending mechanisms are no more those typical of laser bending of tubes (UM), in fact the tongue can be considered as a plate attached to a tube by one side. This kind of tube geometry could be used to generate connections between mechanical parts by means of a no-contact technique. If a high specific power laser is used (such as CO<sub>2</sub> laser), it could cut the slot when focused on the tube surface and bend the slot in defocused conditions. HDPLs do not permit to cut the slot, because their specific power is too low to generate the deep penetration mechanism during processing, therefore the slots were machined. Laser forming tests were performed putting into rotation slotted tubes, made of AISI 304, under a focused HPDL beam, at a speed of 0.628 rad/s. Also these tubes were 20 mm in outer diameter and 1 mm in thickness. In order to provide the rotational speed, the tubes were cut to a length of 50 mm and clamped to a stepping motor. The geometrical features of the tubes are depicted in Figure 13a. In particular, sample (a) had no slots, whereas sample (b) had a U-shaped slot and (c) had 4 symmetric slots along the tube end. The laser treated zone is shown in Figure 13a with a darker color for each sample.

During tests, the laser beam was focused on the external tube surface and the laser power was fixed at 150 W. The tube clamping length was 15 mm. The details about the scanning schemes are reported in Table 1. Initially the laser was focused on the tube external surface and a first scan was performed along the tube circumference. At the end of the scan the laser spot was moved to the initial position to repeat the same scan. Up to a maximum of 20 scans were performed consecutively. At the end of this first set of scans, the tube was left to cool in air. Subsequently the laser spot was moved along the tube length to perform a set of scans on a parallel circumferential line. Finally, the total processed length of the tube ranged from 9.8 to 15.8 mm, the number of scans per circumferential line from 10 to 20. The single laser scan interested the entire tube external circumference apart from the sample (b), for which an angular dimension of 56° was considered to bend only the tongue of Figure 13a. The distance between two consecutive set of scans was 2 mm. As the laser spot maximum axis was aligned to the tube length, a 1.8 mm superposition resulted between successive scans.

In Figure 13b, the picture of the formed tubes is reported. A flare was obtained for the sample (a). In sample (b) the result was similar to the case of sheet metals and the tube wall deformed toward the laser source. However the unprocessed surface of the tongue remained unaltered with the shape of the initial cylindrical surface. Instead, in sample (c) the laser spot was moved from one end to the other one for a distance of almost 16 mm. A complex double curvature surface resulted in the four tongues.

In a further experimentation, two tubes, different in size, were cut to a length of 50 mm and processed with rotational speed of 1.257 rad/s for the small tube and 0.628 rad/s for the big tube. The geometrical features of the slotted tubes are reported in Figure 14a. Initially the laser was focused on the tube external surface, aligned to one of the longitudinal sides of the U-shaped slot; a first scan was performed along the tube circumference, on the part delimited by the slot. At the end of the scan, the laser spot was moved to the initial position to repeat the same scan. Ten scans were performed consecutively; at the end of each scan, the tube was left to cool in air for 80 s. As the laser spot maximum axis was aligned to the tube axis, the axial processed length of the tubes was 3.8 mm. The appearance of the deformed tongues is reported in Figure 14b.

**Table 1. Geometrical parameters for slotted tube forming tests.**

Sample	Tube scanned length [mm]	Number of scans per line	Angular dimension of a single scan [°]	Distance between consecutive set of scans [mm]
A	9.8	20	360	2
B	3.8	10	56	0
C	15.8	20	360	2

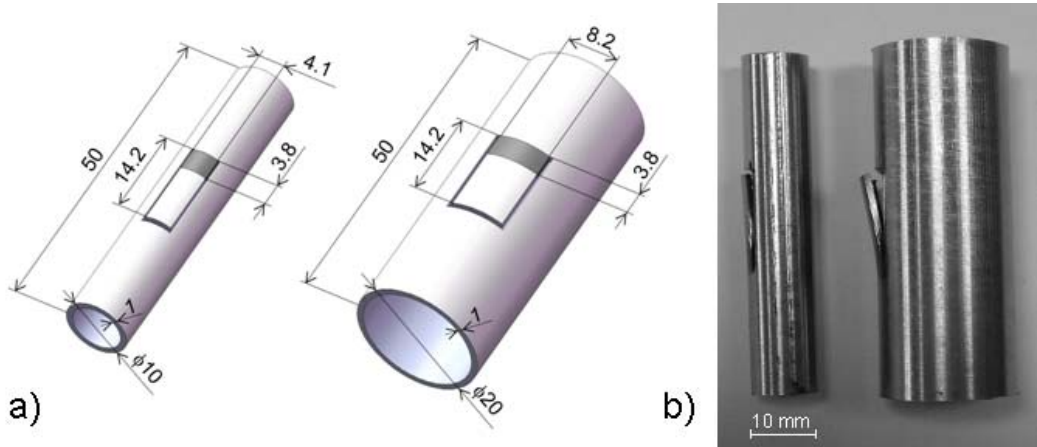


Figure 14. Slotted tubes with different size (a) and aspect of the tubes after laser processing (b).

## NUMERICAL MODELING

Numerical simulation is fundamental for the laser forming design due to its complexity. In the scientific literature, very good agreements were obtained between experimental and numerical data in terms of bending angle or part deformation, by using both analytical and finite element models. The experimental results discussed in the previous section were used for making evidence of this predictability of analytical and discrete models.

In the case of line bending, a simple model can be used in order to predict bending angle if the TGM occurs [44]. Bending angle is expressed as a function of material properties and working parameters:

$$\gamma_s = \frac{1}{5} \left( \frac{2}{\pi} \right)^{1/2} \frac{\beta P \alpha \lambda^{1/2}}{t k(rv)^{1/2}} \quad (1)$$

where the laser power distribution is assumed to be constant over a circular spot with  $r$  radius. This equation (1) was analytically derived. It was also shown that the model is in reasonable agreement with experimental results (using CO<sub>2</sub> and Nd-YAG lasers). This model was chosen only for its simple form that can be easily adapted to the definition of a process map.

Equation (1) refers to a single laser pass, but it can be easily extended to the case of multiple passes, in the hypothesis that the same angle increase occurs at every single laser pass:

$$\gamma_T = n\gamma_S. \quad (2)$$

Combining equation (1) and (2):

$$\gamma_T = \frac{1}{5} \left( \frac{2}{\pi} \right)^{1/2} n \frac{\beta P \alpha \lambda^{1/2}}{tk(rv)^{1/2}} \quad (3)$$

Equation (3) can be arranged in a dimensionless form assuming:

$$N_{Th1} = \frac{\gamma_T tk}{n \alpha \beta P} \quad (4)$$

$$N_{Th2} = \frac{\lambda}{rv} \quad (5)$$

and using equation (4) and (5) in equation (3):

$$\frac{N_{Th1}}{N_{Th2}^{1/2}} = \frac{1}{5} \left( \frac{2}{\pi} \right)^{1/2} \quad (6)$$

Both the defined thermal numbers ( $N_{Th1}$  and  $N_{Th2}$ ) have a physical significance. The first thermal number  $N_{Th1}$  is the efficiency in laser bending. In fact the term  $\gamma_T t/n$  can be considered as the increment after a single laser pass in the sheet length, from the opposite side of the laser exposed surface compared with the length from the side of the laser exposed surface. This length increment is responsible for bending. The term  $\alpha \beta P/k$  represents instead a characteristic length for thermal expansion, being the product (for a reference temperature interval  $\Delta T$ ) of an  $\alpha \Delta T$  term (which is the linear thermal expansion) and a  $\beta P/k \Delta T$  term (which is the characteristic length for heat transfer during laser action). The concept at the basis of the first thermal number is that not all the thermal expansion can produce bending. If a large thermal expansion would be obtained homogeneously inside the sample thickness, no bending would occur.

The second thermal number  $N_{Th2}$  is instead the ratio per unit time between the sample area, which is interested to the heat transfer (as the thermal diffusivity  $\lambda$  can be interpreted), and the sample area which is covered by the laser motion (approximately equal to the term  $rv$ ). In this way  $N_{Th2}$  can be considered the efficiency of heat transfer during laser motion. If  $N_{Th2} \gg 1$  the heat transfer is faster than the laser motion, otherwise if  $N_{Th2} \ll 1$ , the laser moves faster than thermal waves inside the material. Equation (6) shows that laser bending efficiency increases with heat transfer efficiency for every material, processing and geometry condition. However a direct correlation between the term  $N_{Th2}$  and the bending angle is not immediate.

**Table 2. Material properties for process map definition.**

Material	Property	Value
AISI 304	$\alpha$	1.90E-5 K <sup>-1</sup>
	$\lambda$	4.88E-6 m <sup>2</sup> /s
	$k$	19.5 W/m K

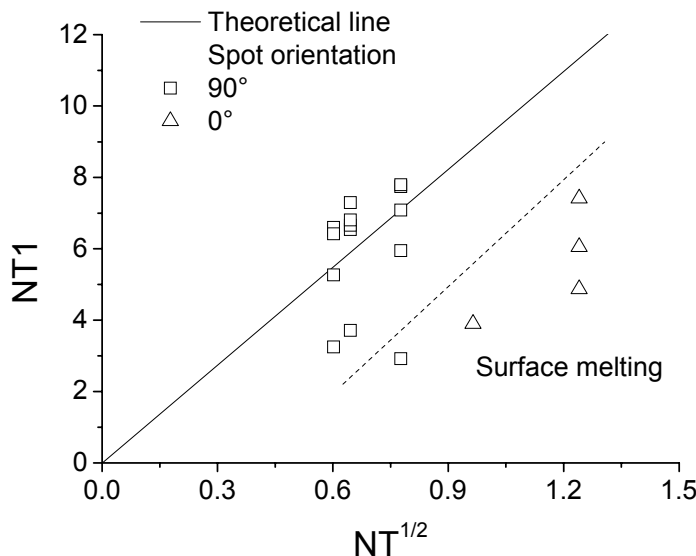


Figure 15. Laser bending process map for stainless steel sheets in all the experimental conditions.

The discussed experimental data in the case of the 1.5 mm thick sheet metals (Figures 2–8) were reported on a process map by using the definitions of equation (4) and (5), i.e. the bending efficiency and the heat transfer efficiency. Table 2 shows material property values used in equation (4) and (5). Additionally, in equation (4) the average of the bending angle increase after a single laser pass was used for the term  $\gamma_T/n$ , and  $\beta$  was fixed equal to 1. It is known that for mild steel the absorption of HPDL radiation is about 45% [4], but, after the first passes, surface oxidation occurs and metal oxides have all very high absorption coefficient [45]. In equation (5) the minimum axis length was used for  $r$  in the case of  $0^\circ$  spot orientation, and the maximum axis length for the case of  $90^\circ$  spot orientation. Figure 15 shows the obtained process map for all the experimental conditions. Every single bending curve is represented by a point. In the same figure, the theoretical curve of equation (6) is superimposed too. Figure 15 shows that equation (6) correctly predicts bending process when surface melting is not present. For stainless steel, experimental data in the case of surface melting are below the theoretical curve because in this case a decrease in bending efficiency  $NT_l$  is mainly present.

Even if analytical models allow researchers to deepen the effect of the involved physical mechanisms in laser forming, finite element analysis is necessary to design complex forming processes. All the forming processes described in the experimental section were carefully modeled by means of finite element models. In the case of line bending, a 3D thermo-

mechanical finite element model was defined to compare numerical and experimental bending angles of the stainless steel sheet metals under different process conditions; the model was built in ANSYS 9 by means of the parametric design language (APDL) to reduce modeling and solution times and to easily change some parameters (such as the sheet thickness or the mesh size). The temperature-dependent material properties of AISI 304 were implemented into the model according to [46]. A bilinear isotropic hardening behavior was implemented to simulate the material properties. The model geometry was built according to the experimental set-up. Initially, a sheet with a thickness of 1.2 mm, a width of 35 mm and a length of 100 mm was modeled (Figure 16a). The model had a finer mesh in the middle, where the laser acted, and a coarse mesh in the remaining parts. The number of element divisions along the sheet thickness was constant and equal to 3. The laser heating was modeled by means of a thermal load in terms of heat flux over a  $3.8 \times 1.2 \text{ mm}^2$  rectangular spot. The dimension of the elements of the finer mesh zone was inferred by the dimension of the spot, setting that the laser spot should cover a total of 2 element facets along the laser path direction. The laser scan was modeled by performing a spot translation along the sheet upper surface. A multi-step analysis was implemented: at each time step, the spot moves overlapping for a half the previous position. Therefore, the resulting time step depended on the mesh size and the scan speed, and was 0.075 s for a speed of 8 mm/s. Two values of the laser power were analyzed: 100 and 150 W. A single laser scan was simulated for the two conditions and a cooling time of 30 s (with a time step of 1 s) was added at the end of each step. Initially, a thermal analysis was carried out by using SOLID70 thermal elements. After obtaining the thermal solution, the thermal elements were converted into SOLID45 structural elements and the thermal solution was used to define the thermal loads of the non-linear structural analysis. Figure 16b shows a typical simulated deformation of a laser irradiated specimen.

In order to calibrate the thermal numerical model, laser heating tests were performed by keeping the sheet in a standstill position; the laser acted on the central position of the sheet for 5 s, with a power of 100 W. At the same time, the temperature of the sheet was acquired at a given distance from the laser spot, on the surface not exposed to laser heating. As a result, the absorption coefficient was set to 0.42 and the heat transfer coefficient was  $10 \text{ W/m}^2 \text{ K}$ . The room temperature was set to  $24^\circ\text{C}$ , according to the measured value during the test.

In Figure 17a a comparison between the temperature curve acquired during the laser heating test and the temperature curve extracted from the thermal model is reported. Therefore, at the end of calibration procedure, a good match of the curves was found. From the thermo-mechanical analysis, the bending angles related to one laser scan and two laser power values (100 and 150 W) were extracted. The bending angle for multiple passes was obtained by multiplying the single-pass value for the number of scans. Figure 17b reports a comparison between experimental and numerical bending angles in the case of a scan rate of 8 mm/s, and the agreement is very good. Higher values of the bending angle are related to a higher number of passes as well as to higher values of laser power. Numerical modeling can predict the effect of the process parameters on the sample deformation. However, the model is able to predict the mechanical effects rather than the thermal ones. In fact, material annealing was not considered in the model.

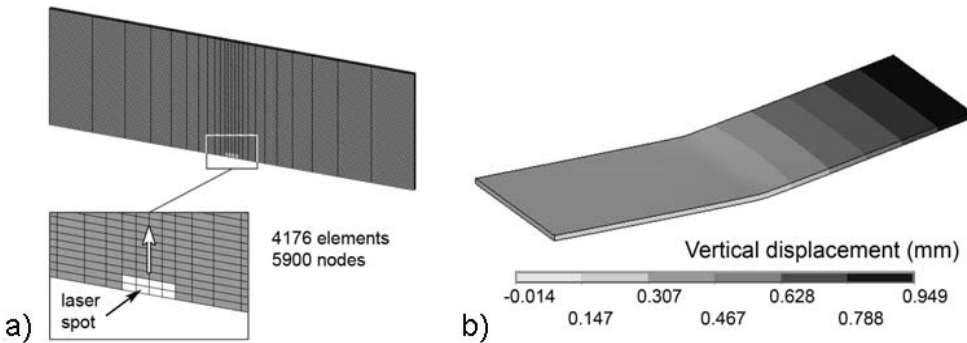


Figure 16. FE modeling of sheet metal forming: a) the discrete model; b) displacement map at the laser power of 150 W and the scanning rate of 8 mm/s, after 1 scan.

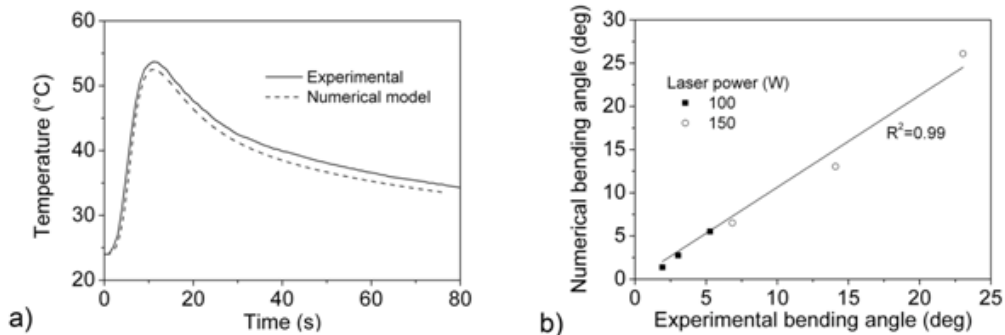


Figure 17. FE simulation of sheet metal forming: a) temperature calibration; b) comparison between experimental and numerical bending angle.

In a further analysis, a single laser scan was simulated in the case of two different scan velocities: 4 mm/s (at 100 and 150 W) and 8 mm/s (at 100, 150 and 200 W). These process conditions refer to the experimental data already reported in Figure 9. The occurrence of the material melting was always avoided. A typical result from the numerical simulation is shown in Figure 18a in terms of temperature and displacement map at given time (3.5 s) and process conditions (scan velocity of 8 mm/s, laser power of 200 W). A comparison between experimental and numerical results is shown in Figure 18b for the sheet bending angle; experimental values were obtained by dividing by 2 the bending angle after 2 passes. The small discrepancy is probably due to the assumption of a constant absorption coefficient. However, the model is able to predict the effect of the change of the main process parameters.

In Figure 19 the evolution of the temperature profile, the stresses and the bending angle is reported in dependence of the time for the same processing conditions of Figure 18a. The temperature profiles are acquired on the top surface of the sample at the start, the middle and the end point of the laser scan. The Von Mises stresses are extracted in the same positions but from the bottom surface. Instead the bending angle is extracted from the vertical displacement of the free end.

The numerical results of Figure 19 may be also generalized to the other laser forming conditions. A peak in the temperature profile is measured when the laser spot passes on the related position. A higher peak is visible in the end point due to the sample pre-heating and

the edge effect. In correspondence of the peak temperature, a peak of the stress is also present. After the laser spot passing, the temperature decreases as well as the stress, but the latter starts to increase again during cooling. At the end, the stress reaches a plateau value depending on the position. Despite of the complex temperature and stress profiles, the bending angle evolution is quite simple. An initial deformation in the opposite direction is present during the first instants of laser exposure, subsequently the trend is rapidly inverted and the bending angle increases linearly during the laser heating. The linear trend disappears when the laser spot approaches the opposite edge. At this point the laser is turned off and the bending angle reaches a stable plateau.

Residual stresses may be extracted by the numerical simulations (a typical stress map is shown in Figure 20a). The plateau value of Von Mises stress of Figure 19 can be considered a numerical prediction of the residual stress. In order to have a comparison between the different numerical solutions, the plateau value of the Von Mises stress was extracted along the laser scan from the side of the bottom surface. The stress distribution is quite complex and two maximums are visible near the edges due to the edge effect. This occurrence suggests that also the measurement of the residual stress is very sensitive to the test location. At 4 mm/s, by increasing the laser power, the residual stress in the central part of the sample increases (Figure 20b). At 8 mm/s the same effect of the laser power is visible (Figure 20c).

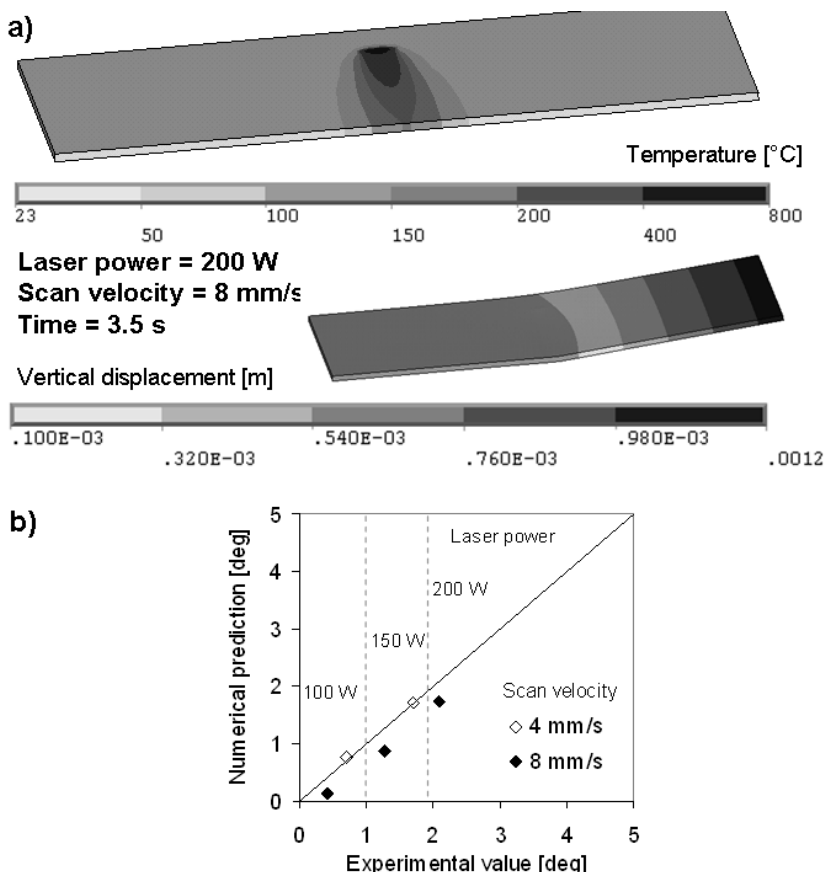


Figure 18. Numerical model results: temperature and displacement maps (a) and comparison between experimental and numerical bending angle (b).

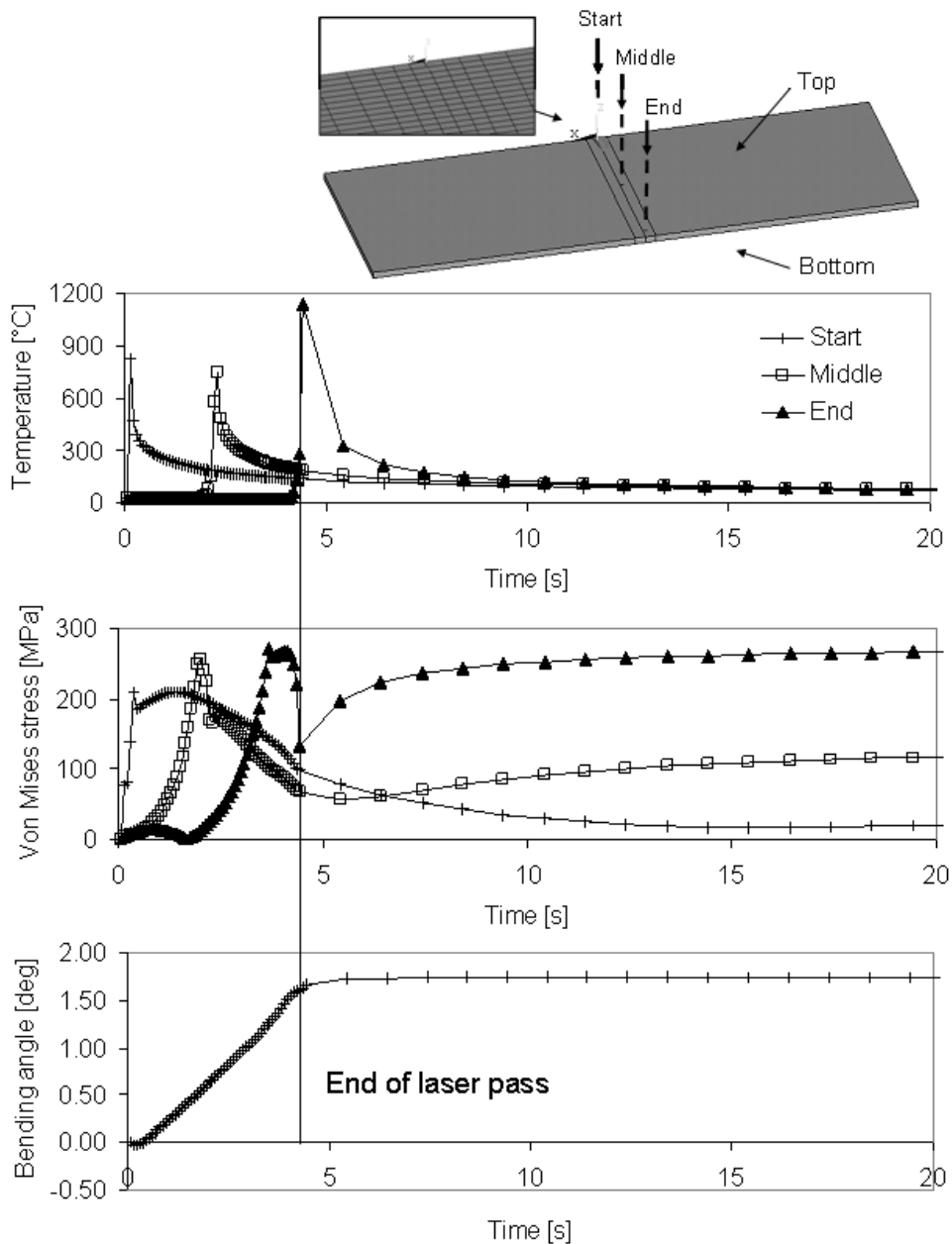


Figure 19. Evolution of temperature, stress and bending angle during laser forming (scan velocity = 8 mm/s, laser power = 200 W).

In the case of tube forming, 3D thermo-mechanical finite element models were also defined. According to the experimental section, the tube was 20 mm in outer diameter, 60 mm in length and 1 mm in wall thickness, and was discretized with a mapped mesh, as Figure 21 shows. In particular, the tube had a fine mesh where the laser acted and in the surrounding zones, whereas a coarse mesh was implemented in the remaining parts. The number of element divisions along the tube thickness was constant and equal to 3. The total number of elements was 5568, the nodes were 7888.

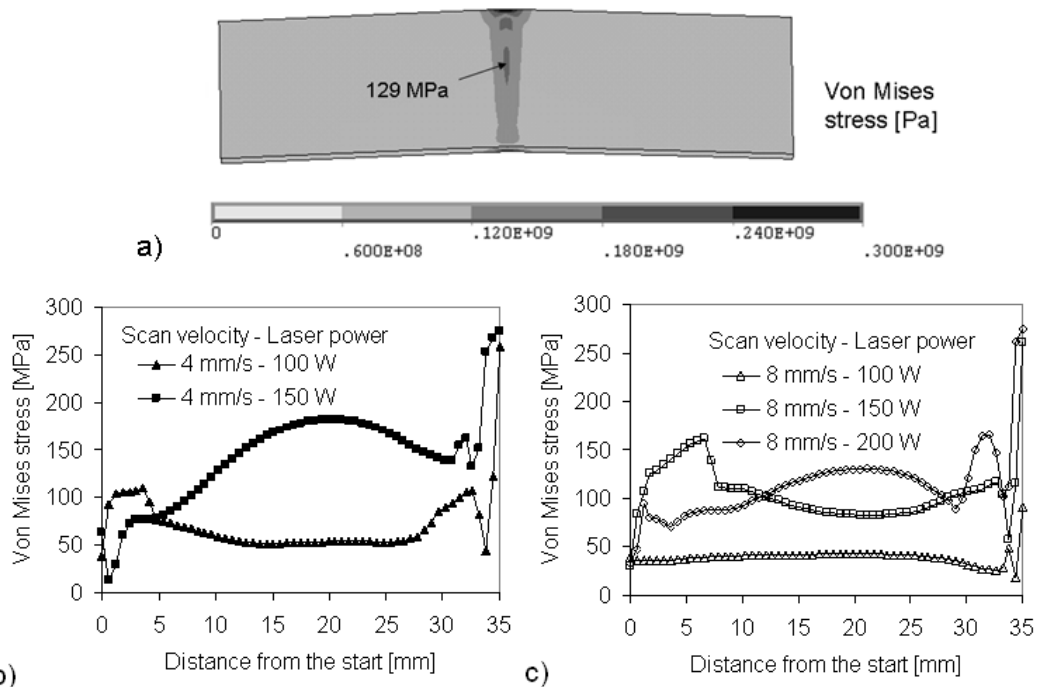


Figure 20. Prediction of residual stresses: (a) Von Mises stress map (scan velocity = 8 mm/s, laser power = 200 W, time = 89 s); residual stress profile on the bottom surface of the sample at the scan velocity of 4 mm/s (b) and 8 mm/s (c).

Also in this case the laser heating was modeled by means of a thermal load in terms of heat flux over a  $3.8 \times 1.2 \text{ mm}^2$  rectangular spot as Figure 21 shows. The size of the elements of the finer mesh zone was inferred by the dimension of the spot, setting that the laser spot should cover a total of 8 elements (2 along the minimum axis and 4 along the maximum axis). The tube rotation was modeled by performing a spot revolution along the external circumference of the tube.

A multi-step analysis was implemented: at each time step, the spot moved so as to overlap for a half the previous position. Therefore the resulting time step depended on the mesh size and the rotational speed, ranging from 0.05 to 0.1 s. Four laser scans were simulated for each condition, and a cooling time of 70 s was added at the end of each heating step. The time step in the cooling phase was fixed to 0.5 s for all the simulations. In order to calibrate the thermal part of the numerical model, laser heating tests were performed by keeping the tube in a standstill position and by acquiring the tube temperature in the point opposite to the laser spot along the external circumference (Figure 10b). Different powers from 40 W to 200 W were set for the laser beam. The tests lasted about 4 min and were used for the calibration procedure of the thermal model. As a result, the absorption coefficient was set to 0.74 and the heat transfer coefficient was  $21 \text{ W/m}^2 \text{ K}$ . Figure 22 shows the good agreement between experimental and numerical data at the end of the calibration procedure.

Numerical solutions were obtained for the power of 150 W and the rotational speeds of 30, 36 and 60 deg/s. During experimentation, in such conditions the average tube temperature was sufficiently controlled during successive scans, thus reducing the cycle time. Due to the discussed numerical procedure, each solution run was divided into 800 steps with a small

difference in the total time step of the heating phases. However, as the cooling phases were much higher in time, the total simulation time is similar for the three conditions (304 s at 30 deg/s, 300 s at 36 deg/s and 292 s at 60 deg/s).

Figure 23a shows the comparison between experimental and numerical results in terms of bending angle after the first 4 scans at the laser power of 150 W. A good agreement was found, showing the validity of the adopted calibration procedure. The effect of the rotational speed on the tube bending is reported in Figure 23b. Higher rotational speeds lead to lower bending angles. Under the laser exposure, the tube deforms downward, whereas in the subsequent cooling phase the tube deformation changes in direction and becomes stable. This mechanism is better shown in Figure 24 where the first two heating steps and the included cooling step are reported. At the beginning of the laser exposure, a sudden increase occurs due to the thermal expansion. The material starts to yield and in the subsequent cooling stage the thermal contraction leads to the tube bending. In the same figure, the displacement maps are shown at the beginning and the end of the first cooling step in the case of 150 W of laser power and 36 deg/s of rotational speed. By decreasing the rotational speed, the slope of the first linear trend increases as well as the final bending angle. However, the tube displacement under heating is an order of magnitude lower than the displacement at the end of the subsequent cooling stage.

The tube deformation due to laser heating is complex as Figure 25 suggests. In this figure, the tube ovalization is reported as a function of time for the three rotational speeds. In tube forming, dimensional accuracy is the main requirement, therefore the problem of the tube ovalization is a key factor for the successful application of this technology. The measure of the tube ovalization is experimentally complex due to the uncertainty in the extraction of the tube cross section. Numerical modeling would help but a proper model calibration is necessary. The ovalization was evaluated by means of the normalized difference between the two orthogonal internal diameters according to the formula shown in the figure. At 30 and 36 deg/s, the ovalization occurs by increasing the vertical diameter whereas the horizontal diameter increases at 60 deg/s. This mismatch is probably dependent on geometrical parameters such as the tube diameter and thickness. Generally, by increasing the laser scans, the tube flattens more and more, and higher ovalizations are observed at lower rotational speeds. An oscillation in the ovalization curve is present during each heating step due to the discussed deformation mechanism. Figure 26 shows the detail of the first heating step: the section of the tube in the case of the maximum and minimum ovalization is also reported at 36 deg/s so as to highlight that the ovalization oscillation depends on the thermal dilatation provided by the laser spot. When this local effect ends, the ovalization curve starts to increase up to a plateau. Plateau values are reported in Figure 25 and a very high difference was found by changing the rotational speed. However, it is not correct to conclude that the higher rotational speed has to be preferred to reduce ovalization. In fact, Figure 27 reports the calculated ovalizations as a function of the bending angle. By studying the curve trends, it is appreciable that a given value of the bending angle would be obtained with higher ovalizations if a higher rotational speed is used. A maximum in the curve at 60 deg/s is observed and it is reasonable to assess that the thermal contribution of the first 4 heating steps is too low to generate a significant tube deformation.

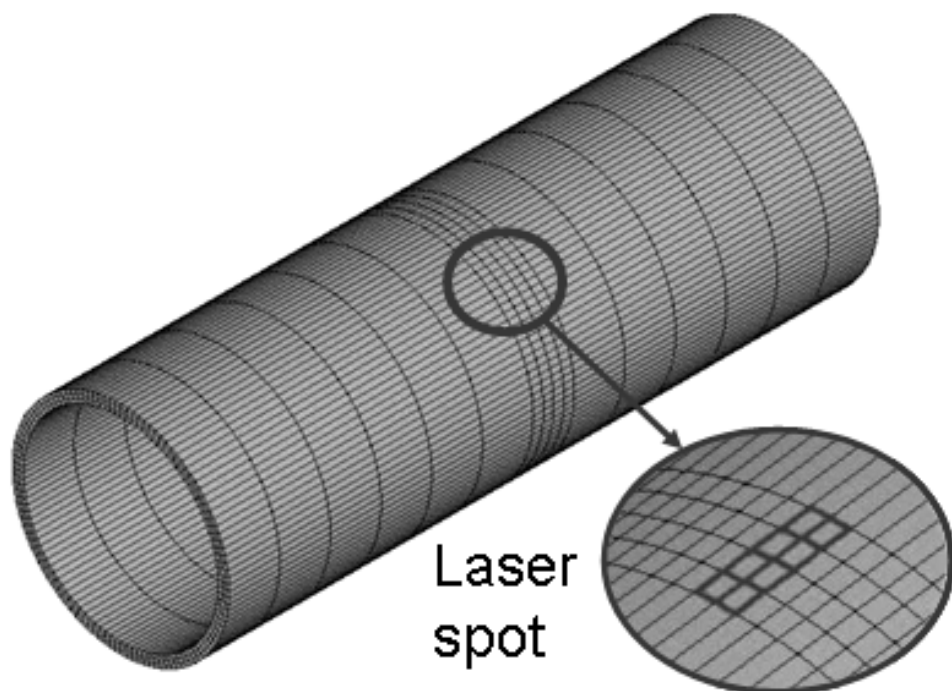


Figure 21. Image of the tube mapped mesh.

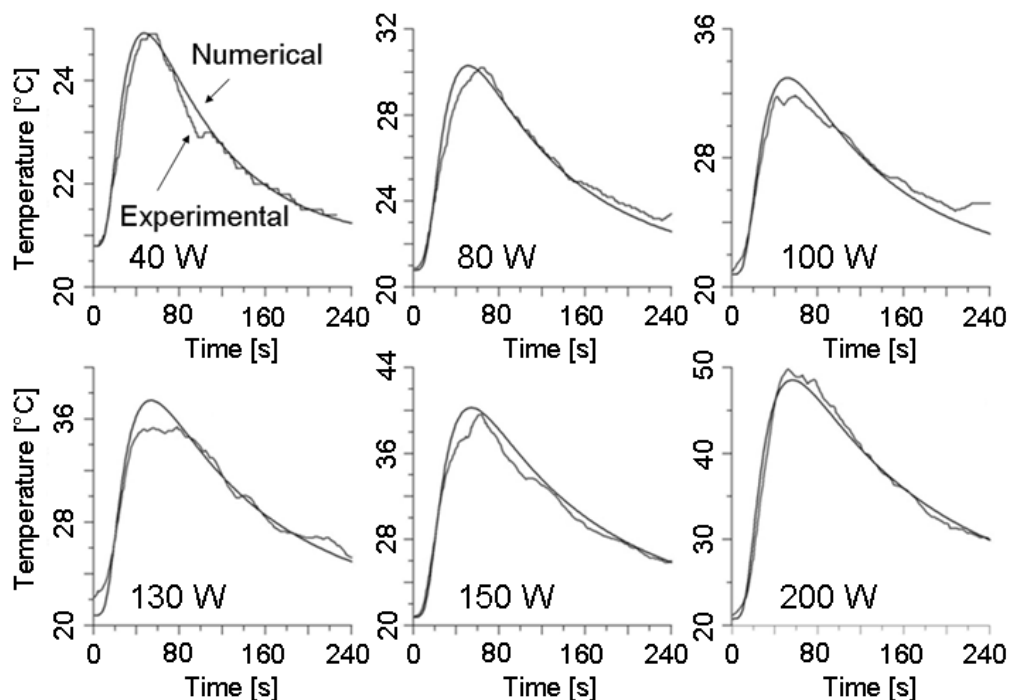


Figure 22. Comparison between numerical and experimental data at the end of the calibration procedure of the thermal model for tube bending.

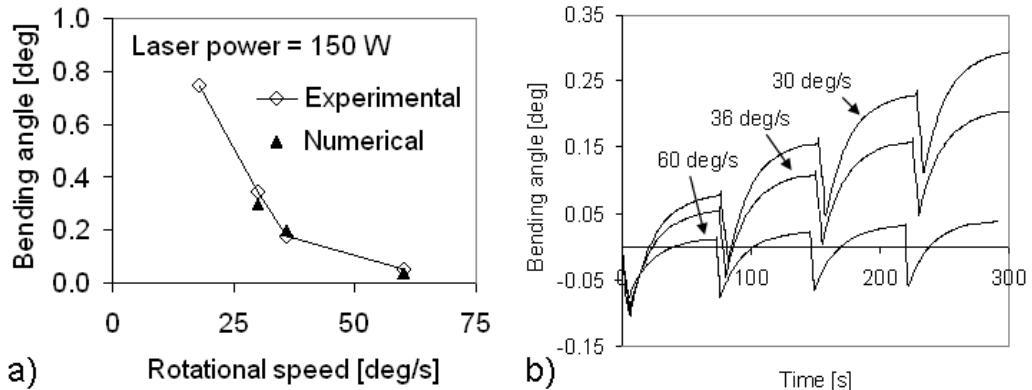


Figure 23. Comparison between experimental and numerical results (a) and numerical prediction of bending angle variation over time (b).

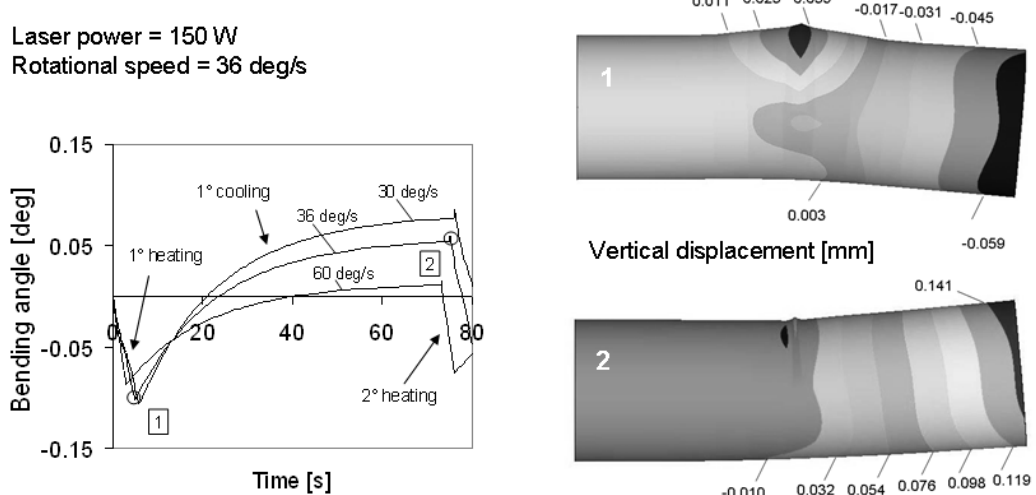


Figure 24. Numerical prediction of the bending angle in the first process stages and related displacement maps.

In order to simulate the forming process of the slotted tubes, the discussed discrete model of the tube has to be changed. Figure 28 shows the case of one of the slotted tubes depicted in Figure 13. The tube geometry was divided into 3 parts for discretizing. The internal part, where the spot acted, was mapped meshed with a fine mesh. Also the two external parts were mapped meshed but with a coarse mesh. The number of element divisions along the tube thickness was left equal to 3 in each part of the tube. The tube rotation was modeled by performing a spot revolution along the portion of the external circumference delimited by the slot boundaries (about 56°). At each time step, the spot moved so as to overlaps for a half the previous position. Fixing the rotational speed to 0.628 rad/s, the resulting time step depended only on the mesh size and was nearly 0.085 s. After each laser heating step, a cooling step of 80 s was simulated. Ten heating-cooling cycles were performed. At the end of the simulation, the radial displacement of a reference node (Figure 28) was evaluated.

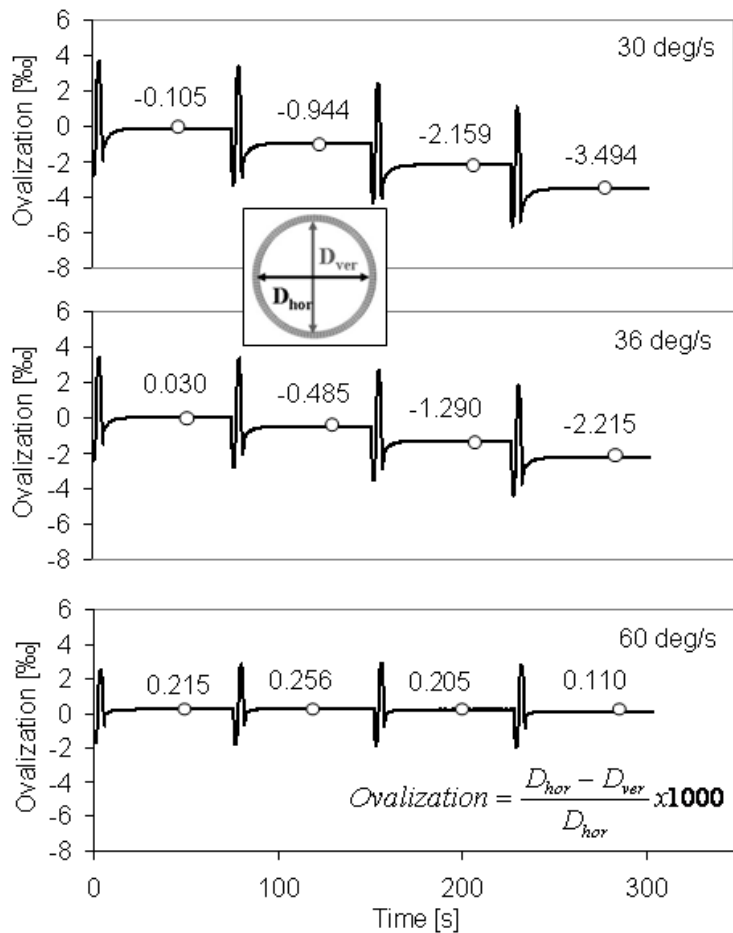


Figure 25. Numerical prediction of the tube ovalization.

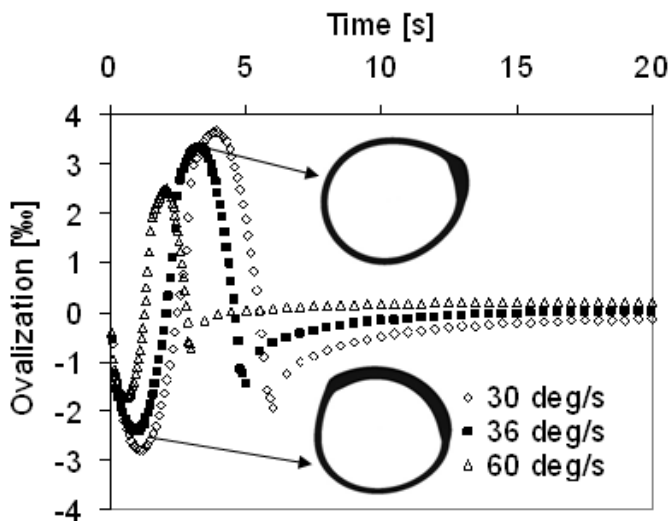


Figure 26. Numerical prediction of the tube ovalization at the beginning of the laser process.

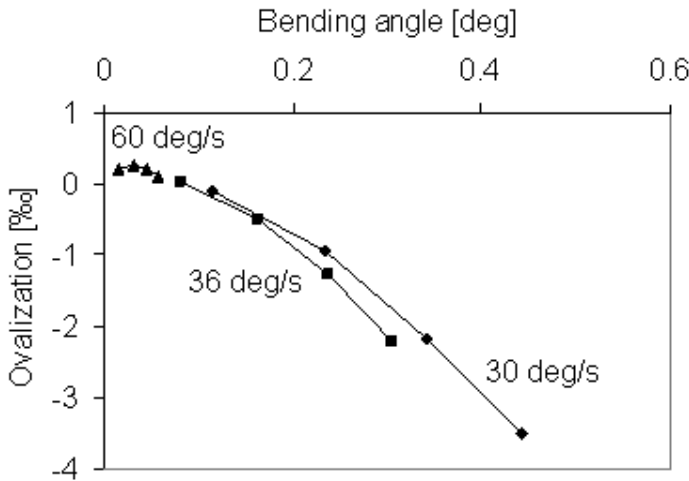


Figure 27. Tube ovalization as a function of the bending angle (numerical results).

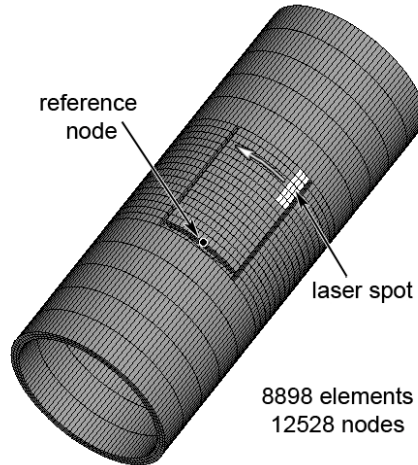


Figure 28. FE model for laser forming of slotted tubes.

Figures 29a and 29b show the results of the numerical simulation in terms of radial displacement of the reference node as a function of time for 1 and 10 scans respectively. As Figure 29a shows, at the beginning of the laser exposure, a sudden increase occurs due to the thermal expansion up to a maximum (point 1). In this case the laser path is too short and the constraining effect of the surrounding material determines this deformation. Subsequently, the radial displacement decreases down to a minimum (point 2). In fact after 1 s, the laser path is sufficiently longer than the spot size (Figure 30). The tongue deforms entering the tube wall and the minimum displacement is negative. As the thermal strains have the same gradient of the temperature, the maximum is on the side of the spot and the tongue bends in the opposite direction. But in this condition, due to the very high temperature, the material starts to yield in the laser processed zone. When the laser spot is sufficiently far from the early processed zone, the material starts to cool. However, due to the previous yielding, the tongue cannot return in the initial configuration but it starts to bend in the opposite direction. Figure 29b shows the

effect of the successive superimposed scans. At the beginning of each step, the same mechanism of Figure 29a is repeated. In particular the relative minimum is always clearly visible. After 800 s of laser processing, over 1.8 mm of total radial displacement is achieved (point 3).

In Figure 31 three displacement maps are reported in correspondence of the above mentioned points. For a better understanding, maps 1 and 2 are shown with a scale factor of 10, map 3 is in true scale. It is evident the complex forming mechanism that leads the tongue to invert twice the bending direction. The numerical simulation was validated by the experimental test on sample (b) of Figure 13. After laser processing, the formed surface of this sheet was analyzed by means of a 3D surface profiling system (Taylor Hobson Talysurf CLI) to acquire the profile of the bent tongue. It was measured a maximum radial displacement of about 2 mm, according to the result of Figure 31.

Numerical modeling was also used to evaluate the effect of the tube diameter on the bending behavior of the tongue. In this case, the rotational speed was fixed at 1.257 rad/s ( $72^\circ/\text{s}$ ) for the tube with a diameter of 10 mm and at 0.628 rad/s ( $36^\circ/\text{s}$ ) for the tube with a diameter of 20 mm, according to the experimental section (Figure 14). Therefore, the rim speed of the laser spot was equal for both tubes. At the end of the simulation, the radial displacement of the reference node (Figure 32) was evaluated, as well as the radial displacement of the nodes in the middle of the tongue, on the external surface, so as to have the profile of the formed tube. In order to make a comparison between experimental and numerical data, the formed surfaces of the tubes of Figure 14b were analyzed by means of the 3D surface profiling and the experimental profiles were filtered because the outline was of interest instead of the roughness profile.

Figure 33a shows the results of the thermal analysis in terms of temperature map, after 0.4 s and 0.98 s for the small and the big tube, respectively. This time corresponds approximately to 5/6 of the first laser scan completion. The larger tube reaches the maximum value of temperature, because in this case the pre-heating effect is more pronounced due to a longer laser path, with respect to the small tube. In both cases, the longitudinal cuts of the slot limit the heat transfer along the tube circumference and the tongue starts to behave like a plate.

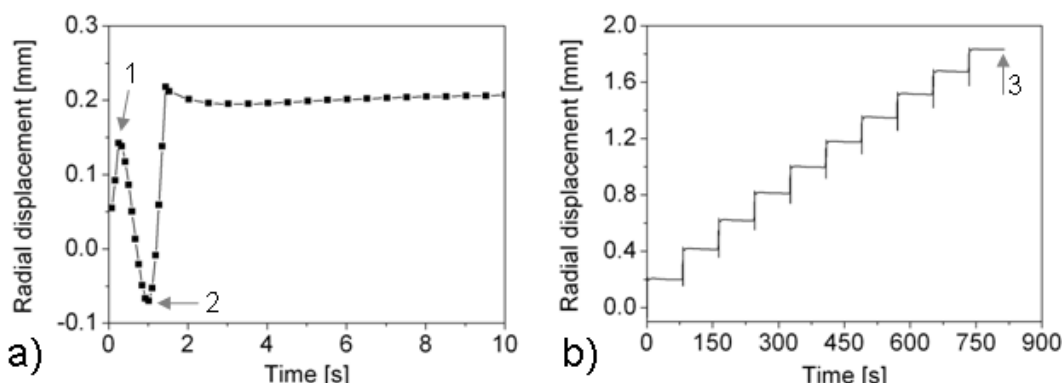


Figure 29. Radial displacement of the reference node during the first scan (a) and during 10 scans (b).

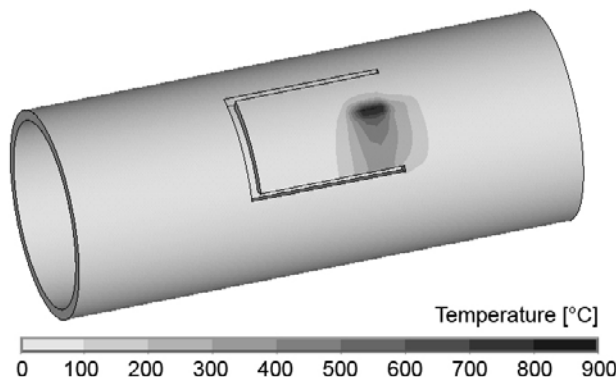


Figure 30. Temperature map after 1 s (point 2).

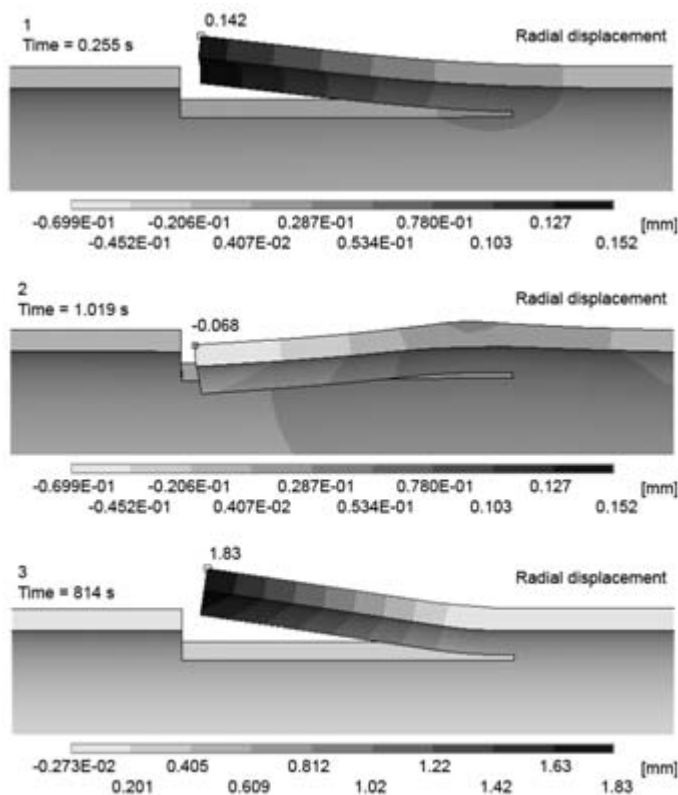


Figure 31. Radial displacement maps (section view) at three different time steps.

Figure 33b shows the radial displacement of the reference node up to 10 scans. It is evident that a higher displacement is generated in the big tube and this difference is dependent on the tongue transverse dimension. The bending curves of Figure 33b are qualitatively similar but actually the tubes exhibit a different behavior during deformation. By increasing the laser scans, the radial displacement of the tongue uniformly increases in both cases. Figures 34a and 34b show the details of the first and the last scan. For the big tube, the mechanism is the same already discussed for Figure 29a. For the small tube, the first sudden

increment in the radial displacement is not present and the tongue immediately starts to enter the tube wall. It is interesting to observe that this different behavior was observed for all the 10 cycles. In fact, Figure 34b refers to the last scan and the numerical curves are very similar to the curves of Figure 34a. Evidently, for the small tube, the size of the tongue is too small and the constraining effect of the surrounding material at the beginning of the laser path is less important.

The radial displacement maps at the end of simulation are shown in Figure 35a in a true scale section view. The tongue deformation is very similar to the metal sheet case even if the tube surface is cylindrical and not flat. The analogy with the laser plate bending case is also confirmed by Figure 33b where a linear dependence of the bending angle on the number of laser scans is predictable.

In Figure 35b a comparison between the profiles from experimentation and numerical simulation is given. The final agreement between experimental and numerical data is very good for both tubes. The unprocessed part of the tongue remains unaltered with the shape of the initial cylindrical surface and this occurrence resulted from both experimental and numerical analyses.

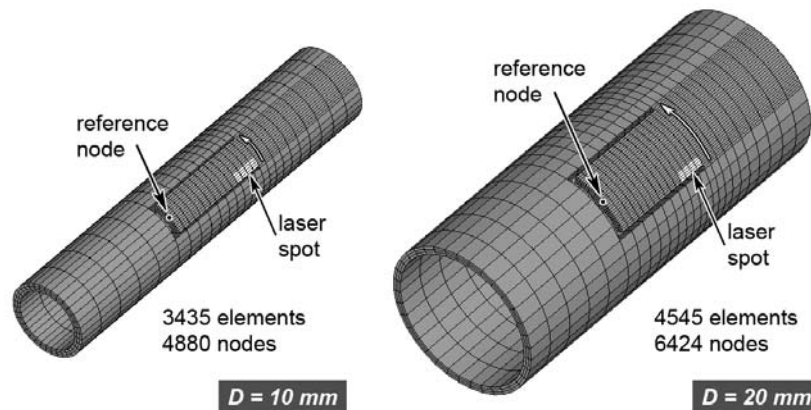


Figure 32. FE models for laser forming of the slotted tubes with different size.

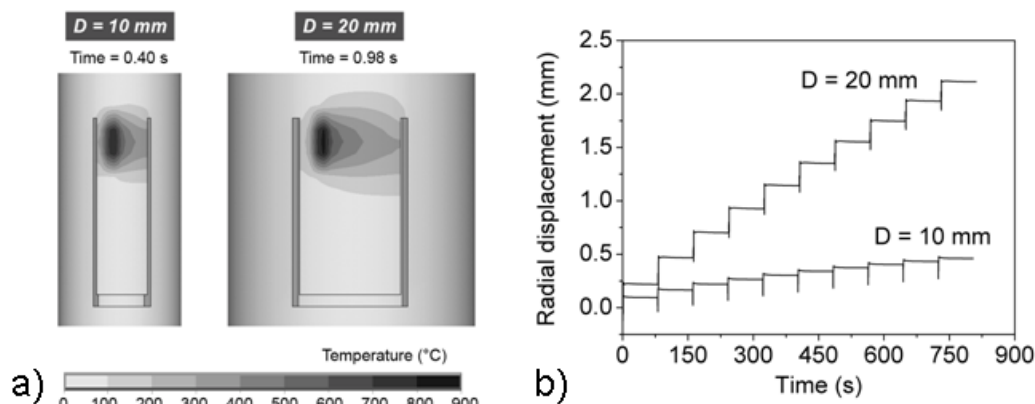


Figure 33. Temperature maps at 5/6 of the first laser scan completion (a) and radial displacement of the reference nodes during 10 scans (b).

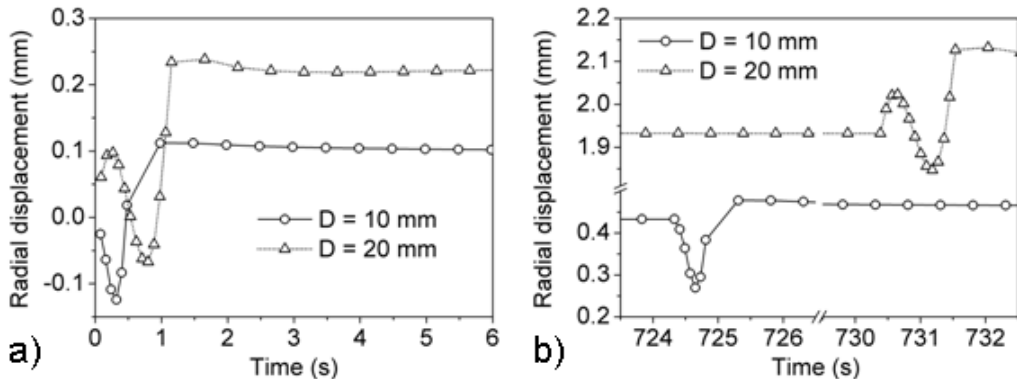


Figure 34. Radial displacement of the reference nodes during the first scan (a) and the last scan (b).

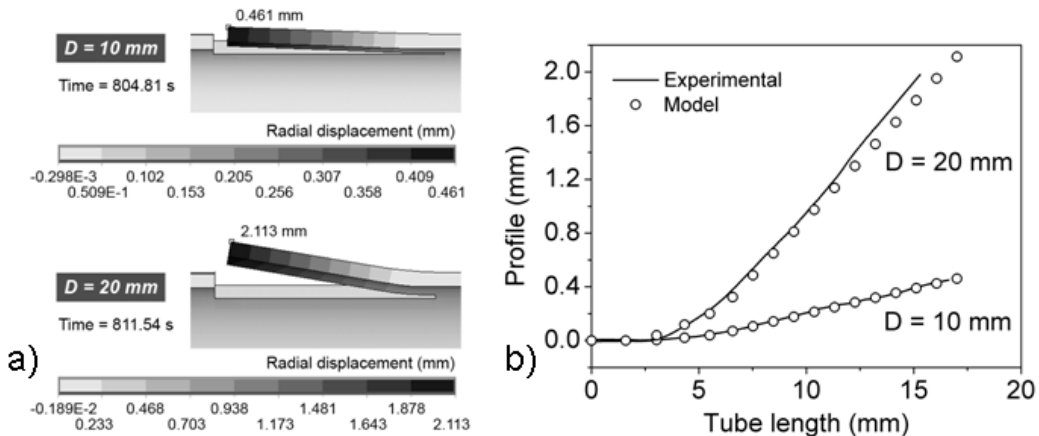


Figure 35. Radial displacement maps (section view) at the end of simulation in true scale, and comparison between the profiles from experimentation and numerical simulation.

## MATERIAL ANALYSIS

Depending on the process parameters and the laser-material interaction, different effects may be observed on the material: from residual stresses to material annealing. Numerical modeling is mandatory to understand the relationship between process parameters and results in laser forming. However, even if good results are generally obtained in terms of prediction of bending angle, the quality of the results may be poor in terms of residual stresses. If multiple scans are carried out, the material annealing cannot be neglected. Numerical simulation may predict the final shape of the laser bent part, but it could be erroneous in the residual stress evaluation. Nevertheless, in order to design a forming process, residual stresses are fundamental and a strain-based approach could be dangerous. Therefore, material analysis is an important step in the study of the laser forming technology.

Residual stresses can be measured by means of X-ray analysis in terms of first and second order stress, namely  $\sigma_I$  and  $\sigma_{II}$ . In fact, X-ray diffraction method is a very useful technique to detect the changes in lattice of the superficial layer subjected to different damage

processes. These changes could be of different nature, such as type of phase, crystalline lattice constants, dimension of mosaic blocks, level of the first and second order stresses, degree of texture, thickness of superficial layer, cohesion forces between atoms, level of dislocation density. In this study, the X-ray diffractograms were carried out by means of a DRON 3 diffractometer equipped with a graphite crystal monochromator. The test was performed on an un-processed metal sheet and 3 bent sheets, which were processed for 6 passes at the scan velocity of 8 mm/s at different laser power (100, 150 and 200 W). The scans ( $\lambda = 1.541 \text{ \AA}$ ) were carried out in the angular domain  $2\theta$  where the typical diffraction of the  $\gamma$ -Fe phase of the stainless steel is visible. The X-ray measures on the treated samples were taken on the convex exterior surface, in the laser beam action zone

The first and second order of residual stress may be directly extracted from the diffractograms. In particular, the first order stress  $\sigma_I$  is given by:

$$\sigma_I = \frac{E}{v} (\cot \theta_s) \Delta \theta \quad (7)$$

where:

$$\Delta \theta = \theta_s - \theta_{in} \quad (8)$$

with  $\theta_s$  the diffraction angle of the peak measured on the stressed sample, and  $\theta_{in}$  the value of the initial un-processed sample:

The second order stress  $\sigma_{II}$  was extracted by the physical width of the diffraction line (311), namely  $\beta_{311}$ . The value of  $\sigma_{II}$  is given by:

$$\sigma_{II} = \frac{E}{v} \eta_{311} \quad (9)$$

where:

$$\eta_{311} = \left( \frac{\Delta d}{d} \right)_{311} = \frac{\beta_{311}}{4 \tan \theta_{311}} \quad (10)$$

and:

$$\beta_{311} = \sqrt{(\beta_{311})_s^2 - (\beta_{311})_{st}^2} \quad (11)$$

with  $\theta_{311}$  the diffraction angle of the line (311),  $(\beta_{311})_s$  the corresponding width for the stressed sample, and  $(\beta_{311})_{st}$  the same value for a standard sample.

In Figure 36 the results of the X-ray analyses are reported. The original diffractograms are shown together with the related bending angle of the samples. In the following Figure 37 a typical microstructure of a bent sample is shown in the laser heated zone (after 6 passes at the scan velocity of 8 mm/s and the laser power of 200 W). The annealing twins are visible; with the laser power increasing, the density of annealing twins increases, as well as the depth of their penetration.

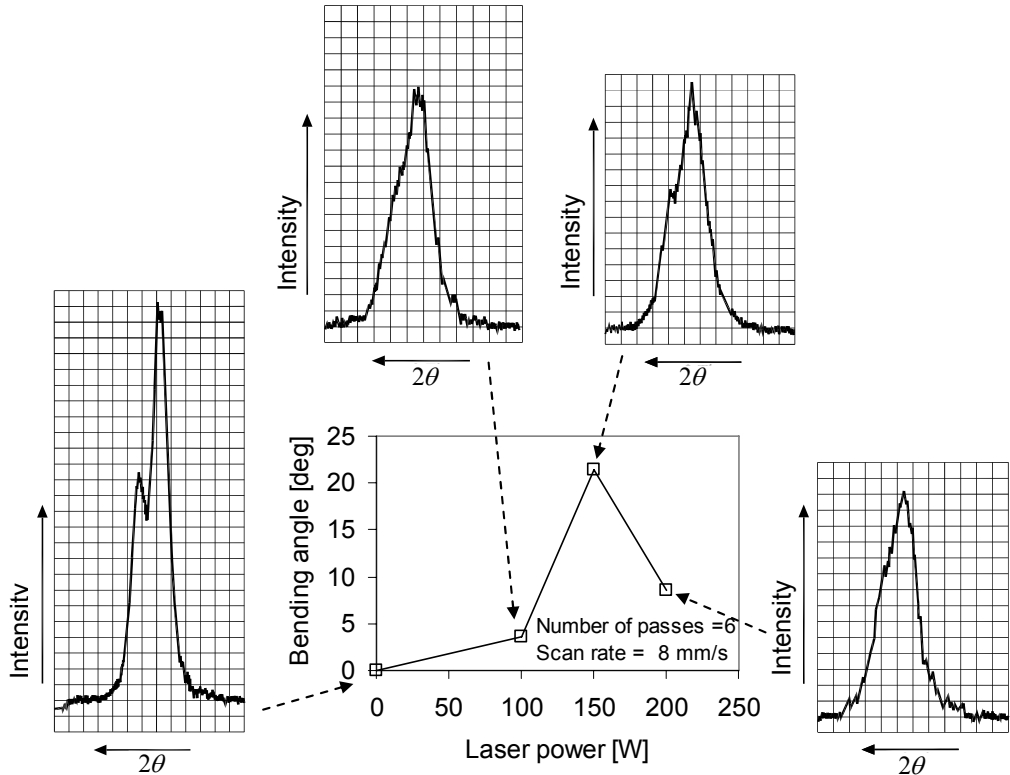


Figure 36. X-ray analyses of un-processed and processed samples.

In Figure 38 the residual stresses experimentally measured (Figure 36) and extracted by equations (7) and (9) are reported. The first order stress,  $\sigma_I$ , measured on the convex exterior surface of the sample has a non-linear variation. By increasing the laser power from 100 to 150 W,  $\sigma_I$  decreases, because of the thermal effect which is more pronounced than the mechanical effect. By increasing the laser power up to 200 W,  $\sigma_I$  increases, which means that the mechanical effect becomes dominant. The second order stress  $\sigma_{II}$  has a stabilization tendency, along with the laser power increasing, which means that the two effects, mechanical and thermal, are mutually compensated. The thermal effect of the laser heating on the material annealing is also shown by the microstructure analysis (Figure 37) as annealing twins are observed in the processed zones of the samples.

In order to measure the effect of the laser bending process, instrumented macro-indentation can be also used. A double indentation is performed on sheets by means of two co-axial small diameter flat indenters made of WC [47]. A very small indentation is left on the sheet, so as to consider this technique a non destructive one, particularly suitable for on-line application. Double indentation tests were carried out on the 1.2 mm thick bent sheets, as shown in Figure 39a. Tests were performed by using a universal material testing machine (MTS Insight 5) opportunely equipped with two indenter holders (upper and lower). Two co-axial flat indenters, 1 mm in diameter, made of WC, were set in the opposite holders. During the test, the applied load was acquired as a function of the penetration depth.

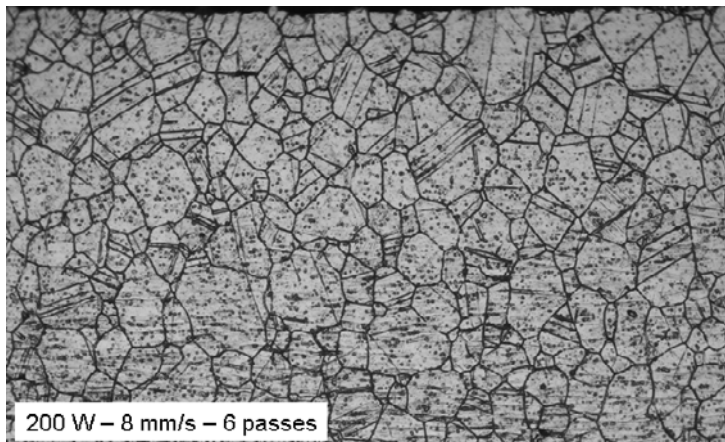


Figure 37. The microstructure of a laser bent sheet metal.

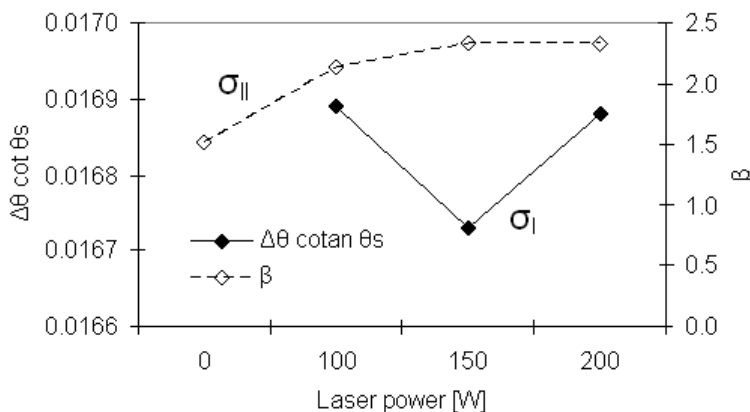


Figure 38. First and second order residual stress (scan velocity = 8 mm/s, number of passes = 6).

Indentations were performed at 0.10 mm/min up to a maximum penetration depth of 0.15 mm, with a pre-load of 50 N. On each side of the bended sheet, 6 indentations were performed at fixed positions, following the grid depicted in Figure 39b. Lower distances form the bending line were not possible due to sample curvature. The value of the indentation load at a fixed penetration depth (0.04 mm) was extracted from each indentation test and used to make a comparison. Five double indentation tests were also performed on an un-processed specimen in the same test conditions. The effect of laser processing on material properties is clearly visible in Figure 39c: the indentation curves are very similar for the un-processed sample and a position far from the laser heated zone, whereas a high difference is present in a position near the bending line. Figure 40 shows the average indentation load at 0.04 mm as a function of the distance from the bending line. The indentation load is lower near the bending line, and rapidly approaches the value of the un-processed sample by increasing the distance from the laser processed zone. With an increase of the laser power or the number of passes, the indentation load decreases. Evidently the material annealing related to the laser heating is prevalent in comparison with the material hardening related to the sample plastic deformation.

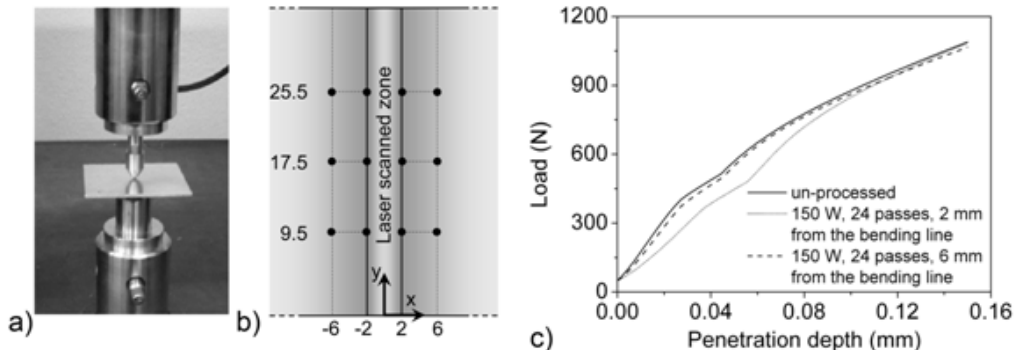


Figure 39. Double indentation tests on laser bent sheets: a) experimental setup; b) indentation grid; c) example of indentation curves.

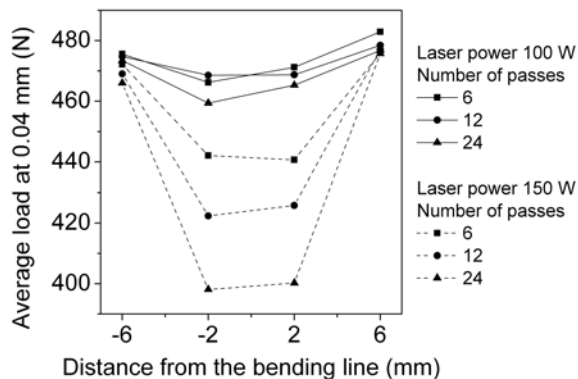


Figure 40. Average indentation load of laser bent sheets.

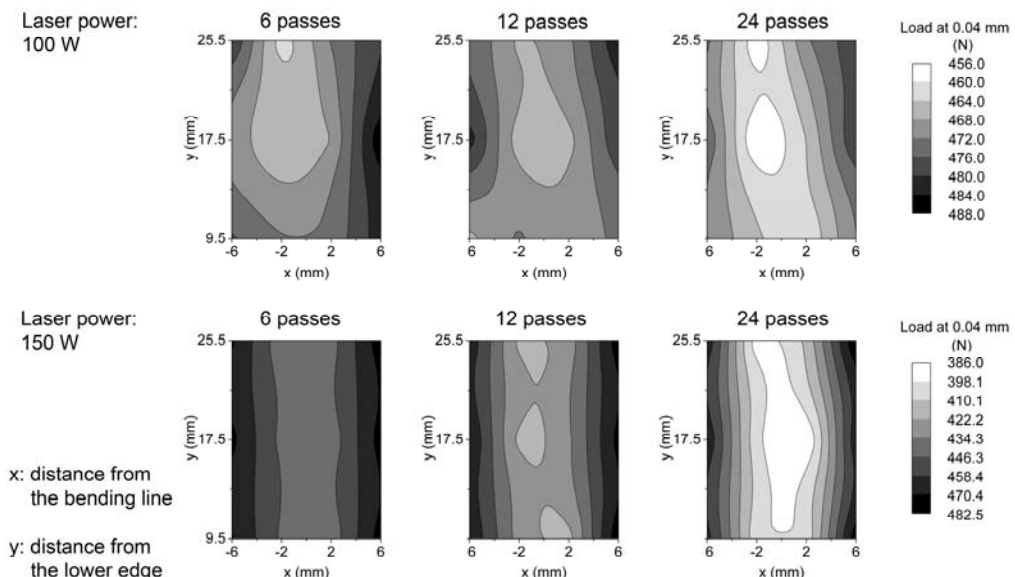


Figure 41. Indentation load maps of bent sheet metals.

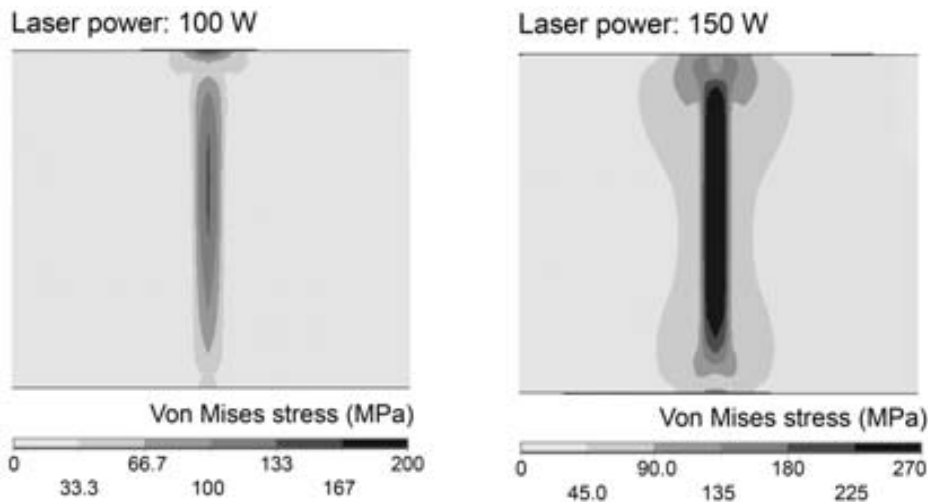


Figure 42. Numerical residual stress (after 1 scan).

The effect of the laser process parameters on the indentation load is more clearly visible in the maps of Figure 41. The load values, extracted from each samples, were arranged in a continuous map by using the Kringing correlation method. For a comparison, Figure 42 shows the numerical prediction of residual stresses at 100 and 150 W after 1 scan. By considering that higher residual stresses are generally related to lower indentation loads, the maps of Figures 41 and 42 should be comparable. However it is evident that only a qualitative analogy may be discussed as the reduction of the indentation load for the processed samples depend mainly on the material annealing (which is not modeled). The effect of the residual stress is not absent but probably secondary.

## CONCLUSION

Laser bending of steel parts is a very attractive process for prototyping or small production runs but the bending mechanism is quite complex. It is particularly critical to evaluate the combined effect of geometrical and process parameters, and numerical modeling is the only method to design a reliable process. Unfortunately, high processing times are necessary. In fact, high bending efficiencies are achieved if the material temperature is low but successive scans result in increasing the average part temperature. The temperature increase of the metal part during time may be detrimental also for the final process accuracy. For example, in tube bending the ovalization is strongly dependent on the rotational speed and lower rotational speeds should be preferred to reduce the tube flattening but a limit in the reduction of the rotational speed is given by the increase of the average tube temperature which may lead to surface melting or material modifications (e.g. softening).

Experimental results showed that a diode laser can be efficiently used to form sheets and tubes. This way, the typical advantages of the laser forming process may be added to the advantages of using diode lasers. Under such conditions, a low power is sufficient to have a good forming efficiency in the case of thin parts. Sheet metals and tubes may be formed in complex shapes; tongues or flares can be made as well and successfully used for tube

assembling or joining. A HPDL could be used also to weld steel parts after forming, even if only by a conduction process. In fact, the ability of diode lasers in performing new processes is very important for industrial applications.

Numerical modeling helps in defining the correct forming strategy. Apart from line bending, it is not possible to predict the result of a forming operation without using any numerical modeling procedure. This is a strong limit as many enterprises prefer to use easier manufacturing processes, therefore laser forming is still confined in research laboratories. The development of simulation softwares for laser forming should overcome this problem but the state of the art of the knowledge is not yet sufficient to achieve this task.

## NOMENCLATURE

$P$	= Laser power [W]
$v$	= Laser scanning rate [mm/s]
$n$	= Number of laser passes
$t$	= Sheet thickness [mm]
$\gamma_s$	= Bending angle after a single laser pass [rad]
$\gamma_T$	= Total bending angle at the end of all the laser passes [rad]
$\beta$	= Absorption coefficient
$\alpha$	= Linear thermal expansion coefficient [ $K^{-1}$ ]
$\lambda$	= Thermal diffusivity [ $m^2/s$ ]
$k$	= Thermal conductivity [W/m K]
$r$	= Spot radius [mm]
$N_{Th1}$	= First thermal number for laser forming
$N_{Th2}$	= Second thermal number for laser forming
$\Delta T$	= Reference temperature interval
$E$	= Elastic modulus
$\nu$	= Poisson's ratio
$\sigma_I$	= First order of residual stress
$\sigma_{II}$	= Second order of residual stress
$\theta$	= Diffraction angle of a X-ray peak
$\beta_{ijk}$	= Physical width of the diffraction line (ijk)

## REFERENCES

- [1] Shi, Y; Yao, Z; Shen, H; Hu, J. *Int J Mach Tools Manuf*, 2006, vol 46, 1689-1697.
- [2] Magee, J; Sidhu, J; Cooke, RL. *Opt Laser Eng*, 2000, vol 34, 339-353.
- [3] Laeng, J; Stewart, JG; Liou, FW. *Int J Prod Res*, 2000, vol 38, 3973-3996.
- [4] Lawrence, J; Schimdt, MJ; Li, L. *Int J Mach Tool Manu*, 2001, vol 41, 967-977.
- [5] Li, W; Yao, L. *Int J Adv Manuf Tech*, 2001, vol 17, 196-203.
- [6] Lee, KC; Lin, J. *Opt Laser Technol*, 2002, vol 34, 639-648.
- [7] Dearden, G; Edwardson, SP. *J Opt A-Pure Appl Opt*, 2003, vol 5, 8-15.
- [8] Geiger, M; Merklein, M; Pitz, M. *J Mater Process Tech*, 2004, vol 151, 3-11.

- [9] Zhang, L; Michaleris, P. *Finite Elem Anal Des*, 2004, vol 40, 383-405.
- [10] Hsieh, H.-S; Lin, J. *Opt Laser Technol*, 2004, vol 36, 431-439.
- [11] McBride, R; Bardin, F; Gross, M; Hand, DP; Jones, JDC; Moore, AJ. *J Phys D Appl Phys*, 2005, vol 38, 4027-4036.
- [12] Yanjin, G; Sheng, S; Guoqun, Z; Yiguo, L. *J Mater Process Tech*, 2005, vol 167, 124-131.
- [13] Zhang, J; Pirzada, D; Chu, CC; Cheng, GJ. *J Manuf Sci Eng*, 2005, vol 127, 157-164.
- [14] Edwardson, SP; Abed, E; Bartkowiak, K; Dearden, G; Watkins, K.G. *J Phys D Appl Phys*, 2006, vol. 39, 382-389.
- [15] Costa Santos, E; Shiomi, M; Osakada, K; Laoui, T. *Int J Mach Tool Manu*, 2006, vol 46, 1459-1468.
- [16] Shi, Y.J; Shen, H; Yao, ZQ; Hu, J. *Acta Metall Sin*, 2006, vol 19, 144-150.
- [17] Shi, Y; Shen, H; Yao, Z; Hu, J; Xia, L. *Comp Mater Sci*, 2006, vol 37, 323-327.
- [18] Shen, H; Shi, Y; Yao, Z; Hu, J. *Comp Mater Sci*, 2006, vol 37, 593-598.
- [19] Shen, H; Shi, Y; Yao, Z; *Proc IME C J Mech Eng Sci*, 2006, vol 220, 507-511.
- [20] Shen, H; Shi, YJ; Yao, ZQ; Hu, J. *Mater Sci Technol*, 2006, vol 22, 981-986.
- [21] Liu, FR; Chan, KC; Tang, CY. *J Laser Appl*, 2006, vol 18, 56-64.
- [22] Cheng, P; Fan, Y; Zhang, J; Yao, Y.L; Mika, D.P; Zhang, W; Graham, M; Marte, J; Jones, M. *J Manuf Sci Eng*, 2006, vol 128, 634-641.
- [23] Cheng, P; Fan, Y; Zhang, J; Yao, Y.L; Mika, D.P; Zhang, W; Graham, M; Marte, J; Jones, M. *J Manuf Sci Eng*, 2006, vol 128, 642-650.
- [24] Shen, H; Zhou, J; Shi, YJ; Yao, ZQ; Hu, J. *Mater Sci Technol*, 2007, vol 23, 483-486.
- [25] Shen, H; Zhou, J; Yao, ZQ. *Proc IME C J Mech Eng Sci*, 2007, vol 221, 993-997.
- [26] Korsunsky, AM; Vorster, WJJ; Zhang, SY; Topić, M; Venter, AM. *Proc IME C J Mech Eng Sci*, 2008, vol 222, 1635-1645.
- [27] Labeas, GN. *J Mater Process Tech*, 2008, vol 207, 248-257.
- [28] Li, W; Yao, YL. *J Manuf Sci Eng*, 2001, vol 123, 674-681.
- [29] Hao, N; Li, L. *Appl Surf Sci*, 2003, vols 208-209, 437-441.
- [30] Hao, N; Li, L. *Appl Surf Sci*, 2003, vols 208-209, 432-436.
- [31] Hsieh, HS; Lin, J. *Opt Laser Technol*, 2005, vol 37, 402-409.
- [32] Zhang, J; Cheng, P; Zhang, W; Graham, M; Jones, J; Jones, M; Yao, Y.L. *J Manuf Sci Eng*, 2006, vol 128, 20-33.
- [33] Safdar, S; Lin, L; Sheikh, MA; Liu, Z. *Opt Laser Technol*, 2007, vol 39, 1101-1110.
- [34] Li, L. *Opt Laser Eng*, 2000, vol 34, 231-253.
- [35] Bachmann, F. *Appl Surf Sci*, 2003, vols 208-209, 125-136.
- [36] Pashby, IR; Barnes, S; Bryden, BG. *J Mater Process Tech*, 2003, vol 139, 585-588.
- [37] Zhu, J; Li, L; Liu, Z. *Appl Surf Sci*, 2005, vol 247, 300-306.
- [38] Casamichele, L; Quadrini, F; Tagliaferri, V. *J Manuf Sci Eng*, 2007, vol 129, 868-873.
- [39] Guglielmotti, A; Quadrini, F; Squeo, EA; Tagliaferri, V. Proceedings of “Esaform2008”, Lyon, France, 23-25 April 2008.
- [40] Guglielmotti, A; Quadrini, F; Squeo, EA; Tagliaferri, V. *Int J Mater Form*, 2009, vol 2, 107-111.
- [41] Gheorghies, C; Nicoara, D; Paunoiu, V; Quadrini, F; Santo, L; Squeo, E.A. *Key Eng Mater*, 2009, vols 410-411, 629-640.
- [42] Gorga, F; Quadrini, F; Squeo, EA; Tagliaferri, V. *J Manuf Technol Res*, 2009, vol 1, 71-84.

- [43] Quadrini, F; Squeo, EA; Tagliaferri, V. Proceedings of Esaform 2009, Enschede, The Netherlands, 2009, 27-29 April.
- [44] Vollertsen, F. *Proceedings of the LANE'1994*, 94, vol 1, 345-359.
- [45] Duley, 1983, Laser processing and analysis of Materials, Plenum Press, New York.
- [46] Chen, J; Young, B. *Eng Struct*, 2006, vol 28, 229-239.
- [47] Quadrini, F; Santo, L; Squeo, EA. *Key Eng Mater*, 2007, vol 344, 127-133.

## ***Chapter 6***

# **LASERS AND LAMPS WITH EXCITATION BY BACKGROUND-ELECTRON MULTIPLICATION WAVE**

**It is devoted to S.I. Yakovlenko's memory**

***A. M. Boichenko***

Head of Kinetic Department A.M. Prokhorov General Physics Institute  
Vavilov street, 38, 119991, Moscow, Russia.

## **ABSTRACT**

It was shown earlier that the ionisation propagation in a gas at about the atmospheric pressure may proceed due to the multiplication of the existing electrons with a low background density rather than the transfer of electrons or photons. It is considered the feasibility of using the plasma produced in the afterglow of this background-electron multiplication wave for pumping plasma lasers (in particular, Penning neon laser and  $\text{Xe}_2^*$  excimer lasers) as well as excilamps.

The Penning neon laser was studied in a  $\text{Ne}-\text{H}_2$  mixture excited by a transverse discharge. Theoretical modeling allowed the conclusion that the laser active medium was excited due to the BEMW passed through the discharge gap. Numerous attempts to pump  $\text{Xe}_2^*$  lasers by a gas discharge instead of a beam have not been successful. Simulations show that it is possible to achieve the laser effect at  $\lambda = 172$  nm as well as to substantially improve the peak specific power of the spontaneous radiation of xenon lamps.

## **1. INTRODUCTION**

Active media of plasma lasers represents recombination-nonequilibrium plasma produced by hard ionizer [1-9]. Widely known representative of such pumping is electron beam pumping. The possibility of new type of gaseous active media powerful pumping resulting to formation of recombination-nonequilibrium plasma is presented. First of all more interesting applications can be associated with laser pumping, especially  $\text{Xe}_2^*$  laser pumping. Another one concerned with spontaneous emission of gases.

It is known that beam-pumped lasers operating on photo-dissociation xenon transitions were the first-realised excimer lasers [10-13] (see also recent reviews [4, 14] and collection [6]). However, numerous attempts to pump  $\text{Xe}_2^*$  lasers by a gas discharge instead of a beam have not been successful. Lasing by  $\text{Kr}_2^*$  dimers in a discharge has been reported [15] and amplification by  $\text{Ar}_2^*$  has been observed [16]. However, so far these results have not been reproduced by other scientific groups. The difficulty consists primarily in the high requirements imposed on the specific pump power. The matter is that the temperature increase to several tenths of an electron-volt leads to the quenching of lasing due to the increase of absorption in photoassociation reactions (for more details, see [4, 6, 8]). As for the ordinary discharge, for a high energy input it overheats the gas. There are grounds to believe that the pumping of rare-gas dimers can be achieved by using the recently realised (see [17-20]) volume nanosecond discharges with a subnanosecond rise time.

In Penning plasma lasers, an inverted population occurs in recombining plasma due to depopulation of the lower level by Penning reactions [1, 3, 6, 21]. Such lasers with neon mixtures are implemented for both beam pumping and pumping in discharge afterglow [6, 21]. In [22-25] Penning neon lasers were excited in the transverse discharge. The possibility of pumping the Penning  $\text{Ne-H}_2$  laser by a multiplication wave was proposed in [26]. The conditions of Penning plasma laser with pumping by a transverse discharge in the cylinder-knife electrode system [27, 28] are examined.

In the present overview the concept of background-electron multiplication wave<sup>1</sup> (BEMW) is described. It is shown that BEMW pumping of a Penning plasma laser at the wavelength  $\lambda = 585.3$  nm  $\text{Ne-H}_2$  mixture [27, 28] in the BEMW afterglow is realized. Then the feasibility of pumping  $\text{Xe}_2^*$  laser by BEMW is discussed. Finally, the excilamp pumping by BEMW is analysed.

## 2. BACKGROUND-ELECTRON MULTIPLICATION WAVE

In [17, 19, 29-38] attention was drawn to the fact that the ionisation in a gas at about the atmospheric pressure can propagate due to multiplication of the existing electrons with a low background density instead of the transfer of electrons or photons. Simply stated, the difference in electron multiplication times at different points in space, which arises from the nonuniformity of the field intensity magnitude, may give rise to the motion of ionisation front not related directly to electron transfer. The preliminary background ionisation may be provided by a small number of runaway electrons as well as by the natural background of radioactivity and cosmic radiation. The background formation is comprehensively discussed in [30].

Such a BEMW [19, 29-32, 36-40] arises at conducting irregularities, for instance, near a conducting surface with small radius of curvature, where an electric field is concentrated. Its front travels in the direction opposite to the gradient of the electric intensity modulus and its speed is proportional to the gas density. In this case, the direction of BEMW propagation is independent of the direction of the electric field. This allowed abandoning the photon hypothesis of streamer formation [41-43] and making an assumption that both anode- and

<sup>1</sup> We use the term 'multiplication wave' to distinguish this process from the commonly considered ionisation wave caused by transfer processes (electron drift and electron heat transfer).

cathode-directed streamers are a multiplication wave [29, 30], the streamer arising from the instability of the multiplication wave front [31].

The BEMW is important to understand many problems of gas discharge physics. For example, the generation mechanism of high-power subnanosecond beams in atmospheric-pressure gases under optimal conditions can be understood namely in the model of BEMW propagation in a dense gas [17, 44-49]. As indicated by experiments, when the rise time of the high-voltage pulse (of the order of one hundred kilovolts) is short enough (ranges into the subnanoseconds), the multiplication wave produces volume ionisation and the streamer has no time to develop. Fast prepulse electrons perform background ionization of gas and prepare BEMW propagation. The beam generation takes place when the multiplication wave approaches the anode and the nonlocal runaway-electron criterion is fulfilled [17, 19, 33-35]. The existence of volume preionization by fast (including runaway) electrons is confirmed by observation of X-rays from the gas-filled volume [50, 51]. A theoretical analysis was performed in [52].

It was also shown that the spatial distribution of the plasma glow between a plane electrode and a spherical (as well as pointed) one occupied a substantial volume for a subnanosecond rise time of the high-voltage pulse [53, 50]. In this case, the geometry of glow regions is nearly the same on changing the sign of the supplied voltage, i.e. is independent of electrode polarity, which may only be attributed to the existence of the multiplication wave, which is independent of the sense of the field.

*Capacitive current.* The BEMW discharge has one more distinctive feature. Even before the voltage reaches a maximum, the discharge current is detected with a very short delay (fractions of a nanosecond) with respect to the time of high voltage applying to the gap [6, 17, 27, 28, 34]. Usually, when a sharp-edge voltage pulse is applied, there is an overvoltage peak even if external preionization is used; only then a current arises and the voltage decreases.

The point is that the gas-discharge gap capacitance changes when the multiplication wavefront moves, which causes a change in the electrode charge. Indeed, if plane capacitor plates being initially at a distance  $d$  are under a voltage  $U$  and approach each other with a velocity  $u_{\text{fr}}$ , the current density on them is given by

$$j = \frac{d}{dt} \left( \frac{U}{2\pi(d - u_{\text{fr}}t)} \right) = \frac{j_0}{(1 - t/\tau_{\text{fr}})^2}, \quad j_0 = U/(2\pi d \tau_{\text{fr}}), \quad \tau_{\text{fr}} = d/u_{\text{fr}} \quad (1)$$

As an example, setting  $U = 100$  kV,  $d = 1$  cm, and  $\tau_{\text{fr}} = 1$  ns, we have  $j_0 = 18$  A/cm. This is in qualitative agreement with measurements.

Note that the above conception of volume-discharge and high-current electron-beam production in a dense gas [17, 33, 34] was called into question in [54], where it was stated that the theory is incorrect from all aspects and all the experiments are doubtful. However, in [55, 56] it was shown that the key critical concepts of [54] are erroneous.

Experimental aspects of BEMW realizations outlined in [19, 20, 47, 49]. Thus, the volume discharges on the basis of background-electron multiplication wave at about an atmospheric pressure have been realised. There is good reason to consider the prospect of using them for pumping lasers and high-pressure lamps.

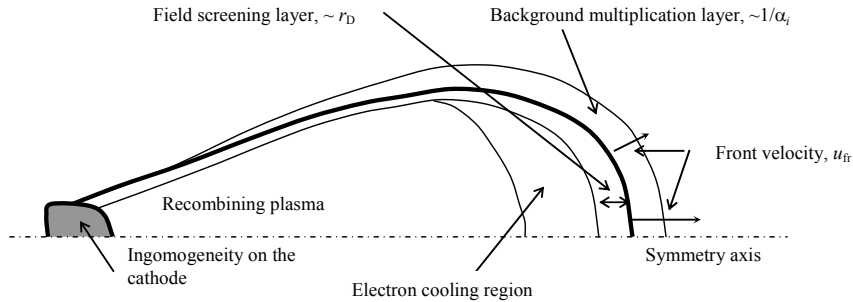


Figure 1. Qualitative view of the discharge based on the background multiplication wave.

### 3. MULTIPLICATION WAVE AND PLASMA LASERS

There are many discharge types: glow, arc, corona, spark discharges, etc. A wealth of papers, reviews, and books are devoted to them [41, 57-60]. However, a pulsed discharge, which is underlain by the BEMW in a nonuniform field, until now has not been considered as a separate form of discharge. At the same time, it possesses several distinguishing features [20, 61].

It turns out that the BEMW is also interesting in relation to the problems of active media excitation. BEMW-based discharges result in the formation of intensely recombining plasma. In recent studies [18-20, 26-28, 36, 37], some specific features of discharges with BEMW were considered. It was shown that plasma formed in afterglow of such discharges is overcooled in the degree of ionisation and promising to obtain lasing on transitions on which lasing in a dense gas was previously achieved with electron-beam pumping and in pulsed discharge afterglow [1-3, 5, 6, 8, 21] (i.e., in recombination-nonequilibrium plasma of plasma lasers). In particular, such plasma is promising also for pumping lasers and lamps with high specific power of radiation.

In BEMW discharge, kinetic processes take place in the following way. Electrons are overheated at the front of multiplication wave. They accelerate in the electric field and ionise the gas. The plasma screens the field behind the multiplication wave front, with the effect that the field-induced heating of electrons is sharply decreased. Electrons begin to cool down due to collisions with gas atoms (Figure 1). Since the degree of ionisation is not high for a high gas density, the electrons are cooled down to a low temperature limited only by recombination heating. In many respects the situation is similar to that which takes place when a dense gas is pumped by a pulsed electron beam. These questions are considered in sufficient detail in the theory of plasma lasers [1-3, 5, 6, 8, 21].

The electron density  $N_e$  behind the multiplication wave can be estimated from the expression

$$E = 2\pi e r_D N_e,$$

where  $E$  is the electric field intensity;  $r_D = (T_e/4\pi e^2 N_e)^{1/2}$  is the Debye radius;  $e$  is the electron charge; and  $T_e$  is the electron temperature. For instance, for  $E \sim 10^5$  V/cm and  $T_e \sim 1$  eV we have  $N_e = E^2/(\pi T_e) \sim 2 \cdot 10^{16}$  cm<sup>-3</sup>. Close values result from calculations of the

multiplication wave propagation between a wire and a cylinder in the atmosphere of xenon [6, 17, 33, 34, 62], which were made on the basis of the diffusion-drift model for xenon elaborated in [63].

Note that producing a plasma of such density with the use of an electron-beam pump requires highly intense electron beams with a current density  $j \sim 100 \text{ kA/cm}^2$ . Lasing by  $\text{Xe}_2^*$  excimers was obtained even for  $j \sim 100 \text{ A/cm}^2$ .

Electrons are cooled due to inelastic and elastic collisions. The time taken to cool down to a temperature  $T_e \sim 0.1 \text{ eV}$  in a helium atmosphere is equal to  $\sim 3 \text{ ns}$  and in the xenon atmosphere to  $\sim 80 \text{ ns}$  (for more details, see below the results of calculations). When employing xenon as the active laser medium it is therefore expedient to add helium in order to speed up the cooling and intensify recombination. However, the main reason for the proposed dilution of xenon by helium is that a uniform discharge in xenon is more difficult to realise.

The dimensions of the overcooled plasma region are controlled by the velocity of the multiplication wave. According to calculations by analytical formulas proposed in [29, 30], to simulations in the framework of the diffusion-drift model [6, 17, 33, 34, 62], and experimental data [6, 17], for a voltage of  $\sim 100 \text{ kV}$  the multiplication wave traverses a distance  $d \sim 1 \text{ cm}$  in less than 1 ns [38]. Therefore, one would expect a transverse dimension of the active medium of about 1 cm.

From the aforesaid it follows that the afterglow plasma of background-electron multiplication wave holds promise for obtaining lasing by those transitions which were observed to lase in a dense gas pumped by an electron beam and in the afterglow of a pulsed discharge [6]:

- by transitions of atomic xenon (this was realised in [64]);
- by transitions of atomic neon in Penning mixtures with hydrogen (this was realised in [27, 28]) and argon;
- by transitions of metal ions (cadmium, zinc, strontium, calcium) mixed with dense rare gases;
- by transitions of exciplex molecules ( $\text{KrF}$ ,  $\text{XeCl}$ , etc.);
- by transitions of rare-gas dimers ( $\text{Xe}_2$ ,  $\text{Kr}_2$ ,  $\text{Ar}_2$ ).

Note at the same time that gas-discharge lasers operating on the gas-plasma transition (i.e. in ionisation-non-equilibrium plasma, in particular, self-terminating lasers), in contrast to plasma lasers operating on the plasma-gas transition (i.e. in recombination-nonequilibrium plasma, see [1-3, 5, 6, 8, 21] for more details), are less promising for pumping by the discharge based on the multiplication wave. This is also indirectly confirmed by experimental results. In [64], the plasma laser on xenon transitions in BEMW discharge afterglow was initiated. However, an attempt to initiate the nitrogen laser using the discharge with multiplication was unsuccessful [64].

#### **4. LAMPS WITH VOLUME BEMW DISCHARGE EXCITATION**

The BEMW is associated with the development of efficient excilamps based on exciplex molecule radiation [65-67]. As is known, large efficiencies (over 50%) are achieved in  $\text{Xe}_2^*$

lamps based on barrier discharges on cathodes with small radius of curvature (e.g., shaped as wires) [68]; currently, such lamps are actively studied [65-72]. Simulation of such excilamps [63, 73, 74] allows the conclusion that volume ionization in them occurs exactly due to BEMW. Only after BEMW passing from a wire to the dielectric barrier, the discharge gap is shorted and quasi-steady charge accumulation on the barrier occurs [37, 63].

In these lamps, a rather long pump pulse duration ( $\sim 1 \mu\text{s}$ ) and not too high electrode voltage ( $\sim 2\text{-}5 \text{ kV}$ ) are used; therefore, they operate at not too high pressures,  $p = 100\text{-}200 \text{ Torr}$ . To develop excilamps with high specific power and to achieve lasing, it is reasonable to use shorter and higher-voltage pulses at about atmospheric and higher pressures.

## 5. PENNING PLASMA LASER AT THE WAVELENGTH $\lambda = 585.3 \text{ nm}$ IN A NE-H<sub>2</sub> MIXTURE

### 5.1. Laser Design and Measurement Techniques

The experiments were performed [27, 28] using a laser excited by a transverse discharge with a simple system of preionization from spark gaps, whose design is close to that described in [75]. The setup allowed space discharge formation in various gas mixtures at elevated pressures. The laser scheme is shown in Figure 2. The pump generator included main and auxiliary circuits. The main circuit was formed by the capacitive storage  $C_0$ , inductance  $L_0$ , and spark gap  $SW_0$ . The auxiliary circuit was intended for preliminary forward pumping of SOS diodes  $D$  and included the capacitor  $C_{Dr}$ , spark switch  $SW_{Dr}$ , and inductance  $L_{Dr}$ . Ten SOS-50-2 diodes were used in the laser, which were connected in parallel to peaking capacitors  $C_1$ . The discharge gap was preionized by radiation of spark gaps placed on both sides from the anode, which were actuated during pulsed charging of peaking capacitors  $C_1$ .

The generator could operate in the mode with inductive energy storage or as an ordinary capacitive generator. In the latter case, the capacitor  $C_{Dr}$  was not used. The discharge current duration under various operating conditions of the generator was 150-250 ns.

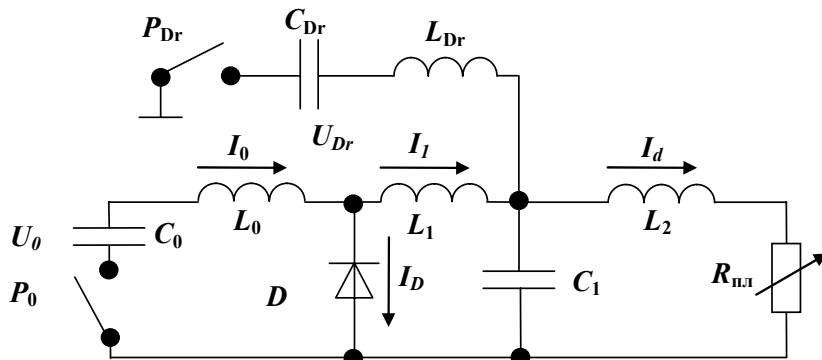


Figure 2. Schematic diagram of the experimental setup:  $SW_0$  and  $SW_{Dr}$  are spark gaps,  $C_0 = 70 \text{ nF}$  is the primary capacitive storage,  $C_1 = 3.6 \text{ nF}$  are peaking capacitors,  $C_{Dr} = 10 \text{ nF}$  is the capacitor for forward pumping of SOS diodes  $D$ ,  $L_0 = 24.5 \text{ nH}$ ,  $L_1 = 2 \text{ nH}$ ,  $L_2 = 11 \text{ nH}$ ,  $L_{Drf} = 3.13 \mu\text{H}$  are circuit inductances,  $U_0$  and  $U_{Dr}$  are charging voltages,  $I_0$ ,  $I_1$ ,  $I_d$  are circuit currents, and  $R_d$  is the discharge resistance.

Cylindrical and knife stainless steel electrodes were used in the laser. The interelectrode gap thickness is  $d = 2.5$  cm, the laser active volume is  $2.5 \times 0.3 \times 72 = 50$  cm<sup>3</sup>. Discharge and lasing characteristics were studied in pure neon and Ne-H<sub>2</sub> mixtures at a mixture pressure up to 0.5 atm.

A plane aluminum mirror was used as a rear mirror. Mirrors with a dielectric coating with the reflectance  $R = 75\%$  or  $95\%$  at  $\lambda = 585$  nm or a quartz plate were placed at the cavity output.

The pulse shape and radiant energy were measured in the far-field region by an FEK-22SP vacuum photodiode. The discharge emission spectrum was measured using a StellarNet EPP2000-C25 spectrometer with a spectral resolution of 0.75 nm and a response function halfwidth of 1.5 nm. To provide the photodiode and spectrograph operation in the linear mode, radiation at their input was attenuated using a sequence of metal grids with known attenuation factors.

In the experiments, the current  $I_d$  through the discharge gap, the discharge current  $I_0$  of the capacitive storage, the current  $I_D$  through SOS diodes, and the laser electrode voltage  $U_d$  were measured. Electrical signals were measured by TDS-220 or TDS-224 digital oscilloscopes.

## 5.2. Experimental Results and Discussion

In the Ne-H<sub>2</sub> mixture, a single line with a wavelength of 585 nm was detected in the lasing spectrum. In pure neon, lasing on the green line ( $\lambda = 540$  nm) was observed. This line appeared after a voltage drop on the laser gap only at a low discharge voltage,  $U_0 \leq 23$  kV, and was localized farther from the knife electrode in discharge regions where the current density decreases. As the discharge voltage increased, the discharge current increased and lasing on  $\lambda = 540$  nm discontinued.

The maximum energies and powers were achieved at neon and hydrogen pressures of  $\sim 150$  and 15-21 Torr, respectively. As the hydrogen pressure increased to  $\sim 40$  Torr, the lasing threshold was not reached at neon admixtures from 10 to 350 Torr. The laser beam aperture was usually  $25 \times 3$  mm<sup>2</sup>. The radiation power distribution over the spot was nonuniform. The radiation power increased in the region with a maximum current density near the knife electrode. In the gap formed by two cylindrical electrodes (the discharge aperture is  $40 \times 20$  mm<sup>2</sup>), lasing was not achieved. The main experiments were performed in a mixture of Ne:H<sub>2</sub> = 165:21 Torr.

The use of the inductive storage instead of the capacitive storage allowed to increase the pulse radiation energy. The maximum lasing energy reached 50  $\mu$ J. The radiation energy also increased with the energy fraction transferred to the discharge circuit inductance of capacitor  $C_0$ , which was controlled by the charging voltage of capacitor  $C_{Dr}$  (see Figure 2).

Figure 3 shows the oscillograms of voltage pulses on the laser gap, discharge current, and lasing pulses under optimal conditions of excitation from generators with capacitive (a) and inductive (b) energy storages. The first voltage peak on the laser gap corresponds to exposure actuation, the discharge is formed at the instant of the second voltage maximum. In both cases, the laser pulse appears at the discharge current pulse end and consists of an intense peak with a duration of  $\sim 100$  ns and a low-intensity tail lasting for 300 ns after the end of pumping. The inductive generator substantially increases the breakdown voltage of the laser

gap and the discharge current rise rate, but reduces the pump pulse duration, which is especially pronounced as charging voltages of capacitors  $C_0$  and  $C_{Dr}$  increase. These factors can improve discharge ignition conditions in the gap with a sharply nonuniform electric field, which results in an increase in the laser beam energy (power) when using the generator with inductive energy storage.

The maximum radiation power of laser beam pulses was achieved using a quartz plate as output mirrors. At a maximum discharge voltage  $U_0 = 36$  kV, the radiation power reached 1.1 kW. An increase in the output mirror reflectance to 75% decreases the peak radiation power by about half; however, the radiation pulse duration significantly increased. Due to this, the radiation pulse energy slightly increased.

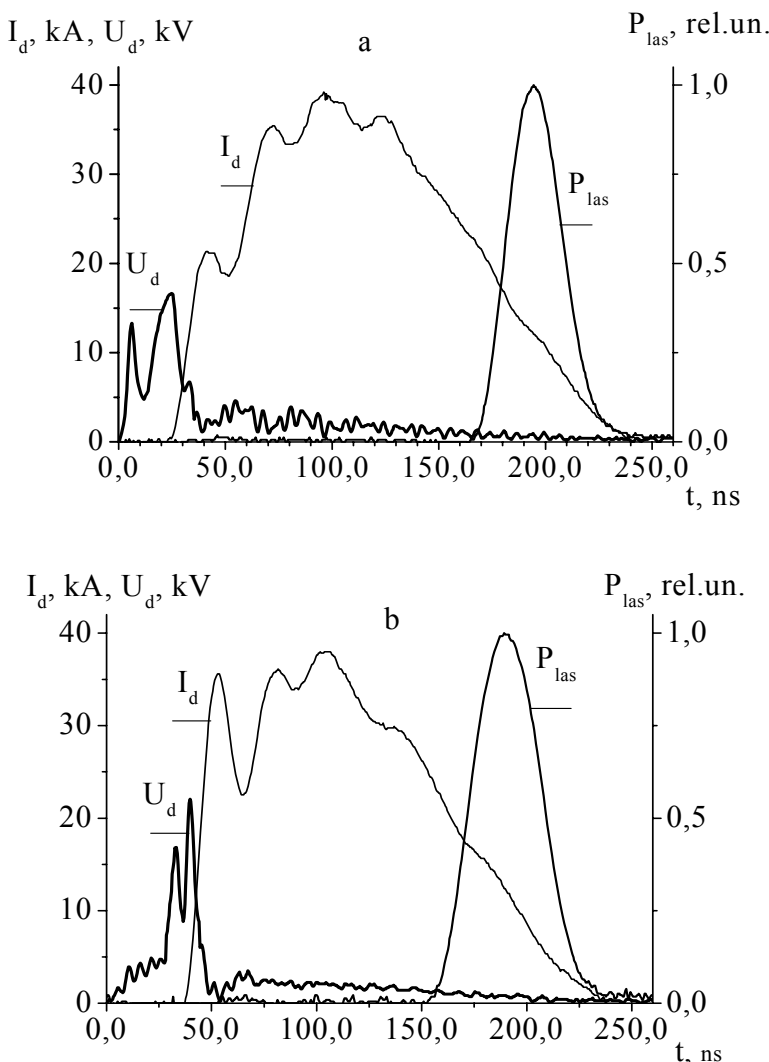


Figure 3. Oscillograms of the voltage at the laser gap, the discharge current, and the temporal shape of the laser pulse for pumping from capacitive (a) and inductive (b) energy storages. The mixture is Ne:H<sub>2</sub> = 11:1 at a pressure of 180 Torr,  $U_1 = 20$  kV,  $U_0 = 33$  kV. A quartz plate is used as the output mirror.

### 5.3. Kinetic Model

In the calculation [27, 28], the kinetic model of the Penning neon plasma laser [76, 77] was used. The model of the neon laser for a He-Ne-Ar-H<sub>2</sub>-N<sub>2</sub> mixture considers ~ 300 plasma-chemical reactions. It includes the following excited atoms, molecules: He<sup>\*</sup>, Ne<sup>\*\*</sup>, Ar<sup>\*</sup>, Ar<sup>\*\*</sup>, Ne<sup>\*\*</sup>, Ne<sup>\*</sup>, He<sup>\*</sup>, HeNe<sup>\*</sup>, Ar<sup>\*</sup>, and ions: He<sup>+</sup>, Ne<sup>+</sup>, Ar<sup>+</sup>, He<sup>+</sup>, Ne<sup>+</sup>, Ar<sup>+</sup>, He<sup>+</sup>, Ne<sup>+</sup>, Ar<sup>+</sup>, HeNe<sup>+</sup>. Four groups of neon states, (3s, 3s'), (3p, 3p'), (4s), (5s), and two separate states, 3p'[1/2]<sub>0</sub> and 3s'[1/2]<sub>1</sub> [76, 77], were included to the neon atom kinetics. Simultaneously with the balance equations of the number of particles, the equations for gas  $T$  and electron  $T_e$  temperatures are considered. When considering the balance of the number of particles and the heat balance, ionization events and events of excitation by beam electrons, triple and dissociative recombination processes, two- and three-particle conversion reactions, Penning and charge exchange reactions, ionization and transitions between excited states during collisions with plasma electrons, spontaneous radiative transitions, and others was considered. In the calculation, the He and Ar component concentrations were set to zero, the effect of N<sub>2</sub> impurity was also neglected. The possibility of lasing on the transition with wavelength  $\lambda = 585.3$  nm was examined. When determining the linewidth, the Doppler broadening and broadening by intrinsic and buffer gases were considered. Non-resonant absorption of operating radiation, caused by photoionization and photodissociation of mixture particles, was taken into account. The calculation was performed in approach of the effective photon lifetime in the cavity (zero-dimensional approach of radiation propagation in the cavity). In this approximation, it is assumed that the radiation intensity is uniform over the cavity volume, i.e., the photon concentration is uniform.

To self-consistently solve unsteady equations for concentrations of various reagents, the balance equation for gas and electron temperatures, and the radiation intensity, the PLASER programm package was used [2, 3, 5, 7-9].

### 5.4. Stage Preceding Lasing

#### 5.4.1. *Background electron formation*

An external voltage applied to the discharge gap results in background electron generation during passage of fast electrons. According to [44, 78], the energy of fast electrons formed in the discharge gap is approximately  $E_e = (2/3) eU$ , where  $U$  is the discharge gap voltage; the fraction of these electrons relative to their total number is approximately  $\eta = 15\text{-}20\%$ . Electrodes (73 cm long each) were a knife blade and a cylinder 4 cm in radius. Hence, the transverse discharge size near the cylindrical electrode is approximately 2 cm. The discharge current near the anode to the end of the background electron generation stage is  $I = 15$  kA (Figure 3(a)). Hence, the electron current density is

$$j = \frac{I}{S} \approx 100 \text{ A/cm}^2 \quad (2)$$

the electron current density of fast electrons is

$$j_b = \frac{\eta I}{S} \approx 20 \text{ A/cm}^2$$

ionization frequency (see [2, 3, 5, 7-9] for more details),

$$v = \frac{2\sigma(E)}{e} j \quad (3)$$

where  $\sigma$  is the ionization cross section,  $j$  is the beam current density, and  $e$  is the electron charge. The ionization frequency corresponding to this current density  $j_b$  at  $U \approx 15$  kV (Figure 3(b),  $E_e \approx 10$  keV) is  $10^4 \text{ sec}^{-1}$ . At such a frequency, an electron density of the order of  $10^{13} \text{ cm}^{-3}$  is formed for the time of fast electron passage through the discharge gap (less than 1 ns) (Figure 4).

Let us estimate what current can be passed through plasma with electron density  $n_e \approx 10^{13} \text{ cm}^{-3}$ . For the electric field strength  $U/d \approx 40 \text{ V/(cm Torr)}$ , we obtain

$$j = eu_d n_e = 86 \text{ A/cm}^2,$$

where the drift velocity ( $u_d = 5.38 \cdot 10^7 \text{ cm/sec}$ ) was taken from [78, 79], which is in good agreement with (2).

Thus, if  $U \approx 15$  kV is applied to the discharge gap, after its passage by fast electrons, an approximate background density of secondary electrons  $n_e \approx 10^{13} \text{ cm}^{-3}$  is formed.

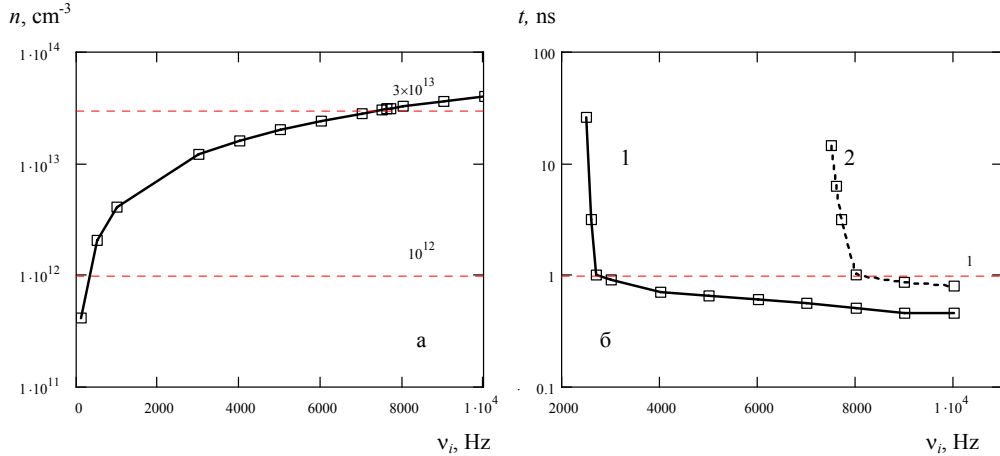


Figure 4. Calculated dependencies of (a) the maximum density of electrons generated due to the ionization frequency and (b) the time of electron density leveling at (1)  $10^{13}$  and (2)  $3 \cdot 10^{13} \text{ cm}^{-3}$ . The half-maximum duration of the ionization frequency action is 1 ns. The mixture pressure is 150 Torr, Ne:H<sub>2</sub> = 5:1.

### 5.4.2. Discharge gap voltage after background electron formation

After passage of fast electrons, the discharge gap resistivity can be estimated as

$$\rho = \frac{mv}{e^2 n_e}$$

where  $v = v_a + v_c$ .

Here the frequency electron-atom collisions is given by

$$v_a = [Ne]v\sigma = [Ne]\sqrt{\frac{3T_e}{m}}\sigma$$

where  $\sigma$  is the transport cross section of elastic electron scattering on the neon atom (it depends weakly on temperature in the low energy region and is approximately equal  $1.5 \cdot 10^{-16} \text{ cm}^2$  [80]), and the Coulomb collision frequency is given by

$$v_c = \frac{4\sqrt{3}\pi e^4 \ln(\Lambda) n_e}{9\sqrt{m T_e^3}}$$

where  $\ln(\Lambda)$  is the Coulomb logarithm ( $\approx 10$ );  $m$  and  $T_e$  are the electron mass and temperature, respectively. Under given conditions,  $[Ne] = 6.4 \cdot 10^{18} \text{ cm}^{-3}$  (the neon pressure is  $\sim 150$  Torr),  $n_e \approx 10^{13} \text{ cm}^{-3}$ ,  $T_e \approx 1 \text{ eV}$ , and the electron-atom collision frequency exceeds the Coulomb collision frequency by more than two orders of magnitude. The plasma resistivity is approximately  $\rho \approx 25 \Omega \text{ cm}$  and the discharge gap voltage decreases to

$$V \approx dE = d\rho j \approx 3-6 \text{ kV}$$

(at  $j = 100-200 \text{ A/cm}^2$ , see Figure 3(a)) according to experimental data.

### 5.4.3. Time of multiplication wave passage through the discharge gap

The problem of the time of multiplication wave passage through the discharge gap (about 2 cm long) in He, Xe, and nitrogen was considered in [40]. Propagation in neon was modeled in [81]. Results for Ne lies in the range between the data for He and Xe. For fields  $E = 7 \text{ V/(cm Torr)}$ , the time of passage should be  $\sim 100 \text{ ns}$ , which is in good agreement (see below) with experimental data (Figure 3(a)).

### 5.4.4. Multiplication wave formation

The electron density  $n_e$  behind the multiplication wave can be estimated from the expression  $E = 2\pi e r_D n_e$ , where  $E$  is the field strength,  $r_D = (T_e/4\pi e^2 n_e)^{1/2}$  is the Debye length, and  $T_e$  is the electron temperature.

For example, under given conditions (at  $E \sim 2-2.5 \text{ kV/cm}$  and  $T_e \sim 0.2-1 \text{ eV}$ ), we have  $n_e = E^2/(\pi T_e) \sim (6.4-1.3) \cdot 10^{13} \text{ cm}^{-3}$ .

## 5.5. Lasing Modeling

Lasing was modeled in two ways. In one case, the initial electron density was taken as  $n_e = 3 \cdot 10^{13} \text{ cm}^{-3}$ . At such electron density, the external field is completely screened, and recombination-nonequilibrium plasma is generated behind the multiplication wave front (see Sec. 5.4.4). In another case, the above electron density is provided by setting the external ionization frequency.

Note that recombination-nonequilibrium plasma formation due to medium excitation by a hard ionizer, e.g., the electron (or ion) beam, is well described by setting the ionization frequency (3). The energy deposition into a corresponding gas component is given by

$$W = E_p v N, \quad (4)$$

where  $E_p$  is the energy expended for electron-ion pair production ( $E_p = 36 \text{ eV}$  for neon) and  $N$  is the density of ionized atoms.

In this case, setting the ionization frequency only models a required electron density ( $n_e = 3 \cdot 10^{13} \text{ cm}^{-3}$ ). In order that modeling results could not affect afterglow of recombination-nonequilibrium plasma, the exposure time was taken small (fractions of nanosecond).

Thus, the initial electron density  $n_e = 3 \cdot 10^{13} \text{ cm}^{-3}$  was modeled in two ways. In the first case, the initial electron density was set as a parameter, the ionization frequency was set to zero. In the second case, the initial electron density arose due to the fictitious ionization frequency action for fractions of a nanosecond.

The time dependencies of the power, energy, and emission efficiency were obtained. The results obtained by two methods, i.e., pumping by an ultrashort beam and setting the initial electron density as a parameter, were compared. In both cases, similar delays of the lasing pulse of the order of 100 ns (Figure 5) were obtained. According to experimental data (Figure 3(a)), lasing begins with a delay of  $\sim 100$  ns after medium breakdown. According to the theoretical treatment, lasing is performed as follows. Each region behind the multiplication wave front begins lasing with a delay of 100 ns. The multiplication wave also moves to the anode about 100 ns. Thus, the lasing pulse beginning and end correspond to emitting regions near the cathode and anode, respectively.

Lasing experiments were performed depending on the mixture pressure at an optimum (from the view point of output energy) ratio of components  $\text{Ne:H}_2 = 5:1$ . Calculation at the same ratio showed that the radiation power and energy optima correspond to hydrogen pressures of  $\sim 40$  and 25 Torr, respectively (Figure 6). The lasing power was also measured at a hydrogen pressure of 20 Torr as a function of the neon pressure in the mixture. The calculated optimum hydrogen pressure is in good agreement with the experimental value (Figure 7).

According to experimental data, the active medium volume was  $2.5 \times 0.3 \times 72 = 50 \text{ cm}^3$ . This volume corresponds to the calculated maximum emitted energy  $E_l \approx 25 \mu\text{J}$  (at a hydrogen pressure  $p_{\text{H}_2} \approx 25$  Torr). It is in good agreement with experimental data (maximum emitted energy  $E_l \approx 50 \mu\text{J}$  at  $p_{\text{H}_2} \approx 20$  Torr).

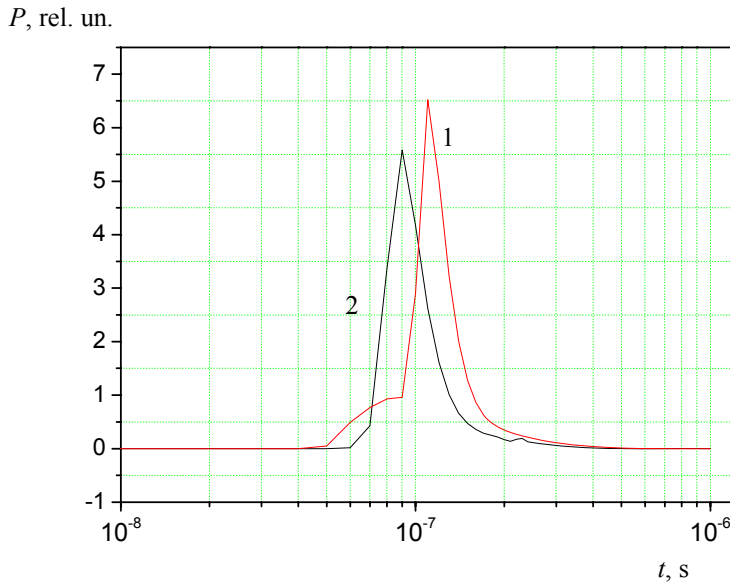


Figure 5. Comparison of two calculation methods: (1) parametric setting of the initial electron density and (2) pumping by an ultrashort electron beam (the half-maximum width is  $\sim 0.1$  ns). The pressure of mixture components is  $p_{\text{Ne}} = 100$  Torr and  $p_{\text{H}_2} = 20$  Torr. The output mirror reflectance is  $R = 75\%$ . The initial electron density is  $n_e = 3 \cdot 10^{13} \text{ cm}^{-3}$ .

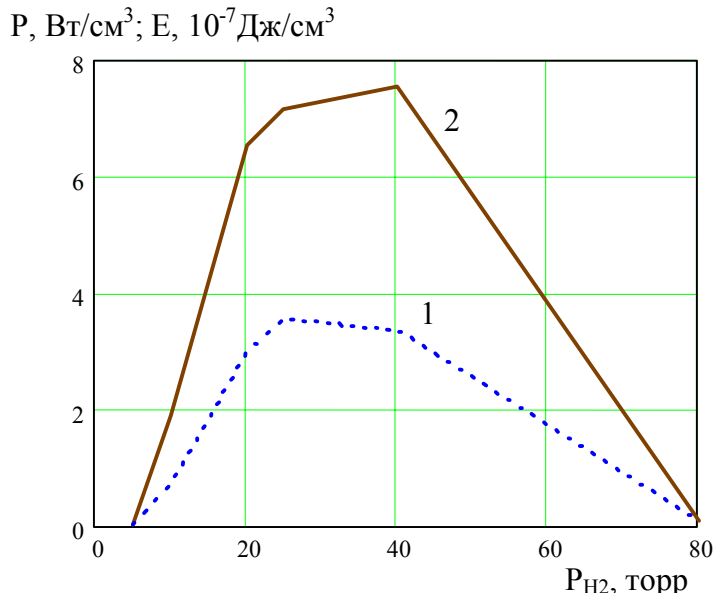


Figure 6. Dependencies of the specific radiation energy (1) and maximum power (2) on the hydrogen pressure. The component ratio is  $\text{Ne:H}_2 = 5:1$ . The output mirror reflectance is  $R = 75\%$ . The initial electron density is  $3 \cdot 10^{13} \text{ cm}^{-3}$ .

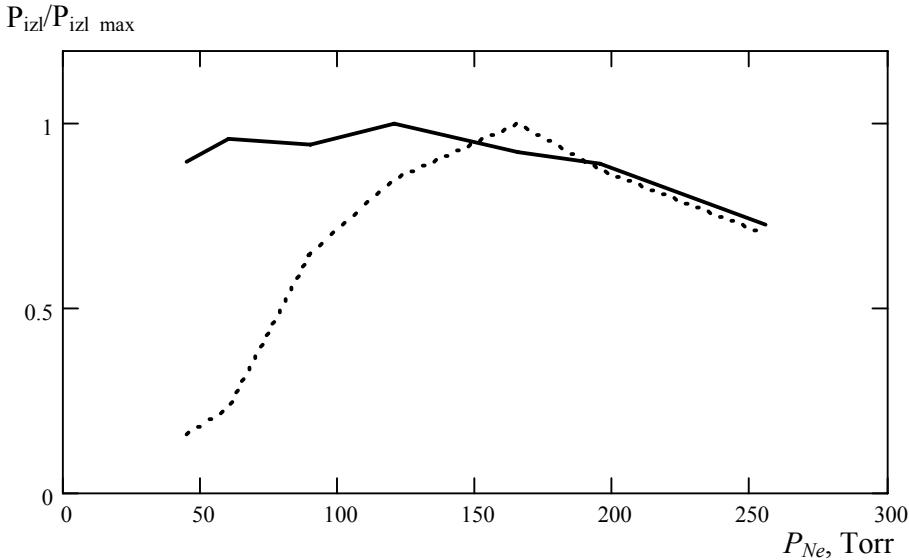


Figure 7. Comparison with experimental data. The dependence of the lasing power on the neon pressure. The hydrogen partial pressure is constant,  $p_{H_2} = 20$  Torr. The dashed and solid curves correspond to the experiment and calculation, respectively.

## 5.6. Some Comments

Note that another interpretation of Figure 3(a) is formally possible. For example, medium breakdown and/or multiplication wave passage correspond to the first stage (a high voltage of  $\sim 15$  kV on the gap), after which a mode similar to the glow discharge mode is reached (a gap voltage decreased to 3-6 kV). The lasing modeling data contradict such an interpretation. At an electric field strength of  $\sim 6\text{-}7$  kV/cm (high voltage stage), the electron density behind the multiplication wave front should exceed  $10^{14}$  cm $^{-3}$ . For initial condition corresponding to electron densities of  $10^{14}\text{-}10^{16}$  cm $^{-3}$ , the lasing pulse develops almost without delay (more precisely, there are two lasing pulses in calculation, the first of which develops almost without delay). Moreover, the passage of the multiplication wave itself at such high electric field strengths, according to [40, 81], should take a time of about 10 ns. Thus, the lasing pulse under these conditions cannot have a characteristic delay of the order of 100 ns as it is in the experiment.

If we interpret the stage with lowered voltage as a stage equivalent to the glow discharge, discharge modeling (see the modeling method description in [7, 8]) with a field strength of about 0.2-2 kV/cm shows that total gas ionization occurs for times shorter than 20 ns. Certainly, total ionization will not actually occur; the field will be earlier superseded from such a discharge region. This also suggests that this stage cannot be considered as a stage similar to the glow discharge.

We note that the discharge was also ignited between two cylindrical electrodes; in this case, the analogy with the glow-type discharge would apparently be more reasonable. However, lasing did not occur in this case. It arose only when the discharge was ignited

between knife and cylindrical electrodes. This circumstance also counts in favor of the multiplication wave existence since its initiation is facilitated by sharp bumps.

The existence of capacitive current also argues in favor of the BEMW discharge. The point is that the discharge current, even before the voltage reaches a maximum, is detected with a very short delay (fractions of a nanosecond) with respect to the time of high voltage applying to the gap (Figure 3). In general, when applying a voltage pulse with a steep leading edge, an overvoltage peak arises even when using external preionization. Only then a current appears and voltage drops. The current development with a short delay can be explained by BEMW propagation. When the multiplication wave front moves, the gas-discharge gap capacitance changes, which causes a change in the electrode charge. Indeed, if planar capacitor plates are initially at distance  $d$  under voltage  $U$  and approach each other with velocity  $u_{fr}$ , the current density on them is given by (1).

As an example, setting  $U = 20$  kV,  $d = 2$  cm, and  $\tau_{fr} = 10$  ns, we have  $j_0 \approx 0.1$  A/cm<sup>2</sup>. It is in qualitative agreement with measurements. Here we present only the estimate for electrodes approaching in vacuum. In a gas medium, this leads to a field strength increase, which in turn can cause an increase in the actual current. For example, it is noted in [22] that the current pulse began at the leading edge of the voltage pulse.

## 6. Xe<sub>2</sub><sup>\*</sup> DIMER LASER

### 6.1. Simulations of Xe<sub>2</sub><sup>\*</sup> Afterglow

As noted above, estimates suggest that a relatively high electron density should be produced after passage of a multiplication wave through the gas. In this case, simulations may be performed by either specifying the required initial electron density or modelling an external hard ionisation source which affords the requisite electron density in a short time (see Sec. 5.6.). The latter approach has been adopted in this study, i.e. the initial electron density is provided by an imaginary electron beam.

We considered the afterglow of a xenon plasma with the initial electron density corresponding to the above estimates (see Sec. 3) for the discharge involving the background-electron multiplication wave. Use was made of the kinetic model of a xenon-helium mixture described in [82]<sup>2</sup>. An investigation was made of the regime whereby the amplified spontaneous emission exerted a weak effect on the population density of the Xe<sub>2</sub><sup>\*</sup> dimer levels. It was assumed that the initial electron density was produced by the pulse of an external electron beam. The beam action was characterised by the ionisation frequency (3). The frequencies for the beam excitation from the ground state were introduced in a similar way. In this case, the energy input to the corresponding gas component is given by the expression (4), where  $E_p = 22$  eV for xenon and 46 eV for helium. For simplicity, the time dependence of the ionisation frequency was assumed to be bell-shaped. The beam pump duration was taken to be short enough in comparison with the characteristic afterglow

---

<sup>2</sup> It is noteworthy that the Xe<sub>2</sub><sup>\*</sup> radiation in the afterglow of a discharge was also considered in a recent paper by Lo et al. [83].

development times. The current density was selected in such a way as to provide a specified electron density.

## 6.2. Kinetic Model

The kinetic equations for particle number balance included 17 components: ions and the excited states of atomic and molecular xenon and helium [18, 20, 61]. In addition, the thermal balance equations were considered for the electron and gas temperatures.

In the description of spontaneous emission we considered two states of the xenon dimer, i.e.,  $\text{Xe}_2(1)$  and  $\text{Xe}_2(2)$  (resonance  $\text{Xe}_2(^1\Sigma_u^+)$  and metastable  $\text{Xe}_2(^3\Sigma_u^+)$  states) were taken into account, which make contributions to the emission band under discussion. In this case, to calculate the specific powers of spontaneous emission, were used the expressions

$$Q_i = A_i \cdot [\text{Xe}_2(i)], \quad Q = Q_1 + Q_2,$$

where  $A_1 = 1.82 \cdot 10^8 \text{ s}^{-1}$ ,  $A_2 = 10^7 \text{ s}^{-1}$  are the spontaneous decay rates;  $[\text{Xe}_2(\dots)]$  are the population densities of the corresponding dimers. The efficiency  $\eta$  of conversion of the energy inputted into the medium to spontaneous radiation was defined as

$$\eta = \frac{\int_0^\infty Q dt}{\int_0^\infty W dt}$$

In present model, advantage was taken of the plasma chemical reaction rate coefficients which had earlier been employed in the simulation of  $\text{XeCl}$  [84, 85] and  $\text{XeF}$  laser [86] kinetics, the Kr-Xe binary mixture kinetics [87], as well as the kinetics of the third continua of xenon [88] (for more details, see [82]). The kinetic model of the Xe-He mixture took into account 132 reactions. The system of kinetic equations was formed and numerically solved with the use of PLASER code package [2, 3, 5, 7-9].

## 6.3. Results of $\text{Xe}_2^*$ Lasing Simulations

The calculated characteristics of Xe- and He-Xe- plasma afterglow are represented in Figures 8-10. The simulations were carried out for different gas pressures  $p$  for the same energy input ( $\sim 74 \text{ mJ cm}^{-3}$ ), the base duration of a discharge pulse was  $\sim 0.1 \text{ ns}$ . Under these conditions, the highest electron density was equal to  $\sim 2 \cdot 10^{16} \text{ cm}^{-3}$ .

One can see that gain in pure xenon arises only for  $p > 1 \text{ atm}$  (Figure 8a). With increasing pressure, the peak value of the gain rises (Figure 9), but the characteristic lifetime of the gain and the time to attainment of the peak gain ( $\sim 1-10 \text{ ns}$ ) shorten in this case. For  $p \approx 2 \text{ atm}$ , the gain is  $\sim 0.02 \text{ cm}^{-1}$ , which is sufficient for the onset of laser oscillation with an active medium of length  $\sim 15 \text{ cm}$ .

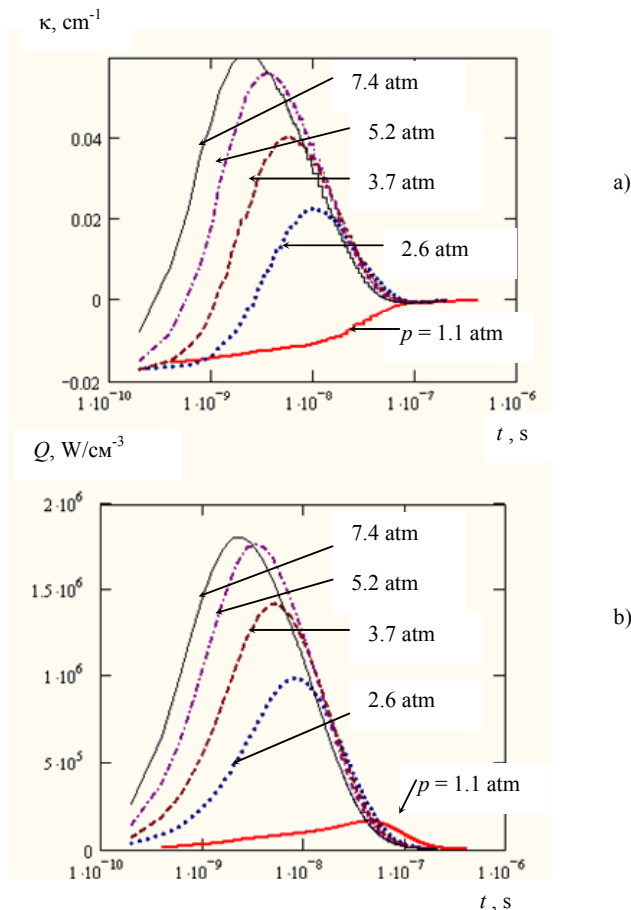


Figure 8. Time dependences of the gain  $\kappa$  (a) and the specific power of spontaneous emission  $Q$  (b) at the  $\lambda \approx 172\text{-nm}$   $\text{Xe}_2^*$  photodissociation transition for different pressures of pure xenon.

It has been known that lasing in pure xenon under beam pumping takes place for  $p > 13$  atm. The point is that a relatively long (50-100 ns) pump by a high-power electron beam is responsible for the heating of the active medium. This substantially strengthens absorption of laser radiation due to photoassociative transitions, which are the reverse of the laser transition. This issue was investigated in sufficient detail in [1-3, 5, 8]. It is possible to substantially lower the threshold pressure by taking advantage of a discharge with a subnanosecond rise time.

It goes without saying that the production of a volume discharge in a dense gas is an intricate task because of the demanding requirements on the steepness of the rise time of the voltage pulse. However, in [64, 89] reported that they managed to achieve this for a helium pressure below 6 atm and a nitrogen pressure below 3 atm. It has also been possible to produce a specific energy input of  $\sim 1 \text{ J cm}^{-3}$  in a time of 5 ns [17]. That is why the production of a volume nanosecond discharge for a xenon pressure of 2 atm and an energy input of  $\sim 0.1 \text{ J cm}^{-3}$  also appears to be a realistic task. To avoid energy input into the discharge upon the shorting of the electrodes, advantage can be taken of a dielectric barrier at the anode, as is done in excilamps (see below).

$\kappa_{\max}$ ,  $\text{cm}^{-1}$ ;  $\eta$ ;  $\tau_{\max}$ , ns

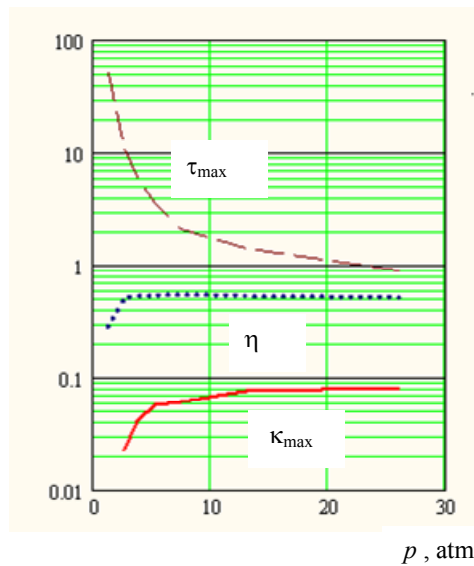


Figure 9. Peak gain  $\kappa_{\max}$ , efficiency  $\eta$  of inputted-energy conversion to spontaneous radiation, and time  $\tau_{\max}$  to attainment of the peak spontaneous emission power for the  $\lambda \approx 172\text{-nm}$   $\text{Xe}_2^*$  transition as functions of pure xenon pressure.

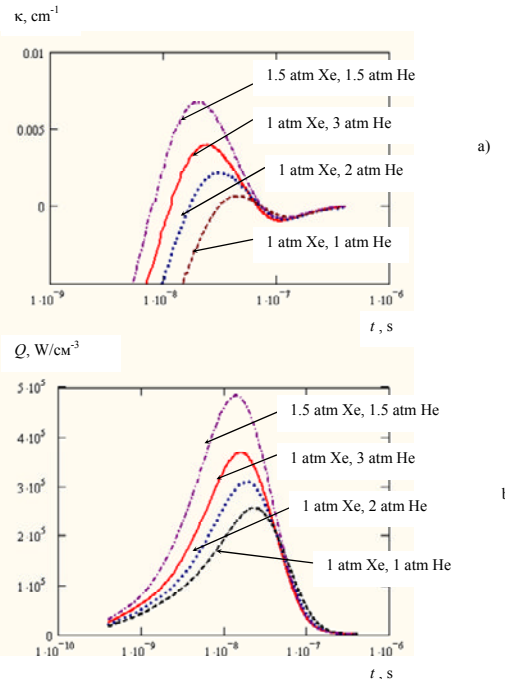


Figure 10. Time dependences of the gain  $\kappa$  (a) and the specific power of spontaneous emission  $Q$  (b) at the  $\lambda \approx 172\text{-nm}$   $\text{Xe}_2^*$  photodissociation transition for different pressures and compositions of xenon-helium mixtures.

To lower the working xenon pressure, it is expedient to employ helium as the buffer gas. Simulations show (Figure 10) that even the addition of 1 atm of helium to xenon at the same pressure gives rise to a positive gain. It is pertinent to note that the gains in pure xenon are higher than in xenon-helium mixtures for the same partial xenon pressures. However, in pure xenon it is more difficult to realise the volume discharge wave.

## 7. MEDIUM-PRESSURE LAMPS

### 7.1. Barrier Excilamps on Xenon Dimers

#### 7.1.1. *Simulation based on the diffusion-drift approximation*

The highest emission efficiency of xenon dimers was achieved in single-barrier excilamps with small-curvature-radius cathodes. The discharge in them is ignited between a thin cathode (a wire at the quartz tube center) and an anode placed on the tube outer surface. For this reason, the discharge formation processes in xenon at a pressure of 100-200 Torr were theoretically and experimentally studied in [63, 72-74]. Let us enlarge on the problems associated with simulation of BEMW propagation.

Plasma formation and electric field screening processes are described by the momentum transport and continuity equations for electrons and ions, as well as by the Poisson equation,

$$\begin{aligned} \mathbf{j}_e &= N_e \mathbf{u}_e = \mathbf{u}_{de}(\mathbf{E}, N) \cdot N_e - D_e(\mathbf{E}, N) \cdot \text{grad}(N_e); \\ \mathbf{j}_i &= N_i \mathbf{u}_i = \mathbf{u}_{di}(\mathbf{E}, N) \cdot N_i - D_i(\mathbf{E}, N) \cdot \text{grad}(N_i); \\ \partial N_e / \partial t + \text{div}(\mathbf{j}_e) &= v_i(\mathbf{E}, N) \cdot N_e - \beta \cdot N_e \cdot N_i; \\ \partial N_i / \partial t + \text{div}(\mathbf{j}_i) &= v_i(\mathbf{E}, N) \cdot N_i - \beta \cdot N_e \cdot N_i; \\ \text{div}(\mathbf{E}) &= 4\pi e(N_i - N_e). \end{aligned} \quad (5)$$

Here  $\mathbf{j}_e$  and  $\mathbf{j}_i$  are electron and ion fluxes,  $\mathbf{u}_e$  and  $\mathbf{u}_i$  are the average electron and ion velocities,  $\mathbf{u}_{de}$  and  $\mathbf{u}_{di}$  are the average electron and ion drift velocities in the external electric field  $\mathbf{E}$ ,  $D_e$  and  $D_i$  are the diffusivities,  $N_e$  and  $N_i$  are the electron and ion densities,  $N$  is the density of neutral xenon atoms, and  $v_i$  is the frequency of xenon atom ionization by electrons, and  $\beta$  is the ion and electron recombination rate.

In [63, 72-74], the cylindrical geometry was considered. The cathode is a cylindrical wire of radius  $r_0 = 0.5$  mm, being under potential  $U_0 \sim -(0.5-5)$  kV. The cathode is adjacent to a xenon-filled discharge gap ( $r_0 < r < r_{\text{bar}}$ ) behind which a dielectric barrier ( $r_{\text{bar}} < r < r_{\text{max}}$ ) is placed, which separates the anode of radius  $r_{\text{max}} \sim 1-2$  cm from the discharge gap.

The dependencies of  $v_i$ ,  $\mathbf{u}_{de}$ ,  $\mathbf{u}_{di}$ ,  $D_e$ , and  $D_i$  appearing on the right-hand sides of Eqs. (5) on the field strength  $\mathbf{E}$  were specified using the formulas obtained from the approximations given in [72, 73].

### 7.1.2. Boundary conditions

The boundary conditions for the set of equations (5) were specified at three points, i.e., on the wire, barrier, and anode (for the field),

$$\left. \frac{\partial N_i}{\partial r} \right|_{r=r_0} = 0, \quad j_e \Big|_{r=r_0} = -\gamma j_i \Big|_{r=r_0}, \quad \varphi \Big|_{r=r_0} = -U_0,$$

$$j_e \Big|_{r=r_{\text{bar}}} = j_i \Big|_{r=r_{\text{bar}}} = 0, \quad \varphi \Big|_{r=r_{\text{max}}} = 0.$$

where  $\gamma = 0.05$  is the secondary electron emission coefficient.

The initial conditions were taken in the form

$$N_e(r,t)|_{t=0} = N_i(r,t)|_{t=0} = N_0 = \text{const}; \quad (6)$$

$$E(r,t)|_{t=0} = E_0(r) = \frac{-U_0}{\ln(r_0/r_{\text{max}})} \cdot \frac{1}{r};$$

$$\varphi(r,t)|_{t=0} = \varphi_0(r) = -U_0 \cdot \frac{\ln(r/r_{\text{max}})}{\ln(r_0/r_{\text{max}})}.$$

These conditions correspond to a low initial charge density (residual from the previous pump pulse) having no effect on the field and potential distributions in the discharge gap.

This problem statement is limited by the fact that it is impossible to consider main types of discharge instability within the one-dimensional model. In particular, it is impossible to describe filament formation. We also note that the diffusion-drift approximation not quite adequately describes the region of recombination-nonequilibrium plasma formed after BEMW passing. However, the set of equations (5) describes the BEMW front for initial condition (6).

### 7.1.3. Nature of ionization processes

The calculations were oriented to the parameters at which the highest efficiency of xenon excilamps was experimentally achieved, i.e., the xenon density  $N = 4.4 \cdot 10^{18} \text{ cm}^{-3}$  and the electrode voltage  $U_0 \sim -(2.5-3) \text{ kV}$ . A series of calculations were performed at various  $U_0$  and  $r_0 = 0.5 \text{ mm}$ ,  $r_{\text{max}} = 15 \text{ mm}$ , and  $r_{\text{bar}} = 13 \text{ mm}$ . In what follows, we present the results for  $U_0 = -2500$  and  $-3000 \text{ V}$  at an initial charge density  $N_0 = 10^6 \text{ cm}^{-3}$ .

The following stages of discharge gap ionization can be distinguished. Initially, the BEMW directed to the anode is formed near the cathode. The multiplication wave travels to the barrier and shorts the discharge gap. Then the charge is accumulated on the barrier and the discharge current decays.

The ionization develops as follows. Near the cathode, in a layer of thickness  $\Delta x \sim 10/a \sim 100 \mu\text{m}$ , intense electron multiplication and wire charge screening by the uncompensated ion charge occur. Then the ionization goes in two directions. First, the multiplication wave

propagates to the anode, in which the electron density is higher than the ion density. Second, the ion density peak is formed near the cathode (Figure 11).

Under weak ionization, the field breaks plasma; hence, the electron density cannot have a peak in the ion peak region (Figure 11(a)). However, even if the ion and electron density peaks coincide, the ion density near the peak somewhat exceeds the electron density. Electrons prevail in the region closer to the anode. As the BEMW propagates, the density of both ions and electrons near the ion peak increases. At a sufficiently strong ionization, the initial field and potential distribution becomes appreciably distorted near the ion peak. In a strong field, this distortion occurs significantly earlier than in a weak field.

When the multiplication wave reaches the anode, the discharge gap becomes as though shortened. Approximately at the same time, the density of both ion and electronic charges near the barrier sharply increases, and the parameters of the near-cathode layer change. In the near-cathode region, the ion and electron density peaks shift to the cathode and spread. The near-cathode layer becomes significantly narrower. As the ionization develops, a field strength dip is formed in the near-cathode region. The potential jump in the near-cathode layer is much smaller than the potential difference  $U_0$  on electrodes due to the small thickness of this layer.

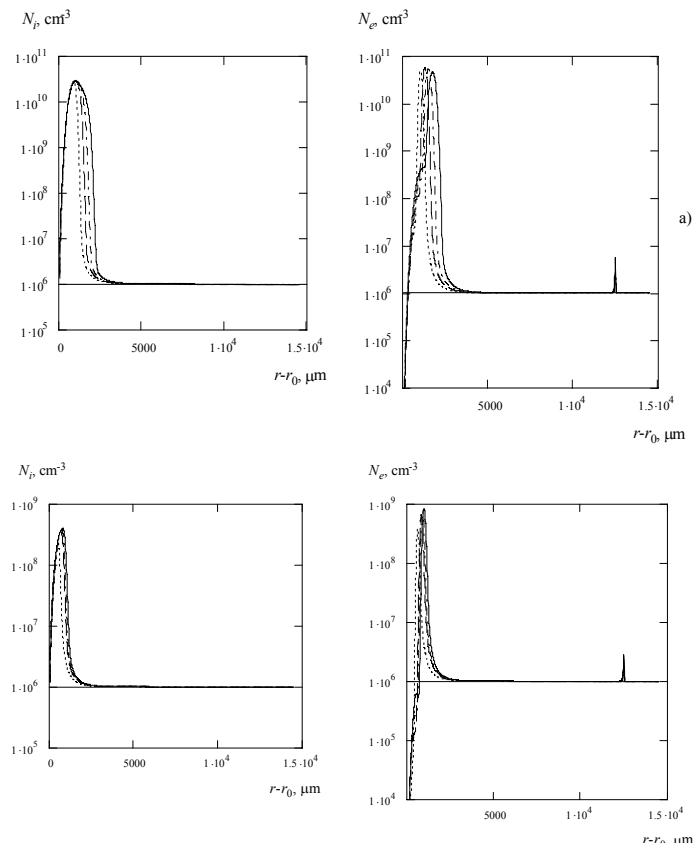


Figure 11. Radial distributions of the ion and electron density at the initial discharge stage at  $U_0 = -3000$  V (a) and  $-2500$  V (b) at different time points: (a) 13 ns (short dashed curves), 18 ns (dashed curves), 23 ns (dash-dotted curves), and 30 ns (solid curves); (b) 7 ns (short dashed curves), 10.5 ns (dashed curves), 11.7 ns (dash-dotted curves), and 14 ns (solid curves).

Since the discharge is the barrier one, the electron current after shortening the discharge gap remains essentially limited. The quasi-steady mode of electronic charge flow from the cathode to the barrier is formed, which is characterized by stationary distributions of plasma and field parameters in a major region of the discharge gap.

Various discharge stages are well traced when considering the time dependence  $J(t)$  of the electron current to the barrier, relative to the tube length (Figure 12). The electron current  $J(t)$  is calculated as the product of the electron flux taken at  $r = 11 \text{ mm} < r_{\text{bar}}$  to the corresponding circumference  $2\pi r$  and to the electron charge.

Initially, when the multiplication wave did not reach the barrier, the electron current is very low. At the instant the multiplication wave reaches the barrier, the electron current peaks. Then the electron current decreases as the electronic charge is accumulated on the barrier,

$$Q(t) = \int_0^t J(t') dt'.$$

The electronic charge and current are taken relative to the tube length.

The charge closing the discharge gap on the barrier per unit length,  $Q_{\text{bl}}$  corresponds to the situation when the total potential difference on the barrier drops,

$$Q_{\text{bl}} = \frac{U_0}{2 \ln(r_{\text{max}} / r_{\text{bar}})}.$$

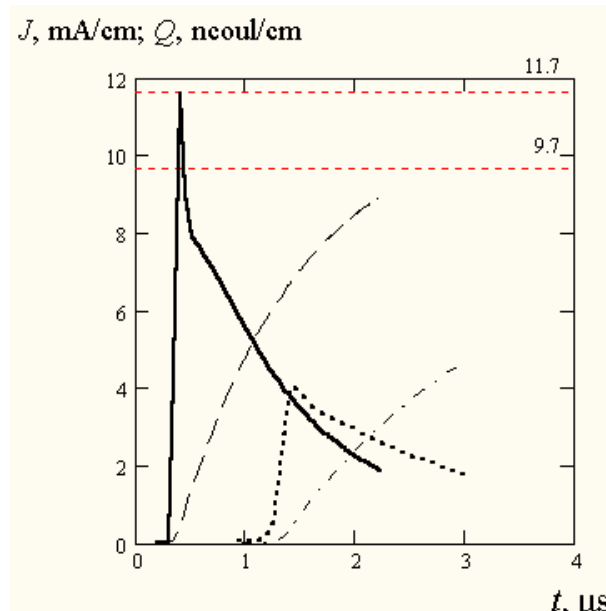


Figure 12. Time dependence of the electron current to the barrier at  $U_0 = -3000 \text{ V}$  (solid curve),  $-2500 \text{ V}$  (dotted curve) and the charge accumulated at the barrier at  $U_0 = -3000 \text{ V}$  (dashed curve),  $-2500 \text{ V}$  (dash-dotted curve). Horizontal dashed lines correspond to the blocking charges at the barrier:  $Q_{\text{bl}} = 11.7 \text{ nC/cm}$  at  $U_0 = -3000 \text{ V}$  and  $Q_{\text{bl}} = 9.7 \text{ nC/cm}$  at  $U_0 = -2500 \text{ V}$ .

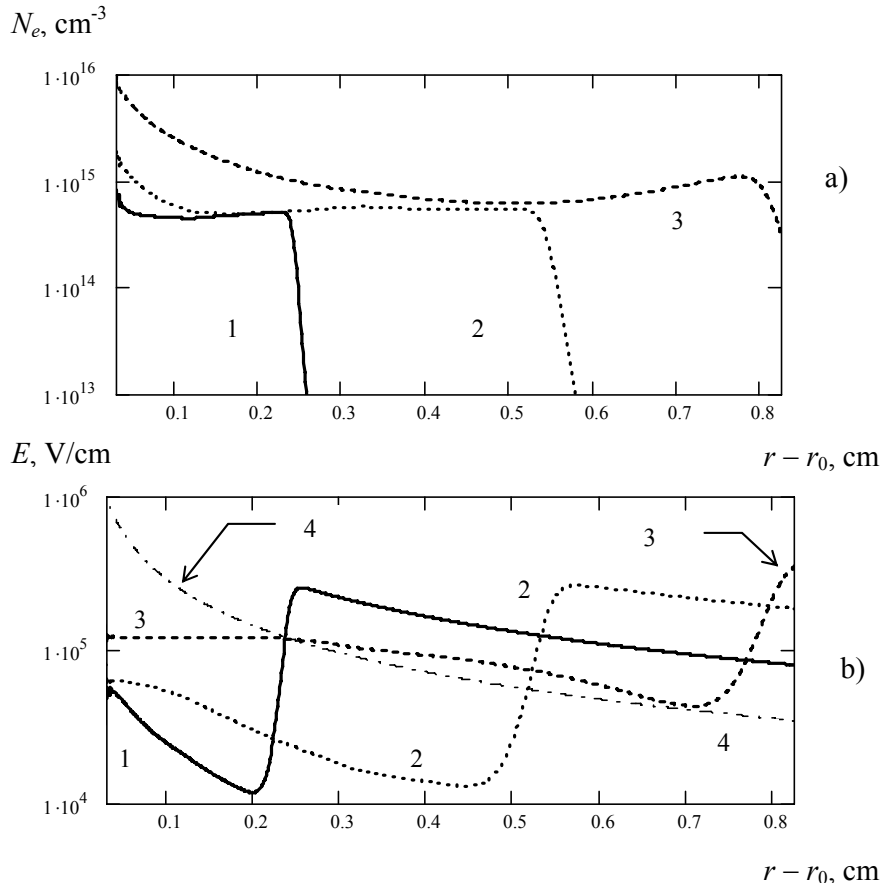


Figure 13. Radial distribution of the (a) electron density and (b) field strength at time points  $t = 1.3$  ns (1), 1.4 ns (2), and 1.5 ns (3). Curve 4 corresponds to the field distribution in empty space  
 $E(r) = \frac{-U}{\ln(r_0/r_1)} \cdot \frac{1}{r}$  at  $U = 100 \text{ kV}$ ,  $r_0 = 0.25 \text{ mm}$ , and  $r_1 = 8 \text{ mm}$ . The time dependence of the set electrode voltage  $U(t)$  was assumed to be linear with peak value  $U_0 = -100 \text{ kV}$  reached at  $t = 1 \text{ ns}$ .

At high voltages  $U_0$ , the current peak is larger, but both the peak appearance time and duration are smaller. The charge at lower voltages  $U_0$  is accumulated more slowly (see Figure 12).

For comparison, we present the result of the BEMW calculation in dense xenon ( $p = 1 \text{ atm}$ ), based on the above model (Figure 13). We can see that the BEMW velocity in dense gas is significantly larger than for low pressures.

## 7.2. On an Increase in the Lamp Intensity on $\text{Xe}_2^*$ Transitions

Let us consider possible power characteristics of  $\text{Xe}_2^*$  lamp according model described in Sec. 6 [18, 20, 61]. It is well known that  $\text{Xe}_2^*$  lamps involving barrier discharges exhibit efficiencies of over 50 % when employing cathodes with a small radius of curvature (for

example, wires) [65, 68]. Experimental [65, 68, 72, 90] and theoretical [63, 72, 73, 91] investigations of these excilamps allow a conclusion that the volume ionisation in them takes place by way of precisely the electron multiplication wave. It is not until the passage of the multiplication wave that the shorting of the discharge gap and the quasistationary charge accumulation at the barrier are realised [63]. However, these lamps operate at not-too-high a pressure ( $p = 100\text{-}200$  Torr), and pump pulse duration is therefore relatively long ( $\sim 1 \mu\text{s}$ ).

To maximise the pulsed output power of these excilamps with retention of their high average efficiency is of interest for some applications. As suggested by our simulations (Figure 8b), to do this requires going over to higher pressures ( $p > 1 \text{ atm}$ ). In this case, it is possible to attain a spontaneous emission specific power of  $1 \text{ MW cm}^{-3}$  for  $p = 2 \text{ atm}$ . Consequently, it is required to employ voltage pulses with a subnanosecond rise time.

Note that according to the calculations of [82] the efficiency of input-energy conversion to the energy of spontaneous emission was high ( $\eta \approx 50\text{-}60\%$ ) for long pump pulses ( $\sim 1 \mu\text{s}$ ) and moderate pressures ( $p = 100\text{-}200$  Torr). For short pulses ( $\sim 0.1 \text{ ns}$ ), as suggested by the simulations outlined above, to attain a high conversion efficiency necessitates directing attention towards higher gas pressures ( $p > 1 \text{ atm}$ ) (Figure 9). We also mention that the optimal input power increases, according to the calculations of [82], with shortening the pump pulse duration. The output efficiency of the lamps depends only slightly on the pressure when it is higher than the optimal one.

The occurrence of the optimum for pressures of  $\sim 5 \text{ atm}$  in our calculations is related to the quenching of excited excimer states by electrons. The characteristic electron quenching time for excimer states for an electron density of  $\sim 2 \cdot 10^{16} \text{ cm}^{-3}$  is equal to  $5 \text{ ns}$ , the excimer production time at a pressure of  $5 \text{ atm}$  is also about  $5 \text{ ns}$ . Furthermore, the heating of gas is also partly responsible for the shift of the optimum towards higher pressures (in comparison with the above pressures  $p = 100\text{-}200$  Torr), because the emission efficiency lowers with increasing gas temperature, and the gas temperature lowers with increasing pressure. For a pressure of  $1 \text{ atm}$ , for instance, by the end of the pumping pulse the gas temperature rises from  $300 \text{ K}$  to a value higher than  $400 \text{ K}$ , while it remains practically invariable for a pressure of  $20 \text{ atm}$ .

## CONCLUSION

Thus, the study performed shows that it is expedient to distinguish one more type of pulsed discharges. In these discharges, ionization in atmospheric-pressure gases propagates not due to electron or photon transport during breakdown, but due to multiplication of background electrons and electrons produced in the gap by fast electrons due to enhancement of the electric field near the cathode and in the gap.

Such a background-electron multiplication wave (BEMW) arises in a nonuniform field on small-curvature-radius conducting surfaces where the electric field is concentrated. Its front moves against the gradient of the electric field magnitude, and the velocity is proportional to the gas pressure. In this case, the electric field direction does not affect the BEMW propagation direction. To obtain the BEMW-based volume discharge, generators with nanosecond pulse rise times and voltages of about  $100 \text{ kV}$  should be used.

An important property of BEMW discharges is that recombination-nonequilibrium plasma (being an active medium of plasma lasers) is formed behind the multiplication front.

All discharge formation and lasing stages of the Penning neon laser in a Ne-H<sub>2</sub> mixture obtained from the theoretical treatment are experimentally confirmed as follows.

- (i) Fast electron formation results in efficient production of secondary electrons with a density of the order of  $n_e = 10^{13} \text{ cm}^{-3}$  in the discharge gap. This stage takes up to 1 ns.
- (ii) After secondary electron formation, the experimental discharge gap voltage drops to 3-6 kV. This value is in good agreement with the value corresponding to Ohm's law at the medium resistivity corresponding to the density of produced secondary electrons.
- (iii) The time 100 ns of the existence of this voltage (3-6 kV) is in good agreement with the time of multiplication wave passage through a medium with obtained parameters.

As a result of the multiplication wave passage, the electron density behind its wave front increases to a value at which the external field is screened. After field screening, electron heating by the field in these regions sharply weakens. Electrons are cooled due to collisions with gas atoms. Since the degree of ionization is low at a high gas density, electrons are cooled to a low temperature limited only by recombination heating; hence, recombination-nonequilibrium plasma is formed. Experimental lasing delays are in good agreement with calculated values.

The optimum ratios of neon and hydrogen in the mixture, radiation energies and powers are also in good agreement with experimental data.

All the above allows us to conclude that the active medium was excited in the case at hand due to multiplication wave passage through the discharge gap.

The consideration also shows that plasma formed in the multiplication wave afterglow of the nanosecond discharge with a subnanosecond front is of interest for developing various plasma lasers, including inert-gas dimer lasers.

In other words, BEMW afterglow plasma is promising to achieve lasing on the transitions on which lasing was previously obtained in dense gas pumped by the electron beam and in a pulsed discharge afterglow. In particular, BEMW afterglow plasma is promising for pumping excimer and exciplex lasers.

Moreover, BEMW discharges are of interest for developing pulsed excilamps with high spontaneous emission pulse power. In particular, such lamps can be of interest for photolytic pumping of lasers intended to generate powerful femtosecond pulses [92-94].

## REFERENCES

- [1] Gudzenko, LI; Yakovlenko, SI. *Plasma Lasers*; Atomizdat: Moscow, SU, 1978. [in Russian].
- [2] *Visible and UV Plasma Lasers*; Yakovlenko, S. I; Ed; Proceedings of the General Physics Institute; Nauka: Moscow, SU, 1989, Vol. 21. [in Russian].
- [3] Yakovlenko, SI. *Las. Phys.*, 1991, vol. 1, 565-589.

- [4] Tarasenko, VF; Yakovlenko, SI. *Quant. Electr.*, 1997, vol. 27, 1111-1119.
- [5] Yakovlenko, SI. In: Plasmatechnical systems. XI.3.2. *Gas and Plasma Lasers*; Fortov, VE; Ed; *Encyclopedia of Low-Temperature Plasma*; Nauka: Moscow, RU, 2000, Introductory Vol. IV, 262-291. [in Russian].
- [6] Gas and Plasma Lasers; Yakovlenko, SI; Ed; *Encyclopedia of Low-Temperature Plasma. Series B: Reference Appendices, Bases, and Databases*; Fortov, VE; Ed; Fizmatlits: Moscow, RU, 2005, Vol. XI-4. [in Russian].
- [7] Boichenko, AM; Tarasenko, VF; Yakovlenko, SI. *Las. Phys.*, 2000, vol. 10, 1159-1187.
- [8] Boichenko, AM; Tarasenko, VF; Yakovlenko, SI. In: *Gas and Plasma Lasers*; Yakovlenko, SI; Ed; *Encyclopedia of Low-Temperature Plasma. Series B: Reference Appendices, Bases, and Databases*; Fortov, VE; Ed; Fizmatlits: Moscow, RU, 2005, Vol. XI-4, 471-503. [in Russian].
- [9] Yakovlenko, SI. In: *Gas Lasers*; M; Endo, RF; Walter, Eds; CRC Press, Taylor and Francis Group: Boca Raton, London, New York, 2007, 369-411.
- [10] Basov, NG; Bogdankevich, OV; Danilychev, VA; Kashnikov, GN; Kerimov, OM; Lantsev, NP. Kratkie Soobshcheniya Fizike, 1970, N7, 68 (in Russian).
- [11] Basov, NG; Balashov, EM; Bogdankevich, OV; Danilychev, VA; Kashnikov, GN; Lantzov, NP; Khodkevich, DD. *J. Luminesc.* 1970, vol. 1-2, 834-841.
- [12] Basov, NG; Danilychev, VA; Popov, YuM; Khodkevich, DD. *JETP Letters*. 1970, vol. 12, 329-330.
- [13] Basov, NG; Danilychev, VA; Popov, Yu. M. *Oyo Butsuri (Japan)*. 1971, vol. 40 (9), 139.
- [14] Molchanov, AG. *Quant. Electr.*, 2003, vol. 33, 37-44.
- [15] Sasaki, W; Shirai, T; Kubodera, S; Kawanaka, J; Igarashi T. *Opt. Lett.*, 2001, vol. 26, 503-505.
- [16] Nakamura, K; Ooguchi, Y; Umegaki, N; Goto, T; Jitsuno, T; Kitamura, T; Takasaki, M; Horiguchi, S. *Proc. SPIE Int. Soc. Opt. Eng.*, 2001, vol. 4747, 286.
- [17] Tarasenko, VF; Yakovlenko, SI. *Phys.-Usp*, 2004, vol. 47, 887-905.
- [18] Boichenko, AM; Yakovlenko, SI. *Quant. Electr.*, 2006, vol. 36, 1176-1180.
- [19] Beams o f Runaway Electrons and Discharges in a Dense Gases, Based on a Wave o f Multiplication o f Background Electrons; Yakovlenko, SI; Ed; Proceedings o f the Prokhorov General Physics Institute; Nauka: Moscow, RU, 2007; vol. 63. [in Russian].
- [20] Tarasenko, VF; Yakovlenko, SI; Boichenko, AM; Kostyrya, ID; Lomaev, MI; Tkachev, AN. *Physics of Wave Phenomena*, 2008, vol. 16, 180-198.
- [21] Derzhiev, VI; Tarasenko, VF; Yakovlenko, SI; Yancharina, AM. In: *Visible and UV Plasma Lasers*; Yakovlenko, S. I; Ed; Proceedings o f the General Physics Institute; Nauka: Moscow, SU, 1989, vol. 21, 5-43. [in Russian].
- [22] Lomaev, MI; Tarasenko, VF. *Opt. Spectrosc.*, 1986, vol. 61, 689.
- [23] Lomaev, MI; Panchenko, AN; Tarasenko, VF. *Sov. J. Quant. Electr.*, 1987, vol. 17, 631.
- [24] Lomaev, MI; Tarasenko, VF. *Sov. Tech. Phys. Lett.*, 1988, vol. 14, 460.
- [25] Lomaev, MI; Tarasenko, VF. *Sov. J. Quant. Electr.*, 1992, vol. 22, 129.
- [26] Fedenev, AA; Yakovlenko, SI. *Las. Phys.*, 2007, vol. 17, 1-4.
- [27] Boichenko, AM; Panchenko, AN; Telminov, AE; AA. Fedenev, AA. *Bulletin of the Lebedev Physics Institute*, 2008, vol. 35, 142-147.
- [28] Boichenko, AM; Fedenev, AA; Panchenko, AN; Tel'minov, AE. *Physics of Wave Phenomena*, 2008, vol. 16, 283-291.

- [29] Yakovlenko, SI. *Tech. Phys. Lett.*, 2004, vol. 30, 354-357.
- [30] Yakovlenko, SI. *Tech. Phys.*, 2004, vol. 49, 1150-1157.
- [31] Yakovlenko, SI. *Tech. Phys. Lett.*, 2005, vol. 31, 169-172.
- [32] Yakovlenko, SI. In: *Gas and Plasma Lasers*; Yakovlenko, S. I; Ed; *Encyclopedia of Low-Temperature Plasma. Series B: Reference Appendices, Bases, and Databases*; Fortov, VE; Ed; Fizmatlits: Moscow, RU, 2005, vol. XI-4, 354-361. [in Russian].
- [33] Tkachev, AN; Yakovlenko, SI. Runaway of Electrons in Dense Gases and Mechanism of Generation of High-Power Subnanosecond Beams. Central Europ. *J. Phys.*, 2004, vol. 2(4), 579-635. ([www.cesj.com/physics.html](http://www.cesj.com/physics.html)).
- [34] Tarasenko, VF; Yakovlenko, SI. *Physica Scripta*, 2005, vol. 72, 41-67.
- [35] Tarasenko, VF; Yakovlenko, SI. *Plasma Dev. Operations*, 2005, vol. 13, 231-279.
- [36] Yakovlenko, SI. Bull. *Lebedev Phys. Inst.*, 2006, vol. 33, N2, 10-12.
- [37] Yakovlenko, SI. *Las. Phys.*, 2006, vol. 16, 403-426.
- [38] Yakovlenko, SI. In: Beams of Runaway Electrons and Discharges in a Dense Gases, Based on a Wave of Multiplication of Background Electrons; Yakovlenko, S. I; Ed; Proceedings of the Prokhorov General Physics Institute; Nauka: Moscow, RU, 2007, vol. 63, 132-147. [in Russian].
- [39] Gundienkov, VA; Yakovlenko, SI. Bull. *Lebedev Phys. Inst.*, 2006, vol. 33, N2, 13-17.
- [40] Gundienkov, VA; Yakovlenko, SI. *Tech. Phys.*, 2006, vol. 51, 1237-1239.
- [41] Kaptsov, PA. *Electronics*; GITTL: Moscow, SU, 1954, [in Russian].
- [42] Raether, H. Electron avalanches and breakdown in gases; Butterworths: London, UK, 1964.
- [43] Lozanskii, ED; Firsov, OB. Theory of a spark; Atomizdat: Moscow, SU, 1975, [in Russian].
- [44] Tarasenko, VF; Yakovlenko, SI. In: Beams of Runaway Electrons and Discharges in a Dense Gases, Based on a Wave of Multiplication of Background Electrons; Yakovlenko, SI; Ed; Proceedings of the Prokhorov General Physics Institute; Nauka: Moscow, RU, 2007; vol. 63, 7-63. [in Russian].
- [45] Tkachev, AN; Yakovlenko, SI. In: Beams of Runaway Electrons and Discharges in a Dense Gases, Based on a Wave of Multiplication of Background Electrons; Yakovlenko, S. I; Ed; Proceedings of the Prokhorov General Physics Institute; Nauka: Moscow, RU, 2007, vol. 63, 64-101. [in Russian].
- [46] Tarasenko, VF; Rybka, DV; Baksht, EKH; Kostyrya, ID; Lomaev, MI. *Instrum. Exp. Tech.*, 2008, vol. 51, 213-219.
- [47] Tarasenko, VF; Yakovlenko, SI. *Physics of Wave Phenomena*, 2008, vol. 16, 207-229.
- [48] Baksht, EKH; Kostyrya, ID; Lomaev, MI; Rybka, DV; Tarasenko, VF. *Physics of Wave Phenomena*, 2008, vol. 16, 199-206.
- [49] Tarasenko, VF; Baksht, EKH; Burachenko, AG; Kostyrya, ID; Lomaev, MI; Rybka, DV. *Plasma Devices and Operations*, 2008, vol. 16, 267-298.
- [50] Kostyrya, ID; Tarasenko, VF; Tkachev, AN; Yakovlenko, SI. *Tech. Phys.*, 2006, vol. 51, 356-361.
- [51] Tarasenko, VF; Yakovlenko, SI; Shunailov, SA; Kostyrya, ID; Tkachev, AN. *Laser Phys.*, 2006, vol. 16, 526-534.
- [52] Tkachev, AN; Yakovlenko, SI. In: Beams of Runaway Electrons and Discharges in a Dense Gases, Based on a Wave of Multiplication of Background Electrons;

- Yakovlenko, SI; Ed; Proceedings o f the Prokhorov General Physics Institute; Nauka: Moscow, RU, 2007, vol. 63, 102-131. [in Russian].
- [53] Kostyrya, ID; Orlovskii, VM; Tarasenko, VF; Tkachev, AN; Yakovlenko, SI. *Tech. Phys. Lett.*, 2005, vol. 31, 457-460.
- [54] Babich, LP. *Phys. Usp.*, 2005, vol. 48, 1015-1038.
- [55] Tarasenko, VF; Yakovlenko, SI. *Phys. Usp.* 2006, vol. 49, 767-770.
- [56] Tarasenko, VF; Yakovlenko, SI. Preprint No. 43; Moscow: A.M. Prokhorov General Physics Institute, *Russian Academy of Sciences*, 2006.
- [57] Loeb, L. *Basic Processes of Electric Discharges in Gases*; GITTL: Moscow, SU, 1950. [in Russian].
- [58] Granovsky, VL. *Electric Current in Gas*; GITTL: Moscow, SU, 1952, vol. 1; Nauka: Moscow, SU, 1971, vol. 2. [in Russian].
- [59] von Engel, A. *Ionized Gases*; Clarendon Press: Oxford, UK, 1965.
- [60] Raizer, YP. *Gas Discharge Physics*; Springer: N.Y., 1991.
- [61] Tarasenko, VF; Yakovlenko, SI; Boichenko, AM; Kostyrya, ID; Lomaev, MI; Tkachev, AN. In: *Beams of Runaway Electrons and Discharges in a Dense Gases, Based on a Wave of Multiplication of Background Electrons*; Yakovlenko, S. I; Ed; *Proceedings of the Prokhorov General Physics Institute*; Nauka: Moscow, RU, 2007, vol. 63, 148-182. [in Russian].
- [62] Tarasenko, VF; Yakovlenko, SI; Orlovskii, VM; Tkachev, AN. *Tech. Phys. Lett.*, 2004, vol. 30, 335-337.
- [63] Tkachev, AN; Yakovlenko, SI. *Laser Phys.*, 2003, vol. 13, 1345-1356.
- [64] Alekseev, SB; Gubanov, VP; Kostyrya, ID; Orlovskii, VM; Skakun, VS; Tarasenko, VF. *Quant. Electr.*, 2004, vol. 34, 1007-1010.
- [65] Kogelschatz, U. In: *International Conference on Atomic and Molecular Pulsed Lasers V* (Tomsk, Russia, 2003); Ed; *Proc. SPIE.*, 2004, vol. 5483, 272-286.
- [66] Lomaev, MI; Skakun, VS; Sosnin, AE; Tarasenko, VF; Shitts, DV; Erofeev, MI. *Phys.-Usp.*, 2003, vol. 46, 193-210.
- [67] Boichenko, AM; Yakovlenko, SI. In: *Gas and Plasma Lasers*; Yakovlenko, SI; Ed; *Encyclopedia of Low-Temperature Plasma. Series B: Reference Appendices, Bases, and Databases*; Fortov, VE; Ed; Fizmatlits: Moscow, RU, 2005, vol. XI-4, 569-608. [in Russian].
- [68] Vollkommer, F; Hitzschke, L. In: Proceedings o f 8th International Symposium on Science and Technology o f Light Sources; Greifswald, Germany, 1998, 51-60.
- [69] Mildren, RP; Carman, RJ. *J. Phys. D: Appl. Phys.*, 2001, vol. 34, L1-L6.
- [70] Tkachev, AN; Yakovlenko, SI. In: *International Conference on Atomic and Molecular Pulsed IV* (Tomsk, Russia, 2001); Ed; *Proc. SPIE*, 2002, vol. 4747, 271.
- [71] Lomaev, MI; Tarasenko, VF; Tkachev, AN; Shitts, DV; Yakovlenko, SI. *Tech. Phys.*, 2004, vol. 49, 790-794.
- [72] Arnold, E; Lomaev, MI; Lisenko, AA; Skakun, VS; Tarasenko, VF; Tkachev, AN; Shitts, DV; Yakovlenko, SI. *Laser Phys.*, 2004, vol. 14, 809-817.
- [73] Tkachev, AN; Yakovlenko, SI. *Laser Phys.*, 2002, vol. 12, 1022-1028.
- [74] Tkachev, AN; Yakovlenko, SI. *Tech. Phys.*, 2003, vol. 48, 190-198.
- [75] Panchenko, AN; Suslov, AI; Tarasenko, VF; Tel'minov, AE. *Quant. Electr.*, 2007, vol. 37, 433-439.
- [76] Karelina, AV; Yakovlenko, SI. *Quant. Electr.*, 1995, vol. 25, 739-745.

- [77] Karelina, AV; Simakova, OV. In: *Gas and Plasma Lasers*; Yakovlenko, SI; Ed; *Encyclopedia of Low-Temperature Plasma. Series B: Reference Appendices, Bases, and Databases*; Fortov, V. E; Ed; Fizmatlits: Moscow, RU, 2005, vol. XI-4, 665-689. [in Russian].
- [78] Tkachev, AN; Fedenev, AA; Yakovlenko, SI. *Tech. Phys.*, 2005, vol. 50, 447-454.
- [79] Eletskii, AV; Smirnov, BM. *Physical Processes in Gas Lasers*; Energoatomizdat: Moscow, SU, 1985, [in Russian].
- [80] Massey, HSW; Burhop, EHS. *Electronic and Ionic Impact Phenomena*; Clarendon: Oxford, UK, 1952.
- [81] Tkachev, AN; Fedenev, AA. *Atmospheric and Oceanic Optics*. 2008, vol. 21, 678-681.
- [82] Boichenko, AM; Yakovlenko, SI; Tarasenko, VF. *Laser and Particle Beams*. 2000, vol. 18, 655-660.
- [83] Lo, D; Shangguan, C; Kochetov, IV; Napartovich, AP. *J. Phys. D: Appl. Phys.*, 2005, vol. 38, 3430-3437.
- [84] Boichenko, AM; Derzhiev, VI; Zhidkov, AG; Yakovlenko, SI. *Sov. J. Quant. Electr.*, 1989, vol. 19, 182-184.
- [85] Boichenko, AM; Yakovlenko, SI. *Quant. Electr.*, 1994, vol. 24, 236-242.
- [86] Boichenko, AM; Derzhiev, VI; Yakovlenko, SI. *Laser Phys.*, 1992, vol. 2, 210-220.
- [87] Boichenko, AM; Yakovlenko, SI. *Sov. J. Quant. Electr.*, 1992, vol. 22, 1094-1097.
- [88] Boichenko, AM; Tarasenko, VF; Fomin, EA; Yakovlenko, SI. *Quant. Electr.*, 1993, vol. 23, 3-25.
- [89] Alekseev, SB; Orlovskii, VM; Tarasenko, VF; Tkachev, AN; Yakovlenko, SI. *Tech. Phys.*, 2005, vol. 50, 1623-1627.
- [90] Arnold, E; Lomaev, MI; Skakun, VS; Tarasenko, VF; Tkachev, AN; Shitts, DV; Yakovlenko, SI. *Laser Phys.*, 2002, vol. 12, 1227-1233.
- [91] Tkachev, AN; Yakovlenko, SI. *Tech. Phys.*, 2003, vol. 48, 190-198.
- [92] Mikheev, LD. *Laser Part. Beams.*, 1992, vol. 10, 473-478.
- [93] Malinovskii, GYA; Mamaev, SB; Mikheev, LD; Moskalev, TYU; Sentis, ML; Cheremiskin, VI; Yalovoi, VI. *Quant. Electr.*, 2001, vol. 31, 617-622.
- [94] Tcheremiskine, VI; Sentis, ML; Mikheev, LD. *Appl. Phys. Lett.*, 2002, vol. 81, 403-405.



## **Chapter 7**

# **PHASE TRANSITIONS AS POSSIBLE SOURCES OF HIGH POWER RADIATION**

***Mark E. Perel'man\****

Racah Institute of Physics, Hebrew University, Jerusalem, Israel.

## **ABSTRACT**

Removal of the latent heat at vapor condensation and/or crystallization (with temperature  $T \ll T_c$ ) occurs, as is shown by theoretical calculations and the resulted experimental data, on characteristic frequencies and their higher harmonics'. Intensity of this radiation can be very high and can explain, in particular, the bright flashes at the phenomenon of sonoluminescence. Under the general laws of the quantum theory these processes can be stimulated by resonant frequencies, therefore it is possible to carry out the laser on such "condensation" radiation. Potential capacity and, in principle, simplicity of such devices should attract to them attention of researchers.

Spectral features of atmospheric clouds correspond to characteristic frequencies of water vapor condensation and of  $\text{CO}_2$ ,  $\text{CH}_4$  condensation, etc. Radiative stimulation of their phase transitions can lead to control of atmospheric processes and of heat fluxes from the Earth, to regularization of its thermal regime.

## **1. INTRODUCTION**

Searches of new opportunities and mechanisms of realization of laser effect are one of the most attractive features of laser physics. In this connection it is possible to pay attention to chemical lasers and a search of their analogs as systems of the greater potential possibilities and power.

Chemical reactions of synthesis with eduction of bound energy, are inevitably leading to a generation of electromagnetic radiation. However, a number of conditions are necessary for realization of the laser effect: a transparency of environment on the basic frequencies of

---

\* Corresponding author: E-mails: m.e.perelman@gmail.com; mark\_perelman@mail.ru

transitions (desirable electro-dipole ones), the narrowness of levels providing their sufficient population density, a sufficient and cleared volume and mass of reagents. Therefore a suitable selection of chemical reactions is critical for practical realization of the laser effect.

Within the frame of thermodynamics and statistical physics the description of phase transitions of the first kind are very close to the description of chemical reactions: the phenomena of vapor condensation, solidification and crystallization also lead to liberation of bound energy. And if these energy liberations occur in the form of electromagnetic radiation, it is possible to think, in principle, about realization of laser-type emission of the latent heat of phase transitions. The most attractive side of such radiators, if they managed to be carried out, would be the cheapness and simplicity of preparation of working substance (e.g. water vapor), and also possible limitlessness of working volume.

On the other hand stimulation of phase transitions by characteristic radiation would have many applications as the control processes in solid state physics, including cristallophysics, in nanotechnology, in the weather control and so on.

The necessity of investigations of removal problems have been put forward and elaborated, in the frame of quantum electrodynamics, in the papers [1], but without concretization of elementary acts.

Thus the investigation of possibilities of realization of this new type of laser sources can be divided onto such parts. First, it must be show that the liberation of latent heat can lead to determined characteristic radiation and corresponding frequencies must be fixed (we followed primary [2]). Then, in the Section 3, the QED theory of this radiation with possibilities of their stimulation must be constructed. In the Section 4 the obvious microscopic considerations allow to establish some additional thermodynamic correlations

Thirdly, the observations data of phenomena, which can be explained by considered radiation, must be described. Then, in the Section 6 features of the atmospheric spectra are described as results of phase transitions of pollution gases [3], this approach can lead to analyses of atmosphere and, in principle, to control of weather processes by radiative stimulating of transitions in clouds.

The unique radiative phenomena that can be connected with latent heat are the sonoluminescence, described in the special Section 7. General results are summed in the Conclusions.

## **2. EMISSION OF LATENT HEAT AT PHASE TRANSITIONS**

All peculiarities of phase transitions should be definable, in principle, by electromagnetic properties of constituents. Thus, the basic parameter of the first-order phase transition, its molar latent heat  $\Lambda(T)$  should be determinable, undoubtedly, via electromagnetic parameters of particles and substances as a whole and via their external parameters. And in the known theory [4] and further in [5] it was shown that such approach leads to the satisfactory estimation of the latent heat of Helium liquefaction.

It may be supposed that the processes of removing of liberated latent heat, i.e. the energy generated during transition, can be examined as a key to such consideration, since the possibilities and channels of such removal can indicate on changes of constituents'

interactions during the transition processes. On the other hand this removing energy can has some special features that can be interesting in applications.

The processes of latent energy removing are not usually considered as a problem at all. Apparently it is tantamount to an implicit assumption that the removal of latent heat (bond energy) at transition into the more condensed phase at constant temperature should be occurred via heat conductivity. Such assumption must be recognized as logically inconsistent: heat conductivity depends on a difference of temperatures and is executing as a continuous process, but phase transition can be executed as a set of discrete processes at the constant temperature.

Note that the imperative existence of certain interrelation of the latent heat generated in the first-order phase transition with optical characteristics of forming phases can be predictable at consideration of certain residual rays [6] or dielectric anomalies [7]: the factor of reflection aspires to unit for the frequencies corresponding to the half of latent heat per atom/molecule of many crystals (cf. [8]).

Here we shall attempt to consider the process of transition into more ordered state microscopically as the conversion, completely or partially, of generated latent heat into electromagnetic transitive radiation of Ginzburg-Frank, [9]. The intensity and spectrum of such phase radiation should depend on existence of suitable electron levels. The observations of this characteristic radiation were executed in some special experiments, they followed a line planned in [1, 8], but their analysis, in our opinion, has not been completed.

Let's notice that some close effects are described as crystalloluminescence. Its effects are investigated for a long time, they including, apparently, displays of several very different phenomena: crystallization including nucleation processes, accumulation of transitions energy on the introduced radiative centers, polymorphic transformations, chemiluminescence, luminescence with fractures and cracks formation, triboluminescence, etc. (e.g. [10]). Such mixture complicates their examination and we try to separate from possible sources of radiation such ones that are caused exclusively by phase transitions of the first kind.

If medium contains particles possessing any electric or magnetic moment, the phase transition of the first kind can be considered as an instantaneous change at the time  $t = 0$  of the dielectric susceptibility of substance and also, probably, the value of moments and positions of particles (it is accepted for simplicity that  $\mu = 1$  and only dipole moments are considered):

$$\boldsymbol{\varepsilon}(t) = \theta(t)\boldsymbol{\varepsilon}_1(\mathbf{t}) + \theta(-t)\boldsymbol{\varepsilon}_2(t); \quad \mathbf{d}(t) = \theta(t)\mathbf{d}_1(\mathbf{t}) + \theta(-t)\mathbf{d}_2(t), \quad (2.1)$$

where  $\theta(t)$  is the Heaviside step function.

The intensity of transient radiation can be calculated directly. But these calculations are not necessary, since they can be simply estimated by the known analogy between transient radiations of (nonrelativistic) charge  $q$  and dipole  $\mathbf{d}$  [9]. So, if a charge  $q$  is entered, under an angle  $\beta$  and with a velocity  $\mathbf{v}$  from vacuum into medium, the intensity of transient emission is

$$W(\omega, \beta) \approx \frac{2q^2\mathbf{v}^2}{\pi c^3} \left| \frac{\varepsilon - 1}{\varepsilon} \right|^2 \sin^2 \beta. \quad (2.2)$$

After averaging over angles it can be assumed that for the transition from radiation of charges to radiation of dipoles such replacement in (2.2) is enough:

$$q^2 \rightarrow \frac{1}{4} (\mathbf{d}_2^2 + \mathbf{d}_1^2)(\omega/v)^2 \approx \frac{1}{2} \mathbf{d}^2(\omega/v)^2. \quad (2.3)$$

Let's specify the expression (2.2) by substitution the usual magnitude  $\epsilon(\omega)$  with only one, for simplicity, resonant frequency:

$$\epsilon(\omega) = 1 + \omega_p^2 / [\omega_0^2 - (\omega + i\Gamma)^2] \approx 1 + \omega_p^2 / 2\omega_0 [(\omega_0 - \omega) - i\Gamma/2], \quad (2.4)$$

where  $\omega_p = \sqrt{4\pi N r_0 c^2}$  is the plasma frequency,  $N$  is the density of scatterers,  $r_0$  is the classical radius of an electron with mass of free particle.

In view of the subsequent integration

$$|\epsilon(\omega) - 1|^2 = \omega_p^4 / 4\omega_0^2 [(\omega_0 - \omega)^2 + \Gamma^2/4] \rightarrow (\pi\omega_p^4 / 2\omega_0^2 \Gamma) \delta(\omega_0 - \omega). \quad (2.5)$$

By integrating (2.2) over angles and frequencies with the help of (2.5), it is received that the energy radiated at the entering of single dipole into condensate is equal to

$$W^R \approx \omega_p^4 d^2 / 6c^3 \Gamma = \pi(c/\Gamma) \sigma_T d^2 N^2, \quad (2.6)$$

where  $d$  is the average value of dipole moments in both substances,  $\sigma_T$  is the Thompson cross-section.

With taking into account the collisional broadening of spectral lines  $\Gamma = c\sigma_T N$  and two determinations of substance polarizability  $\alpha \sim 1/N$  and  $\alpha \sim d^2/3\kappa_B T$ , this relation can be rewritten as  $W_{\text{thr}}^R \approx 3\pi\kappa_B T$ , which is equivalent to the universal expression for molar latent energy of the condensed phase formation  $\Delta H_{\text{form}} = N_A W_{\text{thr}}^R$  consisting from particles with dipole moments:

$$\Delta H_{\text{form}}/T = 3\pi R_{\text{gas}} = 78.2 \text{ J/mol K}, \quad (2.7)$$

where  $R_{\text{gas}}$  is the universal gas constant.

This result proves the universality of correlation between energy of the condensed state formation for dipole particles and temperatures of transition at  $T \ll T_c$ . So, it ascertains that the potential energy of bonds of simple particles at (normal) temperature of phase transition into the condensed phase is  $2\pi$ - times bigger their average kinetic energy.

The numerical evaluations of (2.7) practically coincide with the well-known empirical Trouton's rule for latent energy of vapor condensation:  $\Delta H_{\text{cond}}/T = 80 \text{ J/mole K}$ . Some distinction between energies of formation and boiling can be connected to certain simplifying guesses and approximations of our estimations and does not belittle the general importance of this correlation.

For indicative numerical estimations, one can be taken on  $|\Delta d| \sim 1 D = 10^{18} \text{ CGSE}$ , density of particles of substance  $N \sim 3 \cdot 10^{22} \text{ cm}^{-3}$  and  $\Gamma \sim 10^8$ . From here an estimation  $W^R \sim 5.6 \cdot 10^{13} \text{ erg/particle}$  or a latent molar heat of transition  $\Lambda = N_A W^R \sim 33 \text{ kJ/mole}$  follow at normal temperature and pressure. Such estimations generally correspond to the order of

magnitudes of observable values and support our assumption of removals of latent heat by radiation.

We accept that when the particle (atom, molecule, cluster) enters into a new phase, it radiates the latent heat of transition as one or several quanta which, however, can be thermalized before their exit from the substance. The presence of suitable levels is necessary for realization of the radiation act. But the latent heats of condensation and crystallization are not constants; they change with pressure and/or other extensive parameters.

The most characteristic for substance levels are the levels determined by the gas-crystal transition at the zero, in an ideal, pressure. For monatomic substances it is the heat of atomization, for multi-atomic it can be determined, possibly, as the heat of atomization minus energy of molecules formation.

Thus, for the first time, the connection between thermodynamic and spectral characteristics of substances is established.

Heat of sublimation for many substances is close to the heat of condensation (it must be specially underlined, that for heats of sublimation and/or of atomization the data of different directories are rather inconsistent). Therefore, it is possible to think, that the deep overcooling of vapor is complicated or even is impossible: for a particle almost enough latent heat of condensation exists for its emission with taking into account width of levels. Hence, we can predict the radiation during the crystallization in a vapor phase.

In phenomena of melt crystallization the situation is more complicated. For transition to the radiating level the crystallization heat is not obvious enough, therefore additional energy can be achievable by overcooling and/or to be borrowed from the thermal energy of melt.

So, there are such opportunities of radiation:

1. If radiation has the one-photon character,

$$\hbar\omega_1 = \Lambda/N_A \quad \text{or} \quad \lambda_1 = 120/\Lambda, \quad (2.8)$$

where  $\Lambda$  is expressed in kJ/mole, and lengths of waves in mcm,  $N_A$  is the Avogadro number.

2. The n-photon transition with equal frequencies:

$$\hbar\omega_n = \Lambda/nN_A \quad \text{or} \quad \lambda_1 = 120n/\Lambda. \quad (2.9)$$

Here  $n$  can be connected with the number of formed bonds in condensate, i.e. it can be of the order of coordination number:  $n = 1, 2, 3, \dots$ . The singularities of spectra of condensate media can describe the number of bonds, i.e. their structure for simple substances at least. For monatomic substances the two-photon emission in the  ${}^1S_0$  state with unchanging symmetry of systems are most probable.

3. In the case of more complex molecules transitions with quanta of various frequencies is possible, e.g. for the two-photon case

$$\hbar\omega_1 = \hbar\omega' + \hbar\omega'' \quad \text{or} \quad \lambda'\lambda''/(\lambda' + \lambda'') = \lambda_1 \equiv 120/\Lambda. \quad (2.10)$$

More complicated combinations of frequencies can be similarly considered.

4. Dimers and more complicate formations, clusters, can be examined as single particles and if bound energy of atoms/molecules in them is small enough, wavelengths of radiation for a cluster of M particles will be of the type:

$$\lambda_1^{(M)} \approx 120/M\Lambda, \quad \lambda_n^{(M)} \approx 120n/M\Lambda, \quad (2.11)$$

(Here uncertainties can be connected with differentiation of bonds at formation of little clusters).

5. The more complicated situation with aggregation of M particles and additionally  $q = 1, 2, 3, \dots, m$  ( $m$  is the maximal coordination number) bonds can not be a priori excluded. It will mean the emission of  $(M + q/m)$  times latent energy:

$$\lambda_{n,m}^{(M)} \approx 120n/\Lambda(M + q/m) \quad (2.12)$$

Such expression can be connected with appearing of certain bonds even at a stage of cluster formation.

The removal of all generated bond energy by one photon (the dipole radiation) seems the most simple and just it was assumed in the initial papers [1]. But such process can not be the general feature. In the article [11] is shown that on surfaces always must exist virtual double electromagnetic layers of dipoles or higher moments: they absorb incident electromagnetic waves and generate reflecting and transmitted ones.

In an analogy with these considerations the entering of particles with dipole moments may be considered as formation and subsequent neutralization of the system of anti-parallel dipoles (the anti-parallelism is marked by arrows):

$$\vec{d}(x, y, \Delta z) + \tilde{\vec{d}}(x, y, -\Delta z) \rightarrow A(x, y, 0) + \gamma_1 + \gamma_2 + \dots, \quad (2.13)$$

where through  $A(x, y, 0)$  an neutral "particle", which already had emitted the energy of transition and had been included in substance, is designated. Notice that the interaction between these dipoles takes place in the near field [12], i.e. can be instantaneous [13], the transferring of excitations between anti-parallel dipoles in near field had been supervised experimentally [14].

This dipoles system has the positive charge parity and therefore can be neutralized by emission of two photons, probably of equal frequencies, in the  ${}^1S_0$  state with  $\Delta J = 0$ , i.e. by (4.2) with  $n = 2$ .

The decay rate of dipoles system with emission of two photons, if they are entangled, coincides with the decay rate of single dipole and can be very roughly estimated via the usual expression for such radiation:

$$1/\tau_E \sim \alpha(ka)^2 \omega = (2\pi)^3 d^2 / \hbar \lambda^3. \quad (2.14)$$

With the characteristic values  $d \sim 1$  D;  $\lambda \sim 6$  mcm for water it leads to  $\tau_E \sim 10^{-3}$  sec that leads, for example, to spontaneous drops growth in the vapor phase with the maximal velocity of the order from mcm till tens mcm per second. Such estimation seems non-inconsistent.

This process is equivalent to the emission of one scalar particle and in an accord to the Goldstone theorem of the field theory can lead to changing of system symmetry, e.g. at crystallization in the vapor phase. As one example here can be added that the spectrum of water contains the lines of order of 6 mcm, two photons of which correspond to the generated latent heat at vapor condensation. (Corresponding lines can be determined and shown for many other substances.) The calculations of their probability, i.e. the determination of processes duration, can be carried out by a close analogy with the positronium decay.

The two-photon, the very often, removal of energy generated at the first-order phase transitions may be explicable by such reasons also. The van-der-Waals interaction is describable in QED by the two-photon exchange [15] and the imaginary part of its matrix element is proportional, in the spirit of optical theorem, to probability of emission of two photons. Therefore such removal of latent energy corresponds to the van-der-Waals intermolecular bonds.

### 3. QUANTUM THEORY OF PHASE TRANSITION RADIATION

For revealing quantum features of this radiation, its thresholds, possibilities of radiative stimulating of phase transitions and so on, they must be considered in the frame of QED, by the analogy with consideration in the our article given above.

Let us consider such simple model of media: two phases, e.g. gas and solid or liquid are presented as a system of two levels separated by the latent energy  $\Lambda/N_A$  per particle at constant temperature,  $\Lambda$  is the molar latent heat,  $N_A$  is the Avogadro number. Then the photons generated in the course of transition, i.e. at descent of each particle onto the condensate level, can be thermalized in media or, at some conditions, can be emitted as real photons. Moreover, an existence of induced radiation is not excluded in such picture and it can lead, in principle, to stimulated phase transitions into definite condensate state [1].

The main difference with the QED calculations of atomic radiation, considered in our article above, consists in the kind of electron propagator. Instead of the Low propagator here must be taken the temperature-temporal propagator of bound electron in media (e.g. [16]):

$$G_{v,\lambda}(x_1, x_2; T, \mu) = -i \sum_{N,n} e^{\beta(\Omega + \mu N - E_n)} \langle E_n, N | \{ \psi_v(x_1), \bar{\psi}_\lambda(x_2) \}_+ | E_n, N \rangle, \quad (3.1)$$

where  $\psi_\lambda$  is the wave function of atomic electron,  $n$  are numbers of levels with halfwidths  $T_n$ ; at  $T = 0$  this expression turn into the Low propagator.

For non-ferromagnetic media the Fourier transformation of (3.1) over time takes the form:

$$G_{v,\lambda}(r_1, r_2; \omega) =$$

=

$$-(2\pi)^3 \sum_{N,n,m} e^{\beta(\Omega + \mu N - E_n)} \frac{1}{2s+1} \sum_{\alpha} ((\psi_{\nu}(\mathbf{r}_1))_{n,m}, (\overline{\psi}_{\lambda}(\mathbf{r}_2))_{n,m}) \frac{1 \pm \exp(-\beta\omega_{n,m})}{\omega_{n,m} - \omega - i\Gamma_n}. \quad (3.2)$$

Direct calculations of bound electron-photon interactions at  $T \neq 0$  are not necessary because in all respects they differ only by the extra factor

$$\Delta_n = (1 + \exp(-\beta\omega_0)) \exp[\beta(\Omega + \mu N - E_n)] \quad (3.3)$$

for each electron line from the expressions given in the above article. The number of photons emitted at transition of single particle is not specialized here, if the symmetry of each particle is not changed at the course of transition, the most probable will be emission of two photons in the  ${}^1S^0$  state.

Hence the unique difference of such relations for phase transitions from the formulae of stimulated emission reaction rates consists in a replacement of the flux density threshold values:

$$j^0 \rightarrow j_0^{(\text{phase})} = j^0 / \Delta_1 \Delta_2 \simeq (\sigma \tau \Delta_1 \Delta_2)^{-1}. \quad (3.4)$$

The existence of pole (3.4) in every infinite virial series for bound electron-photon flux interactions leads to the following picture: when the temperature is increasing and the density of thermal radiation in frequency band near resonance becomes equal to (3.4), then the phase transition takes place: a saturation of one type of interactions and the including of following channel of interaction with another features (condensate turns into gas phase and so on).

Let's consider the free energy jump determining the saturation of some  $e-\gamma$  interaction channels. From (3.3) and (3.4) follows

$$\Omega_n = (1/2\beta) \{-\mu N - E_n - \ln \tau_n - \ln[2\sigma j(1 + \cosh \beta \omega_0)]\}. \quad (3.5)$$

At transition from one type of interaction to another the jump of energy is of the order of

$$\Delta \Omega_n = \Omega_{n+1} - \Omega_n \approx -(1/2\beta) \ln(\tau_1/\tau_2) \sim -(1/\beta) \ln(\Gamma/2\omega_0). \quad (3.6)$$

This relation can be rewritten via the molar latent heat and with the universal gas constant  $R_g$  as

$$\Lambda/T \sim R_g \ln(2\omega_0/\Gamma) \quad (3.7)$$

In the infrared range, where characteristic emissions of latent heat may be expected, it can be proposed that  $\omega_0/\Gamma \sim 10^4$ . It leads to  $\Lambda/T \sim 24 \text{ cal/mol}\cdot\text{K}$  that just corresponds to the cited Trouton rule established in 1884 for many substances (non-polar or weakly polar): latent heat and temperature of boiling are connected at normal pressure by the relation of order  $\Lambda_b/T_b \sim 21 \text{ cal/mole}\cdot\text{K}$  (cf. (2.7)). This rule is often used for physicochemical estimations (cf. [1, 2]). However, till now this rule has not been substantiated theoretically; its

sense and significance remained unknown. The estimation (2.19) can be indubitably concretized for different transitions and substances.

#### 4. RECOMBINATION OF COUPLED ANTI-PARALLEL DIPOLES

Let us return to the obvious microscopic considerations that allow the establishment of further thermodynamic correlations

If the particle of condensable gas possesses certain multipole moment, constant or virtual, at the approach to a surface it induces the redistribution of charges in medium, which is describing as the occurrence of a "mirror" moment (charge dislocation) in its near-surface adsorption layer. The arising attraction accelerates the sedimentation of condensable particles on the surface of condensate, i.e. their adsorption and/or phase transition [17].

Let's consider, as well as above, the condensation of vapor atoms or sufficiently simple molecules with the dipole moment  $\mathbf{d}$  on a flat surface of condensate at constant temperature much lower critical one and at such pressure that the vapor can be considered as an ideal gas. Kinetic energies of particle and of its image are equal to  $U_K = (3/2)\kappa_B T$ , the energy of interaction of two identical dipoles on distance  $R$ , averaged over angles, is equal to  $U_R = \mathbf{d}^2/R^3$ .

According to the virial theorem (e.g. [18]) the "temperature" part of potential energy of system, potential of which depends on distance as  $R^n$ , is  $U_T = (2/n)U_K$ , i.e. in our case  $U_T = (2/n)U_K$  for each dipole. Inasmuch as at entering of such particle into condensate its temperature should not be altered, i.e. the kinetic energy and corresponding part of potential energy should be kept, the liberated energy (the latent heat generated in the first-order phase transition of single particle) should be equal

$$\Delta U_b \equiv U_R - |U_T| = \mathbf{d}^2/R^3 - 2\kappa_B T_b. \quad (4.1)$$

In this expression, obviously, dynamic polarizability of atom, retardation and Casimir forces are not taken into account. Their role can be more significant at consideration of completely neutral particles (atoms of noble gases, molecules  $\text{CO}_2$ ,  $\text{CH}_4$ , etc.). It is possible to notice that, apparently, just this circumstance essentially lowers their temperatures of phase transitions in comparison with atoms/molecules possessing such moments (atoms of metals, at which the S-state is basic, e.g. Lithium, can form dimers and more complex aggregates with diversified momenta in a gas state).

Feasibility of the condition (4.1) is determinable, certainly, by an opportunity of approximation of substance polarization via only one "mirror" dipole. Hence the condensable dipole must be completely outside of condensate, i.e. the distance  $R$  in (4.1) should exceed the sizes of particle. Therefore this expression can be unfit or too complicated for consideration of big molecules.

The expression (4.1) can be considered, within the framework of described restrictions, as the strict one; in substances with orientation polarizability (e.g. [19])  $\alpha \approx \alpha_0 + \mathbf{d}^2/3\kappa T$  and therefore it somewhat specifies (2.7):

$$\Delta U_b / \kappa_B T_b = 3(\alpha - \alpha_0) / R^3 - 2. \quad (4.2)$$

In many substances, for which  $\alpha_0$  can be neglected, polarizability is inversely proportional to specific spherical volume, in which dipoles are cooperating, i.e.  $\alpha \sim 3/4\pi R^3$ . Thus, it leads to such form of latent heat per particle:

$$\Delta U_b \approx (4\pi - 2) \kappa_B T_b, \quad (4.3)$$

or, accordingly, for the molar condensation energy,

$$\Lambda_b / T_b \sim 21 \text{ cal/mol K}, \quad (4.4)$$

that just corresponds to (2.7), however now such expression can be already cited as the theorem. But for such generalization the necessary and sufficient conditions must be properly defined.

One more checking of usefulness of (4.1) as the general expression can be carried out as follows. The latent heat of transition into liquid state must tends to zero at approach to the critical temperature and pressure, therefore the general expression (4.1) would be rewritten for critical parameters as

$$d^2 / R_c^3 = 2 \kappa_B T_c. \quad (4.5)$$

Let's check up this relation, as an example, for water. As the critical temperature  $T_c = 647 \text{ K}$  and if the dipole moment keeps its value  $d = 1.855 \text{ D}$ , then  $R_c = 2.68 \cdot 10^8 \text{ cm}$  or the critical density must be of the order of  $\rho_c = 0.372 \text{ g/cm}^3$  at comparison with the experimental value  $\rho_c^{(exp)} = 0.322 \text{ g/cm}^3$ .

But in general it is possible to assert that in spite of all approximations, including constancy of dipole moments, this result seems not unreasonable. It means that the offered theory allows the establishing of correspondence of the critical parameters, at least, for certain substances. Notice that on the other hand, such relation can give possibility for investigation of possible changing of the dipole and other moments of molecules with changing of extensive parameters and for a certain tentative estimation of such changes.

Possible deviations from (3.4) in the scope of conducted discussion are evident. They can occur at approaching of temperature to the critical one, for particles of big sizes, with change of the dipole moment of particles at transition from one phase into another (usually  $|\Delta d| \ll |d|$ ), by virtue of difference of a mirror dipole in dielectrics with the induction dipole (difference is definable by values of dielectric susceptibility of both substances, e.g. [20]), in dependence on the form of condensate surface. All these changes, in principle, need to be taken into account directly in (4.1). More generally we can not assert that the interaction of complex molecules or clusters with condensable surface can be restrictively considered via influence of only one single electromagnetic moment.

It must be noted that the similar rules for processes of solidification of liquids are considerably less definite and practicable. The most simple of them assert that  $\Lambda_m / T_m = 2.5 \pm 0.5 \text{ cal/mole K}$  for simple substances,  $\Lambda_m / T_m = 6 \pm 1 \text{ cal/mole K}$  for inorganic

molecules and  $\Lambda_m/T_m = 13 \pm 3$  cal/mole K for organic ones. The consideration of these processes through proposed transitive radiation of own and induced momenta requires a revealing of "mirror" momenta inside the particles. Therefore their consideration should be much more complicated or would have less definite and more restricted heuristic significance. On the other hand their consideration is possible on the base of relation (3.7) deducted in [8], the Appendix, via assumptions of frequencies and width of emitting levels responsible for phase transitions.

## 5. EXPERIMENTAL DATA AND OBSERVATIONS

Several observations of radiation that can be described as the latent energy removal are known [2]. The most power between them is the gigantic IR excess observed in new born stars and nebulae [21]. Some observations connected with the condensation of water vapor will be mentioned below. But more convincing must be the laboratory investigations.

Let's consider concrete substances in which transitive radiation is experimentally recorded (data of corresponding heats are taken from [22]).

*Aluminum.* The heat of sublimation  $\Lambda_{\text{subl}} \approx 330$  kJ/mole, accordingly, at one-photon transition  $\lambda_1^{(\text{subl})} = 0.364$  mcm that corresponds to observable radiation splash on  $\lambda = 0.36$  mcm [23]. Supervision, however, mark also peak of radiation with  $\lambda = 0.43$  mcm, it corresponds to the heat of condensation into intermediate liquid state before crystallization  $\Lambda_{\text{cond}} = 294$  kJ/mole leading  $\lambda_1^{(\text{cond})} = 0.41$  mcm. It would be interesting to check up the frequency corresponding to the heat of crystallization  $\Lambda_{\text{cryst}} = 10.8$  kJ/mole in deep IR:  $\lambda_{\text{cryst}} = 11.1$  mcm. Note that  $\lambda_1^{(\text{subl})}$  corresponds to the maximum of reflectivity of Al and its minimum is close to 0.75 mcm, i.e. corresponds to two-photon emission of latent energy.

*Copper.* The heat of sublimation  $\Lambda_{\text{subl}} \approx 337.4$  kJ/mole, the heat of condensation into intermediate liquid state before crystallization  $\Lambda_{\text{cond}} = 300.4$  kJ/mole. Accordingly, at two-photon transition for sublimation  $\lambda_2 = 0.71$  and for condensation  $\lambda_2 = 0.8$  mcm that correspond to observable splashes of radiation on  $\lambda = 0.7, 0.8, 0.85$  mcm. Splash in radiation with  $\lambda = 1.5$  mcm can be attributed to four-photon transition of the atom.

*Tellurium.* In the experiment [24] with very rapid crystallization of overcooled Tellurium melt, the increase of radiation intensity in the range 2÷4 microns was observed. If to accept the latent heat of crystallization  $\Lambda_{\text{cryst}} = 17.5$  kJ/mole, with respect to (2.11), it leads to emission of the characteristic radiation corresponding to two-atoms cooperative transition  $\lambda_2 = 3.4$  mcm.

*Sapphire.* The heat of crystallization is 114 kJ/mole. At one-photon transition it leads to  $\lambda = 1.07$  mcm, the observable value  $\lambda = 1.1$  mcm [25].

*Alkali halides and PbCl<sub>2</sub>.* At crystallization of NaCl, NaBr, NaI, KCl, KBr, KI, PbCl<sub>2</sub> the peaks fully complying heat of crystallization are shown [26].

*Lithium fluoride.* At its crystallization the most interesting characteristic spectrum was observed:  $\lambda^{(2.1)} = 4.34$ ,  $\lambda^{(2.2)} = 4.05$ ,  $\lambda^{(2.3)} = 3.45$ ,  $\lambda^{(2.4)} = 2.80$  mcm [23]. For LiF, the latent heat of crystallization  $\Lambda_{\text{cryst}} \approx 26.4$  kJ/mole and coordination number is 6. The observable lengths of waves of radiation with the accuracy of 7% correspond to the formula (2.12) with  $M = 1$ ,  $n = 0$  for  $\lambda^{(2.1)}$ ;  $M = 1$ ,  $n = 1$  for  $\lambda^{(2.2)}$ ,  $M = 1$ ,  $n = 2$  for  $\lambda^{(2.3)}$  and  $M = 1$ ,  $n = 4$  for  $\lambda^{(2.4)}$

*Water.* The heat of sublimation is 46.68 kJ/mole, the heat of condensation into liquid phase at normal conditions is 40.6 kJ/mole and the heat of crystallization is 6.01 kJ/mole. They can lead to such emissions:  $\lambda_{1(\text{subl})} = 2.57$ ,  $\lambda_{1(\text{cond})} = 2.96$ ,  $\lambda_{1(\text{cryst})} = 20$ . In the paper [27] the surpluses of radiation corresponding to sublimation or condensation (an interval 5.2  $\div$  6.4 mcm) and crystallization (32  $\div$  42 mcm), apparently, have been determined, both correspond to two-photon transitions. The peak with  $\lambda \sim 6.7$  mcm fixed from the satellite [28], relates, apparently, to condensating water vapor at the lowered pressure, when it is about 35.8 kJ/mole.

Dimers and more complicated formations are always present in water vapor. So, the peak with  $\lambda = 1.5$  mcm corresponds to condensation of water dimmers  $\lambda = 0.93$  mcm corresponds to three molecules formation and so on (there are some previous supervisions that can be attributed as emissions at water condensation in atmosphere [29] and the most valuable for next section are observations of frequencies that may be attributed as higher harmonics of characteristic phase radiation [30]).

## 6. RADIATIVE TRANSITIONS IN BALANCE OF ATMOSPHERIC HEATING, POSSIBILITY OF THEIR CONTROL

At consideration and comparison of different channels of heat removing from the Earth is usually assumed that latent heat of precipitations (the power of 78 W/cm<sup>2</sup> from 324 W/cm<sup>2</sup> of general flux) is accumulating directly on the Earth surface (e.g. [31]).

Let us show that possible processes of repeated emissions of latent heats at condensation and crystallization of certain atmospheric gases with their subsequent sublimation and anew solidifications can lead to augmentation of the role of this channel of the heat removal from the Earth.

Here must be taken into account that really the emission is connected with formation of bonds between an entering particle and particles in the condensate; for comparatively simple particles can be assumed that all such bonds are identical. As the molecules H<sub>2</sub>O are connected with neighbors by four bonds, at water condensation each molecule establishes two new bonds with the energy  $\hbar\omega_1/2$ . But as in the process of emission energies of some bonds can be accumulated and then emitted as one quantum and such joining can include dimers and even more complex formations, it can be proposed that emitted quanta are described primary by (2.9).

All observable peaks are very wide and this feature must be discussed. At laboratory investigations the variation of energies of condensable or crystallizing particles are restrained by usual equilibrium distributions. But in the case of atmospheric observations there is a natural distribution over altitudes and temperatures. For initial estimation the cited and proved above Trouton rule can be taken into account. It can be supposed that analogical relation, with another and now still undetermined numerical value, would be proposed for transitive emission also. Therefore for considered cases can be assumed such estimation:

$$\Delta\lambda/\lambda \sim \Delta T/T. \quad (6.1)$$

Differences of temperatures within atmosphere evidently can lead to observable values of peaks wideness.

Let's compare experimental (observable, e.g. [31]) data with estimations by the general expression (2.9) for water vapor.

In the Table are written out all its observable maxima from 1 till 6 mcm; they are compared with wave lengths calculated by (2.9) at  $n = 1 \div 7$  with the heat of sublimation  $\Lambda^{(\text{subl})} = 46.68 \text{ kJ/mole}$  and the heat of condensation into liquid phase at normal conditions  $\Lambda^{(\text{cond})} = 40.6 \text{ kJ/mole}$  (the heat of water crystallization  $\Lambda^{(\text{cryst})} = 6.01 \text{ kJ/mole}$  leads to a far IR and is omitted).

All these lines are between radiated wave lengths corresponding to mixture of condensing and sublimation processes. The radiation with  $\lambda \sim 2 \text{ mcm}$  corresponds to dimers or even more complex formations (notice that by their intensities relative to density of dimers can be estimated and so on). Note evident possibilities of splitting these maxi's onto condensation and sublimation types.

**Table: Singularities of water clouds spectra in the Earth atmosphere.**

$\lambda_{\text{observ}}$	0.72 0.81	0.93	1.13	1.42	1.89 2.01-2.05	2.25-3.0	5.9
$n$	7	6	5	4	3	2	1
$\lambda_n^{(\text{subl})}$	0.73	0.86	1.03	1.285	1.71	2.57	5.14
$\lambda_n^{(\text{cond})}$	0.84	0.985	1.18	1.48	1.97	2.96	5.91

In this range are another max's also. The peaks with  $\lambda = 3.1 \text{ mcm}$  and with  $\lambda > 6.5 \text{ mcm}$ , that are not written out here, correspond to the well-known proper vibrations of molecule  $v_1$  ( $\lambda = 3.05$  and  $3.24$  for liquid and solid states correspondingly) and  $v_2$  ( $\lambda \sim 6.06 \div 6.27$  in dependence on phase state).

Now we can briefly consider some other gases that can be organized in clusters or even form drops in the atmosphere:  $\text{CO}_2$ ,  $\text{CH}_4$ ,  $\text{N}_2\text{O}$ , their possible density and temperatures in the upper atmosphere can be, in principle, sufficient for such transitions.

For  $\text{CO}_2$ , the carbon dioxide,  $\Lambda^{(\text{subl})} = 25.23 \text{ kJ/mole}$  and by (2.3)  $\lambda_1 = 4.76 \text{ mcm}$ ,  $\lambda_2 = 2.38 \text{ mcm}$ . Observable peaks are located between  $4.3 \div 4.5 \text{ mcm}$ ,  $2.4 \div 2.8 \text{ mcm}$ . Thus a qualitative correspondence can be claimed. The difference can be connected with the energy needed for bend of pure linear molecule in solid substance.

For  $\text{N}_2\text{O}$ , the nitrous oxide,  $\Lambda^{(\text{subl})} = 23 \text{ kJ/mole}$ ,  $\Lambda^{(\text{cond})} = 16.56 \text{ kJ/mole}$  and correspondingly  $\lambda^{(s)}_1 = 5.2 \text{ mcm}$  and  $\lambda^{(c)}_1 = 7.25 \text{ mcm}$ . They also correspond to observable peaks at 5 and 8 mcm.

For  $\text{CH}_4$ , the methane,  $\Lambda^{(\text{subl})} = 8.22 \text{ kJ/mole}$  and by (2.3)  $\lambda_1 = 14.6 \text{ mcm}$ , but observable peaks are located near to 8 and 5 mcm. Formally they can be attributed to condensation of dimers, trimers, and so on. But for more realistic consideration the knowledge of spectra of corresponding crystals are needed.

Thus it shows that all peaks of water vapors and of some air pollutions are identified as relating to phase transitions. It can lead to simple methods for detection of air pollutions and can be generalized by consideration of other gases. Moreover as processes of solidification

and evaporation can be reiterated and its repeating leads toward several mechanisms of reorganization or canalization of electromagnetic energy in atmosphere.

Possibilities of stimulating phase transitions by external resonant radiation can lead, in principle, to the control of atmospheric processes.

For further development of offered theory some experiments seem needed. The most simple between them can be the establishing a difference of "gases peaks" during daylight hours and nightly. But laboratory investigation of latent energy emission should be also very desirable.

The offered theory can has direct significance for examination of planetary and nebulae atmospheres. So, it can be applied, in particular, to the very old problem of the Great Red Spot of Jupiter: its coloration can be connected, at least particularly, with processes of condensation and crystallization of ammonia and its compounds. But such approach requires laboratory investigations.

## 7. SONOLUMINESCENCE AS UNIQUE EFFECT OF ENERGY CONCENTRATION

The phenomenon of sonoluminescence (SL) consists in the lightening of cavitation bubbles, induced in liquids by acoustical waves (general reviews [32,33]. The investigations of the single-bubble SL even in pure water gave surprising results: the period of irradiation  $T < 50$  psec for acoustical wave with  $f \sim 25$  kHz under compression of the bubble from  $R \sim 40$  mcm till  $R' \sim 0,1$  mcm. Hence it seems that concentration of energy reaches no less than  $10^{12}$  fold, a record value for all known nonnuclear processes, and even approaches to the threshold of D-T reactions.

As yet there is not any adequate or conventional theory, which could elucidate the origin of onset of SL, its spectrum, its influence on some exotical chemical reactions, etc.

We attempt to explain these phenomena on such a way [34]. The cavitation bubbles must be filled by vapor molecules, which will condense on the surfaces under compression with liberating of their latent energy by formation of new  $n$  electron bounds for each molecule ( $n \cong 2$  for water). Therefore the latent energy may be irradiated on the characteristic frequencies. These quanta may be reabsorbed by neighboring resonance bounds and so on (confinement of radiation in the extended two-level system) till possible complete thermalization. But if their density becomes sufficiently big, it may begin the processes of multiphoton harmonics generation, described in our article above [35], for which the liquid is transparent, and it can be just the effect of SL.

In our case the density of phase radiation can be estimated on such manner: under normal conditions into the vapor bubble of radius  $R \approx 40$  mcm enter  $N \sim 7 \cdot 10^{12}$  moleculae of vapor with complete latent energy  $W \sim 5,3$  erg. The rate of single bound radiation can be taken as

$$w = \left(\frac{4}{3}\right) \omega_2^2 |d|^2 \hbar^{-1} = 8.2 \cdot 10^3 \text{ sec}^{-1}, \quad (7.1)$$

where  $d = 1,85$  D is the molecule dipole moment. If the number of excitation in such effectively two-level system (molecules bounds in liquid and vapor states) is sufficiently big, then the Dicke cooperative mechanism may come into effect with time correlation of the impulse of order

$$\tau = (\hbar c / 2\pi) \tilde{R}^2 N_L |d|^2 \omega \sim 4.3 \cdot 10^{-13} \text{ sec}, \quad (7.2)$$

$\tilde{R}$  is the radius of volume with excited molecules across squeezed bubble,  $N_L$  is the Löschmidt number. It gives the duration of the Dicke cooperative flash  $t = \tau \ln(2N) \sim 13$  psec, which does not contradict to the observations [31, 32]. The mean power of cooperative radiation becomes

$$J = \frac{W}{4\pi \tilde{R}^2 t} = 2.4 \cdot 10^{10}, \quad [\text{W}/\text{sn}^2] \quad (7.3)$$

which must be compared with thresholds of multiphoton processes.

The main MPP for our purposes is the high harmonics generation  $N\gamma(\omega) + e \rightarrow e + \gamma(\Omega)$ , where  $\Omega \sim N\omega$ . Its rate could be calculated in the scope of QED via  $(N - 1)$ -order one-connected S-matrix element without account of intermediate states, which can not be developed between fast photon absorptions.

In the MPPs theory it demonstrates that in the strong radiation field sequential photon absorptions are such sufficiently fast, that the electron wave function could not altered between them. As the result the N-photon reaction goes as one-photon process with photon frequency  $N\hbar\omega$ , but with accept of the rate of virtual absorption of N photons.

From (7.3) follows that the threshold for N photon harmonics generation is

$$J \geq J_N = N\hbar\omega / \sigma_{\text{tot}}\tau_2 = 7 \cdot 10^{12} N\hbar\omega^3 [\text{W}/\text{cm}^2] \quad (7.4)$$

( $\hbar\omega$  is in eV-s), which is in agreement with the known experimental data for MPPs. At comparison with (7.3) it gives  $N = 8 \div 10$ , which just present the visible SL spectra. It must be noted that at the Poisson-type quasicontinuous background there can be manifested some peaks, connected with recombination lines of OH and so on, and with resonant lines of dissolvable atoms/molecules, as the probability of their levels occupation may be high enough. So in dilute solutions of alkali salts appear the intensive emission peaks of Li ( $\lambda = 0,67$  mcm, i.e. the radiation with  $N \sim 8$  or 9), Na ( $\lambda = 0,59$  mcm;  $N = 9, 10$ ), K ( $\lambda = 0,77$  mcm,  $N = 7, 8$ ), Ca ( $\lambda = 0,42$  and absence of line with  $\lambda = 0,39$  mcm) etc. It must be marked the spectrum of dodecane with series of broad peaks, corresponding to  $N = 8 \div 12$ . Some chemical reactions in the cavitation bubbles can be considered as photochemical ones, etc.

It may be claimed that the proposed theory is responsible for all present effects of SL and in addition gives the essential arguments in favor of existence of phenomena of radiative phase transitions. On the other hand it can be concluded that further significant increasing of SL power concentration is impossible, since its flashes depend on the position of transparency

band of liquids, but not from the initial acoustical power. Hence this phenomenon does not seem to be a perspective one for cold nuclear reactions.

## CONCLUSION

Let us enumerate the results and some further perspectives.

1. Characteristic radiation corresponding to the first order phase transitions in more ordered states exists and can remove out the latent energy of transition.
2. General quantum view requires an existence of stimulated emission along a spontaneous one. Therefore it predicts possibility of high intensity laser effects realized fast removal of latent energy on the characteristic frequencies and their harmonics.
3. Besides technology the observation of transition radiation may have a big role for climatic problems. Possibility of stimulating phase transitions by resonance irradiation can lead to control of weather processes.
4. In the pure scientific sense must be mentioned that this phenomenon, for the first time, ascertains the internal conformity between the thermodynamic and spectroscopic magnitudes. It demonstrates possibilities and perspectives of spectroscopy of phase transitive radiation and even perspectives for control the speeds and directions of crystallization processes.

## ACKNOWLEDGMENTS

The most part of experimental and observational data were compiled and discussed with V. A. Tatartchenko and J. Lapides, theoretical bases were repeatedly discussed with M. I. Molotsky, I. I. Royzen, M. Ya. Amusia and M. Tsindlekht, all problems were continuously considered with G. M. Rubinstein. I am deeply indebted to them.

## REFERENCES

- [1] Perel'man, M. E. (1971). *Phys.Lett. A*, **32**, 411; *Sov.Phys.-Doklady*, **203**, 1030 (1972); **214**, 539 (1974).
- [2] Perel'man, M. E. & Tatartchenko, V. A. (2008). *Phys. Lett. A*, **372**, 2480.
- [3] Perel'man, M. E. <http://arxiv.org/abs/0905.0471>.
- [4] Schwinger, J., De Raad, L. L. & Milton, K. A. (1978). *Ann. Phys. (NY)*, **115**, 1, 388.
- [5] Milonni, P. W. & Lerner, P. B. (1992). *Phys. Rev. A*, **46**, 1185; Milonni, P. W. (1994). *The Quantum Vacuum*. L.: Academic,.
- [6] Baly, E. C. (1920). *Phil. Mag.*, **40**, 15; Schaefer, C. & Matossi, F. (1930). *Das Ultrarote Spektrum*, B.: Springer, S. 284.
- [7] Kittel, C. (1963). *Quantum Theory of Solids*. NY, Wiley, 320.

- [8] Perel'man, M. E. (2007). *Phil. Mag.*, 87, 3129.
- [9] Ginzburg, V. L. & Tsytovich, V. N. (1979). *Phys. Rep.*, 49, 1; *Transient Radiation and Transient Scattering*. M.: Nauka, 1984 (In Russian).
- [10] Barsanti, M. & Maccarrone, F. (1991). *Riv. Nuovo Cimento* # 14; Chandra, B. P., Verma, P. K. & Ansari, M. H. (1997). *J. Phys. C.*, 9, 7675.
- [11] Perel'man, M. E. (2009). *Int. J. Theor. Phys.* 48, 2579; arXiv: quant-ph/0903.2780
- [12] Perel'man, M. E. (2007). *Ann. Phys. (Leipzig)*, 16, 305.
- [13] Perel'man, M. E. (2005). *Ann. Phys. (Leipzig)*, 14, 733.
- [14] Kawazoe, T. et al. (2005). e-J. *Surf. Sci. Nanotech.*, 3, 74 and references therein.
- [15] Berestetski, V., Lifshitz, E. & Pitaevski, L. (1971). *Relativistic Quantum Theory*. Oxford: Pergamon.
- [16] Lifshitz, E. M. & Pitaevskii, L. P. (1981). *Statistical Physics II*, Pergamon Press, NY.
- [17] Perel'man, M. E., Rubinstein, G. M. & Tatartchenko, V. A. (2008). *Phys. Lett. A*, 372, 4100.
- [18] Hirschfelder, J. O., Curtiss, Ch. F. & Bird, R. B. (1954). *Molecular Theory of Gases and Liquids*. J.Wiley.
- [19] Braun, W. F. (1956). *Dielectrics*. In: *Handbuch der Physik* (Heraus. S.Flügge). XVII, 1. Springer.
- [20] Jackson, J. D. (1962). *Classical Electrodynamics*. J.Wiley.
- [21] Perel'man, M. E. (1981). *Astrophysics*, 17, 213.
- [22] D. R. Lide (Ed.), *Handbook of Chemistry and Physics*. CRC Press, 2003; *Lange's Handbook of Chemistry*. 16th Ed., McGraw-Hill, 2005; P. Patnaik. *Handbook of Inorganic Chemicals*. McGraw-Hill, 2002.
- [23] Molotsky, M. I. & Peregud, B. P. (1981). *Sov. Tech. Phys.*, 26, 369; Abramova, K. B. et al. (1985). *Sov. Opt. Spectr.*, 58, 809.
- [24] Nikolaev, I. V., Kidyarov, B. I. & Kozharo, A. P. (2004). Abst. III Int.Conf. "Kinetics and mechanisms of crystallization", Ivanovo, Russia, 34.
- [25] Tatarchenko, V. A. & Umarov, L. M. (1980). *Sov. Phys. – Crystallography*, 25, 748.
- [26] Tatarchenko, V. A. (1979). *Sov. Phys. – Crystallography*, 24, 238; Umarov, L. M. & Tatarchenko, V. A. (1984). *Sov. Phys – Crystallography*, 29, 670.
- [27] Mestvirishvili, A. N., Directovich, J. G., Grigoriev, S. I. & Perel'man, M. E. (1977). *Phys. Lett.*, 60A, 143.
- [28] Hasler, F. et al. <http://antwrp.gsfc.nasa.gov/apod/ap020323.html>.
- [29] Nichols, L. W. & Lamar, J. (1968). *Applied Optics*, 7, 1757.
- [30] Potter, W. R. & Hoffman, J. G. (1968). *Infrared Physics*, 8, 265; Ayad, M. (1971). *Infrared Physics*, 11, 249.
- [31] Kiehl, J. T. & Trenberth, K. E. (1997). *Bull. Am. Met. Soc.*, 78, 197.
- [32] Brenner, M. P., Hilgenfeldt, S. & Lohse, D. (2002). *Rev. Mod. Phys.*, 74, 425.
- [33] Suslick, K. S. & Flannigan, D. J. (2008). *Ann. Rev. Phys. Chem.*, 59, 659.
- [34] Perel'man, M. E. (1996). In: Int. A. D. Sakharov Conf. Phys., Proc., 2nd, (I. M. Dremin, & A. M. Semikhato, Eds.), World Sc. Pub., Singapore, 1997, 660-3.
- [35] Perel'man, M. E. This collection, Chapter 2.



## ***Chapter 8***

# **APPLICATION OF PULSED LASER DEPOSITION FOR PUTTING MULTI-LAYER COATINGS ON THE INNER SURFACES OF HOLLOW OBJECTS**

*Alexandr Alexandrovich Lozovan,  
Stanislav Vladimirovich Frangulov  
and Denis Vladimirovich Chulkov\**

“MATI”-RSTU named after K.E. Tsiolkovsky  
121552, Orshanskaya street, 3, Moscow, Russian Federation.

## **ABSTRACT**

Presented here are the analysis results of the ability of Pulsed Laser Deposition methods for putting a multi-layer multi-component coating with single-layer thickness in the nano-scale range as well as micro- and nano-composite coatings on the inner surfaces of hollow objects. Also reviewed are mass-transporting processes, occurring during the application of double-component coatings by Pulsed Laser Deposition methods on the inner surface of long tubes of small diameter ( $L/d > 50$   $L \approx 900\text{mm}$ ,  $d \approx 13\text{mm}$ ). With XPS and RBS methods, the structure and composition of double-component multi-layer coatings with single-layer thickness  $\approx 30\text{ nm}$ , obtained on special installation equipped with YAG:Nd<sup>+</sup> Laser LTI-207, is investigated. A device to provide target changing during the deposition process without vacuum braking is developed. We determined conditions of obtaining multi-layer coatings with single-layer thickness in nano-scale range and methods of preliminary inner surfaces cleaning of said objects by means of hollow cathode glowing discharge with partial plasma filling of cathode cavity. We considered different schemes of cleaning inner surfaces of tube-like objects. Possible applications of the presented method for treating of said objects in individual or serial production, instrument decisions providing realization of the presented process and its perspective are discussed.

---

\* Corresponding author: e-mail: plasma@mati.ru

## 1. INTRODUCTION

The use of ion-plasma processes (such as ion implantation, application of coatings) for treatment of intricate shaped product surfaces presents a number of difficulties relating to obtaining uniform surface treatment over the entire surface of the products. The difficulties are aggravated when treating the inside surfaces of hollow products such as tubes. The analysis of papers related to coating deposition onto inner surfaces of tubes by ion-plasma methods showed that the main limiting parameter is the minimal diameter of tubes. Moreover, in most considered processes of deposition, there is a problem of securing of the thickness uniformity along the treated surface.

Ion-plasma methods of coating deposition onto inner surfaces of tubes may be divided into two classes:

- particle flux is formed outside of the cavity under treatment and then transferred to the surface of the cavity;
- source of the particles is inside the cavity.

Solutions of the first type must guarantee good flux controllability to secure the uniformity of deposition along the surface, which is practically impossible with long tubes.

In the second case certain difficulties appear when constructing a deposition device (especially for small cavities), capable of securing controllable process of deposition and at the same time providing simple retuning in case of change in the size of workpieces. Therefore, modification of the inside surfaces of tubes by well-known methods (for instance, magnetron sputtering of coatings [1]) were carried out with tubes of 50 mm or greater inner diameter. The possibility of using a coaxial discharge system [2] for long thin tubes is also doubtful. Modern industry requires tubes with parameters  $d = 5 — 10\text{mm}$ ,  $L/d = 50—100$  ( $L$ —tube length,  $d$  – inner diameter) for such treatment. Thus, the problem of modification of the inner surface of relatively long tubes, small in diameter, is rather pressing.

It is obvious that a plasma source of small size conveyed inside tubes could be exploited for ion-plasma treatment of the inner surfaces of long thin tubes. When treating inner surfaces of straight tubes, this task can be accomplished by means of the laser plasma generated while a target, placed inside the tube, is exposed to pulsed laser irradiation.

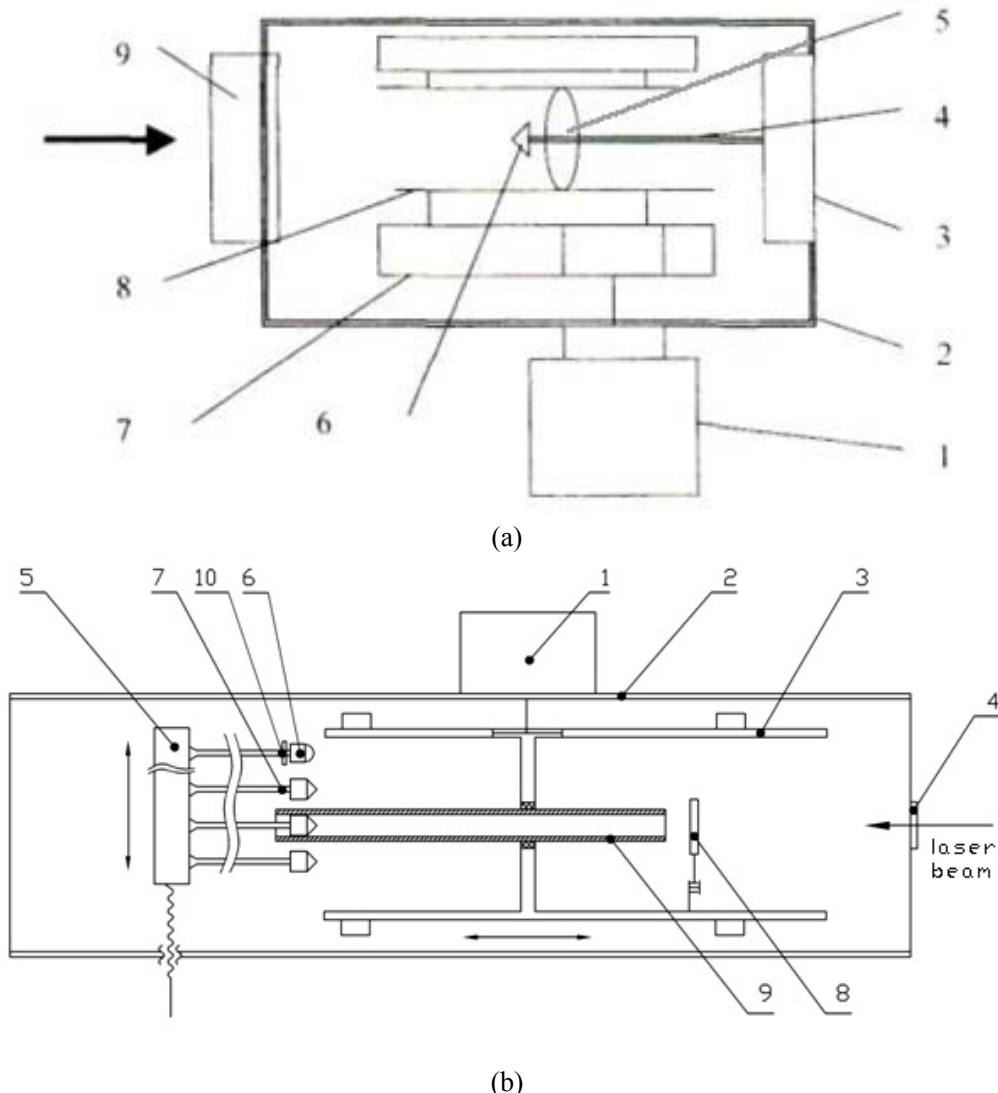
Unique characteristics—high power density, low angular divergence and ability to transfer energy over a long distance—make laser beam a highly suitable instrument for depositing onto inner surfaces of long straight tubes with small diameter.

During the previous years, PLD (Pulsed Laser Deposition) became commonly used for depositing of thin films as a method providing the possibility to obtain films of controllable composition. Composition and structure of metal films essentially depend on the deposition speed and energy of particles, which are noticeably higher in PLD process than in common vapor deposition processes. Intensity of radiation of pulse lasers, used for PLD is in the range  $5 \cdot 10^{12}—10^{14} \text{ W/m}^2$ , that is in the range of intensive vaporization of materials by nanosecond duration of pulse. Thus at the present time PLD method by its own characteristics practically has no alternative for applying coatings onto inner surfaces of long tubes of small diameter.

This method provides precise control of coating thickness, deposition at low temperatures of substrate, sputtering of nanocrystalline and amorphous films with good structure. The

properties of thin films generated by PLD are widely dependent on plasma plume characteristics [6]. The ionic component in plasma plume gives wide abilities of varying of coating properties.

Recently intensive investigations were carried out in the field of developing new nanostructured hard and super hard coatings, notable by high wear and oxidation resistance [7].



- The work chamber of the laser testing bench: 1—turbo-molecular pumps, 2—vacuum chamber, 3—high-voltage transformer, 4—target holder pin, 5—fluoroplastic bush, 6—conical target, 7—longitudinal transposition gear, 8—tube, and 9—door.
- The test bench scheme for applying multi-layer coatings with prior cleaning by discharge: 1—transporter transferring mechanism, 2—vacuum chamber, 3—transporter, 4—window for laser beam, 5—block of targets, 6—anode, 7—target, 8—link with a second anode, 9—processing workpiece, 10—insulator preventing gas flow-out of the tube during cleaning process.

Figure 1. Inner surface treatment process chart.

However, in spite of impressive achievements in creating hard and super hard nanostructured coatings, it would be well to notice, that most of them were applied to outer surfaces of specimens. Applying nanostructured coatings on inner surfaces of cavities of different shape (including tubes) is one of the most complicated tasks of ion-plasma surface modification technology.

Here we present a review of previous and recent results in the field of using the PLD method for applying metal coatings (single-component [8], double-component, multi-layer [9], etc...) on inner surfaces of long tubes with small diameter.

## 2. EXPERIMENTAL EQUIPMENT

The investigations were run on a laser testing bench designed specifically for this purpose and consisting of seven separate units: the processing unit comprising the work chamber and beam with laser beam scanning system, control unit, laser power supply, glow discharge power supply, pulse generator of accelerating voltage and vacuum system.

An LTI-207 laser based on yttrium aluminum garnet activated by neodymium, with pulse pumping and modulated quality was selected as a laser emission source with the following parameters: wavelength  $\lambda = 1.06 \mu\text{m}$ , maximum pulsed ray energy  $W = 1\text{J}$ ; pulse duration  $\tau_1 = 5\text{--}13\text{ns}$ ; pulse frequency  $f = 1\text{--}30 \text{ Hz}$ ; emission divergence  $\gamma = 3 \text{ mrad}$ .

The laser beam enters through the window into the work chamber (Figure 1a) and is scanned over the surface of the conical target (6). Scanning is relied on to extend a lifetime of the target and secure a constant density of vaporizable material (when laser emission has a constant power) since it inhibits the formation of craters on the surface.

The work chamber represents three cylindrical compartments mounted horizontally and joined together into a single vacuum module. The chamber (2) is pumped by two turbo-molecular pumps (1). A high-voltage transformer (3), to which the target holder pin (4) is fixed and connected electrically, is mounted at one end of the chamber. The other end of the pin is supported by a centring fluoroplastic bush (5). There is a door (9) with a window for laser emission fixed at the other end of the chamber. When being treated, the tube (8), conveyed along the chamber axis in the course of spraying, is secured to the longitudinal transposition gear (7) including a rack-and-pinion drive. The target is rigidly connected to the focusing system (the target is fixed firmly to the focus of the optical arrangement), both being coaxial with respect to the tube surface treated.

The focal length is 1.2 m. The focused beam diameter being 0.3–0.4 mm in the working laser mode without modulation, the scanning circle diameter determined by a laser beam trail on a photographic paper is equal to 5 mm at the focusing point. The laser beam trail on the target is 2 mm wide in the modulation mode at maximum power, the scanning circle size being the same. The maximum density of laser emission on the target is  $1.3 \times 10^{13} \text{ W/m}^2$ , which is enough to secure the formation of the plasma flame on targets made of any material. This provides a way of obtaining ions of any solid substances, including those of refractory materials.

To impart additional power to ions of the laser plasma, a high-voltage pulse between the target and the product is applied to the pin of the target holder through the pulse transformer from a high-voltage power generator. The generator operates in standby mode and is triggered

by synchronized pulses from the laser power supply. The pulse duration of the accelerating voltage is chosen on the basis of the relation:

$$\tau_1 < \tau_a < \tau_b,$$

where  $\tau_1$  is the pulse duration of laser emission,  $\tau_a$  the pulse duration of the accelerating voltage, and  $\tau_b$  is the time required to initiate a discharge inside the tube.

To make a fine-tuning of principles of depositing multi-component and multi-layer coatings on inner surfaces of tubes the laser testing bench was modernized (fig 1b). Special device providing alternate (by use of targets of different composition) applying of coating layers and prior surface cleaning in one technological circle.

This device consist of block of targets (5), with several pins holding targets of different composition (7) and one pin holding anode (6) fixed on it. Anode is fixed on the pin through insulator (10), which is preventing flow-out of the orifice gas during the cleaning process. All pins and the block of targets are insulated from each other to prevent appearing of parasitic discharges.

Whole device can make controlled shift perpendicular to the tube axis. Position of each target is also adjustable to provide precision.

Pin's length exceeds the tube's length to allow anode holding pin to push away diaphragm, fixed on one end of the tube to free the way for laser beam.

### 3. THEORY ANALYSIS

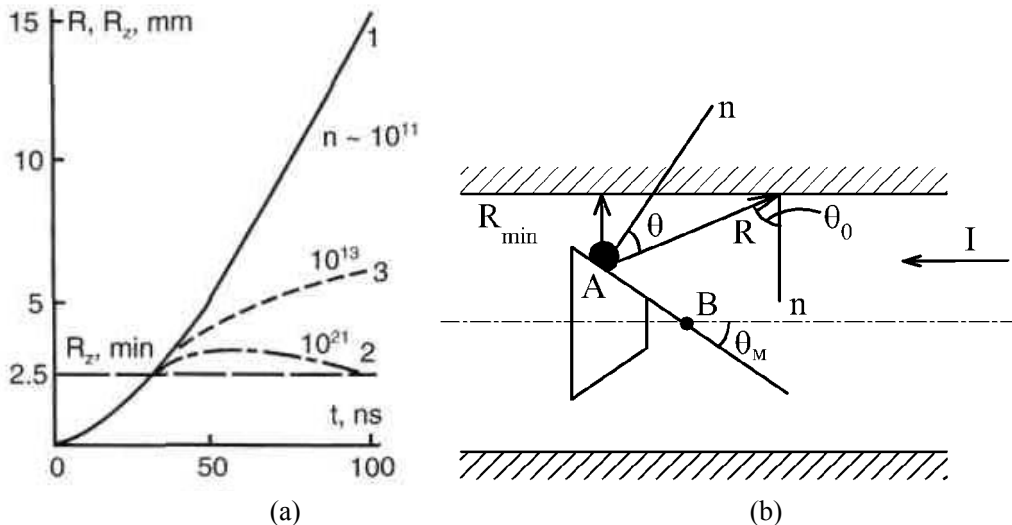
Specificity of mass transfer, occurring during surface cleaning and coating applying in almost closed cavity of tube requires the following:

- definition of optimal scheme and mode of inner surface cleaning of long tubes with small diameter before applying the coating.
- investigation of influence of process geometry on forming of the coating.
- investigation of mass transport processes during applying multi-layer coatings of nano-scale thickness.

**Surface cleaning.** As is well known surface cleaning before deposition is indispensable. After chemical cleaning specimens are cleaned in working chamber by glow discharge plasma or ion beam. At present time the laser surface cleaning becomes more and more widespread. With optimal parameters of laser it is possible to clean the surface with grazing incidence of laser beam, which is positive in our case.

However cleaning by glow discharge plasma was chosen considering following circumstances:

- need in simultaneous impact on considerable part of processing surface for continuous destruction of oxides including recurring deposition of oxygen atoms.
- complexity with using on our laser test bench of additional high speed laser beam scanning system for linear and circular inner surface scanning.



- a) - plasma spread: 1—neutral zone, 2—solid opaque plasma, 3— recombining plasma,  $R$ —size of plasma,  $R_z$ —length from the center of emission zone to different parts of the tube surface,  $t$ —time of process,  $n$ —density of plasma;
- b) - process geometry:  $I$ —course of laser beam.

Figure 2. Diagram of the coating application process:

Inner surface cleaning by glowing discharge plasma represent a hollow cathode discharge. In [8] cleaning of relatively short tubes (300 mm) was configured as cylindrical diode with inner anode where the target holder made of stainless steel played the role of anode. Main objective here was prevention of discharge between outer surface of the tube and chamber, which was achieved by selecting optimal parameters of the process and schemes of power supplying of the discharge.

In case with longer tubes (longer than 1m) realization of diode discharge scheme is technically difficult (for instance – because of anode deflection). A scheme with hollow cathode glowing discharge with short inner anode, conveyed along tube axis during the cleaning process could be used here.

For fast removal of oxygen atoms from the inner volume of the tube the cleaning process should be carried out at a minimal pressure. However thermal load of anode considerably restricts discharge current at low pressures. In hollow cathode discharge plasma we have two types of electrons – fast electrons and slow plasma electrons. In a hollow cathode discharge at low pressure [10], with anode surface area  $S_a \approx (2m/M)^{1/2}S_k$  (where  $S_k$  – cathode surface area,  $m$  и  $M$  – electron and ion mass, respectively) a positive anode potential fall is appearing and increasing with decreasing  $S_a$ . Anode current density becomes more than  $(M/2m)^{1/2}$  times greater (i.e. in two orders) than cathode current density, and so electrons speeded up in the negative volume charge at anode surface able to heat it up to melting temperature.

Thus, in case of inner position of anode and  $S_a < (2m/M)^{1/2}S_k$  it is necessary to secure transfer of slow plasma electrons to anode, preventing reaching of anode surface by fast electrons, in other words – raise the pressure.

In that case energy on anode  $W_a$  will be mainly determined by energy of plasma electrons diffused to anode  $W_{dif}$  and less – by plasma irradiation, which may be neglected. Then, according [11]

$$W_a = W_{dif} = (2\kappa T_e/e)I_a$$

where:  $\kappa$  - Boltzman constant,  $T_e$  – electron temperature,  $e$  – electron charge,  $I_a$  – anode current.

Discharge current may be restricted by using of glowing discharge with partial filling of the cavity by plasma. Therefore the task for experiments with surface cleaning is finding optimal pressure and discharge current.

**Deposition process geometry.** The plasma spread is shown in Figure 2a (plasma spread curves are taken from Ref. [12]) and it has spherical geometry. The rise-up portion of the plasma plume consists of an electron halo. Then, after a neutral zone, there is a collisionless plasma ( $n \approx 10^{11} \text{ cm}^{-3}$ ) followed by a recombining plasma ( $n \approx 10^{18} \text{ cm}^{-3}$ ) and, finally, goes solid opaque plasma ( $n \approx 10^{21} \text{ cm}^{-3}$ ). Spreading electrons and ions of the plasma flame move within self-coordinated field until they collide with the product surface. At this point the ion energy may reach several hundreds of eV. The plasma contains multicharged ions. As Figure 2b illustrates, under certain experimental conditions ( $d = 10 \text{ mm}$ ,  $R_{z \min} = 2.5 \text{ mm}$ ), different parts of the tube surface are exposed to plasma of varied density: the areas near the centre of emission zone (in  $R_{z \min}$  direction) are subjected to solid plasma; with increase in  $R_z$ , the collisionless plasma and recombining plasma act in succession. As this takes place, the density of plasma flow at the tube wall is  $j(z) \sim R_z^{-2}$ .

It is clear that this description of the process is rather approximate since the presence of the tube wall near the plasma plume will distort substantially the process pattern compared to the free plasma spread in vacuum shown in Figure 2a.

Angular distributions of laser plasma particles, both it's neutral and ion component, have great effect on forming of coating. Because of angular distributions of particles, and also because particles flux forming at conic surface disposed inclined to substrate surface, different zones of the surface are exposed to fluxes of considerably different energy density and particles charge state.

As it is known for angular distribution of point source  $f(\theta) = \cos^p \theta$  cross-section of film thickness distribution will be  $d(\theta) = \cos^{p+3} \theta$ , where  $\theta$  – angle between normal to target surface and direction of particle escape (Figure 2b). Then subject to conicity of target and in case of moving of the escape point of plasma A onto the tube axis in point B longitudinal distribution of deposited atoms will be  $d(\theta) \sim \cos \theta_M \cos^{p+3} \theta$ . Thus angular distribution of plasma particles  $f(\theta) = \cos \theta$  will result in longitudinal cross-section of film thickness  $d(\theta) \sim \cos \theta_M \cos^4 \theta$ . In our case the angle  $\theta_M = 45^\circ$ . However described mass transport processes will affect considerably on coating growth.

**Mass transfer influence on forming of multilayer coatings of nano-scale range thickness.** Particles spread of laser plume has rather wide angular distribution. In this case had of atoms to the surface is in the range from  $0^\circ$  to near  $90^\circ$ . As the atoms and ions of laser plume reach the inner surface of tube both deposition and scattering are occurring. In case of

relatively low energy of atomic particles (energy of laser plasma ions is in range of tens to hundreds eV and higher) it is caused by oblique incidence to the surface and dependence of sputtering ratio  $Y(\theta_0)$  and reflection factor  $R(\theta_0)$ . With all this, redeposition of considerable part of sputtered atoms on the tube surface and transfer of reflected particles to more distant from target zones of tube surface are taking place.

Quantitatively erosion of surface by ion sputtering is characterized by sputtering ratio Y, which is found as average amount of extracted from the surface of solid atoms by one incident ion (atom/ion). In our case during plasma spread ions mainly recombine and become fast atoms. However for univocacy of description these incident atomic particles will further be called ions independently of charge state.

During sputtering of multi-component targets partial sputtering ratio of surface  $Y_i$  is used. It is equal to average amount of i-kind atoms extracted by one incident ion  $Y = \sum Y_i$ . [13]

Sputtering ratio depend on ion properties (energy, mass, charge), target properties (mass, structure) and irradiation conditions (hade). Values of Y increase with energy of ions.

Y increases with hade  $\theta_0$  and has a maximum at certain for every material angle of incidence, and then sharply decreases to zero. Approximately for small angle of incidence [13]

$$Y(\theta_0) = Y(0) \cos^{-f} \theta_0,$$

where  $f = 1 \div 1,7$  for different ion-target pairs.

Escape angle distribution of sputtered particles for polycrystalline and amorphous materials under normal irradiation impact angle is a cosine function, thus intensity of sputtered particles flux with S direction is described by [13]

$$I(\theta_s) = I(0) \cos \theta_s,$$

were  $\theta_s$  – escape angle counted from surface normal.

When the angle of ion impact is not normal to surface and the energy of sputtered particles is not big then angular distribution of escaped particles tend to mirroring. The described process of surface sputtering generates flux of sputtered atoms, which mainly will be accumulated on surface again.

A part of impact ions with angle of incidence  $\theta_0$  will be reflected from the tube's wall in compliance with reflection factor value equal to [14]:

$$R(\theta_0) = R(0) + b(1 - \cos \theta_0)^\beta$$

where:  $0.2 < b < 0.6$  and  $1 < \beta < 2.6$  for different target materials. Some of the ions with the highest energy will be implanted in the wall.

Joint action of deposition, sputtering and reflection of atomic particles results in mixing of atoms in forming layer. Taking into account that target is conveyed lengthwise inside the tube, processes with equal impact angle will occur in every surface element. The final result will be superposition of processes shown before.

Finally, presented analysis shown, that an intensive mixing will take place as a result of described mass transfer processes. And that will lead to degradation of the layer boundaries in multi-layer coating.

Finding a function describing such mass transfer seems impossible. Mathematic simulation is also ineffective for various reasons. One of the reasons is roughness of the substrate. In most papers related to applying coatings of nano-scale thickness by PLD an ideally smooth substrates were used (for example – monocrystalline) [15-17]. In our case a polycrystalline polished substrates were used. Thus exact data may be obtained only by experiment.

Additional acceleration of laser plasma ions by applying pulse fields [18-20], was used only for single-layer coatings, as it will increase degradation of layer boundary in case of multi-layer coating.

#### 4. EXPERIMENTAL

**Single layer coatings.** In order for adhesion to be increased, cleaning of the tube inside surface by a glow discharge was performed. X18H10T stainless steel tubes with parameters  $d = 10$  mm,  $L = 300$  mm and foil tubes made of the same material with the same parameters were used as specimens. The specimens were rinsed in acetone and alcohol before treatment. The targets were made of copper and molybdenum.

Adhesion was tested by a film elasticity check procedure (bending the film and checking its elasticity) and was additionally tested by the standard peeling check procedure. In this, scotch tape was affixed to the specimen and torn off sharply and the scotch tape was then examined under the microscope for any evidences of coating being peeled.

The coating thickness was measured by two methods: a visual method with the help of a scanning electron microscope (for  $0.5 \mu\text{m}$  or more thick coatings), and the electron microprobe analysis (EMA) method (for thinner coatings) by means of a "Link-860" attachment to the "Camscan-4" (England) scanning electron microscope which was used to determine the coating composition with the standard processing program ZAF-4.

The following three coating experiments were run:

- I. without surface cleaning by the glow discharge and without ion acceleration;
- II. with surface cleaning by the glow discharge;
- III. with surface cleaning by the glow discharge and with acceleration of sprayed ions of the coating material.

**Long tubes cleaning.** It would be well to notice, that cleaning of inner surface of long ( $L \approx 1\text{m}$  and more) tubes with diameter in range  $\varnothing 10\text{-}20$  mm is difficult task in the view of it's practical realization, quality control and significant duration of the process. In [1] a tube with inner diameter  $d_{in} = 56$  mm and 120 mm long was cleaned with use of magnetic system during 60 min.

How it was shown before, a hollow cathode discharge with inner anode of small surface area may be used avoiding overheating of anode by limited discharge current and partial

filling cathode with discharge plasma. The results of experiments with current distribution along hollow cathode for described scheme are presented further.

Bit-sliced copper hollow cathode with  $d_{in} = 13,5$  mm (Figure 3) consisted of two long sections 430 mm long at each end with five short sections 40 mm long between them. The sections were insulated from each other by insulators < 1 mm thick. Hemispheric anode with radius 4 mm was made of stainless steel and inserted in insulator which completely closed cross-section of tube. Anode had an outlet, which was used to feed gas in discharge gap. The other side of the tube was closed by diaphragm of diameter in range 2-5 mm. Anode was conveyed inside the cathode. Anode position and current of each section were measured. Discharge was run in Ar at a pressure in vacuum chamber 4-54 Pa. Such scheme allowed to measure lengthwise current distribution of cathode at different pressures and diaphragms. To know pressure directly in the tube, an additional experiment was carried out.

Obtained current distributions are shown on Figure 4.

It is evident that with the pressure decreasing a depth of penetration plasma into cathode cavity is also decreasing, which corresponds to data obtained in [22] for hollow cathode discharge with external anode.

By conveying anode inside the tube and controlling voltage of discharge it is possible to carry out successful cleaning of inner surface of cathode on conditions that temperature of cathode and anode will be in acceptable range.

**Multi-layer coatings.** Chemically cleaned tube with diameter  $d_{in} = 13,5$  mm and length  $L=500$  mm made of stainless steel was put in a vacuum chamber. Then the chamber was evacuated to the pressure  $p = 3,5 \cdot 10^{-3}$  Pa and inner surface was cleaned by hollow cathode discharge with partial filling of cavity by plasma. After that Ti/Al and Ti/Nb multilayer coatings with single layer 5-30 nm thick were applied.

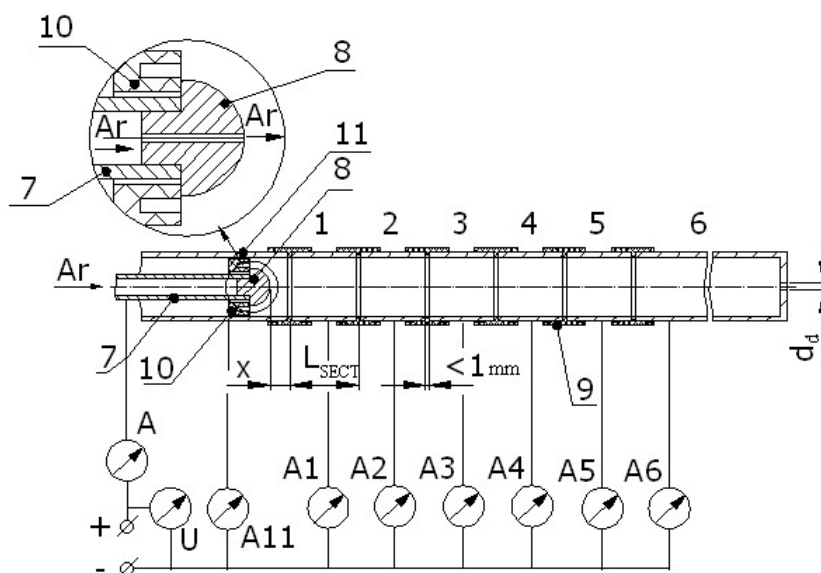


Figure 3. Experiment with bit-sliced cathode. 1-5 – short sections; 6,11 – long sections; 7 – gas and current feeding tube covered by insulator; 8 – anode; 9 – splitting insulator; 10 – anode insulator.

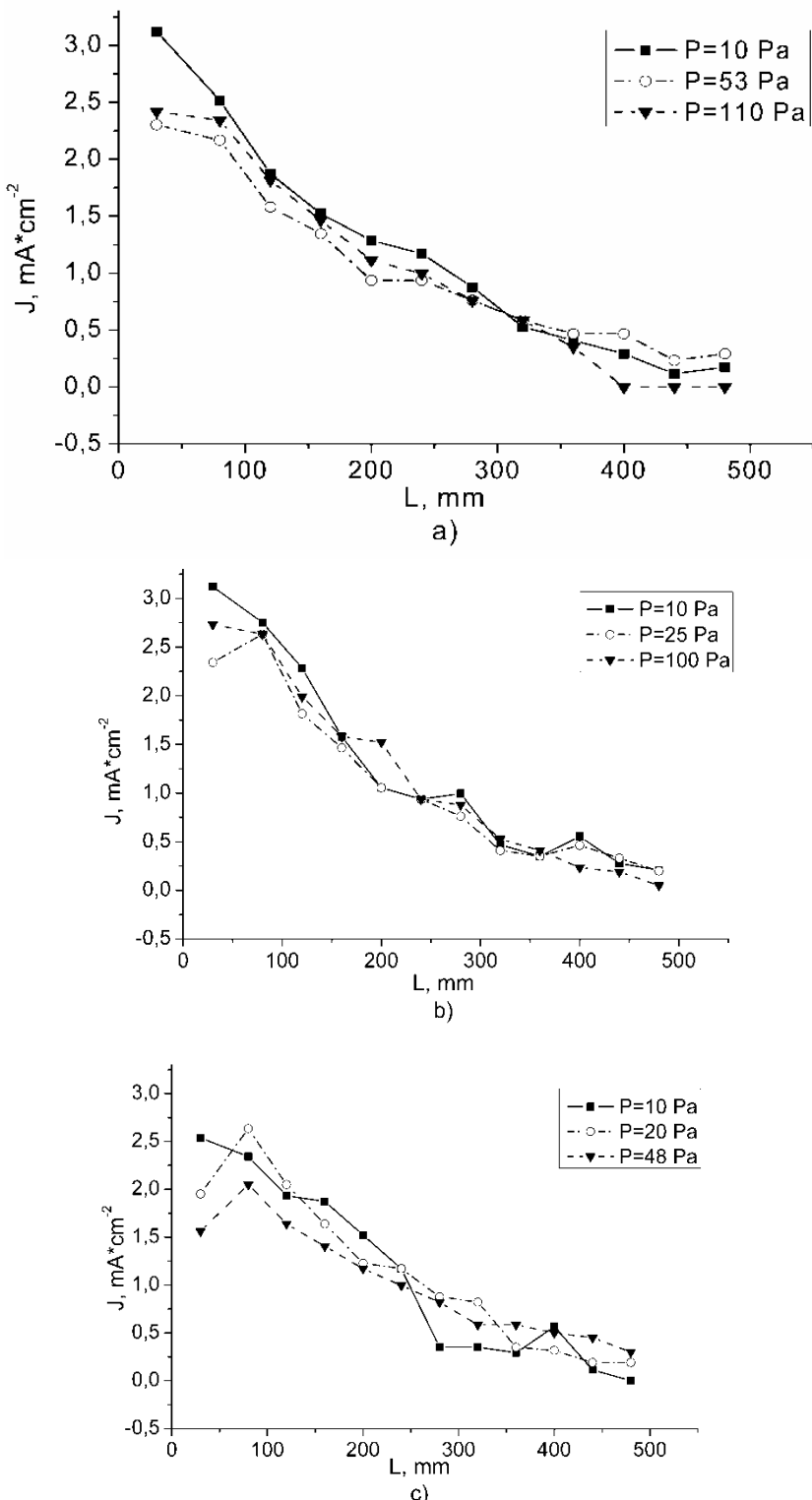


Figure 4. Current distribution along the cathode at different Ar pressure inside the tube. a) – diaphragm  $d_d = 2\text{mm}$ ; b) – diaphragm  $d_d = 3\text{mm}$ ; c) – diaphragm  $d_d = 5\text{mm}$ .

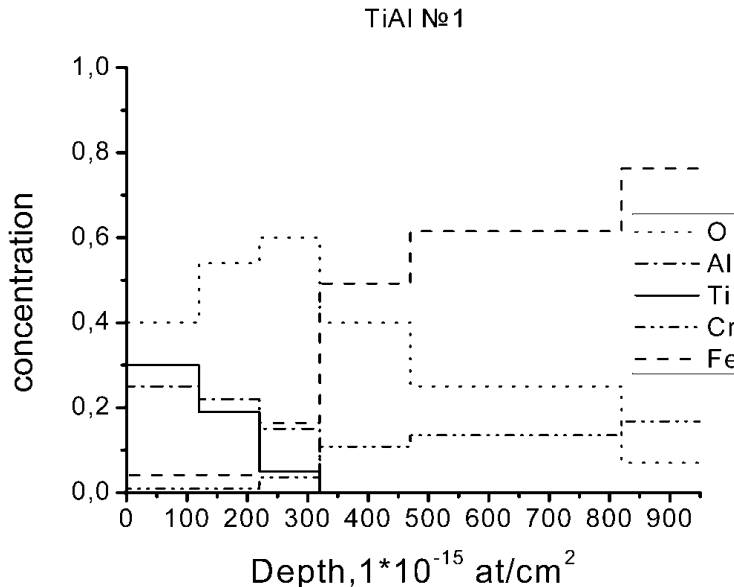


Figure 5. Depth profile of Ti/Al №1 (substrate – stainless steel 12X18H9T). Estimated single layer thickness for Ti – 6.1nm, for Al – 9.1 nm. Applied 5 pairs of layers.

Target changing device able to operate with up to 4 targets of different materials. However to work out the method of depositing multi-layer coatings and for simplifying of composition analysis only two materials were used.

Cross-section element distribution profile was obtained by RBS method. Investigations was carried out on electrostatic accelerator EG-8 at Institute of Nuclear Physics MSU by means of helium ion beam of 2MeV [23] and also on ion-beam complex “Sokol-3” at Institute of Microelectronics Technology and High Purity Materials with energy 1 MeV. The results of RBS analysis are presented on Figure 5 – 8.

Investigation of chemical and phase composition of near-surface layers was carried out by XPS method with XSAM-800 at energy resolution 1eV, stimulating irradiation of Mg K $\alpha$  with energy E=1253,6 eV and pressure P=5÷10<sup>-7</sup> Pa. Size of region being analyzed is 2mm.

As XPS able to analyse surface and a thin near-surface layer, after analysis of one layer etching by Ar<sup>+</sup> was carried out with energy 2,5 keV and current density j=0,4 mA/mm<sup>2</sup> and then the analysis was repeated again and so on. Content of elements and chemical links were determined. The results are shown on Figure 9 and 10.

## 5. RESULTS AND DISCUSSION

**Single layer coatings.** Experiments of type (I) described above demonstrated a satisfactory thickness uniformity and a satisfactory continuity of copper and molybdenum coatings, though their adhesion to the substrate is very poor.

Type (II) experiments showed that while performing cleaning by glow discharge, there is no discharge between the tube and the shell of the vacuum chamber, same at the tube edge where plasma areas of the same size (about 30 cm) are noticed.

Copper spraying carried out after the above-mentioned cleaning shows a satisfactory adhesion during both film elasticity and peeling check procedures. However, for molybdenum the coating peeled when the specimen was bent.

The set of experiments reveal that application of a high-voltage pulse at approx. 9 kV was needed to cause a discharge between the target and the tube because of the small clearance (1 mm).

Copper and molybdenum coatings formed under the conditions of accelerating voltage and preliminary cleaning by the glow discharge demonstrated satisfactory adhesion for up to 2 μm thick coatings for both test procedures. Coating composition was unchanged within the range of the analysis sensitivity (0.5-1% depending on an element's atomic number). Variation in uniformity of the 2 μm thick coatings did not exceed 10%.

Experiments to determine the distribution of coating thickness along the tube longitudinal axis were run for films formed using the third set of coating conditions. This was for Mo deposition on a motionless tube over a period of 30 min. The distribution of coating thickness obtained is shown in Figure 11.

Such distribution is caused not only by the  $j(z) \sim R_z^{-2}$  function but also by ions going out of the plasma flow to the tube wall under the influence of the accelerating voltage. The work of Abramov et al. [26] indicates that, given the longitudinal plasma input to the tube and ignoring recombination, the distribution of coating thickness along the tube axis is also of exponential nature when  $U_a \gg eT_e$  and  $n_{ii}(z)=n_i(z)$  (i.e. when the ion concentration is independent of the radius) which is given by

$$\delta(z) = \delta_0 \exp[-(V_{is}/V_{pl})(2z/d)],$$

where  $V_{is} = (T_e/m_i)^{1/2}$  is the velocity of the ionic sound,  $V_{pl}$  the rate of plasma flow movement,  $\delta_0$  the coating thickness at the tube input (under these experimental conditions  $\delta_0 = \delta_{max}$ ), and  $n_{it}$  is the concentration of ions at the tube wall.

The tube movement distributions are superimposed upon each other during the coating process with the result that each part of the tube surface is treated in the same way and experiences deposition, ion implantation and dynamic ion intermixing. The type of coating treatment can be selected by appropriate choice of the  $I$ ,  $U_a$  or  $\tau_1$  values.

Experiments conducted to determine the greatest possible thickness of Mo coatings that can be applied by the third method have shown that, with coatings of 5 μm or more thickness, areas of considerable peeling are observed, indicating substantial stress within these coatings.

## Cleaning of Long Tubes

Basing on the results of experiments of studying current density distribution along hollow cathode made of copper tube of diameter  $d_{in}=13.5$  mm and length  $L=1060$ mm at different pressures and diaphragms we can say following.

Cathode current density at all studied pressures and diaphragms exceeds  $0.4 \text{ mA}\cdot\text{cm}^{-2}$  over 400 mm from anode. This is satisfactory value for cleaning. It is also noticeable polysemantic character of the current distribution near anode during first 100mm, which is significantly depend on pressure. Current density may both raise or decrease at this length.

Such irregular current distribution was noticed earlier by other authors, but for quite clean surfaces. In this work parameters of discharge were investigated during the stage of cleaning.

Obtained value  $L_o/d_{in} \approx 30$  (where  $L_o$  – zone of effective cleaning) allows significantly increase speed of cleaning and treat long tubes by mean of anode conveying.

Selection of optimal pressure and limitation of discharge current let us transmit heating load mainly to cathode. That resulted in satisfactory thermal condition of cathode and heating of cathode, what is useful both during cleaning and deposition.

**Multilayer coatings.** Analysis of depth distribution of elements of Ti/Al №1 is shown on Figure 5. Two things are calling attention:

- high concentration of oxygen along the depth
- distribution of Ti and Al practically identical, that is evidence of complete mixing of layers.

The thickness of coating is 55 nm.

Distribution, obtained for Ti/Nb №1 (Figure 6) on the same substrate also has high concentration of oxygen and high degree of mixing. Thickness is 40 nm.

Increasing of layer number to 17 in Ti/Nb №2 has no effect (Figure 7). Thickness is 60 nm.

On Figure 8 one can see initial separation of layers. Mixing of atoms with substrate is visible only at the first stage of forming of coating.

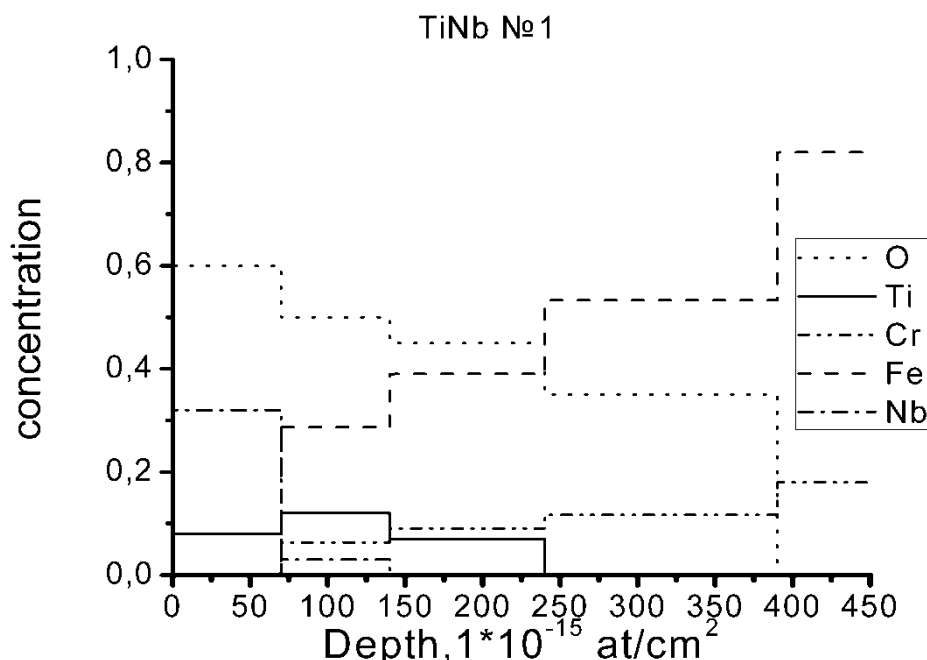


Figure 6. Depth profile of Ti/Nb №1 (substrate – stainless steel 12X18H9T). Estimated single layer thickness for Ti and Nb – 2 nm. Applied 11 pairs of layers.

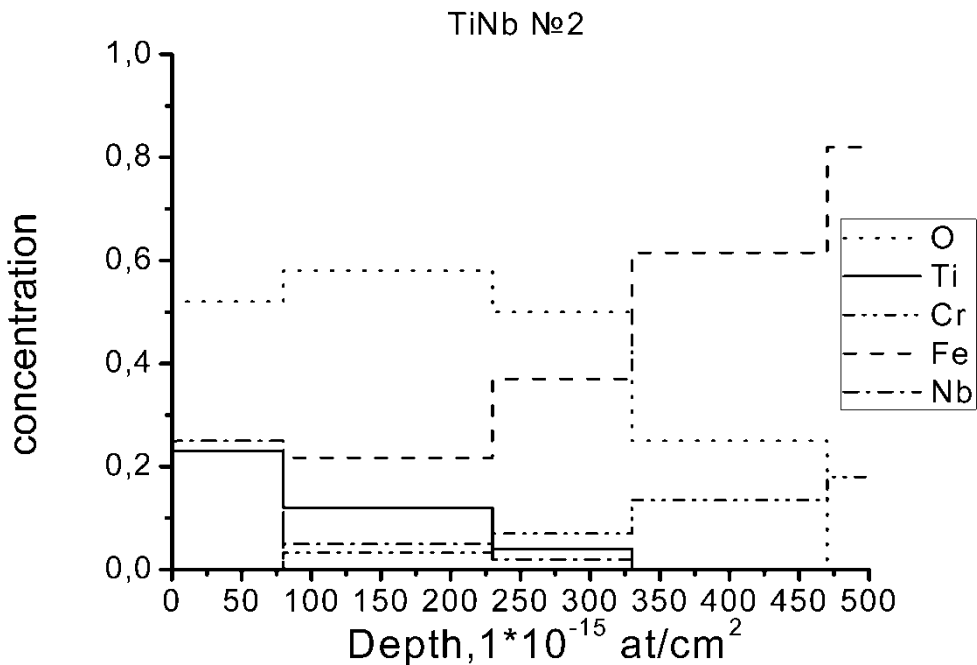


Figure 7. Depth profile of Ti/Nb №2 (substrate – stainless steel 12X18H9T). Estimated single layer thickness for Ti and Nb 1.4 nm. Applied 17 pairs of layers.

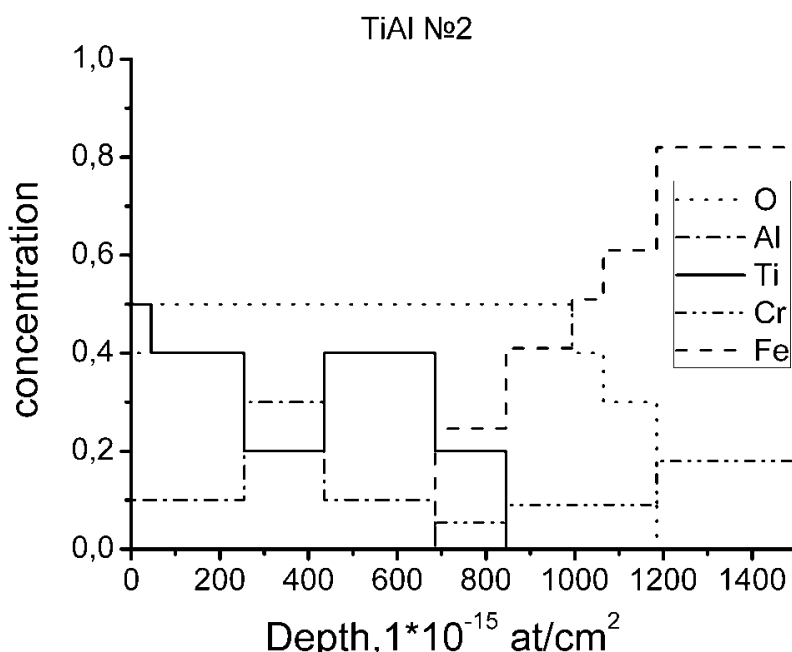


Figure 8. Depth profile of Ti/Al №2 (substrate – stainless steel 12X18H9T). Estimated single layer thickness for Ti and Al – 30 nm. Applied 3 layers.

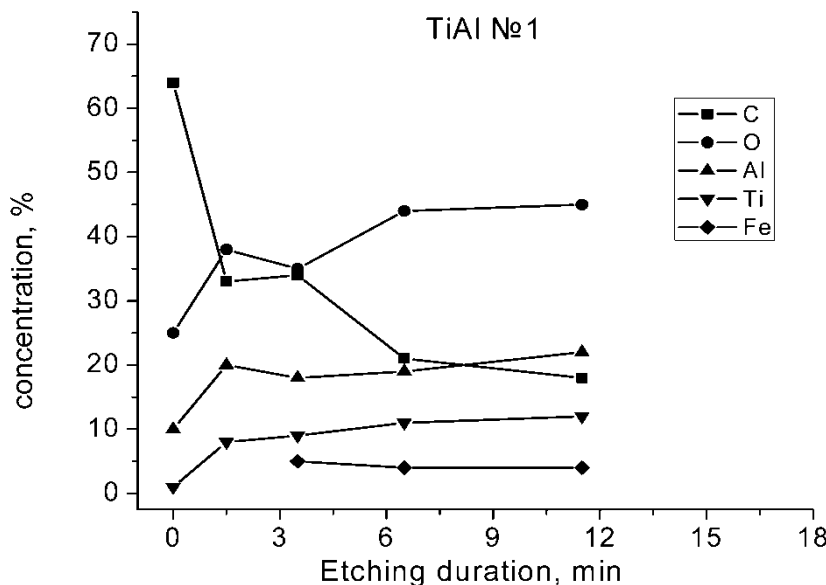


Figure 9. XPS depth profile of Ti/Al №1.

Examined distributions show that while applying very thick layers — in order of several nm — an intensive mixing is occurring. With the increasing of single layer thickness of each material, there gradually starts to form a layered structure, but interpenetration is still significant. High concentration of oxygen at near-surface region also affects the element distribution.

Smaller in comparison with expected thickness of coating on all specimens confirms assumption about mass transport, induced by spraying of substrate and reflection of depositing atoms. Moreover a high oxygen concentration near the surface inserts amendments.

Thus, investigation of implanted specimens was carried out by means of XPS which gives information about not only composition but also about chemical link types of surface elements and of elements in nearest monolayers.

Obtained distributions of elements (Figure 9 and 10) confirmed conclusions based on RBS results.

High concentration of carbon in XPS results call attention. However the reason is well-known. The specimens studied by XPS were studied before by RBS method and it is known that RBS leaves carbon film on the surface of specimen.

XPS spectrum also registered presence of pure metal and oxides of  $\text{TiO}_2$  and  $\text{Al}_2\text{O}_3$ . At the same time  $\text{TiO}_x$  oxides are also present.

Investigations displayed that deposited coating has complicated phase composition, consisting of metals and their oxides. Presence of certain phase at certain depth is determined by ratio of components at thin near-surface layers.

In conclusion it may be stated that such change of phase composition of surface layer with depth is connected with intensive mixing process of atoms of different material layers and substrate.

## CONCLUSION

Proposed scheme of hollow cathode discharge with partial filling of cathode cavity by plasma may be efficiently used for cleaning of long tubes of small diameter by conveying of discharge gap along the cathode.

Combined use of plasma cleaning and heating with proper parameters allows us to carry out high-quality cleaning of inner surface of the tube. It is easier to control the completion of cleaning for the described discharge schemes by current or voltage level of discharge.

The major result of this work is that the use of a pulsed laser evaporation technique for coating of metals over the inner surface of thin tubes has been very promising. The results show strong evidence for the importance of acceleration of the laser plasma ions. These experiments suggest that this technique is essential for adhesion to be increased especially for mono-layer coatings and for improvement of adhesion of the first layer to substrate in multilayer coatings.

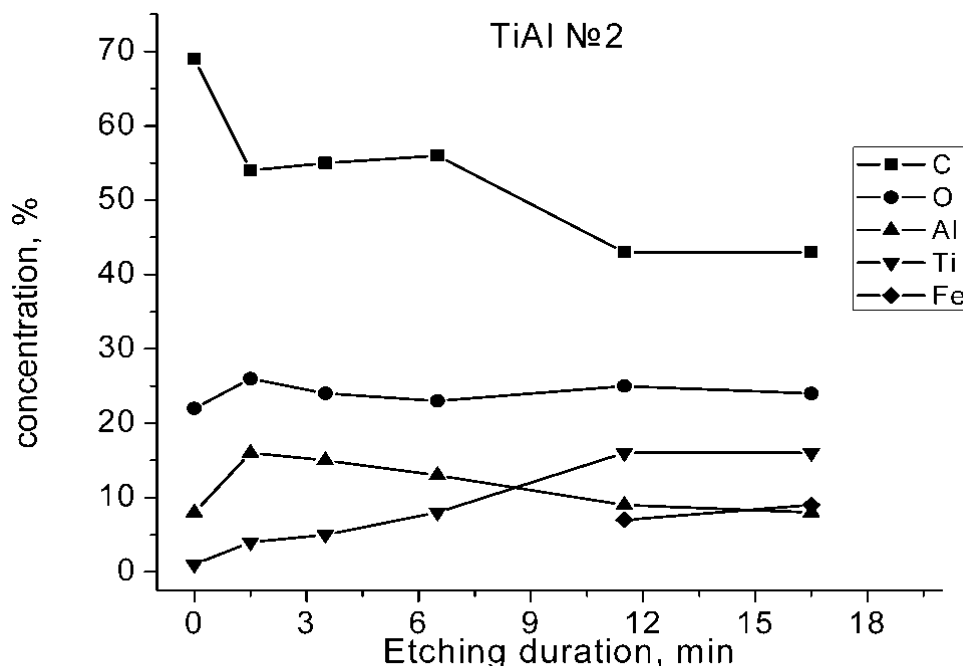


Figure 10. XPS depth profile of Ti/Al №2.

An analysis of processes of mass transfer during PLD-ing on inner surfaces of tubes was carried out. It is ascertained that for thin layers (thickness at 1–10 nm) made by PLD an intensive mixing process leads to the forming of a coating with complicated phase composition.

Shown before mixing process prevents forming of super lattice coating discussed in [7], but obviously multilayer coatings with thickness of single layer in order of tens and hundreds of nm may be created.

However, the present experimental evidence is not enough for a final analysis and further experiments are in progress.

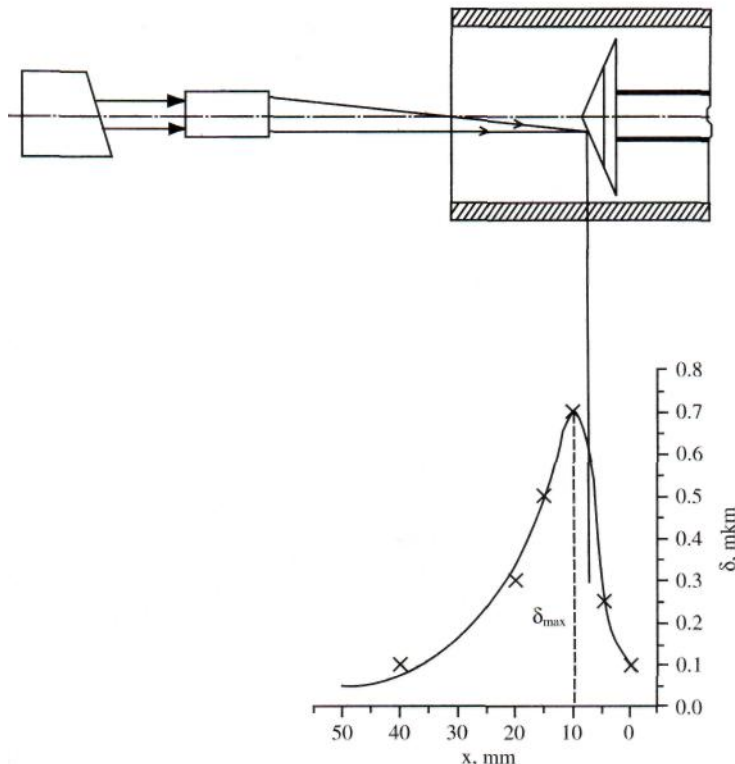


Figure 11. Distribution of coating thickness over the tube longitudinal axis; coating is applied when the tube is motionless:  $\delta$ —thickness of the coating,  $x$ —length along the tube.

## REFERENCES

- [1] Pavlov, DA; Turin, VN; Uchakov, AM. *12th International Conference on Ion-Surface Interaction—1995*, Zvenigorod, Russia, vol. T.2. Moscow: MP Informpoligraf, September, 5-8, 1995. 248-250 in Russian.
- [2] Fetherston Robert, P; Shamim Muhammad, M; Conrad John, R. Apparatus for plasma source ion implantation and deposition for cylindrical surfaces. U.S. Patent Number, 1999, 5, 988, 103. November, 23.
- [3] Ferris, SD; Learn, HJ; Poate, JM. Laser-solid interactions and laser processing. Proceedings of the 1978 Material Research Society, *AIP Conference Proceedings*, 1979, No. 50.
- [4] Jordan, R; Cole, D; Lunney, JG; Mackay, K; Givord, D. *Appl Surf Sci*, 1995, 86, 24-8.
- [5] Draper, CW. Lasers in metallurgy. In: Mukherjee K; Mzumder J; editors. *Proceedings of the Conference of Metallurgical Society of AIME*, Chicago. February, 1981. 67.
- [6] Novodvorsky, OA; Khramova, OD; Filippova, EO; et al. *Optics and Lasers in Engineering*, 32, 2000, 449-457.
- [7] Musil, J. *Surface Coating Technology*, 2000, 125, P.322.
- [8] Lozovan A. *Vacuum*, 2003, 70, 477.

- [9] Lozovan, A; Frangulov, S. *Bulletin of the Russian Academy of Sciences: Physics*. Vol., 2008, 72, No. 7, 953-955.
- [10] Metel, A; Crigoriev, S. Glowing discharge with electrostatic keeping of electrons. Monograph. – M.: *Yanus-K*, MSTU "Stankin", 2005, 296 in Russian.
- [11] Moskalev B. Hollow cathode discharge. M.: *Energiya* 1969.P.184
- [12] Basov, NG; Boiko, VA; Krokhin, OV; Skliskov, GV. *J Exp Theor Phys*, 1966, 51(4) in Russian.
- [13] Sputtering of solids by ion bombardment. Editor R. Berish, 2<sup>nd</sup> Issue-M.: *Mir*. 1986. 448.
- [14] Martynenko, UV. Interaction between plasma and surface. Overal results of science and engeneering. *Plasma physics*. Vol. 3.- M., 1982, C.119-175. in Russian.
- [15] Kazi, IH; Wild, PM; Moore, TN; et al. *Thin Solid Films*, 2003, 433, P.337-343.
- [16] Jen, SU; YU CC; Liv CH; Lee GY. *Thin Solid Films*, 2003, 434, P.316-322.
- [17] Liu, HD.; Zhao, YR; Ramanath, G. et al. *Thin Solid Films*, 2001, 384, P.151-156.
- [18] V. N. Nevolin, V. Yu. Fominskii, A. G. Gnedovets and V. E. Koshmanov. *Technical Physics*, 2005, 50, Vol.6, P. 705-710.
- [19] Fominski, VYu; Nevolin, VN; Romanov, RI; et al. *J. Appl. Phys.*, 2001, Vol. 89. P. 1449-1457.
- [20] Fominski, V; Nevolin, V; Romanov, R. et al. *Thin Solid Films*. 2002, Vol.422/1-2. 39-47.
- [21] Lozovan, A; Frangulov, S. *Svarochnoe Proizvodstvo*, 2009, Vol. 1, in Russian.
- [22] Kraindel, UE; Nikulin, SP. *Technical Physics*, 1992, 62, Vol. 4, P. 89-94 in Russian.
- [23] Burdel, KK., Chechenin, NG. Overal results of science and engeneering. Ser.: Charged particle beams and solid., Vol., 1. M. VINITI, 1990, C. 35 in Russian.
- [24] Doolittle, LR. Algorithms for the rapid simulation of the Rutherford backscattering spectra. *NIM*, B9, 1985, 344-351 in Russian.
- [25] Egorov, VK., Okhulkov, AV. Materials of 22<sup>nd</sup> international debate on physics of interaction between charged particles with crystals. M. MSU, 1993, 167-169 in Russian.
- [26] Abramov, IS; Vildgrube, VG; Kuznetsov, VG; Lisenkov, AA. Industrial developments in the deposition of metallic coatings. In: Soviet Union Conference on Progresivnai texnologii nanesenia metalopokrbitii, *Cheliabinsk. ChPI*, 1986, 57-61 in Russian.



## ***Chapter 9***

# **UNDERGROUND CAVITY 3D DETECTION USING LASER SYSTEM**

***Liu Xiling<sup>1</sup>, Li Xibing<sup>1</sup>, Anthony Comber<sup>2</sup> and Liu Kewei<sup>1</sup>***

<sup>1</sup>School of Resources and Safety Engineering, Central South University,  
Changsha, 410083, China.

<sup>2</sup>Measurement Devices Ltd, Silverburn Crescent, Aberdeen, AB23 8EW, Scotland.

## **ABSTRACT**

Safe and precise cavity detection, especially of dangerous or inaccessible voids, is essential to safe production in a working mine. Conventional underground cavity detection methods are briefly reviewed and their limitations discussed. Accurate 3D laser measurement systems are introduced. One of these laser systems was used to detect inaccessible underground cavities from the surface through boreholes at Luanchuan molybdenum open pit in China. The results from the scanner demonstrated very well the detailed level of information that can be collected in a cavity using this method, with the cavities' layout under various benches being fully mapped. The processed data can be imported into existing models in SURPAC and CAD and the roof and floor elevations from the model of the cavity was used to output sections which would be required at a later design stage. A minimum number of exploration boreholes can be coordinated based on the scanned data which therefore not only fully details the extent of the cavity, but also saves on the costs of exploration drilling. Finally, the advantages and disadvantages of laser detection systems are analysed, and a combination of laser scanning techniques and conventional survey methodology is proposed to detect these unknown underground cavities.

## **1. INTRODUCTION**

The worldwide demand for mineral products is rising due to the increasing shortage of resources and rising consumption resulting from rapidly expanding economies & international trade. These conditions have led in the last few years to a particularly prosperous time for the mining industry. However, in many places, further exploration has been seriously restricted or

been made extremely hazardous due to the presence of various abandoned, & unmapped underground cavities left over from previous mining operations. The disasters caused by cavities have been numerous & disastrous[1]. For example, in Chinese mines in recent years, disasters caused by underground cavities have frequently caused multiple fatalities: 29 people dead in a gypsum mine caused by the collapse of a cavity roof; 81 people dead in a gold mine caused by cavity water inrush in 2001; 13 people dead and 9 injured in a stone mine caused by a cavity roof collapse, 11 people dead in a copper mine cause by cavity water inrush in 2004; 36 people dead and another 33 injured in a gypsum mine caused by cavity roof collapse in 2005; 6 people dead and other 4 injured in a gypsum mine caused by large area roof collapse of an old cavity in 2006. It is clear then that accurate cavity detection & mapping is vital for dealing with such cavities & for ensuring safe mineral exploitation. Similarly, the accurate detection of cavities and voids under highways, construction sites and buildings etc is essential for their operation & the safety of those people who use and work on them.

Regarding conventional detection methods of detecting & mapping out cavities, these have required an understanding of the high precision equipment, of the complex theories behind this equipment, its deployment. It has also required deep analysis of the acquired data and details of the geology in the vicinity of the cavity. However, the geology around the cavity is often very complex & this greatly limits one's ability to interpret results, making accurate detection extremely difficult. Previously, the major goals of attempts to develop methods of cavity detection have been, firstly, designing more precise equipment to take the required observations; studying & interpreting the results of the observations to gain an understanding of the complex geology around the cavity; choosing different detection methods according to different prevailing geological conditions; and adopting multiple detection methods for each cavity. This latter point is to try to ensure that the different techniques verify each other, thus hopefully establishing more accurate & reliable results. However, cavity detection by these conventional methods can still not obtain a sufficiently accurate model of the cavity.

3D laser scanning however, does provide a means of highly accurate modelling of cavities. This method uses a pulsed, infra-red laser, measuring the 'time-of-flight' of the laser pulse to calculate distance measurements. This method is not affected by the geology around the cavity and obtains a very clear visual 3D model of the cavity in a very short time. It is the most accurate way to perform cavity detection.

Currently, the main methods of detecting cavities are: engineering drilling, geophysical exploration, hydrological experiments, gravity observation and magnetic observations. The main cavity detection methods are: micro-gravity method, DC electrical method, transient electromagnetic method (TEM), high-density resistivity method, ground penetrating radar technique, transient Rayleigh wave method, seismic tomography method (CT), shallow seismic exploration and radioactive gas measurement technique etc[2]. Different detection methods are favoured around the world depending on local conditions & preferred technologies. For example, in the USA, comprehensive detection techniques are used, particularly - the electrical method, electromagnetic method, micro-gravity method and seismic method. Japan is one of the leading places in the world for employing geophysical techniques: most commonly, the seismic wave method, electrical method, electromagnetic method and geophysical well logging; electrical method, transient electromagnetic method (TEM), seismic reflecting wave method, electromagnetic wave transmission method and radioactive gas measurement are mostly used in Russia, while ground penetrating radar is

well used in many European countries. Due to severe disasters in China caused by cavity collapses, various geophysical detection techniques have been used to carry out cavity detection[1,2].

There is much ongoing research into different detection techniques. Ground penetrating radar can provide a high resolution map at different levels of a geological body, and carry out scatheless detection of underground objects[3-5]; the high frequency electromagnetic detection method has the advantage of high detecting speed, low cost and a large control area, making it an effective method for geological disaster prevention[6]; based on a 2D simulation model, the 2D electrical method can obtain more accurate results than a conventional electrical method, and cost less than 3D one, making it the most economical method for cavity detection[7-9]; seismic share-wave reflection method can better distinguish the object in shallow stratum, which is difficult for conventional seismic methods to distinguish by detected shallow seismic information[10]. An on-site experimental study was performed in paper [11] aiming at investigating the difficulty of seismic signal interpretation caused by complicated geological condition; BIE (Boundary Integral Equation) was used to analyze shallow seismic measurements in paper [12]; the detection results tested by geological radar method, transient electromagnetic method (TEM), shallow seismic reflecting wave method, transient Rayleigh wave method and high-density resistivity method were commented in paper [13]. In order to overcome the limitations of single detection methods, a combined method which integrates different detection techniques was proposed to carry out cavity detection to achieve more accurate results; and this method was used to perform cavity detection which proved to be valid, especially for complex cavities[2,14-17].

In general, these various conventional methods do not easily produce accurate 3D models of the cavity under investigation. Further, since the detection of abnormalities by these methods is dependent on the rock mass and geological conditions around the cavity, different methods must be used according to the local geological condition. Given the complexity of geological conditions commonly found around cavities, the accurate interpretation of the results is very difficult. For this reason, various methods are combined to overcome the limitation of a single detection method, causing the operation to become more complex & costly.

In recent years, 3D cavity detection methods based on laser range finding techniques have been widely used in mines around the world. Results have proved it to be a very successful method of 3D cavity detection. As early as 1989, AFGANDML853 laser system was tested by the Gaspé mining company, its detection range was limited in 60 meters, and the system was not automated in any way. OPTECHG150 laser rangefinder with 100 meters detection range and 0.05% accuracy was tested also in Gaspé in Feb 1990[18]. A laser detector and automatic scanning equipment were fixed on a rigid rod to measure an excavated space at Noranda's technique centre in 1992 with encouraging performance[19]. Thereafter, laser rangefinders have been increasingly utilised in mines for automatic measurements, with the measured models being imported into existing, integrated mine maps & models[20]. These laser rangefinders and scanners have been used in mines for a wide variety of applications: performing the detection of cavities and excavation spaces; 3D modelling of underground spaces by mounting the laser on a moving vehicle[21]; scanning of rock mass joint surfaces[22], and monitoring vehicles in underground mines and open pits[23] etc. Some of the main manufacturers of laser surveying systems used in these applications are I-SITE in Australia, MDL in United Kingdom, OPTECH in Canada, CYPA in Unite states, RIEGL in

Austria and CALLIDUS in Germany. However, for particular, inaccessible cavities such as those under open pits, cavities under highways or buildings etc, the laser scanner needs to be deployed through a borehole if we want to carry out laser 3D detection as there is no other way of entering the void with laser equipment. This laser system therefore needs to have an extremely small cross-section to fit through the drilled hole. It also needs to be flexible, rugged, easy to deploy & recover, and to incorporate an orientation system to automatically correct the resulting data according to the angle of the instrument during the survey. At present, there are two kinds of laser detection system in the world which are designed to be suitable for surveys of inaccessible cavities: OPTECH's CMS (Cavity Monitoring System) and MDL's C-ALS (Cavity Auto-scanning Laser System). The CMS and C-ALS have been widely used in mines around the world[24-28] since the 1990s, but their application in mines of China commenced just a few years ago[29,30].

There have been many mines in China which have suffered terrible tragedies resulting from underground cavities. An open pit run by Luoyang Luanchuan Molybdenum CO., LTD. is severely threatened by such cavities under the working pit. Detection of cavities needs to be carried out on the surface, rather than from underground, and in this case, the laser instrument needs to be deployed through a borehole. For these reasons, due to its 50mm diameter, the C-ALS is the only suitable system for underground cavity detection in Luanchuan open pit. This is the mine where we choose to use the C-ALS to perform accurate 3D cavity detection with the object of providing detailed information on the layout and extent of the cavities in order to increase the safety of production on the mine.

## 2. CAVITY LASER 3D DETECTION TECHNIQUE

### 2.1. Principle of Laser 3D Detection

A laser is a device which emits light formed by stimulated radiation which is intense, concentrated and highly monochromatic. The lasers used in 3D cavity measurements are generally based on a laser measuring technique called 'time-of-flight'. The basic principle is to measure the time taken for a laser pulse to travel from the receiving optic to the target and back to the receiving optic. This time is then used to calculate the distance travelled,  $L$ , by the laser pulse. The conversion equation is[31]:

$$L = \frac{1}{2}ct$$

where  $c$  is laser propagation speed in the atmosphere, and  $t$  is the time taken for the laser travelling the measuring distance and back to the laser.

The raw data observed by the 3D laser scanner will be as follows: 1) the horizontal and vertical direction of the laser beam based either on the angle of a continuously rotating mirror, used to reflect the laser, or on the angle of the laser head, moved mechanically by motors in the instrument; 2) the distance between the instrument and the measured point, calculated from the laser pulse's 'time-of-flight'; 3) the intensity of the reflection of the scanned point. The data from 1) and 2) are used to calculate the three dimensional coordinate values, and the

reflection intensity is used to colour the measured points according to their signal strength[32].

Commonly, 3D laser scanners will uses the instrument's own internal reference frame shown in Figure 1.

Axes  $x$  and  $y$  are in the cross direction scanning plane and are perpendicular to each other. Axis  $z$  is perpendicular to the cross direction plane. Observation value  $S$  is the range observed with the laser, the horizontal scanning angle  $\alpha$  and vertical scanning angle  $\theta$  of every laser impulse are measured simultaneously through accurate timing. Using this data, the equation for calculating the 3D laser coordinate is[33]:

$$\begin{cases} x = S \cos \theta \cos \alpha \\ y = S \cos \theta \sin \alpha \\ z = S \sin \theta \end{cases}$$

## 2.2. Cavity Auto Scanning Laser System (C-ALS)

Having a small cross-sectional profile and accurate, integrated orientation system, MDL's C-ALS laser scanner was selected to carry out the detection of cavities under the open pit under investigation. C-ALS scans the cavity by using the "time-of-flight" laser measurement technique described above. The C-ALS probe, which incorporates the laser, is just 50mm in diameter. The unit is designed to be deployed down boreholes up to 300 m long, as well as to be deployed uphole and along horizontally holes up to 100 m long. Due to the mechanical rotation of the laser head on the probe, a 3D scan can cover the entire void up to a range of 150 m with an accuracy of  $\pm 5$  cm. The scanned data in its raw form of a 3D 'point cloud' can be processed into a 3D model, and then exported & integrated into most current mining software packages such as SURPAC, VULCAN, AutoCAD, DATAMINE etc[34].

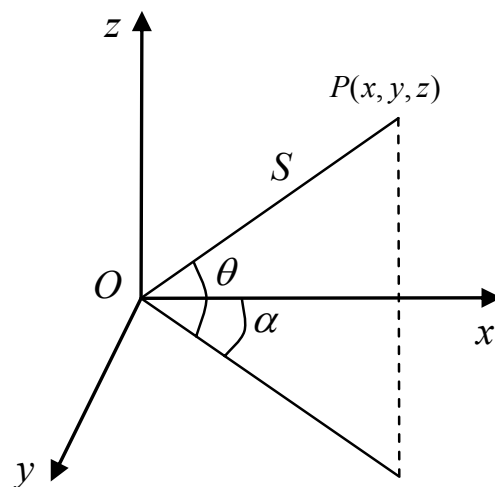


Figure 1. Imaging principle of Laser 3D scanning.

### 2.2.1. System's composition and application

The complete C-ALS system is composed of hardware and software. The full hardware system includes:

- the main probe which houses: the laser scan head, the motors which rotate the scan head horizontally and vertically, and the pitch & roll sensors which monitor the orientation of the probe, allowing the software to automatically align the scan appropriately;
- the nose cone infra-red camera (Figure 2 (a)) which is also integrated into the scanning head. This is used to check the condition of the borehole during deployment, as well as to gauge exactly when the probe enters the cavity;
- Boretrack rods (Figure 2 (b)) for deploying the probe at fixed, regular intervals and to prevent the probe rotating in the borehole which would cause the orientation of the data to be compromised;
- Toughened, load-bearing cable for power, data transmission and to assist deployment and recovery;
- the surface unit (Figure 2 (c)) which manages power & data transmission & which remains on the surface.

The software includes a module for controlling the C-ALS during operations (Figure 3 (a)), a module allowing real-time viewing of the scan as it is carried out (Figure 3 (b)) and 3D modelling software (Figure 3 (c)) for creating surfaces, models & calculating volumes.

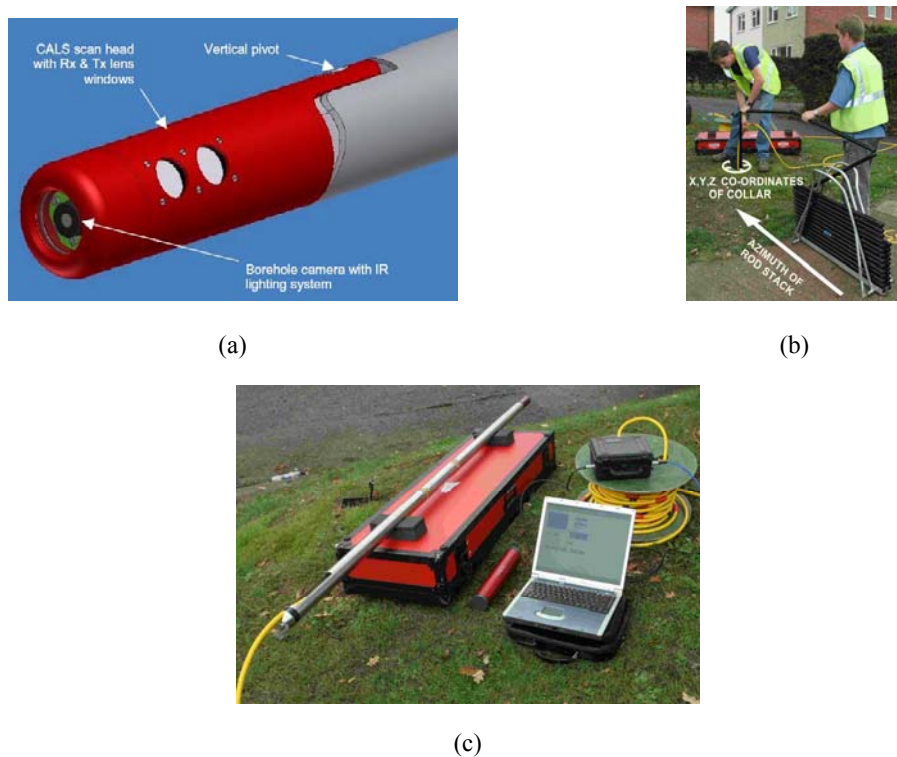


Figure 2. (a) Ore pass survey; (b) Underground space detection; (c) Underground void measurement.

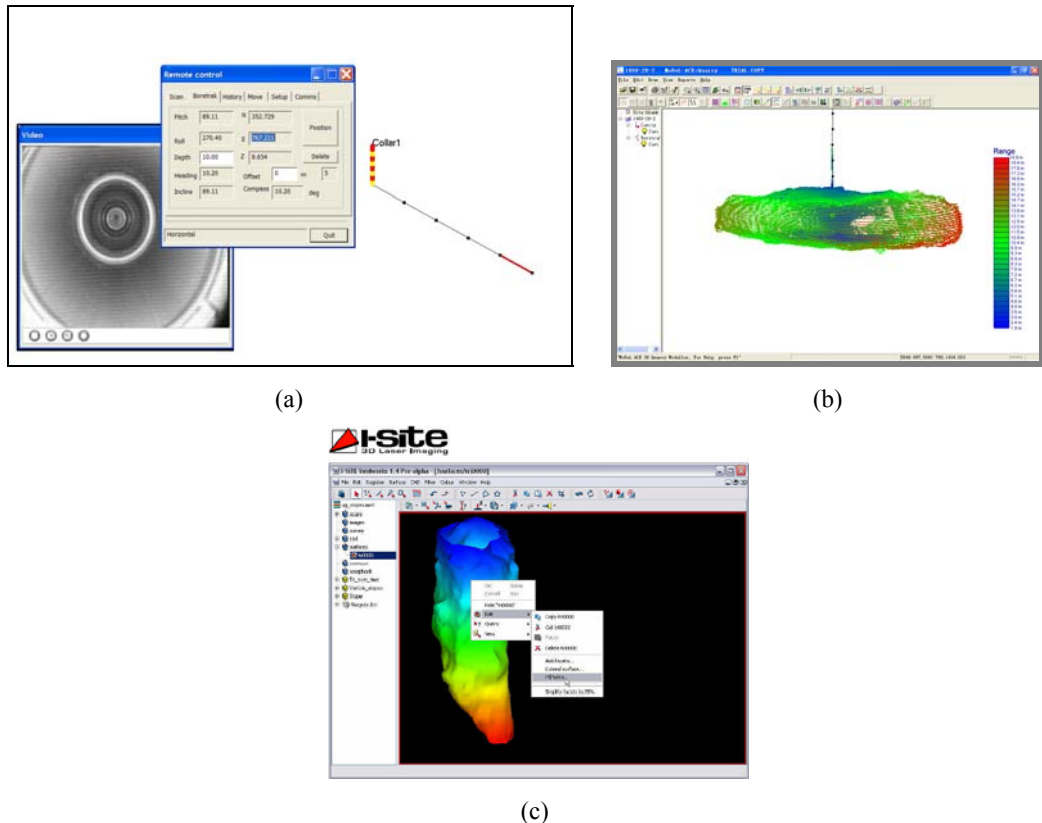


Figure 3. (a) CavityScan software during deployment; (b) CavityScan during a scan; (c) 3D modeling software.

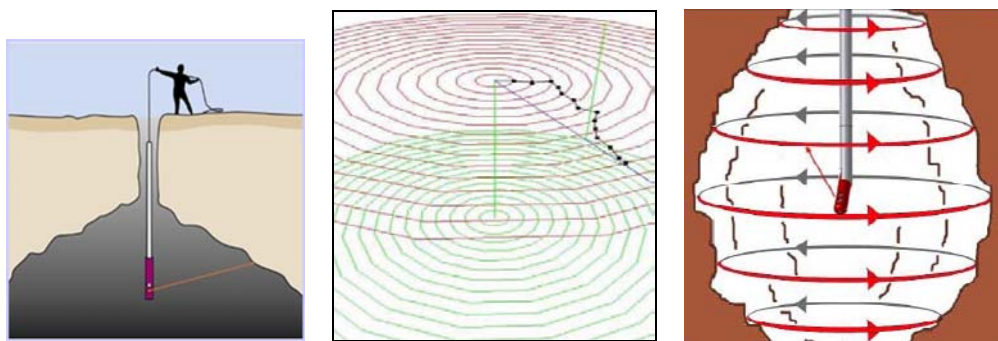


Figure 4. Detection procedure of C-ALS.

Due to the flexibility of the equipment and various customised deployment methods which have been devised, the C-ALS is capable of many different types of cavity scanning operations, including stope surveys, abandoned mine workings, orepass surveys, pillar recovery areas, backfilling areas, silo or ore bin surveys, tunnel profiling, structural monitoring, and surveys of any inaccessible location etc.

### 2.2.2. System detection procedure and data processing

The procedure for using the C-ALS involves the following three steps:

- (1) Deploying the scanner into the cavity while measuring the deviation of the borehole;
- (2) Carrying out the scan through the remote control software module;
- (3) Processing the measured data using modelling software to obtain a 3D cavity model.

Figure 4 shows the detecting procedure of C-ALS.

## 3. C-ALS DETECTION OF CAVITY UNDER OPEN PIT LIMIT IN LUANCHUAN MINE

### 3.1. Present Situation and Problems of Luanchuan Mine

Sandaozhuang mine of Luoyang Luanchuan Molybdenum Co. LTD. is an active mine with  $5.29 \times 10^8$  tons molybdenum and tungsten geological reserves. The average geological grade of molybdenum and tungsten is 0.11%. There are  $6.725 \times 10^5$  tons of metal reserves, with the verified molybdenum reserve comprising 2.52% of the world's total. Sandaozhuang is an open pit mine with 30kt/d production capability and an annual production value of 2 billion RMB. The mine experienced unreasonable underground mining for more than 20 years since the 1980s. There have been massive cavities left by sublevel open stope mining and large numbers of unmapped and abandoned cavities have been left by private mining. There are in total more than 100 cavities of various shapes and sizes, with a combined volume of around  $1 \times 10^7$  m<sup>3</sup> under the open pit. This has left the ore body in a perilous state. Since being excavated, these cavities have suffered ground pressure, weathering and blasting vibration. The rock mass around the cavities is in a fractured and distorted condition, with the cavities' location, size and shape already having altered. As Sandaozhuang open pit continues exploiting the minerals present, the layer between the bench surface and the cavities is becoming thinner. Both workers and their equipment are directly threatened by these underground cavities, and it is possible for fatal accidents to occur at any time due to surface collapse. The major aim of the mine is to deal with those cavities under the open pit, and, for this purpose, it is first vital to accurately detect the shape, location and size of the cavities. Thus, this situation presents a good stage to investigate the suitability of the C-ALS.



Figure 5. Present Sandaozhuang open pit



Figure 6 Deploying the C-ALS to detect cavities.

**Table 1. Detected cavities under various bench.**

Cavity position	Borehole depth /m	Cavity height under borehole /m	Cavity volume /m <sup>3</sup>
Bench 1330	15.2	4.2	647
Bench 1414	14	2.4	174
Bench 1438-1	29.4	70.3	157078
Bench 1438-2	17.8	8.1	2722
Bench 1450	21	7.8	3198
Bench 1462-1	16	5.9	2177
Bench 1462-2	16	5.4	2087

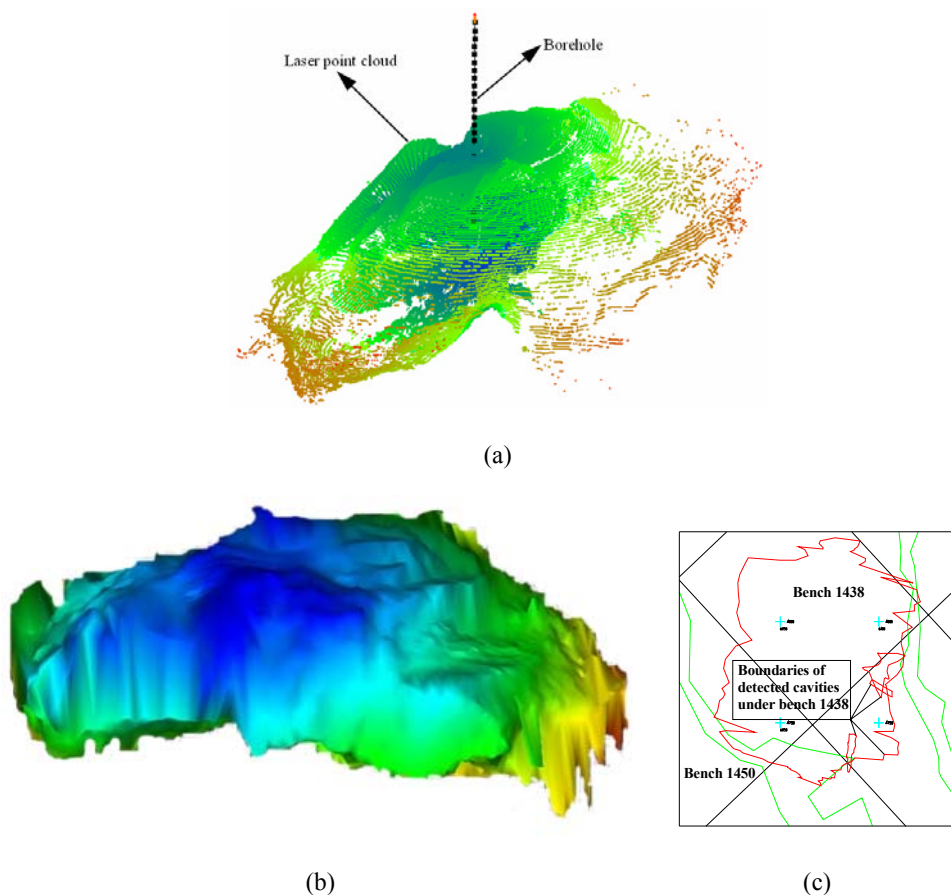


Figure 7. (a) Oriented laser point cloud under bench 1438-1; (b) 3D solid model of cavity under bench 1438-1; (c) Cavity boundary under bench 1438-1 in exploitation ichnography.

### 3.2. Detection Results

The cavities underneath Sandaozhuang open pit will be a source of risk throughout the exploitation of the mine. To illustrate the problem, in Table 1 below are listed the details of

some of the cavities already detected. We know from various surveys that safe mine production is increasingly threatened by those cavities under the open pit boundaries, as the bench blasting continues to progress. The potential danger from these cavities, situated at various depths and with various shapes and volumes, is extremely severe. This is especially true of the largest cavities with complex shapes and which are often interconnected with other adjacent voids.

After each cavity was fully surveyed, the scanned data was edited in CavityScan processing software and a 3D modelling package to form an oriented, geo-referenced point cloud (Figure 7(a)) and 3D solid model (Figure 7(b)), either of which can be exported into SURPAC and CAD. The projective ichnography of the cavity was of most use on-site. This data can be transformed into exploitation ichnography in CAD to outline the cavity boundary (Figure 7(c)).

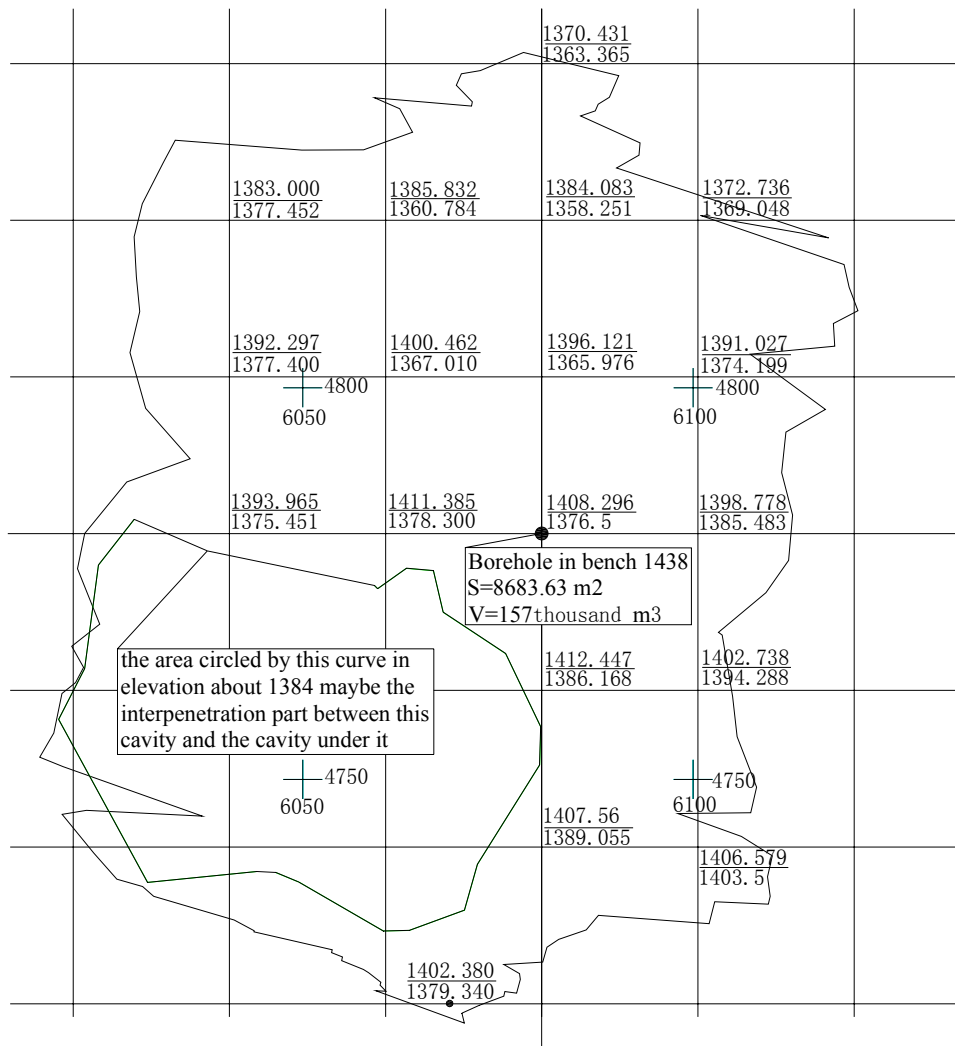


Figure 8. Cavity ichnography with roof and floor elevation of grid intersection point.

### 3.3. Special Cavity Analysis

#### 3.3.1. Huge cavity under bench 1438-1

The cavity under bench 1438-1 is huge, complex and multi-layered and has the cavity under bench 1438-2 in its cap rock, which was of the most concern in July 2007. Detailed detection was carried out through a borehole on the surface of bench 1438-1. In order to provide practical information for cavity disposal and the bench blast, the roof of the cavity and the elevation of the floor were measured at grid intersection points in ichnography taken from the laser point cloud (shown in Figure 12). The grid spacing can be altered according to the required accuracy, with the roof and floor elevation at each specified point measured from the scan data. This data enabled the creation of section charts which would be vital for a later design stage. In Figure 11 (a), there is one area of the cavity which is not covered by the point cloud data. The furthest achievable range to a good reflection surface is about 150 meters of C-ALS and considering this fact, together with an analysis of the other scanned data, we conclude that this part may interconnect with the lower cavity at an elevation of about 1384. The interpenetration part is curve circled in Figure 8.

After the cavity under bench 1438-1 was fully detected, the blast was performed on the thinner cap rock of this huge cavity. The collapsed surface (shown in Figure 9) is spectacular, with an area of 4900 m<sup>2</sup> after the blast. The distance between the surface and the bottom of collapsed pit is about 75 meters as shown in Figure 10. After investigating the collapse on-site, we found small cavities and laneways in its cap rock as shown in Figure 11, this is in agreement with the small cavities and laneways detected during surveys through other boreholes in bench 1438. These are visible in Figure 7 (c). As further blasting continues on, the collapsed surface is enlarging further. Accurate data collected with the C-ALS is constantly providing reliable information for blast design.



Figure 9. Collapsed surface after blast.



Figure 10. Side view of the collapse



Figure 11 Small cavity and laneways in cap rock.

### 3.3.2. Dangerous cavity under bench 1462

Due to the fragmented cap rock, the cavity under bench 1462 was partly collapsed. We drilled two boreholes to deploy the laser probe after investigating the collapsed area. However, this cavity is extremely complex: pillars and collapses make the survey extremely difficult. The scan data showed that the height throughout the cavity is fairly constant. Also, from the point cloud it is apparent that there still have other parts of the cavity beyond the 'line-of-sight' of the laser and thus beyond the extents of the point cloud. These areas are marked in the cavity ichnography—Figure 12. This illustrates that a small number of boreholes are insufficient for a full picture of this cavity. More boreholes need to be drilled, through which the C-ALS can be deployed. The location of the drilling will be based on the data already collected in previous scans. The final cavity shape will be obtained by combining data collected from deployments through numerous boreholes. Figure 13 is the cavity final ichnography under bench 1462 detected through multiple boreholes.

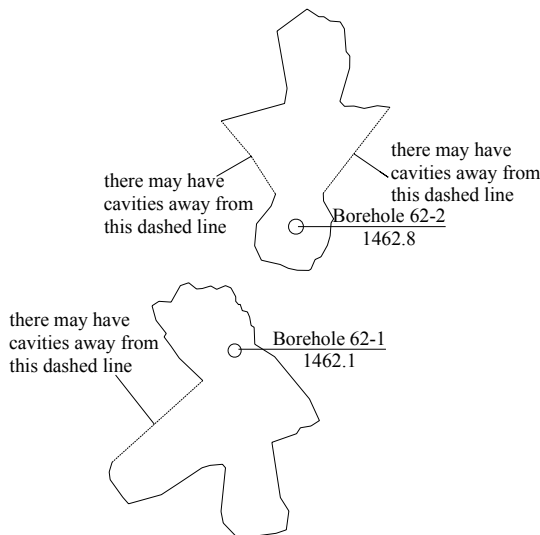


Figure 12. Detected cavity ichnography through two boreholes.



Figure 13. Final cavity ichnography detected through multiple boreholes.

## CONCLUSION

3D laser scanning is an advanced cavity detection method which can detect and survey cavities far more precisely than conventional methods. With a small diameter, high accuracy and unique deployment method, the C-ALS can ensure not only the accurate cavity analysis, but also the safety of the personnel deploying the equipment who are able to remain removed from the dangerous areas being investigated. The unit has proved to be very suitable for underground cavity detection in Sandaozhuang mine of Luoyang Luanchuan Molybdenum Co. LTD.

The detected laser point cloud can be processed to obtain accurate cavity ichnography. The cavity roof and floor elevations at grid intersection points are used to provide detailed information for blast design. Minimal exploration boreholes can be located based on the scanned data which can therefore not only obtain 3D cavity information, but can also save on the cost of exploration drilling.

Laser reflections from water and glass back to the receiving optics is almost zero, and the ability of the laser to measure ranges is limited by the ‘line-of-sight’ within the underground cavity. For these reasons, the influence of water, fog (such as blasting fumes) and humidity in the cavity can have a detrimental affect on laser scanning technology and continues to be further researched. Further, although laser equipment has been used in underground coal mine, the C-ALS is not specifically rated as being intrinsically safe, the detection feasibility of C-ALS in any area where there is risk of flammable gas (such as gas in coal mine) needs to be validated.

In contrast with other, conventional cavity detection methods, operators using a 3D laser scanner will need to know in advance the rough location of the cavity and this will then determine the position of the borehole to be drilled. However, the location of most cavities and voids encountered is unclear, especially if they are inaccessible. Therefore, the 3D laser scanning method described should be combined with the conventional detection methods. The location of the cavity can be determined by conventional detection methods first, and then the borehole position can be chosen, through which the C-ALS can be deployed to carry out an accurate, detailed scan of the void. Data from the C-ALS can then be used to pin-point further locations for drilling and investigation.

## REFERENCES

- [1] Tong Liyuan, Liu Songyu, Qiu Yu, et al. (2004). Current research state of problems associated with mined-out regions under expressway and future development. *Chinese Journal of Rock Mechanics and Engineering*, 23(7), 1198-1202. (in Chinese)
- [2] Yan Changbin, Xu Guoyuan & Zhong Guosheng. (2005). Research of composite prospecting and its application complicated underground mined-out areas. *Journal of Liaoning Technical University*, 24(4), 481-484. (in Chinese)
- [3] Liu Dunwen, Xu Guoyuan, Huang Rendong, et al. (2000). A new technique for prospecting exhausted areas in metal mines. *China Mining Magazine*, 9(4), 34-37. (in Chinese)
- [4] Cheng Jiulong, Hu Kefeng, Wang Yuhe, et al. (2004). Research on detecting of underground mined-out areas by using GPR. *Rock and Soil Mechanics*, 25(Supp), 79-82. (in Chinese)
- [5] Liu Hongjun & Jia Yonggang. (1999). The application of ground penetrating radar survey in probing the underground mined area. *Journal of Geological Hazards and Environment Preservation*, 10(4), 73-76. (in Chinese)
- [6] Xu Baishan, Wang Ende, Chen Qingkai, et al. (2006). Determination of coal mine gob edges by EH-4 system. *Journal of Northeastern University (Natural Science)*, 27(7), 810-813. (in Chinese)

- [7] Hu Yunbing, Wu Yanqing, Song Jing, et al. Simulating model and example analysis of applying electric surveying to detect gob. *Mining Safety and Environmental Protection*, 33(Supp), 39-41. (in Chinese)
- [8] Michael van Schoor. (2002). Detection of sinkholes using 2D electrical resistivity imaging. *Journal of Applied Geophysics*, 50(4), 393-399.
- [9] Ugur Yaramanci. (2000). Geoelectric exploration and monitoring in rock salt for the safety assessment of underground waste disposal sites. *Journal of Applied Geophysics*, 44(2-3), 181-196.
- [10] Xu Baishan, Wang Ende, Tian Gang, et al. (2006). Determination underground water-bearing caves by seismic transverse wave reflection method. *Journal of Northeastern University (Natural Science)*, 27(1), 84-87. (in Chinese)
- [11] Gilles Grandjean, Donatienne Leparoux. (2004). The potential of seismic methods for detecting cavities and buried objects: experimentation at a test site. *Journal of Applied Geophysics*, 56(2), 93-106.
- [12] Bojan B. Guzina, Sylvain Nintcheu Fata, Marc Bonnet. (2002). An Elastodynamic BIE Approach to Underground Cavity Detection. *Electronic Journal of Boundary Elements, BETEQ2001* (2), 223-230.
- [13] Gao Yong, Xu Baishan, Wang Qijun, et al. (2003). Study of geophysical sounding effect on the underground mined-out areas. *Contributions to Geology and Mineral Resources Research*, 18(2), 126-130. (in Chinese)
- [14] Li Xibing, Li Diyuan, Zhao Guoyan, et al. (2006). Detecting, disposal and safety evaluation of the underground goaf in metal mines. *Journal of Mining & Safety Engineering*, 23(1), 24-29. (in Chinese)
- [15] Liu Jinghua, Wang Zhuwen, Zhu Shi, et al. (2005). The geophysical exploration about exhausted area and sinking area in coal mine. *Journal of China Coal Society*, 30(6), 715-719. (in Chinese)
- [16] Shi Zhichun, Zhao Guoyan & Li Faben. (2005). Detection of underground complicated mined-out areas. *Mining Technology*, 5(4), 103-104. (in Chinese)
- [17] Yan Changbin & Xu Guoyuan. (2005). Research of composite geophysical methods and its application in detection complicated mined-out areas. *Journal of Hunan University of Science & Technology (Natural Science Edition)*, 20(3), 10-14. (in Chinese)
- [18] Miller, F., Potvin, Y. & Jacob, D. (1993). Laser measurement of open stope dilution. *Foreign Metal Mining Magazine*, 4, 5-7. (in Chinese)
- [19] Miller Fabien, Potvin Yves & Jacob Denis. (1992). Laser measurement of open stope dilution. *CIM Bulletin*, 85(962), 96-102.
- [20] Shaffer Gray & Stentz Anthony. (2006). Automated surveying of mines using a laser rangefinder. *Emerging Computer Techniques for the Minerals Industry*, 1993: 363-370.
- [21] Huber Daniel, Vandapel Nicolas. Automatic three-dimensional underground mine mapping. *International Journal of Robotics Research*, 25(1), 7-17.
- [22] Fardin, N., Feng, Q. & Stephansson, O. (2003). Application of a new in situ 3D laser scanner to study the scale effect on the rock joint surface roughness. *International Journal of Rock Mechanics & Mining Sciences*, 41(2), 329-335.
- [23] Syddell, M. (2005). Company maps way forward for mining (laser scanning and digital imaging system). *Australian Mining*, 97(4), 30.

- 
- [24] Gilbertson, R. J. (1995). The Application of the cavity monitoring system at olympic dam operations. Proc. Underground Operators Conference, Kalgoorlie, Western Australia, 245-252.
  - [25] Jarosz, A. & Shepherd, L. (2000). Application of cavity monitoring system for the control of dilution and ore loss in open stopes. 11<sup>th</sup> International Congress of ISM, Cracow, Poland: 155-164.
  - [26] John D Lupton. (2004). Cavity monitoring system and stope analysis. *Proceedings, MassMin Chile*, Santiago, Chile, August 2004, 56-62.
  - [27] Stuttle, M. C. (1998). Combined probe drilling and laser surveying for complex underground mapping. *Canadian Mining Journal*, 119(6), 21-23.
  - [28] Stuttle, M. C. (1999). Laser scanning aids underground mine mapping. *Mining Engineering*, 51(3), 45-46.
  - [29] LIU Xi-ling, LI Xi-bing, LI Fa-ben, et al. (2008). 3D cavity detection technique and its application based on cavity auto scanning laser system. *J.Cent.South Univ.Technol.*, 15(2), 285-288
  - [30] Guo Jiang, Luo Zhouquan & Deng Jian. (2005). Application of cavity monitoring system in underground mines. *Chinese Journal of Underground Space and Engineering*, 1(7), 994-996. (in Chinese)
  - [31] LI Xiang-yin, YAO Min-yu, LI Zhuo, et al. (2004). Laser principle technic and application. Harbin : Harbin Institute of Technology Press, (in Chinese)
  - [32] ZHANG Yuan-zhi, HU Guang-yang, LIU Yu-tong, et al. (2001). Application of 3D laser scanning system in engineering projection. *Highway Transportation*, 9, 38-40. (in Chinese)
  - [33] GAO Shan. (2004). Application of the I-SITE 3D laser imagery system in mine survey. *Railway Investigation and Surveying*, 30(6), 38-40. (in Chinese)
  - [34] Measurement Devices Ltd. Cavity Auto Scanning Laser System (C-ALS) Manual. v[1].2.0, 2006, York, UK.

## ***Chapter 10***

# **LASER CLADDING: AN OVERVIEW**

***L. Santo<sup>1</sup> and J. Paulo Davim<sup>2\*</sup>***

<sup>1</sup>Department of Mechanical Engineering, University of Rome “Tor Vergata”, Via del Politecnico 1, 00133 Roma, Italy.

<sup>2</sup>Department of Mechanical Engineering, University of Aveiro, Campus Santiago, 3810-193 Aveiro, Portugal.

## **ABSTRACT**

This chapter presents a basic overview on laser cladding. Among laser technologies, laser cladding has received great attention in recent years, mainly due to the reduced costs of laser sources, the increasing potential for material processing, the development of new coating materials, the emergence of rapid prototyping and other manufacturing applications.

In this chapter the process and different systems for laser cladding have been described, some case studies have been discussed, some predictive models have been proposed, and new perspectives have been discussed. Some aspects and advantages of laser cladding process have been highlighted.

## **INTRODUCTION**

### **What Is Laser Cladding?**

Laser cladding is a non-traditional process mainly used for metallic coating and high-value part surface repair, to increase resistance to wear, corrosion, erosion and oxidation. Other interesting applications are rapid prototyping and low volume manufacturing [1].

During laser cladding process the laser beam is used as the heating source to melt the coating material in order to clad the surface of the substrate. The coating material can be deposited on the substrate by different methods: lateral or coaxial powder injection, pre-placed powder on the substrate, or by wire feeding.

---

\* Corresponding author: E-mail: pdavim@ua.pt

The advantage of laser cladding is the great process flexibility and the possibility of selectively cladding small areas, by depositing different metals and alloys on the substrate to form a layer with thickness ranging from 0.05 to 2 mm and widths as narrow as 0.4 mm.

Due to the intrinsic properties of laser radiation, high input energy, low distortion, avoidance of undesirable phase transformation, controlled shape, minimal diffusion of the substrate elements into the coating, fine microstructure and low porosity in the layer can be obtained. The process is very useful for application in machine-tools and engine manufacturing, in particular for the aircraft and automotive industries.

In the case of layered manufacturing or prototyping technique the integration of laser cladding with CAD/CAM manufacturing systems has been used also to fabricate complex shapes.

Based on its different applications, different names have been given to this technology. For example, researchers use without distinction the terms *laser coating*, *laser powder deposition*, or *laser surfacing* for coating applications. For rapid prototyping they use *selective laser sintering of metals*, or *direct metal laser sintering* in the case of pre-placed powder laser cladding, while *direct metal deposition*, *laser direct casting*, *laser powder fusion*, *shape deposition manufacturing*, or others in powder injection laser cladding process.

## Equipments

The process basically requires a laser system, equipped with a positioning device, that in advanced systems are governed by CAD/CAM software, and with a powder feeder in the case of co-deposition technique [1].

The laser commonly used for cladding are CO<sub>2</sub> lasers, diode-pumped Nd:YAG lasers, and high-power diode lasers (HPDL). Their wavelengths are different, 10.6 μm for CO<sub>2</sub> lasers, 1.06 μm for Nd:YAG lasers, and in the range 0.65-0.98 μm for HPDLs. This causes different laser-material interaction, affecting the material reflectivity, absorption and transmission and consequently the coating deposition.

**Table 1. Main characteristics of commonly used laser in cladding process.**

Characteristics	CO <sub>2</sub>	Nd:YAG diode-pumped	HPDL
Wavelength [μm]	10.6	1.06	0.65-0.98
Maximum power [kW]	45	6	6
Average power density [W/cm <sup>2</sup> ]	10 <sup>6...8</sup>	10 <sup>6...9</sup>	10 <sup>3...5</sup>
Efficiency [%]	5-10	10-12	30
Service period [hour]	1000-2000	5000-10000	5000-10000
Beam parameter product (BPP)[mm × mrad]	12	12	100-1000
Fiber coupling	No	Yes	Yes

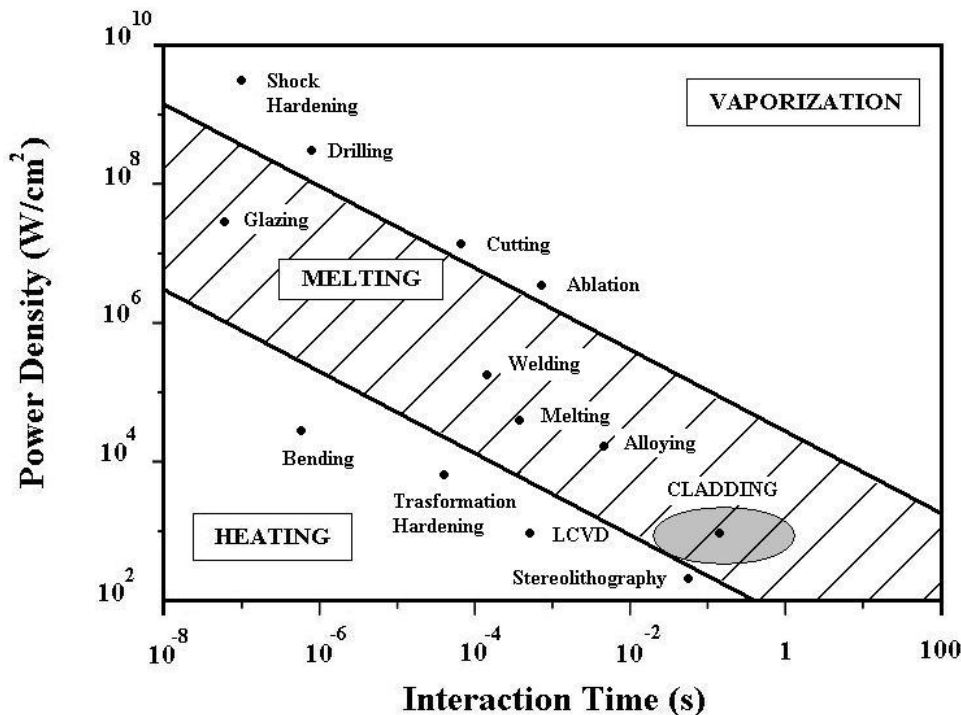


Figure 1. Laser material processing: power density and interaction time [1].

Table 1 reports the main characteristics of lasers for cladding and Figure 1 shows the operating window of laser material processing.

The CO<sub>2</sub> laser is the most commonly used, even if for cladding of small areas on components the pulsed Nd:YAG seems the best choice for the high control of the heat input [2-3].

CO<sub>2</sub> laser and Nd:YAG are already implemented in industry for repairing and regenerating structures and engine part, while recent developments for HPDLs could establish new applications. This is due to the high efficiency of HPDLs and the shape intensity distribution that could not be Gaussian. In fact, its modular structure permits a segmented intensity distribution. In particular it is possible to use a rectangular spot with an uniform power intensity [3-4].

Many kind of powder feeders are used in industry and they can be classified in terms of different principles of operation: gravity-based, mechanical wheel, fluidized-bed and vibrating, even if sometimes a combination of more methods is employed to better perform the deposition. Generally, in the deposition system a carrier gas transports the powder particles from the starting point to the desired location. The powder feeder has to provide a continuous and uniform powder stream, avoiding powder agglomerations. For this reason, it is necessary to control the feed rate in real-time [1].

The choice of a powder feeder strictly depends on the application. It is very difficult to indicate the more suitable, by considering that powders have different size, shape, physical and mechanical properties. Therefore, it is practically impossible to convey each type of them with a steady-state flow using the same feeder machine.

## Process Description

In laser cladding process, a laser heat source is used for depositing a thin layer of a desired metal on a substrate, generating a fusion bond between the two with minimal dilution (see following) of the clad by the substrate. The alloying material can be introduced into the laser melted volume either from pre-deposited layers or directly, by using a co-depositing technique and alloying materials in the form of wire, sheet, paste or powder, as shown in Figure 2.

The cladding with pre-placed powder, also named two-step process, is the simplest method and the powder remains in place until melted, while the area is covered by an inert gas. By means of co-depositing technique, also known as one-step process, the additive material can be supplied out in different ways: wire feeding, paste laser cladding, lateral or coaxial powder injection. In the case of powder injection the carrier gas is used for forming a cladding powder stream blown under the laser beam while it scans the surface of the substrate. A melt pool with a depth corresponding to the thickness of a single clad is generated. It is possible to cover large surfaces, making overlapping tracks. Argon gas is commonly used as shielding and carrier gas.

Figure 3 reports a schematic view of common cladding systems, a) pre-placed cladding material powder and b) blown powder cladding.

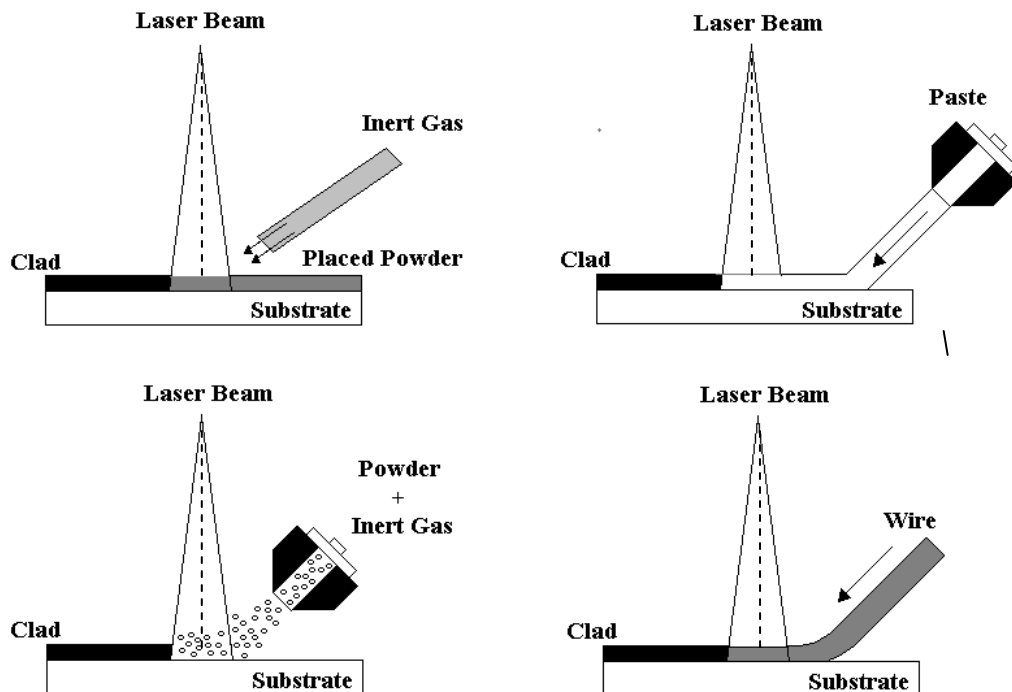


Figure 2. Different methods of laser cladding.

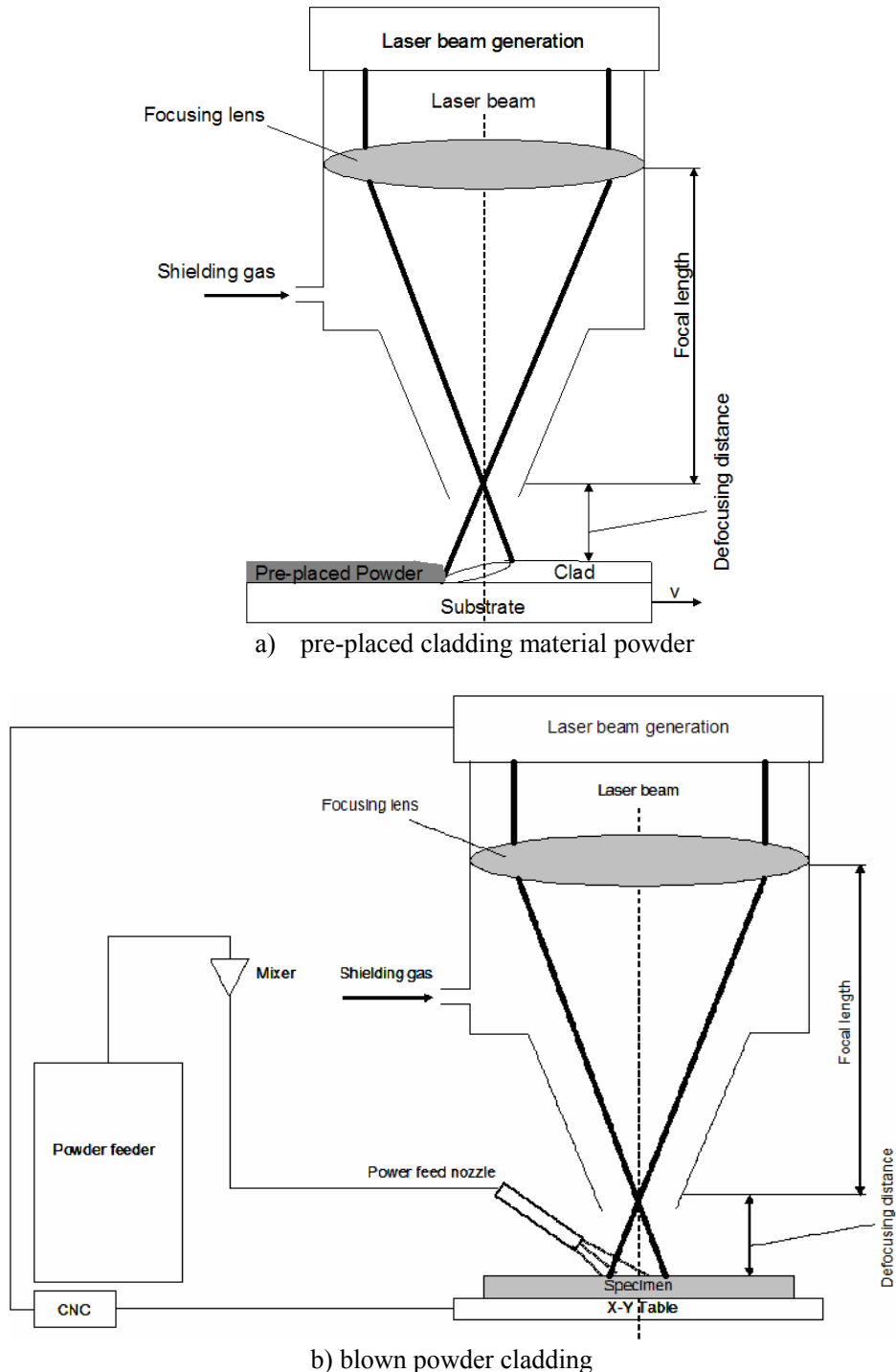


Figure 3. Schematic view of cladding systems [3].

The process with pre-placed powder has usually a small process window, it is time-consuming and sometimes difficult to adapt on complex geometrical shapes. Laser cladding by wire feeding is difficult to control, and it usually leads to high dilution rates. Laser

cladding by powder injection is the most attractive process, as it requires minimum surface preparation and it is applicable for complex geometries. Two ways of feeding powder are available: from a side or coaxially to the laser beam. If the powder stream is delivered coaxially to the laser beam, all the directions of the substrate movement on a plane perpendicular to the laser beam are equivalent, being independent of the cladding direction. Therefore, it is possible to build equivalent tracks independently on the moving direction of the specimen.

The resulting thickness of the clad is typically from 50 µm to 2 mm in one step. When a thicker protection layer is needed, the process can be applied again.

The clad geometry is associated to several parameters, schematically depicted in Figure 4:  $h$  is the clad height,  $w$  is the width,  $\theta$  is the wetting angle and  $b$  is the clad depth, i.e. the thickness of substrate that was melted during the cladding process. The latter represents the thickness of the melted substrate, that after the laser irradiation becomes part of the clad bead.

The wetting angle  $\theta$ , also known as clad angle, can be calculated by the following expression [4-5]:

$$\theta = 180 - 2 \arctan\left(\frac{2h}{w}\right) \quad (1)$$

Many parameters influence the laser cladding process and determine good or poor quality of the clad bead. They are related to the laser, material, motion device, feeder system and environment. The most important are laser power, scanning speed and powder feeding rate, even if several additional parameters play an important role like the beam spot size, the laser beam energy distribution, the amount and sort of shielding and carrier gas, the size, speed and feeding direction of powder particles. Furthermore, the nature and properties of the substrate material cannot be neglected.

In literature [1-3] a lot of indicators of quality assessment have been used: geometry, microstructure, hardness, porosity, residual stress, surface roughness, cracks, dilution.

The last mentioned has two definitions, the first is geometrical, the second is metallurgical.

The geometrical definition of dilution  $d$  is (see Figure 4):

$$dilution = \frac{b}{h+b} \quad (2)$$

According to the metallurgical definition, it may be defined as the percentage of the total volume of the surface layer contributed by melting of the substrate. The dilution generally increases with the increase of laser power, but decreases with the increase of speed.

Besides, in laser cladding, either pre-placed or powder injection, wetting angle and interfacial free energies are important parameters that indicate the quality of the clad. As schematized in Figure 5, the cross sections represent the amount of dilution, corresponding wetting angle  $\theta$ , and interfacial free energies  $\gamma$  [J/m<sup>2</sup>]. Three interfacial energies for laser cladding can be considered as solid-liquid interfacial free energy  $\gamma_{SL}$ , solid-vapour interfacial energy  $\gamma_{SV}$ , and liquid-vapour interfacial energy  $\gamma_{LV}$  [1].

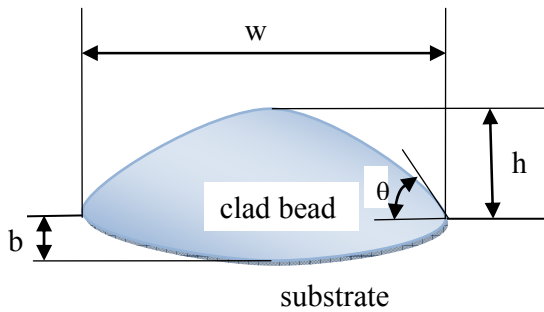


Figure 4. Schematic view of the typical cross section of a clad bead.

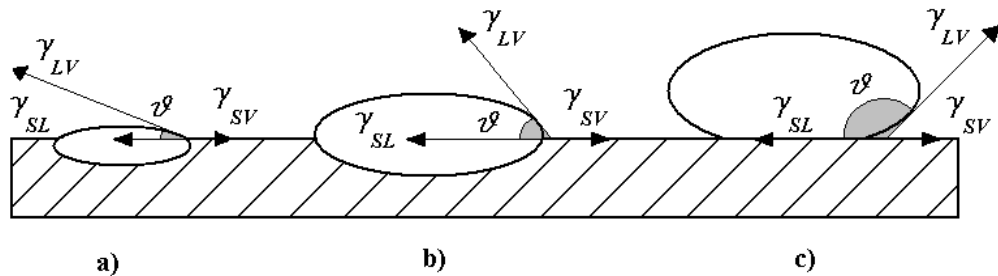


Figure 5. Laser cladding cross sections, associated wetting angle and interfacial free energies: a) high dilution, good wetting, b) ideal clad, c) no dilution, non-wetting [1].

The shape of the clad bead is governed by a balance between the mentioned energies, as shown in Figure 5.

In the applications section, a discussion on process parameters and their influence on clad quality has been reported for each application.

## Governing Equations and Modeling

Several models have been developed on laser cladding process with injection powder into a laser melt pool, that is the most representative method [6-8]. A complete description and modelling is however very complex, because of numerous interactions like laser beam/powder, laser beam/substrate, powder stream/melt pool, powder stream/solid substrate. Physical phenomena like mass and heat transfer, fluid flow, phase transformation are also involved as underlined in [1,4].

They are described as follows.

- The laser beam reaches the substrate, a considerable amount of its energy is directly absorbed by the substrate, a very small part is absorbed by powder particles. The substrate develops a melt pool because of such absorption. The melted particles are simultaneously added into the melt pool. This step of the process can be expressed only by the heat conduction equation.

- Surface tension gradient governs the material flow within the melt pool. As far as the flow penetrates in the substrate, the energy transfer mechanism changes to a mass convection mechanism. During this phenomenon, the melted powder particles are mixed rapidly in the melt pool. This step of the process should be expressed by the momentum, the heat transfer, and continuity equations.

Based on these physical phenomena, heat conduction, momentum, and continuity are the equations that govern the process [1].

In laser cladding process, the laser passes on the additive material at  $t = 0$  and forms the clad, as shown in Figure 6. The transient temperature distribution  $T(x, y, z, t)$  is obtained from the three-dimensional heat conduction in the substrate [1]:

$$\frac{\partial(\rho c_p T)}{\partial t} + \nabla \cdot (\rho c_p U T) - \nabla \cdot (K \nabla T) = Q \quad (3)$$

where  $Q$  is power generation per unit volume of the substrate [ $\text{W/m}^3$ ],  $K$  is thermal conductivity [ $\text{W/m}\cdot\text{K}$ ],  $c_p$  is specific heat capacity [ $\text{J/kg}\cdot\text{K}$ ],  $\rho$  is density [ $\text{kg/m}^3$ ],  $t$  is time [s], and  $U$  is the speed of the workpiece [m/s].

The momentum equation is :

$$\frac{\partial(\rho U)}{\partial t} + (\rho U \nabla) U = \rho g - \nabla p + \mu \nabla \cdot (\nabla U) \quad (4)$$

where  $g$  is acceleration gravity [ $\text{m/s}^2$ ],  $\mu$  is viscosity [ $\text{kg/s}\cdot\text{m}$ ], and  $p$  is pressure [ $\text{N/m}^2$ ].

The last equation is continuity and is represented by

$$\nabla U = 0 \quad (5)$$

The above equations can be solved analytically only in special cases or numerically with assumptions and/or simplifications, adding the boundary conditions.

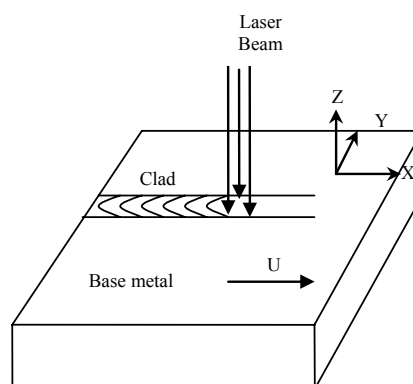


Figure 6. Schematization of laser cladding process.

In literature several steady-state models for laser cladding have been proposed, neglecting the transient response of the process, that plays an important role in the process.

They take into account many important physical phenomena such as thermal conduction, thermocapillary (Marangoni) flow, powder and shield gas forces on melt pool, mass transport, diffusion, laser/powder interaction, melt pool/powder interaction, and laser/substrate interaction in the process zone [1].

## Applications

Many papers discussed laser cladding on steel substrate, a few on aluminium and magnesium [9-25]. The process offers a wide range of possible cladding materials. Some of them are Stellite SF6 (Co based Alloy), *Diamalloy 2002* (WC 12 Co 33 Ni 9Cr 3.5Fe 2Si 2B 0.5C blend, Ni- Cr<sub>3</sub>, Ni-WC, *Tribaloy* (CoMoCrSi), Fe-Mn-C alloy, AISI 431, AISI M2, Ni-20Cr/xAl<sub>2</sub>O<sub>3</sub>, Ni-Cr-B-Si, NiTi, Co-Ti, WC-Si-Ni, used for steel substrate, while Al<sub>2</sub>O<sub>3</sub>, AlSi40, Ni-based alloy /Y<sub>2</sub>O<sub>3</sub> used for aluminium.

Various coatings promote different mechanical and physical properties. Some tests are carried out in order to determine such properties: scanning electron microscope (SEM) analysis to observe microstructures, energy dispersion spectroscopy (EDS) to find the chemical composition, X-ray diffraction (XRD) investigation to analyze clad phases, optical microscopy to study the clad geometry, the liquid penetrant test to reveal surface breaking flaw, wear test to determine the mass loss and wear rate, corrosion and oxidation test, micro-hardness test and nanoindentation test.

Analysis of variance (ANOVA) is used for investigating the influence of processing parameters in the form of single-cladding layer and hardness of coating; study for the prediction of the geometric form of clad is made by using multiple analysis regression.

Two case studies are proposed in the following section. The former is focused on a metal matrix composite obtained by laser cladding. The latter deals with a statistical method for the prediction of the geometric form of clad using multiple regression analysis.

## Case Study: Laser Cladding of Ni-Based Alloy/Y<sub>2</sub>O<sub>3</sub> Powder on 6061aluminium Alloy

In [26] laser cladding of Ni-based alloy/Y<sub>2</sub>O<sub>3</sub> powder on 6061aluminium alloy was carried out by using 3 kW CW Nd:YAG laser. Metal matrix composite was obtained. It is composed of aluminium, Ni-based alloy, refining and dispersion strengthening Y<sub>2</sub>O<sub>3</sub>, and particle hardening W, Cr. The chemical composition of 6061 Al alloy and Ni-based alloy powder are reported in Table 2. The specimens are 60x50x30 mm<sup>3</sup> in dimensions. Argon atmosphere was used for performing the tests.

The average grain size of mixture powder was 30 mm. To prepare Ni-based alloy + Y<sub>2</sub>O<sub>3</sub> deposited materials, four kinds of pressed compacts 1 mm in thickness were obtained. They were preset on the surface of aluminium after a thermal treatment (dried at 120° C). Subsequently, the Nd-YAG laser was used for obtaining the matrix composite material. The process conditions were: the laser power 1688 W, the overlap ratio 30%, the scanning speed

10 mm/s, the gas flow rate 1.4 L min<sup>-1</sup>, and four compositions of cladding materials ( Ni-based alloy + 0%, 2%, 6%, 8 % Y<sub>2</sub>O<sub>3</sub> respectively).

After laser cladding the specimens were characterized along the position of cross-section direction and longitudinal direction.

The microstructure and morphology, phase identification, element diffusion, and composition analysis of Ni-based alloy/ Y<sub>2</sub>O<sub>3</sub>-deposited metal and of substrate interface were examined by using optical observation, SEM, electron probe micro-analyzer (EPMA) with EDS, and XRD. In addition, the micro-hardness distribution and corrosion-resistance property were investigated.

The corrosion rate was calculated by following equation 5:

$$\nu_{loss} = \frac{(m_0 - m_1)}{St} \quad (6)$$

where  $\nu_{loss}$  is corrosion rate,  $m_0$  is mass before corrosion,  $m_1$  is mass after corrosion,  $S$  is surface area of specimen, and  $t$  is corrosion time.

For instance, the SEM observation of morphology distribution in the case of Ni-based alloy and 2% Y<sub>2</sub>O<sub>3</sub> as clad metal on 6061 aluminium substrate shows that the weld bead of deposited metal/aluminium substrate with well-metallurgical bonding is obtained with acicular structure, free from faults such as porosity and slags. The SEM observations show also that the interface reaction has occurred near the fusion line and that the addition of Y<sub>2</sub>O<sub>3</sub> alters the microstructures, as more fine microstructures are obtained, and promotes shorter transition zones near deposited metals/6061 aluminium substrate interface.

Micro-hardness investigations of clad metal shows that the micro-hardness is much higher (780-1100 HV<sub>02</sub>) than of aluminium substrate (62 HV<sub>02</sub>), as expected.

Corrosion rate of aluminium substrate is nearly the double of deposited metal (16.5889 gm<sup>-2</sup>h<sup>-1</sup>, 8.2451 gm<sup>-2</sup>h<sup>-1</sup> and 6.3669 gm<sup>-2</sup>h<sup>-1</sup> for Al alloy, Ni-based alloy and Ni-based alloy + 8 % Y<sub>2</sub>O<sub>3</sub> respectively).

By using different cladding materials, coatings with higher micro-hardness and better corrosion resistance can be obtained. Also by increasing the Y<sub>2</sub>O<sub>3</sub> percentage the micro-hardness increases and consequently the corrosion rate of coating metal decreases.

## Case Study: Experimental Study for the Prediction of the Geometric form of Clad Using Multiple Regression Analysis

In [27] laser cladding of nickel alloy *Diamalloy 2002* on 100 Mn Cr W4 (DIN) steel plates was carried out by using a 6 kW CO<sub>2</sub> continuous laser, a three/axis CNC controlled table, a powder feeder, and a coaxial cladding head. After the process the specimens were sectioned transversally to study the clad track by using a shop microscopy.

A plan of experiments with 27 tests with repetition was performed to evaluate the effect of the process parameters (laser power, scanning velocity, and powder flow rate) on the geometry of the clad. The main aim was to establish a model by using multiple regression analysis (MRA) between process parameters and the geometry of single-cladding layer. Finally, further experimental tests were used for making a comparison with the foreseen results.

**Table 2. Chemical composition of 6061 alloy and Ni-based alloy powder [26]**

Materials	Si	Fe	Ni	Cu	Co	Mn	Mg	Cr	Mo	C	Zn	W	Al
6061 Al	0.4-0.8	0.7	-	0.15-0.4	-	0.15	0.8-1.2	0.04-0.35	0.15	-	0.25	-	Bal.
Ni-based Alloy	-	6	48	-	8	-	14	5	1	-	12	6	

**Table 3. Experimental results of the measurement of the clad geometry as a function of process parameters [27].**

Test number	Processing parameters			$h^a$ Clad height	$w^a$ Clad width	$P^a$ Penetration Depth
	$P$ (kW)	$V$ (mm/s)	$C$ (g/min)	(mm)	(mm)	(mm)
1	2	5	5	0.410	4.392	0.866
2	2	5	7.5	0.610	4.737	0.876
3	2	5	11	0.756	5.156	0.991
4	2	10	5	0.358	4.455	0.795
5	2	10	7.5	0.380	4.683	0.889
6	2	10	11	0.695	4.954	0.943
7	2	15	5	0.255	4.683	0.606
8	2	15	7.5	0.420	4.741	0.741
9	2	15	11	0.570	4.893	0.886
10	3	5	5	0.430	4.321	0.815
11	3	5	7.5	0.451	4.784	0.889
12	3	5	11	0.781	5.621	0.921
13	3	10	5	0.321	4.653	0.795
14	3	10	7.5	0.493	4.893	0.815
15	3	10	11	0.682	5.383	0.793
16	3	15	5	0.318	4.671	0.764
17	3	15	7.5	0.483	4.829	0.794
18	3	15	11	0.644	4.805	0.832
19	4	5	5	0.650	4.850	1.24
20	4	5	7.5	0.732	4.990	1.512
21	4	5	11	0.912	5.290	1.716
22	4	10	5	0.550	4.880	1.143
23	4	10	7.5	0.620	4.950	1.473
24	4	10	11	0.754	5.061	1.704
25	4	15	5	0.510	4.830	1.24
26	4	15	7.5	0.420	4.970	1.138
27	4	15	11	0.653	5.020	1.629

<sup>a</sup> All measurements are repeated (mean values)

Table 3 shows the results in terms of clad height ( $h$ ), clad width ( $w$ ) and penetration depth ( $p$ ) as a function of the process parameters: laser power, scanning velocity and powder mass flow rate.

**Table 4. Comparison between the experimental results and the values obtained by MRA model [27].**

Geometric form of clad (P=4 kW, V=5 mm/s and C=11 g/min)	Experimental (V <sub>exp</sub> )	Model (V <sub>m</sub> )	Error (%)
Clad width, w (mm)	5.62	5.28	6.0
Clad height, h (mm)	0.79	0.85	7.6
Depth penetration, p (mm)	1.24	1.50	20.1

From Table 3 it is possible to observe that the value of  $h$  increases with the increase of laser power and powder mass flow, while it decreases with the increase of scanning velocity. This means that with a higher scanning velocity, a lower laser power and powder mass flow it is possible to obtain a smaller clad height. It is also evident that  $p$  increases with the increase of laser power, and it decreases with the increasing of scanning velocity. The clad width  $w$  increases with the increasing of powder mass flow rate.

By applying the multiple linear analysis regression, that is a statistical technique to analyze multifactor data, the following relationship are obtained [27] :

$$w = 3.94 + 0.000119 \times P - 0.0077 \times V + 0.082 \times C \quad R=0.86 \quad (7)$$

$$h = 0.099 + 0.0000748 \times P - 0.0162 \times V + 0.049 \times C \quad R=0.69 \quad (8)$$

$$p = -0.0168 + 0.000289 \times P - 0.013 \times V + 0.039 \times C \quad R=0.66 \quad (9)$$

where,  $P$  is the laser power in kW,  $V$  is the scanning velocity in mm/s, and  $C$  is the powder mass flow rate in g/min.

Table 4 shows instead the comparison between the predicted values for geometric clad using the MRA Eqs. 7-9 respectively, and the experimental results.

From Table 4 it is evident that the calculated errors for clad width and for clad height are good, while those calculated for depth penetration are too high.

### Case Study: Investigation on Technological and Scientific Spreading of Laser Cladding

In [28] an analysis of the patents and scientific publications in the laser cladding field, for the period ranging from 1985-2007, was performed by using some strategies. All the laser cladding processes and all the substrates used for coating, repairing and 3D fabrication were taken into account. For the technological activities (patents) the used dataset were USPTO's US Granted (US), and US application (US-A), the European Patent Office (EP), Patent Cooperation Treaty (PCT-WO), the Japan Patent Office through Wisdomain Inc's FOCUS product, PlusPat database on Questel-Orbit, regional patent offices (France and Germany), INPADOC database; for the scientific activities (scientific publications) ISI's Web of Science®database was the main used database.

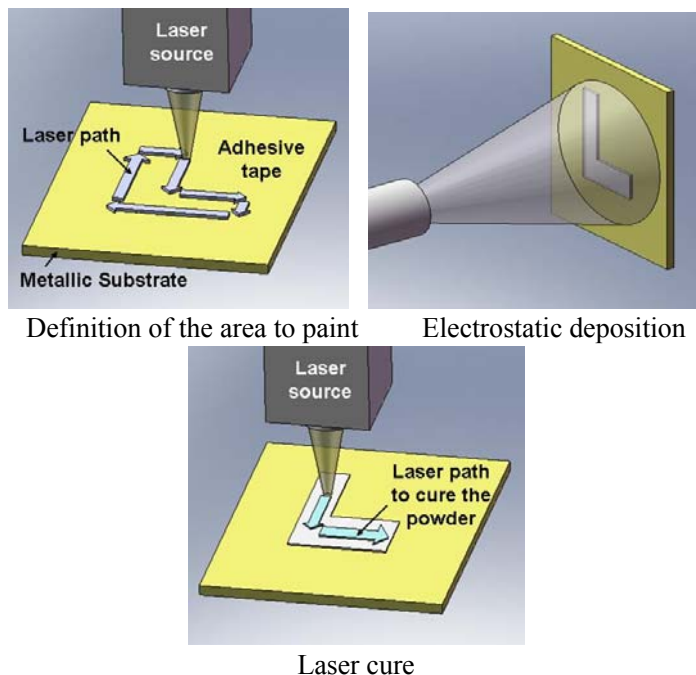


Figure 7. System scheme.

The main results of the analysis were as follows. The number of patents increased from 9 to 28 between 1984 and 1985, whereas the highest number was 43 in 1997. In the following years the number was in the range 23-42 per year. Toyota and Nissan have the highest number of patents, 51 and 49, respectively. Their research and development activities were mainly performed between 1985 and 1992 for Toyota, and 1993 and 2001 for Nissan. The patents primarily protect applications related to the laser cladding of valve seats, pistons and cylinders for automotive engines. General Electric Co. ranks 3<sup>rd</sup> with 36 patents from 1989 to 2001, for applications mainly related to the rebuilding of turbine blades (aeronautic or electric). For the number of the scientific papers, an exponential growth of publication activity was recorded from 1985 to 2007. 588 scientific publications were recorded by using ISI's Web of Science® database, while 2115 records by using also other databases as (Inspec, EI compendex, Metadex, Weldasearch, Aluminium Industry Abstract) until 2007. In the last case different kinds of publications including proceedings were considered.

By comparing the results it has been noted an high increase of the number of the scientific publications in the laser cladding field, while that does not occur for the patents. The one great increase of patents after 1985 is probably correlated to the first high-power CO<sub>2</sub> laser, higher than 1 kW.

In any case this states that great and growing interest is addressed to this specific topic.

## New Perspectives

A lot of papers were written on laser cladding, showing the great interest for this topic and several attempts were made to optimize the process, mainly in terms of coating performance,

process modelling and process control. There is a significant growth of the research activity in Asia, particularly in China. Europe is also active, with specific research on aluminium components [28].

Future works could concern the development of self-governing machines for the process, which cannot only deposit a wide range of alloys, but can also make complex shapes. Other research efforts could focus on increasing the speed of the process, because the current processing speed is still slow, compared to the competitive techniques such as plasma and thermal spraying. Efforts should be also dedicated to the process modelling, after a better understanding of the process and of the relationship between laser energy, process speed, powder feed rate, and mechanical and metallurgical properties. In repair application of large parts it could be useful to build a laser cladding system that works in-situ, without removing the components, which means to develop new accurate positioning devices. This will be very useful also for rapid prototyping application to build very complex shapes.

Further fields of development are surely the micro and nano-technologies. In particular, laser cladding process can be used for the microstructure fabrication and some papers deals with these topics.

Finally, for coating application a new idea was proposed for future industrial application: the diode laser cure of thermosetting powders on metallic surface [29-31]. It has been developed for aesthetic purposes, in order to make writings and to personalize parts, but it can be also interesting for functional application when applied to small parts. The physical principle is different from traditional laser cladding one, because no melting of the substrate occurs, but a paint coating is obtained. The process can be divided in two main phases, in the first an electrostatic deposition of commercial thermosetting powder is performed on metallic surfaces, in the second the laser beam passes on the powder following a fixed path and cures it, making the coating. In order to obtain a high definition of the borders, a further preliminary phase has been put, the generation of the area to paint by using an adhesive tape. The adhesive tape can be cut by laser, corresponding to the area to paint, then it can be removed to allow the powder deposition and laser cure. Figure 7 shows a scheme of the new system. This way the process can be performed to produce the coating in a completely automatic process, as shown in [29-30].

By using an AISI 304 steel sheet substrate, 90x90x1mm<sup>3</sup> in size, subjected to cataphoresis treatment, and epoxy-polyester powders, the diode laser power was found in the range 50-65 W for a scan speed of 1 or 2 mm/s. Very good results in terms of aspect and adhesion to the substrate were found, demonstrating that the diode laser is a useful tool to cover small parts using a thermosetting powder.

Future work will be necessary to thoroughly understand the physical phenomena involved in the process and to characterize the coating and the adhesion.

## REFERENCES

- [1] Ehsan Toyserkani, Amir Khajepour, Stephen Corbin, *Laser Cladding*, 2004, CRC Press.
- [2] Hans Gedda, Laser Surface Cladding A Literature Survey, *Technical Report*, 2000, ISSN:1402-1536.
- [3] Santo, L. Int. J. Surface Science and Engineering, 2008, Vol. 2, No. 5, 327, 336.

- [4] de Oliveira, U; Ocelik, V; Th. JM. De Hosson, *Surface and Coating Technology*, 2005, 197, pp.127-136.
- [5] Paulo Davim, J; Oliveira, C; Cardoso, A. *Journal of Engineering Manufacture, part B*, 2006, 220 pp. 1549-1554.
- [6] Nan Yang Optics & Laser Technology, 2009, 41, 94-98.
- [7] Plati, A; Tan, J.C; Golosnoy, IO; Persoons, R; van Acker, K; Clyne, TW. *Advanced Engineering Materials*, 2006, 7, 619-624.
- [8] Jendrzejewski, R; Sliwinski, G; Krawczuk, M; Ostachowicz, W. *Surface & Coatings Technology*, 2006, 201, 3328-3334.
- [9] Knut Partes; Carlo Giolli; Francesca Borgioli; Ugo Bardi; Thomas Seefeld; Frank Vollertsen *Surface & Coatings Technology*, 2008, 202, 2208-2213.
- [10] Viswanathan, A; Sastikumar, D; Harish Kumar, AK. *Nath Surface & Coatings Technology*, 2009, 203, 1618-1623.
- [11] Janne Nurminen; Jonne Nakkila; Petri Vuoristo *International Journal of Refractory Metals & Hard Materials*, 2009, 27, 472-478.
- [12] Navas, C; Conde, A; Fernandez, BJ; Zubiri, F; de Damborenea, J. *Surface & Coating Technology*, 2005, 194, 136-142.
- [13] Feng, J; Ferreira, MGS; Vilar, R. *Surface & Coatings Technology*, 1966, 88, 212-218.
- [14] Cheng, FT; Lo, KH; Man, HC. *Materials Science & Engineering*, 2004, 380, 20-29.
- [15] Chengyun Cui, Zuoxing Guo, Yuhua Liu, Qiongqiong Xie, Zheng Wang, Jiandog Hu, Yuan Yao, *Optics & Laser Technology*, 2007, 39, 1544-1550.
- [16] Paul, CP; Alemohammad, H; Toyserkani, E; Khajepour, A; Corbin, S. *Materials Science & Engineering*, 2007, 464, 170-176.
- [17] Sun, S; Durandet, Y; Brandt, M. *Surface & Coatings Technology*, 2005, 14, 225-231.
- [18] Anjos, MA; Vilar, R; Qiu, YY. *Surface & Coatings Technology*, 1997, 92, 142-149.
- [19] Hamidreza Alemohammad, Shahrzad Esmaeili, Ehsan Toyserkani, *Materials Science & Engineering*, 2007, 456, 156-161.
- [20] Dawei Zhang, Xinpeng Zhang, *Surface & Coatings Technology*, 2005, 190, 212-217.
- [21] Tobar, MJ; Amado, JM; Alvarez, C; Garcia, A; Varala, A; Yanez, A. *Surface & Coatings Technology*, 2008, 202, 2297-2301.
- [22] Conde, A; Zubiri, F; de Damborenea, J. *Materials Science and Engineering A*, 2002, 334, 233-238.
- [23] Guojian Xu, Muneharu Kutsuna, Zhongjie Liu, Katsusige Yamada, *Surface & Coatings Technology*, 2006, 201, 1138-1144.
- [24] Dubourg, L; Ursescu, D; Hlawka, F; Cornet, A. *Wear*, 2005, 258, 1745-1754.
- [25] Godfrey, C; Onwubolu, J; Paulo Davim; Carlos Oliveira; A. Cardoso *Optics & Laser Technology*, 2007, 39, 1130-1134.
- [26] Pei Quan Xu; Hong Ying Gong; Guo Xiang Xu; Jian Ping He; Zhi Shui Yu *J Mater Sci* 2008, 43, 1559-1567.
- [27] Paulo Davim, J; Carlos Oliveira; A. Cardoso *Materials and Design*, 2008, 29, 554-557.
- [28] Dubourg, L; Archambeault, J. *Surface & Coatings Technology* 2008, 202, 5863-5869.
- [29] Italian Patent n° IT:RM2008A000580.

- [30] Santo L; Tagliaferri V; Trovalusci F; Proceedings of ASME 2009 International Manufacturing Science and Engineering Conferenze (MSEC2009), October 4-7, 2009, West Lafayette, Indiana, USA,
- [31] Quadrini, F; Santo L; Tagliaferri V; Trovalusci F., *Polymer-Plastics Technology and Engineering*, in press.

## ***Chapter 11***

# **LASER PROTOTYPING OF POLYMER-BASED NANOPLASMONIC COMPONENTS**

***Andrey L. Stepanov<sup>a,b\*</sup>, Roman Kiyani<sup>a</sup>, Carsten Reinhardt<sup>a</sup>  
and Boris N. Chichkov<sup>a</sup>***

<sup>a</sup>Laser Zentrum Hannover, 30419 Hannover, Germany

<sup>b</sup>Kazan Physical-Technical Institute, Russian Academy of Sciences, 420029 Kazan,  
Russian Federation

## **ABSTRACT**

Growing interest in the field of surface plasmon polaritons comes from a rapid advance of nanostructuring technologies. The application of two-photon polymerization by pulse laser technique for the fabrication of dielectric and metallic SPP-structures, which can be used for localization, guiding, and manipulation of plasmonic waves on a subwavelength scale, are studied. This fast technology is based on nonlinear absorption of near-infrared femtosecond laser pulses. Excitation, propagation, and interaction of SPP waves with nanostructures are controlled and studied by leakage radiation imaging. It is demonstrated that created nanostructures are very efficient for the excitation and focusing of plasmonic waves on the metal film. Examples of passive and active plasmonic components are presented and discussed.

## **INTRODUCTION**

Miniaturization is a central guideline in modern science and technology. Semiconductor electronic devices, which are fabricated today in industry, are characterized by low heat dissipation and limited propagation speed of electrical signals [1, 2]. An alternative, allowing a solution of these problems, is to use an optical data transmission. Therefore, miniaturized light sources and detectors are required as key elements for modern telecommunication and interconnector systems to combine with or to replace conventional electronic devices,

---

\* Corresponding author: e-mail: a.stepanov@lzh.de ; anstep@kfti.knc.ru

sensors, and actuators. Nowadays, both improved preparation and analytical methods allow the realization of structures in the range of *nanometers*. Many physical properties of material structures are dramatically modified when their sizes are reduced below one micrometer and thereby, approach the length scales of the effective light wavelengths. It is expected that the understanding and application of these novel effects will allow the development of a wealth of new methods and devices for applications in medicine, electronics, photonics, and material science.

Research at the nanoscale level has already been conducted for many years, whereas in optics, only first attempts towards nanophotonics have been undertaken recently. The miniaturization of conventional optical elements such as, for example, waveguides as well as the resolving power of optical microscopes is restricted by the diffraction limit. In the visible spectral range, this limit corresponds to about half a micron. A promising solution to overcome the diffraction limit is to use optics based on light field coupled to collective electron oscillations at the interface of a metal and a dielectric [3, 4]. Such mixed photon/electron surface modes are known as surface plasmon polaritons (SPPs) [5]. When SPP waves are excited on metal nanostructures, the surface structure dimension rather than the exciting light wavelength determines the special SPP electromagnetic field profile. This allows the overcoming of the diffraction limit and the realization of optical devices at the nanoscale dimensions.

As a propagating electromagnetic wave, SPPs in an extended metal structure can be used for the guiding of light fields, corresponding to *signal transfer* or *optical addressing* [6, 7]. A dispersion relation characterizes SPP waves and predicts that the plasmon wavelength is smaller than the vacuum light wavelength for any given light frequency [5, 7]. The metals of choice are usually gold or silver, as these metals possess high concentration of free conducting electrons and show SPP wave modes in the visible or near-infrared spectral range.

In summary, propagating SPPs in surface nanostructures can be used for electromagnetic signal transfer and nanoscale light field manipulation. Propagating plasmon effects can lead to the realization of nanoscale plasmon-based (*plasmonic*) optical devices. SPP waves can provide an interface between macrooptics and plasmonic nanocomponents. Examples demonstrating the broad prospects of SPP nanodevices:

- in analogy to electronics higher integration densities and easier fabrication techniques allow the realization of 2D- and 3D-devices using SPPs modes;
- the ongoing increase of the computer processor frequency can soon lead to a situation when the processor will be working faster than the communication speed via electrical signals in metal wires. Faster intra- and inter-chip connections are required. Conventional optical waveguides cannot be miniaturized to meet the demand of present and future integration densities. Instead of that, SPP waveguides could serve as optical interconnects with nanoscale sections;
- as mixed photon/electron oscillations, SPP waves could offer an elegant solution for the transformation of optical and electrical signals in a new generation of electro-optical devices.

The aim of this article is to present a short overview of the state-of-the-art in 2D- and 3D-laser nanomanufacturing by two-photon polymerization (2PP) technique and recent progress in the field of SPP and SPP-based nanodevices.

## LASER NANOMANUFACTURING OF SPP OPTICAL ELEMENTS

The possibility of very high localization of laser energy has led to more and more advanced laser applications. Particularly, the interaction of lasers with polymers and dielectrics is of high technological interest. The adaptation of polymers to laser characteristics and vice versa is very challenging from the scientific and technological points of view. A method which has recently attracted considerable attention is 2PP using femtosecond lasers [8-13], where complicated microstructures can be produced in photosensitive materials. It is very attractive 2D and 3D rapid microstructuring technology which provides much better structural resolution and quality than the well-known stereo-lithography (SL) technique. In spite of 2PP being a very young technology (ten years old), there are already several very nice and informative reviews published on this subject [14-16].

The very important distinction between the 2PP and SL technologies is that in the case of 2PP, near-infrared (IR) laser pulses, and in the case of SL, ultraviolet (UV) laser radiation are used for curing of photosensitive materials. From the first glance, it does not look like a big difference whether multiphoton (IR) or single photon (UV) absorption initiate polymerization processes. Taking into account that photosensitive materials are usually transparent in the infrared and are highly absorptive in the UV range, one can initiate polymerization with IR laser pulses within the volume and fabricate 3D structures, whereas with UV laser radiation, due to single photon absorption, polymerization also occurs at the surface. 3D structures made with tightly focused UV light have usually poor resolution. Therefore, for the fabrication of 3D structures, SL is used as a planar technology with layer-by-layer polymerization steps, whereas 2PP is a truly high-resolution 3D technology.

In this study the novel optical SPP components were produced by 2PP technique which is a very attractive technology for the fabrication of 3D structures on dielectric substrates with resolutions down to 100 nm. For 2PP and 3D material processing, usually near-infrared Ti:sapphire femtosecond laser oscillators working at a wavelength around 800 nm are applied. When femtosecond laser pulses are tightly focused into the volume of a photosensitive material (or photoresist), they initiate the 2PP process by two-photon absorption in certain photostarters and subsequent polymerization. After illumination of the desired structures inside the resist volume and development, e.g., washing out of non-illuminated regions, the polymerized material remains in the prescribed 3D structure. This allows the fabrication of any computer-generated 3D structure by direct laser recording into the volume of a photosensitive material.

The dielectric SPP elements are fabricated on glass or metal substrates by 2PP of the inorganic-organic hybrid polymer ORMOCER and the commercial lithographic resist maN-1405, both provided by microresist technology GmbH. The polymer can be polymerized by using a radical photoinitiator Irgacure 369 from Ciba Specialty Chemicals Inc.. The lithographic resist undergoes a bond cleavage upon illumination. Both materials change their refractive index during this process, allowing real-time observation of the polymerization.

For the fabrication of dielectric structures by 2PP, a femtosecond oscillator, Spectra-Physics Model Tsunami, is used. This system delivers laser pulses at a wavelength of 780 nm with a pulse duration of 80 fs (FWHM), and a repetition rate of 80 MHz. In present experiments, the average laser power of up to 40 mW is applied. The schematic of the setup used for the sample preparation is shown in Figure 1

Femtosecond laser pulses are focused by an immersion-oil objective (Nikon, 100x magnification, 1.3 NA). In case of the ORMOCEP, a liquid polymer droplet is sandwiched between the substrate and a cover glass with the thickness of 150  $\mu\text{m}$ . Their separation is fixed by a plastic frame with the size of 18 x 18 mm<sup>2</sup> and thickness of 100  $\mu\text{m}$ . For fabrication of surface structures, the laser beam is focused through the cover glass and the ORMOCEP layer on the substrate surface. During structuring, the laser beam can additionally be scanned along the sample surface by a galvo-scanner system from Scanlab. After completion of the 2PP and development of the surface polymer structures, the samples are washed in isobutyl-methylketon (4-methyl-2-pentanone) to remove remaining liquid material. At the final fabrication stage, 50-nm-thin gold films can be deposited on the dried samples with surface dielectric structures by electron or thermal sputtering / evaporation.

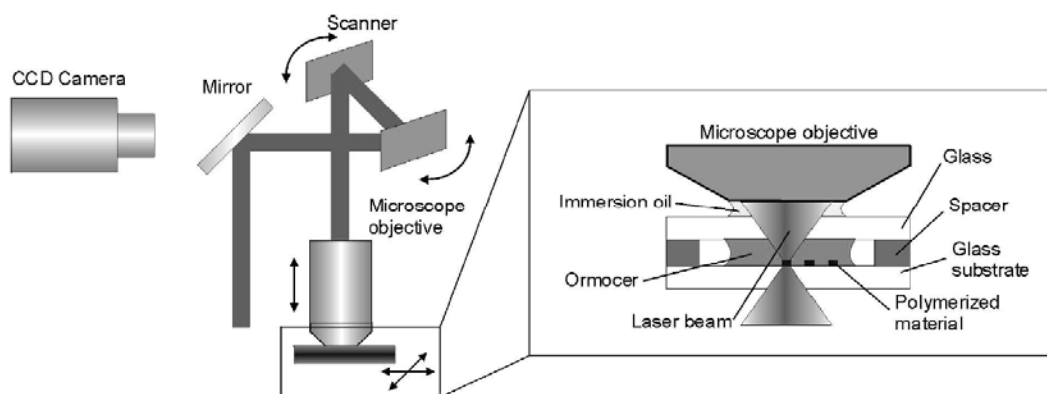


Figure 1. Schematic of the experimental setup for sample preparation by 2PP.

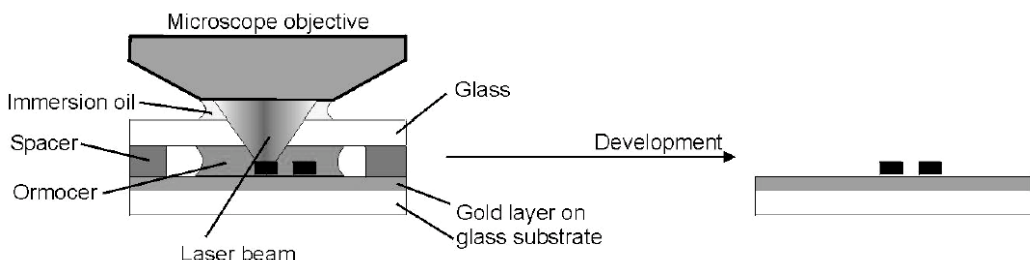


Figure 2. Schematic of setup for the fabrication of SPP surface structures from ORMOCEP.

Dielectric SPP structures can also be fabricated directly on the gold film, see Figure 2. Laser-induced polymerization on the reflecting metal surface is more problematic due to

interference effects and poor polymer adhesion to metals. 2PP of ORMOCEER on a gold layer is possible for a smaller range of laser powers compared to the 2PP on a glass substrate. Simultaneously the required threshold power for 2PP process decreases. The first effect is related to adhesion problems and laser heating of the gold layer. The reduction of the 2PP threshold can be explained by the interference of the incoming and reflected laser beams in the vicinity of the gold surface. In the interference maxima the polymerization threshold is reduced due to higher intensity. In addition, the high intensity laser pulse creates free electrons by multiphoton photoelectric effect which can also influence the polymerization process. Possible laser heating effects at the gold surface can result in a chemical destruction of the material. To avoid these effects, the interaction time of the laser beam with the material (and the gold surface) should be possibly short. Therefore, for fabrication of line structures, the laser beam is scanned with a velocity of 40  $\mu\text{m/s}$ . Multiple scanning of the fabricated structures reduces the 2PP threshold, since the total illumination time increases. With this procedure polymerization was observed in a range of laser powers between 8 mW and 16 mW. However, for powers exceeding 16 mW the possibility of structural defects during the fabrication process strongly increases. This can be explained by field enhancement effects at point-like inhomogeneities on the sputtered gold surface. The visibility of the interference pattern can be further reduced when a structure is written several times with a gradually increasing laser power, starting from the lowest power of 6 mW. With this procedure also the possibility of structural defects decreases. In this case, the field enhancement effects at point-like inhomogeneities are reduced due to a thin layer of polymerized material created during the first lower power scan.

Fabrication of dielectric SPP structures from maN-1405 is accomplished in a similar way. The resist is spin coated onto the substrate surface to the desired thickness, e. g. 500 nm layer thickness for 3000 rpm. The laser beam is then focused without immersion oil as depicted in Figure 3. The structures are scanned twice at laser powers around 20 mW.

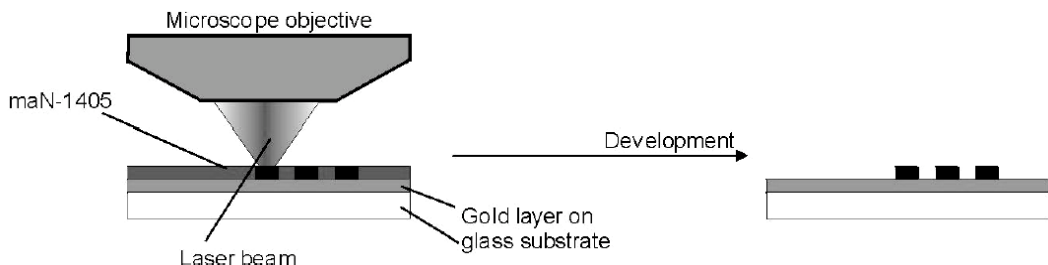


Figure 3. Schematic of setup for the fabrication of SPP surface structures from maN-1405.

Structuring by 2PP of ORMOCEER on transparent dielectric substrates has been studied in details. Some examples of 3D structures are shown in Figure 4. In contrast, the fabrication of polymerized structures by 2PP directly on metal surfaces has not been explored so far. Laser-induced polymerization on the reflecting metal surface is more problematic due to interference effects and poor polymer adhesion to metals.

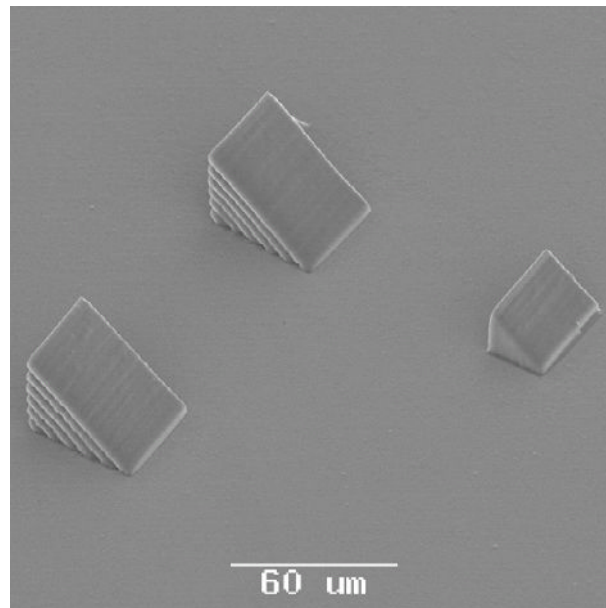


Figure 4. Prisms with optical quality fabricated by 2PP.

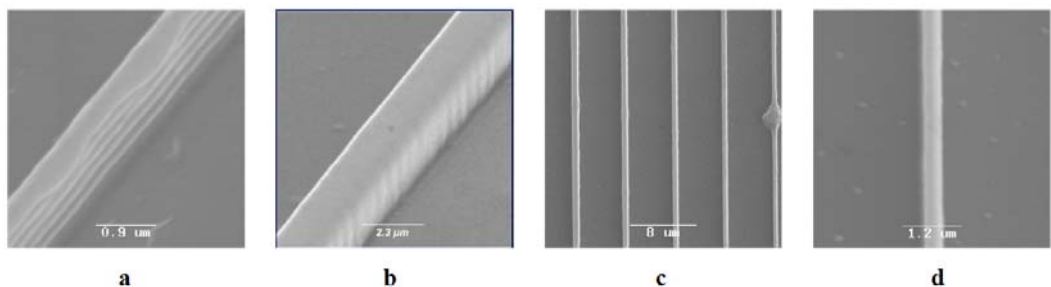


Figure 5. Comparison of laser fabricated dielectric line structures from ORMOCER on a) a metal covered and b) a bare glass substrate and maN-1405 on gold (c,d).

## FABRICATION OF OPTICAL WAVEGUIDING DIELECTRIC COMPONENTS

A scanning electron microscope (SEM) is used for the visual inspection of the fabricated samples. In Figure 5, SEM images of waveguide structures fabricated from ORMOCER on gold and glass surfaces are shown. Longitudinal modulations of the waveguide sidewalls due to interference of the incoming and reflected beam are evident in the structure fabricated on the gold surface by a single scan (Figure 5a), whereas they are not observed in the case of transparent glass substrate (Figure 5b). Structures fabricated from maN-1405 are generally less high, so that interference does not cause any problems. Lines of different width can be realized by adjusting of the applied laser power (Figure 5c and Figure 5d). Examples of dielectric couplers fabricated by 2PP of the ORMOCER and bond cleavage of maN-1405 on gold surfaces are shown in Figure 6 a and Figure 6b, respectively.

Longitudinal modulations of the waveguide sidewalls (Figure 4a) are evident in the structure fabricated on the gold surface, whereas they are not observed in the case of transparent glass substrate. This modulation appears due to the interference effects. The measured period of the interference pattern is 251 nm. This value is in good agreement with the interference period  $d = \lambda/2 n_{uc} \sim 254$  nm, determined by the half of the laser wavelength in uncured ORMOCECER. The slight transversal modulation of the sidewalls observed on the glass substrate can be addressed to small mechanical vibrations in the system. To compare resolution limits of 2PP technique on transparent (glass) and reflecting (gold) substrates, single polymerized voxels are fabricated in Ormocer on different surfaces using the same experimental setup. The diameter of the voxels fabricated on the glass and gold surfaces are

measured as a function of the applied laser power. The experimental results are fitted by a simple expression, where  $\sigma_2 = 3 \cdot 10^{-55}$  cm<sup>4</sup>s is the effective two-photon polymerization cross section measured before, and  $t=80$  fs is the laserpulse duration. The number of applied laser pulses  $n=v t$  is determined by the repetition rate  $v=80$  MHz of the laser system and the illumination time of a single voxel  $t$ , which has been set to  $t=200$  ms in these experiments. The dimensionless parameter  $C=\ln[\rho_0/(\rho_0 - \rho_{th})]$  depends on the primary initiator density  $\rho_0$  and the threshold density of radicals required for polymerization  $\rho_{th}$ . For the used Ormocer material we have  $\rho_0=1.5$  wt.% and  $\rho_{th}=0.25$  wt.%. The photon flux is defined by  $N_0 = 2PT (\pi r_0^2 \tau v h \omega)$ , where  $r_0$  is the beam radius,  $P$  is the average laser power,  $\omega$  is the laser frequency, and  $T$  is the factor taking into account light transmittance through the scanner and microscope objective,  $T=0.20$  in the present case.

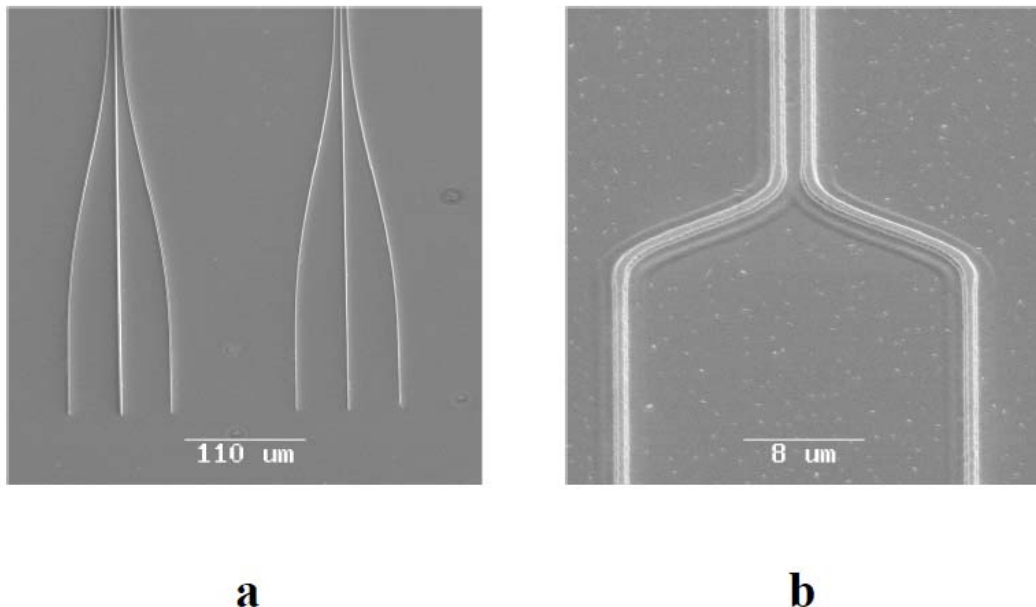


Figure 6. Example of coupling structures fabricated from ORMOCECER (a) and maN-1405 (b).

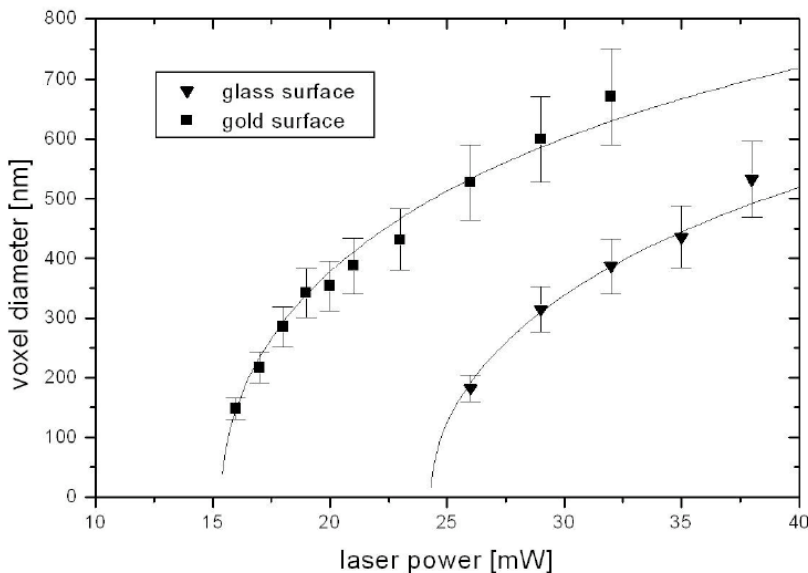


Figure 7. Comparison of the structuring parameters on gold and glass.

The experimental measurements of the voxel diameter and the results of the calculations are shown in Figure 7. In calculations of the voxel diameter on the glass surface, the beam radius  $r_0 = 520$  nm is used as a single fit parameter. To reproduce the experimental data for the voxel diameter on the gold surface, the influence of the reflected beam has to be taken into account. In this case the experimental data can be reproduced by replacing the photon flux  $N_0$  by  $1.6 \cdot N_0$ . This value is well below the maximum possible flux enhancement in the interference maxima given by a factor of 4. The reason for this is that, in our experiments, tightly focused laser pulses with a focus position slightly above the surface are used. Therefore, the reflected beam is divergent and has lower intensity. The interference enhancement factor of 1.6 corresponds to the expected value. Possible laser heating effects at the gold surface can result in a chemical destruction of the ORMOCEP material. To avoid these effects, the interaction time of the laser beam with the material (and the gold surface) should be possibly short. Therefore, for the fabrication of the line structures the laser beam is scanned with the velocity of 40  $\mu\text{m}/\text{s}$ .

To reduce the visibility of the interference pattern and to create more smooth structures, waveguides have been written two times keeping the laser power constant. Multiple scanning of the fabricated structures reduces the 2PP threshold, since the total illumination time increases. With this procedure polymerization was observed in a range of laser powers between 8 mW and 16 mW. However, for powers exceeding 16 mW the possibility of structural defects during the fabrication process strongly increases. This can be explained by field enhancement effects at point-like inhomogeneities on the sputtered gold surface. The visibility of the interference pattern can be further reduced when a structure is written several times with a gradually increasing laser power, starting from the lowest power of 6 mW. With this procedure also the possibility of structural defects decreases. In this case, the field enhancement effects at point-like inhomogeneities are reduced due to a thin layer of polymerized material created during the first lower power scan. To fabricate SPP structures

like waveguides, bends, and beam splitters with a smooth surface quality, the laser power is set initially to 6 mW and is gradually increased to 14 mW. For every laser power the structure is scanned two times. The resulting structures still show a weak interference pattern close to the metal surface but have much better surface quality. SEM pictures of a bend and y-splitter fabricated with this procedure are shown in Figure 8.

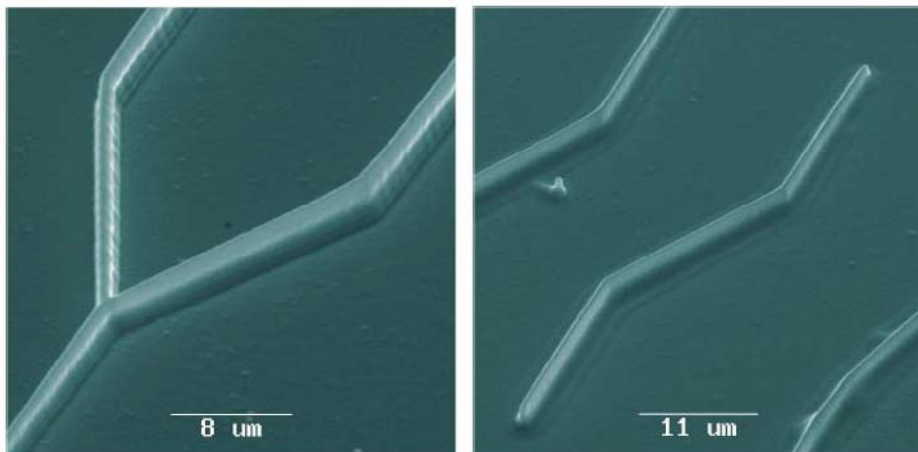


Figure 8. Structures fabricated on gold with multiple scanning.

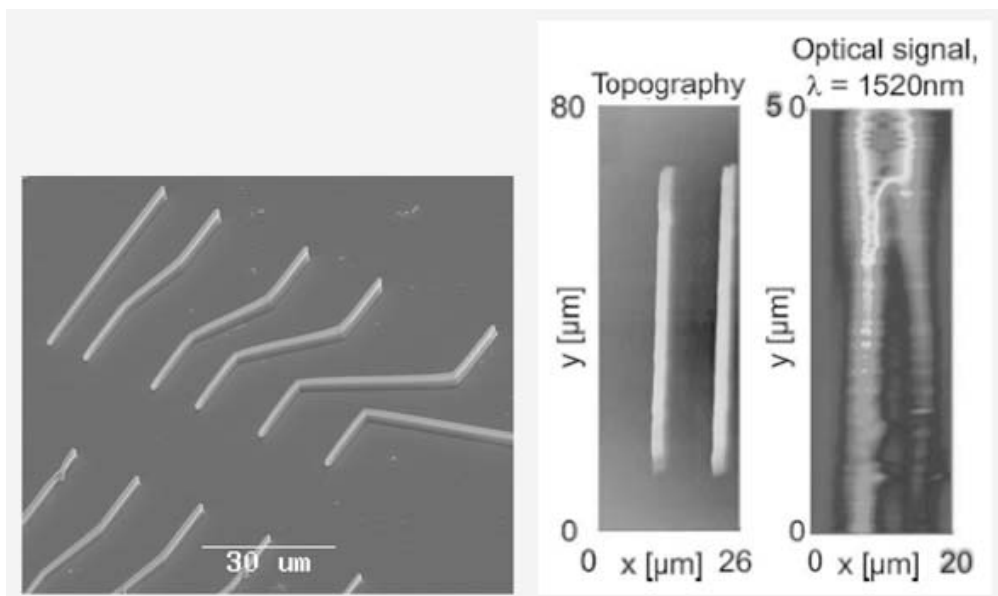


Figure 9. SPP near-field intensity distribution (right) of waveguide demonstrating guiding of SPP waves.

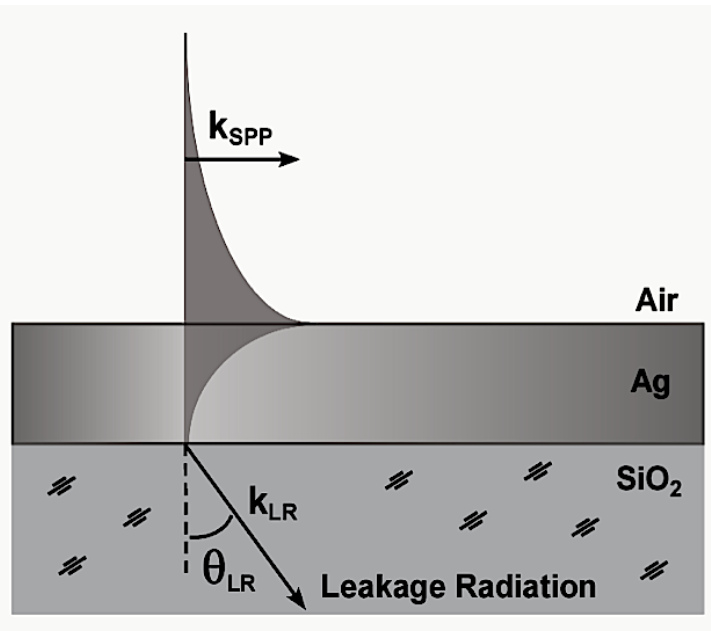


Figure 10. Plasmon excitation on topological surface structures and emission of leakage radiation.

SPP device technology makes use of the properties of surface waves – electromagnetic excitations propagating along and bound to interface between a metal and a dielectric. The intrinsically two-dimensional nature of SPPs is ideally suited for the planar waveguide realization, which can be implemented from polymers. Guiding properties of the dielectric SPP structures was studied with straight 60  $\mu\text{m}$  long ridges fabricated by 2PP. The SPPs are launched at the gold–air interface by a focused laser beam at a wavelength tip of 1520 nm in the Kretschmann-excitation configuration. The topography of the polymer ridges and the SPP near-field distribution imaged with a scanning near-field optical microscope are shown in Figure 9 [17]. It can be seen that a relatively wide SPP beam is partially coupled into, propagating along, and coupled out of the polymer ridge. At the same time, the rest of the (diverging) SPP beam continues to propagate along the air–gold interface and is reflected by the neighbouring ridge.

## LEAKAGE RADIATION IMAGING

The intensity decay length of a plane SPP wave in a metal film located between two dielectric media defines its intrinsic decay length  $L_{int}=1/2k''$ , where  $k''$  is defined as the imaginary part of the complex surface plasmon wave vector  $k_{SPP}=k'+ik''$ . Intrinsic losses are caused by inelastic scattering of conduction electrons, scattering of electrons at interfaces, and leakage radiation (LR). Leakage radiation is emitted from the interface between the metal thin film and a higher-refractive-index dielectric medium (Figure 10), for example, glass [18]. When the electromagnetic plasmon field crosses the metal film and reaches the substrate, leakage radiation appears at a characteristic angle with respect to the interface normal. This

radiation permits the detection of SPPs in the far-field [19, 20] and this approach was used in our study.

The experimental setup used for leakage radiation imaging is shown in Figure 11. For the local excitation of SPPs, the linearly polarized light from a Ti:Sapphire laser at wavelengths between 760 and 900 nm is focused through a microscope objective onto the surface of nanostructured gold or silver films. LR is detected by means of an oil immersion objective in optical contact with the glass substrate. By focusing this objective on the metal/glass interface, this radiation can be collected and either imaged or focused onto a photo-detector. The distribution of SPP is photo- or videotaped with a charge-coupled-device (CCD) camera. Each pixel element of an image captures the flux of LR emerging from the corresponding position at the metal-air interface. The latter is a direct quantitative measure of the SPP intensity at this position.

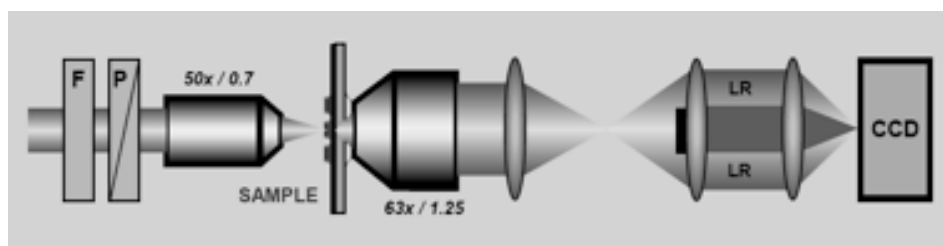


Figure 11. Experimental scheme of leakage radiation microscope. SPPs are excited by laser light on a structured metal film on a glass substrate. F (gray) filter, P polarizer.

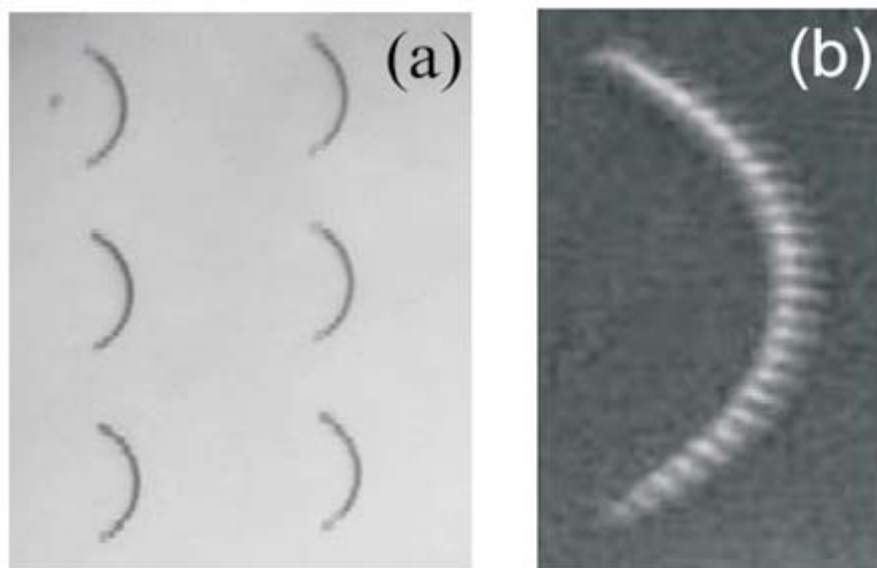


Figure 12. SEM image of (a) the sample with several surface structures, (b) an individual structure. The radius of the curved chains of nanoparticles is equal to  $10 \mu\text{m}$ . The particle in-plane size (diameter) and inter-particle distance are 350 nm and 850 nm, respectively.

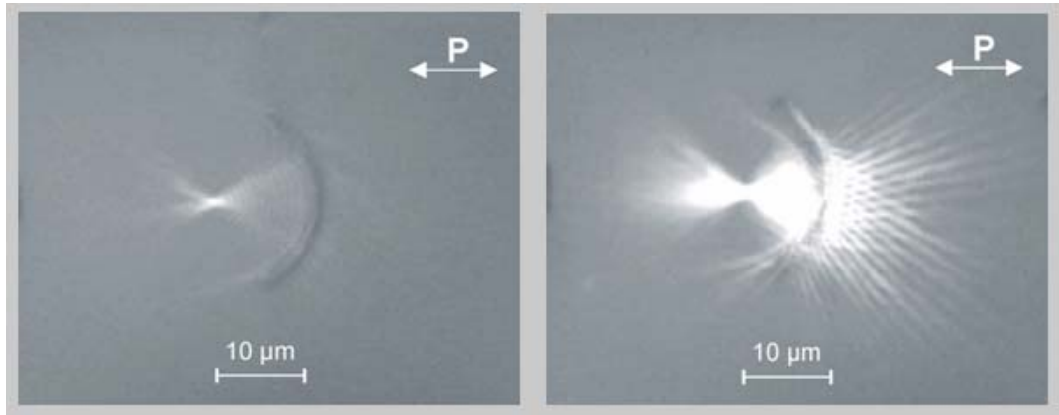


Figure 13. Experimental LR image of the SPP focusing by the surface structure. The arrow indicates the incident light polarization.

## NANOPLASMONIC COMPONENTS

SPP wave focusing on the flat metal surface was studied with a curved (circular) line of nanoparticles. Scanning electron microscope (SEM) os these structures are presented in Figure 12. Focusing of SPPs by the curved chains of nanoparticles was observed with by LR for moderate sizes of the incident laser beam (Figure 13, left). The SPP excitation was obtained by a focusing laser beam (at normal incidence) directed to the centre of the chain. The exciting laser spot was, in this case (Figure 13, right), equal to approximately  $10 \mu\text{m}$  in diameter. Interference of divergent SPPs excited by different particles results in the SPP focusing with a focal point located at the centre of curvature of the nanoparticle chain. As can seen, the focal SPP waist is very well localized and has relatively small value. In addition to the SPP focusing one can see that there is a system of SPP rays on the other side from the nanoparticle chain. The origin of this effect is again in the interference between the SPPs produced by the individual particles. Details of the numerical modelling of plasmon focusing efficiency are presented in [21].

When the incident laser spot is decreased down to  $3 \mu\text{m}$ , the SPP focusing effect becomes less pronounced (Figure 14), since only a few scattering centers are excited by the laser beam. The position where the laser beam is focused on the structure is indicated by the dashed circles. The SPP focal waist broadens resulting in a nearly parallel and relatively narrow SPP beam. In such case it is possible to control the propagation direction of the narrow SPP beam (always directed perpendicular to a local tangent of the particle chain) simply by changing the incident laser spot position along the chain (Figure 14). This effect is useful for the SPP manipulation in complex micro-optical elements utilizing chains of separated scatterers.

2PP provides possibilities for the realization and investigation of plasmon propagation on 3D surface structures. The schematic of first experiment is shown in Figure 15, where plasmons are excited on the left defect structure and propagate over a ramp structure. In this case leakage radiation from plasmons on the ramp structure is less visible compared to the leakage radiation from SPPs on the plane surface.

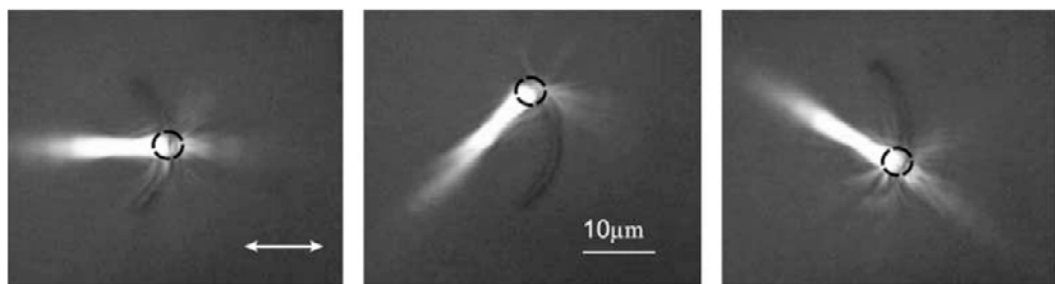


Figure 14. LR images of the SPPs excited by the surface structure. The diameter of the incident light spot for the SPP excitation (dashed circles) is equal to  $3\text{ }\mu\text{m}$ . (a) The exciting laser spot is at the centre of the structure, (b) and (c) the laser spot is shifted away from the centre. The arrow indicates the incident light polarization.

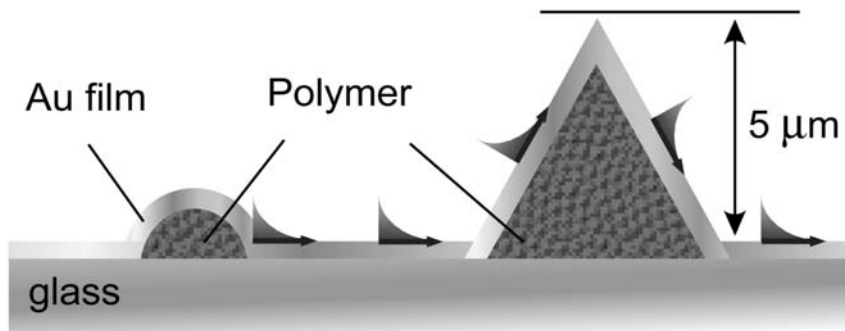


Figure 15. Schematic of a 3D surface structure for SPP propagation.

The LRM image together with the corresponding SEM image of the test structure is demonstrated in Figure 16. This result clearly indicates that SPPs can propagate on smoothly curved surfaces with curvatures larger than the SPP wavelength.

In conclusion, laser fabrication of dielectric 2D and 3D surface plasmon polariton (SPP) structures on metal surfaces by two photon induced polymerization of a high refractive index inorganic–organic hybrid polymer has been studied. Optical properties of the fabricated dielectric SPP structures have been investigated by leakage radiation microscopy of the propagating SPPs. Effective excitation and focusing of the SPPs have been demonstrated with dielectric structures. The demonstrated results on excitation and manipulation of SPP fields and the simplicity of laser fabrication technique provide interesting prospects for the realization of future plasmonic devices.

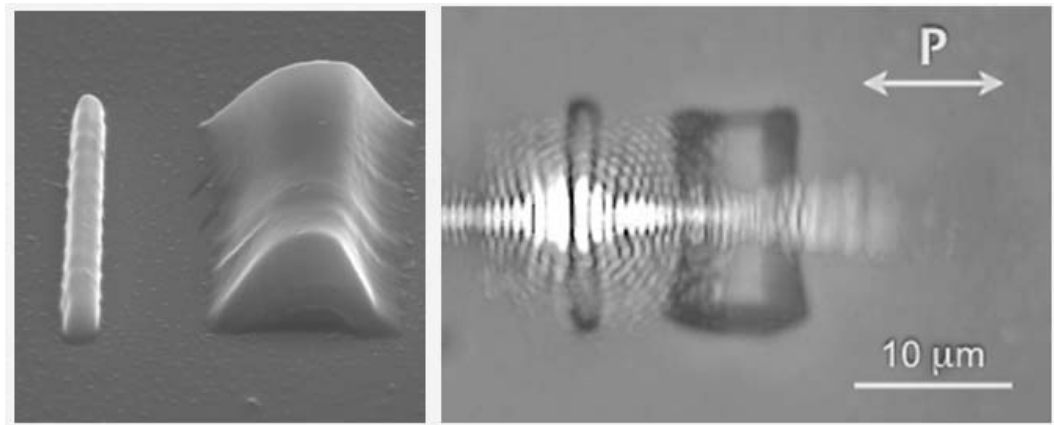


Figure 16. SEM image of the 3D structure fabricated by 2PP (left) and LR image of the SPPs excited on the ridge and propagating over the 3D structure (left).

## ACKNOWLEDGMENTS

The author (A.L.S.) is grateful to the Alexander Humboldt Foundation (Germany) and the Austrian Scientific Foundation in the frame of the Lise Meitner program for financial support.

## REFERENCES

- [1] Wong, H. & Ieai, H. (2005). *Physics World*, 18, 40.
- [2] Hitz, B. (2005). *Photonics spectra*, 39, 52.
- [3] Barnes, W. L., Dereux, A. & Ebbesen, T. W. (2003). *Nature*, 424, 824.
- [4] Ozbay, E. (2006). *Science*, 311, 189.
- [5] Raether, H. (1988). Surface Plasmons (Springer Tracts in Modern Physics: Berlin).
- [6] Weeber, J. C., Lacroute, Y. & Dereux, A. (2003). *Phys. Rev. B*, 68, 115401.
- [7] Drezet, A., Hohenau, A., Koller, D., Stepanov, A. L., Ditlbacher, H., Steinberger, B., Aussnegg, F.R., Leitner, A. & Krenn, J. R. (2008). *Mater. Sci. Eng. B*, 149, 220.
- [8] Maruo, S., Nakamura, O. & Kawata, S. (1997). 22, 132.
- [9] Cumpston, B. H., Ananthvel, S. P., Barlow, S., Dyer, D. L., Ehrlich, J. E., Erskine, L., Heikal, A. A., Kuebler, S. M., Lee, I. Y. S., McCord-Maughon, D., Qin, J. , Röckel, H., Rumi, M., Wu, X. L., Marder, S. R. & Perry, J. W. (1999). *Nature*, 398, 51.
- [10] Kawata, S., Sun, H. B. Tanaka, T. & Tanaka, K. *Nature*, (2001). 412, 697.
- [11] Serbin, J., Egbert, A., Ostendorf, A., Chichkov, B., Houbertz, R., Domann, G., Schulz, J., Cronauer, C., Frohlich, L. & Popall, M. (2003). *Opt. Lett.* 28, 301.
- [12] Deubel, M., von Freymann, G., Wegener, M., Pereira, S., Busch, K. & Soukoulis, C. M. (2004). *Nature materials.*, 3, 444.
- [13] Serbin, J., Ovsianikov, A. & Chichkov, B. (2004). *Opt. Express*, 12, 5221.
- [14] Sun, H. B. & Kawata, S. (2004). Two-photon polymerization and 3D lithographic microfabrication (Springer: Berlin).

- [15] Blanco, A., Busch, K., Deubel, M., Enkrich, C., von Freymann, G., Hermatschweiler, M., Koch, W., Linden, S., Meisel, D. C. & Wegener, M. (2004). Three-dimensional lithography of photonic-crystal in photonic crystal. Eds. K., Busch, S., Lölkes, R. B., Wehrspohn, H., Föll., (Wiley-VCH,).
- [16] Prasad, P. N. (2004). *Nanophotonics* (John Wiley & Sons).
- [17] Reinhardt, C., Passinger, S., Chichkov, B., Murquart, C., Radko, I. & Bozhevolnyi, S. *Opt. Lett.*, 31, 1307 (2006).
- [18] Raether, H. (1988). *Surface plasmons* (Springer: Berlin,).
- [19] Stepanov, A. L., Krenn, J. R., Ditlbacher, H., Honenau, A., Drezet, A., Steinberger, B., Leitner, A. & Aussenneg, F. R. (2005). *Opt. Lett.*, 30, 1524.
- [20] Kiyan, R., Reinhardt, C., Passinger, S., Stepanov, A. L., Hohenau, A., Krenn, J. R. & Chichkov, B. N. (2007). *Opt. Express*, 15, 4205.
- [21] Evlyukhin, A. B., Stepanov, A. L., Kiyan, R. & Chichkov, B. N. (2008). *J. Opt. Soc. Am. B*, 25, 1011.



## ***Chapter 12***

# **STRUCTURED BEAMS IN LASER REFRACTOGRAPHY APPLICATIONS**

***I.L. Raskovskaya, B.S. Rinkevichyus, and A.V. Tolkachev***

V.A. Fabrikant Physics Department, Moscow Power Engineering Institute  
(Technical University), Moscow, Russia

## **ABSTRACT**

In this chapter, the applications of structured laser beams in laser refractography technology are considered. The basic principles of laser refractography, a new method for diagnostics of optically inhomogeneous media and flows are described. This technology is based on the refraction of the structured laser beams in transparent inhomogeneity, digital registration and computer processing of the refraction pattern. The experimental setup allowed quantitative visualization of the transparent media by using 2D- or 3D-refractograms. The 3D-refractograms are used for visualization of the boundary layer near the hot or cold ball in water that are present. The problem of laser sheet (plane structured laser beam) also cylindrical beam propagation in media with radial variation of the temperature and refractive index is solved and the trajectories of geometrical rays are calculated. The comparison of the parameters for experimental and corresponding calculated refractograms allows recognizing the temperature fields in the boundary layer, i.e., gives quantitative information. The method is modified for studying edge effects and micro layers in liquids and gases. Due to nearly inertialess measurements, laser refractography can be used for diagnostics of fast and transient processes.

**Keywords:** Laser beam, structured laser beam, refraction, laser refractography, quantitative visualization.

## **1. INTRODUCTION**

Laser beams have been widely used for diagnostics in the fields of acoustic pressure, temperature, density, and flow velocity in transparent media [1-5]. First of all, optical

measurements do not distort the fields under study because the energy being absorbed by the medium is quite low in most cases. In addition, laser methods almost have no inertial errors which makes it possible to perform precision measurements of fast processes. The possibility to perform remote measurements is an additional advantage of these methods. Laser methods can be used to study the refraction index field, which can be subsequently recalculated into the field of another physical quantity being sought. The modern stage of development of laser and computational techniques is characterized by the advent of visible semiconductor lasers, commercial production of Diffraction Optical Elements (DOE), digital video and photo cameras with the number of pixels exceeding millions, and the development of new effective digital methods for optical image processing. All these factors have made it possible to create optical diagnostic methods for inhomogeneous media at a qualitatively new scientific and technical level by developing methods for obtaining information on the medium or a flow in the chosen cross section (2D-diagnostics) and in the bulk (3D-diagnostics).

Refraction methods for diagnostics of flows have been revived in recent years due to the above-listed factors. Array photodetectors and computers have made it possible to work out new methods of laser gradient refractometry (speckle method [6], as well as computer-laser [7] and Background Oriented Shadow (BOS) methods [8]). High-quality laser beams of various shapes are produced by using simple optical systems. Scanning and multichannel refractometric systems with computer-assisted image processing have been developed [5]. Main laser refraction gradient methods for diagnostics of flows and corresponding laser beams are shown in Figure 1.

*Laser refractography (LR)* [4] is a new technology of laser diagnostic for optically inhomogeneous media such as liquid, gas and plasma flows. Laser refractography is based on refraction of structured laser beams in optically inhomogeneous media and digital recording of the refraction pattern. This method is a quantitative integral method used for studying transparent stationary and nonstationary media.

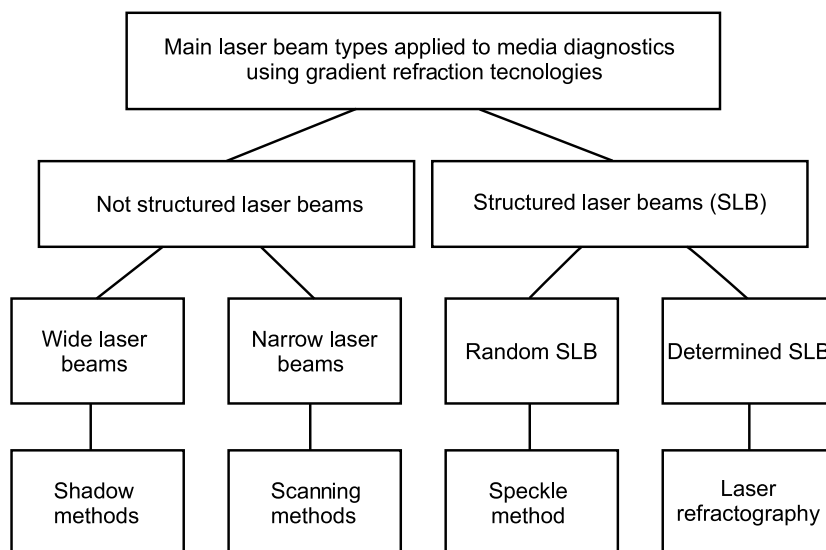


Figure 1. Main laser gradient refraction methods.



A) Dot laser beam near a hot cylindrical inhomogeneity      b) Astigmatic Gaussian laser beam near a cooled ball in water      c) Besselian laser beam near a hot ball in water

Figure 2. Typical 2D-refractograms of SLB.

Single Line	Crosshair	Parallel Lines	Concentric Circles
Single Dot	Single Circle	Dot Line	Dot Matrix

Figure 3. The main types of SLB.

## 2. MAIN TYPES OF THE STRUCTURED LASER BEAMS

*Structured Laser Beam (SLB)* is a spatially amplitude-modulated radiation obtained mainly with the help of DOE [9-10]. DOE is a previous or reflective plate with a phase micro relief calculated in the diffraction theory context. An evolution of microelectronics and laser techniques has made it possible in a practical manner to create a DOE with a complex zone profile and unique characteristics, unattainable in the context of traditional optics. The most perspective for use in LR are DOE that focus laser radiation into thin lines or small areas, which corresponds to a structured beam with an intensity modulation. The structured laser beam passing through a medium forms a 2D-refraction pattern on the screen, whose shape is determined by the type of SLB and the spatial distribution of the refractive index depending on temperature, pressure, density, salinity and other parameters of the medium [11]. In this case, beam structure elements are directly traced in its section and refractograms (refraction

pattern) are of a contour graphic nature (Figure 2), which was actually the reason for the "refractography" term to appear.

The main types of SLB sources are given in Figure 3 and classified according to the shape of 3D geometrical figures formed by the beams from the sources of line-, plane- and cone-structured laser radiation. The two-dimensional figures shown in Figure 3 are cross sections of the beams formed by a family of geometrical optics rays from the source. Combining the main types of sources, we can also create other sources adapted to the structure of inhomogeneities and to the shape of the surface of bodies near which the boundary layers are studied. For the diagnostics of spatial inhomogeneities, it is expedient to form measuring "networks" of elementary sources.

Obviously, the above approach is valid in the geometrical optics approximation. Hence, to determine the range of applicability of the method, the error associated with diffraction effects in actual measuring devices should be estimated. For example, plane-structured laser radiation, also known as the "laser sheet" (LS), is actually an astigmatic Gaussian laser beam with an elliptical cross section whose diffractional divergence is determined by using the familiar quasi-optical methods. The complex amplitude of the Gaussian astigmatic laser beam at  $z = 0$  (at the entrance to the medium) be  $E(x,y,0)$ :

$$E(x, y, 0) = \exp \{i[kx \sin \alpha]\} A^0(x, y, 0), \quad (1)$$

where  $A^0(x, y, z)$  is the beam envelope in the medium

$$A^0(x, y, z) = A_x^0(x, z) A_y^0(y, z) = \frac{A^0(0, 0, z_F)}{\sqrt{1 + D^2}} \exp \left\{ -\frac{x^2}{w_1^2(1 + D^2)} - \frac{y^2}{w_2^2(1 + D^2)} \right\}, \quad (2)$$

where  $A_x^0(x, z)$ ,  $A_y^0(y, z)$  are corresponding  $x$  and  $y$  depended components,  $z_F$  is the waist coordinate and

$$D = \frac{(z - z_F)}{R_F}. \quad (3)$$

with  $R_F$  – confocal radius.

The laser beam with elliptical cross section has two effective radii at the waist  $w_1$  ( $x$ -axis direction) and  $w_2$  ( $y$ -axis direction). There is laser sheet when  $w_1 \ll w_2$  or  $w_2 \ll w_1$ . Laser sheet forming can be done using cylindrical lenses or DOE. Refractograms of the Gaussian laser beam with elliptical cross section (plane beam or LS) are shown on Figure 2 b.

The cylindrical or conical beams correspond to the Besselian beam. Besselian beam is a laser radiation model that has a number of peculiarities: intensity distribution in its section defines by Besselian functions of different orders; the beam has a central symmetry and is practically non-diffractive (i.e., its structure is invariable when the beam spreads through space).

The use of Besselian beams in optically heterogeneous medium diagnostics is rather perspective thanks to a high spatial radiation concentration within tight laser cord or tube boundaries. It allows to obtain tight laser probes and investigate with their help heterogeneous

mediums or flows on a long distances. Besselian beam of zero order defines by Besselian function of the same order in cylindrical coordinates  $(r, \psi, z)$  when spreading along  $z$  axis; amplitude distribution is

$$E(r, \psi, z) = AJ_0(k_0 nr \sin \theta_0) \exp(ik_0 nz \cos \theta_0), \quad (4)$$

where  $A$  – field amplitude,  $J_0(x)$  – first kind Besselian function of zero order,  $\theta_0$  – angular beam parameter,  $n$  – medium refraction index,  $k_0$  – mode number for vacuum.

Beam amplitude does not depend on  $\psi$  angle, i.e. the beam has a central symmetry. Beam phase changes in  $z$  axis direction with the velocity  $v = c/(n\cos\theta_0)$ , more than  $v = c/n$ , while amplitude doesn't depend on  $z$ . Using spectral approach Besselian beam can be presented as a result of interference of plane waves, spreading with an  $\theta_0$  angle to  $z$  axis, the resulting interference field is practically concentrated in an area, bounded by first zero of the  $J_0(x)$  function.

The easiest way to obtain a Besselian beam is the use of cone lenses – axions [9]. Besselian beam appears as a result of interference of plane waves spreading with the same angle to axion axis. Interference figure will look like bright central beam circled with a system of rings.

Besselian beam forming can also be done using DOE. Refractograms of the Besselian beams are shown on Figure 2 c.

### 3. PLANE SLB REFRACTION IN A SPHERICAL INHOMOGENEITY

For developing the method for constructing theoretical refraction patterns, LS refraction is studied [11-13] in a spherical layered medium with refractive index  $n = n(r)$ . Figure 4 illustrates the geometry of the problem. A laser beam in the form of LS 1 at right angles to the  $x$  axis propagates along the  $z$  axis. The origin of coordinates coincides with the centre of spherical inhomogeneity 2. The projection of the laser sheet is observed on screen 3 in a plane perpendicular to the  $z$  axis and located at a distance  $z_1$  from the origin. The Cartesian and spherical coordinates are related by the expressions:  $x = r \sin \theta \cos \varphi$ ,  $y = r \sin \theta \sin \varphi$ ,  $z = r \cos \theta$ .

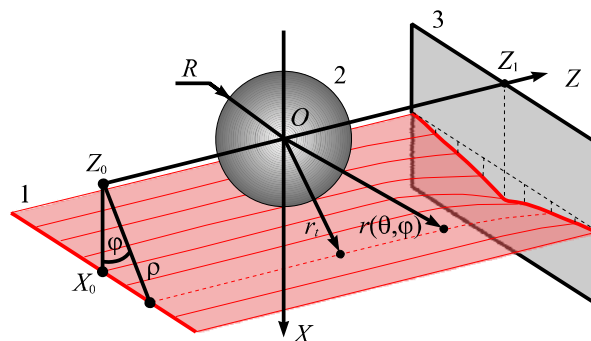


Figure 4. Geometrical parameters need for refractograms calculation: 1 – laser sheet; 2 - spherical inhomogeneity; 3 - screen.

For  $z = z_0$ , the LS equation has the form  $x = x_0$ . The impact parameter  $\rho$  of a beam lying in the LS is determined by angle  $\varphi$  (beam parameter)

$$\rho(\varphi) = \frac{x_0}{\cos \varphi}. \quad (5)$$

In the case of spherical symmetry, this beam remains in the plane defined by parameter  $\varphi$  and its trajectory is described by the dependence  $r(\theta, \varphi)$ . The trajectories of beams are calculated using the relations describing their propagation in the spherical inhomogeneity [14]. The method for determining the trajectory of propagation of a beam in such a medium involves the splitting of the trajectory into two segments: from the point of entrance to the turning point and from the turning point to the plane of observation. In the case considered here, the turning point is determined by the minimal distance  $r_t$  from the beam trajectory to the origin (centre of the inhomogeneity) and can be determined from the equation

$$r_t n(r_t) = n_0 \rho(\varphi), \quad (6)$$

where  $n_0$  is the unperturbed refractive index (for  $z = z_0$ ).

The radial coordinate of the beam at the input to the medium (for  $z = z_0$ ) is given by

$$r_0(\varphi) = \sqrt{\rho^2(\varphi) + z_0^2}. \quad (7)$$

The angle  $\theta_0$  characterizes the direction of the beam entering the medium:

$$\theta_0(\varphi) = \frac{\pi}{2} + \operatorname{arctg} \frac{z_0}{\rho(\varphi)}. \quad (8)$$

The angle corresponding to the turning point is given by

$$\theta_t(\varphi) = \theta_0(\varphi) + \int_{r_0(\varphi)}^{r_t(\varphi)} \frac{n_0 x_0 dr}{r \cos \varphi \sqrt{n^2(r)r^2 - n_0^2 \rho^2(\varphi)}}. \quad (9)$$

The equation of the trajectory of the beam up to the turning point has the form

$$\theta(r, \varphi) = \theta_0(\varphi) + \int_{r_0(\varphi)}^r \frac{n_0 x_0 dr}{r \cos \varphi \sqrt{n^2(r)r^2 - n_0^2 \rho^2(\varphi)}}, \quad (10)$$

while the equation for the trajectory beyond the turning point is

$$\theta(r, \varphi) = \theta_t(\varphi) + \int_r^{r_t(\varphi)} \frac{n_0 x_0 dr}{r \cos \varphi \sqrt{n^2(r)r^2 - n_0^2 \rho^2(\varphi)}}. \quad (11)$$

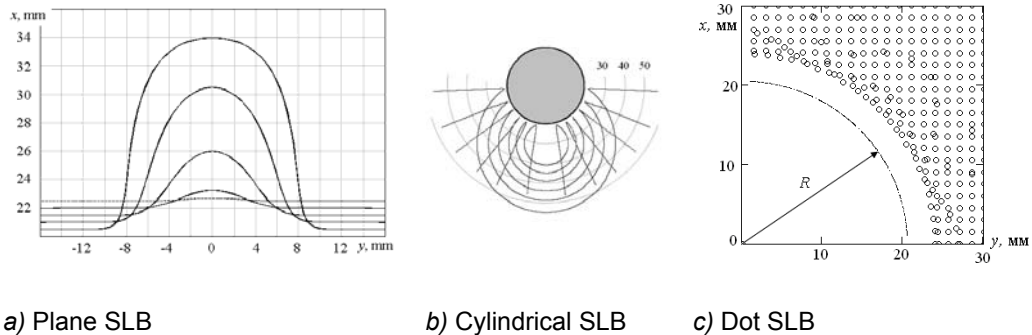


Figure 5. Calculated 2D-refractograms of the main SLB near a heated ball in water.

Relations (9) and (10) form the basis for calculating refraction of the laser sheet in a spherical inhomogeneity. The angle  $\varphi$  is a parameter specifying an arbitrary beam in the LS, which allows us to describe the entire family of beams belonging to the laser sheet. The radial coordinate  $r(z_1, \varphi)$  of the beam on the screen lying in plane  $z = z_1$  can be determined from the relation

$$r \cos \theta(r, \varphi) = z_1, \quad (12)$$

while the coordinates of laser sheet projection on the screen can be found from the equations

$$\begin{aligned} x(z, \varphi) &= r(z, \varphi) \sin \theta(r(z, \varphi), \varphi) \cos \varphi, \\ y(z, \varphi) &= r(z, \varphi) \sin \theta(r(z, \varphi), \varphi) \sin \varphi. \end{aligned} \quad (13)$$

These relations define the structure of refraction pattern for the given spherical inhomogeneity. For the cylindrical SLR we use the same equations (6-13) but instead of (5)

$$\rho_{1,2}(\varphi) = \xi_0 \cos \varphi \pm \sqrt{r_i^2 - \xi_0^2 \sin^2 \varphi}, \quad (14)$$

where  $\rho_{1,2}$  are two benches of the solution  $\rho(\varphi)$  for the cylindrical surface of radius  $r_i$  with the axis  $(\xi_0, 0)$ .

#### 4. 2D- AND 3D-REFRACTOGRAMS

*2D-refractograms* [4] is the 2D-image of a source of spatially structured radiation formed by an optical system whose role is played by the medium under study. In this respect, the refractography technique is close to the BOS method in which images of the structured screen with randomly distributed points are studied in natural light passing through an optically inhomogeneous medium. The fundamental difference between laser refractography and the BOS method is the use of coherent laser radiation which allows a quantitative diagnostics of the medium and an analysis of interference effects carrying additional information. Moreover,

observation of laser radiation scattered by small particles makes it possible to visualize the region under investigation. 2D-retraction patterns can be used for quick diagnostics of inhomogeneities even without subsequent computer processing. Figure 5 shows typical 2D-refractograms of the main SLB near a heated ball in water.

*3D-refractograms* is a 3D image of the surface formed by the rays from SLB refracted in the medium (Figure 6), and can be obtained from the entire body of experimental and theoretical 2D-refraction patterns for various cross sections with the help of a special technique [4]. A 3D-refraction pattern can be visualized experimentally in scattered radiation.

2D- and 3D-refraction patterns are recorded with a digital video camera attached to the PC used for their processing. By comparing experimental and theoretical refraction patterns we can reconstruct the inhomogeneity profile and verify the numerical methods of computing the flow parameters.

## 5. SLB REFRACTOGRAMS FOR A SPHERICAL TEMPERATURE BOUNDARY LAYER

Note that all optical methods in fact describe the field of the refractive index, which can be subsequently transformed into the temperature field  $T(x,y)$  or the field of some other parameter. Following [15], we shall analyze thermal processes assuming that for laser wavelength  $0.6328 \mu$ , the temperature dependence of the refractive index of water is determined by the approximate dependence  $n(t)$  [4]. The mathematical simulation of refraction of a LS in a spherically symmetric thermal boundary layer around a sphere of radius  $R$  is performed for the radial temperature dependence described by the expression

$$T(r) = T_0 + \Delta T e^{-\frac{(r-R-\Delta R)^2}{a^2}}, \quad (15)$$

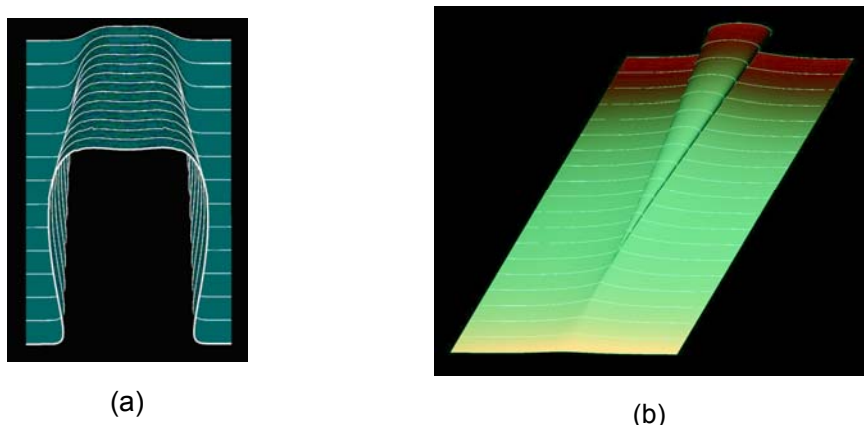


Figure 6. Calculated 3D-refractograms of the LS propagating near hot (a) and cold (b) ball in water

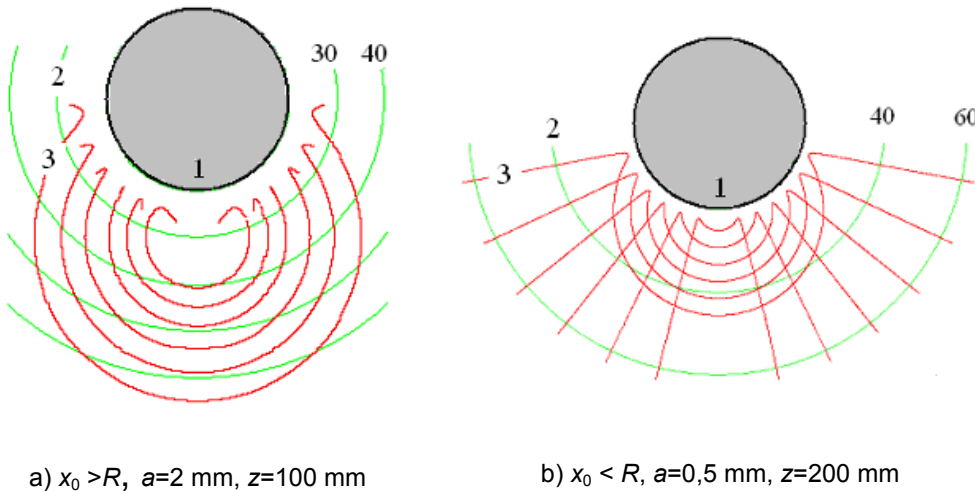


Figure 7. Typical calculated 2D-refractograms of the cylindrical SLB propagating in water under a hot ball at  $T=90^\circ\text{C}$ ,  $R=20$  mm: 1-ball, 2-coordinate lines, 3-cylindrical SLR 2D-refractograms.

where  $T_0$ ,  $\Delta T$ ,  $\Delta R$ , and  $a$  are model parameters of the temperature field. The parameter  $T_0$  is determined by the temperature of the walls of a cell filled with a liquid, temperature  $T(R)$  is equal to the temperature  $T_s$  at the surface of the sphere, and the ratio  $\Delta T/a$  corresponds to the temperature field gradient in a boundary layer of thickness  $a$ . For a hot sphere,  $\Delta T > 0$ , while for a cold sphere, we have  $\Delta T < 0$ .

For example, figure 6a shows 3D-refractograms for model of temperature distribution (15) in the vicinity of a hot sphere in water. Figure 6b shows 3D-refractograms for model of temperature distribution (15) in the vicinity of a cooled sphere in water with parameters  $R = 25.4$  mm,  $T_0 = 70$   $^\circ\text{C}$ ,  $\Delta T = -57$   $^\circ\text{C}$ ,  $\Delta R = -1$  mm,  $a = 2$  mm,  $x_0 = 25.5$  mm and distance  $z$  increasing.

A typical feature of the "cold" spherical in homogeneity in water is the formation of a loop on refractograms. For temperature gradients close to zero, a characteristic extremum (Figure 6b) is observed on the loop directly at the surface of the sphere, which is associated with a slight deviation of beams in this region. The temperature distribution in the layer in this case is nearly Gaussian. No extremum is formed for an exponential distribution.

Thus, visualization of an inhomogeneity in the medium with the help of refraction patterns makes it possible to carry out quick diagnostics of the type of the inhomogeneity and draw conclusions about the temperature distribution in a thin boundary layer. The formation of a loop on the refraction pattern is directly linked with the presence of axial caustics [4] that can be visualized experimentally.

Figure 7 shows typical 2D-refractograms of the cylindrical SLB for model of temperature distribution (15) in the vicinity of a hot sphere in water at  $T=90^\circ\text{C}$ ,  $R=20$  mm. Figure 8 shows typical calculated 3D-refractograms of the cylindrical SLB at the same conditions.

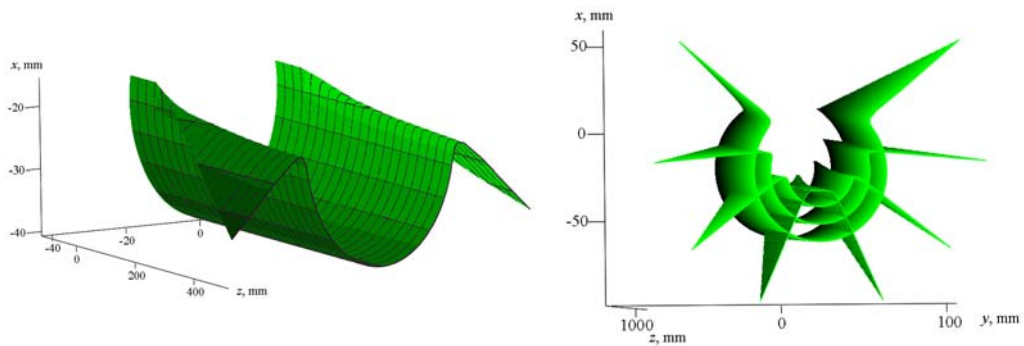


Figure 8.Calculated 3D-refractograms for a cylindrical SLB propagating in water under a hot ball.

## 6. EXPERIMENTAL SETUP USING STRUCTURED BEAMS FOR TEMPERATURE PROFILE RECONSTRUCTION

Figure 9 shows a principal scheme of the experimental setup for visualization of thermal physical processes under natural nonstationary convection [15] in a liquid in a vicinity of heated (cooled) bodies with the help of SLB.

The setup consists of laser 1 with a DOE fixed on it's frame, and an adjusting bench 2. At the exit from DOE, an SLB 3 is formed and directed into water-filled cuvette 5 with a heated or cooled object 4 in it. The object's temperature is measured by means of thermocouple and digital voltmeter. Refraction image is viewed on a semitransparent screen 6. This image is recorded by the digital video camera 7. Signal from camera 7 are transmitted to the personal computer 8. The metal object was then heated to a temperature of 50–100°C, or cooled to 9–10°C and then immersed in a vessel filled with water. After this, video recording of the refraction pattern on screen was performed for several minutes. The recorded image of the refraction pattern was loaded into a computer and processed with the help of a special software.

Figure 10 shows the experimental 2D-refractograms of the SLB propagating near the surface of the typical bodies. The measuring technique provides simultaneous diagnostics of the process in the region of passage of SLB in the boundary layer immediately over the sphere.

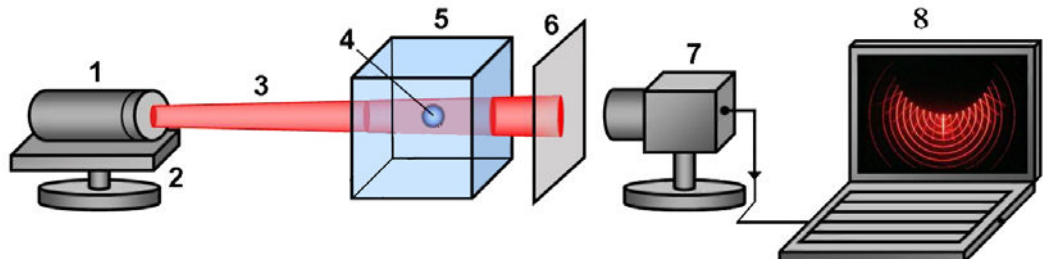


Figure 9. The experimental setup scheme: 1 – laser, 2 – adjusting bench, 3 – SLB, 4 – object, 5 – cuvette, 6 – semitransparent screen, 7,8 – digital video camera, 9 – computer.

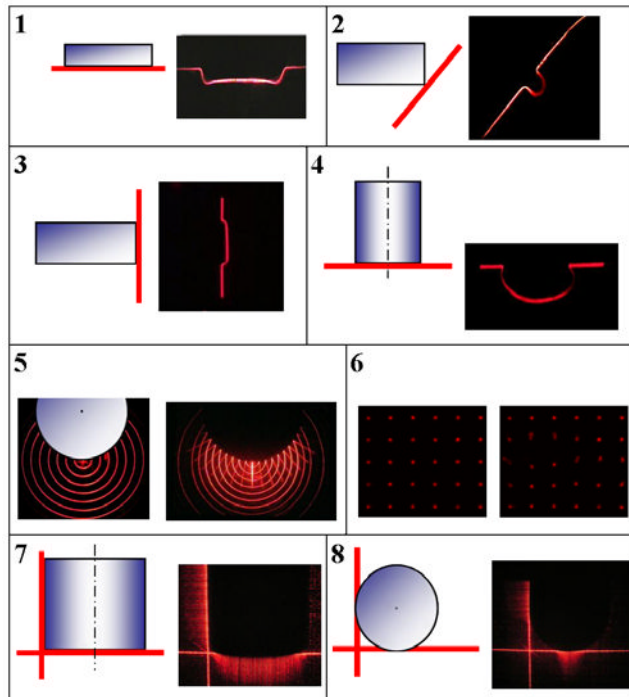


Figure 10. The library of typical experimental 2D-refractograms.

Even a preliminary observation of the refraction patterns depicted for example in Figure 2 makes it possible to draw qualitative conclusions concerning the evolution of the inhomogeneity in the layer using the library of typical refractograms. These calculated or experimental (Figure 10) libraries allow carrying out quick diagnostics of the process.

The technique of the temperature profile quantitative diagnostics for the boundary layer is performed on the basis of the method described in [4]. The digitized experimental refraction pattern is compared with the set of library refraction patterns calculated for the given setup and for various parameters of the temperature layer for the given model. The criterion of minimization of the mean square deviation is used for selecting the theoretical refraction pattern having the best coincidence with the experimental one. The temperature profile corresponding to the chosen theoretical refraction pattern is chosen as the measured profile.

## 7. STRUCTURED BEAMS APPLICATION TO ACOUSTIC FIELD VISUALIZATION AND DIAGNOSTICS

The distortions of the envelope  $I_0(x,0)$  of the laser beam with an elliptical cross-section (laser sheet) in the presence of a traveling acoustic wave are considered. The laser sheet intensity  $I(x,0)$  modulation allows to solve the inverse problem of the acoustic field parameters investigation [16]. Figure 11 shows the geometric parameters of the problem on consideration.

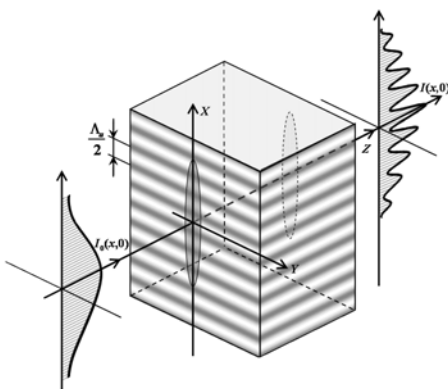


Figure 11. The geometric illustration of the mathematical model.

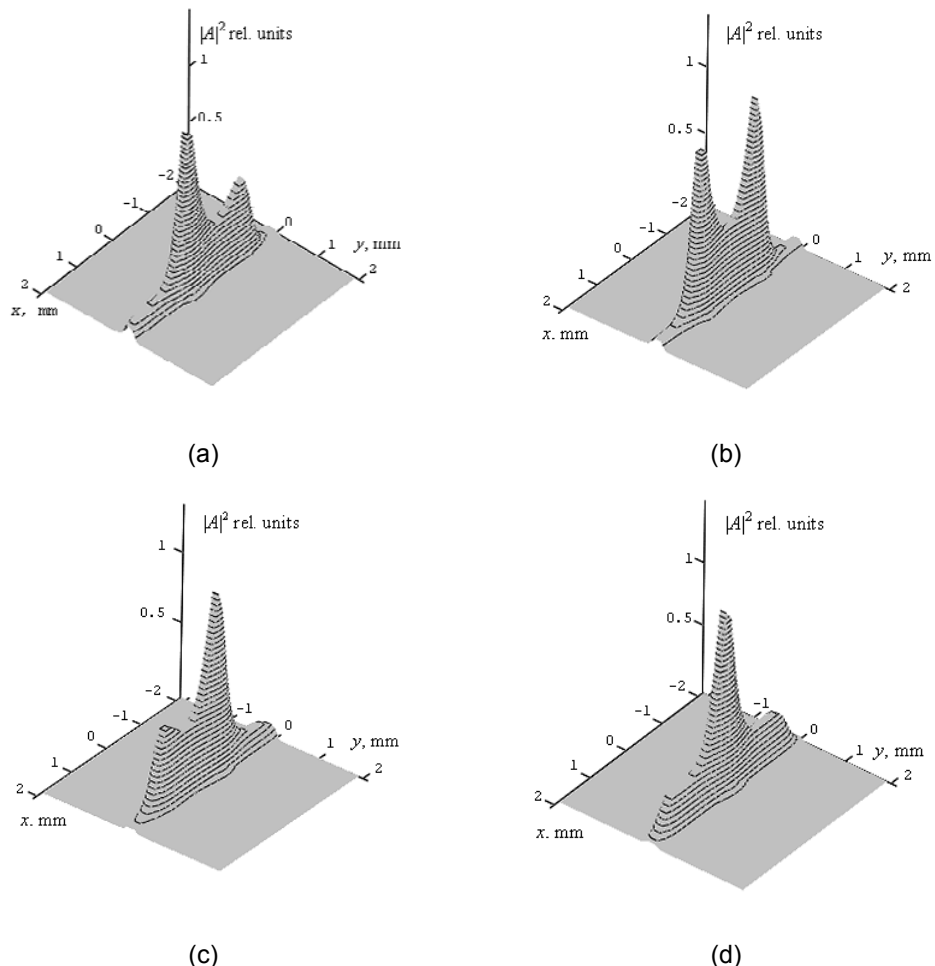


Figure 12. The beam intensity envelope in the media with acoustic wave  $\Lambda_a=1$  mm,  $w=1$  mm,  $\delta n=3 \cdot 10^{-5}$  at different distances  $z$ : a – 110 mm, b – 115 mm, c – 120 mm, d – 125 mm.

Parameters  $K_a$  and  $k$  are the acoustic and optical wave vectors, where its absolute values are respectively:

$$K_a = \frac{2\pi}{\Lambda_a}, \quad k = \frac{2\pi}{\lambda}, \quad (16)$$

and  $\Lambda_a$  and  $\lambda$  are the acoustic and optical wavelengths in the medium. The refractive index of the medium modulated by the standing acoustic wave can be represented

$$n(x, t) = n_0(1 + 2\delta n \sin(\Omega_a t) \cos(K_a x)), \quad \delta n = \frac{\Delta n}{n_0} \ll 1, \quad (17)$$

where  $\Omega_a$  - the acoustic frequency,  $t$  - time,  $n_0$  - the refractive index of the unperturbed medium and  $\Delta n$  - the maximum deviation from  $n_0$ .

The computer simulation technology based on representing of the beam field as a spatial spectrum and describe propagation of each spectral component in the inhomogeneous medium in the approximation of geometrical optics using methods of eikonal and amplitude perturbation.

Figure 12 shows the variation of beam intensity envelope  $I=|A|^2$  in the media with acoustic wave at different distances  $z$  for the case when sheet radius  $w \approx \Lambda_a$ .

## CONCLUSION

The use of the structured beams in laser refractography application appreciably expands capabilities of traditional gradient laser methods.

Firstly, the right choice of a beam structure elements' configuration allows us to *adapt* measurements for a certain heterogeneity type, for example, for an investigation of boundary micro layers near surfaces of different shapes.

Secondly, a beam structure of elements' plurality and their spatial extension make it possible to conduct measurements *simultaneously* in chosen areas of a medium under consideration; that is important for dynamic heterogeneities diagnostics, for time-dependent convection flows, for example.

Thirdly, the main informative parameter in quantitative diagnostics is a beam structure element displacement because of a refraction in a heterogeneity. Measuring of this displacement is possible thanks to elements' *identification*, since discrete and regular beam structure nature allows us to define which initial structure element an element of refractogram corresponds to.

In fact the use of structured beams in LR allows us to accomplish a multi-channel medium probe with a spatial division of identifiable channels as well as with an ability to spatially adapt to a medium under investigation form. A refractogram can be interpreted as a two-dimensional discrete multiway signal, which makes it possible to use correlation analysis methods for its processing for heterogeneity profile reconstruction. Listed structured beam

features allows us to talk about the fact that LR technology provides opportunities not only to render optical heterogeneities, but also to accomplish quantitative diagnostics of them.

In a certain sense, a refraction pattern is a 'portrait' of the medium under study and can be compared with the set of elementary refraction patterns of typical inhomogeneities. This makes it possible to perform quick diagnostics of the medium right in the course of observations. The use of SLB also allows a 3D visualization of the beam caustics and to trace their formation by analyzing the evolution of 2D-refraction patterns.

Various combinations, orientation and arrangement of elementary sources of SLB make it possible to adapt the measuring setup to the structure of the inhomogeneity. In view of the extended nature of the radiation source, a simultaneous diagnostics of processes can be carried out in various regions. It follows from the above technique of measuring the temperature of boundary layers that the possibility of quantitative diagnostics of parameters of the medium (reconstruction of the inhomogeneity profile from a comparison of the experimental and theoretical refraction patterns) is a significant advantage of the laser refractography technique.

Because refraction measurements are virtually inertialess, structured beams can be used for diagnostics of stationary as well as rapid transient processes, including thermal processes in liquids, gases and plasma, natural convection in liquids in the vicinity of heated or cooled bodies, ultrasonic flows, and mixing of various liquids in apparatuses used in chemical technology. Moreover, structured beams in laser refractography technique can be adapted for diagnostics of boundary layers and edge effects, as well as for studying processes in micro- and nanochannels due to the possibility of formation of narrow probe beams.

## REFERENCES

- [1] Rinkevichius, B. S. (1998). *Laser Diagnostics in Fluid Mechanics*. New-York, NY: Begell House, Inc. 341.
- [2] Karasik, A. Ya., Rinkevichius, B. S. & Zubov, V. A. (1995). *Laser Interferometry Principles*. Ed. B. S. Rinkevichius. Mir Publishers: Moscow, CRC Press: Boca Raton ;, 448.
- [3] Settles, G. S. (2001). Schlieren and shadowgraph techniques: visualizing phenomena in a transparent media. Springer-Verlag: Berlin, 376.
- [4] Evtikhieva, O. A., Raskovskaya, I. L. & Rinkevichyus, B. S. (2008). *Laser refractography*. Fizmatlit: Moscow, 176 (in Russian).
- [5] Gumennik, Y. V. & Rinkevichius, B. S. (1990). The flow visualization by schlieren methods with Fuco knife and scanning light beam. In: *Flow visualization V*, ed. R. Reznicek. Hemisphere Pub., N.Y., pp. 113-118.
- [6] Shatokhina, N. A., Rinkevichius, B. S., Sultanov, T. T. & Zubov, V. A. (1997). Using specle interferometry for the analysis of the refractive index gradient distribution in fluid and gas flows. In: *Laser anemometry. Advances and applications*. Eds. B. Ruck, A. Leder, & D. Dopheide, Karlsruhe, pp. 399-406.
- [7] Evtikhieva, O. A., Rinkevichyus, B. S. & Tolkachev, A. V. (2004). The computer aided laser refractive method for investigation of optical inhomogeneous flows. *Measur. Techniq.*, Vol. 47, No. 6.

- [8] Skornyakova, N. M., Popova, E. M., Rinkevichyus, B. S. & Tolkachev, A. V. (2004). The investigation of heat transfer by Background Oriented Shlieren Method. In: *CD-ROM Proc. 12th International Symposium on Application of Laser Techniques to Fluid Mechanics*. Lisbon.
- [9] Soifer, V. A. (Ed.) (2007). *Diffraction Computer Optics*. Fizmatlit: Moscow, 736 (in Russian).
- [10] Evtikhieva, O. A., Rinkevichyus, B. S. & Tolkachev, A. V. (2006). Visualization of nonstationary free convection in liquids with structured laser beam. *Proc. 12th International Symposium on Flow Visualization*. September 10-14, Geottingen, paper 051.
- [11] Raskovskaya, I. L., Rinkevichyus, B. S. & Tolkachev, A. V. (2007). Laser refractography of optically inhomogeneous media. *Quantum electronics*, Vol.37, No.12, 1176-1180,
- [12] Lapitski, K. M., Raskovskaya, I. L. & Rinkevichyus, B. S. (2006). Quantitative visualization of transparent spherical temperature layer. *Proc. 12th International Symposium on Flow Visualization*. September 10-14, Geottingen, paper 055.
- [13] Lapitskiy, K. M., Raskovskaya, I. L. & Rinkevichyus, B. S. (2008). Modeling of edge effects influence on the laser beam refraction in a temperature inhomogeneity. *Measur. Techn.*, Vol.51, No.7, pp. 740-746.
- [14] Kravtsov, Yu. A. & Orlov, Yu. I. (1980). *Geometrical Optics of Inhomogeneous Media* Nauka: Moscow, (in Russian).
- [15] Artyomov, V. I., Evtikhieva, O. A., Lapitski, K. M., Rinkevichyus, B. S., Tolkachev, A. V. & Jankov, G. G. (2005). Investigation of Unstable Temperature Field of Free Convection by COLAR Method. *Optical Methods of Flow Investigation. Proc. 8th Sci. and Tech. Conf.*, Ed. Y. N.Dubnitshev, B.S.Rinkevichyus. Moscow, Russia, June 28-July 1, (Moscow Power Energ. Inst. Publ.:, Moscow), 478-481.
- [16] Raskovskaya, I. L. (2004). Propagation of a Laser Beam through a Medium in the Presence of an Acoustic Wave. *Journal of Communications Technology and Electronics*, Vol.49, No. 11, pp.1293- 1297.



## Chapter 13

# OPTICAL BREAKDOWN IN GASES INDUCED BY HIGH-POWER IR CO<sub>2</sub> LASER PULSES

***J. J. Camacho<sup>1</sup>, L. Díaz<sup>2</sup>, M. Santos<sup>2</sup>, L. J. Juan<sup>1</sup>  
and J. M. L. Poyato<sup>1\*</sup>***

<sup>1</sup>Departamento de Química-Física Aplicada. Facultad de Ciencias. Universidad Autónoma de Madrid. Cantoblanco. 28049-Madrid. Spain

<sup>2</sup>Instituto de Estructura de la Materia, CFMAC, CSIC, Serrano 121. 28006-Madrid, Spain

## ABSTRACT

This chapter reviews some fundamentals of laser-induced breakdown spectroscopy (LIBS) and describes some experimental studies developed in our laboratory on gases such as nitrogen, oxygen and air. LIBS of these gases at different pressures, in the spectral range ultraviolet-visible-near infrared (UV-Vis-NIR), was excited by using a high-power transverse excitation atmospheric (TEA) CO<sub>2</sub> laser ( $\lambda=9.621$  and  $10.591\text{ }\mu\text{m}$ ;  $\tau_{\text{FWHM}}=64\text{ ns}$ ; and different laser power densities). The spectra of the generated plasmas are dominated by emission of strong atomic, ionic species and molecular bands. Excitation temperatures were estimated by means of atomic and ionic lines. Electron number densities were deduced from the Stark broadening of several ionic lines. The characteristics of the spectral emission intensities from different species have been investigated as functions of the gas pressure and laser irradiance. Optical breakdown threshold intensities in different gases have been measured experimentally. The physical processes leading to laser-induced breakdown of the gases have been analyzed. Plasma characteristics in LIBS of air were examined in detail on the emission lines of N<sup>+</sup>, O<sup>+</sup> and C by means of time-resolved optical-emission spectroscopy (OES) technique. The results show a faster decay of continuum and ionic spectral species than of neutral atomic and molecular ones. The velocity and kinetic energy distributions for different species were obtained from time-of-flight (TOF) OES measurements. Excitation temperature and electron density in the laser-induced plasma were estimated from the analysis of spectral data at various times from the laser pulse incidence. Temporal evolution of electron density has been used for the estimation of the three-body recombination rate constant.

\* Corresponding author: E-mails: j.j.camacho@uam.es; luisol@cfmac.csic.es; magna@iem.cfmac.csic.es; jml.poyato@uam.es.

## 1. INTRODUCTION

A remarkable demonstration of the interaction of radiation with matter is the plasma production which occurs when a powerful laser is focused in a gas. Strong pulses of infrared (IR) laser light can cause breakdown and plasma formation in gases which are usually transparent at these wavelengths. By this means gases are transformed into opaque, highly conducting plasmas in times of the order of nanoseconds. If the radiant energy in the focus exceeds the threshold value for breakdown, as happens with high-power lasers (ruby, Nd:YAG, CO<sub>2</sub>, excimer, etc), the gas becomes highly ionized and the plasma thus produced will practically absorb the beam. In atmospheric air, for example, laser-beam-induced breakdown is characterized by a brilliant flash of bluish-white light at the lens focus accompanied by a distinctive cracking noise. This transformation from neutral gas into hot plasma takes place in three quite distinct stages: initiation, formative growth, and plasma development accompanied by shock wave generation and propagation in the surrounding gas. A fourth and final stage, extinction, follows.

The formation of laser-induced breakdown (LIB) plasma in a gas has been investigated since its discovery by Maker *et al* [1] resulting in several studies that have been summarized by different authors [2-16]. Several hundred papers describing various aspects of the phenomenon have been published, and a healthy controversy appears to be in existence concerning the mechanisms by which gases can become almost perfect conductors under the influence of short-duration pulses of long-wavelength light alone. The LIB plasma develops a shock wave into the ambient medium and the gas is heated to high temperatures [17]. It is evident that after breakdown, the plasma becomes very opaque and an abrupt shutoff of the laser transmitted light occurs. Due to the many experimental parameters involved in the LIB, an exhaustive investigation of the plasma would involve the processing of an impressive number of records. To investigate LIB of gases several diagnostic techniques have been employed in the last years. Optical emission spectroscopy (OES) is a powerful tool to get information on the LIB species. Because of the transient features of the plume created by LIB, OES technique with time and space resolution is especially appropriate to obtain information about the behaviour of the created species in space and time as well as the dynamics of the plasma evolution. Although OES gives only partial information about the plasma particles, this diagnostic technique helped us to draw a picture of the plasma in terms of the emitting chemical species, to evaluate their possible mechanisms of excitation and formation and to study the role of gas-phase reactions in the plasma expansion process.

The objectives of this work are: (i) to show some fundamentals of laser-induced breakdown spectroscopy (LIBS) and, (ii) to review of our recent results on LIBS analysis of chemical species in gases plasmas induced by high-power IR CO<sub>2</sub> laser, adding some new results. This chapter describes the experimental results obtained from UV-Visible-near IR spectra of LIB plasmas generated by carbon dioxide laser pulses in gases such as N<sub>2</sub>, O<sub>2</sub> and air. The major parts of this work are already published by us in different journals [18-21]. We consider here only research on the plasma induced when a high-intensity laser radiation is focused in a gas. The emission observed in the laser-induced plasma region is due to electronic relaxation of excited atoms, ions and molecular bands of different diatomic molecules. Excitation temperatures and electron number densities were calculated by means of different atomic and ionic lines. Estimates of vibrational and rotational temperatures of

some molecules electronically excited species are also reported. The characteristics of the spectral emission intensities from different species have been investigated as functions of the gas pressure and laser irradiance. Optical breakdown threshold intensities in the different studied gases have been determined.

For air we discuss the dynamics of the plume expansion and formation of different atomic, ionic and molecular species for different delay times with respect to the beginning of the laser pulse. The velocity and kinetic distributions for the different species were obtained from the time-of-flight (TOF) measurements using time-resolved OES. Possible mechanisms for the production of these distributions are discussed. Line intensities from different atomic and ionic species were used for determining electron temperature and Stark-broadened profiles of some lines were employed to calculate electron density. The temporal behavior of electron number density has been employed for the estimation of three-body recombination rate constant and recombination time. The present paper is aimed at discussing thermo-chemical processes produced by a high-power IR CO<sub>2</sub> pulsed laser on several gases and at evaluating LIB changes which are of fundamental importance in establishing the mechanisms responsible for the plasma emission.

## 1.1. Laser-Induced Breakdown Spectroscopy (LIBS)

Excellent textbooks and reviews about the fundamentals of laser-induced breakdown spectroscopy (LIBS) and examples of various processes are readily available today [13-16]. LIBS, also sometimes called laser-induced plasma spectroscopy, is a technique of atomic-molecular emission spectroscopy which utilizes a highly-power laser pulse as the excitation source. LIBS can analyze any matter regardless of its physical state, being it solid, liquid or gas. Because all elements emit light when excited to sufficiently high energy, LIBS can detect different species (atomic, ionic and molecular) and limited only by the power of the laser as well as the sensitivity and wavelength range of the spectrograph/detector. Basically LIBS makes use of OES and is to this extent very similar to arc/spark emission spectroscopy. LIBS operates by focusing the laser onto a small volume of the sample; when the laser is triggered it breaks a very small amount of gas which instantaneously generates a plasma plume with temperatures of about 10000–30000 K. At these temperatures, the gas dissociates (breakdown) into excited ionic and atomic species. At the early time, the plasma emits a continuum of radiation which does not contain any known information about the species present in the plume and within a very small timeframe the plasma expands at supersonic velocities and cools. At this point the characteristic atomic/ionic and molecular emission lines of the species can be observed. The delay between the emission of the continuum and characteristic radiation is of the order of 1  $\mu$ s, this is one of the reasons for temporally gating the detector. LIBS is technically similar and complementary to a number of other laser-based techniques (Raman spectroscopy, laser-induced fluorescence etc). In fact devices are now being manufactured which combine these techniques in a single instrument, allowing the atomic, molecular and structural characterization of a sample as well as giving a deeper insight into physical properties. A typical LIBS system consists of a pulsed laser and a spectrometer with a wide spectral range and a high sensitivity, fast response rate and time

gated detector. The principal advantages of LIBS over the conventional analytical spectroscopic techniques are its simplicity and the sampling speed.

## 1.2. Laser Parameters

The variables that can influence the LIBS measurements are mainly the laser properties i.e. wavelength, energy, pulse duration, focusing spot size, shot-to-shot energy fluctuations, ambient conditions, physical properties of the sample and the detection window (delay time and gate width). How these parameters affect the precision and accuracy of LIBS are addressed below. In LIBS a high-power laser is used to breakdown a gaseous sample in the form of plasma. The primary energy related parameters influencing the laser-gas interaction are the laser peak power  $P_W$  (or radiant pulse energy per time, in W) and the laser peak intensity  $I_W$  (power density or irradiance; energy per unit area and time,  $\text{W cm}^{-2}$ ) given by

$$P_W = E_W / \tau_{\text{FWHM}}^{\text{Las}}, \quad (1.1)$$

$$I_W = P_W / \pi r^2, \quad (1.2)$$

where  $E_W$  (in J) is the pulse energy,  $\tau_{\text{FWHM}}^{\text{Las}}$  (in s) is the laser pulse duration of the full width at half maximum (FWHM) and  $\pi r^2$  is the focal spot area ( $\text{cm}^2$ ). The fluence  $\Phi_W$  (in  $\text{J cm}^{-2}$ ) on the focused spot area, the photon flux density  $F_{\text{ph}}$  ( $\text{photon cm}^{-2} \text{s}^{-1}$ ), electric field  $F_E$  ( $\text{V cm}^{-1}$ ) and pressure radiation  $p_R$  (in Pa) are given by

$$\Phi_W = E_W / \pi r^2, \quad (1.3)$$

$$F_{\text{ph}} = I_W \lambda / hc, \quad (1.4)$$

$$F_E = \sqrt{I_W / c \epsilon_0}, \quad (1.5)$$

$$p_R = 2I_W / c, \quad (1.6)$$

where  $\lambda$  is the laser wavelength,  $h$  is the Planck constant,  $c$  is the speed of light, and  $\epsilon_0$  is the electric constant. In Eq. (1.6) we suppose that the laser radiation is totally reflected and therefore the pressure radiation can be doubled. The laser peak intensity  $I_W$ , fluence, photon flux, electric field and pressure radiation are inversely proportional to the focused spot area. For LIBS, the peak intensity  $I_W$  (and the other properties  $\Phi_W$ ,  $F_{\text{ph}}$ ,  $F_E$  and  $p_R$ ) that can be delivered to the sample is more important than the absolute value of the laser power. For the formation of plasma, the laser irradiance needs to exceed the threshold value, typically of the order of several  $\text{GW cm}^{-2}$  for a nanosecond laser pulse. If the laser energy is very close to the breakdown threshold, the pulse-to-pulse fluctuations can cause the plasma condition to be

irreproducible, which results in poor measurement precision. The intensities of the emission lines are proportional to the laser energy while the laser plasma is in the optical thin region. When the laser energy increases further, it produces very dense and hot plasma that can absorb laser energy. This will lead to an increase in the continuum emission and a decrease in the signal intensity. Besides, the laser pulse duration and the shot-to-shot fluctuations can also affect the signal reproducibility and hence LIBS precision.

### 1.3. Focal Properties

The laser power density at the focal volume is inversely proportional to the focused spot size. For a laser beam with a Gaussian profile, the focused beam waist  $w_0$  is given by

$$w_0 = \frac{\lambda f}{\pi w_s}, \quad (1.7)$$

where  $f$  is the focal length of the lens and  $w_s$  is the radius of the unfocused beam. The higher laser power density at the focal point can be achieved by reducing the focused beam waist using a shorter focal length lens. On the other hand, the angular spread in laser light generated by the diffraction of plane waves passing through a circular aperture consists of a central, bright circular spot (the Airy disk) surrounded by a series of bright rings. The beam divergence angle  $\theta$ , measured to edges of Airy disk, is given by  $\theta=2.44\lambda/d$ , where  $\lambda$  is the laser wavelength and  $d$  is the diameter of the circular aperture. It can be shown that a laser beam, with beam divergence  $\theta_i$ , incident on a lens of focal length  $f$ , whose diameter is several times larger than the width of the incident beam, is focused to a diffraction-limited spot of diameter approximately equal to  $f\theta_i$ . If the focal region of the laser beam is assumed to be cylindrical in shape, the spot size in terms of length  $l$ , can be approximated as

$$l = (\sqrt{2} - 1)\theta_i f^2 / d. \quad (1.8)$$

## 2. OPTICAL BREAKDOWN IN GASES

Optical breakdown in gases leads to the generation of free electrons and ions, electrons in gases are either bound to a particular molecule or are quasifree when they have sufficient kinetic energy to move without being captured by local molecular energy potentials. Thus, transitions bound and quasi-free states are the equivalent of ionization of molecules in gases. The optical breakdown process describes in greater detail by Raizer [2-3, 23], starts when a laser beam with sufficient power density is focused down, and a sufficient radiation flux density is achieved, leading to a discharge/spark. This discharge is somewhat similar to the discharge induced by a sufficient electric field between the electrodes of a spark plug in an internal combustion engine. The temperature and pressure of the gas in the region of this discharge will be increased significantly as the energy of the laser is absorbed to cause this so called laser induced optical breakdown. The energy deposition into a gas by a focused laser

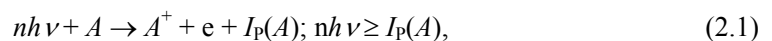
beam can be described by four progressive steps: (i) initial release of electrons by multiphoton effect; (ii) ionization of the gas in the focal region by the cascade release of electrons; (iii) absorption and reflection of laser energy by the gaseous plasma, rapid expansion of the plasma and detonation wave formation; and (iv) the propagation of the detonation wave into the surrounding gas and relaxation of the focal plasma region.

## 2.1. LIB Plasma

Plasma is a local assembly of atoms, molecules, ions and free electrons, overall electrically neutral, in which the charged species often act collectively. The LIB plasma is initiated by a single laser pulse. If we consider the temporal evolution of LIB plasma, at early times the ionization grade is high. As electron-ion recombination proceeds, neutral atoms and molecules form. A recombination occurs when a free electron is captured into an ionic or atomic energy level and gives up its excess kinetic energy in the form of a photon. LIB plasmas are characterized by a variety of parameters, the most basic being the degree of ionization. A weakly ionized plasma is one in which the ratio of electrons to other species is less than 10%. At the other extreme, high ionized plasmas may have atoms stripped of many of their electrons, resulting in very high electron to atom/ion ratios. LIB plasmas typically, for low power laser intensities, fall in the category of weak ionized plasmas. At high laser power densities, LIB plasmas correspond to strong ionized plasmas.

## 2.2. Initiation Mechanism: Multiphoton Ionization (MPI) and Electron Impact Ionization (EII)

Plasma is initiated by electron generation and electron density growth. The conventional LIB plasma can be initiated in two methods: **multiphoton ionization** (MPI) and **electron impact ionization** (EII) both followed by electron cascade. EII is sometimes denominated as cascade ionization process or avalanche ionization due to **inverse bremsstrahlung** (IB) heating of electrons. MPI involves the simultaneous absorption of a number of photons  $n$ , required to equal the ionization potential  $I_p(A)$  of an atom or molecule  $A$



where  $n$  is the number of photons needed to strip off an electron, which corresponds to the integer part of the quantity:

$$n = \frac{I_p + \varepsilon_{osc}}{h \nu} + 1. \quad (2.2)$$

Here  $\varepsilon_{osc}$  is the oscillation energy of a free electron in the alternating electric field. Within the classical microwave breakdown theory [22], a free electron oscillates in the alternating electric field  $E$  of the laser electromagnetic wave with frequency  $\omega$  and wavelength  $\lambda$  ( $\mu\text{m}$ ), and its oscillation energy,

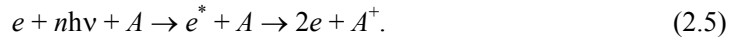
$$\varepsilon_{\text{osc}}[eV] = \frac{e^2 E^2}{4m\omega^2} = \frac{e^2}{4m\pi c^3} I_w \lambda^2 = 4.67 \times 10^{-14} I_w \lambda^2, \quad (2.3)$$

remains constant. In Eq. (2.3)  $e$  is the electron charge and  $I_w$  is the laser intensity [irradiance, power density or flux density in W/cm<sup>2</sup>; Eq. 1.2]. The probability of MPI  $W_{\text{MPI}}$ , by absorbing simultaneously  $n$  laser photons to strip off an electron, is expressed by the classical formula [23]

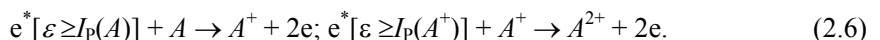
$$W_{\text{MPI}}[\text{s}^{-1}] \cong \omega n^{3/2} \left( 1.36 \frac{\varepsilon_{\text{osc}}}{I_p} \right)^n = 1.88 \times 10^{15} \lambda^{2n-1} n^{3/2} \left\{ \frac{6.35 \times 10^{-14} I_w}{I_p} \right\}^n, \quad (2.4)$$

where  $I_p$  is in eV. Besides, the probability of simultaneous absorption of photons decreases with the number of photons  $n$  necessary to cause ionization. Therefore, the MPI rate is proportional to  $I_w^n$  and inversely proportional to  $I_p^n$ .

EII process consists on the absorption of light photon by free or quasifree electrons, producing electrons with enough kinetic energy  $e^*$  to ionize one atom or molecule



Two conditions must co-exist for EII to initiate: (i) an initial electron must reside in the focal volume; and (ii) the initial electron must acquire energy which exceeds the ionization energy of the material in the focus. These free or quasifree electrons can be produced by the effect of cosmic ray ionization (natural ionization), by means of MPI, or by a breakdown induced in some impurity. The equilibrium number of free electrons and ions per cm<sup>3</sup> in the atmosphere at the earth's surface is about 500 [24]. The electron cascade ionization process requires the presence of either free electrons or excited atoms or molecules in the focal region for their initiation, but the possibility of a free electron or an excited atom produced by natural causes being present there during the laser flash can be discounted, as Tozer pointed out [25]. They occur naturally in the earth's atmosphere, produced at a rate of about 10 cm<sup>-3</sup>s<sup>-1</sup> at the earth's surface by the presence of local radioactivity and the passage of ultraviolet radiation and cosmic rays. Most electrons become rapidly attached to electronegative atoms and molecules to form negative ions. The mean lifetime of a free electron in the atmosphere is about 10<sup>-7</sup> s, so that the aggregate life of free electrons is about 10<sup>-6</sup> s when liberated at the rate of  $\approx 10$  cm<sup>-3</sup>s<sup>-1</sup>. The probability of finding a free electron in the focal region  $\approx 10^{-4}$  cm<sup>3</sup> during a laser flash  $\approx 10^{-8}$  s is thus entirely negligible, as is the chance for finding an excited atom. One concludes that the laser light itself produces the initiatory electrons. These electrons in the focal volume gain sufficient energy, from the laser field through IB collision with neutrals, to ionize atoms, molecules or ions by inelastic electron-particle collision resulting in two electrons of lower energy being available to start the process again



Thus a third species (atom-molecule/ion) is necessary for conserving momentum and energy during optical absorption. The recurring sequences of IB absorption events and

subsequent EII lead to a rapid growth in the number of free electrons, if the laser intensity is sufficient to overcome the losses of free electrons through diffusion out of the focal volume and through recombination. The MPI mechanism dominates electron generation only for low exciting wavelengths. Therefore initial EII becomes a problem at a higher wavelength because neither cascade nor MPI can furnish sufficient number of electrons. At higher laser intensities, electric field of the laser is able to pull an outer shell electron out of its orbit. After the initial electron ejection the LIB plasma is commonly maintained by the absorption of optical energy and the EII. Electrons in the laser field will gain energy through electron-neutral IB collisions and will lose energy by elastic and inelastic collisions with the neutral species through excitation of rotational and vibrational degree of freedom of molecules and excitation of electronic states. While some electrons will be lost by attachment, new electrons will be produced by ionizing collisions. At high laser intensity, few electrons will be generated with energy larger than the ionization energy. The wavelength-resolved emission spectra from the laser plasma are not expected to vary due to the plasma origin. However plasma origin may be relevant, if the enhancement is observed between UV, visible and IR excitation wavelengths.

Once that LIB plasma is formed, its growth is governed by the continuity rate equation for the electron density [26] due to the combined effect of EII and MPI

$$\frac{dn_e}{dt} = v_i n_e + W_n I_w^n N - v_a n_e - v_r n_e^2 + D_e \nabla^2 n_e, \quad (2.7)$$

where  $v_i$  is the impact ionization rate,  $W_n$  is the multiphoton ionization rate coefficient,  $I_w$  is the intensity of the laser beam,  $n$  is the number of photons required for MPI,  $N$  is the number of atoms/molecules per unit volume,  $v_a$  is the attachment rate,  $v_r$  is the recombination rate and  $D_e$  is the electron diffusion coefficient. The term  $dn_e/dt$  is the net rate of change in electron concentration at a point in the focal volume at a time  $t$  after the release of initiatory electrons. On the right side of the equation (2.7), the first term is the electron generation due to impact ionization. The second term on the right is MPI rate. The third, fourth and fifth terms are sink terms which represent electron attachment, recombination and diffusion, respectively. Impact ionization is defined by multiplying the number of electrons per unit volume to the impact ionization rate  $v_i$ . The impact ionization rate refers to the rate at which electrons are generated as a result of ionizing collisions. At high laser intensity, a few new electrons can be generated and gain energy larger than their ionization energy which leads to the generation of new electrons by impact ionization, thereby leading to the cascade growth. Recombination losses are usually not important in the breakdown forming stage.

### 2.3. Electron attachment, recombination and diffusion

Electron attachment is the rate of electron attachment  $v_a$  multiplied by the number of electrons per unit volume. The LIB plasma typically loose electrons to the neutral species via the attachment mechanism in the form of three-body attachment or two-body dissociative attachment. Three-body attachment is:  $e + AB + X \rightarrow AB^- + X$ , where  $X$  appears to be a facilitator that allows the electrons to be gained by  $AB$  even through  $X$  remains unchanged

throughout the process. Two-body dissociative attachment is:  $e + AB \rightarrow A^- + B$ . In this mechanism the electrons must exhibit a threshold electron energy that is equal to the difference between the dissociative energy of  $AB$  and the attachment energy of  $A$ , which results in the separation of  $A$  and  $B$ .

Electron recombination is the rate of electron recombination  $v_R$  multiplied to the number of electrons per unit volume. When the electron density is high, such as during the last stage of cascade breakdown, the LIB plasma can lose electrons to ions through electron-ion recombination. Similar to the electron attachment, three-body recombination and two-body recombination occurs as:  $e + AB^+ + X \rightarrow AB + X$ ,  $e + AB^+ \rightarrow A + B$ . The electron-ion recombination rate has been studied theoretically for a three-body recombination by Gurevich and Pitaevskii [27]

$$v_R = 8.8 \times 10^{-27} \frac{n_e^2}{T_e^{3.5}} [s^{-1}], \quad (2.8)$$

where  $n_e$  is the electron density in cm<sup>-3</sup> and  $T_e$  is the electron temperature in eV. The electron diffusion term is expressed as  $D_e \nabla^2 n_e$  [Eq. (2.7)]. This loss mechanism, more important for a small diameter laser beam, is the diffusion of electrons out of the focal volume. Morgan [6] referred to the combined effect of diffusion and cascade ionization as the responsible for top-hat intensity profile. By imposing an electron skin at the edge of the intensity profile, they found that the electron density grows exponentially as

$$\langle v_e \rangle = \frac{2.408 D_e}{r^2}, \quad (2.9)$$

where  $\langle v_e \rangle$  is the average electron velocity,  $D_e$  is electron diffusion coefficient and  $r$  is the radius of the beam. The equation (2.9) is intended to be an upper boundary for diffusion losses only because laser beams typically have a radial distribution closer to the Gaussian rather than top-hat distribution.

In LIB plasmas, the decrease of electron density  $n_e$  is mainly due to recombination between electrons and ions in the plasma. These processes correspond to the so-called radiative recombination and three-body recombination processes in which a third body may be either a heavy particle or an electron. The electron number density  $n_e$  (cm<sup>-3</sup>) in the laser induced plasma is governed by the kinetic balance equation [28, 29]

$$\frac{dn_e}{dt} = k_{\text{ion}} n_e N_i - k_{\text{rec}} n_e^3, \quad (2.10)$$

where  $N_i$  indicates the concentration of heavy particles (neutrals and ions) and  $k_{\text{ion}}$  (cm<sup>3</sup> s<sup>-1</sup>) and  $k_{\text{rec}}$  (cm<sup>6</sup> s<sup>-1</sup>) denote the rate constants of ionization ( $e + A \rightarrow A^+ + 2e$ ) and tree-body electron-ion recombination ( $2e + A^+ \rightarrow A^* + e$ ), respectively. The excess of energy in three-body electron-ion recombination is deposited as kinetic energy to a free electron, which

participates in the recombination process as a third body partner. The three-body electron-ion recombination energy can be converted into radiation in the process of radiative electron-ion recombination ( $e + A^+ \rightarrow A^* \rightarrow A + h\nu$ ). The cross section of this process is relatively low and it can be competitive with three-body electron-ion recombination only when the plasma density is low. If  $dn_e/dt=0$  an equilibrium condition can be established; if  $dn_e/dt \neq 0$ , then the ionization ( $dn_e/dt > 0$ ) or the three-body recombination ( $dn_e/dt < 0$ ) prevails and departure from equilibrium occurs [28]. The second derivative of  $Y=dn_e/dt$  with respect to the electron number density is given by

$$\frac{d^2Y}{dn_e^2} = -6k_{rec}n_e. \quad (2.11)$$

The recombination time can be determined by the value of the rate constant of the recombination process as  $t_{rec}=1/(n_e^2 k_{rec})$  [29].

In summary, the process of plasma initiation essentially consists of the formation of free or quasi-free electrons by interplay of MPI and EII. Therefore, two mechanisms MPI and EII can initiate a conventional LIB plasma formation. After the LIB plasma formation the temporal growth is governed by the equation (2.7). The recombination of these two source terms (MPI and EII) and three sink terms (electron attachment, electron recombination and electron diffusion) controls the development of the conventional LIB plasma. The decrease of  $n_e$  is mainly due to the so-called radiative recombination and three-body recombination processes in which a third body may be either a heavy particle or an electron. These mechanisms that directly affect the temporal development of the LIB plasma, determine the necessary spectroscopic techniques required to spectrally resolve elemental species inside the LIB plasma.

## 2.4. Optical Breakdown Threshold Intensities

The minimum power density required to form a plasma is called the breakdown threshold; different types of laser, sample, and environmental conditions will have different breakdown thresholds. Breakdown thresholds of solids and liquids are usually much lower than those for gases. The principal method of investigation has been to measure the beam intensity required for electron liberation and the minimum intensity needed to produce breakdown as a function of the radiation wavelength and pressure of a variety of gases. Precise measurements of the intensities of laser radiation required to release initiatory electrons or to lead to breakdown are made only with the greatest difficulty. The difficulties arise on account of the imprecise definition of the extent of the focal region and inaccurate knowledge of the spatial-temporal characteristics of the beam intensity within the focal region, which, in turn, lead to uncertainties in the absolute value of the instantaneous radiation intensity. The parameters which characterize a focused laser beam are its polarization, wavelength, line width, duration, divergence and the temporal and spatial distribution of intensity. For a given pulse these are functions of the laser and focusing system governed by the mode structure within the laser cavity, by the aberration functions of the lens or focusing mirror, and by the beam diameter at the lens or mirror. In specifying the electron

liberation or breakdown threshold intensities all these factors should ideally be specified, but, regrettably, in the literature there is often inadequate detail and essential features of experimental procedures are frequently omitted. In consequence many published data are of little value, serving merely to indicate orders of magnitude and broad trends only rather than absolute values in well-defined conditions. For these reasons data published by various workers are often contradictory, and reliable interpretation is sometimes difficult to make.

For gases to breakdown, a certain concentration of electrons has to be reached before the end of the laser pulse. Laser-induced breakdown is frequently defined [5, 30] as an electron density multiplication during the laser pulse by a factor of 10<sup>13</sup> corresponding to 43 electron generations. In fact, multiplying the natural electron density by 10<sup>13</sup> leads to  $n_e \approx 10^{16} \text{ cm}^{-3}$  which is the electron density of plasmas at atmospheric pressure for which electron-ion IB dominates electron-neutral IB. With respect to electron-neutral IB, the electron-ion IB has a much higher efficiency as a result of the long range Coulomb interaction, and a plasma with an electron density  $n_e = 10^{16} \text{ cm}^{-3}$  is quasi instantaneously completely ionized.

The condition for optical breakdown is taken to occur when the number density of the induced electrons equals the critical density for the laser wavelength. The critical plasma density  $n_e^{\text{crit}} [\text{cm}^{-3}] = m \omega^2 / 4\pi e^2 \cong 1.1 \times 10^{21} / \lambda^2 [\mu\text{m}]$  ( $n_e^{\text{crit}} \cong 10^{19} \text{ cm}^{-3}$  for CO<sub>2</sub> laser) is the density where the electron plasma frequency equals to the laser frequency. When the electron density exceeds the critical density the sample is not transparent any more. Energetic electrons produce excited species through impact excitation, dissociation and ionization of gas molecules. According to the microwave theory [22], electrons gain energy from the laser radiation field by elastic collisions with neutral atoms at the rate:  $(d\varepsilon/dt)_{\text{gain}} = (e^2 F_E^2 / m) \cdot [\nu_c^2 / (\omega^2 + \nu_c^2)]$ , where  $F_E$  and  $\omega$  are the root-mean-square electric field and angular frequency of the radiation and  $\nu_c$  is the electron-neutral collision frequency.

Several models have been developed to describe the optical breakdown and to compute the breakdown threshold. Chan *et al.* [30] proposed a model based on the energy balance of electrons neglecting their energy distribution. According to this work, breakdown occurred if the laser heating of electrons by IB induces a gain of electron energy that overcomes the energy losses. Thus, one requires a laser power density (power threshold density)

$$I_{\text{las}} \geq \frac{m c I_p}{4\pi e^2 \ln 2} \frac{\omega^2 + \nu_c^2}{\nu_c} \left[ \frac{43}{\tau_{\text{las}}} \ln 2 + \frac{D_e}{\Lambda^2} + \frac{2m \langle \varepsilon \rangle \ln 2 \nu_c}{M I_p} + \left( \alpha + \frac{\beta}{\Lambda^2} \right) \nu_c \right], \quad (2.12)$$

where  $m$  and  $e$  are the mass and charge of electrons,  $c$  is the light velocity, and  $I_p$  and  $M$  are the ionization potential and the atomic mass of the gas. The terms  $\omega$ ,  $\nu_c$ ,  $\tau_{\text{las}}$ ,  $D_e$ ,  $\Lambda$  and  $\langle \varepsilon \rangle$  are the laser frequency, effective electron-neutral collision frequency, laser pulse duration, diffusion coefficient, diffusion length and average electron energy, respectively. The terms  $\alpha$  (dimensionless) and  $\beta$  (length<sup>2</sup>) are two parameters which depend on the atomic structure of the gas. The terms inside the brackets represent various loss terms. The first term in the brackets stands for the generation of 43 electrons necessary for breakdown. The second, third, and fourth terms take into account the electron energy loss due to diffusion out of the focal volume, elastic and inelastic collisions, respectively. The loss due to electron attachment is very low and therefore not considered in Eq. (2.12). The losses due to elastic and inelastic

collisions are proportional to  $v_c$  that increases linearly with the gas pressure  $p$ . At low pressure, collisional loss can be neglected and electron heating by IB varies linearly with  $p$  according to  $v_c^2 \ll \omega$ . Thus, the threshold decreases with  $p$  in the low-pressure range. When increasing  $p$  to sufficiently high values, the collisional losses overcome the terms of electron generation and diffusion loss. If  $v_c^2 \ll \omega$  still holds, both gain and loss terms are proportional to  $p$  and the threshold is pressure independent. In the high pressure range ( $v_c^2 \gg \omega$ ) the gain by IB diminishes as  $p^{-1}$  and the threshold increases. Thus, it exists an optimum pressure for which the optical breakdown threshold is minimum. According to Eq. (2.12), the breakdown power threshold density in general is directly proportional to the ionization potential of the gas. Moreover, the breakdown threshold passes through a minimum at the pressure when laser angular frequency  $\omega$  is equal to the effective electron-neutral collision frequency  $v_c$  as indicated by the term outside the brackets. Depending on their relative magnitudes, breakdown may be termed to be limited, diffusion limited or attachment limited [30].

Time-limited breakdown occurs if the first term in the brackets dominates, that is when the laser pulse duration  $\tau_{\text{las}}$  is so short that the growth rate of electron density required to induce a visible breakdown exceeds any losses. Thus, the threshold power density varies inversely with pulse duration and the breakdown is determined by the product of the intensity times the pulse duration. Diffusion-limited processes occur when the second term in the brackets dominates, that is for gas breakdown to take place in a small focal volume at low gas pressure. The breakdown power density threshold in this case decreases as  $\Lambda^{-2}$  with the focal size and it also decreases as  $p^{-2}$  with the gas pressure in the range of pressure so that  $\omega \gg v_c$ . The third and fourth terms are the attachment and elastic collision losses. They are relatively unimportant and are dependent on the type and masses of the gas. For inert gases, the attachment loss can be completely neglected. The last term is the energy loss due to inelastic collision and it should be important for molecular gases because the large number of excited states they possess. Because the attachment rate and collision frequency are assumed to be proportional to the gas pressure  $p$ , these three terms are independent of the gas pressure.

At low pressure and in particular for small waist, the electron diffusion out of the focal volume is the dominating loss term. The electron diffusion length  $\Lambda$  can be estimated assuming a focal volume of cylindrical shape with radius

$$r = \frac{f\Theta}{2}, \quad (2.13)$$

and length  $l = (\sqrt{2} - 1) \frac{f^2 \Theta}{d}$  (Eq. 1.8), where  $f$  is the focal length of the focussing lens,  $\Theta$  the angle of laser beam divergence, and  $d$  the laser beam diameter incident on the lens. For a Gaussian laser beam, one has

$$\frac{1}{\Lambda^2} = \left( \frac{2.405}{r} \right)^2 + \left( \frac{\pi}{l} \right)^2, \quad (2.14)$$

For a large numerical opening ( $\geq f/5$ ), Eq. (2.14) is simplified to  $\Lambda = r/2.405$ . Using this expression with  $r$  from Eq. (2.13) and computing the electron diffusion coefficient as

$$D_e = \frac{2\langle\varepsilon\rangle}{3m\nu_{\text{eff}}}, \quad (2.15)$$

the energy loss due to electron diffusion is evaluated. With respect to the loss due to elastic collisions, the energy loss by diffusion can be neglected if

$$\nu_{\text{eff}} \gg \frac{4.81\sqrt{I_p M}}{\sqrt{3m}\Theta}. \quad (2.16)$$

A large dispersion of breakdown threshold values exists in literature. It is attributed to the large number of parameters on which the optical breakdown depends. Several mechanisms have been found to reduce the threshold of optical breakdown. Smith and Haught [31] observed threshold lowering by Penning effect during ruby laser breakdown in a high-pressure Ar atmosphere when adding 1% Ne. The phenomenon was due to Ar ionization by collisions with excited Ne atoms which were produced by a resonant excitation process. However, the threshold lowering was at maximum of about 50% [31]. For CO<sub>2</sub> laser radiation, a resonant excitation process can be excluded because of the small photon energy and the Penning effect does not contribute to optical breakdown threshold lowering in the far IR spectral range. For laser radiation of sufficiently high photon energy, the presence of impurities with low ionization energy led to the threshold lowering [32] that was attributed to multiphoton ionization. However, this effect was not observed for CO<sub>2</sub> laser radiation. Gas impurities with the lowest ionization potential like hydrocarbon radicals require at least the simultaneous absorption of more than 50 photons that is a process of vanishing probability. Contrarily, molecular species such as hydrocarbon or other radicals brake the ionization avalanche. They have many vibrational and rotational excitation levels which cause electron energy loss by inelastic collisions [see Eq. (2.12)].

Several authors [33, 34] reported threshold lowering when initiating the breakdown by ablation of a solid target. A threshold reduction by a factor of 10<sup>2</sup> was observed for CO<sub>2</sub> laser radiation [33]. The threshold lowering was explained by shock wave generation as an effect of strong material ablation. The shock wave heats up the surrounding gas which is instantaneously transformed in a strongly ionized plasma. The optical breakdown from solid material ablation has been shown to be a multistage plasma initiation process that is characterized by three thresholds [34]: (i) the material ablation threshold  $I_{\text{vap}}$ ; (ii) the breakdown threshold of the evaporated material  $I_{\text{vap}}^*$ ; and (iii) the breakdown threshold of the surrounding gas  $I_{\text{gas}}^*$ . It is noted that  $I_{\text{vap}}^*$  and  $I_{\text{gas}}^*$  are the thresholds of preionized vapour and the gas, respectively. For the case of CO<sub>2</sub> laser ablation, the initial ionization stage of the ablated material vapour is  $n_e/n_{\text{vap}} < 10^{-5} - 10^{-4}$  [34],  $n_{\text{vap}}$  being the ablated material vapor density. As a consequence of preionization, the number of electrons generations necessary for complete ionization is strongly reduced (<<43). Thus, the electron generation term can be neglected in Eq. (2.12). The diffusion loss can be also neglected according to the relative large volume preionized by the shock wave. In the case of rare gases, the loss by inelastic collisions is much smaller than that due to elastic collisions and the avalanche ionization is determined by the balance between IB heating of electrons and losses by elastic collisions. The breakdown threshold (in W/cm<sup>2</sup>) given by Eq. (2.12) is simplified to [34]

$$I_{\text{las}} \geq I_{EC}^* = 1.8 \times 10^7 \frac{I_p}{M}, \quad (2.17)$$

where the ionization potential is in eV and the atomic mass of the gas is in atomic mass units. The index *EC* stands for elastic collisions to recall that only this loss term has been taken into account. Barchukov *et al.* [33] proposed a threshold criterion similar to Eq. (2.17) with a three times larger numerical constant. The difference is due to the average electron energy which was supposed to be equal to the ionization potential by Barchukov *et al.* [33] while  $\langle \varepsilon \rangle = (1/3)I_p$  was taken for Eq. (2.17).

## 2.5. Laser-Plasma Interaction

The interaction between the laser radiation and free electrons of the plasma is described by the Drude model considering the electron motion in the laser field as a harmonic oscillator. For collision frequencies  $\omega_p^2 \gg \nu_c^2$ , where  $\omega_p$  is the plasma frequency. The dielectric constant is given by  $\epsilon \approx 1 - \omega_p^2/\omega^2$ , where  $\omega$  is the laser frequency. Optical breakdown in gases at atmospheric pressure leads to an electron density equal to the critical density (for CO<sub>2</sub> laser radiation  $n_e^{\text{crit}} \cong 10^{19} \text{ cm}^{-3}$ ). In the region where the critical density is reached, the plasma frequency is equal to the laser frequency and  $n = \sqrt{\epsilon} = 0$ . The plasma is thus completely reflecting in the corresponding zone. Only a few authors have investigated the laser beam reflection by the plasma. In fact, the studies show that breakdown plasmas reaching the critical density absorb most of the incident laser energy [35-37]. The fraction of reflected radiation is small because of strong absorption in the zone adjacent to the plasma sheet of critical density. Donaldson *et al.* [36] showed that 80% of incident laser energy was absorbed in a zone of weak thickness where the electronic density varied from  $0.83n_e^{\text{crit}}$  to  $n_e^{\text{crit}}$  when generating breakdown with a (Nd:YAG) laser of  $\tau_{\text{las}}=35 \text{ ps}$  and  $I_W=10^{14} \text{ Wcm}^{-2}$ . Offenberger and Burnett [35] measured the reflected and transmitted power of TEA-CO<sub>2</sub> laser pulses during breakdown in hydrogen. The reflected power was always below 2% of the incident laser power. The major absorption mechanism of CO<sub>2</sub> laser radiation during breakdown ignition is electron-neutral IB. Once strongly ionized plasma is formed, the electron impact ionization or electron-ion IB dominates as a result of the long range Coulomb interaction between charged particles.

Several experimental and theoretical studies have been performed to investigate the IB effect. Among numerous expressions for the determination of the IB absorption coefficient [2, 5, 36] the formula

$$\alpha_{\text{IB}} = 3.69 \times 10^8 \frac{n_e^2 \sum_i f_i Z_i^2}{\sqrt{T_e} \nu^3} \left(1 - e^{-h\omega/2\pi k_B T}\right) [\text{cm}^{-1}], \quad (2.18)$$

proposed by Spitzer [38] was used by many authors to estimate the laser energy absorption by the plasma. Here,  $T_e$  and  $n_e$  are in K and cm<sup>-3</sup>, respectively. The factors  $f_i$  are the fractional

abundances of ions,  $Z_i$  the corresponding ion charge. In the case of CO<sub>2</sub> laser radiation, one has  $(1 - e^{-h\omega/2\pi k_B T}) \approx h\omega/2\pi k_B T$  and Eq. (2.18) simplifies for a singly ionized plasma to

$$\alpha_{IB} = 1.8 \times 10^{-35} \frac{n_e^2}{T_e^{3/2}} \text{ [cm}^{-1}\text]}, \quad (2.19)$$

where  $T_e$  is in eV. Equation (2.19) shows that the efficiency of IB absorption decreases with increasing electron temperature. At high plasma temperatures, other absorption mechanisms dominate. They have been made in evidence during studies of laser-plasma interaction related to thermonuclear fusion using power densities several orders of magnitude higher than breakdown thresholds.

## 2.6. Absorption wave Propagation

After breakdown ignition, the strongly absorbing plasma will propagate in the direction opposite to the laser beam. The absorption wave formation has been observed in many experiments using CO<sub>2</sub> laser sources [33, 35, 39]. The theoretical analyses of optical breakdown and absorption wave propagation performed by Raizer [2] using a hydrodynamic model have been widely accepted and became a standard theory in the field. According to this model, the laser-induced absorption waves propagate by the following stepwise mechanisms: (i) A small plasma zone is heated up by the laser beam. It reaches the critical density and strongly absorbs the laser radiation. (ii) The electron density in the adjacent zones increases. (iii) The adjacent preionized zone that is irradiated by the laser beam is heated up and becomes absorbent. Thus, the strongly absorbing plasma zone propagates in the direction opposite to the laser beam.

Three different propagation modes are distinguished. The breakdown wave is characterized by the following propagation mechanism: (i) breakdown occurs initially in the region of the highest laser power density and later in the zones of lower power density. The expansion of high pressure plasma compresses the surrounding gas and drives a shock wave. Thus, the breakdown propagates in the direction opposite to the laser beam. The plasma also tends to expand back along the beam path toward the laser, a phenomenon known as moving breakdown. The velocity of the breakdown wave is given by

$$v_{bw} = \frac{w_0}{t_b \operatorname{tg}\varphi}, \quad (2.20)$$

where  $w_0$  and  $\varphi$  are the minimum radius and opening angle of the focused laser beam, respectively. For example, for our typical experimental conditions with the CO<sub>2</sub> laser, taking  $w_0=0.05$  cm,  $t_b=100$  ns and  $\operatorname{tg}\varphi=0.2$ , the breakdown wave propagates with  $v_{bw}=2.5 \times 10^6$  cm/s;

(ii) Propagation through the detonation wave mechanisms occurs when rapid heating of the gas in the region of strong absorption induces a spherical shock wave. The latter propagates into the surrounding gas that is heated and preionized. The part of the preionized gas that is further illuminated by the laser beam absorbs the laser radiation and becomes opaque. Thus, the absorption zone follows the shock wave. The propagation velocity of the detonation wave is given by

$$v_{bw} = \left[ 2(\gamma^2 - 1) \frac{I_w}{\rho_0} \right]^{1/3}, \quad (2.21)$$

where  $\gamma$  and  $\rho_0$  are the adiabatic constant of the gas and the specific mass, respectively. The specific energy that is injected into the gas is

$$\epsilon_{bw} = \frac{\gamma}{(\gamma^2 - 1)(\gamma + 1)} v_{bw}^2. \quad (2.22)$$

It is noted that detonation wave propagation velocity and injected specific energy are independent of the atomic structure of the gas. The gas influences the detonation wave propagation only through its specific mass and adiabatic constant. Thus, a change of gas nature is equivalent to a pressure variation if  $\gamma$  is unchanged. Consequently, the detonation wave propagation velocity in Ar is equal to that in Xe at three times lower pressure. For Xe at atmospheric pressure and  $I_w = 10^8 \text{ W cm}^{-2}$ , the detonation wave propagates with a velocity of  $6 \times 10^5 \text{ cm s}^{-1}$  and heats up the gas to a temperature of 28 eV. The temperature is obtained by assuming an ideal gas, for which the specific energy is related to the temperature by  $\epsilon_{bw} = (3/2) k_B T N_A / M$ . Here,  $k_B$ ,  $T$ ,  $N_A$  and  $M$  are Boltzmann's constant, plasma temperature, Avogadro's constant and mass, respectively.

(iii) For  $I_w > 10^{10} \text{ W cm}^{-2}$ , the plasma is heated up to  $T < 10^2 \text{ eV}$ . According to the high temperature, the plasma strongly radiates in the UV and soft X-ray spectral range ionizing thus the surrounding gas. Once preionized, the gas in the zone illuminated by the laser beam absorbs the laser radiation and a laser sustained radiation wave propagates in the direction opposite to the laser beam. The dominating propagation mechanism of the absorption wave depends on the experimental conditions. Breakdown waves are formed in the case of very small opening angle of the focused laser beam whereas radiation waves occur at very high laser power density. For moderate power density and sufficiently wide opening angle, the optical breakdown propagates as a detonation wave.

A portion of the laser pulse energy is absorbed by the expanding plasma generating three different types of waves: (i) laser-supported combustion (LSC) waves; (ii) laser-supported detonation (LSD) waves; and (iii) laser-supported radiation (LSR) waves [40]. They differ in their predictions of the opacity and energy transfer properties of the plasma to the surrounding gas. At low-power laser regime ( $I_w < 1 \text{ MW/cm}^2$ ), LSC waves are produced, which comprise of a precursor shock, that is separated from the absorption zone and the plasma. The shock wave results in an increase in the ambient gas density, temperature and pressure, whereas the shock edges remain transparent to the laser light. At medium-power laser regime ( $1 \text{ MW/cm}^2 < I_w < 4 \text{ GW/cm}^2$ ), the precursor shock is sufficiently strong and the shocked gas is hot enough to begin absorbing the laser radiation without requiring additional heating by energy from the plasma. The laser absorption zone follows directly behind the shock wave and moves at the same velocity. In this case a LSD wave is produced and has been modelled by several Raizer [2-3, 23]. The propagation of the LSD wave is controlled by the absorption of the laser energy. At high-power laser regime ( $I_w > 4 \text{ GW/cm}^2$ ), the plasma is so hot that, prior to the arrival of the shock wave, the gas is heated to temperatures at which laser absorption begins. Laser radiation is initiated without any density change and the pressure profile results mainly from the strong local heating of the gas rather than a propagating shock

wave. The LSR wave velocity increases much more rapidly with irradiance than those of the LSC and LSD waves.

### 3. LIB PLASMA ANALYSIS

In contrast to conventional spectroscopy, where one is mainly concerned with the structure of an isolated atom and molecule, the radiation from the plasma also depends on the properties of the plasma in the intermediate environment of the atomic or molecular radiator. This dependence is a consequence of the long-range Coulomb potential effects which dominate the interactions of ions and electrons with each other and with existing neutral particles. These interactions are reflected in the characteristic radiations in several ways. They can control population densities of the discrete atomic states, spectral shift and broadening by Stark effect, decrease of ionization potentials of the atomic species, cause continuum radiation emissions and emission of normally forbidden lines. Generally, the radiation emitted from self-luminous plasma can be divided into bound-bound (b-b), bound-free (b-f), and free-free (f-f) transitions.

#### 3.1. Local Thermodynamic Equilibrium (LTE)

Plasma description starts by trying to characterize properties of the assembly of atoms, molecules, ions and electrons rather than individual species. If thermodynamic equilibrium exists, then plasma properties can be described through the concept of temperature. Thermodynamic equilibrium is rarely complete, so physicists have settled for a useful approximation, local thermodynamic equilibrium (LTE). In LTE model it is assumed that the distribution of population densities of the electrons is determined exclusively through collisional processes and that they have sufficient rate constants so that the distribution responds instantaneously to any change in the plasma conditions. In such circumstances each process is accompanied by its inverse and these pairs of processes occur at equal rates by the principle of detailed balance. Thus, the distribution of population densities of the electrons energy levels is the same as it would be in a system in complete thermodynamic equilibrium. The population distribution is determined by the statistical mechanical law of equipartition among energy levels and does not require knowledge of atomic cross sections for its calculation. Thus, although the plasma density and temperature may vary in space and time, the distribution of population densities at any instant and point in space depends entirely on local values of density, temperature, and chemical composition of plasma. If the free electrons are distributed among the energy levels available for them, their velocities have a Maxwellian distribution

$$dn_v = n_e 4\pi \left( \frac{m}{2\pi k_B T_e} \right)^{3/2} \exp\left(-\frac{mv^2}{2k_B T_e}\right) v^2 dv, \quad (3.1)$$

where  $n_e$  is the electron density,  $m$  is the electron mass,  $k_B$  is the Boltzmann constant,  $T_e$  is the electron temperature and  $v$  is the electron velocity. For the bound levels the distributions of

population densities of neutrals and ions are given by the Boltzmann (3.2) and Saha (3.3) equations

$$\frac{N_j}{N_i} = \frac{g_j}{g_i} \exp\left(-\frac{(E_j - E_i)}{k_B T_e}\right), \quad (3.2)$$

$$\frac{N_{z+1,k} n_e}{N_{z,k}} = \frac{g_{z+1,k}}{g_{z,k}} 2 \left( \frac{2\pi m k_B T_e}{h^2} \right)^{3/2} \exp\left(-\frac{I_p_{z,k}}{k_B T_e}\right), \quad (3.3)$$

where  $N_i$ ,  $N_j$ ,  $N_{z+1,k}$  and  $N_{z,k}$  are the population densities of various levels designated by their quantum numbers  $j$  (upper),  $i$  (lower) and  $k$  (the last for the ground level) and ionic charge  $z$  and  $z+1$ . The term  $g_{z,i}$  is the statistical weight of the designated level,  $E_j$  and  $E_i$  are the energy of the levels  $j$  and  $i$  and  $I_p_{z,k}$  is the ionization potential of the ion of charge  $z$  in its ground level  $k$ . Equations (3.1)-(3.3) describe the state of the electrons in an LTE plasma. For complete LTE of the populations of all levels, including the ground state, a necessary condition is that electron collisional rates for a given transition exceed the corresponding radiative rates by about an order of magnitude [41]. This condition gives a criterion [42] for the critical electron density of the level with energy  $\Delta E = E_j - E_i$

$$n_e^{\text{crit}} \geq \frac{5}{8\sqrt{\pi}} \left( \frac{\alpha}{a_0} \right)^3 z^7 \left( \frac{\Delta E}{z^2 E_H} \right)^3 \sqrt{\left( \frac{k_B T_e}{z^2 E_H} \right)} \cong 1.6 \times 10^{12} T_e^{1/2} (\Delta E)^3, \quad (3.4)$$

where  $\alpha$  is fine-structure parameter,  $a_0$  is Bohr radius, and  $E_H$  is the hydrogen ionization potential. In the numerical relationship of Eq. (3.4),  $n_e^{\text{crit}}$  is given in  $\text{cm}^{-3}$ ,  $T_e$  in K and  $\Delta E$  (energy difference between the two neighboring states) in eV. Many plasmas of particular interest do not come close to complete LTE, but can be considered to be only in partial thermodynamic equilibrium in the sense that the population of sufficiently highly excited levels are related to the next ion's ground state population by Saha-Boltzmann relations, respective to the total population in all fine-structure levels of the ground state configuration [41]. For any atom or ion with simple Rydberg level structure, various criteria were advanced for the minimum principal quantum number  $n_{\text{crit}}$  for the lowest level, often called thermal or collision limit, for which partial thermodynamic equilibrium remains valid to within 10%. One criterion with quite general validity is given by Griem [42]:

$$n_{\text{crit}} \approx \left[ \frac{10z^7}{2\sqrt{\pi} n_e} \left( \frac{\alpha}{a_0} \right)^3 \right]^{2/17} \left( \frac{k_B T_e}{z^2 E_H} \right)^{1/17}. \quad (3.5)$$

### 3.2 Line Radiation

Line radiation from plasma occurs for electron transitions between the discrete or bound energy levels in atoms, molecules or ions. In an optically thin plasma of length  $l$  along the

line of sight [43], the integrated emission intensity  $I_{ji}$  of a spectral line arising from a transition between bound levels  $j$  and  $i$  is given by

$$I_{ji} = \frac{A_{ji} h \nu_{ji}}{4\pi} \int N_j ds = h \nu_{ji} A_{ji} N_j l, \quad (3.6)$$

where  $N_j$  is the population density of the upper level  $j$ ,  $h\nu_{ji}$  is the photon energy (energy difference between levels  $j$  and  $i$ ), and  $A_{ji}$  is the spontaneous transition probability or Einstein  $A$  coefficient. The integration is taken over a depth of plasma viewed by the detector, and the intensity of radiation is measured in units of power per unit area per unit solid angle. Transition probabilities can be sometimes expressed via the oscillator strength  $f_{ji}$ . This is defined as the ratio of the number of classical oscillators to the number of lower state atoms required to give the same line-integrated absorption [44]. Its relationship to the Einstein coefficient is

$$f_{ji} = \frac{4\pi\epsilon_0}{e^2} \frac{mc^3}{8\pi^2\nu_{ji}} \frac{g_j}{g_i} A_{ji}. \quad (3.7)$$

The usefulness of  $f_{ji}$  is that it is dimensionless, describing just the relative strength of the transition. The detailed values of  $A_{ji}$ ,  $g_i$ , and  $g_j$  can be obtained from reference compilations or from electronic databases, i.e by NIST [45].

### 3.3. Continuum Radiation

The origins of continuum radiation are both bound-free and free-free transitions. Free-free emission or IB radiation is due to the interaction of free electrons with positively charged ions. In free-bound emission (recombination radiation), a free electron is captured by an ion in a bound level. The energy of the photon given off is the difference between original energy of the electron and its new energy in whatever level of whatever atom it ends up in. Since this difference can have any value, the result of many free-bound transitions is a continuous spectrum. Transitions between two free energy levels can occur in plasmas increasing the energy exchanges of charged particles. Classically, this takes place because a moving charge radiates when it is accelerated or retarded. For most cases of practical importance, these free-free transitions are classified as bremsstrahlung or cyclotron spectra. In bremsstrahlung, the acceleration of charged particle takes place via the Coulomb field of charged particles. In cyclotron radiation, the acceleration is due to the gyration of charged particles in a magnetic field. The total continuum radiation at any particular frequency  $I(v)$  is the sum of the contributions from all such processes having components at the specified frequency. Thus

$$I(v)dv = \frac{1}{4\pi} \int n_e \sum_i N_i \left[ \gamma(i, T_e, v) + \sum_p \alpha(i, j, T_e, v) \right] h\nu ds dv, \quad (3.8)$$

where  $\gamma(i, T_e, v)$  is the atomic probability of a photon of frequency  $v$  being produced in the field of an atom or ion (specified by  $i$ ) by an electron of mean kinetic temperature  $T_e$  making

free-free transition;  $\alpha(i, j, T_e, v)$  is the corresponding probability where the electron makes a free-bound transition into a level  $j$ . As before, the integration is taken over the plasma depth  $s$ .

### 3.4. Line Broadening; Determination of Electron Number Density from Stark Broadening of Spectral Lines

The shape of the spectral lines in the LIB has been studied since the first observation of the laser-induced breakdown in early 1960s. It plays an important role for the spectrochemical analysis and quantification of the plasma parameters. The observed spectral lines are always broadened, partly due to the finite resolution of the spectrometers and partly to intrinsic physical causes. In addition, the center of the spectral lines may be shifted from its nominal central wavelength. The principal physical causes of spectral line broadening are the Doppler, resonance pressure, and Stark broadening. There are several reasons for this broadening and shift. These reasons may be divided into two broad categories: broadening due to local conditions and broadening due to extended conditions. Broadening due to local conditions is due to effects which hold in a small region around the emitting element, usually small enough to assure LTE. Broadening due to extended conditions may result from changes to the spectral distribution of the radiation as it traverses its path to the observer. It also may result from the combining of radiation from a number of regions which are far from each other.

#### 3.4.1. Natural broadening

The uncertainty principle relates the lifetime of an excited state (due to the spontaneous radiative decay) with the uncertainty of its energy. This broadening effect results in an unshifted Lorentzian profile. The FWHM of natural broadening for a transition with a natural lifetime of  $\tau_{ji}$  is:  $\Delta\lambda_{FWHM}^N = \lambda^2 / \pi c \tau_{ji}$ . The natural lifetime  $\tau_{ji}$  is dependent on the probability of spontaneous decay:  $\tau_{ji} = 1/A_{ji}$ . Natural broadening is usually very small compared with other causes of broadening.

#### 3.4.2. Doppler broadening

The Doppler broadening is due to the thermal motion of the emitting atoms, molecules or ions. The atoms in a gas which are emitting radiation will have a distribution of velocities. Each photon emitted will be "red" or "blue" shifted by the Doppler effect depending on the velocity of the atom relative to the observer. The higher the temperature of the gas, the wider the distribution of velocities in the gas. Since the spectral line is a combination of all of the emitted radiation, the higher the temperature of the gas, the broader will be the spectral line emitted from that gas. This broadening effect is described by a Gaussian profile and there is no associated shift. For a Maxwellian velocity distribution the line shape is Gaussian, and the FWHM may be estimated as (in Å):

$$\Delta\lambda_{FWHM}^D = 7.16 \times 10^{-7} \cdot \lambda \cdot \sqrt{T/M}, \quad (3.9)$$

being  $\lambda$  the wavelength in Å,  $T$  the temperature of the emitters in K, and  $M$  the atomic mass in amu.

### 3.4.3. Pressure broadening

The presence of nearby particles will affect the radiation emitted by an individual particle. There are two limiting cases by which this occurs: (i) Impact pressure broadening: The collision of other particles with the emitting particle interrupts the emission process. The duration of the collision is much shorter than the lifetime of the emission process. This effect depends on both the density and the temperature of the gas. The broadening effect is described by a Lorentzian profile and there may be an associated shift. (ii) Quasistatic pressure broadening: The presence of other particles shifts the energy levels in the emitting particle, thereby altering the frequency of the emitted radiation. The duration of the influence is much longer than the lifetime of the emission process. This effect depends on the density of the gas, but is rather insensitive to temperature. The form of the line profile is determined by the functional form of the perturbing force with respect to distance from the perturbing particle. There may also be a shift in the line center. Pressure broadening may also be classified by the nature of the perturbing force as follows: (i) *Linear Stark broadening* occurs via the linear Stark effect which results from the interaction of an emitter with an electric field, which causes a shift in energy which is linear in the field strength ( $\sim E$  and  $\sim 1/r^2$ ); (ii) *Resonance broadening* occurs when the perturbing particle is of the same type as the emitting particle, which introduces the possibility of an energy exchange process ( $\sim E$  and  $\sim 1/r^3$ ); (iii) *Quadratic Stark broadening* occurs via the quadratic Stark effect which results from the interaction of an emitter with an electric field, which causes a shift in energy which is quadratic in the field strength ( $\sim E$  and  $\sim 1/r^4$ ); (iv) *Van der Waals broadening* occurs when the emitting particle is being perturbed by Van der Waals forces. For the quasistatic case, a Van der Waals profile is often useful in describing the profile. The energy shift as a function of distance is given in the wings by e.g. the Lennard-Jones potential ( $\sim E$  and  $\sim 1/r^6$ ).

### 3.4.4. Stark broadening

Stark broadening of spectral lines in the plasma occurs when an emitting species at a distance  $r$  from an ion or electron is perturbed by the electric field. This interaction is described by the Stark effect. The linear Stark effect exists for hydrogen and for all other atoms. Stark broadening from collisions of charged species is the primary mechanism influencing the emission spectra in LIBS. Stark broadening of well-isolated lines in the plasma can be used to determine the electron number density  $n_e(\text{cm}^{-3})$ . In the case of a non-H-like line, an estimation of the Stark width (FWHM) and line shift of the Stark broadened lines is given as [41-44]:

$$\Delta\lambda_{\text{FWHM}}^{\text{Stark}} = 2W\left(\frac{n_e}{10^{16}}\right) + 3.5A\left(\frac{n_e}{10^{16}}\right)^{1/4} \left(1 - BN_D^{-1/3}\right) W\left(\frac{n_e}{10^{16}}\right), \quad (3.10)$$

$$\Delta\lambda^{\text{Shift}} = D\left(\frac{n_e}{10^{16}}\right) \pm 2A\left(\frac{n_e}{10^{16}}\right)^{1/4} \left(1 - BN_D^{-1/3}\right) W\left(\frac{n_e}{10^{16}}\right), \quad (3.11)$$

where  $W$  is the electron impact parameter or half-width,  $A$  is the ion impact parameter both in Å,  $B$  is a coefficient equal to 1.2 or 0.75 for ionic or neutral lines, respectively,  $D$  (in Å) is the electron shift parameter and  $N_D$  is the number of particles in the Debye sphere

$N_D = 1.72 \times 10^9 T^{3/2} n_e^{-1/2}$ . The electron and the ion impact parameters are functions of temperature. The first term on the right side of Eq. (3.10) refers to the broadening due to the electron contribution, whereas the second one is the ion broadening. The minus sign in Eq. (3.11) applies to the high-temperature range of those few lines that have a negative value of  $D/W$  at low temperatures. Since for LIB conditions Stark broadening is predominantly by electron impact, the ion correction factor can safely be neglected, and Eq. (3.10) becomes

$$\Delta\lambda_{\text{FWHM}}^{\text{Stark}} \approx 2W \left( \frac{n_e}{10^{16}} \right). \quad (3.12)$$

The coefficients  $W$  are independent of  $n_e$  and slowly varying functions of electron temperature. A comprehensive list of width and shift parameters  $W$ ,  $A$  and  $D$  is given by Griem [42].

In the quasi-static approximation, the interaction between slowly moving ions and radiating species can be approximated by a perturbation which remains nearly constant over the whole time that the species is radiating. Hydrogen and hydrogen-like ions exhibits linear Stark effect. The FWHM (in Å) of a hydrogen or H-like ion spectral line, in the quasi-static approximation, is given by [41, 42]

$$\Delta\lambda_{\text{FWHM}}^{\text{Stark}} = 8.16 \times 10^{-19} \left( 1 - 0.7 N_D^{-1/3} \right) \lambda_0^2 (n_2^2 - n_1^2) (Z_p^{1/3} - Z_e) n_e^{2/3}, \quad (3.13)$$

where  $\lambda_0$  is the wavelength line centre,  $n_2$  and  $n_1$  are the principal quantum numbers of the upper and lower states, respectively,  $Z_p$  and  $Z_e$  are the nuclear charge on the perturbing ion and the emitting species (atom or ion) and  $n_e$  is the electron number density in cm<sup>-3</sup>. Although the line shapes do depend on the electron contribution, the FWHM are generally insensitive. Eq. (3.13) represents a very good estimate of the Stark broadening in those hydrogenic lines that do not have a strong undisplaced Stark component as for example  $L_\beta$ ,  $L_\delta$ ,  $H_\beta$  (Balmer) and  $H_\delta$  transitions. On the other hand, the FWHM of hydrogenic lines with strong central Stark components are dominated by interaction of the electrons with the emitting hydrogenic species such as  $L_\alpha$  and  $H_\alpha$  transitions. Such lines have a Lorentzian line shape and FWHM for  $L_\alpha$  transition in the impact approximation is given by

$$\Delta\lambda_{\text{FWHM}}^{\text{Stark}} \approx 1.62 \times 10^{-17} \frac{n_e}{\sqrt{T}} \left( 13.76 - \log \frac{n_e^{1/2}}{T} \right), \quad (3.14)$$

where  $\Delta\lambda_{\text{FWHM}}^{\text{Stark}}$  is in Å,  $T$  is in K and  $n_e$  is in cm<sup>-3</sup>. It is seen from Eqs. (3.13) and (3.14) that the ion broadening, in the quasi-static approximation, varies as  $n_e^{2/3}$  and is independent of the temperature whereas the collisional broadening varies approximately as  $n_e$  and it is very much temperature dependent. It is to be noted the electron densities determined from Eqs. (3.13) and (3.14) are only crude estimations and one must compute the entire line profile to extract the total line width for an accurate estimation of  $n_e$ .

### 3.5. Determination of Excitation, Vibrational and Rotational Temperatures

The excitation temperature  $T_{\text{exc}}$  can be calculated according to the Boltzmann equation under the assumption of LTE (Section 3.1). The significance of this temperature depends on the degree of equilibrium within the plasma. For plasma in LTE, any point can be described by its local values of temperature, density, and chemical composition. By considering two lines  $\lambda_{ji}$  and  $\lambda_{nm}$  of the same species, characterized by different values of the upper energy level ( $E_j \neq E_n$ ), the relative intensity ratio can be used to calculate the plasma excitation temperature

$$T_{\text{exc}} = \frac{E_j - E_n}{k_B \ln \left[ \frac{I_{nm} \cdot \lambda_{nm} \cdot g_j \cdot A_{ji}}{I_{ji} \cdot \lambda_{ji} \cdot g_n \cdot A_{nm}} \right]} . \quad (3.15)$$

When selecting a line pair, it is advisable to choose two lines as close as possible in wavelength and as far apart as possible in excitation energy. This is to limit the effect of varying the spectral response of the detection system. The use of several lines instead of just one pair leads to greater precision of the plasma excitation temperature estimation. In fact, though the precision of the intensity values can be improved by increasing the signal intensity, the transition probabilities  $A_{ji}$  reported in the literature exhibit significance degree of uncertainty (5-50%). The excitation temperature can be calculated from the relative intensities of a series of lines from different excitation states of the same atomic or ionic species from the slope of the Boltzmann plot  $\ln[I_{ji} \lambda_{ji} / g_j A_{ji}]$  versus  $E_j/k_B$

$$\ln \left[ \frac{I_{ji} \cdot \lambda_{ji}}{g_j \cdot A_{ji}} \right] = C - \frac{E_j}{k_B \cdot T_{\text{exc}}} , \quad (3.16)$$

where  $I_{ji}$  is the emissivity ( $\text{W m}^{-3} \text{ sr}^{-1}$ ) of the emitted  $j \rightarrow i$  spectral line,  $\lambda_{ji}$  is the wavelength,  $g_j=2J_j+1$  is the statistical weight,  $A_{ji}$  is the Einstein transition probability of spontaneous emission,  $E_j/k_B$  is the normalized energy of the upper electronic level and  $C=\ln(hcN_j/4\pi Q(T))$  ( $Q(T)$  is the partition function). The values of the  $\lambda_{ji}$ ,  $g_j$ ,  $A_{ji}$  and  $E_i$  for selected atomic or ionic lines can be obtained from the NIST Atomic Spectral Database [45]. A set of selected spectral lines can be chosen based on their relative strengths, accuracies and transition probabilities.

The emission spectra of the diatomic species reveal a relatively complex structure which is due to the combination of the electronic transitions from the different rotational and vibrational states [46-48]. The emission intensities of the molecular bands can be analyzed in order to calculate the molecular vibrational temperature  $T_{\text{vib}}$ . For a plasma in LTE, the intensity of an individual vibrational  $v'-v''$  band  $I_{v'-v''}$  is given by

$$\ln \left( \frac{I_{v'-v''} \cdot \lambda_{v'-v''}^4}{q_{v'-v''}} \right) = A - \frac{G(v') h c}{k_B \cdot T_{\text{vib}}} , \quad (3.17)$$

where  $A$  is a constant,  $\lambda_{v'-v''}$  is the wavelength corresponding to the band head,  $q_{v'-v''} = \left| \int_0^{\infty} \Psi_{v'}(R) \Psi_{v''}(R) dR \right|^2$  is the Franck-Condon factor and  $G(v')h c/k_B$  is the normalized energy of the upper vibrational level. A line fit to  $\ln(I_{v'-v''} \cdot \lambda_{v'-v''}^4 / q_{v'-v''})$  as a function of the upper normalized electronic-vibrational energies has a slope equal to  $-1/T_{\text{vib}}$ .

On the other hand, the emission intensities of the rotational lines of a vibrational band can be analyzed in order to estimate the effective rotational temperature  $T_{\text{rot}}$ . In this case it is necessary to consider the Hund's coupling case for the both electronic states implied in the transition. From the assignment of the rotational spectrum it is possible to estimate the effective rotational temperature by considering the  $J$  value for the maximum of the band  $T_{\text{rot}} = (2B_v h c/k_B)(J_{\max} + 1/2)^2$ ,

being  $B_v$  the rotational constant for  $v'$  vibrational level and  $J_{\max}$  the total angular momentum at the maximum.

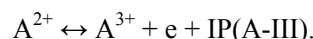
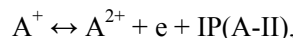
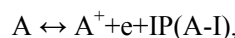
Another method for estimating the vibrational and rotational temperatures is based on a simulation program of the spectra. Software developed in our laboratory [49] calculated the spectra of a diatomic molecule by summing the intensity of all rovibrational levels and convoluting the results with the instrumental line shape of the optical system. The emission intensity  $I_{v',J-v'',J''}$  of a molecular line can be approximated by

$$I_{v',J-v'',J''} \approx \frac{64\pi^4 \tilde{V}_{v',J-v'',J''}^4}{3(2J'+1)} N_{v',J} \bar{R}_e^2 q_{v',v''} S_{J,J''}, \quad (3.18)$$

where  $\tilde{V}_{v',J-v'',J''}$  is the wavenumber of the transition,  $2J'+1$  is the rotational degeneracy of the upper state,  $N_{v',J}$  is the population in the initial (upper) state,  $\bar{R}_e$  is the average electronic transition moment,  $q_{v',v''}$  is the Franck-Condon factor and  $S_{J,J''}$  is the Hönl-London factor [50]. Spectrum simulations are based on comparison of experimental and calculated spectra for different rotational and vibrational population distributions which depend on temperature.

### 3.6. Ionization Degree of the Plasmas: Saha Equation

In plasma there is a continuous transition from gases with neutral atoms to a state with ionized atoms, which is determined by an ionization equation. The transition between gas and plasma is essentially a chemical equilibrium, which shifts from the gas to the plasma side with increasing temperature. Let us consider the first three different ionization equilibria of an atom  $A$ :



For each ionization equilibrium, considering the atoms and ions in their ground electronic state, the LTE between ionization and recombination reactions at temperature  $T$  is described by the Saha equation (see Eq. 3.3)

$$\frac{n_e \cdot N_i}{N_0} = \frac{g_e \cdot g_i}{g_0} \frac{(2\pi m k_B T)^{3/2}}{h^3} e^{-I_p/k_B T}, \quad (3.19)$$

where  $n_e = N_i$  are the electron and ion densities in the different ionization equilibria in the second member of ionization equilibria. From this equation, ionization degree  $n_e \cdot N_i / N_0$  can be estimated.

#### 4. EXPERIMENTAL DETAILS

LIBS is a plasma based method that uses instrumentation similar to that used by other spectroscopic methods (atomic emission spectroscopy, laser-induced fluorescence etc). A typical LIBS apparatus utilizes a pulsed laser that generates the powerful optical pulses used to form the plasma. Principles of laser operation in general and the operation of specific lasers are described in detail in numerous books. The discussion here will be limited to the fundamentals of the operation of the transversely excited atmospheric (TEA) carbon dioxide laser used in this work. The CO<sub>2</sub> laser is a near-infrared gas laser capable of very high power and with the highest efficiency of all gas lasers ( $\approx 10\text{-}20\%$ ) and for cw operation the highest output power. Although CO<sub>2</sub> lasers have found many applications including surgical procedure, their popular image is as powerful devices for cutting, drilling, welding or as weapons for military applications. The linear CO<sub>2</sub> molecule has three normal modes of vibration, labelled  $v_1$  (symmetry stretch),  $v_2$  (bending vibration) and  $v_3$  (asymmetric stretch). The fundamental vibration wavenumbers are 1354, 673 and 2396 cm<sup>-1</sup>, respectively. The vibrational state of the molecule is described by the number of vibrational quanta in these modes. The bending vibrational mode is twofold degenerate and can have a vibrational angular momentum along the CO<sub>2</sub> axis. The number of quanta of this vibrational angular momentum is stated as an upper index to the vibrational  $v_2$  quanta. The upper laser level (00<sup>0</sup>1) denotes the ground vibrational state for the mode  $v_1$ , the ground vibrational state for the mode  $v_2$  which is doubly degenerate, and the first excited vibrational state for the mode  $v_3$ . The active medium is a gas discharge in a mixture of He, N<sub>2</sub> and CO<sub>2</sub>. By electron impact in the discharge excited vibrational levels in the electronic ground states of N<sub>2</sub> and CO<sub>2</sub> are populated. The vibrational levels  $v = 1$  in the N<sub>2</sub> molecule and ( $v_1, v_2, v_3$ ) = (00<sup>0</sup>1) in the CO<sub>2</sub> molecule are near-resonant and energy transfer from the N<sub>2</sub> molecule to the CO<sub>2</sub> molecule becomes very efficient. This populates the (00<sup>0</sup>1) level in CO<sub>2</sub> preferentially, creates inversion between the (00<sup>0</sup>1) and the (02<sup>0</sup>0) levels, and allows laser oscillations on many rotational transitions between these two vibrational states in the wavelength range 9.6-10.6 μm. The main laser transitions in CO<sub>2</sub> occur between the excited states of the mode  $v_3$ (00<sup>0</sup>1) and the symmetric stretching mode  $v_1$ (10<sup>0</sup>0) (10.6 μm) or the bending mode  $v_2$ (01<sup>1</sup>0) (9.6 μm). A single line can be selected by a Littrow-grating, forming one of the resonator end mirrors. Helium atoms do not take part directly in the excitation of CO<sub>2</sub> molecules but do play

an important role in heat-transfer from the gas mixture to the tube walls, as well as facilitating the depopulation of the lower vibrational levels in CO<sub>2</sub>, contributing in this way to the maintenance of the population inversion. The power of CO<sub>2</sub> lasers depends on their configuration. The laser used in these experiments was a transversely excited atmospheric (TEA) CO<sub>2</sub> laser in which the gas-flow is transverse to the laser cavity's axis. The pressure in the tube is close to atmospheric pressure. The CO<sub>2</sub>:N<sub>2</sub>:He mixture is exchange in a continuous way, enhancing the output power of the laser. The laser can achieve a power of 50 MW. The optical materials used in lasers emitting radiation in the infrared range are obviously different than those used in the visible range. For example, materials such as germanium (Ge) or gallium arsenide (GaAs) are completely opaque in the visible range, while being transparent in the infrared range. Some materials, such as zinc selenide (ZnSe), are transparent in both spectral ranges. Typical materials transparent in the IR range are: NaCl or CsI. Metal mirrors (copper, molybdenum) are used in the IR range, owing to their small absorption (and large reflectivity) as well as their large heat capacity which enables removal of heat from the active medium.

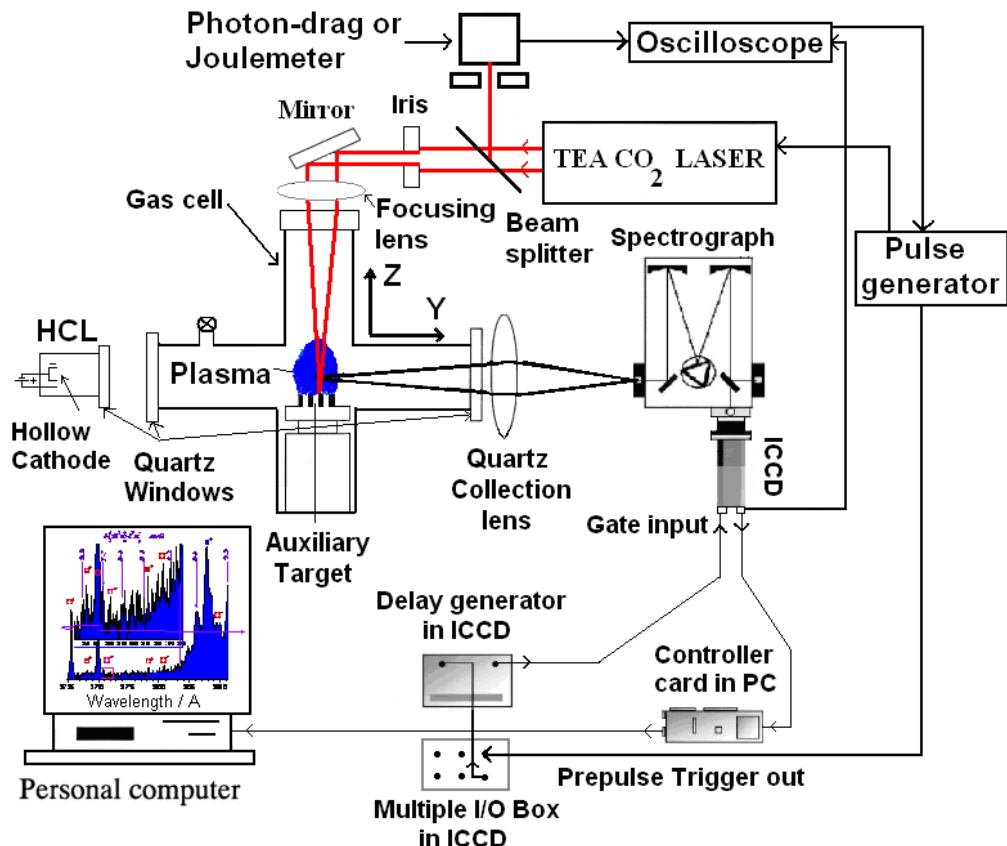


Figure 1. Schematic diagram of the experimental set-up used for time-resolved TEA-CO<sub>2</sub> pulsed laser gas breakdown diagnostics.

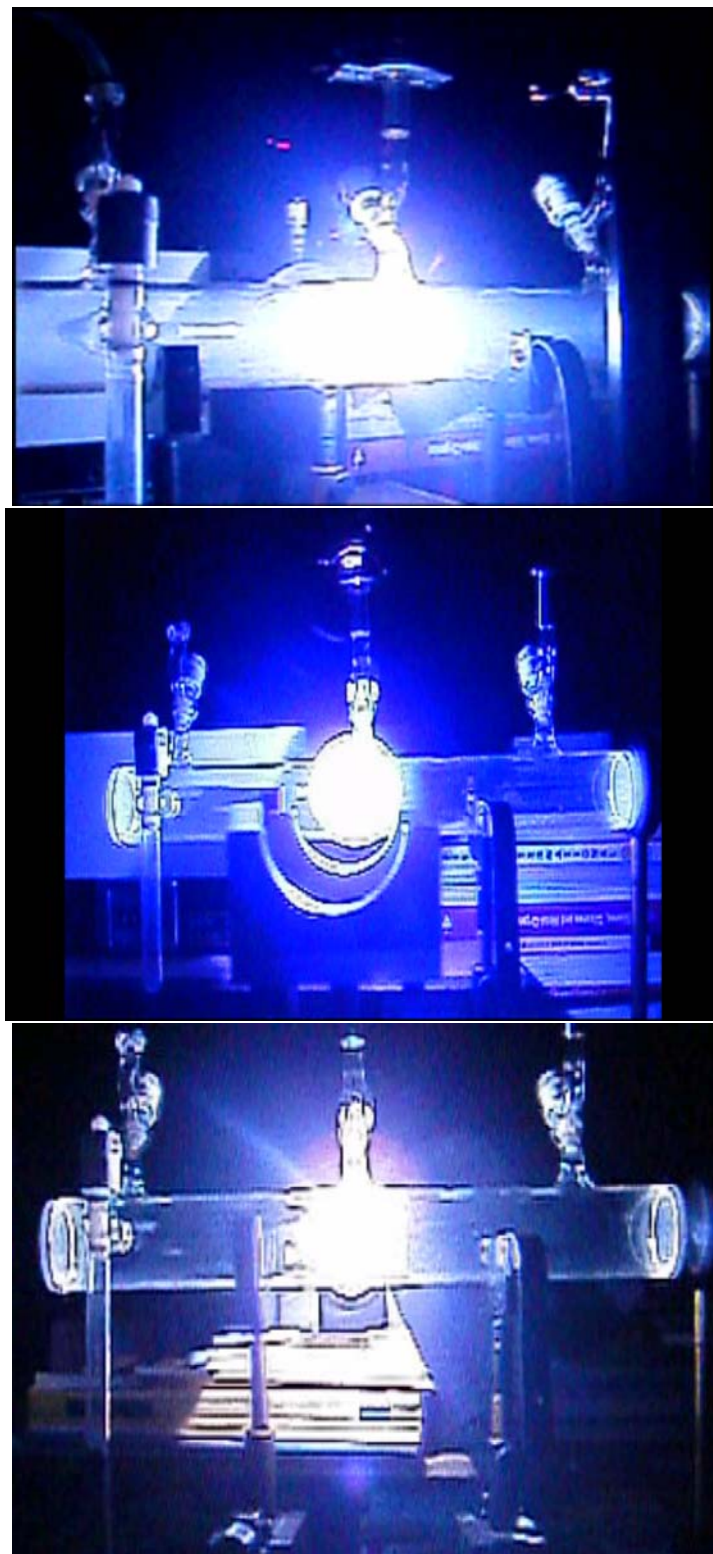


Figure 2. (Continued)

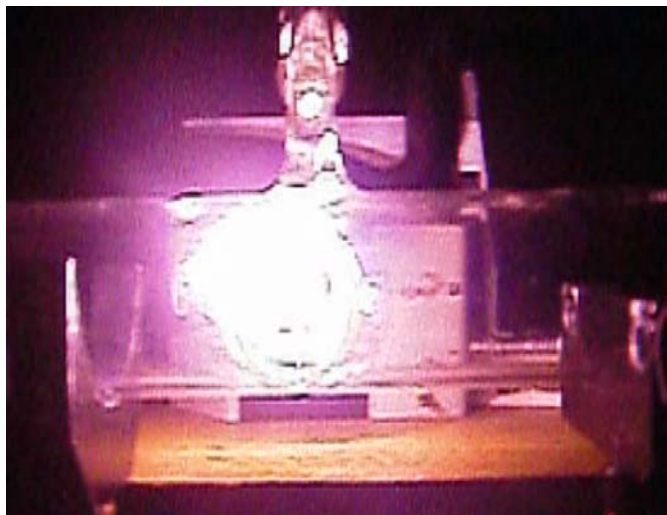


Figure 2. Four images of the LIB of nitrogen at atmospheric pressure ( $\lambda=9.621\text{ }\mu\text{m}$  and power density of  $4.5\text{ GW}\times\text{cm}^{-2}$ ), oxygen at  $49.0\text{ kPa}$  ( $\lambda=10.591\text{ }\mu\text{m}$  and power density of  $1.93\text{ GW}\times\text{cm}^{-2}$ ), air at atmospheric pressure ( $\lambda=9.621\text{ }\mu\text{m}$  and intensity of  $5.86\text{ GW}\times\text{cm}^{-2}$ ) and He at atmospheric pressure ( $\lambda=10.591\text{ }\mu\text{m}$  and power density of  $6.31\text{ GW}\times\text{cm}^{-2}$ ) at different times of the experiment induced by a TEA-CO<sub>2</sub> laser pulse. Laser beam direction is from right to left.

A schematic diagram of the experimental configuration used for time-resolved TEA-CO<sub>2</sub> pulsed laser gas breakdown diagnostics is shown in Figure 1. The experiments were carried out with a transverse excitation atmospheric (TEA) CO<sub>2</sub> laser (Lumonics model K-103) operating on an 8:8:84 mixture of CO<sub>2</sub>:N<sub>2</sub>:He, respectively. The laser is equipped with frontal Ge multimode optics (35 % reflectivity) and a rear diffraction grating with 135 lines mm<sup>-1</sup> blazed at 10.6 μm. The laser pulse repetition rate was usually 1 Hz. The divergence of the emitted laser beam is 3 mrad. The laser delivered up to 3.16 J at a wavelength of 10.591 μm, leading to an estimated power of 49.5 MW (Eq. 1.1), intensity (power density or irradiance) of  $6.31\text{ GW cm}^{-2}$  (Eq. 1.2), fluence of  $403\text{ J}\square\text{cm}^{-2}$  (Eq. 1.3), photon flux of  $3.1\square10^{29}\text{ photon}\square\text{cm}^{-2}\square\text{s}^{-1}$  (Eq. 1.4), electric field of  $1.54\text{ MV}\square\text{cm}^{-1}$  (Eq. 1.5) and radiation pressure of 421 kPa (Eq. 1.6) on the focal position. The focused-spot area ( $7.85\times10^{-3}\text{ cm}^2$ ) of the laser beam was measured with a pyroelectric array detector (Delta Development Mark IV). The temporal shape of the TEA-CO<sub>2</sub> laser pulse, monitored with a photon drag detector (Rofin Sinar 7415), consisted in a prominent spike of a FWHM of around 64 ns carrying ~90% of the laser energy, followed by a long lasting tail of lower energy and about 3 μs duration. The primary laser beam was angularly defined and attenuated by a diaphragm of 17.5 mm diameter before entering to the gas cell. A beam splitter was used to redirect 10% of the laser pulse energy on a pyroelectric detector (Lumonics 20D) or on a photon-drag detector (Rofin Sinar 7415) for energy and temporal shape monitoring and triggering, respectively, through a digital oscilloscope (Tektronix TDS 540). The laser-pulse energy was varied with the aid of several calibrated CaF<sub>2</sub> attenuating plates. The shot-to-shot fluctuation of the laser energy was approximately 5%. In time-resolved gas breakdown, the pulsed laser light was focused by a NaCl lens of 24 cm focal lens onto the surface of a 0.7 mm×0.7 mm stainless steel mesh in gas at atmospheric pressure. This allows us to fix the focal position for LIB at any fluence inducing strong gas breakdown plasma. No lines from metals were found in the spectra,

meaning that the metal mesh was practically never ablated. The high purity gases (~99.99 %) were placed in a medium-vacuum cell equipped with a NaCl window for the laser beam and two quartz windows for optical access. The gas is initially at ambient temperature (298 K). The cell was evacuated with the aid of a rotary pump, to a base pressure of 4 Pa that was measured by a mechanical gauge. Optical emission from the plume was imaged by a collecting optical system onto the entrance slit of different spectrometers. The light emitted from the laser-induced plasma was optically imaged 1:1, at right angles to the normal to the focal volume, by a quartz lens (focal length 4 cm, *f*-number = *f*/2.3) onto the entrance slit of the spectrometer. The distance between gas plasma axis and entrance slit was typically *y*=16 cm. Optical emission accompanying the laser-induced gas plasma was viewed in a *XZ* parallel plane to the front face of the metal mesh for different distances *z* along the plasma *Y* axis. Two spectrometers were used: 1/8 m Oriel spectrometer (10 and 25 μm slits) with two different gratings (1200 and 2400 grooves/mm<sup>-1</sup>) in the spectral region 2000-11000 Å at a resolution of ~1.3 Å in first-order (1200 grooves mm<sup>-1</sup> grating), and an ISA Jobin Yvon Spex (Model HR320) 0.32 m equipped with a plane holographic grating (2400 grooves mm<sup>-1</sup>) in the spectral region 2000-7500 Å at a resolution of ~0.12 Å in first-order. Two detectors were attached to the exit focal plane of the spectrographs and used to detect the optical emissions from the laser-induced plasma: an Andor DU420-OE (open electrode) CCD camera (1024x256 matrix of 26x26 μm<sup>2</sup> individual pixels) with thermoelectric cooling working at -30 °C; A 1024x1024 matrix of 13x13 μm<sup>2</sup> individual pixels ICCD (Andor iStar DH-734), with thermoelectric cooling working at -20 °C. The low noise level of the CCD allows long integration times and therefore the detection of very low emission intensities. The spectral window in high-resolution experiments was about 12 nm. The intensity response of the detection systems was calibrated with a standard (Osram No.6438, 6.6-A, 200-W) halogen lamp and Hg/Ar pencil lamp. Several (Cu/Ne, Fe/Ne and Cr/Ar) hollow cathode lamps (HCL) were used for the spectral wavelength calibration of the spectrometers.

In time-resolved measurements, for synchronization, the CO<sub>2</sub> laser was operated at the internal trigger mode and ICCD detector was operated in external and gate modes. The external trigger signal generated by the laser was fed through the scope and delay generator into the back of the ICCD detector head. The total insertion delay ( $45 \pm 2$  ns) is the total length of time taken for the external trigger pulse to travel through the digital delay generator and gater so that the ICCD will switch on. The time jitter between the laser and the fast ICCD detector gate was about  $\pm 2$  ns. The delay time *t*<sub>d</sub> is the time interval between the arrival of the laser pulse on the metal mesh and the activation of the ICCD detector. The gate width time *t*<sub>w</sub> is the time interval during which the plasma emission is monitored by the ICCD. Both parameters were adjusted by the digital delay generator of the ICCD detector. The CO<sub>2</sub> laser pulse picked up with the photon drag detector triggered a pulse generator (Stanford DG 535) through the scope and this pulse was used as external trigger in the ICCD camera. The laser pulse and the gate monitor output were displayed in a digital oscilloscope. In this way, by using the output of the photon drag detector, the oscilloscope, the delay pulse generator and the gate monitor output of the ICCD camera, the gate width time *t*<sub>w</sub> and the delay time *t*<sub>d</sub> could be adjusted without insertion time.

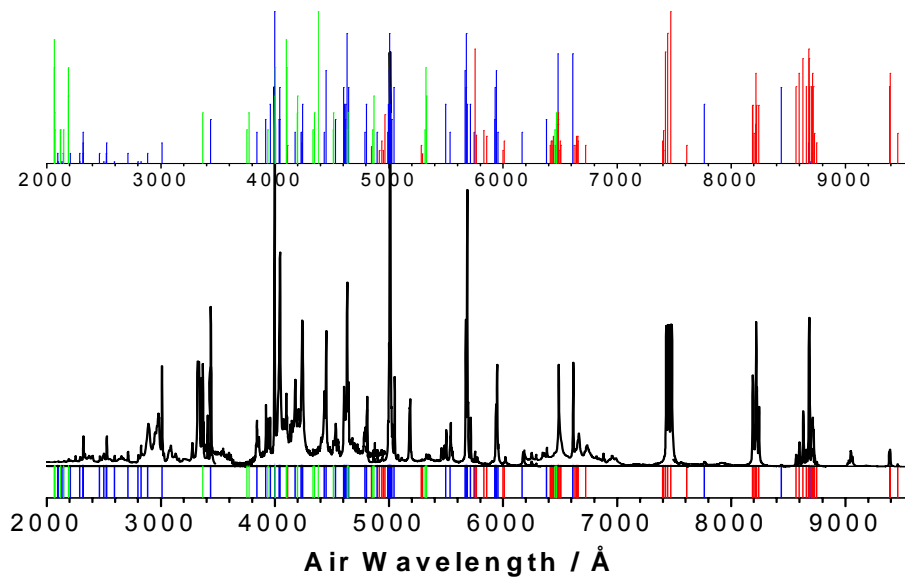


Figure 3. An overview of the LIB emission spectrum of nitrogen at a pressure of  $1.2 \times 10^5$  Pa, excited by the 9P(28) line at  $1039.36\text{ cm}^{-1}$  of the TEA CO<sub>2</sub> laser, compared with atomic lines of N (red), N<sup>+</sup> (blue) and N<sup>2+</sup> (green).

## 5. RESULTS AND DISCUSSION

When a gas is irradiated by CO<sub>2</sub> laser lines of sufficient power, a visible breakdown occurs. The onset of LIB in air is a sudden dramatic event involving the production of more than  $\sim 10^{16}$  electron-ion pairs and the emission of radiation characteristic of the gas-plasma. Figure 2 shows a series of images of the LIB nitrogen (up to the left), oxygen (up to the right), air (below to the left) and helium (below to the right) plasma at different times of the experiment. Although the laser-induced plasma appears spatially uniform to the naked eye, it is indeed elongated along the direction of the incoming carbon dioxide laser beam. For a laser power density around  $4.5\text{ GW}\times\text{cm}^{-2}$ , the laser-induced plasma may be  $\approx 6\text{ cm}$  long and a few centimeters in diameter. A number of plasma lobes can be distinguished as well as diffuse, luminous cloud surrounding the central plasma core. The observations of the LIB geometry during the experiments indicate that the actual plasma region is not spherical, but elongated in the direction of the laser beam propagation. There is an expansion back toward the laser that essentially fills the converging cone of the CO<sub>2</sub> laser radiation. The growth of the plasma in the direction opposite to the laser beam had lead to the model of a radiation-supported detonation wave (Section 2.6). A shock wave propagates from the focal region (a point at the centre of the cell) into the gas and absorption of energy from the laser beam drives the shock wave, causing it to spread. The structure of the LIB plasma is complex, and indeed there may be several distinct plasma regions produced along the laser beam axis. This multiple collinear plasmas in gases at pressures around the atmospheric level are observable by the naked eye. The CO<sub>2</sub> laser pulse remains in the focal volume after the plasma formation for some significant fraction of its duration and the plasma formed can be heated to very high temperatures and pressures by IB absorption. Since plasmas absorb radiation much more

strongly than ordinary matter, plasmas can block transmission of incoming laser light to a significant degree; a phenomenon known as plasma shielding [51]. The high temperatures and pressures produced by plasma absorption can lead to thermal expansion of the plasma at high velocities, producing an audible acoustic signature, shock waves, and cavitation effects. The plasma also tends to expand back along the beam path toward the laser, a phenomenon known as moving breakdown. The shock wave heats up the surrounding gas which is instantaneously transformed in strongly ionized plasma.

## 5.1. LIBS of Nitrogen

In this section we present our results on the large-scale plasma produced in nitrogen gas at room temperature and pressures ranging from  $4 \times 10^3$  to  $1.2 \times 10^5$  Pa by high-power TEA-CO<sub>2</sub> LIB plasma [18]. The time-integrated spectrum of the generated plasma is dominated by emission of strong N<sup>+</sup> and N and very weak N<sup>2+</sup> atomic lines and molecular features of N<sub>2</sub><sup>+</sup>(B<sup>2</sup>Σ<sub>u</sub><sup>+</sup>-X<sup>2</sup>Σ<sub>g</sub><sup>+</sup>), N<sub>2</sub><sup>+</sup>(D<sup>2</sup>Π<sub>g</sub>-A<sup>2</sup>Π<sub>u</sub>), N<sub>2</sub>(C<sup>3</sup>Π<sub>u</sub>-B<sup>3</sup>Π<sub>g</sub>) and very weak N<sub>2</sub>(B<sup>3</sup>Π<sub>g</sub>-A<sup>3</sup>Σ<sub>u</sub><sup>+</sup>). Figure 3 displays an overview of the optical emission spectrum of LIDB in nitrogen (2000–9565 Å) compared with atomic lines of N, N<sup>+</sup> and N<sup>2+</sup> [45]. Strong atomic N<sup>+</sup> lines dominate the spectrum but, atomic N lines (about 3 times weaker) and very weak N<sup>2+</sup> lines (about  $10^{-2}$ - $10^{-3}$  times weaker) also are present. The assignments of the atomic N (mainly in the 5700–9565 Å spectral region), N<sup>+</sup> (2000–6000 Å) and N<sup>2+</sup> (2000–5500 Å) individual lines are indicated by stick labels. In the upper part of Figure 3 we indicate in a column graph, the relative intensities of atomic observed N, N<sup>+</sup> and N<sup>2+</sup> lines tabled in NIST Atomic Spectral Database [45]. There is a good agreement between line intensities tabulated in NIST and the measured intensities observed here for N, N<sup>+</sup> and N<sup>2+</sup>. The spectrum of Figure 3 has been obtained with six successive exposures on the CCD detector using a 1/8 m Oriel spectrometer (1200 grooves/mm grating). In addition to identified atomic lines, molecular bands associated to N<sub>2</sub><sup>+</sup> and N<sub>2</sub> diatomic molecules are observed. The analysis of the molecular emission has already been used for a long time to get information on the structure and symmetry of excited states [46-48]. Studies of the electronic spectra of N<sub>2</sub> and N<sub>2</sub><sup>+</sup> in a number of discharge tubes, such as electrodeless microwave discharges and conventional *ac* and *dc* discharges, are well known. In many electrical discharges, the most prominent electronic transitions of N<sub>2</sub> are the first positive B<sup>3</sup>Π<sub>g</sub>-A<sup>3</sup>Σ<sub>u</sub><sup>+</sup> system (between 480 and 2530 nm) and the second positive C<sup>3</sup>Π<sub>u</sub>-B<sup>3</sup>Π<sub>g</sub> system (between 270 and 550 nm) [52]. For the electronic states implied in the electronic transitions of N<sub>2</sub>(C-B and B-A) and N<sub>2</sub><sup>+</sup>(B-X and D-A) the vibrational quanta  $\Delta G(v+\frac{1}{2})$  in the upper and lower electronic states have similar magnitudes and therefore the vibrational transitions with  $\Delta v=v'-v''$  constant (sequences) appear quite close. The known part of the C-B second positive system of molecular nitrogen consist of the  $\Delta v = 4, 3, 2, 1, 0, -1, -2, -3, -4, -5, -6$  and -7 triple-headed band sequence, all degraded to the violet. A sharp cutting-off of the rotational in  $v'=4$  vibrational level of the C state is observed, which Herzberg [53] attributed to a predissociation. Pannetier *et al* [54] observed the 5-5 band of the C-B system with band-head at 3259.2 Å. Also Tanaka and Jursa [55] studied this band system with high intensity in the aurora afterglow observed for weak red-degraded triplet bands originate from  $v'=5$  (C<sup>3</sup>Π<sub>u</sub>). Perturbations of various types in the C<sup>3</sup>Π<sub>u</sub> state of molecular nitrogen were also observed. Moreover, the most prominent electronic transitions of N<sub>2</sub><sup>+</sup> are the first negative B<sup>2</sup>Σ<sub>u</sub><sup>+</sup>-X<sup>2</sup>Σ<sub>g</sub><sup>+</sup> system (between 280 and 590 nm) and the A<sup>2</sup>Π<sub>u</sub>-X<sup>2</sup>Σ<sub>g</sub><sup>+</sup> Meinel

system (550 and 1770 nm) [52]. The A-X Meinel bands for nitrogen cation were first identified in the aurora borealis [56]. The analysis of these band systems of  $N_2$  and  $N_2^+$  was accomplished in the early work of many authors and played an important part in the development of our understanding of the spectra of diatomic molecules.

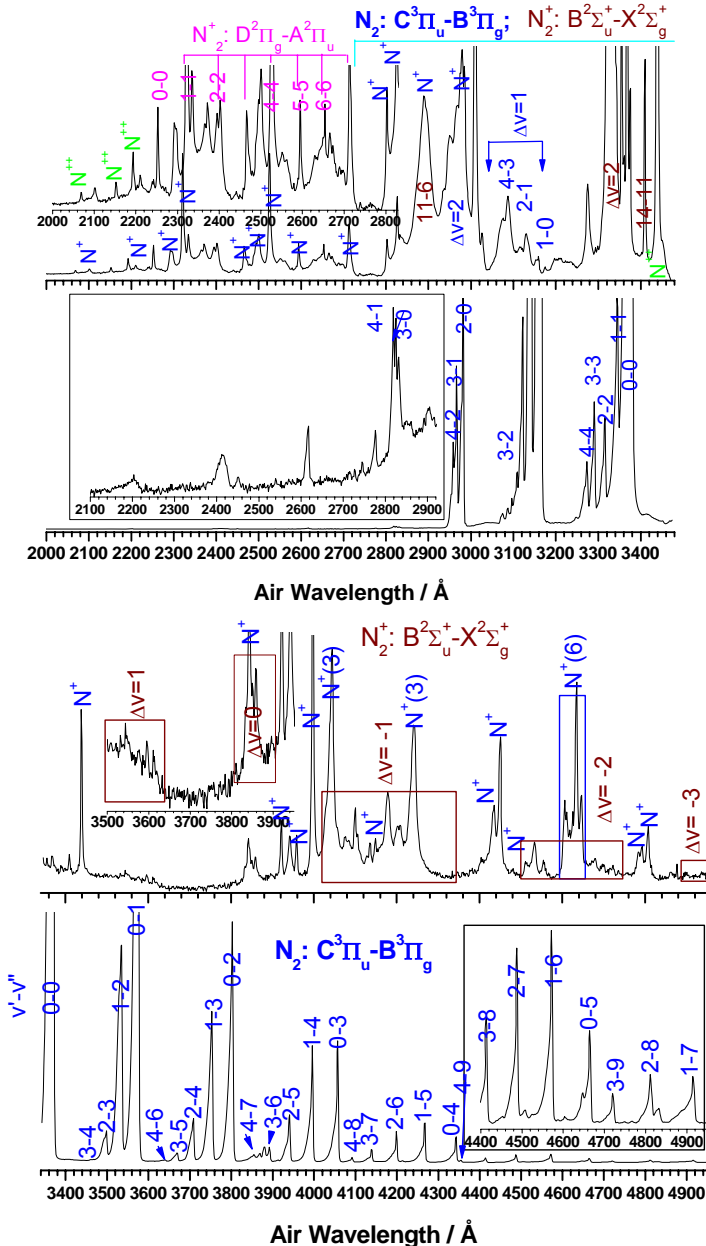


Figure 4. (Continued)

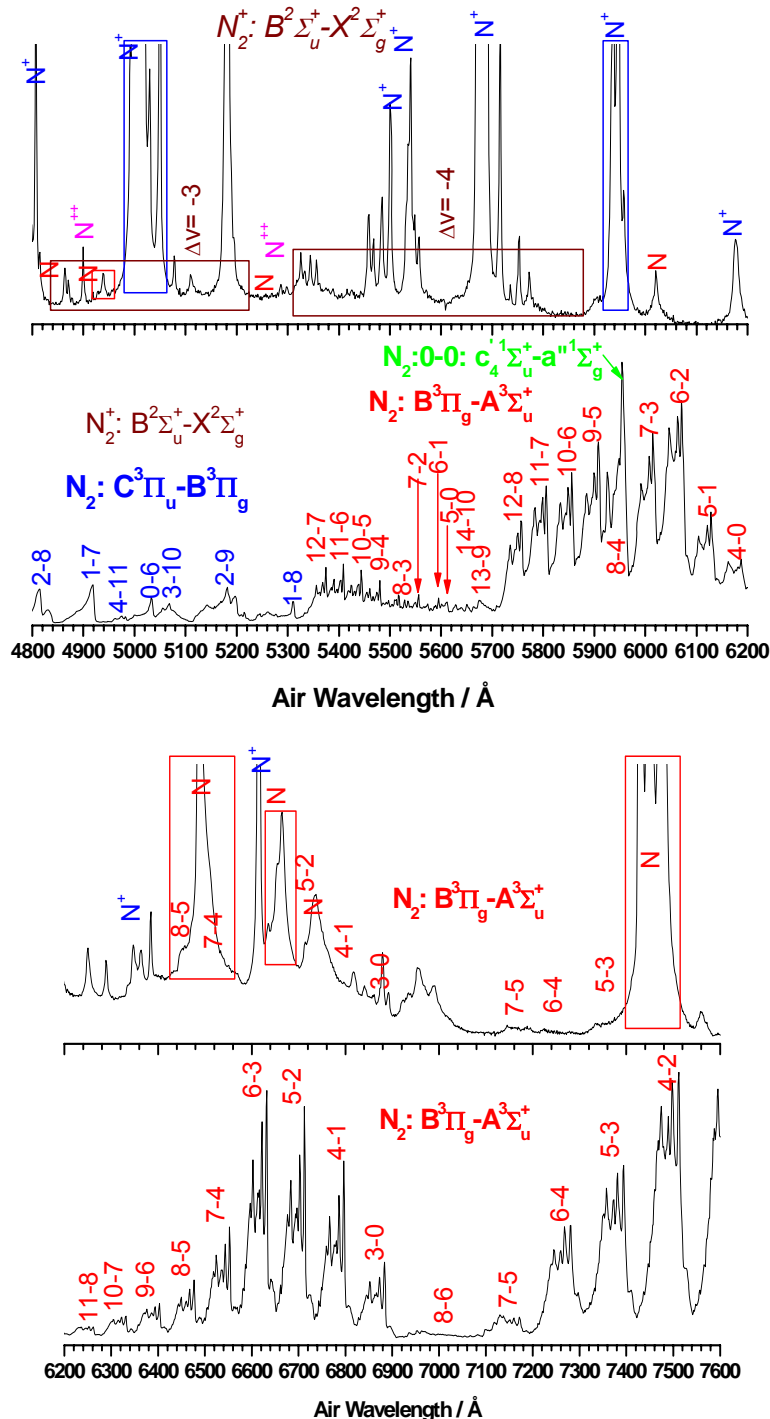


Figure 4. (Continued)

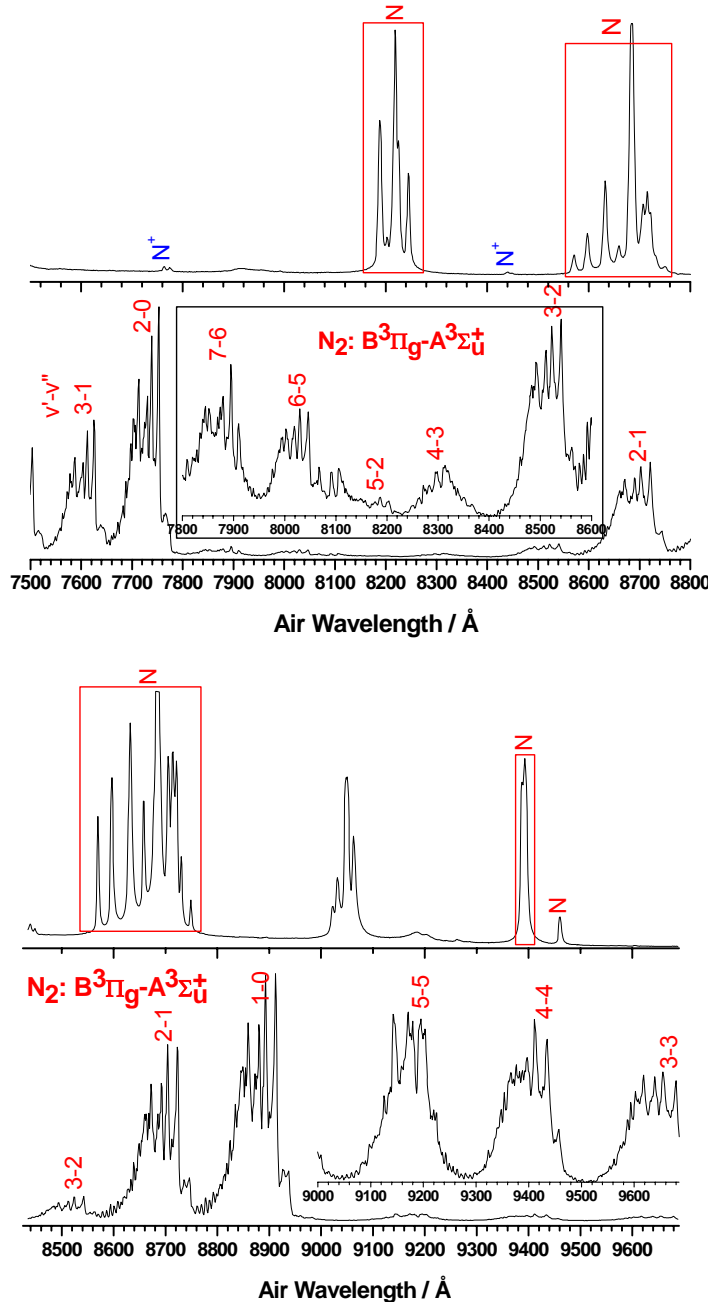


Figure 4. An overview of the low-resolution emission spectra observed in the 2000–9690 Å region. Upper panel: LIDB in nitrogen at a pressure of  $1.2 \times 10^5$  Pa, excited by the  $9P(28)$  line at  $1039.36 \text{ cm}^{-1}$  of the  $\text{CO}_2$  laser; Lower panel: dc electric glow discharge spectrum of nitrogen at low pressure.

In order to assign the molecular features of the LIDB in nitrogen, its spectrum is compared to that of the *dc* electric glow discharge at low pressure (~5 Torr). Typical spectra recorded with the oriel spectrometer (25  $\mu\text{m}$  slit and grating of 1200 grooves/mm) after  $\text{CO}_2$  laser excitation and in the cathode glow discharge of  $\text{N}_2$  are given in Figure 4. A global analysis of the latter allows one to distinguish the second positive C-B system (between 270

and 530 nm) and the first positive B-A system (between 570 and 970 nm) of N<sub>2</sub> and very weak emissions corresponding to the first negative B-X system of N<sub>2</sub><sup>+</sup> ions. Moreover, spectroscopic measurements performed on the dc electric glow in N<sub>2</sub> spectrum showed that although numerous molecular bands appear, nitrogen atomic lines are not present. Besides, the second positive system of N<sub>2</sub> and the first negative system of N<sub>2</sub><sup>+</sup> spectra are frequently observed simultaneously in plasma containing nitrogen. In the glow discharge in N<sub>2</sub> at 5977.4 Å, the 0-0 band of the c<sub>4</sub>  $^1\Pi_u$ -a<sup>”</sup>  $^1\Sigma_g^+$  Ledbetter Rydberg series [57] of nitrogen is observed overlapped with the 8-4 band sequence of the first positive B-A system. The LIB emission spectrum of N<sub>2</sub> (Figure 4) shows six red-degraded heads in the region 225-275 nm which were readily assigned to the  $\Delta\nu=0$  ( $\nu=0, 1, \dots, 6$ ) band sequence of the D<sup>2</sup> $\Pi_g$ -A<sup>2</sup> $\Pi_u$  Janin-d'Incan system [52] of N<sub>2</sub><sup>+</sup>. In the spectral range between 2700-5300 Å, the second positive system of N<sub>2</sub>(C-B) and the first negative system of N<sub>2</sub><sup>+</sup>(B-X) spectra are observed simultaneously. Table 1 lists the different molecular species that have been observed in the LIB spectrum of nitrogen.

**Table 1.- List of the most intense observed molecular bands in the LIB in nitrogen, corresponding electronic transition and wavelength in Å (air) for the major band heads.**

Molecule	Name system	Observed band system	Major band heads (Å) ( $\nu'$ , $\nu''$ )
N <sub>2</sub> <sup>+</sup>	Janin-d'Incan	D <sup>2</sup> $\Pi_g$ - A <sup>2</sup> $\Pi_u$	2343 (0, 0); 2398 (1, 1); 2456 (2, 2); 2516 (3, 3); 2579 (4, 4); 2645 (5, 5); 2714 (6, 6)
N <sub>2</sub> <sup>+</sup>	First negative	B <sup>2</sup> $\Sigma_u^+$ - X <sup>2</sup> $\Sigma_g^+$	2861.7 (11, 6); 3033.0 (11, 7); 3065.1 (15, 10); 3076.4 (4, 1); 3078.2 (3, 0); 3291.6 (5, 3); 3293.4 (4, 2); 3298.7 (3, 1); 3308.0 (2, 0); 3319.9 (8, 6); 3349.6 (18, 13); 3381.5 (10, 8); 3419.6 (14, 11); 3447.3 (23, 16); 3460.8 (17, 13); 3493.4 (12, 10); 3532.3 (5, 3); 3538.3 (4, 3); 3548.9 (3, 2); 3563.9 (2, 1); 3582.1 (1, 0); 3588.6 (16, 13); 3612.4 (10, 9); 3806.8 (5, 5); 3818.1 (4, 4); 3835.4 (3, 3); 3857.9 (2, 2); 3884.3 (1, 1); 3914.4 (0, 0); 4110.9 (6, 7); 4121.3 (5, 6); 4140.5 (4, 5); 4199.1 (2, 3); 4236.5 (1, 2); 4278.1 (0, 1); 4459.3 (7, 9); 4466.6 (6, 8); 4490.3 (5, 7); 4515.9 (4, 6); 4554.1 (3, 5); 4599.7 (2, 4); 4651.8 (1, 3); 4709.2 (0, 2); 4864.4 (7, 10); 4881.7 (6, 9); 4913.2 (5, 8); 4957.9 (4, 7); 5012.7 (3, 6); 5076.6 (2, 5); 5148.8 (1, 4); 5228.3 (0, 3); 5485.5 (4, 8); 5564.1 (3, 7); 5653.1 (2, 6); 5754.4 (1, 5); 5864.7 (0, 4)
N <sub>2</sub>	Second positive	C <sup>3</sup> $\Pi_u$ -B <sup>3</sup> $\Pi_g$	2953.2 (4, 2); 2962.0 (3, 1); 2976.8 (2, 0); 3116.7 (3, 2); 3136.0 (2, 1); 3159.3 (1, 0); 3268.1 (4, 4); 3285.3 (3, 3); 3311.9 (2, 2); 3338.9 (1, 1); 3371.3 (0, 0); 3500.5 (2, 3); 3536.7 (1, 2); 3576.9 (0, 1); 3641.7 (4, 6); 3671.9 (3, 5); 3710.5 (2, 4); 3755.4 (1, 3); 3804.9 (0, 2); 3857.9 (4, 7); 3894.6 (3, 6); 3943.0 (2, 5); 3998.4 (1, 4); 4059.4 (0, 3); 4094.8 (4, 8); 4141.8 (3, 7); 4200.5 (2, 6); 4269.7 (1, 5); 4343.6 (0, 4); 4355.0 (4, 9); 4416.7 (3, 8); 4490.2 (2, 7); 4574.3 (1, 6); 4667.3 (0, 5); 4723.5 (3, 9); 4814.7 (2, 8); 4916.8 (1, 7); 5031.5 (0, 6); 5066.0 (3, 10); 5179.3 (2, 9); 5309.3 (1, 8)

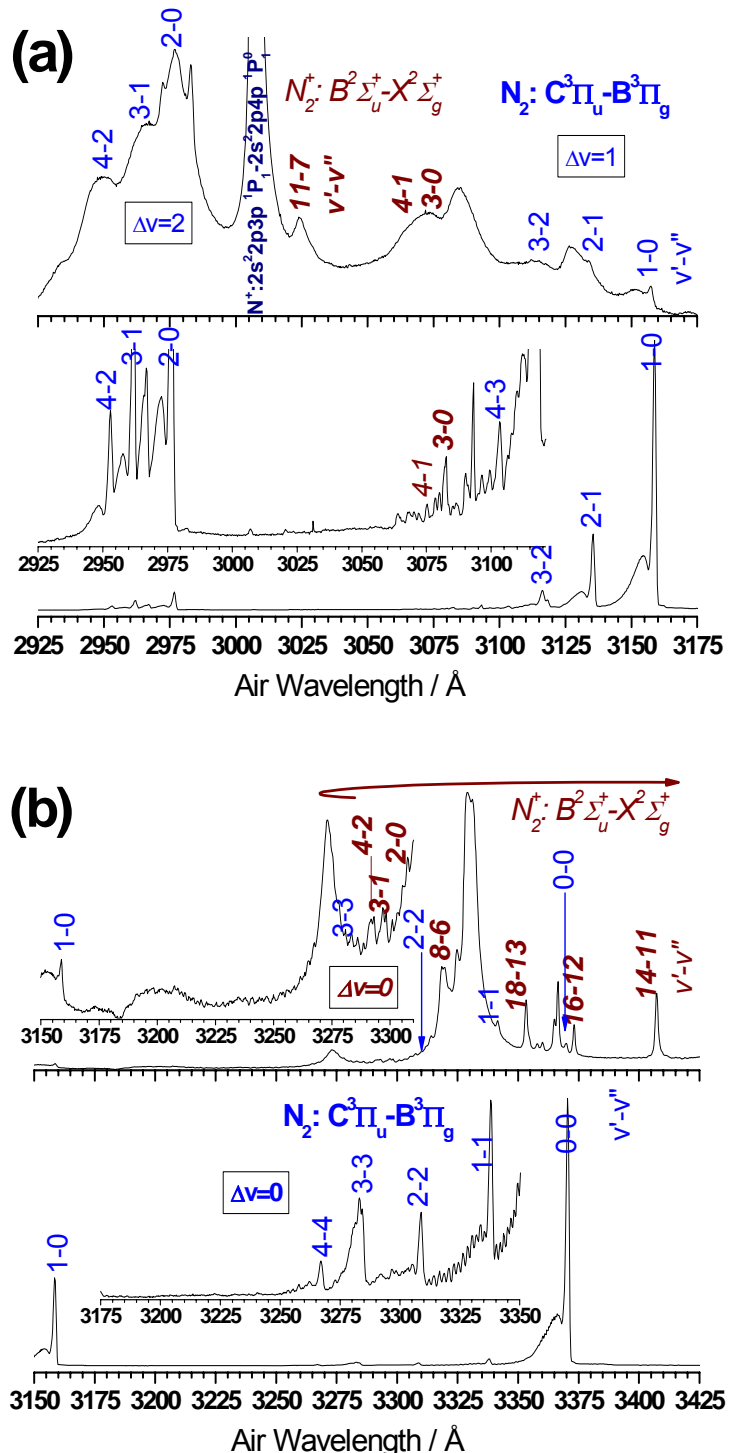


Figure 5. (Continued)

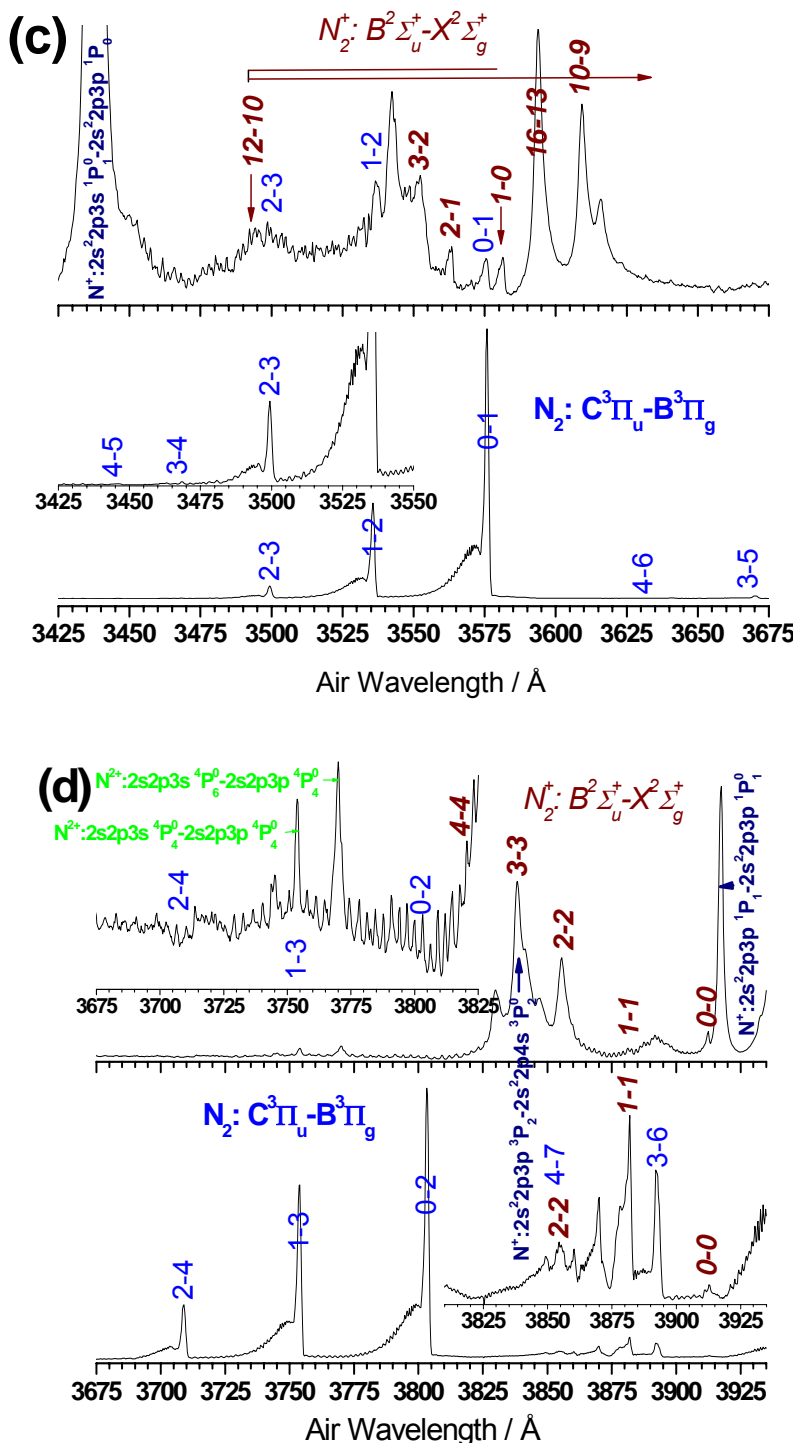


Figure 5. (Continued)

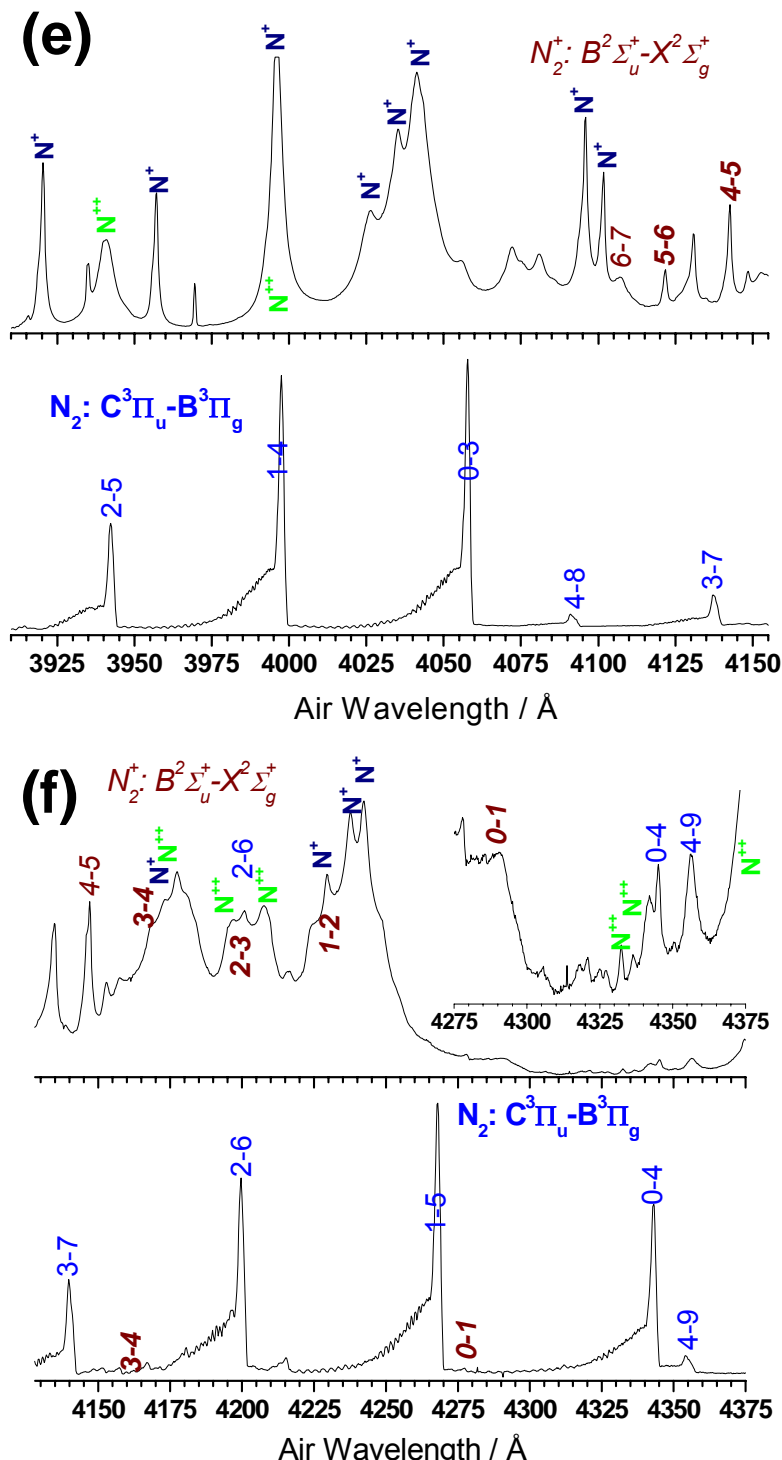


Figure 5 (a)-(f). Comparison between high-voltage dc electric discharge (lower panels) and LIDB (upper panels) emission spectra for nitrogen in several spectral regions.

In order to investigate the different electronic bands of N<sub>2</sub> and N<sub>2</sub><sup>+</sup> both LIDB and high-voltage dc electric glow discharge spectra were recorded with a resolution of ~0.12 Å by a ISA Jobin Yvon Spex 0.32 m spectrometer. The high-resolution of LIB spectrum allowed us to resolve partially the vibrational bands of the second positive C-B system of N<sub>2</sub> and the first negative B-X system of N<sub>2</sub><sup>+</sup>. Both spectra have been obtained with forty successive exposures on the CCD camera in the spectral region 2000-7500 Å. In the high-resolution spectra, no new processes were detected but allow us to identify unequivocally the band structure of the different transitions. As examples, Figure 5(a)-(f) shows a comparison between two spectra, the lower one obtained for the high-voltage dc electric discharge, and the upper one recorded in the LIB experiment. We indicate with italic the position of the band-head ( $v'-v''$ ) of first negative system of N<sub>2</sub><sup>+</sup>(B-X) while in regular typeface the bands of the second positive system of N<sub>2</sub>(C-B). The upper panel of Figure 5(a) shows the LIB emission spectrum of nitrogen in the spectral region 2925-3175 Å of nitrogen. Assignment of the emission band heads is shown in table 1 and indicated also on the spectra. The two sets of three blue degraded band heads (2925-2980 Å) and (3105-3165 Å) are readily assigned to the  $\Delta v=2$  and  $\Delta v=1$  sequences of the second positive system of N<sub>2</sub>(C-B), respectively. The series of bands between 3020-3095 Å belong to any of the bands 11-7, 4-1 and 3-0 of the first negative system of N<sub>2</sub><sup>+</sup>(B-X). The lower panel, corresponding to the dc electric glow discharge of nitrogen at low pressure, shows practically the same bands with different intensity distributions and spectral widths. In the spectrum of the lower panel of Figure 5(b) (nitrogen electric glow discharge) we easily identified five bands of the  $\Delta v=0$  sequence and the 1-0 band of the second positive system of N<sub>2</sub>(C-B). The main intensity is observed for the dominant transition N<sub>2</sub>(C,  $v'=0$ )→(B,  $v''=0$ ) which corresponds to the most intense nitrogen laser line at 3371 Å. However, this simple picture changes drastically in the LIB emission spectrum of nitrogen excited by the CO<sub>2</sub> laser, being now the 0-0 band very weak. A large number of additional strong bands mainly in the region 3260-3410 Å are detected in the LIDB spectrum and can be attributed to emissions from the first negative system of N<sub>2</sub><sup>+</sup> (especially for  $\Delta v=2$ ). The B-X system of N<sub>2</sub><sup>+</sup> has been observed over a wide range of vibrational levels. The highest values so far observed are  $v'=29$  for the excited B state and  $v''=23$  for the X state. The main bands of this system lie in the -2≤ $\Delta v$ ≤2 with  $v'<5$  sequences and all of these bands are blue degraded. However under certain circumstances many more bands, some red degraded, are observed, most being tail bands of these sequences. The observed bands with  $v'\leq 7$  and also those with  $8\leq v'\leq 11$  and  $\Delta v<-1$  are shaded to the violet. All the observed bands with  $v'\geq 12$  and those with  $v'=10$  and 11,  $\Delta v\geq 0$  are shaded to the red although some bands appear headless. These bands are so-called tail bands taking place a reversal in the successions of the bands in the sequence. Moreover, in the bands of the first negative system of N<sub>2</sub><sup>+</sup> have been observed numerous rotational line displacements and intensities anomalies arising from perturbations in the B state. The perturbing state is A<sup>2</sup>Π<sub>u</sub>. In the Deslandres table listing the observed band heads, there is a pronounced gap in on arm of the Condon locus, and a less marked one in the other [52]. Franck-Condon factors indicate that the missing bands should be as intense as many of the observed. The few bands observed in the region of the gap are 8-6 and 9-8, which are headless and the 10-9 and 10-8 which have no definite heads. The missing bands coincide with the strong bands of either first negative system of N<sub>2</sub><sup>+</sup>(B-X) or the second positive system of N<sub>2</sub>(C-B), and are difficult to detect. In the spectrum of the lower panel of Figure 5(c) corresponding to the nitrogen electric glow discharge we easily identified several bands of the  $\Delta v=-1$  sequence and two weak 4-6 and 3-5

bands of the second positive system of  $\text{N}_2(\text{C-B})$ . In this spectral region (3425-3675 Å) the most intense bands are due to the transitions  $\text{N}_2(\text{C}, v'=0) \rightarrow (\text{B}, v''=1)$  and  $\text{N}_2(\text{C}, v'=1) \rightarrow (\text{B}, v''=2)$ , also present in the LIB emission spectrum of nitrogen in the upper panel of Figure 5(c). As in the previous cases, the LIB emission spectrum excited by the  $\text{CO}_2$  laser changes drastically regarding the emission spectrum of nitrogen electric glow discharge. In it a large number of additional strong bands corresponding mainly to the  $\Delta v=+1$  sequence B-X band system of  $\text{N}_2^+$  are detected which are partially overlapped by the weak bands of the C-B system of  $\text{N}_2$ . For low  $v'$  the 1-0, 2-1, 3-2 ... bands of the B-X system of  $\text{N}_2^+$  are degraded to shorter wavelengths and for high  $v'$  values the bands are degraded to longer wavelengths (tail bands). In the nitrogen electric glow discharge spectrum [lower panel of Figure 6(d)] we identified 3-6, 4-7, 0-2, 1-3 and 2-4 bands of the second positive system of  $\text{N}_2(\text{C-B})$  and 0-0, 1-1 and 2-2 bands of the first negative system of  $\text{N}_2^+$ . In this spectral region (3675-3935 Å) the most intense band is the 0-2 band of  $\text{N}_2(\text{C-B})$ . The LIB emission spectrum in this region hardly shows bands of the second positive system of  $\text{N}_2(\text{C-B})$ . However, this emission spectrum exhibits a large number of bands corresponding mainly to the  $\Delta v=0$  sequence B-X band system of  $\text{N}_2^+$ . In the spectra of the lower panel of figs. 5(d)-(f) (nitrogen electric glow discharge) we identified several bands of the second positive system of  $\text{N}_2(\text{C-B})$ , indicated on the spectra, and some very weak bands of the first negative system of  $\text{N}_2^+$ . As in the previous cases, the spectra change drastically in the LIDB emission of nitrogen excited by the  $\text{CO}_2$  laser. A large number of  $\text{N}^+$  and  $\text{N}^{2+}$  atomic lines and additional strong bands of the first negative system of  $\text{N}_2^+$  are now present.

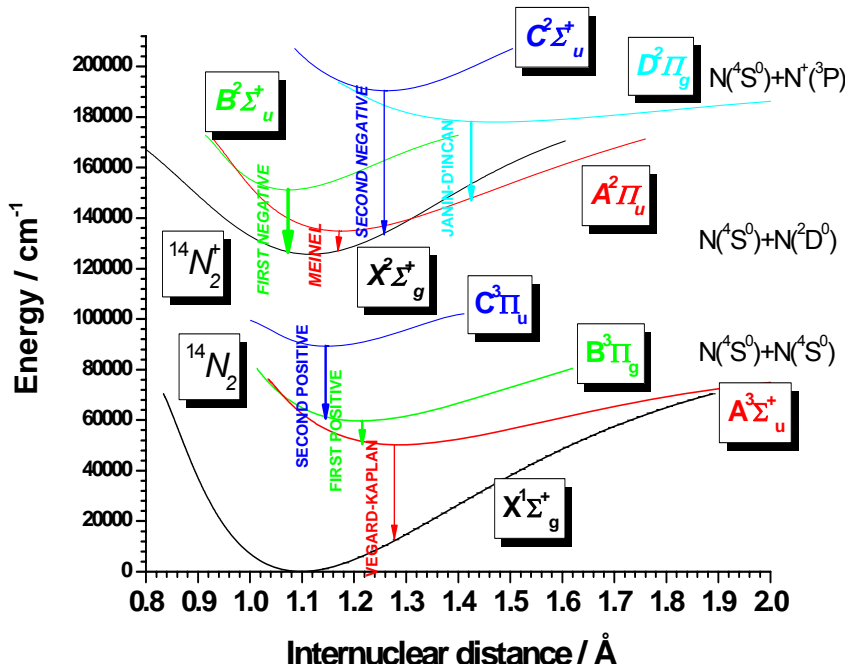


Figure 6. RKR potential energy curves for some bound electronic states of  $\text{N}_2$  and  $\text{N}_2^+$ .

To understand the different processes involved in the analyzed emission, Rydberg-Klein-Rees (RKR) potential energy curves for some bound electronic states of N<sub>2</sub> and N<sub>2</sub><sup>+</sup> have been calculated. The potential energy curves for the X<sup>1Σ<sub>g</sub><sup>+</sup>, A<sup>3Σ<sub>u</sub><sup>+</sup>, B<sup>3Π<sub>g</sub>, C<sup>3Π<sub>u</sub> states of N<sub>2</sub> and X<sup>2Σ<sub>g</sub><sup>+</sup>, A<sup>2Π<sub>u</sub>, B<sup>2Σ<sub>u</sub><sup>+</sup>, C<sup>2Σ<sub>u</sub><sup>+</sup> and D<sup>2Π<sub>g</sub> states of N<sub>2</sub><sup>+</sup> were obtained from the experimental information reported by Huber and Herzberg [58] and Laher and Gilmore [59]. Figure 6 shows the calculated RKR potentials and associated transitions for electronic states of N<sub>2</sub> and N<sub>2</sub><sup>+</sup> which can be relevant to interpret the results of the present work. Many perturbations are known in molecular states of nitrogen although a depth explanation of these features in terms of mixing of electronic states is not yet available. A useful graphical summary of many potential energy curves has been reported by Gilmore [60]. Perturbations are often accompanied by complex intensity irregularities as happens in the first negative system of N<sub>2</sub><sup>+</sup>. Whereas the vibrational and rotational constants run quite normal for the X<sup>2Σ<sub>g</sub><sup>+</sup> state of N<sub>2</sub><sup>+</sup>, this is not at all the case for the B<sup>2Σ<sub>u</sub><sup>+</sup> electronic state. Both the  $B_v$  and  $G(v)$  curves versus the vibrational quantum number  $v$  have unusual shapes. This can be interpreted as caused by a strong mutual vibrational perturbation between the B<sup>2Σ<sub>u</sub><sup>+</sup> and C<sup>2Σ<sub>u</sub><sup>+</sup> states of the same species of N<sub>2</sub><sup>+</sup> (see Figure 6). As this perturbation is homogeneous (i.e.,  $ΔΛ=0$ ) the shifts in both levels will be nearly independent of  $J$  producing that the B<sup>2Σ<sub>u</sub><sup>+</sup> potential curve to flatten out in the middle of its energy range. The minimum of the C<sup>2Σ<sub>u</sub><sup>+</sup> potential energy curve should be moved to smaller internuclear distances. There are also observed numerous rotational perturbations in the B-X system of N<sub>2</sub><sup>+</sup>, caused by an interaction between the A<sup>2Π<sub>u</sub> and the B<sup>2Σ<sub>u</sub><sup>+</sup> states.</sup></sup></sup></sup></sup></sup></sup></sup></sup></sup></sup></sup></sup></sup></sup></sup></sup>

The excitation temperature  $T_{exc}$  was calculated from the relative intensities of some N<sup>+</sup> ionic lines (3400–4800 Å spectral region) according to the Boltzmann equation (3.16). The estimated excitation temperature was  $T_{exc}=21000±1300$  K. However, if the excitation temperature is determined using only the relative intensities of N atomic lines (7300–8800 Å spectral region) a value of  $T_{exc}=7900±1300$  K is obtained. This behaviour is observed by other authors [61] and may be interpreted to result from the different emissivity distributions of neutral atoms and ion lines. The emissivity of the ion lines is produced, on the average, near the inner region with higher temperature. On the contrary, the emissivity of the neutral atom lines comes, on the average, from the low temperature region close to the plasma front, where the neutral atom density is higher. The intensity measurements correspond to the integration of the local emissivity values along the line-of-sight, integrated in turn in the perpendicular directions. As a consequence, the neutral atom Boltzmann plot provides a temperature value which is a certain average of the low-temperature values in the plasma (7900 K), whereas the temperature obtained from the ion Boltzmann plot (21000 K) averages the values existing in the high-temperature region. On the other hand, we have carried out simulations of the  $Δv=+1$  sequence of B-X band of N<sub>2</sub><sup>+</sup> for different vibrational temperatures finding that a value around 20000 K reasonably reproduces the experimental spectrum. Also, if we consider a temperature of 7900 K the ionization degree obtained by means of the Saha equation is of 0.00064. Such a low ionization degree does not justify the observed emission spectra of N<sup>+</sup> and N<sub>2</sub><sup>+</sup>. Keeping in mind these results, the temperature obtained from relative intensity of N<sup>+</sup> atomic lines (21000±1300 K) was chosen as the first approximation for the excitation temperature.

**Table 2. Laser parameters for the TEA CO<sub>2</sub> LIB experiments of oxygen.**

Laser $\lambda$ (μm)	Energy $E_W$ (mJ)	Power $P_W$ (MW)	Intensity $I_W$ (GW cm <sup>-2</sup> )	Fluence $\Phi_W$ (J cm <sup>-2</sup> )	Photon Flux, $F_{ph}$ (ph. cm <sup>-2</sup> s <sup>-1</sup> )	Electric Field $F_E$ (MV cm <sup>-1</sup> )
9.621	2685	42.1	5.36	342	$2.60 \times 10^{29}$	1.50
9.621	2256	35.4	4.50	287	$2.18 \times 10^{29}$	1.37
9.621	1732	27.1	3.46	220	$1.67 \times 10^{29}$	1.20
9.621	1209	19.0	2.41	154	$1.17 \times 10^{29}$	1.01
9.621	503	7.88	1.00	64.0	$4.86 \times 10^{28}$	0.65
10.591	3161	49.5	6.31	402	$3.36 \times 10^{29}$	1.63
10.591	2145	33.6	4.28	273	$2.28 \times 10^{29}$	1.34
10.591	1481	23.2	2.96	189	$1.58 \times 10^{29}$	1.11
10.591	968	15.2	1.93	123	$1.03 \times 10^{29}$	0.90
10.591	624	9.78	1.25	79.5	$6.64 \times 10^{28}$	0.72
10.591	436	6.83	0.87	55.5	$4.64 \times 10^{28}$	0.60

## 5.2. LIBS of Oxygen

In this section we present our recent results on LIBS in oxygen gas and pressures ranging from 4.6 to 75 kPa was studied using a high-power transverse excitation atmospheric CO<sub>2</sub> laser ( $\lambda=9.621$  and 10.591 μm;  $\tau_{FWHM}=64$  ns; power densities ranging from 0.87 to 6.31 GW·cm<sup>-2</sup>) [20]. For the present experiments the measured focused-spot area was  $7.85 \times 10^{-3}$  cm<sup>2</sup>. This value is higher than the calculated area ( $2.2 \times 10^{-4}$  cm<sup>2</sup>) obtained from the beam waist (Eq. 1.7). This fact is due to the non-Gaussian profile of the CO<sub>2</sub> laser beam. Moreover the CO<sub>2</sub> laser beam passes through a circular aperture of diameter 17.5 mm. For this diaphragm the calculated divergence angle for the laser beams at 9.621 and 10.591 μm are 1.3 and 1.5 mrad, respectively. Thus, considering the total beam divergence (~4.4 mrad), the calculated diameter of the focused TEA-CO<sub>2</sub> laser (beam waist) is 1.06 mm, which is very similar to the measured value (~1 mm). If the focal region of the laser beam is assumed to be cylindrical in shape, the spot size in terms of length  $l$  (Eq. 1.8) of the focused TEA-CO<sub>2</sub> laser is 6.0 mm, which is similar to the measured value (~7 mm). For the different pulse laser energies measured in LIB of oxygen, the calculated laser peak power (Eq. 1.1), intensity (Eq. 1.2), fluence (Eq. 1.3), photon flux (Eq. 1.4), electric field (Eq. 1.5) and pressure radiation (Eq. 1.6) are given in Table 2.

Figures 7(a-f) display an overview of the low-resolution LIB emission spectrum (2320-9690 Å) in oxygen at a pressure of 53.2 kPa, excited by the 10P(20) line of the CO<sub>2</sub> laser, and assignment of the atomic lines of O, O<sup>+</sup>, O<sup>2+</sup>, N and N<sup>+</sup> [45]. Strong atomic O lines dominate the spectrum but, ionic O<sup>+</sup> lines (about 8 times weaker) and weak O<sup>2+</sup> lines (about 150 times weaker) also are present. Some atomic and ionic nitrogen lines were also present, as well as, the first negative band system 330-400 nm corresponding to the transition  $B^2\Sigma_u^+ - X^2\Sigma_g^+$  in N<sub>2</sub><sup>+</sup>. In the acquisition of the spectrum of the Figure 7(d-f) a cut-off filter was used to suppress the second order intense UV oxygen atomic lines. This cut-off filter produces a decrease of the intensity with regard to the spectra of the Figure 7(a-c). In order to get more

insight into LIB of oxygen and to obtain an unambiguous assignment of the emission lines, we have scanned the corresponding wavelength regions with higher resolution ( $\sim 0.10 \text{ \AA}$  in first-order), which was sufficient to distinguish clearly between nearly all observed lines. The spectra have been obtained with fifty successive exposures on the ICCD camera in the spectral region 1900-7500  $\text{\AA}$ . As example, Figure 8(a-f) shows several spectra recorded in the LIB experiment. These LIB emission spectra were recorded under the following experimental conditions: oxygen pressure of 48.8 kPa, excitation line 10P(20) at 10.591  $\mu\text{m}$  and CO<sub>2</sub> laser power density 4.28 GW·cm<sup>-2</sup>. Figs. 8(a-f) display some details of the large features found in Figs. 7(a-f). No new features were observed in these high-resolution spectra. In these Figures, multiplet transitions between different  $J$  levels for O<sup>+</sup> and O<sup>2+</sup> are observed. In some cases these multiplet structures are not completely resolved due to Stark broadening of ionic lines. The spectral features clearly show the complexity of the relaxation process and bring out the possibility of cascading processes.

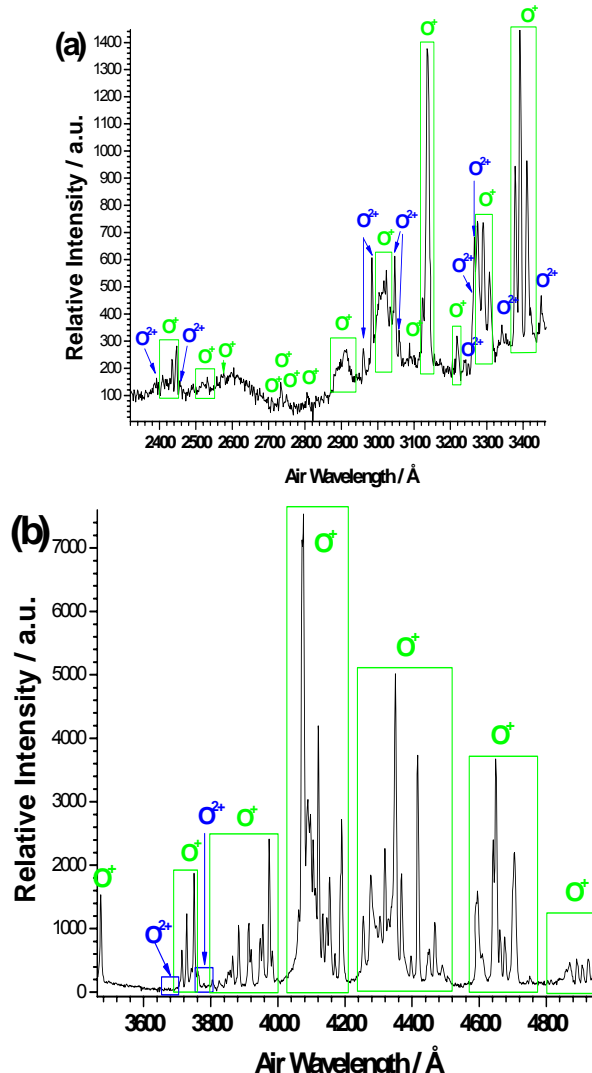


Figure 7. (Continued)

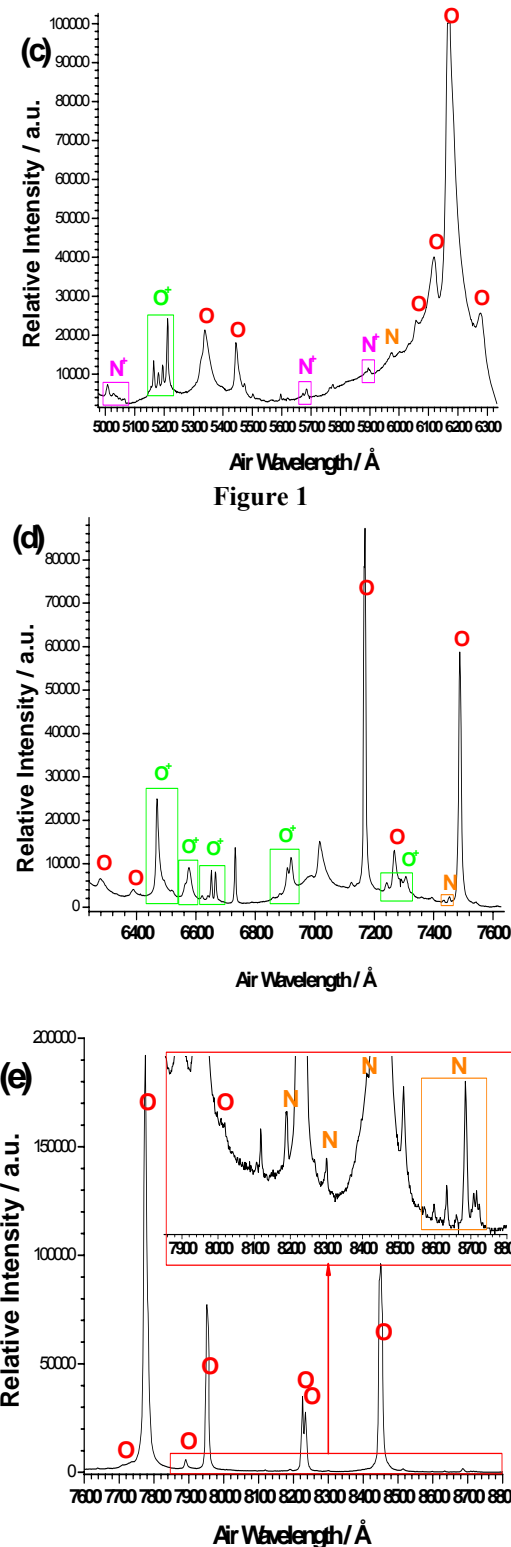


Figure 1

Figure 7. (Continued)

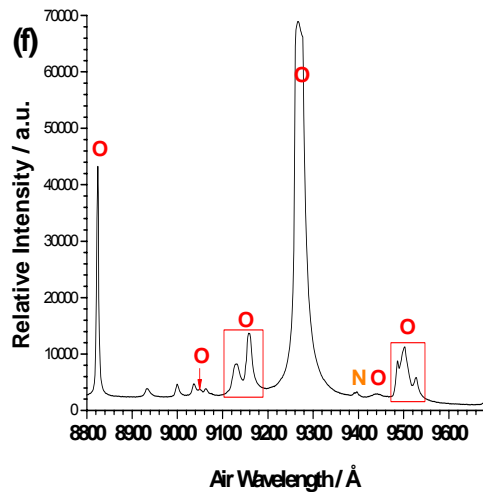


Figure 7(a-f). Low-resolution LIB emission spectrum observed in the 2320-9690 Å region in oxygen at a pressure of 53.2 kPa, excited by the 10P(20) line of the TEA-CO<sub>2</sub> laser at 10.591 μm and a power density of 0.87 GW×cm<sup>-2</sup>, and assignment of the atomic lines of O, O<sup>+</sup>, O<sup>2+</sup>, N and N<sup>+</sup>.

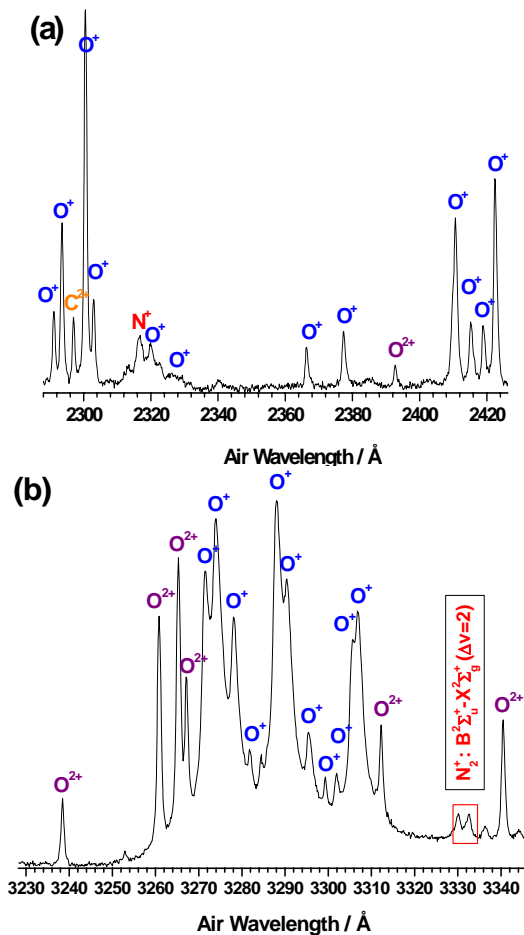


Figure 8. (Continued)

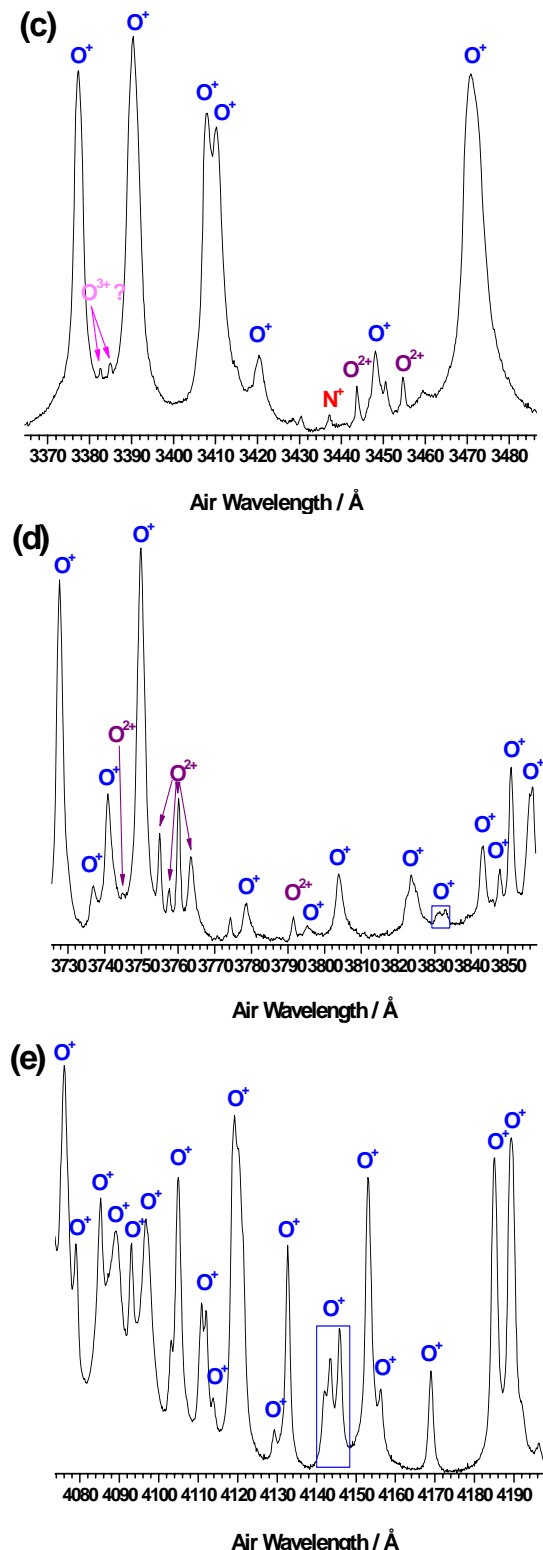


Figure 8. (Continued)

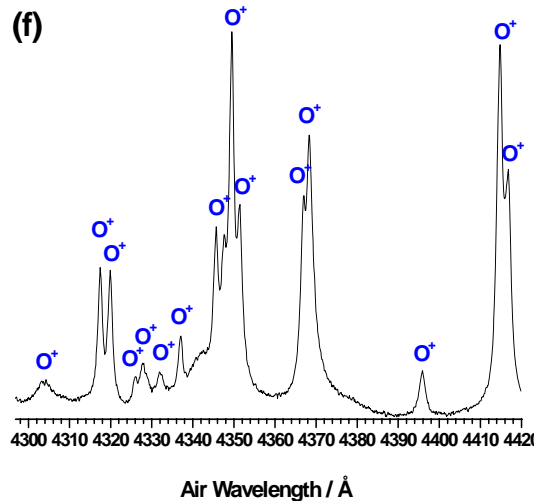
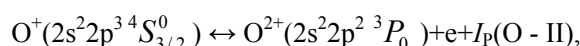
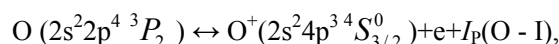


Figure 8 (a-f). High-resolution LIB emission spectrum observed in several spectral regions in oxygen at a pressure of 48.8 kPa, excited by the CO<sub>2</sub> laser at 10P(20) line (10.591 μm) with a power density of 4.28 GW×cm<sup>-2</sup>, and assignment of some atomic lines of O<sup>+</sup>, O<sup>2+</sup>, and N<sup>+</sup>.

The excitation temperature was calculated from the relative intensities of several O<sup>+</sup> (3270–3310 Å spectral region) and O<sup>2+</sup> (2900–3350 Å spectral region) atomic lines and the slope of the Boltzmann plot (Eq. 3.16). The values of the  $\lambda_{ki}$ ,  $g_k$ ,  $A_{ki}$  and  $E_k$  for O<sup>+</sup> and O<sup>2+</sup> selected atomic lines were obtained from the NIST Atomic Spectral Database [45]. The excitation temperatures were determined under the following experimental conditions: oxygen pressure of 48.8 kPa, excitation line 10P(20) at 10.591 μm and CO<sub>2</sub> laser power density 4.28 GW×cm<sup>-2</sup>. The obtained excitation temperatures, in the case of O<sup>+</sup> and O<sup>2+</sup>, were  $23000 \pm 3000$  K and  $31500 \pm 1600$  K, respectively (Figure 9). This behavior can be due to the different quenching rate coefficients between each species. Also this fact may be interpreted to result from the different emissivity distributions of single ionized and double ionized oxygen lines.

When LIB is produced in oxygen under high intensity laser radiation, some molecules can obtain an energy that exceeds the binding energy. Also some of their electrons become so energetic that the atoms and molecules ionize. Taking into account our experimental spectral observations, at these high temperatures oxygen becomes a mixture mainly of primary O<sub>2</sub>, O, O<sup>+</sup>, O<sup>2+</sup> and electrons. The transition between a gas and plasma is essentially a chemical equilibrium which shifts from the gas to plasma side with increasing temperature. Let us consider the first two different ionization equilibria of oxygen:



where the first two ionization potentials for oxygen are  $I_p(\text{O - I}) = 13.618$  eV, and  $I_p(\text{O - II}) = 35.121$  eV [62]. Taking into account the consideration of section 3.6, we can obtain the ionization degree. Figure 10 shows the ionization degree  $N_i/(N_0 + N_i)$  of O and O<sup>+</sup>,

plotted as a function of the gas temperature  $T$  at a constant total pressure  $P=(N_0+n_e+N_i)k_B T$  of 53.2 kPa. The graph shows that oxygen is already fully ionized at thermal energies well below the first ionization-energy of 13.618 eV (equivalent to 158000 K). If we consider a temperature of 23000 K, the ionization degrees of O and O<sup>+</sup> obtained by means of the Saha equation are 0.994 and 0.022, respectively. For  $T=31500$  K, the ionization degrees of O and O<sup>+</sup> obtained by means of the Saha equation are 0.999 and 0.34, respectively. These so high values of the ionization degrees justify the observed emission spectra.

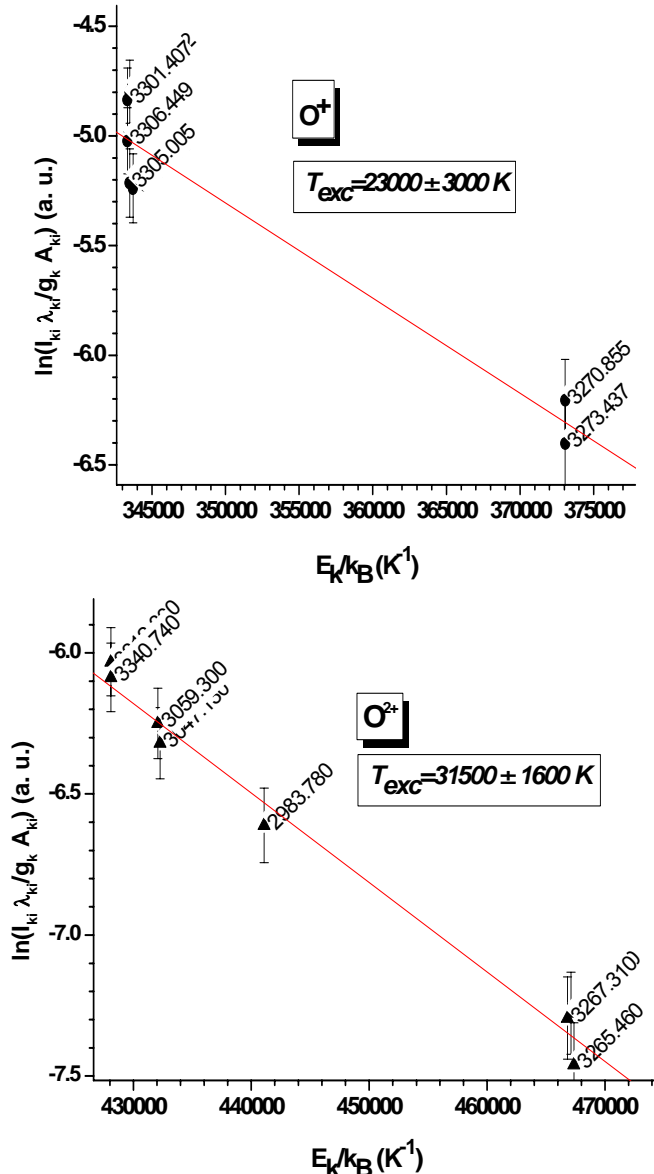


Figure 9. Linear Boltzmann plots for several O<sup>+</sup> and O<sup>2+</sup> transition lines used to calculate plasma temperature,  $T_{\text{exc}}$ . Plots also show linear fit to the data.

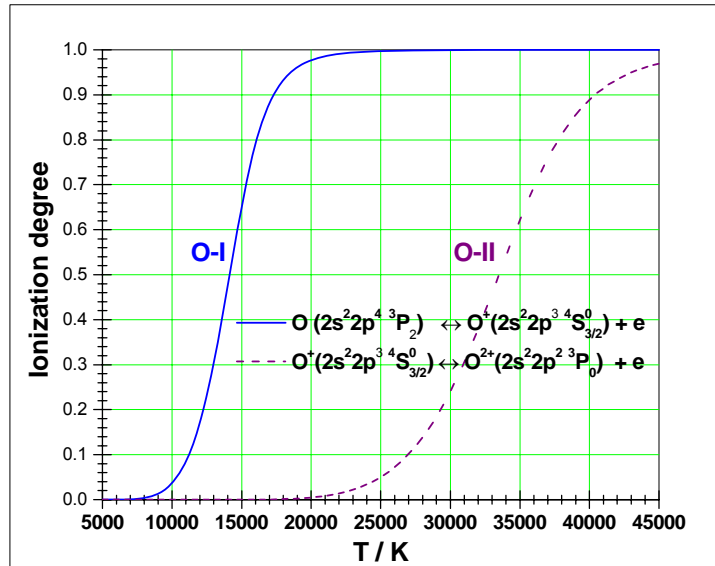


Figure 10. Temperature dependence of the ionization degree  $N_i/(N_0 + N_i)$  of atomic oxygen O and oxygen singly ionized O<sup>+</sup> at a constant pressure of 53.2 kPa.

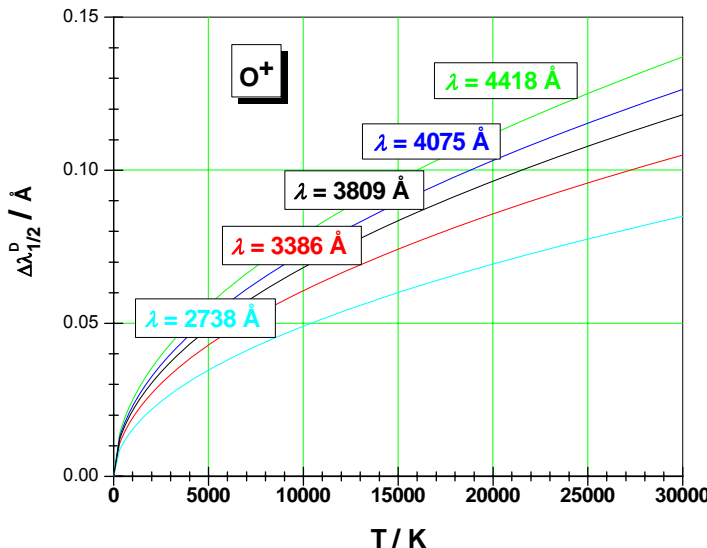


Figure 11. Doppler line widths for some lines of O<sup>+</sup>.

The electron number density was obtained by considering the discussion reported in section 3.4. The Doppler line widths for some lines of O<sup>+</sup> for different temperatures are shown in Figure 11. In our experiments, for O<sup>+</sup> lines, the Doppler line widths are 0.07–0.12 Å at 23000 K. The choice of plasma emission for  $n_e$  measurements is made to ensure that the O<sup>+</sup> spectral lines are sensitive enough to Stark effect and do not suffer from interference by other species. The estimation of electron density  $n_e$  has been carried out by measuring the broadening of the spectral profiles of isolated lines of O<sup>+</sup> (2738, 3386, 3809, 4075, and 4418 Å) from the high-resolution spectra. The electron impact parameters for the different O<sup>+</sup> lines

were approximated to a first-order exponential decay. The electron number densities of the laser-induced plasma were determined from the high-resolution emission spectra in oxygen at a pressure of 48.8 kPa, excited by the CO<sub>2</sub> laser at 10.591 μm with a power density of 4.28 GW×cm<sup>-2</sup>. A Lorentz function was used to fit the spectra. In order to extract the Stark broadening from the total experimentally measured line broadening, we have to previously deconvolute the different effects that contribute to the broadening of the spectral line: The instrumental, Doppler and Stark broadenings. Electron densities in the range (3.5-16.5)×10<sup>16</sup> cm<sup>-3</sup>, with an estimated uncertainty of 10%, were determined from the Stark broadening [Eq. (3.12)] data of several singly ionized oxygen lines.

At the evaluated temperature of 23000 ± 3000 K, Eq. (3.4) yields  $n_e \approx (0.54-2.3) \times 10^{16} \text{ cm}^{-3}$ . These electron densities are lower to deduced values from the Stark broadening (3.5-16.5)×10<sup>16</sup> cm<sup>-3</sup>, approximately one order of magnitude. Based on these calculations, the validity of the LTE assumption is supported.

The interactions between the incoming laser radiation and the gas sample depend upon numerous variables related to the laser and the gas. These variables include laser wavelength, energy, spatial and temporal profile of the laser beam, and the thermal properties of the sample. The incident beam is partially reflected and partially absorbed by the bulk to a degree that depends on the nature of the gas and the temperature it reaches under laser irradiation. LIBS spectra of oxygen obtained by laser irradiation at the different wavelengths are compared in Figure 12. These high-resolution LIB emission spectra in oxygen were obtained to a pressure of 48.8 kPa, excited by two TEA-CO<sub>2</sub> laser wavelengths at 10.591 μm ( $I_w=6.31 \text{ GW}\times\text{cm}^{-2}$ ) and 9.621 μm ( $I_w=5.36 \text{ GW}\times\text{cm}^{-2}$ ). The spectral range was chosen in order to detect both single and double ionized oxygen species. Also this spectral region has been selected to show differences in signal intensity and background emission in detail. The first remark that we should make is that the background continuum emission after the same optimization was performed on the data acquisition window is much stronger for spectrum produced by the 10.591 μm laser line. This is due to the higher laser power density ( $I_w=6.31 \text{ GW}\times\text{cm}^{-2}$ ) and the higher absorption in the plasma caused by the IB, whose cross-section is proportional to  $\lambda^3[1-\exp(-hc/\lambda k_B T)]^{-1}$  or approximately  $\lambda^2$  ( $T$  is the electron temperature during the electron avalanche or cascade growth of ionization and  $\lambda$  is the laser excitation wavelength). The spectral lines of O<sup>+</sup> and O<sup>2+</sup>(2983.78, 3017.63, 3023.45, 3043.02, 3047.13, 3059.30 Å) were clearly observed. It is clear that the ionic spectral lines for both O<sup>+</sup> and O<sup>2+</sup> were enhanced by a factor of 4 when the LIBS is induced by the TEA-CO<sub>2</sub> laser at 10.591 μm. Besides, the irradiation at this wavelength favors the formation of the doubly ionized species (~ 30%), as it is obtained from the ratio of the intensities of the O<sup>2+</sup> and O<sup>+</sup> lines. Moreover, plasma electron densities were determined from Stark broadening of the O<sup>2+</sup> double ionized line at 2983.78 Å. The measured electron densities for the LIB emission spectra in oxygen were (3.5±0.2)×10<sup>16</sup> cm<sup>-3</sup> and (3.2±0.2)×10<sup>16</sup> cm<sup>-3</sup> for excitation at 10.591 μm and 9.621 μm, respectively. Values of the electron impact half-width  $W$  for O<sup>2+</sup> were taken from the reported values given by Sreckovic *et al* [63]. It is noted that the emission intensity for O<sup>+</sup> and O<sup>2+</sup> shows different picture than the electron density possibly due to the effect of the laser wavelength.

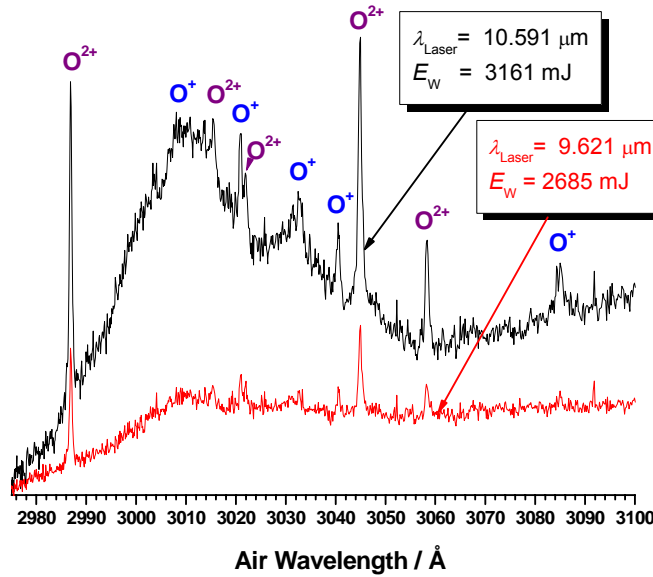


Figure 12. High-resolution LIB emission spectra in oxygen at a pressure of 48.8 kPa, excited by two TEA-CO<sub>2</sub> laser wavelengths at 10.591  $\mu\text{m}$  ( $E_w=3161 \text{ mJ}$ ) and 9.621  $\mu\text{m}$  ( $E_w=2685 \text{ mJ}$ ).

To see the effect laser irradiance the measurements were also carried out at different laser fluences. Optical emission spectra of the oxygen plasma plume at a pressure of 48.8 kPa as a function of the laser intensity are shown in Figs. 13(a) and 13(b). These spectra were recorded after the incidence of only one pulse of the TEA-CO<sub>2</sub> laser. The data were measured at a delay of 20 ms. An increase of atomic/ionic emission intensity and of the doubly ionized O<sup>2+</sup> formation respect to O<sup>+</sup> with increasing the laser irradiance was observed. Also the background increases with the laser power. At higher laser power densities (6.31-4.28 GW cm<sup>-2</sup>), the spectral lines are more broadened than at lower power densities as a result of the high pressure associated with the plasma. It is assumed that at higher laser fluence the LIB plasma is more energetic and more ionized.

The emission characteristics of the laser-induced plasma are influenced by the composition of the gas atmosphere. The pressure of the gas is one of the controlling parameters of the plasma characteristics, as well as the factors related to the laser energy absorption. Also the presence of air gas (vacuum conditions) during the LIB process has consequences on the expansion dynamics. An interesting observation was the effect of the oxygen pressure. Nanosecond TEA CO<sub>2</sub>-laser produced plasma emission has been characterized as a function of oxygen pressure. Experiments were performed in the pressure interval from 8 to 50 kPa and at pulse energy of 3161 mJ. Figure 14 shows LIB emission spectra at various oxygen pressures, excited by the 10.591  $\mu\text{m}$  line at a power density of 6.31 GW cm<sup>-2</sup>. As can be seen in Figure 14, the intensities of different spectral lines of O<sup>+</sup> and O<sup>2+</sup> increase with decreasing pressure, reach a maximum at about 12.5 kPa, and then decrease for lower pressures. Characteristic emission lines from O<sup>+</sup> and O<sup>2+</sup> elements exhibited significant enhancement in signal intensity at a few kPa oxygen pressure as compared to high pressures below atmospheric pressure. However, the ratio of the intensities among the O<sup>2+</sup> and O<sup>+</sup> lines remains the same at all pressures. The measurements indicate enhancement due to a longer lifetime of the plasma expanding to a larger size at lower oxygen pressures. Further reduction

in oxygen pressure down to  $\sim 12.5$  kPa resulted in a decrease in signal intensity, as a result of a reduction of collisional excitation of the emission lines which occurs when the plasma plume expands into the oxygen atmosphere.

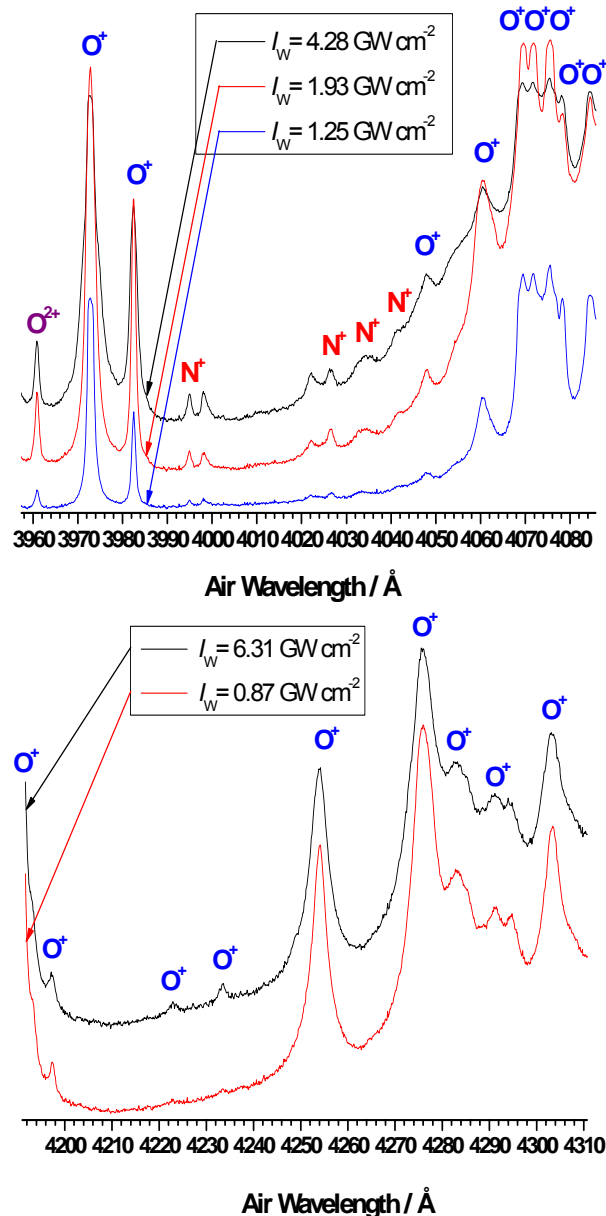


Figure 13 (a-b). High-resolution LIB in oxygen (at a pressure of 48.8 kPa) emission spectra observed in the (a) 3957-4085 Å and (b) 4195-4310 Å regions, excited by two TEA-CO<sub>2</sub> laser wavelengths at 10.591 μm as a function of the laser power density.

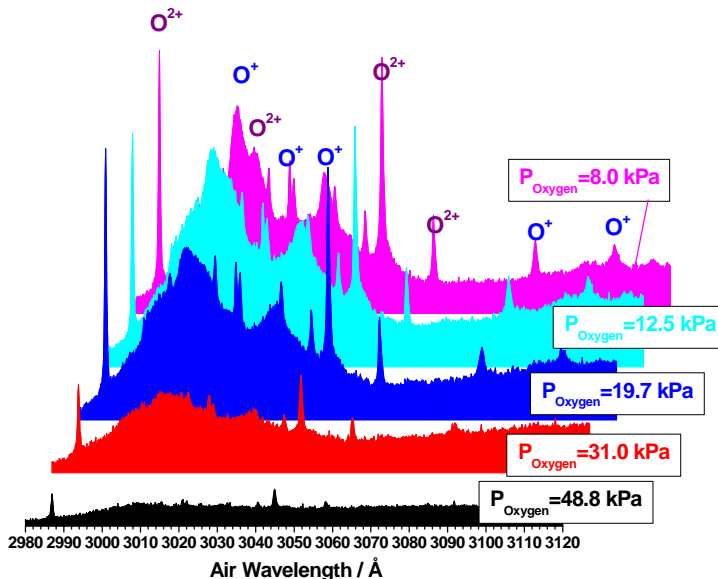


Figure 14. High-resolution LIB emission spectra at various oxygen pressures, excited by the TEA-CO<sub>2</sub> laser ( $10.591 \mu\text{m}$ ) at a power density of  $6.31 \text{ GW cm}^{-2}$ .

### 5.3. LIBS of Air

A spectroscopic study of ambient air plasma, initially at room temperature and pressures ranging from 32 to 101 kPa, produced by TEA-CO<sub>2</sub> laser ( $\lambda=9.621$  and  $10.591 \mu\text{m}$ ;  $\tau_{\text{FWHM}} \approx 64$  ns; power densities ranging from 0.29 to  $6.31 \text{ GW cm}^{-2}$ ) has been carried out in an attempt to clarify the processes involved in laser-induced breakdown (LIB) air plasma. To understand the detailed aspects of laser-beam interaction with air and recombination processes following the breakdown, OES studies of the emission spectra from the plasma offer the most convenient method. The strong emission observed in the plasma region is mainly due to electronic relaxation of excited N, O and ionic fragments N<sup>+</sup>. The medium-weak emission is due to excited species O<sup>+</sup>, N<sup>2+</sup>, O<sup>2+</sup>, C, C<sup>+</sup>, C<sup>2+</sup>, H, Ar and molecular band systems of N<sub>2</sub><sup>+</sup>(B<sup>2</sup>S<sub>u</sub><sup>+</sup>-X<sup>2</sup>S<sub>g</sub><sup>+</sup>), N<sub>2</sub>(C<sup>3</sup>P<sub>u</sub>-B<sup>3</sup>P<sub>g</sub>), N<sub>2</sub><sup>+</sup>(D<sup>2</sup>P<sub>g</sub>-A<sup>2</sup>P<sub>u</sub>) and OH(A<sup>2</sup>S<sup>+</sup>-X<sup>2</sup>Π). Figure 15(a-f) displays an overview of the low-resolution LIB emission spectrum in air at atmospheric pressure, excited by the 10P(20) line of the CO<sub>2</sub> laser with an intensity of  $2.2 \text{ GW cm}^{-2}$ , and assignment of the atomic lines of N, O, C, C<sup>+</sup>, H, Ar, N<sup>+</sup>, O<sup>+</sup>, N<sup>2+</sup>, O<sup>2+</sup>, C<sup>2+</sup> tabulated in NIST Atomic Spectral Database [45] and molecular bands of N<sub>2</sub><sup>+</sup>(B<sup>2</sup>S<sub>u</sub><sup>+</sup>-X<sup>2</sup>S<sub>g</sub><sup>+</sup>), N<sub>2</sub><sup>+</sup>(D<sup>2</sup>P<sub>g</sub>-A<sup>2</sup>P<sub>u</sub>), N<sub>2</sub>(C<sup>3</sup>P<sub>u</sub>-B<sup>3</sup>P<sub>g</sub>) and OH(A<sup>2</sup>S<sup>+</sup>-X<sup>2</sup>Π). Strong atomic N<sup>+</sup>, N and O lines dominate the spectrum but, atomic lines of C, C<sup>+</sup>, H, Ar, O<sup>+</sup>, N<sup>2+</sup>, O<sup>2+</sup>, C<sup>2+</sup> also are present. LIB spectrum of air was compared with the LIB spectra obtained in our laboratory for nitrogen [18] and oxygen [20]. The spectra have been obtained at higher resolution with fifty successive exposures on the ICCD camera in the spectral region 2000-7500 Å. As examples, Figure 16(a-l) shows several spectra recorded in the air LIB experiment. These LIB emission spectra were recorded under the following experimental conditions: air pressure of  $\sim 101$  kPa, excitation line 9P(28) at  $9.621 \mu\text{m}$  and laser irradiance of  $5.36 \text{ GW cm}^{-2}$ . Note that spectra of Figs. 15(a-f) and 16(a-l)

were excited by two different laser wavelengths. No new features were observed in these high-resolution spectra. In these Figures, multiplet transitions between different  $J$  levels for  $\text{N}^+$  and  $\text{O}^+$  are observed. In some cases these multiplet structures are not completely resolved due to Stark broadening of atomic/ionic lines. The spectral features clearly show the complexity of the relaxation process. In Figures 16(a-l), a rather complex structure is observed, in consequence of the overlapping between rovibrational lines of different molecular band systems and atomic/ionic lines. Figure 16(a) displays the overlapping between some bands of the  $\text{N}_2^+(\text{D}^2\Pi_g\text{-A}^2\Pi_u)$  system and some lines of  $\text{N}^+$ ,  $\text{O}^+$ ,  $\text{C}^{2+}$  and  $\text{O}^{2+}$ . In this spectrum the predominant emitting species is the triplet structure of  $\text{N}^+ 2s^2 2p(^2\text{P}^0)4d ^3\text{F}_{3,2,4} \rightarrow 2s^2 2p(^2\text{P}^0)4d ^3\text{D}_{2,1,3}$  around 2317 Å overlapped with the 0-0 band of the  $\text{N}_2^+(\text{D-A})$  system. In the spectrum of Figure 16(b), the most intense emitting species is the line of  $\text{C} 2s^2 2p(^2\text{P}^0)3s ^1\text{P}^0_1 \rightarrow 2s^2 2p^2 ^1\text{S}_0$  at 2478.56 Å, and several ionic lines of  $\text{O}^+ 2s^2 2p(^3\text{P})4p ^2\text{D}_{5/2} \rightarrow 2s^2 2p(^1\text{D})3s ^2\text{D}_{5/2}$  at 2425.56 Å,  $\text{O}^+ 2s^2 2p(^1\text{D})3p ^2\text{D}_{3/2} \rightarrow 2s^2 2p(^3\text{P})3s ^2\text{P}_{1/2}$  at 2433.53 Å, and the doublet  $\text{O}^+ 2s^2 2p(^1\text{D})3p ^2\text{D}_{3/2,5/2} \rightarrow 2s^2 2p(^3\text{P})3s ^2\text{P}_{3/2}$  at 2444.25 Å and 2445.54 Å, respectively. Several medium intensity ionic lines of  $\text{N}^+$  also overlapped with different bands of  $\text{N}_2^+(\text{D-A})$  and many weak lines of  $\text{O}^{2+}$  and  $\text{O}^+$  are also present. In the spectrum of Figure 16(c), the most intense emitting species is the line of  $\text{N}^+ 2s^2 2p(^2\text{P}^0)4s ^1\text{P}^0_1 \rightarrow 2s^2 2p(^2\text{P}^0)3p ^1\text{P}_1$  at 3006.83 Å. This Figure displays the overlapping between the  $\text{N}_2(\text{C-B})$   $v'=2-v''=0$  band,  $\text{OH}(\text{A-X}) \Delta v=0$  sequence and many weak lines of  $\text{O}^+$  and  $\text{O}^{2+}$ . In the spectrum of Figure 16(d),  $\text{N}_2^+(\text{B}^2\Sigma_u^+ \text{-X}^2\Sigma_g^+) \Delta v=2$  sequence and many weak lines of  $\text{O}^+$  and  $\text{O}^{2+}$  are recorded. This spectrum shows the reversal of the bands from  $v'=11$ , which is due to the overlap between high vibrational quantum number bands with low quantum number bands. So, the first vibrational bands of  $\text{N}_2^+(\text{B-X})$  (2-0, 3-1, 4-2 ... and 10-8) are shaded to the violet and after reversal (11-9, 12-10, 13-12 ...) are shaded to the red. In the spectrum of Figure 16(e), the most intense emitting species is the line of  $\text{N}^+ 2s^2 2p(^2\text{P}^0)3p ^1\text{S}_0 \rightarrow 2s^2 2p(^2\text{P}^0)3s ^1\text{P}^0_1$  at 3437.15 Å. Many medium intensity ionic lines of  $\text{O}^+$  and  $\text{O}^{2+}$ , weak molecular bands of  $\text{N}_2(\text{C-B})$  and  $\text{N}_2^+(\text{B-X})$  are also present. Surprisingly, the relative intensity of the 0-0 band head in the  $\text{N}_2(\text{C-B})$  system is very weak. In the spectrum of Figure 16(f), many medium intensity rovibrational molecular bands of  $\text{N}_2(\text{C-B}; \Delta v=-1$  sequence) and  $\text{N}_2^+(\text{B-X}; \text{mainly } \Delta v=1 \text{ sequence})$  are observed. In the spectrum of Figure 16(g), the most intense emitting species are the lines of  $\text{O}^+ 2s^2 2p(^3\text{P})3p ^4\text{S}^0_{3/2} \rightarrow 2s^2 2p(^3\text{P})3s ^4\text{P}_{3/2}$  at 3727.32 Å,  $\text{O}^+ 2s^2 2p(^3\text{P})3p ^4\text{S}^0_{3/2} \rightarrow 2s^2 2p(^3\text{P})3s ^4\text{P}_{5/2}$  at 3749.49 Å,  $\text{N}^+ 2s^2 2p(^2\text{P}^0)4s ^3\text{P}^0_2 \rightarrow 2s^2 2p(^2\text{P}^0)3p ^3\text{P}_2$  at 3838.37 Å and  $\text{N}_2^+(\text{B-X}) \Delta v=0$  sequence. Several weak intensity ionic lines of  $\text{O}^+$  and  $\text{O}^{2+}$  also overlapped with different bands of  $\text{N}_2^+(\text{B-X})$  are also present. As in the spectrum of Figure 16(d) a reversal of the bands for high vibrational levels is produced. So, the first vibrational bands of  $\text{N}_2^+(\text{B-X})$  (0-0, 1-1, 2-2, ...) are shaded to the violet and after reversal are shaded to the red. In the spectrum of Figure 16(h), several strong intensity ionic lines of  $\text{N}^+$ ,  $\text{O}^+$  and  $\text{N}^{2+}$  also overlapped with different bands of  $\text{N}_2^+(\text{B-X}) \Delta v=0$  sequence. The relative intensity of the 0-0 band head at 3914.9 Å in the  $\text{N}_2^+(\text{B-X})$  system is quite weak and partially overlapped with one  $\text{O}^+$  line. Nevertheless, the 0-0 band is the most intense of their band sequence. In this spectrum, many weak intensity rovibrational molecular bands of  $\text{N}_2^+(\text{B-X})$  can be appreciated. The strong emission observed in Figures 16(i-l) is mainly due to the relaxation of excited ionic fragments  $\text{N}^+$  and  $\text{O}^+$ . In Figure 16(j) various ionic lines overlap with molecular bands of  $\text{N}_2^+(\text{B-X})$  transitions and produce rather complex structure, but this high-resolution spectra allow for a precise attribution of almost all observed

transitions. The six lines of single ionized nitrogen between 4600-4650 Å correspond to the multiplet structure of  $N^+ 2s^2 2p(^2P^0)3p(^3P^0) \rightarrow 2s^2 2p(^2P^0)3s(^3P^0)$ . As it can see, the LIB of air includes mainly contributions of both nitrogen and oxygen. It should be noted that the nitrogen and oxygen line intensities maintain the proportions of the air composition.

On the other hand, excitation temperatures of  $23400 \pm 700$  K and  $26600 \pm 1400$  K were estimated by means of  $N^+$  and  $O^+$  ionic lines, respectively. Electron number densities of the order of  $(0.5\text{-}2.4) \times 10^{17}$  cm<sup>-3</sup> and  $(0.6\text{-}7.5) \times 10^{17}$  cm<sup>-3</sup> were deduced from the Stark broadening of several ionic  $N^+$  and  $O^+$  lines, respectively.

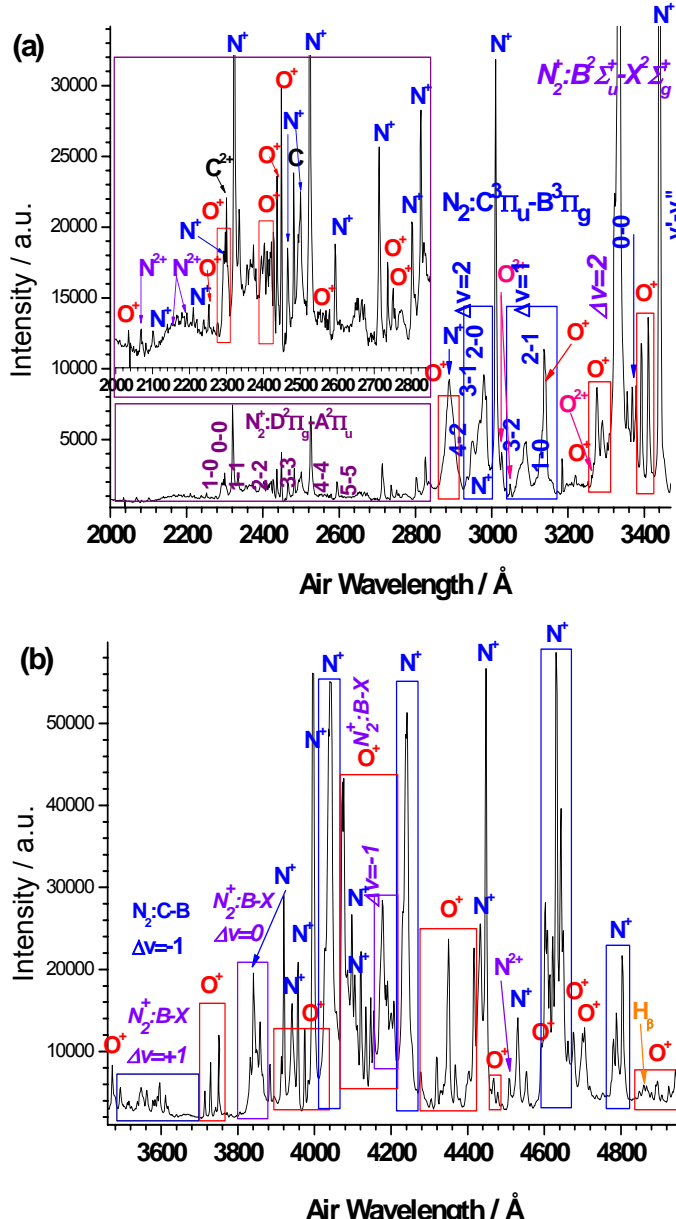


Figure 15. (Continued)

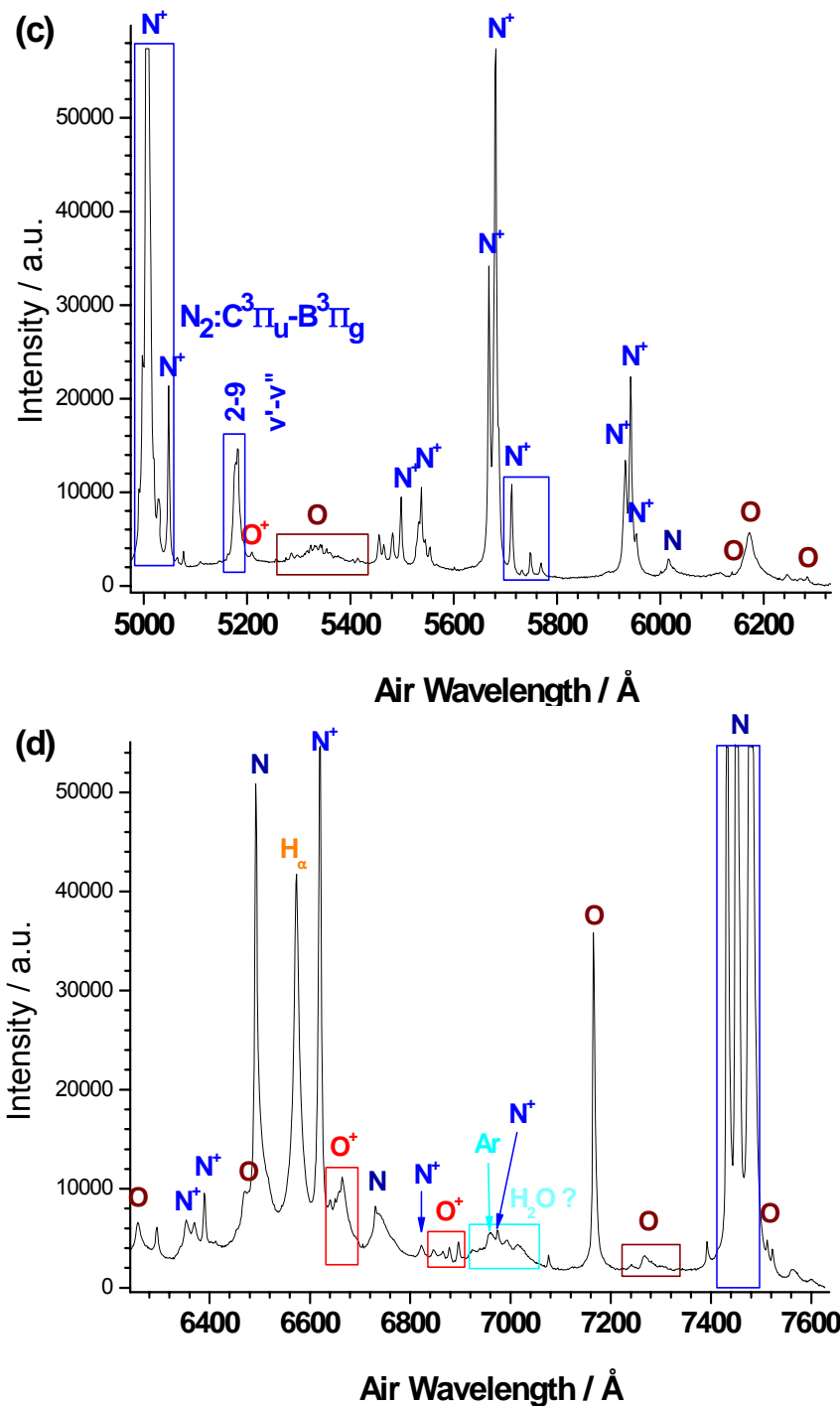


Figure 15. (Continued)

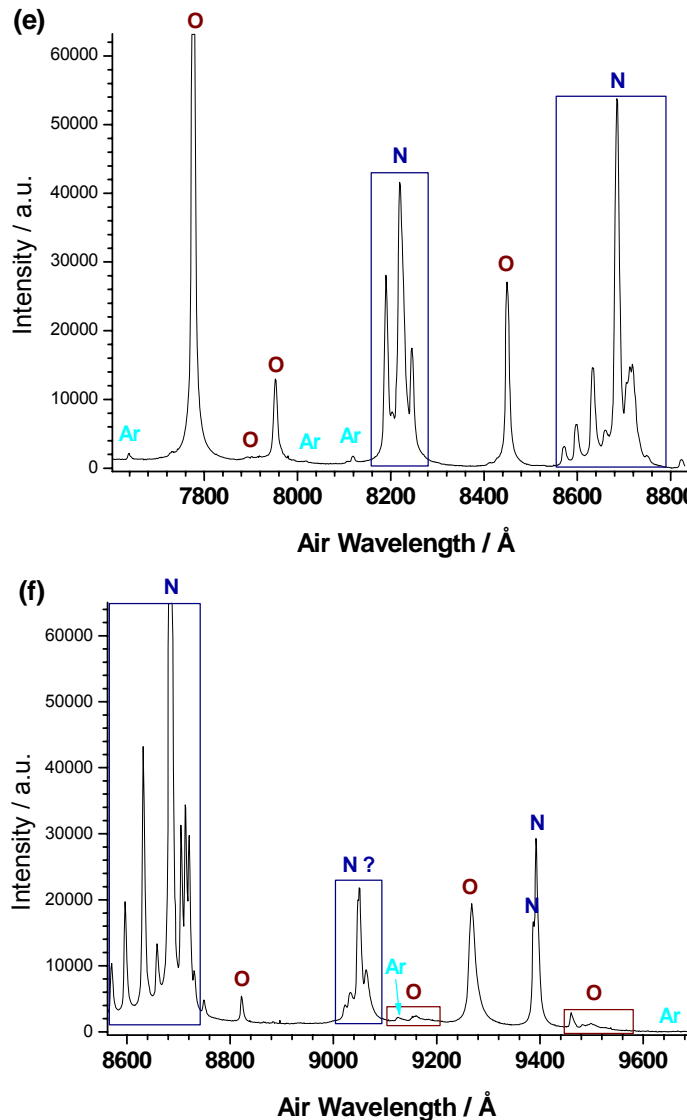


Figure 15 (a-f) Low-resolution LIB emission spectrum observed in the 2000-9690 Å region in ambient air at atmospheric pressure, excited by the TEA-CO<sub>2</sub> laser at 10.591 μm and a power density of 2.2 GW×cm<sup>-2</sup>, and assignment of the atomic lines of N, O, C, C<sup>+</sup>, H, Ar, N<sup>+</sup>, O<sup>+</sup>, N<sup>2+</sup>, O<sup>2+</sup>, C<sup>2+</sup> and molecular bands of N<sub>2</sub><sup>+</sup>(B<sup>2</sup>Σ<sub>u</sub><sup>+</sup>-X<sup>2</sup>Σ<sub>g</sub><sup>+</sup>) and N<sub>2</sub>(C<sup>3</sup>Π<sub>u</sub>-B<sup>3</sup>Π<sub>g</sub>)

LIBS spectra obtained by laser irradiation at the different wavelengths are compared in Figure 17. These high-resolution LIB emission spectra in air were obtained at atmospheric pressure, excited by two TEA-CO<sub>2</sub> laser wavelengths at 10.591 μm ( $I_W=6.31$  GW×cm<sup>-2</sup>) and 9.621 μm ( $I_W=5.36$  GW×cm<sup>-2</sup>). The spectral range was chosen in order to detect the emission lines of different atomic, single and double ionized species (C, C<sup>+</sup>, N<sup>+</sup>, O<sup>+</sup>, O<sup>2+</sup>). Both spectra have been obtained after the incidence of only one laser pulse. The relative intensities for different species practically do not change with the laser wavelength. The atomic C line at 2478.56 Å was enhanced when the LIBS is induced by the CO<sub>2</sub> laser at 10.591 μm. This fact is probably due to a self-absorption process in such resonance line. Figure 18 shows high-

resolution LIB emission spectra in air at atmospheric pressure, excited by the CO<sub>2</sub> laser line at 9.621 μm ( $I_w=5.36 \text{ GW/cm}^2$ ), recorded with cell and without cell. We see similar intensities for O<sup>+</sup> and different bands of N<sub>2</sub><sup>+</sup>(B-X) Δv=0 sequence in both spectra. However, the intensity of N<sup>+</sup> and N<sup>2+</sup> lines was increased when the LIB is with cell. Also, there is a line in the spectra at ~3860 Å, possible due to H<sub>2</sub>, which intensity increases without cell. This fact is probably caused by differences in relative humidity of air in both situations.

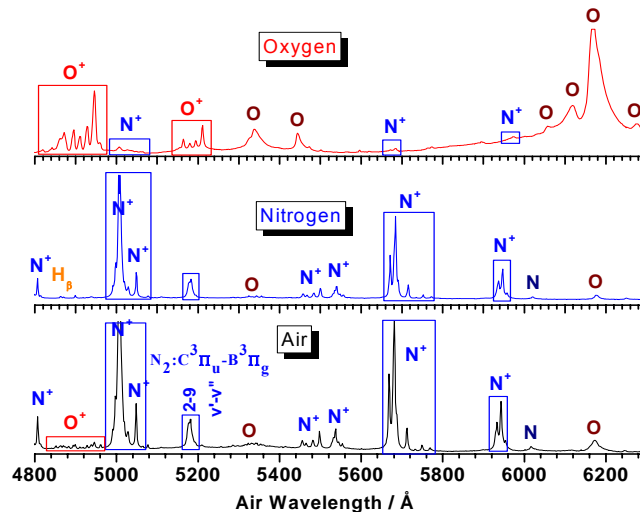


Figure 16. Low-resolution LIB emission spectra in air, nitrogen and oxygen, excited by the TEA-CO<sub>2</sub> laser at 10.591 μm and a power density of ~1 GW×cm<sup>-2</sup>, and assignment of the atomic lines of N, O, H, N<sup>+</sup>, O<sup>+</sup> and 2-9 molecular band of N<sub>2</sub>(C<sup>3</sup>Π<sub>u</sub>-B<sup>3</sup>Π<sub>g</sub>).

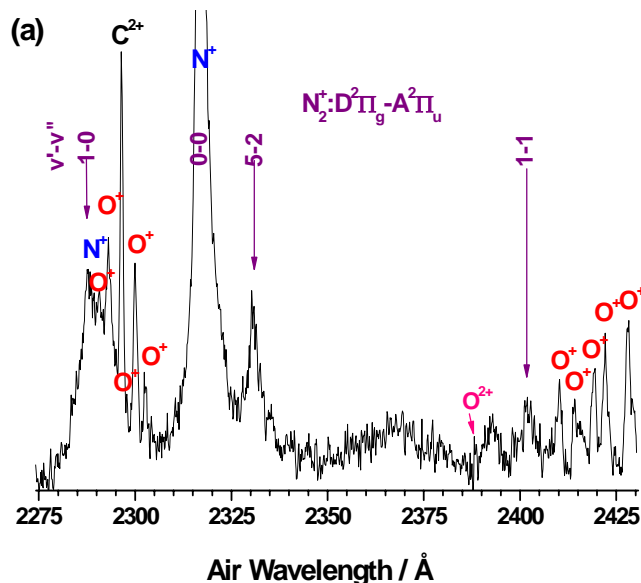


Figure 16. (Continued)

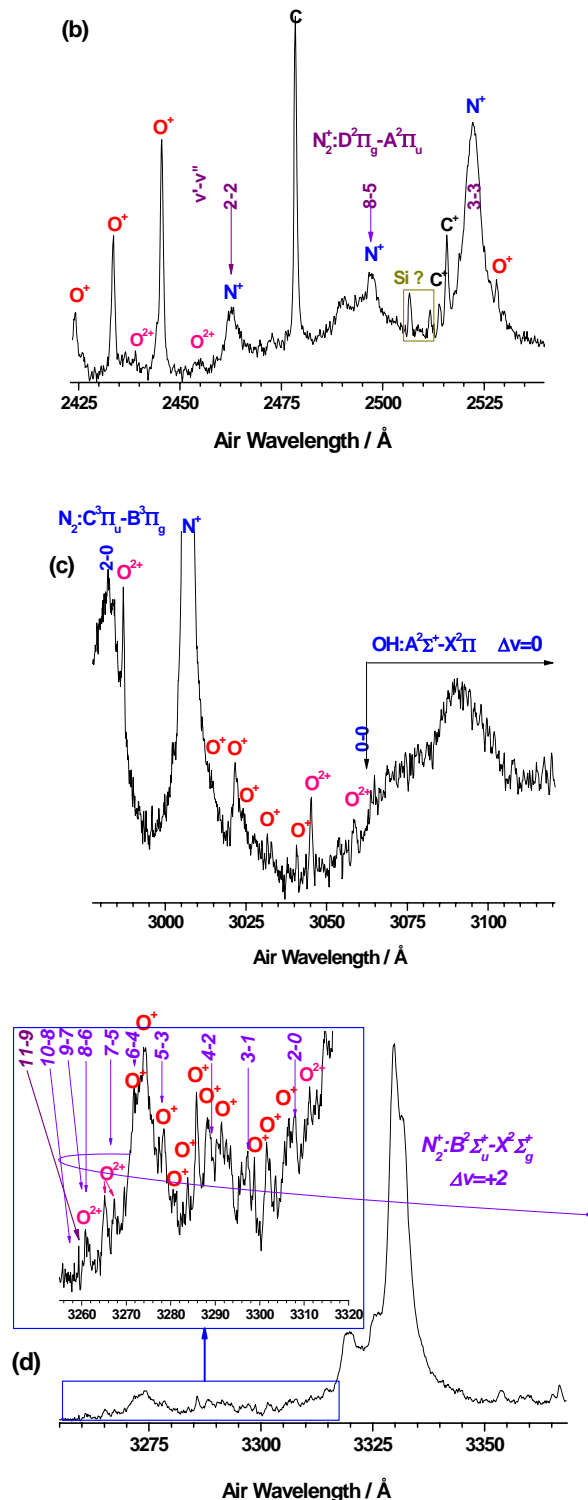


Figure 16. (Continued)

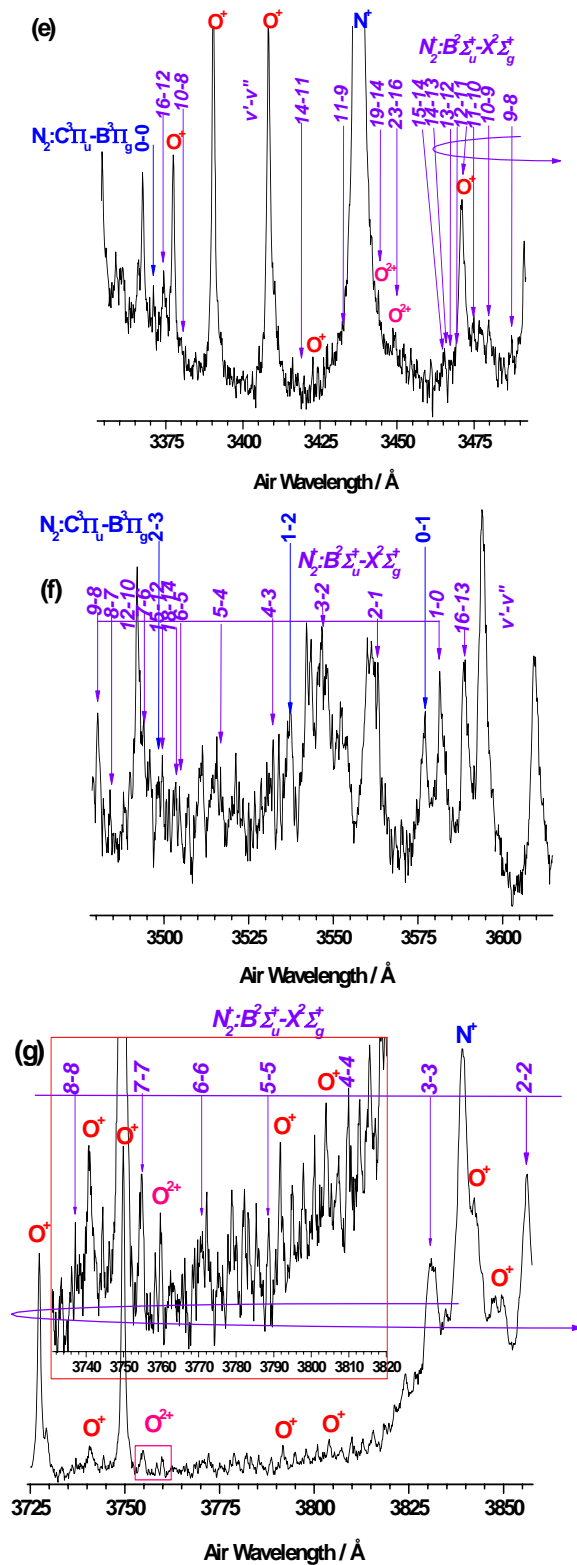


Figure 16. (Continued)

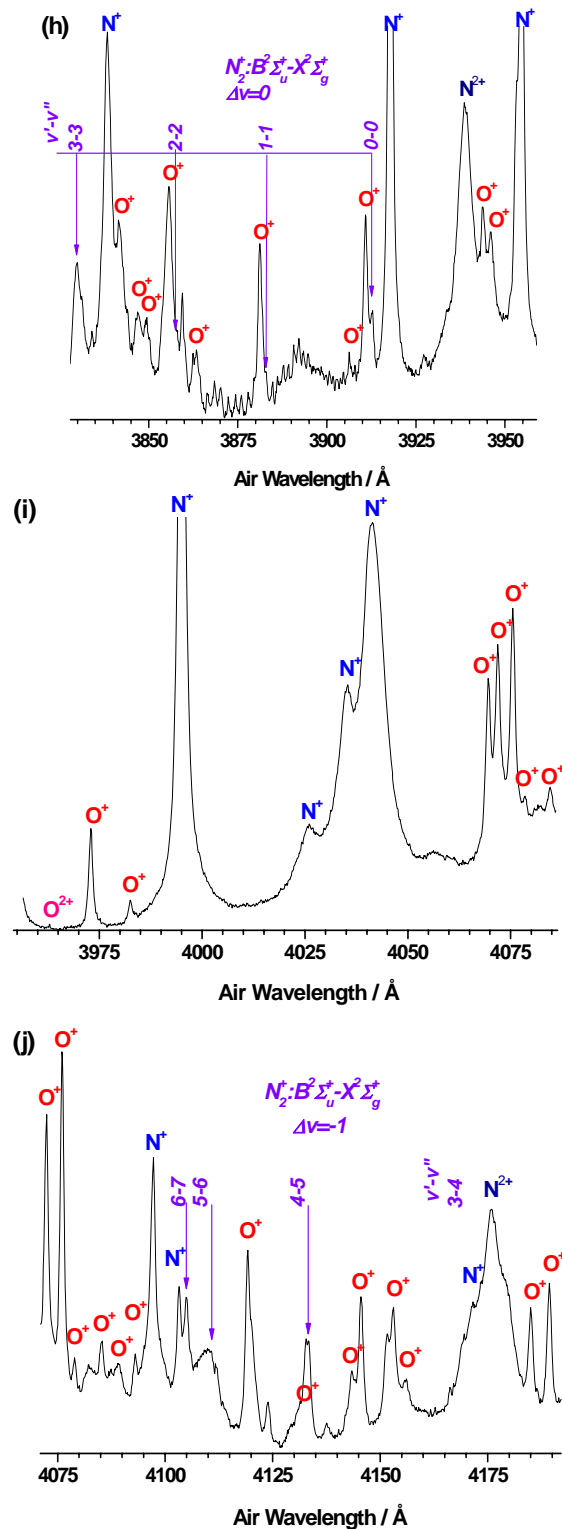


Figure 16. (Continued)

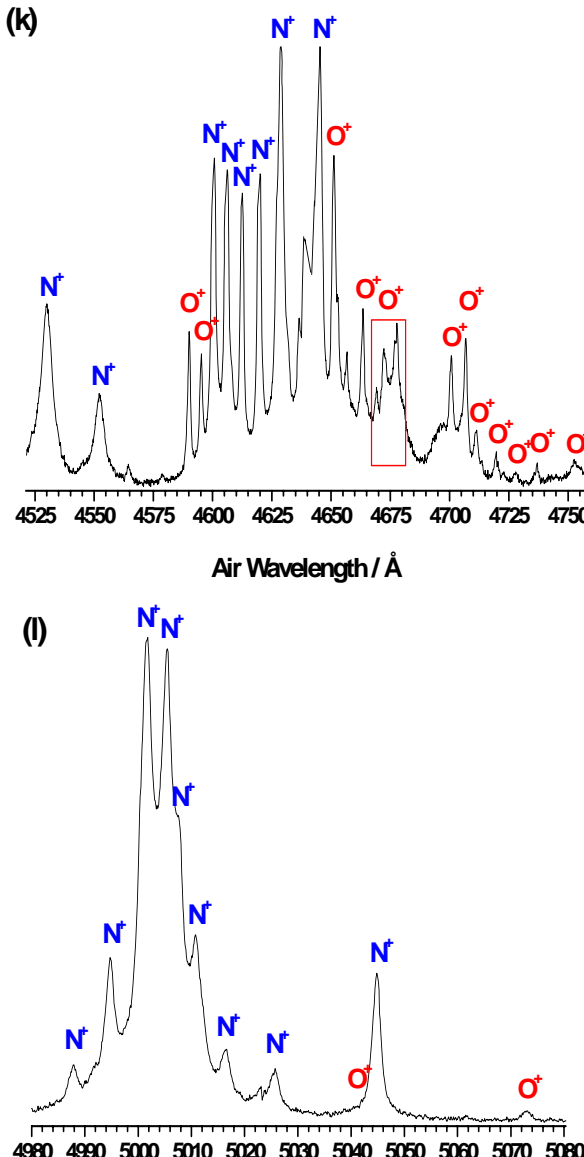


Figure 16 (a-l) High-resolution LIB emission spectrum observed in several spectral regions in ambient air at atmospheric pressure, excited by the CO<sub>2</sub> laser at 9.621 μm with a power density of 5.36 GW×cm<sup>-2</sup>, and assignment of some atomic lines of N<sup>+</sup>, O<sup>+</sup>, N<sup>2+</sup>, O<sup>2+</sup>, and band heads of the molecular bands of N<sub>2</sub><sup>+</sup>(B<sup>2</sup>Σ<sub>u</sub><sup>+</sup>-X<sup>2</sup>Σ<sub>g</sub><sup>+</sup>), N<sub>2</sub>(C<sup>3</sup>Π<sub>u</sub>-B<sup>3</sup>Π<sub>g</sub>), N<sub>2</sub><sup>+</sup>(D<sup>2</sup>Π<sub>g</sub>-A<sup>2</sup>Π<sub>u</sub>) and OH(A<sup>2</sup>Σ<sup>+</sup>-X<sup>2</sup>Π).

To see the effect that the laser irradiance has on the air breakdown measurements were also carried out at different laser intensities. Low-resolution LIB emission spectra of the air plasma at atmospheric pressure, excited by the TEA-CO<sub>2</sub> laser wavelength at 9.621 μm, as a function of the laser intensity is shown in Figure 19. These spectra were recorded after the incidence of only one pulse of the TEA-CO<sub>2</sub> laser. An increase of atomic/ionic emission intensity with increasing the laser irradiance was observed. Also the background increases with the laser power. At higher laser power densities (6.31-4.00 GW cm<sup>-2</sup>), the spectral lines are more broadened than at lower power densities as a result of the high pressure associated

with the plasma. It is assumed that at higher laser fluence the LIB plasma is more energetic and more ionized. In order to see the effect of the laser intensity on molecular band emission, high-resolution LIB emission spectra of the air plasma at atmospheric pressure, (excited by the TEA-CO<sub>2</sub> laser wavelength at 9.621 μm) as a function of the laser intensity is shown in Figure 20. The assignment of this spectrum can be found in Figure 4(f). An increase of molecular band intensity of N<sub>2</sub><sup>+</sup>(B<sup>2</sup>Σ<sub>u</sub><sup>+</sup>-X<sup>2</sup>Σ<sub>g</sub><sup>+</sup>) and N<sub>2</sub>(C<sup>3</sup>Π<sub>u</sub>-B<sup>3</sup>Π<sub>g</sub>) with increasing the laser intensity was observed.

Nanosecond TEA CO<sub>2</sub>-laser produced plasma emission has been characterized as a function of air pressure. Figure 21 shows LIB emission spectra in the pressure interval from 32 to 101 kPa, excited by the TEA-CO<sub>2</sub> laser (10.591 μm) at a power density of 6.31 GW cm<sup>-2</sup>. As can be seen in Figure 21, the intensities of different spectral lines of C, N<sup>+</sup>, O<sup>+</sup>, O<sup>2+</sup> and N<sub>2</sub><sup>+</sup>(D-A) molecular bands increase with increasing pressure, reach a maximum at about 79.6 kPa, and then decrease with higher pressures. The measurements indicate enhancement due to a longer lifetime of the plasma expanding to a larger size at lower air pressures ( $p < 79.6$  kPa). Further increase in air pressure above to ~ 79.6 kPa resulted in a decrease in signal intensity, as a result of a reduction of collisional excitation of the emission lines which occurs when the plasma plume expands into the air atmosphere.

The detection of the N<sub>2</sub><sup>+</sup>(B-X) bands is of particular interest since it provides an estimation of the effective vibrational and rotational temperatures. The emission intensities of the N<sub>2</sub><sup>+</sup> Δv=-1 and Δv=0 band sequences were analyzed in order to estimate the molecular vibrational temperature  $T_{\text{vib}}$  (see section 3.5). Two Boltzmann plots (Equation 3.17) of the band intensities against the vibrational energy at the laser irradiance 5.36 GW cm<sup>-2</sup> are given in Figure 22(a-b) along with the corresponding Franck-Condon factors. The estimated effective vibrational temperatures were  $T_{\text{vib}}=12100 \pm 700$  K and  $12000 \pm 900$  K, respectively. On the other hand, the emission intensities of the 0-0 (B<sup>2</sup>Σ<sub>u</sub><sup>+</sup>-X<sup>2</sup>Σ<sub>g</sub><sup>+</sup>) band of N<sub>2</sub><sup>+</sup> were analyzed in order to estimate the effective rotational temperature  $T_{\text{rot}}$ . In <sup>2</sup>Σ-<sup>2</sup>Σ transitions both electronic states belong to Hund's (b) coupling case ( $\Delta N=\pm 1$ ) [46-48]. Each line of the R and P branches are doublet since they separate in two sublevels with  $J=N\pm\frac{1}{2}$  each one subscripted with  $i=1, 2$  (1 for  $J=N+\frac{1}{2}$  and 2 for  $J=N-\frac{1}{2}$ ).

$$R_i(N) = \tilde{\nu}_0 + F'_i(N+1) - F''_i(N), \quad (5.1)$$

$$P_i(N) = \tilde{\nu}_0 + F'_i(N-1) - F''_i(N). \quad (5.2)$$

In Eqs. (5.1) and (5.2) the Q-branch forms satellite branches, whose intensities are much lower than the main ones, very close to the corresponding R and P branches lines (called R-form or P-form Q branches) with wavenumbers:

$$^RQ_{21}(N) = \tilde{\nu}_0 + F'_{i2}(N+1) - F''_1(N), \quad (5.3)$$

$$^PQ_{12}(N) = \tilde{\nu}_0 + F'_{i2}(N-1) - F''_2(N). \quad (5.4)$$

The subscripts 21 and 12 indicate the transition which takes place from a term of the  $F_2$  series to one of the  $F_1$  series or vice versa:

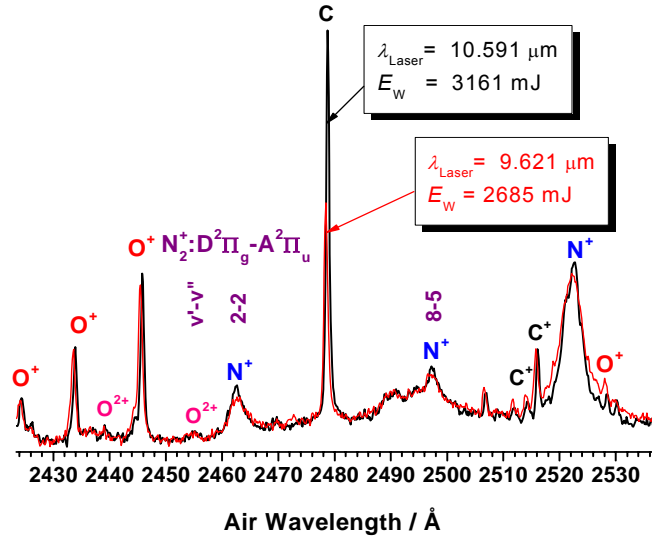


Figure 17. High-resolution LIB emission spectra in air at atmospheric pressure, excited by two TEA-CO<sub>2</sub> laser wavelengths at 10.591  $\mu\text{m}$  ( $I_w=6.31 \text{ GW/cm}^2$ ) and 9.621  $\mu\text{m}$  ( $I_w=5.36 \text{ GW/cm}^2$ ).

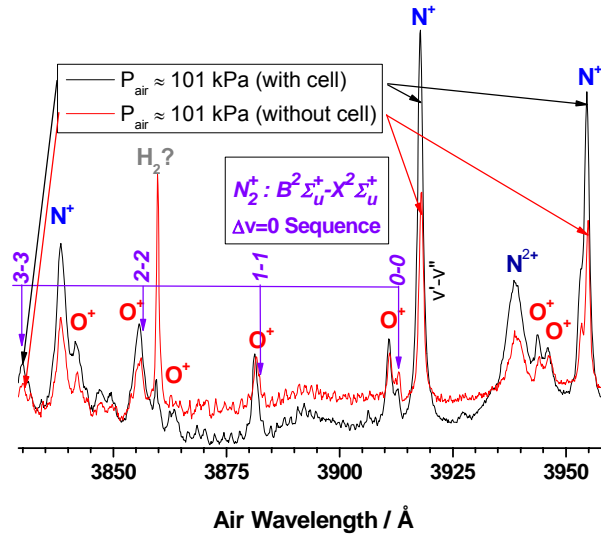


Figure 18. High-resolution LIB emission spectra in air at atmospheric pressure, excited by the TEA-CO<sub>2</sub> laser line at 9.621  $\mu\text{m}$  ( $I_w=5.36 \text{ GW/cm}^2$ ) recorded with cell and without cell.

$$F_1(N = J - \frac{1}{2}) = B_v N(N + 1) + \dots + \gamma \frac{N}{2}, \quad (5.5)$$

$$F_2(N = J + \frac{1}{2}) = B_v N(N + 1) + \dots - \gamma \frac{N + 1}{2}. \quad (5.6)$$

In Eqs. (5.1)-(5.6)  $N$  is the total angular momentum excluding spin of nuclear rotation,  $\tilde{\nu}_0$  is the wavenumber of the pure vibrational transition,  $B_v$  is rotational spectroscopic

constant and  $\gamma$  is the spin-rotation coupling constant. Moreover, in the case of a molecule with two identical nuclei such as N<sub>2</sub><sup>+</sup>, relative line intensities are affected by the nuclear spin ( $I=1$ ). The nuclear spin governs the intensities through the Pauli exclusion principle; all wavefunctions are antisymmetric with respect to the interchange of fermions (half-integer spin particle) and symmetric with respect to the interchange of bosons (integer spin particle). Then the ratio of the statistical weights of the symmetric and antisymmetric rotational levels is  $I+1/I$  for bosons or  $I/I+1$  for fermions. In the case of N<sub>2</sub><sup>+</sup> the B<sup>2</sup>Σ<sub>u</sub><sup>+</sup> electronic state has only odd  $J$  values and then the ratio of the statistical weights of the symmetric and antisymmetric rotational levels is 2/1.

The assignment of rotational spectrum of 0-0 B<sup>2</sup>Σ<sub>u</sub><sup>+</sup>-X<sup>2</sup>Σ<sub>g</sub><sup>+</sup> band of N<sub>2</sub><sup>+</sup>, recorded in experimental conditions indicated above, is shown in Figure 23(a). In Figure 23(b) we display the calculated fortrat diagram for  $P_1$ ,  $P_2$ ,  $R_1$ ,  $R_2$ , <sup>R</sup>Q<sub>12</sub> and <sup>P</sup>Q<sub>21</sub> branches corresponding to this band. The alternation of the intensities of the rotational lines is observed.

To estimate the effective rotational temperature, we consider the  $J$  value for the maximum of the 0-0 band (B-X) of N<sub>2</sub><sup>+</sup> ( $J_{\max}$ ) (Section 3.5)

$$T_{\text{rot}} = \frac{2B_0hc}{k_B} \left( J_{\max} + \frac{1}{2} \right)^2, \quad (5.7)$$

being  $B_0$  the rotational constant for  $v'=0$  and  $J_{\max}$  the total angular momentum at the maximum. This effective rotational temperature is found to be  $T_{\text{rot}}=1900 \pm 100$  K. As in any gas, temperature in LIB plasma is determined by the average energies of the plasma species (e<sup>-</sup>, N<sub>2</sub>, O<sub>2</sub>, Ar, H, N, O, C, OH, N<sub>2</sub><sup>+</sup>, N<sup>+</sup>, O<sup>+</sup>, N<sup>2+</sup>, O<sup>2+</sup>, C<sup>+</sup>, C<sup>2+</sup> etc) and their relevant degrees of freedom (translational, rotational, vibrational, and those related to electronic excitation). Thus, LIB plasmas, as multi-component systems, are able to exhibit multiple temperatures. In LIB for plasma generation in the laboratory, energy from the laser electric field is first accumulated by the electrons and, subsequently, is transferred from the electrons to the heavy particles. Electrons receive energy from the electric field and, by collision with a heavy particle, lose only a small portion of that energy. That is why the electron temperature in plasma is initially higher than that of heavy particles. Subsequently, collisions of electrons with heavy particles (Joule heating) can equilibrate their temperatures, unless time or energy are not sufficient for the equilibration (such as in LIB and pulsed discharges). The temperature difference between electrons and heavy neutral particles due to Joule heating in the collisional weakly ionized plasma is conventionally proportional to the square of the ratio of the electric field  $E$  to the pressure  $p$ . Only in the case of small values of  $E/p$  do the temperatures of electrons and heavy particles approach each other. Numerous plasmas are characterized by multiple different temperatures related to different plasma particles and different degrees of freedom. Plasmas of this kind are usually called non-thermal plasmas. Although the relationship between different plasma temperatures in non-thermal plasmas can be quite sophisticated, it can be conventionally presented in LIB strongly ionized plasmas as  $T_e$  (electron temperature) >  $T_i$  (ions or excitation temperature) >  $T_{\text{vib}}$  >  $T_{\text{rot}}$ . In LIB non-thermal plasma studied here, electron temperature is about 10 eV, ions temperature ~2 eV, vibrational temperature ~1 eV, rotational temperature ~0.2 eV, whereas the gas temperature is close to rotational temperature.

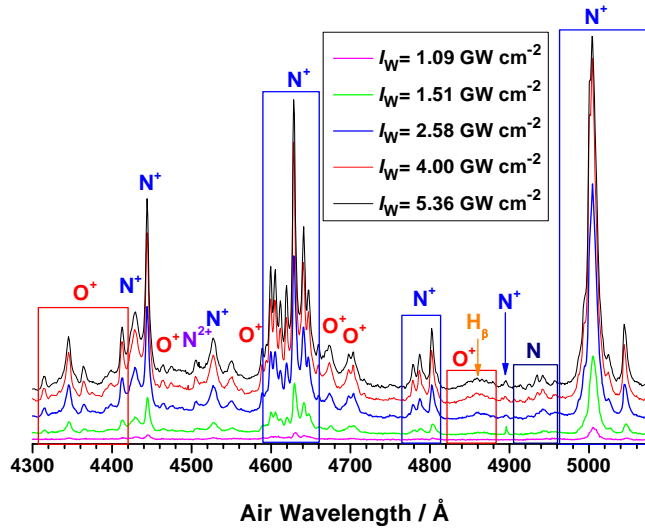


Figure 19. Low-resolution LIB emission spectra in air at atmospheric pressure observed in the 4300–5080 Å region, excited by the TEA-CO<sub>2</sub> laser wavelength at 9.621 μm, as a function of the laser power density.

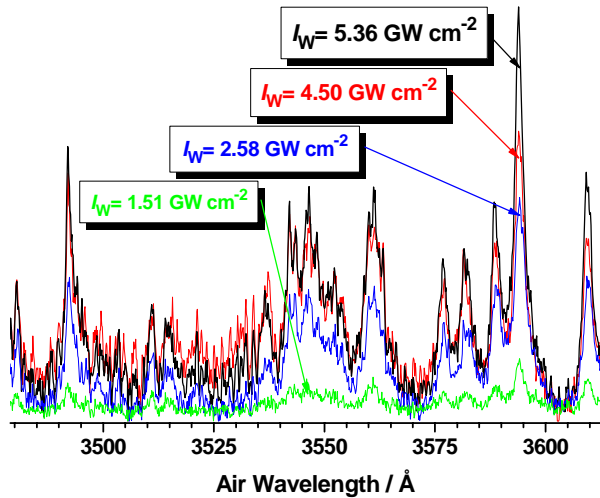


Figure 20. High-resolution LIB emission spectra in air at atmospheric pressure, excited by the TEA-CO<sub>2</sub> laser wavelength at 9.621 μm, as a function of the laser intensity.

The strong atomic and ionic lines observed in LIB spectra of air indicate the high degree of excitation/ionization and the high rate of the N<sub>2</sub>, O<sub>2</sub> dissociation processes achieved in the plasma. As we mentioned in section 2.2, when a high-power laser beam of intensity  $I_w$  interacts with a gas, electrons involving the formation of laser-induced plasma can be generated through two main processes: MPI and EII both followed by electron cascade. The ionization rate in MPI varies as  $I_w^n$  where  $n$  is the number of photons needed to strip off an electron. MPI is relatively improbable for nitrogen and oxygen atoms or molecules in the ground state [N(2s<sup>2</sup>2p<sup>3</sup> 4S<sup>0</sup><sub>3/2</sub>), O(2s<sup>2</sup>2p<sup>4</sup> 3P<sub>2</sub>), N<sub>2</sub>(X<sup>1</sup>Σ<sub>g</sub><sup>+</sup>) and O<sub>2</sub>(X<sup>3</sup>Σ<sub>g</sub><sup>-</sup>)], since their high

ionization potentials (14.534, 13.618, 9.567 and 12.070 eV, respectively), means that more than 100 photons are required for these processes. Besides, the probability of simultaneous absorption of photons decreases with the number of photons  $n$  necessary to cause ionization. In general, this probability is  $W_{MPI} \propto \Phi_W^n \propto F_E^{2n}$ . Calculations of MPI probability (Eq. 2.4) for N, O, N<sub>2</sub> and O<sub>2</sub> give  $W_{MPI}=0$  s<sup>-1</sup> for the CO<sub>2</sub> laser at  $\lambda=9.621$  μm and  $I_W=4.5$  GW×cm<sup>-2</sup>. For example, for a 193 nm (ArF) at the laser intensity  $I_W=1$  GW×cm<sup>-2</sup> ( $n=2$ ), the probability of MPI for O<sub>2</sub> gives  $W_{MPI}=1058$  s<sup>-1</sup>. EII consists on the absorption of light photon by free or quasifree electrons. These electrons in the focal volume gain sufficient energy, from the laser field through IB collisions with neutrals, to ionize mainly nitrogen and oxygen atoms, molecules or ions by inelastic electron-particle collision resulting in two electrons of lower energy being available to start the process again. EII is the most important process for the longer wavelengths used in this work. On the other hand, we have made experimental measurements of breakdown threshold laser intensities of N<sub>2</sub>, O<sub>2</sub> and ambient air (Section 2.4). The threshold power density is dependent on the kind of laser, laser wavelength, pulse length, beam size of the focal volume, and gas pressure. Breakdown thresholds of solids and liquids are usually lower than for gases. Experimental threshold power densities for air is measured for the TEA-CO<sub>2</sub> laser at  $\lambda=10.591$  μm. The threshold power densities for air at a given pressure are measured in the two following manners. First the cell was evacuated with the aid of a rotary pump, to a base pressure of 4 Pa that was measured by a mechanical gauge and then it was filled with air up to the desired pressure. The TEA-CO<sub>2</sub> laser was fired and its energy transmitted through the cell was increased until the breakdown was observed in 50% of laser pulses. The threshold was easily determined because it was always associated with the appearance of a blued bright flash of light in the focal region, with a cracking noise, and the abrupt absorption of the laser pulse transmitted through the focal region. Another way to measure the threshold was to induce a previous breakdown at a pressure over the desired value, later the pressure is lowered and the energy adjusted until the breakdown begins with some probability, usually around 50%. This method is similar to induce the breakdown with energy in excess and to attenuate the laser until the spark disappears. In these cases it could be that initial free electrons have been produced by previous breakdowns and they are the seed of the avalanche process. In this last method the obtained threshold value is normally lower. The present experiments have shown that when high laser energy was used, air breakdown occurred easily and it was reproducible. When the laser energy was reduced to its threshold power density value, air breakdown became a sporadic event. Such sporadic behavior might be due to the difficulty of generating the seed electrons at the breakdown threshold values.

Figure 24 shows the measured breakdown threshold intensity for air, N<sub>2</sub> [18] and O<sub>2</sub> [20] as a function of pressure. We have measured the breakdown threshold intensity in air at atmospheric pressure finding  $4.5 \times 10^9$  W×cm<sup>-2</sup> ( $1.3 \times 10^6$  V×cm<sup>-1</sup>) for an air fresh charge and  $1.1 \times 10^9$  W×cm<sup>-2</sup> ( $6.4 \times 10^5$  V×cm<sup>-1</sup>) for an air non-fresh charge. As can be seen from Figure 24, if a breakdown has been previously induced in the gas (open symbol), the pressure range to induce the breakdown is bigger and the power density is lower than when no previous breakdown is induced (solid symbol). The number of free electrons is higher in conditions of previous breakdown than in the case of no previous breakdown, lowering the threshold for the plasma initiation. This has been observed by different authors. LIB threshold intensity of air at atmospheric pressure has been measured by Alcock *et al* [ $\sim 4 \times 10^{10}$  W×cm<sup>-2</sup> (Ruby, 0.3472 μm) and  $\sim 10^{11}$  W×cm<sup>-2</sup> (0.6943 μm)] [64], Haught *et al* ( $\sim 4 \times 10^{14}$  W×cm<sup>-2</sup>) [65], De Michelis

( $\sim 4 \times 10^{10} \text{ W} \cdot \text{cm}^{-2}$ ) [66], Ireland *et al* ( $\sim 4 \times 10^{10} \text{ W} \cdot \text{cm}^{-2}$ ) [67], Aaron *et al* ( $\sim 4 \times 10^{14} \text{ W} \cdot \text{cm}^{-2}$ ) [68], Phuoc and White ( $\sim 2.5 \times 10^{12} \text{ W} \cdot \text{cm}^{-2}$ ) [69], Tomlinson *et al* [ $\sim 2 \times 10^{11} \text{ W} \cdot \text{cm}^{-2}$  (Ruby, 0.69  $\mu\text{m}$ ) and  $\sim 7 \times 10^{10} \text{ W} \cdot \text{cm}^{-2}$  (Nd:YAG, 1.06  $\mu\text{m}$ )] [70], Chan *et al* [ $\sim 1.5 \times 10^9 \text{ W} \cdot \text{cm}^{-2}$  ( $\text{CO}_2$ , 10.6  $\mu\text{m}$ ,  $\Lambda$ (diffusion length)= $4.8 \times 10^{-3} \text{ cm}$ ),  $\sim 3 \times 10^9 \text{ W} \cdot \text{cm}^{-2}$  ( $\Lambda=3.2 \times 10^{-3} \text{ cm}$ ), and  $\sim 7 \times 10^9 \text{ W} \cdot \text{cm}^{-2}$  ( $\Lambda=1.6 \times 10^{-3} \text{ cm}$ )] [30], Kawahara ( $\sim 7 \times 10^{10} \text{ W} \cdot \text{cm}^{-2}$ , Nd:YAG, 1.06  $\mu\text{m}$ )] [71] and Zhuzhukalo *et al* [ $\sim 7 \times 10^{10} \text{ W} \cdot \text{cm}^{-2}$  (focal length = 1.4 m) and  $\sim 2 \times 10^{10} \text{ W} \cdot \text{cm}^{-2}$  (focal length = 14 m)] [72]. Alcock *et al* [64] reported a decrease of the breakdown threshold intensity from  $\sim 9 \times 10^{10}$  to  $\sim 4 \times 10^{10} \text{ W} \cdot \text{cm}^{-2}$  at 0.3472  $\mu\text{m}$  and  $\sim 2 \times 10^{11}$  to  $\sim 1 \times 10^{11} \text{ W} \cdot \text{cm}^{-2}$  at 0.6943  $\mu\text{m}$  for air pressures between  $\sim 200$  Torr and  $\sim 800$  Torr. Chang *et al* [30] reported for several gases ( $\text{O}_2$ ,  $\text{N}_2$ , air, He, and Ne) that the threshold power density decreases as the pressure increases and that it decreases as the focal volume increases. For air they reported a slow decrease with a minimum of the breakdown threshold intensity from  $\sim 1.5 \times 10^9$  to  $\sim 1 \times 10^9 \text{ W} \cdot \text{cm}^{-2}$  at  $\Lambda=4.8 \times 10^{-3} \text{ cm}$ ,  $\sim 3 \times 10^9$  to  $\sim 1.5 \times 10^9 \text{ W} \cdot \text{cm}^{-2}$  at  $\Lambda=3.2 \times 10^{-3} \text{ cm}$ , and  $\sim 10 \times 10^9$  to  $\sim 5 \times 10^9 \text{ W} \cdot \text{cm}^{-2}$  at  $\Lambda=1.6 \times 10^{-3} \text{ cm}$  for air pressures between  $\sim 200$  Torr and  $\sim 10000$  Torr. In this work, they used a  $\text{CO}_2$  laser and the focal diameter range from  $0.75 \times 10^{-2}$  to  $3 \times 10^{-2} \text{ cm}$ . Phuoc and White [69] reported a decrease of the breakdown threshold intensity from  $\sim 2 \times 10^{13}$  to  $\sim 2 \times 10^{12} \text{ W} \cdot \text{cm}^{-2}$  at 0.532  $\mu\text{m}$  and  $\sim 8 \times 10^{12}$  to  $\sim 1 \times 10^{12} \text{ W} \cdot \text{cm}^{-2}$  at 1.064  $\mu\text{m}$  for air pressures between 50 Torr and 3000 Torr. It has to be noted that we have obtained similar threshold power densities for air than those given by Chan [30], but lower values than reported in Refs. [64-72]. This fact can be related in part to the used focal length (24 cm) and beam size in the focal region ( $7.85 \times 10^{-3} \text{ cm}^2$ ) that is one order of magnitude, at least, higher than the values commonly used in the literature, favoring the probability of existence of free electrons to seed the process and decreasing the threshold laser intensity due to the lack of the diffusion losses.

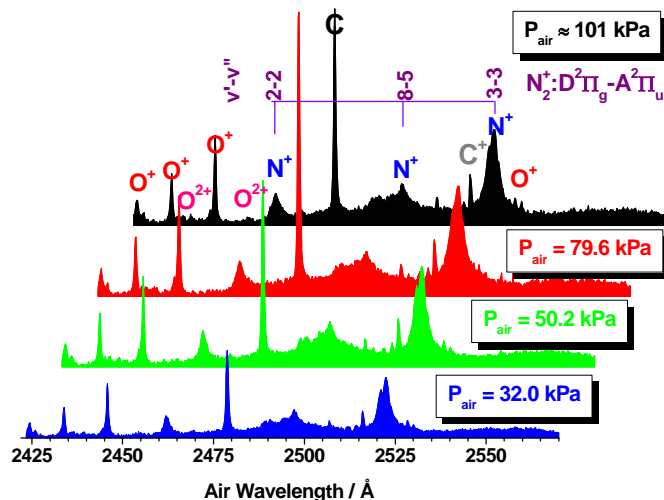


Figure 21. High-resolution LIB emission spectra at various air pressures, excited by the TEA- $\text{CO}_2$  laser (10.591  $\mu\text{m}$ ) at a power density of  $6.31 \text{ GW} \cdot \text{cm}^{-2}$ .

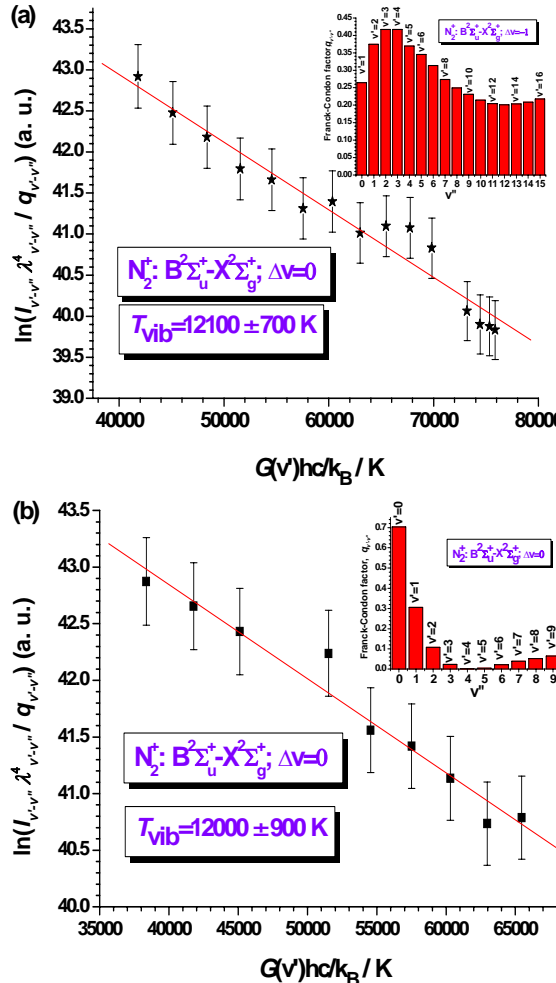


Figure 22. Left (a) panel: Linear Boltzmann plot of the N<sub>2</sub><sup>+</sup> (B-X)  $\Delta\nu=-1$  band sequence intensity versus the normalized energy of the upper vibrational level; Right (b) panel: Linear Boltzmann plot of the N<sub>2</sub><sup>+</sup> (B-X)  $\Delta\nu=0$  band sequence intensity versus the normalized energy of the upper vibrational level; Experimental conditions: laser power density of 5.36 GW cm<sup>-2</sup> and atmospheric pressure. Plots also show linear fit to the data and the corresponding Franck-Condon factors.

It has been established [3-10] that the threshold photon flux density or equivalently the threshold power density for MPI varies with  $p^{-1/n}$ , where  $p$  is the gas pressure and  $n$  is the number of simultaneously absorbed photons (see section 2.4). Therefore, MPI predicts a very weak dependence of the threshold power density on pressure. However, as we can see from Figure 24, the breakdown threshold power density in air versus pressure shows a minimum around  $5 \times 10^4$  Pa if previous breakdown have existed and  $8 \times 10^4$  Pa without previous breakdown. Therefore, it can be seen from Figure 24 that the pressure dependence is not in harmony with MPI which predicts a very weak  $p^{-1/n}$  dependence for the threshold power density, while it is in qualitative agreement with electron cascade. A minimum in the variation of the threshold power density versus pressure is predicted by the classical theory [2-3, 23]. In our experiments, a minimum in the threshold power density versus pressure curve (Figure 24) is observed. Therefore, starting from our experimental observations and

calculations, we can conclude that although, the first electrons must appear via MPI or natural ionization, electron impact is the main mechanism responsible for the breakdown in air.

### 5.3.1. Temporal evolution of the LIB plasma

The absorption of light and heating of a gas is of primary significance for important practical problems (the fire ball of an explosion, the heating of artificial satellites during re-entry into the atmosphere, detection of environmental pollutants, ignition systems, laser machining, inertially confined fusion, etc). In this section, time-resolved OES analysis for the plasma produced by high-power tunable IR CO<sub>2</sub> pulsed laser breakdown of air is presented [21]. In these series of experiments, the CO<sub>2</sub> pulsed laser ( $\lambda=10.591\text{ }\mu\text{m}$ , 64 ns (FWHM), 47-347 J/cm<sup>2</sup>) was focused onto a metal mesh target under air as host gas at atmospheric pressure [21]. It was found that the CO<sub>2</sub> laser is favorable for generating strong, large volume air breakdown plasma, in which the air plasma was then produced. While the metal mesh target itself was practically never ablated, the air breakdown is mainly due to electronic relaxation of excited N, O, C, H, Ar and ionic fragments N<sup>+</sup>, O<sup>+</sup>, N<sup>2+</sup>, O<sup>2+</sup>, C<sup>+</sup> and molecular band systems of N<sub>2</sub><sup>+</sup>(B<sup>2</sup>S<sub>u</sub><sup>+</sup>-X<sup>2</sup>S<sub>g</sub><sup>+</sup>; D<sup>2</sup>P<sub>g</sub>-A<sup>2</sup>P<sub>u</sub>), N<sub>2</sub>(C<sup>3</sup>P<sub>u</sub>-B<sup>3</sup>P<sub>g</sub>) and OH(A<sup>2</sup>S<sup>+</sup>-X<sup>2</sup>P<sub>g</sub>).

The difficulties arise on account of the imprecise definition of the extent of the focal region which, in turn lead to inadequate or inaccurate knowledge of the spatial-temporal characteristic of the beam intensity within the focal region for gases. On the other hand, it is well known that a pure gas plasma, due to the gas breakdown process, is produced when a TEA CO<sub>2</sub> laser is focused onto a metal sample at a gas pressure of around 1 atm, in which case practically all the laser irradiance is absorbed in the gas plasma [33, 73]. It is expected that, in some medium range pressures between 0.01 torr and 1 atm, both gas plasma and target plasmas are produced. In such a case, some interaction inevitable takes place between the gas and the target laser induced plasmas. The plasma is a mixture of electrons, atoms, molecules and ions, and mass from both the ablated target and the ambient gas. The interaction between the ejected mass (plume) and the surrounding air slows the expansion of the plasma. If a metal mesh is used as a target, low amount (if any) of ablated material will be formed and the spatial origin of gas breakdown process will be accurately defined independently of the laser fluence. After its formation in the vicinity of the metal mesh surface, the air breakdown plasma propagates towards the laser source at a supersonic speed. The shock wave heats up the surrounding air which is instantaneously transformed in strongly ionized plasma.

Two different types of spectra were recorded: time-integrated and time-resolved. In the acquisition of time-integrated spectra, a good signal to noise ratio has been obtained averaging each spectrum over several successive laser pulses. Typically the signals from 20 laser pulses are averaged and integrated over the entire emission time. In time-resolved measurements, the delay  $t_d$  and width  $t_w$  times were varied. It was verified that the plasma emission was reproducible over more than 7 ablation events by recording the same spectrum several times. The temporal history of LIB air plasma is illustrated schematically in Figure 25. The time for the beginning of the CO<sub>2</sub> laser pulse is considered as the origin of the time scale ( $t=0$ ). Inserts illustrate some emission spectra recorded at different delay and width times at two observed distances of  $z=2.5$  and 5 mm. The temporal shape of the CO<sub>2</sub> laser pulse is also shown.

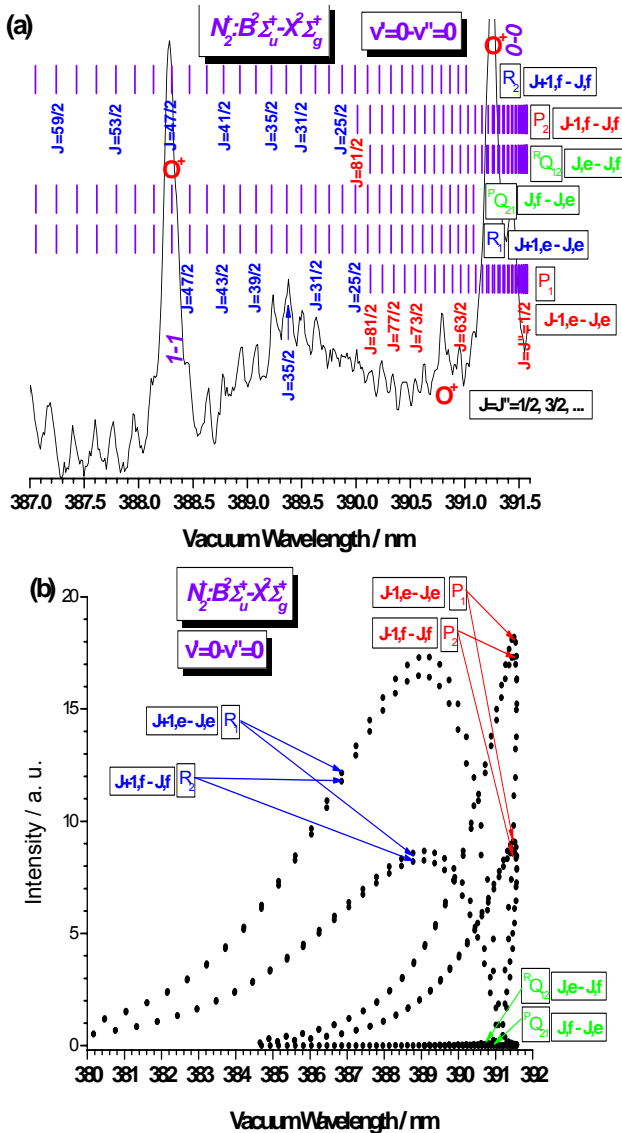


Figure 23. (a) Detailed LIB spectrum of air and partial rotational assignments of the 0-0  $B^2\Sigma_u^+ - X^2\Sigma_g^+$  band of  $N_2^+$ . (b) Calculated fortrat diagram for  $P_1$ ,  $P_2$ ,  $R_1$ ,  $R_2$ ,  $R^* Q_{12}$  and  $P^* Q_{21}$  branches in the 0-0 band (B-X) of  $N_2^+$  at  $T_{\text{rot}}=1950$  K.

The LIB spectra of air were measured at different delay and width times. In a first set of experimental measurements, the spectra have been obtained in the spectral region 2423-2573 Å, at a delay time ranging from 0 to 30 µs at 0.5 µs intervals and at an observed distance  $z$  from 1 to 10 mm. The spectral range was chosen in order to detect both single and double ionized oxygen species, several single ionized nitrogen lines and atomic carbon. Figure 26 illustrates the time-resolved evolution from laser-induced ( $106 \text{ J/cm}^2$ ) air plasma monitored at 0, 0.1, 0.7, 2, 3, 4, and 5 µs gate delays for a fixed gate width time of 0.5 µs and  $z=2.5$  mm. One can see that after the laser pulse, the plasma emission consists in an intense continuum. This continuum radiation is emitted by the laser-induced plasma as a result of free-free and

free-bound transitions. As seen in Figure 26 during the initial stages after laser pulse ( $t_d \leq 0.5 \mu\text{s}$ ), continuum emission dominates the spectrum. As time evolves ( $0.5 \mu\text{s} \leq t_d \leq 3.5 \mu\text{s}$ ),  $\text{N}^+$ ,  $\text{O}^+$  and  $\text{O}^{2+}$  emissions dominate the spectrum. These ionic lines decrease quickly for higher delay times, being detected up to  $\sim 4.5 \mu\text{s}$ . The emission lines become progressively narrower as a consequence of the electron number density distribution. It points out that the electron density and excitation temperature must decrease during the plasma expansion. As the delay is increased ( $t_d > 3.5 \mu\text{s}$ ) C atomic emission line dominates the spectrum. This atomic line decreases for higher delay times, being detected up to  $\sim 30 \mu\text{s}$ . The maximum intensity of continuum and spectral lines is reached after a characteristic time, depending on the observation distance  $z$ . Figure 27 shows time-resolved emission spectra from LIB ( $106 \text{ J/cm}^2$ ) in air collected at different distances ( $z=1$  and  $7.5 \text{ mm}$ ) and recorded at 2, 3, 4, and  $5 \mu\text{s}$  gate delays for a fixed gate width time of  $0.5 \mu\text{s}$ . By analyzing Figures 26 and 27 it is possible to see that C atoms are produced both in the ablated target and in the air breakdown. When the spectra were recorded near the target surface ( $z < 2.5 \text{ mm}$ ), the main contribution of C atoms is due to the target surface. For  $z > 2.5 \text{ mm}$ , practically the spectrum is due to air breakdown. At far away distances from the metal mesh target surface, the plasma front arrives later than for close distances. Figure 28 displays several time-resolved emission spectra from LIB ( $106 \text{ J/cm}^2$ ) in air monitored at 1, 2.5, 5, and  $7.5 \text{ mm}$  observed distances and after the laser pulse ( $t_d < 0.5 \mu\text{s}$ ). In this Figure, one can see that at short time after the TEA CO<sub>2</sub> laser pulse, the plasma emission consists in an intense continuum that decreases with distance. Figure 29 shows time-resolved emission spectra from laser-induced air plasma ( $106 \text{ J/cm}^2$ ) recorded at  $t_d=3 \mu\text{s}$  with  $t_w=0.5 \mu\text{s}$  monitored at 1, 2.5, 5, 7.5 and  $10 \text{ mm}$ . In these recording conditions, the most intense plasma is monitored at 5 mm from the mesh target surface.

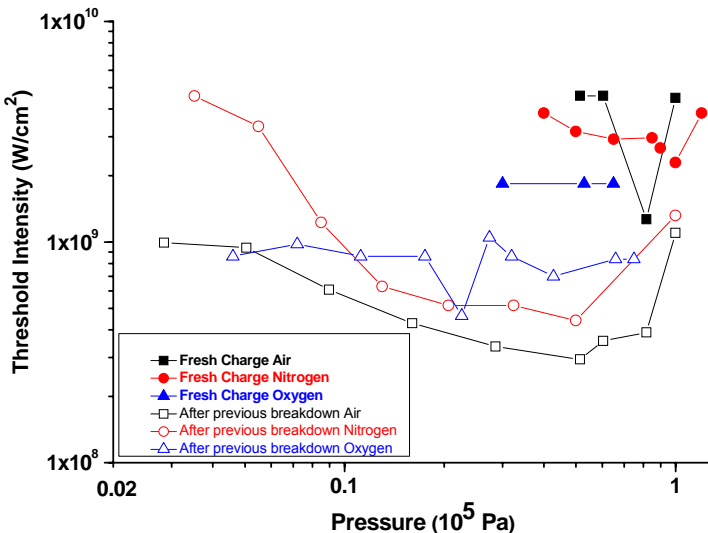


Figure 24. Experimental laser-induced breakdown thresholds excited by the TEA-CO<sub>2</sub> laser ( $10.591 \mu\text{m}$ ) in air (square), nitrogen [18] (circle) and oxygen [20] (triangle) for different pressures. Solid: fresh charge (without previous breakdown); Open: after previous breakdown.

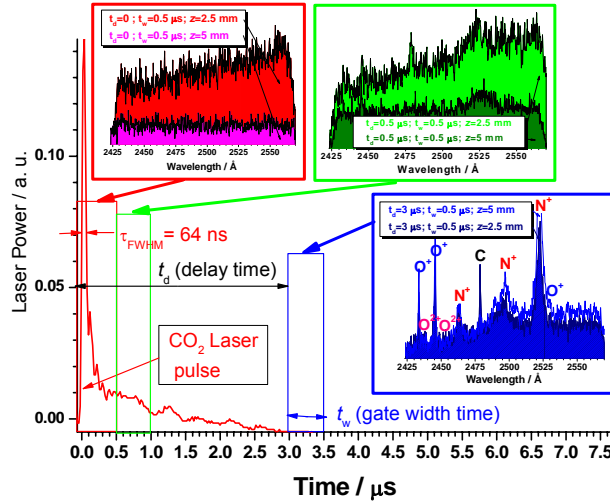


Figure 25. A schematic overview of the temporal history of LIB air plasma. Here  $t_d$  is the delay time and  $t_w$  is the gate width time during which the plasma emission is monitored. Insets plots illustrate some spectra observed at different delay times (0, 0.5 and 3  $\mu$ s) for a fixed gate width time of 0.5  $\mu$ s and  $z=2.5$  and 5 mm. The temporal shape of the CO<sub>2</sub> laser pulse is also shown.

Figure 30 displays the temporal evolution of the LIBS air plasma (160 J/cm<sup>2</sup>) in the spectral region 3725–3860 Å region monitored at 2.5, 3 and 4  $\mu$ s gate delays for a fixed gate width time of 0.5  $\mu$ s ( $z=1$  cm) and time-integrated spectrum ( $t_d=0$  and  $t_w>>30$   $\mu$ s). The inset plot shows the assignment of some ionic lines of N<sup>+</sup>, O<sup>+</sup> and O<sup>2+</sup> and band heads of different molecular bands of N<sub>2</sub><sup>+</sup>(B<sup>2</sup> $\Sigma_u^+$ -X<sup>2</sup> $\Sigma_g^+$ ;  $\Delta v=0$  sequence) [see Figure 17(g)]. At early times ( $t_d<1$   $\mu$ s) (not shown), the plasma emission consists in a weak continuum. When the delay increases, some ionic lines of N<sup>+</sup>, O<sup>+</sup> and O<sup>2+</sup> and band heads of the molecular bands of N<sub>2</sub><sup>+</sup>(B<sup>2</sup> $\Sigma_u^+$ -X<sup>2</sup> $\Sigma_g^+$ ) enhanced steeply as a consequence of the expansion and heating of the air plasma. At longer times ( $t_d>3$   $\mu$ s), the ion lines significantly decrease steeply in intensity as a consequence of the expansion and cooling of the plasma plume and its recombination into ground state ions. At  $t_d>4$   $\mu$ s, N<sup>+</sup> and O<sup>+</sup> ionic lines and N<sub>2</sub><sup>+</sup> rovibrational lines disappear. Figure 31 shows the temporal evolution of the LIBS air plasma (71 J/cm<sup>2</sup>) in the spectral region 3830–3960 Å region monitored at 2, 3 and 4  $\mu$ s gate delays for a fixed gate width time of 0.5  $\mu$ s ( $z=1$  cm) and time-integrated spectrum ( $t_d=0$  and  $t_w>>30$   $\mu$ s). This plot also shows the assignment of some ionic lines of N<sup>+</sup>, O<sup>+</sup> and N<sup>2+</sup> and band heads of different molecular bands of N<sub>2</sub><sup>+</sup>(B<sup>2</sup> $\Sigma_u^+$ -X<sup>2</sup> $\Sigma_g^+$ ;  $\Delta v=0$  sequence). At early times ( $t_d<1$   $\mu$ s) (not shown), the plasma emission consists in a continuum. When the delay increases, some ionic lines of N<sup>+</sup>, O<sup>+</sup> and N<sup>2+</sup> and band heads of the molecular bands of N<sub>2</sub><sup>+</sup>(B<sup>2</sup> $\Sigma_u^+$ -X<sup>2</sup> $\Sigma_g^+$ ) enhanced as a consequence of the air plasma expansion. At longer times ( $t_d>3$   $\mu$ s), the ion lines significantly decrease steeply in intensity. At  $t_d>5$   $\mu$ s, N<sup>+</sup>, N<sup>2+</sup> and O<sup>+</sup> ionic lines and N<sub>2</sub><sup>+</sup> rovibrational lines disappear. Figure 32 displays the temporal progress of the LIBS air plasma in the spectral window 4070–4195 Å observed at 2.5, 3 and 4  $\mu$ s gate delays for a fixed gate width time of 0.5  $\mu$ s ( $z=1$  cm) and time-integrated spectrum ( $t_d=0$  and  $t_w>>30$   $\mu$ s). The assignments of some ionic lines of N<sup>+</sup>, O<sup>+</sup> and N<sup>2+</sup> and band heads of different molecular bands of N<sub>2</sub><sup>+</sup>(B<sup>2</sup> $\Sigma_u^+$ -X<sup>2</sup> $\Sigma_g^+$ ;  $\Delta v=-1$  sequence) are indicated. As before, at early times ( $t_d<1$   $\mu$ s), the plasma emission consists in a weak continuum. When the delay increases, some ionic lines of N<sup>+</sup>, O<sup>+</sup> and N<sup>2+</sup>

and band heads of the molecular bands of  $\text{N}_2^+$ ( $\text{B}^2\Sigma_u^+ - \text{X}^2\Sigma_g^+$ ) enhanced. At longer times ( $t_d > 3 \mu\text{s}$ ), the ion lines significantly decrease steeply in intensity. At  $t_d > 4 \mu\text{s}$ ,  $\text{N}^+$ ,  $\text{N}_2^{2+}$  and  $\text{O}^+$  ionic lines and  $\text{N}_2^+$  rovibrational lines disappear.

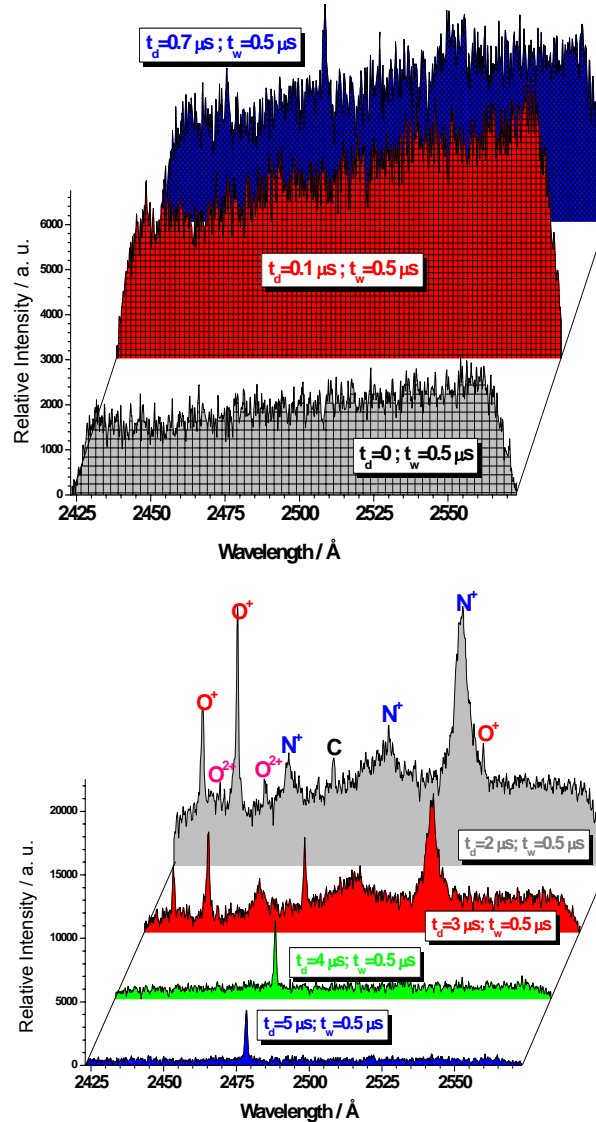


Figure 26. Time-resolved emission spectra from laser-induced ( $106 \text{ J/cm}^2$ ) air plasma observed in the region  $2423-2573 \text{ \AA}$  monitored at 0, 0.1, 0.7, 2, 3, 4, and 5  $\mu\text{s}$  gate delays for a fixed gate width time of  $0.5 \mu\text{s}$  and  $z=2.5 \text{ mm}$ .

### 5.3.2. Time of flight, velocity, kinetic energy and electron density

Space-and-time resolved OES measurements could be used to estimate plasma expansion rate and kinetic energy. The temporal evolution of spectral atomic, ionic and molecular line intensities at a constant distance from the target can be used to construct the time-of-flight (TOF) profile. TOF studies of the emission provide fundamental information regarding the

time taken for a particular species to evolve after the laser-induced plasma has been formed. Specifically, this technique gives an indication of the velocity of the emitted species. A coarse estimation of the velocity for the different species in the plume can be inferred from the time resolved spectra by plotting the intensities of selected emission lines versus the delay time, and then calculating the velocity by dividing the distance from the target by the time where the emission peaks. This method for determination of plasma velocity should be used with care due to the superposition of both expansion and forward movements of the plasma plume. We assumed a plasma model consisting in two plasmas [74]: primary plasma that acts as initial explosion energy source and emits an intense continuum emission background for a short time just above the surface of the auxiliary target; secondary plasma expands with time around the primary plasma. The secondary plasma is formed by the excitation from the shock wave and by the emitting of atomic, ionic and molecular species characterized by a low background signal.

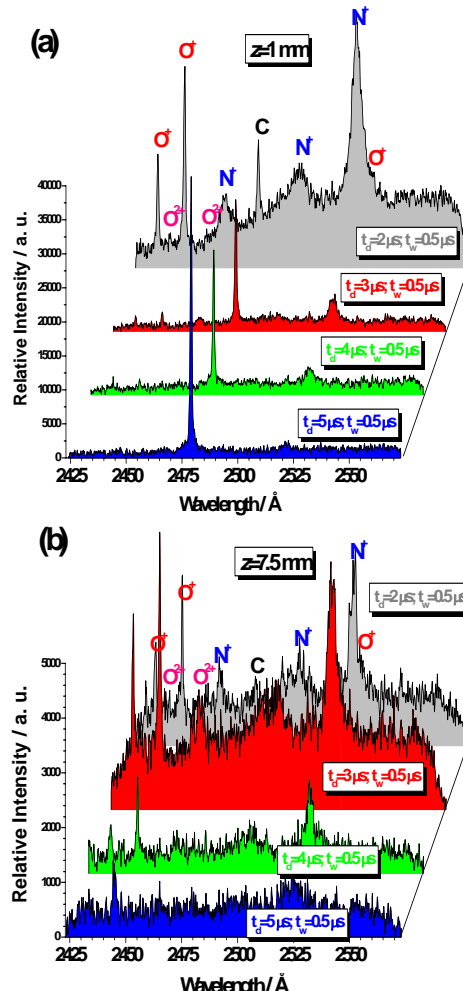


Figure 27. Time-resolved emission spectra from laser-induced ( $106 \text{ J/cm}^2$ ) air plasma observed in the region  $2423\text{--}2573 \text{ \AA}$  monitored at 2, 3, 4, and 5  $\mu\text{s}$  gate delays for a fixed gate width time of  $0.5 \mu\text{s}$  and (a)  $z=1 \text{ mm}$ ; (b)  $z=7.5 \text{ mm}$ .

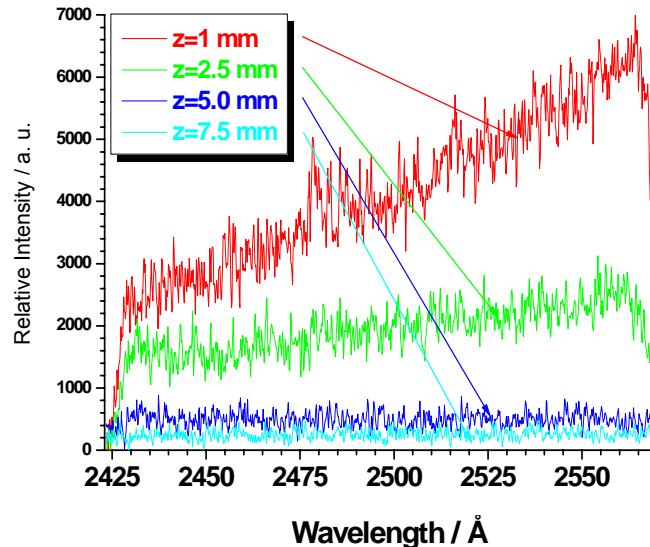


Figure 28. Time-resolved emission spectra from LIB ( $106 \text{ J/cm}^2$ ) in air at 1, 2.5, 5, and 7.5 mm along the plasma expansion direction (Z-axis) and recorded at  $t_d=0$  and  $t_w=0.5 \mu\text{s}$ .

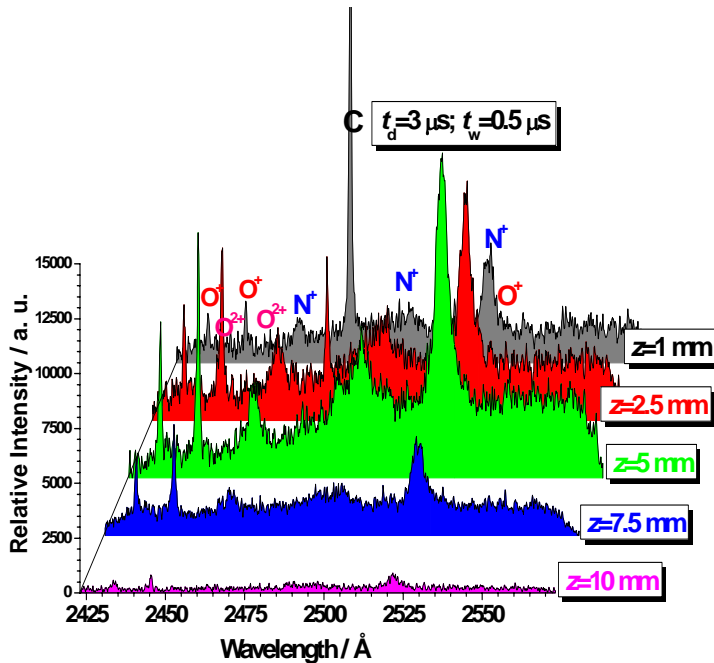


Figure 29. Time-resolved emission spectra from laser-induced air plasma ( $106 \text{ J/cm}^2$ ) observed in the region  $2423$ - $2573 \text{ \AA}$  at  $t_d=3 \mu\text{s}$  for  $t_w=0.5 \mu\text{s}$  monitored at 1, 2.5, 5, 7.5 and 10 mm along the plasma expansion direction.

Figure 33(a) displays the TOF profiles for the air breakdown experiments induced by  $\text{CO}_2$  laser pulses ( $106 \text{ J/cm}^2$ ), of continuum radiation,  $\text{O}^+(2433.53 \text{ \AA})$ ,  $\text{O}^+(2455.53 \text{ \AA})$ ,  $\text{N}^+(2461.27 \text{ \AA})$ ,  $\text{N}^+(2478.56 \text{ \AA})$ ,  $\text{N}^+(2522.23 \text{ \AA})$  and  $\text{C}(2478.56 \text{ \AA})$  lines as a function of the delay time. We notice the appearance of a strong maximum for continuum background for a

delay of 1  $\mu$ s at  $z=5$  mm. When  $t_d$  increases, the continuum drops steeply as a consequence of the reduction of electron density and temperature as the plume expands. For O<sup>+</sup> and N<sup>+</sup> ionic species and C atomic, the maxima appear for a delay of 2.5, 3 and 4.5  $\mu$ s, respectively. The emission intensity of O<sup>+</sup> and N<sup>+</sup> ionic lines decreases more rapidly than the emission intensity of the C lines. The time duration of ionic species was nearly 5  $\mu$ s, while the time duration of C atomic emission was nearly 20  $\mu$ s. The experimental TOF distributions  $N(t)$  are essentially number density distributions. They are converted to flux distributions  $dN/dt$  by employing a correction factor  $z/t$ , where  $z$  means the flight distance along the plasma expansion and  $t$  is the delay time after the laser pulse incidence. It should be mentioned that the estimation of velocity distributions assumes that the emitting species are generated on the assisting metal mesh target. The velocity distributions that are derived from these TOF distributions are displayed in Figure 33(b). At the laser fluence used in this series of experiments (106 J/cm<sup>2</sup>) and  $z=5$  mm, TOF distributions present different characteristics. Thus, the velocity distributions of ionic species O<sup>+</sup>(2445.54 Å) and N<sup>+</sup>(2522.23 Å) are comparatively wider (~3.7 and ~4 km/s (FWHM), respectively) than the velocity distribution of carbon neutral species [~1.2 km/s (FWHM)]. The velocity distributions of O<sup>+</sup>, N<sup>+</sup> and C lines species are centred at about 2, 1.7 and 1.1 km/s, respectively. From TOF spectra, the translational kinetic energy can be deduced [ $KE=(1/2)m(z/t)^2$ ] by measuring the time  $t$  required to transverse the distance from the target to the detector  $z$ . The kinetic energy obtained for some species are plotted in Figure 34. We have observed small atomic and ionic average kinetic energies. As we have stated above, for a better understanding of the physical mechanisms underlying the plasma emission breakdown in air, LIB spectra were obtained by varying both the distance  $z$  (up to 10 mm) with respect to the auxiliary metal mesh and the laser energy. It is expected, in fact, that these two parameters would affect strongly the dynamic evolution of the plasma and the shock wave induced by the CO<sub>2</sub> laser. Different lines originating from atomic and ionic species of both nitrogen and oxygen were analyzed. O<sup>+</sup> doublet ( $2s^22p^2(^1D)3p\ ^2D^0_{3/2,5/2}\rightarrow2s^22p^2(^3P)3s\ ^2P_{3/2}$ ) at ~2445 Å and N<sup>+</sup> triplet ( $2s^22p(^2P^0)4d\ ^3D^0_{1,2,3}\rightarrow2s^22p(^2P^0)3p\ ^3P_{0,1,2}$ ) at ~2522 Å were chosen as representative of ionized lines. The energies of the lower levels of both multiplets are high (189068.514 for O<sup>+</sup> and 170572.61, 170607.89 and 170666.23 cm<sup>-1</sup> for N<sup>+</sup>) so that the self-absorption effect can be neglected. Figures 35 and 36 show TOF and velocity distributions of multiplet structures of N<sup>+</sup>(~2522 Å) and O<sup>+</sup>(~2445 Å) at different distances (1, 2.5, 5, 7.5 and 10 mm) as for a laser fluence of 106 J/cm<sup>2</sup>. The temporal emission features are affected by the presence of strong continuum at short distances ( $z\leq3$  mm) and at early delay time. But at distances greater than 3 mm, the continuum radiation is considerably reduced and the interference of continuum on the TOF distributions is negligible. The spike observed in TOF and velocity profiles is the prompt signal that is used as a time maker. By the shift of the TOF peaks for each distance it is possible to calculate approximately the mean velocities of LIB along the propagation axis Z. The measured peak velocities of multiplet structures of N<sup>+</sup>(~2522 Å) and O<sup>+</sup>(~2445 Å) monitored at 1, 2.5, 5, 7.5 and 10 mm (for a laser fluence of 106 J/cm<sup>2</sup>) are 0.5, 1, 1.7, 2.1 and 3.6 km/s and 0.5, 1, 2, 2.5 and 5 km/s, respectively. The peak velocities of N<sup>+</sup> and O<sup>+</sup> increase with the distance from the target surface. This is due to the initial acceleration of the ablated partials from zero velocity to a maximum velocity. Also we have studied OES of the air plasma by varying the laser energy. We observed that when the laser fluence is increased, the N<sup>+</sup> and O<sup>+</sup> TOF distributions broaden and move towards lower delay times. On the other hand, plasma temperature was

determined from the emission line intensities of several  $\text{N}^+$  and  $\text{O}^+$  ionized lines observed in the laser-induced plasma of air for a delay time of 3  $\mu\text{s}$  and a distance of  $z=5$  mm. The obtained excitation temperatures, in the case of  $\text{N}^+$  and  $\text{O}^+$ , were  $23400 \pm 900$  K and  $26600 \pm 1300$  K, respectively. For  $\text{N}^+$  and  $\text{O}^+$  lines, the Doppler line widths vary between 0.08-0.17 Å at 23400 K and 0.11-0.13 Å at 26600 K, respectively.

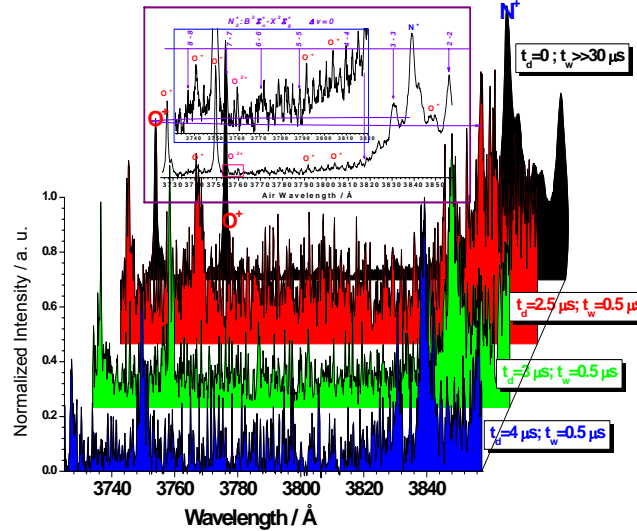


Figure 30. Time-resolved emission spectra from laser-induced ( $160 \text{ J/cm}^2$ ) air plasma observed in the region 3725-3860 Å monitored at 2.5, 3 and 4  $\mu\text{s}$  gate delays for a fixed gate width time of 0.5  $\mu\text{s}$  ( $z=1$  cm) and time-integrated spectrum ( $t_d=0$  and  $t_w>>30 \mu\text{s}$ ). The inset plot shows the assignment of some ionic lines of  $\text{N}^+$ ,  $\text{O}^+$  and  $\text{O}^{2+}$  and band heads of the molecular bands of  $\text{N}_2^+(\text{B}^2\Sigma_u^+ - \text{X}^2\Sigma_g^+)$ .

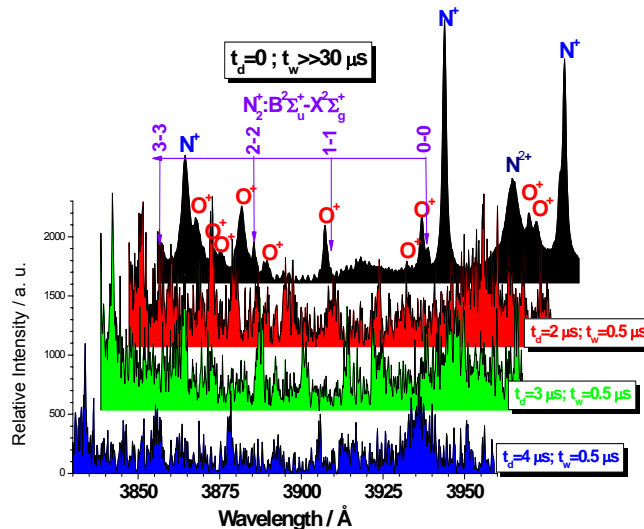


Figure 31. Time-resolved emission spectra from laser-induced air plasma ( $71 \text{ J/cm}^2$ ) observed in the region 3830-3960 Å monitored at 2, 3 and 4  $\mu\text{s}$  gate delays for a fixed gate width time of 0.5  $\mu\text{s}$  ( $z=1$  cm) and time-integrated spectrum ( $t_d=0$  and  $t_w>>30 \mu\text{s}$ ). The assignments of some ionic lines of  $\text{N}^+$ ,  $\text{O}^+$  and  $\text{N}^{2+}$  and band heads of the molecular bands of  $\text{N}_2^+(\text{B}^2\Sigma_u^+ - \text{X}^2\Sigma_g^+)$  are indicated.

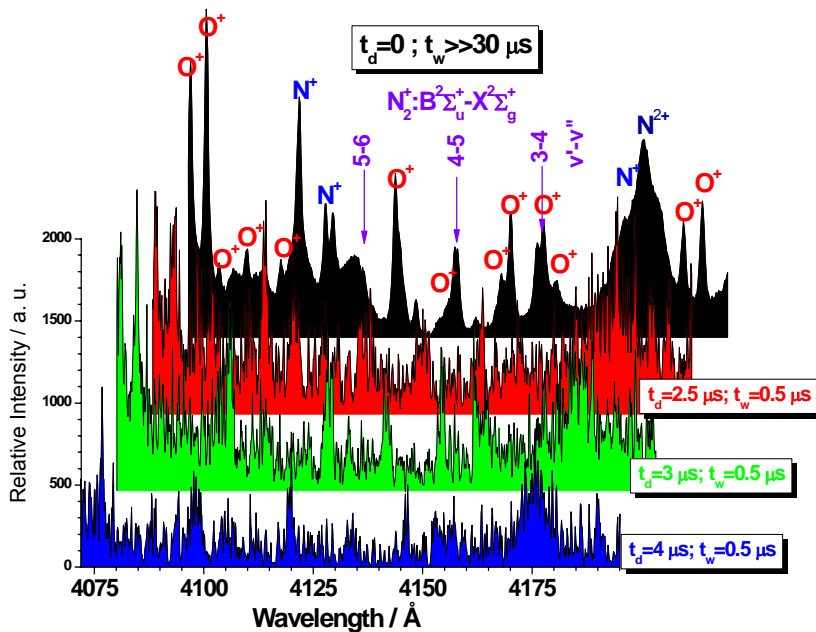


Figure 32. Time-resolved emission spectra from laser-induced air plasma ( $71 \text{ J/cm}^2$ ) observed in the region  $4070\text{-}4195 \text{ Å}$  monitored at  $2.5$ ,  $3$  and  $4 \mu\text{s}$  gate delays for a fixed gate width time of  $0.5 \mu\text{s}$  ( $z=1 \text{ cm}$ ) and time-integrated spectrum ( $t_d=0$  and  $t_w>>30 \mu\text{s}$ ). The assignments of some ionic lines of  $\text{N}^+$ ,  $\text{O}^+$  and  $\text{N}^{2+}$  and band heads of the molecular bands of  $\text{N}_2^+$  ( $\text{B}^2\Sigma_u^+ \text{-} \text{X}^2\Sigma_g^+$ ) are indicated.

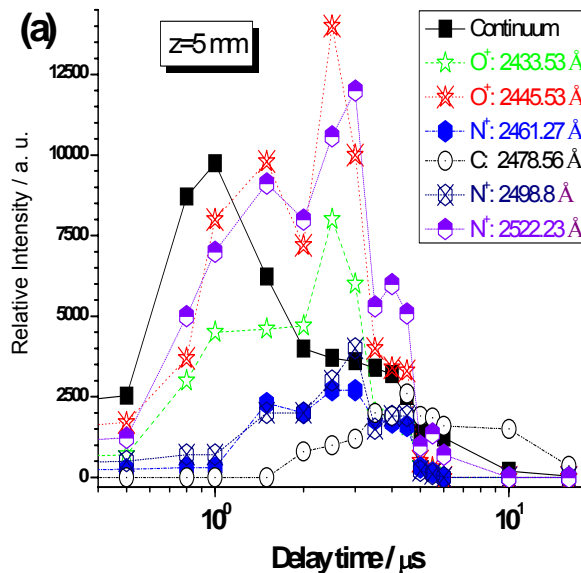


Figure 33. (Continued)

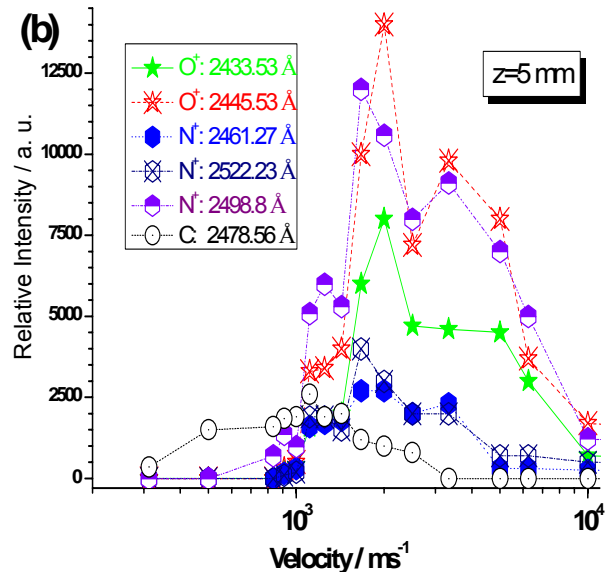


Figure 33. (a) Number density TOF distributions of continuum radiation,  $\text{O}^+$ (2433.53; 2445.54 Å),  $\text{N}^+$ (2461.27; 2478.56; 2522.23 Å) and C(2478.56 Å) lines as a function of delay time (fixed gate width time of 0.5  $\mu\text{s}$ ) for a laser fluence of 106 J/cm<sup>2</sup> and  $z=5$  mm. (b) Velocity distributions derived from the experimental TOF profiles for the indicated species.

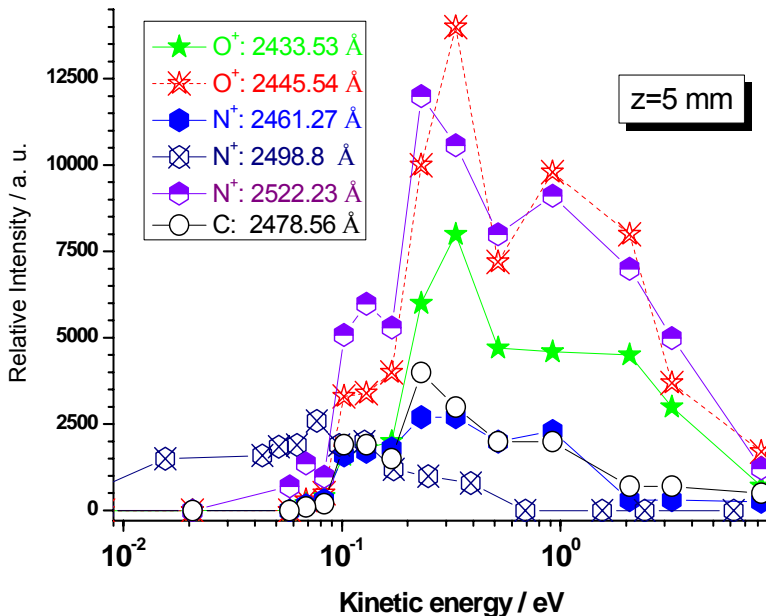


Figure 34. Kinetic energy distributions of  $\text{O}^+$ (2433.53 Å),  $\text{O}^+$ (2445.54 Å),  $\text{N}^+$ (2461.27 Å),  $\text{N}^+$ (2478.56 Å),  $\text{N}^+$ (2522.23 Å) and C(2478.56 Å) lines derived from the TOF spectra at  $z=5$  mm.

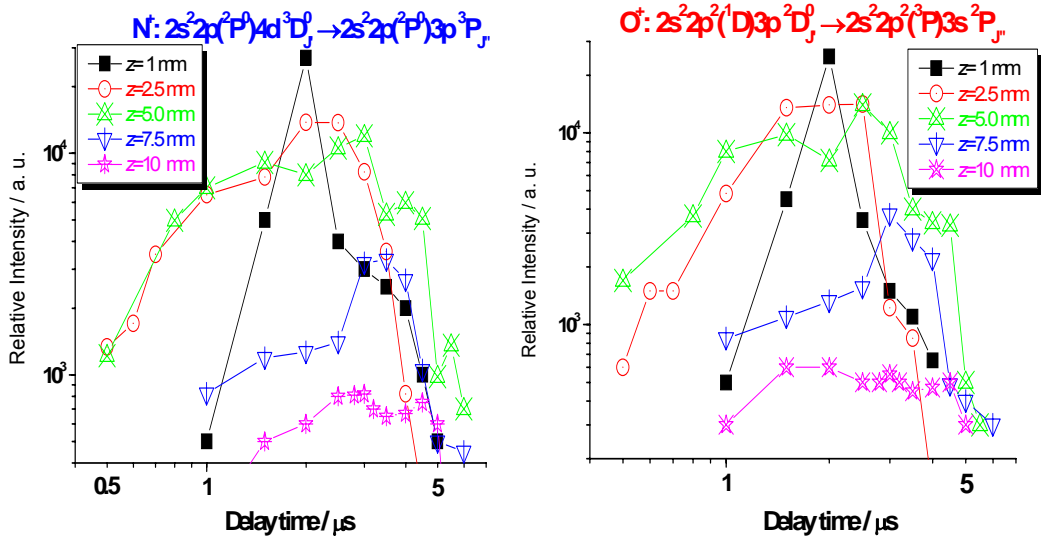


Figure 35. Number density TOF profiles of multiplet structures of  $\text{N}^+$  ( $\sim 2522 \text{ \AA}$ ) and  $\text{O}^+$  ( $\sim 2445 \text{ \AA}$ ) at 1, 2.5, 5, 7.5 and 10 mm as a function of delay time for a laser fluence of  $106 \text{ J/cm}^2$ .

The  $\text{N}^+$  triplet ( $2s^2 2p(^2P^0) 4d \ ^3D_{1,2,3} \rightarrow 2s^2 2p(^2P^0) 3p \ ^3P_{0,1,2}$ ) at  $\sim 2522 \text{ \AA}$  was identified as candidate for electron-density measurements. By substituting the Stark line widths at different time delays in Eqn. (3.12) and the corresponding value of Stark broadening  $W$  ( $0.372 \text{ \AA}$  from Griem [41] at plasma temperature of  $23400 \text{ K}$ ), we obtain the electron density. Figure 37 gives the time evolution of electron density and its first derivative with respect to time by setting the gate width of the intensifier at  $0.5 \text{ \mu s}$ . These values have been obtained by Stark broadening of the  $\text{N}^+$  TOF curves at  $z = 5 \text{ mm}$  and for a laser fluence of  $106 \text{ J/cm}^2$ . The initial electron density at  $0.1 \text{ \mu s}$  is approximately  $1.3 \times 10^{16} \text{ cm}^{-3}$ . Afterwards, the density increases and reaches a maximum ( $1.7 \times 10^{17} \text{ cm}^{-3}$ ) at  $\sim 0.8 \text{ \mu s}$ , and then decrease as the time is further increased. At shorter delay times ( $< 0.1 \text{ \mu s}$ ), the line to continuum ratio is small and the density measurement is sensitive to errors in setting the true continuum level. For times  $> 0.1 \text{ \mu s}$ , the line to continuum ratio is within the reasonable limits and the values of electron density shown in Figure 37 should be reliable. After  $6 \text{ \mu s}$ , the electron density is about  $2.7 \times 10^{16} \text{ cm}^{-3}$ . For a long time  $> 6 \text{ \mu s}$ , subsequent decreased  $\text{N}^+$  emission intensities result in poor signal-to-noise ratios, and there exists a limitation in the spectral resolution. The decrease of  $n_e$  is mainly due to recombination between electrons and ions in the plasma. These processes correspond to the so-called radiative recombination and three-body recombination processes in which a third body may be either a heavy particle or an electron. The electron number density  $n_e$  ( $\text{cm}^{-3}$ ) in the laser induced plasma is governed by the kinetic balance equation 2.10. By considering the discussion reported in section 2.3, the equilibrium condition can be established at  $0.8 \text{ \mu s}$  (dynamical equilibrium) and  $t > 2 \text{ \mu s}$  (stationary equilibrium). For  $t \leq 0.8 \text{ \mu s}$  the ionization prevails while for  $0.8 \text{ \mu s} < t < 2 \text{ \mu s}$  the three-body recombination dominates. In the case of TEA-CO<sub>2</sub> laser at a laser fluence of  $106 \text{ J/cm}^2$  and  $z = 5 \text{ mm}$ , the recombination rate constant estimated is approximately  $5 \times 10^{-28} \text{ cm}^6 \text{ s}^{-1}$  (Eq. 2.11). The recombination time can be determined by the value of the rate constant of the recombination process as  $t_{\text{rec}} = 1/(n_e^2 k_{\text{rec}})$  obtaining  $t_{\text{rec}} \approx 0.4-3 \text{ \mu s}$ .

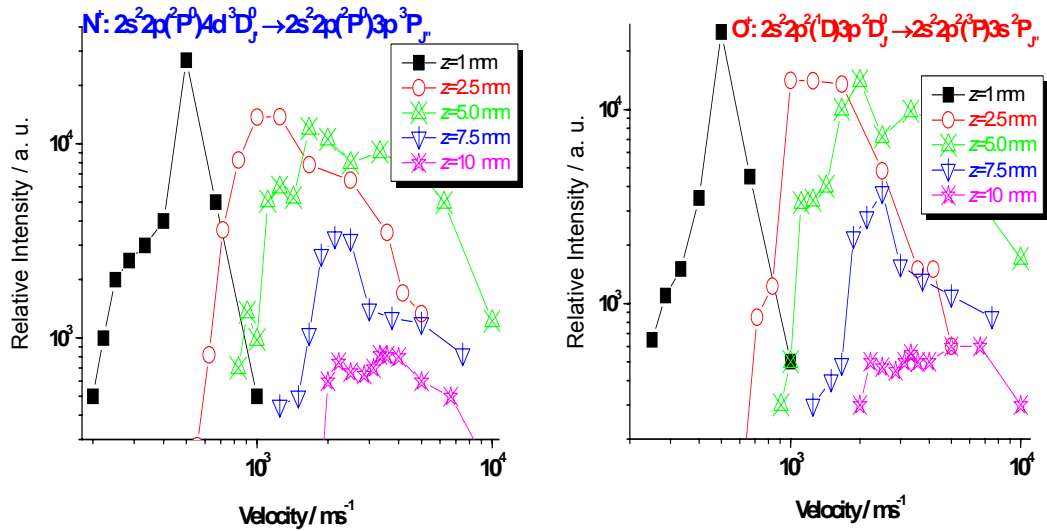


Figure 36. Velocity profiles of multiplet structures of  $\text{N}^+$  ( $\sim 2522 \text{ \AA}$ ) and  $\text{O}^+$  ( $\sim 2445 \text{ \AA}$ ) at 1, 2.5, 5, 7.5 and 10 mm as a function of delay time for a laser fluence of  $106 \text{ J/cm}^2$ .

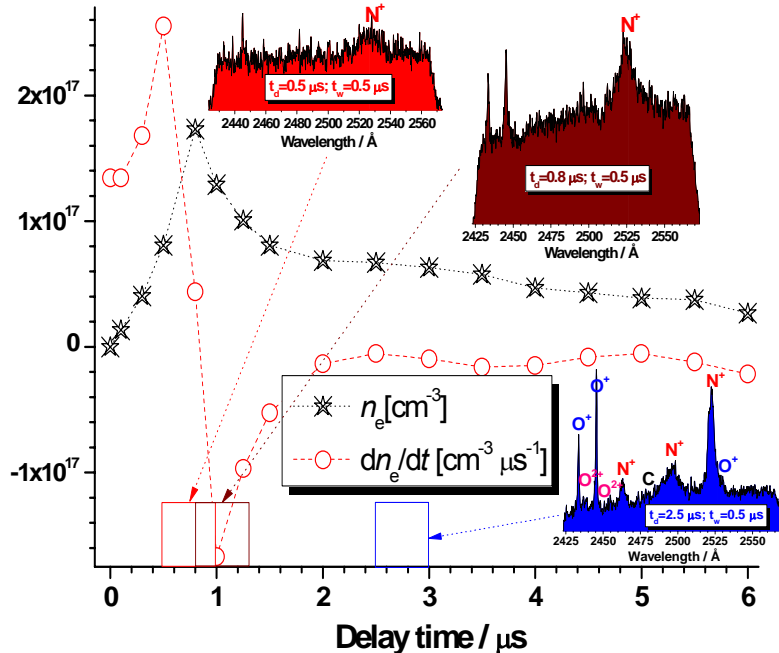


Figure 37. The temporal evolution of electron density  $n_e$  and  $dn_e/dt$  for different delay times from plasma ignition and  $z = 5 \text{ mm}$ . Inset plots illustrate some spectra observed at different delay times.

Optical emission accompanying TEA-CO<sub>2</sub> nanosecond LIB in air is very long lived ( $\sim 20 \mu\text{s}$ ) relative to the average radiative lifetimes of the excited levels that give rise to the observed emission lines. All of the emission lines of N, N<sup>2+</sup>, O, O<sup>+</sup> and O<sup>2+</sup> expected in the 2000-10000  $\text{\AA}$  wavelength range are observed, illustrating that the excited species giving

rise to the optical emission are produced by non-specific mechanism during the TEA CO<sub>2</sub> LIB process. However, a direct excitation-de-excitation mechanism cannot explain the observed emission spectra. Electron impact ionization would explain the emission intensity variation with the time for N, N<sup>+</sup>, N<sup>2+</sup>, O, O<sup>+</sup> and O<sup>2+</sup> species. On the other hand, the formation of the excited molecular species would happen in the gas phase by collisions between atomic or ionic species present in the plume at times far away from the plasma ignition. The emission process at this plasma stage is divided into two different process associated, respectively with the shock formation and the plasma cooling. During the former, the atoms, molecules and ions gushing out from the laser focal region are adiabatically compressed against the surrounding gas. During the latter stage the temperature of the plasma and consequently the emission intensities of atomic lines and molecular bands decrease gradually.

## CONCLUSION

This article reviews some fundamentals of LIBS and some experimental studies developed in our laboratory on N<sub>2</sub>, O<sub>2</sub> and air gases using a high-power IR CO<sub>2</sub> pulsed laser. In this experimental study we used several laser wavelengths ( $\lambda=9.621$  and  $10.591\text{ }\mu\text{m}$ ) and laser intensity ranging from 0.87 to  $6.31\text{ GW cm}^{-2}$ . The spectra of the generated plasmas are dominated by emission of strong atomic, ionic species and molecular bands. For the assignment of molecular bands a comparison with conventional emission sources was made. Excitation, vibrational and rotational temperatures, ionization degree and electron number density for some species were estimated by using different spectroscopic methods. The characteristics of the spectral emission intensities from different species have been investigated as functions of the gas pressure and laser irradiance. Optical breakdown threshold intensities in different gases have been measured experimentally. The physical processes leading to laser-induced breakdown of the gases have been analyzed. Plasma characteristics in LIBS of air were examined in detail on the emission lines of N<sup>+</sup>, O<sup>+</sup> and C by means of time-resolved OES technique. The results show a faster decay of continuum and ionic spectral species than of neutral atomic and molecular ones. The velocity and kinetic energy distributions for different species were obtained from TOF measurements. Excitation temperature and electron density in the laser-induced plasma were estimated from the analysis of spectral data at various times from the laser pulse incidence. Temporal evolution of electron density has been used for the estimation of the three-body recombination rate constant.

## ACKNOWLEDGMENTS

We gratefully acknowledge the support received in part by the DGICYT (Spain) Projects: MEC: CTQ2007-60177/BQU and MEC: CTQ2008-05393/BQU for this research.

## REFERENCES

- [1] Maker, PD; Terhune, RW; Savage, CM. Proc. 3rd Int. Conf. Quantum Electronics; (*Paris: Dunod*) 1963, Vol. 2, 1559.
- [2] Raizer, YP. Breakdown and heating of gases under the influence of a laser beam; Soviet Physics: *Uspekhi*. Vol. 8, Nº 5, 1966.
- [3] Raizer, YP. Laser-Induced discharge phenomena; Consultants Bureau: New York. 1977.
- [4] Bebb, HB; Gold, A. Multiphoton Ionization of Hydrogen and Rare Gas Atoms; Physics of Quantum Electronics; ed P L Kelly et al McGraw-Hill: New York. 1966.
- [5] De Michelis, C. IEEE J. Quantum Electron. 1969, 5, 188-202.
- [6] Morgan, CG. *Rep. Prog. Phys.*, 1975, 38, 621-665.
- [7] Bekefi, G. Principles of Laser Plasma; Wiley: New York. 1976.
- [8] Lyman, JL; Quigley, GP; Judd, OP. Multiple-Photon Excitation and Dissociation of Polyatomic Molecules; Ed. Cantrell, CD. Springer: Berlin., 1980.
- [9] Rosen, DI; Weyl, GJ. *Phys. D. Appl. Phys.*, 1978, 20, 1264-1276.
- [10] Gamal, YE. *EDJ. Phys. D. Appl. Phys.*, 1988, 21, 1117-1120.
- [11] Smith, DC. Laser induced gas breakdown and plasma interaction 38<sup>th</sup> Aerospace Sciences Meeting and Exhibit. *Reno: Nevada.*, 2000.
- [12] Yueh, FY; Singh, JP; Zhang, H. Encyclopedia of Analytical Chemistry (Laser-Induced Breakdown Spectroscopy, Elemental Analysis); ed R A Meyers. Wiley: *Chichester.*, 2000.
- [13] Cremers, DA; Radziemski, LJ. Handbook of Laser-Induced Breakdown Spectroscopy; Wiley: Chichester., 2006.
- [14] Mizolek, AW; Palleschi, V; Schechter, I. Laser-Induced Breakdown Spectroscopy; Cambridge University Press: *Cambridge.*, 2006.
- [15] Singh, JP; Thakur, SN. Laser-Induced Breakdown Spectroscopy; Elsevier:, New York. 2007.
- [16] Yong-Ill, L. Laser Induced Breakdown Spectrometry; Nova Science Publishers: New York 2000.
- [17] Marpaung, AM; Kurniawan, H; Tjia, MO; Kagawa, KJ. *Phys. D. Appl. Phys.*, 2001, 34, 758-771.
- [18] Camacho, JJ; Poyato, JML; Diaz, L; Santos, MJ. *Phys. B: At. Mol. Opt. Phys.*, 2007, 40, 4573-4590.
- [19] Camacho, JJ; Poyato, JML; Diaz, L; Santos, MJ. *Appl. Phys.*, 2007, 102, 103302-10.
- [20] Camacho, J. J; Santos, M; Diaz, L; Poyato, J. M. *L. J. Phys. D. Appl. Phys.*, 2008, 41, 215206-13.
- [21] Camacho, JJ; Santos, M; Diaz, L; Juan, LJ; Poyato, JML. 2009 (Submitted for publication)
- [22] MacDonald, AD. Microwave Breakdown in Gases; Wiley: New York. 1966.
- [23] Raizer, YP. Gas Discharge Physics; Springer: *Berlin, Heidelberg.*, 1991.
- [24] Kopczynski, TL; Bogdan, M; Kalin, AW; Schotwau, HJ; Kneubuhl, FH. *Appl. Phys. B: Photophys. Laser Chem.*, 1992, 54, 526-530.
- [25] Tozer, BA. *Phys. Rev.*, 1965, 137, 1665-1667.

- [26] Radziemski, LJ; Cremers, DA; Laser-induced plasma and applications; New York: Dekker. 1989.
- [27] Gurevich, A; Pitaevskii, L. Sov. Phys. *JETP*., 1962, 19, 870-871.
- [28] Capitelli, M; Capitelli, F; Eletskii, A. Spectrochim. *Acta B*., 2000, 55, 559-574.
- [29] Capitelli, M; Casavola, A; Colonna, G; Giacomo, AD. Spectrochim. *Acta B*., 2004, 59, 271-289.
- [30] Chan, CH; Moody, CD; McKnight, WBJ. *Appl. Phys.*, 1973, 44, 1179-1188.
- [31] Smith, DS; Haught, AF. *Phys. Rev. Lett.*, 1966, 16, 1085-1088.
- [32] Young, M; Hercher, M. *J. Appl. Phys.*, 1967, 38, 4393-4400.
- [33] Barchukov, AI; Bunkin, FV; Konov, VI; Lubin, AA. Sov. Phys. *JETP*, 1974, 39, 469-477.
- [34] Hermann, J; Boulmer-Leborgne, C; Mihailescu, IN; Dubreuil, B. *J. Appl. Phys.*, 1993, 73, 1091-1099.
- [35] Offenberger, AA; Burnett, NH. *J. Appl. Phys.*, 1972, 43, 4977-4980.
- [36] Donaldson, TP; Balmer, JE; Zimmermann, JA. *J. Phys. D: Appl. Phys.*, 1980, 13, 1221-1233.
- [37] Meyerand, RG; Haught, AF. *Phys. Rev. Lett.*, 1964, 13, 7-9.
- [38] Spitzer, L. Physics of Fully Ionised Gases; John Wiley: New York. 1962.
- [39] Hermann, J; Boulmer-Leborgne C; Dubreuil, B; Mihailescu, IN. *J. Appl. Phys.*, 1993, 74, 3071-3079.
- [40] Ready, JF. Effect of high power laser radiation; Academic Press., New York. 1971.
- [41] Griem, HR. Principles of plasma spectroscopy; University Press: Cambridge., 1997.
- [42] Griem, HR. *Phys. Rev.*, 1962, 128, 515-523.
- [43] Huddlestone, RH; Leonard, SL. Plasma Diagnostic Techniques; Academic Press: New York. 1965.
- [44] Hutchinson, IH. Principles of plasma diagnostic; University Press: Cambridge. 2002.
- [45] NIST Atomic Spectra Database online at <http://physics.nist.gov/PhysRefData/ASD/index.html>
- [46] Herzberg, G. Spectra of diatomic molecules; Van Nostrand: New York. 1950.
- [47] Steinfeld, JI. An introduction to modern molecular spectroscopy; MIT Press: London. 1986.
- [48] Bernath, PF. Spectra of atoms and molecules; Oxford University Press: New York. 1995.
- [49] Camacho, JJ; Pardo, A; Martin, E; Poyato, JMLJ. *Phys. B, At. Mol. Opt. Phys.*, 2006, 39, 2665-2679.
- [50] Kovacs, I. Rotational Structure in the Spectra of Diatomic Molecules; Hilger: London. 1969.
- [51] Drogoff, LB; Margotb, J; Chakera, M; Sabsabi, M; Barthelemy, O; Johnstona, TW; Lavillea, S; Vidala, F; Kaenela, VY. Spectrochim. *Acta Part B*., 2001, 56, 987-1002.
- [52] Lofthus, A; Krupenie, PHJ. *Phys. Chem. Ref. Data.*, 1977, 6, 113-307.
- [53] Herzberg, G. Ergeb. Exakten Naturwiss. 1931, 10, 207-284.
- [54] Pannetier, G; Marsigny, GL; Guenebaut, HCR. *Acad. Sci. Paris.*, 1961, 252, 1753-1755.
- [55] Tanaka, Y; Jursa, ASJ. *Opt. Soc. Amer.*, 1961, 51, 1239-1245.
- [56] Meinel, AB. *Astrophys. J.*, 1950, 112, 562-563.
- [57] Ledbetter, JW. Jr. *J. Mol. Spectrosc.*, 1972, 42 100-111.

- 
- [58] Huber, KP; Herzberg, G. Molecular spectra and Molecular structure. IV. Constants of diatomic molecules; Van Nostrand Reinhold: New York. 1979.
  - [59] Laher, RR; Gilmore, FR. *J. Phys. Chem. Ref. Data.*, 1991, 20, 685-712.
  - [60] Gilmore, FRJ. *Quant. Spectrosc. Radiat. Transfer.*, 1965, 5, 369-389.
  - [61] Aguilera, JA; Aragon, C. *Spectrochim. Acta B.*, 2004, 59, 1861-1876.
  - [62] Martin, WC; Zalubas, RJ. *Phys. Chem. Ref. Data.*, 1983, 12, 323-379.
  - [63] Sreckovic, A; Dimitrijevic, MS; Djenize, S. *Astron. and Astroph.*, 2001, 371, 354-359.
  - [64] Alcock, AJ; Kato, K; Richardson, MC. *Opt. Comm.*, 1968, 6, 342-343.
  - [65] Haught, AF; Meyerand, RG; Smith, DC. *Physics of Quantum Electronics*; In P. L. Kelley, B. Lax, & P. E. Tannenwald (Eds.), MacGraw-Hill: New York. 1966. 509.
  - [66] De Michelis, C. *Opt. Comm.*, 1970, 2, 255-256.
  - [67] Ireland, CLM; Morgan, CG. *J. Phys. D: Appl. Phys.*, 1973, 6, 720-729.
  - [68] Aaron, JM; Ireland, CLM. *Morgan, CG. J. Phys. D: Appl. Phys.* 1974, 7, 1907-1917.
  - [69] Phuoc, TX; White, CM. *Opt. Comm.*, 2000, 181, 353-359.
  - [70] Tomlinson, RG; Damon, EK; Buscher, HT. *Physics of Quantum Electronics*; In P. L. Kelley, B. Lax, & P. E. Tannenwald (Eds.), MacGraw-Hill., New York. 1966. 520.
  - [71] Kawahara, N; Beduneau, JL; Nakayama, T; Tomita, E; Ikeda, Y. *Appl. Phys.*, B 2007, 86, 605-614.
  - [72] Zhuzhukalo, EV; Kolomiiskii, AN; Nastoyashchii, AF; Plyashkevich, LN. *J. Quantum Electron.*, 1981, 11, 670-671.
  - [73] Marcus, S; Lowder, JE; Mooney, DL. *J. Appl. Phys.*, 1976, 47, 2966-2968.
  - [74] Kagawa, K; Yokoi, S. *Spectrochim. Acta*, B 1982, 37, 789-795.

## Chapter 14

# MACHINING STEEL XC42 BY HIGH-POWER CONTINUOUS CO<sub>2</sub> LASER (PHYSICAL PROCESS DESCRIPTION, ENERGETIC AND THERMAL MODELING)

***Neila Jebbari<sup>1</sup>, Mohamed Mondher Jebbari<sup>2</sup>, Annie Tarrats-Saugnac<sup>3</sup> and Jean Paul Longuemard<sup>3</sup>***

<sup>1</sup> Faculté des Sciences de Tunis, L.P.M.C., Département de physique,  
Campus Universitaire 2090 Al-Manar, Tunis, Tunisie

<sup>2</sup> Faculté des Sciences de Tunis, Département de Physique,  
Campus Universitaire 2090 Al-Manar, Tunis, Tunisie

<sup>3</sup> Ecole Centrale de Paris, Grande Voie des Vignes 92 295  
Chatenay Malabry Cedex, France

## ABSTRACT

Manufacturers who use laser cutting are interested in the optimization of productivity and the subsequent quality of components made by the laser cutting process. Both aspects are governed by the selection of appropriate laser process parameters. These parameters include laser power, assist gas and cutting speed. The last parameter must be able to provide a good quality of machined components. The inert gas is used to minimize the number of laser process parameters. So, only the absorbed energy by steel  $E_a$  contributes in the machining processes.  $E_a$  depends on power laser, interaction time and absorbed coefficient.

Good quality of components made by the laser cutting process is deduced from groove specific characteristic parameters like the width ( $L_s$ ), the groove depth ( $P_r$ ) and the width of the Thermal Affected Zone ( $Z_{TAZ}$ ).

The condition that must be used to write the energy balance is to fix the adequate assumption. The energy balance will give the theoretical values of the characteristic machining parameters and will permit the evaluation of lost energy if the energy quantity able to create the TAZ is calculated from the resolution of the heat propagation equation.

---

\* E-mail: neila2710@yahoo.fr

## INTRODUCTION

The description of the physical and dynamic nature of the laser cutting process, in the first paragraph, fixes the measured values of the specific characteristic parameters of the groove: the interaction time ( $t_i$ ), the melt-solid interaction time ( $t_{TAZ}$ ) and the laser illuminated surface ( $S_T$ ) considered as heat source.

In the second step, the experimental behavior permits us to determine the values of incidence angles that must be used to calculate the theoretical absorbed coefficient ( $A$ ).

The third paragraph details the experimental results which permitted us to establish how the parameters of machining can act on the parameters of the groove. One can establish the relations driving the groove width with the impact diameter ( $L_S$ ,  $D$ ), the groove depth with the absorbed power ( $P_r$ ,  $E_a$ ) and the TAZ width with the machining parameters.

The last paragraph deals with the evaluation of the part of energy that serves to heat the removed solid volume ( $E_{c_1}$ ), the conduction energy quantity enable us to create the TAZ ( $E_{c_2}$ ) and the energy lost in the medium ( $\Delta E_I$ ).

## DYNAMIC NATURE OF LASER CUTTING PROCESS

The high-power continuous CO<sub>2</sub> laser beam is the machining tool that illuminates the material surface to be machined [1-2]. The used laser wavelength drives the Drude interaction laser-matter, where the main quantity of absorbed energy is converted into heat by photonic effects. So the absorbed laser energy transformed in thermal motion agitates the molecules and warms-up the material. According to the thermal properties of the material, this heat quantity will be diffused toward the material core. Various studies, focused on laser machining [3-12], led to the following dynamic nature of the laser cutting process.

In the first step, when the movement of the beam starts up, the absorbed laser energy increases with the area of the enlightened surface, so the warm-up of the material increases. The temperature of the enlightened surface arise from the ambient temperature  $T_a$  to the merger temperature  $T_f$ . The energy, brought in that way by laser beam, is sufficient to heat and to melt the material [13]. The melted material flows from the surface towards the depth creating the cutting front. The cutting front propagates from the center of the thermal fields with a front speed ( $V_f$ ). The motion of the beam laser, relative to the piece, is called cutting or machining speed ( $V$ ).

After this first step, which one can describe as a transitional mode, appears a periodic and permanent mode.

In fact, the laser lights up two surfaces: the first one, on the top of the piece, has a crescent-like form and the other one, in the lower part, looks like a half inclined cylinder. However, and since the front speed  $V_f$ , is greater than the machining speed  $V$  [4], the surface in crescent form disappears because it is outside the influence of the beam. Then the laser interacts directly with the half inclined cylinder surface form which leads the laser beam to reach the depth  $P_r$ .

The beam progress has constant speed  $V$ , the laser lights-up again the two kinds of surfaces and this process takes place periodically.

In the same manner, to cut or to groove [14-17], one can provide an optimum pressure gas jet to remove the melted piece beneath the laser beam.

The temporal period  $t_i$  of this mechanism corresponds to the duration of time where one point, of the surface, remains illuminated by the laser beam (Figure 1). If  $D$  is the laser beam diameter (impact diameter), taken at the surface of the sample, the temporal period  $t_i$  can be written as:

$$t_i = \frac{D}{V} \quad (1)$$

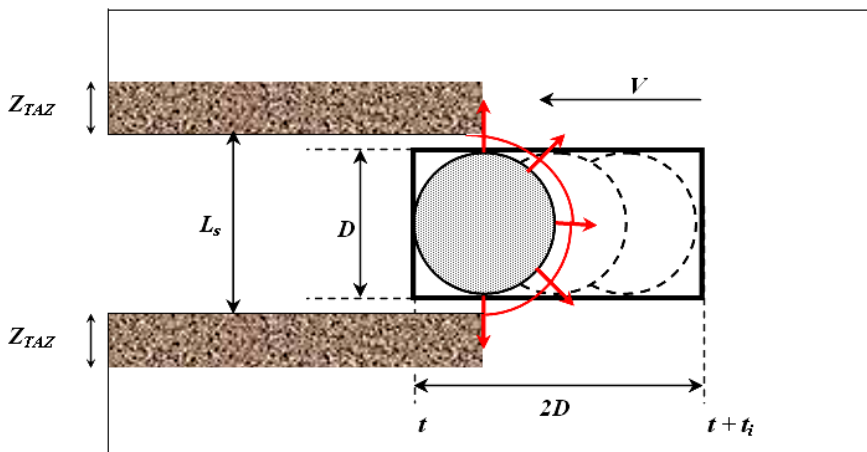


Figure 1. Illuminated surface  $S_T$  during the interaction time  $t_i$  ( $S_T=2D^2$ ).

From the irradiated surface towards the exterior of the sample, the heat propagation on the top of the surface remains isotropic. Then one can consider that the groove width is the same in all directions and the melted surface is bigger than the impact surface.

The second assumption is to consider that the enlightened surface and the energy absorbed by the crescent are superior in the direction of manufacturing than in the extremities which allow uniform streaks to appear at the superior zone level of the internal surface groove (Figure 2).

At this stage, the beam is out of interaction with the superior level of the groove surface; it interacts only with deeper levels and does not act any more on the width of the groove. This assumption can lead us to suppose that the groove width  $L_s$  does not depend on increasing power or decreasing speed, but it must depend only on the impact diameter  $D$  and on the thermal material properties.

The calculation of the absorption coefficient must take account of some assumptions: The laser beam in deeper levels interacts with an inclined surface, so the incidence angle may vary on large range of values (Figure 3). On the other hand, the metallic properties impose the skin effect penetration [18]; the totality of absorption takes place on the surface excluding neither bulk absorption nor transmission. At the interface melt-solid (the inclined surface), the temperature is the same as that of fusion.

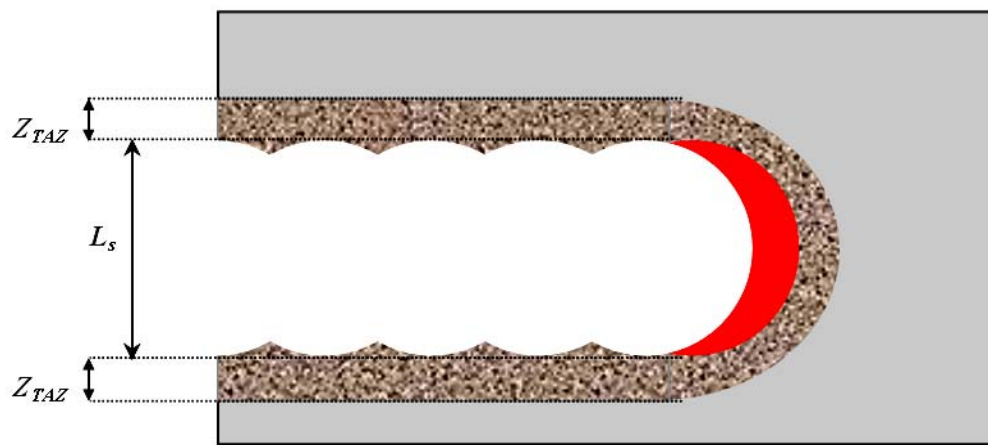


Figure 2. Regularly spaced striations in the upper part of cutting surface (top view)

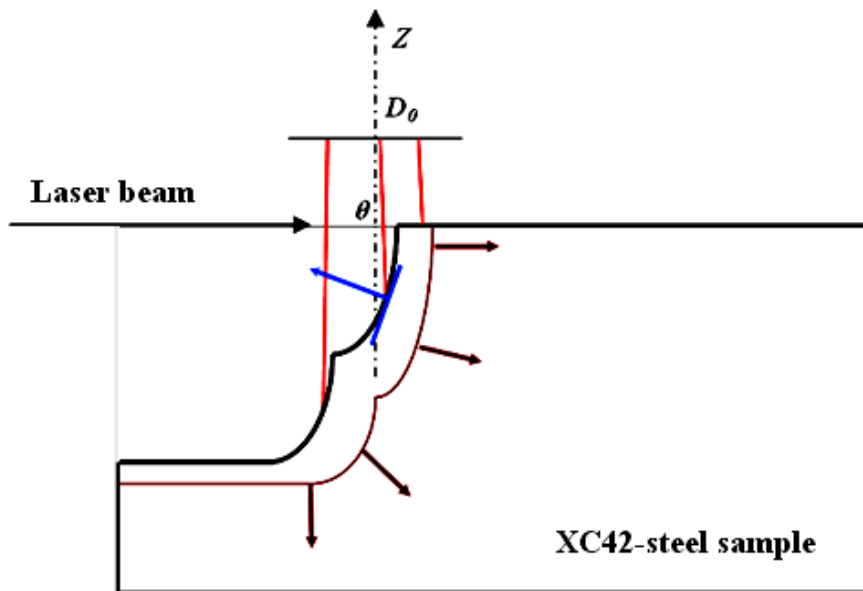


Figure 3. Incidence angle  $\theta$  at each point of the front surface

The machined materials usually present a phase change named thermal affected zone (**TAZ**) which is caused by the dissipated heat in the un-removed material.

The total surface  $S_T$  enlightened by the laser during the time of interaction  $t_i$  (Figure 1) serves to maintain the temperature of the melted front simulated as heat source and it can be supposed equal to:

$$S_T = 2D^2 \quad (2)$$

The principal parameters contributing in the manufacturing mechanism are defined and some of them will be calculated such as the impact diameter D and the average absorption coefficient A. Other parameters like the laser power P or the machining speed V will be fixed according to the needs of user.

The absorbed laser energy E<sub>a</sub> during a temporal period is then written as:

$$E_a = AP \frac{D}{V} \quad (3)$$

This quantity of energy is sufficient to manufacturing a groove characterized by the parameters: L<sub>s</sub>, TAZ and P<sub>r</sub>. Well on for the cut, the optimized thickness e takes place of P<sub>r</sub>.

## IMPACT DIAMETER AND ABSORPTION COEFFICIENT

### Impact Diameter (D)

To determine the values of the waist  $D_0$  and the impact diameter  $D$  at z height, a laser beam is assumed to be Gaussian [7]. The propagation equation solution proves that the Gaussian beam is characterised by a complex curvature ray. The imaginary term contains the impact diameter  $D$  of the laser beam. From the propagation law and according to the shape of the laser resonant cavity, the relation between  $D_0$  and  $D(z)$  is:

$$D = D_0 \sqrt{1 + \left( \frac{4\lambda z}{\pi D_0^2} \right)^2} \quad (4)$$

The resonant cavity of the used laser is constituted in one side by a plan mirror and in the other side by a spherical half-reflecting mirror. This specific shape of the resonant cavity and the **127 mm** focal length lens placed **4 m** behind the cavity makes it possible to determine the value of the waist:  $D_0 = 0.096 \text{ mm}$ .

### Absorption Coefficient (A)

The sample surface is not treated and the maximum intensity attained by the CO<sub>2</sub> continuous laser is lower than critical plasma intensity, it is in the order of  $10^7 \text{ W/cm}^2$ . So this laser can provide just enough energy to melt XC42 steel. In this case the absorbed power A, depends mainly on surface temperature and incidence angle  $\theta$ . The beam, being a Gaussian one, presents some divergence, but this latter is relatively weak to affect the A value. On the other hand the melting front curve which is directly irradiated by the beam is relatively important (Figure 3). To each point of the front surface corresponds an incidence angle  $\theta$  and an absorbing coefficient  $A(T_f, \theta)$ . In a first approximation, one can consider that the absorbing power of the irradiated surface is the average  $\langle A(T_f, \theta) \rangle$ :

$$\langle A(T_f, \theta) \rangle = A = \frac{\sum_{i=0}^{i=n-1} \langle A(T_f, i\Delta\theta) \rangle}{n} \quad (5)$$

with  $(n-1)\Delta\theta = 90^\circ$ .

To calculate the absorption capacity of each of those angles, in the case of metals in infrared wave lengths, it is necessary to calculate the reflection power  $R$  [18-19].

In metallic behavior, absorption takes place over a very low penetration distance and may be assimilated to a surface absorption. One can write:

$$A = 1 - \langle R_p \rangle \quad (6)$$

For XC42-steel obtained average absorption capacity is around of 25%, for a  $p$ -polarization.

## CHARACTERISTIC PARAMETERS OF THE GROOVE OR CUT

### Groove Width ( $L_s$ )

During the grooving process, for several values of  $P$  and  $V$ , the experimental results show that the groove width  $L_s$  remains the same and evolves linearly as a function of impact diameter  $D$  according to the relationship:

$$L_s = \alpha D + \beta \quad (7)$$

Where  $\alpha$  and  $\beta$  are constants depending only on the optical and thermal properties of the material.

For XC42,  $\alpha = 0.8$  and  $\beta = 0.16 \text{ mm}$  [20].

### Thermal Affected Zone Width ( $Z_{taz}$ )

The TAZ are characterized mechanically by micro-toughness and optically by optical microscope [1]. The measurements make it possible to estimate the width of the TAZ at optimal morphology of the groove [21].

The experimental TAZ widths  $Z_{TAZ}$  are measured at the top of the groove and the average values of the  $Z_{TAZ}$  are reported on experimental curves.

Figure 4 represents the evolution of the experimental value of the TAZ width as a function of impact diameter  $D$ .  $Z_{TAZ}$  increases to reach a maximum at  $D = 0.17 \text{ mm}$ , then it decreases toward a limit value. This result confirms the optimization between the interaction time (increasing with  $D$ ) and the laser power density (decreasing with  $D$ ) [20].

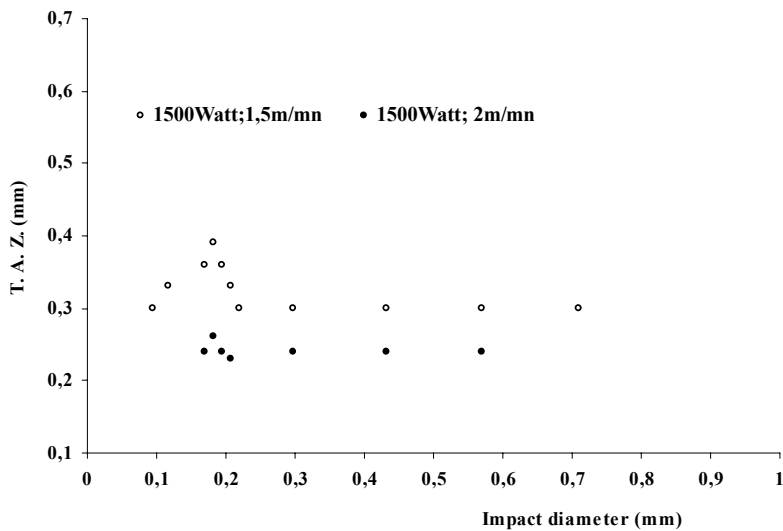


Figure 4. Influence of impact diameter on the Thermal Affected Zone (T.A.Z.)

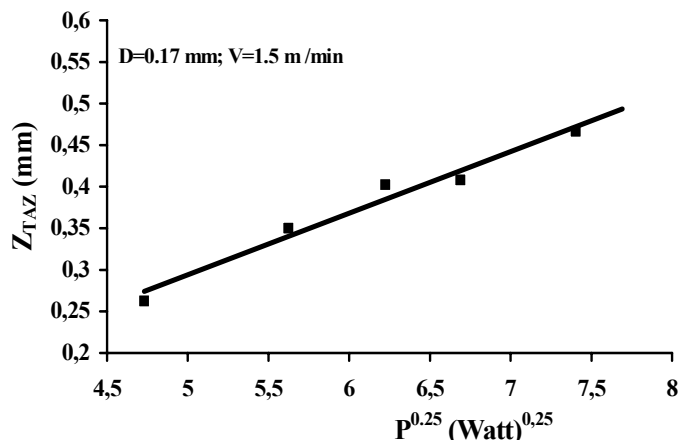


Figure 5. Influence of laser power on the Thermal Affected Zone (TAZ)

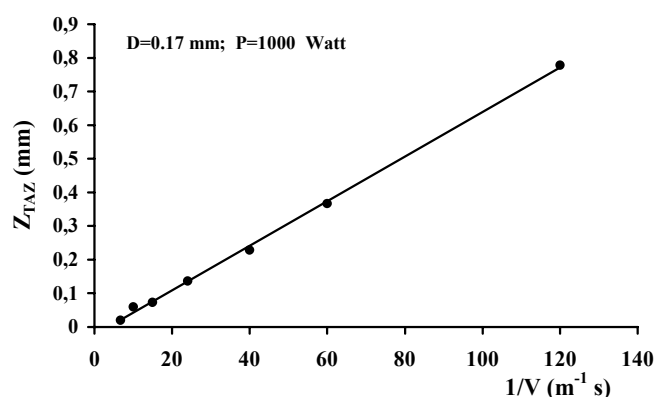


Figure 6. Influence of machining speed on the Thermal Affected Zone (TAZ).

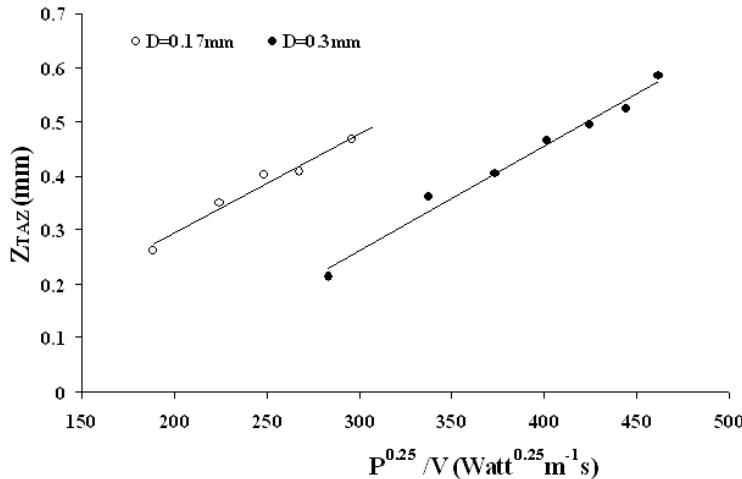


Figure 7. Influence of laser power on the Thermal Affected Zone (TAZ).

These evolutions are repetitive and can be fitted as a function of power and speed parameters. Figure 5 shows that  $Z_{TAZ}$  evolves linearly with  $\sqrt[4]{P}$  and at the same time it is linear with  $V^I$  (Figure 6).

In general, the width of the TAZ evolves as a linear function with  $P^{1/4} \times V^{-1}$  and can be written as:

$$Z_{TAZ} = \gamma \frac{\sqrt[4]{P}}{V} + \delta \quad (8)$$

Figure 7 shows that  $\gamma$  and  $\delta$  depend on impact beam diameter  $D$ .

At optimal value of impact diameter ( $D = 0.17\text{ mm}$ ) and from the fitting curves of the  $Z_{TAZ}$  (Figure 7), it could be deduced that  $\gamma = 0.0012\text{ mm}^{0.75}(\text{Kg s})^{-0.25}$  and  $\delta = 0.027\text{ mm}$ .

During the interaction time  $t_i$ , the laser power melts a preheated volume  $V_f$ . At the same time, the quantity of heat is diffused by conduction from the melted zone to the material core [21]. As a result, the zone having the temperature greater or equal to  $720\text{ }^\circ\text{C}$  will change the structure and will be the TAZ.

Let us suppose that this heat, put down on the surface  $S_T$ , is transferred in the core of the material during the presence of the melted matter, whose temperature is approximately equal to the fusion temperature. The surface  $S_T$  is simulated as the heat source and  $t$  the time of the melted matter maintained on this surface. So,  $t$  can be defined as the interaction time between the melted surface and the solid surface, it is called "melt-solid interaction time".

This heat will be diffused by conduction, perpendicularly to the melted surface  $S_T$ , in the  $Z$  direction. The zone situated between the surface  $S_T$ , with a fusion temperature  $T_f$ , and the parallel surface with the temperature  $T_{TAZ}$ , is called Thermal Affected Zone, defined by the thickness  $Z_{TAZ}$  and the temperature  $T_{TAZ}$ . The general heat equation in the case of a semi-infinite medium is:

$$\Delta T(X, Y, Z, t) - \frac{1}{d} \frac{\partial T(X, Y, Z, t)}{\partial t} = 0 \quad (9)$$

where:

- $T(X, Y, Z, t)$  is the temperature inside the metal,
- $d$  is the thermal diffusivity of the steel.

At the last conditions, using method of changing variables ( $u = \frac{Z}{2\sqrt{dt}}$ ), heat equation

solution is:

$$\frac{T - T_0}{T_f - T_0} = erfc\left(\frac{Z}{2\sqrt{dt}}\right) \quad (10)$$

Where  $t$  is the time needed to keep the front  $Z$  at the temperature  $T$ . If the temperature  $T$  is imposed to be the TAZ temperature ( $T_{TAZ}$ ), the time  $t$  will be defined as the needed time to create the TAZ.

Using the value of the temperature  $T = T_{TAZ} = 720^\circ C$ , for XC42, in relation (10) the interaction time ( $t = t_{TAZ}$ ) between the melted surface and the solid surface can be obtained:

$$\frac{T_{TAZ} - T_0}{T_f - T_0} \approx 0,45 \approx erfc\left(\frac{Z_{TAZ}}{2\sqrt{dt_{TAZ}}}\right) \Rightarrow \frac{Z_{TAZ}}{2\sqrt{dt_{TAZ}}} \approx \frac{1}{2} \Rightarrow Z_{TAZ} \approx \sqrt{dt_{TAZ}} \quad (11)$$

### Melt-Solid Interaction Time ( $t_{TAZ}$ )

To determine the evolution of the melt-solid interaction time  $t_{TAZ}$  the relations (8) and (11) are used. For optimum value of impact diameter  $D=0.17 \text{ mm}$ , deduced value of  $t_{TAZ}$  is equal to:

$$t_{TAZ} = \frac{Z_{TAZ}^2}{d} = \frac{1}{d} \left( 0.0012 \frac{P^{0.25}}{V} + 0.027 \right)^2 \quad (12)$$

To calculate the limit of the TAZ,  $Z_{TAZ}$ , it is more precise to use the melt-solid interaction time  $t_{TAZ}$  in the thermal model. The use of the laser-matter interaction time  $t_i$  to calculate  $Z_{TAZ}$  leads to a divergence with the experimental results.

At this stage, it is interesting to compare the melt-solid interaction time  $t_{TAZ}$  to the laser-matter interaction time  $t_i$  ( $t_i = \frac{D}{V}$ ). To be able to do it, it should be put in mind that the melt-

solid surface  $S_T$  requires to be constant and equal to the sum of illuminated surfaces during the laser-matter interaction  $t_i$  ( $S_T = 2D^2$ ).

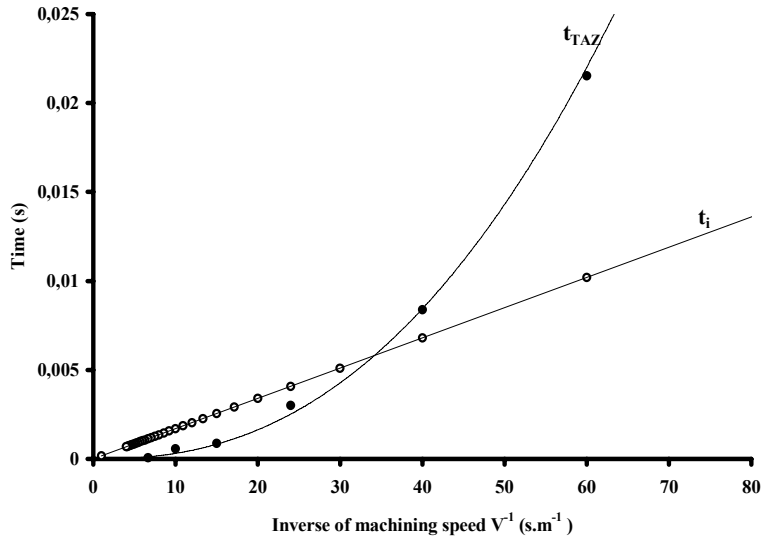


Figure 8. Influence of machining speed on the laser-matter interaction time  $t_i$  and on the melt–solid interaction time  $t_{TAZ}$

Figure 8 shows the evolutions of  $t_i$  and  $t_{TAZ}$  versus the inverse of machining speed  $V$ . At low speed,  $t_{TAZ}$  is higher than  $t_i$ . The low speed implies a big quantity of melted matter, thus this big quantity of melted volume will maintain the surface  $S_T$  in the melt state for a long time (higher than  $t_i$ ). Conversely, at high speed, the melt volume is less important and the surface will stay at fusion temperature for a short time (lower than  $t_i$ ).

## Groove Depth (Pr)

### - Assumptions

In order to model the machining process, it is assumed that:

1. The laser-metal is considered a locally isolated system.
2. During  $t_i$ , the conduction energy  $E_c$  (heating energy) is proportional to the absorbed energy  $E_a$ :

$$E_c = b E_a \quad (13)$$

where  $E_a$  is the unique source of energy.

3. The volume  $V_f$  brought to melting during the interaction time is equal to the product of the groove depth  $P_r$  and the melted surface  $S$  during the interaction:

$$V_f = P_r S \quad (14)$$

where  $S$  is equal to:

$$S = \pi \left( \frac{L_s}{2} \right)^2 \quad (15)$$

4. The energy  $E_f$  required to change the phase of the volume  $V_f$  is:

$$E_f = \rho L_f V_f \quad (16)$$

Where  $\rho L_f$  is the latent melting energy per unit volume [19].

5. The volume brought to melting is locally removed.

#### - Energy Balance

The energy balance must be studied during the interaction time  $t_i$ . The initial state will be defined by the energy already stored, by conduction, in the metal not yet irradiated by the laser beam. Let  $W_i$  be the energy of that state:  $W_i = E_c$

The final state energy  $W_f$  corresponds to the laser energy  $E_a$  brought to the metal minus the quantity  $E_f$  corresponding to the change phase energy:  $W_f = E_a - E_f$ .

The system being isolated, so  $W_f - W_i = 0$ , then:

$$E_c = E_a - E_f \quad (17)$$

Substituting relations (3, 13-16) in (17), the following is obtainable:

$$b = 1 - \frac{\rho L_f \pi \left( \frac{L_s}{2} \right)^2 P_r}{A P \frac{D}{V}} \quad (18)$$

The proportional coefficient  $b$  depends only on the type of material and not on machining parameters. For XC42 these is  $b = 0.86$  [20].

#### - Calculation Of $P_r$

Since  $b$  is independent on machining parameters and remains constant for the same material it is sufficient to determine  $b$ , for any machined material, to deduce previously the depth of the groove. From (7) and (18) one can write:

$$P_r = \frac{(1-b) A P \frac{D}{V}}{\rho L_f \pi \left( \frac{\alpha D + \beta}{2} \right)^2} \quad (19)$$

## MODELING THE CONDUCTION ENERGY ( $E_c$ )

From the energy balance model [20], the characteristics of the groove related to the machining parameters have been obtained. In this paper, the heat suitable model is added in order to calculate the predicted TAZ width which will be compared to the experimental results.

In the case of machining laser, the time of interaction being very short (some milliseconds) and the heat would not have the time to be dissipated in the air. The convection is slower than conduction so, owing energy lost by convection, the conduction energy  $E_c$  dissipated, deduced from energetic balance, is distributed in three quantities  $E_{c_1}$ ,  $E_{c_2}$  and  $\Delta E_l$ :

$$E_c = E_{c_1} + E_{c_2} + \Delta E_l \quad (20)$$

- $E_{c_1}$  is the energy that serves to heat the part of solid volume, that would be removed, from the ambient temperature  $T_\theta$  to the fusion temperature  $T_f$ :

$$E_{c_1} = \int_{T_\theta}^{T_f} \rho(T) V_f C(T) dT \quad (21)$$

where  $\rho(T)$  is the specific mass and  $C(T)$  the specific capacity.

For  $T_\theta = 20^\circ\text{C}$  and  $T_f = 1500^\circ\text{C}$ ,  $E_{c_1} = 9.08 \cdot 10^9 V_f$  (Joule) is obtained.

- $E_{c_2}$  is the energy dissipated in the metal helping to create the TAZ. The energy  $E_{c_2}$  can be imposed to be the quantity  $Q$  of heat, diffused by conduction from the melted surface to the core:

$$E_{c_2} = Q \quad (22)$$

The quantity  $Q$  is detailed and calculated in the next section

- $\Delta E_l$  is the lost energy. This quantity of energy is supposed to be a part of energy  $E_a$  dissipated in the evacuated melted matter.

## Required Energy $E_{c_2}$ to Create the Taz

The density  $\Phi$  of heat flux and the quantity  $Q$  of heat traversing surface  $S_T$ , during the time  $t$ , and causing the TAZ are equal to:

$$\Phi(z = 0, t) = \frac{K(T_f - T_\theta)}{\sqrt{\pi t d}} \quad (23)$$

$$Q(z = 0, t) = \frac{S_r 2K(T_f - T_\theta)}{\sqrt{\pi d}} \sqrt{t} \quad (24)$$

where  $K$  is the thermal conductivity.

Using the relations (2), (11), (24) and ( $\frac{K}{d} = \rho C$ ), the following is reached:

$$E_{c_2} = Q(z = 0, t) = \frac{4 \rho C (T_f - T_\theta)}{\sqrt{\pi}} D^2 Z_{TAZ} \quad (25)$$

## Lost Energy ( $\Delta E_l$ )

The following relation is used to calculate  $\Delta E_l$ :

$$\Delta E_l = E_c - E_{c_1} - E_{c_2} = bE_a - \int_{T_\theta}^{T_f} \rho(T) V_f C(T) dT - Q \quad (26)$$

The bigger quantity of lost energy is observed at higher power and increases with the machining speed (Figure 9). This is in well agreement with dissipated energy phenomena where the high power yields to put high quantity of energy in the system. Some quantity of this energy is stored in the melted volume before being evacuated.

In the grooving experiments, the melted volume flows out in the bottom of the groove and cuts a channel with a characteristic evacuated length  $l_e$ . In fact, a part of the called lost energy  $\Delta E_l$  serves to further deepen the groove.

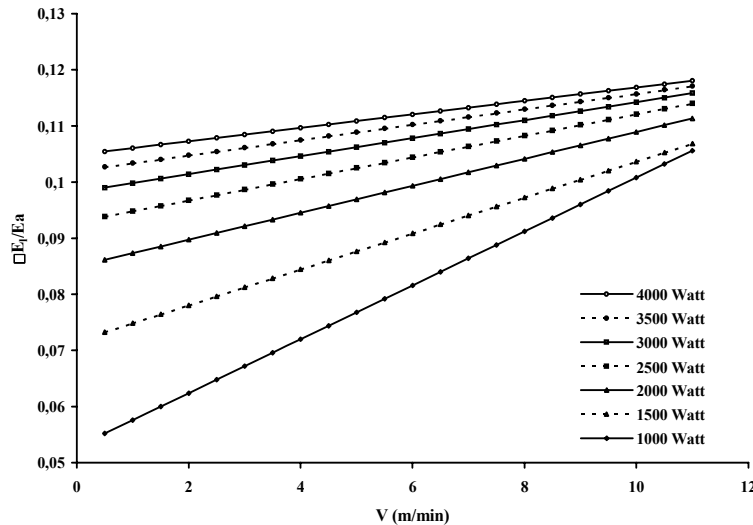


Figure 9. Influence of machining speed on the lost energy

Figure 9, represents the evolution of the ratio  $\Delta E_l/E_a$  versus the machining speed  $V$ . For any power the curves are linear but the slope  $\kappa$  decreases with increasing power (Table 1):

$$\frac{\Delta E_l}{E_a} = \kappa V + \mu \quad (27)$$

where  $\kappa$  and  $\mu$  depend on the laser power  $P$ . For  $D = 0.2 \text{ mm}$  the following is obtained:

$$\kappa = 4.8 P^1 (s m^{-1}) \text{ and } \mu = 5.5 10^{-3} P^{0.5} - 4 10^{-5} P - 0.081$$

**Table 1. Effect of laser power on slope curve of equation:  $\frac{\Delta E_l}{E_a} = \kappa V + \mu$**

P (Watts)	1000	1500	2000	2500	3000	3500	4000
$\kappa$ (min /m)	0.0048	0.0032	0.0024	0.0019	0.0016	0.0014	0.0012
$\mu$	0.0528	0.0717	0.0849	0.0929	0.0982	0.102	0.1049

## CONCLUSION

This chapter clarified some laser machining mechanisms. We used an energetic model, considering the system to be locally isolated and assuming that the laser beam interacts with a preheated surface during the laser–matter interaction time. The absorbed power melts a part of the material and preheats the part that would be manufactured during the following interaction time.

The proposed dynamic of the machining processes explain the experimental results. The coherence between experimental and theoretical results is available only at optimal

conditions. In fact the relationship (19) shows the evolution of the depth of the groove as a function of three parameters: the laser beam power, the machining speed and the impact diameter.

On the basis of this relationship, the depth  $P_r$  depends on interaction time ( $t_i = \frac{D}{V}$ ) and on power density  $(\frac{P}{(\alpha D + \beta)^2})$ . So the depth  $P_r$  passes by a maximum when the impact diameter  $D$  is equal to the ratio  $\beta/\alpha$ . This ratio is the optimal value of the impact diameter to obtain the best parameters of the groove with minimum of laser energy.

Experimentally at normal incidence, when value of impact diameter is equal to the waste  $D_\theta$  (focus beam), one obtains non parallel cut walls and non repetitive groove characteristics. This result is basically due to the feed-back effect (return by reflection of a part of the beam into the resonant cavity). For greater diameters, the lost convection energy is more important and one cannot neglect it in the energetic model [20].

To calculate the width of the TAZ ( $Z_{TAZ}$ ), it is more precise to use the melt-solid interaction time ( $t_{TAZ}$ ) in the thermal model than to use the interaction time ( $t_i$ )

If the gas used to remove the melted matter is oxygen, an extra energy ( $E_{ex}$ ) due to the metal oxidation appears to be a major component in the process. For this reason, writing the energy balance according to the appropriate assumptions will permit the calculation of the new characteristic parameters of the groove. So the effect of the extra energy due to the oxidation must be taken into consideration.

## REFERENCES

- [1] Steen, W.M. *J Opt A: Pure Appl Opt*, 2003, 5, S3–7.
- [2] Ciofini, M.; Lapucci, A.; Lolli, S. *J Opt A: Pure Appl Opt* 2003, 5, 186–191.
- [3] Arata, Y.; Maruo, H.; Miyamoto, I.; Takeuchi, S. *Proceedings of symposium on electron and ion beam science and technology*, Washington, 1986, 111–128.
- [4] Yuan, S. *PhD thesis*, Institut National des Sciences appliquées de Lyon, 1989.
- [5] Arata, Y.; Maruo, H.; Miyamoto, I.; Takeuchi, S. *Trans JWRI*, 1979, 8, 15–26.
- [6] Arata, Y.; Maruo, H.; Miyamoto, I.; Takeuchi, S. *Trans JWRI*, 1981, 10, 129–39.
- [7] Vannes, A.B. *Laser et industrie de transformation; Technique et documentation*; Lavoisier: Paus, 1986, 225.
- [8] Kogelnik, H.; T.L.I.: *Appl Opt*, 1966, 5.
- [9] Jebbari, N.; Tarrats-Saugnac, A.; De Contencin, F.X. *OPTO*, 1992, 536.
- [10] Jebbari, N.; Tarrats-Saugnac, A.; Melhaoui, A. *Mécanique Industrielle et Matériaux*, 1995, 48, 232
- [11] Jebbari, N.; Tarrats-Saugnac, A. *Mécanique et optique*; I.S.L., Saint Louis, 25 April 1995
- [12] Chrissolouris, G. *Laser Machining – Theory and practice*; Springer: Berlin, Heidelberg, 1991
- [13] Pantelis, D. *Techniques de l'ingénieur, traité généralités A 1 095*, 1–18.

- 
- [14] Kamalu, J.N.; Steen, W.M. *Lasers in metallurgy, held at the 110<sup>th</sup> American institute of mining, metallurgical and petroleum engineers (AIME) annual meeting*, Chicago, IL, 1981, 263–77
  - [15] Adams, M.J. *Proceedings of conference on advanced in welding processes*; Abington, Cambridge, UK: Welding Institute; 14–16 April 1971. p. 140–146.
  - [16] Babenko, V.P.; Tychinskii, V.P. *Sov J Quantum Electron*, 1973, 2, 399
  - [17] Kechmair, D. *PhD thesis*, Université de Paris — Sud centre d'Orsay, 1989.
  - [18] Born, M.; Wolf, E. *Principles of Optics*, 5th edition; Pergamon Press: Oxford, 1975
  - [19] *Metals handbook*; ninth edition —Volume 2—Properties of pure metals. 741–759.
  - [20] Jebbari, N.; Jebbari, M.; Ahdad, F.; Tarrats-Saugnac A.; Longuemard, J.P. *Appl Phys B*, 2000, 70, 99–103
  - [21] Jebbari, N.; Jebbari, M.M.; Saadallah, F.; Tarrats-Saugnac, A.; Bennaceur R.; Longuemard, J.P. *Opt. Laser Technol.* 2008, 40, 864–873.

# INDEX

## A

- abortion, 74  
absorption coefficient, 260, 261, 262, 265, 428, 503, 505  
acceleration, vii, 44, 65, 67, 81, 95, 99, 112, 115, 124, 125, 126, 166, 339, 347, 374, 433, 491  
accelerator, 112, 124, 127, 342  
accidental, 14  
accidents, 358  
accounting, 71, 74  
accuracy, 2, 68, 80, 177, 197, 238, 245, 266, 279, 324, 353, 355, 361, 363, 418  
acetone, 227, 237, 249, 339  
acid, 184  
ACM, 93  
acoustic, 50, 54, 132, 207, 399, 409, 410, 411, 445  
acoustical, 326, 328  
actuators, 207, 384  
adaptation, 385  
adhesion, 34, 63, 212, 339, 342, 343, 347, 380, 387  
adiabatic, 23, 58, 106, 430  
adjustment, 200  
adsorption, 209, 219, 238, 239, 240, 241, 321  
AFM, 176, 177, 180, 181, 183, 184, 186, 187, 188, 189, 190, 191, 192, 193, 194, 195, 196, 197, 198, 199, 207  
aggregates, 321  
aggregation, 318  
aid, 209, 227, 442, 481  
AIP, 91, 92, 209, 210, 214, 222, 348  
Albert Einstein, 96  
alcohol, 227, 339  
  
algorithm, 26, 49, 50, 51  
alkali, 328  
alkaline, 176  
alloys, 86, 88, 247, 368, 380  
ALS, 354, 355, 356, 357, 358, 361, 362, 363, 364, 366  
alternative, viii, 66, 96, 159, 161, 332, 383  
alters, 376  
aluminium, 375, 376, 380  
aluminum, 39, 41, 42, 238, 247, 248, 289, 323, 334  
ambient air, 161, 165, 467, 471, 476, 481  
amendments, 346  
ammonia, 1, 237, 326  
amorphization, 35  
amorphous, 193, 195, 197, 332, 338  
amplitude, 17, 29, 38, 39, 99, 106, 108, 132, 135, 139, 145, 152, 170, 172, 173, 401, 402, 403, 411  
Amsterdam, 157, 158  
analog, 99, 151  
analytical models, 260  
angular momentum, 438, 439, 478, 479  
anisotropy, 140  
annealing, 208, 223, 247, 261, 274, 275, 276, 277, 279  
Annealing, 86, 88  
anode, 284, 285, 288, 291, 294, 299, 301, 302, 303, 333, 335, 336, 337, 339, 340, 343, 344  
anomalous, 100  
ANOVA, 375  
appendix, 64  
aqueous solutions, 210, 213  
argon, 212, 218, 220, 223, 287  
argument, 38, 199  
arsenide, 192, 440  
ASD, 499  
ASI, 157  
Asia, 380  
aspect ratio, 161, 185  
assessment, 365, 372  
assignment, 438, 456, 459, 461, 467, 471, 472, 476, 477, 479  
assumptions, 17, 19, 34, 46, 68, 96, 323, 374

- asymptotically, 110  
atmosphere, 209, 210, 213, 214, 215, 218, 219, 220,  
  222, 225, 226, 228, 229, 230, 232, 287, 314, 324,  
  325, 326, 354, 375, 421, 427, 465, 477, 484  
atmospheric pressure, ix, 283, 284, 285, 425, 428,  
  430, 440, 442, 465, 467, 471, 476, 478, 480, 481,  
  483, 484  
atomic force microscopy (AFM), 85, 89, 207  
atomic positions, 30, 57  
attachment, 339, 422, 423, 424, 425, 426  
attribution, 468  
Au nanoparticles, 218  
Australia, 353, 366  
Austria, 354  
automatic scanning, 353  
averaging, 49, 69, 109, 122, 123, 129, 138, 140, 152,  
  316, 484  
Avogadro number, 317, 319  
avoidance, 368
- B**
- back, 9, 12, 56, 57, 58, 59, 65, 68, 112, 132, 164,  
  180, 184, 354, 364, 429, 443, 444  
backscattered, 227  
backscattering, 349  
band gap, 38, 75  
bandwidth, 163  
barrier, 112, 288, 299, 301, 302, 303, 304, 305  
baths, 227  
BCS theory, 150  
behavior, ix, 12, 17, 20, 28, 39, 40, 43, 77, 172, 180,  
  220, 228, 233, 234, 239, 245, 247, 256, 261, 271,  
  272, 417, 461, 481, 502  
bell, 297  
bell-shaped, 297  
bending, 33, 44, 245, 246, 247, 248, 249, 250, 251,  
  252, 253, 254, 255, 256, 257, 258, 259, 260, 261,  
  262, 263, 264, 266, 267, 268, 270, 271, 272, 273,  
  274, 275, 276, 277, 279, 280, 339, 439  
Bessel, 38  
bias, 213  
binding, 138, 142, 153, 206, 461  
binding energy, 138, 142, 153, 206, 461  
binomial distribution, 114, 116, 137  
biocompatibility, 206  
biocompatible, 208  
biomedical applications, 208  
biophysics, 2  
biosensors, 208  
black body, 117, 142  
blocks, 275  
Bohr, 142, 153, 157, 432  
boiling, 15, 19, 188, 316, 321  
Boltzmann constant, 431  
Boltzmann distribution, 138  
bonding, 78, 376  
bonds, 30, 80, 141, 316, 317, 318, 319, 324  
boreholes, x, 351, 355, 361, 362, 363, 364  
Bose, 4, 129, 138, 139, 152, 154, 155  
Bose-Einstein, 4, 138, 139, 152, 154, 155  
bosons, 479  
boundary conditions, 12, 26, 27, 33, 48, 51, 54, 56,  
  59, 60, 63, 169, 172, 173, 302, 374  
bounds, 326, 327  
branching, 170  
breakdown, xi, 176, 183, 289, 294, 296, 306, 309,  
  415, 416, 417, 418, 419, 420, 421, 422, 423, 424,  
  425, 426, 427, 428, 429, 430, 434, 440, 442, 444,  
  467, 476, 481, 483, 484  
bremsstrahlung, 97, 420, 433  
broadband, 183  
bubble, 326, 327  
bubbles, 326, 328  
buffer, 196, 209, 215, 224, 291, 301  
buildings, 352, 354  
butane, 237
- C**
- CAD, x, 246, 351, 360, 368  
cadmium, 287  
calcium, 287  
calibration, 261, 262, 265, 266, 267, 443  
CAM, 368  
Canada, 353  
capacitance, 285, 297  
capillary, 116  
carbon, 208, 237, 247, 248, 249, 326, 346, 416, 439,  
  444, 485, 491  
carbon dioxide, 326, 416, 439, 444  
carbon film, 346  
carbon monoxide, 237  
carbon nanotubes, 208  
carrier, 73, 74, 75, 76, 77, 81, 237, 369, 370, 372  
casting, 368  
catalyst, 208, 209, 213, 217, 218, 221, 223, 225, 227  
cathode, x, 285, 294, 301, 302, 303, 304, 306, 331,  
  336, 339, 340, 341, 343, 344, 347, 349, 443, 448  
cation, 209, 446  
cavitation, 326, 328, 445  
cavities, x, 207, 332, 334, 351, 352, 353, 354, 355,  
  358, 359, 361, 363, 364, 365  
CEA, 157  
cell, 9, 26, 27, 28, 36, 48, 49, 50, 52, 59, 61, 63, 65,  
  68, 69, 71, 79, 80, 82, 163, 407, 442, 444, 472,  
  478, 481  
ceramic, 209, 215, 217

- CH4, ix, 313, 325, 326  
channels, vii, 7, 9, 95, 96, 105, 138, 314, 320, 324, 411  
charge density, 302  
charged particle, vii, 95, 99, 137, 349, 428, 433  
chemical bonds, 143  
chemical reactions, 166, 212, 291, 314, 326, 328  
chemical stability, 206  
chemical vapor deposition, 210  
chemiluminescence, 315  
Chile, 366  
China, x, 218, 219, 224, 351, 353, 354, 364, 365, 380  
cholesterol, 237  
cladding, x, 248, 367, 368, 369, 370, 371, 372, 373, 374, 375, 376, 378, 379, 380  
cladding layer, 375, 376  
classical, vii, 3, 6, 8, 19, 26, 29, 47, 55, 60, 80, 95, 101, 106, 114, 115, 117, 118, 123, 127, 128, 133, 134, 139, 213, 225, 316, 420, 421, 433, 483  
cleaning, x, 208, 331, 333, 335, 336, 337, 339, 340, 342, 343, 344, 347  
cleavage, 385, 388  
clouds, ix, 313, 314, 325  
clusters, 26, 50, 108, 213, 228, 229, 232, 318, 323, 325  
coal mine, 364, 365  
coatings, ix, 167, 175, 176, 182, 183, 211, 331, 332, 333, 334, 335, 337, 339, 340, 342, 343, 344, 347, 349, 375, 376  
coherence, 133, 163  
cohesion, 275  
collisions, 4, 5, 18, 36, 37, 38, 39, 145, 151, 155, 212, 230, 286, 287, 291, 293, 307, 422, 425, 427, 428, 435, 479, 481  
colors, 178  
combined effect, 279, 422, 423  
combustion, 419, 430  
communication, 384  
compatibility, 119  
competition, 113, 228, 232  
complement, 15  
complexity, 55, 68, 246, 258, 335, 353, 457, 468  
compliance, 338  
complications, vii, 95, 112  
components, x, 33, 59, 103, 116, 131, 138, 149, 211, 232, 248, 294, 295, 298, 346, 369, 380, 383, 385, 402, 433, 436  
composites, 247  
composition, ix, 116, 148, 166, 199, 212, 227, 331, 332, 335, 339, 342, 343, 346, 347, 356, 375, 376, 377, 431, 437, 465, 469  
compounds, 213, 326  
comprehension, 131  
Compton scattering, 112, 125  
computation, 137  
computer simulations, 182  
computing, 406, 426  
concentration, 65, 150, 238, 239, 240, 291, 326, 328, 343, 344, 346, 384, 402, 422, 423, 425  
conception, 96, 130, 155, 285  
concordance, 114, 117  
concrete, 106, 323  
condensation, ix, 139, 154, 155, 208, 313, 314, 316, 317, 319, 321, 322, 323, 324, 325, 326  
condensed media, 153  
conductance, 237  
conductivity, 3, 10, 11, 12, 14, 15, 16, 17, 29, 50, 77, 138, 148, 149, 151, 162, 174, 190, 280, 315, 374, 513  
configuration, 44, 45, 168, 192, 193, 194, 195, 197, 198, 250, 254, 270, 392, 411, 432, 440, 442  
confinement, 8, 15, 29, 46, 55, 60, 64, 65, 67, 327  
conformity, 120, 136, 137, 151, 328  
conjecture, 106  
conjugation, 164, 165  
conservation, 32, 37, 38, 51, 76, 80, 113, 114, 127, 129, 132, 133  
construction, 232, 352  
construction sites, 352  
consumption, 63, 351  
continuity, 169, 301, 342, 374, 422  
contracts, 246  
control, ix, 39, 51, 76, 148, 149, 165, 200, 245, 248, 313, 314, 326, 328, 332, 334, 347, 353, 358, 366, 369, 371, 394, 431  
convection, 374, 408, 411, 412, 413, 512, 515  
convective, 44  
convergence, 96, 105, 108, 111  
conversion, 166, 207, 291, 298, 300, 306, 315, 354  
conversion reaction, 291  
convex, 275, 276  
cooling, 4, 14, 34, 40, 41, 42, 43, 55, 64, 66, 67, 81, 82, 132, 245, 246, 248, 249, 256, 261, 263, 265, 266, 268, 287, 443  
Cooper pairs, 149  
correlation, 28, 29, 55, 65, 143, 147, 150, 153, 248, 256, 259, 279, 316, 327, 411  
correlation analysis, 411  
correlation function, 28, 29  
correlations, 28, 29, 138, 139, 140, 141, 142, 143, 144, 148, 155, 314, 321  
corrosion, 367, 375, 376  
cosine, 338  
cosmic rays, 421  
cost-effective, 176  
costs, x, 245, 248, 351, 367

- Coulomb, 38, 39, 79, 80, 100, 125, 131, 140, 153, 293, 425, 428, 431, 433
- Coulomb interaction, 39, 79, 80, 140, 425, 428
- coupling, 4, 5, 8, 9, 10, 15, 16, 17, 36, 41, 43, 47, 48, 49, 50, 51, 54, 55, 60, 61, 79, 207, 246, 368, 389, 438, 477, 479
- covalent, 80
- covalent bond, 80
- covalent bonding, 80
- CPU, 37
- crack, 46, 70, 91
- cracking, 220, 416, 481
- CRC, 308, 329, 380, 412
- critical density, 322, 425, 428, 429
- critical points, 144
- critical temperature, 142, 143, 322
- cross-sectional, 234, 355
- crystal lattice, 59
- crystal structure, 6, 30, 31, 63, 79, 80, 235
- crystalline, 28, 31, 56, 57, 58, 60, 64, 65, 191, 195, 197, 212, 275
- crystallites, 65, 66, 219
- crystallization, ix, 20, 66, 313, 314, 315, 317, 319, 323, 324, 325, 326, 328, 329
- crystals, viii, 36, 46, 145, 159, 160, 175, 183, 208, 218, 222, 224, 229, 232, 234, 315, 326, 349
- curing, 385
- CVD, 209
- cycles, 227, 268, 273
- cyclotron, 433
- D**
- damping, 145
- danger, 360
- data analysis, 28, 180
- data processing, 358
- database, 378, 379
- debates, 6, 19
- decay, xi, 43, 100, 105, 298, 319, 392, 415, 434, 464
- decisions, x, 331
- decomposition, 19, 96, 97, 100, 101, 103, 105, 106, 108, 109
- deduction, 108, 155
- defects, 35, 59, 199, 236, 237, 387, 390
- deficiency, 98, 212
- definition, vii, 10, 37, 48, 50, 69, 71, 73, 95, 97, 102, 117, 121, 131, 134, 137, 138, 139, 140, 143, 144, 145, 151, 258, 260, 335, 372, 380, 424, 484
- deformation, 8, 29, 32, 45, 46, 61, 64, 65, 67, 71, 77, 81, 246, 247, 248, 258, 261, 263, 266, 270, 272, 273, 277
- degenerate, 152, 439
- degenerate electron gas, 152
- degradation, 339
- degree of crystallinity, 31
- degrees of freedom, 112, 114, 116, 117, 479
- delocalization, 148
- density fluctuations, 30
- deposition rate, 227
- deposits, 209
- derivatives, 154
- desorption, 89, 227
- destruction, 64, 167, 188, 189, 335, 387, 390
- detachment, 124
- detection, x, 228, 326, 351, 352, 353, 354, 355, 356, 358, 361, 363, 364, 365, 366, 393, 418, 437, 443, 477, 484
- detection techniques, 352, 353
- detonation, 420, 429, 430, 444
- deviation, 28, 32, 40, 42, 166, 167, 358, 407, 409, 411
- DFT, 35, 36, 37, 79, 80
- diamond, viii, 160, 162, 185, 190, 192, 200, 211
- diamond grains, 191
- diamonds, 56, 57, 59, 60, 162, 190, 192, 200
- diaphragm, 164, 335, 340, 341, 442, 456
- dielectric constant, 428
- dielectrics, 3, 37, 322, 385
- differential equations, 9, 39
- differentiation, 318
- diffraction, viii, 6, 44, 97, 164, 176, 177, 179, 180, 185, 205, 235, 275, 280, 384, 401, 402, 419, 442
- diffusion, 5, 9, 36, 47, 48, 51, 61, 62, 73, 74, 75, 166, 188, 194, 195, 228, 232, 287, 301, 302, 368, 375, 376, 422, 423, 424, 425, 426, 427, 482
- diffusion process, 61, 73, 74, 232
- diffusion time, 232
- diffusivities, 301
- diffusivity, 55, 259, 280
- dimensionality, 206
- dimer, 297, 298, 307
- diode laser, ix, 245, 246, 248, 249, 250, 279, 368, 380
- diodes, 207, 288, 289
- dipole, 79, 110, 141, 143, 145, 146, 314, 315, 316, 318, 319, 321, 322, 327
- dipole moment, 141, 145, 146, 315, 316, 318, 321, 322, 327
- dipole moments, 146, 315, 316, 318, 322
- disaster, 353
- discharges, 284, 285, 286, 288, 305, 306, 307, 335, 445, 479
- discretization, 9, 28, 48, 49, 50, 52
- dislocation, 64, 275, 321
- dispersion, 39, 79, 98, 100, 101, 128, 131, 132, 133, 151, 154, 219, 375, 384, 427

displacement, 65, 129, 254, 262, 263, 266, 268, 270, 271, 272, 273, 274, 411  
dissociation, 119, 232, 236, 284, 425, 480  
distortions, 59, 60, 409  
distribution function, 7, 37, 38, 39, 40, 42, 75  
divergence, 116, 164, 332, 334, 402, 419, 424, 426, 442, 456  
division, 117, 125, 130, 411  
donor, 235  
doped, 207  
Doppler, 125, 126, 291, 434, 463, 492  
drying, 208

**E**

earth, 421  
eating, 286, 307  
elaboration, 71, 73  
elastic deformation, 32, 65  
elasticity, 68, 339, 343  
electric field, 38, 39, 137, 284, 286, 290, 292, 296, 301, 306, 418, 419, 420, 422, 425, 435, 442, 456, 479  
electrical breakdown, 148  
electrical conductivity, 138, 151  
electrical properties, 208  
electrical resistance, 237  
electricity, 3, 207  
electrodeposition, 210  
electrodes, 289, 296, 297, 299, 303, 419  
electromagnetic, 1, 98, 104, 127, 138, 140, 141, 144, 148, 155, 163, 313, 314, 315, 318, 323, 326, 352, 353, 384, 392, 420  
electromagnetic wave, 163, 318, 352, 384, 420  
electromagnetic waves, 163, 318  
electron beam, 200, 283, 286, 287, 295, 297, 299, 307  
electron beam pumping, 283  
electron charge, 286, 292, 304, 337, 421  
electron density, xi, 4, 12, 36, 37, 39, 286, 292, 293, 294, 295, 296, 297, 298, 303, 305, 306, 307, 415, 417, 420, 422, 423, 425, 426, 428, 429, 431, 432, 463, 464, 486, 488, 491, 495, 496, 497  
electron gas, 3, 37, 39, 40, 41, 42, 43, 152  
electron microscopy, viii, 205  
electron state, 121  
electronic structure, 12  
electron-phonon, 4, 5, 7, 8, 9, 10, 13, 14, 15, 16, 17, 32, 36, 37, 38, 39, 40, 41, 45, 47, 48, 49, 51, 54, 55, 60, 61, 63, 79, 81  
electron-phonon coupling, 4, 5, 8, 9, 10, 15, 36, 41, 47, 48, 49, 51, 54, 55, 60, 61  
electrostatic force, 80  
emission source, 334, 497  
emitters, 208, 434  
energy density, 74, 75, 76, 162, 183, 184, 187, 188, 189, 190, 191, 192, 195, 197, 199, 337  
energy emission, 326  
energy of system, 321  
energy transfer, 5, 15, 18, 19, 36, 37, 40, 43, 49, 50, 54, 55, 56, 64, 74, 245, 374, 430, 439  
energy-momentum, 102, 127, 129  
engines, 379  
England, 339  
entropy, 20, 21, 23, 24, 55, 56, 57, 142  
environment, 55, 176, 208, 213, 237, 313, 372, 431  
environmental conditions, 424  
environmental contaminants, 227  
epitaxial films, 162, 190  
epitaxial growth, 196  
epoxy, 380  
equality, 102, 117, 119, 145, 146, 154  
equating, 117, 135  
equilibrium, 3, 4, 5, 7, 8, 9, 15, 17, 20, 22, 23, 24, 27, 28, 29, 34, 37, 39, 42, 45, 46, 47, 50, 51, 56, 57, 60, 63, 66, 79, 117, 213, 287, 325, 421, 424, 431, 432, 437, 438, 439, 461  
equilibrium state, 20  
erosion, 338, 367  
estimating, 143, 247, 438  
etching, 175, 176, 177, 178, 181, 183, 184, 185, 190, 342  
ethanol, 213, 237  
Eulerian, 247  
Europe, 380  
European Community, 201  
evanescent waves, 129, 130, 131  
evaporation, 6, 44, 166, 188, 208, 209, 210, 212, 326, 347, 386  
evolution, xi, 3, 5, 9, 14, 20, 24, 39, 45, 46, 48, 51, 54, 55, 56, 64, 262, 263, 401, 409, 412, 415, 416, 420, 484  
examinations, 100, 107  
excimer lasers, ix, 211, 212, 213, 283, 284  
exciton, 206, 235  
exclusion, 479  
execution, 107  
experimental condition, 68, 187, 260, 337, 343, 429, 430, 457, 461, 467, 479  
exploitation, 352, 359, 360  
explosion energy, 489  
exposure, 238, 239, 245, 254, 263, 266, 270, 289, 294  
extinction, 416  
extraction, 49, 266  
extrapolation, 28

**F**

fabricate, 368, 385, 390  
 fabrication, viii, x, 43, 159, 185, 378, 380, 383, 384, 385, 386, 387, 390, 395  
 factorials, 104  
 family, 402, 405  
 fast processes, 400  
 Fata, 365  
 fatalities, 352  
 fatigue, 247  
 faults, 376  
 FCC, 51, 54, 63, 64  
 feeding, 165, 340, 367, 370, 371, 372  
 FEM, 91  
 Fermi, 3, 4, 5, 7, 11, 17, 18, 35, 37, 39, 40, 41, 42, 43, 61, 73, 74, 75, 79, 118, 136, 142, 148, 150, 153, 157, 158  
 Fermi energy, 39, 40, 42, 142, 148  
 Fermi level, 4, 18  
 Fermi surface, 148  
 Fermi-Dirac, 3, 4, 5, 17, 18, 35, 37, 39, 41, 73, 74, 79  
 fermions, 479  
 ferromagnetic, 166, 185, 320  
 Feynman, 96, 100, 103, 113, 153  
 fiber, 160, 175, 182, 207, 248  
 fiber optics, 160  
 field theory, 96, 97, 100, 319  
 filament, 302  
 film thickness, 11, 12, 63, 72, 81, 168, 172, 173, 174, 183, 188, 213, 337  
 film-substrate interface, 65  
 filters, 163  
 financial support, 396  
 finite differences, 77  
 Finland, 159  
 fire, 484  
 first principles, 45  
 flame, 334, 337  
 flare, 257  
 flat panel displays, 161, 208  
 flexibility, 200, 245, 357, 368  
 flight, xi, 130, 139, 212, 352, 354, 355, 415, 417  
 flow, 8, 9, 33, 44, 66, 67, 68, 69, 196, 232, 238, 239, 240, 246, 304, 333, 335, 337, 343, 369, 373, 375, 376, 377, 378, 399, 406, 412, 440  
 flow rate, 376, 377, 378  
 fluctuations, 27, 28, 29, 49, 52, 69, 71, 100, 102, 109, 117, 199, 238, 418  
 fluid, 207, 373, 412  
 fluorescence, 417, 439  
 fluoride, 324

focusing, x, 6, 7, 211, 249, 334, 383, 393, 394, 395, 417, 418, 424  
 Fourier, 33, 97, 174, 320  
 fractures, 315  
 fragmentation, 19  
 France, 157, 159, 281, 378, 501  
 free energy, 320, 372, 433  
 free surface energy, 220  
 freedom, 112, 114, 116, 117, 422, 479  
 friction, 78  
 FTIR, 131  
 fulfillment, 172  
 fusion, 133, 368, 370, 376, 429, 484, 503, 508, 510, 512  
 fuzzy logic, 247  
 FWHM, xi, 236, 386, 415, 418, 434, 435, 436, 442, 456, 467, 484, 491

**G**

GaAs, viii, 90, 93, 160, 162, 192, 194, 195, 196, 197, 198, 199, 200, 440  
 gallium, 192, 440  
 gas jet, 503  
 gas phase, 221, 225, 230, 320, 497  
 gas sensors, 237  
 gases, xi, 18, 116, 138, 139, 154, 155, 211, 213, 237, 283, 285, 287, 291, 306, 309, 314, 324, 325, 326, 399, 412, 415, 416, 417, 419, 424, 425, 426, 427, 428, 438, 443, 444, 481, 482, 484  
 gauge, 100, 356, 443, 481  
 Gaussian, 6, 11, 33, 44, 49, 51, 62, 77, 114, 369, 401, 402, 407, 419, 423, 426, 434, 456, 505  
 gel, 210  
 General Electric, 379  
 generalization, 102, 103, 134, 322  
 generation, vii, 1, 2, 19, 35, 64, 67, 95, 96, 97, 99, 100, 109, 111, 113, 136, 161, 207, 285, 291, 313, 327, 374, 380, 384, 416, 419, 420, 422, 425, 427, 479  
 generators, 289, 306  
 geology, 352  
 geometrical optics, 402, 411  
 geometrical parameters, 185, 266  
 germanium, 440  
 Germany, 1, 72, 82, 221, 310, 354, 378, 383, 396  
 Gibbs, 8, 86  
 glass, viii, 33, 34, 63, 160, 172, 174, 175, 176, 228, 364, 385, 386, 387, 388, 389, 390, 392, 393  
 glow discharge, 296, 334, 335, 339, 342, 343, 448, 453  
 glucose, 237  
 goals, 352

gold, 2, 33, 40, 61, 67, 68, 210, 221, 352, 384, 386, 388, 389, 390, 391, 392, 393  
 grain, 19, 61, 97, 135, 191, 221, 375  
 grain boundaries, 61  
 grains, 136, 190, 191, 192, 219, 222  
 graph, 103, 105, 113, 153, 238, 239, 251, 445, 462  
 graphite, 191, 192, 208, 228, 275  
 gratings, 160, 161, 163, 164, 175, 176, 185, 443  
 gravity, 352, 369, 374  
 grazing, 335  
 grids, 289  
 groups, viii, 26, 80, 135, 205, 211, 213, 214, 215, 225, 230, 240, 284, 291  
 growth mechanism, 214, 215, 219, 221, 222, 226, 231, 233, 234, 241  
 growth rate, 426  
 growth temperature, 231

## H

$H_2$ , ix, 283, 284, 288, 289, 290, 291, 292, 294, 295, 307, 472  
 halogen, 443  
 halogens, 124  
 Hamiltonian, 99, 107, 108, 119  
 hands, 109  
 hardening, 245, 248, 261, 277, 375  
 hardness, 79, 162, 190, 206, 208, 372, 375, 376  
 harm, 483  
 harmonics, vii, ix, 95, 96, 97, 99, 109, 111, 112, 113, 114, 115, 116, 117, 118, 136, 313, 324, 327, 328  
 harmony, 483  
 heat capacity, 10, 20, 22, 23, 24, 39, 40, 50, 64, 74, 75, 77, 152, 440  
 heat conductivity, 11, 15, 16, 17, 77, 138, 174, 315  
 heat release, 167, 186  
 heat removal, 324  
 heat transfer, 168, 200, 259, 260, 261, 265, 271, 373, 374, 413  
 heating rate, 7, 9, 245  
 heavy particle, 423, 424, 479  
 Hebrew, 95, 313  
 height, 28, 29, 176, 183, 188, 189, 192, 194, 224, 230, 359, 362, 372, 377, 378  
 helium, 218, 287, 297, 298, 299, 300, 301, 342, 444  
 heterogeneity, 135, 411  
 heterogeneous, 24, 26, 27, 28, 58, 402  
 heterostructures, viii, 160, 196, 199, 201  
 heuristic, 323  
 Higgs, 101  
 high power density, 332  
**high pressure**, 217, 218, 234, 288, 426, 429, 465, 476  
 high resolution, 353

high tech, 385  
 high temperature, 5, 16, 43, 150, 209, 249, 270, 416, 430, 444, 461  
 higher quality, 236, 241  
 high-speed, 165  
 highways, 352, 354  
 histogram, 198  
 Holland, 157, 158  
 homogeneity, 407  
 homogenous, 37  
 host, 484  
 human, 208  
 humidity, 364, 472  
 hybrid, 46, 47, 51, 68, 78, 207, 385, 395  
 hydro, 208  
 hydrocarbon, 427  
 hydrodynamic, 6, 44, 46, 61, 66, 67, 68, 81, 429  
 hydrofluoric acid, 184  
 hydrogen, 142, 237, 287, 289, 294, 295, 296, 307, 428, 432, 435, 436  
 hydrological, 352  
 hydrophilic, 208  
 hydrophobic, 208  
 hydrostatic pressure, 26, 59, 60  
 hydrothermal, 210  
 hydrothermal synthesis, 210  
 hypothesis, 59, 143, 259, 284

## I

IBM, 63, 91  
 identification, 30, 138, 376, 411  
 identity, 102, 103  
 illumination, 208, 385, 387, 389, 390  
 imagery, 366  
 images, 2, 169, 174, 184, 186, 187, 189, 190, 191, 197, 198, 209, 210, 214, 219, 220, 222, 223, 224, 228, 229, 230, 231, 233, 238, 249, 388, 395, 405, 442, 444  
 imaging, x, 73, 163, 365, 383, 393  
 imaging systems, 163  
 immersion, 160, 386, 387, 393  
 impact energy, 212  
 implementation, 46, 49, 51  
 impurities, 427  
 in situ, 201, 365  
 InAs/GaAs, 162  
 incidence, viii, xi, 36, 159, 160, 163, 165, 166, 167, 176, 197, 200, 201, 335, 338, 394, 415, 465, 471, 476, 491, 497, 502, 503, 505, 515  
 inclusion, 82, 153, 191  
 India, 219, 223  
 Indiana, 381  
 indicators, 372

- indices, 98, 127, 128, 129, 138, 143, 155  
 individuality, 138  
 induction, 140, 145  
 industrial, 208, 246, 248, 256, 280, 380  
 industrial application, 246, 248, 256, 280, 380  
 industry, 1, 332, 351, 369, 383  
 inelastic, 36, 287, 392, 421, 422, 425, 426, 427, 481  
 inequality, 139  
 inert, xi, 208, 212, 307, 370, 426, 501  
 inertia, 127, 129, 141, 145, 146, 246  
 infinite, 51, 96, 136, 168, 200, 320  
 infrared, x, xi, 163, 320, 383, 384, 385, 415, 416, 439, 506  
 inherited, 200  
 inhomogeneities, 387, 390, 402, 406, 412  
 inhomogeneity, xi, 399, 401, 403, 404, 405, 406, 407, 409, 412, 413  
 initial state, 96, 104, 105, 136  
 initiation, 11, 59, 127, 297, 416, 421, 424, 427, 481  
 injection, 367, 368, 370, 372, 373  
 inorganic, 323, 385, 395  
 insertion, 443  
 insight, 417, 457  
 inspections, 234, 235, 240, 388  
 instabilities, 6, 26, 28  
 instability, 285, 302  
 insulators, 7, 8, 47, 73, 78, 80, 340  
 integrated circuits, 190  
 integrated optics, viii, 159, 161, 175, 182, 185, 200  
 integration, 39, 47, 49, 50, 52, 55, 57, 69, 77, 104, 105, 126, 130, 207, 316, 368, 384, 433, 434, 443, 455  
 integrity, 255  
 interaction process, 10, 46, 47  
 interactions, vii, 3, 16, 19, 29, 35, 45, 78, 80, 95, 98, 101, 102, 109, 116, 135, 136, 137, 138, 139, 140, 141, 143, 146, 150, 155, 315, 320, 348, 373, 431, 464  
 interface, 5, 6, 26, 27, 28, 29, 61, 376, 384, 392, 393  
 interference, viii, 7, 97, 105, 123, 134, 159, 160, 161, 163, 165, 166, 176, 187, 188, 189, 194, 197, 200, 387, 388, 389, 390, 394, 403, 405, 463  
 intermolecular, 319  
 internal combustion, 419  
 international trade, 351  
 interstitials, 236, 237  
 interval, 4, 5, 6, 104, 121, 122, 123, 129, 148, 152, 232, 259, 280, 324, 443, 465, 477  
 intrinsic, 163, 201, 206, 237, 291, 368, 392, 434  
 inversion, 249, 439  
 investment, 248  
 ion beam, 36, 37, 79, 82, 176, 335, 342, 515  
 ion bombardment, 3, 44, 81, 349  
 ion implantation, 332, 343, 348  
 ionic, xi, 79, 80, 208, 333, 343, 415, 416, 417, 420, 432, 435, 437, 455, 456, 464, 465, 467, 469, 476, 480, 484, 486, 487, 488, 491, 492, 493, 497  
 ionization energy, 421, 422, 427  
 ionization potentials, 431, 461, 481  
 IOP, 209, 210, 214, 220, 222, 224  
 IR, 163, 175, 181, 200, 212, 281, 323, 325, 385, 415, 416, 417, 422, 427, 440, 484, 497  
 IR spectra, 416, 427  
 IR transmission, 181  
 Ireland, 482  
 iron, 1, 174, 175, 188  
 irradiation, viii, 1, 3, 4, 7, 8, 17, 19, 23, 35, 36, 39, 40, 41, 42, 45, 46, 51, 54, 56, 59, 60, 63, 67, 74, 109, 111, 153, 160, 161, 183, 247, 326, 328, 332, 337, 338, 342, 372, 464, 471  
 irradiations, 255  
 island, 192, 195, 198, 199, 228  
 isotropic, 127, 130, 131, 138, 145, 261, 503  
 isotropy, 38, 39  
 Israel, 95, 313  
 Italy, 205, 225, 245, 367
- J**
- Japan, 93, 218, 220, 223, 308, 352, 378  
 JEM, 228  
 Jerusalem, 95, 313  
 jewelry, 162, 192, 200  
 joining, 96, 280, 325  
 Jordan, 91, 100, 348  
 Joule heating, 479
- K**
- kinematics, 112, 117, 124  
 kinetic energy, xi, 35, 36, 48, 49, 73, 75, 119, 120, 121, 130, 132, 140, 152, 154, 212, 229, 232, 316, 321, 415, 419, 420, 421, 423, 488, 491, 497  
 kinetic equations, 19, 29, 46, 298  
 kinetic model, 291, 297, 298  
 kinetics, vii, viii, 6, 9, 19, 26, 32, 46, 56, 60, 68, 95, 96, 128, 133, 165, 291, 298  
 Klein-Gordon, 100  
 knots, 194  
 Korea, 221
- L**
- L1, 288, 310  
 L2, 172, 288  
 Lafayette, 381  
 Lagrangian, 247  
 Landau theory, 137, 144, 149, 155

- language, 138, 261  
Laplace transformation, 169  
laser ablation, viii, 20, 159, 167, 205, 210, 211, 212, 213, 214, 218, 221, 225, 228, 234, 235, 236, 427  
laser rangefinders, 353  
lasers, ix, 1, 2, 109, 127, 136, 161, 175, 176, 209, 212, 213, 232, 246, 248, 258, 279, 283, 284, 285, 286, 287, 307, 313, 332, 354, 368, 369, 385, 416, 439  
lasing threshold, 289  
lattice, 4, 5, 7, 8, 9, 10, 12, 13, 14, 15, 16, 17, 18, 20, 29, 30, 32, 36, 37, 39, 43, 46, 47, 48, 49, 50, 51, 52, 53, 54, 55, 56, 59, 60, 61, 63, 64, 66, 70, 71, 74, 76, 77, 79, 81, 82, 145, 199, 237, 274, 347  
law, 11, 32, 33, 80, 114, 116, 120, 147, 151, 154, 307, 431, 505  
laws, ix, 32, 99, 114, 129, 131, 132, 133, 313  
leakage, x, 383, 392, 393, 394, 395  
LED, 207  
left-handed, 98  
lens, 211, 226, 249, 416, 419, 424, 426, 442  
lenses, 402, 403  
liberation, 106, 122, 123, 314, 424  
LIBS, xi, 415, 416, 417, 418, 435, 439, 445, 456, 464, 467, 471, 487, 497  
lifetime, 291, 298, 334, 421, 434, 435, 465, 477  
light beam, 117, 412  
light transmission, 180, 181  
light transmittance, 389  
limitation, 8, 19, 32, 68, 246, 344, 353  
limitations, x, 19, 43, 47, 227, 351, 353  
linear, vii, 10, 11, 17, 20, 24, 27, 28, 39, 40, 44, 48, 57, 95, 97, 98, 108, 117, 127, 129, 145, 238, 247, 256, 259, 261, 263, 266, 273, 276, 289, 305, 326, 335, 378, 435, 436, 439, 462, 483, 508, 514  
linear dependence, 11, 17, 20, 57, 108, 273  
linear function, 10, 39  
links, 139, 146, 154, 342  
liquefaction, 314  
liquid interfaces, 58  
liquid phase, 5, 6, 22, 23, 24, 26, 28, 30, 52, 54, 55, 57, 58, 324, 325  
liquids, xi, 213, 323, 326, 328, 399, 412, 413, 424, 481  
Lithium, 89, 321, 324  
lithography, viii, 2, 160, 161, 162, 166, 190, 200, 221, 385, 397  
local order, 26, 30, 31, 44, 54, 55, 57, 58, 64, 65, 70  
localization, x, 61, 134, 383, 385  
location, 263, 357, 358, 362, 364, 369  
locus, 453  
logging, 352  
London, 82, 88, 158, 308, 309, 438, 499  
long distance, 332, 403  
losses, 5, 76, 392, 422, 423, 425, 426, 427, 482  
low power, 279, 420  
low temperatures, 43, 151, 332, 436  
low-intensity, 289  
low-power, 430  
low-temperature, 17, 237, 455  
LSD, 430  
LTD, 354, 358, 363  
luminescence, 315  
lying, 167, 218, 404, 405
- M**
- machines, 380  
magnesium, 249, 375  
magnetic, 97, 138, 141, 143, 146, 162, 166, 185, 315, 339, 352, 433  
magnetic field, 433  
magnetic moment, 97, 141, 146, 315  
magnetron, 209, 332  
magnetron sputtering, 209, 332  
maintenance, 440  
manipulation, x, 383, 384, 394, 395  
manufacturing, x, 165, 245, 247, 248, 280, 367, 368  
mapping, 352, 365, 366  
market, 248  
mask, viii, 160, 176, 177, 178, 179, 190, 224, 226, 227  
masking, 162  
mass loss, 375  
mass transfer, 335, 339, 347  
mass transfer process, 339  
mass-transport, ix, 331  
material surface, 2, 3, 5, 6, 7, 44, 77, 81  
materials science, viii, 205, 206  
matrix, 38, 96, 97, 99, 102, 103, 104, 105, 106, 108, 109, 118, 119, 143, 247, 319, 327, 375, 443  
Maxwell equations, 127, 128  
MBE, 163, 196, 201, 209, 210  
measurement, x, 103, 177, 178, 238, 240, 254, 263, 351, 352, 355, 356, 365, 377, 419, 495  
measures, 275  
mechanical energy, 207  
mechanical properties, 369  
media, x, 97, 101, 112, 115, 127, 128, 129, 130, 131, 132, 133, 134, 138, 145, 146, 150, 151, 153, 154, 158, 214, 283, 286, 317, 319, 320, 392, 399, 400, 410, 411, 412, 413  
medium composition, 149  
melt, 6, 8, 56, 59, 81, 188, 317, 323, 367, 370, 373, 374, 375  
melting temperature, 9, 20, 21, 22, 23, 24, 29, 34, 52, 56, 57, 64, 66, 72, 218, 228, 336

- melts, 20, 57  
 memory, 63, 283  
 mercury, 136  
 mesons, 118  
 metal ions, 287  
 metal oxide, 237, 260  
 metal oxides, 260  
 metallurgy, 348  
 metal-semiconductor, 207  
 methane, 326  
 methanol, 237  
 microelectronics, viii, 159, 401  
 microfabrication, 396  
 micrometer, 384  
 microscope, 339, 375, 388, 389, 392, 393, 394  
 microscopy, viii, 205, 207, 375, 376, 395  
 microstructure, 247, 275, 276, 277, 368, 372, 376, 380  
 microstructures, 375, 376, 385  
 microwave, 210, 420, 425, 445  
 military, 439  
 minerals, 358  
 mines, 352, 353, 354, 364, 365, 366  
 miniaturization, 384  
 mining, 351, 353, 355, 358, 365, 516  
 Ministry of Education, 201  
 mirror, 71, 72, 73, 127, 133, 136, 165, 289, 290, 295, 321, 322, 323, 354, 424, 505  
 MIT, 499  
 mixing, 238, 338, 339, 344, 346, 347, 412, 455  
 mobility, 148, 212, 232  
 MOCVD, 209  
 modeling, ix, 7, 12, 17, 37, 43, 45, 46, 62, 68, 70, 71, 72, 73, 78, 81, 82, 245, 247, 261, 262, 266, 271, 274, 279, 280, 283, 294, 296, 357  
 models, ix, x, 3, 8, 10, 33, 37, 45, 46, 68, 70, 71, 73, 78, 79, 81, 82, 116, 245, 246, 247, 258, 260, 264, 273, 294, 351, 353, 356, 367, 373, 375, 425  
 modulation, 173, 174, 175, 187, 197, 334, 389, 401, 409  
 modulus, 6, 32, 38, 40, 280, 284  
 mole, 21, 142, 143, 144, 153, 316, 317, 321, 323, 324, 325, 326  
 molecular dynamics, 66, 146  
 molecular mass, 151  
 molybdenum, x, 339, 342, 343, 351, 358, 440  
 momentum, 32, 37, 38, 39, 66, 96, 102, 106, 113, 117, 119, 120, 121, 122, 123, 125, 127, 129, 130, 132, 133, 137, 141, 151, 153, 154, 155, 301, 374, 421, 438, 439, 478, 479  
 monochromator, 235, 275  
 monolayers, 346  
 morphological, 200  
 morphology, viii, 2, 3, 6, 162, 178, 185, 187, 192, 195, 197, 199, 201, 205, 219, 222, 228, 229, 230, 232, 239, 240, 376, 506  
 mosaic, 70, 275  
 Moscow, 158, 283, 307, 308, 309, 310, 311, 331, 348, 399, 412, 413  
 motion, 6, 18, 19, 34, 43, 44, 47, 48, 49, 50, 52, 53, 54, 55, 61, 67, 73, 81, 129, 211, 213, 249, 255, 259, 284, 372, 428, 434, 502  
 motors, 354, 356  
 movement, 125, 127, 343, 372  
 MPI, 63, 99, 106, 118, 120, 121, 137, 420, 421, 422, 424, 480, 483  
 MPP, 99, 105, 107, 118, 122, 123, 135, 136, 327  
 MRA, 376, 378  
 MTS, 276  
 multi-component systems, 479  
 multidimensional, 61, 81  
 multilayered structure, 201  
 multiple regression, 375, 376  
 multiple regression analysis, 375, 376  
 multiplication, ix, 283, 284, 285, 286, 287, 293, 294, 296, 297, 302, 303, 304, 306, 307, 425  
 multiplier, 111
- N**
- NaCl, 324, 440, 442  
 naming, 148  
 nanobelts, 207  
 nanoclusters, 225  
 nanocomposites, 91  
 nanocrystalline, 66, 81, 332  
 nanodevices, 384, 385  
 nanodots, 36, 210, 218  
 nanoelectronics, 162  
 nanoimprint, 183  
 nanoindentation, 375  
 nanometer, 160, 162, 166, 183  
 nanometer scale, 162, 183  
 nanometers, viii, 159, 166, 185, 384  
 nanonails, 218  
 nanoparticles, 185, 208, 213, 218, 220, 225, 230, 233, 393, 394  
 nanophotonics, 162, 384  
 nanorods, 207, 209, 210, 213, 214, 218, 219, 221, 223, 224, 225  
 nanostructures, viii, x, 2, 3, 45, 46, 61, 62, 73, 81, 82, 160, 161, 162, 185, 200, 201, 205, 206, 207, 208, 209, 210, 211, 213, 214, 215, 219, 220, 225, 230, 231, 232, 234, 237, 383, 384  
 nanotechnology, 162, 201, 314  
 nanowires, 207, 208, 213, 214, 218, 220, 223  
 Nanyang Technological University, 222

- National University of Singapore, 222  
 NATO, 157  
 natural, 49, 72, 109, 111, 115, 121, 135, 140, 143,  
   153, 180, 284, 325, 405, 408, 412, 421, 425, 434,  
   484  
 needles, 206, 221  
 negativity, 132  
 neodymium, 334  
 neon, ix, 283, 284, 287, 289, 291, 293, 294, 296, 307  
 Netherlands, 282  
 network, 219  
 neutralization, 318  
 Nevada, 498  
 New York, 82, 83, 84, 86, 88, 90, 92, 156, 243, 282,  
   308, 498, 499, 500  
 New Zealand, 224  
 Newton, 19, 241  
 nickel, 55, 92, 376  
 NIR, xi, 415  
 NIST, 433, 437, 445, 461, 467, 499  
 nitride, 211, 213  
 nitrogen, xi, 237, 287, 293, 299, 415, 442, 444, 445,  
   448, 449, 452, 453, 455, 456, 467, 472, 480, 485,  
   486, 491  
 nitrogen dioxide, 237  
 nitrogen gas, 445  
 nitrous oxide, 326  
 noble gases, 321  
 noble metals, 4, 16, 17, 43  
 nodes, 264, 271, 273, 274  
 noise, 416, 443, 481, 484, 495  
 nonequilibrium, 4, 7, 8, 19, 24, 29, 32, 35, 37, 38,  
   43, 45, 46, 56, 60, 61, 62, 68, 73, 77, 79, 81, 286,  
   287, 294, 307  
 nonlocality, 98  
 non-thermal, 43, 479  
 non-uniform, 192, 233, 249  
 normal, 28, 59, 64, 65, 66, 128, 131, 132, 153, 166,  
   167, 176, 197, 213, 218, 221, 232, 233, 316, 317,  
   321, 324, 325, 327, 337, 338, 392, 394, 439, 443,  
   455, 515  
 normal conditions, 153, 324, 325, 327  
 n-type, 237  
 nuclear, 8, 45, 105, 138, 162, 328, 436, 478  
 nuclear charge, 436  
 nucleation, 5, 6, 8, 19, 24, 25, 26, 29, 58, 60, 66, 81,  
   209, 216, 219, 220, 221, 222, 225, 228, 231, 232,  
   233, 315  
 nuclei, 6, 24, 25, 26, 30, 72, 479  
 nucleus, 6, 19  
 numerical tool, 29
- O**
- observations, 20, 225, 234, 239, 314, 315, 323, 324,  
   325, 327, 352, 376, 412, 444, 461, 483  
 Ohmic, 207  
 oil, 386, 387, 393  
 omentum, 129  
 opacity, 430  
 operator, 99, 102, 103, 119  
 optical absorption coefficient, 168  
 optical coefficients, 207  
 optical microscopy, 375  
 optical properties, 17, 182  
 optical pulses, 439  
 optical systems, 31, 400  
 optical transmission, 177, 178, 179, 180, 182, 183  
 optics, viii, 6, 7, 35, 37, 78, 82, 96, 159, 160, 161,  
   165, 175, 182, 185, 200, 364, 384, 401, 402, 411,  
   442  
 optimization, xi, 464, 501, 506  
 opto-electronic, 207  
 optoelectronics, 202, 206  
 orbit, 422  
 organic, 323, 385, 395  
 orientation, 30, 70, 185, 222, 234, 235, 249, 250,  
   251, 252, 253, 254, 260, 322, 354, 355, 356, 412  
 originality, 69  
 oscillation, 266, 298, 420  
 oscillations, 55, 57, 97, 107, 384, 439  
 oscillator, 164, 165, 386, 428, 433  
 oxidation, 166, 210, 260, 333, 367, 375, 515  
 oxide, 196, 208, 210, 212, 220, 228, 229, 326  
 oxides, 260, 335, 346  
 oxygen plasma, 208, 465  
 ozone, 209
- P**
- PACS, 160  
 parabolic, 39  
 paradox, 126, 127, 137  
 paradoxical, 127  
 parallelism, 318  
 paramagnetic, 166  
 Paris, 157, 498, 499, 501, 516  
 particle beams, 349  
 partition, 437  
 passive, x, 98, 383  
 patents, 378, 379  
 patterning, viii, 160, 161, 162, 183, 185, 187, 199  
 PCT, 378  
 percolation, 228

- periodic, 4, 26, 27, 36, 51, 54, 56, 59, 60, 71, 72, 160, 161, 162, 163, 165, 166, 168, 176, 182, 183, 185, 189, 190, 192, 194, 199, 200, 210, 502
- permit, xii, 257, 501, 515
- perovskite, 36
- perturbation, 39, 40, 132, 411, 436, 455
- perturbations, 3, 453, 455
- petroleum, 516
- phase conjugation, 164
- phase shifts, 97
- phase transformation, 6, 19, 24, 26, 29, 34, 45, 46, 47, 49, 61, 68, 73, 77, 79, 81, 255, 368, 373
- phase transitions, viii, ix, 96, 98, 101, 138, 140, 141, 142, 143, 155, 313, 314, 315, 319, 320, 321, 323, 326, 328
- phonon, 4, 5, 7, 9, 10, 13, 14, 15, 17, 18, 37, 38, 39, 40, 41, 42, 43, 49, 54, 61, 74, 77, 83, 84, 85, 86, 87, 90, 92
- phonons, 4, 5, 7, 9, 11, 15, 17, 29, 37, 38, 39, 40, 42, 43, 51, 73, 74, 77, 151, 152
- photochemical, 167, 328
- photodetectors, 165, 207, 400
- photoionization, 291
- photoluminescence, viii, 205, 225, 235, 237
- photonic, viii, 114, 159, 160, 175, 183, 208, 397, 502
- photonic crystals, viii, 159, 160, 175, 183, 208
- phononics, 175, 207, 384
- physical and mechanical properties, 369
- physical mechanisms, ix, 3, 64, 77, 245, 248, 260
- physical properties, 20, 167, 206, 237, 375, 384, 417, 418
- physicists, 431
- physicochemical, 321
- physics, viii, 1, 3, 4, 19, 35, 46, 77, 96, 98, 105, 139, 155, 158, 162, 176, 285, 309, 313, 314, 349, 499
- piezoelectric, 207
- piezoelectric properties, 207
- piezoelectricity, 206, 207
- pitch, 356
- PL, viii, 205, 235, 236, 237, 238, 239, 240, 241
- PL emission, 238, 241
- PL spectrum, 236, 238
- planar, 161, 163, 164, 175, 183, 297, 385, 392
- Planck constant, 418
- plane waves, 403, 419
- planetary, 326
- planning, vii, 95
- plasmons, 394, 397
- plastic, 6, 8, 29, 32, 33, 61, 64, 67, 68, 69, 71, 81, 246, 247, 248, 249, 277, 386
- plastic deformation, 6, 8, 29, 32, 61, 64, 67, 68, 71, 81, 246, 277
- plasticity, 46, 68
- play, 35, 37, 46, 167, 199, 212, 372, 439
- PLD, viii, 205, 209, 210, 211, 212, 213, 214, 215, 218, 221, 224, 225, 226, 230, 332, 333, 334, 339, 347
- plurality, 411
- Poisson, 114, 123, 133, 280, 301, 328
- Poisson distribution, 114, 123
- Poisson equation, 301
- Poland, 366
- polar coordinates, 28
- polarity, 285
- polarizability, 316, 321, 322
- polarization, 39, 104, 116, 117, 132, 140, 164, 165, 166, 179, 183, 192, 193, 194, 195, 197, 198, 201, 321, 394, 395, 424, 506
- polarization planes, 166
- polarized light, 180, 393
- pollutants, 484
- pollution, 314
- polycrystalline, 72, 185, 190, 191, 192, 195, 219, 338
- polycrystalline diamond, 185, 190, 191, 192
- polyester, 380
- polyimide, viii, 160, 161, 185, 189, 190
- polyimide film, 161, 185, 189, 190
- polymer, 143, 207, 385, 386, 387, 392, 395
- polymer blends, 207
- polymer molecule, 143
- polymer structure, 386
- polymerization, x, 146, 383, 385, 386, 387, 389, 390, 395, 396
- polymerization process, 385, 387
- polymerization processes, 385
- polymers, 385, 392
- polystyrene, 221
- poor, 80, 163, 248, 274, 342, 372, 385, 387, 419, 495
- population, 284, 297, 298, 314, 431, 432, 433, 438, 440
- population density, 297, 314, 433
- pores, 210
- porosity, 368, 372, 376
- porous, 219
- Portugal, 367
- powder, 208, 216, 223, 367, 368, 369, 370, 371, 372, 373, 374, 375, 376, 377, 378, 380
- powders, 210, 369, 380
- powers, 250, 252, 254, 255, 256, 265, 289, 298, 307, 387, 390
- predictability, 258
- prediction, 20, 57, 263, 268, 269, 274, 279, 375
- predictive model, x, 367
- predictive models, x, 367
- preference, 6, 76

prevention, 336, 353  
 probability, 38, 108, 113, 114, 115, 117, 119, 120, 121, 124, 134, 319, 328, 421, 427, 433, 434, 437, 481, 482  
 probe, 17, 44, 355, 356, 362, 366, 376, 411, 412  
 process control, 380  
 production, x, 32, 185, 212, 231, 236, 245, 279, 285, 294, 299, 306, 307, 331, 351, 354, 358, 360, 400, 416, 417, 444  
 productivity, xi, 161, 163, 183, 501  
 program, 138, 339, 396, 438  
 propagators, 99, 100  
 proportionality, 142, 154  
 proposition, 107, 127, 154  
 protection, 372  
 prototype, 246  
 prototyping, 246, 279, 368  
 pseudo, 130  
 PUB, 157  
 Puerto Rico, 219  
 pulsed laser, viii, 3, 44, 48, 51, 60, 66, 159, 161, 162, 166, 167, 175, 176, 185, 189, 190, 192, 193, 194, 195, 196, 197, 201, 209, 210, 211, 212, 247, 332, 347, 417, 439, 440, 442, 484, 497  
 pulsed laser deposition, 210, 211  
 pumping, ix, 164, 226, 283, 284, 285, 286, 287, 288, 289, 290, 294, 295, 299, 306, 307, 334  
 pumps, 333, 334  
 pure line, 326  
 pure water, 326  
 pyramidal, 232

**Q**

QDs, 162, 185  
 QED, 96, 97, 99, 100, 103, 106, 112, 113, 123, 130, 136, 137, 138, 139, 153, 155, 314, 319, 327  
 quality control, 339  
 quanta, 111, 114, 116, 117, 122, 135, 136, 137, 138, 142, 317, 318, 325, 327, 439, 445  
 quantization, 96, 136  
 quantum, vii, ix, 95, 96, 97, 98, 101, 110, 119, 120, 121, 122, 123, 128, 133, 134, 138, 141, 162, 185, 196, 201, 207, 313, 314, 319, 325, 328, 432, 436, 455, 468  
 quantum dots, 162  
 quantum electrodynamics, vii, 95, 96, 119, 133, 314  
 quantum optics, 96  
 quantum theory, ix, 96, 134, 313  
 quantum well, 185, 196, 201  
 quartz, 33, 34, 218, 221, 289, 290, 301, 443  
 quasiclassical, 96, 120  
 quasi-equilibrium, 75  
 quasiparticles, 4, 154

**R**

radar, 352, 353, 364  
 radial distribution, 423  
 Raman spectroscopy, 417  
 random, 28, 49, 207  
 rapid prototyping, x, 245, 367, 368, 380  
 Rayleigh, 117, 218, 352, 353  
 reaction rate, 99, 104, 105, 106, 108, 109, 111, 117, 118, 122, 123, 136, 137, 209, 298, 320  
 reactive ion, 177, 178  
 reactivity, 232, 236  
 reagents, 291, 314  
 real time, 14, 16  
 reality, 98  
 recall, 428  
 recombination, xi, 74, 112, 283, 286, 287, 291, 294, 301, 302, 307, 328, 343, 415, 417, 420, 422, 423, 424, 433, 439, 467, 487, 495, 497  
 recombination processes, 74, 291, 423, 424, 467  
 reconstruction, 411, 412  
 recovery, 238, 239, 356, 357  
 recrystallization, 61, 66, 166  
 rectification, 164  
 redistribution, 6, 18, 26, 37, 53, 54, 61, 321  
 reference frame, 355  
 refining, 375  
 reflection, vii, 51, 55, 65, 95, 99, 127, 131, 132, 133, 134, 135, 136, 164, 175, 180, 315, 338, 346, 353, 354, 361, 365, 420, 428  
 reflectivity, 11, 62, 165, 323, 368, 440, 442  
 refraction gradient, 400  
 refraction index, 128, 130, 400, 403  
 refractive index, xi, 160, 176, 179, 207, 385, 395, 399, 401, 403, 404, 406, 411, 412  
 refractometry, 400  
 refractory, 334  
 regional, 378  
 regression, 375, 378  
 regular, 161, 162, 175, 176, 185, 189, 190, 192, 227, 356, 411, 453  
 relationship, 170, 248, 274, 378, 380, 432, 433, 479, 506, 515  
 relaxation, 3, 4, 7, 8, 9, 10, 13, 14, 15, 17, 23, 30, 31, 32, 33, 34, 42, 43, 47, 50, 55, 56, 59, 60, 61, 64, 65, 67, 69, 74, 199, 416, 420, 457, 467, 484  
 relaxation process, 457, 468  
 relaxation time, 8, 9, 10, 13, 14, 15, 17, 42, 43, 74  
 reliability, 245, 248  
 renormalization, 111, 153  
 repair, 367, 380  
 research and development, 201, 379  
 reserves, 358

- resistance, 65, 229, 237, 288, 333, 367, 376  
 resistivity, 293, 307, 352, 353, 365  
 resolution, xii, 17, 28, 36, 44, 66, 161, 165, 166, 235, 238, 289, 342, 353, 385, 389, 416, 434, 443, 448, 453, 456, 459, 461, 463, 464, 465, 466, 467, 471, 472, 476, 478, 480, 482, 495, 501  
 resonator, 117, 439  
 resources, 351  
 restructuring, 3, 6, 8, 20, 44, 45, 67  
 retardation, 321  
 retention, 306  
 rings, 403, 419  
 risk, 359, 364  
 Robotics, 365  
 rods, 206, 218, 219, 220, 221, 222, 223, 224, 225, 230, 234, 239, 356  
 rolling, 189  
 Rome, 245, 367  
 room temperature, 37, 42, 148, 150, 165, 207, 227, 235, 237, 238, 261, 445, 467  
 root-mean-square, 425  
 roughness, 28, 29, 271, 339, 365, 372  
 routines, 93  
 runaway, 284, 285  
 Russia, 159, 163, 283, 310, 329, 348, 352, 399, 413  
 Russian, 159, 163, 201, 307, 308, 309, 310, 311, 329, 331, 348, 349, 383, 412, 413  
 Russian Academy of Sciences, 163, 310, 349, 383  
 Rutherford, 349  
 Rydberg atoms, 231
- |          |
|----------|
| <b>S</b> |
|----------|
- safety, 352, 354, 363, 365  
 salinity, 401  
 salts, 328, 365  
 sampling, 36, 418  
**sapphire**, 215, 216, 217, 218, 219, 221, 222, 225, 385  
 satellite, 324, 477  
 saturation, vii, 95, 105, 106, 108, 109, 124, 135, 140, 146, 147, 150, 153, 320  
 scalar, 319  
 scaling, 50, 80  
 scanning electron, viii, 205, 394  
 Scanning Electron Microscopy, 228  
 scatter, 166, 180, 199  
 scattering, vii, 19, 32, 95, 96, 97, 98, 99, 100, 103, 106, 109, 112, 113, 114, 117, 125, 128, 133, 134, 135, 136, 137, 139, 145, 146, 148, 152, 155, 165, 218, 220, 293, 337, 392, 394  
 Schottky, 207, 228  
 Schrödinger equation, 97, 99, 107  
 search, 63, 119, 120, 313  
 searching, 132, 241  
 secret, 162, 192, 200  
 security, 200  
 sedimentation, 321  
**seed**, 216, 217, 224, 481, 482  
 seeds, 221, 223  
 seismic, 352, 353, 365  
 selecting, 336, 409, 437  
 self-assembling, viii, 160, 162, 192, 193, 200, 201  
**SEM**, viii, 2, 205, 209, 210, 214, 219, 220, 221, 222, 223, 224, 225, 228, 229, 230, 231, 232, 233, 234, 235, 238, 239, 375, 376, 388, 391, 393, 394, 395, 396  
 semiconductor, viii, 160, 161, 162, 166, 190, 192, 200, 207, 237, 400  
 semiconductors, 3, 7, 8, 37, 47, 73, 77, 78, 79, 82, 168, 185, 197, 237  
 sensing, viii, 205, 206, 237, 238, 239, 240, 241  
 sensitivity, 30, 161, 239, 343, 417  
 sensors, 207, 208, 237, 356, 384  
 separation, 52, 64, 65, 70, 344, 386, 423  
 series, 20, 21, 22, 34, 57, 59, 96, 98, 105, 106, 108, 136, 185, 192, 249, 254, 255, 256, 302, 320, 328, 419, 437, 444, 449, 453, 477, 484, 491  
 Shanghai, 218  
 shape, ix, 6, 14, 26, 28, 63, 67, 68, 77, 179, 185, 197, 221, 227, 230, 231, 233, 234, 245, 246, 249, 257, 273, 274, 289, 290, 334, 358, 362, 368, 369, 373, 401, 402, 419, 426, 434, 436, 438, 442, 456, 484  
 sharing, 26  
 shear, 6, 32  
 shock, 2, 30, 46, 61, 416, 427, 429, 430, 444, 484, 489, 491, 497  
 shock waves, 46, 445  
 shortage, 351  
 short-term, 112, 117  
**Si<sub>3</sub>N<sub>4</sub>**, 207  
 sign, 100, 131, 132, 133, 139, 285, 436  
 signals, 238, 239, 289, 383, 384, 484  
 signs, 55, 100, 133  
**silica**, viii, 34, 70, 72, 160, 161, 162, 172, 173, 174, 175, 176, 177, 178, 179, 180, 182, 183, 184, 185, 189, 190, 215, 218, 225  
**silica glass**, viii, 160, 172, 173, 174, 176, 177  
 silicon, 78, 172, 173, 174, 175, 192, 194, 209, 215, 216, 217, 218, 219, 222, 223, 225, 227, 228, 235, 238  
 silver, 135, 384, 393  
 similarity, 143, 247  
 Singapore, 222, 330  
 single crystals, 195, 199, 207  
 singular, 100, 101  
 singularities, 98, 99, 140, 317

- sintering, 368  
sites, 5, 193, 219, 221, 222, 225, 228, 231, 233, 365  
skin, 133, 134, 135, 146, 154, 423  
SLAC, 157  
smoothing, 132  
software, 249, 355, 356, 357, 358, 360, 368, 408  
solar, 175, 207  
sol-gel, 210  
solid phase, 20, 22, 23  
solid state, 139, 161, 314, 325  
solid surfaces, viii, 159, 160, 163, 164, 200  
solidification, 66, 67, 70, 81, 314, 323, 326  
solid-state, 56  
sound speed, 39  
Soviet Union, 349  
space-time, 140  
Spain, 159, 415, 497  
spark discharges, 286  
spatial, 6, 8, 9, 28, 29, 36, 37, 43, 46, 50, 52, 55, 61, 62, 97, 102, 103, 107, 122, 123, 161, 164, 165, 168, 172, 173, 174, 175, 187, 190, 192, 199, 200, 285, 401, 402, 411, 424, 464, 484  
spawning, 6  
species, xi, 208, 212, 213, 219, 220, 227, 228, 229, 230, 231, 232, 234, 236, 237, 415, 416, 417, 420, 421, 422, 424, 425, 427, 431, 435, 436, 437, 449, 455, 461, 463, 464, 467, 471, 479  
specific heat, 169, 374  
Specific Heat, 90  
Specord M, 177  
spectral component, 411  
spectroscopic methods, 439, 497  
spectroscopy, xi, 328, 375, 415, 416, 417, 431, 439  
speed, 5, 8, 15, 19, 39, 116, 121, 128, 130, 134, 165, 246, 248, 254, 255, 256, 257, 261, 265, 266, 268, 271, 279, 284, 287, 332, 335, 344, 353, 354, 372, 374, 375, 380, 383, 384, 418, 484  
speed of light, 418  
spin, 103, 387, 478  
sporadic, 481  
SPR, 237  
sputtering, 209, 210, 212, 332, 338, 386  
stability, 13, 40, 50, 52, 59, 60, 69, 164, 165, 206  
stabilization, 107, 120, 121, 238, 276  
stages, 4, 121, 163, 222, 223, 228, 268, 302, 304, 307, 416, 486  
stainless steel, ix, 211, 226, 245, 247, 248, 249, 250, 251, 252, 253, 254, 260, 261, 275, 289, 336, 339, 340, 342, 344, 345, 442  
standard model, 36  
Stark effect, 431, 435, 436, 463  
stars, 323  
stationary distributions, 304  
statistical analysis, 198  
statistics, 3, 7, 37, 73, 74  
steel, ix, xi, 211, 226, 227, 245, 246, 247, 248, 249, 250, 251, 252, 253, 254, 256, 260, 261, 275, 279, 280, 289, 336, 339, 340, 342, 344, 345, 375, 376, 380, 442, 501, 505, 506, 509  
steel plate, 376  
stoichiometry, 212  
storage, viii, 159, 160, 162, 166, 185, 288, 289, 290  
strain, 32, 162, 163, 192, 195, 199, 201, 246, 247, 274  
strains, 247, 249, 270  
strategies, 378  
strength, 5, 8, 9, 10, 15, 36, 40, 43, 55, 60, 63, 115, 292, 293, 296, 297, 301, 303, 305, 355, 433, 435  
stress, 8, 15, 32, 33, 44, 55, 59, 60, 64, 65, 67, 195, 196, 199, 246, 248, 249, 263, 264, 265, 274, 275, 276, 277, 279, 280, 343, 372  
stretching, 439  
strontium, 287  
structural defects, 387, 390  
structural modifications, 35  
structuring, 6, 67, 77, 82, 386, 390  
substances, 137, 155, 314, 316, 317, 319, 320, 322, 323, 334  
substitutes, 47  
substitution, 110, 125, 128, 143, 148, 152, 316  
substrates, viii, 160, 161, 162, 172, 174, 175, 176, 182, 183, 185, 189, 190, 192, 196, 199, 200, 209, 218, 220, 221, 225, 227, 228, 339, 378, 385, 387, 389  
subtraction, 100, 129  
superconductivity, 138, 149, 150, 211  
superlattice, 200  
superposition, 20, 119, 249, 257, 338, 489  
supply, 334, 335  
suppression, 112  
surface area, 27, 53, 336, 339, 376  
surface diffusion, 166, 228  
surface layer, 51, 195, 342, 346, 372  
surface modification, viii, 6, 60, 159, 161, 166, 197, 200, 334  
surface region, 9, 23, 29, 47, 51, 346  
surface roughness, 365, 372  
surface structure, 45, 67, 384, 386, 387, 392, 393, 394, 395  
surface treatment, 248, 332, 333  
surface wave, 162, 167, 392  
surfactants, 213  
surgical, 1, 439  
surplus, 116  
surpluses, 324  
susceptibility, 101, 134, 140, 145, 146, 148, 315, 322

- swelling, 189  
 switching, 67, 240  
 symmetry, 33, 36, 68, 101, 197, 317, 319, 320, 402, 403, 404, 439, 445  
 synchronization, 52, 68, 164, 443  
 synthesis, 163, 210, 313
- |   |
|---|
| T |
|---|
- Taiwan, 223  
 target zone, 338  
 targets, 12, 45, 51, 54, 61, 62, 115, 116, 124, 127, 333, 334, 335, 338, 339, 342  
 technological developments, 176  
 telecommunication, 384  
 TEM, 210, 214, 352, 353  
 temperature dependence, 5, 8, 15, 17, 21, 22, 23, 57, 406  
 temperature gradient, 5, 6, 8, 15, 17, 31, 34, 44, 46, 55, 62, 66, 74, 75, 81, 246, 249, 407  
 temporal, vii, 11, 51, 55, 62, 77, 81, 95, 96, 97, 98, 99, 100, 102, 103, 105, 109, 113, 117, 120, 133, 137, 138, 139, 155, 290, 319, 417, 420, 424, 442, 464, 484, 487, 488, 491, 496, 503, 505  
 tensile, 55, 65, 81  
 tensile stress, 55, 65  
 tension, 34, 44, 374  
 terraces, 231  
 test procedure, 343  
 Thailand, 220  
 thermal analysis, 261, 271  
 thermal energy, 2, 6, 7, 26, 43, 52, 54, 55, 56, 143, 317  
 thermal equilibrium, 4, 5, 9, 39, 79  
 thermal evaporation, 208, 209, 210  
 thermal expansion, 8, 15, 20, 22, 51, 162, 195, 196, 220, 246, 248, 249, 259, 266, 270, 280, 445  
 thermal load, 261, 265, 336  
 thermal plasma, 479  
 thermal properties, 172, 464, 502, 506  
 thermal stability, 59  
 thermal treatment, 375  
 thermalization, 4, 5, 7, 17, 35, 36, 37, 39, 40, 116, 117, 226  
 thermodynamic, 23, 112, 117, 144, 148, 150, 154, 314, 317, 321, 328, 431, 432  
 thermodynamic equilibrium, 431, 432  
 thermodynamic parameters, 23, 148  
 thermodynamic properties, 150  
 thermodynamics, 55, 72, 314  
 Thermoelastic, 89  
 thermo-mechanical, 247, 248, 261, 264  
 thermonuclear, vii, 95, 99, 127, 137, 429  
 thermosetting, 380  
 thin film, 63, 161, 162, 200, 211, 212, 213, 223, 332, 333, 392  
 Thomson, 118  
 threatened, 354, 358, 360  
 three-dimensional, 59, 365, 374  
 threshold, xi, 6, 11, 39, 43, 44, 54, 60, 111, 112, 122, 123, 124, 135, 136, 176, 183, 190, 195, 299, 320, 326, 327, 387, 389, 390, 415, 416, 417, 418, 423, 424, 425, 426, 427, 428, 481, 483  
 time frame, 7  
 time variables, 104  
 timing, 355  
 Titanium, 84, 89  
 topological, 392  
 total energy, 14, 20, 51, 52, 53, 54, 55, 74, 75, 136  
 total internal reflection, 98  
 toughness, 506  
 Toyota, 379  
 tracking, 9  
 trade, 351  
 trajectory, 404  
 transduction, 237  
 transfer, ix, 5, 15, 18, 19, 35, 36, 37, 40, 43, 49, 54, 55, 56, 64, 74, 98, 99, 125, 155, 168, 176, 198, 199, 200, 212, 245, 259, 260, 261, 265, 271, 283, 284, 332, 336, 337, 373, 374, 384, 413, 430, 439  
 transformation, 6, 24, 26, 29, 34, 46, 47, 61, 68, 73, 77, 79, 81, 99, 107, 130, 169, 174, 320, 368, 373, 384, 416, 515  
 transformations, vii, 19, 46, 68, 77, 95, 315  
 transient emission, 315  
 transistors, 207  
 transition metal, 4, 17  
 transitions, 105, 111, 138, 143, 148, 154, 155, 236, 284, 286, 287, 291, 299, 307, 314, 315, 318, 321, 324, 325, 419, 431, 432, 433, 436, 437, 439, 445, 453, 455, 457, 468, 477  
 translation, 261  
 translational, 479, 491  
 transmission, 128, 163, 175, 176, 177, 178, 179, 180, 181, 182, 183, 352, 356, 368, 383, 445, 503  
 transparency, 313  
 transparent, vii, x, 63, 65, 95, 97, 99, 127, 128, 130, 133, 137, 182, 191, 207, 327, 385, 387, 388, 389, 399, 400, 412, 413, 416, 425, 430, 440  
 transparent medium, 127  
 transport, 4, 5, 18, 35, 36, 38, 46, 47, 54, 61, 73, 74, 75, 79, 80, 207, 293, 301, 306, 335, 337, 346, 375  
 transport processes, 335, 337  
 travel, 354, 443  
 trial, 70  
 triggers, 8  
 Tsunami, 386

TTM, 9, 10, 12, 17, 18, 19, 29, 32, 36, 37, 41, 43, 46, 47, 48, 50, 51, 52, 54, 60, 62, 63, 64, 65, 67, 68, 69, 70, 71, 73, 74, 77, 78, 79, 80, 81, 82

tunneling, 97, 98, 100, 155

twins, 275, 276

two-dimensional, viii, 64, 66, 159, 162, 165, 167, 168, 182, 185, 189, 192, 194, 200, 392, 402, 411

## U

ultraviolet, xi, 84, 161, 207, 238, 385, 415, 421

uncertainty, 97, 98, 101, 106, 113, 116, 118, 121, 132, 136, 141, 154, 200, 266, 434, 437, 464

uniform, 129, 162, 165, 174, 192, 200, 213, 226, 233, 249, 253, 287, 291, 332, 369, 444

United Kingdom, 353

universal gas constant, 316, 320

universality, 316

UV, xi, 161, 162, 163, 166, 175, 176, 182, 183, 184, 185, 192, 193, 194, 195, 200, 207, 208, 211, 212, 307, 308, 349, 385, 415, 416, 422, 430, 456

## V

vacancies, 236, 237

vacuum, x, 39, 100, 102, 105, 127, 130, 132, 134, 161, 164, 165, 180, 209, 211, 213, 214, 226, 227, 289, 297, 315, 331, 333, 334, 337, 340, 342, 384, 403, 443, 465

validity, 112, 266, 432, 464

van der Waals, 79, 435

vapor, ix, 188, 208, 210, 228, 232, 313, 314, 316, 317, 319, 321, 323, 324, 325, 326, 327, 332, 427

vapor-liquid-solid, 208

vapor-solid (VS), 209

variables, 97, 99, 107, 249, 256, 418, 464

variation, xi, 6, 26, 55, 99, 146, 149, 199, 238, 247, 268, 276, 325, 399, 411, 430, 483

vector, 30, 38, 39, 44, 45, 103, 104, 392

versatility, 199, 213

vibration, 176, 207, 247, 358, 439

visible, xi, 6, 28, 40, 45, 163, 200, 231, 235, 251, 254, 262, 263, 271, 275, 277, 279, 328, 344, 361, 384, 394, 400, 415, 422, 426, 440, 444

vision, viii, 96

visualization, xi, 399, 407, 408, 412, 413

VLS, 208, 209, 215, 216, 217, 219, 221, 223, 224, 225

voids, x, 351, 352, 360, 364

## W

waste disposal sites, 365

water, ix, xi, 176, 213, 256, 313, 314, 319, 322, 323, 324, 325, 326, 327, 352, 364, 365, 399, 401, 405, 406, 407, 408

water vapor, ix, 313, 314, 323, 324, 325, 326

wave number, 39

wave propagation, 287, 429, 430

wave vector, 38, 39, 392, 411

waveguide, 388, 389, 391, 392

wavelengths, viii, 116, 180, 205, 212, 227, 231, 234, 241, 318, 368, 384, 393, 411, 416, 422, 454, 464, 465, 466, 468, 471, 478, 481

weak interaction, 141

wealth, 286, 384

weapons, 439

wear, 333, 367, 375

weathering, 358

welding, 248, 439

wettability, 208

wetting, 221, 372, 373

wide band gap, 206

wires, 206, 218, 288, 306, 384

workers, 358, 425

writing, 103, 109, 515

## X

xenon, ix, 283, 284, 287, 297, 298, 299, 300, 301, 302, 305

XPS, ix, 331, 342, 346, 347

X-ray analysis, 274

x-ray diffraction, viii, 205

X-ray diffraction, 235, 274, 375

X-rays, 285

XRD, viii, 205, 235, 375, 376

## Y

yield, 32, 33, 249, 266, 270

## Z

Zener, 121

zinc, viii, 205, 206, 207, 208, 209, 210, 213, 217, 218, 220, 225, 227, 228, 235, 236, 237, 287, 440

ZnO, viii, 205, 206, 207, 208, 209, 210, 211, 213, 214, 215, 216, 217, 218, 219, 221, 222, 223, 224, 225, 226, 227, 228, 229, 230, 231, 236, 237, 240, 241

ZnO nanorods, 207, 209, 210, 214, 221, 225

ZnO nanostructures, 206, 207, 208, 209, 210, 211, 213, 215, 225, 237